





**รายงานวิจัยฉบับสมบูรณ์**

# สมบัติทางไฟฟ้าของสารเซรามิกเฟร์โรอิเล็กตริกที่มีตะกั่วเป็นฐานภายใต้ความเค้นอัด

**โดย**

**ผู้ช่วยศาสตราจารย์ ดร. รัตติกร ยิ้มนิรัญ**

**พฤษภาคม 2552**

สัญญาเลขที่ RMU5080021

# รายงานวิจัยฉบับสมบูรณ์

# สมบัติทางไฟฟ้าของสารเซรามิก เฟร์โรอิเล็กตริกที่มีตะกั่วเป็นฐานภายใต้ความเค้นอัด

ผู้ช่วยศาสตราจารย์ ดร. รัตติกร ยิ้มนิรัญ
ภาควิชาฟิสิกส์และวัสดุศาสตร์ คณะวิทยาศาสตร์
มหาวิทยาลัยเชียงใหม่

สนับสนุนโดยสำนักงานคณะกรรมการการศึกษาอุดมศึกษา
และสำนักงานกองทุนสนับสนุนการวิจัย

(ความเห็นในรายงานนี้เป็นของผู้วิจัย สกอ. และ สกว.ไม่จำเป็นต้องเห็นด้วยเสมอไป)

# กิตติกรรมประกาศ

ผู้วิจัยใคร่ขอขอบพระคุณ สำนักงานคณะกรรมการการศึกษาอุดมศึกษา (สกอ.) และสำนักงานกองทุนสนับสนุนการวิจัย (สกว.) ที่ได้ให้การสนับสนุนงานวิจัยและพัฒนาครั้งนี้ ผ่านทางทุนเพิ่มขีดความสามารถด้านการวิจัยของอาจารย์รุ่นกลาง ประจำปี พ.ศ. 2550 ขอขอบคุณภาควิชาฟิสิกส์และวัสดุศาสตร์ คณะวิทยาศาสตร์ มหาวิทยาลัยเชียงใหม่ ที่ช่วยอำนวยความสะดวกในการใช้เครื่องมือ อุปกรณ์ และ สถานที่ จนทำให้งานวิจัยเรื่องนี้สามารถดำเนินการจนสำเร็จผลได้ด้วยดี ขอขอบคุณผู้ร่วมงานและนักศึกษาทุกท่าน ที่มีส่วนช่วยเหลือผู้วิจัยให้ดำเนินงานชิ้นนี้สำเร็จลุล่วงได้ดี โดยเฉพาะ ดร. อธิพงศ์ งามจารุโรจน์ ดร. สุพัตรา วงศ์แสนใหม่ ดร. อนุรักษ์ ประสาทเขตต์การณ์ ดร. ปิยชนน์ เกษสุวรรณ ดร. เรวดี วงศ์มณีรุ่ง ดร. อรวรรณ คำมั่น ดร. นราธิป วิทยากร ดร. วรรณวิลัย วิทยากร คุณเมืองใจ อุ่นเรือน คุณณัฐพงศ์ วงศ์ดำเนิน คุณธนพงศ์ สารีอินธ์ คุณจิรภา ตั้งศรีตระกูล คุณศศิพร ประเสริฐปาลิฉัตร และคุณนฤทธ์ ตรีอำนรรค ขอขอบคุณผู้ช่วยศาสตราจารย์ ดร.ยงยุทธ เหล่าศิริถาวร สำหรับด้านงานคำนวณและงานด้านฟิสิกส์อื่นๆ ขอขอบคุณรองศาสตราจารย์ ดร.สุพล อนันตา ที่ได้ให้ความช่วยเหลือส่งเสริมเกื้อกูลในการทำงานเสมอมานับตั้งแต่วันเริ่มต้น ตลอดจนเป็นกำลังใจให้กันเสมอที่จะสู้และอยู่รอดในการทำวิจัยในสภาวะที่ยากที่จะกล่าวได้ ผู้วิจัยต้องขอบคุณความร่วมมือที่ได้รับอย่างดีจากนักวิจัยที่ปรึกษาและเพื่อนร่วมงานในต่างประเทศ ได้แก่ Prof. Amar Bhalla แห่ง University of Texas at San Antonio Prof. Xiaoli Tan แห่ง Iowa State University และ Prof. David Cann แห่ง Oregon State University

ท้ายที่สุดนี้ขอมอบความดีทั้งหมดให้แทนคำขอบคุณสำหรับ คุณวิภา ยิ้มนิรัญ ภรรยา และด.ช. รัญชน์ ยิ้มนิรัญ ลูกชาย คงไม่มีความสำเร็จใดๆเกิดขึ้นได้ถ้าปราศจากความรักและความเข้าใจ รอยยิ้มแห่งความสุข คำปลอบเมื่อยามท้อ ตลอดจนกำลังใจและความอดทนที่ครอบครัวมอบให้ผู้วิจัยตลอดมาจนสามารถมาถึง ณ วันนี้ได้

***"ขอขอบคุณทุกคนอีกครั้งที่ร่วมสุขและร่วมทุกข์ด้วยกันมาตลอด"***

"*Despite all the struggles we have had to face and endure; at last my friends, we still make it to where we have planned all along via our own way*"

**This work is dedicated to my two "*teachers*" who have inspired me and recently passed away during the course of this work**

**Drs. Robert E. Newnham and Anthony J. Moulson**

(ผู้ช่วยศาสตราจารย์ ดร. รัตติกร ยิ้มนิรัญ)

หัวหน้าโครงการ

# บทคัดย่อ

**รหัสโครงการ :** RMU5080021

**ชื่อโครงการ :** สมบัติทางไฟฟ้าของสารเซรามิกเฟร์โรอิเล็กตริกที่มีตะกั่วเป็นฐานภายใต้ความเค้นอัด

**ชื่อนักวิจัย :** ผศ.ดร. รัตติกร ยิ้มนิรัญ

ภาควิชาฟิสิกส์และวัสดุศาสตร์ คณะวิทยาศาสตร์ มหาวิทยาลัยเชียงใหม่

**E-mail Address :** rattikornyimnirun@yahoo.com

**ระยะเวลาโครงการ :** 25 มิถุนายน 2550 ถึง 25 มิถุนายน 2552

ในการวิจัยนี้ได้ทำการศึกษาสมบัติทางไฟฟ้าภายใต้ความเค้นอัดของสารเซรามิกเฟร์โรอิเล็กตริกที่มีตะกั่วเป็นฐานที่สำคัญ กล่าวคือ PT PZT PIN PMN PZN PCoN PNN PZN-PZT PMN-PT PIN-PT PCoN-PZT และ PNN-PZT โดยสามารถแบ่งผลงานที่ได้จากโครงการวิจัยนี้ออกเป็น 4 กลุ่มใหญ่ กล่าวคือ 1. กระบวนการเตรียมผงและเซรามิก 2. สมบัติไดอิเล็กตริกและทางไฟฟ้าอื่นๆของสารเซรามิก 3. อิทธิพลของความเค้นแบบแกนเดี่ยวต่อสมบัติไดอิเล็กตริกและทางไฟฟ้าอื่นๆของสารเซรามิกทั้งหมดที่กล่าวมาข้างต้น และ 4. การศึกษาหาองค์ความรู้ใหม่ด้านอื่นๆที่ถือเป็นการต่อยอดจากผลงานที่ได้ศึกษามาในเบื้องต้น ซึ่งกลุ่มผู้วิจัยได้ประสบความสำเร็จในการเตรียมผงและเซรามิกด้วยการใช้เทคนิคผสมออกไซด์ร่วมกับเทคนิคการบดย่อยละเอียด โดยได้ทราบถึงเงื่อนไขที่เหมาะสมต่อการเตรียมผงให้มีความบริสุทธิ์สูง และพบเงื่อนไขในการเผาที่เหมาะสมต่อการเตรียมเซรามิกแต่ละชนิดที่กล่าวมาเหล่านี้ให้มีความบริสุทธิ์และความหนาแน่นสูง และจากการตรวจสอบคุณลักษณะเฉพาะและคุณสมบัติทางไฟฟ้าต่างๆของเซรามิกที่เตรียมได้ก็พบว่าสารเซรามิกที่เตรียมได้นั้นแสดงคุณลักษณะเฉพาะเป็นสารเซรามิกเฟร์โรอิเล็กตริกแบบปกติ หรือสารเซรามิกเฟร์โรอิเล็กตริกกลุ่มรีแลกเซอร์ หรือสารเซรามิกที่แสดงลักษณะผสมกันระหว่างเซรามิกเฟร์โรอิเล็กตริกแบบปกติและสารเซรามิกเฟร์โรอิเล็กตริกกลุ่มรีแลกเซอร์ ทั้งนี้ขึ้นกับชนิดของสารเซรามิกและอัตราส่วนผสม และจากการศึกษาอิทธิพลของความเค้นแบบแกนเดี่ยวต่อสมบัติไดอิเล็กตริกและทางไฟฟ้าอื่นๆของสารเซรามิกก็พบว่าความเค้นมีผลอย่างชัดเจนในการเปลี่ยนแปลงสมบัติต่างๆในสารเซรามิกทุกระบบ โดยมีทิศทางและอัตราการเปลี่ยนแปลงที่ขึ้นอยู่กับชนิดของสารเซรามิกและอัตราส่วนผสม ท้ายที่สุดนั้นผลการศึกษาในโครงการวิจัยนี้ได้นำไปสู่ผลงานการตีพิมพ์ในระดับนานาชาติแล้วกว่า 50 เรื่อง

**คำหลัก:** ความเค้นแบบแกนเดี่ยว; สมบัติทางไฟฟ้า; สารเซรามิกเฟร์โรอิเล็กตริก

# Abstract

**Project Code :** RMU5080021

**Project Title :** Electrical Properties of Lead-Based Ferroelectric Ceramics Under Compressive Stress

**Investigators :** Asst. Prof. Dr. Rattikorn Yimnirun

Department of Physics and Materials Science, Faculty of Science, Chiang Mai University

**E-mail Address :** rattikornyimnirun@yahoo.com

**Project Period :** June 25, 2007 to June 25, 2009

In this study, effects of uniaxial stress on the electrical properties of important ceramics in PT PZT PIN PMN PZN PCoN PNN PZN-PZT PMN-PT PIN-PT PCoN-PZT and PNN-PZT systems were investigated. The outputs of this project can be divided into 4 main groups; namely, 1. powder and ceramic fabrication, 2. dielectric and other electrical properties, 3. effects of uniaxial stress on dielectric and other electrical properties of all the prepared ceramics, and 4. new body of knowledge arised from the above-mentioned studies. We have successfully prepared powders and ceramics by using the mixed-oxide technique in conjunction with the vibro-milling technique and found suitable conditions for preparing high purity powders and for fabricating each ceramic to high purity and density. From the characterization and electrical properties measurements, the prepared ceramics exhibit either normal or relaxor or mixed ferroelectric characteristics, depending upon the type of ceramics and composition ratio. Similarly, the uniaxial stress studies also indicate that the applied stress impose significant influence on the electrical properties with the direction and rate of change depending on the type of ceramics and composition ratio. Finally, the results from this project have resulted in more than 50 international publications.

**Keywords :** Uniaxial Stress; Electrical Properties; Ferroelectric Ceramics

# Executive Summary

แบเรียมไทเทเนต ($BaTiO_3$) หรือ BTเลดไทเทเนต ($PbTiO_3$) หรือ PT เลดเซอร์โคเนตไทเทเนต ($Pb(Zr,Ti)O_3$) หรือ PZT เลดแมกนีเซียมไนโอเบต ($Pb(Mg_{1/3}Nb_{2/3})O_3$) หรือ PMN เลดซิงค์ไนโอเบต ($Pb(Zn_{1/3}Nb_{2/3})O_3$) หรือ PZN เลดนิกเกิลไนโอเบต ($Pb(Ni_{1/3}Nb_{2/3})O_3$) หรือ PNN เลดโคบอลท์ไนโอเบต ($Pb(Co_{1/3}Nb_{2/3})O_3$) หรือ PCoN และ เลดอินเดียมไนโอเบต ($Pb(In_{1/2}Nb_{1/2})O_3$) หรือ PIN ล้วนแล้วแต่เป็นสารซรามิกเฟร์โรอิเล็กตริก (ferroelectrics) ที่ถูกพัฒนาขึ้นมาเพื่อใช้ประโยชน์ในอุปกรณ์อิเล็กทรอนิกส์ประเภทต่างๆ อย่างไรก็ตามโดยทั่วไปแล้ว ในสภาวะการใช้งานจริงของอุปกรณ์อิเล็กทรอนิกส์ที่ผลิตจากสารเซรามิกเฟร์โรอิเล็กตริกดังที่กล่าวมาแล้วนั้น สารเซรามิกมักจะอยู่สภาวะภายใต้ความเค้น ซึ่งอาจจะเกิดจากความเค้นเชิงกลภายนอกระหว่างการใช้งาน หรือความเค้นเชิงกลภายในอันเกิดจากการที่สารเซรามิกเหล่านี้ ดังนั้นข้อมูลเกี่ยวกับสมบัติไดอิเล็กตริกภายใต้อิทธิพลของความเค้น จึงมีความสำคัญอย่างมากต่อการออกแบบ การจัดสร้างและการใช้งานของอุปกรณ์อิเล็กทรอนิกส์ที่ผลิตจากสารเซรามิกเฟร์โรอิเล็กตริกเหล่านี้ ดังนั้นผู้วิจัยจึงทำการศึกษาอย่างเป็นระบบถึงอิทธิพลของความเค้นต่อสมบัติทางไฟฟ้าของสารเซรามิกเฟร์โรอิเล็กตริกที่สำคัญ กล่าวคือ PT PZT PIN PMN PZN PCoN PNN PZN-PZT PMN-PT PIN-PT PCoN-PZT และ PNN-PZT โดยสามารถแบ่งผลงานที่ได้จากโครงการวิจัยนี้ออกเป็น 4 กลุ่มใหญ่ กล่าวคือ 1. กระบวนการเตรียมผงและเซรามิก 2. สมบัติไดอิเล็กตริกและทางไฟฟ้าอื่นๆของสารเซรามิก 3. อิทธิพลของความเค้นแบบแกนเดี่ยวต่อสมบัติไดอิเล็กตริกและทางไฟฟ้าอื่นๆของสารเซรามิกทั้งหมดที่กล่าวมาข้างต้น และ 4. องค์ความรู้ใหม่ด้านอื่นๆที่ถือเป็นการต่อยอดจากผลงานที่ได้ศึกษามาในเบื้องต้น ซึ่งกลุ่มผู้วิจัยได้ประสบความสำเร็จในการเตรียมผงและเซรามิกด้วยการใช้เทคนิคผสมออกไซด์ร่วมกับเทคนิคการบดย่อยละเอียด โดยได้ทราบถึงเงื่อนไขที่เหมาะสมต่อการเตรียมผงให้มีความบริสุทธิ์สูง และพบเงื่อนไขในการเผาที่เหมาะสมต่อการเตรียมเซรามิกแต่ละชนิดที่กล่าวมาเหล่านี้ให้มีความบริสุทธิ์และความหนาแน่นสูง และจากการตรวจสอบคุณลักษณะเฉพาะและคุณสมบัติทางไฟฟ้าต่างๆของเซรามิกที่เตรียมได้ก็พบว่าสารเซรามิกที่เตรียมได้นั้นแสดงคุณลักษณะเฉพาะเป็นสารเซรามิกเฟร์โรอิเล็กตริกแบบปกติ หรือสารเซรามิกเฟร์โรอิเล็กตริกกลุ่มรีแลกเซอร์ หรือสารเซรามิกที่แสดงลักษณะผสมกันระหว่างเซรามิกเฟร์โรอิเล็กตริกแบบปกติและสารเซรามิกเฟร์โรอิเล็กตริก กลุ่มรีแลกเซอร์ ทั้งนี้ขึ้นกับชนิดของสารเซรามิกและอัตราส่วนผสม และจากการศึกษาอิทธิพลของความเค้นแบบแกนเดี่ยวต่อสมบัติไดอิเล็กตริกและทางไฟฟ้าอื่นๆของสารเซรามิกก็พบว่าความเค้นมีผลอย่างชัดเจนในการเปลี่ยนแปลงสมบัติต่างๆในสารเซรามิกทุกระบบ โดยมีทิศทางและอัตราการเปลี่ยนแปลงที่ขึ้นอยู่กับชนิดของสารเซรามิกและอัตราส่วนผสม

# เนื้อหางานวิจัย

## 1. ความสำคัญและที่มาของปัญหาที่ทำการวิจัย

สารเซรามิกเฟร์โรอิเล็กตริกสามารถแบ่งได้เป็น 2 ประเภทใหญ่ๆ จากลักษณะของการเปลี่ยนแปลงเฟสและการตอบสนองต่อความถี่ คือ สารเซรามิกเฟร์โรอิเล็กตริกแบบปกติ (normal ferroelectrics) และสารเซรามิกเฟร์โรอิเล็กตริกกลุ่มรีแลกเซอร์ (relaxor ferroelectrics) ซึ่งในกลุ่มแรกนั้นการเปลี่ยนเฟสจะเกิดขึ้นอย่างรวดเร็ว (sharp transition) บริเวณอุณหภูมิคูรี (Curie temperature: $T_C$) และมีสมบัติไดอิเล็กตริกที่ไม่ค่อยขึ้นกับความถี่ ในขณะที่สารเซรามิกในกลุ่มที่สองนั้นจะเกิดการเปลี่ยนเฟสแบบช้าๆ (diffuse phass transition) และมีสมบัติไดอิเล็กตริกที่เปลี่ยนแปลงกับความถี่อย่างชัดเจน ตัวอย่างสารเซรามิกเฟร์โรอิเล็กตริกแบบปกติที่สำคัญได้แก่ แบเรียมไทเทเนต ($BaTiO_3$) หรือ BT เลดไทเทเนต ($PbTiO_3$) หรือ PT และเลดเซอร์โคเนตไทเทเนต ($Pb(Zr,Ti)O_3$) หรือ PZT ในขณะตัวอย่างของสารเซรามิกเฟร์โรอิเล็กตริกกลุ่มรีแลกเซอร์ ที่สำคัญประกอบด้วย เลดแมกนีเซียมไนโอเบต ($Pb(Mg_{1/3}Nb_{2/3})O_3$) หรือ PMN เลดซิงค์ไนโอเบต ($Pb(Zn_{1/3}Nb_{2/3})O_3$) หรือ PZN เลดนิกเกิลไนโอเบต ($Pb(Ni_{1/3}Nb_{2/3})O_3$) หรือ PNN เลดโคบอลท์ไนโอเบต ($Pb(Co_{1/3}Nb_{2/3})O_3$) หรือ PCoN และ เลดอินเดียมไนโอเบต ($Pb(In_{1/2}Nb_{1/2})O_3$) หรือ PIN ซึ่งสารเหล่านี้ล้วนแล้วแต่เป็นสารที่ถูกพัฒนาขึ้นมาเพื่อใช้ประโยชน์ในอุปกรณ์อิเล็กทรอนิกส์ประเภทต่างๆ เช่น ตัวเก็บประจุไฟฟ้า ตัวต้านทาน เทอร์มิสเตอร์ เซนเซอร์ แอกทัวเอเทอร์ ทรานสดิวเซอร์ หม้อแปลงไฟฟ้า บัซเซอร์ในลำโพง อุปกรณ์ตรวจสอบตำหนิหรือรอยร้าวในวัสดุแบบไม่ทำลาย ตัวบังคับการสั่นของหัวเข็มในเครื่องมือขูดหินปูน อุปกรณ์ทำความสะอาดเครื่องมือทางการแพทย์ด้วยอัลตร้าโซนิกส์ หัวตรวจวัดอัลตร้าซาวด์ หัวตรวจวัดความดันโลหิต และหุ่นยนต์ขนาดจิ๋วสำหรับใช้ในการตรวจอวัยวะภายในแบบไร้สาย เป็นต้น [1-9] ซึ่งโดยหลักการพื้นฐานแล้ววัสดุที่มีศักยภาพเหมาะสมสำหรับการนำมาประยุกต์ใช้ในงานต่างๆเหล่านี้นั้น จะต้องมีคุณลักษณะที่สำคัญอันได้แก่ การมีค่าสภาพยอมสัมพัทธ์ที่เหมาะสม ในช่วงของอุณหภูมิและความถี่สำหรับการทำงานของอุปกรณ์ มีค่าสัมประสิทธิ์ไฟฟ้าเชิงกลคู่ควบสูง สามารถทำการจัดเรียงไดโพลภายในเนื้อสารได้ง่าย มีการสูญเสียของพลังงานในระหว่างการใช้งานที่ต่ำ มีอายุการใช้งานนานและที่สำคัญต้องสามารถทำการเตรียมได้ง่าย โดยมีค่าใช้จ่ายไม่มากและปลอดภัย สามารถหาวัตถุดิบได้ง่าย และต้องการอุณหภูมิเผาที่ไม่สูงมากนัก เป็นต้น ซึ่งโดยทั่วไปแล้วนั้น การผสมผสานของคุณสมบัติที่ดีต่างๆเหล่านี้ไม่สามารถพบได้ในวัสดุเดี่ยวๆตัวใดตัวหนึ่งที่กล่าวมาในข้างต้นได้ เนื่องจากวัสดุแต่ละชนิดต่างก็มีข้อดีและข้อเสียที่แตกต่างกันไปในลักษณะที่มีความเฉพาะตัวมาก ดังนั้นการศึกษาวิจัยเพื่อค้นหาวัสดุชนิดใหม่ๆ ที่อาศัยหลักการนำเอาวัสดุหลักๆที่มีอยู่เดิมมารวมเข้าด้วยกัน ที่สามารถจะผสมผสานข้อดีและช่วยบรรเทาข้อเสียของแต่ละวัสดุที่เป็นองค์ประกอบหลักได้อย่างลงตัว จึงเป็นวิธีการหนึ่งที่ได้รับความสนใจอย่างมากทั้งในแวดวงวิชาการและในวงการอุตสาหกรรม ทำ

ให้ในปัจจุบันมีสารเซรามิกเฟร์โรอิเล็กตริกชนิดใหม่ๆที่มีความสลับซับซ้อนยิ่งขึ้นจำนวนมากเกิดขึ้นมาเช่น BT-PT, BT-PZT, PZT-PZN, PMN-PT, PMN-PZN, PMN-PZT, PIN-PT, PIN-PMN, PIN-PZN, PNN-PZT, PCoN-PZT, BT-PMN-PZN, PT-PMN-PZN, PMN-PT-BT, PZT-PZN-PMN และ PMN-PT-PIN เป็นต้น [1-3,10-20] และงานวิจัยทางด้านนี้ส่วนใหญ่เน้นถึงการศึกษาถึงอิทธิพลของปัจจัยหลักในกระบวนการผลิตที่มีต่อพฤติกรรมการเกิดเฟส โครงสร้างจุลภาคและสมบัติไดอิเล็กตริก สมบัติเฟร์โรอิเล็กตริกและสมบัติไฟฟ้าเชิงกลของสารเซรามิกที่ผลิตขึ้น [10-24]

เลดไทเทเนต ($PbTiO_3$) หรือ PT นั้นเป็นสารเฟร์โรอิเล็กตริกที่มีสมบัติพิโซอิเล็กตริก (piezoelectrics) และไพโรอิเล็กตริก (pyroelectrics) โดดเด่นมากตัวหนึ่งและเหมาะสำหรับการนำไปใช้ในงานที่ต้องมีอุณหภูมิและความถี่สูงๆอย่างมาก [3-7] แต่ก็ติดอยู่ตรงที่ว่ามีค่าเตตระกอนอลิตี้ (tetragonality) หรือ c/a สูงมากๆ (~ 1.065) [3] ทำให้ PT เป็นสารที่มีความเครียดภายในสูงมากดังนั้นการเตรียมเป็นชิ้นงานเซรามิกจึงกระทำได้ยากมาก เพราะชิ้นงานจะแตกออกเป็นเสี่ยงเสมอ จึงนิยมทำการเติมสารเจือเพื่อลดความเครียดภายในเนื้อสาร หรือไม่ก็นำไปรวมกับสารชนิดอื่นๆก่อนจะนำไปใช้งานต่อไป เช่น BT-PT, PZT, PZN-PT และ PMN-PT เป็นต้น [1,2,25-27]

เลดเซอร์โคเนตไทเทเนต $Pb(Zr,Ti)O_3$ หรือ PZT นั้นเป็นสารละลายของแข็งระหว่าง $PbZrO_3$ กับ $PbTiO_3$ ที่ถูกจัดเป็นต้นแบบของสารเซรามิกพิโซอิเล็กตริกที่มีการศึกษาค้นคว้ากันอย่างกว้างขวางมาก โดยนิยมนำมาใช้ในที่จุดเตาแก๊ส บัซเซอร์ในลำโพง หัวฉีดหมึกในปริ้นส์เตอร์ โซนาร์ และทรานสดิวเซอร์ที่ใช้กันในเครื่องอัลทราโซนิกส์ เป็นต้น [2-5] เนื่องจาก PZT เป็นสารที่มีค่าตัวประกอบไฟฟ้าเชิงกลคู่ควบ (~ 0.65) และอุณหภูมิคูรี (> 400 $^{o}$ซ) สูงกว่า BT มาก จึงเหมาะสำหรับการนำไปใช้ในอุปกรณ์ทรานสดิวเซอร์พลังงานสูงที่ต้องมีการใช้งานที่อุณหภูมิสูง นอกจากนี้ PZT ยังเป็นสารที่มีค่าสภาพยอมสัมพัทธ์ใกล้เคียงกับ BT แต่ว่าต้องการอุณหภูมิเผาซินเตอร์ที่ต่ำกว่า (~ 1200 $^{o}$ซ) PZT เป็นสารที่สามารถทำการโพลลิ่ง (poling) เพื่อจัดเรียงไดโพลภายในสารได้ง่ายกว่า BT และยังมีช่วงของค่าสภาพยอมสัมพัทธ์กว้างกว่า BT มาก [5,7] นอกจากนี้ สมบัติเฟร์โรอิเล็กตริก พิโซอิเล็กตริก และไพโรอิเล็กตริกที่สำคัญของสาร PZT นั้นสามารถควบคุมได้โดยการปรับเปลี่ยนที่ค่าอัตราส่วนของ Zr ต่อ Ti ทำให้สามารถสร้างสาร PZT ที่มีค่าสภาพยอมสัมพัทธ์ได้หลากหลายมาก ซึ่งค่าอัตราส่วนของZr/Tiที่ 52/48 53/47 และ 55/45 จะเป็นสูตรที่ได้รับความนิยมสูงมากเพราะเป็นสูตรที่อยู่แถวบริเวณแนว Morphotropic Phase Boundary (MPB) ที่มีทั้งเฟสของPZTแบบเตตระกอนอลและรอมโบฮีดรอลอยู่ร่วมกัน ทำให้สาร PZT ที่มีสัดส่วนทางเคมีอยู่แถวบริเวณนี้มีค่าสภาพยอมสัมพัทธ์และค่าสัมประสิทธ์พิโซอิเล็กตริกคู่ควบสูงมาก [1,3] สำหรับข้อด้อยของสาร PZTนั้นก็มีอยู่หลายประการคือ เป็นสารที่มีค่าการสูญเสียทางไดอิเล็กตริกสูง (~ 4.0%) มีความล้า (fatigue) และการสูญเสียของพลังงานสูงมาก (มีสมบัติ Hysteresis ซึ่งไม่เป็นที่ต้องการในการใช้งานที่ต้องการความละเอียดอ่อน) เมื่อผ่านการใช้งานทำให้มีอายุการใช้งานสั้น และที่สำคัญ PZT เป็นสารที่มี

อุณหภูมิคูรีค่อนข้างสูง ($T_C \sim 200 - 400$ °ซ ขึ้นกับค่า Zr/Ti) ทำให้การใช้ประโยชน์สูงสุดของสารถูกจำกัดอยู่ที่อุณหภูมิสูงๆเท่านั้น [1-3]

สารเฟร์โรอิเล็กตริกกลุ่มรีแลกเซอร์ (relaxor ferroelectrics) เช่น เลดแมกนีเซียมไนโอเบต ($Pb(Mg_{1/3}Nb_{2/3})O_3$) หรือ PMN ซึ่งถือว่าเป็นต้นแบบของพวกรีแลกเซอร์นั้นเป็นสารที่พึ่งถูกพัฒนาขึ้นมาภายหลัง PZT แต่ว่ามีค่าสภาพยอมสัมพัทธ์สูงและมีช่วงอุณหภูมิที่เหมาะสำหรับการใช้งานกว้างมากกว่าสาร PZT โดยครอบคลุมถึงช่วงอุณหภูมิห้อง นอกจากนี้ PMN ยังเป็นสารที่ต้องการอุณหภูมิสำหรับเผาซินเตอร์ต่ำกว่า PZT (< 1200 °ซ) ทำให้สามารถใช้วัสดุที่มีจุดหลอมเหลวต่ำเช่น เงิน ทองแดง หรือ เงินผสมปัลลาเดียม ซึ่งมีราคาถูกมาทำเป็นขั้วไฟฟ้าได้ [3,28] PMN เป็นสารที่มีลักษณะเฉพาะทางจุลภาคที่ส่งผลทำให้มีการสูญเสียพลังงานต่ำเมื่อผ่านการใช้งานและไม่มีสมบัติ Hysteresis ทำให้มีประสิทธิภาพในการส่งถ่ายพลังงานสูงกว่าสาร PZT ในปัจจุบันจึงนิยมนำสาร PMN มาใช้ในพวกตัวเก็บประจุไฟฟ้าแบบหลายชั้นและอุปกรณ์อิเล็กทรอนิกส์ที่ต้องการความละเอียดอ่อนสูงๆเช่น หัววัดทรานสดิวเซอร์ทางการแพทย์ และตัวขับเร้า (acturtors) เป็นต้น [5-7] แต่อย่างไรก็ตาม PMN ก็เป็นสารที่มีค่าสัมประสิทธิ์ไฟฟ้าเชิงกลคู่ควบต่ำกว่า PZT มาก และยังมีพฤติกรรมทางไดอิเล็กตริกที่เปลี่ยนแปลงตามความถี่ของสัญญาณอีกด้วย [3,5] และที่สำคัญการเตรียมสาร PMN ให้มีความบริสุทธิ์สูงนั้นกระทำได้ยากกว่าการเตรียมสาร PZT เนื่องจากจะพบว่ามีการเกิดเฟสไพโรคลอร์ (pyrochlores) ที่เป็นสารประกอบของ $PbO\text{-}Nb_2O_5$ เกิดขึ้นปะปนอยู่เสมอ และส่งผลในแง่ลบต่อสมบัติทางไฟฟ้าของเซรามิก PMN [29-31]

ในช่วงสองทศวรรษที่ผ่านมา เลดซิงค์ไนโอเบต ($Pb(Zn_{1/3}Nb_{2/3})O_3$) หรือ PZN เป็นสารเฟร์โรอิเล็กตริกกลุ่มรีแลกเซอร์ที่ได้รับความสนใจมากเป็นพิเศษ เนื่องจากมีสมบัติไดอิเล็กตริก สมบัติพิโซอิเล็กตริก และสมบัติอิเล็กโทรสตริกทีฟที่โดดเด่นมาก โดยผลึกเชิงเดี่ยวของ PZN มีค่าสัมประสิทธิ์สมบัติพิโซอิเล็กตริก ($d_{33}$) ค่าความเครียดที่ถูกเหนี่ยวนำจากสนามไฟฟ้า (s) และค่าคงที่ไฟฟ้าเชิงกลคู่ควบ ($k_{33}$) ที่สูงถึง 2500 pm/V 1.7% และ 90% ตามลำดับ ทำให้เกิดความสนใจอย่างกว้างขวางในการที่จะนำสาร PZN ไปประยุกต์ใช้ในแอกทัวเอเทอร์และหัวตรวจวัดอัลตร้าซาวด์ [9,14,15,32,33] อย่างไรก็ตาม สาร PZN ในรูปแบบที่เป็นเซรามิกก็มีความยากลำบากในการเตรียมมากเนื่องจากจะเกิดเฟสไพโรคลอร์ที่มีผลทำให้สมบัติทางไฟฟ้าของเซรามิก PZN ลดลง และโดยทั่วไปจะต้องการทำให้เกิดเสถียรภาพของเฟสเพอรอฟสไกด์ด้วยการเติมสารอื่น เช่น BT หรือ PZT ลงไป หรือการเตรียมสารด้วยวิธีเคมีกล (mechanochemical) [34] นอกจากนี้ ยังได้มีการพบว่า นอกจาก PZN แล้ว เลดนิกเกิลไนโอเบต ($Pb(Ni_{1/3}Nb_{2/3})O_3$) หรือ PNN เลดโคบอลท์ไนโอเบต ($Pb(Co_{1/3}Nb_{2/3})O_3$) หรือ PCoN ซึ่งก็เป็นสารเฟร์โรอิเล็กตริกกลุ่มรีแลกเซอร์ก็ได้รับความสนใจมากเป็นพิเศษ เนื่องสารละลายของแข็งระหว่าง PZT และ PZN PNN และ PCoN นั้นมีมีสมบัติไดอิเล็กตริก สมบัติพิโซอิเล็กตริก และสมบัติอิเล็กโทรสตริกทีฟที่โดดเด่นมาก ทำให้ได้รับการศึกษาอย่างกว้างขวาง [35-39]

เลดอินเดียมไนโอเบต ($Pb(In_{1/2}Nb_{1/2})O_3$) หรือ PIN เป็นสารเฟร์โรอิเล็กตริกกลุ่มรีแลกเซอร์ที่ได้รับความสนใจเนื่องจากความพิเศษที่ว่า PIN สามารถเปลี่ยนลักษณะของโครงสร้างไปมาระหว่างแบบมีระเบียบ (order) และแบบไม่มีระเบียบ (disorder) ด้วยการอบอุ่น (annealing) ที่อุณหภูมิที่เหมาะสม โดยเมื่อ PIN อยู่ในสถานะแบบไม่มีระเบียบนั้นจะมีสมบัติเฟร์โรอิเล็กตริกและมีโครงสร้างแบบ pseudo-cubic โดยอุณหภูมิที่ค่าคงที่ไดอิเล็กตริกมีค่าสูงสุด ($T_m$) อยู่ที่ 66 °ซ ในขณะที่ในสถานะแบบมีระเบียบนั้น PIN จะเปลี่ยนไปเป็นสารแอนตีเฟร์โรอิเล็กตริกที่มีโครงสร้างแบบออทรอรอมบิค (orthorhombic) ซึ่งมีอุณหภูมิการเปลี่ยนเฟสที่ 190 °ซ [15,17,40]

โดยทั่วไปแล้วนั้น เนื่องจากวัสดุแต่ละชนิดต่างก็มีข้อดีและข้อเสียที่แตกต่างกันไปในลักษณะที่มีความเฉพาะตัวมาก ดังนั้นการศึกษาวิจัยเพื่อค้นหาวัสดุชนิดใหม่ๆ ที่อาศัยหลักการนำเอาวัสดุหลักๆที่มีอยู่เดิมมารวมเข้าด้วยกัน ที่สามารถจะผสมผสานข้อดีและช่วยบรรเทาข้อเสียของแต่ละวัสดุที่เป็นองค์ประกอบหลักได้อย่างลงตัว จึงเป็นวิธีการหนึ่งที่ได้รับความสนใจอย่างมากทั้งในแวดวงวิชาการและในวงการอุตสาหกรรม โดยเฉพาะการรวมกันระหว่างสารเซรามิกเฟร์โรอิเล็กตริกแบบปกติ เช่น PT และ PZT และสารเซรามิกเฟร์โรอิเล็กตริกกลุ่มรีแลกเซอร์ เช่น PMN PZN PNN PCoN และ PIN นั้นจะได้รับความสนใจเป็นพิเศษ เนื่องจากมีสมบัติที่โดดเด่นมาก ทำให้ในปัจจุบันมีสารเซรามิกเฟร์โรอิเล็กตริกชนิดใหม่ๆที่มีความสลับซับซ้อนยิ่งขึ้นจำนวนมากเกิดขึ้น [10-24]

ในช่วงหลายปีที่ผ่านมานี้การพัฒนาสารเฟร์โรอิเล็กตริกชนิดใหม่ๆที่มี PMN เป็นองค์ประกอบหลักเริ่มได้รับความสนใจเพิ่มมากขึ้นเรื่อยๆนับตั้งแต่มีการค้นพบว่าสารในระบบ PMN-PT สูตรที่มีปริมาณของ PT ไม่เกิน 30% นั้นมีค่าสภาพยอมสัมพัทธ์ที่สูงมาก (~ 24000) และมีศักยภาพเหมาะสำหรับการพัฒนาไปใช้ในพวกตัวขับเร้าจุลภาค (microactuators) หรือตัวเก็บประจุไฟฟ้าได้ [41-43] แต่ก็ยังมีข้อด้อยอยู่ที่การมีค่าการสูญเสียทางไดอิเล็กตริกที่สูงใกล้เคียงกับสาร PZT และมีค่าตัวประกอบคุณภาพเชิงกลที่ต่ำ นอกจากนี้ยังต้องใช้เวลาในการเผาซินเตอร์ที่นานมาก [41,42]

สารเซรามิกเฟร์โรอิเล็กตริก PZN-PZT นอกจากจะมีเสถียรภาพของเฟสเพอรอพสไกต์ที่ดีแล้วนั้น ยังมีสมบัติไดอิเล็กตริกและสมบัติพิโซอิเล็กตริกที่ดี โดยมีค่าสัมประสิทธิ์สมบัติพิโซอิเล็กตริก ($d_{33}$) ค่าความเครียดที่ถูกเหนี่ยวนำจากสนามไฟฟ้า (2 kV/mm) (s) และค่าคงที่ไฟฟ้าเชิงกลคู่ควบ ($k_p$) ที่สูงถึง 430 pC/N 0.24% และ 67% ตามลำดับ ซึ่งเหมาะสมที่จะนำไปประยุกต์ใช้ในแอกทัวเอเทอร์ หม้อแปลงไฟฟ้า และมอเตอร์กำลังสูง ทั้งนี้สารเซรามิกเฟร์โรอิเล็กตริก PZN-PZT ยังสามารถซินเตอร์ได้ที่อุณหภูมิที่ต่ำกว่า 1100 °ซ [44,45] นอกจากนี้ ยังพบว่าสารเฟร์โรอิเล็กตริกในกลุ่มเดียวกันกล่าวคือ PNN-PZT และ PCoN-PZT ก็ยังสมบัติไดอิเล็กตริกและสมบัติพิโซอิเล็กตริกที่โดดเด่นไม่แพ้ PZN-PZT จึงมีการศึกษาอย่างแพร่หลายเช่นกัน [35-39] อย่างไรก็ตาม ถึงแม้ว่าสารที่มีพื้นฐานมาจาก PZN นั้นจะมีสมบัติที่น่าสนใจมาก แต่สารเหล่านั้นมักจะไม่สารถใช้งานที่อุณหภูมิที่สูงเกิน 85 °ซ ทั้งนี้เนื่องจากอุณหภูมิคูรีที่ค่อนข้างต่ำ [15]

ดังนั้นจึงมีความต้องการสารที่มีค่าคงที่ไฟฟ้าเชิงกลคู่ควบที่มากและอุณหภูมิคูรีที่สูงกว่า 250 °ซ สาร PIN-PT เป็นหนึ่งในสารที่ได้รับความสนใจเป็นพิเศษเนื่องจากเป็นสารเฟร์โรอิเล็กตริกกลุ่มรีแลกเซอร์ที่มีอุณหภูมิคูรีที่สูงกว่า 250 °ซ [15]

อย่างไรก็ตามโดยทั่วไปแล้ว ในสภาวะการใช้งานจริงของอุปกรณ์อิเล็กทรอนิกส์ที่ผลิตจากสารเซรามิกเฟร์โรอิเล็กตริกดังที่กล่าวมาแล้วนั้น สารเซรามิกมักจะอยู่สภาวะภายใต้ความเค้น ซึ่งอาจจะเกิดจากความเค้นเชิงกลภายนอกระหว่างการใช้งาน เช่น แอกทัวเอเทอร์และทรานสดิวเซอร์ เป็นต้น หรือความเค้นเชิงกลภายในอันเกิดจากการที่สารเซรามิกเหล่านี้ซึ่งมีสมบัติพิโซอิเล็กตริกจะเกิดการเปลี่ยนแปลงรูปร่างภายใต้อิทธิพลของสนามไฟฟ้าซึ่งส่งผลให้เกิดความเค้นกระทำต่อสารเซรามิก เช่น ตัวเก็บประจุไฟฟ้า เทอร์มิสเตอร์ เซนเซอร์ หม้อแปลงไฟฟ้า และหัวตรวจวัดอัลตร้าซาวด์ เป็นต้น ดังนั้นข้อมูลเกี่ยวกับสมบัติทางไฟฟ้าต่างๆ โดยเฉพาะ สมบัติไดอิเล็กตริก สมบัติเฟร์โรอิเล็กตริก และสมบัติไฟฟ้าเชิงกล ภายใต้อิทธิพลของความเค้น จึงมีความสำคัญอย่างมากต่อการออกแบบ การจัดสร้างและการใช้งานของอุปกรณ์อิเล็กทรอนิกส์ที่ผลิตจากสารเซรามิกเฟร์โรอิเล็กตริกเหล่านี้ ซึ่งการศึกษาเหล่านี้นอกจากจะช่วยเสริมข้อมูลที่จำเป็นในการพัฒนาและการนำไปประยุกต์ใช้ของสารเซรามิกเฟร์โรอิเล็กตริกแล้ว ยังสามารถเสริมองค์ความรู้พื้นฐานในเรื่องโครงสร้างของโดเมน (domain structure) และการเคลื่อนที่ของโดเมน (domain motion) [46,47] ซึ่งเป็นกลไกที่สำคัญที่มีอิทธิพลต่อสมบัติไดอิเล็กตริกและสมบัติไฟฟ้าเชิงกลในสารเซรามิกเฟร์โรอิเล็กตริก ส่งผลให้ในช่วงที่ผ่านมาได้เริ่มมีการศึกษาถึงอิทธิพลของความเค้นต่อสมบัติทางไดอิเล็กตริก สมบัติเฟร์โรอิเล็กตริก และไฟฟ้าเชิงกลของสารเซรามิกในระบบต่างๆ เช่น PZT PMN-PT PZT-BT PIN-PT PZN-PZT และ PMN-PZT เป็นต้น แต่ยังคงอยู่ในวงที่จำกัดเมื่อเปรียบเทียบกับจำนวนของสารเซรามิกเฟร์โรอิเล็กตริกใหม่ๆที่ได้รับการพัฒนาขึ้นมา ทำให้งานวิจัยที่เป็นระบบในประเด็นของอิทธิพลของความเค้นต่อสมบัติต่างๆของสารเซรามิกเฟร์โรอิเล็กตริกที่สำคัญที่ปรากฏในวารสารงานวิจัยในระดับนานาชาติยังมีจำนวนที่ค่อนข้างน้อย [20,46-54]

ด้วยเหตุผลดังกล่าวมาข้างต้น ดังนั้นในช่วงระยะเวลา 7 ปีที่ผ่านมาทางผู้วิจัยจึงได้ทำการศึกษาอย่างเป็นระบบถึงอิทธิพลของความเค้นต่อสมบัติทางไฟฟ้าของสารเซรามิกเฟร์โรอิเล็กตริกที่สำคัญ กล่าวคือ สารเซรามิกเฟร์โรอิเล็กตริกระบบเดี่ยว เช่น BT PT PZT PZN PMN PIN เป็นต้น สารเซรามิกเฟร์โรอิเล็กตริกระบบคู่ที่สำคัญที่เกิดจากการผสมสารในระบบเดี่ยว เช่น PZT-BT PMN-PT PZN-PZT PIN-PT เป็นต้น และ สารเซรามิกเฟร์โรอิเล็กตริกที่มีความซับซ้อนมากและไม่เป็นที่ปรากฏมาก่อน คือ PZTBT-PMNT โดยโครงการวิจัยแรกที่ได้รับทุนส่งเสริมนักวิจัยรุ่นใหม่ ประจำปี 2545 (TRG-4580054) มุ่งเน้นความสำคัญไปที่การศึกษาถึงสมบัติไดอิเล็กตริกและไฟฟ้าเชิงกลของสารเซรามิกในระบบ PMN-PZT ภายใต้อิทธิพลของความเค้นแบบแกนเดี่ยว ซึ่งผลการศึกษาที่ได้มีการนำไปสู่การสร้างองค์ความรู้พื้นฐานใหม่ซึ่งนำไปสู่การตีพิมพ์ผลงานในระดับนานาชาติถึง 5 เรื่อง และต่อมาในโครงการศึกษาต่อเนื่องที่ได้รับทุนพัฒนานักวิจัย (เมธีวิจัย สกว) ประจำปี 2547 (RSA-4780002) ผู้วิจัยได้ทำการศึกษา

เพื่อสร้างองค์ความรู้พื้นฐานใหม่ที่จำเป็นสำหรับการทำความเข้าใจในธรรมชาติของสมบัติไดอิเล็กตริกของสารเซรามิกเฟร์โรอิเล็กตริกภายใต้ความเค้นของสารเซรามิกในระบบที่มีที่สำคัญกล่าวคือ สารเซรามิกเฟร์โรอิเล็กตริกระบบเดี่ยว เช่น BT PT PZT PZN PMN PIN เป็นต้น สารเซรามิกเฟร์โรอิเล็กตริกระบบคู่ที่สำคัญที่เกิดจากการผสมสารในระบบเดี่ยว เช่น PZT-BT PMN-PT PZN-PZT PIN-PT เป็นต้น และ สารเซรามิกเฟร์โรอิเล็กตริกที่มีความซับซ้อนมากและไม่เป็นที่ปรากฏมาก่อน คือ PZTBT-PMNT ทั้งนี้มีผลการศึกษาเป็นที่น่าพอใจและเป็นที่ยอมรับโดยทั่วไปในระดับนานาชาติ โดยในโครงการดังกล่าวนี้ได้มีการการตีพิมพ์ผลงานในระดับนานาชาติถึง 45 เรื่อง อย่างไรก็ตาม ด้วยระยะเวลาที่จำกัดทำให้ยังไม่ได้มีการศึกษาถึงอิทธิพลของความเค้นต่อสมบัติเฟร์โรอิเล็กตริกของสารเซรามิกทั้งหมดที่ได้ศึกษามา (ยกเว้นเพียง PMN-PZT) เพื่อเป็นการสร้างองค์ความรู้ที่สมบูรณ์แบบมากขึ้นผู้วิจัยจึงมีความประสงค์ที่จะทำการศึกษาถึงอิทธิพลของความเค้นต่อสมบัติเฟร์โรอิเล็กตริกของสารเซรามิกที่ได้กล่าวมาข้างต้น และนอกจากนี้ยังจะได้ขยายการศึกษาเพื่อครอบคลุมสารเซรามิกเฟร์โรอิเล็กตริกที่สำคัญที่ได้รับการศึกษาอย่างกว้างขวางในช่วงที่ผ่านมาเนื่องจากมีคุณลักษณะทางไฟฟ้าที่โดดเด่นกล่าวคือสารเซรามิกในระบบ PCoN-PZT และ PNN-PZT

กล่าวโดยสรุปในโครงการวิจัยปัจจุบันที่ดำเนินการนี้ จะเป็นการพัฒนาองค์ความรู้ใหม่แบบรวบยอดของอิทธิพลของความเค้นต่อสมบัติทางไฟฟ้าของสารเซรามิกเฟร์โรอิเล็กตริกที่สำคัญ เพื่อเป็นแนวทางในการนำองค์ความรู้ที่ได้รับจากการวิจัยนี้ไปใช้ในภาคปฏิบัติเพื่อพัฒนาการออกแบบ การจัดสร้างและการใช้งานของอุปกรณ์อิเล็กทรอนิกส์ที่ผลิตจากสารเซรามิกเฟร์โรอิเล็กตริกเหล่านี้ให้มีประสิทธิภาพสูงขึ้น นอกจากนี้แล้ว โครงการวิจัยนี้ยังเป็นการสร้างผลงานวิจัยแบบต่อเนื่องซึ่งมุ่งเน้นการใช้องค์ความรู้ที่ได้รับจากโครงการวิจัยจากทุนส่งเสริมนักวิจัยรุ่นใหม่และทุนพัฒนานักวิจัยของผู้วิจัยเองมาประยุกต์ใช้ และยังเป็นการส่งเสริมให้เกิดการเชื่อมโยงด้านการวิจัยระหว่างนักวิจัยในประเทศโดยการนำผลการวิจัยจากนักวิจัยท่านอื่นที่มีความร่วมมืออย่างใกล้ชิดซึ่งได้รับทุนส่งเสริมนักวิจัยรุ่นใหม่และทุนพัฒนานักวิจัยมาใช้ประโยชน์ในโครงการวิจัยนี้ [55-57] ซึ่งโครงการทั้งสองดังกล่าวนั้นได้มุ่งเน้นไปที่การการศึกษาถึงอิทธิพลของปัจจัยหลักในกระบวนการผลิตที่มีต่อพฤติกรรมการเกิดเฟส โครงสร้างจุลภาคและสมบัติไดอิเล็กตริกของสารเซรามิกในระบบ PZN PMN PNN และ PCoN ซึ่งผลการศึกษาเหล่านี้สามารถนำมาใช้โดยตรงในการเลือกเงื่อนไขที่เหมาะสมในการเตรียมสารเซรามิกที่มีความบริสุทธิ์และความหนาแน่นสูง รวมทั้งสมบัติไดอิเล็กตริกที่ดี มาใช้ในการศึกษาในโครงการวิจัยนี้ จะเห็นได้ว่าโครงการวิจัยนี้ นอกจากจะให้องค์ความรู้ที่สามารถนำไปใช้ในภาคปฏิบัติแล้ว ยังจะนำไปสู่ความรู้ความเข้าใจพื้นฐานใหม่ๆเกี่ยวกับสารเซรามิกเฟร์โรอิเล็กตริกที่สำคัญอันจะเป็นพื้นฐานในการพัฒนาประเทศและผลงานที่ได้ยังสามารถที่จะตีพิมพ์ในวารสารวิชาการระดับนานาชาติได้ นอกจากนี้ยังเป็นการพัฒนาวิชาชีพอาจารย์ให้มีศักยภาพในการผลิตนักศึกษาระดับปริญญาเอกได้

**2. วัตถุประสงค์ของการวิจัย**

1. เพื่อศึกษากระบวนการเตรียมผงและเซรามิกในระบบ PCoN PNN PZT PCoN-PZT และ PNN-PZT
2. เพื่อศึกษาอิทธิพลของความเค้นอัดต่อสมบัติไดอิเล็กตริกและสมบัติเฟร์โรอิเล็กตริกของสารเซรามิกระบบเดี่ยว PCoN และ PNN
3. เพื่อศึกษาอิทธิพลของความเค้นอัดต่อสมบัติไดอิเล็กตริกและสมบัติเฟร์โรอิเล็กตริกของสารเซรามิกระบบคู่ PCoN-PZT และ PNN-PZT
4. เพื่อศึกษาอิทธิพลของความเค้นอัดต่อสมบัติเฟร์โรอิเล็กตริกของสารเซรามิกระบบเดี่ยว PT PZT PIN PMN และ PZN
5. เพื่อศึกษาอิทธิพลของความเค้นแบบแกนเดี่ยวต่อสมบัติเฟร์โรอิเล็กตริกของสารเซรามิก ระบบคู่ PZN-PZT PMN-PT และ PIN-PT
6. เพื่อศึกษาความสัมพันธ์ระหว่างสมบัติไดอิเล็กตริกและสมบัติเฟร์โรอิเล็กตริกภายใต้ความเค้นอัดของแต่ละองค์ประกอบและสมบัติดังกล่าวของสารเซรามิกระบบคู่

**3. ระเบียบวิธีวิจัย**

ขั้นตอนการวิจัยในโครงการนี้จะถูกแบ่งออกเป็น 3 ส่วนหลัก คือ 1) การศึกษาการเตรียมผงและเซรามิกในระบบ PZT PNN PCoN PNN-PZT และ PCoN-PZT ด้วยการใช้เทคนิคผสมออกไซด์ เพื่อหาเงื่อนไขในการเตรียมผงและสารเซรามิกที่มีความบริสุทธิ์และความหนาแน่นสูง โดยใช้องค์ความรู้บางส่วนจากโครงการของ รองศาสตราจารย์ ดร. สุพล อนันตา และ ดร. นราธิป วิทยากร 2)การศึกษาอิทธิพลของความเค้นอัดต่อสมบัติเฟร์โรอิเล็กตริกของสารเซรามิกระบบ PMN-PT PIN-PT และ PZN-PZT โดยเป็นการศึกษาต่อเนื่องจากโครงการวิจัยที่ได้รับทุนพัฒนานักวิจัย ปี 2547 ของผู้วิจัยเอง ซึ่งเน้นเฉพาะการศึกษาอิทธิพลของความเค้นอัดต่อสมบัติไดอิเล็กตริกของสารเซรามิกดังกล่าว และ 3) การศึกษาอิทธิพลของความเค้นอัดต่อสมบัติไดอิเล็กตริกและสมบัติเฟร์โรอิเล็กตริกของสารเซรามิกระบบของสารเซรามิกระบบเดี่ยว PZT PNN และ PCoN และสารเซรามิกระบบคู่ PNN-PZT และ PCoN-PZT ที่เตรียมขึ้นได้

ดังนั้นเพื่อให้เกิดความต่อเนื่องของการดำเนินการวิจัยระหว่างโครงการนี้และโครงการที่เกี่ยวข้อง จึงต้องมีการวางแผนงานการวิจัยโดยมีรายละเอียดของระเบียบวิธีวิจัยดังนี้ (โดยใช้ระยะเวลารวม 2 ปีในการดำเนินการทั้งหมด (จากที่วางแผนไว้ในเบื้องต้น 3 ปี))

1 ศึกษาค้นคว้ารวบรวมข้อมูลจากผลงานวิจัยและเอกสารทางวิชาการที่เกี่ยวข้อง

2 ทำการติดตั้งและตรวจสอบเครื่องมืออัดแรงเพื่อใช้ในการวัดสมบัติไดอิเล็กตริกและสมบัติเฟร์โรอิเล็กตริกของสารเซรามิกภายใต้ความเค้นอัด และทำการติดตั้งและตรวจสอบอุปกรณ์อื่นๆที่จะใช้งานให้มีความพร้อม

3 เตรียมผงและเซรามิกในระบบ $Pb(Ni_{1/3}Nb_{2/3})O_3$ หรือ PNN ด้วยการใช้เทคนิคผสมออกไซด์ โดยศึกษาหาเงื่อนไขที่เหมาะสมต่อการเตรียมผงให้มีความบริสุทธิ์สูง และศึกษาหาเงื่อนไขในการเผาที่เหมาะสมต่อการเตรียมเซรามิกเหล่านี้ให้มีความบริสุทธิ์และความหนาแน่นสูง

4 เตรียมผงและเซรามิกในระบบ $Pb(Co_{1/3}Nb_{2/3})O_3$)หรือ PCoN ด้วยการใช้เทคนิคผสมออกไซด์ โดยศึกษาหาเงื่อนไขที่เหมาะสมต่อการเตรียมผงให้มีความบริสุทธิ์สูง และศึกษาหาเงื่อนไขในการเผาที่เหมาะสมต่อการเตรียมเซรามิกเหล่านี้ให้มีความบริสุทธิ์และความหนาแน่นสูง

5 เตรียมผงและเซรามิกในระบบ $Pb(Zr_{1/2}Ti_{1/2})O_3$ หรือ PZT ด้วยการใช้เทคนิคผสมออกไซด์ โดยศึกษาหาเงื่อนไขที่เหมาะสมต่อการเตรียมผงให้มีความบริสุทธิ์สูง และศึกษาหาเงื่อนไขในการเผาที่เหมาะสมต่อการเตรียมเซรามิกเหล่านี้ให้มีความบริสุทธิ์และความหนาแน่นสูง

6 ทำการตรวจสอบคุณลักษณะเฉพาะและคุณสมบัติของผงและเซรามิกที่เตรียมได้

7 ทดสอบอิทธิพลของความเค้นอัดต่อสมบัติเฟร์โรอิเล็กตริก (Polarization-Electric Field (P-E) Loops) ของสารเซรามิกระบบเดี่ยว PT และ PMN ด้วยเครื่องมืออัดแรงแบบแกนเดี่ยว

8 ทดสอบอิทธิพลของความเค้นอัดต่อสมบัติเฟร์โรอิเล็กตริก (Polarization-Electric Field (P-E) Loops) ของสารเซรามิกระบบคู่ PMN-PT ด้วยเครื่องมืออัดแรงแบบแกนเดี่ยว

9 สรุปความสัมพันธ์ระหว่างสมบัติเฟร์โรอิเล็กตริกภายใต้ความเค้นอัดของ PT และ PMN และสมบัติดังกล่าวของสารเซรามิกระบบ PMN-PT

10 อภิปรายผลการศึกษา และการเตรียมผลงานเพื่อการตีพิมพ์

11 เตรียมผงและเซรามิกในระบบ (1-x)PZT-xPNN เมื่อ x มีค่าเป็น 0.0, 0.1, 0.2, 0.3, 0.4, และ 0.5 ด้วยเทคนิคผสมออกไซด์โดยใช้สารที่เตรียมได้จาก ข้อ 8.3 และ 8.5 ที่มีความบริสุทธิ์สูงเป็นสารตั้งต้น โดยศึกษาหาเงื่อนไขที่เหมาะสมต่อการเตรียมผง

ให้มีความบริสุทธิ์สูง และศึกษาหาเงื่อนไขในการเผาที่เหมาะสมต่อการเตรียมเซรามิกเหล่านี้ให้มีความบริสุทธิ์และความหนาแน่นสูง

12 เตรียมผงและเซรามิกในระบบ (1-x)PZT-xPCoN เมื่อ x มีค่าเป็น 0.0, 0.1, 0.2, 0.3, 0.4, และ 0.5 ด้วยเทคนิคผสมออกไซด์โดยใช้สารที่เตรียมได้จาก ข้อ 8.4 และ 8.5 ที่มีความบริสุทธิ์สูงเป็นสารตั้งต้น โดยศึกษาหาเงื่อนไขที่เหมาะสมต่อการเตรียมผงให้มีความบริสุทธิ์สูง และศึกษาหาเงื่อนไขในการเผาที่เหมาะสมต่อการเตรียมเซรามิกเหล่านี้ให้มีความบริสุทธิ์และความหนาแน่นสูง

13 ทำการตรวจสอบคุณลักษณะเฉพาะและคุณสมบัติของผงและเซรามิกที่เตรียมได้

14 ทดสอบอิทธิพลของความเค้นอัดต่อสมบัติเฟร์โรอิเล็กตริก (Polarization-Electric Field (P-E) Loops) ของสารเซรามิกระบบเดี่ยว PT และ PIN ด้วยเครื่องมืออัดแรงแบบแกนเดี่ยว

15 ทดสอบอิทธิพลของความเค้นอัดต่อสมบัติเฟร์โรอิเล็กตริก (Polarization-Electric Field (P-E) Loops) ของสารเซรามิกระบบคู่ PIN-PT ด้วยเครื่องมืออัดแรงแบบแกนเดี่ยว

16 สรุปความสัมพันธ์ระหว่างสมบัติเฟร์โรอิเล็กตริกภายใต้ความเค้นอัดของ PT และ PIN และสมบัติดังกล่าวของสารเซรามิกระบบ PIN-PT

17 ทดสอบอิทธิพลของความเค้นอัดต่อสมบัติเฟร์โรอิเล็กตริก (Polarization-Electric Field (P-E) Loops) ของสารเซรามิกระบบเดี่ยว PZT และ PZN ด้วยเครื่องมืออัดแรงแบบแกนเดี่ยว

18 ทดสอบอิทธิพลของความเค้นอัดต่อสมบัติเฟร์โรอิเล็กตริก (Polarization-Electric Field (P-E) Loops) ของสารเซรามิกระบบคู่ PZN-PZT ด้วยเครื่องมืออัดแรงแบบแกนเดี่ยว

19 สรุปความสัมพันธ์ระหว่างสมบัติเฟร์โรอิเล็กตริกภายใต้ความเค้นอัดของ PZT และ PZN และสมบัติดังกล่าวของสารเซรามิกระบบ PZN-PZT

20 อภิปรายผลการศึกษาและการเตรียมผลงานเพื่อการตีพิมพ์

21 ทดสอบอิทธิพลของความเค้นอัดต่อสมบัติไดอิเล็กตริก (ค่าคงที่ไดอิเล็กตริก ($\varepsilon_r$) และการสูญเสียทางไดอิเล็กตริก (tan $\delta$)) ของสารเซรามิกระบบเดี่ยว PZT และ PNN ด้วยเครื่องมืออัดแรงแบบแกนเดี่ยว

22 ทดสอบอิทธิพลของความเค้นอัดต่อสมบัติไดอิเล็กตริก (ค่าคงที่ไดอิเล็กตริก ($\varepsilon_r$) และการสูญเสียทางไดอิเล็กตริก (tan $\delta$)) ของสารเซรามิกระบบคู่ PNN-PZT ด้วยเครื่องมืออัดแรงแบบแกนเดี่ยว

23 ทดสอบอิทธิพลของความเค้นอัดต่อสมบัติไดอิเล็กตริก (ค่าคงที่ไดอิเล็กตริก ($\varepsilon_r$) และการสูญเสียทางไดอิเล็กตริก (tan $\delta$)) ของสารเซรามิกระบบเดี่ยว PZT และ PCoN ด้วยเครื่องมืออัดแรงแบบแกนเดี่ยว

24 ทดสอบอิทธิพลของความเค้นอัดต่อสมบัติไดอิเล็กตริก (ค่าคงที่ไดอิเล็กตริก ($\varepsilon_r$) และการสูญเสียทางไดอิเล็กตริก (tan $\delta$)) ของสารเซรามิกระบบคู่ PCoN-PZT ด้วยเครื่องมืออัดแรงแบบแกนเดี่ยว

25 สรุปความสัมพันธ์ระหว่างสมบัติไดอิเล็กตริกภายใต้ความเค้นอัดของ PZT PNN และ PCoN และสมบัติดังกล่าวของสารเซรามิกระบบ PNN-PZT และ PCoN-PZT

26 ทดสอบอิทธิพลของความเค้นอัดต่อสมบัติเฟร์โรอิเล็กตริก (Polarization-Electric Field (P-E) Loops) ของสารเซรามิกระบบเดี่ยว PZT และ PNN ด้วยเครื่องมืออัดแรงแบบแกนเดี่ยว

27 ทดสอบอิทธิพลของความเค้นอัดต่อสมบัติเฟร์โรอิเล็กตริก (Polarization-Electric Field (P-E) Loops) ของสารเซรามิกระบบคู่ PNN-PZT ด้วยเครื่องมืออัดแรงแบบแกนเดี่ยว

28 ทดสอบอิทธิพลของความเค้นอัดต่อสมบัติเฟร์โรอิเล็กตริก (Polarization-Electric Field (P-E) Loops) ของสารเซรามิกระบบเดี่ยว PZT และ PCoN ด้วยเครื่องมืออัดแรงแบบแกนเดี่ยว

29 ทดสอบอิทธิพลของความเค้นอัดต่อสมบัติเฟร์โรอิเล็กตริก (Polarization-Electric Field (P-E) Loops) ของสารเซรามิกระบบคู่ PCoN-PZT ด้วยเครื่องมืออัดแรงแบบแกนเดี่ยว

30 สรุปความสัมพันธ์ระหว่างสมบัติสมบัติเฟร์โรอิเล็กตริกภายใต้ความเค้นอัดของ PZT PNN และ PCoN และสมบัติดังกล่าวของสารเซรามิกระบบ PNN-PZT และ PCoN-PZT

31 อภิปรายผลการศึกษาและสรุปผลการวิจัย ตลอดจนข้อเสนอแนะในรูปแบบการเขียนรายงานฉบับสมบูรณ์ และการเตรียมผลงานเพื่อการตีพิมพ์

**4. ประโยชน์ที่ได้รับจากโครงการวิจัยนี้**

1 องค์ความรู้ใหม่ในเรื่องกระบวนการเตรียมผงและเซรามิกในระบบ PNN PCoN PZT PNN-PZT และ PCoN-PZT

2 องค์ความรู้ใหม่ในเรื่องของอิทธิพลของความเค้นอัดต่อสมบัติไดอิเล็กตริกของสารเซรามิกระบบเดี่ยว PZT PNN และ PCoN

3 องค์ความรู้ใหม่ในเรื่องของอิทธิพลของความเค้นอัดต่อสมบัติไดอิเล็กตริกของสารเซรามิกระบบคู่ PNN-PZT และ PCoN-PZT

4 ความรู้ความเข้าใจถึงความสัมพันธ์ระหว่างสมบัติไดอิเล็กตริกภายใต้ความเค้นอัดของแต่ละองค์ประกอบและสมบัติดังกล่าวของสารเซรามิกระบบคู่

5 องค์ความรู้ใหม่ในเรื่องของอิทธิพลของความเค้นอัดต่อสมบัติเฟร์โรอิเล็กตริกของสารเซรามิกระบบเดี่ยว PMN PT PIN PZN PZT PNN และ PCoN

6 องค์ความรู้ใหม่ในเรื่องของอิทธิพลของความเค้นอัดต่อสมบัติเฟร์โรอิเล็กตริกของสารเซรามิกระบบคู่ PMN-PT PIN-PT PZN-PZT PNN-PZT และ PCoN-PZT

7 ความรู้ความเข้าใจถึงความสัมพันธ์ระหว่างสมบัติเฟร์โรอิเล็กตริกภายใต้ความเค้นอัดของแต่ละองค์ประกอบและสมบัติดังกล่าวของสารเซรามิกระบบคู่

8 ผลงานวิจัยในรูปของสิ่งตีพิมพ์ ได้แก่สิ่งตีพิมพ์ในวารสารทางวิชาการต่างๆ การนำเสนอผลงานในการประชุมวิชาการและสัมมนา หรือหนังสือตำราวิชาการ เพื่อเป็นการพัฒนาวิชาชีพอาจารย์ให้มีศักยภาพในการผลิตนักศึกษาระดับปริญญาเอกได้

9 องค์ความรู้ใหม่ที่จะนำไปใช้ประกอบการเรียนการสอนและการปรับปรุงกระบวนวิชาในหลักสูตรวัสดุศาสตร์ทั้งในระดับปริญญาตรีและระดับบัณฑิตศึกษาที่ผู้วิจัยรับผิดชอบอยู่ต่อไป

10 นักวิจัยรุ่นกลางที่มีความรู้ทางด้านสารเซรามิกเฟร์โรอิเล็กตริกกลุ่มเพอรอพสไกต์และแนวทางในการกำหนดหัวข้อวิทยานิพนธ์สำหรับการพัฒนาบุคลากรทางด้านวัสดุศาสตร์ที่เกี่ยวข้องทั้งในระดับปริญญาโท และเอก สาขาวัสดุศาสตร์อย่างต่อเนื่อง

11 การเชื่อมโยงด้านการวิจัยระหว่างนักวิจัยในประเทศท่านอื่นซึ่งได้รับทุนผู้รับทุนพัฒนาศักยภาพในการทำงานวิจัยของอาจารย์รุ่นใหม่และรุ่นกลางที่มีความร่วมมือกันอย่างใกล้ชิด รวมทั้งกับนักวิจัยชั้นนำในระดับนานาชาติ

12 แนวทางการพัฒนาชุดโครงการวิจัยและการสร้างความร่วมมือของกลุ่มนักวิจัยภายในสถาบันต้นสังกัดและระหว่างกลุ่มวิจัยต่างๆที่สนใจในเรื่องที่เกี่ยวข้องกันทั้งในและต่างประเทศ

**5. สรุปผลที่ได้จากโครงการวิจัยนี้**

เมื่อพิจารณาจากวัตถุประสงค์ของโครงการวิจัยทั้ง 6 ข้อแล้ว โดยสรุปสามารถแบ่งองค์ความรู้ใหม่ที่ได้จากโครงการวิจัยนี้ออกเป็น 4 กลุ่มใหญ่ กล่าวคือ

1. องค์ความรู้ใหม่ในเรื่องกระบวนการเตรียมผงและเซรามิกในระบบ PNN PCoN PZT PNN-PZT และ PCoN-PZT และความสัมพันธ์ระหว่างสมบัติไดอิเล็กตริกและสมบัติเฟร์โรอิเล็กตริกของสารเซรามิกระบบดังกล่าว
2. องค์ความรู้ใหม่ในเรื่องอิทธิพลของความเค้นอัดต่อสมบัติเฟร์โรอิเล็กตริกของสารเซรามิกระบบเดี่ยว PT PZT PIN PMN และ PZN และสารเซรามิกระบบคู่ PZN-PZT PMN-PT และ PIN-PT พร้อมทั้งความสัมพันธ์ระหว่างสมบัติเฟร์โรอิเล็กตริกภายใต้ความเค้นอัดของแต่ละองค์ประกอบและสมบัติดังกล่าวของสารเซรามิกระบบคู่
3. องค์ความรู้ใหม่ในเรื่องอิทธิพลของความเค้นอัดต่อสมบัติไดอิเล็กตริกและสมบัติเฟร์โรอิเล็กตริกของสารเซรามิกระบบเดี่ยว PCoN และ PNN และ สารเซรามิกระบบคู่ PCoN-PZT และ PNN-PZT พร้อมทั้งความสัมพันธ์ระหว่างสมบัติไดอิเล็กตริกและสมบัติเฟร์โรอิเล็กตริกภายใต้ความเค้นอัดของแต่ละองค์ประกอบและสมบัติดังกล่าวของสารเซรามิกระบบคู่
4. องค์ความรู้ใหม่ด้านอื่นๆที่ถือเป็นการต่อยอดจากผลงานที่ได้ศึกษามาในเบื้องต้น

ซึ่งผลงานที่ได้ใน 4 กลุ่มนั้น ถือเป็นผลงานที่เกี่ยวข้อง*โดยตรง*กับโครงการวิจัยนี้ ดังจะได้กล่าวถึงในรายละเอียดต่อไป

**ส่วนที่ 1:** สำหรับองค์ความรู้ใหม่ในเรื่องกระบวนการเตรียมผงและเซรามิกในระบบ PNN PCoN PZT PNN-PZT และ PCoN-PZT นั้น กลุ่มผู้วิจัยได้ประสบความสำเร็จในการเตรียมผงและเซรามิกในระบบ $Pb(Ni_{1/3}Nb_{2/3})O_3$ หรือ PNN $Pb(Zr_{0.52}Ti_{0.48})O_3$ $Pb(Co_{1/3}Nb_{2/3})O_3$)หรือ PCoN และ $Pb(Zr_{1/2}Ti_{1/2})O_3$ หรือ PZT ด้วยการใช้เทคนิคผสมออกไซด์ โดยศึกษาหาเงื่อนไขที่เหมาะสมต่อการเตรียมผงให้มีความบริสุทธิ์สูง และศึกษาหาเงื่อนไขในการเผาที่เหมาะสมต่อการเตรียมเซรามิก เหล่านี้ให้มีความบริสุทธิ์และความหนาแน่นสูง นอกจากนี้ก็ได้เตรียมผงและเซรามิกในระบบ (1-x)PZT-xPNN และ (1-x)PZT-xPCoN เมื่อ x มีค่าเป็น 0.1, 0.2, 0.3, 0.4 และ 0.5 ด้วยการใช้เทคนิคผสมออกไซด์เช่นกัน ส่วนองค์ความรู้ใหม่ในเรื่องของสมบัติไดอิเล็กตริกและทางไฟฟ้าอื่นๆของสารเซรามิกในทุกระบบนั้น ได้รับโดยตรงจากการทำการตรวจสอบคุณลักษณะเฉพาะและคุณสมบัติต่างๆของเซรามิกที่เตรียมได้ ผลงาน

ที่ได้รับนั้นได้ถูกนำไปตีพิมพ์ในวารสารทางวิชาการต่างๆ ดังต่อไปนี้ (ทั้งนี้ รายละเอียดได้ถูกนำเสนอในแต่ละผลงานแล้ว และในกรณีที่เป็นผลงานตีพิมพ์ในวารสารวิชาการนานาชาติสามารถค้นคว้าเพิ่มเติมได้ในภาคผนวก)

*ผลงานตีพิมพ์ในวารสารวิชาการนานาชาติ (จำนวน 11 เรื่อง)*

1. O. Khamman, **R. Yimnirun**, and S. Ananta, "Effect of calcination conditions on phase formation and particle size of lead nickel niobate powders synthesized by using $Ni_4Nb_2O_9$ precursor" *Materials Letters,* 61, pp 4466-4470 (2007)
2. N. Vittayakorn, S. Wirunchit, S. Traisak, **R. Yimnirun**, G. Rujijanagul, "Development of Perovskite and Phase Transition in Lead Cobalt Niobate Modified Lead Zirconate Titanate System" *Current Applied Physics,* 8, pp 128-133 (2008)
3. Anurak Prasatkhetragarn, Naratip Vittayakorn, Supon Ananta, **Rattikorn Yimnirun** and David P. Cann, "Synthesis, dielectric and ferroelectric properties of ceramics in the *(1-x)*$Pb(Zr_{1/2}Ti_{1/2})O_3$ – *(x)*$Pb(Co_{1/3}Nb_{2/3})O_3$ system" *Japan Journal of Applied Physics*, 47(2), pp 998-1002 (2008).
4. O. Khamman, **R. Yimnirun**, and S. Ananta, "Effect of vibro-milling time on phase formation and particle size of nickel niobate nanopowders" *Materials Science and Engineering B*, 150(1), pp 12-17 (2008)
5. Orawan Khamman, **Rattikorn Yimnirun**, Supon Ananta, "Effect of Niobate B-Site Precursor of Phase Formation of PNN Powders" *J. Alloys and Compounds*, 465, pp522-526 (2008).
6. Muangjai Unruan, Naratip Vittayakorn, Rewadee Wongmaneeruang, Anurak Prasatkhetragarn, Supon Ananta and **Rattikorn Yimnirun**, "Synthesis and Properties of $Pb(Co_{1/3}Nb_{2/3})O_3$ Ceramics" *J. Alloys and Compounds*, 466, pp 264-267 (2008).
7. S. Ananta,, **R. Yimnirun**, and O. Khamman "Effect of nickel niobate B-site precursors on phase formation, microstructure and dielectric properties of perovskite PNN ceramics" *Functional Materials Letters*, 1(3), pp 229-233 (2008)
8. P. Ketsuwan, Y. Laosiritaworn, S. Ananta, **R. Yimnirun**, "Electrical Properties of Nb-Doped $Pb(Zr_{0.52}Ti_{0.48})O_3$ Ceramics" *International Journal of Modern Physics B*, 23, pp 105-111 (2009)

9. Anurak Prasatkhetragarn, Athipong Ngamjarurojana, Yongyut Laosiritaworn, Supon Ananta, **Rattikorn Yimnirun**, and David Cann, “Effects of Zr/Ti ratio on phase formation and electrical properties of $0.8Pb(Zr_{1/2}Ti_{1/2})O_3$-$0.2Pb(Co_{1/3}Nb_{2/3})O_3$ ceramics” *Current Applied Physics*, 9, pp 802-806 (2009)
10. Anurak Prasatkhetragarn, Piyachon Ketsuwan, Supon Ananta, **Rattikorn Yimnirun**, and David Cann “Phase Formation, Microstructure and Dielectric Properties of $(1-x)Pb(Zr_{1/2}Ti_{1/2})O_3–xPb(Co_{1/3}Nb_{2/3})O_3$ Ceramics” *Materials Letters,* 63, pp 1281-1284 (2009)
11. Anurak Prasatkhetragarn, Athipong Ngamjarurojana, Yongyut Laosiritaworn, Supon Ananta, **Rattikorn Yimnirun**, and David Cann, “Effects of sintering conditions on phase formation and electrical properties of $0.8Pb(Zr_{1/2}Ti_{1/2})O_3$-$0.2Pb(Co_{1/3}Nb_{2/3})O_3$ ceramics” *Current Applied Physics* (2009) *in press*

*ผลงานตีพิมพ์ในวารสารประกอบการประชุมวิชาการระดับนานาชาติ (จำนวน 1 เรื่อง)*

1. W. Laosiritaworn, O. Khamman, S. Ananta, **R. Yimnirun** and Y. Laosiritaworn, “Artificial Neural Network Modeling of Ceramics Powder Preparation: application to $NiNb_2O_6$” *Ceramics International,* 34(4), pp 809-812 (2008).

**ส่วนที่ 2:** ในส่วนนี้นั้นถือเป็นผลงานหลักของโครงการวิจัยนี้ โดยเป็นองค์ความรู้ใหม่ในเรื่องของอิทธิพลของความเค้นแบบแกนเดี่ยวต่อสมบัติเฟร์โรอิเล็กตริกของสารเซรามิกระบบเดี่ยว PT PZT PIN PMN และ PZN และสารเซรามิกระบบคู่ PZN-PZT PMN-PT และ PIN-PT ซึ่งได้จากการใช้เครื่องมืออัดแรงแบบแกนเดี่ยวประกอบในการวัดสมบัติไดอิเล็กตริก เช่น ค่าคงที่ไดอิเล็กตริก ($\varepsilon_r$) และการสูญเสียทางไดอิเล็กตริก (tan $\delta$) และสมบัติอื่นๆ เช่น สมบัติเฟร์โรอิเล็กทริกฮิสเทอรีซิส (วงวน P-E) ของสารเซรามิกในทุกระบบที่กล่าวมาภายใต้ความเค้นแบบแกนเดี่ยว และผลงานที่ได้นั้นก็ได้ถูกนำไปตีพิมพ์ในวารสารทางวิชาการต่างๆ ดังต่อไปนี้ (รายละเอียดได้ถูกนำเสนอในแต่ละผลงานแล้ว และในกรณีที่เป็นผลงานตีพิมพ์ในวารสารวิชาการนานาชาติสามารถค้นคว้าเพิ่มเติมได้ในภาคผนวก)

*ผลงานตีพิมพ์ในวารสารวิชาการนานาชาติ (จำนวน 20 เรื่อง)*

1. S. Wongsaenmai, W. Qu, S. Ananta, **R. Yimnirun**, and X. Tan, “Effect of Ba-substitution on the structure and properties of $Pb_{0.8}Ba_{0.2}In_{0.5}Nb_{0.5}O_3$ ceramics” *Applied Physics A,* 88, pp 757-761 (2007).

2. S. Wongsaenmai, **R. Yimnirun,** S. Ananta, R. Guo, and, A. Bhalla, "Thermal Expansion Measurement in the Relaxor Ferroelectric PIN-PT System" *Materials Letters*, 62, pp 352-356 (2008)
3. M. Unruan, S. Wongsaenmai, Y. Laosiritaworn, S. Ananta, and **R. Yimnirun**, "Changes in Dielectric Properties of $Pb(In_{1/2}Nb_{1/2})O_3$-$PbTiO_3$ Ceramics Under Compressive Stress Applied Parallel and Perpendicular to Electric Field" *J. Phys. D: Appl. Phys.,* 41*,* pp 541-545 (2008)*.*
4. Supattra Wongsaenmai, Xiaoli Tan, Supon Ananta, and **Rattikorn Yimnirun**, "Dielectric and Ferroelectric Properties of Fine Grains $Pb(In_{1/2}Nb_{1/2})O_3$–$PbTiO_3$ Ceramics" *Journal of Alloys and Compounds*, 454, pp 331-339 (2008).
5. **R. Yimnirun**, N. Wongdamnern, N. Triamnak, M. Unruan, A. Ngamjarurojana, S. Ananta, and Y. Laosiritaworn, "Stress-Dependent Scaling Behavior of Sub-Coercive Field Dynamic Ferroelectric Hysteresis in $Pb(Zn_{1/3}Nb_{2/3})O_3$-Modified $Pb(Zr_{1/2}Ti_{1/2})O_3$ Ceramic" *J. Applied. Physics,* 103 (8)*,* pp 086105-1-3 (2008).
6. R. Wongmaneerung, **R. Yimnirun,** S. Ananta,. A. Bhalla, and R. Guo, "Thermal Expansion Measurement in the PMN-PT Ceramic Systems" *J. Alloys and Compounds,* 461, pp 565-569 (2008)*.*
7. Muangjai Unruan, Athipong Ngamjarurojana, Yongyut Laosiritaworn, Supon Ananta, and **Rattikorn Yimnirun**, "Influences of Perpendicular Compressive Stress on Ferroelectric Properties of Electrostrictive and Piezoelectric $Pb(Mg_{1/3}Nb_{2/3})O_3$-$PbTiO_3$ Ceramics" *J. Applied Physics.* 104, 034101 (2008).
8. M. Unruan, R. Wongmaneerung, A. Ngamjarurojana, S. Ananta, Y. Laosiritaworn, and **R. Yimnirun,** "Changes of Ferroelectric Properties of Lead Magnsium Niobate-Lead Titanate Ceramics Under Compressive Stress" *J. Applied Physics.* 104, 064107 (2008)
9. **R. Yimnirun**, N. Wongdamnern, N. Triamnak, M. Unruan, A. Ngamjarurojana, S. Ananta, and Y. Laosiritaworn, "Stress-Dependent Scaling Behavior of Sub-Coercive Field Dynamic Ferroelectric Hysteresis in $0.4Pb(Zn_{1/3}Nb_{2/3})O_3$-$0.6Pb(Zr_{1/2}Ti_{1/2})O_3$ Ceramic" *J. Physics: Condensed Matters.* 20, 415202 (2008)
10. **R. Yimnirun**, N. Wongdamnern, N. Triamnak, T. Sareein, M. Unruan, A. Ngamjarurojana, S. Ananta, and Y. Laosiritaworn, "Power-law Scaling of Sub-Coercive Field Dynamic Ferroelectric Hysteresis in $0.3Pb(Zn_{1/3}Nb_{2/3})O_3$-

$0.7Pb(Zr_{1/2}Ti_{1/2})O_3$ Ceramic" *J. Physics D: Applied. Physics,* 41, 205415 (2008)

11. **R. Yimnirun**, N. Wongdamnern, N. Triamnak, M. Unruan, A. Ngamjarurojana, S. Ananta, and Y. Laosiritaworn, "Stress-Dependent Scaling Behavior of Sub-Coercive Field Dynamic Ferroelectric Hysteresis in $0.5Pb(Zn_{1/3}Nb_{2/3})O_3$-$0.5Pb(Zr_{1/2}Ti_{1/2})O_3$ Ceramic" *J. Applied. Physics,* **104***,* pp 104103-1-4 (2008)
12. **Rattikorn Yimnirun**, Narit Triamnak, Muangjai Unruan, Athipong Ngamjarurojana, Yongyut Laosiritaworn, and Supon Ananta, "Ferroelectric Properties of $Pb(Zr_{1/2}Ti_{1/2})O_3$—$Pb(Zn_{1/3}Nb_{2/3})O_3$ Ceramics Under Compressive Stress" *Current Applied Physics*, 9, pp 249-252 (2009)
13. R. Wongmaneerung, **R. Yimnirun**, S. Ananta, "Processing and Properties of $Pb(Mg_{1/3}Nb_{2/3})O_3$-$PbTiO_3$ Based Ceramics" *Current Applied Physics*, 9, pp 268-273 (2009).
14. **R. Yimnirun**, S. Wongsaenmai, S. Ananta, N. Triamnak, "Dielectric Properties of PIN-PT Ceramics Under Compressive Stress" *Current Applied Physics,* 9, pp 422-425 (2009).
15. **R. Yimnirun** "Dielectric Properties of PMN-PT Prepared by Mixed Oxide Method" *International Journal of Modern Physics B*, 23(3), pp 403-410 (2009)
16. R. Wongmaneerung, **R. Yimnirun**, and S. Ananta, "Effect of two-stage sintering on phase formation, microstructure and dielectric properties of perovskite PMN ceramics derived from a corundum $Mg_4Nb_2O_9$ precursor" *Materials Chemistry and Physics*, 114, pp 569-575 (2009)
17. S. Wongsaenmai, S. Ananta, and **R. Yimnirun**, "Effects of Addition of BT on Structural Phase Formation and Electrical Properties of Relaxor Ferroelectric $Pb(In_{0.5}Nb_{0.5})_{(1-x)}Ti_{(x)}O_3$ ceramics" *J. Alloys and Compounds,* 474, pp 241-245 (2009)
18. R. Wongmaneerung, A. Rujiwatra, **R. Yimnirun**, and S. Ananta, "Fabrication and Dielectric Properties of Self-reinforced Lead Titanate Nanocomposites" *J. Alloys and Compounds,* 475, pp 473-478 (2009)
19. R. Wongmaneerung, P. Singjai, **R. Yimnirun** and S. Ananta, "Effects of SiC nanofibers Addition on Microstructure and Dielectric Properties of Lead Titanate Ceramics" *J. Alloys and Compounds,* 475, pp 456-462 (2009)
20. R. Wongmaneerung, **R. Yimnirun**, and S. Ananta, "Effect of Magnasium Niobate Precursors on Phase Formation, Microstructure and Dielectric

Properties of Perovskite Lead Magnesium Niobate Ceramics" *J. Alloys and Compounds* (2008) *in press*

*ผลงานตีพิมพ์ในวารสารประกอบการประชุมวิชาการระดับนานาชาติ (จำนวน 2 เรื่อง)*

1. **R. Yimnirun**, S. Wongsaenmai, R. Wongmaneerung, N. Wongdamnern, A. Ngamjarurojana, S. Ananta, and Y. Laosiritaworn, " Stress- and Temperature-Dependent Scaling Behavior of Dynamic Hysteres-is in Soft PZT Bulk Ceramics" *Physica Scripta*, T129, pp 184-189 (2007)
2. A. Ngamjarurojana, S. Ural, S.H. Park, S. Ananta, **R. Yimnirun**, and K. Uchino, "Piezoelectric Properties of Low Temperature Sintering in $Pb(Zr,Ti)O_3$ - $Pb(Zn,Ni)_{1/3}Nb_{2/3}O_3$ Ceramics for Piezoelectric Transformer Applications" *Ceramics International,* 34(4), pp 705-708 (2008).

**ส่วนที่ 3:** เช่นเดียวกับส่วนที่ 2 ในส่วนนี้นั้นถือเป็นผลงานหลักของโครงการวิจัยนี้ โดยองค์ความรู้ใหม่ในเรื่องอิทธิพลของความเค้นอัดต่อสมบัติไดอิเล็กตริกและสมบัติเฟร์โรอิเล็กตริกของสารเซรามิกระบบเดี่ยว PCoN และ PNN และ สารเซรามิกระบบคู่ PCoN-PZT และ PNN-PZT พร้อมทั้งความสัมพันธ์ระหว่างสมบัติไดอิเล็กตริกและสมบัติเฟร์โรอิเล็กตริกภายใต้ความเค้นอัดของแต่ละองค์ประกอบและสมบัติดังกล่าวของสารเซรามิกระบบคู่นั้น ได้จากการใช้เครื่องมืออัดแรงแบบแกนเดี่ยวประกอบในการวัดสมบัติไดอิเล็กตริก เช่น ค่าคงที่ไดอิเล็กตริก ($\varepsilon_r$) และการสูญเสียทางไดอิเล็กตริก ($\tan \delta$) และสมบัติอื่นๆ เช่น สมบัติเฟร์โรอิเล็กทริกฮิสเทอรีซิส (วงวน P-E) ของสารเซรามิกในทุกระบบที่กล่าวมาภายใต้ความเค้นแบบแกนเดี่ยว และผลงานที่ได้นั้นก็ได้ถูกนำไปตีพิมพ์ในวารสารทางวิชาการต่างๆ ดังต่อไปนี้ (รายละเอียดได้ถูกนำเสนอในแต่ละผลงานแล้ว และในกรณีที่เป็นผลงานตีพิมพ์ในวารสารวิชาการนานาชาติสามารถค้นคว้าเพิ่มเติมได้ในภาคผนวก)

*ผลงานตีพิมพ์ในวารสารวิชาการนานาชาติ (จำนวน 3 เรื่อง)*

1. Muangjai Unruan, Anurak Prasatkhetragarn, Yongyut Laosiritaworn, Supon Ananta, and **Rattikorn Yimnirun**, "Dielectric Properties of PZT-PCN Ceramics Under Compressive Stress" *Physica Scripta,* 77, pp 571-574 (2008).
2. Muangjai Unruan , Anurak Prasatkhetragarn, Yongyut Laosiritaworn, Supon Ananta, and **Rattikorn Yimnirun**, "Changes in Dielectric Properties of $Pb(Zr_{1/2}Ti_{1/2})O_3$-$Pb(Co_{1/3}Nb_{2/3})O_3$ Ceramics Under Compressive Stress

Applied Perpendicular to Electric Field" to *J. Phys. D:Applied Physics,* **41**, pp 245405 (2008)

3. Muangjai Unruan , Anurak Prasatkhetragarn, Athipon Ngamjarurojana, Yongyut Laosiritaworn, Supon Ananta, and **Rattikorn Yimnirun**, "Changes in Dielectric and Ferroelectric Properties of $Pb(Zr_{1/2}Ti_{1/2})O_3$-$Pb(Ni_{1/3}Nb_{2/3})O_3$ Ceramics Under Compressive Stress" *J. Applied Physics,* **105***,* (2009)

**ส่วนที่ 4**: ในส่วนนี้ เป็นการศึกษาหาองค์ความรู้ใหม่ด้านอื่นๆที่ถือเป็นการต่อยอดจากผลงานที่ได้ศึกษามาในเบื้องต้น ซึ่งผลงานที่ได้มีความหลากหลายและเป็นจุดเริ่มต้นในการวิจัยอีกหลายๆโครงการของผู้ที่มีส่วนร่วมในโครงการวิจัยนี้ และผลงานที่ได้นั้นก็ได้ถูกนำไปตีพิมพ์ในวารสารทางวิชาการต่างๆ ดังต่อไปนี้ (รายละเอียดได้ถูกนำเสนอในแต่ละผลงานแล้ว และในกรณีที่เป็นผลงานตีพิมพ์ในวารสารวิชาการนานาชาติสามารถค้นคว้าเพิ่มเติมได้ในภาคผนวก)

*ผลงานตีพิมพ์ในวารสารวิชาการนานาชาติ (จำนวน 12 เรื่อง)*

1. Yongyut Laosiritaworn, Supon Ananta**,** and **Rattikorn Yimnirun**, "Effects of Temperature Gradient of Magnetic Properties of Ising Thin-Film", *Physical Review B,* 75, pp 054417 (2007)
2. Prasit Thongbai, Chivalrat Masingboon, Santi Maensir, T. Yamwong, S. Wongsaenmai, and **R. Yimnirun**, "Giant dielectric behavior of $CaCu_3Ti_4O_{12}$ subjected to post-sintering annealing and uniaxial stress" *J. Phys.: Condensed Matter,* 19, pp 236208-1-10 (2007).
3. R. Wongmaneerung, X. Tan, R.W. McCullum, S. Ananta, and **R. Yimnirun**, Cation-, dipole-, and spin-order in $Pb(Fe_{2/3}W_{1/3})O_3$-based magnetoelectric multiferroic compounds" *Applied Physics Letters,* 90, 242905 (2007)
4. **R. Yimnirun**, R. Wongmaneerung, S. Wongsaenmai, A. Ngamjarurojana, S. Ananta, and Y. Laosiritaworn, "Temperature Scaling of Dynamic Hysteresis in Hard Lead Zirconate Titanate Bulk Ceramic" *Applied Physics A*, 89, pp 737-741 (2007).
5. Prasit Thongbai, Santi Maensiri, Teerapon Yamwong, and **Rattikorn Yimnirun** "Giant dielectric properties of $CaCu_3Ti_4O_{12}$/(Li, Ti)-doped NiO composites subjected to post-sintering annealing and compressive stress" *J. Applied Physics*, 103, pp 114107-1-6 (2008).

6. **Rattikorn Yimnirun,** "Scaling Behavior of Dynamic Hysteresis in PZT-Based Ferroelectric Bulk Ceramics" *Functional Materials Letters*, 1(2), pp 133-137 (2008).
7. M. Unruan, T. Sareein, J. Tangsritrakul, S. Prasertpalichatr, A. Ngamjarurojana, S. Ananta, and **R. Yimnirun**, "Changes in Dielectric and Ferroelectric Properties of $Fe^{3+}/Nb^{5+}$ Hybrid-Doped Barium Titanate Ceramics Under Compressive Stress" *J. Applied Physics,* **104**, pp 124102-1-5 (2008)
8. N. Wongdamnern, A. Ngamjarurojana, Y. Laosiritaworn, S. Ananta, and **R. Yimnirun**, "Dynamic Ferroelectric Hysteresis Scaling in $BaTiO_3$ Single Crystals" *Journal of Applied Physics,* 105, 044109 (2009)
9. O. Khamman, X. Tan, S. Ananta, and **R. Yimnirun**, "The morphotropic phase boundary and electrical properties of $(1-x)Pb(Zn_{1/2}W_{1/2})O_3$—$xPb(Zr_{0.5}Ti_{0.5})O_3$ ceramics" *J. Materials Science*, 44, pp 1868-1872 (2009)
10. T. Sareein, M. Unruan, A. Ngamjarurojana, S. Jiansirisomboon, A. Watcharapasorn, and **R. Yimnirun**, "Influences of Compressive Stress and Aging on Dielectric Properties of Sodium Bismuth Titanate Ceramics" *Physics Letters A,* 373, pp 1583-1587 (2009)
11. **Rattikorn Yimnirun**, Muangjai Unruan, Rewadee Wongmaneerung, Orawan Khamman, Wanwilai Chaisan, and Supon Ananta, "Dielectric Properties of Complex Perovskite PZBT-PMNT Ceramic Under Compressive Stress" *International Journal of Modern Physics B* (2009) *accepted*
12. A. Chaipanich, N. Jaitanong and **R. Yimnirun**, "Ferroelectric Hysteresis Behavior in 0-3 PZT-Cement Composites: Effects of Frequency and Electric Field" *Ferroelectric Letters* (2009) *accepted*

*ผลงานตีพิมพ์ในวารสารประกอบการประชุมวิชาการระดับนานาชาติ (จำนวน 5 เรื่อง)*

1. W. Chaisan, **R. Yimnirun**, S. Ananta, " Effects of Compressice Stress of Ferroelectric Properties of BT Ceramics" *Physica Scripta*, T129, pp 205-208 (2007)
2. N. Wongdamnern, N. Triamnak, A. Ngamjarurojana, Y. Laosiritaworn, S. Ananta, and **R. Yimnirun**, "Comparative Studies of Dynamic Hysteresis Responses in Hard and Soft PZT Ceramics" *Ceramics International,* 34(4), pp 731-734 (2008).

3. Y. Laosiritaworn, S. Ananta, J. Poulter, and **R. Yimnirun**, “Monte Carlo investigation of hysteresis properties in ferroelectric thin-films under the effect of uniaxial stresses” *Ceramics International*, 35*,* pp 181-184 (2009)
4. W. Chaisan, **R. Yimnirun**, and S. Ananta, “Preparation and characterization of ceramic nanocomposites in the PZT–BT system” *Ceramics International,* 35*,* pp 121-124 (2009)
5. W. Chaisan, **R. Yimnirun**, and S. Ananta, “Effect of vibro-milling time on phase formation and particle size of barium titanate nanopowders” *Ceramics International*, 35*,* pp 173-176 (2009)

## เอกสารอ้างอิง


1. B. Jaffe, W.R. Cook Jr., and H. Jaffe, *Piezoelectric Ceramics*, Academic Press, 1971.
2. Y. Xu, *Ferroelectric Materials and Their Applications*, North-Holland, 1991.
3. A.J. Moulson and J.M. Herbert, *Electroceramics*, Chapman and Hall, 1993.
4. R.E. Newnham and G.R. Ruschau, *Am. Ceram. Soc. Bull*. **75**[10] 51 (1996).
5. K. Uchino, *Piezoelectric Actuators and Ultrasonic Motors*, Kluwer Academic, 1997.
6. J.F. Scott, *Ferroelectrics*, **206/207**, 365 (1998).
7. G.H. Haertling, *J. Am. Ceram. Soc.* **82**[4] 797 (1999).
8. A.S. Bhalla, R. Guo and R. Roy, Mat. Res. Innovat. **4**, 3 (2000)
9. S.E.E Park and W. Hackenberger, *Current Opinion Sol. State Mat. Sci.* **6**, 11 (2002).
10. H. Chen, X. Guo and Z. Meng, *Mater. Chem.Phys.* **75**, 202 (2002).
11. R. Zuo, L. Li, X. Hu and Z. Gui, *Mater. Lett*. **54**, 185 (2002).
12. Y. H. Chen, K. Uchino, M. Shen and D. Viehland, *J. Appl. Phys.* **90(3)**, 1455 (2001).
13. H. Chen, J. Long and Z. Meng, *Mater. Sci. Eng*. **B99**, 433 (2003).
14. S. Priya, K. Uchino and D. Viehland, *Appl. Phys. Lett*. **81(13)**, 2430 (2002).
15. N. Yasuda, H. Ohwa, M. Kume, K. Hayashi, Y. Hosono and Y. Yamashita, *J. Cryst. Growth*. **229**, 299 (1999).
16. E. F. Alberta and A. S. Bhalla, *Mater. Lett*. **40**, 114 (1999).
17. E. F. Alberta and A. S. Bhalla, *Mater. Lett*. **29**, 127 (1996).
18. H. Ouchi, *J. Am. Ceram. Soc.* **51** 169 (1968).
19. C.H. Wang, *J. Eur. Ceram. Soc*. **22** 2033 (2002).

20. R. Yimnirun, S. Ananta, E. Meechoowas and S. Wongsaenmai, *J. Phys. D: Appl. Phys*. **36,** 1615 (2003).
21. R. Yimnirun, S. Ananta and P. Laoratanakul, *Mater. Sci. Eng. B* **112,** 79 (2004).
22. W. Chaisan, R. Yimnirun, S. Ananta and D. Cann, *Mater. Lett.*, **59,** 3732 (2005).
23. R. Yimnirun, S. Ananta and P. Laoratanakul, *J. Eur. Ceram. Soc* **25,** 3225 (2005).
24. R. Tipakontitikul, S. Ananta, and R. Yimnirun, *Curr. Appl. Phys.* **6**, 307 (2006).
25. H. Cai, Z. Gui and L.T. Li, *Mat. Sci. Eng. B-Solid* **83**, 137 (2001).
26. A.S. Bhalla, R. Guo and E.F. Alberta, *Mater. Lett.* **54**, 264 (2002).
27. R. Yimnirun, R. Tipakontitikul, and S. Ananta, *Int. J. Mod. Phys. B* **20**, 2415 (2006).
28. T.R. Shrout and J.P. Dougherty, *Ceramic Transactions: Ceramic Dielectrics*, American Ceramic Society, Westerville, O.H. **8**, 3 (1990).
29. S. Ananta and N.W. Thomas, *J. Eur. Ceram. Soc*. **19**, 1873 (1999).
30. S. Wongsaenmai, Y. Laosiritaworn, S. Ananta, and R. Yimnirun, *Mater. Sci. Eng. B* **128**, 83 (2006).
31. A.L. Costa, C. Galassi, G. Fabbri, E. Roncari and C. Capiani, *J. Eur. Ceram. Soc*. **21**, 1165 (2001).
32. J. Kuwata, K. Uchino and S. Nomura, *Jpn. J. Appl. Phys., Part 1*, **21**, 1298 (1982).
33. S.E. Park and T.R. Shrout, *J. Appl. Phys.* **82**, 1804 (1997).
34. B.D. Stojanovic, *J. Mater. Proc. Tech.* **143-144**, 78 (2003).
35. N. Vittayakorn, G. Rujijanagul, T. Tunkasiri, X. Tan, and D. P. Cann, *Mat. Sci. Eng. B* **108**, 258 (2004).
36. N. Vittayakorn, G. Rujijanagul, T. Tunkasiri, X. Tan and D. P. Cann, *J. Mat. Res.* **18**, 2882 (2003)
37. N. Vittayakorn, G. Rujijanagul, X, Tan, M. A. Marquardt, and D. P. Cann, *J. Appl. Phys.* **96(9)**, 5103 (2004)
38. N. Vittayakorn, G. Rujijanagul, X, Tan, and D. P. Cann, *J. Electroceramics* (*in press)*
39. N. Vittayakorn, G. Rujijanagul, X, Tan, and D. P. Cann, *Curr. Appl. Phys.* (*in press*).
40. E.F. Alberta and A.S. Bhalla, *J. Phys. Chem. Solids*, **63**, 1759 (2002).
41. H.K. Guo, X.G. Tang, J.X. Zhang, S.W. Shan, M.M. Wu and Y.J. Luo, *J. Mater. Sci. Lett.* **17**, 1567 (1998).
42. M. Lejeune and J.P. Boilot, *Mater. Res. Bull*. **17**, 1245 (1982).
43. K. Chen, C. Li, X. Zhang and Y. Huang, *Mater. Lett*. **57**, 20 (2002).
44. H. Fan and H.E. Kim, *J. Appl. Phys.* **91(1)**, 317 (2002).

45. N. Vittayakorn, S. Uttiya, G. Rujijanagul, and D. P. Cann, *J. Phys. D: Appl. Phys.*, **38**, 2942 (2005)
46. R. Yimnirun, Y. Laosiritaworn, and S. Wongsaenmai, *J. Phys. D: Appl. Phys.* **39,** 759 (2006).
47. Q.M. Zhang, J. Zhao, K. Uchino and J. Zheng, *J. Mater. Res.* **12[1],** 226 (1997).
48. D. Viehland, J.F. Li, E. McLaughlin, J. Powers, R. Janus and H. Robinson, *J. Appl. Phys.* **95(4)**, 1969 (2004).
49. I.J. Fritz, *J. Appl. Phys.* **49(9)**, 4922 (1978).
50. D. Viehland and J. Powers, *Appl. Phys. Lett.* **78(20)**, 3112 (2001).
51. R. Yimnirun, *Ferroelectrics* **331**, 9 (2006).
52. J. Zhao, A.E. Glazounov and Q.M. Zhang, *Appl. Phys. Lett.* **74(3)**, 4362 (1999).
53. R. Yimnirun, M. Unruen, Y. Laosiritaworn, and S. Ananta, *J. Phys. D: Appl. Phys.* **39**, 3097 (2006).
54. R. Yimnirun, S. Wongsaenmai, A. Ngamjarurojana, and S. Ananta, *Curr. Appl. Phys,* **6** 520 (2006).
55. รัตติกร ยิ้มนิรัญ, อิทธิพลของความเค้นแบบแกนเดี่ยวต่อสมบัติไดอิเล็กตริกและไฟฟ้าเชิงกลของสารเซรามิกในระบบ PMN-PZT, รายงานฉบับสมบูรณ์ โครงการทุนส่งเสริมนักวิจัยรุ่นใหม่, สนับสนุนโดยสำนักงานกองทุนสนับสนุนการวิจัย (สกว.) พ.ศ. 2545.
56. สุพล อนันตา, อิทธิพลของปัจจัยในกระบวนการเตรียมต่อการเกิดเฟส โครงสร้างจุลภาค และสมบัติไดอิเล็กตริกของสารเซรามิก PBZT-PMNT, รายงานฉบับสมบูรณ์ โครงการทุนพัฒนานักวิจัย, สนับสนุนโดยสำนักงานกองทุนสนับสนุนการวิจัย (สกว.) พ.ศ. 2546.
57. รัตติกร ยิ้มนิรัญ, อิทธิพลของความเค้นแบบแกนเดี่ยวต่อสมบัติไดอิเล็กตริกของสารเฟร์โรอิเล็กตริกเซรามิก, รายงานฉบับสมบูรณ์ โครงการทุนพัฒนานักวิจัย, สนับสนุนโดยสำนักงานกองทุนสนับสนุนการวิจัย (สกว.) พ.ศ. 2547.

# Output จากโครงการวิจัยที่ได้รับทุนจาก สกอ. และ สกว.

**1. ผลงานตีพิมพ์ในวารสารวิชาการนานาชาติ จำนวนทั้งสิ้น 46 เรื่องได้แก่ (*รายละเอียดในภาคผนวก*)**

1. Yongyut Laosiritaworn, Supon Ananta**,** and **Rattikorn Yimnirun**, "Effects of Temperature Gradient of Magnetic Properties of Ising Thin-Film", *Physical Review B,* 75, pp 054417 (2007).
2. Prasit Thongbai, Chivalrat Masingboon, Santi Maensir, T. Yamwong, S. Wongsaenmai, and **R. Yimnirun**, "Giant dielectric behavior of $CaCu_3Ti_4O_{12}$ subjected to post-sintering annealing and uniaxial stress" *J. Phys.: Condensed Matter,* 19, pp 236208-1-10 (2007).
3. R. Wongmaneerung, X. Tan, R.W. McCullum, S. Ananta, and **R. Yimnirun**, Cation-, dipole-, and spin-order in $Pb(Fe_{2/3}W_{1/3})O_3$-based magnetoelectric multiferroic compounds" *Applied Physics Letters,* 90, 242905 (2007)
4. S. Wongsaenmai, W. Qu, S. Ananta, **R. Yimnirun**, and X. Tan, "Effect of Ba-substitution on the structure and properties of $Pb_{0.8}Ba_{0.2}In_{0.5}Nb_{0.5}O_3$ ceramics" *Applied Physics A,* 88, pp 757-761 (2007).
5. O. Khamman, **R. Yimnirun**, and S. Ananta, "Effect of calcination conditions on phase formation and particle size of lead nickel niobate powders synthesized by using $Ni_4Nb_2O_9$ precursor" *Materials Letters,* 61, pp 4466-4470 (2007)
6. **R. Yimnirun**, R. Wongmaneerung, S. Wongsaenmai, A. Ngamjarurojana, S. Ananta, and Y. Laosiritaworn, "Temperature Scaling of Dynamic Hysteresis in Hard Lead Zirconate Titanate Bulk Ceramic" *Applied Physics A*, 89, pp 737-741 (2007).
7. N. Vittayakorn, S. Wirunchit, S. Traisak, **R. Yimnirun**, G. Rujijanagul, "Development of Perovskite and Phase Transition in Lead Cobalt Niobate Modified Lead Zirconate Titanate System" *Current Applied Physics,* 8, pp 128-133 (2008)
8. S. Wongsaenmai, **R. Yimnirun,** S. Ananta, R. Guo, and, A. Bhalla, "Thermal Expansion Measurement in the Relaxor Ferroelectric PIN-PT System" *Materials Letters*, 62, pp 352-356 (2008)

9. Anurak Prasatkhetragarn, Naratip Vittayakorn, Supon Ananta, **Rattikorn Yimnirun** and David P. Cann, "Synthesis, dielectric and ferroelectric properties of ceramics in the *(1-x)*$Pb(Zr_{1/2}Ti_{1/2})O_3$ – *(x)*$Pb(Co_{1/3}Nb_{2/3})O_3$ system" *Japan Journal of Applied Physics*, 47(2), pp 998-1002 (2008).
10. M. Unruan, S. Wongsaenmai, Y. Laosiritaworn, S. Ananta, and **R. Yimnirun**, "Changes in Dielectric Properties of $Pb(In_{1/2}Nb_{1/2})O_3$-$PbTiO_3$ Ceramics Under Compressive Stress Applied Parallel and Perpendicular to Electric Field" *J. Phys. D: Appl. Phys.,* 41*,* pp 541-545 (2008)*.*
11. Supattra Wongsaenmai, Xiaoli Tan, Supon Ananta, and **Rattikorn Yimnirun**, "Dielectric and Ferroelectric Properties of Fine Grains $Pb(In_{1/2}Nb_{1/2})O_3$–$PbTiO_3$ Ceramics" *Journal of Alloys and Compounds*, 454, pp 331-339 (2008).
12. Muangjai Unruan, Anurak Prasatkhetragarn, Yongyut Laosiritaworn, Supon Ananta, and **Rattikorn Yimnirun**, "Dielectric Properties of PZT-PCN Ceramics Under Compressive Stress" *Physica Scripta,* 77, pp 571-574 (2008).
13. **R. Yimnirun**, N. Wongdamnern, N. Triamnak, M. Unruan, A. Ngamjarurojana, S. Ananta, and Y. Laosiritaworn, "Stress-Dependent Scaling Behavior of Sub-Coercive Field Dynamic Ferroelectric Hysteresis in $Pb(Zn_{1/3}Nb_{2/3})O_3$-Modified $Pb(Zr_{1/2}Ti_{1/2})O_3$ Ceramic" *J. Applied. Physics,* 103 (8)*,* pp 086105-1-3 (2008).
14. O. Khamman, **R. Yimnirun**, and S. Ananta, "Effect of vibro-milling time on phase formation and particle size of nickel niobate nanopowders" *Materials Science and Engineering B*, 150(1), pp 12-17 (2008)
15. Prasit Thongbai, Santi Maensiri, Teerapon Yamwong, and **Rattikorn Yimnirun** "Giant dielectric properties of $CaCu_3Ti_4O_{12}$/(Li, Ti)-doped NiO composites subjected to post-sintering annealing and compressive stress" *J. Applied Physics*, 103, pp 114107-1-6 (2008)*.*
16. R. Wongmaneerung, **R. Yimnirun,** S. Ananta,. A. Bhalla, and R. Guo, "Thermal Expansion Measurement in the PMN-PT Ceramic Systems" *J. Alloys and Compounds,* 461, pp 565-569 (2008)*.*
17. Muangjai Unruan, Athipong Ngamjarurojana, Yongyut Laosiritaworn, Supon Ananta, and **Rattikorn Yimnirun**, "Influences of Perpendicular Compressive Stress on Ferroelectric Properties of Electrostrictive and

Piezoelectric $Pb(Mg_{1/3}Nb_{2/3})O_3$-$PbTiO_3$ Ceramics" *J. Applied Physics.* 104, 034101 (2008).

18. Orawan Khamman, **Rattikorn Yimnirun**, Supon Ananta, "Effect of Niobate B-Site Precursor of Phase Formation of PNN Powders" *J. Alloys and Compounds*, 465, pp522-526 (2008).
19. Muangjai Unruan, Naratip Vittayakorn, Rewadee Wongmaneeruang, Anurak Prasatkhetragarn, Supon Ananta and **Rattikorn Yimnirun**, "Synthesis and Properties of $Pb(Co_{1/3}Nb_{2/3})O_3$ Ceramics" *J. Alloys and Compounds*, 466, pp 264-267 (2008).
20. M. Unruan, R. Wongmaneerung, A. Ngamjarurojana, S. Ananta, Y. Laosiritaworn, and **R. Yimnirun,** "Changes of Ferroelectric Properties of Lead Magnsium Niobate-Lead Titanate Ceramics Under Compressive Stress" *J. Applied Physics.* 104, 064107 (2008)
21. **R. Yimnirun**, N. Wongdamnern, N. Triamnak, M. Unruan, A. Ngamjarurojana, S. Ananta, and Y. Laosiritaworn, "Stress-Dependent Scaling Behavior of Sub-Coercive Field Dynamic Ferroelectric Hysteresis in $0.4Pb(Zn_{1/3}Nb_{2/3})O_3$-$0.6Pb(Zr_{1/2}Ti_{1/2})O_3$ Ceramic" *J. Physics: Condensed Matters.* 20, 415202 (2008)
22. **R. Yimnirun**, N. Wongdamnern, N. Triamnak, T. Sareein, M. Unruan, A. Ngamjarurojana, S. Ananta, and Y. Laosiritaworn, "Power-law Scaling of Sub-Coercive Field Dynamic Ferroelectric Hysteresis in $0.3Pb(Zn_{1/3}Nb_{2/3})O_3$-$0.7Pb(Zr_{1/2}Ti_{1/2})O_3$ Ceramic" *J. Physics D: Applied. Physics,* 41, 205415 (2008)
23. **Rattikorn Yimnirun,** "Scaling Behavior of Dynamic Hysteresis in PZT-Based Ferroelectric Bulk Ceramics" *Functional Materials Letters*, 1(2), pp 133-137 (2008).
24. S. Ananta,, **R. Yimnirun**, and O. Khamman "Effect of nickel niobate B-site precursors on phase formation, microstructure and dielectric properties of perovskite PNN ceramics" *Functional Materials Letters*, 1(3), pp 229-233 (2008)
25. Muangjai Unruan , Anurak Prasatkhetragarn, Yongyut Laosiritaworn, Supon Ananta, and **Rattikorn Yimnirun**, "Changes in Dielectric Properties of $Pb(Zr_{1/2}Ti_{1/2})O_3$-$Pb(Co_{1/3}Nb_{2/3})O_3$ Ceramics Under Compressive Stress

Applied Perpendicular to Electric Field" to *J. Phys. D:Applied Physics,* **41**, pp 245405 (2008)

26. **R. Yimnirun**, N. Wongdamnern, N. Triamnak, M. Unruan, A. Ngamjarurojana, S. Ananta, and Y. Laosiritaworn, "Stress-Dependent Scaling Behavior of Sub-Coercive Field Dynamic Ferroelectric Hysteresis in $0.5Pb(Zn_{1/3}Nb_{2/3})O_3$-$0.5Pb(Zr_{1/2}Ti_{1/2})O_3$ Ceramic" *J. Applied. Physics,* **104***,* pp 104103-1-4 (2008)
27. M. Unruan, T. Sareein, J. Tangsritrakul, S. Prasertpalichatr, A. Ngamjarurojana, S. Ananta, and **R. Yimnirun**, "Changes in Dielectric and Ferroelectric Properties of $Fe^{3+}$/$Nb^{5+}$ Hybrid-Doped Barium Titanate Ceramics Under Compressive Stress" *J. Applied Physics,* **104**, pp 124102-1-5 (2008)
28. **Rattikorn Yimnirun**, Narit Triamnak, Muangjai Unruan, Athipong Ngamjarurojana, Yongyut Laosiritaworn, and Supon Ananta, "Ferroelectric Properties of $Pb(Zr_{1/2}Ti_{1/2})O_3$—$Pb(Zn_{1/3}Nb_{2/3})O_3$ Ceramics Under Compressive Stress" *Current Applied Physics*, 9, pp 249-252 (2009)
29. R. Wongmaneerung, **R. Yimnirun**, S. Ananta, "Processing and Properties of $Pb(Mg_{1/3}Nb_{2/3})O_3$-$PbTiO_3$ Based Ceramics" *Current Applied Physics*, 9, pp 268-273 (2009).
30. **R. Yimnirun**, S. Wongsaenmai, S. Ananta, N. Triamnak, "Dielectric Properties of PIN-PT Ceramics Under Compressive Stress" *Current Applied Physics,* 9, pp 422-425 (2009).
31. P. Ketsuwan, Y. Laosiritaworn, S. Ananta, **R. Yimnirun**, "Electrical Properties of Nb-Doped $Pb(Zr_{0.52}Ti_{0.48})O_3$ Ceramics" *International Journal of Modern Physics B*, 23, pp 105-111 (2009)
32. **R. Yimnirun** "Dielectric Properties of PMN-PT Prepared by Mixed Oxide Method" *International Journal of Modern Physics B*, 23(3), pp 403-410 (2009)
33. R. Wongmaneerung, **R. Yimnirun**, and S. Ananta, "Effect of two-stage sintering on phase formation, microstructure and dielectric properties of perovskite PMN ceramics derived from a corundum $Mg_4Nb_2O_9$ precursor" *Materials Chemistry and Physics*, 114, pp 569-575 (2009)

34. N. Wongdamnern, A. Ngamjarurojana, Y. Laosiritaworn, S. Ananta, and **R. Yimnirun**, "Dynamic Ferroelectric Hysteresis Scaling in $BaTiO_3$ Single Crystals" *Journal of Applied Physics,* 105, 044109 (2009)
35. S. Wongsaenmai, S. Ananta, and **R. Yimnirun**, "Effects of Addition of BT on Structural Phase Formation and Electrical Properties of Relaxor Ferroelectric $Pb(In_{0.5}Nb_{0.5})_{(1-x)}Ti_{(x)}O_3$ ceramics" *J. Alloys and Compounds,* 474, pp 241-245 (2009)
36. R. Wongmaneerung, A. Rujiwatra, **R. Yimnirun**, and S. Ananta, "Fabrication and Dielectric Properties of Self-reinforced Lead Titanate Nanocomposites" *J. Alloys and Compounds,* 475, pp 473-478 (2009)
37. R. Wongmaneerung, P. Singjai, **R. Yimnirun** and S. Ananta, "Effects of SiC nanofibers Addition on Microstructure and Dielectric Properties of Lead Titanate Ceramics" *J. Alloys and Compounds,* 475, pp 456-462 (2009)
38. Anurak Prasatkhetragarn, Athipong Ngamjarurojana, Yongyut Laosiritaworn, Supon Ananta, **Rattikorn Yimnirun**, and David Cann, "Effects of Zr/Ti ratio on phase formation and electrical properties of $0.8Pb(Zr_{1/2}Ti_{1/2})O_3$-$0.2Pb(Co_{1/3}Nb_{2/3})O_3$ ceramics" *Current Applied Physics*, 9, pp 802-806 (2009)
39. O. Khamman, X. Tan, S. Ananta, and **R. Yimnirun**, "The morphotropic phase boundary and electrical properties of (1-*x*)$Pb(Zn_{1/2}W_{1/2})O_3$—*x*$Pb(Zr_{0.5}Ti_{0.5})O_3$ ceramics" *J. Materials Science*, 44, pp 1868-1872 (2009)
40. T. Sareein, M. Unruan, A. Ngamjarurojana, S. Jiansirisomboon, A. Watcharapasorn, and **R. Yimnirun**, "Influences of Compressive Stress and Aging on Dielectric Properties of Sodium Bismuth Titanate Ceramics" *Physics Letters A,* 373, pp 1583-1587 (2009)
41. Anurak Prasatkhetragarn, Piyachon Ketsuwan, Supon Ananta, **Rattikorn Yimnirun**, and David Cann "Phase Formation, Microstructure and Dielectric Properties of $(1-x)Pb(Zr_{1/2}Ti_{1/2})O_3$–$xPb(Co_{1/3}Nb_{2/3})O_3$ Ceramics" *Materials Letters,* 63, pp 1281-1284 (2009)
42. Muangjai Unruan , Anurak Prasatkhetragarn, Athipon Ngamjarurojana, Yongyut Laosiritaworn, Supon Ananta, and **Rattikorn Yimnirun**, "Changes in Dielectric and Ferroelectric Properties of $Pb(Zr_{1/2}Ti_{1/2})O_3$-

$Pb(Ni_{1/3}Nb_{2/3})O_3$ Ceramics Under Compressive Stress" *J. Applied Physics* (2009)

43. R. Wongmaneerung, **R. Yimnirun**, and S. Ananta, "Effect of Magnasium Niobate Precursors on Phase Formation, Microstructure and Dielectric Properties of Perovskite Lead Magnesium Niobate Ceramics" *J. Alloys and Compounds* (2008) *in pres*
44. Anurak Prasatkhetragarn, Athipong Ngamjarurojana, Yongyut Laosiritaworn, Supon Ananta, **Rattikorn Yimnirun**, and David Cann, "Effects of sintering conditions on phase formation and electrical properties of $0.8Pb(Zr_{1/2}Ti_{1/2})O_3$-$0.2Pb(Co_{1/3}Nb_{2/3})O_3$ ceramics" *Current Applied Physics* (2009) *in press*
45. **Rattikorn Yimnirun**, Muangjai Unruan, Rewadee Wongmaneerung, Orawan Khamman, Wanwilai Chaisan, and Supon Ananta, "Dielectric Properties of Complex Perovskite PZBT-PMNT Ceramic Under Compressive Stress" *International Journal of Modern Physics B* (2009) *accepted*
46. A. Chaipanich, N. Jaitanong and **R. Yimnirun**, "Ferroelectric Hysteresis Behavior in 0-3 PZT-Cement Composites: Effects of Frequency and Electric Field" *Ferroelectric Letters* (2009) *accepted*

## 2. การนำผลงานวิจัยไปใช้ประโยชน์

### 2.1 เชิงพาณิชย์

ในการวิจัยนี้ถึงแม้ไม่ได้มุ่งหวังในด้านการนำผลงานไปใช้ประโยชน์ในเชิงพาณิชย์ แต่มุ่งเน้นในการสร้างองค์ความรู้ใหม่ แต่อุปกรณ์ที่ถูกพัฒนาขึ้นมาใช้ประกอบการศึกษา ซึ่งได้แก่ ชุดอุปกรณ์ในการวัดสมบัติทางไฟฟ้าภายใต้ความเค้นนั้น สามารถนำไปประยุกต์ใช้ในการวัดสมบัติดังกล่าวทั้งในกรณีที่ไม่มีความเค้นและกรณีที่มีความเค้นในวัสดุตัวอื่นๆได้ ซึ่งสามารถที่จะลดการสั่งซื้ออุปกรณ์ที่มีความคล้ายคลึงจากต่างประเทศได้

### 2.2 เชิงนโยบาย

ผลการวิจัยที่ได้จากโครงการนี้ได้ถูกนำไปใช้ในการกำหนดแผนและทิศทางการวิจัยของกลุ่มผู้วิจัยที่ชัดเจนขึ้น ดังจะเห็นได้จากการเสนอหัวข้อวิจัยเพื่อขอรับทุนพัฒนาศักยภาพการทำงานวิจัยของอาจารย์รุ่นใหม่และรุ่นกลาง ประจำปี 2550-2551 ของ

อดีตผู้ร่วมวิจัยหลายท่าน จากสำนักงานกองทุนสนับสนุนการวิจัยและสำนักงานคณะกรรมการการอุดมศึกษา ซึ่งเป็นการวิจัยต่อเนื่องจากโครงการวิจัยนี้ เพื่อเป็นการส่งเสริมให้เกิดการวิจัยแบบมีทิศทางมากขึ้น

**2.3 เชิงสาธารณะ**

โครงการวิจัยนี้ได้ก่อให้เกิดเครือข่ายความร่วมมือในการวิจัยมากขึ้นระหว่างนักวิจัยรุ่นกลางและนักวิจัยรุ่นใหม่ทั้งในและต่างประเทศ เช่นความร่วมมืออย่างใกล้ชิดในการวิจัยกับ รศ. ดร. สุพล อนันตา ภาควิชาฟิสิกส์และวัสดุศาสตร์ คณะวิทยาศาสตร์ มหาวิทยาลัยเชียงใหม่ ซึ่งเน้นการวิจัยด้านกระบวนการผลิตเซรามิก ในขณะที่ผู้วิจัยได้มีส่วนร่วมในการวัดสมบัติทางไฟฟ้าของเซรามิกที่ผลิตขึ้น นอกจากนี้ก็มีความร่วมมือกับ ผศ. ดร. ยงยุทธ เหล่าศิริถาวร ภาควิชาฟิสิกส์และวัสดุศาสตร์ คณะวิทยาศาสตร์ มหาวิทยาลัยเชียงใหม่ ที่นำความรู้เรื่องฟิสิกส์คณานามาประกอบการคำนวณหลายๆอย่าง และการร่วมมืออย่างเหนียวแน่นกับ อ.ดร. อธิพงศ์ งามจารุโรจน์ ในการพัฒนาอุปกรณ์และเครื่องมือในการวัดต่างๆ นอกจากนี้ยังได้มีการสร้างความร่วมมือด้านการวิจัยกับนักวิจัยในต่างประเทศคือ Prof. David Cann แห่ง Oregon State University และ Prof. Xiaoli Tan แห่ง Iowa State University สหรัฐอเมริกา และที่สำคัญที่สุดผู้วิจัยได้รับความรู้ในการวิจัยจากนักวิจัยอาวุโสจากต่างประเทศคือ Prof. Robert Newnham Prof. L. Eric Cross Prof. Kenji Uchino แห่ง The Pennsylvania State University สหรัฐอเมริกา และ Prof. Amar Bhalla แห่ง University of Texas at San Antonio สหรัฐอเมริกา

**2.4 เชิงวิชาการ (พัฒนาการเรียนการสอน/สร้างนักวิจัยใหม่)**

ผลงานที่ได้จากการวิจัยนี้ได้ถูกนำไปใช้ประกอบการเรียนการสอนในหลายๆ กระบวนวิชาของสาขาวิชาวัสดุศาสตร์ ในระดับบัณฑิตศึกษา เช่น MATS 701 Characterization and Properties of Materials MATS 703 Fabrication Processes of Materials MATS 723 Ferroelectric Materials MATS 743 Electroceramics และ MATS 745 Physical Properties of Crystals นอกจากนี้ผู้วิจัยยังนำผลงานบางส่วนไปประกอบการเขียนตำราเรื่อง สมบัติทางไฟฟ้าของเซรามิกเฟร์โรอิเล็กทริก (Electrical Properties of Ferroelectric Ceramics) สำหรับในส่วนของการสร้างนักวิจัยใหม่นั้น นอกจากประโยชน์โดยตรงที่เกิดกับผู้วิจัยเองแล้ว โครงการวิจัยนี้ได้มีส่วนในการฝึกฝนทักษะการวิจัยและการเผยแพร่ผลงานให้กับนักศึกษาทั้งในระดับปริญญาตรีและระดับบัณฑิตศึกษาในฐานะผู้ช่วยวิจัยร่วมกับหัวหน้าโครงการ และผลงานวิจัยที่ได้สามารถนำไปตีพิมพ์ในวารสาร

ทางวิชาการทั้งในและต่างประเทศ รวมทั้งการนำเสนอผลงานในที่ประชุมทางวิชาการระดับนานาชาติ (ดังแสดงใน output และผลงานอื่น ๆ) ซึ่งมีผลให้เกิดการพัฒนานักวิจัยรุ่นใหม่และรุ่นกลางมากขึ้น

**3. อื่น ๆ (ผลงานตีพิมพ์ในวารสารวิชาการและการเสนอผลงานในที่ประชุมวิชาการนานาชาติ)**

**3.1 ผลงานตีพิมพ์ในวารสารประกอบการประชุมวิชาการระดับนานาชาติ (Proceedings of International Conferences) จำนวนทั้งสิ้น 8 เรื่องได้แก่**

1 **R. Yimnirun**, S. Wongsaenmai, R. Wongmaneerung, N. Wongdamnern, A. Ngamjarurojana, S. Ananta, and Y. Laosiritaworn, " Stress- and Temperature-Dependent Scaling Behavior of Dynamic Hysteres-is in Soft PZT Bulk Ceramics" *Physica Scripta*, T129, pp 184-189 (2007)

2 W. Chaisan, **R. Yimnirun**, S. Ananta, " Effects of Compressice Stress of Ferroelectric Properties of BT Ceramics" *Physica Scripta*, T129, pp 205-208 (2007)

3 N. Wongdamnern, N. Triamnak, A. Ngamjarurojana, Y. Laosiritaworn, S. Ananta, and **R. Yimnirun**, "Comparative Studies of Dynamic Hysteresis Responses in Hard and Soft PZT Ceramics" *Ceramics International,* 34(4), pp 731-734 (2008).

4 W. Laosiritaworn, O. Khamman, S. Ananta, **R. Yimnirun** and Y. Laosiritaworn, "Artificial Neural Network Modeling of Ceramics Powder Preparation: application to $NiNb_2O_6$" *Ceramics International,* 34(4), pp 809-812 (2008).

5 A. Ngamjarurojana, S. Ural, S.H. Park, S. Ananta, **R. Yimnirun**, and K. Uchino, "Piezoelectric Properties of Low Temperature Sintering in $Pb(Zr,Ti)O_3$ - $Pb(Zn,Ni)_{1/3}Nb_{2/3}O_3$ Ceramics for Piezoelectric Transformer Applications" *Ceramics International,* 34(4), pp 705-708 (2008).

6 Y. Laosiritaworn, S. Ananta, J. Poulter, and **R. Yimnirun**, "Monte Carlo investigation of hysteresis properties in ferroelectric thin-films under the effect of uniaxial stresses" *Ceramics International*, 35*,* pp 181-184 (2009)

7 W. Chaisan, **R. Yimnirun**, and S. Ananta, "Preparation and characterization of ceramic nanocomposites in the PZT–BT system" *Ceramics International,* 35*,* pp 121-124 (2009)

8 W. Chaisan, **R. Yimnirun**, and S. Ananta, “Effect of vibro-milling time on phase formation and particle size of barium titanate nanopowders” *Ceramics International*, 35, pp 173-176 (2009)

**3.2 การเสนอผลงานในที่ประชุมวิชาการนานาชาติจำนวนทั้งสิ้น 49 เรื่องได้แก่**

1. **R. Yimnirun**, S. Wongsaenmai, R. Wongmaneerung, N. Wongdamnern, A. Ngamjarurojana, S. Ananta, and Y. Laosiritaworn, “ Stress- and Temperature-Dependent Scaling Behavior of Dynamic Hysteresis in Soft PZT Bulk Ceramics” ISFM-2007, Hangzhou, China (May 2007). ***Invited Talk***
2. S. Wongsaenmai, S. Ananta, **R. Yimnirun**, R. Guo, A. Bhalla, “Correlation of Ordered-Disordered State and Electrical Properties of BT and PT Substituted PIN Systems” ICMAT-2007, Singapore (July 2007)
3. **R. Yimnirun**, S. Wongsaenmai, R. Wongmaneerung, M. Unruan, N. Wongdamnern, A. Ngamjarurojana, Y. Laosiritaworn, and S. Ananta, “Temperature- and Stress-Dependent Scaling of Ferroelectric Hysteresis in Soft and Hard PZT Bulk Ceramics” MS&T 2007, Detroit, USA (September 2007) ***Invited Talk***
4. R. Wongmaneerung, **R. Yimnirun**, and S.Ananta, “Dielectric Properties of PMN-PT Ceramics” Thailand’s First Nano Conference, Chiang Mai, Thailand (August 2007)
5. **R. Yimnirun**, “Scaling Behavior of Dynamic Hysteresis in PZT Ceramics”, *The 2nd Progress in Advances in Materials and Technology in Thailand Meeting*, Khon Kaen, (2008) ***Invited Talk***
6. **Rattikorn Yimnirun**, Jirapa Tangsritrakul, Saroj Rujirawat, and Sukit Limpijumnong, “Experimental Identification of Mn Site in $BaTiO_3$ by Synchrotron X-Ray Absorption Near-Edge Structure” *The 6th Asian Meeting of Ferroelectrics (AMF-6)*, Taiwan (August 2008) ***Invited Talk***
7. **R. Yimnirun**, N. Triamnak, M. Unruan, S. Wongsaenmai, A. Ngamjarurojana, Y. Laosiritaworn, and S. Ananta, “Dielectric and Ferroelectric Properties of Complex Perovskite Ceramics Under Compressive Stress” ISFM-2007, Hangzhou, China (May 2007).
8. W. Chaisan, **R. Yimnirun**, S. Ananta, “ Effects of Compressive Stress of Ferroelectric Properties of BT Ceramics” ISFM-2007, Hangzhou, China (May 2007).

9. Muangjai Unruan , Anurak Prasatkhetragarn, Yongyut Laosiritaworn, Supon Ananta, and **Rattikorn Yimnirun**, “Effects of Compressive Stress on Dielectric Properties of PZT-PCN Ceramics” ICMAT-2007, Singapore (July 2007)
10. N. Wongdamnern, S. Ananta, Y. Laosiritaworn, and **R. Yimnirun**, “Stress-Dependent Scaling Behavior of Dynamic Hysteresis in Hard Lead Zirconate Titanate Ceramic” ICMAT-2007, Singapore (July 2007)
11. R. Wongmaneerung, **R. Yimnirun,** S. Ananta,. A. Bhalla, and R. Guo, “Thermal Expansion Measurement in the 0.9PMN-0.1PT Ceramics” ICMAT-2007, Singapore (July 2007)
12. O. Khamman, **R. Yimnirun**, and S. Ananta, “A Two-Stage Solid State Reaction of Lead Nickel Niobate Powders” MS&T 2007, Detroit, USA (September 2007)
13. P. Ketsuwan, Y. Laosiritaworn, S. Ananta, **R. Yimnirun**, and D. P. Cann, “Effect of Nb-Doping on Electrical Properties of $Pb(Zr_{0.52}Ti_{0.48})O_3$ Ceramics” MS&T 2007, Detroit, USA (September 2007)
14. P. Ketsuwan, A. Prasatkhetragarn, N. Vittayakorn, C. C. Huang, S. Ananta, **R. Yimnirun**, B. J. Gibbons, D. P. Cann, “$Bi(Zn_{1/2}Ti_{1/2})O_3$-$ABO_3$ effect for alkaline base perovskite” ISAF 2008, Santa Fe, NM, USA (February 2008)
15. P. Ketsuwan, S. Ananta, Y. Laosiritaworn, **R. Yimnirun**, David P. Cann, “Impedance and Dielectric Properties of Nb-Doped $Pb(Zr_{0.52}Ti_{0.48})O_3$ Ceramics” *The International Conference on Smart Materials: Smart/Intelligent Materials and Nanotechnology-2008 (SmartMat’08 and* IWOFM-2), April 22-25. 2008, Chiang Mai, Thailand.
16. A. Ngamjarurojana , S. Ananta, **R. Yimnirun**, “Effect of $Al_2O_3$ Addition on Dielectric, Piezoelectric and Ferroelectric Properties of $0.2Pb(Zn_{1/3}Nb_{2/3})O_3$–$0.8Pb(Zr_{1/2}Ti_{1/2})O_3$ Ceramics” *The International Conference on Smart Materials: Smart/Intelligent Materials and Nanotechnology-2008 (SmartMat’08 and* IWOFM-2), April 22-25. 2008, Chiang Mai, Thailand.
17. S. Prasertpalichatr, M. Unruan, S. Rujirawat, S. Limpijumnong, **R. Yimnirun**, “Dielectric and Ferroelectric Aging Effect of $Fe^{3+}$/$Nb^{5+}$ Hybrid-Doped Barium Titanate Ceramics” *The International Conference on Smart Materials: Smart/Intelligent Materials and Nanotechnology-2008 (SmartMat’08 and* IWOFM-2), April 22-25. 2008, Chiang Mai, Thailand.

18. M. Unruan, R. Wongmaneerung, Y. Laosiritaworn, S. Ananta, **R. Yimnirun**, "Changes in Ferroelectric Properties of 0.7PMN–0.3PT Ceramics with Compressive Stress" *The International Conference on Smart Materials: Smart/Intelligent Materials and Nanotechnology-2008 (SmartMat'08 and* IWOFM-2), April 22-25. 2008, Chiang Mai, Thailand.
19. N. Wongdamnern, A. Ngamjarurojana, S. Ananta, Y. Laosiritaworn, **R. Yimnirun**, "Scaling Behavior of Dynamic Hysteresis in Hard PZT Bulk Ceramics Under Influence of Compressive Stress and Temperature" *The International Conference on Smart Materials: Smart/Intelligent Materials and Nanotechnology-2008 (SmartMat'08 and* IWOFM-2), April 22-25. 2008, Chiang Mai, Thailand.
20. A. Prasatkhetragarn, S. Ananta, **R. Yimnirun**, David P. Cann, "Effect of Temperature Treatment on Dielectric Properties of $0.8Pb(Zr_{1/2}Ti_{1/2})O_3$ - $0.2Pb(Co_{1/3}Nb_{2/3})O_3$ Ceramics" *The International Conference on Smart Materials: Smart/Intelligent Materials and Nanotechnology-2008 (SmartMat'08 and* IWOFM-2), April 22-25. 2008, Chiang Mai, Thailand.
21. C. Silawongsawat, T. Sareein, A. Ngamjarurojana, S. Maensiri**, R. Yimnirun**, S. Ananta, "Effect of Calcination Conditions on Phase Formation and Characterization of $BiFeO_3$ Powders Synthesized By a Solid-State Reaction" *The International Conference on Smart Materials: Smart/Intelligent Materials and Nanotechnology-2008 (SmartMat'08 and* IWOFM-2), April 22-25. 2008, Chiang Mai, Thailand.
22. S. Chandarak, T. Sareein, A. Ngamjarurojana, S. Maensiri, S. Ananta, **R. Yimnirun**, "Effect of Calcination Conditions on Phase Formation and Characterization of $BiFeO_3$-$BaTiO_3$ Powders Synthesized By a Solid-State Reaction" *The International Conference on Smart Materials: Smart/Intelligent Materials and Nanotechnology-2008 (SmartMat'08 and* IWOFM-2), April 22-25. 2008, Chiang Mai, Thailand.
23. Muangjai Unruan , Athipong Ngamjarurojana, Yongyut Laosiritaworn, Supon Ananta, And **Rattikorn Yimnirun**, "Dielectric Properties of $Pb(Zr_{1/2}Ti_{1/2})O_3$-$Pb(Zn_{1/3}Nb_{2/3})O_3$ Ceramics Under Compressive Stress Applied Perpendicular to Electric Field" *The 6$^{th}$ Asian Meeting of Ferroelectrics (AMF-6)*, Taiwan (August 2008)

24. M. Unruan, A. Prasatkhetragarn, A. Ngamjarurojana, Y. Laosiritaworn, S. Ananta and **R. Yimnirun**, "Ferroelectric Properties of $Pb(Zr_{1/2}Ti_{1/2})O_3$-$Pb(Zn_{1/3}Nb_{2/3})O_3$ Ceramics under Compressive Stress Applied Perpendicular to Electric Field" *The 6th Asian Meeting of Ferroelectrics (AMF-6)*, Taiwan (August 2008)
25. irapa Tangsritrakul, Muangjai Unruan, Piyachon Ketsuwan, Narit Triamnak, Saroj Rujirawat, Tanawadee Dechakupt, Supon Ananta, And **Rattikorn Yimnirun**," Effects Of Iron Addition On Electrical Properties And Aging Behavior Of Barium Titanate Ceramics" *The 6th Asian Meeting Of Ferroelectrics (Amf-6)*, Taiwan (August 2008)
26. Anurak Prasatkhetragarn, Supon Ananta, and **Rattikorn Yimnirun**, "Effect of Zr/Ti Ratio on Phase Formation and Electrical Properties of $0.2Pb(Co_{1/3}Nb_{2/3})O_3 - 0.8Pb(Zr_xTi_{1-x})O_3$ Ceramics" *The 6th Asian Meeting of Ferroelectrics (AMF-6)*, Taiwan (August 2008)
27. Anurak Prasatkhetragarn, Supon Ananta, and **Rattikorn Yimnirun**, "Effects of Sintering Conditions on Phase Formation and Electrical Properties of $0.2Pb(Co_{1/3}Nb_{2/3})O_3 - 0.8Pb(Zr_{1/2}Ti_{1/2})O_3$ Ceramics" *The 6th Asian Meeting of Ferroelectrics (AMF-6)*, Taiwan (August 2008)
28. P. Ketsuwan, C. C. Huang, S. Ananta, **R. Yimnirun**, D. P. Cann, "Electrical Conductivity And Dielectric And Ferroelectric Properties Of Chromium Doped Lead Zircronate Titanate Ceramic" *The 6th Asian Meeting of Ferroelectrics (AMF-6)*, Taiwan (August 2008)
29. P. Ketsuwan, C. C. Huang, S. Ananta, **R. Yimnirun**, D. P. Cann, "Effects Of Niobium Doping On Dielectric And Ferroelectric Properties Of Chromium Modified Lead Zircronate Titante Ceramics" *The 6th Asian Meeting of Ferroelectrics (AMF-6)*, Taiwan (August 2008)
30. Sasiporn Prasertpalichatr, Muangjai Unruan, Jirapa Tangsritrakool, Supon Ananta, and **Rattikorn Yimnirun**, "Dielectric and Ferroelectric Aging Effect of $Fe^{3+}/Nb^{5+}$ Hybrid-Doped Barium Titanate Ceramics" *The 6th Asian Meeting of Ferroelectrics (AMF-6)*, Taiwan (August 2008)
31. N. Wongdamnern, Y. Laosiritaworn, A. Ngamjarurojana, S. Ananta, and **R. Yimnirun**, "Stress-Dependent Scaling Behavior of PZT-PZN Ceramics Under Sub-Coercive Field Condition" *The 6th Asian Meeting of Ferroelectrics (AMF-6)*, Taiwan (August 2008)

32. Thanapong Sareein, Athipong Ngamjarurojana, Supon Ananta, and **Rattikorn Yimnirun**, "Dielectric and Ferroelectric Properties of KNN-BNT Ceramic Systems" *The 6th Asian Meeting of Ferroelectrics (AMF-6)*, Taiwan (August 2008)
33. A.Ngamjarurojana, **R. Yimnirun**, S. Ananta"Effect of. VibroMilling Time on Phase Formation and Particle Size of $ZnNb_2O_6$ Nano- powders" *The 6th Asian Meeting on Electroceramics (AMEC-6)*, Japan (October 2008)
34. M. Unruan, A. Prasatkhetragarn, A. Ngamjarurojana, Y. Laosiritaworn, S. A nanta, **R. Yimnirun** "Ferroelectric Properties of $Pb(Zr_{1/2}Ti_{1/2})O_3$-$Pb(Zn_{1/3}Nb_{2/3})O_3$ Ceramics under compressive stress applied perpendicular to electric field" *The 6th Asian Meeting on Electroceramics (AMEC-6)*, Japan (October 2008)
35. L. Srisombat, O. Khamman, **R. Yimnirun**, S. Ananta, T.R. Lee "XPS Chara cterization of Relaxor Perovskite PNN Ceramics Prepared By Corundum Pr ecursor Method" *The 6th Asian Meeting on Electroceramics (AMEC-6)*, Japan (October 2008)
36. Wimalin S. Laosiritaworn, **Rattikorn Yimnirun**, Yongyut Laosiritaworn "Artifi cial Neural Network Modeling of Ferroelectric Hysteresis: An Application to Soft Lead Zirconate Titanate Ceramics" *The 6th Asian Meeting on Electroceramics (AMEC-6)*, Japan (October 2008)
37. W. C. Vittayakorn, **R. Yimnirun**, S. Ananta"Composition, Structure and Pro perties of PZT-BT Ceramics Prepared by Two-stage Sintering" *The 6th Asian Meeting on Electroceramics (AMEC-6)*, Japan (October 2008)
38. Jirapa Tangsritrakul, Muangjai Unruan, Piyachon Ketsuwan, Narit Triamna k, Tanawadee Dechakupt, Supon Ananta, **Rattikorn Yimnirun**, Saroj Rujira wat"Effects of Iron Addition on Aging Behavior of Barium Titanate Ceramics " *The 6th Asian Meeting on Electroceramics (AMEC-6)*, Japan (October 2008)
39. Piyachon Ketsuwan, Supon Ananta, **Rattikorn Yimnirun**, Chien-Chih Huang,David P. Cann "Dielectric Properties of Lidoped $Bi_{0.2}K_{0.8}(Zn_{0.1}Ti_{0.1})Ta_{0.8}O_3$ Ceramics"
40. S. Prasertpalichatr, J. Tangsritrakul, T. Sareein, M. Unruan, A. Ngamjaruroj ana, **R. Yimnirun**"Effect of Compressive Stress on Aging Behavior of

Hybrid-doped $Fe^{3+}/Nb^{5+}$ $BaTiO_3$ Ceramics" *The 6th Asian Meeting on Electroceramics (AMEC-6)*, Japan (October 2008)

41. S. Ananta, R. Wongmaneerung, L. Srisombat, **R. Yimnirun**"Potential of M icrostructural Engineering Technique for Fabrication of Highly Dense Perov skite Lead Titante Ceramics" *The 6th Asian Meeting on Electroceramics (AMEC-6)*, Japan (October 2008)
42. T. Sareein, M. Unruan, A. Ngamjarurojana, S. Ananta, **R. Yimnirun**"Effects of Compressive Stress on Dielectric and Ferroelectric Properties.of Lead-Free $(Bi_{1/2}Na_{1/2})TiO_3$-$(K_{1/2}Na_{1/2})NbO_3$ Ceramic Systems" *The 6th Asian Meeting on Electroceramics (AMEC-6)*, Japan (October 2008)
43. A. Thongon, S. Ananta, **R. Yimnirun**, S. Choopun, Y. Laosiritaworn "Monte Carlo simulations of nanopowders from mechanical milling" *The 6th Asian Meeting on Electroceramics (AMEC-6)*, Japan (October 2008)
44. A. Thongon, S. Ananta, **R. Yimnirun**, S. Choopun, Y. Laosiritaworn "Modeling of Nano Structure via a Spinodal Decomposition" *The 6th Asian Meeting on Electroceramics (AMEC-6)*, Japan (October 2008)
45. Sukrit Sucharitakul, Sasiporn Prasertpalichat, Yongyut Laosiritaworn, **Rattikorn Yimnirun** "Pinched Hysteresis Scaling in HybridDoped $BaTiO_3$" *The 6th Asian Meeting on Electroceramics (AMEC-6)*, Japan (October 2008)
46. Yongyut Laosiritaworn, **Rattikorn Yimnirun**, Ruyan Guo, Amar S. Bhalla " Stress Dependence of Dielectric Properties in Relaxor Ferroelectric : Monte Carlo Investigation" *The 6th Asian Meeting on Electroceramics (AMEC-6)*, Japan (October 2008)
47. Sukrit Sucharitakul, **Rattikorn Yimnirun**, Yongyut Laosiritaworn,"Hybrid-Doped Ferroelectric Modeling via Monte Carlo Simulation" *The 6th Asian Meeting on Electroceramics (AMEC-6)*, Japan (October 2008)
48. Piyachon Ketsuwan, Supon Ananta, **Rattikorn Yimnirun**, Chien-Chih Huang, David P. Cann "Dielectric and Ferroelectric Properties of (Cr,N b) doped Lead Zircronate Titanate Ceramics" *The 6th Asian Meeting on Electroceramics (AMEC-6)*, Japan (October 2008)
49. N. Wongdamnern, A. Ngamjarurojana, S. Ananta, Y. Laosiritaworn, **R. Yim nirun**,"ScalingBehavior of SubCoercive Field Dynamic Hysteresis in $BaTiO_3$ Single Crystal" *The 6th Asian Meeting on Electroceramics (AMEC-6)*, Japan (October 2008)

# ภาคผนวก

## Re-Print หรือ Pre-Print หรือ Accepted Manuscript

## ของ

## ผลงานตีพิมพ์ในวารสารวิชาการนานาชาติ

## (จำนวน 46 เรื่อง)

**และ**

**ผลงานที่ตีพิมพ์ในวารสารประกอบการประชุมวิชาการระดับนานาชาติ (Proceedings of International Conferences)**

**(จำนวน 8 เรื่อง)**

# Temperature effects in the magnetic properties of two-dimensional Ising square lattices: A Monte Carlo investigation

Yongyut Laosiritaworn,* Supon Ananta, and Rattikorn Yimnirun
*Department of Physics, Faculty of Science, Chiang Mai University, Chiang Mai 50200, Thailand*
(Received 3 November 2006; revised manuscript received 5 January 2007; published 22 February 2007)

The magnetic behavior of a two-dimensional nearest-neighbor Ising model with the presence of linear temperature variation in a thermal steady state was studied using the Wolff Monte Carlo simulation. The technique consists of fixing the temperatures of boundary spins, while the temperature field in the interior linearly varies with distance. It is found that with increasing the temperature difference between the two boundaries, the magnetization greatly reduces in magnitude while the susceptibility peaks tend to spread out over a temperature range. The detailed descriptions of these magnetization and susceptibility behaviors are elucidated from their spatial variation. The extraction of the "critical temperatures" is taken via the fourth-order cumulant of the magnetization. The critical temperatures are found to reduce slightly with increasing the temperature difference. This implies the vulnerability of the magnetization and susceptibility properties to the temperature variation in ferromagnetic materials, and to use such materials in temperature variation environments must be done with caution.

DOI: 10.1103/PhysRevB.75.054417 PACS number(s): 75.10.Dg, 05.10.Ln, 75.40.Cx

## I. INTRODUCTION

Magnetic thin films have been known to be very important in terms of fundamental and technological interest, especially in the magnetic recording technology.[1,2] Many contributions have been taken to provide understanding of these systems in detail.[3,4] However, there are still incomplete pictures describing their magnetic properties especially in nonequilibrium states. For instance, the theoretical studies usually investigate the thin-film problems by considering the system in contact with only a single heat bath, which means that the temperature of the whole system is fixed. As a result, the conventional thermal equilibrium investigation may not be useful in understanding the magnetic materials used in some applications, which operate at some fluctuating temperatures. For instance, in heat-assisted magnetic recording, the media temperature is nonuniformly raised by laser irradiation.[5] In such applications, there occurs a heat flux flowing among regions from high to low temperatures, resulting in local variation in temperature. Therefore, the approximation on using a single (average) temperature in the calculation is clearly inadequate since important thermodynamics is missing. On the other hand, magnetic properties strongly depend on thermal fluctuation. Therefore, the variation in temperatures makes the problem very complex, so experimental and theoretical investigations of this issue cannot be taken trivially. Consequently, it is of great interest and challenge to find how magnetic properties respond to the variation in temperature field. To date, there are few studies on this effect of temperature variation on magnetic systems; i.e., they are mainly restricted to the thermal properties such as heat conductivity.[6,7] A particular study on the field uses nonequilibrium simulations to calculate thermal conductivity in a two-dimensional (2D) Ising system based on microcanonical algorithm,[8] which was later extended to include external magnetic field.[9]

Therefore, in this study, the understanding of the effect of temperature variation, but restricted only to thermal steady state, on magnetic system has been extended by performing Monte Carlo simulation to investigate magnetic properties, i.e., the magnetization and the magnetic susceptibility including their spatial resolution. The simulation considers the use of Ising model, which has been proven to be useful in many areas starting from biological systems[10,11] to financial problems[12,13] and statistical mechanics, with the ultrathin film or 2D structure. Also, in magnetic material problems, both theoretical[14,15] and experimental investigations[16–18] have also shown, in terms of critical exponents, that the 2D Ising system is very useful for the study of magnetic behavior in thin ferromagnetic films. To outline, the study investigates how the overall average magnetic properties, such as the magnetization and the magnetic susceptibility, depend on temperature supplied to the boundary spins from the heat baths and heat bath temperature differences by means of Monte Carlo simulations. Next, the study investigates the variation of these magnetic properties in terms of spatial resolution to observe how local magnetic behavior plays a part in overall average magnetic properties. Then, the "critical temperature," which is defined to be the temperature (of a lower temperature heat bath) where the order parameter of the system vanishes at thermodynamic limit, is extracted to examine how the temperature variation affects the critical phenomena. These are followed by a conclusion, which summarizes a prominent finding from the study, and a suggestion on how the topic would benefit the community.

## II. METHODOLOGY

In this study, we consider the Ising Hamiltonian

$$H = -J\sum_{\langle ij\rangle} S_i S_j, \tag{1}$$

where the spins $S_{i(j)}$ take on the values $\pm 1$ and the sum includes only first nearest-neighbor pairs. The units $J$ and $J/k_B$ are used for temperatures and energies, respectively. The

 ©2007 The American Physical Society

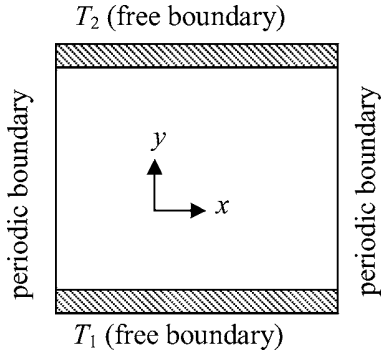



FIG. 1. The setup system structure showing its boundary conditions and its temperature constraint on the free boundaries, i.e., $T_1$ at $y=1$ and $T_2$ at $y=L$, where $T_1 \leqslant T_2$.

considered system is a 2D structure where periodic and free boundary conditions are used for the $x$ and $y$ directions, respectively. The simulations are carried out with total number of spins $N=L_x \times L_y$, where $L_x$ and $L_y$ represent the number of magnetic (atomic) sites along the $x$ and $y$ directions of the system. A rule of thumb in performing Monte Carlo simulations is to choose $L_x$ and $L_y$ as large as possible to minimize finite-size effect. Therefore, in this study we use $L_x=L_y=L$ ranging from 40 to 100 in steps of 10, which are still computationally feasible and fairly large. Actually, these chosen $L$ are picked from the $L$ that the correction to scaling is not significantly needed in the investigation of critical properties.[19] In fact, the finite-size effect causes the deviation in any physical properties between those of the finite system and of the infinite system especially close to critical point. This can be described using the critical behavior of the magnetic interaction. For instance, in a paramagnetic phase, the correlation length of the same spin is small. However, on approaching the critical point from above, the correlation length starts to grow and blows up if the considered system is very large ($L$ tends to infinity). Nevertheless, for finite $L$, the divergence of the correlation length is not permitted since the largest value of the correlation length itself is $L$. Furthermore, due to finite-size effect, which arises from the free surfaces (if there are any), or the periodic image (if the periodic boundary condition is chosen), the rate of correlation growing in the finite-size system and the infinite system is different, and this alters the magnetic properties in the finite system from the infinite system. For example, it is very obvious that the magnetization in the finite system does not cease down to zero at the critical point.

Next, in applying temperatures to the system, along the $y$ direction, at $y=1$ and $L_y$, the fixed temperatures $T_1$ and $T_2$ where $T_1 < T_2$ (see Fig. 1) are supplied to the boundary spins. Due to the temperature variation, starting from the $y=1$ side, the temperature steadily increases from $T_1$ and reaches $T_2$ at the opposite side. In this nonequilibrium state, the heat flux passes from the $T_2$ side to the $T_1$ side, while local temperatures along the pathway can be determined from the heat conduction formula,

$$\frac{1}{A}\frac{dQ}{dt} = -K\frac{dT}{dx}, \tag{2}$$

where $K$ is the thermal conductivity and $dT/dx$ refers to the one-dimensional temperature gradient. However, when the system relaxes to its steady state, the ratio $dQ/dt$ is maintained and the resulting temperature gradient becomes a constant. As a result, at this steady state, the temperature $T$ is linearly proportional to the distance away from the $T_1$ side and it can be estimated that

$$T_y = T_1 + \left(\frac{T_2 - T_1}{L_y - 1}\right)y, \tag{3}$$

where $y$ is the distance away from $T_1$ and $T_y$ is the local temperature at $y$. Because the study considers the system only in its steady state, the local temperature $T_y$ is therefore fixed at the distance $y$ throughout the simulation, giving rise to various local thermal equilibria for each specific distance $y$ in the system.

In this study, we consider the temperature difference between the two heat baths $\Delta T=T_2-T_1$ ranging from 0.0 to 2.8 $J/k_B$ with steps of 0.4 $J/k_B$, and $T_1$ ranging from 0.1 to 3.4 $J/k_B$ with steps of 0.1 $J/k_B$. With these $\Delta T$ and $T_1$ ranges, it is possible to investigate the system in several cases. For instance, both $T_1$ and $T_2$ are in ferromagnetic phase, $T_1$ is in ferromagnetic but $T_2$ is in paramagnetic phase, and both $T_1$ and $T_2$ are in paramagnetic phase. Note that without temperature variation, the 2D Ising critical temperature $T_C$, which splits paramagnetic out of ferromagnetic phase, is $T_C=2/\ln(1+\sqrt{2}) \approx 2.269\ J/k_B$.[20]

Next, in updating the spin configurations during Monte Carlo simulations, a series of successive spin configurations are chosen via importance sampling under the condition of ergodicity and detailed balance. A very popular algorithm, which satisfies these conditions, is the Metropolis algorithm,[21] where a particular spin configuration is different from its previous configuration by only a single spin flip. The probability in accepting a new spin configuration, which is generated from the previous study, is $p=\exp(-\Delta E/k_B T_y)$, where $\Delta E$ is the energy difference associated with the flip and $T_y$ is the local temperature attached to the flipped spin. However, instead of using the conventional Metropolis algorithm, we consider the Wolff algorithm[22] because the Wolff greatly reduces the correlation time $\tau$. This is due to the fact that the updated probability in Metropolis algorithm depends only on an energy difference from a single spin flip. Therefore, this results in a large correlation time $\tau$ among successive spin configurations.[23,24] In the following, the large $\tau$ brings a large statistical error of the magnetization $\langle(\delta m)^2\rangle$ because[23,24]

$$\langle(\delta m)^2\rangle = \frac{1}{n}(\langle m^2\rangle - \langle m\rangle^2)\left(1 + 2\frac{\tau}{\delta t}\right), \tag{4}$$

where, at large enough $n$, $\tau=\Sigma(\langle m_0 m_i\rangle - \langle m^2\rangle)/(\langle m^2\rangle - \langle m\rangle^2)$ is the integrated correlation time and $\delta t$ is the time interval between two successive configurations, and $n$ is the number of configurations being sampled. As can be seen from the above equation, the smaller the $\tau$, the lower the statistical

error. Therefore, one can see the benefit of using the Wolff algorithm upon the Metropolis algorithm since the Wolff provides a smaller $\tau$ in the same system. For example, close to critical temperature in 2D Ising model, the correlation time $\tau$ scales with the system size $L$ as $\tau \propto L^z$, and the gives $z=0.25\pm0.01$,[25] while the Metropolis gives $z=2.1665\pm0.0012$.[26]

In using the Wolff algorithm to make configuration updates, a cluster of the same direction spins is made and flipped. In creating the cluster, a seed spin is randomly chosen and then its neighboring spins, at temperature $T_y$, are added to form a group with a probability

$$p = 1 - \exp\left(-\frac{2J}{k_B T_y}\right). \tag{5}$$

Then, the procedure is repeated for the just added spins until no more spins are added to the cluster. Next all the spins in the cluster are flipped to their opposite directions, i.e., $S_i$ to $-S_i$.

In this Monte Carlo study, with the chosen Wolff algorithm, we first waited for each simulation at least for 1000 Monte Carlo steps per site (MCS) from its initial state (disordered state) to allow the system to relax to its steady state before taking any measurements. After that, during the simulation, the magnetization and the energy are measured when the number of flipped spins exceeds or is equal to $N$. The global average of the magnetization per spin is defined as $m=(1/N)\Sigma_i S_i$, and in each simulation, $N'=50\,000$ configurations are used to calculate the expectation of the magnetization per spin, i.e.,

$$\langle m \rangle = \frac{1}{N'} \sum_{t}^{N'} |m_t|. \tag{6}$$

It is also of interest to observe how the free boundaries play their roles on the microscopic magnetic properties. This is so since the effect of average exchange interaction on a single magnetic spin strongly depends on its neighboring. At the free boundary, the smaller number of nearest-neighbor sites causes the smaller magnitude of average exchange interaction, whereas in the interior the spin feels more bulklike (homogeneously). So the variation of magnetic properties from the free boundary to the interior of the system is expected. Therefore, the spatial dependence of the magnetic properties, i.e., $m_y$ and $\chi_y$, for distance $y$ away from the $T_1$ side, is calculated to observe the free boundary effect (for which the temperature variation is not yet turned on) and the temperature variation effects on the local magnetic properties. Specifically, the study considers the variation of $m_y$ and $\chi_y$ as a function of the distance $y$ away from the $T_1$ side to the direction toward the $T_2$ side. For convenience, only $y$ that is a multiple of lattice spacing unit is considered, and all spins at the same distance $y$ are defined to have local magnetization and local susceptibility per spins in the absence of external field as $m_y=(1/L)\Sigma_{i\in y}S_i$ and $\chi_y=L(\langle m_y^2\rangle - \langle m_y\rangle^2)/k_B T_y$. Note that we have applied the thermal equilibrium formalism to microscopically investigate the thermal steady state because all spins at the same distance $y$ are virtually attached to the same heat bath at temperature $T_y$. In this way, it means that we first consider the region to be small enough to experience only a single and stable temperature, and then the thermal equilibrium technique is applied to study this microscopic region. After that, the dependence of the magnetic properties on the spatial temperature is calculated and the overall magnetic properties are extracted by averaging the microscopic properties. Note that if the system has not yet arrived at the steady state, everywhere except at the boundary the spins we will notice the spatial temperatures to change in time and the thermal equilibrium technique cannot be applied to such case.

Next, based on the local magnetic susceptibility $\chi_y$, the global (average) magnetic susceptibility at zero field is defined as

$$\chi \equiv \left.\frac{\partial m}{\partial h}\right|_{h\to 0} = \frac{1}{L}\sum_y \left.\frac{\partial m_y}{\partial h}\right|_{h\to 0} = \frac{1}{L}\sum_y \chi_y$$
$$= \sum_y \frac{1}{k_B T_y}(\langle m_y^2\rangle - \langle m_y\rangle^2). \tag{7}$$

Also in this study, the critical behavior is investigated via the critical temperature $T_C$. Note that the term critical temperature used in this context is the temperature that the magnetization of the whole system vanishes at the thermodynamic limit. In this temperature variation study, at a particular temperature, some parts of the system may already lie in paramagnetic state, but if there are still some other parts residing in ferromagnetic state, the whole system is categorized to be ferromagnetic since there still exists finite magnetization. Then, $T_C$ is defined if and only if the magnetization is completely destroyed by the thermal fluctuation that spreads throughout the system (in the infinite sized system). However, due to computational limitation, the simulations have to be performed in finite sizes where their finite-size effects must be taken into account. Therefore, in this study, the temperature $T_C$ is phenomenologically located via the fourth-order cumulant $U_L$ of the magnetization per spin,[27]

$$U_L = 1 - \frac{\langle m^4\rangle}{3\langle m^2\rangle^2}, \tag{8}$$

where, at critical point, $U_L$ should be independent of $L$; i.e., for differing sizes $L$ and $L'$, $(U_L/U_{L'})_{T=T_C}=1$. The reason in using Eq. (8), which was created to study thermal equilibrium systems to extract the critical temperature $T_C$, is based on the fact that the correlation length of the magnetization diverges (or the spontaneous symmetry breaking occurs throughout the system) at the critical point. Thus, no matter how large the system size $L$ is, $U_L$ should be the same at the critical point. Therefore, in this study of thermal steady state, for a specific value of $\Delta T$, the critical temperature is defined in terms of $T_1$ (the lower temperature heat bath), which allows the correlation length of global magnetization to diverge at the thermodynamic limit and results in $(U_L/U_{L'})_{T=T_C}=1$. In fact, instead of $T_1$, one may define the critical temperature in terms of $T_2$ if it is desired. However, in this study, the lower temperature of the two heat baths is

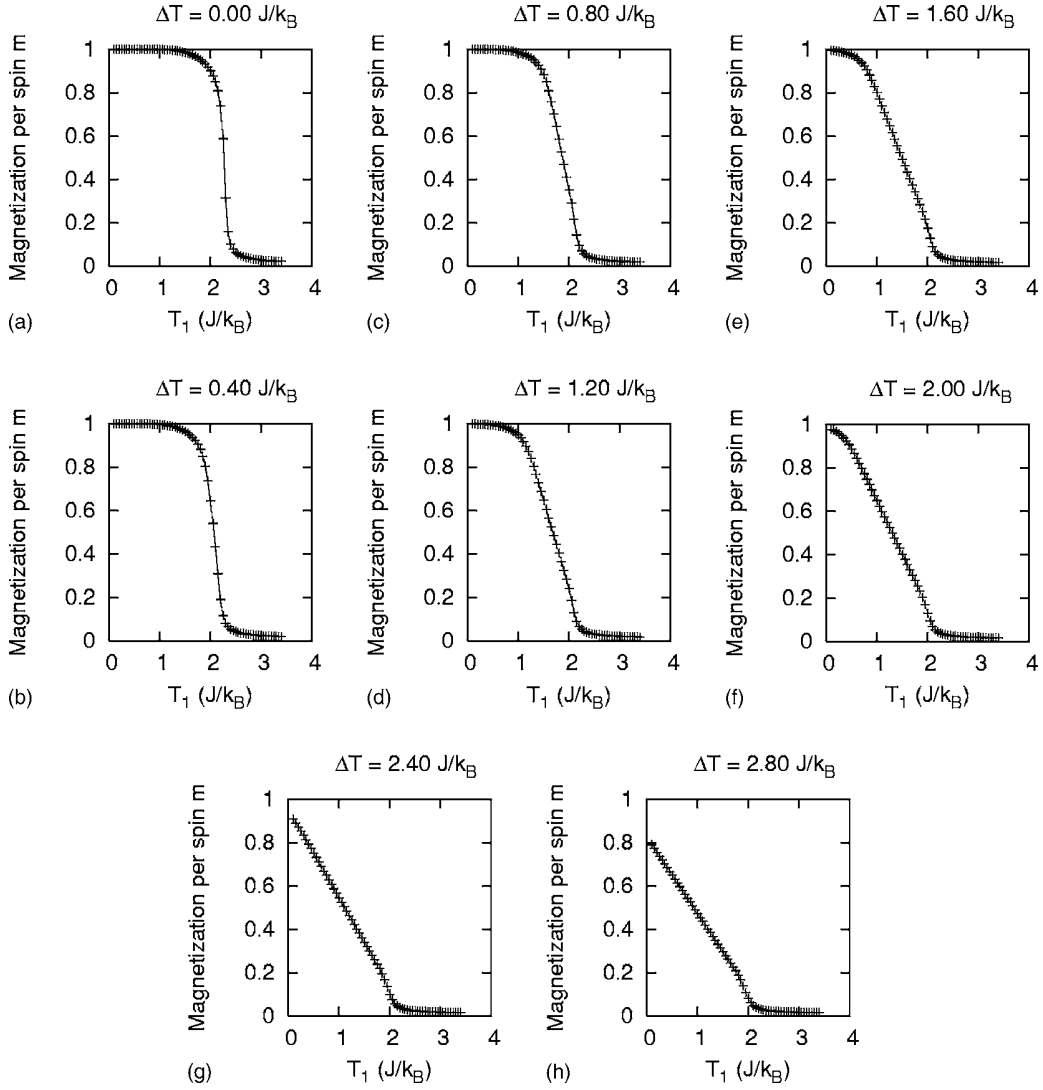



FIG. 2. Magnetization per spin $m$ as a function of temperature $T_1$ for various $\Delta T = T_2 - T_1$.

preferred to define the critical temperature.

Nevertheless, owing to finite-size effects, the cumulant curves obtained from Eq. (8) for different $L$'s do not exactly cross at the same temperature. Therefore, the critical temperature is estimated from $T_C(b=L/L')$ at the limit $(\ln b)^{-1} \rightarrow 0$.[24,27] To maximize the efficiency of this $T_C$ calculation, for each system, a single long simulation is only performed at a temperature $T_0$ and the histogram method[28,29] is used to extrapolate $U_L$ to a temperature nearby in order to find the cumulant crossing points on a fine scale. The temperature $T_0$ is guessed from the temperature at the center of the cumulant crossing points. Approximately $2 \times 10^5$ spin configurations, which are found to compromise between calculation time and statistical error, are used to create the histograms. To exclude the data obtained from temperatures too far from the simulated temperature $T_0$, the range of the extrapolation obeys $|U(T) - U(T_0)| \leq \sigma_E$, where $U = \langle E \rangle$ is the average of the energy and $\sigma_E$ is a standard deviation of $E$ at $T_0$.[30]

## III. RESULTS AND DISCUSSIONS

### A. Overall magnetization and magnetic susceptibility profiles

From the simulations, the magnetization $m$ and susceptibility $\chi$ profiles for various $T_1$ and temperature difference $\Delta T = T_2 - T_1$ are obtained and shown in Figs. 2 and 3. As can be seen from Fig. 2, with increasing $\Delta T$, the magnetization $m$ tends to decrease. This is because the larger $\Delta T$ is, the greater the temperature is at the hotter part of the system (close to the $T_2$ side). Then, at this hotter part, the magnetic spins experience larger thermal fluctuation, resulting in smaller local magnetization magnitude. Consequently, on the overall average, the magnetization reduces with increasing $\Delta T$. Note that even the magnetization significantly reduces in magnitude at large $\Delta T$, the critical point (the temperature where magnetization curve has the maximum slope) only slightly changes. This is due to the fact that there are still some parts of the system, connecting to lower temperature $T_1$, which reside in ferromagnetic phase even magnetic order

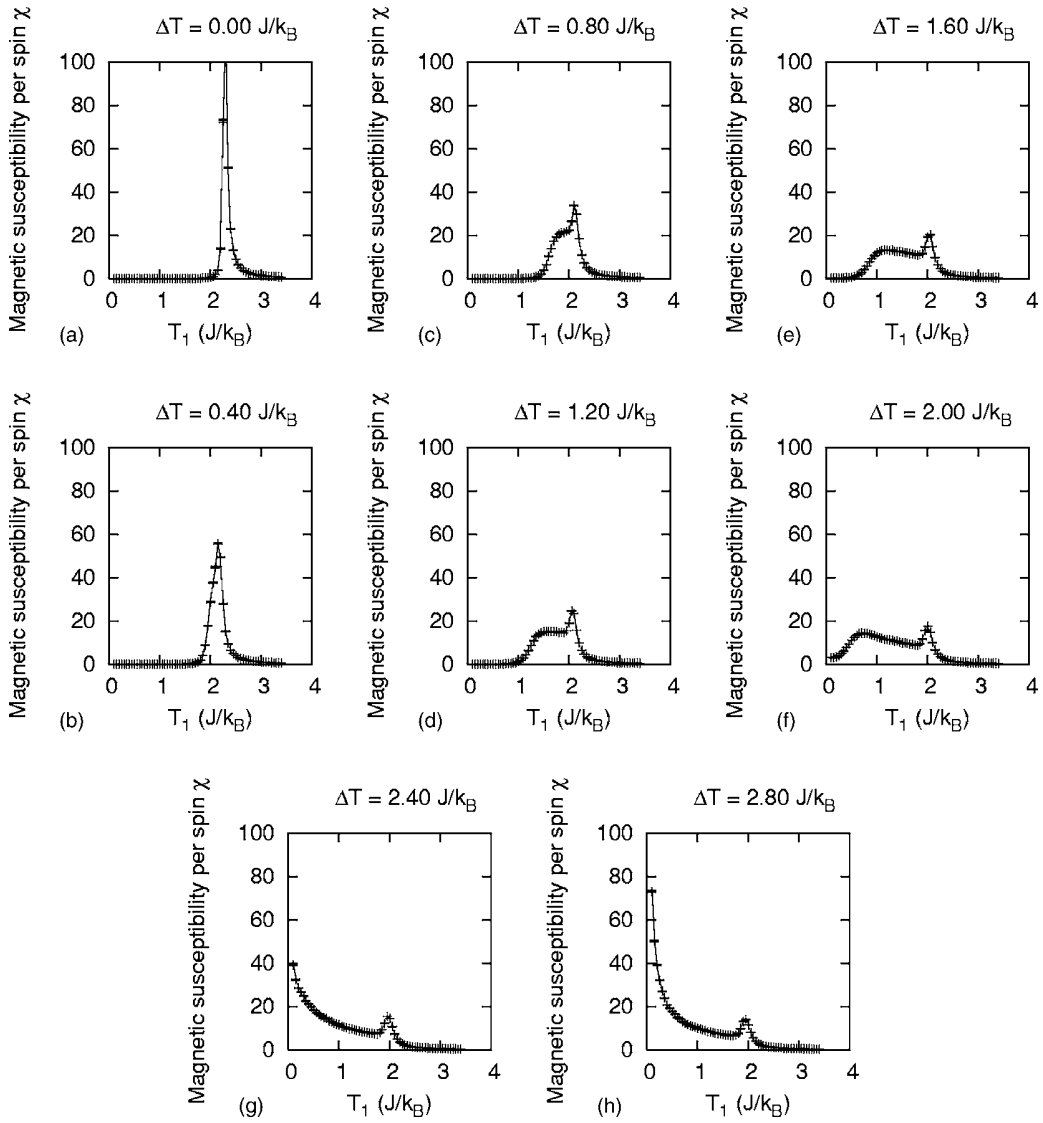
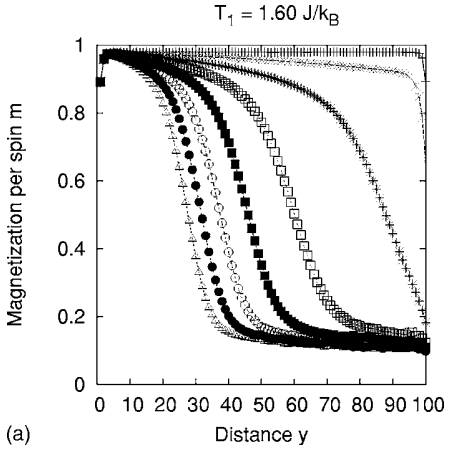



FIG. 3. Magnetic susceptibility per spin $\chi$ as a function of temperature $T_1$ for various $\Delta T = T_2 - T_1$.

of the other parts has already been destroyed. Therefore, the whole system presents some finite magnetization and preserves the overall ferromagnetic behavior. This phenomenon is similar to those found in magnetic thin films where exchange interaction varies from layer to layer.[31] In Ref. 31, because of the differences in exchange interaction magnitude, the magnetic orders from different layers are not destroyed at the same temperature. Therefore, the true critical temperature is defined to be the largest eigenvalue (temperature) that allows the susceptibility to diverge (under the framework of mean-field theory), which is the first encounter of temperature in which the overall magnetization is completely destroyed by the thermal fluctuation if the system is heated from its ferromagnetic phase.

On the other hand, the results for magnetic susceptibility $\chi$, as in Fig. 3, show a broader range of phase transition for $\Delta T > 0$. This is very different from the case $\Delta T = 0$ where the susceptibility blows up only at the normal 2D Ising critical temperature $T_C \approx 2.269\ J/k_B$. This is due to the fact that the susceptibility is representative of magnetization fluctuation which severely increases in magnitude at the critical point. As for $\Delta T > 0$, there is temperature variation, making the temperature field rise in magnitude from $T_1$ to $T_2$. Consequently, different parts of the system experience different local temperatures. Some parts may already reach the critical point where others may not. Each part of the system will not highlight the critical behavior at the same temperature $T_1$. For example, at $T_1 = 1.60\ J/k_B$ and $\Delta T = 0.6\ J/k_B$, the spins close to the $T_1$ boundary are lying in ferromagnetic state and their local susceptibility will be very small. On the other hand, the spins close to the $T_2 = 2.00\ J/k_B$ boundary will start to exhibit large thermal induced magnetization fluctuation since this temperature $T_2$ is close to $T_C$. Therefore, the local susceptibility for spins close to $T_2$ will be fairly large. Another example is the case where $T_1 = 2.20\ J/k_B$ and $\Delta T = 0.2\ J/k_B$. The local susceptibility will be large for spins close to $T_1$, but will be small for spins close to $T_2$ because these spins are already lying in paramagnetic state. These two examples



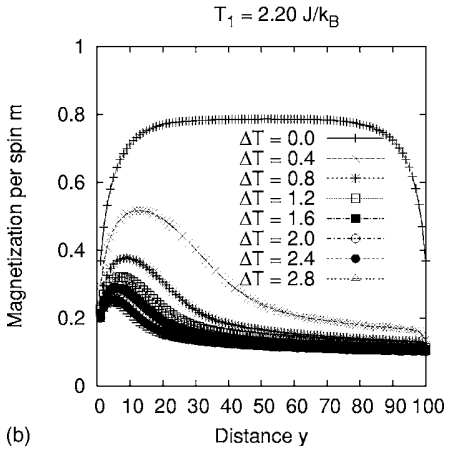
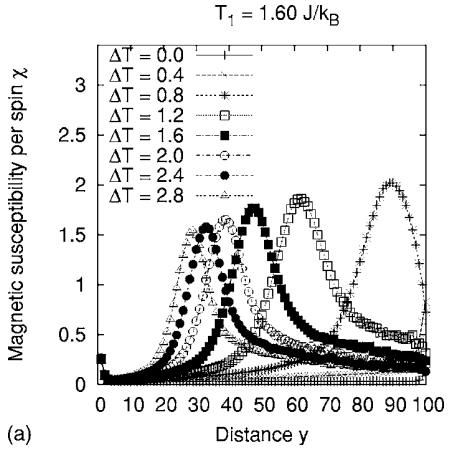




FIG. 4. Spatial variation of magnetization per spin $m$ as a function of distance $y$ away from the $T_1$ boundary for various $\Delta T$ at (a) $T_1=1.60\ J/k_B$ and at (b) $T_1=2.20\ J/k_B$. The legends to symbols in (a), which are the same as those in (b), are removed for visual aids.



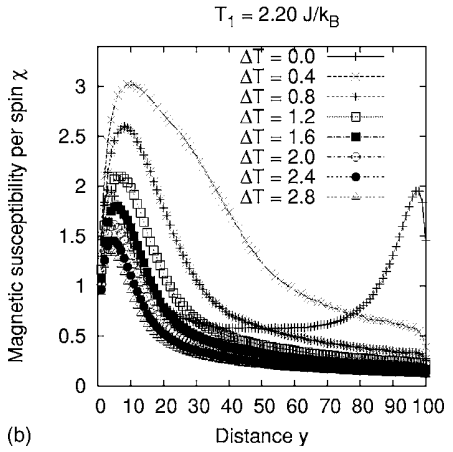




FIG. 5. Spatial variation of magnetic susceptibility per spin $\chi$ as a function of distance $y$ away from the $T_1$ boundary for various $\Delta T$ at (a) $T_1=1.60\ J/k_B$ and at (b) $T_1=2.20\ J/k_B$.

can be used to describe the susceptibility phenomena in Fig. 3. Even $T_1$ is smaller than the normal 2D $T_C$, but with help from $\Delta T$, there will be some interior parts of the system which will exhibit critical behavior. This results in a broader range of the susceptibility peak on the temperature $T_1$ scale. Nevertheless, the peak is not as sharp as the $\Delta T=0\ J/k_B$ system because in the case of $\Delta T=0\ J/k_B$, all spins contribute in magnetization fluctuation at the same temperature, i.e., $T_C$. A more detailed description of this broader range can be given by looking at spatial variation of the magnetic properties (see Figs. 4 and 5).

### B. Spatial variation of magnetization and magnetic susceptibility

The study has found that the temperature variation has a strong effect on the local (spatial) magnetic properties. For example, Fig. 4 shows the spatial variation of magnetization per spin $m$ as a function of distance $y$ away from the $T_1$ boundary for various temperature differences $\Delta T=0.0$, 0.4, 0.8, 1.2, 1.6, 2.0, 2.4, and 2.8 $J/k_B$ at (a) $T_1=1.60\ J/k_B$ and at (b) $T_1=2.20\ J/k_B$. Starting with $\Delta T=0\ J/k_B$, all spins experience the same temperature throughout the system. All parts of the system have the same magnetic behavior; i.e., all local magnetization and local susceptibility show the critical behavior at the same $T_C$, which is about 2.269 $J/k_B$ for normal infinite size 2D Ising system. The spins on both $T_1$ and $T_2$ boundaries have a lower magnetization magnitude than those from other spins in the interior (see Fig. 4). This is due to the fact that the spins inside are coupled with four nearest-neighbor spins, while spins at the edges ($y=1$ and $y=L$) experience the free boundary and are coupled with only three nearest-neighbor spins. Therefore, the spins close to the $T_1$ and $T_2$ boundaries are more susceptible to the thermal fluctuation and result in a smaller magnetization magnitude. On the other hand, the spins which reside in the interior experience a higher level of ferromagnetic interaction, causing more spins to point to the same direction and yield a higher magnitude of magnetization. These results agree well with previous Ising model investigations that the spins at the free boundaries have smaller magnetization magnitudes compared with those in the interior.[32,33]

However, with increasing $\Delta T>0$, the temperature variation induced by temperature gradient in the system linearly raises the temperature $T$ from the $T_1$ boundary to $T_2$ boundary. This makes the local magnetic properties vary, which is

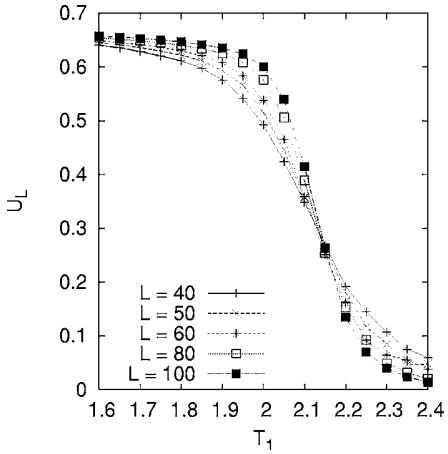



FIG. 6. The fourth-order cumulant of the magnetization for $\Delta T=1.20\ J/k_B$ system as a function of $T_1$. From the figure, it can be estimated that the crossing points take place between $T_1=2.10$ and $2.20\ J/k_B$, therefore, the critical temperature will lie in this region.

very different from the $\Delta T=0$ case. Looking at Fig. 4(a) as an example, at $T_1=1.60\ J/k_B$ and $\Delta T<0.669\ J/k_B$, both $T_1$ and $T_2$ are smaller than the normal $T_C\approx 2.269\ J/k_B$, and the whole system experiences ferromagnetic coupling. Therefore, finite magnetization behavior can be found throughout the system. Nevertheless, the magnetization reduces in magnitude from the $T_1$ boundary to the $T_2$ boundary due to a higher level of thermal fluctuation. On the other hand, for $\Delta T>0.669\ J/k_B$, the spins at and close to the $T_2$ boundary experience paramagnetic interaction because $T_2$ is greater than the normal 2D Ising $T_C$. Consequently, the magnetization reduces very sharply from the $T_1$ to the $T_2$ boundary. This detailed description can also be applied to understand the magnetization behavior in Fig. 4(b). Therefore, these are the reasons why the magnetization declines with increasing $\Delta T$ (e.g., see Fig. 2), which could be very useful in designing sensor applications such as the temperature sensor from magnetic materials.[34] In addition, as one may see in Fig. 4, the distance $y$ away from the $T_1$ boundary is a "thermometer," which indicates the rise of temperature from $T_1$ to $T_2$. This is why the results in Fig. 4 are more or less similar to some subfigures in Fig. 2. Note that the magnetization does not completely reduce to zero because of the finite-size effect.

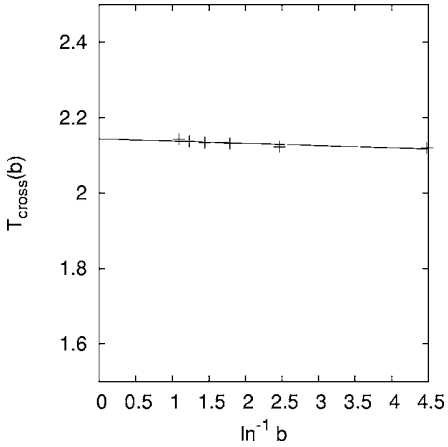



FIG. 7. The extraction of critical temperature $T_C$ for $\Delta T=1.20\ J/k_B$ via the extrapolation of $T_{cross}(b)$ to the limit $\ln^{-1}(b)\rightarrow 0$, where $T_{cross}$ is the temperature that $U_L=U_{L'}$ where $L'=40$ and $L=50$, 60, 70, 80, 90, and 100, and $b=L/L'$. The line is drawn from linear least-squares fit, which gives $T_C=2.14393\pm 0.00393\ J/k_B$.

TABLE I. Critical temperature $T_C$ obtained from Monte Carlo simulation for various temperature differences between the two free boundaries.

| $\Delta T=T_2-T_1$ | $T_C$ |
|---|---|
| 0.0 | 2.26926±0.00018 |
| 0.4 | 2.19187±0.00312 |
| 0.8 | 2.16802±0.00273 |
| 1.2 | 2.14393±0.00393 |
| 1.6 | 2.13046±0.00367 |
| 2.0 | 2.11466±0.00406 |
| 2.4 | 2.09977±0.00640 |
| 2.8 | 2.08514±0.00510 |

Apart from the magnetization results, the temperature variation has a similar effect on the spatial magnetic susceptibility. For instance, at $\Delta T=0$ in Fig. 5(a), the whole system experiences the same temperature $T=T_1=T_2=1.60\ J/k_B$, which is smaller than $T_C$. The system is then far from the critical point and the thermally induced magnetization fluctuation (the susceptibility) is small. However, for $\Delta T=0$ in Fig. 5(b), the temperature $T=T_1=T_2=2.20\ J/k_B$ is close to $T_C$, so the magnetization starts to fluctuate strongly and the susceptibility starts growing (resulting in peaks) near the boundary $T_1$ and $T_2$ ends. In this $\Delta T=0$ case, the interior spins have a smaller susceptibility because there are more (average) number of neighbor spins which provides a higher magnetic interaction, and this interaction behaves as a buffer to the magnetization fluctuation. Similar to magnetization results, for $\Delta T>0$, the distance $y$ indicates the rise of temperature. In Fig. 5, with increasing $\Delta T$, the susceptibility peaks move toward the $T_1$ boundary since some parts inside the system have already reached $T_C$ and this $T_C$ moves towards the $T_1$ end with increasing $\Delta T$.

### C. Critical temperatures

On the other hand, in looking at the critical property, i.e., $T_C$, the fourth-order cumulant in Eq. (8) is found useful. The crossing of $U_L$ is found for the whole range $\Delta T=0.0$–$2.8\ J/k_B$ in this study. An example for the cumulant crossing for $\Delta T=1.2\ J/k_B$ is shown in Fig. 6. As mentioned earlier, to minimize the finite-size effect, an extrapolation of $T_C(b=L/L')$ to the limit $(\ln b)^{-1}\rightarrow 0$ is performed (e.g., see Fig. 7). The critical temperatures $T_C$ at this thermodynamic limit are presented in Table I and plotted as a function of temperature difference $\Delta T=T_2-T_1$ (see Fig. 8). As can been seen, for $\Delta T=0$ which is in the absence of temperature variation, the value of $T_C$ agrees well with the exact solution, which is about $2.269\ J/k_B$ for normal infinite size 2D Ising model. This definitely assures the validity of the simulation codes.

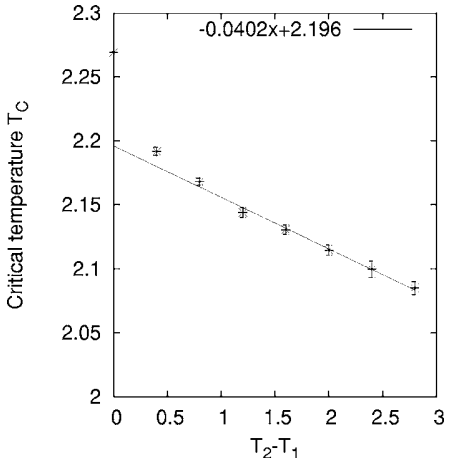



FIG. 8. Critical temperatures $T_C$ obtained from 2D Ising simulations for various $\Delta T=T_2-T_1$. The straight line is a linear least-squares fit to the data for $T_2-T_1 \geqslant 0.8\ J/k_B$.

However, for $\Delta T>0$, $T_C$ reduces very sharply from $\Delta T=0$ to $\Delta T=0.8\ J/k_B$ and afterward reduces slightly for $\Delta T>0.8\ J/k_B$. As can be seen in Fig. 8, it is possible to assign a linear fit to $T_C$ for the range $\Delta T>0.8\ J/k_B$, which gives $T_C(\Delta T)=-0.0402(\Delta T)+2.196$. As evident from the linear fit in Fig. 8, the slope to the fitted function $dT_C/d(\Delta T)=-0.0402$ is rather small. This indicates that even if $T_C$ reduces with increasing $\Delta T$, it does not significantly change in magnitude. This implies that the temperature variation has some minor effects on the critical point by shifting $T_C$ to a smaller value with increasing $\Delta T$. This is so since the greater temperature difference brings more thermal fluctuation into the system so the transition from a ferromagnetic state to the parameter magnetic state occurs at a lower temperature. However, the change is not substantial because the paramagnetic state is defined for a magnetic state that all finite magnetizations are destroyed. Nevertheless, though the temperature variation brings a higher thermal fluctuation to the $T_2$ boundary causing the spins to align randomly and the local average magnetization close to this $T_2$ ceases down to zero, the spins close to the lower temperature side $T_1$ is still intact to the heat bath $T_1$ with a temperature smaller than the normal $T_C$. Therefore, some parts of the system still lie in ferromagnetic state. Hence, the overall average magnetization is not completely destroyed resulting in finite magnetization. As a result, unlike other magnetic properties, such as the sharp reduction in magnetization magnitude and the spreading out of susceptibility peaks over a temperature range, $T_C$ changes very slightly.

## IV. CONCLUSION

In this study, the effects of linear temperature variation on magnetic properties, i.e., the magnetization, the magnetic susceptibility, and the critical temperature, in the thermal steady state are investigated. In the absence of temperature difference ($\Delta T=0$ or $T_1=T_y=T_2$), the result (e.g., $T_C$) was found to agree well with the theoretical exact solution of the thermal equilibrium 2D Ising problem. This assures the validity of the simulation codes. However, when the temperature variation is turned on, the temperature difference at the boundaries supplies thermal fluctuation to the spins in the system with different magnitudes, and this makes the magnetization and the susceptibility become spatially dependent. The hotter and the colder parts of the system tend to show paramagnetic and ferromagnetic behaviors, respectively. The interference between these two behaviors turns out to be the reason why the average magnetization sharply reduces and the susceptibility peak becomes broader, while the critical temperature slightly decreases with increasing the temperature difference. The detailed descriptions of the phenomena are given via the investigation of spatial variation of the corresponding magnetic properties. To conclude, the study provides a detailed understanding of how the magnetic properties behave in response to the temperature variation in thermal steady state in ultrathin film, which may be another step closer in modeling real magnetic materials.

## ACKNOWLEDGMENTS

The authors would like to acknowledge the Commission on Higher Education (Thailand) and the Thailand Research Fund for financial support.

*Corresponding author. FAX: +66 53 943445. Email address: yongyut_laosiritaworn@yahoo.com

[1] A. Moser, K. Takano, D. T. Margulies, M. Albrecht, Y. Sonobe, Y. Ikeda, S. Sun, and E. E. Fullerton, J. Phys. D **35**, r157 (2002).
[2] T. Osaka, T. Asahi, J. Kawaji, and T. Yokoshima, Electrochim. Acta **50**, 4576 (2005).
[3] P. J. Jensen and K. H. Bennemann, Surf. Sci. Rep. **61**, 129 (2006).
[4] F. Aguilera-Granja and J. L. Morán-López, Solid State Commun. **74**, 155 (1990).
[5] Shengbin Hu, Baoxi Xu, Hongxing Yuan, Yunjie Chen, Jun Zhang, and Rong Ji, J. Magn. Magn. Mater. **303**, e62 (2006).
[6] R. Harris and M. Grant, Phys. Rev. B **38**, 9323 (1988).
[7] M. Neek-Amal, R. Moussavi, and H. R. Sepangi, Physica A **371**, 424 (2006).
[8] M. Creutz, Phys. Rev. Lett. **50**, 1411 (1983).
[9] S. S. Mak, Phys. Lett. A **196**, 318 (1995).
[10] S. V. Buldyrev, N. V. Dokholyan, A. L. Goldberger, S. Havlin, C.-K. Peng, H. E. Stanley, and G. M. Viswanathan, Physica A **249**, 430 (1998).
[11] H. E. Stanley, S. V. Buldyrev, A. L. Goldberger, Z. D. Goldberger, S. Havlin, R. N. Mantegna, S. M. Ossadnik, C.-K. Peng, and M. Simons, Physica A **205**, 214 (1994).
[12] D. Horváth, M. Gmitra, and Z. Kuscsik, Physica A **361**, 589 (2006).
[13] A. Krawiecki and J. A. Hołyst, Physica A **317**, 597 (2003).

[14] K. Binder and P. C. Hohenberg, Phys. Rev. B **9**, 2194 (1974).
[15] M. Bander and D. L. Mills, Phys. Rev. B **38**, 12015 (1988).
[16] Y. Li and K. Baberschke, Phys. Rev. Lett. **68**, 1208 (1992).
[17] H. J. Elmers, J. Hauschild, H. Höche, U. Gradmann, H. Bethge, D. Heuer, and U. Köhler, Phys. Rev. Lett. **73**, 898 (1994).
[18] M. J. Dunlavy and D. Venus, Phys. Rev. B **69**, 094411 (2004).
[19] A. M. Ferrenberg and D. P. Landau, Phys. Rev. B **44**, 5081 (1991).
[20] B. M. McCoy and T. T. Wu, *The Two-Dimensional Ising Model* (Harvard University Press, Cambridge, MA, 1973).
[21] N. Metropolis, A. W. Rosenbluth, M. N. Rosenbluth, A. H. Teller, and E. Teller, J. Chem. Phys. **21**, 1087 (1953).
[22] U. Wolff, Phys. Rev. Lett. **62**, 361 (1989).
[23] H. Müller-Krumbhaar and K. Binder, J. Stat. Phys. **8**, 1 (1973).
[24] K. Binder and D. W. Heermann, *Monte Carlo Simulation in Statistical Physics* (Springer-Verlag, Berlin, 1992).
[25] P. D. Coddington and C. F. Baillie, Phys. Rev. Lett. **68**, 962 (1992).
[26] M. P. Nightingale and H. W. J. Blöte, Phys. Rev. Lett. **76**, 4548 (1996).
[27] K. Binder, Z. Phys. B: Condens. Matter **43**, 119 (1981).
[28] A. M. Ferrenberg and R. H. Swendsen, Phys. Rev. Lett. **61**, 2635 (1988).
[29] A. M. Ferrenberg and D. P. Landau, Phys. Rev. B **44**, 5081 (1991).
[30] M. E. J. Newman and G. T. Barkema, *Monte Carlo Methods in Statistical Physics* (Clarendon, Oxford, 1999).
[31] S. S. A. Razee, J. B. Staunton, L. Szunyogh, and B. L. Györffy, Phys. Rev. B **66**, 094415 (2002).
[32] Q. Hong, Phys. Rev. B **41**, 9621 (1990).
[33] Y. Laosiritaworn, J. Poulter, and J. B. Staunton, Phys. Rev. B **70**, 104413 (2004).
[34] H. Osada, S. Chiba, H. Oka, H. Hatafuku, N. Tayama, and K. Seki, J. Magn. Magn. Mater. **272-276**, e1761 (2004).

IOP PUBLISHING JOURNAL OF PHYSICS: CONDENSED MATTER

J. Phys.: Condens. Matter **19** (2007) 236208 (10pp) doi:10.1088/0953-8984/19/23/236208

# Giant dielectric behaviour of $CaCu_3Ti_4O_{12}$ subjected to post-sintering annealing and uniaxial stress

**Prasit Thongbai[1], Chivalrat Masingboon[1], Santi Maensiri[1,4], Teerapon Yamwong[2], Supattra Wongsaenmai[3] and Rattikorn Yimnirun[3]**

[1] Integrated Nanotechnology Research Center (INRC) and Small & Strong Materials Group (SSMG), Department of Physics, Faculty of Science, Khon Kaen University, Khon Kaen, 40002, Thailand
[2] National Metals and Materials Technology Center (MTEC), Thailand Science Park, Pathumthani, 12120, Thailand
[3] Department of Physics, Faculty of Science, Chiang Mai University, Chiang Mai, 50200, Thailand

E-mail: sanmae@kku.ac.th and santimaensiri@gmail.com

Received 21 March 2007, in final form 18 April 2007
Published 8 May 2007
Online at stacks.iop.org/JPhysCM/19/236208

**Abstract**

This paper reports the influences of the post-sintering annealing in argon and uniaxial compressive pre-stress on the giant dielectric properties of the $CaCu_3Ti_4O_{12}$ ceramics sintered at 1100 °C in air for 6 and 16 h. The $CaCu_3Ti_4O_{12}$ ceramic sintered at 1100 °C for 6 h exhibited high $\varepsilon'$ of $\sim 1 \times 10^4$ whereas the $CaCu_3Ti_4O_{12}$ ceramic sintered at 1100 °C for 16 h possessed one order of magnitude higher dielectric constant ($\varepsilon' \sim 2 \times 10^4$). The dielectric behaviour of both samples exhibits Debye-like relaxation, and can be explained based on a Maxwell–Wagner model. Post-sintering annealing in argon for 5 h leads to a significant increase in $\varepsilon'$ for $CaCu_3Ti_4O_{12}$ ceramic sintered at 1100 °C for 16 h but a slight decrease in $\varepsilon'$ for the $CaCu_3Ti_4O_{12}$ ceramic sintered at 1100 °C for 6 h. The $\varepsilon'$ of the 16 h sintered $CaCu_3Ti_4O_{12}$ ceramic after annealing in argon increases with increasing temperatures, and exhibits a peak at about 150 °C, which is closely related to the oxygen vacancies. The dielectric behaviour of this argon-annealed sample follows the UDR law. The dielectric properties of the argon-annealed samples change significantly with the applied compressive stress (the absolute change can reach 25% at a maximum stress of 130 MPa). However, the changes in dielectric properties with the stress in the samples subjected to different sintering times follow opposing trends. The mechanisms responsible for this difference are discussed.

(Some figures in this article are in colour only in the electronic version)

[4] Author to whom any correspondence should be addressed.

 © 2007 IOP Publishing Ltd Printed in the UK 

## 1. Introduction

Dielectric materials that have high dielectric constant and good thermal stability and are Ba/Pb free have particularly attracted ever-increasing attention for their practical applications in microelectronics such as capacitors and memory devices. Recently, calcium copper titanate ($CaCu_3Ti_4O_{12}$), a non-ferroelectric material with a cubic perovskite-related crystal structure, has generated considerable interest because it exhibits a giant dielectric constant of $\varepsilon \sim 10^4$ for polycrystalline ceramics [1–8] and $\varepsilon \sim 10^5$ for single crystals [9] in the kilohertz region over a large temperature range (from 100 to 600 K). This material does not undergo any structural change over the same temperature range, although its dielectric constant abruptly decreases to less than 100 below 100 K, showing a Debye-type relaxation [1, 2, 9]. It has also been reported [6] that the colossal dielectric constant of close to $10^6$ at room temperature can be obtained in $CaCu_3Ti_4O_{12}$ after annealing in flowing argon at 1000 °C for 6 h, and was attributed to the increase in concentration of oxygen vacancies and hence charge carriers. Fang and his co-worker [10] also studied the effects of post-annealing conditions on the dielectric properties of $CaCu_3Ti_4O_{12}$ thin films deposited on $Pt/Ti/SiO_2/Si$ substrates by pulsed laser deposition. They observed that post-sintering annealing in nitrogen atmosphere produced strong low-frequency dielectric relaxation as the annealing temperature increases, whereas annealing in oxygen atmosphere at high temperature suppressed the relaxation and decreased the dielectric constant of the thin films. Most recently, the influence of post-sintering annealing on dielectric properties of $CaCu_3Ti_4O_{12}$ was further investigated by Wang and Zhang [11, 12]. They showed that the annealing treatments on $CaCu_3Ti_4O_{12}$ in reducing (nitrogen) and oxidizing (oxygen) atmospheres have significant changes in dielectric properties near room temperature. These results support the results reported in [6] and strongly suggest that the concentration of oxygen plays an important role in the dielectric properties of $CaCu_3Ti_4O_{12}$.

So far, several explanations for the origin of the colossal dielectric property of $CaCu_3Ti_4O_{12}$ material have been proposed to be due to either intrinsic or extrinsic effects. Since the giant dielectric response of this material was found to be very sensitive to the microstructure (such as grain size) and processing conditions (such as sintering temperature and time, cooling rate, and partial pressure) [3, 5–8], more investigations tend to indicate that the high dielectric constant originates from the extrinsic effect such as internal barrier layer capacitor (IBLC) [3–5], contact-electrode effect [13, 14], and special inhomogeneity of local dielectric response [15]. Although still unclear, the IBLC explanation of the extrinsic mechanism is widely accepted at the present stage [16–21].

In addition to its interesting dielectric property, $CaCu_3Ti_4O_{12}$ has remarkably strong linear current–voltage characteristics without the addition of dopants [22]. These excellent properties render this material particularly attractive for a wide range of applications. However, in some practical applications, dielectric ceramics may be subjected to mechanical or thermal stresses, causing changes in their properties. A prior knowledge of how the material properties change under different load conditions is therefore crucial for proper design of a device and for suitable selection of materials for a specific application. Despite this fact, material constants used in many design calculations are often obtained from a stress free measuring condition, which in turn may lead to incorrect or inappropriate device designs. However, the stress dependence of the permittivity in this highly dielectric material has not been thoroughly studied. It is therefore important to determine the properties of $CaCu_3Ti_4O_{12}$ material as a function of applied stress.

In the present study, we investigate the influences of the post-sintering annealing in argon and uniaxial compressive pre-stress on the giant dielectric properties of the $CaCu_3Ti_4O_{12}$ ceramics sintered at 1100 °C in air for 6 and 16 h. The mechanisms responsible for the giant dielectric properties are discussed.

## 2. Experiment details

$CaCu_3Ti_4O_{12}$ powders were prepared by a conventional mixed oxide technique using the powders of $CaCO_3$ (99.95% purity; CERAC, USA), CuO (99.9% purity; CERAC, USA) and $TiO_2$ (99.5% purity; CERAC, USA). A stoichiometric mixture of the starting materials was ball-milled in ethanol for 24 h with a polyethylene bottle and zirconia balls. The mixed slurry was dried and then calcined at 950 °C in air for 8 h. The calcined powders were ground and passed through a 106 $\mu$m sieve to break up large agglomerates. Green bodies were prepared from the sieved powders using uniaxial pressing in a 16 mm die with an applied pressure of 100 MPa. The compacts were pressureless-sintered at 1100 °C in air for 6 and 16 h. The final dimensions of the samples were ∼12 mm in diameter and ∼3 mm in height. A post-annealing process was carried out in flowing argon (99.999% purity) at 1000 °C for 5 h. Throughout this paper, we assign symbols of CCTO-6 and CCTO-16 for the bulk samples of $CaCu_3Ti_4O_{12}$ sintered at 1100 °C in air for 6 and 16 h, respectively, and assign symbols of CCTO-6–Ar and CCTO-16–Ar for the bulk samples of CCTO-6 and CCTO-16 after post-sintering annealing under flowing argon at 1000 °C for 5 h.

The $CaCu_3Ti_4O_{12}$ ceramics were characterized by x-ray diffraction (XRD) (Philips PW3710, The Netherlands), and scanning electron microscopy (SEM) (LEO 1450VP, UK). The dielectric response of the samples was measured using a Hewlett Packard 4194A impedance gain phase analyser over the frequency ranges from 100 Hz to 1 MHz and at an oscillation voltage of 1 V. The measurements were performed over the temperature ranges from −30 to 160 °C using an inbuilt cooling–heating system. Each measured temperature was kept constant with an accuracy of ±1 °C. Silver paint was coated on both surfaces of the samples and dried overnight. The dielectric properties of the samples after post-sintering annealing were measured under the influence of the compressive stress through spring-loaded pins connected to an $LCZ$-meter (Hewlett Packard 4276A) at the frequency of 1 kHz and room temperature (25 °C). The details of the system are described in elsewhere [23].

## 3. Results and discussion

The microstructure of all the sintered ceramics revealed by scanning electron microscopy (figures 1(a) and (b)) shows polycrystalline grains with estimated grain sizes of 7.7 ± 1.9 and 9.0 ± 1.9 $\mu$m for CCTO-6 and CCTO-16. Figure 1(c) shows XRD patterns of the sintered ceramics before and after post-sintering annealing, confirming a main phase of $CaCu_3Ti_4O_{12}$ (JCPDS card no 75-2188) in all the samples. The values of lattice parameter $a$ calculated from the XRD spectra are 0.7387 ± 0.000 03, 0.7385 ± 0.000 04, 0.7389 ± 0.000 03, and 0.7391 ± 0.000 07 nm for CCTO-6, CCTO-16, CCTO-6–Ar, and CCTO-16–Ar, respectively. The values of $a$ for CCTO-6 and CCTO-16 are slightly lower than the 0.7391 nm reported by Subramanian *et al* [1]. Post-annealing in argon results in an increase in the values of $a$ for CCTO-6–Ar and CCTO-16–Ar, which are close to 0.7391 nm.

Figures 2(a) and (b) show the real and imaginary parts of dielectric dispersion for the samples of CCTO-6 and CCTO-16, measured using a Hewlett Packard 4194A impedance gain phase analyser at the frequency ranges from 100 Hz to 1 MHz with an oscillation voltage of 1 V at various temperatures. It is clearly seen from figure 2(a) that both samples exhibit the giant dielectric permittivity of $\sim 1 \times 10^4$ for CCTO-6 and $\sim 2 \times 10^4$–$2.5 \times 10^4$ for CCTO-16 at low frequencies and each sample has a similar dielectric behaviour. First, all of the samples exhibit the Debye-like relaxation [2, 9, 14, 16]. This behaviour is similar to that observed in CCTO ceramics reported in the literature [3, 4, 7, 8, 17, 24, 25]. Second, $\varepsilon'$ has little frequency dependence below the relaxation frequency. Third, the relaxation peak in both samples shifts to higher frequency at higher temperature.

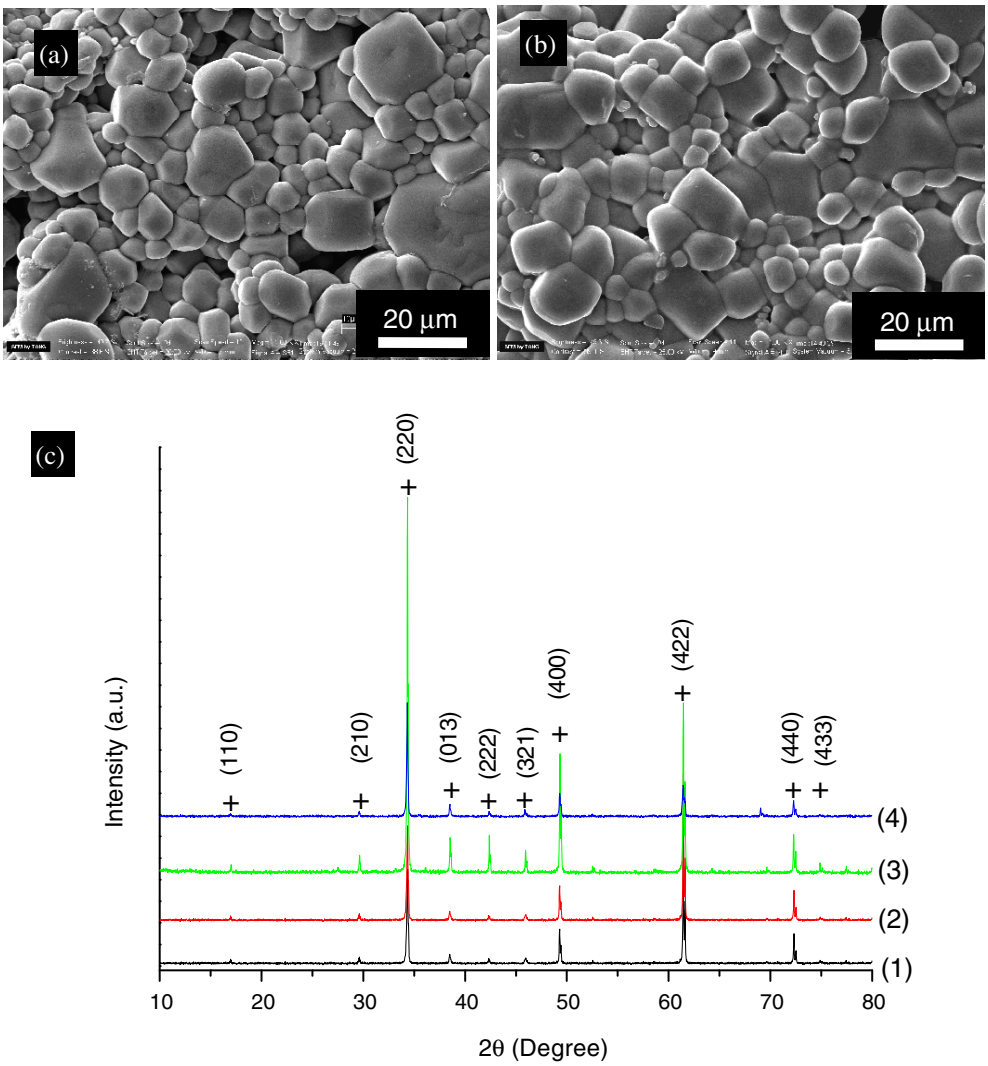



**Figure 1.** (a) and (b) SEM micrographs of sintered CCTO-6 and CCTO-16, respectively. (c) XRD patterns of the sintered materials of CCTO-6 and CCTO-16 before and after annealing at 1000 °C for 5 h under flowing argon. (1) CCTO-6, (2) CCTO-16, (3) CCTO-6–Ar, and (4) CCTO-16–Ar.

The Debye-like relaxation for CCTO-6 and CCTO-16 (figures 2(a) and (b)) can be fitted to the empirical Cole–Cole equation [26]:

$$\varepsilon^*(\omega) = \varepsilon'(\omega) - \mathrm{i}\varepsilon''(\omega) = \varepsilon_\infty + [(\varepsilon_\mathrm{s} - \varepsilon_\infty)/1 + (\mathrm{i}\omega\tau)^\alpha] \quad (1)$$

where $\varepsilon_\mathrm{s}$ and $\varepsilon_\infty$ are the static and high-frequency limits of the dielectric constant, respectively, $\tau$ is the most probable relaxation time, and $\alpha$ is a constant with values between zero and unity. For an ideal Debye relaxation $\alpha = 1$. If $\alpha < 1$, this implies that the relaxation has a distribution of relaxation times, leading to a broader peak shape than a Debye peak as shown in figure 2(b). The solid lines in figures 2(a) and (b) are the fitted results with $\alpha = 0.92$ for CCTO-6 and $\alpha = 0.91$ for CCTO-16. Figure 2(c) shows the plot of log $\tau$ versus $1/T$, in which the solid line

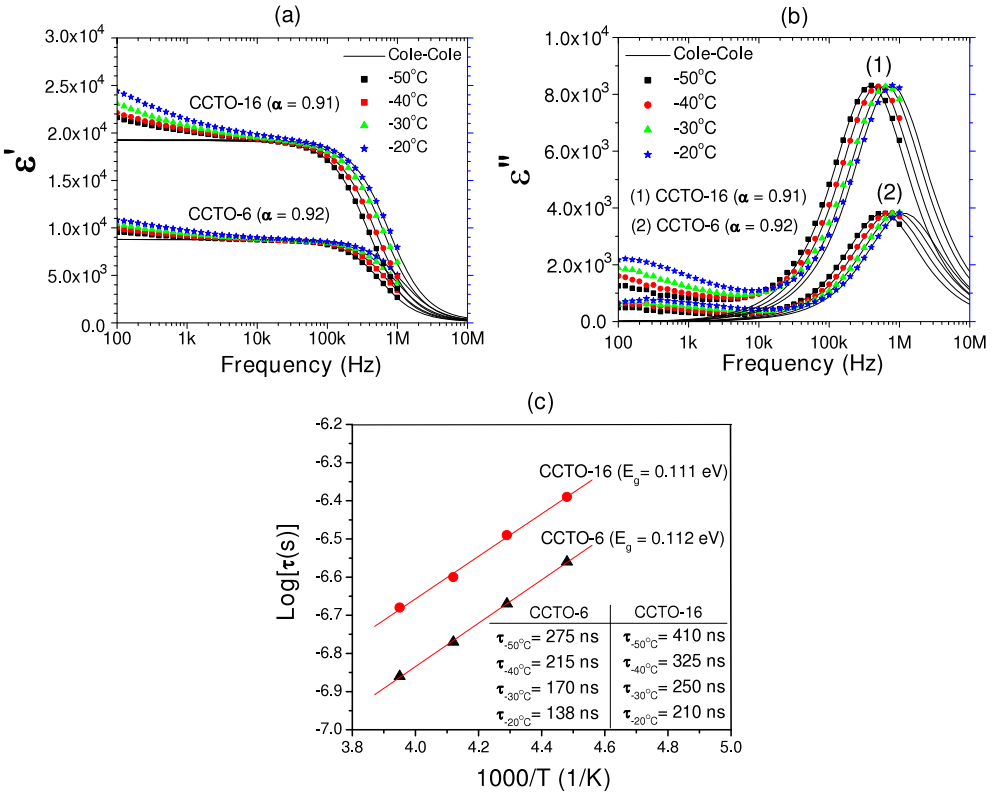



**Figure 2.** (a) Frequency dependence of the dielectric dispersion showing $\varepsilon'$ at several temperatures for the sintered materials of CCTO-6 and CCTO-16. (b) Frequency dependence of the dielectric dispersion showing $\varepsilon''$ at several temperatures for the sintered materials of CCTO-6 and CCTO-16. (c) Arrhenius plot of dielectric relaxation time for the CCTO-6 and CCTO-16 samples. Solid lines in (a) and (b).

is the fitted result obeying the Arrhenius law, i.e.

$$\tau = \tau_0 \exp(E/k_B T) \tag{2}$$

where $\tau_0$ is the pre-exponential factor, $E$ is the activation energy for the relaxation, $k_B$ is the Boltzmann constant, and $T$ is the absolute temperature. $\tau$ is calculated from the relations $\omega\tau = 1$ and $\omega = 2\pi f_p$, where $\omega$ is the angular frequency and $f_p$ is the characteristic frequency corresponding to the peak of $\varepsilon''$. Activation energies of the low-frequency relaxation determined from the slopes of the graphs (figure 2(c)) were obtained to be 0.112 for CCTO-6 and 0.111 eV for CCTO-16. Both values are comparable to the reported values of 0.067 eV [16], 0.08 eV [3, 17], 0.093 eV [18], 0.059–0.076 eV [19], and 0.084–0.132 eV [7] for the grains of $CaCu_3Ti_4O_{12}$.

Since the dielectric response in both CCTO-6 and CCTO-16 shows the Debye-like relaxation which is approximately equal to the pure Debye functional form of a Maxwell–Wagner relaxation, the giant dielectric behaviour of both samples can be explained by using the Maxwell–Wagner relaxation model. The Maxwell–Wagner relaxation can be described by an equivalent circuit consisting of a series array of two subcircuits, one representing grain effects and one grain boundaries [8]. In each subcircuit, the resistor and capacitor are in parallel. From this equivalent circuit, the static permittivity ($\varepsilon'_s$) and dielectric relaxation time ($\tau$) can

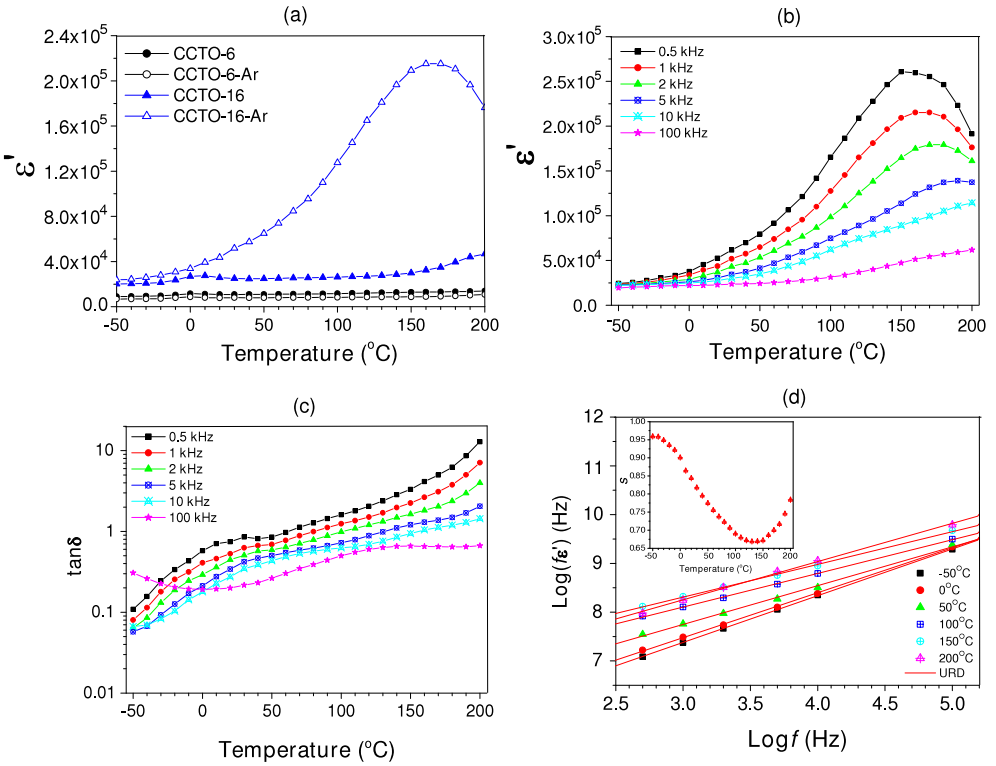



**Figure 3.** (a) Temperature dependence of $\varepsilon'$ at frequency of 100 Hz for the sintered materials of CCTO-6 and CCTO-16 before and after annealing at 1000 °C for 5 h under flowing argon. (b) Temperature dependence of $\varepsilon'$ at various frequencies for the CCTO-16 after annealing at 1000 °C for 5 h under flowing argon. (c) Temperature dependence of $\tan\delta$ at various frequencies for the CCTO-16 after annealing at 1000 °C for 5 h under flowing argon.

be calculated as

$$\varepsilon'_{\mathrm{s}} = (R_{\mathrm{g}}^2 C_{\mathrm{g}} + R_{\mathrm{gb}}^2 C_{\mathrm{gb}})/[C_0(R_{\mathrm{g}} + R_{\mathrm{gb}})^2] \tag{3}$$

and

$$\tau = [R_{\mathrm{g}} R_{\mathrm{gb}}(C_{\mathrm{g}} + C_{\mathrm{gb}})]/(R_{\mathrm{g}} + R_{\mathrm{gb}}), \tag{4}$$

where $R_{\mathrm{g}}$, $R_{\mathrm{gb}}$ and $C_{\mathrm{g}}$, $C_{\mathrm{gb}}$ are the resistance and capacitance of grains and grain boundaries, respectively [27]. Since $R_{\mathrm{gb}} \gg R_{\mathrm{g}}$, and $C_{\mathrm{gb}}$ is also much larger than $C_{\mathrm{g}}$ [3, 8], the effective dielectric permittivity ($\varepsilon'_{\mathrm{s}}$) of the sample at frequencies much lower than the relaxation frequency $1/(2\pi\tau)$ can therefore be obtained approximately from equation (3),

$$\varepsilon'_{\mathrm{s}} = C_{\mathrm{gb}}/C_0 \tag{5}$$

and we can approximate $\tau$ from equation (4) using

$$\tau \approx R_{\mathrm{g}} C_{\mathrm{gb}} = \tau_{\mathrm{g}}(C_{\mathrm{gb}}/C_{\mathrm{g}}) \tag{6}$$

where $\tau = R_{\mathrm{g}} C_{\mathrm{g}}$ is the response time of the grains [8]. Since $C_{\mathrm{g}}$ and $C_{\mathrm{gb}}$ have been reported to be independent of temperature [3, 8], $\tau$ and $\tau_{\mathrm{g}}$ have the same temperature dependence and the electrical response of grains has the same activation energy as that of the observed dielectric relaxation (figure 3(c)). On the basis of this analysis, we conclude that the activation

energies for the response of the grains in the samples of CCTO-6 and CCTO-16 are 0.112 and 0.111 eV, respectively. It is noted that the relation $\varepsilon'_s = C_{gb}/C_0$ implies that $\varepsilon'_s$ is determined only by the ratio between the grain boundary capacitance $C_{gb}$ and the vacuum capacitance of the sample $C_0$, and $\varepsilon'_s$ is constant when $C_{gb}$ is unchanged with temperature and frequency. Liu *et al* [28] observed a constant dielectric permittivity in wide temperature and frequency ranges in $Bi_{2/3}Cu_3Ti_4O_{12}$ because of its constant $C_{gb}$. Therefore, we attribute the differences in dielectric response observed in CCTO-6 and CCTO-16 to the differences in their grain boundary capacitances.

Figure 3(a) compares dielectric constant $\varepsilon'$ of CCTO-6 and CCTO-16 before and after post-sintering annealing, showing a significant increase in $\varepsilon'$ for the CCTO-16 after post-sintering annealing (CCTO-16–Ar) but a slight decrease in $\varepsilon'$ for the CCTO-6 after post-sintering annealing (CCTO-6–Ar). The $\varepsilon'$ of CCTO-16–Ar increases with increasing temperatures, and interestingly exhibits a peak at about 150 °C. This behaviour is important in explaining the effect of post-sintering annealing under a reducing atmosphere in the $CaCu_3Ti_4O_{12}$ system, and thus we further consider the dielectric behaviour of the CCTO-16 in detail. Figures 3(b) and (c) show temperature dependences of $\varepsilon'$ and $\tan\delta$ over the frequencies of 500 Hz–100 kHz. $\varepsilon'$ exhibits a peak around 150 °C (at 1 kHz) (figure 3(a)), whereas $\tan\delta$ increases near-exponentially with increasing temperature without a visible anomaly in the vicinity of 150 °C (figure 3(b)). This implies that the peak in $\varepsilon'$ is not likely caused by the relaxation process. From figure 3(b), upon increasing the measured frequency, the peak position of $\varepsilon'$ is shifted to higher temperatures and the peak height decreases, which is typical of a thermally activated Debye-like behaviour. The obvious upturn in $\tan\delta$ at low temperatures for the curves of high frequencies (at 100 kHz) shown in figure 3(c) is due to the relaxation widely studied before in the $CaCu_3Ti_4O_{12}$ system. This dielectric behaviour observed in CCTO-16–Ar is similar to that of the $CaCu_3Ti_4O_{12}$ sample after post-sintering annealing under nitrogen at 920 °C for 2 h, reported by Wang and Zhang [12]. In their report, the dielectric peak was observed at around 67 °C (340 K) (hereafter referred to as the 67 °C peak) and can be eliminated by annealing in oxidizing ($O_2$) atmosphere and created by annealing in reducing ($N_2$) atmosphere. This strongly suggests that the 67 °C peak is closely related to oxygen vacancies which made the grains of the $CaCu_3Ti_4O_{12}$ ceramic more conductive. Therefore, Wang and Zhang [12] proposed that the 67 °C peak was linked with the conductivity, the dielectric behaviour of the $CaCu_3Ti_4O_{12}$ after annealing in $N_2$ atmosphere followed the universal dielectric law (UDR) [29], and $\varepsilon'$ can be calculated as

$$\varepsilon' = [\tan(s\pi/2)\sigma_0 f^{s-1}]/\varepsilon_0, \tag{7}$$

where $\sigma_0$ and the frequency exponent $s$ are temperature dependent and $\varepsilon_0$ is the electric permittivity of free space. This equation can be rewritten as $f\varepsilon' = A(T)f^s$ with the temperature-dependent constant $A(T) = \tan(s\pi/2)\sigma_0/\varepsilon_0$. Hence, at a given temperature, a straight line with a slope of $s$ should be obtained if $\log_{10}(f\varepsilon')$ is plotted as a function of $\log_{10} f$. Since the URD-law model is typically valid for materials with hopping localized charge carriers, Wang and Zhang [12] confirmed that the charge carriers in the $CaCu_3Ti_4O_{12}$ after annealing in $N_2$ atmosphere are localized and not free charge carriers. This rules out the space-charge polarization as the origin of the 67 °C peak. To confirm this model, we plotted $\log_{10}(f\varepsilon')$ as a function of $\log_{10} f$ for the CCTO-16–Ar as shown in figure 3(c). As expected, straight lines with slopes of $s$ were obtained. The values of the parameter $s$ deduced from linear fitting are presented in the inset of figure 3(c). It is seen from figure 3(c) that with increasing temperature the slope of the linear temperature dependence changes from a negative to a positive value at the transition temperature ~150 °C. This result is consistent with that observed in $CaCu_3Ti_4O_{12}$ after annealing in $N_2$ atmosphere with the transition temperature

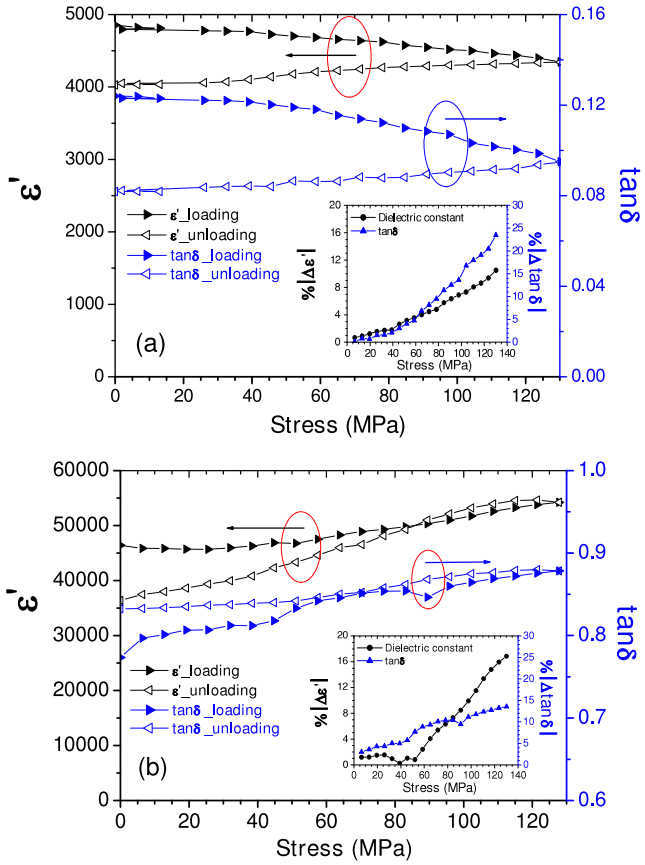



**Figure 4.** Uniaxial stress dependence of $\varepsilon'$ and $\tan\delta$ at a frequency of 100 Hz for the samples of (a) CCTO-6 and (b) CCTO-16 after annealing at 1000 °C for 5 h under flowing argon.

at ∼67 °C. The change in slope implies an alternation of the polarization mechanism [12]. According to our post-sintering annealing results, we conclude that the $\varepsilon'$ peak is unlikely to be caused by a relaxation process. The ∼150 °C peak is closely related to the oxygen vacancies and the dielectric behaviour follows the UDR law. Annealing the $CaCu_3Ti_4O_{12}$ sample in argon atmosphere at high temperatures would increase the concentration of the oxygen vacancies as obtained in the nitrogen-annealed $CaCu_3Ti_4O_{12}$ reported by Wang and Zhang [12].

Figures 4(a) and (b) show the stress dependent dielectric properties for CCTO-6–Ar and CCTO-16–Ar, respectively. It is clearly observed that the dielectric properties of both samples change significantly with the applied compressive stress (the absolute change can reach 25% at the maximum stress of 130 MPa). However, the changes in dielectric properties with the stress in the samples subjected to different sintering times follow opposing trends. For the CCTO-6–Ar, both $\varepsilon'$ and $\tan\delta$ decrease with increasing stress, and, interestingly, continue to decrease upon the reduction of the applied stress (figure 4(a)). On the other hand, the dielectric properties of the CCTO-16–Ar sample increase when the stress is increased and decrease when the stress is gradually reduced, as shown in figure 4(b). To explain these observations, at least qualitatively, one needs to consider the different bases in the dielectric behaviours of the two ceramics. Clearly, the very high dielectric constant observed in CCTO ceramics is attributable to highly resistive grain boundaries [18, 30]. Interestingly, the CCTO-

16–Ar ceramic, which has been subjected to longer sintering (16 h), also possessed one order of magnitude higher dielectric constant, possibly due to higher concentration of the acceptor state (oxygen vacancies) available in the grain boundaries of the ceramic [31]. With lower concentrations of acceptor states, the CCTO-6–Ar should contain more mobile dipoles that can easily be activated by the applied stress. Hence, this leads to a stress-induced ageing mechanism, as reported previously [32–34], that results in the decrease in the dielectric constant and dielectric loss. This stress-induced ageing is irreversible, as the dielectric properties continue to decrease even upon reduction of the applied stress (figure 4(a)). On the other hand, in the case of the CCTO-16–Ar ceramic, with higher concentration of the acceptor states, there are competing mechanisms between the stress-induced ageing and the elastic deformation. Initially, with the stress-induced ageing mechanism still dominating, most of the acceptor states come to rest at the grain boundaries and stabilize the stress influence, as it is observed that the dielectric properties are rather stable at lower stress level [32–34]. A further increase in the compressive stress may result in a slight decrease in the grain boundary thickness. The effective dielectric properties of this ceramic, which can be regarded as the boundary layer capacitor (BLC) [16–21, 31], therefore increase, and the decrease in the effective dielectric properties follows with the reduction of the stress, as observed in figure 4(b).

## 4. Conclusion

The giant dielectric behaviour of polycrystalline $CaCu_3Ti_4O_{12}$ ceramics subjected to post-sintering annealing and under uniaxial stress was investigated. The dielectric behaviour of both CCTO-6 and CCTO-16 samples exhibits Debye-like relaxation, and can be explained based on the Maxwell–Wagner model. A significant increase in $\varepsilon'$ was observed for the CCTO-16 after post-sintering annealing in argon (CCTO-16–Ar), whereas a slight decrease in $\varepsilon'$ was observed for the CCTO-6 after post-sintering annealing in argon (CCTO-6–Ar). The $\varepsilon'$ of CCTO-16–Ar increases with increasing temperatures, and interestingly exhibits a peak at about 150 °C. The $\varepsilon'$ peak at 150 °C is unlikely to be caused by a relaxation process but is closely related to the oxygen vacancies. The dielectric properties of both CCTO-6–Ar and CCTO-16–Ar samples change significantly with the applied compressive stress, and this can be explained by the stress-induced ageing mechanism.

## Acknowledgments

The authors would like to thank the Electron Microscopy Unit, Faculty of Science, Khon Kaen University, for providing SEM facilities. This work is supported by The Integrated Nanotechnology Research Center (INRC), Khon Kaen University, and The Postgraduate Education Development (PED) in Physics Program, The Commission on Higher Education, The Ministry of Education, Thailand.

## References

[1] Subramanian M A, Li D, Duan N, Reisner B A and Sleight A W 2000 *J. Solid State Chem.* **151** 323
[2] Ramirez A P, Subramanian M A, Gardela M, Blumberg G, Li D, Vogt T and Shapiro S M 2000 *Solid State Commun.* **115** 217
[3] Sinclair D C, Adams T A, Morrison F D and West A R 2002 *Appl. Phys. Lett.* **80** 2153
[4] Adams T B, Sinclair D C and West A R 2002 *Adv. Mater.* **18** 1321
[5] Fang T T and Shiau H K 2004 *J. Am. Ceram. Soc.* **87** 2072
[6] Bender B A and Pan M J 2005 *Mater. Sci. Eng.* B **117** 339

[7] Shao S F, Zhang J L, Zheng P, Zhong W L and Wang C L 2006 *J. Appl. Phys.* **99** 084106
[8] Liu J, Sui Y, Duan C G, Mei W N, Smith R W and Hardy J R 2006 *Chem. Mater.* **18** 3878
[9] Homes C C, Vogt T, Shapiro S M, Wakimoto S and Ramirez A P 2001 *Science* **293** 673
[10] Fang L, Shen M and Cao W 2004 *J. Appl. Phys.* **95** 6483
[11] Wang C C and Zhang L W 2006 *Appl. Phys. Lett.* **88** 042906
[12] Wang C C and Zhang L W 2006 *Phys. Rev.* B **74** 024106
[13] Lunkenheimer P, Bobnar V, Pronin A V, Ritus A I, Volkov A A and Loidl A 2002 *Phys. Rev.* B **66** 052105
[14] Lunkenheimer P, Fichtl R, Ebbinghaus S G and Loidl A 2004 *Phys. Rev.* B **70** 172102
[15] Cohen M H, Neaton J B, He L X and Vanderbilt D 2003 *J. Appl. Phys.* **94** 3299
[16] Zhang L and Tang Z J 2004 *Phys. Rev.* B **70** 174306
[17] West A R, Adams T B, Morrison F D and Sinclair D C 2004 *J. Eur. Ceram. Soc.* **24** 1439
[18] Chiodeli G, Massarotti V, Capsoni D, Bini M, Azzoni C B, Mozzati M C and Lupotto P 2004 *Solid State Commun.* **132** 241
[19] Capsoni D, Bini M, Massarotti V, Chiodelli G, Mozzatic M C and Azzoni C B 2004 *J. Solid State Chem.* **177** 4494
[20] Kalinin S V, Shin J, Veith G M, Baddorf A P, Lobanov M V, Runge H and Greenblatt M 2005 *Appl. Phys. Lett.* **86** 102902
[21] Fang T T, Mei L T and Ho H F 2006 *Acta Mater.* **54** 2867
[22] Chung S, Kim I and Kang S 2004 *Nat. Mater.* **3** 774
[23] Yimnirun R, Moses P J, Mayer R J and Newnham R E 2003 *Rev. Sci. Instrum.* **74** 3429
[24] Aygun S, Tan X, Maria J P and Cann D 2005 *J. Electroceram.* **15** 203
[25] Zhang J L, Zheng P, Wang C L, Zhao M L, Li J C and Wang J F 2005 *Appl. Phys. Lett.* **87** 142901
[26] Cole K S and Cole R H 1941 *J. Chem. Phys.* **9** 341
[27] Hippel V 1954 *Dielectrics and Waves* (New York: Wiley)
[28] Liu J, Duan C, Yin W, Mei W N, Smith R W and Hardy J R 2004 *Phys. Rev.* B **70** 144106
[29] Jonscher A K 1983 *Dielectric Relaxation in Solids* (London: Chelsea Dielectric Press)
[30] Chen W P, Xiang W, Guo M S, You W C, Zhao X Z and Chan H L W 2006 *J. Alloys Compounds* **422** L9–12
[31] Moulson A J and Herbert J M 2003 *Electroceramics* (Chichester: Wiley)
[32] Yimnirun R, Ananta S, Ngamjarurojana A and Wongsaenmai S 2006 *Curr. Appl. Phys.* **6** 520
[33] Yimnirun R, Unruan M, Laosiritaworn Y and Ananta S 2006 *J. Phys. D: Appl. Phys.* **39** 3097
[34] Yimnirun R 2006 *Int. J. Mod. Phys.* B **20** 3409

# Cation, dipole, and spin order in $Pb(Fe_{2/3}W_{1/3})O_3$-based magnetoelectric multiferroic compounds

R. Wongmaneerung and X. Tan[a)]
*Department of Materials Science and Engineering, Iowa State University, Ames, Iowa 50011*

R. W. McCallum
*Materials and Engineering Physics Program, Ames Laboratory, U.S. DOE, Ames, Iowa 50011*

S. Ananta and R. Yimnirun
*Department of Physics, Faculty of Science, Chiang Mai University, Chiang Mai 50200, Thailand*

(Received 6 March 2007; accepted 17 May 2007; published online 11 June 2007)

Long range 1:1 cation order was developed in $Pb(Fe_{2(1-x)/3}Sc_{2x/3}W_{1/3})O_3$ solid solution compounds by high temperature solid state reaction. It is found that the degree of cation order directly influences the saturation magnetization in these single phase compounds. A high saturation magnetization ($\sim 0.61\mu_B$/f.u.) was observed for $x=0.15$ at 10 K under 5 T. A ferrimagnetic structure was suggested to take into account for the observed magnetic behavior. These compounds also display a saturated electrical polarization of $\sim 15\ \mu C/cm^2$ at 40 kV/cm at 120 K. © *2007 American Institute of Physics*. [DOI: 10.1063/1.2748098]

Magnetoelectric multiferroic compounds, combining a spontaneous electrical polarization with a net magnetization, have attracted worldwide interest recently due to their great potentials for fundamental research and practical applications.[1–3] However, all the known magnetic ferroelectric oxides either have a low transition temperature or display an extremely small polarization/magnetization. Among these multiferroic compounds, those with the $ABO_3$ perovsite structure show the highest magnetic transition temperatures and the largest electrical polarizations.[3] Considering the fact that most magnetic perovskite oxides have an antiferromagnetic order due to a superexchange coupling between magnetic ions on the *B* site,[4] Baettig and Spaldin[5] and Baettig *et al.*[6] proposed to introduce spontaneous magnetization via *ferrimagnetism* and predicted that $Bi(Fe_{1/2}Cr_{1/2})O_3$ would display an electrical polarization of 80 $\mu C/cm^2$ and a saturation magnetization of $1\mu_B/ABO_3$ f.u. if $Fe^{3+}$ and $Cr^{3+}$ occupy separate *B* sublattices ($B'$ and $B''$) to form a double perovskite structure. The Neel temperature was calculated to be low (<100 K), though. However, such a double perovskite structure with long range *B*-site cation order is not likely to form since $Fe^{3+}$ and $Cr^{3+}$ have the same charge and close ionic sizes. $Bi(Fe_{1/2}Cr_{1/2})O_3$ is, thus, expected to adopt a simple perovskite structure with random occupancy of $Fe^{3+}$ and $Cr^{3+}$ on *B* site. Recent experimental work confirmed that the $Bi(Fe_{1/2}Cr_{1/2})O_3$ epitaxial thin film is isostructural to $BiFeO_3$ with a rhombohedral distortion.[7] A saturation magnetization of only $0.26\mu_B$/f.u. was measured at room temperature due to the absence of long range cation order. In addition, the film was found to be very leaky with an induced polarization of only 2.8 $\mu C/cm^2$ at 82 kV/cm. In the bulk form, $Bi(Fe_{1/2}Cr_{1/2})O_3$ shows neither *B*-site cation order nor any ferri—or ferromagnetic order down to 2 K.[8]

In contrast, a few ferroelectric Pb-based complex perovskite oxides have been reported to display long range 1:1 *B*-site cation order, such as $Pb(Sc_{1/2}Ta_{1/2})O_3$,[9] La-doped $Pb(Mg_{1/3}Nb_{2/3})O_3$,[10,11] and $Pb(Sc_{2/3}W_{1/3})O_3$.[12] The multiferroic $Pb(Fe_{2/3}W_{1/3})O_3$ compound also shows 1:1 cation order, however, the chemical order is very weak and the cation ordered domains are limited to the nanometer scale (<5 nm).[13–15] Developing long range cation order in $Pb(Fe_{2/3}W_{1/3})O_3$ for large saturation magnetization has been experimentally attempted previously with $Mg^{2+}$ doping[16] and $Co^{2+}$ doping.[17] The present work aims to enhance cation order in $Pb(Fe_{2/3}W_{1/3})O_3$ through solid solution with $Pb(Sc_{2/3}W_{1/3})O_3$, both of which have a *B*-cation ratio of 2:1. Magnetic as well as ferroelectric properties are assessed as a function of the degree of *B*-site cation order.

Ceramics in the solid solution $(1-x)Pb(Fe_{2/3}W_{1/3})O_3-xPb(Sc_{2/3}W_{1/3})O_3$($x=0.09, 0.15, 0.21$), or $Pb(Fe_{2(1-x)/3}Sc_{2x/3}W_{1/3})O_3$, were prepared via a solid state reaction method with high purity powders (better than 99.9%). Proportional amount of $Fe_2O_3$, $WO_3$, and $Sc_2O_3$ powders were mixed and calcined at 900 °C for 24 h. Then appropriate amount of PbO powder was mixed and a second calcination was carried out at 850 °C for 2 h. Ceramic pellets were formed by sintering at 890 °C for 2 h followed by a slow cooling procedure at 9 °C/h to 800 °C. The surface layers of the sintered disks were removed before x-ray diffraction experiments. Dielectric characterization was performed with a *LCR* meter (HP-4284A, Hewlett-Packard) in conjunction with an environmental chamber (9023, Delta Design). A heating rate of 3 °C/min was used during measurement. The polarization hysteresis measurement was carried out with a standardized ferroelectric test system (RT-66A, Radiant technologies). A Quantum Design 5T MPMS was used for magnetic characterization.

X-ray diffraction indicates that the as-sintered ceramics are phase pure and display a pseudocubic perovskite structure, as shown in Fig. 1. The lattice parameters increase with $Sc^{3+}$ content and were determined to be 3.9760, 3.9837, and 4.0004 Å for ceramics of $x=0.09$, 0.15, and 0.21, respectively. This is consistent with the fact that $Sc^{3+}$ has a larger ionic radius than both $Fe^{3+}$ and $W^{6+}$. Furthermore, $(\frac{1}{2}\frac{1}{2}\frac{1}{2})$-type superlattice peaks get strengthened as $Sc^{3+}$ content increases, as revealed clearly by the inset in Fig. 1. In

[a)]Electronic mail: xtan@iastate.edu

 © 2007 American Institute of Physics
Downloaded 13 Feb 2008 to 202.28.27.3. Redistribution subject to AIP license or copyright; see http://apl.aip.org/apl/copyright.jsp

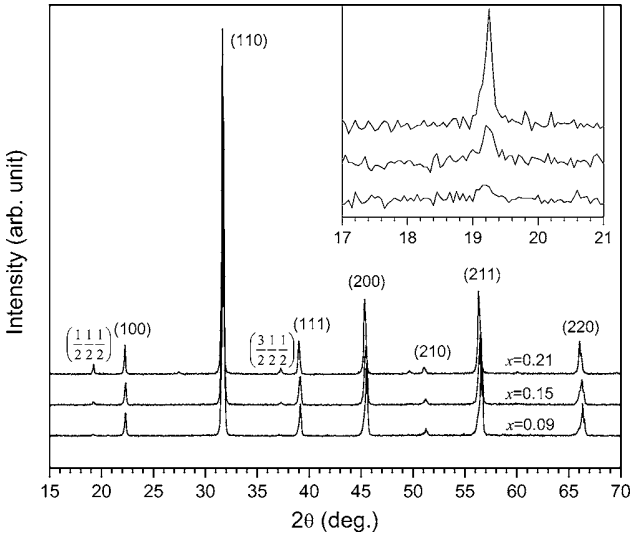



FIG. 1. X-ray diffraction pattern of the sintered $Pb(Fe_{2(1-x)/3}Sc_{2x/3}W_{1/3})O_3$ ceramics. Major peaks are indexed on the basis of a simple cubic perovskite structure. The $(\frac{1}{2}\frac{1}{2}\frac{1}{2})$-type superlattice peaks due to *B*-site cation order are also indexed. The inset shows the close view of the $(\frac{1}{2}\frac{1}{2}\frac{1}{2})$ superlattice peak.

complex perovskite oxides, the presence of the $(\frac{1}{2}\frac{1}{2}\frac{1}{2})$ superlattice peak is an indication of the development of 1:1 *B*-site cation order and the intensity of this superlattice peak has been routinely used to calculate the ordering parameter *S*.[10,11] This parameter ranges from 0 to 1, with 0 marking the complete disorder and 1 marking the complete order. The ordering parameters *S* are calculated to be 0.26, 0.55, and 0.81 for ceramics of $x=0.09$, 0.15, and 0.21, respectively. The double perovskite model,

$$Pb[Sc_{2x/3}Fe_{(1/2-2x/3)}][Fe_{1/6}W_{1/3}]O_3,$$

was used for the calculation.

The dielectric response of these ceramic pellets was examined and the result is shown in Fig. 2. It is noted that broad peaks appear for all three compositions. At 100 kHz, the maximum relative permittivities $\varepsilon_m$ were measured to be 5130 at 198 K, 5460 at 206 K, and 4160 at 198 K for ceramics of $x=0.09$, 0.15, and 0.21, respectively. It appears that the ceramic with $x=0.15$ behaves slightly abnormally. The

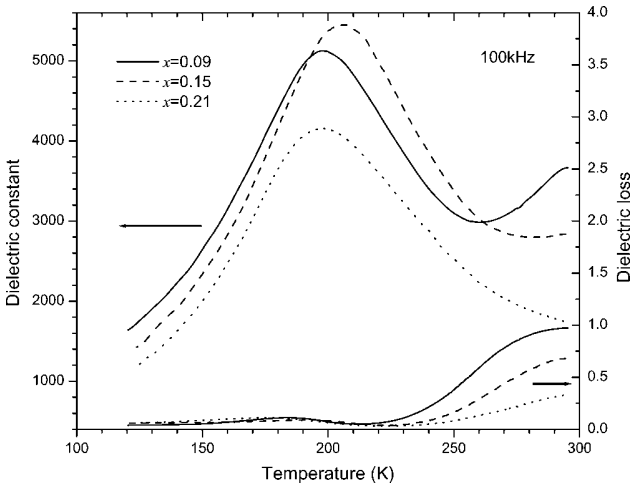



FIG. 2. Relative dielectric permittivity and dielectric loss of the $Pb(Fe_{2(1-x)/3}Sc_{2x/3}W_{1/3})O_3$ ceramics as a function of temperature at 100 kHz.

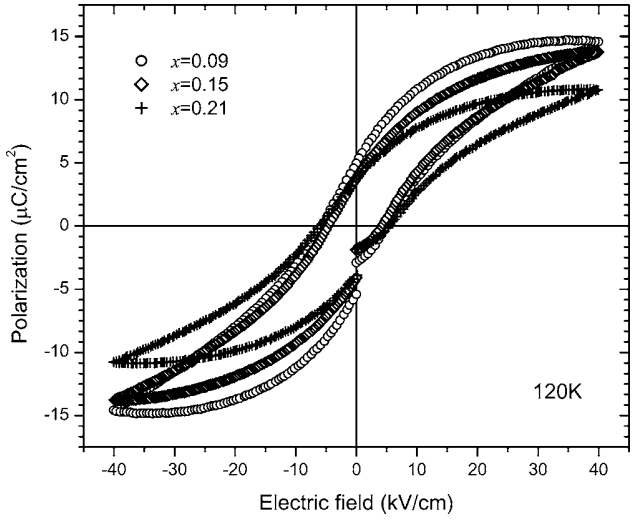



FIG. 3. Polarization vs electric field hysteresis loops measured at 4 Hz at 120 K in the $Pb(Fe_{2(1-x)/3}Sc_{2x/3}W_{1/3})O_3$ ceramics. Well defined saturated loops are observed.

dielectric loss is relatively low for all three ceramics, especially under 230 K. Compared to pure $Pb(Fe_{2/3}W_{1/3})O_3$ ($\varepsilon_m=11\,700$ at $T_m=190$ K at 100 kHz),[13] solid solution with $Pb(Sc_{2/3}W_{1/3})O_3$ leads to a slight higher $T_m$ but a much lower $\varepsilon_m$ value.

The low dielectric loss at low temperatures allows the electric field-induced polarization measurement under quasistatic fields. The electrical polarization versus electric field hysteresis loop was evaluated at 4 Hz at 120 K. As shown in Fig. 3, saturated loops were recorded for all three compositions. Saturation polarizations of 14.6, 13.8, and 10.9 $\mu C/cm^2$ for ceramics of $x=0.09$, 0.15, and 0.21, respectively, were measured at the peak electric field of 40 kV/cm at this temperature. Remanent polarizations of 5.2, 4.0, and 3.8 $\mu C/cm^2$ for $x=0.09$, 0.15, and 0.21, respectively, were recorded. The coercive fields were determined to be 5.5, 4.5, and 5.5 kV/cm for $x=0.09$, 0.15, and 0.21, respectively. Therefore, strong ferroelectricity with large electrical polarizations and low coercive fields is demonstrated in the $Pb(Fe_{2(1-x)/3}Sc_{2x/3}W_{1/3})O_3$ solid solution.

The magnetization under weak field indicates a clear transition from paramagnetic to ferrimagnetic at ~224, ~245, and ~222 K for the ceramics of $x=0.09$, 0.15, and 0.21, respectively. Compared to pure $Pb(Fe_{2/3}W_{1/3})O_3$ ($T_N=370$ K),[13–15] incorporating Sc decreases the transition temperature, which can be attributed to the dilution of the magnetic cations. The magnetization under a strong magnetic field of 5 T for the three ceramics is shown in Fig. 4. Interestingly, the ceramic of $x=0.15$ shows the highest magnetization. The saturation magnetizations at 10 K under 5 T were determined to be $0.22\mu_B/ABO_3$ f.u., $0.61\mu_B/ABO_3$ f.u., and $0.48\mu_B/ABO_3$ f.u. for $x=0.09$, 0.15, and 0.21, respectively. The saturation magnetizations observed in these ceramics are about one order of magnitude higher than disordered perovskite compounds[3,15] and are even two times as high as single crystalline $Bi(Fe_{1/2}Cr_{1/2})O_3$ epitaxial thin films.[7]

We believe that the observed magnetic behavior is dictated by the *B*-site cation order in the ceramics. As mentioned previously, the solid solution can be expressed as a double perovskite compound $Pb[Sc_{2x/3}Fe_{(1/2-2x/3)}]$

Downloaded 13 Feb 2008 to 202.28.27.3. Redistribution subject to AIP license or copyright; see http://apl.aip.org/apl/copyright.jsp

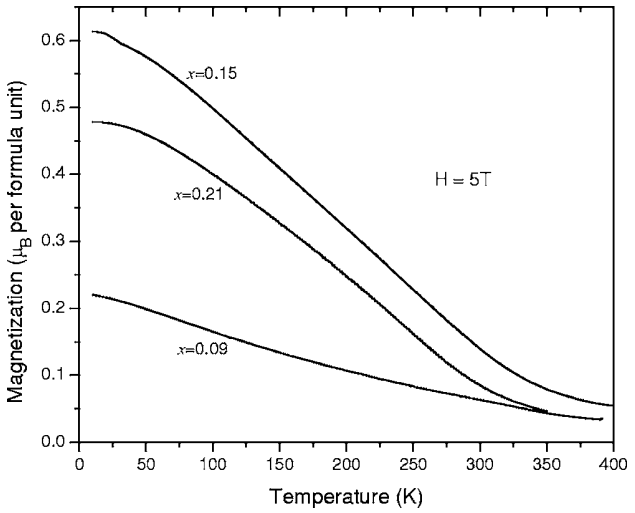



FIG. 4. Magnetization vs temperature during cooling under 5 T in the $Pb(Fe_{2(1-x)/3}Sc_{2x/3}W_{1/3})O_3$ ceramics.

$\times[Fe_{1/6}W_{1/3}]O_3$ when it is fully ordered. We denote the sublattice occupied by $[Sc_{2x/3}Fe_{(1/2-2x/3)}]$ as $B'$, while the one occupied by $[Fe_{1/6}W_{1/3}]$ as $B''$. Due to the superexchange coupling between the $Fe^{3+}$ cations, an antiferromagnetic order is developed on the magnetic moment of $Fe^{3+}$ between the two *B*-site sublattices. Therefore, the measured magnetization depends on the partition of the $Fe^{3+}$ cations on the two sublattices. For $0.00 \leqslant x \leqslant 0.50$, the double perovskite model $Pb[Sc_{2x/3}Fe_{(1/2-2x/3)}][Fe_{1/6}W_{1/3}]O_3$ indicates that the $B'$ sublattice has more $Fe^{3+}$ cations than the $B''$ sublattice and the difference is $(1-2x)/3$ $Fe^{3+}$ ions/f.u. The magnetization data above $T_c$ indicate that the magnetic moment for each $Fe^{3+}$ in the paramagnetic state is roughly $3\mu_B$. Therefore, we estimate that in the ordered state, the saturation magnetization of our double peroskite model for the composition series will be $(1-2x)\mu_B$/f.u. for a fully ordered structure. This is a straight line with respect to $x$ and is plotted in Fig. 5.

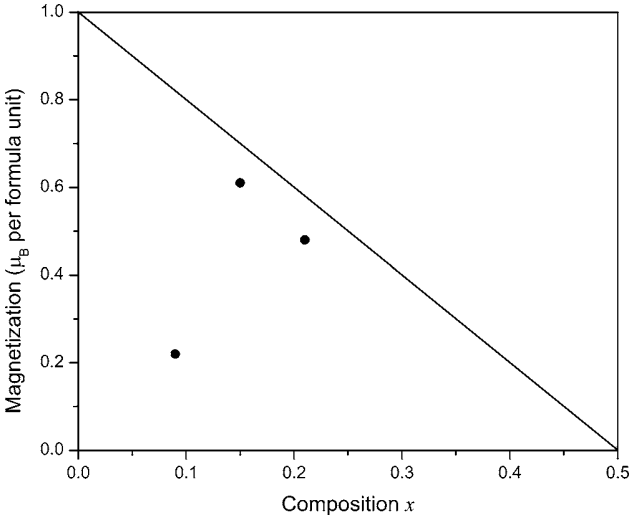



FIG. 5. Predicted linear relation between the saturation magnetization and the composition $x$ in the $Pb(Fe_{2(1-x)/3}Sc_{2x/3}W_{1/3})O_3$ solid solution system based on the ferrimagnetic double perovskite model. The dark dots mark the measured saturation magnetizations.

The three dark dots in Fig. 5 are the measured saturation magnetization at 10 K under 5 T for the ceramics of $x=0.09$, 0.15, and 0.21, respectively. The experimental values of the saturation magnetization correspond to 27%, 87%, and 83% of the predicted values from the straight line for each composition, respectively. For the ceramics of $x=0.15$ and 0.21, it is clear that the experimental data match the ferrimagnetic double perovskite model quite well. The large discrepancy between the experimental data and the ferrimagnetic model for $x=0.09$ is due to the weak long range *B*-site cation order. As mentioned in the x-ray diffraction section, the cation ordering parameters *S* are 0.26, 0.55, and 0.81 for the ceramics of $x=0.09$, 0.15, and 0.21, respectively. It is interesting to note that the values of the chemical order parameter *S* are in good agreement with the percentage of the predicted saturation magnetization in these ceramics, especially for $x=0.09$ and $x=0.21$. Clearly there is a direct correlation between the degree of the long range cation order and the achieved saturation magnetization. The low saturation magnetization measured in the ceramic of $x=0.09$ is due to antisite occupancy of the *B*-site cations. For the ceramic of $x=0.15$, we believe that the ordering parameter *S* is under estimated due to the small size of cation ordered domains.

In summary, long range cation order is developed in ceramics of $Pb(Fe_{2(1-x)/3}Sc_{2x/3}W_{1/3})O_3$ solid solution prepared with a simple solid state reaction method. Saturated polarization versus electric field hysteresis loops were observed for all three ceramics under quasistatic electric fields. Large electrical polarizations (14.6 $\mu C/cm^2$ for $x=0.09$) were measured at 40 kV/cm at 120 K. Direct correlation between the measured saturation magnetization and the degree of *B*-site cation order is observed. Ultrahigh saturation magnetization ($0.61\mu_B/ABO_3$ f.u.) was measured in the ceramic of $x=0.15$.

This work was supported by the Short Term Innovative Research (STIR) program at the Army Research Office through Grant No. W911NF-06-1-0417. Research at Ames Laboratory (RWM) is supported by the U.S. Department of Energy, Basic Energy Sciences, under Contract No. DE-AC02-07CH11358. Three of the authors (R.W., S.A., and R.Y.) are grateful to the Thailand Research Fund.

[1] S. W. Cheong and M. Mostovoy, Nat. Mater. **6**, 13 (2007).
[2] N. A. Spaldin and M. Fiebig, Science **309**, 391 (2005).
[3] M. Fiebig, J. Phys. D **38**, R123 (2005).
[4] J. Kanamori, J. Phys. Chem. Solids **10**, 87 (1959).
[5] P. Baettig and N. A. Spaldin, Appl. Phys. Lett. **86**, 012505 (2005).
[6] P. Baettig, C. Ederer, and N. A. Spaldin, Phys. Rev. B **72**, 214105 (2005).
[7] R. Nechache, C. Harnagea, A. Pignolet, F. Normandin, T. Veres, L. P. Carignan, and D. Menard, Appl. Phys. Lett. **89**, 102902 (2006).
[8] M. R. Suchomel, C. I. Thomas, M. Allix, M. J. Rosseinsky, A. M. Fogg, and M. F. Thomas, Appl. Phys. Lett. **90**, 112909 (2007).
[9] N. Setter and L. E. Cross, J. Appl. Phys. **51**, 4356 (1980).
[10] J. Chen, H. M. Chan, and M. P. Harmer, J. Am. Ceram. Soc. **72**, 593 (1989).
[11] M. A. Akbas and P. K. Davies, J. Am. Ceram. Soc. **80**, 2933 (1997).
[12] P. Juhas, I. Grinberg, A. M. Rappe, W. Dmowski, T. Egami, and P. K. Davies, Phys. Rev. B **69**, 214101 (2004).
[13] P. M. Vilarinho and J. L. Baptista, J. Eur. Ceram. Soc. **11**, 407 (1993).
[14] L. Zhou, P. M. Vilarinho, and J. L. Baptista, J. Eur. Ceram. Soc. **18**, 1383 (1998).
[15] W. Qu, X. Tan, R. W. McCallum, D. P. Cann, and E. Ustundag, J. Phys.: Condens. Matter **18**, 8935 (2006).
[16] G. A. Smolenskii, V. A. Isupov, N. N. Krainik, and A. I. Agranovskaya, Izv. Akad. Nauk SSSR, Ser. Fiz. **25**, 1333 (1961).
[17] K. Uchino and S. Nomura, Ferroelectrics **17**, 505 (1978).

**Downloaded 13 Feb 2008 to 202.28.27.3. Redistribution subject to AIP license or copyright; see http://apl.aip.org/apl/copyright.jsp**

Appl. Phys. A 88, 757–761 (2007)
DOI: 10.1007/s00339-007-4064-z

**Applied Physics A**
**Materials Science & Processing**

S. WONGSAENMAI[1]
W. QU[2]
S. ANANTA[1]
R. YIMNIRUN[1]
X. TAN[2,✉]

# Effect of Ba-substitution on the structure and properties of $Pb_{0.8}Ba_{0.2}[(In_{1/2}Nb_{1/2})_{1-x}Ti_x]O_3$ ceramics

[1] Department of Physics, Faculty of Science, Chiang Mai University, Chiang Mai 50200, Thailand
[2] Department of Materials Science and Engineering, Iowa State University, Ames, IA 50011, USA

**Received: 29 December 2006/Accepted: 14 April 2007**
**Published online: 14 June 2007 •** **© Springer-Verlag 2007**

**ABSTRACT** Ferroelectric ceramics with formula $Pb_{0.8}Ba_{0.2}[(In_{1/2}Nb_{1/2})_{1-x}Ti_x]O_3$ (PBINT) ($x = 0.0, 0.1, 0.2, 0.3, 0.4$ and 0.5) were prepared via a two-step solid state reaction method. It was found that ceramics with compositions in the range of $x = 0.0 \sim 0.3$ showed a pseudo-cubic structure, whereas the ceramic with $x = 0.5$ displayed a tetragonal structure. All compositions showed significant frequency dispersion in their dielectric properties. The remanent polarization $P_r$ as well as the coercive field $E_c$, measured at room temperature, increases with the Ti content. The experimental results obtained in this system are summarized into a phase diagram, with the morphotropic phase boundary (MPB) located at $x = 0.4$. Compared with the $Pb[(In_{1/2}Nb_{1/2})_{1-x}Ti_x]O_3$ solid solution system, incorporating Ba in the A-site leads to a significant decrease in the dielectric maximum temperature $T_{max}$, a suppression of the dielectric relaxation parameter $\gamma$, and a shift of the MPB composition to a higher Ti content.

**PACS** 77.84.Dy; 77.80.Bh; 77.22.Ch

## 1 Introduction

Lead-based relaxor ferroelectric compounds have been extensively investigated because of their unique dielectric, ferroelectric and piezoelectric properties [1–3]. One of these compounds is $Pb(In_{1/2}Nb_{1/2})O_3$ (PIN), which can be prepared as crystals with different degrees of cation order [4–10]. Due to the charge and size difference between the $In^{3+}$ (0.800 Å) and $Nb^{5+}$ (0.64Å) [11], long range In/Nb cation order on the B-site in the $ABO_3$ perovskite structure can be developed by extended thermal annealing. Most importantly, the cation order was observed to have significant impact on the ferroelectric property of PIN. Disordered PIN is a relaxor ferroelectric with a pseudo-cubic structure and a broad dielectric maximum [4–7]. In contrast, ordered PIN shows an antiferroelectric behavior with an orthorhombic structure [6–8]. A sharp peak in the dielectric constant vs. temperature relation is observed around 145 °C [8]. Compared to other relaxor compounds, such as the extensively studied $Pb(Mg_{1/3}Nb_{2/3})O_3$, the high transition temperature of PIN is very attractive, offering better thermal stability in transducer applications [12].

Synthesis of phase pure PIN ceramic with the solid state reaction method has been a challenge due to its small tolerance factor ($t = 0.964$) [13–15]. The presence of a minor amount of cubic pyrochlore phases is detrimental to the dielectric and ferroelectric properties. The wolframite method, as used by Grove [13] for the preparation of perovskite PIN ceramic, is not effective in suppressing the pyrochlore phase formation. The addition of excess $In_2O_3$ was found to be capable of improving the perovskite phase yield [13, 14]. The perovskite phase can also be stabilized with the solid solution method, where the B-site ($In_{1/2}Nb_{1/2}$) is substituted with Ti to form the $Pb(In_{1/2}Nb_{1/2})O_3$-$PbTiO_3$ (PIN-PT) solid solution [16–20] or the A-site Pb is substituted with Ba to form the $Pb(In_{1/2}Nb_{1/2})O_3$-$Ba(In_{1/2}Nb_{1/2})O_3$ (PIN-BIN) solid solution [21]. It is interesting to notice that In/Nb cation order is often observed in PIN single crystals but not polycrystalline ceramics [4–10], while complete cation order is present in the compound of $Ba(In_{1/2}Nb_{1/2})O_3$ [22–24]. In addition, $BaTiO_3$ is also known to be effective at stabilizing the perovskite phase for compounds with small tolerance factors [25].

The present study was initially intended to introduce long range In/Nb cation order in PIN ceramics by forming solid solutions with BIN and, at the same time, to stabilize the perovskite phase. Alternatively, Ti substitution at B-site is known to disrupt the long range cation order [26]. For that reason, the degree of cation order in PIN ceramics may be manipulated by controlling the amount of Ba and Ti addition. Therefore, the ultimate goal is to investigate the effect of the B-site cation order on the electric dipole order in the ceramics. In addition, the role of Ba substitution may be elucidated by comparing the data with our recent work on the PIN-PT solid solution [20].

## 2 Experimental

$Pb_{0.8}Ba_{0.2}[(In_{1/2}Nb_{1/2})_{1-x}Ti_x]O_3$ ($x = 0.0, 0.1, 0.2, 0.3, 0.4$ and 0.5, abbreviated as PBINT hereafter) powders were synthesized by a two-step solid state reaction method. The wolframite $InNbO_4$ was first prepared from oxide powders of $Nb_2O_5$ and $In_2O_3$. Mixed powders were milled with a vibratory mill for 6 h in isopropanyl alcohol. After drying, the mixture was calcined at 1100 °C for 2 h to obtain the intermediate precursor $InNbO_4$. The wolframite precursor was

✉ Fax: +1-515-2945444, E-mail: xtan@iastate.edu

then mixed with appropriate amounts of PbO, $BaCO_3$, and $TiO_2$. Excess amounts of PbO (2 wt. %) and $In_2O_3$ (2 wt. %) were added at this stage. The mixture was milled again for 6 h. After drying, the mixture was calcined in air at temperatures between 1050 and 1250 °C with dwell time of 2 hours and a heating/cooling rate of 20 °C/min inside closed alumina crucibles. Pellets 12.7 mm in diameter and ∼ 1 mm thick were pressed with 1 wt. % PVA binder. The pressed pellets were sintered in a double crucible configuration at temperatures 1300 °C (for $x = 0.0$) and 1250 °C (for $x = 0.1 \sim 0.5$) for 2 h with a heating/cooling rate of 5 °C/min. To minimize PbO loss, the pellets were buried in protective powders of the same composition.

The crystal structure of the sintered ceramics and the degree of cation order was analyzed with X-ray diffraction (XRD) at a step size of 0.05° and a duration time of 1 s. The grain morphology of the ceramics was examined with scanning electron microscopy (SEM). The ferroelectric domain structure was observed with transmission electron microscopy (TEM). The density of ceramics was determined with the Archimedes method. The dielectric properties were measured with an LCR meter (HP-4284A, Hewlett-Packard) in conjunction with an environmental chamber (9023, Delta Design). A heating rate of 2 °C/min and frequencies of 100, 1000 and 10 000 Hz were used during measurement. Ferroelectric hysteresis loops were evaluated at ±30 kV/cm at temperatures of 25, −20, −50 and −80 °C with a standardized ferroelectric test system (RT-66A, Radiant Technologies).

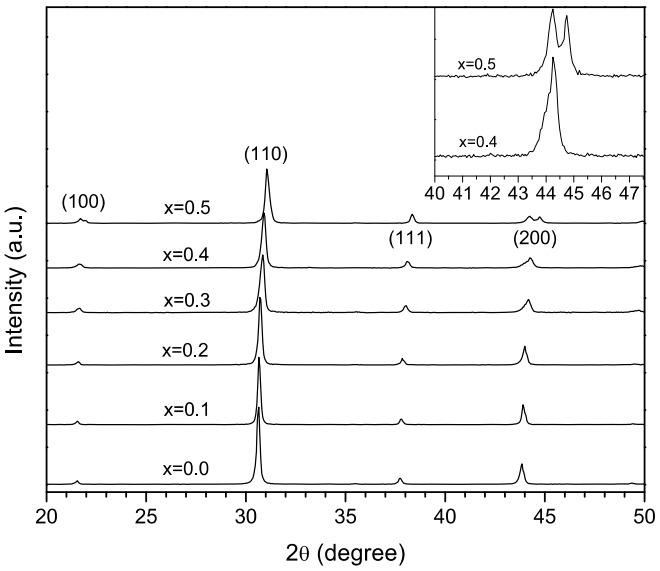



**FIGURE 1** X-ray diffraction spectra of the $Pb_{0.8}Ba_{0.2}[(In_{1/2}Nb_{1/2})_{1-x}Ti_x]O_3$ ceramics. The *inset* shows the close view of the (200) peak in ceramics of $x = 0.4$ and 0.5

## 3 Results and discussion

### 3.1 *Structure of the PBINT ceramics*

Figure 1 shows the X-ray diffraction pattern of the $Pb_{0.8}Ba_{0.2}[(In_{1/2}Nb_{1/2})_{1-x}Ti_x]O_3$ ceramics. It is evident that the as-sintered ceramics are in pure perovskite phase within the detection limit of X-ray powder diffraction, indicating that the addition of Ba and Ti stabilizes the perovskite structure. The splitting of the (200) peak in the composition of $x = 0.5$ indicates a tetragonal symmetry. For compositions of $x = 0.0$ through 0.3, a pseudo-cubic structure was observed. For the ceramic with $x = 0.4$, a broad (100) peak and a distorted (200) peak were noticed. A closer view of the (200) peak for the ceramics with $x = 0.4$ and 0.5 is shown in the inset. It, therefore, appears that the morphotropic phase boundary (MPB) which separates the pseudo-cubic phase from the tetragonal phase in this system is located around $x = 0.4$. Increase in the Ti content leads not only to a structural transition from pseudo-cubic to tetragonal, but also to a decrease in the lattice parameters and the unit cell volume. The decrease in lattice parameter is expected since the radius of $Ti^{4+}$ (0.605 Å) is much smaller than the average radius 0.72 Å for $(1/2In^{3+} + 1/2Nb^{5+})$ [11]. These observations are similar to those of our recent work on the PIN-PT ceramics [20]. It is interesting to notice that the substitution of 20 at. % Pb with Ba on the A-site pushes the MPB composition from $x = 0.3$ to $x = 0.4$.

The X-ray diffraction pattern was collected with $2\theta$ starting from 15° in order to detect a possible superlattice peak $(\frac{1}{2}\ \frac{1}{2}\ \frac{1}{2})$ between 18.5° and 19.0° (spectra with $2\theta < 20°$ were not shown in Fig. 1). This extra peak is the signature of the B-site In/Nb 1 : 1 order. Unfortunately, the $(\frac{1}{2}\ \frac{1}{2}\ \frac{1}{2})$ peak is absent for all as-sintered ceramics. Since Ti is known to disrupt B-site cation order in complex perovskite [26], additional attempts were made to the $Pb_{0.8}Ba_{0.2}(In_{1/2}Nb_{1/2})O_3$ composition (with no Ti addition). Another pellet of this composition was sintered at 1250 °C for 2 h (a lower temperature was used

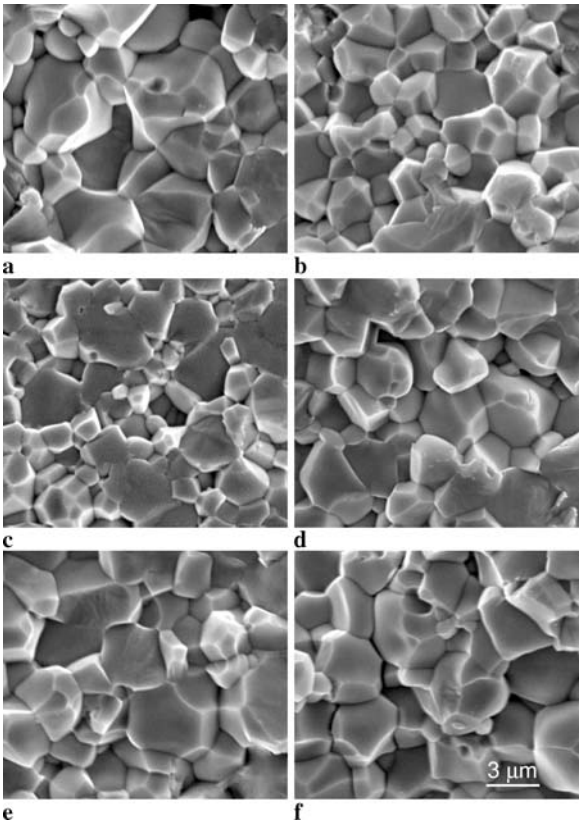



**FIGURE 2** SEM micrographs of the $Pb_{0.8}Ba_{0.2}[(In_{1/2}Nb_{1/2})_{1-x}Ti_x]O_3$ ceramics. (**a**) $x = 0.0$, (**b**) $x = 0.1$, (**c**) $x = 0.2$, (**d**) $x = 0.3$, (**e**) $x = 0.4$, (**f**) $x = 0.5$

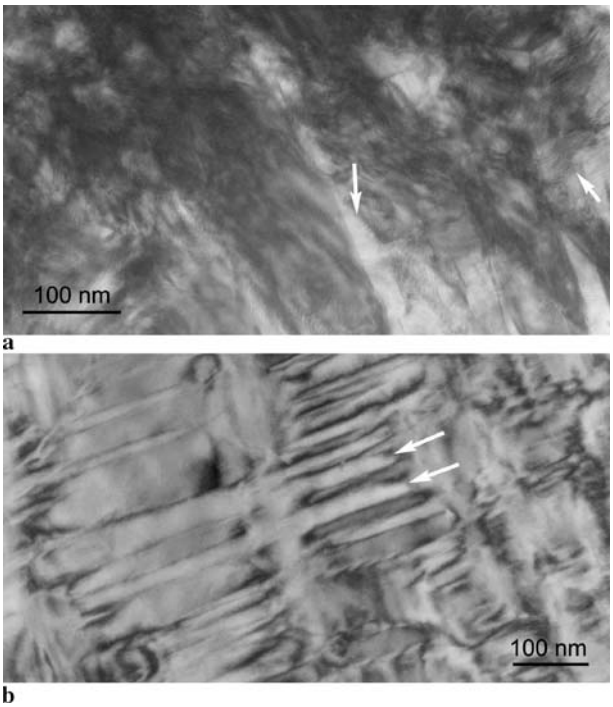



**FIGURE 3** TEM bright field micrographs of the $Pb_{0.8}Ba_{0.2}[(In_{1/2}Nb_{1/2})_{1-x}Ti_x]O_3$ ceramics with [110] zone axis. (**a**) $x = 0.3$. The bright *arrow* in the right points at the disrupted domains while the one in the middle points at a large ferroelectric domain. (**b**) $x = 0.5$. The two bright *arrows* point at two parallel 90° ferroelectric domains

hoping that it was below the order/disorder transition temperature), cooled at a slow rate of 12 °C/h to 830 °C, followed by furnace cool to room temperature. Slow scan (step size 0.05, duration time 2 s) X-ray diffraction was performed for $2\theta$ in the range of 15° to 20°. Again, no superlattice $(\frac{1}{2}\frac{1}{2}\frac{1}{2})$ peak was detected, indicating that long range In/Nb cation order was not developed under the present processing conditions. The absence of long range chemical order, even with the presence of 20 at. % Ba on the A-site, was further confirmed by TEM observations. We speculate that the absence of cation order may be attributed to the fact that In/Nb order is hard to develop in PIN polycrystalline ceramics [4–10]. The results indicate that Ba substitution is effective in stabilizing the perovskite phase but not in enhancing the In/Nb cation order.

The grain morphology of the sintered ceramics was examined by SEM and is shown in Fig. 2. Dense microstructure with uniform grains is evident for all ceramics. The average grain size, determined with the linear intercept method, and the relative density are listed in Table 1. It is found that all the ceramics have a grain size of $2 \sim 3$ μm and a relative density above 90%. The ceramic with $x = 0.0$ (Fig. 2a) shows large grain size and high relative density as a result of a higher sintering temperature (1300 °C). For ceramics with $x = 0.1$ through 0.5, which were sintered at 1250 °C, increase in the Ti content substituting for $(In_{1/2}Nb_{1/2})$ on the B-site leads to an increase in both grain size and relative density, indicating an increasing sinterability of the ceramics.

| Composition ($x$) | Average grain size (μm) | Relative density (%) |
|---|---|---|
| 0.0 | 3.5 | 97 |
| 0.1 | 2.3 | 90 |
| 0.2 | 2.4 | 93 |
| 0.3 | 2.5 | 94 |
| 0.4 | 3.0 | 97 |
| 0.5 | 3.2 | 99 |

**TABLE 1** Average grain size and relative density of the $Pb_{0.8}Ba_{0.2}[(In_{1/2}Nb_{1/2})_{1-x}Ti_x]O_3$ ceramics

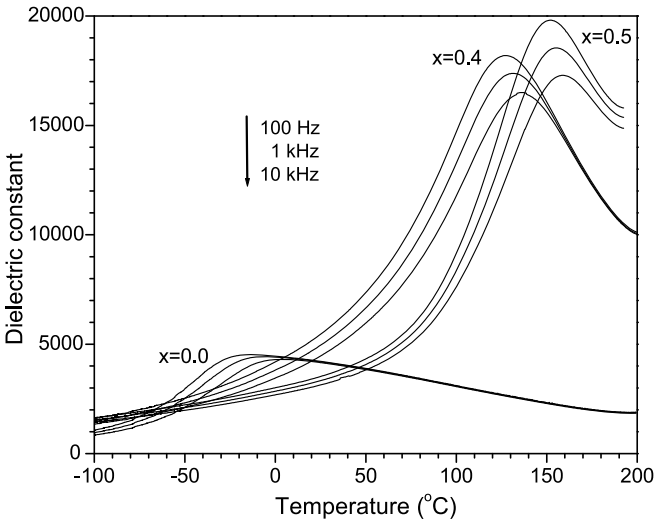



**FIGURE 4** The frequency dispersion of the dielectric constant of the $Pb_{0.8}Ba_{0.2}[(In_{1/2}Nb_{1/2})_{1-x}Ti_x]O_3$ ceramics with $x = 0.0$, 0.4, and 0.5

The subgrain structure of the ceramics was further analyzed with TEM (Fig. 3). Selected area electron diffraction did not show any $(\frac{1}{2}\frac{1}{2}\frac{1}{2})$-type superlattice spots, even in the slowly cooled $Pb_{0.8}Ba_{0.2}(In_{1/2}Nb_{1/2})O_3$ ceramic. The absence of In/Nb cation order revealed by X-ray diffraction was, therefore, further confirmed. The ferroelectric domain structure shows dramatic change over the composition range. For the $Pb_{0.8}Ba_{0.2}(In_{1/2}Nb_{1/2})O_3$ ceramic, a faint contrast was observed in the bright field image for the polar nanodomains (not shown). For the ceramic with $x = 0.3$, a mixture of large ferroelectric domains (a couple of hundred nanometers) and disrupted domains with complicated contrast were observed (Fig. 3a). For the ceramic with $x = 0.5$, large regular lamellar ferroelectric domains were found (Fig. 3b). They have similar morphologies as those in other tetragonal ferroelectric crystals [27] and are, therefore, ferroelectric 90° domains.

### 3.2 *Dielectric and ferroelectric properties*

The temperature dependence of the dielectric constant in the PBINT system was measured and is shown in Fig. 4. All of the compositions show a broad peak at $T_{max}$ and very low dielectric loss. The properties measured at 1 kHz are listed in Table 2. It is found that $T_{max}$ generally increases with increasing Ti content. The maximum dielectric permittivity $\varepsilon_{max}$ also follows this trend. Compared with our recent work on PIN-PT ceramics [20], it is evident that substituting Pb with Ba leads to a significant decrease in $T_{max}$. For example, $T_{max}$ is 155 °C for $Pb_{0.8}Ba_{0.2}[(In_{1/2}Nb_{1/2})_{0.5}Ti_{0.5}]O_3$ while 375 °C for $Pb[(In_{1/2}Nb_{1/2})_{0.5}Ti_{0.5}]O_3$. This indicates that Ba on the A-site is much weaker than Pb for ferroelectricity.

Figure 4 also shows a considerable frequency dispersion in the dielectric behavior. The results are quite similar to those in PIN-PT ceramics [20]. The relative permittivity $\varepsilon_r$ vs. temperature $T$ in ferroelectrics generally obeys the relation

$$\frac{1}{\varepsilon_r} - \frac{1}{\varepsilon_{max}} = B(T - T_{max})^{\gamma} \quad (1)$$

at temperatures above the dielectric peak [28–30]. Equation (1) corresponds to the Curie–Weiss law observed in normal ferroelectrics such as $BaTiO_3$ when $\gamma = 1$. Equation (1) becomes the quadratic relationship suggested for ideal relaxor ferroelectrics when $\gamma$ equals to 2 [1]. Therefore, the parameter $\gamma$ has been used as an indicator of the degree of dielectric relaxation. For all of the ceramics studied in this work, fitting the 1 kHz dielectric constant data leads to the quantitative variation of $\gamma$ with composition, as listed in Table 2. Compared to PIN-PT ceramics [20], the PBINT ceramics show a lower dielectric relaxation parameter at the same Ti content (e. g., 1.52 vs. 1.62 at $x = 0.5$).

The ferroelectric hysteresis loops of the PBINT ceramics were measured at a series of temperature at and below room temperature. Figure 5 shows the observed $P$ vs. $E$ loops at 25 °C and −80 °C. It is found that the hysteresis loops open up as Ti content increases at both temperatures. The ceramics with $x = 0.4$ and 0.5 show well-defined hysteresis loops at both temperatures, indicating the presence of a normal ferroelectric state with long range polar order. For the ceramic with the composition of $x = 0.3$, a slim loop was observed at room temperature while a fairly square loop was found at −80 °C. For the ceramics with $x = 0.0$ through 0.2, nonlinear curves were observed at 25 °C, while slim loops were observed at the low temperature. Measurements of the remanent polarization ($P_r$) and coercive field ($E_c$) from the hysteresis loops indicate that increasing Ti content from $x = 0.3$ to 0.4 leads to a significant jump in $P_r$ at both temperatures. In contrast, this composition change shows almost no increase in $E_c$ at room temperature. Therefore, the ceramic with $x = 0.4$ exhibits a high $P_r$ and a moderate $E_c$, indicating that it is the composition with the best ferroelectric properties in this system. This result also suggests that $x = 0.4$ is the morphotropic phase boundary composition, consistent with the X-ray diffraction analysis.

The monotonic increase in both $P_r$ and $E_c$ with Ti content at room temperature in the present PBINT system is in sharp contrast to that in the PIN-PT ceramics. The $P_r$ at room temperature in the PIN-PT ceramics was observed to reach a peak at the MPB composition of $x = 0.3$ and then decrease sharply with further increase in Ti content in the tetragonal phase [20].

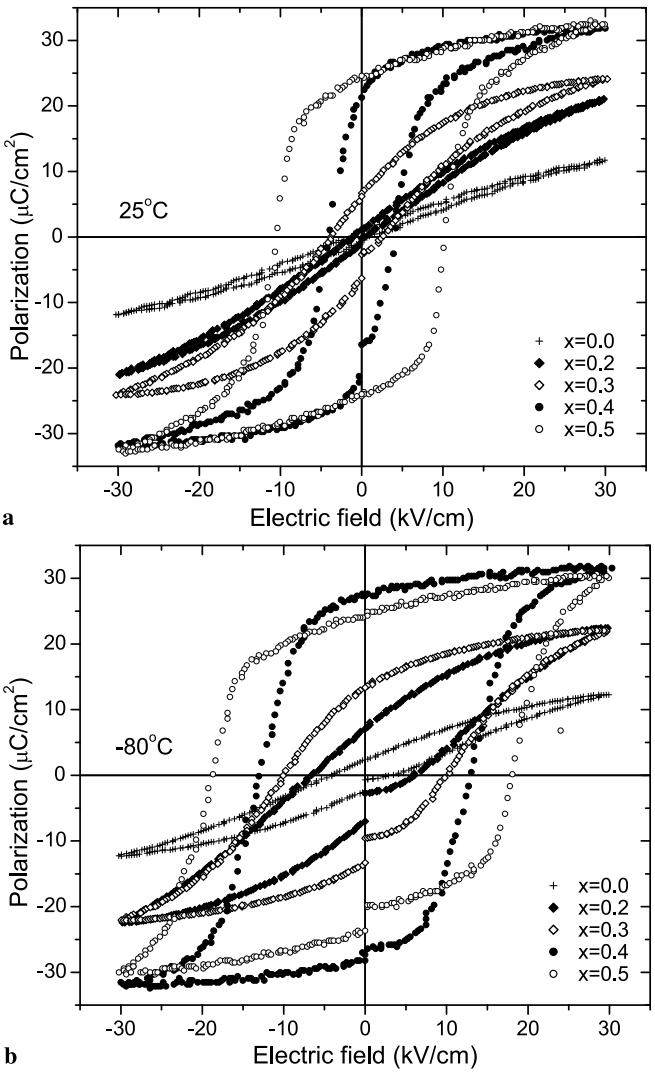



**FIGURE 5** The polarization vs. electric field hysteresis loops measured from the $Pb_{0.8}Ba_{0.2}[(In_{1/2}Nb_{1/2})_{1-x}Ti_x]O_3$ ceramics at 4 Hz. (**a**) 25 °C, (**b**) −80 °C

Therefore, substitution of Pb with Ba improves the room temperature ferroelectric properties of PBINT.

All of these structure and property changes in PBINT from the PIN-PT can be traced back to the Ba-substitution. The $6s^2$ lone pair electrons on Pb cations were shown to be essential for strong ferroelectricity and the tetragonal distortion [31]. Substituting Pb on the A-site with Ba weakens the ferroelectric dipole order and the tetragonal distortion tendency. As a consequence, a lower $T_{max}$ and a higher Ti content at MPB

| Composition ($x$) | $T_{max}$ (°C) | Dielectric properties at $T_{max}$ | | Dielectric properties at 25 celsius | | Relaxation parameter ($\gamma$) |
|---|---|---|---|---|---|---|
| | | $\varepsilon_{max}$ | $\tan\delta$ | $\varepsilon_r$ | $\tan\delta$ | |
| 0.0 | −5 | 4450 | 0.018 | 4189 | 0.005 | 1.83 |
| 0.1 | −14 | 4820 | 0.018 | 4463 | 0.021 | 1.71 |
| 0.2 | 26 | 7591 | 0.029 | 7587 | 0.030 | 1.65 |
| 0.3 | 77 | 10177 | 0.032 | 5326 | 0.076 | 1.63 |
| 0.4 | 131 | 17376 | 0.036 | 4953 | 0.068 | 1.59 |
| 0.5 | 155 | 18541 | 0.049 | 3333 | 0.039 | 1.52 |

**TABLE 2** Dielectric properties of the $Pb_{0.8}Ba_{0.2}[(In_{1/2}Nb_{1/2})_{1-x}Ti_x]O_3$ ceramics at 1 kHz

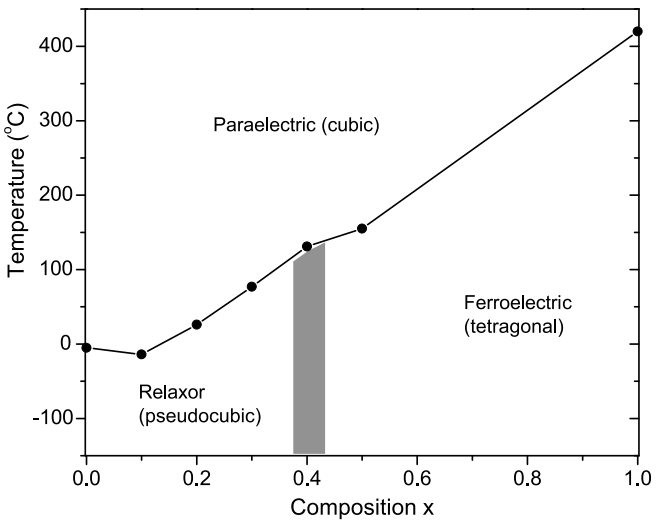



**FIGURE 6** The proposed phase diagram for the $Pb_{0.8}Ba_{0.2}[(In_{1/2}Nb_{1/2})_{1-x}Ti_x]O_3$ system based on the structure analysis and properties measurement

were observed. Because of the low $T_{max}$ in the PBINT ceramics, even at $x = 0.5$ (155 °C), the electrical dipole order has not yet frozen at room temperature, leading to a high switchable polarization. The suppression of the dielectric relaxation parameter $\gamma$ in PBINT seems to be caused by Ba-substitution as well. $BaTiO_3$ appears to have the lowest $\gamma$ among ferroelectric perovskite oxides [29].

The structure and properties of the $Pb_{0.8}Ba_{0.2}[(In_{1/2}Nb_{1/2})_{1-x}Ti_x]O_3$ system discussed above can be summarized into a phase diagram as shown in Fig. 6. The Curie point for $Pb_{0.8}Ba_{0.2}TiO_3$ ($x = 1.0$) is determined by assuming the solid solution follows the rule of mixture [32]:

$$T_c(°C) = 0.8 \times 490 + 0.2 \times 130\,. \quad (2)$$

Three phases are identified: the cubic paraelectric, the pseudocubic relaxor ferroelectric and the tetragonal normal ferroelectric. The cubic paraelectric phase is inferred from the general phase transition trend in the perovskite family of ferroelectric oxides [32]. The morphotropic phase boundary is denoted by the shaded area around $x = 0.4$.

## 4 Conclusion

Complex perovskite ceramics $Pb_{0.8}Ba_{0.2}[(In_{1/2}Nb_{1/2})_{1-x}Ti_x]O_3$ ($x = 0.0, 0.1, 0.2, 0.3, 0.4$ and $0.5$) were successfully prepared via a two-step solid state reaction method. The failure of the development of long range cation order in this system indicates that Ba-substitution is effective in stabilizing the perovskite phase but not in enhancing the cation order. Compared to the PIN-PT solid solution system, replacing the Pb on the A-site with Ba leads to dramatic changes in the structure and properties. The MPB composition shifts from $x = 0.3$ for PIN-PT to $x = 0.4$ for PBINT. The $T_{max}$ is significantly lower in PBINT than for the PIN-PT with the same Ti content (185 ~ 220 °C lower for $x = 0.1$ through 0.5). There is also a slight suppression of the dielectric relaxation parameter $\gamma$ in the PBINT system. The remanent polarization $P_r$ measured at room temperature shows a monotonic increase with Ti content in the PBINT system. While for the PIN-PT solid solution, $P_r$ peaks at the MPB composition and then sharply decreases with further increase in Ti content in the tetragonal phase. All of these changes can be explained based on the fact that Ba cations on the A-site are weaker than Pb cations for ferroelectricity.

**ACKNOWLEDGEMENTS** The authors are grateful to the Thailand Research Fund (TRF), the Commission on Higher Education (CHE) and the Graduate School of Chiang Mai University for financial support.

## REFERENCES

1 G.A. Smolensky, J. Phys. Soc. Japan. **28**, 26 (1970)
2 L.E. Cross, Ferroelectrics **76**, 241 (1987)
3 T.R. Shrout, A. Halliyal, Am. Ceram. Soc. Bull. **66**, 704 (1987)
4 P. Groves, J. Phys. C Solid State Phys. **19**, 5103 (1986)
5 N. Yasuda, S. Shibuya, J. Phys.: Condens. Matter **1**, 10613 (1989)
6 A. Kania, K. Roleder, G.E. Kugel, M. Hafid, Ferroelectrics **135**, 75 (1992)
7 K. Nomura, H. Terauchi, N. Yasuda, H. Ohwa, J. Kor. Phys. Soc. **32**, S989 (1998)
8 N. Yasuda, H. Ohwa, J. Ohhashi, K. Nomura, H. Terauchi, M. Iwata, Y. Ishibashi, J. Kor. Phys. Soc. **32**, S996 (1998)
9 C.A. Randall, D.J. Barber, P. Groves, R.W. Whatmore, J. Mater. Sci. **23**, 3678 (1988)
10 C. Elissalde, F. Weill, J. Ravez, Mater. Sci. Eng. B **25**, 85 (1994)
11 R.D. Shannon, Acta Cryst. **A32**, 751 (1976)
12 Y. Guo, H. Luo, T. He, Z. Yin, Solid State Commun. **123**, 417 (2002)
13 P. Groves, Ferroelectrics **65**, 67 (1985)
14 E.F. Alberta, A.S. Bhalla, Mater. Lett. **29**, 127 (1996)
15 F.G. Jones, C.A. Randall, S.J. Jang, T.R. Shrout, Ferroelectr. Lett. **12**, 55 (1990)
16 U. Kodama, M. Osada, O. Kumon, T. Nishimoto, Ceram. Bull. **48**, 1122 (1969)
17 E.F. Alberta, A.S. Bhalla, J. Kor. Phys. Soc. **32**, S1265 (1998)
18 N. Yasuda, M. Sakaguchi, Y. Itoh, H. Ohwa, Y. Yamashita, M. Iwata, Y. Ishibashi, Japan. J. Appl. Phys. **42**, 6205 (2003)
19 C. Augier, M. Phamthi, H. Dammak, P. Gaucher, J. Eur. Ceram. Soc. **25**, 2429 (2005)
20 S. Wongsaenmai, X. Tan, S. Ananta, R. Yimnirun, J. Alloys Compd., in press (2007)
21 M. Tanaka, M. Sadamoto, J. Phys.: Condens. Matter **5**, L689 (1993)
22 P. Groves, Phase Trans. **5**, 197 (1985)
23 B.P. Burton, E. Cockayne, Phys. Rev. B **60**, R12542 (1999)
24 V. Ting, Y. Liu, R.L. Withers, L. Noren, M. James, J.D. Fitzgerald, J. Solid State Chem. **179**, 551 (2006)
25 A. Halliyal, U. Kumar, R.E. Newnham, L.E. Cross, Am. Ceram. Soc. Bull. **66**, 671 (1987)
26 P. Juhas, I. Grinberg, A.M. Rappe, W. Dmowski, T. Egami, P.K. Davies, Phys. Rev. B **69**, 214101 (2004)
27 Y.H. Hu, H.M. Chan, X.W. Zhang, M.P. Harmer, J. Am. Ceram. Soc. **69**, 594 (1986)
28 H.T. Martirena, J.C. Burfoot, Ferroelectrics **7**, 151 (1974)
29 K. Uchino, S. Nomura, Ferroelectr. Lett. **44**, 55 (1982)
30 N. Vittayakorn, G. Rujijanagul, X. Tan, M.A. Marqardt, D.P. Cann, J. Appl. Phys. **96**, 5103 (2004)
31 R.E. Cohen, Nature **358**, 136 (1992)
32 A.J. Moulson, J.M. Herbert, *Electroceramics: Materials, Properties, Applications*, 2nd edn. (John Wiley & Sons, New York, 2003)

Available online at www.sciencedirect.com
ScienceDirect
Materials Letters 61 (2007) 4466–4470
materials letters
www.elsevier.com/locate/matlet

# Effect of calcination conditions on phase formation and particle size of lead nickel niobate powders synthesized by using $Ni_4Nb_2O_9$ precursor

O. Khamman, R. Yimnirun, S. Ananta *

*Department of Physics, Faculty of Science, Chiang Mai University, Chiang Mai 50200, Thailand*

Received 24 November 2006; accepted 8 February 2007
Available online 16 February 2007

**Abstract**

An approach to synthesize lead nickel niobate, $Pb(Ni_{1/3}Nb_{2/3})O_3$ or PNN, powders with a modified two-stage mixed oxide synthetic route has been developed. Novel intermediate phase of nickel diniobate ($Ni_4Nb_2O_9$) was employed as a B-site precursor, with the formation of the PNN phase investigated as a function of calcination conditions by TG-DTA and XRD techniques. Morphology, particle size and chemical composition have been determined via a combination of SEM and EDX techniques. It has been found that the unreacted PbO and $Pb_{1.45}Nb_2O_{6.26}$ phases tend to form together with PNN, depending on calcination conditions. It is seen that optimization of calcination conditions can lead to a 100% yield of PNN in a cubic phase.
© 2007 Elsevier B.V. All rights reserved.

*Keywords:* Lead nickel niobate; Nickel diniobate; Perovskite; Calcination; Powders-solid-state reaction

## 1. Introduction

Lead nickel niobate, $Pb(Ni_{1/3}Nb_{2/3})O_3$ or PNN, one of the important compounds in the family of perovskite relaxor ferroelectrics, has been known to possess excellent dielectric broadening and electrostrictive properties [1,2]. PNN-based ceramics have been extensively investigated for their applications in multilayer capacitors, electrostrictive actuator, and electromechanical transducer devices [1–3]. However, the performance of these materials is often limited by the coexistence of a low permittivity pyrochlore phase with the perovskite phase [2,4]. Thus, there has been a great deal of interest in the preparation of single-phase PNN powders as well as in the sintering and electrical properties of PNN-based ceramics [3–7].

The mixed oxide synthetic route is probably one of the most fundamental, practical routine methods which has been used, developed and modified in both scientific research and industrial mass production for many years [5–7]. In general, PNN powders synthesized by a mixed oxide method have spatial fluctuations in their compositions. The extent of the fluctuation depends on the characteristics of the starting powders as well as on the processing schedule. Similar problem of pyrochlore formation has been encountered in the preparation of lead magnesium niobate (PMN) powders, where the use of the B-site precursor $MgNb_2O_6$ was proposed by Swartz and Shrout [8] as an effective way of producing PMN powder in high yield. The reaction sequence through which PNN is formed by solid-state reaction, where the use of the B-site precursor $NiNb_2O_6$ has been proposed in analogous to the fabrication of PMN, has been widely investigated by many researchers but with varying conclusions [5–10]. Whereas some workers have been prompted to investigate synthetic route different from the mixed oxide approach, e.g. solution combustion [11], co-precipitation [12], and hydrothermal [13]. The overall aim of the work described here is to refine the two-stage mixed oxide method further. Since, to date, the potential of the $Ni_4Nb_2O_9$ [14,15] as a key precursor for the preparation of PNN has not yet been reported. Moreover, its effect on the formation of perovskite PNN phase under various calcination conditions is very interesting and nonexistent in the literature. Thus, in this work, an attempt has been made to synthesize the lead nickel niobate powders via a rapid vibro-milling technique by employing a novel intermediate phase of nickel diniobate

* Corresponding author. Tel.: +66 53 943367; fax: +66 53 943445.
*E-mail address:* Suponananta@yahoo.com (S. Ananta).

0167-577X/$ - see front matter © 2007 Elsevier B.V. All rights reserved.
doi:10.1016/j.matlet.2007.02.019

($Ni_4Nb_2O_9$) as a key B-site precursor. The phase formation and morphology of the powders calcined at various conditions will be studied and discussed.

## 2. Experimental procedure

The starting materials were commercially available lead oxide, PbO (JCPDS file number 77–1971), nickel oxide, NiO (JCPDS file number 73–1519) and niobium oxide, $Nb_2O_5$ (JCPDS file number 30–0873) (Aldrich, 99% purity). These three oxide powders exhibited an average particle size in the range of 3.0–5.0 μm. The following reaction sequences are proposed for the formation of PNN:

$$4NiO(s) + Nb_2O_5(s) \rightarrow Ni_4Nb_2O_9(s) \quad (1)$$

$$12PbO(s) + 3Nb_2O_5(s) + Ni_4Nb_2O_9(s) \rightarrow 12Pb(Ni_{1/3}Nb_{2/3})O_3(s) \quad (2)$$

First, an intermediate phase of $Ni_4Nb_2O_9$ was prepared from the reaction between NiO and $Nb_2O_5$ at 1250 °C for 0.5 h, with heating/cooling rates of 30 °C/min applied, as reported earlier [15]. $Pb(Ni_{1/3}Nb_{2/3})O_3$ was then synthesized by the solid-state reaction of thoroughly ground mixtures of PbO, $Nb_2O_5$ and $Ni_4Nb_2O_9$ powders that were milled in the required stoichiometric ratio. Powder-processing was carried out in a manner similar to that employed in the preparation of other materials, as described previously [16–18]. A vibratory laboratory mill (McCrone Micronizing Mill) was carried out for 30 min with corundum cylindrical media in isopropyl alcohol (IPA). After drying at 120 °C for 2 h, the reaction of the uncalcined powders taking place during heat treatment was investigated by themogravimetric and differential thermal analysis (TG-DTA, Shimadzu), using a heating rate of 10 °C/min in air from room temperature up to 1100 °C. Based on the TG-DTA results, the mixture was calcined in air at various conditions in closed alumina crucible, in order to investigate the formation of lead nickel niobate.

All powders were subsequently examined by room temperature X-ray diffraction (XRD; Siemens-D500 diffractometer), using Ni-filtered $CuK_\alpha$ radiation to identify the phases formed and optimum calcination conditions for the formation of $Pb(Ni_{1/3}Nb_{2/3})O_3$ powders. Powder morphologies and particle sizes were directly imaged, using scanning electron microscopy (SEM; JEOL JSM-840A). EDX spectra were quantified with the virtual standard peaks supplied with the Oxford Instrument eXL software.

## 3. Results and discussion

The TG-DTA simultaneous analysis of a powder mixed in the stoichiometric proportion of $Pb(Ni_{1/3}Nb_{2/3})O_3$ is displayed in Fig. 1. The TG curve shows three distinct weight losses, i.e. ~25–150 °C,.450–700 °C and 750–1000 °C. In the temperature range from room temperature to ~150 °C, both exothermic and endothermic peaks are observed in the DTA curve, in consistent with the first weight loss. These observations can be attributed to the decomposition of the organic species (i.e. polyethylene milling jar, rubber gloves, skin, etc.) from the milling process [16–18]. Corresponding to the second fall in specimen weight, by increasing the temperature up to ~700 °C, the solid-state reaction occurred between PbO and $NiNb_2O_6$ [4–7]. The broad exothermic characteristics in the

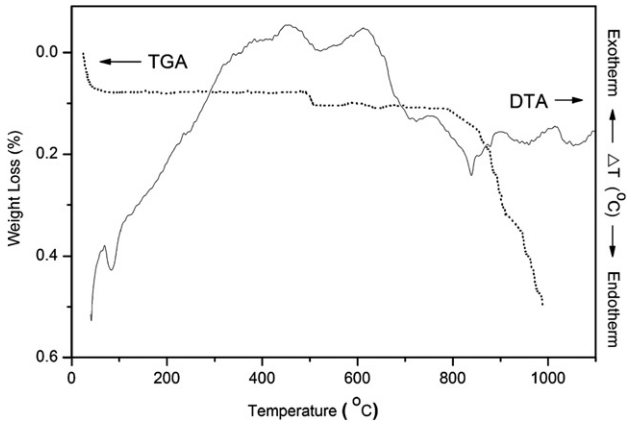



Fig. 1. TG-DTA curves for the mixture of $PbO–Nb_2O_5–Ni_4Nb_2O_9$ powder.

DTA curve represent that reaction, which has maxima at ~450 and 600 °C. Above 700 °C, the DTA curve shows that there are other small peaks at ~750, 900 and 1025 °C, however, it is to be noted that there is no obvious interpretation of these peaks. This is supported by a large fall in sample weight over the same temperature range. These data were used to define the range of calcination temperatures for XRD investigation to between 550 and 1150 °C.

To further study the phase development with increasing calcination temperature in the powders, they were calcined for 2 h in air at various temperatures, up to 1150 °C, followed by phase analysis using XRD. As shown in Fig. 2, for the uncalcined powders and the powders calcined at 550 °C, only X-ray peaks of precursors PbO (●), $Nb_2O_5$ (o) and $Ni_4Nb_2O_9$ (+), which could be matched with JCPDS file numbers 77–1971 [19], 30–0873 [20] and 46–0525 [21], respectively, are present, indicating that no reaction had yet been triggered during the milling or low firing processes. As the temperature increased to 600 °C, the intensity of the precursor phases of $Nb_2O_5$ and $Ni_4Nb_2O_9$ has been found to completely disappear, and crystalline $Pb(Ni_{1/3}Nb_{2/3})O_3$ (▼) started to appear, accompanying with PbO and $Pb_{1.45}Nb_2O_{6.26}$ as separated phases in the powder. This observation agrees well with those derived from the TG-DTA results. For the present work, there are no significant differences between the powders calcined at temperatures ranging from 600 to 800 °C. Further increase of the calcination temperature to 800 °C does not result in very much increase in the amount of $Pb(Ni_{1/3}Nb_{2/3})O_3$, whereas PbO and $Pb_{1.45}Nb_2O_{6.26}$ remain unchanged. This $Pb_{1.45}Nb_2O_{6.26}$ phase was indexable according to a cubic pyrochlore structure with lattice parameters $a$=1056 pm, space group *Fd3m* (no. 227), in consistent with JCPDS file numbers 84–1731 [22].

Upon calcination at 900 °C, the desired $Pb(Ni_{1/3}Nb_{2/3})O_3$ phase becomes the predominant phase and is the only detectable phase in the powders, after calcination at 1050 °C, consistent with the TG-DTA results. This $Pb(Ni_{1/3}Nb_{2/3})O_3$ phase was indexable according to a cubic perovskite structure with lattice parameters $a$=403 pm, space group *Pm3m* (no. 221), in consistent with JCPDS file numbers 34–0103 [23] and literature [7,13]. However, for the present study, it can be seen that at the temperature range of 1100–1150 °C, some peaks of the pyrochlore $Pb_{1.45}Nb_2O_{6.26}$ phase reappear, mixing with the major phase of $Pb(Ni_{1/3}Nb_{2/3})O_3$. This could be attributed mainly to the PbO volatilization, leading to the decomposition of the perovskite phase to the pyrochlore phase, in agreement with the TG-DTA observations at the same temperature range and also the literature [7].

Apart from the calcination temperature, the effect of dwell time was also found to be quite significant. From Fig. 3, it can be seen that the single-phase of $Pb(Ni_{1/3}Nb_{2/3})O_3$ (yield of 100% within the limitations of the XRD technique) was found to be possible in powders calcined at 1050 °C with dwell time of 0.5 h or more (Fig. 3(d,e)) and 1000 °C for at least 5 h (Fig. 3(c)). The observation that the dwell time effect may also play an important role in obtaining a single-phase perovskite product is also consistent with other similar systems [16–18]. In earlier works [3,7,9], long heat treatments at ~1000–1200 °C for at least 4 h were proposed for the formation of $Pb(Ni_{1/3}Nb_{2/3})O_3$ by a mixed oxide synthetic route with columbite $NiNb_2O_6$ precursor, although no details on phase formation

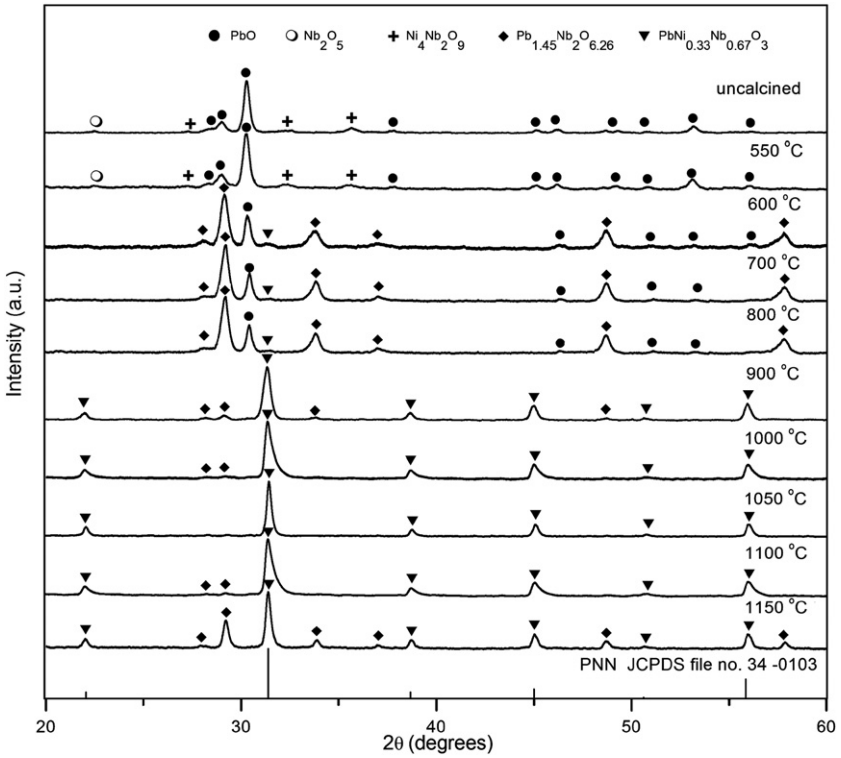



Fig. 2. XRD patterns of PNN powders calcined at various temperatures for 2 h with heating/cooling rates of 10 °C/min.

were provided. However, in the present study where corundum $Ni_4Nb_2O_9$ was employed as key precursor, it was found that there are no significant differences between the powders calcined at 1050 °C with dwell time of 0.5–2 h, as shown in Fig. 3. This observation could be attributed to the effectiveness of $Ni_4Nb_2O_9$ precursor, vibro-milling and a carefully optimized reaction. Most importantly, this study suggests that a rapid vibro-milling method can significantly lower the optimum calcination temperature and dwell time for formation of single-phase $Pb(Ni_{1/3}Nb_{2/3})O_3$ powders.

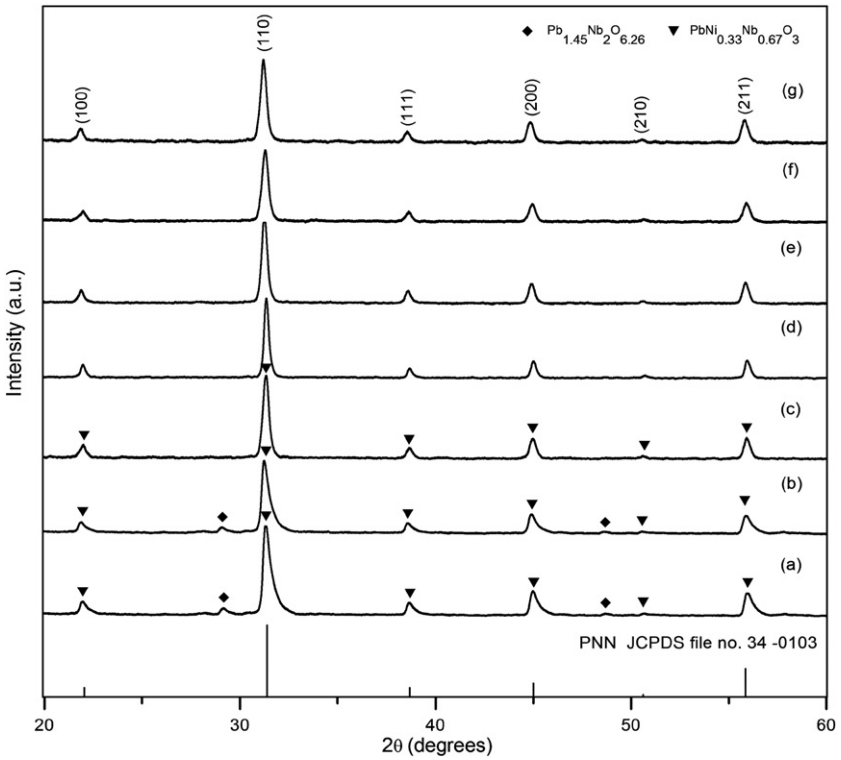



Fig. 3. XRD patterns of PNN powders calcined at 1000 °C with heating/cooling rates of 30 °C/min for (a) 3, (b) 4 and (c) 5 h; at 1050 °C with heating/cooling rates of 10 °C/min for (d) 1 and (e) 0.5 h; and at 1050 °C for 0.5 h with heating/cooling rates of (f) 20 and (g) 30 °C/min.

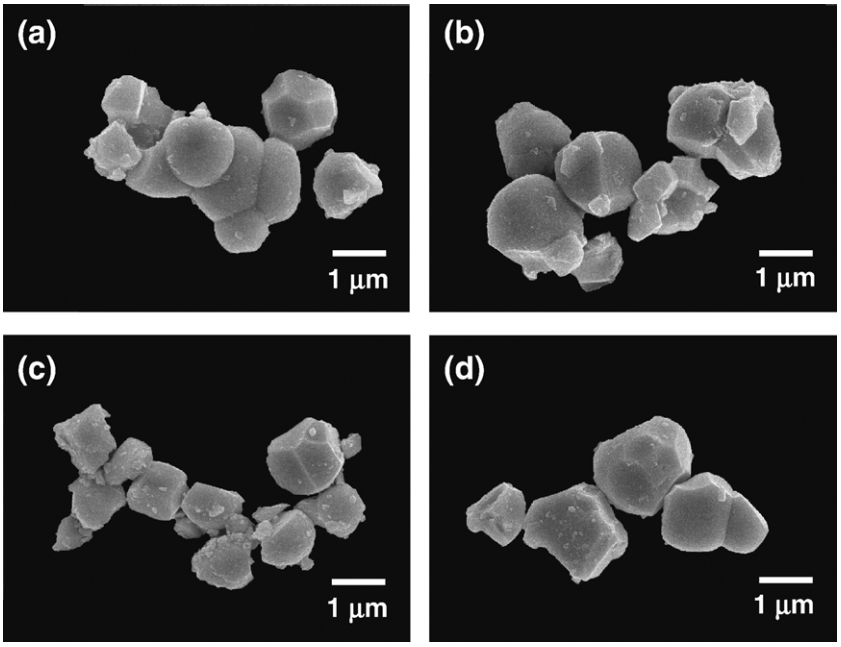



Fig. 4. SEM micrographs of the PNN powders calcined at 1050 °C for 0.5 h with heating/cooling rates of (a) 10, (b) 20 and (c) 30 °C/min; and (d) 2 h with heating/cooling rates of 10 °C/min.

In the present study, an attempt was also made to calcine $Pb(Ni_{1/3}Nb_{2/3})O_3$ powders under various heating/cooling rates. In this connection, it is shown that for the powders calcined at 1050 °C for 0.5 h, the yield of $Pb(Ni_{1/3}Nb_{2/3})O_3$ phase did not vary significantly with different heating/cooling rates, ranging from 10 to 30 °C/min (Fig. 3(e–g)). The observation that faster heating/cooling rates are required for the mixtures containing low-melting point oxide constituent (PbO), is in good agreement with early results reported in other similar systems [17,24].

Based on the TG-DTA and XRD data, it may be concluded that, over a wide range of calcination conditions, single-phase $Pb(Ni_{1/3}Nb_{2/3})O_3$ cannot be straightforwardly formed via a solid-state mixed oxide synthetic route, unless a careful design of calcination condition is performed. It is well documented that powders prepared by a conventional mixed oxide method have spatial fluctuations in their compositions. The extent of the fluctuation depends on the characteristics of the starting powders as well as the processing schedules [15–17]. It should be noted that no evidence of the pyrochlore $Pb_2Nb_2O_7$ [24], $Pb_3Nb_2O_8$ [12] and $Pb_3Nb_4O_{13}$ [25,26] was found in this study, nor was there any indication of the $Pb_{15}NiNb_{10}O_{41}$ reported by Balzer and Langbein [26] being present. The experimental work carried out here suggests that the optimal calcination conditions for single-phase $Pb(Ni_{1/3}Nb_{2/3})O_3$ (with impurities undetected by XRD technique) is 1050 °C for 0.5 h with heating/cooling rates as fast as 30 °C/min, without any addition of excess PbO or NiO [7]. Moreover, the formation temperature and dwell time for the production of $Pb(Ni_{1/3}Nb_{2/3})O_3$ powders observed in this work are also close to those reported earlier [5,6,9] but with faster heating/cooling rates. This clearly emphasizes the advantages of a combination between a corundum $Ni_4Nb_2O_9$ precursor, a rapid vibro-milling technique (only 30 min) and a carefully optimized reaction.

The morphological evolution during calcination was investigated by scanning electron microscopy (SEM). Micrographs of $Pb(Ni_{1/3}Nb_{2/3})O_3$ powders calcined at various dwell times and heating/cooling rates are illustrated in Fig 4. The influence of calcination conditions on the particle size is also given in Table 1. After calcination at 1050 °C with different dwell times and heating/cooling rates, the powders have similar morphology. In general, the particles are agglomerated and irregular in shape, with a substantial variation in particle size, particularly in samples calcined with faster heating/cooling raters (Fig. 4(c)). The results indicate that averaged particle size tend to increase with dwell times but seems to decrease with faster heating/cooling rates (Table 1).

As expected, it is seen that longer heat treatment leads to larger particle sizes and hard agglomeration (Fig. 4(d)). As shown in Fig. 4(a)–(c), as well as in Table 1, by increasing the heating/cooling rates, averaged particle size tends to decrease whilst the degree of agglomeration tends to increase. This observation could be attributed to the mechanism of surface energy reduction of the fine powders, i.e. the smaller the powder the higher the specific surface area [27]. This finding is also similar to that in $Pb(Mg_{1/3}Nb_{2/3})O_3$ powders synthesized by Wongmaneerung et al. [24]. To the authors' knowledge, the present data are the first results for the morphology–calcination relationship of $Pb(Ni_{1/3}Nb_{2/3})O_3$ powders prepared by the solid-state reaction. It is also of interest to point out that mass production of single-phase $Pb(Ni_{1/3}Nb_{2/3})O_3$ powders with the smallest particle size ~0.38 μm (estimated from SEM micrographs) can be achieved by employing a simple solid-state reaction combined with a rapid vibro-milling technique. In addition, EDX analysis using a 20 nm probe on a large number of particles of the calcined powders confirms that the parent composition is $Pb(Ni_{1/3}Nb_{2/3})O_3$ powders, in good agreement with XRD results.

## 4. Conclusions

The solid-state mixed oxide method via a rapid vibro-milling technique is explored in the preparation of single-phase $Pb(Ni_{1/3}Nb_{2/3})O_3$ powders by using $Ni_4Nb_2O_9$ as a novel B-site precursor. The calcination conditions have been found to show pronounced effects on phase formation and particle size of the calcined PNN powders. This work demonstrated that single-phase of lead nickel niobate powders with particle size ranging

Table 1
Particle size data of PNN powders calcined at various conditions

| Calcination conditions | | | Particle size range (average) (±0.1 μm) |
|---|---|---|---|
| Temperature (°C) | Dwell time (h) | Rates (°C/min) | |
| 1050 | 0.5 | 10 | 0.80–1.44 (1.18) |
| 1050 | 0.5 | 20 | 0.58–1.87 (1.08) |
| 1050 | 0.5 | 30 | 0.38–1.45 (0.92) |
| 1050 | 1 | 10 | 0.70–1.70 (1.22) |
| 1050 | 2 | 10 | 0.70–1.75 (1.30) |

from 0.38–1.45 μm can be produced via this technique by using a calcination temperature of 1050 °C for 0.5 h, with heating/cooling rates of 30 °C/min. The resulting PNN powders exhibit similar morphology and variety of agglomerated particle sizes, depending on calcination conditions.

## Acknowledgments

We thank the Thailand Research Fund (TRF), the Commission on Higher Education (CHE), the Faculty of Science and the Graduate School, Chiang Mai University for all supports.

## References

[1] A.J. Moulson, J.M. Herbert, Electroceramics, 2nd ed., Wiley, Chichester, 2003.
[2] G. Haertling, J. Am. Ceram. Soc. 82 (1999) 797.
[3] F. Levassort, P. Tran-Huu-Hue, E. Ringaard, M. Lethiecq, J. Eur. Ceram. Soc. 21 (2001) 1361.
[4] T.R. Shrout, A. Halliyal, Am. Ceram. Soc. Bull. 66 (1987) 704.
[5] E.F. Alberta, A.S. Bhalla, J. Phys. Chem. Solids 63 (2002) 1759.
[6] L.C. Veitch, B.S. Thesis, The Pennsylvania State University, University Park, PA 1982.
[7] C.H. Lu, W.J. Hwang, Ceram. Int. 22 (1996) 373.
[8] S.L. Swartz, T.R. Shrout, Mater. Res. Bull. 17 (1982) 1245.
[9] E.F. Alberta, A.S. Bhalla, Mater. Lett. 54 (2002) 47.
[10] Y. Sasaki, A. Nagai, T. Yoshimoto, NIST Spec. Publ. 804 (1991) 99.
[11] M.M.A. Sekar, A. Halliyal, J. Am. Ceram. Soc. 81 (1998) 380.
[12] Y. Yoshikawa, Key Eng. Mater. 206–213 (2002) 87.
[13] C.H. Lu, W.J. Hwang, Jpn. J. Appl. Phys. 38 (1999) 5478.
[14] H. Ehrenberg, G. Wltschek, H. Weitzel, F. Trouw, J.H. Buettner, T. Kroener, H. Fuess, Phys. Rev., B 52 (1995) 9595.
[15] O. Khamman, R. Yimnirun, S. Ananta. Mater. Lett. (in press), doi:10.1016/j.matlet.2006.09.056.
[16] R. Wongmaneerung, R. Yimnirun, S. Ananta, Mater. Lett. 60 (2006) 1447.
[17] R. Tipakontitikul, S. Ananta, Mater. Lett. 58 (2004) 449.
[18] O. Khamman, W. Chaisan, R. Yimnirun, S. Anantam, Mater. Lett. (in press), doi:10.1016/j.matlet.2006.10.063.
[19] Powder Diffraction File No. 77–1971, International Centre for Diffraction Data, Newton Square, PA, 2000.
[20] Powder Diffraction File No. 33–0873, International Centre for Diffraction Data, Newton Square, PA, 2000.
[21] Powder Diffraction File No. 46–0525, International Centre for Diffraction Data, Newton Square, PA, 2000.
[22] Powder Diffraction File No. 84–1731, International Centre for Diffraction Data, Newton Square, PA, 2000.
[23] Powder Diffraction File No. 34–0103, International Centre for Diffraction Data, Newton Square, PA, 2000.
[24] R. Wongmaneerung, T. Sarakonsri, R. Yimnirun, S. Ananta, Mater. Sci. Eng., B 132 (2006) 292.
[25] A.I. Agranovskaya, Bull. Acad. Sci. U.S.S.R., Phys. Ser. 1 (1960) 1271.
[26] B. Balzer, H. Langbein, Cryst. Res. Technol. 32 (1997) 955.
[27] J.S. Reeds, Principles of Ceramic Processing 2nd ed., Wiley, New York, 1995.

Appl. Phys. A 89, 737–741 (2007)
DOI: 10.1007/s00339-007-4156-9

**Applied Physics A**
**Materials Science & Processing**

R. YIMNIRUN✉
A. NGAMJARUROJANA
R. WONGMANEERUNG
S. WONGSAENMAI
S. ANANTA
Y. LAOSIRITAWORN

# Temperature scaling of ferroelectric hysteresis in hard lead zirconate titanate bulk ceramic

Department of Physics, Faculty of Science, Chiang Mai University, Chiang Mai 50200, Thailand

**Received: 21 February 2007/Accepted: 4 June 2007**
**Published online: 28 June 2007 •** **© Springer-Verlag 2007**

**ABSTRACT** The temperature scaling of the ferroelectric hysteresis was investigated in hard lead zirconate titanate (PZT) bulk ceramic. The power-law temperature scaling relations were obtained for hystersis area $\langle A \rangle$, remnant polarization $P_r$, and coercivity $E_C$ in the forms of $\langle A \rangle \propto T^{-0.9650}$, $P_r \propto T^{-0.0261}$, and $E_C \propto T^{-0.8823}$, respectively, which are mostly comparable to those of its soft counterpart. The observation that $P_r$ decayed more slowly with temperature than in soft PZT was attributed to the presence of the complex defects in hard PZT. However, the product of $P_r$ and $E_C$ still provided the similar scaling law on the $T$ dependence in comparison with $\langle A \rangle$.

**PACS** 77.80.-e; 77.80.Fm; 77.84.-s; 77.84.Dy

## 1 Introduction

Acceptor-doped lead zirconate titanate ($Pb(Zr_{1-x}Ti_x)O_3$ or PZT) or commercially known as hard PZT ceramics have been employed extensively in applications that require hard piezoelectric properties, such as ultrasonic motors and high power transformers [1]. The ferroelectric characteristics of hard PZT are also different from those of the soft PZT, as a result of complex defects present [2–4]. The difference in the behaviors has also been investigated extensively [5–12]. In hard PZT, the oxygen vacancies are introduced, trapped at the domain walls, then form electric dipoles with the acceptor atoms. These dipoles called complex defects act as pinning points for the domain wall and the domain wall motion is reduced. The complex defects are absent in the soft PZT ceramics, hence the domain walls can move more easily. Therefore, hard PZT ceramics typically show higher coercivity ($E_C$) than soft ones [2, 3, 9, 11]. Dielectric and piezoelectric properties of the two ceramic types are also significantly different [2–7].

From both the fundamental and practical viewpoints, the temperature and thermal history have been found to impose significant effects on the ferroelectric hysteresis behavior of the hard PZT, which have also been attributed to the presence and response of the complex defects to the temperature [5, 6, 9, 12–16]. Earlier, we proposed the scaling of the area of the hysteresis with field amplitude and frequency for hard PZT bulk ceramics [17], which is interestingly very similar to that for the soft PZT bulk ceramics reported previously [18]. This observation suggested little influence of the complex defects to the dynamic behavior. However, as stated above, the complex defects are reportedly responsible for temperature-related behaviors in the hard PZT ceramics. To this connection, an investigation of the temperature scaling of dynamic hysteresis of the hard PZT ceramic with comparison to that of the soft PZT ceramic will provide insight to roles of complex defects to the temperature-dynamic hysteresis behavior. It is, therefore, the aim of this study to establish experimentally the temperature scaling of the ferroelectric hysteresis for hard PZT bulk ceramic.

✉ Fax: 6653-943-445, E-mail: rattikornyimnirun@yahoo.com

## 2 Experimental

The polarization–electric field ($P$–$E$) hysteresis loops of commercial hard PZT ceramic discs (APC-840, APC International, Ltd., USA) with diameter of 8 mm and thickness of 1 mm were obtained by a modified Sawyer–Tower circuit over temperature range 298–453 K with $E_0$ up to 40 kV/cm ($f$ was fixed at 40 Hz). The electric field was applied to a sample by a high voltage AC amplifier (Trek 610D) with the input sinusoidal signal from a function generator (HP 3310A). The $P$–$E$ loops were recorded by a digital oscilloscope (HP 54645A, 100 MHz). Each loop was obtained after 20 sampling cycle to average out the noise deformation. The hysteresis loop obtained was very consistent with that obtained by a standardized ferroelectric testing unit, RT66A (Radiant Technologies Inc., NM), which ensures the reliability of the measurements. It should be noted that the Curie temperature ($T_C$) of the hard PZT used was determined experimentally from dielectric measurement to be 593 K.

## 3 Results and discussion

Figure 1 displays the hysteresis loops profile for various electric field amplitudes $E_0$ at a fixed $T = 373$ K (Fig. 1a), and for various temperatures at a fixed $E_0 =$ 35 kV/cm (Fig. 1b). From the $P$–$E$ loops, it is obvious that both $E_0$ and $T$ play a crucial role on the hysteresis area $\langle A \rangle$. For example, in Fig. 1a, with increasing $E_0$, a transition from a minor loop at low field to a saturated $s$-shape loop at high

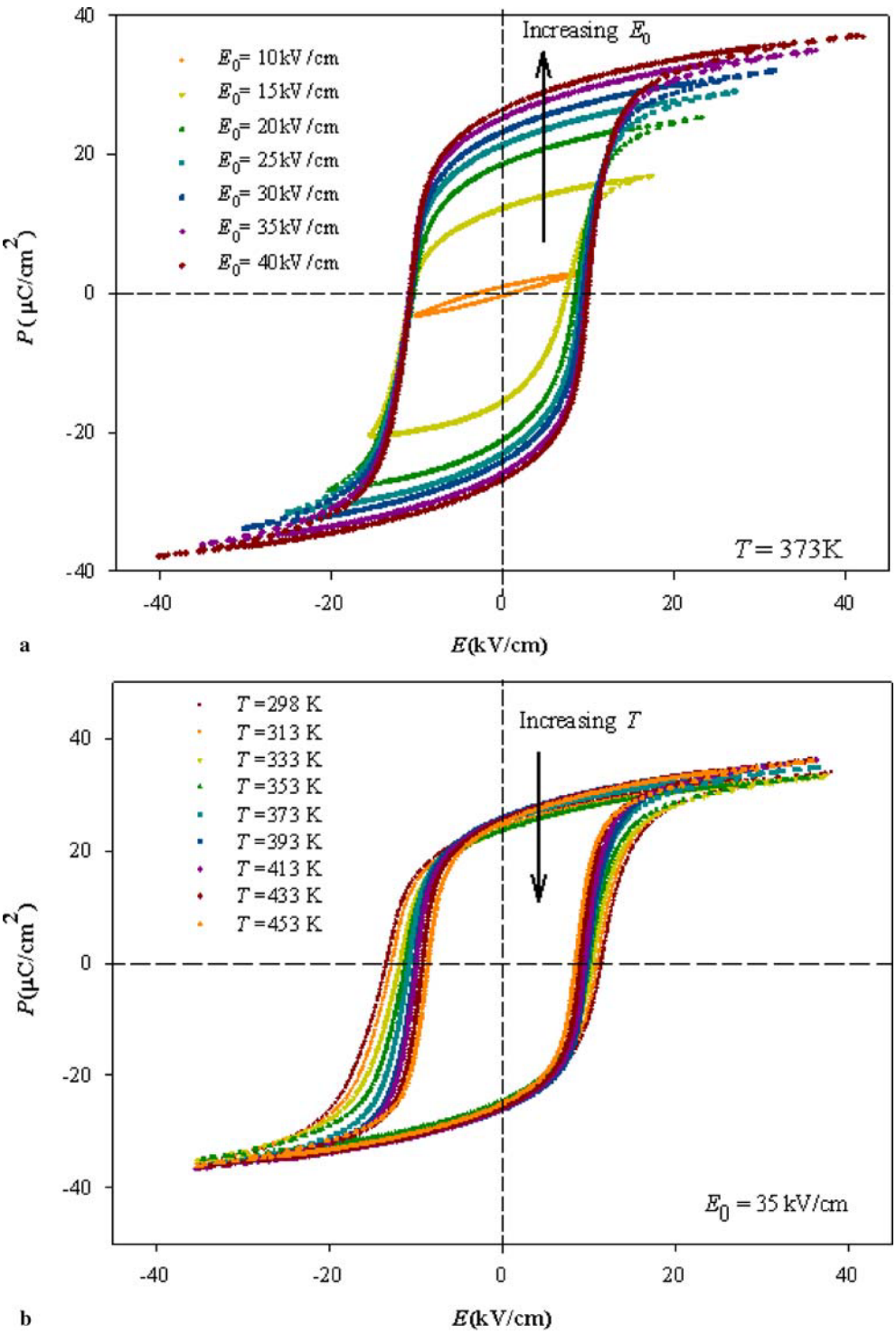



**FIGURE 1** Hysteresis loops for hard PZT ceramic (**a**) at $T = 373$ K with varying $E_0$, and (**b**) at $E_0 = 35$ kV/cm with varying $T$

field occurs. This is expected because with higher field there is more electrical energy supplied into the system resulting in more 'electrical driving force' acting on electric dipole moments [3]. Consequently, the polarization has more tendencies to follow the external electric field which in turns reduces the phase lag between the polarization and the field signals. As a result, the saturated loops are obtained at the high fields instead of the minor loops at low fields. Additionally, slightly asymmetric $P$–$E$ loops are also observed in the hard PZT, as displayed in Fig. 1. The observation could be attributed to the presence of the complex defects, which provide the internal bias-field [3, 5, 7, 11]. Therefore, the ferroelectric interaction between these defect dipoles, which are trapped near domain walls, and the other dipoles in the domains makes the polarization switching and domain re-orientation processes, as well as the domain wall motions, more difficult in one field direction than the other direction. This results in asymmetric loops, and the differences between $E_C^+$ and $E_C^-$, and $P_r^+$ and $P_r^-$, as observed in Fig. 1. On the other hand, as suggested in Fig. 1b, with increasing temperature, the loop area is slowly reduced in

size. This is caused by that higher temperature provides higher thermal fluctuation to the polarization order parameter which reduces the ferroelectric interaction among the dipoles [3]. Therefore, even $E_0$ is fixed, the polarization direction is easily tuned with the electric field at higher temperatures due to the smaller ferroelectric interaction providing a reduction in the coercivity ($E_C$). Interestingly, the remnant polarization ($P_r$) is seen to be rather stable with temperature, which is very different from what was observed in soft PZT, as reported earlier [19]. The interpretation for this observation is not obvious, but could be related to the complex defects present only in hard PZT, as will be discussed later. Nonetheless, the hysteresis loop area is still seen to reduce with increasing the temperature generally because of the strong reduction in $E_C$. More interestingly, the observed temperature dependence of these hysteresis parameters prompts a question whether these parameters scale with temperature the same way as in the soft PZT ceramic. For better comparison with the soft PZT case, this present study will only focus on the scaling relations for very well-saturated loops at fields above 25 kV/cm.

Figure 2 shows the relation between $\langle A \rangle$ and $T$ in a double logarithmic form, from which one would see a similar decreasing trend for all $E_0$. This implies a power law relation between the hysteresis area and temperature i.e., $\langle A \rangle \propto T^{\gamma}$. By the least square-fitting method, the exponent $\gamma = -0.9650$ was obtained. As plotted in Fig. 2, the dependence of the area with temperature can be fitted (solid line) very well (with $R^2 \sim 0.97$) by

$$\langle A \rangle \propto T^{-0.9650} . \tag{1}$$

The temperature scaling relation of the hysteresis area $\langle A \rangle$ obtained for hard PZT is very much comparable to that obtained for soft PZT, as reported earlier in the form of $\langle A \rangle \propto T^{-1.1024}$ [19].

Additionally, Fig. 3 shows the relation between $E_C$ and $T$ in a double logarithmic plot. As being evident, the power-law temperature scaling relation seems suitable for $E_C$. It is found that the dependence of $E_C$ on $T$ can be fitted very well (with $R^2 \sim 0.99$) by

$$E_C \propto T^{-0.8823} . \tag{2}$$

When compared to that of soft PZT with a linear relation (i.e., the power exponent is equal to one) [19], the scaling relations of $E_C$ for both types of PZT are still comparable.

Though in soft PZT ceramic the $P_r$ was seen to scale strongly with $T$ in the power-law form, i.e., $P_r \propto T^{-1.2322}$ [19], the $P_r$ of hard PZT ceramic is surprisingly observed to be rather stable with temperature (with very small reduction over wide temperature range), as shown in Fig. 3. An attempt was made to fit the data and found very weak power-law decay of area with temperature in the form of

$$P_r \propto T^{-0.0261} . \tag{3}$$

It is interesting to observe that the temperature scaling behaviors for the hard PZT bulk ceramic are, to some extent, similar to those of the soft counterpart [19], particularly for $\langle A \rangle$ and $E_C$. By a direct comparison, the power-law exponents for the two ceramics are not significantly different. More importantly, the similar temperature scaling behaviors for the two types of ceramics suggest that though the complex defects contribute greatly to the difference on the electrical properties, they contribute only slightly to the temperature-dependent dynamic behaviors.

Nonetheless, a noticeable difference in the temperature scaling behavior of $P_r$ between the soft and hard PZT ceramics still requires explanation. In hard PZT, $P_r$ is seen to decrease more slowly with increasing temperature than in soft PZT. Increasing temperature provides the reduction in ferroelectric interaction between dipoles, which results in the decrease of $P_r$ and $E_C$ with increasing temperature in similar rates of decay, as observed in soft PZT [19]. However,

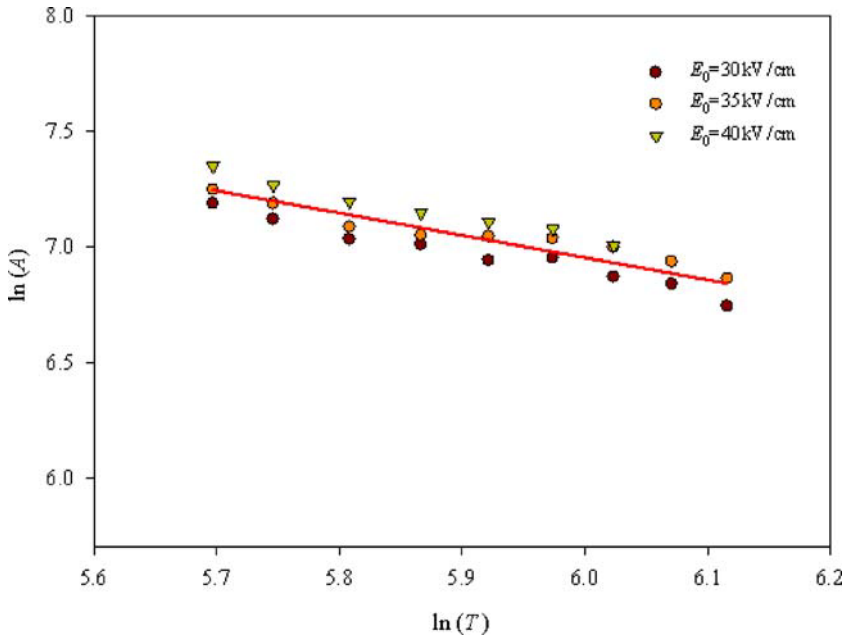



**FIGURE 2** Double logarithmic plot between ln($A$) and ln($T$)

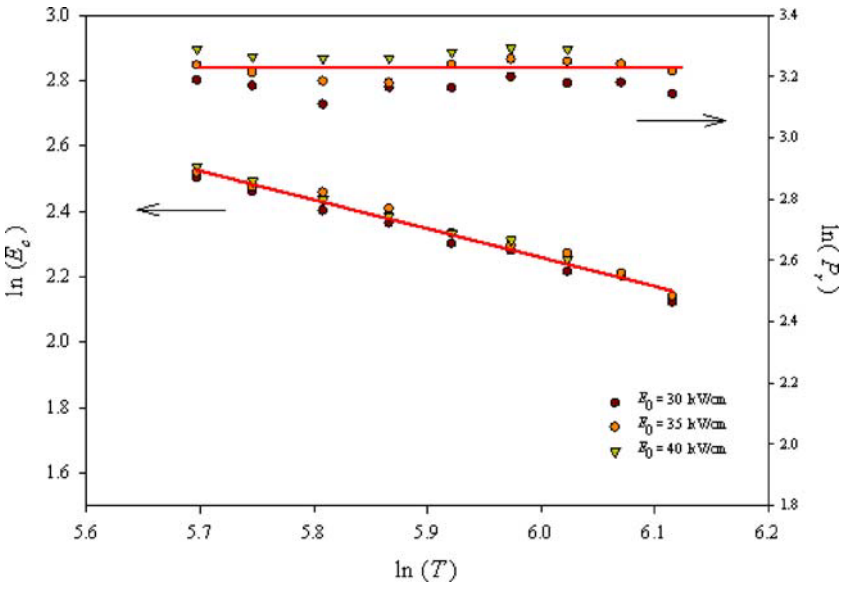



**FIGURE 3** Double logarithmic plots between $\ln(P_r)$ and $\ln(T)$, and $\ln(E_C)$ and $ln(T)$

this is not the case in hard PZT as $P_r$ is seen to decay more slowly with temperature than $E_C$, as seen from (2) and (3) and Fig. 1b. The reasons could be attributed to the difference in short-range ferroelectric interaction between the trapped defect dipoles and the neighboring dipoles under high field (where $E_C$ is determined) and under zero field (where $P_r$ is determined) conditions [5, 7, 15]. With an addition of an electrical driving force under high field condition, the majority of dipoles can switch more easily with increasing temperature, resulting in strong decay in $E_C$ with temperature. On the other hand, without an electrical field, the thermal energy alone cannot provide enough driving force for the re-orientation of the majority of dipoles, particularly those nearby the trapped defect dipoles; hence, $P_r$ is seen to decay very slowly with increasing temperature. The internal bias-field from the defect dipoles also causes the difference in temperature decay between $E_C^+$ and $E_C^-$, and $P_r^+$ and $P_r^-$, as observed in Fig. 1b.

Even though the temperature-scaling relations of $P_r$ and $E_C$ obtained for hard PZT are slightly different from those of soft PZT, particularly $P_r$, and as approaching saturation the hysteresis area can be roughly estimated with $(2P_r)(2E_C)$ [16, 20], it is of interest to check if the product of $P_r$ and $E_C$ in the case of hard PZT would still provide a similar scaling law on the $T$ dependence in comparison with $\langle A \rangle$, as observed in soft PZT case. By using (2) and (3), it is then found that

$$(2E_C)(2P_r) \approx 4(T^{-0.9084}) . \quad (4)$$

The scaling of 'area' in this way on the temperature should have the exponent $\gamma$ of $-0.9084$, which is very similar to that extracted from the $\ln\langle A \rangle$ and $\ln T$ plot (which the exponent $\gamma$ has a value of $-0.9650$). Therefore, these two scaling methods seem to agree. So once the scaling of area to the temperature is found, it is possible to guess how the $E_C$ would scale with $T$ if the scaling relation between $P_r$ and $T$ is known or vice versa. The same conclusion was reached in the soft PZT ceramic case [19].

## 4 Conclusions

In hard PZT bulk ceramic, the power-law temperature scaling relations are obtained for hystersis area $\langle A \rangle$, remnant polarization $P_r$, and coercivity $E_C$ in the forms of $\langle A \rangle \propto T^{-0.9650}$, $P_r \propto T^{-0.0261}$, and $E_C \propto T^{-0.8823}$, respectively, which are mostly comparable to those of its soft counterpart. The observation that $P_r$ decays more slowly with temperature than in soft PZT is attributed to the presence of the complex defects in hard PZT. However, the product of $P_r$ and $E_C$ still provides the similar scaling law on the $T$ dependence in comparison with $\langle A \rangle$, as also reported for soft PZT case. Most importantly, this study suggests that, while the complex defects contribute greatly to the difference in many electrical behaviors between soft and hard PZT ceramics, they show very little influence on the temperature-dependent dynamic hysteresis behavior.

**ACKNOWLEDGEMENTS** Financial supports from the Thailand Research Fund (TRF) and Commission on Higher Education (CHE) are gratefully acknowledged.

## REFERENCES

1 K. Uchino, *Piezoelectric Actuators and Ultrasonic Motors* (Kluwer, Boston, 1997), p. 129
2 B. Jaffe, W.R. Cook, H. Jaffe, *Piezoelectric Ceramics* (Academic, New York, 1971), p. 271
3 M.E. Lines, A.M. Glass, *Principles and Applications of Ferroelectrics and Related Materials* (Clarendon, Oxford, 1977), p. 102
4 K. Uchino, *Ferroelectric Devices* (Dekker, New York, 2000), p. 145
5 K. Carl, K.H. Hardtl, Ferroelectrics **17**, 473 (1978)
6 Q.M. Zhang, H. Wang, N. Kim, L.E. Cross, J. Appl. Phys. **75**, 454 (1994)
7 T. Tsurumi, T. Sasaki, H. Kakemoto, T. Harigai, S. Wada, Japan. J. Appl. Phys. Part 1 **43**, 7618 (2004)
8 M.H. Lente, A. Picinin, J.P. Rino, J.A. Eiras, J. Appl. Phys. **95**, 2646 (2004)
9 Q. Tan, J. Li, D. Viehland, Appl. Phys. Lett. **75**, 418 (1999)
10 M. Morozov, D. Damjanovic, N. Setter, J. Eur. Ceram. Soc. **25**, 2483 (2005)
11 W. Chang, A.H. King, K. Bowman, Appl. Phys. Lett. **88**, 242 901 (2006)
12 S.K. Pandey, O. P Thakur, A. Kumar, C. Prakash, R. Chatterjee, T.C. Goel, J. Appl. Phys. **100**, 014 104 (2006)

13 Q. Tan, D. Viehland, J. Am. Ceram. Soc. **81**, 328 (1998)
14 B.S. Li, G.R. Li, Q.R. Yin, Z.G. Zhu, A.L. Ding, W.W. Cao, J. Phys. D Appl. Phys. **38**, 1107 (2005)
15 O. Lohse, D. Bolten, S. Tiedke, T. Schneller, R. Waser, Proc. IEEE-ISAF 98 **1**, 27 (1998)
16 G.L. Yuan, J.-M. Liu, S.T. Zhang, D. Wu, Y.P. Wang, Z.G. Liu, H.L.W. Chan, C.L. Choy, Appl. Phys. Lett. **84**, 954 (2004)
17 R. Yimnirun, R. Wongmaneerung, S. Wongsaenmai, A. Ngamjarurojana, S. Ananta, Y. Laosiritaworn, Appl. Phys. Lett. **90**, 112906 (2007)
18 R. Yimnirun, Y. Laosiritaworn, S. Wongsaenmai, S. Ananta, Appl. Phys. Lett. **89**, 162901 (2006)
19 R. Yimnirun, R. Wongmaneerung, S. Wongsaenmai, A. Ngamjarurojana, S. Ananta, Y. Laosiritaworn, Appl. Phys. Lett. **90**, 112908 (2007)
20 J.-M. Liu, H.P. Li, C.K. Ong, L.C. Lim, J. Appl. Phys. **86**, 5198 (1999)

Available online at www.sciencedirect.com
ScienceDirect
Current Applied Physics 8 (2008) 128–133
Current Applied Physics
An official journal of the KPS
www.elsevier.com/locate/cap
www.kps.or.kr

# Development of perovskite and phase transition in lead cobalt niobate modified lead zirconate titanate system

Naratip Vittayakorn [a,*], Supamas Wirunchit [a], Sakda Traisak [a], Rattikorn Yimnirun [b], Gobwut Rujijanagul [b]

[a] *Materials Science Research Unit, Department of Chemistry, Faculty of Science, King Mongkut's Institute of Technology Ladkrabang, Bangkok 10520, Thailand*

[b] *Department of Physics, Faculty of Science, Chiang Mai University, Chiang Mai 50200, Thailand*

Received 19 December 2006; received in revised form 28 May 2007; accepted 15 June 2007
Available online 29 June 2007

**Abstract**

Ferroelectric lead zirconate titanate–lead cobalt niobate ceramics with the formula $(1-x)Pb(Zr_{1/2}Ti_{1/2})O_3$–$xPb(Co_{1/3}Nb_{2/3})O_3$ where $x = 0.0$–$0.5$ were fabricated using a high temperature solid-state reaction method. The formation process, the structure and homogeneity of the obtained powders have been investigated by X-ray diffraction method as well as the simultaneous thermal analysis of both differential thermal analysis (DTA) and thermogravimetry analysis (TGA). It was observed that for the binary system $(1-x)Pb(Zr_{1/2}Ti_{1/2})O_3$–$xPb(Co_{1/3}Nb_{2/3})O_3$, the change in the calcination temperature is approximately linear with respect to the PCoN content in the range $x = 0.0$–$0.5$. In addition, X-ray diffraction indicated a phase transformation from a tetragonal to a pseudo-cubic phase when the fraction of PCoN was increased. The dielectric permittivity is remarkably increased by increasing PCoN concentration. The maximum value of remnant polarization $P_r$ (25.3 μC/cm$^2$) was obtained for the 0.5PZT–0.5PCoN ceramic.
© 2007 Elsevier B.V. All rights reserved.

*PACS:* 77.22.−d; 77.80.Bh; 77.84.Dy; 61.10.Nz; 77.80.Dj

*Keywords:* Ferroelectric; Relaxor ferroelectric; Perovskite

## 1. Introduction

Since the late 1960s, lead titanate:lead zirconate ceramic (generally known as $Pb(Zr_{1-x}Ti_x)O_3$ or PZT), near the tetragonal–rhombohedral morphotropic phase boundary has been considered an important material for a wide range of piezoelectric, pyroelectric and ferroelectric device applications such as transducers, computer memory and display and pyroelectric sensors [1,2]. Most commercial PZT ceramics are thus designed in the vicinity of the morphotropic phase boundary (MPB) with various doping in order to achieve optimum properties [1,2]. Recently, many piezoelectric ceramic materials have been developed from binary systems containing a combination of relaxor and normal ferroelectric materials [3] which yield high dielectric permittivities {e.g. $Pb(Zn_{1/3}Nb_{2/3})O_3$–$PbTiO_3$ (PZN–PT) [4,5], $Pb(Zr_{1/2}Ti_{1/2})O_3$–$Pb(Ni_{1/3}Nb_{2/3})O_3$ (PZT–PNN) [6]}, excellent piezoelectric coefficients {e.g. $Pb(Zn_{1/3}Nb_{2/3})O_3$–$PbTiO_3$ (PZN–PT) [4,5], $Pb(Zr_{1/2}Ti_{1/2})O_3$–$Pb(Zn_{1/3}Nb_{2/3})O_3$ (PZN–PZT) [7], $Pb(Sc_{1/3}Nb_{2/3})O_3$–$PbTiO_3$ (PSN–PT) [8,9]}, and high pyroelectric coefficients {e.g. $Pb(Ni_{1/3}Nb_{2/3})O_3$–$PbTiO_3$–$PbZrO_3$(PNN–PT–PZ) [10]}.

Lead cobalt niobate ($Pb(Co_{1/3}Nb_{2/3})O_3$, PCoN) is a typical relaxor ferroelectric characterized by a high dielectric constant, a broad diffuse phase transition near −70 °C and low firing temperature [11]. Though the paraelectric–ferroelectric transition temperature of PCoN is below room temperature, it can be easily shifted upward with the

* Corresponding author. Tel.: +66 89 700 2136; fax: +66 2 326 4415.
*E-mail address:* naratipcmu@yahoo.com (N. Vittayakorn).

1567-1739/$ - see front matter © 2007 Elsevier B.V. All rights reserved.
doi:10.1016/j.cap.2007.06.002

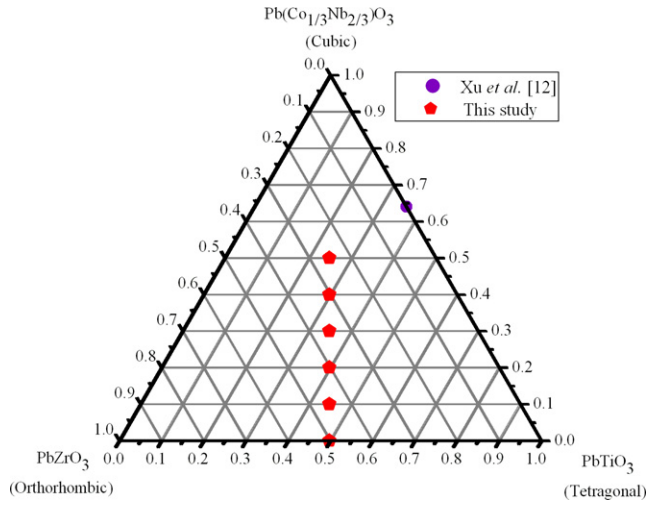



Fig. 1. Compositions studied in the $PbTiO_3$–$PbZrO_3$–$Pb(Co_{1/3}Nb_{2/3})O_3$ ternary system.

addition of $PbTiO_3$ (PT), which is a normal ferroelectric compound with a phase transition at 490 °C. So the PCoN-based relaxors are one of the most attractive materials for multilayer ceramic capacitors and electrostrictive actuators [2].

Since PCoN is a relaxor ferroelectrics with a broad dielectric peak near $T_c \approx -70$ °C and PZT (Zr/Ti = 50/50) is a normal ferroelectric with a sharp maximum permittivity at $T_c \sim 390$ °C, the curie temperature in PZT–PCoN system can be engineered over a wide range of temperature by controlling the amount of PCoN in the system. However, the PZT–PCoN ceramics have not been obtained as yet. Fig. 1 schematically shows the pseudo-ternary composition range which was studied in this work compared with other studies [2]. In order to get more information about combination of relaxor and normal ferroelectric materials and to recognize the properties of PZTCoN ceramics, this paper attempted to carry out the synthesis of the quasi-binary solid solution $(1-x)Pb(Zr_{0.5}Ti_{0.5})O_3$–$xPb(Co_{1/3}Nb_{2/3})O_3$, with $x = 0.0$–$0.5$ using a solid-sate reaction method and to report some properties of obtained ceramics.

## 2. Experimental

Ceramics of $(1-x)Pb(Zr_{0.5}Ti_{0.5})O_3$–$xPb(Co_{1/3}Nb_{2/3})O_3$(PZT–PCoN) with $x = 0$–$0.5$ were synthesized using the solid-state reaction method. The CoO (99.9%), $Nb_2O_5$ (99.9%), PbO (Fluka, >99% purity) $TiO_2$ (99.8%) and $ZrO_2$ (99%) were mixed and milled in ethyl alcohol for 18 h using a ball-milling. After drying at 120 °C for 2 h, the reaction of the uncalcined powders taking place during heat treatment was investigated by differential thermal analysis (DTA; Shimadzu) and thermogravimetry analysis (TGA; Shimadzu), using a heating rate of 10 °C/min in air from room temperature up to 1400 °C. Based on the TG–DTA results, the mixture was calcined at various temperatures ranging from 650 to 900 °C, dwell times 4 h and heating/cooling rates ranging 20 °C/min, in closed alumina crucible, in order to investigate the perovskite phase formation. The calcined powders, with polyvinyl alcohol (PVA) added as binder, were pressed into pellets of 15 mm diameter and ~2 mm thickness, which were then sintered at 1100–1200 °C in Pb-atmosphere for 4 h in a closed alumina crucible. X-ray diffraction (XRD; Philips PW 1729 diffractometer) using Cu $K_\alpha$ radiation was used to determine the phases formed and optimum firing temperatures for the formation of desired phase. For measuring the dielectric and ferroelectric characteristics, the specimens were polished to 1 mm thickness. After ultrasonic cleaning in ethanol bath, silver-paste was coated on the polished samples on both sides by the screen printing method, and then subsequently, fired at 650 °C for 30 min. For the dielectric properties measurement, capacitance was measured at 1 kHz using an automated measurement system consisted of an LCR meter (HP-4284, Hewlett–Packard Inc.). The dielectric constant is then calculated from $\varepsilon_r = Cd/\varepsilon_0 A$, where $C$ is the capacitance of the sample, $d$ and $A$ are the thickness and the area of the electrode, respectively, and $\varepsilon_0$ is the dielectric permittivity of vacuum ($8.854 \times 10^{-12}$ F/m). The ferroelectric hysteresis loop parameters were measured with aid of a home-built Sawyer–Tower circuit.

## 3. Results and discussion

The TG–DTA simultaneous analysis of a powder mixed in the stoichiometric proportions of PZT–PCoN is illustrated in Fig. 2. In the temperature range from room temperature to ~350 °C, the sample shows both exothermic and endothermic peaks in the DTA curve, in consistent with a slight drop in weight loss at the same temperature range. These observations can be attributed to the decomposition of the organic species from the milling process [12,13]. The different temperature, intensities, and shapes of the thermal peaks probably are related to the different natures of the organic species and consequently, caused

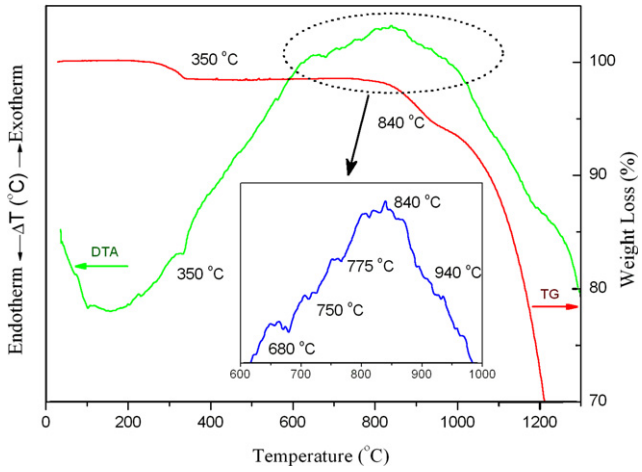



Fig. 2. DTA–TG curves for the mixture of PZT–PCoN powder.

by the removal of species differently bounded in the network [13]. In the temperature range 650–900 °C, both exothermic and endothermic peaks are observed in the DTA curve. The enlarged zone of this DTA curve shows that the endothermic peak at ~750 °C should be correlated to the phase transition of perovskite structure, because no weight loss could be found in the TG curve and that is also in accordance to literature data [14,15]. The last endothermic peak centered at ~840 °C may be caused by the decomposition of lead oxide. As a result, crystallization of PZT–PCoN powders is established above ~750 °C. Further increase in temperature or heating time will promote crystallization of perovskite phase powders. These data were used to define the range of temperatures (650–950 °C) for XRD investigation. To study the phase development with increasing calcination temperature, all compositions were calcined at various temperatures for 4 h in air with constant heating/cooling rates of 20 °C/min, followed by phase analysis using XRD technique.

XRD patterns of the calcined 0.7PZT–0.3PCoN powders at different calcination temperatures are illustrated Fig. 3. The XRD results show that the pyrochlore phase $Pb_xNb_yO_z$ pyrochlore phases was dominant at calcination temperatures below 700 °C. In the work by Chen et al. [12] it was reported that in the lead–niobium pyrochlore system the cubic $Pb_3Nb_4O_{13}$, pyrochlore phase (ICDD No. 25–443) forms first around 580 °C. At higher temperatures, it transforms to $Pb_2Nb_2O_7$, (ICDD No. 40–828) and finally to $Pb_3Nb_2O_8$, (ICDD No. 30–712) with increased calcination temperatures. At 700 °C, the pyrochlore phase began to decrease and disappeared completely at 750 °C. The yield of the perovskite phase increased significantly until at 750 °C, a single-phase of perovskite phase was formed. The studies also reflect the growth of crystallinity in the powders with the increasing heat-treatment temperatures. The results of the X-ray diffraction measurement support the DTA observation (Fig. 2) that the perovskite phase is formed at approximately 750 °C. The relationship between the relative content of perovskite phase and the calcination temperature is illustrated in Fig. 4. The relative content of perovskite phase is calculated based on the value of $(I_{Pe(110)}/(I_{Pe(110)} + I_{Py(222)}))$, where $I_{Pe(110)}$ and $I_{Py(222)}$ indicate the intensity of the (1 1 0) diffraction peak of perovskite phase and the intensity of the (2 2 2) diffraction peak of the pyrochlore phase, respectively. Based on the XRD data obtained here together with the % phase perovskite, it may be conclude that the change in the calcination temperature is approximately linear with respect to the PCoN content in the range $x = 0.0$–0.5. With an increase in $x$, the calcination temperature shifts up to high temperatures. The XRD patterns of $(1-x)$PZT–$x$PCoN ceramics with various $x$ values are shown in Fig. 5. The patterns show single-phase perovskite-structured ceramics with $x \leqslant 0.4$. Evidence for the pyrochlore or other second phases was not detected in the patterns. Pyrochlore peaks, identified with "*" in Fig. 5, were found in the samples with $x = 0.5$. These results indicated that the presence of PCoN in the solid solution decreases the structural stability of PZT perovskite phase by its tolerance factor and electronegativity [16].

The $PbZrO_3$–$PbTiO_3$ phase diagram predicts that at room temperature $Pb(Zr_{1/2}Ti_{1/2})O_3$ falls within the tetragonal phase field near the MPB. The crystal symmetry for pure PCoN is cubic at room temperature. Below $T_{max} \approx -70$ °C, the symmetry changes to rhombohedral. Therefore, with increasing $x$ the crystal symmetry should change due to the effects of the increased PCoN fraction and the decrease in $T_C$. It is well know that in the pseudo-cubic phase, the {2 0 0} profile will show a single narrow peak because all the planes of {2 0 0} share the same lattice parameters, while in the tetragonal phase, the {2 0 0} profile should be split into two peaks with the intensity height of the former being half of the latter because the

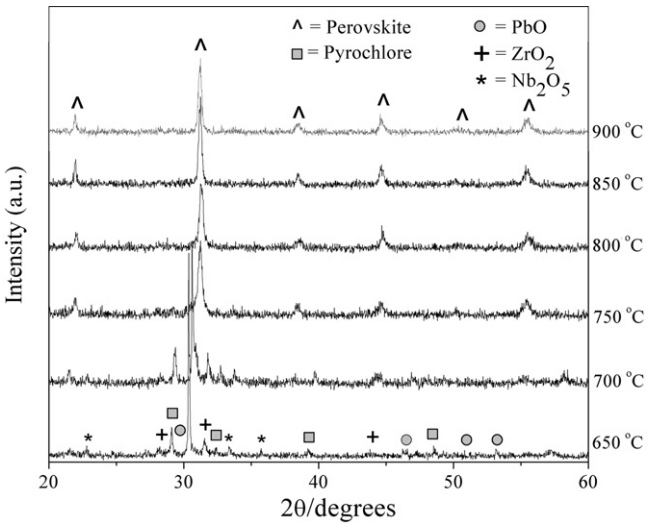



Fig. 3. XRD patterns of 0.7PZT–0.3PCoN powder calcined at various temperature for 4 h.

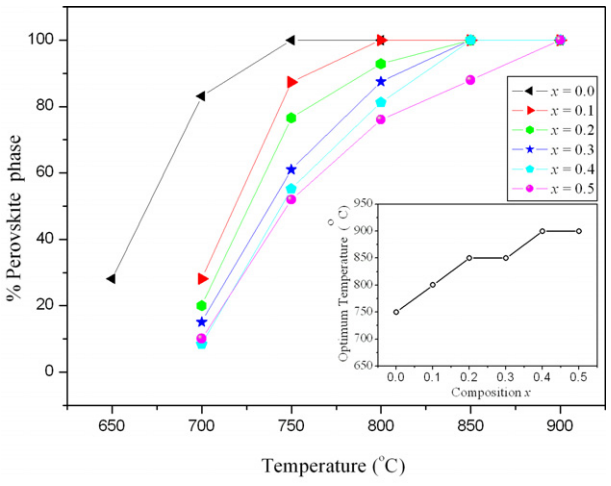



Fig. 4. Percentage of perovskite phase as a function of calcinations temperature for $(1 - x)$PZT–$x$PCoN powder.

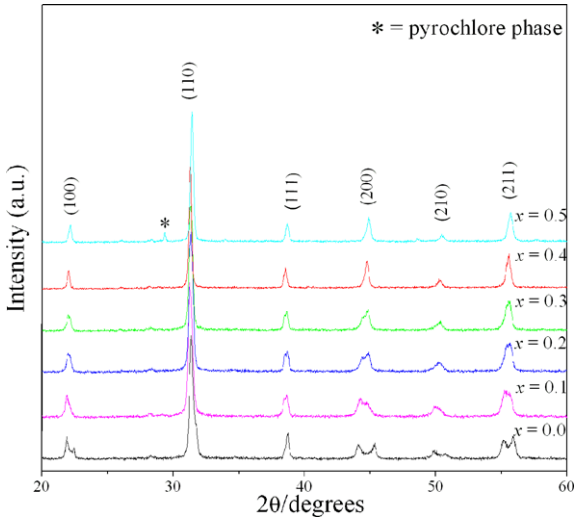



Fig. 5. XRD patterns of $(1-x)$PZT–$x$PCoN ceramics.

lattice parameters of (200) and (020) are the same but are slightly different from those of (002).

Based on the careful XRD study of {200} reflections in Fig. 6, we can find that a phase transformation from the tetragonal structure to the pseudo-cubic structure occurs with increasing PCoN content. The ceramics exist as tetragonal phase which is indicated by the splitting of $(002)_T$ and $(200)_T$ peaks in the $2\theta$ range from 43.5° to 46.5° at $x = 0.10$. As PCoN content increases from $x = 0.1$ to 0.3, the ceramics coexist as tetragonal and pseudo-cubic phase revealed by the coexistence of $(002)_T$ and $(200)_R$ peaks in the $2\theta$ range from 43.5° to 45.5°. To a first approximation, it could be said that the composition with $x = 0.1$–0.2 is close to the morphotropic phase boundary (MPB) of the $Pb(Zr_{0.50}Ti_{0.50})O_3$–$Pb(Co_{1/3}Nb_{2/3})O_3$ system, where the structure of the PZT–PCoN compositions is gradually changing from tetragonal to pseudo-cubic. Electrical data described later further supports this assumption.

The ceramics with $x = 0.50$ exist as pseudo-cubic phase revealed by the single $(200)_R$ peak. It is interesting to note that the influence of the addition of $Pb(Co_{1/3}Nb_{2/3})O_3$ on the phase transition of the $Pb(Zr_{1/2}Ti_{1/2})O_3$ system is similar to that of $Pb(Zr_{1/2}Ti_{1/2})O_3$–$Pb(Ni_{1/3}Nb_{2/3})O_3$, $Pb(Zr_{1/2}Ti_{1/2})O_3$–$Pb(Mg_{1/3}Nb_{2/3})O_3$ and $Pb(Zr_{1/2}Ti_{1/2})O_3$–$Pb(Zn_{1/3}Nb_{2/3})O_3$ systems [6,17–19].

The dielectric properties of $(1-x)$PZT–$x$PCoN, $x = 0.0$–0.5 are illustrated in Fig. 7. With increasing concentration of PCoN, the dielectric constant tends to increase. The effect of increasing the dielectric constant at room temperature with increasing PCoN content is interpreted to be due to the possibility of the decrease of the transition temperature to near room temperature. Because of when PCoN is added into PZT, the transition temperature of the PZT–PCoN ceramics are shifted towards the room temperature; hence the dielectric properties measured at room temperature are increased. Other authors have reported a similar behavior [6,20]. Fig. 8 shows the saturated loops of 0.9PZT–0.1PCoN samples with difference electric fields strengths. It is clearly evident that the shape of hysteresis various greatly with the electric fields strength. At 5 kV/cm electric fields strength, a near-linear relationship of P–E is observed. This result is due to the fact that the electric field is not large enough to switch any domains. At 10 kV/cm electric fields, the polarization nonlinearity is developed in both regions of the positive and negative fields. These results clearly demonstrate that the electric field strength of 10 kV/cm is of enough energy to constrain realignment of some domains in the direction of the applied fields. No evidence of pinning effect or asymmetric loop was detected in all electric fields strength. At 25 kV/cm electric field strength, the loop reveals fully developed symmetric hysteresis loop. This shows that the electric fields strength of 25 kV/cm has of enough energy to constrain realignment of all domains in the direction of the electric fields.

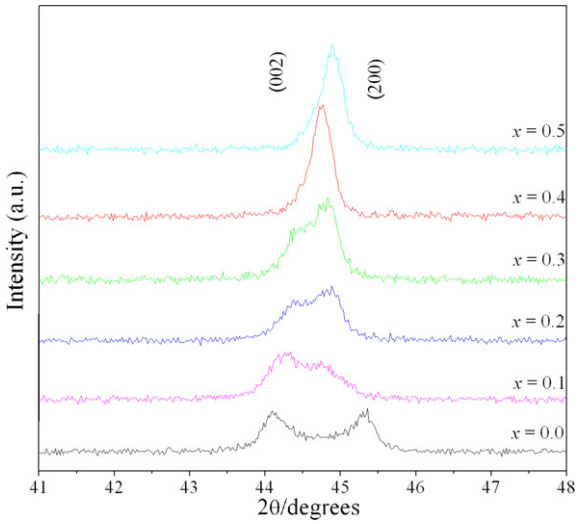



Fig. 6. XRD pattern of the (200) peak of $(1-x)$PZT–$x$PCoN, $x = 0.0$–0.1 ceramics.

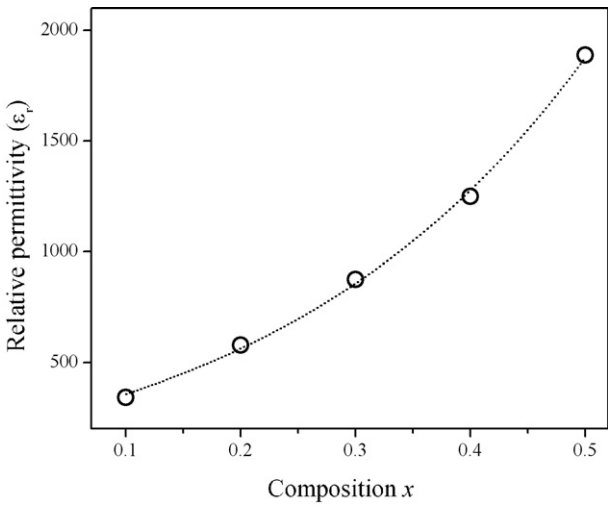



Fig. 7. Relative permittivity of $(1-x)$PZT–$x$PCoN as a function of compositions.

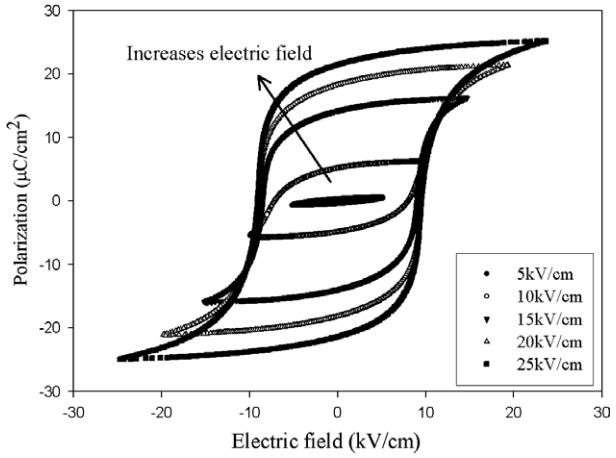



Fig. 8. Polarization of $(1-x)$PZT–$x$PCoN ceramics with $x = 0.1$ as a function of electric fields.

Fig. 9 illustrates the $P$–$E$ curves of the samples with $x = 0.0$, 0.1 and 0.5 measured at 25 kV/cm. All compositions show symmetry in shape and reveal rectangular hysteresis loops. From the fully saturated loops, the remanent polarization $P_r$ and coercive field $E_c$ were determined. The values of $P_r$ and $E_c$ for composition $x = 0.1$ are 21.4 μC/cm$^2$ and 9 kV/cm, respectively, whereas for composition $x = 0.0$ the remanent polarization $P_r$ is 15.2 μC/cm$^2$. At the composition $0.0 \leqslant x \leqslant 0.5$, the hysteresis loop has a typical "square" form stipulated by switching of a domain structure in an electrical field, which is typical of a phase that contains long-range cooperation between dipoles. That is characteristic of a ferroelectric micro-domain state. Room temperature values of $P_r$ are found to be ~15.2, 21.4 and 25.3 μC/cm$^2$ for composition $x = 0.0$, 0.1 and 0.5 samples, respectively. The results on other compositions are also listed Table 1.

It is seen that the samples with compositions $x = 0.1$ and 0.5 exhibit the highest saturation and remnant polarization among all the ceramics studied. As indicated by the above

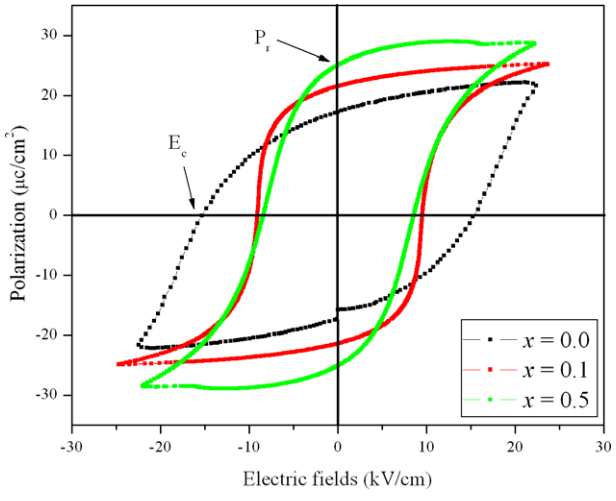



Fig. 9. Hysteresis loops of the $(1-x)$PZT–$x$PCoN ceramics with $x = 0.0$, 0.1 and 0.5 measured at 25 kV/cm.

Table 1
Polarization hysteresis data as a function of $x$ in the $(1-x)$PZT–$x$PCoN system

| Composition | $P_s$ (μC/cm$^2$) | $P_r$ (μC/cm$^2$) | $E_c$ (kV/cm) |
|---|---|---|---|
| $x = 0.0$ | 19.3 | 15.2 | 16.7 |
| $x = 0.1$ | 25.0 | 21.4 | 9.0 |
| $x = 0.2$ | 10.1 | 9.5 | 9.7 |
| $x = 0.3$ | 12.5 | 7.6 | 8.4 |
| $x = 0.4$ | 13.9 | 8.6 | 9.8 |
| $x = 0.5$ | 28.7 | 25.3 | 9.3 |

XRD, the composition with $x = 0.1$ contains both tetragonal and pseudo-cubic phases, so it should favor a strong ferroelectric effect due to the increased ease of reorientation during poling by transformation of a number of 180° domains into 90° ones. From the present results, it also can be revealed that the MPB coexisting in the tetragonal and pseudo-cubic phases in the present system is a broad composition region of $x \sim 0.1$, which exhibits high ferroelectric properties around the center of the MPB. Recent literature reviews [18,21] show that there are 2 MPBs in the PZT–PZN system; first, the separated tetragonal phase with rhombohedra phase at the composition 0.8PZT–0.2PZN and the second MPB showing transformation relaxor pseudo-cubic ferroelectric to normal pseudo-cubic ferroelectric at the composition 0.5PZT–0.5PZN [7]. It is interesting to note that the composition $x = 0.5$ in PZT–PCoN system may be attributed to the transition from normal ferroelectric to relaxor ferroelectric which is similar to the PZT–PZN and PZT–PNN system [6,7,21].

## 4. Conclusions

The effect of PCoN modification on the phase formation and transition mechanism of perovskite PZT–PCoN ceramics has been investigated for various chemical compositions. X-ray diffraction has indicated that except at $x = 0.5$, complete solid solutions occur across the entire compositional range of the $(1-x)Pb(Zr_{0.5}Ti_{0.5})O_3$–$xPb(Co_{1/3}Nb_{2/3})O_3$ system. PZT ceramic was identified by XRD as a single-phase material with a perovskite structure having tetragonal symmetry, while the mixed compositions showed a gradual change from tetragonal to pseudo-cubic symmetry, with a possible morphotropic phase boundary (MPB) between the two phases near the 0.9PZT–0.1PCoN composition. Ferroelectric and dielectric properties of the PZT–PCoN ceramics were investigated. The maximum value of remnant polarization $P_r$ (25.3 μC/cm$^2$) was obtained for the 0.5PZT–0.5PCoN ceramic. Most importantly, this study showed that the addition of PCoN could improve the ferroelectric behavior in PZT ceramics.

## Acknowledgements

This work was supported by the Thailand Research Fund (TRF), the Commission on Higher Education (CHE), National Research Council of Thailand (NRCT),

Thailand Graduate Institute of Science and Technology (TGIST) and King Mongkut's Institute of Technology Ladkrabang (KMITL).

## References

[1] K. Uchino, Ferroelectric Devices, Marcel Dekker, Inc., New York, 2000.
[2] Y. Xu, Ferroelectric Materials and Their Application, Elsevier Science Publishers B.V., 1991.
[3] S.-E. Park, T.R. Shrout, IEEE Tr. UFFC. 44 (1997) 1140.
[4] J. Kuwata, K. Uchino, S. Nomura, Ferroelectrics 37 (1981) 579.
[5] M.L. Mulvihill, L.E. Cross, W. Cao, K. Uchino, J. Am. Ceram. Soc. 80 (1997) 1462.
[6] N. Vittayakorn, G. Rujijanagul, X. Tan, M.A. Marquardt, D.P. Cann, J. Appl. Phys. 96 (2004) 5103.
[7] H. Fan, H.-E. Kim, J. Mater. Res. 17 (2002) 180.
[8] O. Furukawn, Y. Yamashita, M. Harata, T. Takahashi, K. Inagai, Jpn. J. Appl. Phys. 24 (1985) 96.
[9] V.J. Tennery, K.W. Hang, R.E. Novak, J. Am.Ceram. Soc. 51 (1968) 671.
[10] D. Luff, R. Lane, K.R. Brown, H.J. Marshallsay, Trans. J. Br. Ceram. Soc. 73 (1974) 251.
[11] G.A. Smolenskii, A.L. Agranovskaya, Sov. Phys.-Tech. Phys. (1958) 1380.
[12] A. Ngamjarurojana, O. Khamman, R. Yimnirun, S. Ananta, Mater. Lett. 60 (2006) 2867.
[13] N. Vittayakorn, S. Wirunchit, Smart Mater. Struct. 16 (2007) 851.
[14] R. Wongmaneerung, R. Yimnirun, S. Ananta, Mater. Lett. 60 (2006) 2666.
[15] R. Wongmaneerung, T. Sarakonsri, R. Yimnirun, S. Ananta, Mater. Sci. Eng. B 130 (2006) 246.
[16] T.R. Shrout, A. Halliyal, Am. Ceram. Soc. Bull. 66 (1987) 704.
[17] N. Vittayakorn, C. Puchmark, G. Rujijanagul, X. Tan, D.P. Cann, Curr. Appl. Phys. 6 (2006) 303.
[18] N. Vittayakorn, G. Rujijanagul, X. Tan, H. He, M.A. Marquardt, D.P. Cann, J. Electroceram. 16 (2006) 141.
[19] S. Wongsaenmai, Y. Laosiritaworn, S. Ananta, R. Yimnirun, Mater. Sci. Eng. B 128 (2005) 83.
[20] N. Vittayakorn, G. Rujijanagul, T. Tunkasiri, X. Tan, D.P. Cann, J. Mater. Res. 18 (2003) 2882.
[21] H. Fan, H.-E. Kim, J. Appl. Phys. 91 (2002) 317.

Available online at www.sciencedirect.com
ScienceDirect
Materials Letters 62 (2008) 352–356
materials letters
www.elsevier.com/locate/matlet

# Thermal expansion measurements in the relaxor ferroelectric PIN–PT system

Supattra Wongsaenmai [a,*], Rattikorn Yimnirun [a,c,1], Supon Ananta [a], Ruyan Guo [b], Amar S. Bhalla [b,2]

[a] Department of Physics, Faculty of Science, Chiang Mai University, Chiang Mai 50200, Thailand
[b] Materials Research Laboratory, The Pennsylvania State University, University Park, PA 16802, USA
[c] NANOTEC Center of Excellence at Chiang Mai University, Chiang Mai 50200, Thailand

Received 11 February 2007; accepted 11 May 2007
Available online 18 May 2007

**Abstract**

Thermal expansion was measured for the ceramic compositions $(1-x)Pb(In_{0.5}Nb_{0.5})O_3-(x)PbTiO_3$ ($x=0.0$, 0.1, 0.2 and 0.3) prepared via the wolframite method. The deviation from the straight line below Burns temperature for all the compositions was due to the dynamic polarization fluctuations. Burns temperature was determined and found to increase with increasing PT concentration. The local polarization was calculated from the thermal expansion data. The calculated local polarization and the measured reversible spontaneous polarization were compared and the relaxor behavior of the PIN–PT compositions was analyzed.
© 2007 Elsevier B.V. All rights reserved.

*Keywords:* PIN–PT; Relaxor ferroelectric; Thermal expansion; Burns temperature; Glassy polarization phase

## 1. Introduction

Relaxor behavior in the perovskite mixed oxides has been the topic of several reports. There are several models which attempted to explain the exact behavior of the relaxor but none can completely explain their interesting properties. The composition fluctuation model by Smolenskii [1] proposed that the different local Curie temperatures lead to broad diffuse phase transition. Cross proposed the origin of polarization mechanism analogous to the superparamagnetic cluster material [2]. The broad distribution and frequency dispersion of the dielectric properties originate from slowing down of polarization reorientation in each cluster. The glass-like behavior was considered by Viehland to extend Cross' model and was analogous to the magnetic spin glass [3]. The freezing temperature was defined as the macroscopic polarization emergence. The glassy polarization phase of relaxor ferroelectrics has been considered after Burns' and Dacol's measurements of the optic index of refraction, $n(T)$, dependence on the temperature [4–7]. The deviation from linear behavior of $n(T)$ was observed starting at Burns temperature ($T_d$) which is much higher than the transition temperature ($T_m$). This behavior was interpreted in terms of the local polar regions of randomly orientated irreversible polarization ($P_d$) and of very small number of unit cells, which grow with the reducing temperature. The local polarization exists above the transition temperature while disappears or is unmeasurable above Burns temperature [5]. Several other techniques, including refractive index measurements [4], Raman scattering [8], neutron powder diffraction [9], neutron elastic scattering [10], dynamic light scattering [11] and dielectric measurements [12-13] have also been used to measure Burns temperature and to explain the glass-like behavior. Thermal expansions which are related to the square of the polarization can be used to study phase transition, thermal expansion coefficient and anisotropies to estimate the dynamic polarization in the relaxor systems. Therefore, Burns temperature and local polarization can be detected by this technique [14,15].

$Pb(In_{0.5}Nb_{0.5})O_3$–PIN is a member of the relaxor family with a 1:1 stoichiometry at B-site and which can be converted from disordered state into ordered state by thermal treatment [16]. The disordered state of PIN exhibits a relaxor behavior and

* Corresponding author. Tel.: +66 53 943445.
*E-mail addresses:* wongsaenmai@yahoo.com (S. Wongsaenmai), rattikornyimnirun@yahoo.com (R. Yimnirun), asb2@psu.edu (A.S. Bhalla).
[1] Tel.: +66 53 943367.
[2] Tel.: +1 814 8659232.

0167-577X/$ - see front matter © 2007 Elsevier B.V. All rights reserved.
doi:10.1016/j.matlet.2007.05.029

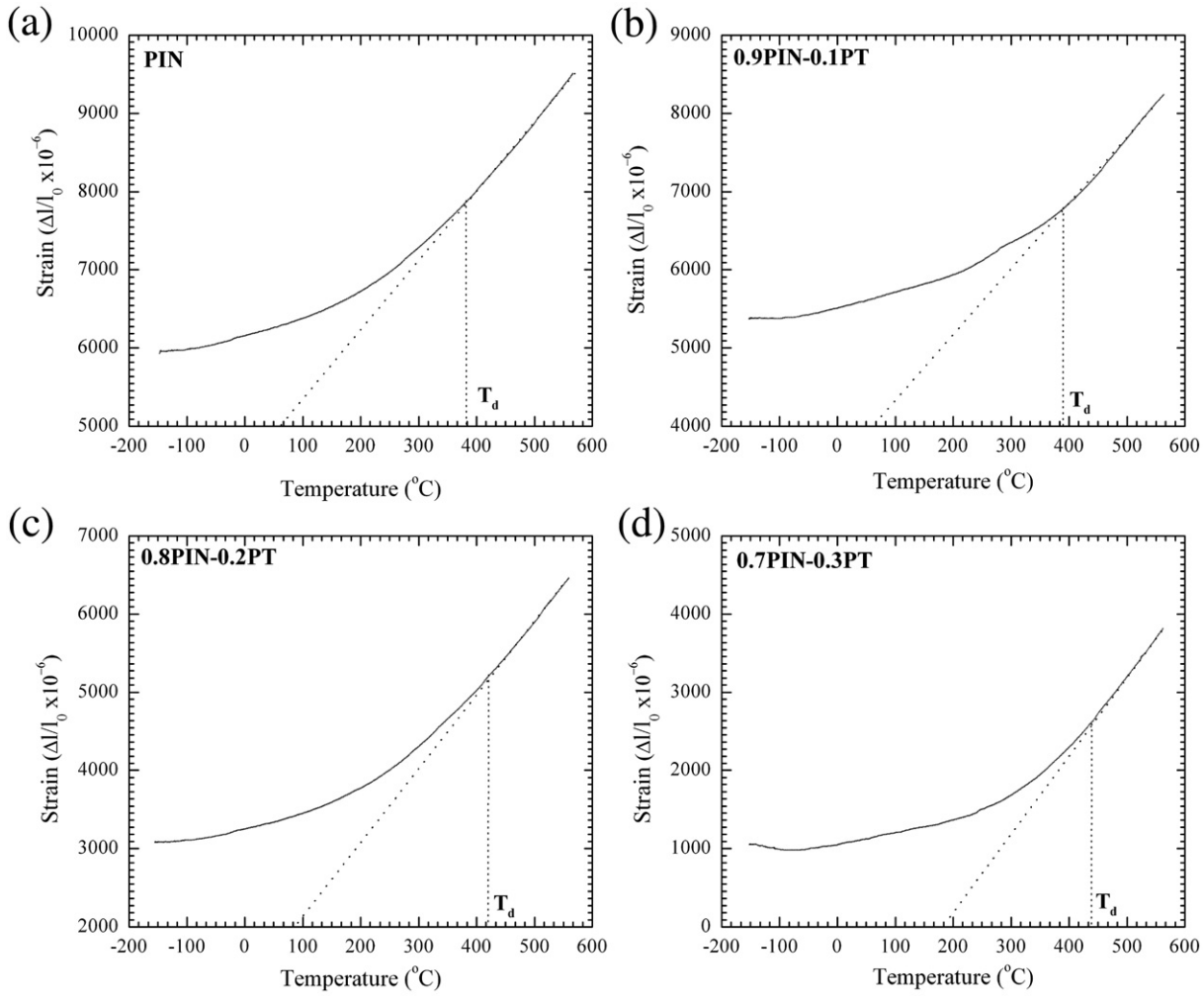



Fig. 1. Temperature dependence of the strain for $(1-x)$PIN–$(x)$PT system (a) $x=0.0$, (b) $x=0.1$, (c) $x=0.2$ and (d) $x=0.3$.

shows a broad dielectric maximum near 66°C [17,18]. The ordered state of PIN shows an antiferroelectric behavior with a sharp steep in the dielectric constant vs. temperature curve observed at 168°C [18,19]. There are several reports, which attempted to investigate the properties of the solid solution of relaxor ferroelectric PIN and normal ferroelectric PT, including the relaxor behavior analysis from the dielectric properties, the deviation of the Curie–Weiss law and the glass-like behavior using the Vogel–Fulcher relation [20,21]. The relaxor behavior analyzed from the thermal expansion measurement has been studied in several relaxor ferroelectric systems e.g. PMN–PT, PMN, PZN, PLZT and tungsten bronze structure family [5,7,14,22–24]. Though studies on dielectric and ferroelectric properties of the PIN-based system have been reported [25,26], there have been no thermal expansion measurement and analysis of relaxor behavior of the PIN-based system.

In this paper, the relaxor behavior of PIN–PT system was analyzed from the thermal expansion data. The glassy polarization and the relaxor behavior were studied and Burns temperature and the local polarizations were estimated. The results showed the Burns temperature between 380°C and 435°C for all of the compositions. The local polarization was calculated and compared with the reversible spontaneous polarization measurement.

## 2. Experimental

The powders of $(1-x)Pb(In_{0.5}Nb_{0.5})O_3$–$(x)PbTiO_3$ ($x=0.0$, 0.1, 0.2 and 0.3, abbreviated as PIN–PT) were synthesized by a two-step solid solution reaction method [27]. The wolframite $InNbO_4$ was first prepared from oxide powder of $In_2O_3$ and $Nb_2O_5$ [28]. Mixed powder was milled and calcined at 1100°C

Table 1
The parameters derived from the thermal expansion measurement of $(1-x)$PIN–$(x)$PT system

| Composition ($x$) | $T_m$ (°C) at 1 kHz | $T_d$ (°C) | Properties at room temperature | | |
|---|---|---|---|---|---|
| | | | $\alpha\times10^{-6}$ (°C$^{-1}$) | $P_s$ (μC/cm$^2$) | $P_d$ (μC/cm$^2$) |
| 0.0 | 70 | 380 | 2.2 | 7.6 | 16.0 |
| 0.1 | 144 | 391 | 2.9 | 15.2 | 17.7 |
| 0.2 | 208 | 420 | 3.4 | 18.7 | 19.9 |
| 0.3 | 279 | 435 | 4.0 | 23.3 | 24.1 |

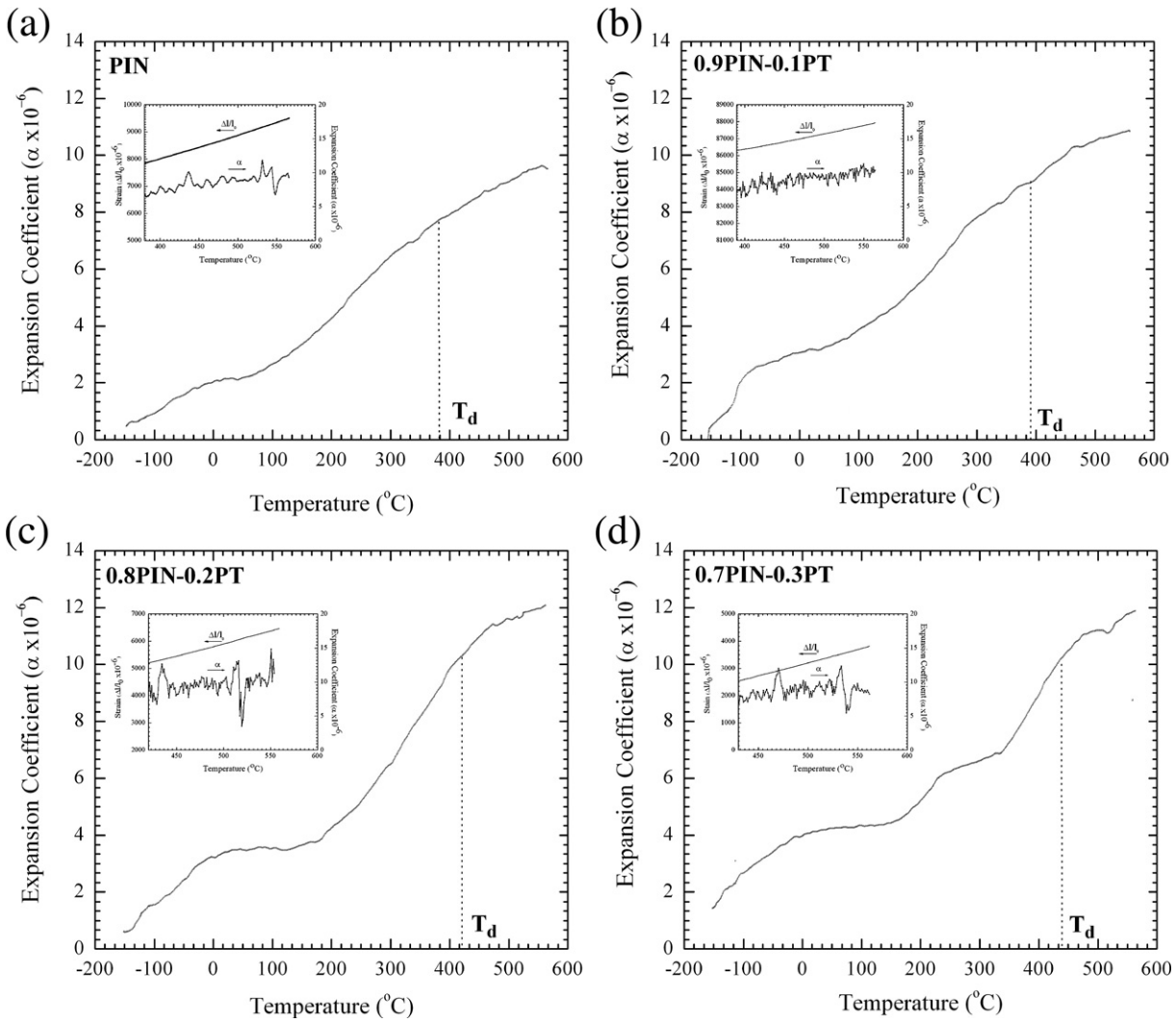



Fig. 2. Temperature dependence of thermal expansion coefficient (α) for $(1-x)$PIN–$(x)$PT system (a) $x=0.0$, (b) $x=0.1$, (c) $x=0.2$ and (d) $x=0.3$. (Inset shows a closer look at temperature dependence of $\Delta l/l$ and α above Burns temperature.)

temperature for 2h to obtain the intermediate precursor $InNbO_4$ [29]. The wolframite precursor was then mixed with reagent grade powder of PbO, $TiO_2$ for PIN–PT. Excess amounts of PbO (2%) and $In_2O_3$ (2%) were added at this stage. The mixtures were milled again following the intermediate precursor stage. After drying, the mixtures were calcined at temperature between 800°C and 1000°C with soaking time of 2h [30]. Pellets were pressed with 1% PVA. The pressed pellets were sintered with the soaking time of 2h in a double crucible configuration at temperature from 1100°C to 1125°C. To prevent PbO loss, the pellets were buried in protective powders.

The ceramics of PIN–PT were cut to rectangular bars with dimension 5mm × 1mm × 1mm. The effect of temperature on sample expansion (strain) was measured with a linear voltage-differential transformer (LVDT) dilatometer (Series 6500, theta industries, Inc., NY). The measurements were performed over the temperature range −145°C and 550°C with heating rate of 2°C/min, as reported in other relaxor ferroelectric systems [31,32]. However, it should also be noted that these measurements could be rate dependent, and further investigation is of interest.

## 3. Results and discussion

The thermal strain dependences of temperature of PIN–PT ceramics are shown in Fig. 1. There is no clear anomaly of the thermal strain at transition temperature. This behavior differs from the normal ferroelectrics which generally show an abrupt discontinuity (first orders) at the transition temperature and follow the linear relationship above transition temperature. The deviation from the straight line or linear relationship below the Burns temperature was observed for all the compositions. The values of Burns temperature were in the temperature range from 380°C to 435°C depending on PT concentration, as shown in Table 1. The Burns temperature is much higher than the transition temperature for pure PIN and other relaxor ferroelectric systems [6,25,26]. The difference between transition temperature and Burns temperature also decreases with increasing PT concentration.

Similar behavior has been reported in other quadratic relationships with the polarization such as the deviation from the straight line at transition temperature in the refractive index and birefringence measurements [33]. The increase of Burns temperature due to addition of PT was attributed to stronger correlation between the polar and slightly anisotropic normal PT ferroelectric [10]. Therefore, the increase of PT concentration leads to decrease of closeness of the

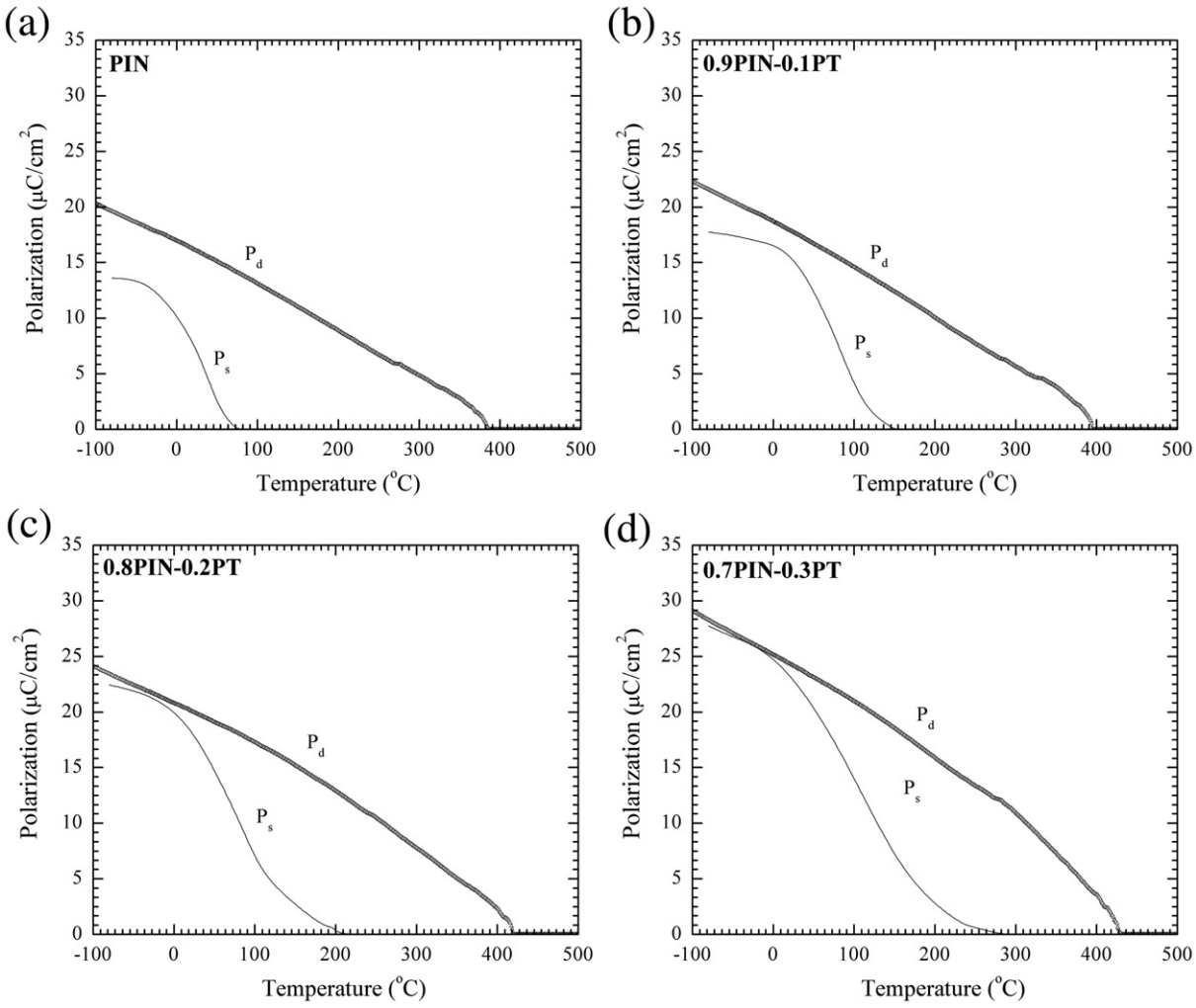



Fig. 3. Comparison of $P_d$ and $P_s$ of both $(1-x)$PIN–$(x)$PT system (a) $x=0.0$, (b) $x=0.1$, (c) $x=0.2$ and (d) $x=0.3$.

transition and Burns temperatures. This contribution follows with the decrease in relaxor ferroelectric nature in PIN ceramics which eventually decrease the degree of relaxor behavior with increasing PT concentration. At temperatures high above Burns temperature the correlation between thermal strain and temperature shows a linear relationship leading to no polarization effect.

The thermal expansion coefficient (α), defined as $\alpha_T = dx_T/dT$ [32], is calculated and listed in Table 1. The small thermal expansion coefficient values are similar to those reported for other relaxor ferroelectrics [34]. The plots of the thermal expansion coefficient vs. temperature are shown in Fig. 2. The thermal expansion coefficient gradually changes with temperature above Burns temperature, and then thermal expansion coefficient decreases more steeply below Burns temperature. Though the linear relation of strain vs. temperature above Burns temperature was shown in Fig. 1, the thermal expansion coefficients were found to change with temperature. The small fluctuations were shown in the inset of Fig. 2. The possible origin of this temperature dependence and fluctuation is not clear, but could be attributed to differential calculation error over small temperature range. Similar problem has also been reported earlier [24]. Probably, the results of the thermal expansion coefficient calculation are not suitable for defining Burns temperatures. Therefore, strain vs. temperature measurement is more suitable for Burns temperature identification.

The observation can be explained due to the results of the glassy polarization phase which occurs from charge difference of ions on the B-site in highly disordered state at the high temperature leading to the strong breaking of the translational symmetry [6]. Then, the random orientation, unstable reversible polarization and very small size of local polarization arise below Burns temperature.

The glassy polarization phase was interpreted with local polarization ($\overline{P}^2_d$) existent below Burns temperature. It is known that there is no stable and finite local polarization ($P=0$) above dielectric transition maxima temperature but there is a stable and finite square of polarization ($\overline{P}^2 \neq 0$). These dynamic local polarizations above transition temperature can be detected by the quadratic relationship with the thermal expansion behavior and can be measured. The polarization is calculated from the relationship between total thermal strain (or linear thermal expansion) and electrostriction as shown below.

$$x_{11} = \alpha(T - T_0) + (Q_{11} + 2Q_{12})\overline{P}^2 \quad (1)$$

where α is the thermal expansion coefficient, $T_0$ is the reference temperature and $Q_{11}$ and $Q_{12}$ are the electrostrictive coefficients [35]. In this paper the electrostrictive coefficient of a typical perovskite structure $PbTiO_3$ was used for the calculation of $\overline{P}^2$ [36] as it is assumed that for most materials electrostrictive coefficients are of the same range.

Fig. 3 shows the temperature dependence of the polarization. The local polarization ($P_d$) was calculated from Eq. (1) using the thermal strain data. The reversible spontaneous polarization ($P_r$) was obtained from ferroelectric (P–E) hysteresis measurement. The local polarization curves show slow decrease to zero at Burns temperature while the reversible polarization drops to zero at the transition temperature. The gradual change of reversible polarization near transition temperature is due to the distribution of polar nano-region in relaxor ferroelectric. On the other hand, the local polarization shows a gradual decrease with temperature up to the Burns temperature. The separation of both polarization curves above the transition temperature also suggests the existence of the dynamic nature of the local polarization. The value of the local polarization is closer to the reversible polarization at low temperature indicating development of stable polarization with reducing temperature. If the temperature is low enough to freeze the dynamic behavior of the polarization, the reversible polarization value will be equal to the local polarization [7]. However, it is found that the local polarization is far from the reversible polarization value at low temperature for pure PIN and the composition of $x=0.1$, suggesting the presence of enough dynamic polar regions. Similar separation of the polarizations at low temperature has also been observed in PMN and PZN [6].

## 4. Conclusions

The relaxor behavior of the ceramics of compositions $(1-x)Pb(In_{0.5}Nb_{0.5})O_3$–$(x)PbTiO_3$ ($x=0.0$, 0.1, 0.2 and 0.3) prepared via the wolframite method was studied by the thermal expansion measurement over the temperature range −145 °C and 550 °C. It was found that the thermal expansion exhibits a linear relation with temperature at high temperature, and starts to deviate at Burns temperature between 380 °C and 435 °C. Pure PIN shows the Burns temperature far above the transition temperature, and the difference between these temperatures is lower with increasing PT concentration. The deviation from linear behavior was interpreted with the existence of the dynamic polarization between the transition temperature and Burns temperature. The local dynamic polarization was calculated from the thermal expansion data and compared with the reversible spontaneous polarization measurement. The separation of both polarizations was very clear at high temperature, while it was closer at temperature below $T_m$. The results confirm that the local polarization exists in PIN–PT and increase as the temperature decreases below $T_m$.

## Acknowledgements

This work was supported by the Thailand Research Fund (TRF), Commission on Higher Education (CHE), Graduate School of Chiang Mai University and Ministry of University Affairs, the National Nanotechnology Center (NANOTEC), NSTDA, Ministry of Science and Technology, through its program of Center of Excellence Network, Thailand, and the relaxor & metamaterials grants of NSF/DMR, USA.

## References

[1] G.A. Smolenskii, Jpn. J. Appl. Phys. 28 (1970) 1970.
[2] L.E. Cross, Ferroelectrics 76 (1987) 246.
[3] D. Viehland, S.J. Jang, L.E. Cross, J. Appl. Phys. 68 (6) (1990) 2916.
[4] G. Burns, F.H. Dacol, Solid State Commun. 42 (1) (1982) 9.
[5] G. Burns, F.H. Dacol, Phys. Rev., B 28 (5) (1983) 2527.
[6] G. Burns, F.H. Dacol, Solid State Commun. 48 (10) (1983) 853.
[7] G. Burns, F.H. Dacol, Ferroelectrics 52 (1983) 103.
[8] G. Burns, F.H. Dacol, Solid State Commun. 58 (1986) 567.
[9] J. Zhao, A.E. Glazounov, Q.M. Zhang, B. Toby, Appl. Phys. Lett. 72 (1998) 1048.
[10] D. La-Orauttapong, J. Toulouse, Z.-G. Ye, W. Chen, R. Erwin, J.L. Robertson, Phys. Rev., B 67 (2003) 134110.
[11] W. Kleemann, P. Licinio, T. Woike, R. Pankrath, Phys. Rev. Lett. 86 (2001) 6014.
[12] D. Viehland, S.J. Jang, L.E. Cross, M. Wuttig, Phys. Rev., B 46 (1992) 8003.
[13] J. Dec, W. Kleemann, V. Bobnar, Z. Kutnjak, A. Levstik, R. Pirc, R. Pankrath, Europhys. Lett. 55 (2001) 781.
[14] A.S. Bhalla, R. Guo, L.E. Cross, G. Burns, F.H. Dacol, R.R. Neurgaonkar, Phys. Rev., B 36 (4) (1987) 2030.
[15] A.S. Bhalla, R. Guo, L.E. Cross, G. Burns, F.H. Dacol, R.R. Neurgaonkar, Ferroelectrics 106 (1990) 161.
[16] C.A. Randall, A.S. Bhalla, Jpn. J. Appl. Phys. 29 (2) (1990) 327.
[17] E.F. Alberta, A.S. Bhalla, Mater. Lett. 29 (1996) 127.
[18] E.F. Alberta, A.S. Bhalla, J. Phys. Chem. Solids 63 (2002) 1759.
[19] M. Iwata, S. Katagiri, H. Orihara, M. Maeda, I. Zusuki, H. Ohwa, N. Yasuda, Y. Ishibashi, Ferroelectrics 301 (2004) 179.
[20] S. Wongsaenmai, A.S. Bhalla, R. Guo, S. Ananta, R. Yimnirun, Ferroelectr. Lett. 34 (2007) 36.
[21] A.A. Bokov, M.A. Leshchenko, M.A. Malitskaya, I.P. Raevski, J. Phys., Condens. Matter 11 (1999) 4899.
[22] H. Arndt, G. Schmidt, Ferroelectrics 79 (1988) 149.
[23] G. Burns, F.H. Dacol, Ferroelectrics 104 (1990) 25.
[24] M.V. Gorev, I.N. Flerov, P.H. Sciau, V.S. Bondarev, A.G. LehMann, Ferroelectrics 307 (2004) 127.
[25] S. Wongsaenmai, R. Yimnirun, S. Ananta, J. Alloy. Compd. (in press).
[26] S. Wongsaenmai, R. Yimnirun, S. Ananta, Appl. Phys. A. (in press).
[27] S. Wongsaenmai, R. Yimnirun, S. Ananta, J. Mater. Sci. 128 (2007) 83.
[28] S. Wongsaenmai, R. Yimnirun, S. Ananta, Mater. Letter. 61 (2007) 2426.
[29] S. Wongsaenmai, O. Khamman, S. Ananta, R. Yimnirun, J. Electroceram. (in press).
[30] N. Yasuda, M. Fujie, Jnp. J. Appl. Phys. 31 (1992) 3128.
[31] D.K. Agrawal, R. Roy, H.A. Mckinstry, Mater. Res. Bull. 22 (1987) 83.
[32] V. Mueller, L. Läger, H. Beige, H.-P. Abicht, Thomas Müller, Solid State Commun. 129 (2004) 757.
[33] G. Burns, Phase Transit. 5 (1985) 261.
[34] L.E. Cross, S.J. Jang, R.E. Newhnam, S. Nomura, K. Uchino, Ferroelectrics 23 (1980) 187.
[35] L.E. Cross, Ferroelectrics 76 (1987) 241.
[36] S. Nomura, K. Uchino, Ferroelectrics 41 (1982) 117.

Japanese Journal of Applied Physics
Vol. 47, No. 2, 2008, pp. 998–1002

©2008 The Japan Society of Applied Physics

# Synthesis and Dielectric and Ferroelectric Properties of Ceramics in $(1-x)Pb(Zr_{1/2}Ti_{1/2})O_3$–$(x)Pb(Co_{1/3}Nb_{2/3})O_3$ System

Anurak PRASATKHETRAGARN*, Naratip VITTAYAKORN[1], Supon ANANTA, Rattikorn YIMNIRUN, and David P. CANN[2]

*Department of Physics, Faculty of Science, Chiang Mai University, Chiang Mai 50200, Thailand*
[1]*Department of Chemistry, Faculty of Science, King Mongkut's Institute of Technology Ladkrabang, Bangkok 10520, Thailand*
[2]*Materials Science, Department of Mechanical Engineering, Oregon State University, Corvallis, OR 97331, U.S.A.*

(Received August 16, 2007; revised September 28, 2007; accepted October 26, 2007; published online February 15, 2008)

Ceramics in a PZT–PCN system with the formula $(1-x)Pb(Zr_{1/2}Ti_{1/2})O_3$–$(x)Pb(Co_{1/3}Nb_{2/3})O_3$, where $x = 0.1$–$0.5$, were prepared using a solid-state mixed-oxide technique (the columbite-wolframite precursor method). The phase formation behavior and microstructure were studied using X-ray diffraction (XRD) analysis and scanning electron microscopy (SEM), respectively. The dielectric and ferroelectric properties of the compounds were studied and discussed. Phase-pure perovskites of PZT–PCN ceramics were obtained over a wide compositional range. In addition, the XRD, dielectric, and ferroelectric properties confirmed that the morphotropic phase boundary (MPB) composition between the tetragonal and pseudo cubic phases of this system lied between $0.2 \leq x \leq 0.3$. [DOI: 10.1143/JJAP.47.998]

KEYWORDS: ferroelectric properties, perovskites, MPB, phase transition

## 1. Introduction

Lead-based perovskite-type solid solutions consisting of ferroelectric and relaxor materials have attracted more and more fundamental and practical attention because of their excellent dielectric, piezoelectric, and electrostrictive properties, which are useful in actuating and sensing applications.[1)] Recently, many piezoelectric ceramic materials have been developed from binary systems containing a combination of relaxor and normal ferroelectric materials[2)] that yield high dielectric permittivities [e.g., $Pb(Zn_{1/3}Nb_{2/3})O_3$–$PbTiO_3$ (PZN–PT)[3,4)] and $Pb(Zr_{1/2}Ti_{1/2})O_3$–$Pb(Ni_{1/3}Nb_{2/3})O_3$ (PZT–PNN)[5)]], excellent piezoelectric coefficients [e.g., $Pb(Zn_{1/3}Nb_{2/3})O_3$–$PbTiO_3$ (PZN–PT),[3,4)] $Pb(Zr_{1/2}Ti_{1/2})O_3$–$Pb(Zn_{1/3}Nb_{2/3})O_3$ (PZN–PZT),[6)] and $Pb(Sc_{1/3}Nb_{2/3})O_3$–$PbTiO_3$ (PSN–PT)[7,8)]], and high pyroelectric coefficients [e.g., $Pb(Ni_{1/3}Nb_{2/3})O_3$–$PbTiO_3$–$PbZrO_3$ (PNN–PT–PZ)[9)]]. Of the lead-based complex perovskites, lead zirconate titanate [$Pb(Zr_{1/2}Ti_{1/2})O_3$ or PZT] ceramics have been investigated from both fundamental and applied viewpoints.[10)] A solid solution of $Pb(Zr_{1-x}Ti_x)O_3$ (PZT) was found to host exceptionally high value for dielectric and piezoelectric properties for compositions close to the morphotropic phase boundary (MPB). This MPB is located at a $PbTiO_3$:$PbZrO_3$ of $\sim 1:1$ and separates the Ti-rich tetragonal phase from the Zr-rich rhombohedral phase.[10)] Furthermore, it has a high $T_C$ of 390 °C, which allows piezoelectric devices to be operated at relatively high temperatures. Most commercial PZT ceramics are designed in the vicinity of the MPB with various doping methods in order to achieve high properties.

Lead cobalt niobate (PCN) is a perovskite relaxor ferroelectric with a broad diffuse phase transition near −70 °C.[11)] The structure is cubic at room temperature (RT). In this compound, the octahedral sites of the crystal are randomly occupied by $Co^{2+}$ and $Nb^{5+}$ ions.[12)] Malkov and Venevtsev have indicated that there are large deviations in the temperatures at which the permittivity is maximum ($T_m$) for single-crystal and ceramic samples.[13)] The effects of the DC bias on the dielectric properties have been reported as a function of temperature for single-crystal $Pb(Co_{1/3}Nb_{2/3})O_3$ with a diffuse phase transition.[14)] Although the paraelectric–ferroelectric transition temperature of PCN is below RT, it can be easily shifted upward with the addition of $PbTiO_3$ (PT), which is a normal ferroelectric compound with a phase transition at 490 °C.[15)] In addition, it is well known that the addition of PZT enhances the piezoelectric, dielectric, and ferroelectric properties in a solid solution with a relaxor ferroelectric such as PZT–PZN,[16,17)] PZT–PNN,[5)] and PZT–PMN.[18)] On the basis of this approach, solid solutions of PZT and PCN are expected to synergistically combine the properties of both the normal ferroelectric PZT and relaxor ferroelectric PCN, which could exhibit piezoelectric and dielectric properties that are better than those of the single-phase PZT and PCN.[12,19)] There have been no systematic studies on the electrical properties of ceramics within a wide composition range between PZT and PCN.

The overall purpose of this study is to determine the phase transition, grain size, and composition dependence of the dielectric properties and ferroelectric behavior of ceramics in a $(1-x)Pb(Zr_{1/2}Ti_{1/2})O_3$–$(x)Pb(Co_{1/3}Nb_{2/3})O_3$ (where $x = 0.1$–$0.5$) binary system prepared using the columbite-wolframite precursor method.

## 2. Experimental Procedure

Reagent-grade oxides of PbO, CoO, $Nb_2O_5$, $ZrO_2$, and $TiO_2$ (anatase-structure) were used as raw materials. The columbite $CoNb_2O_6$ and wolframite $ZrTiO_4$ precursors were weighed and introduced into the batch calculations. $CoNb_2O_6$ and $ZrTiO_4$ powders were prepared at calcination temperatures of 1100 and 1450 °C for 2 h, respectively. In the present work, $(1-x)Pb(Zr_{1/2}Ti_{1/2})O_3$–$(x)Pb(Co_{1/3}Nb_{2/3})O_3$ samples with compositions of $x = 0.1$–$0.5$ were prepared from $ZrTiO_4$, $CoNb_2O_6$, and PbO powders. PZT–PCN powders were synthesized using the solid-state reaction of these raw materials and mixed by a vibro-milling technique in ethanol for 1 h. PbO excess of 2.0 mol % was constantly added to compensate for lead losses during calcination and sintering.[17)] After drying, the product was calcined in an alumina crucible at a temperature of 950 °C.

*E-mail address: Prasatkhetragarn@yahoo.com

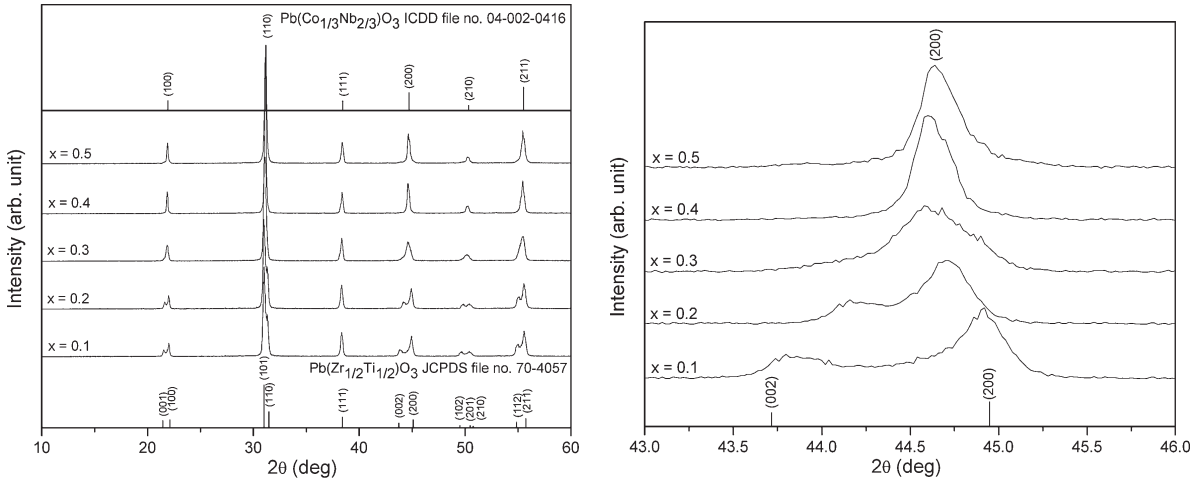



Fig. 1. XRD patterns of $(1-x)$PZT–$(x)$PCN ceramics, where $x = 0.1$–$0.5$.

The calcined powders were pressed hydraulically to form disc-shaped pellets with a diameter of 10 mm and a thickness of 1 mm, with 1 wt % poly(vinyl alcohol) (PVA) added as a binder. The pellets were sintered at 1200 °C for 2 h at a heating/cooling rate of 5 °C/min. The phase structure of the powders was analyzed via X-ray diffraction (XRD; Siemens-D500 diffractometer) analysis using Cu K$\alpha$ radiation. The microstructures of the sintered samples were examined using scanning electron microscopy (SEM; JEOL JSM-840A). The dielectric properties of the samples were measured using an automated measurement system. This system consisted of an LCR meter (Hewlett-Packard HP-4284A) in connection with a Delta Design 9023 temperature chamber and a sample holder (Norwegian Electroceramics) capable of high-temperature measurement. The ferroelectric properties were examined using a simple Sawyer–Tower circuit.[18)]

## 3. Results and Discussion

The XRD patterns of $(1-x)$PZT–$(x)$PCN ceramics with various $x$ values are shown in Fig. 1. It can be seen that a complete crystalline solution of the perovskite structure is formed throughout the entire compositional range without the presence of pyrochlore or unwanted phases. From the XRD data, the $Pb(Zr_{1/2}Ti_{1/2})O_3$ ceramic is identified as a single-phase material with a perovskite structure having tetragonal symmetry, which was matched with JCPDS file no. 70-4057. The XRD patterns of the PZT–PCN compositions show a range in symmetry between the tetragonal and pseudo cubic perovskite types.[20)] For a better comparison, ICDD file no. 04-002-0416 for $Pb(Co_{1/3}Nb_{2/3})O_3$ with pseudo cubic structural symmetry is also displayed in Fig. 1. It is clear that the crystal symmetry should change owing to the effects of increasing the PCN fraction and a corresponding decrease in $T_C$. It is well known that in the pseudo cubic phase, the (200) profile will show a single narrow peak, while in the tetragonal phase, the (200) profile should be split into two peaks. More interestingly, the composition at $x = 0.3$ exhibited peak broadening at a $2\theta$ of $\sim$44–45°, indicating the structural transformation from the tetragonal phase, characterized by the shifting of the (002)/(200) peaks to the pseudo cubic phase. This observation is obviously associated with the composition showing the coexistence of two symmetries, which in this case are the tetragonal and pseudo cubic phases. To a first approximation, it could be said that the composition with $x = 0.3$ is close to the MPB of the $(1-x)$PZT–$(x)$PCN system, where the structure of the PZT–PCN compositions gradually changes from tetragonal to pseudo cubic. The electrical data described later on will further support this assumption.

The SEM images in Fig. 2 reveal that the addition of PCN resulted in significant changes in the microstructure of the ceramics. Some grains are observed to have irregular shapes with both open and close pores as a result of the high rate of the evaporation of PbO during the sintering.[17)] The images also show that the grain size of the ceramics varied considerably from 0.43 to 19.56 μm (Table I). However, the average grain size significantly decreased with an increase in the content of PCN. It can also be seen that the maximum density is obtained in the 0.7PZT–0.3PCN ceramics, while the minimum density is observed in the 0.5PZT–0.5PCN ceramics. Interestingly, the density results can be correlated to the microstructure because high-density 0.7PZT–0.3PCN ceramics show high degrees of grain close packing, whereas low-density 0.5PZT–0.5PCN ceramics contain many closed pores.

The dielectric properties of $(1-x)$PZT–$(x)$PCN, where $x = 0.1$–$0.5$, are illustrated in Fig. 3. At RT, with an increase in the concentration of PCN, the dielectric constant tends to increase because the transition temperature of the PZT–PCN ceramics shift across RT; hence, the value of the dielectric properties measured at RT increased, as shown in Table II. Other authors have reported a similar behavior.[5)] The temperature dependence of the dielectric constant for the compositions of the $(1-x)$PZT–$(x)$PCN system show broad dielectric peaks with an increase in the concentration of PCN, which indicate a diffuse phase transition. The diffuse phase transition may have been caused by a decrease in grain size; the observed difference in the degree of diffuseness could be a result of the grain size variation, as shown in Table II,[21)] and chemical inhomogenieties within the $(1-x)$PZT–$(x)$PCN solid solution.[20)]

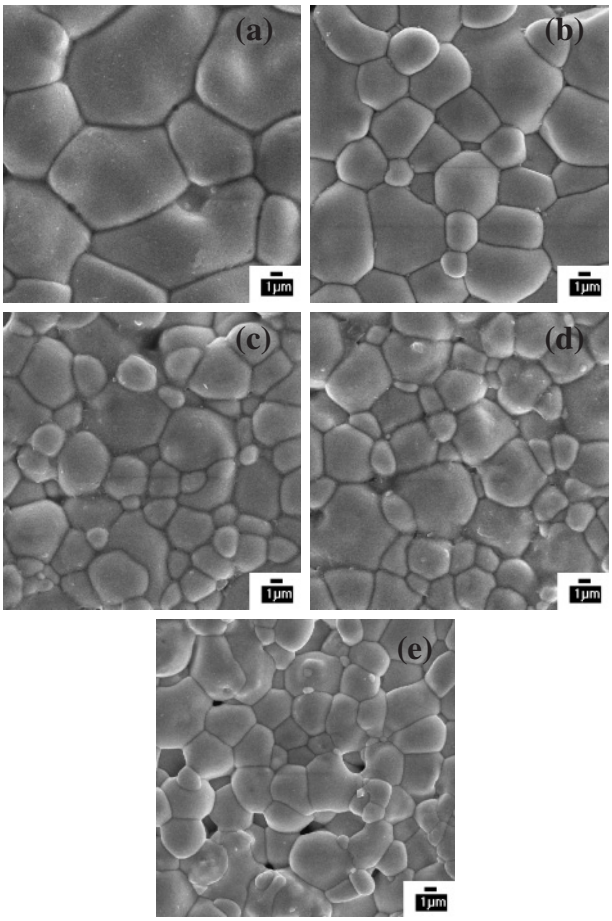



Fig. 2. SEM images of $(1-x)$PZT–$(x)$PCN ceramics with various compositions: $x =$ (a) 0.1, (b) 0.2, (c) 0.3, (d) 0.4, and (e) 0.5.

Table I. Physical characteristics of $(1-x)$PZT–$(x)$PCN ceramics, where $x = 0.1$–$0.5$.

| Ceramics ($x = 0.1$–$0.5$) | Density ($g/cm^3$) | Grain size range (μm) | Average grain size (μm) |
|---|---|---|---|
| 0.9PZT–0.1PCN | $7.39 \pm 0.05$ | 4.54–19.56 | $7.45 \pm 0.05$ |
| 0.8PZT–0.2PCN | $7.46 \pm 0.05$ | 2.60–12.35 | $4.13 \pm 0.05$ |
| 0.7PZT–0.3PCN | $7.62 \pm 0.05$ | 0.43–9.48 | $2.82 \pm 0.05$ |
| 0.6PZT–0.4PCN | $7.42 \pm 0.05$ | 0.60–10.75 | $2.77 \pm 0.05$ |
| 0.5PZT–0.5PCN | $7.31 \pm 0.05$ | 0.47–9.53 | $2.61 \pm 0.05$ |

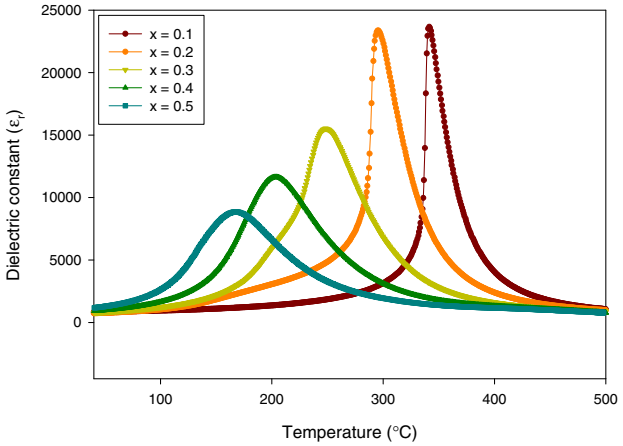



Fig. 3. (Color online) Dielectric constant ($\varepsilon_r$) of $(1-x)$PZT–$(x)$PCN ceramics at 100 kHz.

It should be noted that the formation of MPB could be clearly seen by the crystal structure analysis as described earlier. As is well known, the value of the dielectric and ferroelectric properties of a solid solution with MPB usually maximize approximately at the MPB. An anomaly at the MPB has been observed by our group in solid solution $(x)$PZT–$(1-x)$PNN.[5] However, no anomalies approximately at the MPB in the dielectric properties (Table II) could be found in the present work. In addition, the ferroelectric properties at approximately $x = 0.3$ are only slightly different from those of other compositions ($x = 0.2$, 0.4), rather than being "anomalously high". This could possibly be caused by a substitution of $Ni^{2+}$ by $Co^{2+}$ in the B-site, which shifts the MPB composition from $x = 0.2$ in the PZT–PNN system to $0.2 \leq x \leq 0.3$ in PZT–PCN. Since in this current work, we only started with compositions at 0.1 intervals, the exact MPB composition could not be clearly identified. However, as seen in Table II, the argument that the MPB composition should fall between $0.2 \leq x \leq 0.3$ in PZT–PCN is supported by all the XRD and electrical data, which show drastic decreases in the value of the electrical properties in compositions with $x > 0.3$.

The temperature dependence of the dielectric constant ($\varepsilon_r$) measured at 100 kHz for the $(1-x)$PZT–$(x)$PCN samples with $x = 0.1$–$0.5$ is shown in Fig. 3. In an ideal solid solution of PZT and PCN, the transition temperature is expected to vary linearly between 341 and 167 °C. As shown in Table II, the Curie temperature decreased as expected with an increase in PCN content. However, the $\varepsilon_r$ peaks became broader with increasing PCN content at $x \geq 0.3$. It was confirmed that the composition with $0.2 \leq x \leq 0.3$ is close to the morphotropic phase boundary (MPB) of the $(1-x)Pb(Zr_{1/2}Ti_{1/2})O_3$–$(x)Pb(Co_{1/3}Nb_{2/3})O_3$ system.

Table II. Dielectric and ferroelectric properties of $(1-x)$PZT–$(x)$PCN ceramics, where $x = 0.1$–$0.5$.

| Ceramics ($x = 0.1$–$0.5$) | $T_C$ (°C) | Dielectric properties | | | | Ferroelectric properties (at 25 °C) | | | Loop squareness ($R_{sq}$) |
|---|---|---|---|---|---|---|---|---|---|
| | | $\varepsilon_{max}$ | $\varepsilon_{RT}$ | $\gamma$ | $\delta$ | $P_r$ ($\mu C/cm^2$) | $P_s$ ($\mu C/cm^2$) | $E_c$ (kV/cm) | |
| 0.9PZT–0.1PCN | 341.40 | 23700 | 740 | 1.52 | 14.72 | 2.9 | 4.1 | 8.45 | 1.52 |
| 0.8PZT–0.2PCN | 295.50 | 23400 | 800 | 1.68 | 15.73 | 20.1 | 21.6 | 6.84 | 1.91 |
| 0.7PZT–0.3PCN | 248.40 | 15500 | 840 | 1.81 | 16.55 | 20.9 | 22.6 | 6.92 | 1.94 |
| 0.6PZT–0.4PCN | 203.50 | 11600 | 910 | 1.82 | 16.68 | 18.6 | 20.3 | 6.30 | 1.93 |
| 0.5PZT–0.5PCN | 167.50 | 8900 | 1180 | 1.97 | 16.92 | 14.5 | 15.2 | 6.10 | 1.92 |

To further understand the dielectric behavior of the PZT–PCN system, the ferroelectric transition can analyzed through the Curie–Weiss relationship. For normal ferroelectrics such as PZT and PCN, above the Curie temperature, the dielectric constant follows the following equation:

$$\varepsilon = \frac{c}{T - T_0}, \tag{1}$$

where $c$ is the Curie constant and $T_0$ is the Curie–Weiss temperature.[10,21,23] For a ferroelectric with a diffuse phase transition such as the PZT–PCN solid solutions, the following equation applies:

$$\frac{1}{\varepsilon} \approx (T - T_m)^2, \tag{2}$$

The above equation has been shown to be valid over a wide temperature range compared with the normal Curie–Weiss law [eq. (1)].[24,25] In eq. (2), $T_m$ is the temperature at which the dielectric constant is maximum. If the local Curie temperature distribution is Gaussian, the reciprocal permittivity can be written in the form:[5,24]

$$\frac{1}{\varepsilon} = \frac{1}{\varepsilon_m} + \frac{(T - T_m)^\gamma}{2\varepsilon_m \delta^2}, \tag{3}$$

where $\varepsilon_m$ is the maximum permittivity, $\gamma$ is the diffusivity, and $\delta$ is the diffuseness parameter. For $(1-x)$PZT–$(x)$PCN compositions, the diffusivity ($\gamma$) and diffuseness parameter ($\delta$) can be estimated from the slope and intercept of the dielectric data shown in Fig. 4, and tabulated in Table II.

$\gamma$ and $\delta$ are both material constants depending on the composition and structure of the material.[5] $\gamma$ is the expression of the degree of dielectric relaxation, while $\delta$ is used to measure the degree of diffuseness of the phase transition. In a material with a "pure" diffuse phase transition described by the Smolenskii–Isutov relation [eq. (2)], $\gamma$ is expected to be 2.[26] The mean value of the diffusivity ($\gamma$) is extracted from these plots by fitting a linear equation. The values of $\gamma$ vary between 1.52 and 1.97, which confirms that diffuse phase transition occurs in the PZT–PCN system. It is important to note that in perovskite ferroelectrics, it has been established that $\gamma$ and $\delta$ can be affected by microstructure features, density, and grain size.[18] For PZT-rich ceramics, $\gamma$ and $\delta$ increase with an increase in PCN content, confirming the diffuse phase transitions in PZT–PCN solid solutions. It is clear that the addition of PCN increases the degree of disorder in $(1-x)$PZT–$(x)$PCN over the compositional range $0.1 \leq x \leq 0.5$ with the highest degree of diffuseness exhibited in the 0.5PZT–0.5PCN composition. It should also be mentioned here that different dielectric behaviors could also be caused by grain size variation,[21] as noted in Table I.

The polarization–field ($P$–$E$) hysteresis loops of $(1-x)$PZT–$(x)$PCN ceramics measured at 15 kV/cm are shown in Fig. 5. A series of well-developed and mostly symmetric hysteresis loops are observed for all compositions. It is seen that the remanent polarization ($P_r$) varies significantly across the compositional range. However, the coercive field $E_c$ is relatively constant, as shown in Table II. The ferroelectric parameters obtained from the $P$–$E$ loops are plotted in Fig. 6. The remnant polarization ($P_r$) and saturated polarization ($P_s$) increased from $P_r = 2.9\,\mu C/cm^2$ and $P_s = 4.1\,\mu C/cm^2$ in 0.9PZT–0.1PCN to reach maximum values of $P_r = 20.9\,\mu C/cm^2$ and $P_s = 22.6\,\mu C/cm^2$ in 0.7PZT–0.3PCN. At higher PCN contents, they then drop to $P_r = 14.5\,\mu C/cm^2$ and $P_s = 15.2\,\mu C/cm^2$ in 0.5PZT–0.5PCN. However, it should be noted that the $P_r$ (2.9 $\mu C/cm^2$) for the composition $x = 0.1$ in the present work is

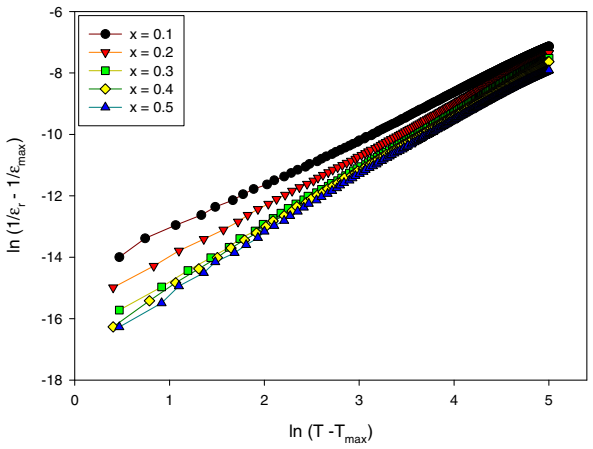



Fig. 4. (Color online) Variation of $\ln(1/\varepsilon_r - 1/\varepsilon_{max})$ vs $\ln(T - T_{max})$ of $(1-x)$PZT–$(x)$PCN ceramics.

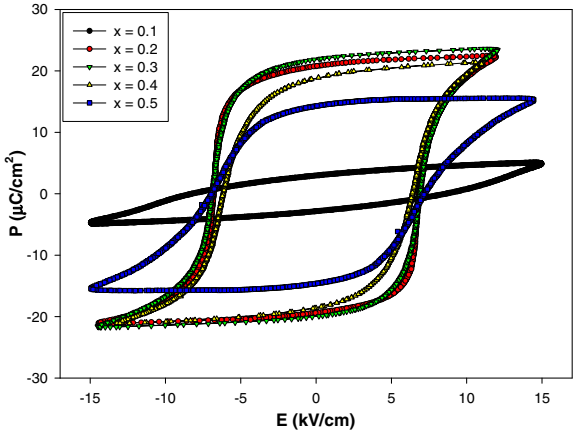



Fig. 5. (Color online) Effect of composition ($x$) on $P$–$E$ hysteresis loops for $(1-x)$PZT–$(x)$PCN ceramics with $x = 0.1$–0.5.

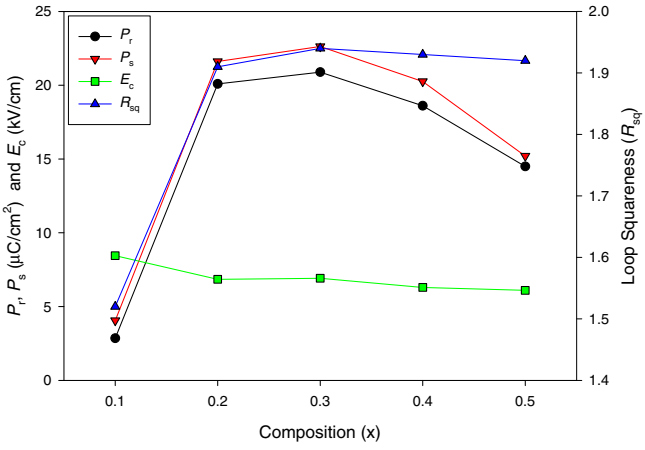



Fig. 6. (Color online) Remnant polarization ($P_r$), saturation polarization ($P_s$), coercive field ($E_c$), and loop squareness ($R_{sq}$) of $(1-x)$PZT–$(x)$PCN ceramics.

lower than the $P_r$ ($\sim 15\,\mu C/cm^2$) in a previous study,[20] probably due to the fact that the solid-state conventional mixed oxide method used in the previous study[20] yielded two MPB compositions at $x = 0.1$ and 0.5, which is different from the columbite–wolframite method used in this study, which showed only one MPB composition at approximately $0.2 \leq x \leq 0.3$. It is well known that ferroelectric values, such as $P_r$, $P_s$, and $E_c$, show maximum values approximately at the MPB composition.

An empirical relationship between remnant polarization ($P_r$), saturation polarization ($P_s$) and polarization at the fields above the coercive field was derived by Haertling and Zimmer.[27] This permits the quantification of changes in the hysteresis behavior for the $(1-x)$PZT–$(x)$PCN samples through the following equation:

$$R_{sq} = \frac{P_r}{P_s} + \frac{P_{1.1E_c}}{P_s}, \quad (4)$$

where $R_{sq}$ is the squareness of the hysteresis loop and $P_{1.1E_c}$ is the polarization at an electric field equal to 1.1 times the coercive field ($E_c$). For an ideal hysteresis loop, $R_{sq}$ is equal to 2.0. As listed in Table II, the loop squareness parameter $R_{sq}$ increased from 1.52 in 0.9PZT–0.1PCN to reach the maximum value of 1.94 in 0.7PZT–0.3PCN before decreasing to 1.92 in the 0.5PZT–0.5PCN composition. This observation is in good agreement with the *P–E* hysteresis loops, as depicted in Fig. 5. The results imply that the addition of 30 mol % PCN into PZT results in an optimized square *P–E* loop.

## 4. Conclusion

In this study, ceramics within the $(1-x)Pb(Zr_{1/2}Ti_{1/2})O_3$–$(x)Pb(Co_{1/3}Nb_{2/3})O_3$ solid solution system (where $x = 0.1$–$0.5$) were successfully prepared using a solid-state mixed-oxide technique. The PZT ceramic was identified by XRD analysis as a single-phase tetragonal perovskite, while the addition of PCN resulted in a gradual shift from tetragonal symmetry to pseudo cubic symmetry, with a possible MPB between the two phases located near the 0.7PZT–0.3PCN composition. However, the dielectric and ferroelectric properties did not show anomalously high value for the dielectric and ferroelectric properties at the 0.7PZT–0.3PCN composition, indicating that the MPB composition shifted to $0.2 \leq x \leq 0.3$ in the PZT–PCN system.

## Acknowledgements

This work was supported by the Commission on Higher Education (CHE), the Thailand Research Fund (TRF), the Faculty of Science, and the Graduate School of Chiang Mai University.

1) A. J. Moulson and J. M. Herbert: *Electroceramics: Materials, Properties, Applications* (Wiley, Chichester, U.K., 2003).
2) S.-E. Park and T. R. Shrout: IEEE Trans. Ultrason. Ferroelectr. Freq. Control **44** (1997) 1140.
3) J. Kuwata, K. Uchino, and S. Nomura: Ferroelectrics **37** (1981) 579.
4) M. L. Mulvihill, L. E. Cross, W. Cao, and K. Uchino: J. Am. Ceram. Soc. **80** (1997) 1462.
5) N. Vittayakorn, G. Rujijanagul, X. Tan, M. A. Marquardt, and D. P. Cann: J. Appl. Phys. **96** (2004) 5103.
6) H. Fan, G.-T. Park, J.-J. Choi, J. Ryu, and H.-E. Kim: J. Mater. Res. **17** (2002) 180.
7) O. Furukawa, Y. Yamashita, M. Harata, T. Takahashi, and K. Inagaki: *5th Meet. Ferroelectric Materials and Their Applications, Kyoto, 1985*, Jpn. J. Appl. Phys. **24** (1985) Suppl. 24-3, p. 96.
8) V. J. Tennery, K. W. Hang, and R. E. Novak: J. Am. Ceram. Soc. **51** (1968) 671.
9) D. Luff, R. Lane, K. R. Brown, and H. J. Marshallsay: Trans. J. Br. Ceram. Soc. **73** (1974) 251.
10) L. E. Cross: Mater. Chem. Phys. **43** (1996) 108.
11) G. A. Smolenskii and A. L. Agranovskaya: Sov. Phys. Tech. Phys. **3** (1958) 1380.
12) T. Kudo, T. Yazaki, F. Naito, and S. Sugaya: J. Am. Ceram. Soc. **53** (1970) 326.
13) B. A. Malkov and Y. N. Venevtsev: Izv. Akad. Nauk Neorg. Mater. **13** (1977) 1468 [in Russian].
14) V. D. Saĺniov, Y. S. Kuźminov, and Y. N. Venevtsev: Izv. Akad. Nauk Neorg. Mater. **7** (1971) 1277 [in Russian].
15) C. Xu, Z. Duan, X. Wang, D. Yang, and K. Chen: J. Cryst. Growth **281** (2005) 543.
16) N. Vittayakorn, C. Puchmark, G. Rujijanagul, X. Tan, and D. P. Cann: Curr. Appl. Phys. **6** (2006) 303.
17) N. Vittayakorn, G. Rujijanagul, T. Tankasiri, X. Tan, and D. P. Cann: Mater. Sci. Eng. B **108** (2004) 258.
18) R. Yimnirun, S. Ananta, and P. Laoratanakul: J. Eur. Ceram. Soc. **25** (2005) 3235.
19) T. Hachiga, S. Fujimoto, and N. Yasuda: J. Phys. D **20** (1987) 1291.
20) N. Vittayakorn, S. Wirunchit, S. Traisak, R. Yimnirun, and G. Rujijanagul: Curr. Appl. Phys. **8** (2008) 128.
21) R. Yimnirun, S. Ananta, and P. Laoratanakul: Mater. Sci. Eng. B **112** (2004) 79.
22) I. W. Chen, P. Li, and Y. Wang: J. Phys. Chem. Solids **57** (1996) 1525.
23) G. H. Haertling: J. Am. Ceram. Soc. **82** (1999) 797.
24) A. Halliyal, U. Kumar, R. E. Newnham, and L. E. Cross: Am. Ceram. Soc. Bull. **66** (1987) 671.
25) R. D. Shannon and C. T. Prewitt: Acta Crystallogr., Sect. B **25** (1969) 925.
26) Y.-M. Chiang, D. P. Birnie, and W. D. Kingery: *Physical Ceramics* (Wiley, Chichester, U.K., 1997) p. 522.
27) G. H. Haertling and W. J. Zimmer: Am. Ceram. Soc. Bull. **45** (1966) 1084.

J. Phys. D: Appl. Phys. **41** (2008) 085406 (5pp) doi:10.1088/0022-3727/41/8/085406

# Changes in dielectric properties of $Pb(In_{1/2}Nb_{1/2})O_3$-$PbTiO_3$ ceramics under compressive stress applied parallel and perpendicular to an electric field

**M Unruan, S Wongsaenmai, Y Laosiritaworn, S Ananta and R Yimnirun**[1]

Department of Physics, Faculty of Science, Chiang Mai University, Chiang Mai, 50200, Thailand

E-mail: rattikornyimnirun@yahoo.com

Received 16 November 2007, in final form 25 January 2008
Published 12 March 2008
Online at stacks.iop.org/JPhysD/41/085406

**Abstract**

The influences of compressive stress on the dielectric properties of $(1-x)Pb(In_{1/2}Nb_{1/2})O_3$–$xPbTiO_3$ ($x = 0.1$–$0.5$) ceramics was investigated in this study. The dielectric properties were measured under compressive stress applied parallel and perpendicular to electric field. The results clearly showed that the superimposed compression stress had pronounced effects on the dielectric properties of PIN–PT ceramics. In general, with increasing compressive stress the dielectric constant of the ceramics increased and decreased when the stress was applied parallel and perpendicular, respectively, to the electric field direction. The dielectric loss tangent, however, decreased in both stress cases. The observations were mainly interpreted in terms of competing influences of the domain switching through non-180° domain walls, clamping of domain walls, de-ageing and the stress-induced decrease in the switchable part of spontaneous polarization.

(Some figures in this article are in colour only in the electronic version)

## 1. Introduction

There has been a great deal of interest in lead indium niobate, $Pb(In_{1/2}Nb_{1/2})O_3$ (PIN), because it can be obtained in a disordered state and can be made to exhibit a transition from the disordered state to the ordered state by long-time thermal annealing. In the disordered state, PIN is a relaxor ferroelectric (RFE) with rhombohedral symmetry. On the other hand, the ordered PIN structure is antiferroelectric (AFE) with orthorhombic symmetry [1]. However, the temperature related to the maximum dielectric constant ($T_{max}$) of PIN in the RFE phase is low (at 1 kHz, $T_{max} = 66\,^{\circ}C$) [2, 3]. Thus, to enhance the dielectric properties of PIN (as well as increasing $T_{max}$), lead titanate, $PbTiO_3$ (PT) is added to PIN with compositions $(1-x)$PIN–$x$PT (for $x = 0.1$–$0.5$).

Piezoelectric and ferroelectric ceramics are widely used in devices such as actuators and transducers. However, when they are used in devices specified above, these ceramics are often subjected to self-induced or environmental stresses [4–6]. A prior knowledge of the effects of stresses on the material properties is crucial for proper design of a device and for suitable selection of materials for a specific application [7–9]. Therefore, it is very important to obtain experimental data, as well as to better understand how these materials behave under stress [10–12]. Recently, the compressive stress dependence of dielectric properties has been studied in materials such as $BaTiO_3$ (BT), $Pb(Zr_{0.52}Ti_{0.48})O_3$ (PZT), $Pb(Mg_{1/3}Nb_{2/3})O_3$ (PMN), $Pb(Mg_{1/3}Nb_{2/3})O_3$–$PbTiO_3$ (PMN–PT), $Pb(Mg_{1/3}Nb_{2/3})O_3$–$Pb(Zr_{0.52}Ti_{0.48})O_3$ (PMN–PZT) and $Pb(Zr_{0.52}Ti_{0.48})O_3$–$BaTiO_3$ (PZT–BT) [13–22]. The results clearly showed that the effects of stress on the dielectric properties depended significantly on ceramic compositions and stress levels. Practically, there have been many previous reports on the electrical properties of PIN and PT ceramics, but there has been no systematic study on the influence of an applied stress on the dielectric properties of the PIN–PT ceramics. Earlier investigation has

[1] Author to whom any correspondence should be addressed.

 © 2008 IOP Publishing Ltd Printed in the UK

**Table 1.** Characteristics of PIN–PT ceramics with optimized processing conditions (measured at 10 kHz) [28, 29].

| Ceramic | Sintering temperature (°C) | Density (g cm$^{-3}$) | $T_{max}$ (°C) | Room-temperature stress-free dielectric properties | |
|---|---|---|---|---|---|
| | | | | $\varepsilon_r$ | tan $\delta$ |
| 0.9PIN–0.1PT | 1100 | 7.78 | 134 | 2275 | 0.105 |
| 0.8PIN–0.2PT | 1125 | 7.85 | 213 | 863 | 0.053 |
| 0.7PIN–0.3PT | 1125 | 7.81 | 292 | 689 | 0.028 |
| 0.6PIN–0.4PT | 1125 | 7.85 | 355 | 1132 | 0.049 |
| 0.5PIN–0.5PT | 1125 | 7.80 | 398 | 483 | 0.083 |

already revealed the significance of stress-induced ferroelectric phase transition in PIN-based materials [23]. Therefore, it is the aim of this study to determine the dielectric properties of the $(1-x)$PIN–$x$PT ceramics as a function of compressive stress. Comparison between the changes in the dielectric properties under compressive stress applied parallel and perpendicular to the electric field direction is reported.

## 2. Experimental method

In this study, $(1-x)Pb(In_{1/2}Nb_{1/2})O_3$–$xPbTiO_3$ (for $x = 0.1$–0.5) ceramics were prepared from the two stage mixed-oxide method. First, $InNbO_4$ was first prepared from oxide powders of $Nb_2O_5$ and $In_2O_3$. The powders were mixed by a rapid vibratory mill for 30 min in alcohol. After drying, the mixture was calcined at 1100 °C for 2 h to obtain the intermediate precursor $InNbO_4$ [24]. Next, the precursor was mixed with an appropriate amount of PbO and $TiO_2$ by a rapid vibratory mill for 30 min. For optimization purposes, the mixtures were calcined at temperatures between 800 and 900 °C for 2 h. After calcination, the powders were pressed hydraulically to form disc-shaped pellets of 10 mm in diameter and 3 mm thick, with 3 wt% polyvinyl alcohol as a binder. Finally, the disc-shaped pellets were sintered in air at temperatures between 1100 and 1125 °C for 2 h. The sintering temperature was determined from the maximum density and phase purity. The sintering temperature of 1100 °C was the optimized condition for 0.9PIN–0.1PT, and 1125 °C for the other compositions, as listed in table 1. The detailed preparation process is given elsewhere [25]. Before studying the dielectric properties under compressive stress, the sintered specimens were cut as rectangular bars (typical dimensions $6\times2\times2$ mm$^3$) and lapped to obtain parallel faces. After coating with silver paint as an electrode at the faces, the specimens were heated at 750 °C for 12 min to ensure contact between the electrode and the surface of the ceramic.

To study the effects of stress on the dielectric properties of the ceramic, the compressometer was constructed for simultaneous applications of the mechanical stress and the electric field [26]. The compressometer cell, consisting of a cylindrical brass cell with a heavy brass base, a brass ram and a precisely guided loading platform, provided true uniaxial stress during mechanical loading. The compressive stress was supplied by the servohydraulic load frame and the applied stress level was monitored with the pressure gauge of the load frame. Measurements were performed as a function of mechanical pre-stress applied discretely [27]. For the case of the compressive stress applied parallel to the electric field direction, the specimen bar was carefully placed between the two alumina blocks and the electric field was applied to the specimen via the copper shims attached to the alumina blocks. For the case of stress perpendicular to the electrical field, the electrodes were applied on the other two opposite faces with silver wire attached to the electrodes for electrical measurement. The low-field dielectric properties were measured by an LCR-meter (Instrek LCR-821) with an applied voltage of 1 V. The room temperature (25 °C) capacitance and the dielectric loss tangent were determined at a frequency of 10 kHz. The dielectric constant was then calculated from a parallel-plate capacitor equation, e.g. $\varepsilon_r = Cd/\varepsilon_0 A$, where $C$ is the capacitance of the specimens, $d$ and $A$ are, respectively, the thickness and the area of the electrode and $\varepsilon_0$ is the dielectric permittivity of vacuum ($8.854\times10^{-12}$ F m$^{-1}$). In addition, it should also be noted that the dielectric properties could be affected by the collapse of the structure of silver paint electrode under compressive stress. Therefore, a careful examination of the specimens' electrodes was taken after the measurements, and there was no clear evidence of the collapse of the electrodes. This is probably due to the relatively low stress level used.

## 3. Results and discussion

Since this work reports the dielectric properties of PIN–PT ceramics under the application of compressive pre-stress, the following paragraph is only served as preliminary information on structural and dielectric characteristics under stress-free conditions, which are important in the discussion of the influence of stress on the dielectric properties of the ceramics. More information on the above mentioned characteristics can be found in previous publications [28, 29]. By the x-ray diffraction method, the phase and structural information of the PIN–PT ceramics was established [29]. In general, pseudo-cubic symmetry was observed at low PT contents ($x = 0.1$, 0.2 and 0.3). However, by the influence of PT, the tetragonal symmetry had developed in the compositions $x = 0.4$ and 0.5. The dielectric constant ($\varepsilon_r$) was also measured as functions of both temperature and frequency, as previously described in detail in previous publications [28, 29]. In compositions $x = 0.4$ and 0.5, the dielectric properties were nearly independent of frequency, except in the vicinity of the phase transformation temperature; a typical characteristic of normal ferroelectrics. At low PT contents, the dielectric behaviour was shifted towards that of relaxor materials. The dielectric properties of the compositions with $x \leqslant 0.3$ exhibited a diffuse phase transition with dielectric peak broadening. As listed in table 1, the high value of dielectric constant under stress-free conditions at room temperature is obtained in ceramic composition with $x = 0.4$ because of its vicinity to the morphotropic phase boundary (MPB) of the PIN–PT system, as reported earlier [1, 28, 29]. In addition, the high room temperature dielectric constant for $x = 0.1$ composition is due to the fact that dielectric maximum temperature ($T_{max}$)

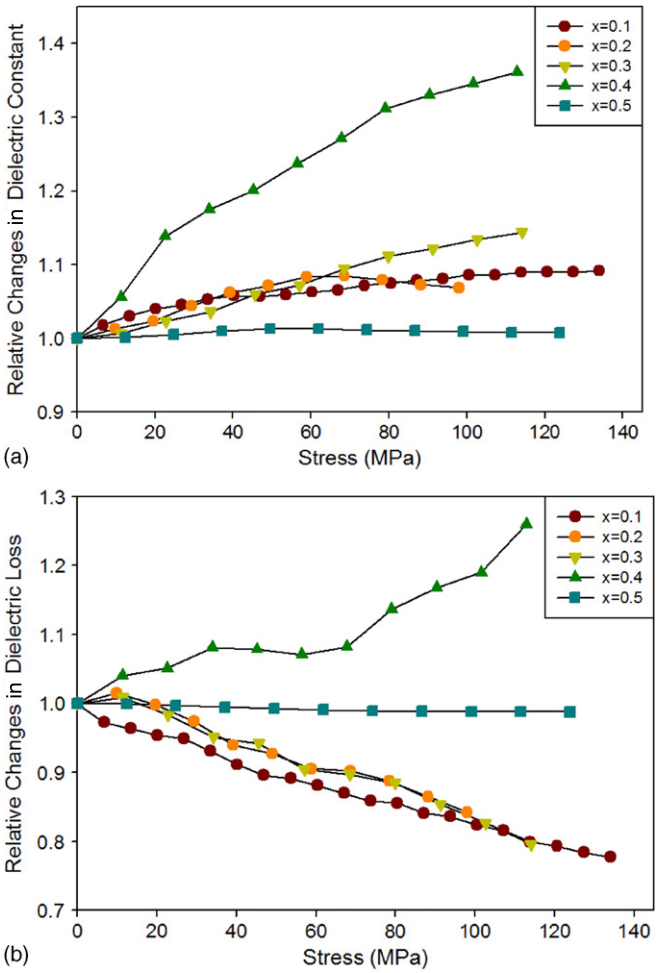



**Figure 1.** (*a*) Relative changes in dielectric constant ($\varepsilon_r$) and (*b*) relative changes in dielectric loss tangent ($\tan\delta$) with compressive stress applied parallel to the electric field direction for $(1-x)$PIN–$x$PT ceramics (measured at 25 °C and 10 kHz).

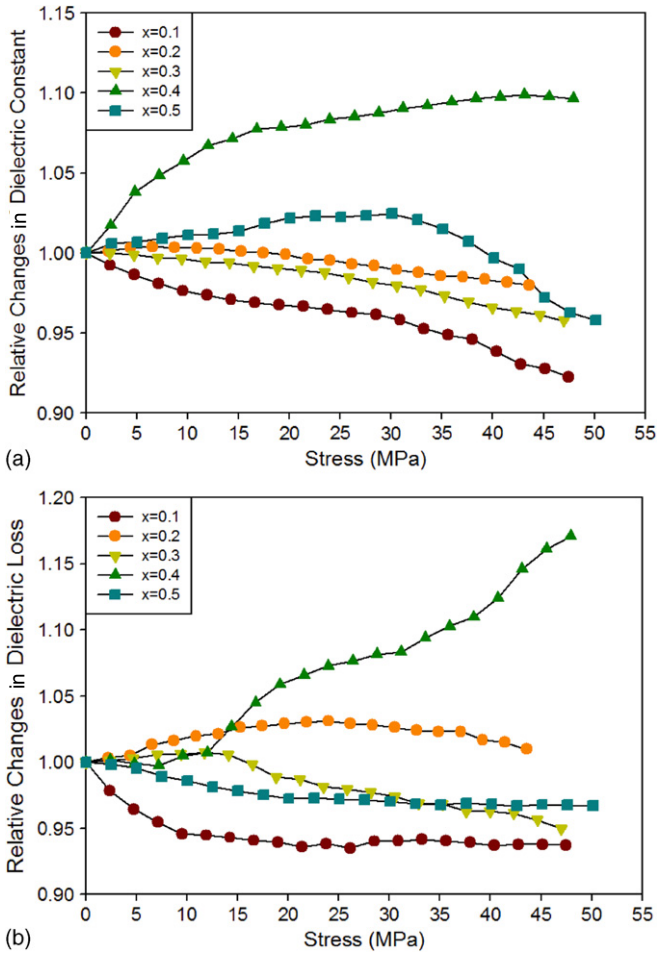



**Figure 2.** (*a*) Relative changes in dielectric constant ($\varepsilon_r$) and (*b*) relative changes in dielectric loss tangent ($\tan\delta$) with compressive stress applied perpendicular to the electric field direction for $(1-x)$PIN–$x$PT ceramics (measured at 25 °C and 10 kHz).

of 134 °C is much closer to room temperature than $T_{max}$ of other compositions. Hence, the dielectric peak is on the rise in this composition, and results in a higher room temperature dielectric constant value than that of other compositions.

The room temperature dielectric properties at 10 kHz of $(1-x)$PIN–$x$PT ceramics as a function of compressive stress are depicted in figures 1 and 2. For better comparison, the dielectric properties of each composition under stress are normalized to the stress-free values. In addition, the measurements were performed with the mechanical stress increased to maximum stress, then gradually removed to zero. The results showed only slightly different dielectric properties between loading and unloading conditions, which differ from results previously observed in other ceramic systems and PIN–PT with poled specimens, likely caused by the stress-induced depoling mechanism at high stress [21, 30–32]. Therefore, the averaged changes in the dielectric properties with stress are plotted in figures 1 and 2. Clearly, there are observable changes in both the dielectric constant and the dielectric loss tangent with stress, in both cases of the compressive stress being applied either parallel or perpendicular to the electric field direction.

For the case of stress parallel to the electric field direction, as depicted in figures 1(*a*) and (*b*), the changes in the dielectric properties with stress can be divided into three groups. As shown in figure 1(*a*), for the pseudo-cubic compositions ($x = 0.1$–$0.3$), the dielectric constant increases noticeably (5–12%) when the stress reaches 100 MPa. On the other hand, the dielectric loss tangent ($\tan\delta$) is seen to decrease significantly (20–25%) with increasing stress, as displayed in figure 1(*b*). Interestingly, for the tetragonal composition ($x = 0.5$), the dielectric properties (both dielectric constant and dielectric loss tangent) show very little change with stress. More interestingly, the dielectric properties of the composition with $x = 0.4$, which is very close to the MPB of PIN–PT system (at $x \sim 0.37$ [33]), increase significantly with the applied stress (30% at maximum stress). It is also noticed that the changes in the dielectric properties with the compressive stress obtained in this study are in parts similar to those for BT, PZT, PMN–PZT and PMN–PT systems in earlier investigations [13, 14]. Other investigations on commercial hard and soft PZT ceramics also observed similar changes in the dielectric properties with the compressive stress applied parallel to the electric field direction [20, 21, 31].

For the case of stress applied perpendicular to the electric field direction, as depicted in figures 2(*a*) and (*b*), the changes in the dielectric properties with stress are significantly different from the parallel stress case. As shown in figure 2(*a*), for the pseudo-cubic compositions ($x = 0.1$–$0.3$), the dielectric constant decreases with the applied stress, as opposed to the parallel stress case. Interestingly, for the tetragonal compositions ($x = 0.5$), the dielectric constant first increases with stress, then decreases with further increase in the applied stress. On the other hand, the dielectric constant of the near MPB composition $x = 0.4$ still shows an increasing trend with applied stress. It is of interest to observe that the changes in the dielectric loss tangent with stress of all compositions are similar to those in the case of the parallel stress, as shown in figure 2(*b*). For the case of the compressive stress applied perpendicular to the direction of the electric field, only a few previous experimental works have been carried out on some commercial hard and soft PZT ceramics, and PMN–PT ceramics [21, 30, 31, 34]. Interestingly, the results observed in this study are in general very similar to those obtained earlier in PZT and PMN–PT ceramics mentioned above.

To understand these experimental results, at least qualitatively, various effects have to be considered. When a compressive stress is applied to the ferroelectric materials, the domain structure in the material will change to maintain the domain energy at a minimum because the stress will move some of the polarization away from its polar direction; during this process some of the domains engulf other domains or change shape irreversibly. Under a stress, the domain structure of ferroelectric ceramics may undergo domain switching through non-180° domain walls, de-ageing and clamping of domain walls [15, 18, 21, 31].

The experimental observations, both the drastic change and the very little change cases, can be attributed to competing influences, in an opposite way, of the intrinsic contribution of domains and the extrinsic contribution of re-polarization and growth of micro-polar regions. Under the applied compressive stress, the non-180° domain wall density increases. Hence the increase in the dielectric constant is observed. The de-ageing mechanism, which also increases the dielectric constant [14–16, 21], is also expected to play a role here. Therefore, a combination of the domain switching and the de-ageing mechanisms is believed to be a reason for the increase in the dielectric constant. On the other hand, the stress clamping of domain walls, which results in a decrease in domain wall mobility, and the stress-induced decrease in the switchable part of spontaneous polarization are expected to play a role in the decrease of the dielectric constant [14, 21, 31]. In addition, the continuous decrease in the dielectric constant can also be attributed to the switching of 90° domains, which causes the significant decrease in the dielectric constant. With all these possible mechanisms stated, one can easily understand the experimental results obtained. In the case of parallel stress, a combination of the domain switching and the de-ageing mechanisms is believed to be a reason for the increase in the dielectric constant in all compositions, as shown in figure 1(*a*). In addition, a large increase in the dielectric constant of the near MPB composition, i.e. 0.6PIN–0.4PT, is attributed to more domain states in the composition which combines six possible domain states from the tetragonal phase with 8 possible domain states from the pseudo-cubic (or rhombohedral) phase [7], hence a much larger non-180° domain wall density and a larger change are observed. This mechanism still dominates in the case of the perpendicular stress for the same composition, which results in an increase in the dielectric constant, while the other compositions show a slight decrease in the dielectric constant when the stress is applied perpendicular to the direction of the electric field, as depicted in figure 2(*a*). This observation suggests that the stress clamping of domain walls and the stress-induced decrease in the switchable part of spontaneous polarization play a key role in controlling the change in the dielectric constant with the stress applied in the perpendicular direction to the electric field. It should also be noticed that the dielectric constant of 0.5PIN–0.5PT are rather stable under applied stress when compared with the near MPB 0.6PIN–0.4PT composition. This suggests the influence of different structures. As stated above, the 0.6PIN–0.4PT composition contains mixed tetragonal–rhombohedral phases with more possible domain states (14), while the 0.5PIN–0.5PT contains mainly tetragonal phases with only six domain states, hence much smaller changes in dielectric properties. In addition, since the measurements were carried out at room temperature, which is far below the transition temperature of 398 °C for the 0.5PIN–0.5PT composition, the domain is much less mobile and the change in the dielectric properties is also much less. This also explains why the change in the dielectric properties with the applied stress of this composition is much less than that of other non-MPB compositions with much lower transition temperatures. In addition, a little decrease in the dielectric constant after a full cycle of stress application has been observed and attributed to the stress-induced decrease in the switchable part of spontaneous polarization at high stress and the irreversible 90° domain switching [15, 31].

The cause of the stress dependence of the dielectric loss tangent is a little more straightforward. In both the parallel and the perpendicular stress cases, as observed in figures 1(*b*) and 2(*b*), the clamping of the domain walls under compressive stress results in a decrease in domain wall mobility and reduces the dielectric loss tangent in the $x = 0.1$–$0.3$ compositions [21, 31]. This is a reversible effect with the domain wall mobility returning to near the original values when the applied stress is removed, as stated earlier that the dielectric properties return to near their original values after a stress cycle. On the other hand, it should be noted that a noticeable increase in the dielectric loss tangent of the 0.6PIN–0.4PT composition is observed, as seen in figures 1(*b*) and 2(*b*). Similarly to the dielectric constant changes with stress, this is mainly attributed to more available domain states of 14 and hence more domain wall mobility in this near MPB composition. Moreover, the de-ageing mechanism is also expected to play a role in the increase in dielectric response with stress in this composition. During the ageing process, some of the domain walls become pinned by impurities and structural imperfections. When a large enough stress is applied to the aged samples, it causes structural changes and redistribution of impurities. As a

result, the domain walls that were pinned during ageing can become active again. This de-ageing can increase the dielectric responses, as clearly observed in the 0.6PIN–0.4PT composition in both the parallel and the perpendicular stress cases. As stated earlier, the rather immobile domains in the 0.5PIN–0.5PT composition explain a near constant of the dielectric constant and loss under applied stress. It should also be noted that the competing influence between the domain clamping and de-ageing mechanisms can be a cause of a slight difference in the dielectric loss response to the applied stress. These results clearly demonstrate that the contribution of each mechanism to the dielectric responses of the PIN–PT ceramics depends on the compositions and the stress level and direction.

## 4. Conclusions

In this study, the dielectric properties of PIN–PT ceramics with a formula $(1-x)Pb(In_{1/2}Nb_{1/2})O_3$–$xPbTiO_3$ (for $x = 0.1$–$0.5$) prepared by the two stage mixed-oxide method are measured under the compressive stress applied both parallel and perpendicular to the electric field direction. The results clearly show that the superimposed compression stress has pronounced effects on the dielectric properties of the PIN–PT ceramics. In general, with increasing compressive stress the dielectric constant of the ceramics increases and decreases when the stress is applied parallel and perpendicular, respectively, to the electric field direction. The dielectric loss tangent, however, decreases in both stress cases. The observations are mainly interpreted in terms of competing influences of the intrinsic contribution, and the extrinsic contribution from domain switching through non-180° domain walls, clamping of domain walls, de-ageing and the stress-induced decrease in the switchable part of spontaneous polarization.

## Acknowledgments

This work was jointly supported by the Thailand Research Fund (TRF), Commission on Higher Education (CHE), Royal Golden Jubilee PhD program, Faculty of Science and Graduate School of Chiang Mai University.

## References

[1] Alberta E F and Bhalla A S 1998 *J. Korean Phys. Soc.* **32** 1265
[2] Halliyal A, Kumar U, Newnham R E and Cross L E 1987 *Am. Ceram. Soc. Bull.* **66** 671
[3] Belsick J R, Halliyal A, Kumar U and Newnham R E 1987 *Am. Ceram. Soc. Bull.* **66** 664
[4] Kuwata J, Uchino K and Nomura S 1982 *Japan. J. Appl. Phys.* **21** 1298
[5] Park S and Shrout T R 1997 *J. Appl. Phys.* **82** 1804
[6] Viehland D and Powers J 2001 *Appl. Phys. Lett.* **78** 3112
[7] Cross L E 1987 *Ferroelectric* **76** 241
[8] Uchino K 1997 *Piezoelectric Actuators and Ultrasonic Motors* (Boston, MA: Kluwer)
[9] Stansfield D 1991 *Underwater Electroacoustic Transducers* (Bath, UK: Bath University Press)
[10] Lynch C S 1996 *Acta. Mater.* **44** 4137
[11] Zhou D, Wang Z and Kamlah M 2005 *J. Appl. Phys.* **97** 084105
[12] Hilczer A, Szafranski M and Kosec M 2007 *Ferroelectric Lett.* **34** 29
[13] Yimnirun R, Ananta S and Chamunglap S 2007 *Mater. Chem. Phys.* **102** 165
[14] Yimnirun R, Ananta S, Ngamjarurojana A and Wongsaenmai S 2006 *Curr. Appl. Phys.* **6** 520
[15] Yang G, Liu S F, Ren W and Mukherjee B K 2000 *Proc. SPIE Symp. Smart Struct. Mater.* **3992** 103
[16] Yimnirun R, Unruan M, Laosiritaworn Y and Ananta S 2006 *J. Phys. D: Appl. Phys.* **39** 3097
[17] Yimnirun R 2006 *Int. J. Mod. Phys.* B **20** 3409
[18] Zhou D, Kamlah M and Munz D 2005 *J. Eur. Ceram. Soc.* **25** 425
[19] Wongsaenmai S, Ananta S, Meechoowas E and Yimnirun R 2003 *J. Phys. D: Appl. Phys.* **36** 1615
[20] Krueger H 1967 *J. Acoust. Soc. Am.* **42** 636
[21] Zhang Q M, Zhao J, Uchino K and Zheng J 1997 *J. Mater. Res.* **12** 226
[22] Steiner O, Tagantsev A K, Colla E L and Setter N 1999 *J. Eur. Ceram. Soc.* **19** 1243
[23] Nomura K, Shingai T, Ishino S, Terauchi H, Yasuda N and Ohwa H 1999 *J. Phys. Soc. Japan* **68** 39
[24] Yasuda N and Fujie M 1992 *Japan. J. Appl. Phys.* **31** 3128
[25] Wongsaenmai S, Khamman O, Ananta S and Yimnirun R 2008 *J. Electroceram.* at press, doi: 10.1007/s10832-007-9311-3
[26] Yimnirun R, Ananta S, Ngamjarurojana A and Wongsaenmai S 2005 *Appl. Phys. A: Mater. Sci. Proc.* **81** 1227
[27] Yimnirun R, Laosiritaworn Y and Wongsaenmai S 2006 *J. Phys. D: Appl. Phys.* **39** 759
[28] Wongsaenmai S, Bhalla A, Tan X, Ananta S and Yimnirun R 2007 *Ferroelectric Lett.* **34** 36
[29] Wongsaenmai S, Tan X, Ananta S and Yimnirun R 2008 *J. Alloys Compounds* at press, doi: 10.1016/j.jallcom.2006.12.053
[30] Zhao J, Glazounov A E and Zhang Q M 1999 *Appl. Phys. Lett.* **74** 436
[31] Yang G, Liu S F, Ren W and Mukherjee B K 2001 *Ferroelectrics* **262** 207
[32] Triamnak N, Wongsaenmai S, Ananta S and Yimnirun R 2007 *Ceram. Int.* submitted
[33] Augier C, Pham-Thi M, Dammak H and Gaucher P 2005 *J. Eur. Ceram. Soc.* **25** 2429
[34] Krueger H 1967 *J. Acoust. Soc. Am.* **43** 583

Provided for non-commercial research and education use.
Not for reproduction, distribution or commercial use.




This article appeared in a journal published by Elsevier. The attached copy is furnished to the author for internal non-commercial research and education use, including for instruction at the authors institution and sharing with colleagues.

Other uses, including reproduction and distribution, or selling or licensing copies, or posting to personal, institutional or third party websites are prohibited.

In most cases authors are permitted to post their version of the article (e.g. in Word or Tex form) to their personal website or institutional repository. Authors requiring further information regarding Elsevier's archiving and manuscript policies are encouraged to visit:

http://www.elsevier.com/copyright

Author's personal copy

ELSEVIER

Journal of Alloys and Compounds 454 (2008) 331–339

Journal of ALLOYS AND COMPOUNDS

www.elsevier.com/locate/jallcom

# Dielectric and ferroelectric properties of fine grains $Pb(In_{1/2}Nb_{1/2})O_3$–$PbTiO_3$ ceramics

Supattra Wongsaenmai [a], Xiaoli Tan [b], Supon Ananta [a], Rattikorn Yimnirun [a,*]

[a] *Department of Physics, Faculty of Science, Chiang Mai University, Chiang Mai 50200, Thailand*
[b] *Department of Materials Science and Engineering, Iowa State University, Ames, IA 50011, USA*

Received 3 October 2006; accepted 10 December 2006
Available online 20 December 2006

**Abstract**

The dielectric and ferroelectric properties of $(1-x)Pb(In_{1/2}Nb_{1/2})O_3$–$xPbTiO_3$ (when $x = 0.1$, 0.2, 0.3, 0.4, and 0.5) ceramics prepared by an oxide-mixing method via a vibro-milling technique were investigated. Fine grains ceramics were achieved with average grain size of 1–2 μm, indicating advantage of the vibro-milling technique used. While PIN ceramic exhibited relaxor behavior, the dielectric properties of PIN–PT ceramics showed a mixed relaxor and normal ferroelectric behavior, with more normal ferroelectric behavior observed with increasing PT content. In addition, the ferroelectric properties of the ceramics in PIN–PT system changed from the relaxor ferroelectric behavior in PIN ceramic to the normal ferroelectric behavior in PIN–PT ceramics. These results clearly show the significance of the added PT in reducing the relaxor ferroelectric behavior in PIN ceramic. Finally, the existence of the MPB composition between $x = 0.3$ and 0.4 has been confirmed from the XRD analysis, and dielectric and ferroelectric properties measurements.
© 2006 Elsevier B.V. All rights reserved.

*Keywords:* Dielectric properties; Ferroelectric properties; Mixed-oxide; PIN–PT

## 1. Introduction

Lead-based perovskite-type solid solutions consisting of the ferroelectric and relaxor materials have attracted a growing fundamental and practical interest because of their excellent dielectric, piezoelectric and electrostrictive properties which are useful in actuating and sensing applications [1–3]. Among the lead-based complex perovskites, lead magnesium niobate–lead titanate ($(1-x)Pb(Mg_{1/3}Nb_{2/3})O_3$–$xPbTiO_3$ or PMN-PT) and lead zinc niobate–lead titanate ($(1-x)Pb(Zn_{1/3}Nb_{2/3})O_3$–$xPbTiO_3$ or PZN-PT) have attracted much attention due to their superior electrical properties [4–7]. However, the major disadvantage of the two ceramic systems is relatively low Curie temperatures ($T_C$) of the morphotropic phase boundary (MPB) compositions, i.e. lower than 200 °C for the two systems [5–8]. This low $T_C$ comes with the expenses of more temperature dependent properties and less polarization stability, which in turn restrict the operating temperature range to less than 100 °C [7,8]. Interestingly, the MPB composition of the lead indium niobate–lead titanate ($(1-x)Pb(In_{1/2}Nb_{1/2})O_3$–$xPbTiO_3$ or PIN–PT) solid solution system has been reported to possess $T_C$ higher than 250 °C [8–13], and therefore potential for high temperature applications. Many previous studies have focused on the processing and properties of PIN–PT single crystals, particularly the MPB composition [9,12,14,15], while the information on PIN–PT ceramics is still limited [8,10,13]. In addition, most of the PIN–PT ceramics studied were prepared by the mixed-oxide method with a conventional ball-milling technique, which resulted in coarse grains ceramics [11,13], even though it is well known that fine grains ceramics usually show superior electrical properties [16,17]. Recently, a vibro-milling technique has been employed to produce nano-sized powders which can be used to fabricate ceramics with fine grain microstructure [18–20]. Therefore, as an extension to the research on the PIN–PT ceramics, the overall purpose of this study was to systematically determine the dielectric and ferroelectric properties of ceramics in the $(1-x)Pb(In_{1/2}Nb_{1/2})O_3$–$xPbTiO_3$ (when $x = 0.0$, 0.1, 0.2, 0.3, 0.4, and 0.5) system prepared by the mixed-oxide method via the vibro-milling technique. The vibro-milling technique

* Corresponding author. Tel.: +66 53 943 367; fax: +66 53 943 445.
*E-mail addresses:* rattikor@chiangmai.ac.th, rattikornyimnirun@yahoo.com (R. Yimnirun).

0925-8388/$ – see front matter © 2006 Elsevier B.V. All rights reserved.
doi:10.1016/j.jallcom.2006.12.053

Author's personal copy



was employed to explore the potential in obtaining fine grains ceramics, which would in turn lead to superior electrical properties.

## 2. Experimental

The $Pb(In_{1/2}Nb_{1/2})O_3$–$PbTiO_3$ ceramics used in this study were prepared from $Pb(In_{1/2}Nb_{1/2})O_3$ and $PbTiO_3$ starting powders obtained via the vibro-milling technique. In this technique, a vibratory laboratory mill (McCrone Micronizing Mill) was employed. A total of 48 polycrystalline corundum milling media with a powder weight of 20 g was kept constant in each batch. The milling operation was carried out in isopropanal inert to the polypropylene jar [18–20]. Initially, pure-phase PIN powders were obtained via a well-known wolframite method [21,22], while PT powders were prepared by a mixed-oxide method [23]. With the wolframite method, the single-phase indium niobate ($InNbO_4$) powders were first prepared by mixing starting indium oxide ($In_2O_3$) and niobium oxide ($Nb_2O_5$) (Aldrich, 99.9% purity) powders by employing the vibro-milling technique for 0.5 h and then calcining the mixed powders at 900 °C for 4 h with heating/cooling rates of 30 °C/min [24]. This yielded a so-called wolframite ($InNbO_4$) powder. The wolframite precursor powders were subsequently vibro-milled with lead oxide (PbO) (Fluka, 99% purity) for 0.5 h. The mixed powders were calcined at 1100 °C for 2 h with heating/cooling rates of 10 °C/min to form a single-phase PIN [25]. It should, however, be noted that to obtain the pure-phase PIN powders 2 mol% excess of $In_2O_3$ and PbO had to be added to compensate the loss during calcination [25]. With a more conventional oxide-mixing route, PT powders were prepared from PbO and titanium oxide ($TiO_2$) (Riedel-de Haën, 99% purity) starting powders. These powders were vibro-milled for 0.5 h and later calcined at 600 °C for 2 h with heating/cooling rates of 5 °C/min [23]. The $(1-x)Pb(In_{1/2}Nb_{1/2})O_3$–$xPbTiO_3$ (when $x = 0.0, 0.1, 0.2, 0.3, 0.4$, and 0.5) ceramics were then prepared from the PIN and PT powders by the same mixed-oxide method. The PIN and PT powders were weighed in the required stoichiometric ratio and vibro-milled for 0.5. The thoroughly mixed powders were then pressed hydraulically to form disc-shaped pellets 10 mm in diameter and 2 mm thick, with 3 wt.% polyvinyl alcohol as a binder. The pellets were placed on the alumina powder-bed inside alumina crucible and surrounded with atmosphere powders of the same composition. Finally, the pellets were sintered at 1175 °C (1050 °C for PIN) for 2 h with heating/cooling rates of 10 °C/min.

The densities of the sintered ceramics were measured by Archimedes method. The phase formations of the sintered specimens were studied by an X-ray diffractometer (XRD; Siemen-D500 diffractometer). The microstructure analyses were undertaken by a scanning electron microscopy (SEM: JEOL Model JSM 840A). Grain size was determined from SEM micrographs by a linear intercept method. The dielectric properties were evaluated with a computer-controlled dielectric measurement system consisted of a precision LCR-meter (Hewlett Packard, model 4284A), a temperature chamber (Delta Design, model 9023), and a sample holder (Norwegian Electroceramics) capable of high temperature measurement. The room temperature ferroelectric polarization versus electric field (*P–E*) measurements was made using a standardized ferroelectric test system (RT-66A, Radiant Technologies) with an applied field of 30–60 kV/cm.

## 3. Results and discussion

The XRD patterns of $(1-x)$PIN–$x$PT ceramics with various $x$ values are shown in Fig. 1(a). It can be seen that a complete crystalline solution of perovskite structure is formed throughout the composition range without the presence of pyrochlore or unwanted phases. From the patterns, PIN ceramic is identified as a single-phase material with a perovskite structure having cubic symmetry which could be matched with JCPDS file no. 87-0304. The XRD patterns of the PIN–PT compositions show a combination between PIN and PT patterns, showing a perovskite structure having the symmetry varying between pseudo-cubic and tetragonal types. For better comparison, the

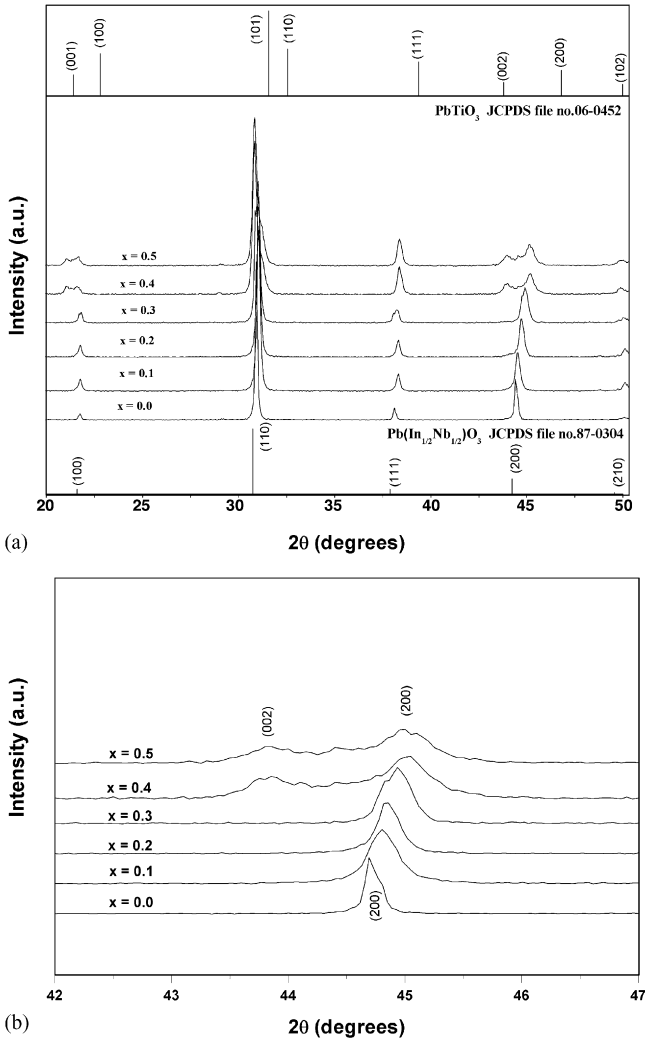



Fig. 1. (a) XRD patterns of $(1-x)$PIN–$x$PT ceramics and (b) selected region of the diffraction patterns.

JCPDS file no. 06-0452 for PT with a tetragonal structural symmetry is also displayed in Fig. 1(a). More interestingly, the composition with $x = 0.3$ began to exhibit broadening of peaks at $2\theta \approx 21.5°$, 30.5°, and 44.5° for (1 0 0)/(0 0 1), (1 1 0)/(1 0 1), and (2 0 0)/(0 0 2), respectively. Fig. 1(b) shows the broadened peaks at $2\theta \sim 44.5$–45°, indicating the structural transformation from the pseudo-cubic phase to the tetragonal phase, characterized by (2 0 0)/(0 0 2) peaks. This observation is obviously associated with the composition with coexistence of two symmetries, which in this case are tetragonal and pseudo-cubic phases. To a first approximation, it could be said that the composition between $x = 0.3$ and 0.4 is close to the morphotropic phase boundary (MPB) of the $Pb(In_{1/2}Nb_{1/2})O_3$–$PbTiO_3$ system, where the structure of the PIN–PT compositions is gradually changing from pseudo-cubic to tetragonal. Earlier studies have reported the MPB composition for PIN–PT system at $x \sim 0.37$ [9–12]. Electrical data described later further support this observation.

SEM micrographs in Fig. 2 reveal fine grains microstructure in all PIN–PT ceramics with little variation of the average grain

Author's personal copy



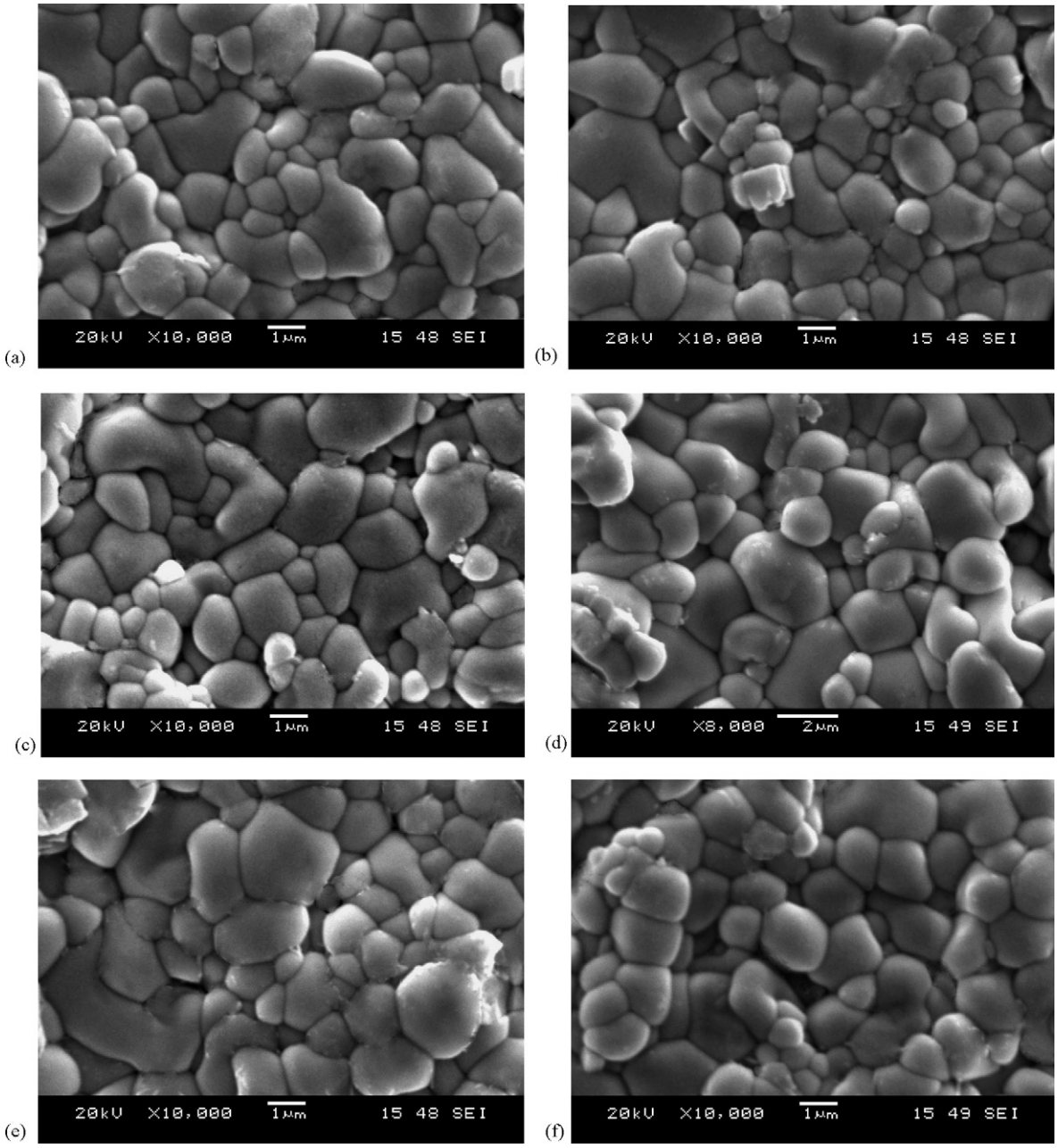



Fig. 2. SEM micrographs of $(1-x)$PIN–$x$PT with various compositions: (a) $x=0.0$, (b) $x=0.1$, (c) $x=0.2$, (d) $x=0.3$, (e) $x=0.4$, and (f) $x=0.5$.

size between 1 and 2 μm. The average grain size, as well as the density, does not vary significantly with the ceramic compositions, as listed in Table 1. However, it should be noticed that the microstructure of all the compositions also represents two distinct grain sizes, i.e. large grains (∼2 μm) and submicron grains. Earlier study on PIN–PT ceramics prepared with the conventional ball-milling method has also reported bimodal grain sizes but with large grains over 10 μm and fine grains about 1–2 μm [10]. Clearly, this shows the advantage of the vibro-milling technique in producing fine grains PIN–PT ceramics.

The dielectric properties, e.g. dielectric constant ($\varepsilon_r$) and $\tan\delta$, are measured as functions of both temperature and frequency, as shown in Fig. 3(a)–(f). As listed in Table 1 and plotted separately in Fig. 4, the maximum dielectric constant increases steadily with increasing PT content up to 30 mol% ($\varepsilon_r$ increases from 4310 in PIN to 16028 in 0.7PIN–0.3PT). Then a drop in the dielectric constant is observed with further increase in PT content to 40 mol%. This supports the XRD observation that the MPB composition should lie between compositions $x=0.3$ and 0.4. It should also be noted that a rise in the dielectric constant with more PT content (50 mol%) is possibly caused by large thermal conduction at high temperature [26]. Furthermore, as listed in Table 1, since the transition temperature of PT is very high (490 °C) [27], it is expected to observe that the transition temperature increases with increasing amount of PT in the PIN–PT system. This is clearly evident in Fig. 4. Again, it should also be noted here that, as shown in Fig. 3, the dielectric properties of most compositions increase significantly at high temperature

Author's personal copy



Table 1
Physical features and dielectric properties of $(1-x)$PIN–$x$PT ceramics (measured at 1 kHz)

| $x$ | Density (g/cm$^3$) | Grain size (μm) | $T_{max}$ (°C) | $\varepsilon_r$ at | | $\Delta T = T_{m,100\,kHz} - T_{m,100\,Hz}$ (°C) | Diffusivity ($\gamma$) |
|---|---|---|---|---|---|---|---|
| | | | | $T_{max}$ | 25 °C | | |
| 0.0 | 7.83 | 1.22 ± 0.08 | 71 | 4310 | 3345 | 26.2 | 1.89 |
| 0.1 | 7.51 | 1.29 ± 0.10 | 175 | 7120 | 2336 | 8.0 | 1.83 |
| 0.2 | 7.95 | 1.41 ± 0.12 | 210 | 10,733 | 1659 | 5.4 | 1.75 |
| 0.3 | 8.09 | 1.84 ± 0.16 | 267 | 16,028 | 1056 | 1.6 | 1.70 |
| 0.4 | 7.98 | 1.51 ± 0.16 | 327 | 11,867 | 1291 | 1.0 | 1.65 |
| 0.5 | 7.95 | 1.33 ± 0.10 | 375 | 15,038 | 573 | 0.4 | 1.62 |

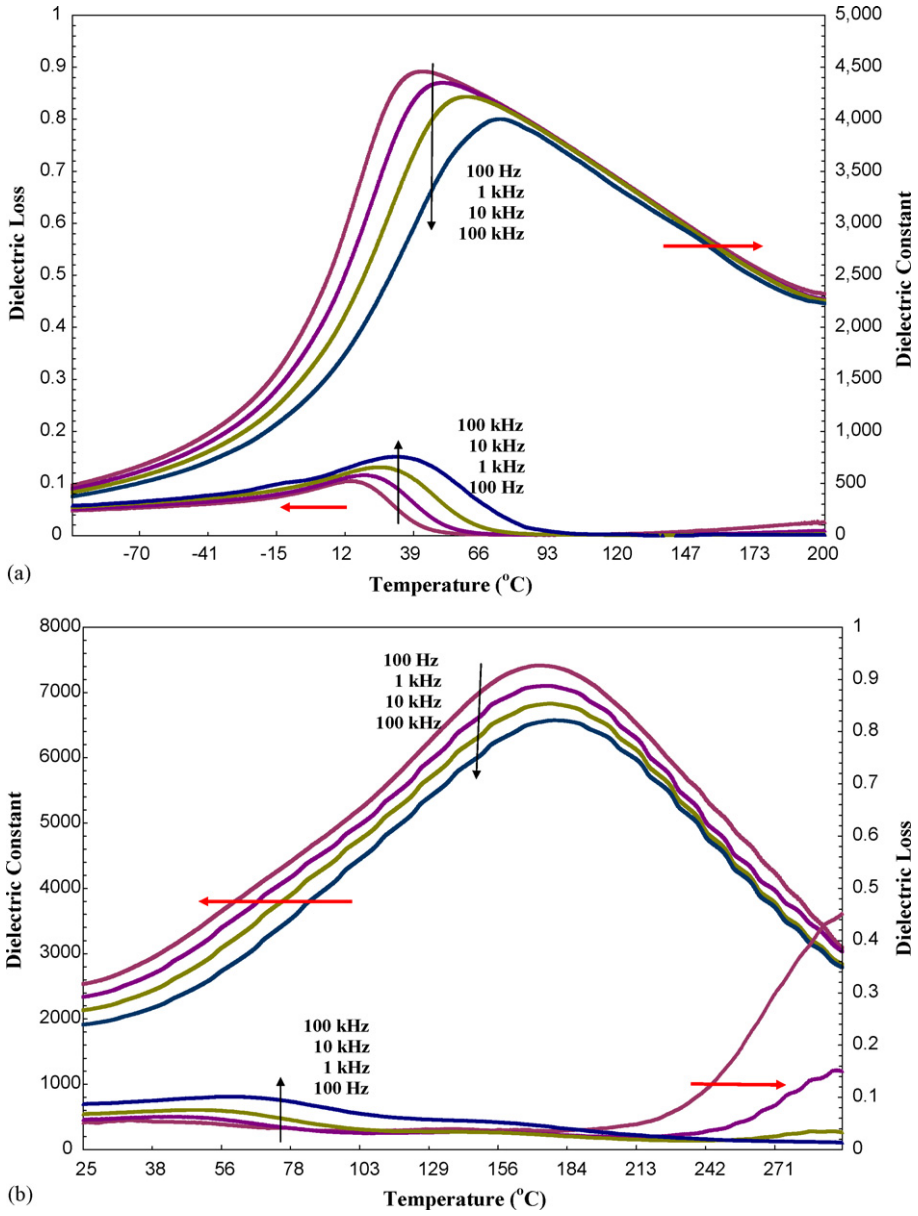



Fig. 3. (a) Temperature and frequency dependences of dielectric properties of PIN ceramic. (b) Temperature and frequency dependences of dielectric properties of 0.9PIN–0.1PT ceramic. (c) Temperature and frequency dependences of dielectric properties of 0.8PIN–0.2PT ceramic. (d) Temperature and frequency dependences of dielectric properties of 0.7PIN–0.3PT ceramic. (e) Temperature and frequency dependences of dielectric properties of 0.6PIN–0.4PT ceramic. (f) Temperature and frequency dependences of dielectric properties of 0.5PIN–0.5PT ceramic.

Author's personal copy



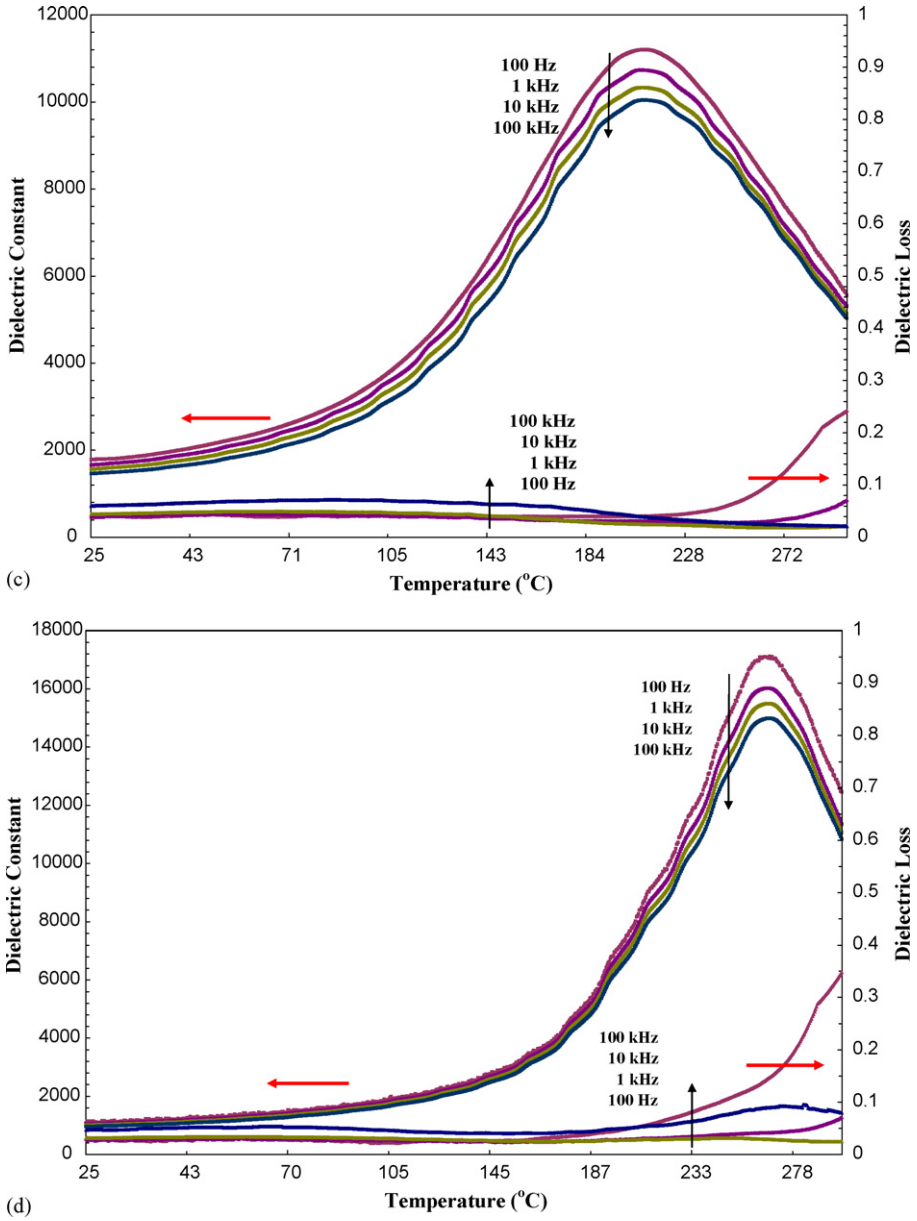



Fig. 3. (*Continued*)

as a result of thermally activated space charge conduction [26].

The dielectric properties of PIN ceramic, as plotted in Fig. 3(a), change significantly with temperature and frequency. Both dielectric constant ($\varepsilon_r$) and dielectric loss tangent ($\tan\delta$) exhibit strong temperature-frequency dependence below the transition temperature, indication of a typical relaxor ferroelectric behavior. In this case, the temperatures of maximum dielectric constant and dielectric loss tangent are shifted to higher temperature with increasing frequency. The maximum value of the dielectric constant decreases with increasing frequency, while that of the dielectric loss tangent increases. The dielectric properties then become frequency independence above the transition temperature [2,26]. While PIN exhibits a relaxor ferroelectric behavior, PT is a normal ferroelectric with nearly frequency-independent dielectric properties [27]. When PT is added to form the binary system with PIN, the dielectric behavior of PIN–PT should shift towards that of normal ferroelectric materials. As seen in Fig. 3(b)–(f), the dielectric properties exhibit a mixture of both normal and relaxor characteristics, in which the transition temperature is not shifted with frequency as much as for the PIN ceramic and the dielectric properties exhibit weaker temperature-frequency dependence below the transition temperature. This frequency dispersion in the dielectric properties can be quantified with $\Delta T = T_{m,100\,kHz} - T_{m,100\,Hz}$, which can be used as a rough estimate for more relaxor behavior with higher $\Delta T$. As listed in Table 1, an addition of PT results in smaller $\Delta T$. These results indicate the decreasing of relaxor behavior with increasing PT content [28]. Consequently, the dielectric peaks have become sharper with increasing PT content. Similar tendency has also been observed in several prior investigations [4–7,9,11].

Author's personal copy



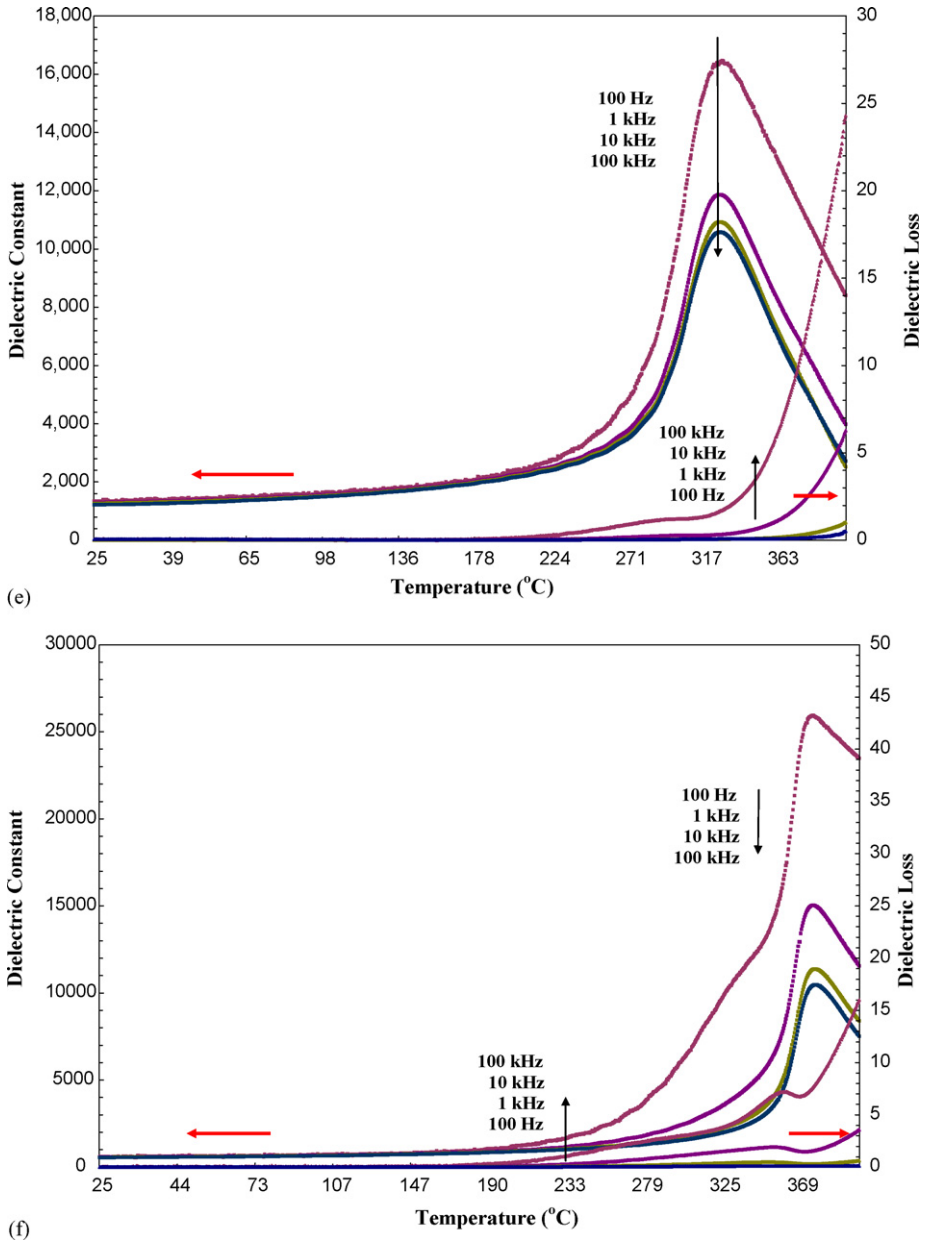



Fig. 3. (*Continued*).

The degree of broadening or diffuseness in the observed dielectric variation could also be estimated with the diffusivity ($\gamma$) using the expression $\ln(1/\varepsilon_r - 1/\varepsilon_{max})$ versus $(T - T_{max})^{\gamma}$. The value of $\gamma$ can vary from 1, for normal ferroelectrics with a normal Curie–Weiss behavior, to 2, for completely disordered relaxor ferroelectrics [6,26]. The values of $\gamma$ listed in Table 1 vary between 1.89 and 1.62, which confirms that diffuse phase transitions (DPT) occur in PIN–PT ceramics with a high degree of disorder. This observation clearly quantifies the decreasing of relaxor behavior with increasing PT content, as discussed earlier. Decreasing trend of $\gamma$ value with increasing of PT content observed in PIN–PT system agrees with the previous study [29].

The dependence of temperature of maximum dielectric constant ($T_m$) on frequency of PIN–PT system can be explained with Vogel–Fulcher equation:

$$\varpi = f_0 \exp\left[\frac{-E_a}{k(T_m - T_f)}\right] \quad (1)$$

where $f_0$, $E_a$ and $T_f$ are the Debye frequency, the activation energy and the static freezing temperature, respectively [30]. The Debye frequency, the activation energy and the static freezing temperature obtained by fitting the experimental data with Eq. (1) are listed in Table 2. From Eq. (1), it is known that the activation energy is an internal energy of the cluster, which concerns with an anisotropy energy, $K_{anis}$ and the cluster volume, $V$ [31]. The fitting results show that the activation energy increases with increasing PT content for PIN–PT system, indicating that PT induces the increasing of the anisotropy energy and the cluster

Author's personal copy



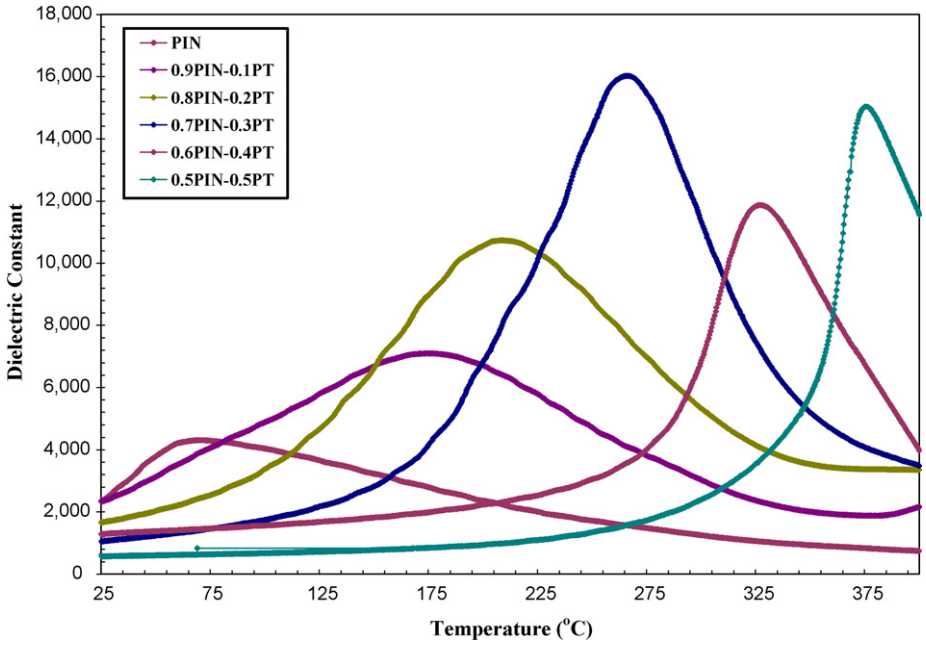



Fig. 4. Temperature dependence of dielectric constant of $(1-x)$PIN–$x$PT ceramics (measured at 1 kHz).

volume. It can be implied that size of isolated cluster or ordering increase with increasing PT contents [30,31]. For relaxor ferroelectrics, the value of Debye frequency concerns with size of polar nano-region and interaction between polar nano-regions [30]. In general, the stronger interaction and larger size show the smaller of the Debye frequency value [31]. Therefore, it can be implied that the increasing PT content shows marked effect in decreasing relaxor behavior by increasing size of and interaction between polar nano-regions, in good agreement with the observations discussed earlier. Similar observation has also been reported in other relaxor-based systems [32].

Fig. 5 illustrates a series of polarization ($P$–$E$) hysteresis loops for the PIN–PT ceramics. It is clearly evident that the shape of $P$–$E$ loops varies greatly with the ceramic compositions. The hysteresis curve of PIN ceramic is of a "slim" loop type, a characteristic of the suppressed ferroelectric interaction [2,26]. This is typically found in the relaxor ferroelectrics with polar nano-regions. The hysteresis loops of PIN–PT ceramics become more developed showing large remnant polarization ($P_r$: remaining polarization when electric field is decreased to zero) and large saturated polarization ($P_s$) with increasing PT content up to 30 mol%. The hysteresis loops are of a typical "square" form as a result of domain switching in an applied field. This is a typical characteristic of a phase that contains long-range interaction between dipoles in the ferroelectric micro-domain state [26]. From the loops, the polarizations ($P_r$ and $P_s$) and the coercive field $E_C$ (indicating an electric field required to zero the polarization) are determined and listed in Table 3. In addition, the ferroelectric characteristic of the ceramics can be assessed with the hysteresis loop squareness ($R_{sq}$) which is typically understood to be the ratio of $P_r/P_s$ where $P_r$ is the remnant polarization at zero electric field and $P_s$ is the saturated polarization obtained at some finite field strength below the dielectric breakdown. Jin et al. [33] used the loop squareness to measure not only the deviation in the polarization axis but also that in the electric field axis with the empirical expression $R_{sq} = (P_r/P_s) + (P_{1.1E_c}/P_r)$, where $P_{1.1E_c}$ is the polarization at the field equal to $1.1E_c$. For the ideal square loop, $R_{sq}$ is equal to 2.00. As listed in Table 3, the value of $R_{sq}$ increases with increasing PT content up to 30 mol%.

These results clearly indicate that an addition of PT induces the normal ferroelectric behaviors of PT into the PIN–PT ceramic system. More interestingly, it should also be noticed that a conclusion drawn from the XRD analysis and dielectric properties measurements discussed earlier that the MPB composition should exist between $x = 0.3$ and 0.4 is supported further

Table 2
The parameters obtained from fitting Vogel–Fulcher equation for $(1-x)$PIN–$x$PT ceramics

| $x$ | $T_f$ (K) | $f_0$ (Hz) | $E_a$ (eV) |
|---|---|---|---|
| 0.0 | 310 | $3.9 \times 10^{10}$ | 0.042 |
| 0.1 | 434 | $3.0 \times 10^{10}$ | 0.015 |
| 0.2 | 471 | $2.8 \times 10^{10}$ | 0.010 |
| 0.3 | 535 | $2.6 \times 10^{10}$ | 0.004 |
| 0.4 | 599 | $2.3 \times 10^{10}$ | 0.002 |
| 0.5 | 649 | $1.4 \times 10^{10}$ | 0.001 |

Table 3
Ferroelectric properties of $(1-x)$PIN–$x$PT ceramics

| $x$ | Ferroelectric properties (at 25 °C) | | | Loop squareness ($R_{sq}$) |
|---|---|---|---|---|
| | $P_r$ (μC/cm$^2$) | $P_s$ (μC/cm$^2$) | $E_C$ (kV/cm) | |
| 0.0 | – | – | – | – |
| 0.1 | 6.46 | 14.25 | 6.57 | 0.73 |
| 0.2 | 15.52 | 19.63 | 9.47 | 1.31 |
| 0.3 | 20.43 | 27.05 | 8.58 | 0.97 |
| 0.4 | 5.65 | 11.99 | 11.68 | 0.59 |
| 0.5 | 1.28 | 3.75 | 8.70 | 0.46 |

Author's personal copy



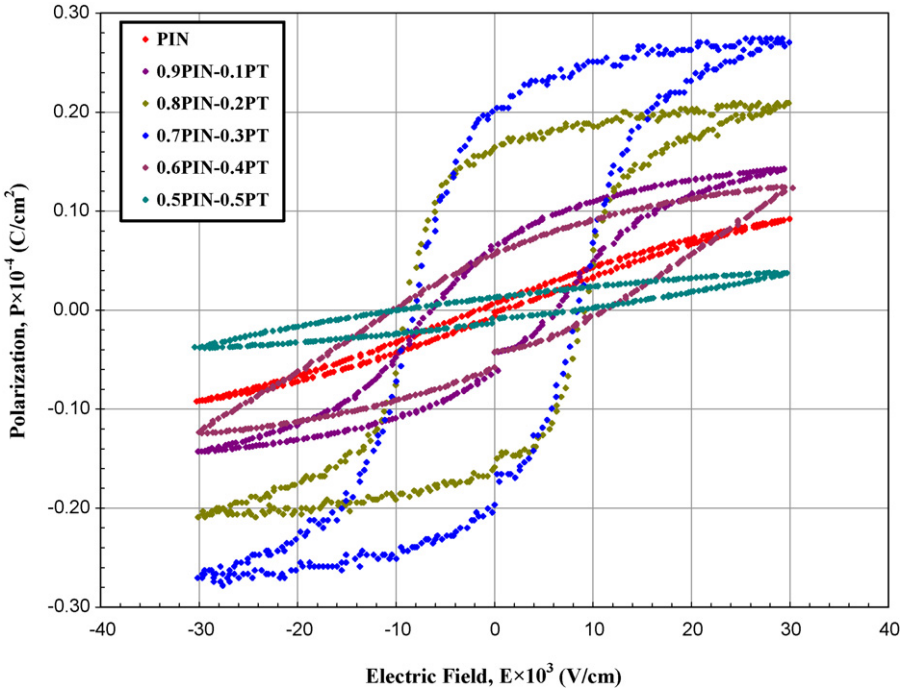



Fig. 5. *P–E* hysteresis loops of $(1-x)$PIN–$x$PT ceramics.

by the ferroelectric properties, as seen from a strong enhancement of polarization values with increasing PT content up to $x=0.3$, then a sudden drop of the polarization values with further increase in PT content. Finally, it is worthy noting that the fine grains PIN–PT ceramics obtained via the vibro-milling technique used in this study yield slightly better dielectric properties than the coarse grains PIN–PT ceramics in previous investigations [10–13]. However, as only very few investigations have been performed on PIN–PT ceramics, further investigations are still needed for more thoroughly and better comparison.

## 4. Conclusion

The $(1-x)Pb(In_{1/2}Nb_{1/2})O_3$–$xPbTiO_3$ (when $x=0.1$, 0.2, 0.3, 0.4, and 0.5) ceramics were prepared by an oxide-mixing method via a vibro-milling technique. The dielectric properties of the ceramics were determined as functions of both temperature and frequency with an automated dielectric measurement system, while the room temperature ferroelectric properties were measured by means of a standardized ferroelectric test system. The dielectric measurement took place over the temperature range of 25 and 400 °C with measuring frequency between 100 Hz and 100 kHz. Fine grains ceramics were achieved with average grain size of 1–2 μm, indicating advantage of the vibro-milling technique used. The results indicated that the dielectric properties of PIN ceramic were of relaxor ferroelectric behavior. The dielectric properties of PIN–PT ceramics showed a mixed relaxor and normal ferroelectric behavior, with more normal ferroelectric behavior observed with increasing PT content. The *P–E* hysteresis loop measurements demonstrated that the ferroelectric properties of the ceramics in PIN–PT system changed from the relaxor ferroelectric behavior in PIN ceramic to the normal ferroelectric behavior in PIN–PT ceramics. These results clearly show the significance of the added PT in reducing the relaxor ferroelectric behavior in PIN ceramic. More interestingly, XRD analysis, and dielectric and ferroelectric properties measurements also indicated the existence of the MPB composition between $x=0.3$ and 0.4. Finally, the fine grains PIN–PT ceramics showed slightly better dielectric properties than the coarse grains ceramics in previous investigations.

## Acknowledgments

The authors would like to express their gratitude for financial supports from the Thailand Research Fund (TRF), Commission on Higher Education (CHE), Graduate School and Faculty of Science of Chiang Mai University, and Ministry of University Affairs in Thailand.

## References

[1] K. Uchino, Ferroelectric Devices, Marcel Dekker, New York, 2000.
[2] G.H. Haertling, J. Am. Ceram. Soc. 82 (1999) 797–818.
[3] L.E. Cross, Mater. Chem. Phys. 43 (1996) 108–115.
[4] S.E. Park, T.R. Shrout, J. Appl. Phys. 82 (1997) 1804–1811.
[5] J. Kuwata, K. Uchino, S. Nomura, Jpn. J. Appl. Phys. 21 (1982) 1298–1302.
[6] R. Yimnirun, Int. J. Mod. Phys. B, in press.
[7] G. Xu, H. Luo, Y. Guo, Y. Gao, H. Xu, Z. Qi, W. Zhong, Z. Yin, Solid State Commun. 120 (2001) 321–324.
[8] N. Yasuda, H. Ohwa, M. Kume, Y. Yamashita, Jpn. J. Appl. Phys. 39 (2000) 5586–5588.
[9] N. Yasuda, H. Ohwa, D. Hasegawa, H. Hosono, Y. Yamashita, M. Iwata, Y. Ishibashi, Ferroelectrics 270 (2002) 247–252.
[10] M. Pham-Thi, C. Augier, H. Dammak, P. Gaucher, Ultrasonics 44 (2006) e627–e631.
[11] C. Augier, M. Pham-Thi, H. Dammak, P. Gaucher, J. Eur. Ceram. Soc. 25 (2005) 2429–2432.

Author's personal copy



[12] Y. Guo, H. Luo, T. He, Z. Yin, Solid State Commun. 123 (2002) 417–420.
[13] E.F. Alberta, A.S. Bhalla, J. Phys. Korea 32 (1998) s1265–s1269.
[14] N. Yasuda, M. Sakaguchi, Y. Itoh, H. Ohwa, Y. Yamashita, M. Iwata, Y. Ishibashi, Jpn. J. Appl. Phys. 42 (2003) 6205–6208.
[15] N. Yasuda, H. Ohwa, M. Kume, K. Hayashi, Y. Hosono, Y. Yamashita, J. Cryst. Growth 229 (2001) 299–304.
[16] B. Jaffe, W.R. Cook, H. Jaffe, Piezoelectric Ceramics, Academic Press, New York, 1971.
[17] Y.H. Xu, Ferroelectric Materials and their Applications, North Holland, Los Angeles, 1991.
[18] R. Wongmaneerung, R. Yimnirun, S. Ananta, Mater. Lett. 60 (2006) 2666–2671.
[19] R. Wongmaneerung, T. Sarnkonsri, R. Yimnirun, S. Ananta, Mater. Sci. Eng. B 130 (2006) 246–253.
[20] A. Ngamjarurojana, O. Khamman, R. Yimnirun, S. Ananta, Mater. Lett. 60 (2006) 2867–2872.
[21] S. Wongsaenmai, R. Yimnirun, S. Ananta, Mater. Lett., in press.
[22] E.F. Alberta, A.S. Bhalla, Mater. Lett. 29 (1996) 127–129.
[23] R. Wongmaneerung, R. Yimnirun, S. Ananta, Mater. Lett. 60 (2006) 1447–1452.
[24] S. Wongsaenmai, R. Yimnirun, S. Ananta, J. Mater. Sci., in press.
[25] S. Wongsaenmai, O. Khamman, S. Ananta, R. Yimnirun, J. Electroceram., in press.
[26] L.E. Cross, Ferroelectrics 76 (1987) 241–267.
[27] R. Wongmaneerung, R. Yimnirun, S. Ananta, Appl. Phys. A 86 (2007) 249–255.
[28] C. Lei, K. Chen, X. Zhang, J. Wang, Solid State Commun. 123 (2002) 445–450.
[29] M. Kuwabara, S. Takahashi, K. Goda, K. Oshima, K. Watanabe, Jpn. J. Appl. Phys. 31 (1992) 3241–3244.
[30] D. Viehland, S.-J. Jang, L.E. Cross, J. Appl. Phys. 68 (1990) 2916–2921.
[31] D. Viehland, S.-J. Jang, L.E. Cross, M. Wutting, Phys. Rev. B 46 (1992) 8003–8006.
[32] G. Singh, V.S. Triwari, V.K. Waghawan, Solid State Commun. 129 (2004) 665–670.
[33] B.M. Jin, J. Kim, S.C. Kim, Appl. Phys. A 65 (1997) 53–56.

Phys. Scr. **77** (2008) 045702 (4pp) doi:10.1088/0031-8949/77/04/045702

# Dielectric properties of PZT–PCN ceramics under compressive stress

**Muangjai Unruan, Anurak Prasatkhetragarn, Yongyut Laosiritaworn, Supon Ananta and Rattikorn Yimnirun**

Department of Physics, Faculty of Science, Chiang Mai University, Chiang Mai, 50200, Thailand

E-mail: rattikornyimnirun@yahoo.com

Received 16 November 2007
Accepted for publication 12 March 2008
Published 3 April 2008
Online at stacks.iop.org/PhysScr/77/045702

**Abstract**

In this study, ceramics in PZT–PCN systems with a formula $(1-x)Pb(Zr_{1/2}Ti_{1/2})O_3$–$(x)Pb(Co_{1/3}Nb_{2/3})O_3$ ($x = 0.1$–$0.5$) were prepared by a solid-state mixed-oxide technique. The phase formation and microstructure were studied using x-ray diffraction (XRD) and scanning electron microscopy (SEM), respectively. Effects of compressive stress on the dielectric properties of PZT–PCN ceramics were investigated at stress up to 230 MPa using a compressometer. The results clearly showed that the dielectric constant of the PZT–PCN ceramics increased significantly with increasing applied stress, while the dielectric loss tangent showed an opposing trend. The experimental observations have been attributed to a combination of the domain switching and the deaging mechanisms from the application of the compressive stress.

PACS numbers: 77.80.−e, 77.80.Fm, 77.84.−s

(Some figures in this article are in colour only in the electronic version.)

## 1. Introduction

A family of ferroelectric materials which are of great interest due to their high polarizability is lead-based relaxor ferroelectrics. Much attention for this type of material has been focused on lead magnesium niobate ($Pb(Mg_{1/3}Nb_{2/3})O_3$ or PMN), which is widely accepted as a prototype for relaxor material. However, there is a series of relaxor materials based on $Pb(B_{1/3}Nb_{2/3})O_3$ system that also possesses interesting properties. This current study is focused on lead cobalt niobate ($Pb(Co_{1/3}Nb_{2/3})O_3$ or PCN). However, the temperature related to the maximum dielectric constant ($T_{max}$) of PCN in relaxor phase is very low ($T_{max} = -70\,^{\circ}C$). Thus, in order to increase $T_{max}$ of PCN, lead zirconate titanate ($PbZr_{0.5}Ti_{0.5}O_3$ or PZT) was added to PCN to form a solid solution of PZT–PCN ceramics. The solid solutions between PZT and PCN are expected to synergistically combine the properties of both normal ferroelectric PZT and relaxor ferroelectric PCN, which could exhibit better piezoelectric and dielectric properties than those of the single-phase PZT and PCN [1, 2]. Our recent investigations have already revealed very interesting electrical properties of PZT–PCN ceramic systems [3, 4]. More importantly, when used this type of material is often subjected to self-induced or external stress. Information on the material properties under stress is critical for designing and selecting material for specific applications. Earlier studies on the influence of stress on electrical properties of other systems, i.e. PMN–PT, PMN–PZT, etc [5–7] indicate the importance of this subject matter. However, there has been no study on the effects of stress on electrical properties of PZT–PCN ceramics. It is, therefore, of interest to investigate the influence of compressive stress on properties of the PZT–PCN ceramics.

## 2. Experimental procedure

The reagent-grade oxides of PbO, CoO, $Nb_2O_5$, $ZrO_2$ and $TiO_2$ (anatase-structure) were used as raw materials. The columbite $CoNb_2O_6$ and wolframite $ZrTiO_4$ precursors were used as starting materials for PZT–PCN ceramics. The $CoNb_2O_6$ and $ZrTiO_4$ powders were prepared at calcination temperatures at 1100 and 1450 °C for 2 h, respectively. In the present work, the $(1-x)Pb(Zr_{1/2}Ti_{1/2})O_3$–$(x)Pb(Co_{1/3}Nb_{2/3})O_3$ with ($x = 0.1$–$0.5$) compositions were prepared from $ZrTiO_4$, $CoNb_2O_6$ and PbO powders. The

 © 2008 The Royal Swedish Academy of Sciences Printed in the UK

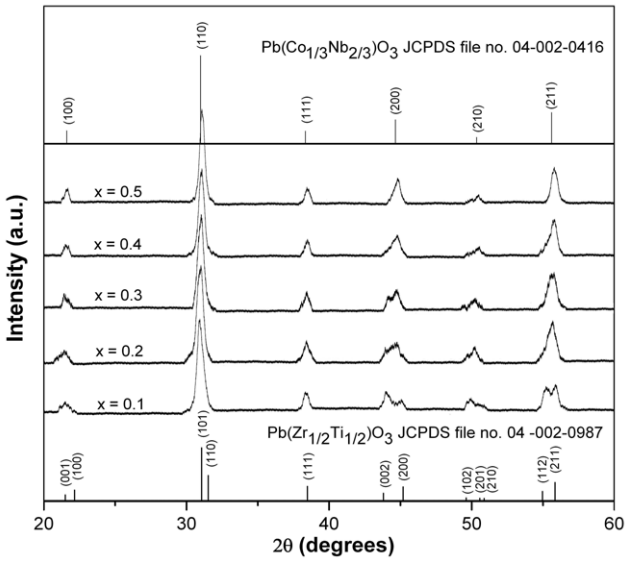



**Figure 1.** The XRD patterns of $(1-x)$PZT–$(x)$PCN ceramics.

PZT–PCN powders were synthesized by the solid-state reaction of these raw materials and mixed by the vibro-milling technique in ethanol for 1 h. A constant PbO excess of 2.0 mol.% was added to compensate for lead losses during calcination and sintering [8]. After drying, the product was calcined in alumina crucibles at temperatures between 900 and 950 °C. The calcined powders were pressed hydraulically to form disc-shape pellets 10 mm in diameter and 1 mm thick, with 1 wt.% polyvinyl alcohol (PVA) added as a binder. The pellets were sintered at 1200 °C for 2 h with heating/cooling rates 5 °C $\text{min}^{-1}$. The phase structure of the powders was analyzed by x-ray diffraction (XRD; Siemens-D500 diffractometer) using the $\text{CuK}_\alpha$ radiation. The microstructures of the sintered samples were examined using scanning electron microscopy (SEM; JEOL JSM-840A).

For dielectric property characterizations under compressive stress, the sintered samples were lapped to obtain parallely faced disc-shaped specimens, and the faces were then coated with silver paint as electrodes. To study the effects of the compressive stress on the dielectric properties, a compressometer was employed [7, 9]. Measurements were performed as a function of mechanical stress applied discretely between 0 and 230 MPa. The measurements were carried out on the samples for loading and unloading conditions. During the measurements, a desired stress was first applied to the sample and the dielectric properties were then recorded. The dielectric properties were measured through the LCR-meter (Instrek LCR-821). The room temperature (25 °C) capacitance and the dielectric loss tangent were obtained at a frequency of 1 kHz under compressive stress up to 230 MPa. The dielectric constant was then calculated from a parallel-plate capacitor equation, e.g. $\varepsilon_r = \text{Cd}/\varepsilon_0\text{A}$, where C is the capacitance of the specimens, d and A are, respectively, the thickness and the area of the electrode, and $\varepsilon_0$ is the dielectric permittivity of vacuum ($8.854 \times 10^{-12}$ F $\text{m}^{-1}$).

## 3. Results and discussion

The XRD patterns of $(1-x)$PZT–$(x)$PCN ceramics with various $x$ values are shown in figure 1. It can be seen that a complete crystalline solution of perovskite structure is formed throughout the whole composition range without the presence of pyrochlore or unwanted phases. From the patterns, $\text{Pb}(\text{Zr}_{1/2}\text{Ti}_{1/2})\text{O}_3$ ceramic is identified as a single-phase material with a perovskite structure having tetragonal symmetry which could be matched with ICDD file no. 04-002-0987. The XRD patterns of the PZT–PCN compositions show a combination between PZT and PCN patterns, showing a perovskite structure having symmetry varying between tetragonal and pseudo-cubic types [3, 4]. For better comparison, the ICDD file no. 04-002-0416 for $\text{Pb}(\text{Co}_{1/3}\text{Nb}_{2/3})\text{O}_3$ with a pseudo-cubic structural symmetry is also displayed in figure 1. More interestingly, the composition with $x = 0.3$ exhibited broadening of peaks at $2\theta \sim 44$–$45°$, indicating the structural transformation from the tetragonal phase, characterized by (002)/(200) peaks, to the pseudo-cubic phase. This observation is obviously associated with the composition with coexistence of two symmetries, which in this case are tetragonal and pseudo-cubic phases. To a first approximation, it could be said that the composition with $x = 0.3$ is close to the morphotropic phase boundary (MPB) of he $(1-x)$ $\text{Pb}(\text{Zr}_{1/2}\text{Ti}_{1/2})\text{O}_3$–$(x)\text{Pb}(\text{Co}_{1/3}\text{Nb}_{2/3})\text{O}_3$ system, where the structure of the PZT–PCN compositions is gradually changing from tetragonal to pseudo-cubic phases [3, 4].

SEM micrographs in figure 2 reveal that the PCN-modification increases degrees of grain close-packing behavior of PZT ceramics. Some grains are observed to have irregular shapes with both open and closed pores as a result of a high rate of evaporation of PbO during the sintering process [8].

The micrographs also show that the grain size of the ceramics varies considerably from <0.47 to 19.6 $\mu$m. Furthermore, the average grain size decreases significantly with increasing PCN in the ceramic compositions. It can also be noticed that the maximum density is obtained in 0.7PZT–0.3PCN ceramics, while the minimum density is observed in 0.5PZT–0.5PCN ceramics. Interestingly, the density results can be correlated to the microstructure as high-density 0.7PZT–0.3PCN ceramics show high degrees of grain close packing, whereas low-density 0.5PZT–0.5PCN ceramics contain many pores.

The experimental results of the compressive stress dependence of the dielectric properties of the ceramics in the PZT–PCN system are shown in figures 3 and 4. There is a significant change of both the dielectric constant and the dielectric loss tangent of the ceramics when the applied stress increases from 0 to 230 MPa. The changes of the dielectric constant with the applied stress can be divided into three different groups. For PZT-rich compositions (0.9PZT–0.1PCN and 0.8PZT–0.2PCN), the dielectric constant increases with applied stress. It can be seen that the dielectric constant is enhanced by approximately 10% at 230 MPa applied stress. For the compositions near MPB of the $(1-x)\text{Pb}(\text{Zr}_{1/2}\text{Ti}_{1/2})\text{O}_3$–$(x)\text{Pb}(\text{Co}_{1/3}\text{Nb}_{2/3})\text{O}_3$ system, the dielectric constant increases more than other compositions with the increasing applied stress. The changes in the dielectric constant 30% at 230 MPa applied stress are obviously higher than that observed in PZT-rich compositions. For PCN-rich composition (0.5PZT–0.5PCN), the dielectric

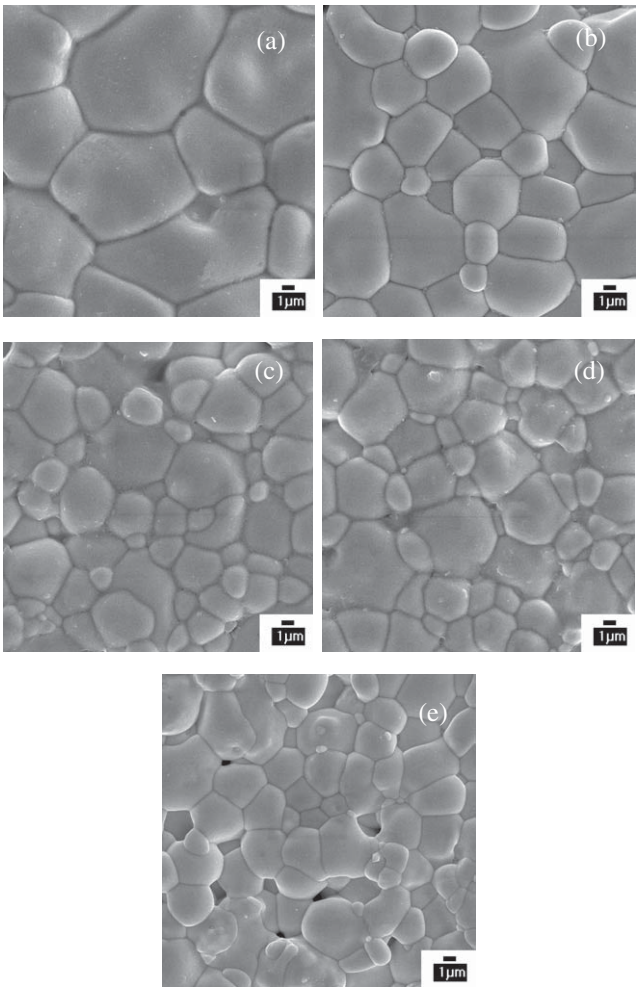



**Figure 2.** SEM micrographs of $(1-x)$PZT–$(x)$PCN with various compositions: (a) $x = 0.1$, (b) $x = 0.2$, (c) $x = 0.3$, (d) $x = 0.4$ and (e) $x = 0.5$.

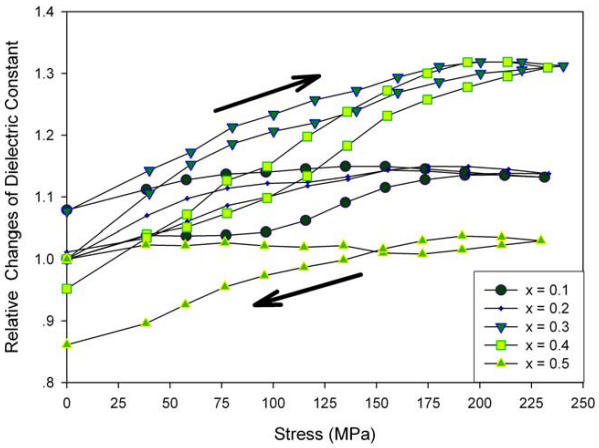



**Figure 3.** Relative changes of the dielectric constant as a function of compressive stress for $(1-x)$PZT–$(x)$PCN ceramics.

constant rises only slightly (<3%) when the applied stress increases to the maximum amplitude. The dielectric loss tangent for all compositions is found to decrease significantly and linearly when the applied stress is raised from 0 to 230 MPa. The largest changes occur in PZT-rich compositions (0.9PZT–0.1PCN and 0.8PZT–0.2PCN) with

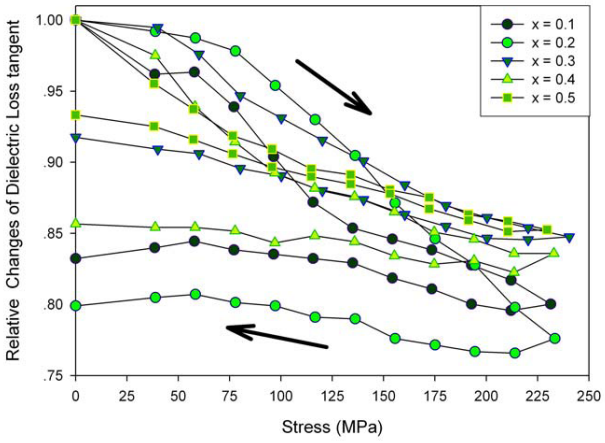



**Figure 4.** Relative changes of the dielectric loss tangent as a function of compressive stress for $(1-x)$PZT–$(x)$PCN ceramics.

the dielectric loss tangent decreasing nearly by 20%. For other compositions, the dielectric loss tangent decreased nearly 15% at 230 MPa applied stress.

To understand these experimental results, various effects have to be considered. Normally, the properties of ferroelectric materials are derived from both the intrinsic contribution, which is the response from a single domain, and extrinsic contributions, which are from domain wall motions [10–12]. When a mechanical stress is applied to a ferroelectric material, the domain structure in the material will change to maintain the domain energy at a minimum; during this process some of the domains engulf other domains or change shape irreversibly. Under a stress, the domain structure of ferroelectric ceramics may undergo domain switching, clamping of domain walls, de-aging and de-poling [13, 14]. In this study, the results on the compressive stress dependence of the dielectric properties can easily be explained with the above statements. When the compressive stress is applied in the direction parallel to the polar axis direction, the stress will move some of the polarization away from the polar axis direction resulting in a change in domain structures [10–13]. This change increases the non-180° domain wall density. Hence the increase of the dielectric constant with the applied stress is observed. The de-aging mechanism is also expected to play a role here [10, 12]. Therefore, a combination of the domain switching and the de-aging mechanisms is believed to be a reason for the increase of the dielectric constant with increasing applied stress in the PZT–PCN system, as shown in figure 3. The stress dependence of the dielectric loss tangent, as depicted in figure 4 is caused by the stress-induced de-aging mechanism. The de-aging in the materials normally causes the decrease of the dielectric loss tangent observed in some compositions [11]. This is an irreversible effect with the dielectric constant and dielectric loss tangents not returning to their original values after a stress cycle, as seen in figures 3 and 4.

## 4. Conclusions

In this study, ceramics in the $(1-x)$Pb$(Zr_{1/2}Ti_{1/2})O_3$–$(x)$Pb$(Co_{1/3}Nb_{2/3})O_3$ system (when $x = 0.1$–$0.5$) were successfully prepared by a solid-state mixed-oxide technique (the columbite–wolframite precursor method). PZT ceramic

was identified by XRD as a single-phase material with a perovskite structure having tetragonal symmetry, while the mixed compositions showed a gradual change from tetragonal to pseudo-cubic symmetry, with a possible MPB between the two phases near the 0.7PZT–0.3PCN composition. The dielectric properties under the compressive stress of the PZT–PCN ceramics are observed at stress levels up to 230 MPa using a compressometer. The results clearly show that the dielectric constant of the PZT–PCN ceramics increase significantly with increasing applied stress. Larger changes in the dielectric properties with the applied stress are observed in the compositions near MPB of the $(1-x)Pb(Zr_{1/2}Ti_{1/2})O_3-(x)Pb(Co_{1/3}Nb_{2/3})O_3$ system. However, the dielectric loss tangent of all compositions decreases with increasing applied stress. This study shows that the applied stress has significant influences on the dielectric properties of the PZT–PCN ceramics.

## Acknowledgments

This work was supported by the Commission on Higher Education (CHE), Thailand Research Fund (TRF), Royal Golden Jubilee PhD. Program, the Faculty of Science and the Graduate School of Chiang Mai University.

## References

[1] Kudo T, Yazaki T, Naito F and Sugaya S 1970 *J. Am. Ceram. Soc.* **53** 326
[2] Hachiga T, Fujimoto S and Yasuda N 1987 *J. Phys. D: Appl. Phys.* **20** 1291
[3] Vittayakorn N, Wirunchit S, Traisak S, Yimnirun R and Rujijanagul G 2008 *Curr. Appl. Phys.* **8** 128
[4] Prasartkhetragarn A, Vittayakorn N, Ananta S, Yimnirun R and Cann D P 2008 *Japan J. Appl. Phys.* **47** 998
[5] Yimnirun R, Unruan M, Laosiritaworn Y and Ananta S 2006 *J. Phys. D: Appl. Phys.* **39** 3097
[6] Triamnak N, Unruan M, Ananta S and Yimnirun R 2007 *J. Electroceram.* at press
[7] Yimnirun R, Ananta S, Meechoowas E and Wongsaenmai S 2003 *J. Phys. D: Appl. Phys.* **36** 1615
[8] Vittayakorn N, Rujijanagul G, Tunkasiri T, Tan X and Cann D P 2004 *Mater. Sci. Eng.* B **108** 258
[9] Yimnirun R, Ananta S, Ngnamjarurojana A and Wongsaenmai S 2006 *Appl. Phys.* A **6** 520
[10] Yang G, Ren W, Liu S F, Masys A J and Mukherjee B K 2000 *Proc. IEEE Ultrason. Symp.* **2** 1005
[11] Audigier D, Richard C, Descamps C, Troccaz M and Eyraud L 1994 *Ferroelectrics* **154** 219
[12] Fritz I J 1978 *J. Appl. Phys.* **49** 4922
[13] Yang G, Liu S F, Ren W and Mukherjee B K 2000 *Proc. SPIE Symp. Smart Struct. Mater.* **3992** 103
[14] Steiner O, Tagantsev A K, Colla E L and Setter N 1999 *J. Euro. Ceram. Soc.* **19** 1243

# Stress-dependent scaling behavior of subcoercive field dynamic ferroelectric hysteresis in $Pb(Zn_{1/3}Nb_{2/3})O_3$-modified $Pb(Zr_{1/2}Ti_{1/2})O_3$ ceramic

R. Yimnirun,[a] N. Wongdamnern, N. Triamnak, M. Unruan, A. Ngamjarurojana, S. Ananta, and Y. Laosiritaworn
*Department of Physics, Faculty of Science, Chiang Mai University, Chiang Mai 50200, Thailand*

(Received 6 February 2008; accepted 19 February 2008; published online 23 April 2008)

Scaling behavior of subcoercive field dynamic ferroelectric hysteresis under influence of stress was investigated in $Pb(Zn_{1/3}Nb_{2/3})O_3$-modified $Pb(Zr_{1/2}Ti_{1/2})O_3$ (PZT) bulk ceramic. The scaling relation of hysteresis area $\langle A \rangle$ against frequency $f$, field amplitude $E_0$, and stress $\sigma$ for the minor loops takes a form of $\langle A - A_{\sigma=0} \rangle \propto f^{-0.42} E_0^{3.65} \sigma^{0.24}$, which is very similar to that of soft and hard PZT ceramics. However, slightly faster responses to $f$ and $E_0$ indicate the ease of polarization orientation in this simpler domain structure ceramic as compared to commercial PZT ceramics.
© *2008 American Institute of Physics*. [DOI: 10.1063/1.2907755]

The dynamic hysteresis characteristics have become important consideration since hysteresis area $\langle A \rangle$ as a function of the field amplitude $E_0$ and frequency $f$ presents lots of information critical for many ferroelectric applications.[1,2] Theoretical studies have been carried out to understand the dynamic response of hysteresis curves in spin and polarization systems.[3–7] In particular, attention is focused on scaling law

$$\langle A \rangle \propto f^m E_0^n, \tag{1}$$

where $m$ and $n$ are exponents that depend on the dimensionality and symmetry of the system. Based on three-dimensional models, it has been suggested that $m=1/3$ and $n=2/3$ as $f \to 0$, whereas $m=-1$ and $n=2$ as $f \to \infty$.[3,5,8] Experimental investigations on a few thin-film systems have also been reported with variation in the scaling relations obtained.[9–12] On the contrary, there are only few reports on the scaling behavior studies of ferroelectric hysteresis loops of bulk ferroelectric ceramics.[13–16] More importantly, in many applications the ceramic specimens are often subjected to mechanical loading, either from the design of the device itself or from operating conditions which induce stresses.[1,17] Therefore, a prior knowledge of how the material properties change under different load conditions in materials is inevitably crucial for proper design of a device and for suitable selection of materials for a specific application.[18–22]

Previous works on $Pb(Zn_{1/3}Nb_{2/3})O_3$ (PZN)-modified PZT (or PZN-PZT) have reported excellent electrical properties suitable for various applications.[23–25] Interestingly, transmission electron microscopy study has revealed a clear regular lamellar 90° domain configuration in 0.9PZT-0.1PZN ceramic with tetragonal symmetry.[26] Therefore, the 0.9PZT-0.1PZN ceramic was chosen for this study. Practically, ferroelectric ceramics are used under subcoercive field condition in most applications; it is therefore of interest to obtain scaling relations for such condition. This present work is aimed at obtaining the stress-dependent scaling behavior of subcoercive field dynamic ferroelectric hysteresis in 0.9PZT-0.1PZN ceramic.

The disk-shaped samples of tetragonal-structure 0.9PZT-0.1PZN ceramic with diameter of 10 mm and thickness of 1 mm were used in this study. The dynamic hysteresis ($P$-$E$) loops were characterized at room temperature (25 °C) by using a modified Sawyer–Tower circuit with $f$ covering from 2 to 100 Hz and $E_0$ from 0 to 18 kV/cm. The electric field was applied to a sample by a high voltage ac amplifier (Trek 610D) with the input sinusoidal signal from a function generator (HP 3310A). The $P$-$E$ loops were recorded by a digital oscilloscope (HP 54645A, 100 MHz). The detailed descriptions of this system were explained elsewhere.[21] The compressive stress, applying parallel to the electric field direction, was supplied by the servohydraulic load frame and monitored with the pressure gauge. The $P$-$E$ loops were recorded as a function of mechanical stress discretely applied between 0 and 173 MPa for each applied field and frequency. At each constant stress, the loop was obtained after 20 sampling cycles to average out the noise deformation.

The hysteresis profiles for various frequencies $f$, field amplitude $E_0$, and stress $\sigma$ are obtained and shown in Figs. 1(a)–1(c). For a particular applied stress, as expected, the dependence of the loop pattern and area $\langle A \rangle$ on $f$ and $E$ is remarkable. At fixed $E_0$, the loop area $\langle A \rangle$ and remnant polarization ($P_r$) decrease with an increase of frequency, as shown in Fig. 1(a). The dependence of the hysteresis loop on $E_0$ is depicted in Fig. 1(b). Similar observations have also been reported in soft and hard PZT ceramics.[27–29] In addition, the $P$-$E$ loop area $\langle A \rangle$ is found to steadily decrease with increasing the stress. Several previous investigations also reported similar stress-dependent behavior.[20–22]

To obtain the suitable scaling relation for the bulk ceramic, one can first follow the suggested scaling law given in Eq. (1) to directly determine exponents $m$ and $n$ from the experimental data. By plotting $\langle A \rangle$ against $f$ at fixed $E_0$, one obtains the exponent $m$. On the other hand, the exponent $n$ can be obtained from plotting $\langle A \rangle$ against $E_0$ at fixed $f$. As plotted in Fig. 2, it is revealed that the experimental data can

[a]Author to whom correspondence should be addressed. Electronic mail: rattikornyimnirun@yahoo.com.

 © 2008 American Institute of Physics

Downloaded 27 Apr 2008 to 202.28.244.211. Redistribution subject to AIP license or copyright; see http://jap.aip.org/jap/copyright.jsp

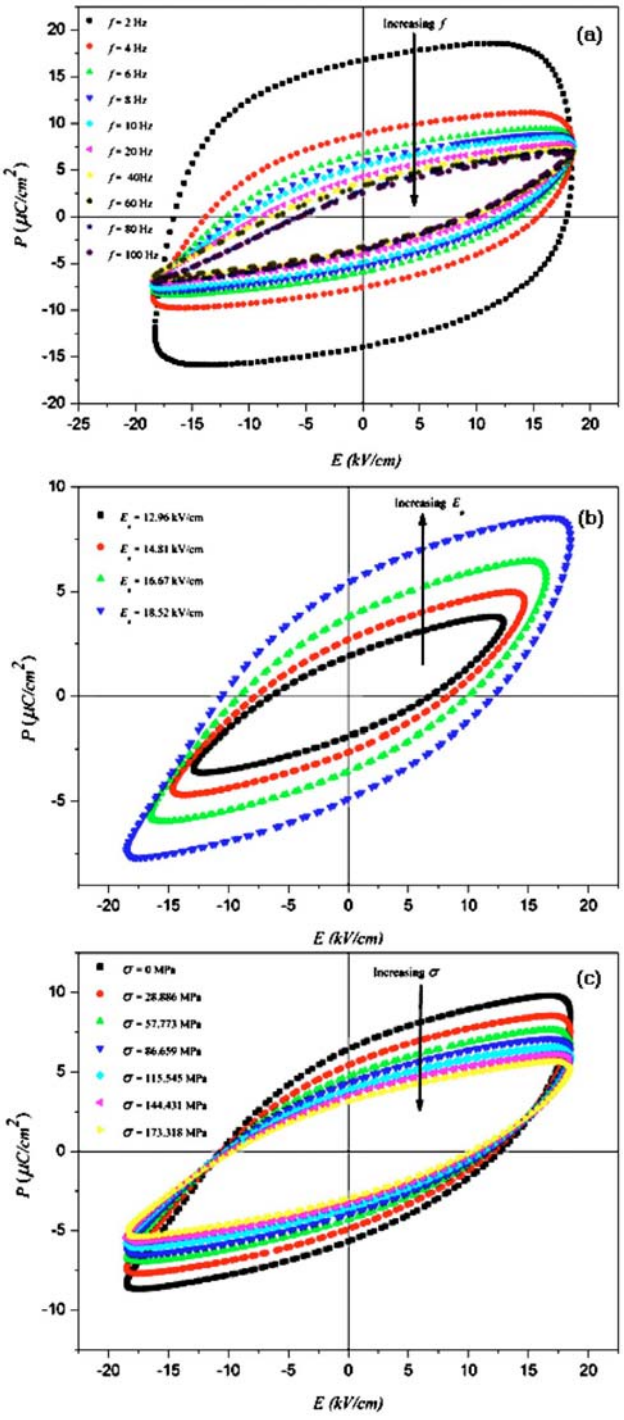



FIG. 1. (Color online) Hysteresis loops under subcoercive field condition for 0.9PZT-0.1PZN ceramic (a) at various $f$ ($E_0$=18.5 kV/cm and $\sigma$ =27 MPa), (b) at various $E_0$ ($f$=10 Hz and $\sigma$=27 MPa), and (c) at various $\sigma$ ($f$=10 Hz and $E_0$=18.5 kV/cm).

be fitted (with $R^2$=0.99), within the measured uncertainty, by

$$\langle A\rangle \propto f^{-0.42}E_0^{3.65}. \tag{2}$$

Here, the first interesting observation is that the minor-loop scaling in PZN-modified PZT bulk ceramics is generally similar to that of PZT thin film,[5,9] as well as that of minor loop of PZT bulk ceramics.[13,15] As explained in our previous investigation,[13] this was attributed to the fact that

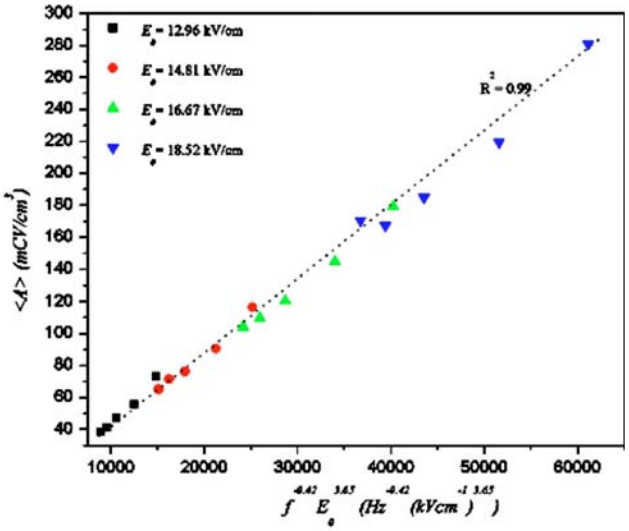



FIG. 2. (Color online) Scaling of hysteresis area $\langle A\rangle$ against $f^{-0.42}E_0^{3.65}$ for 0.9PZT-0.1PZN ceramic under subcoercive field condition.

main polarization orientation mechanism in thin films and in subcoercive field condition for bulk ceramics likely is from the 180° domain reversal. This explains why the scaling behavior of PZT bulk ceramics at low E fields is similar to that of thin films. More importantly, the scaling relation obtained in Eq. (2) indicates that $\langle A\rangle$ more quickly decays with $f$ and more quickly grows with $E_0$ than the minor-loop scaling relations obtained earlier for commercial soft PZT bulk ceramic with $\langle A\rangle \propto f^{-0.33}E_0^3$.[13] This clearly indicates the ease of the polarization orientation process in tetragonal 0.9PZT-0.1PZN ceramics with a clear regular lamellar 90° domain configuration[26] that leads to faster polarization orientation kinetics, as compared to complex domain structures of commercial PZT bulk ceramics which require higher energy barrier for the polarization orientation process.

To investigate the scaling behavior under the effect of applied stresses, instead of including only the field amplitude $E_0$ and the frequency term $f$, the scaling relation should also include the stress ($\sigma$) term, i.e.,

$$\langle A\rangle \propto f^m E_0^n \sigma^p. \tag{3}$$

However, due to increasing number of exponents, to simplify the problem, the validity of the scaling law $\langle A\rangle(\sigma) \propto f^{-0.42}E_0^{3.65}$ is assumed for all applied stresses. Consequently, the area $\langle A\rangle$ for each stress is plotted against $f^{-0.42}E_0^{3.65}$, as shown in Fig. 3(a), and it can be seen from the least-square linear fits that reasonably good linear relations can be found. As a result, the condition of universality having $m$=−0.42 and $n$=3.65 in 0.9PZT-0.1PZN bulk ceramic is confirmed. Consequently, $\langle A\rangle \propto (a+b\sigma^c)f^{-0.42}E_0^{3.65}$ may be written and by substituting the fitted parameters, it is found that

$$\langle A\rangle - \langle A_{\sigma=0}\rangle = \langle A - A_{\sigma=0}\rangle \propto f^{-0.42}E_0^{3.65}\sigma^{0.24}, \tag{4}$$

where $\langle A_{\sigma=0}\rangle$ refers to stress-free hysteresis area which will be a dominant term for zero stress. The data collapsing of the scaling area from all $f$, $E_0$, and $\sigma$ was found to confirm Eq. (4), as evident in Fig. 3(b). Note that from the appearance of

Downloaded 27 Apr 2008 to 202.28.244.211. Redistribution subject to AIP license or copyright; see http://jap.aip.org/jap/copyright.jsp

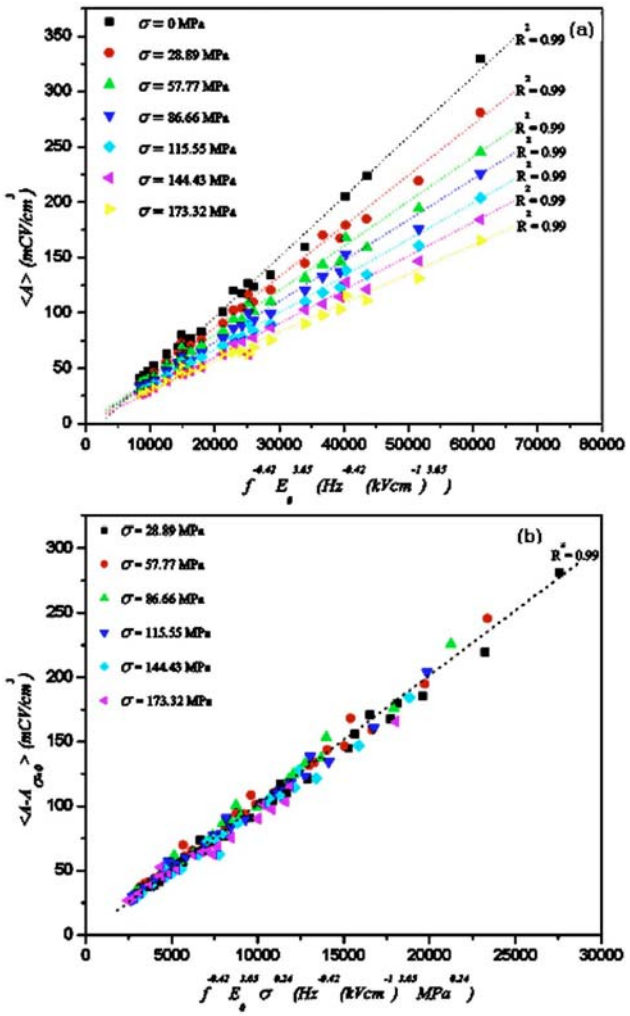



FIG. 3. (Color online) (a) Scaling of hysteresis area $\langle A \rangle$ against $f^{-0.42}E_0^{3.65}$ at various $\sigma$, (b) the collapse of the scaling area $\langle A - A_{\sigma=0} \rangle$ against $f^{-0.42}E_0^{3.65}\sigma^{0.24}$ on a same linear line (with small fluctuation) for 0.9PZT-0.1PZN ceramic under subcoercive field condition.

stress $\sigma$, $\langle A - A_{\sigma=0} \rangle$, referring to the difference in energy dissipation between understress and stress-free conditions, increases with increasing stress suggesting a decay of $\langle A \rangle$ with $\sigma$ at a rate of $\sigma^{0.24}$, as observed in experiments. As a result, it can be concluded that the difference of the hysteresis area between understress and stress-free condition scales with frequency, field amplitude, and stress via exponents $m=-0.42$, $n=3.65$, and $p=0.24$. However, at a particular fixed stress, Eq. (4) gives $f^{-0.42}E_0^{3.65}$ which is the original form for how the area scales with the frequency and the field amplitude.

In summary, the scaling behavior of the subcoercive field dynamic ferroelectric hysteresis of PZN-modified PZT bulk ceramics under the effect of mechanical stress has been investigated. The scaling relation for the minor loops takes the form of $\langle A - A_{\sigma=0} \rangle \propto f^{-0.42}E_0^{3.65}\sigma^{0.24}$, which is very similar to that of soft and hard PZT ceramics. However, slightly faster responses to $f$ and $E_0$ indicate the ease of polarization orientation in this simpler domain structure ceramic as compared to commercial PZT ceramics. As a result, this study suggests that the domain structures play partial role in controlling dynamic hysteresis behavior of ferroelectric materials.

Financial supports from the Thailand Research Fund (TRF), Commission on Higher Education (CHE), Royal Golden Jubilee Ph.D. Program, Faculty of Science, and Graduate School of Chiang Mai University are gratefully acknowledged.

[1] K. Uchino, *Ferroelectric Devices* (Dekker, New York, 2000).
[2] O. Auciello, J. F. Scott, and R. Ramesh, Phys. Today **51**, 22 (1998).
[3] M. Rao, H. R. Krishnamurthy, and R. Pandit, Phys. Rev. B **42**, 856 (1990).
[4] M. Acharyya and B. K. Chakrabarti, Phys. Rev. B **52**, 6560 (1995).
[5] J.-M. Liu, H. L. W. Chan, C. L. Choy, Y. Y. Zhu, S. N. Zhu, Z. G. Liu, and N. B. Ming, Appl. Phys. Lett. **79**, 236 (2001).
[6] H. B. Zuo, M. F. Zhang, J. C. Han, and J. M. Liu, Mater. Lett. **61**, 2697 (2007).
[7] M. Sarjala, E. T. Seppälä, and M. J. Alava, Physica B **403**, 418 (2008).
[8] M. Rao and R. Pandit, Phys. Rev. B **43**, 3373 (1991).
[9] J.-M. Liu, H. L. W. Chan, C. L. Choy, and C. K. Ong, Phys. Rev. B **65**, 014416 (2001).
[10] B. Pan, H. Yu, D. Wu, X. H. Zhou, and J.-M. Liu, Appl. Phys. Lett. **83**, 1406 (2003).
[11] Y.-H. Kim and J.-J. Kim, Phys. Rev. B **55**, R11933 (1997).
[12] J.-H. Park, C.-S. Kim, B.-C. Choi, B. K. Moon, J. H. Jeong, and I. W. Kim, Appl. Phys. Lett. **83**, 536 (2003).
[13] R. Yimnirun, Y. Laosiritaworn, S. Wongsaenmai, and S. Ananta, Appl. Phys. Lett. **89**, 162901 (2006).
[14] R. Yimnirun, S. Wongsaenmai, S. Ananta, and Y. Laosiritaworn, Appl. Phys. Lett. **89**, 242901 (2006).
[15] R. Yimnirun, R. Wongmaneerung, S. Wongsaenmai, A. Ngamjarurojana, S. Ananta, and Y. Laosiritaworn, Appl. Phys. Lett. **90**, 112908 (2007).
[16] R. Yimnirun, R. Wongmaneerung, S. Wongsaenmai, A. Ngamjarurojana, S. Ananta, and Y. Laosiritaworn, Appl. Phys. Lett. **90**, 112906 (2007).
[17] K. Uchino, *Piezoelectric Actuators and Ultrasonic Motors* (Kluwer Academic, Boston, 1997).
[18] J. Zhao, A. E. Glazounov, and Q. M. Zhang, Appl. Phys. Lett. **74**, 436 (1999).
[19] D. Viehland and J. Powers, J. Appl. Phys. **89**, 1820 (2001).
[20] D. Zhou, M. Kamlah, and D. Munz, J. Eur. Ceram. Soc. **25**, 425 (2005).
[21] R. Yimnirun, Y. Laosiritaworn, and S. Wongsaenmai, J. Phys. D **39**, 759 (2006).
[22] R. Yimnirun, S. Ananta, A. Ngamjarurojana, and S. Wongsaenmai, Appl. Phys. A: Mater. Sci. Process. **81**, 1227 (2005).
[23] X. P. Jiang, J. W. Fang, H. R. Zeng, B. J. Chu, G. R. Li, D. R. Chen, and Q. R. Yin, Mater. Lett. **44**, 219 (2000).
[24] H. Fan and H. E. Kim, J. Appl. Phys. **91**, 317 (2002).
[25] N. Vittayakorn, G. Rujijanagul, T. Tunkasiri, X. Tan, and D. P. Cann, J. Mater. Res. **18**, 2881 (2003).
[26] N. Vittayakorn, G. Rujijanagul, X. Tan, and D. P. Cann, J. Electroceram. **16**, 141 (2006).
[27] D. A. Hall and P. J. Stevenson, Ferroelectrics **228**, 139 (1999).
[28] J. E. Garcia, R. Perez, and A. Albareda, J. Phys. D **34**, 3279 (2001).
[29] M. Morozov, D. Damjanovic, and N. Setter, J. Eur. Ceram. Soc. **25**, 2483 (2005).

Downloaded 27 Apr 2008 to 202.28.244.211. Redistribution subject to AIP license or copyright; see http://jap.aip.org/jap/copyright.jsp

ELSEVIER

Materials Science and Engineering B 150 (2008) 12–17

MATERIALS SCIENCE & ENGINEERING B

www.elsevier.com/locate/mseb

# Effect of vibro-milling time on phase formation and particle size of nickel niobate nanopowders

O. Khamman, R. Yimnirun, S. Ananta *

*Department of Physics, Faculty of Science, Chiang Mai University, Chiang Mai 50200, Thailand*

Received 3 December 2007; received in revised form 8 January 2008; accepted 12 January 2008

**Abstract**

A columbite-type phase of nickel niobate, $NiNb_2O_6$, nanopowder was synthesized by a solid-state reaction via a rapid vibro-milling technique. The effect of milling time on the phase formation and particle size of $NiNb_2O_6$ powder was investigated. Powder samples were characterized using DTA, XRD, SEM and laser diffraction techniques. It was found that the smallest particle size of 32 nm was achieved at 25 h of vibro-milling after which a higher degree of particle agglomeration was observed on continuation of milling to 35 h. In addition, by employing an appropriate choice of the milling time, a narrow particle size distribution curve was also observed.
© 2008 Elsevier B.V. All rights reserved.

*Keywords:* Nickel niobate; Milling; Nanopowders; Phase formation; Particle size

## 1. Introduction

Earlier works concerning the columbite-type nickel niobate ($NiNb_2O_6$) have been directed towards determining microwave dielectric, magnetic and optical properties [1,2]. Recently, this compound is also a potential material for the development of wireless communication and lithium batteries [3,4]. Moreover, it is well established as a key precursor for the successful preparation of single-phase ferroelectric perovskite $Pb(Ni_{1/3}Nb_{2/3})O_3$ (PNN)-based ceramics, which is becoming increasingly important for multilayer ceramic capacitor, electrostrictor, ultrasonic transducer and actuator applications [5,6].

There has been a great deal of interest in the preparation of single-phase PNN powders as well as in the sintering and electrical properties of PNN-based ceramics [7–9]. In general, the constituents NiO and $Nb_2O_5$ are first mixed and reacted together to form $NiNb_2O_6$, prior to mixing and reacting with PbO in the second step of calcination at elevated temperature. Interestingly, this mixed oxide route has been employed with minor modifications in the synthesis of $NiNb_2O_6$ itself [8,9]. However, powders prepared by a mixed oxide route have spatial fluctuations in their compositions. The extent of the fluctuation depends on the characteristics of the starting powders as well as on the processing schedule.

Recently, the studies of nanoparticles are also a very attractive field [10,11]. The evolution of a method to produce nanopowders of precise stoichiometry and desired properties is complex, depending on a number of variables such as starting materials, processing history, temperature, etc. The advantage of using mechanical milling for preparation of nanosized powders lies in its ability to produce mass quantities of powders in the solid-state using simple equipment and low-cost starting precursors [11]. Although some research has been done in the preparation of $NiNb_2O_6$ powders via a vibro-milling technique [8,12], to our knowledge a systematic study regarding the influence of milling time on the preparation of $NiNb_2O_6$ powders has not yet been reported. Thus, in the present study, the effect of milling time on phase formation and particle size of nickel niobate powders was investigated in this connection. The potential of the vibro-milling technique as a simple method to obtain usable quantities of single-phase nickel niobate powders at low temperature and with nanosized particles was also examined.

## 2. Experimental

The starting materials were commercially available nickel oxide, NiO (JCPDS file number 73-1519) and niobium oxide, $Nb_2O_5$ (JCPDS file number 30-873) (Aldrich, 99.9% purity).

* Corresponding author. Tel.: +66 53 943 376; fax: +66 53 943 445.
*E-mail address:* suponananta@yahoo.com (S. Ananta).

0921-5107/$ – see front matter © 2008 Elsevier B.V. All rights reserved.
doi:10.1016/j.mseb.2008.01.006

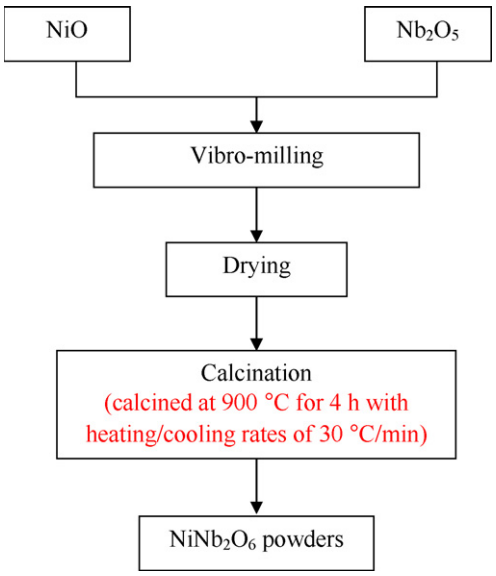



Fig. 1. Preparation route for $NiNb_2O_6$ powders.

The two oxide powders exhibited an average particle size in the range of 3.0–5.0 μm. $NiNb_2O_6$ powders were synthesized by the solid-state reaction of these raw materials. Powder-processing (Fig. 1) was carried out in a manner similar to that employed in our previous works [11–13]. A vibratory laboratory mill (McCrone Micronizing Mill) powered by a 1/30 HP motor was employed for preparing the stoichiometric $NiNb_2O_6$ powders. The grinding vessel consists of a 125 ml capacity polypropylene jar fitted with a screw-capped, gasketless, polythene closure. The jar is packed with an ordered array of identical, cylindrical, grinding media of polycrystalline corundum (instead of employing zirconia media under alcohol [8,9]). A total of 48 milling media cylinder with a powder weight of 20 g was kept constant in each batch. The milling operation was carried out in isopropanal inert to the polypropylene jar. Various milling times ranging from 0.5 to 35 h were selected in order to investigate the phase formation characteristic of nickel niobate and the smallest particle size. After drying at 120 °C for 2 h, the reaction of the uncalcined powders taking place during heat treatment was investigated by differential thermal analysis technique (DTA, Shimadzu) at a heating rate of 10 °C/min in air from room temperature up to 900 °C. Based on the DTA result and literature [8,12], the mixture was calcined at 900 °C (in closed alumina crucible) for 4 h with heating/cooling rates of 30 °C/min.

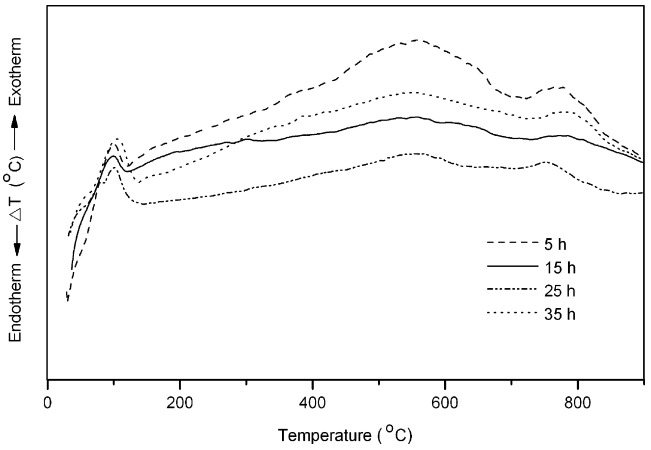



Fig. 2. DTA analysis for the mixture of NiO and $Nb_2O_5$ powders milled at different times.

All powders were subsequently examined by room temperature X-ray diffraction (XRD; Siemens-D500 diffractometer), using Ni-filtered Cu Kα radiation to identify the phases formed and optimum milling time for the production of $NiNb_2O_6$ powders having the smallest particle size. The relative amount of columbite and secondary phases was determined from XRD patterns of the samples by measuring the major characteristic peak intensities for the columbite (3 1 1) or $I_P$ and secondary (+) phases or $I_S$. The following qualitative equation was used [14].

$$\text{Columbite phase (wt\%)} = \frac{I_P}{I_P + I_S} \times 100 \quad (1)$$

The crystalline lattice constants and average particle size were also estimated from XRD patterns [15]. The particle size distributions of the powders were determined by laser diffraction technique (DIAS 1640 laser diffraction spectrometer) with the particle sizes and morphologies of the powders observed by scanning electron microscopy (JEOL JSM-840A SEM). The particle sizes of $NiNb_2O_6$ powders milled at different times obtained from different measuring techniques are provided in Table 1.

## 3. Results and discussion

The DTA results for the powders milled at different times are compared and displayed in Fig. 2. In general, similar thermal characteristics are observed in all cases, consistent with

Table 1
Effect of milling time on the phase formation and particle size of $NiNb_2O_6$ powders measured by different techniques

| Milling time (h) | Columbite phase (wt%) | XRD | | | | SEM | | Laser scattering | |
|---|---|---|---|---|---|---|---|---|---|
| | | *A* (nm) | *a* (Å) | *b* (Å) | *c* (Å) | *D* (nm) | *P* (nm) | *D* (nm) | *P* (nm) |
| 0.5 | 87 | 173.40 | 15.72 | 4.96 | 4.98 | 900 | 560–1400 | 3200 | 400–5000 |
| 1 | 92 | 93.69 | 15.50 | 5.00 | 5.02 | 820 | 500–1300 | 2500 | 320–5000 |
| 5 | 100 | 73.12 | 15.01 | 5.24 | 5.02 | 708 | 467–1160 | 1500 | 250–3000 |
| 15 | 100 | 59.44 | 14.71 | 5.32 | 5.00 | 545 | 167–949 | 450 | 250–750 |
| 25 | 100 | 34.54 | 15.64 | 4.99 | 4.99 | 120 | 32–164 | 240 | 40–750 |
| 35 | 100 | 20.57 | 15.52 | 5.05 | 5.00 | 250 | 63–570 | 690 | 45–6000 |

*A*: crystallite size; *a*, *b*, and *c*: lattice parameters; *D*: average particle size; *P*: particle size range or distribution.

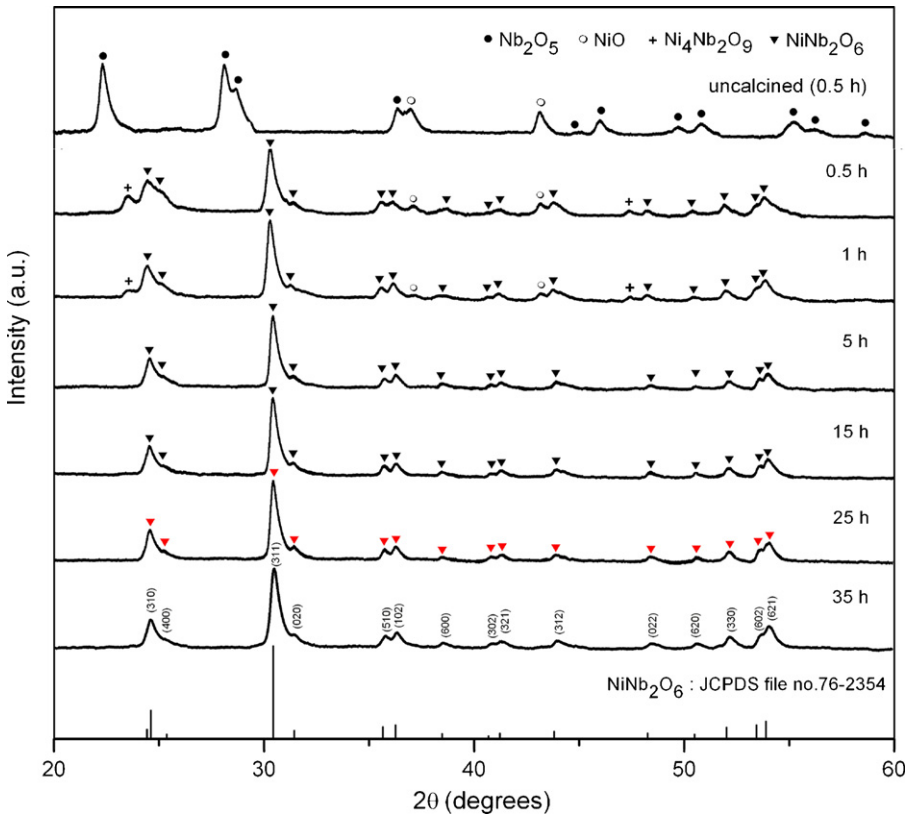



Fig. 3. XRD patterns of $NiNb_2O_6$ powders milled at different times (calcined at 900 °C for 4 h with heating/cooling rates of 30 °C/min).

our previous work [12]. In the temperature range from room temperature to ~150 °C, all samples show both exothermic and endothermic peaks in the DTA curves. These observations can be attributed to the decomposition of the organic species originating from the milling process [11–13]. Increasing the temperature up to ~900 °C, the solid-state reaction occurred between NiO and $Nb_2O_5$ [12,16]. The broad exotherm with several peaks in the DTA curves represents that reaction, which has a maximum at ~550 and 750 °C. The slightly different temperature, intensities and shapes of the thermal peaks for the powders are probably related to the different sizes of the powders subjected to different milling times [9,11].

To further study the effect of milling time on phase formation, each of the powders milled for different times was calcined at 900 °C for 4 h in air, followed by phase analysis using XRD. For the purpose of estimating the concentrations of the phase present, Eq. (1) has been applied to the powder XRD patterns obtained, as given in Table 1. As shown in Fig. 3, for the uncalcined powder subjected to 0.5 h of vibro-milling, only X-ray peaks of precursors NiO (◯) and $Nb_2O_5$ (●) are present, indicating that no reaction had been initiated during the milling process. However, after calcination, it is seen that the columbite-type $NiNb_2O_6$ becomes the predominant phase in the powder milled for 0.5 h, indicating that the reaction has occurred to a considerable extent. It is seen that traces of unreacted NiO and $Nb_2O_5$ precursors and corundum-type $Ni_4Nb_2O_9$ earlier reported by the authors [16] have been found along with the $NiNb_2O_6$ parent phase at a milling time of 1 h or less. This observation could be attributed mainly to the poor mixing capability under short milling time, similar with other work [11–13]. With milling time of 5 h or more, it is apparent that a single-phase columbite $NiNb_2O_6$ (yield of 100% within the limitations of the XRD technique) was found to be possible after the same calcination process was applied.

In general, the strongest reflections found in the majority of these XRD patterns indicate the formation of the $NiNb_2O_6$. These can be matched with JCPDS file number 76-2354 for the orthorhombic phase, in space group *Pbcn* (no. 60) with cell parameters $a = 1403$ pm, $b = 568.7$ pm and $c = 503.3$ pm [17], consistent with other works [12,18]. It should be noted that no

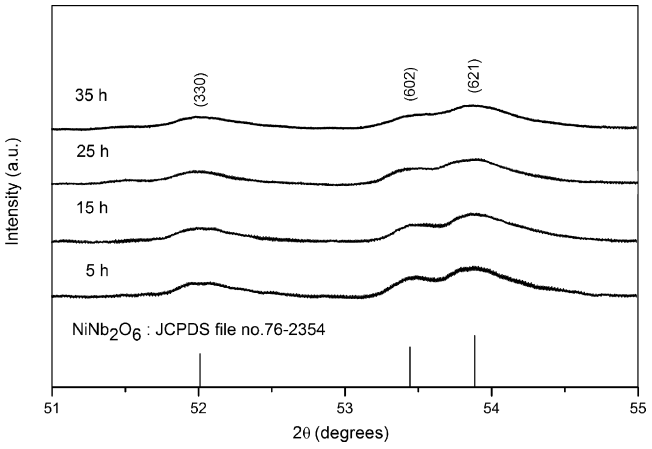



Fig. 4. Enlarged zone of XRD patterns showing (6 0 2) and (6 2 1) peaks broadening as a function of milling times.

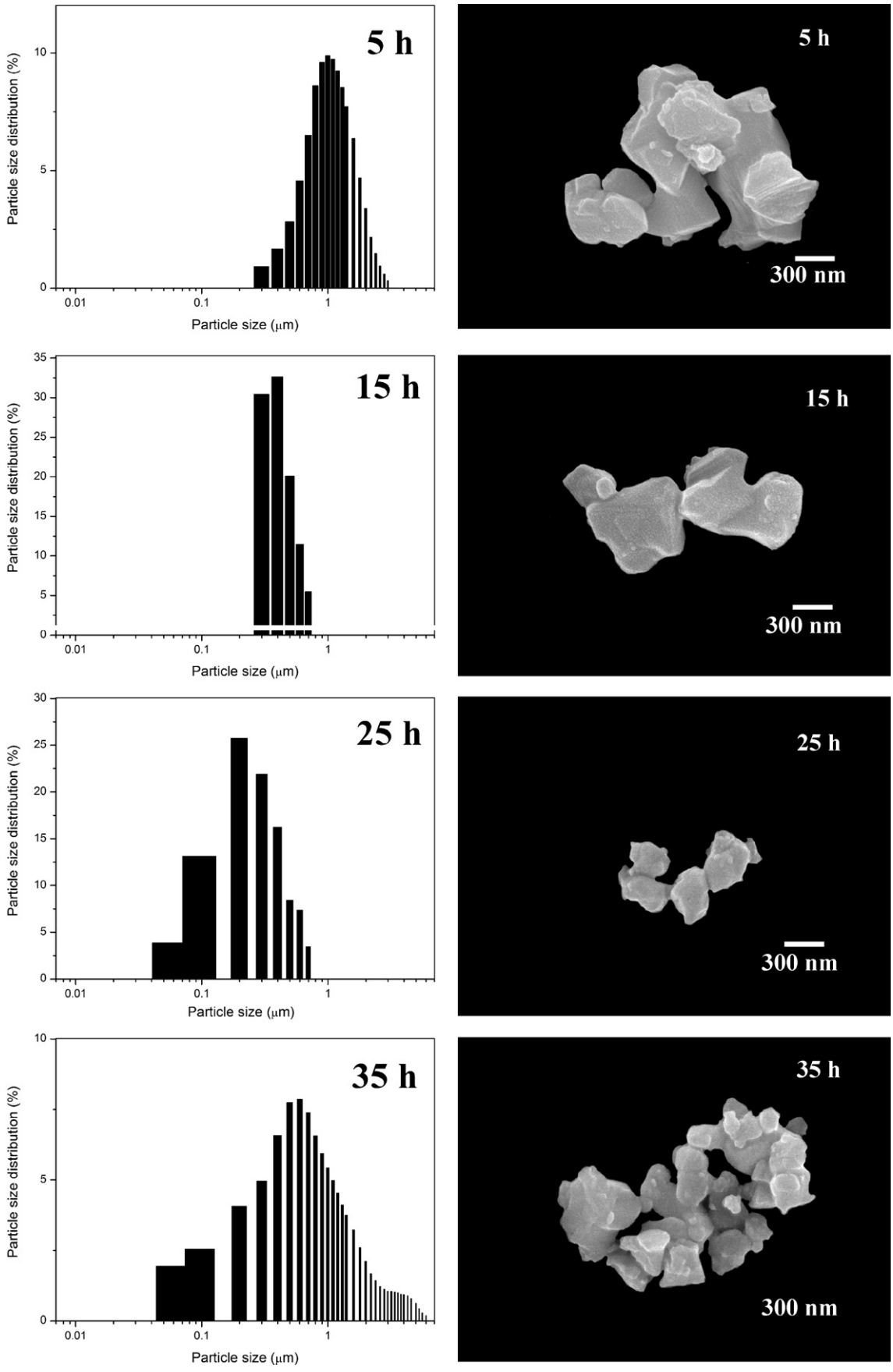



Fig. 5. SEM micrographs and particle size distribution of $NiNb_2O_6$ powders milled at different times.

evidence for the introduction of impurity due to wear debris from the milling process was observed in any of the calcined powders (within the milling periods of 0.5–35 h), demonstrating the effectiveness of the vibro-milling technique for the production of high purity $NiNb_2O_6$ nanopowders, without any introduction of excess NiO [9]. Moreover, it has been observed that with increasing milling time, all diffraction lines broaden, e.g. (6 0 2) and (6 2 1) peaks at $2\theta \sim 53$–$54^\circ$ (Fig. 4), an indication of a continuous decrease in particle size and of the introduction of lattice strain. These observations indicate that the prolonged milling treatment affects the particle size and evolution of crystallinity of the phase formed (Table 1), in good agreement with other similar system [14,19]. For $NiNb_2O_6$ powders, the longer the milling time, the finer is the particle size, down to a certain level. The results suggest that the steady state of the vibro-milling is attained at ~25 h of milling. Moreover, it is worthy to note that, in this condition, the mean crystalline size is close to ~35 nm. Also, the relative intensities of the Bragg peaks for the powders tend to decrease with the increase of milling time. However, it is well documented that, as Scherer's analysis provides only a measurement of the extension of the coherently diffracting domains, the particle sizes estimated by this method can be significantly under estimated [11,20]. In addition to strain, factors such as dislocations, stacking faults, heterogeneities in composition and instrumental broadening can contribute to peak broadening, making it almost impossible to extract a reliable particle size solely from XRD [15,21].

In this connection, scanning electron microscopy was also employed for particle size measurement (Table 1). The morphological evolution of the powders and their corresponding particle size distributions as a function of milling time were also revealed, as illustrated in Fig. 5. At first sight, the morphological characteristic of $NiNb_2O_6$ powders with various milling times is similar for all cases. In general, the particles are agglomerated and basically irregular in shape, with a substantial variation in particle sizes. The powders consist of primary particles nanometers in size. Increasing the milling time over the range 5–35 h, the average size of the $NiNb_2O_6$ particles decreases significantly, until at 25 h, the smallest particle size (estimated from SEM micrographs to be ~32 nm) is obtained. However, it is also of interest to point out that larger particle size was obtained for a milling time longer than 25 h. This may be attributed to the occurrence of hard agglomeration with strong inter-particle bonds within each aggregate resulting from dissipated heat energy of prolong milling [11,22]. Fig. 5 also illustrates that vibro-milling has slightly changed the shape of the particles which become more rounded at long milling times. At the same time, the particle size is reduced. Fracture is considered to be the major mechanism at long milling times. As shown in Fig. 5, after milling times of 5, 15 and 25 h, the powders exhibit a single peak covering the size ranging from 40 to 3000 nm. With milling time of 25 h, a uniform particle size distribution with a much lower degree of particle agglomeration (<1 μm) is found. However, upon further increase of milling time up to 35 h, a bimodal distribution curve with peak broadening between 45 and 6000 nm is observed. First is a monomodal distribution corresponding to the primary size of the $NiNb_2O_6$ particles. The second group (peak) is believed to arise mainly from particle agglomeration. The results obtained for $NiNb_2O_6$ powders milled for different times via different techniques are also compared in Table 1. Variations in these data may be attributed mainly to the formation of hard and large agglomerations, as observed in the SEM results.

In this work, it is seen that the optimum milling time for the production of the smallest nanosized high purity $NiNb_2O_6$ powder was found to be at 25 h. The finding of this investigation indicates a strong relationship between the vibro-milling process and the yield of $NiNb_2O_6$ nanopowders. However, in case of the vibro-milling technique, other factors such as the milling speed, milling scale and type of milling media also need to be taken into account.

## 4. Conclusions

The results infer that the milling time influences not only the development of the solid-state reaction of nickel niobate phase but also the particle size and morphology. The resulting $NiNb_2O_6$ powders have a range of particle size, depending on vibro-milling times. Production of a single-phase nickel niobate nanopowder can be successfully achieved by employing a combination of 25 h milling time and calcination condition of 900 °C for 4 h, with heating/cooling rates of 30 °C/min.

## Acknowledgements

This work was supported by the Thailand Research Fund (TRF), the Commission on Higher Education (CHE), the National Nanotechnology Center (NANOTEC) through its program of Center of Excellence Network and the Faculty of Science, Chiang Mai University.

## References

[1] R.C. Pullar, J.D. Breeze, N.M. Alford, J. Am. Ceram. Soc. 88 (2005) 2466.
[2] C. Heid, H. Weitzel, F. Bourdarot, R. Calemczuk, T. Vogt, H. Fuess, J. Phys. Condens. Mater. 8 (1996) 10609.
[3] D. Prabhakaran, F.R. Wondre, A.T. Boothroyd, J. Cryst. Growth 250 (2003) 72.
[4] A.M. Cruz, N.L. Alcaraz, A.F. Fuentes, L.M. Torres-Martinez, J. Power Sources 81/82 (1999) 255.
[5] A.J. Moulson, J.M. Herbert, Electroceramics, 2nd ed., Wiley, Chichester, 2003.
[6] Y. Xu, Ferroelectric Materials and their Applications, North-Holland, New York, 1991.
[7] T. Zhong, Y.D. Hou, M.K. Zhu, B.C. Xu, J.L. Tang, J.B. Liu, H. Wang, H. Yan, Mater. Lett. 59 (2005) 1169.
[8] E.F. Alberta, A.S. Bhalla, Mater. Lett. 54 (2002) 47.
[9] C.H. Lu, H.J. Hwang, Ceram. Int. 22 (1996) 373.
[10] N. Setter, R. Waser, Acta Mater. 48 (2000) 151.
[11] R. Wongmaneerung, R. Yimnirun, S. Ananta, Mater. Lett. 60 (2006) 1447.
[12] O. Khamman, R. Yimnirun, S. Ananta, Mater. Lett. 61 (2007) 639.
[13] A. Udomporn, S. Ananta, Mater. Lett. 58 (2004) 1154.
[14] S. Ananta, Mater. Lett. 58 (2004) 2781.
[15] H. Klug, L. Alexander, X-Ray Diffraction Procedures for Polycrystalline and Amorphous Materials, 2nd ed., Wiley, New York, 1974.
[16] O. Khamman, R. Yimnirun, S. Ananta, Mater. Lett. 61 (2007) 2565–2570.

[17] Powder Diffraction File no. 76-2354. International Centre for Diffraction Data, Newtown Square, PA, 2000.
[18] J. Ye, Z. Zou, A. Matsushita, Int. J. Hydrogen Energy 28 (2003) 651.
[19] A. Ngamjarurojana, O. Khamman, R. Yimnirun, S. Ananta, Mater. Lett. 60 (2006) 2867.
[20] C. Suryanarayana, Prog. Mater. Sci. 46 (2001) 1.
[21] A. Revesz, T. Ungar, A. Borbely, J. Lendvai, Nanostruct. Mater. 7 (1996) 779.
[22] P.C. Kang, Z.D. Yin, O. Celestine, Mater. Sci. Eng. A-Struct. 395 (2005) 167.

# Giant dielectric properties of $CaCu_3Ti_4O_{12}$/(Li,Ti)-doped NiO composites subjected to postsintering annealing and compressive stress

Prasit Thongbai,[1] Santi Maensiri,[1,a)] Teerapon Yamwong,[2] and Rattikorn Yimnirun[3]
[1]*Department of Physics, Faculty of Science, Khon Kaen University, Khon Kaen 40002, Thailand*
[2]*National Metals and Materials Technology Center (MTEC), Thailand Science Park, Pathumthani 12120, Thailand*
[3]*Department of Physics, Faculty of Science, Chiang Mai University, Chiang Mai 50200, Thailand*

(Received 22 August 2007; accepted 29 March 2008; published online 9 June 2008)

We report the effects of postsintering annealing in argon and compressive prestress on the giant dielectric properties of $CaCu_3Ti_4O_{12}$–$Li_{0.3}Ti_{0.02}Ni_{0.68}O$ composites in the frequency range from 100 Hz to 1 MHz. After postsintering annealing, all compounds investigated still display a Debye-like relaxation, which can be interpreted based on the Maxwell–Wagner model. The dielectric behavior and the effect of compressive prestress of $CaCu_3Ti_4O_{12}$ and $CaCu_3Ti_4O_{12}$–$Li_{0.3}Ti_{0.02}Ni_{0.68}O$ after annealing are closely related to the oxygen vacancies in the grain boundaries. © *2008 American Institute of Physics*. [DOI: 10.1063/1.2937238]

## I. INTRODUCTION

Giant dielectric ceramics with good thermal stability and Ba/Pb-free have recently attracted much attention due to their potential applications in microelectronics such as capacitors and memory devices. Giant-permittivity dielectric response with weakly temperature-dependent permittivity has been observed in $CaCu_3Ti_4O_{12}$ (CCTO) ($\varepsilon' \sim 10^4$ for polycrystalline ceramics and $\varepsilon' \sim 10^5$ for single crystals),[1–3] NiO-based ceramic ($\varepsilon' \sim 10^4$–$10^5$),[4–8] $Ba_4YMn_3O_{11.5}$ ($\varepsilon' \sim 10^4$),[9] and CuO ($\varepsilon' \sim 10^4$).[10] Most recently, our group[11] reported the giant values of $\varepsilon' \sim 10^5$ observed in polycrystalline $CaCu_3Ti_4O_{12}$ ceramics reinforced with 10 mol % of 39 nm $Li_{0.3}Ti_{0.02}Ni_{0.68}O$ (LTNO) nanoparticles. The dielectric behavior of these composites exhibits Debye-like relaxation, which can be explained based on the Maxwell–Wagner model, and the dielectric dispersions of the composites arise from the internal barrier layer capacitor (IBLC) effect.[12,13]

Interestingly, the colossal dielectric constant of $\sim 10^6$ at room temperature can also be obtained in $CaCu_3Ti_4O_{12}$ after annealing in argon at 1000 °C for 6 h, and this enhancement was attributed to the increase in concentration of oxygen vacancies and hence charge carriers.[14] The influence of postsintering annealing on dielectric properties of $CaCu_3Ti_4O_{12}$ was further investigated by Wang and Zhang.[15,16] They showed that the annealing treatment on $CaCu_3Ti_4O_{12}$ in reducing (nitrogen) and oxidizing (oxygen) atmospheres has strong effects on dielectric properties of the $CaCu_3Ti_4O_{12}$. These results support the results reported in Ref. 14 and strongly suggest that the concentration of oxygen plays an important role in the dielectric properties of $CaCu_3Ti_4O_{12}$. In addition to its interesting dielectric property, $CaCu_3Ti_4O_{12}$ has remarkably strong nonlinear current-voltage characteristics without the addition of dopants.[13] These excellent properties render this material particularly attractive for a wide range of applications. However, in some practical applications, dielectric ceramics may be subjected to mechanical or thermal stresses causing changes on their properties. A prior knowledge of how the material properties change under different load conditions is therefore crucial for proper design of a device and for suitable selection of materials for a specific application. Despite that fact, material constants used in many design calculations are often obtained from a stress-free measuring condition, which in turn may lead to incorrect or inappropriate device designs.

Most recently, we observed that postsintering annealing in argon for 5 h leads to a significant increase in $\varepsilon'$ for $CaCu_3Ti_4O_{12}$ ceramic, which is closely related to the oxygen vacancies.[17] The dielectric properties of the argon-annealed samples were also found to change significantly with the applied compressive stress (the absolute change can reach 25% at a maximum stress of 130 MPa), which could be explained by the stress-induced aging mechanism.[17] The stress dependence of the permittivity in $CaCu_3Ti_4O_{12}$-based ceramics has not been thoroughly studied. Herein, we investigate the influences of the postsintering annealing in argon and compressive prestress on the giant dielectric properties of the $(1-x)CaCu_3Ti_4O_{12}\cdot xLi_{0.3}Ti_{0.02}Ni_{0.68}O$ (CCTO-LTNO) composites sintered in air at 1100 °C for 16 h.

## II. EXPERIMENT

The sample preparations of $(1-x)CaCu_3Ti_4O_{12}\cdot xLi_{0.3}Ti_{0.02}Ni_{0.68}O$ ($x=0$, 0.1, 0.25, and 0.5) composites are given in our previous publication.[11] The dimensions of the samples were ~12 mm in diameter and ~3 mm in height. Here, we assign symbols of CCTO, 10%LTNO, 25%LTNO, and 50%LTNO, for the sintered samples of $(1-x)CaCu_3Ti_4O_{12}\cdot xLi_{0.3}Ti_{0.02}Ni_{0.68}O$, with $x=0$, 0.1, 0.25, and 0.5, respectively. A postsintering annealing process was carried out in flowing argon (99.999% purity) at 1000 °C for 5 h, and we assign symbols of CCTO-Ar, 10%LTNO-Ar, 25%LTNO-Ar, and 50%LTNO-Ar, for the sintered samples of CCTO, 10%LTNO, 25%LTNO, and 50%LTNO, after argon annealing. The sintered ceramics were characterized by x-ray diffraction (XRD) (Philips PW3710, The Netherlands)

a)Electronic address: santimaensiri@gmail.com and sanmae@kku.ac.th.

 © 2008 American Institute of Physics

Author complimentary copy. Redistribution subject to AIP license or copyright, see http://jap.aip.org/jap/copyright.jsp

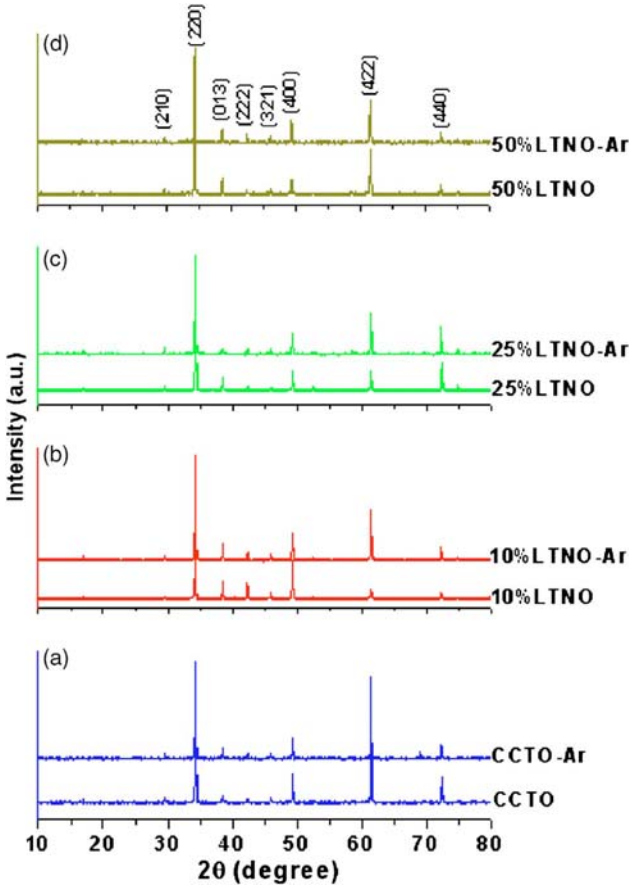



FIG. 1. (Color online) XRD patterns of the sintered materials of CCTO and CCTO-LTNO before and after annealing at 1000 °C for 5 h under flowing argon. (a) CCTO, (b) 10%LTNO, (c) 25%LTNO, and (d) 50%LTNO.

and scanning electron microscopy (SEM) (LEO 1450VP, UK). The frequency and temperature dependences of dielectric properties for the as-sintered samples were measured using a Hewlett Packard 4194A impedance gain phase analyzer. Silver paste was used as the electrode, and it was coated on both surfaces of the sample and dried overnight. The dielectric properties of the samples after postsintering annealing were measured under the influence of the compressive stress through spring-loaded pins connected to an inductance capacitance impedance (LCZ) meter (Hewlett Packard 4276A) at the frequency of 100 kHz at room temperature (25 °C). The details of the system are described elsewhere.[18]

## III. RESULTS AND DISCUSSION

Figure 1 shows XRD patterns of the sintered ceramics before and after postsintering annealing, confirming only a main phase of $CaCu_3Ti_4O_{12}$ in all the samples with no diffraction peaks of LTNO and other possible impurities such as $TiO_2$, CuO, $CaTiO_3$, and $NiTiO_3$. The values of lattice parameter $a$ calculated from XRD spectra are shown in Table I; these values are close to 0.7391 nm of that reported in literature.[1] Higher concentrations of LTNO did not result in any noticeable shift in lattice parameter, suggesting that the added LTNO is most likely present in the microstructure either in the grain boundaries or as a second phase. Moreover,

TABLE I. Lattice parameter $a$ and activation energies ($E_a$) for CCTO-LTNO ceramics before and after postannealing sintering.

| | Lattice parameter (nm) | | Activation energy (eV) | |
|---|---|---|---|---|
| Materials | Before | After | Before | After |
| CCTO | 0.7385 | 0.7391 | 0.112 | 0.112 |
| 10%LTNO | 0.7385 | 0.7391 | 0.112 | 0.112 |
| 25%LTNO | 0.7388 | 0.7389 | 0.116 | 0.112 |
| 50%LTNO | 0.7387 | 0.7392 | 0.116 | 0.112 |

the values of lattice parameter of the CCTO-LTNO composites after postsintering annealing also did not result in any noticeable shift in lattice parameter. Their values show little change, which is comparable to the values of samples before postsintering. These results indicate that the postannealing sintering treatments did not change the crystal structure—the structure of all samples remains cubic and centric.

Microstructures of the sintered composites ceramics were revealed by SEM. The samples were fractured in order to observe their composite morphologies. Figures 2(a)–2(d) show SEM micrographs of the sintered samples revealing polycrystalline grains with estimated grain sizes of $9.0 \pm 1.9$, $8.8 \pm 1.7$, $12.4 \pm 2.8$, and $13.4 \pm 2.7$ $\mu$m for CCTO, 10%LTNO, 25%LTNO, and 50%LTNO, respectively. No change in grain size of the samples before and after annealing was observed. It is important to note that the thickness of grain boundary cannot be accurately measured by SEM technique. However, the thickness of grain boundary was estimated to about 50–200 nm for CCTO ceramic. It is seen from the backscattered electron images of the fracture surfaces of the samples [Figs. 2(e)–2(h)] that a large portion of porosity increases with increasing amount of LTNO, as can be clearly observed in the microstructures of 25%LTNO and 50%LTNO. The LTNO nanoparticles distribute inhomogeneously and form clusters or agglomerates and locate between grain boundaries of CCTO matrix (indicated by arrows). It is noted that no diffraction peaks of LTNO and the other possible layer is impurities were detected by XRD, but the inhomogeneous distribution of LTNO was observed by the backscattered SEM images of the fracture surfaces of the CCTO-LTNO composites. This indicates that the outmost layer of the composites is LTNO and other possible impurity deficient. Similar observation was reported for $CaCu_3Ti_4O_{12}$/Ag composites having the Ag deficient in the outmost layer and Ag rich in the inner part of the composites.[19]

Figure 3 shows the real ($\varepsilon'$) and imaginary ($\varepsilon''$) parts of dielectric dispersion for the Ar-annealed samples, measured at −50 °C over the frequency range of 100 Hz–1 MHz. It is clearly seen from Fig. 3(a) that all of the samples exhibit the giant dielectric constant ($\varepsilon' \sim 1 \times 10^4 - 3.5 \times 10^4$) below the relaxation frequency ($f < 100$ kHz). The drastic decrease in the real parts of dielectric spectra of all samples is seen in the frequency range above 20 kHz, accompanied by the appearance of corresponding peaks in the imaginary parts of dielectric spectra, as shown in Fig. 3(b). Moreover, the relaxation peak in all samples shifts to higher frequency at a higher temperature (not shown). The dielectric behavior of all

Author complimentary copy. Redistribution subject to AIP license or copyright, see http://jap.aip.org/jap/copyright.jsp

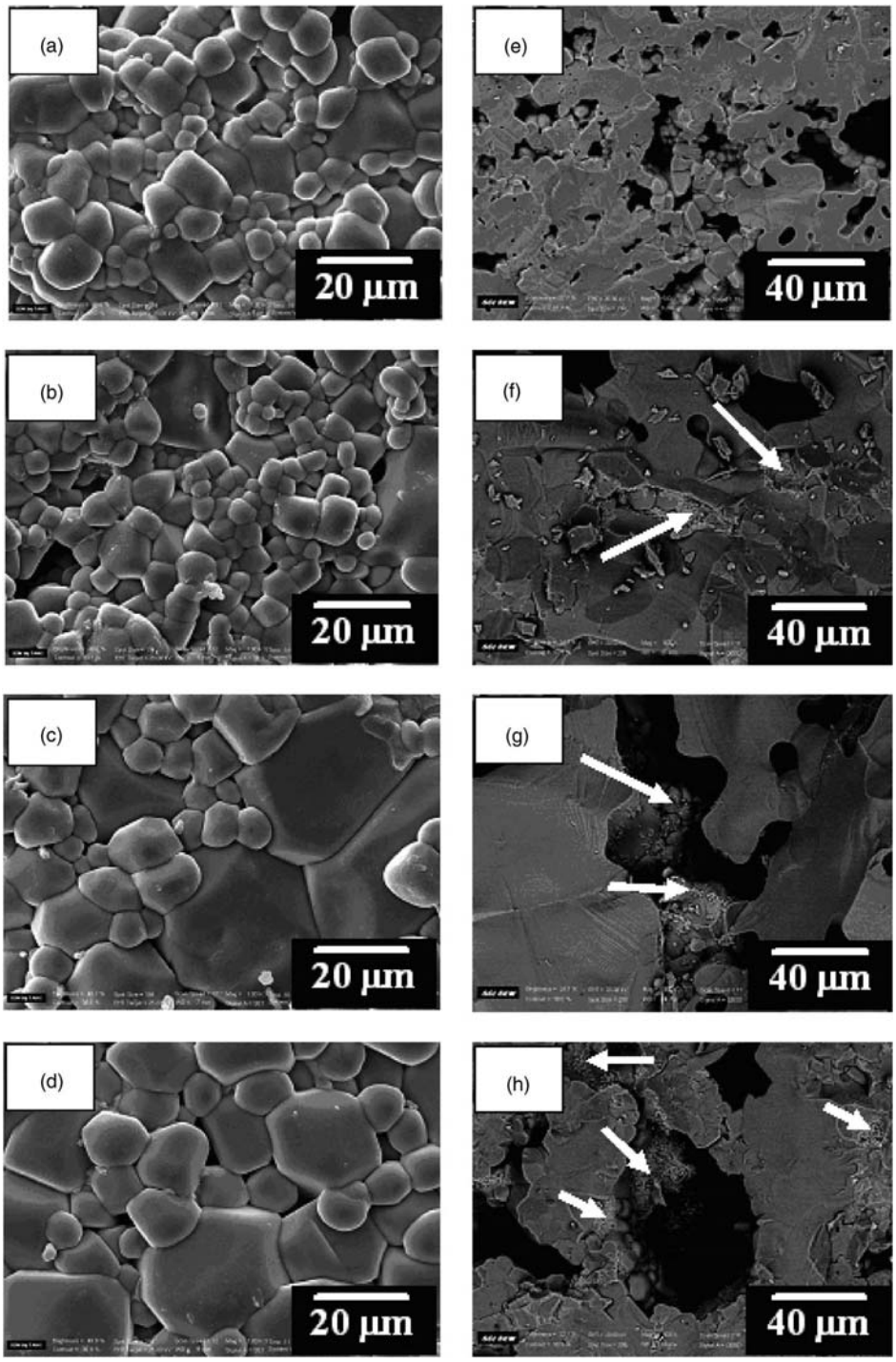



FIG. 2. SEM micrographs of the ceramic samples sintered in air at 1100 °C for 16 h: (a) CCTO, (b) 10%LTNO, (c) 25%LTNO, and (d) 50%LTNO; (e)-(d) show the backscattered SEM micrograph of fracture surface of CCTO, 10%LTNO, 25%LTNO, and 50%LTNO, respectively.

samples after postsintering annealing still exhibits a Debye-like relaxation similar to that of the as-sintered samples. The dielectric behavior of the nonannealed and annealed samples can be interpreted based on the Maxwell–Wagner model and their dielectric dispersions arise from the IBLC effect.[11,17] This behavior is also similar to that observed in $CaCu_3T_{i4}O_{12}$ ceramics reported in literatures.[2,17,20–22]

The $E_a$ values of the low-temperature relaxation determined from the slopes of Arrhenius plot of log $\tau$ vs $1/T$ [the inset of Fig. 3(b)] were obtained to be ~0.112 eV for all of the Ar-annealed samples. Annealing in argon results in a slight decrease in $E_a$ values of the 25%LTNO-Ar and 50%LTNO-Ar, whereas the $E_a$ values of CCTO-Ar and 10%LTNO-Ar do not change with annealing treatment and show the same value of 0.112 eV. This value is comparable to the reported values of 0.067,[23] 0.08,[12,24] 0.093,[25] 0.059–0.076,[26] and 0.084–0.132 eV (Refs. 20 and 22) for the grains of $CaCu_3T_4O_{12}$. The $E_a$ values are also tabulated in Table I. Based on the Maxwell–Wagner model, it is seen that the $E_a$ of the dielectric process is approximately equal to that of the grain conduction process.[17,21] Thus, the postsintering annealing does not change the electrical properties of the part of grains in CCTO matrix.

Figure 4 shows the dielectric constant ($\varepsilon'$) and loss tan-

Author complimentary copy. Redistribution subject to AIP license or copyright, see http://jap.aip.org/jap/copyright.jsp

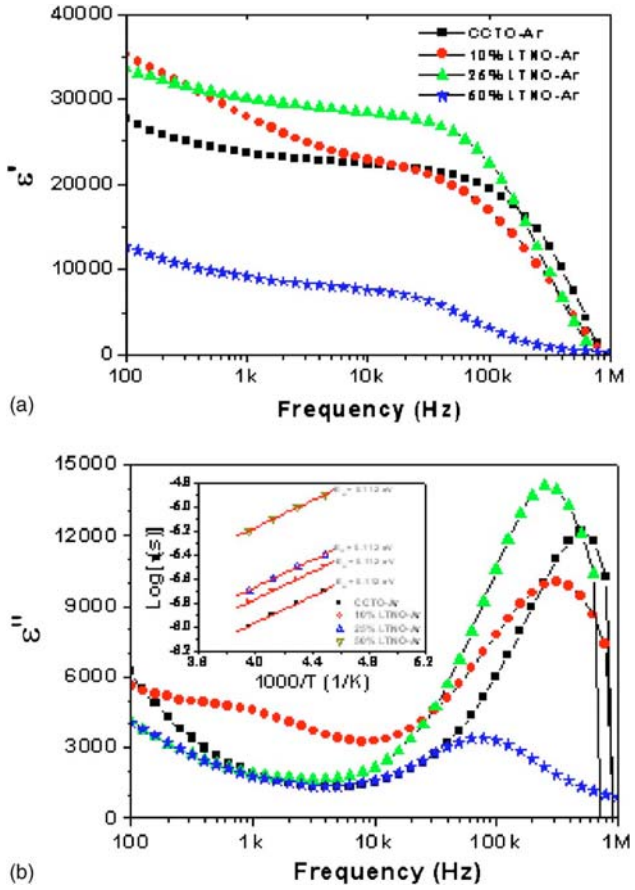



FIG. 3. (Color online) The frequency dependence of dielectric dispersions of CCTO ceramic and CCTO-LTNO composites after postsintering annealing in argon at 1000 °C measured at −50 °C. (a) the real part $\varepsilon'$ and (b) the imaginary part $\varepsilon''$. The inset displays the Arrhenius plot of log $\log(\tau)$ vs $1000/T$.

gent (tan $\delta$) of CCTO and CCTO-Ar, 25%LTNO, and 25%LTNO-Ar. Figure 4(a) shows a significant increase in $\varepsilon'$ at low frequency for the CCTO after postsintering annealing (CCTO-Ar), accompanied by the increase in tan $\delta$ at the same frequency range. At high frequency, the $\varepsilon'$ value of CCTO-Ar gradually decreases to the $\varepsilon'$ value of CCTO. For the 25%LTNO and 25%LTNO-Ar [Fig. 4(b)], the $\varepsilon'$ values of these composite samples show a little change after annealing. The dramatic increase in $\varepsilon'$ for CCTO-Ar is closely related to the oxygen vacancies, as previously reported.[17] Annealing the $CaCu_3Ti_4O_{12}$ sample in argon atmosphere at high temperature would increase the concentration of the oxygen vacancies and thus increase $\varepsilon'$ values, as obtained in the nitrogen-annealed $CaCu_3Ti_4O_{12}$ reported by Wang and Zhang.[16]

At present, the extrinsic effect of IBLC is widely accepted as the origin of the giant dielectric response in both (Li, Ti)-doped NiO (Refs. 4 and 5) and $CaCu_3Ti_4O_{12}$.[12,13,15–17,20–27] However, many aspects for the origin of semiconducting grains and insulating grain boundary regions for CCTO ceramics remain unclear. Li *et al.*[28] proposed that the grain and grain boundary regions in CCTO ceramics may consist of the same phase but with slightly different compositions. Sinclair *et al.*[12] reported that heat treatment of CCTO pellets in $N_2$ at 1000 °C caused a significant change in electrical properties at room temperature, in which the resistance of grain boundary ($R_{gb}$) decreased by two orders of magnitude but the resistance of grain remained unchanged. They proposed a plausible explanation that the semiconductivity of the grains arises from a small but significant loss of oxygen during ceramic processing in air at high temperatures, whereas furnace cooling allows reoxidation to occur along the grain boundary regions, which converts these regions into insulators. From this proposal, it implied that the grain boundary region (the shell of grain) of CCTO ceramic is the nonoxygen vacancy region. Interestingly, the low-$R_{gb}$ value of the sample after heat treatment in $N_2$ can be reverted to the high-$R_{gb}$ value of the as sample by annealing in oxygen.[29] From these results, it is strongly believed that the electrical properties of grain boundary have a close relation to the stoichiometry of oxygen at this region. Therefore, the difference in dielectric properties for our CCTO and CCTO-Ar is greatly affected by the oxygen vacancies at the grain boundary. These indicate that an oxygen at the grain boundary for our CCTO ceramic has been oxidized during annealing treatment in argon, and the reoxidation process during furnace cooling has been limited by annealing in this reducing atmosphere. Hence, the thickness of grain boundary layers for the CCTO-Ar has reduced to a thinner layer compared to CCTO.

In our previous work,[17] the dielectric behavior of CCTO has been interpreted based on the Maxwell–Wagner model. From this model, Liu *et al.*[21] estimated the dielectric constant of bulk CCTO, i.e., $\varepsilon'_s \approx \varepsilon_{gb}(d_g+d_{gb})/d_{gb}$, where $\varepsilon_{gb}$ is the dielectric constant of grain boundary layer, and $d_g$ and $d_{gb}$ are the thicknesses of grain and grain boundary layers, respectively. Therefore, the increase in the dielectric constant of CCTO-Ar is possibly due to the decrease in its $d_{gb}$. Bueno *et al.*[30] used dielectric spectroscopy to examine CCTO to demonstrate that at low frequency, the contribution of the grain boundary can be separated from the total dielectric response. At present, we propose that the increment of $\varepsilon'$ for CCTO-Ar at low frequency is contributed by grain boundaries, which arise from the loss of oxygen and limited reoxidation during furnace cooling. This suggests that the annealing treatment modifies the defect equilibrium at this region. At high frequency, the $\varepsilon'$ of CCTO-Ar slightly changes, as compared to the $\varepsilon'$ of CCTO. This corresponds to the unchanged value of $E_a$ for the grains of the samples before and after postsintering annealing. In contrast, the values of $\varepsilon'$ and tan $\delta$ for the 25%LTNO-Ar are unchanged with Ar annealing over the measured frequencies. We think that annealing in argon does not cause a significant change in the total polarization at the grain boundary of the 25%LTNO-Ar because there are LTNO nanoparticles located between grain boundaries of the CCTO matrix.[11] This suggests that the LTNO has more contribution on polarization at this region than the grain boundary of CCTO matrix.

Figures 5(a) and 5(b) show the stress dependent dielectric properties of CCTO-Ar and 25%LTNO-Ar, respectively. It is clearly observed that the dielectric properties of both samples change significantly with applied compressive stress. The absolute change of $\varepsilon'$ can reach 16% and 7% at

Author complimentary copy. Redistribution subject to AIP license or copyright, see http://jap.aip.org/jap/copyright.jsp

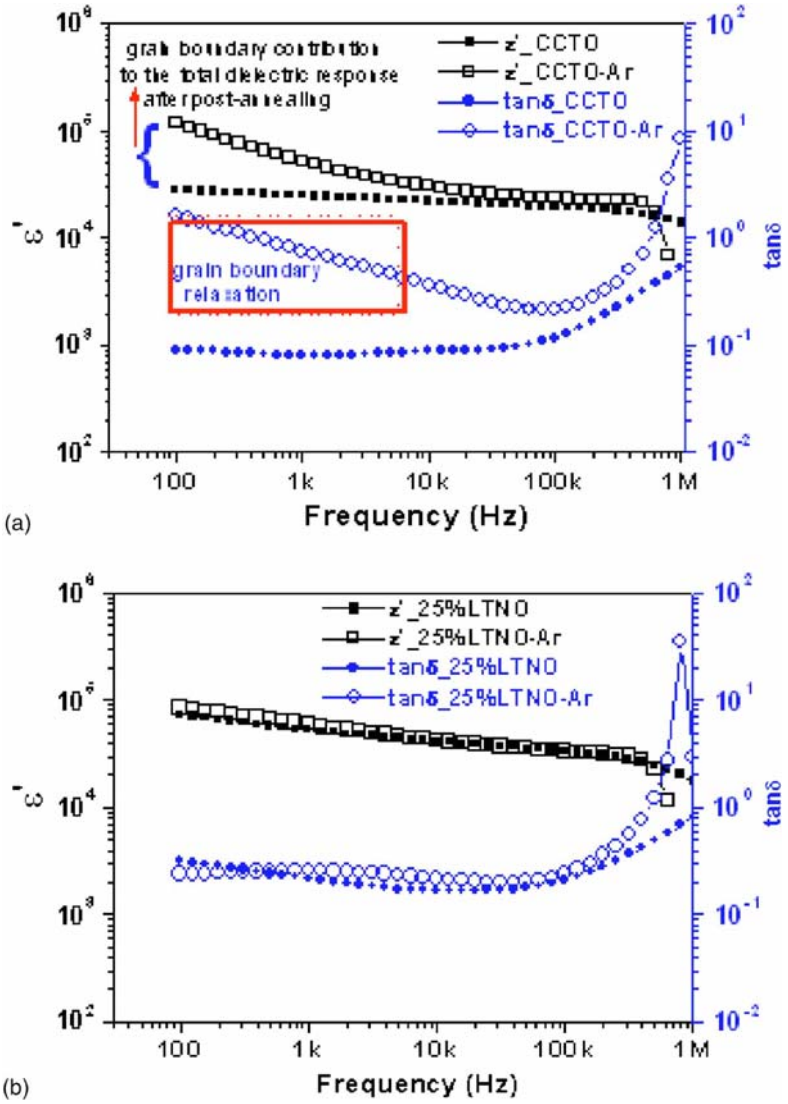



FIG. 4. (Color online) Room temperature $\varepsilon'$ and tan $\delta$ of (a) CCTO and (b) 25%LTNO, before and after postsintering annealing.

the maximum stress of 130 MPa for CCTO-Ar and 25%LTNO-Ar, respectively. However, the changes in dielectric properties with the stress in the CCTO-Ar and 25%LTNO-Ar follow opposing trends. For the CCTO-Ar, both $\varepsilon'$ and tan $\delta$ increase with increasing stress and interestingly continue to decrease upon the reduction of the applied stress [Fig. 5(a)]. On the other hand, the dielectric properties of the 25%LTNO-Ar sample decrease when the stress is increased in the range of 0–40 MPa, and beyond this range, $\varepsilon'$ and tan $\delta$ are almost unchanged with compressive stress [Fig. 5(b)]. As previously discussed,[17] the CCTO-Ar possesses very much higher concentration of the oxygen vacancies in the grain boundaries, as compared to the 25%LTNO-Ar. With lower concentration of oxygen vacancies, 25%LTNO-Ar should contain more mobile dipoles that can easily be activated by the applied stress. Hence, this leads to a stress-induced aging mechanism,[17,31] which results in the decrease in $\varepsilon'$ and tan $\delta$ at the low stress level. In the case of the CCTO-Ar, with very high concentration of the oxygen vacancies, there are competing mechanisms between the stress-induced aging and the elastic deformation. Initially, with the stress-induced aging mechanism still dominating, most of the oxygen vacancies come to rest at the grain boundaries and stabilize the stress influence, as it is observed that the dielectric properties are rather stable at a lower stress level.[17,31] A further increase in the compressive stress may result in a slight decrease in the grain boundary thickness. The effective dielectric properties of this ceramic, which can be regarded as the IBLC,[12] therefore increase, and the decrease in the effective dielectric properties follows with the reduction of the stress, as observed in Fig. 5(a). Here, we attribute that the differenes in the absolute change of $\varepsilon'$ under compressive stress are closely related to the concentration of oxygen vacancies in the grain boundary.

## IV. CONCLUSION

In conclusion, the giant dielectric behaviors of polycrystalline $CaCu_3Ti_4O_{12}$ and $CaCu_3Ti_4O_{12}$–$Li_{0.3}Ti_{0.02}Ni_{0.68}O$ composites subjected to postsintering annealing and compressive stress were investigated. The dielectric behavior of all samples after postsintering annealing still exhibits a Debye-like relaxation. A significant increase in $\varepsilon'$ was observed for CCTO-Ar at low frequency, whereas an unchange

Author complimentary copy. Redistribution subject to AIP license or copyright, see http://jap.aip.org/jap/copyright.jsp

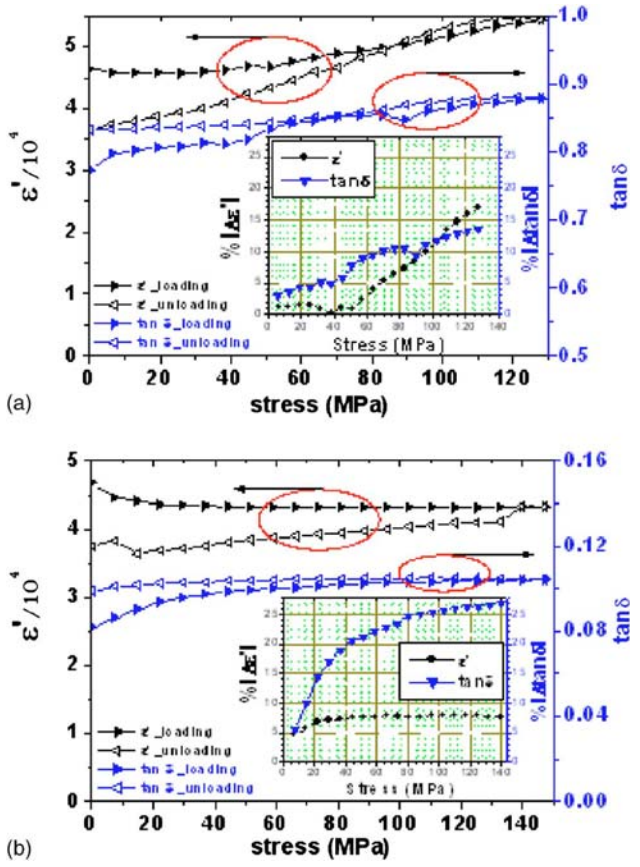



FIG. 5. (Color online) Compressive stress dependence of $\varepsilon'$ and tan $\delta$ at a frequency of 100 kHz for the samples of (a) CCTO-Ar and (b) 25% after annealing at 1000 °C for 5 h under flowing argon. The insets of Figs. 5(a) and 5(b) show the absolute change (%) of $\varepsilon'$ and tan $\delta$. Here, $\%|\Delta\varepsilon'|$ and $\%|\Delta \tan \delta|$ are defined as $|(\varepsilon'_\sigma - \varepsilon'_0)/\varepsilon'_0| \times 100(\%)$ and $|(\tan \delta_\sigma - \tan \delta_0)/\tan \delta_0| \times 100(\%)$, respectively, where $(\varepsilon'_\sigma, \varepsilon'_0)$, and $(\tan \delta_\sigma, \tan \delta_0)$, are the dielectric constants and dissipation factors with the applied compressive stress and without the applied compressive stress, respectively.

in $\varepsilon'$ was observed for 25%LTNO-Ar. The dielectric properties of both CCTO-Ar and 25%LTNO-Ar samples change significantly with the applied compressive stress, and this can be explained by the stress-induced aging mechanism. The different bases in dielectric behaviors of the two ceramics can be explained by the level of concentration of oxygen vacancies in the grain boundaries after postsintering annealing.

## ACKNOWLEDGMENTS

This work is financially supported by The Thailand Research Fund (TRF), and The Commission on Higher Education (CHE), The Ministry of Education, Thailand. P.T. would like to thank the Thailand Graduate Institute of Science and Technology (TGIST) for his PhD scholarship.

[1] M. A. Subramanian, D. Li, N. Duan, B. A. Reisner, and A. W. Sleight, J. Solid State Chem. **151**, 323 (2000).
[2] A. P. Ramirez, M. A. Subramanian, M. Gardela, G. Blumberg, D. Li, T. Vogt, and S. M. Shapiro, Solid State Commun. **115**, 217 (2000).
[3] C. C. Homes, T. Vogt, S. M. Shapiro, S. Wakimoto, and A. P. Ramirez, Science **293**, 673 (2001).
[4] J. Wu, C. W. Nan, Y. Lin, and Y. Deng, Phys. Rev. Lett. **89**, 217601 (2002).
[5] S. Maensiri, P. Thongbai, and T. Yamwong, Acta Mater. **55**, 2851 (2007).
[6] Y. Lin, J. Wang, L. Jiang, Y. Chen, and C. W. Nan, Appl. Phys. Lett. **85**, 5664 (2004).
[7] P. K. Jana, S. Sarkar, and B. K. Chaudhuri, Appl. Phys. Lett. **88**, 182901 (2006).
[8] Y. Lin, L. Jiang, R. Zhao, and C. W. Nan, Phys. Rev. B **72**, 014103 (2005).
[9] X. Kuang, C. Bridges, M. Allix, J. B. Claridge, H. Hughes, and M. J. Rosseinsky, Chem. Mater. **18**, 5130 (2006).
[10] S. Sarkar, P. K. Jana, B. K. Chaudhuri, and H. Sakata, Appl. Phys. Lett. **89**, 212905 (2006).
[11] S. Maensiri, P. Thongbai, and T. Yamwong, Appl. Phys. Lett. **90**, 202908 (2007).
[12] D. C. Sinclair, T. B. Adams, F. D. Morrison, and A. R. West, Appl. Phys. Lett. **80**, 2153 (2002).
[13] S. Y. Chung, I. L. D. Kim, and S. J. L. Kang, Nat. Mater. **3**, 774 (2004).
[14] B. A. Bender and M. J. Pan, Mater. Sci. Eng., B **117**, 339 (2005).
[15] C. C. Wang and L. W. Zhang, Appl. Phys. Lett. **88**, 042906 (2006).
[16] C. C. Wang and L. W. Zhang, Phys. Rev. B **74**, 024106 (2006).
[17] P. Thongbai, C. Masingboon1, S. Maensiri, T. Yamwong, S. Wongsaenmai, and R. Yimnirun, J. Phys.: Condens. Matter **19**, 236208 (2007).
[18] R. Yimnirun, P. J. Moses, R. J. Mayer, and R. E. Newnham, Rev. Sci. Instrum. **74**, 3429 (2003).
[19] C. C. Wang, Y. J. Yan, L. W. Zhang, M. Y. Cui, G. L. Xie, and B. S. Cao, Scr. Mater. **54**, 1501 (2006).
[20] S. F. Shao, J. L. Zhang, P. Zheng, W. L. Zhong, and C. L. Wang, J. Appl. Phys. **99**, 084106 (2006).
[21] J. Liu, Y. Sui, C. G. Duan, W. N. Mei, R. W. Smith, and J. R. Hardy, Chem. Mater. **18**, 3878 (2006).
[22] J. L. Zhang, P. Zheng, C. L. Wang, M. L. Zhao, J. C. Li, and J. F. Wang, Appl. Phys. Lett. **87**, 142901 (2005).
[23] L. Zhang and Z. J. Tang, Phys. Rev. B **70**, 174306 (2004).
[24] A. R. West, T. B. Adams, F. D. Morrison, and D. C. Sinclair, J. Eur. Ceram. Soc. **24**, 1439 (2004).
[25] G. Chiodelli, V. Massarotti, D. Capsoni, M. Bini, C. B. Azzoni, M. C. Mozzati, and P. Lupotto, Solid State Commun. **132**, 241 (2004).
[26] D. Capsoni, M. Bini, V. Massarotti, G. Chiodelli, M. C. Mozzatic, and C. B. Azzoni, J. Solid State Chem. **177**, 4494 (2004).
[27] C. Masingboon, S. Maensiri, T. Yamwong, P. Anderson, and S. Seraphin, Appl. Phys. A: Mater. Sci. Process. **91**, 87 (2008).
[28] M. Li, A. Feteira, D. C. Sinclair, and A. R. West, Appl. Phys. Lett. **88**, 232903 (2006).
[29] T. B. Adams, D. C. Sinclair, and A. R. West, J. Am. Ceram. Soc. **89**, 10 (2006).
[30] P. R. Bueno, M. A. Ramírez, J. A. Varela, and E. Longo, Appl. Phys. Lett. **89**, 191117 (2006).
[31] R. Yimnirun, M. Unruan, Y. Laosiritaworn, and S. Ananta, J. Phys. D: Appl. Phys. **39**, 3097 (2006).

Author complimentary copy. Redistribution subject to AIP license or copyright, see http://jap.aip.org/jap/copyright.jsp

ELSEVIER

Journal of Alloys and Compounds 461 (2008) 565–569

Journal of ALLOYS AND COMPOUNDS

www.elsevier.com/locate/jallcom

# Thermal expansion properties of PMN–PT ceramics

Rewadee Wongmaneerung [a,b,*], Ruyan Guo [b], Amar Bhalla [b], Rattikorn Yimnirun [a], Supon Ananta [a]

[a] *Department of Physics, Faculty of Science, Chiang Mai University, Chiang Mai 50200, Thailand*
[b] *Pennsylvania State University, Materials Research Laboratory, PA, USA*

Received 5 June 2007; received in revised form 10 July 2007; accepted 14 July 2007
Available online 27 July 2007

**Abstract**

Thermal expansion properties of $(1-x)$PMN–$x$PT ceramics were determined in the temperature range of approximately −150 to +550 °C by dilatometer thermal expansion measurement. We reported the temperature-dependent measurements of the strain, thermal expansion coefficient and the magnitude of polarization ($P_d$). The anomaly behaviors were observed at Burns temperature ($T_d$). From the experimental data, it appeared that far above the ferroelectric phase transition temperature, up to $T_d$, these materials possessed a local randomly oriented polarization $P_d$. Various aspects of understanding the polarization behavior and other effects in this ferroelectric system were also examined and discussed.
© 2007 Elsevier B.V. All rights reserved.

*Keywords:* Thermal expansion; Polarization; Relaxors; Perovskites

## 1. Introduction

Relaxor ferroelectrics, such as lead magnesium niobate (PMN), lead zinc niobate (PZN) and strontium barium niobate (SBN) attract considerable interest owing to rich diversity of their physical properties and possible applications in various technological schemes. These relaxors possess very large dielectric constants; attractive for capacitors, exceptionally large electrostrictive coefficients; important for actuators and micropositioners and large electro-optic constants [1,2].

The main features of the relaxors are connected with their structural inhomogeneity or disorder and with the presence of polar nanodomains in non-polar matrix. The structural investigations and physical properties studies reveal three peculiar temperatures: $T_d$, $T_c$ and $T_m$. $T_d$, so-called the Burn temperature, is the temperature where randomly oriented polar nanoregions become detectable within the otherwise non-polar paraelectric phase of several ferroelectrics. Originally observed in $BaTiO_3$ due to the characteristic anomaly of the refractive index [3], polar precursor clusters were later on detected in $PbTiO_3$ [4], $KNbO_3$ [5] and in the relaxor ferroelectrics PLZT [6], PMN, PZN [7] and SBN [8]. The polar regions are formed in the course of cooling at a temperature $T_d \approx 350\,^{\circ}C$, which is considerably higher than the temperature $T_m$ ($T_m \approx -10\,^{\circ}C$ for PMN). At temperature below $T_d$, the temperature dependences of the birefringence and the elongation per unit length $\Delta l/l$ for PMN deviate from linear behavior (characteristic of higher temperatures), which is associated with the formation of polar nanoregions and increase in their total volume with a decrease in the temperature [9–11]. $T_c$, Curie temperature, is the temperature where the sample will undergo a cooperative ferroelectric phase transition. $T_m$ is the temperature of the dielectric permittivity maximum, leading to an isotropic relaxor state with random orientation of polar domains [2].

A variety of experimental techniques, including refractive index measurements [3], Raman scattering [12], second-harmonic-generation (SHG) measurement [13], neutron powder diffraction [14], neutron elastic scattering [15], dynamic light scattering [16] and dielectric measurements [17–19] has been employed to confirm the existence (and value) of $T_d$. It was pointed out by Bhalla et al. [8] that due to electrostrictive coupling between the lattice strain and the polar nanoregions, $T_d$ should also be detectable from thermal expansion measurements. Indeed, deviations from the linear temperature dependence of the thermal strain had been observed at tempera-

* Corresponding author at: Department of Physics, Faculty of Science, Chiang Mai University, Chiang Mai 50200, Thailand. Tel.: +6681 8854973.
*E-mail address:* re_nok@yahoo.com (R. Wongmaneerung).

0925-8388/$ – see front matter © 2007 Elsevier B.V. All rights reserved.
doi:10.1016/j.jallcom.2007.07.086

ture $T \geq T_m$ in PLZT [20] and SBN [8], and had been attributed to the condensation of randomly oriented local polarization at $T_d$ [3].

In this work, we studied thermal expansion of $(1-x)$PMN–$x$PT ceramics with end member compositions and compositions close to a morphotropic phase boundary (MPB), i.e., $x = 0$, 0.2, 0.3, 0.35 and 1.0. Thermal expansion and thermal expansion coefficient data were then reported. Moreover, it is always a challenge to measure the temperature dependence of the polarization of these relaxor ferroelectrics over the entire temperature range. In this study, we also reported polarization values from the ferroelectric hysteresis ($P$–$E$) and thermal expansion measurements. From the phenomenological approach [8], it is known that the $P_d$ values can be extracted by using the relation;

$$x_{ij} = \frac{\Delta l}{l} = Q_{ijkk} P_k^2 \quad (1)$$

where $x_{ij}$ is the strain, $\Delta l/l$ is the thermal expansion, $Q_{ijkk}$ is the electrostrictive coefficient and $P_k$ is the polarization. Electrostrictive coefficients ($Q$) are determined in paraelectric phase and considered constant.

## 2. Experimental

The compositions of the ceramics in this investigation are $(1-x)Pb(Mg_{1/3}Nb_{2/3})O_{3-x}PbTiO_3$, $x = 0$, 0.20, 0.30, 0.35 and 1.0, and these samples were prepared from B-site precursor mixed oxide synthetic route, as reported earlier [21,22]. Pure $PbTiO_3$ powders were synthesized by a simple mixed oxide method [23]. Starting precursors were PbO, MgO, $Nb_2O_5$ and $TiO_2$. Ceramic fabrication was achieved by adding 3 wt% polyvinyl alcohol binder, prior to pressing as pellets in a pseudo-uniaxial die press at 100 MPa. Each pellet was placed in an alumina crucible together with an atmosphere powder of identical chemical composition. Sintering was carried out with a dwell time of 2 h, with constant heating/cooling rates of 20 °C/min and then heated to a sintering temperature of 1100–1250 °C. For PT ceramics, in order to achieve sinterable product, the samples were sintered using two-stage sintering [24], three sets of the first sintering temperature were assigned for the two-stage sintering case: 700, 800 and 900 °C. The second sintering temperature was set at 1200 °C. Sintering was carried out with a dwell time of 2 h at each step, with constant heating/cooling rates of 1 °C/min.

For thermal expansion measurement, all samples were cut in bar shape (5 mm long and 1 mm thick), placed inside a fused silica holder, heated at a rate of 2 °C/min from −100 to 450 °C and the thermal expansion was measured as a function of temperature using a linear voltage-differential transformer (LVDT) dilatometer. The LVDT has an advantage over the other transformers as it gives a linear output for every unit displacement. The polarization hysteresis measurement was carried out with a standardized ferroelectric test system (RT-66A, Radiant technologies).

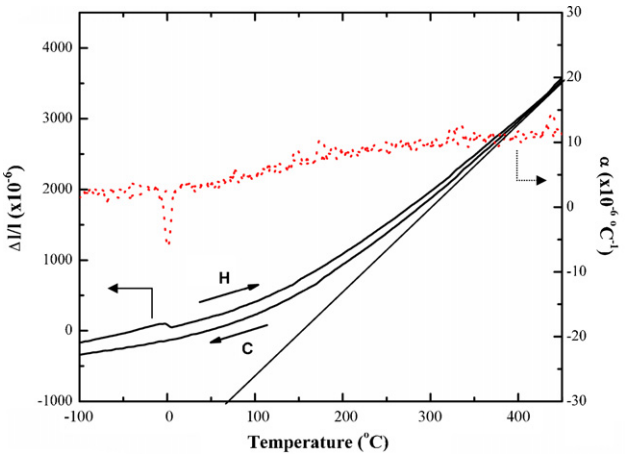



Fig. 1. Thermal expansion ($\Delta l/l$) and thermal expansion coefficient ($\alpha$) as a function of temperature for pure PMN ceramics (H = heating cycle and C = cooling cycle).

## 3. Results and discussion

The results of dilatometric measurements of $(1-x)$PMN–$x$PT ceramics are presented in Figs. 1–3 (solid line is thermal expansion and dot line is thermal expansion coefficient). The dependence of $\Delta l/l$ for pure PMN ceramic in the course of heating and cooling is shown in Fig. 1. The thermal expansion is very low with low thermal expansion coefficient near room temperature or near the Curie point. The temperature of the dielectric permittivity maximum, $T_m$ of this ceramic occurs at around −10 °C, in good agreement with the previously published values [1,20]. Table 1 lists the thermal expansion and transition temperature of PMN–PT compositions, derived from the thermal strain versus temperature measurements. Fig. 2(a–c) indicate that the respective paraelectric–ferroelectric phase transition occurs at ∼100, 120 and 175 °C, for samples with $x = 0.2$, 0.3 and 0.35, respectively. The phase transition temperatures are consistent with literatures [21,22]. Most of these compositions exhibit low thermal expansion coefficient near the Curie temperature. The values of thermal expansion coefficient in the temperature range of −100 to 100 °C, as determined from heating cycle for 0.8PMN–0.2PT, 0.7PMN–0.3PT and 0.65PMN–0.35PT are

Table 1
Various important features of the thermal expansion measurements in the selected PMN–PT ceramics

| Sample | $T_c$ (°C) | Thermal expansion coefficient ($\times 10^{-6}$ °C$^{-1}$)[a] | Calculates $P_s$ at room temperature (μC/cm$^2$)[b] |
|---|---|---|---|
| PMN | −10 | 1.6 | 72.97 |
| 0.8PMN–0.2PT | 100 | 2.0 | 94.58 |
| 0.7PMN–0.3PT | 120 | 2.4 | 56.33 |
| 0.65PMN–0.35PT | 175 | 3.2 | 54.76 |
| PT (700/1200 °C) | 489 | −64 | 74.99 |
| PT (800/1200 °C) | 481 | −70 | 75.49 |
| PT (900/1200 °C) | 478 | −83 | 76.85 |

[a] The estimate precision of these values is approximately ±0.01%.
[b] The estimate precision of these values is approximately ±0.1%.

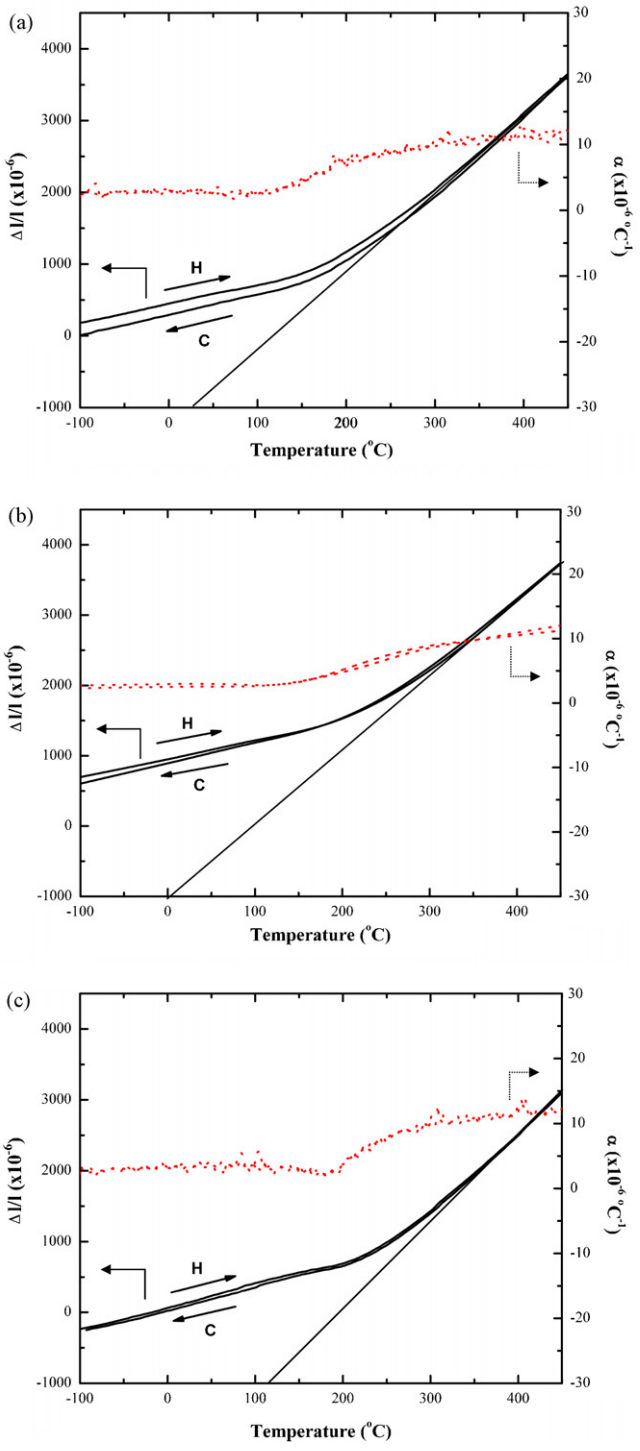



Fig. 2. Thermal expansion ($\Delta l/l$) and thermal expansion coefficient ($\alpha$) as a function of temperature for $(1-x)$PMN–$x$PT ceramics: (a) $x=0.20$, (b) $x=0.30$ and (c) $x=0.35$.

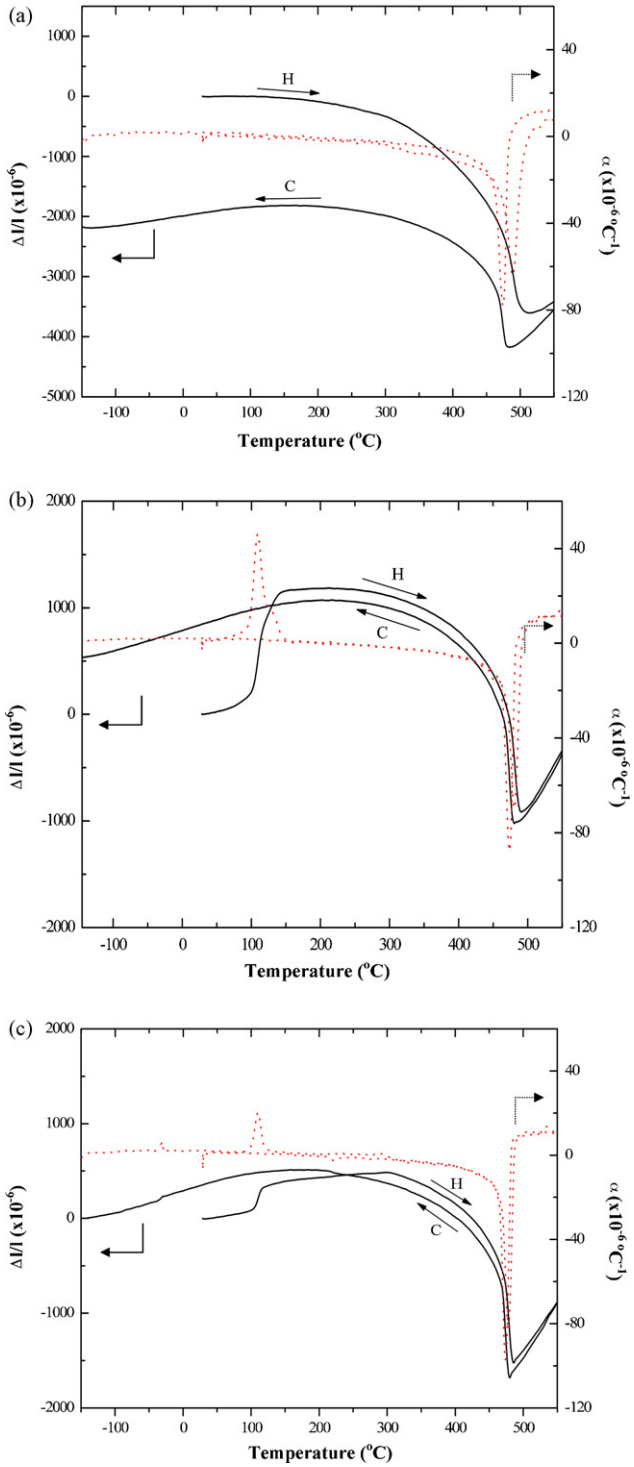



Fig. 3. Thermal expansion ($\Delta l/l$) and thermal expansion coefficient ($\alpha$) as a function of temperature for PT ceramics doubly sintered at (a) 700/1200, (b) 800/1200 and (c) 900/1200 °C.

$2\times10^{-6}$, $2.4\times10^{-6}$ and $3.2\times10^{-6}\,^{\circ}C^{-1}$, respectively. Furthermore, the highest temperature data, far above $T_c$, can be approximated by a straight line, as can be seen in the figures. The deviation from this linear high-temperature behavior occurs at 325 °C for $x=0.2$, at 350 °C for $x=0.3$ and at 360 °C for $x=0.35$.

The results of the thermal expansion for double sintered PT ceramics, shown in Fig. 3(a–c), indicate that the respective paraelectric–ferroelectric phase transition occur at around 489 °C for 700/1200 °C PT, at 481 °C for 800/1200 °C PT and at 478 °C for 900/1200 °C PT samples. It should be noted that the thermal expansion behavior of PT differs significantly from

that of pure PMN and PMN–PT. This can be explained by the fact that PT is a normal ferroelectric, whereas pure PMN and PMN–PT ceramics are relaxor ferroelectric. Moreover, the other reason is possible; their structures are different (structure of PT is tetragonal, pure PMN and PMN–PT is cubic). The thermal expansion coefficients change sharply at the $T_c$, as determined from heating of three unpoled samples and the values are $-64 \times 10^{-6}$, $-70 \times 10^{-6}$ and $-83 \times 10^{-6}\,^{\circ}C^{-1}$, respectively. The phase transition temperature values are slightly different in the three samples. However, they are in good agreement with literatures [25,26]. Furthermore, the thermal expansion (or strain) curve in these samples is linear at temperatures above $T_c \approx 490\,^{\circ}C$. At temperatures below Curie temperature, these linear thermal expansions are superimposed by a ceramic's spontaneous polarization. Following a thermal cycle, an unpoled ceramic will obviously return very much to the state of distortion it had before the cycle except for 700/1200 °C PT ceramic. The thermal expansion could not be highly reproducible that may be related to the average grain sizes which are smaller than that observed in the other two samples (not show in this paper). It should also be noticed in Fig. 3(b and c) that the anomaly occurs between 100 and 150 °C during heating cycle. This is believed to be due to space charges, as well as moisture, accumulated on the sample surfaces, which then disappeared during cooling cycle.

On analyzing the deviation of the strain from the high-temperature linear behavior and by using Eq. (1), $P_d$ values can be obtained at various temperatures. Using the values of $Q_{11} = 0.123 \times 10^{-2}\ m^4/C^2$ and $Q_{12} = -0.049 \times 10^{-2}\ m^4/C^2$ [27] for $x = 0$, 0.20, 0.30 and 0.35, $P_d$ values can be calculated, as plotted in Fig. 4. When calculating the spontaneous strains of the rhombohedral at a particular temperature, the cubic cell constant should be extrapolated to that temperature accounting for the thermal expansion. A linear extrapolation from above the transition temperature can be made over a narrow range with fairly good accuracy. In Fig. 4, we calculated the $P_d$, really $((P_d^2)^{1/2})$, values obtained from $\Delta l/l$. Also plotted is the normal reversible polarization data, $P_r$, determined from the *P–E* measurements. It is evident that the polarization calculated from the strain is larger than $P_r$ and extends several hundred degrees above $T_c$ due to quadratic electrostrictive effects. Moreover, for temperatures well below $T_c$, although not equal, $P_d$ and $P_r$ are comparable; they are obtained by totally independent techniques. It has been known that the ferroelectric–paraelectric

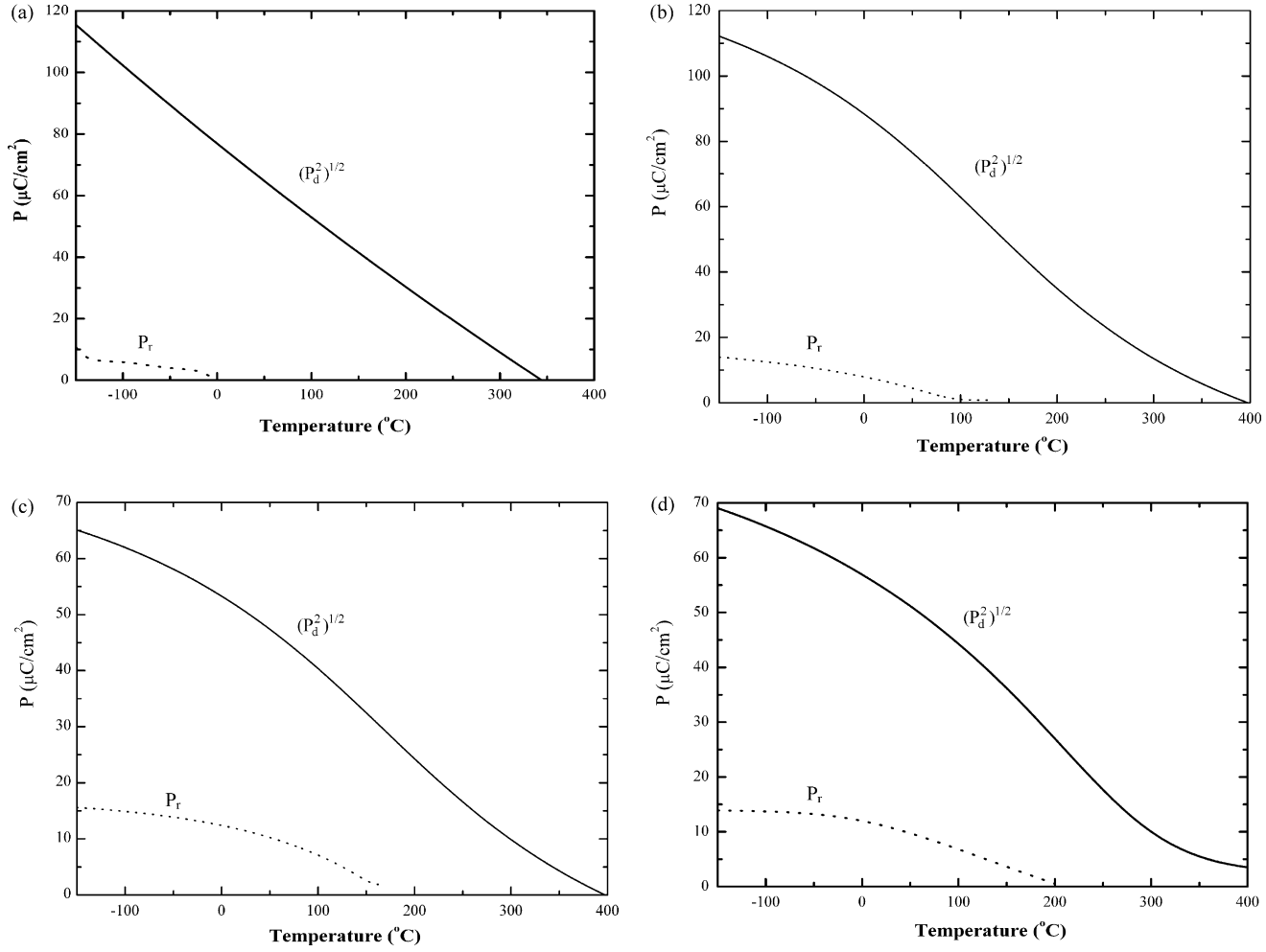



Fig. 4. $(P_d^2)^{1/2}$ as a function of temperature for $(1-x)$PMN–$x$PT ceramics from Eq. (1) and the reversible ferroelectric polarizations $P_r$ (dot lines): (a) $x = 0$, (b) $x = 0.20$, (c) $x = 0.30$ and (d) $x = 0.35$.

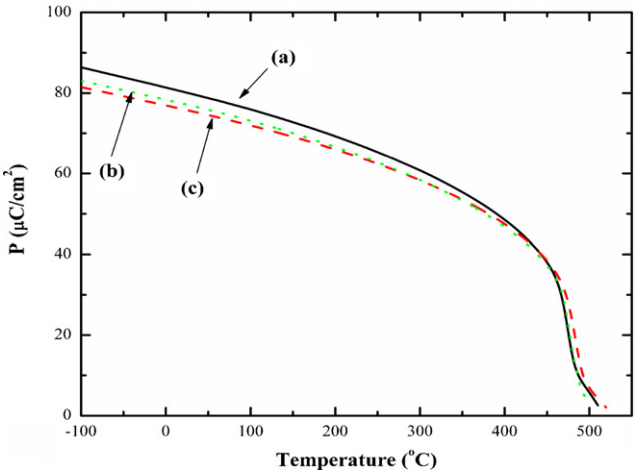



Fig. 5. $(P_d^2)^{1/2}$ as a function of temperature for PT ceramics from Eq. (1): (a) 700/1200, (b) 800/1200 and (c) 900/1200 °C.

phase transition becomes more diffuse when the PT content decreases, indication of a more pronounced relaxor behavior. Ceramic with $x = 0.20$ shows more pronounced relaxor behavior, for which the $P_d$ decays slowly with temperature compared to the other compositions ($x = 0.30$ and 0.35). Nevertheless, all $x = 0.20$, 0.30 and 0.35 show similar $T_d$ value, even though there are differences in their compositions. These $T_d$ values are several hundred degrees above the ferroelectric $T_c$ (≈100 °C for $x = 0.2$, 120 °C for $x = 0.3$ and 175 °C for $x = 0.35$) indicating glassy polarization behavior over the range [6,7]. It seems that at ≈$T_d$ small local regions of the sample begin to show a polarization due to a favorable arrangement of the atoms. The strain measurements can detect this effect because $P_d^2$ rather than $P_d$ contributes to these terms. Once local regions of polarization occur, the cooperative effect that occurs at $T_c$ can be understood.

For PT sample, using the values of $Q_{11} = 8.9 \times 10^{-2}$ m$^4$/C$^2$ and $Q_{12} = -2.6 \times 10^{-2}$ m$^4$/C$^2$ [28]. The result is plotted in Fig. 5. When calculating the spontaneous strains of the tetragonal at a particular temperature, the cubic cell constant should be extrapolated to that temperature accounting for the thermal expansion. In Fig. 5, the $P_d$ values calculated from the thermal expansion data are shown. The agreement in the $P_s$ values is excellent. The values are also in good agreement not only in magnitude but also in the $T_c$ values with the earlier reported results [29,30]. All samples sintered under different conditions, the polarization behaviors are slightly different. However, for the 800/1200 and 900/1200 °C ceramics, the magnitude of $P_d$ and trend of polarization behavior are similar to those of 700/1200 °C PT ceramic. The sharpness of the transition increases and the hyteresis space gradually decreases for the samples sintered at higher temperature in first step of the two-stage sintering process. It should be noted that the polarization behavior at high temperature of PMN–PT samples differs from PT samples because the PMN–PT samples have diffuse phase transition whereas PT has the first-order phase transition [25,26].

## 4. Conclusion

In this work, an anolmaly behavior of thermal expansion in $(1-x)$PMN–$x$PT ceramics was observed. High temperature anomaly is connected with symmetry change and polar nanodomains arising at the Burns temperature $T_d$. The obtained results are in good agreement with the reported values and also suggesting that thermal strain data can be used for reliable estimating the polarization.

## Acknowledgements

We thank the Thailand Research Fund (TRF) and the Commission on Higher Education (CHE), the Thailand Toray Science Foundation (TTSF), the Graduate School of Chiang Mai University and NSF Relaxor program, Materials Research Laboratory and MRI of Penn State University for all the support.

## References

[1] L.E. Cross, Ferroelectrics 76 (1987) 241–267.
[2] G.A. Samara, J. Phys. Condens. Matter 15 (2003) R367–R411.
[3] G. Burns, F.H. Dacol, Solid State Commun. 42 (1982) 9–12.
[4] W. Kleemann, F.J. Schäfer, D. Rytz, Phys. Rev. B 34 (1986) 7873–7879.
[5] W. Kleemann, F.J. Schäfer, M.D. Fontana, Phys. Rev. B 30 (1984) 1148.
[6] G. Burns, F.H. Dacol, Phys. Rev. B 28 (1983) 2527–2530.
[7] G. Burns, F.H. Dacol, Solid State Commun. 48 (1983) 853–856.
[8] A.S. Bhalla, R. Guo, L.E. Cross, G. Burns, F.H. Dacol, R.R. Neurgaonkar, Phys. Rev. B 36 (1987) 2030–2035.
[9] N.N. Krainik, L.A. Markova, V.V. Zhdanova, Ferroelectrics 90 (1989) 119–124.
[10] P. Bonneau, P. Garnier, C. Calvarin, J. Solid State Chem. 91 (1991) 350–361.
[11] M. Damdekalne, K. Bormanis, L. Chakare, A. Sternberg, Ferroelectrics 186 (1996) 293–296.
[12] G. Burns, F.H. Dacol, Solid State Commun. 58 (1986) 567–571.
[13] T. Heinz, G. Burns, N. Halas, Bull. Am. Phys. Soc. 31 (1986) 603.
[14] J. Zhao, A.E. Glazounov, Q.M. Zhang, B. Toby, Appl. Phys. Lett. 72 (1998) 1048–1050.
[15] D. La-Orauttapong, J. Toulouse, Z.-G. Ye, W. Chen, R. Erwin, J.L. Robertson, Phys. Rev. B 67 (2003) 134110–134120.
[16] W. Kleemann, P. Licinio, T. Woike, R. Pankrath, Phys. Rev. Lett. 86 (2001) 6014–6017.
[17] D. Viehland, S.J. Jang, L.E. Cross, M. Wutting, Phys. Rev. B 46 (1992) 8003–8006.
[18] V. Bovtun, J. Petzelt, V. Porokhonskyy, S. Kamba, Y. Yakimenko, J. Eur. Ceram. Soc. 21 (2001) 1307–1311.
[19] J. Dec, W. Kleemann, V. Bobnar, Z. Kutnjak, A. Levstik, R. Pirc, R. Pankrath, Europhys. Lett. 55 (2001) 781–787.
[20] S.L. Swartz, T.R. Shrout, W.A. Schulze, L.E. Cross, J. Am. Ceram. Soc. 67 (1984) 311–315.
[21] H. Arndt, G. Schmidt, Ferroelectrics 79 (1988) 149–152.
[22] S. Ananta, N.W. Thomas, J. Eur. Ceram. Soc. 19 (1999) 155–163.
[23] R. Wongmaneerung, R. Yimnirun, S. Ananta, Mater. Lett. 60 (2006) 2666–2671.
[24] S. Ananta, N.W. Thomas, J. Eur. Ceram. Soc. 19 (1999) 2917–2930.
[25] G. Shirane, S. Hoshino, J. Phys. Soc. Jpn. 6 (1951) 265–270.
[26] G. Shirane, R. Pepinsky, B.C. Frazer, Acta Crystallogr. 9 (1956) 131–140.
[27] G. Robert, M.D. Maeder, D. Damjanovic, N. Setter, J. Am. Ceram. Soc. 84 (2001) 2869–2872.
[28] M.J. Huan, E. Furman, S.J. Jang, H.A. McKinstry, L.E. Cross, J. Appl. Phys. 62 (1987) 3331–3338.
[29] V.G. Gavrilyachenko, R.I. Spinko, M.A. Martynenko, E.G. Fesenko, Fiz. Tverd. Tela 12 (1970) 1532–1534.
[30] F. Jona, G. Shirane, Ferroelectric Crystal, Pergamon Press, Oxford, 1962.

# Influences of perpendicular compressive stress on the dielectric and ferroelectric properties of electrostrictive and piezoelectric $Pb(Mg_{1/3}Nb_{2/3})O_3$-$PbTiO_3$ ceramics

Muangjai Unruan, Athipong Ngamjarurojana, Yongyut Laosiritaworn, Supon Ananta, and Rattikorn Yimnirun[a)]
*Department of Physics, Faculty of Science, Chiang Mai University, Chiang Mai 50200, Thailand*

(Received 26 February 2008; accepted 26 May 2008; published online 1 August 2008)

The dielectric and ferroelectric properties of $(1-x)Pb(Mg_{1/3}Nb_{2/3})O_3$-$(x)PbTiO_3$ or $(1-x)$PMN-$(x)$PT $(x=0.1-0.4)$ ceramics were measured under compressive stress applied perpendicular to the electric field. For the dielectric properties, the experimental results revealed that the superimposed perpendicular compression stress reduced the dielectric constant but increased the dielectric loss tangent of all the compositions. On the other hand, for the ferroelectric properties the applied stress noticeably enhanced the dissipation energy, the polarizations, and the coercive field of all the compositions. These results were interpreted through the non-180° ferroelastic domain switching processes, the stress clamping of domain walls, the deaging mechanism, and the stress induced enhancement in the switchable part of spontaneous polarization. More importantly, the influences of the stress applied in the perpendicular direction to the electric field were generally opposite to those of the parallel stress. © *2008 American Institute of Physics*.
[DOI: 10.1063/1.2960518]

## I. INTRODUCTION

Perovskite relaxor ferroelectric lead magnesium niobate, $Pb(Mg_{1/3}Nb_{2/3})O_3$ (PMN), and its solid solution with normal ferroelectric lead titanate, $PbTiO_3$ (PT), the so-called PMN-PT, are of great interest due to their high polarizabilities and excellent combined electrical properties suitable for various electronic device applications. These compounds have dielectric constants in excess of 20 000, making them potential candidates for capacitive applications. In addition, they also exhibit large electrostrictive coefficients at temperatures above their phase transition temperatures. This behavior extends their use to transducer and actuator applications.[1–5] In general, the $(1-x)Pb(Mg_{1/3}Nb_{2/3})O_3$-$(x)PbTiO_3$ or $(1-x)$PMN-$(x)$PT ceramic compositions with $x<0.2$ have been studied for electrostrictive applications,[4–7] while those with $x>0.2$ can be utilized as piezoelectric materials.[4,6,8,9] The differences between the electrostrictive and piezoelectric compositions of PMN-PT are due to differences in the degree of long-range polar order.[4,7,10] In the compositions with lower PT content, relaxor ferroelectric characteristics with polar clusters or nanodomains are observed.[4,11,12] On the other hand, long-range polar order with normal micron-sized ferroelectric domains exists in the compositions with higher PT content.[4,9,10]

Practically, when used in specific applications PMN-PT ceramics are often subjected to mechanical loading, either deliberately in the design of the device itself or because the device is used to change shapes as in many smart structure applications or the device is used under environmental stresses.[8,13–17] A prior knowledge of how the material properties change under different load conditions is crucial for proper design of a device and for suitable selection of materials for a specific application. Despite this fact, material constants used in any design calculations are often obtained from a stress-free measuring condition, which in turn may lead to incorrect or inappropriate actuator and transducer designs. It is therefore important to determine the properties of these materials as a function of applied stress. Previous investigations on the stress dependence of the electrical properties of many ceramic systems have clearly emphasized the importance of the matter.[7,15,18–23] Recently, the stress dependence of dielectric and ferroelectric properties has been investigated in several perovskite-based materials such as $BaTiO_3$ (BT), $Pb(Zr_{0.52}Ti_{0.48})O_3$ (PZT), PMN, PZT-BT, PMN-PZT, and $Pb(Zn_{1/3}Nb_{2/3})O_3$ (PZN)-PZT.[19–22,24–26] Since PMN-PT ceramics are practically employed in many electromechanical devices, there have been previous reports on the electromechanical properties of electrostrictive 0.9PMN-0.1PT and piezoelectric 0.7PMN-0.3PT ceramics under various mechanical and electrical loading conditions.[7,15,23,27] In addition, our previous investigation on the influence of the applied stress on the dielectric properties of PMN-PT ceramic systems also revealed that the superimposed compression stress significantly reduced both the dielectric constant and the dielectric loss tangent of 0.9PMN-0.1PT ceramics, while the changes were not as significant in the other PMN-PT ceramic compositions.[24] The results clearly showed that the effects of stress on the dielectric properties depended significantly on the ceramic chemical compositions and stress levels. In addition, significant changes in the ferroelectric properties of PMN-PT ceramics under the compressive stress applied parallel to the electric field were observed in our recent investihgation.[28] Previously, many investigations also reported the electrical properties of ferroelectric ceramics under the influences of the

[a)]Electronic mail: rattikornyimnikirun@yahoo.com.

 © 2008 American Institute of Physics

Downloaded 14 Apr 2009 to 202.28.246.2. Redistribution subject to AIP license or copyright; see http://jap.aip.org/jap/copyright.jsp

TABLE I. Characteristics of PMN-PT ceramics with optimized processing conditions (Refs. 24, 28, and 32).

| Ceramic | Density[a] ($g/cm^3$) | Grain size range ($\mu m$) | Average grain size[b] ($\mu m$) | $T_m$ or $T_C$ (1 kHz) (°C) | Stress-free dielectric properties[c] $\varepsilon_r$ | tan $\delta$ | Stress-free ferroelectric properties[d] $\langle A \rangle$ ($kJ/m^3$) | $P_{sat}$ ($\mu C/cm^2$) | $P_r$ ($\mu C/cm^2$) | $E_c$ (kV/cm) | Stress-free differential permittivity |
|---|---|---|---|---|---|---|---|---|---|---|---|
| 0.9PMN-0.1PT | 7.98 | 0.42–3.66 | 2.07 | 45 | 5321 | 0.082 | 57 | 12.3 | 1.7 | 1.5 | 13 062 |
| 0.8PMN-0.2PT | 7.94 | 0.44–3.02 | 2.02 | 100 | 2674 | 0.045 | 121 | 14.1 | 6.6 | 2.8 | 15 439 |
| 0.7PMN-0.3PT | 7.86 | 0.41–2.80 | 1.72 | 150 | 2019 | 0.050 | 184 | 12.9 | 7.5 | 4.5 | 9126 |
| 0.6PMN-0.4PT | 7.83 | 0.41–3.45 | 1.93 | 210 | 1223 | 0.024 | 235 | 9.7 | 6.1 | 8.2 | 5013 |

[a]The estimated precision of the density is ±1%.
[b]The estimated precision of the average grain size is ±1%.
[c]Measured at 1 V/mm (25 °C and 1 kHz).
[d]Measured at 25 °C and 50 Hz.

compressive stress applied perpendicular to the electric field.[20,22,27,29–31] Therefore, as an extension of our previous investigations on PMN-PT ceramics,[24,28] it is the aim of this study to examine the dielectric and ferroelectric properties of the electrostrictive and piezoelectric PMN-PT ceramic compositions under compressive stress applied perpendicular to the electric field.

## II. EXPERIMENTAL METHOD

As described in our previous investigations,[24,28] dense perovskite-phase electrostrictive 0.9PMN-0.1PT and 0.8PMN-0.2PT ceramics and piezoelectric 0.7PMN-0.3PT and 0.6PMN-0.4PT ceramics with uniform microstructure and similar density values used in this study were prepared from PMN and PT powders by the mixed-oxide columbite precursor method. Details of the ceramic processing and characterizations were already provided elsewhere.[32] Table I summarizes the physical characteristics of the PMN-PT ceramics used in this study. More importantly, since the physical and microstructure features of all the ceramic compositions are not significantly different, these parameters should not play an important role in the composition-dependent ferroelectric properties under compressive stress.

Before studying the dielectric and ferroelectric properties under compressive stress, the sintered specimens were cut as rectangular bars (approximate dimensions of $6 \times 2 \times 2$ $mm^3$) and lapped to obtain parallel faces. After coating with silver paint as electrode at the faces, the specimens were heated at 750 °C for 12 min with heating/cooling rates of 10 °C/min to ensure the contact between the electrode and surface of ceramics. The electrodes were applied on the other two opposite faces with silver wire attached to the electrodes for electrical measurement. To study the effects of the compressive stress on the dielectric and ferroelectric properties, the uniaxial compressometer was constructed for simultaneous applications of the mechanical stress and the electric field.[33–35] Figure 1 shows a schematic of the experimental setup with stress and electric field applied perpendicularly. The compressometer cell consisting of a cylindrical brass cell with a heavy brass base, a brass ram, and a precisely guided loading platform provided true uniaxial stress during mechanical loading. The compressive stress was supplied by the servohydraulic load frame and the applied stress level was monitored with the pressure gauge of the load frame. Measurements were performed as a function of mechanical stress applied discretely between 0 and 170 MPa depending on the samples. The low-field dielectric properties were measured by an *LCR* meter (Instrek LCR-821) with an applied voltage of 1 V. The room temperature (25 °C) capacitance and the dielectric loss tangent were determined at a frequency of 1 kHz. The dielectric constant was then calculated from a parallel-plate capacitor equation, e.g., $\varepsilon_r = Cd/\varepsilon_0 A$, where $C$ is the capacitance of the specimens, $d$ and $A$ are, respectively, the thickness and the area of the electrode, and $\varepsilon_0$ is the dielectric permittivity of vacuum ($8.854 \times 10^{-12}$ F/m). The room temperature (25 °C) ferroelectric hysteresis ($P$-$E$) loops were characterized by using a computer controlled modified Sawyer–Tower circuit. The electric field of 15–20 kV/cm was applied to a sample by a high voltage ac amplifier (Trek, model 610D) with input sinusoidal signal with a frequency of 50 Hz from a signal generator (Goodwill, model GAG-809). The parameters obtained from the loops were the saturation polarization ($P_{sat}$), the remanent polarization ($P_r$), and the coercive field ($E_c$), which were defined as the points where the loops reach the maximum polarization, cross the zero field, and cross the zero polarization, respectively. The measurements reported were for the samples during their first mechanical stress cycle. It should also be noted that the reported ferroelectric

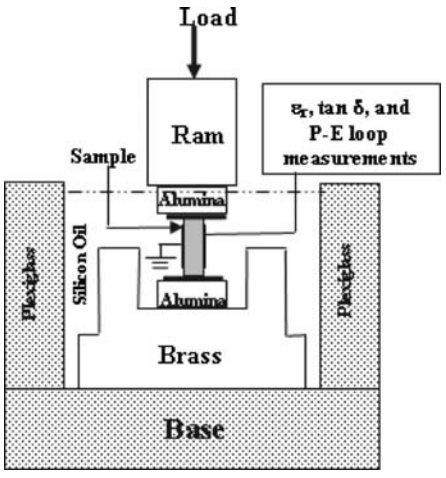



FIG. 1. A schematic of the experimental setup showing stress and electric field applied perpendicularly.

Downloaded 14 Apr 2009 to 202.28.246.2. Redistribution subject to AIP license or copyright; see http://jap.aip.org/jap/copyright.jsp

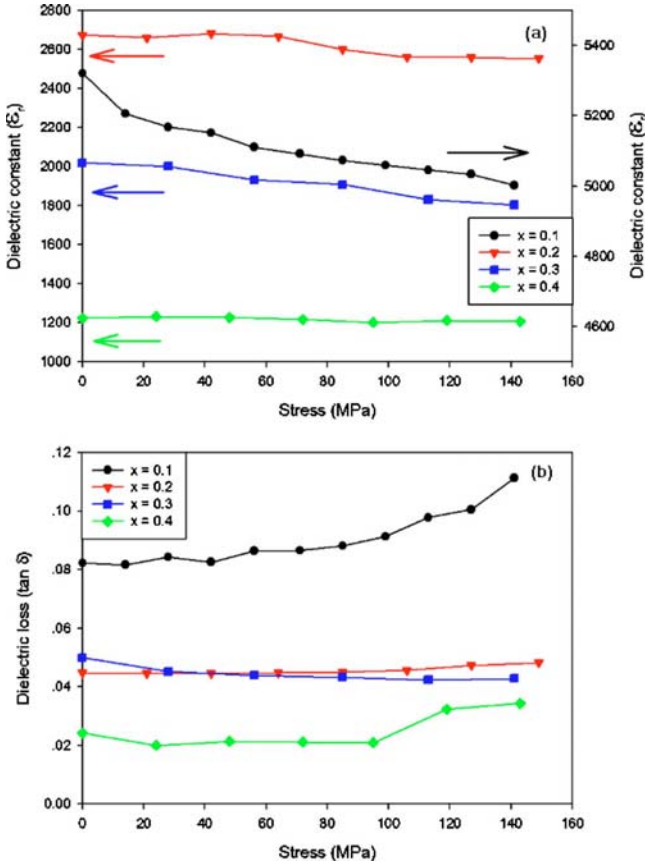



FIG. 2. (Color online) Changes in the dielectric properties of $(1-x)$PMN-$(x)$PT ceramics with compressive stress applied perpendicular to the electric field: (a) dielectric constant ($\varepsilon_r$) and (b) dielectric loss (tan $\delta$) (measured at 25 °C and 1 kHz).

parameters were obtained after a total of 10 cycles of the electric field was applied to the sample at each constant stress level.

## III. RESULTS AND DISCUSSION

### A. Dielectric properties under perpendicular stress

The room temperature dielectric properties at 1 kHz of $(1-x)$PMN-$(x)$PT ceramics as a function of compressive stress are depicted in Fig. 2. Clearly, there are observable changes in both the dielectric constant [Fig. 2(a)] and the dielectric loss tangent [Fig. 2(b)] with the stress applied perpendicular to the electric field direction. As seen in Fig. 2(a), the dielectric constant is seen to decrease with increasing stress in all the compositions. The decrease in the dielectric constant varies from approximately 12% in the near morphotropic phase boundary (MPB) piezoelectric 0.7PMN-0.3PT composition to 4%–5% in the electrostrictive 0.9PMN-0.1PT and 0.8PMN-0.2PT compositions and to 2% in the tetragonal piezoelectric 0.6PMN-0.4PT composition at a maximum applied stress of 150 MPa. However, since the dielectric constant of the sample was measured through the capacitance, there is a change in sample capacitance due to the geometrical deformation under stress. The variation in the sample dielectric constant $(\Delta\varepsilon_r)$ can be expressed as $\varepsilon_r^* X^*[(1+2\upsilon)/E]$, where $X$ is the applied stress, $\upsilon$ is the Poisson ratio, and $E$ is the Young modulus.[24,35] By applying the estimated values of $\upsilon \sim 0.3$ and $E \sim 100$ GPa for PMN-PT ceramics[7,23,27,36] and $\varepsilon_r$ given in Table I, it can be estimated that at the maximum stress of 150 MPa, the variation in the sample dielectric constant due to the geometrical deformation is $<0.5\%$. Therefore, this variation should not be an important factor in the variation in the dielectric constant under stress seen in Fig. 2(a). Interestingly, the changes in the dielectric constant of the PMN-PT systems with the perpendicular stress are generally similar to those of the parallel stress obtained in our previous investigation.[24]

On the other hand, when the maximum stress of 150 MPa is reached the dielectric loss tangent (tan $\delta$) is generally seen to increase from the stress-free value, as displayed in Fig. 2(b). However, while the dielectric loss tangent for the electrostrictive 0.9PMN-0.1PT and 0.8PMN-0.2PT compositions increases continuously with increasing stress, that for the piezoelectric 0.7PMN-0.3PT and 0.6PMN-0.4PT compositions first decreases slightly, then slowly increases at a higher applied stress. For the case of the compressive stress applied perpendicular to the direction of the electric field, only a few previous experimental works have been carried out on some commercial hard and soft PZT ceramics, $Pb(In_{1/2}Nb_{1/2})O_3$ (PIN)-PT and PMN-PT ceramics.[20,27,29,37,38] Interestingly, the results observed in this current study are generally very similar to those obtained earlier in the Pb-based perovskite ceramics mentioned above.

To understand these experimental results, at least qualitatively, various effects have to be considered. Normally, the properties of ferroelectric materials are derived from both the intrinsic contribution of domains and extrinsic contributions of repolarization and growth of micropolar regions.[19–23] When a compressive stress is applied to the ferroelectric materials, the domain structure in the materials will change to maintain the domain energy at a minimum; during this process some of the domains engulf other domains or change shape irreversibly. Under the applied stress, the domain structure of ferroelectric ceramics may undergo domain switching through non-180° domain walls, deaging, clamping of domain walls, and stress induced decrease in the switchable part of spontaneous polarization.[21,23,39]

The situation for the PMN-PT system is quite complex because this system is a mixing between the relaxor ferroelectric PMN and the normal ferroelectric PT. Therefore, there is a competing mechanism between the two types of materials depending on temperature and chemical composition. Since 0.9PMN-0.1PT is a relaxor ferroelectric with $T_m \sim 45$ °C and the experiment was carried out at room temperature (~25 °C), which is slightly below the $T_m$, the experimental observation, which shows decreases in dielectric constant with increasing stress, can be attributed to competing influences of the intrinsic contribution of nonpolar matrix and the extrinsic contribution of repolarization and growth of micropolar regions. Since the dielectric response of both contributions is affected by the applied stress in an opposite way, the behavior of 0.9PMN-0.1PT depends on the ratio between the micropolar region and the nonpolar matrix; in this case the nonpolar matrix still dominates.[21,22,37] Hence, the dielectric constant of the 0.9PMN-0.1PT ceramics is ob-

Downloaded 14 Apr 2009 to 202.28.246.2. Redistribution subject to AIP license or copyright; see http://jap.aip.org/jap/copyright.jsp

served to decrease, while the dielectric loss tangent increases with increasing the compressive stress. The dielectric response to the applied stress is therefore slightly lower in the electrostrictive 0.8PMN-0.2PT composition with a higher micropolar region content at room temperature.

The decrease in the dielectric constant for the piezoelectric compositions with a drastic change in 0.7PMN-0.3PT and a very little change in 0.6PMN-0.4PT can be attributed to influences of the polarization and domains. Under the applied compressive stress, the stress clamping of domain walls, which results in a decrease in domain wall mobility, and the stress induced decrease in the switchable part of spontaneous polarization are expected to play a role in the decrease in the dielectric properties of the two compositions.[20,37] In addition, the continuous decrease in the dielectric constant can also be attributed to the switching of 90° domains, which causes the significant decrease in the dielectric constant. A larger decrease in the dielectric constant of the near MPB composition, i.e., 0.7PMN-0.3PT, is attributed to more domain states in the composition that combines six possible domain states from the tetragonal phase with eight possible domain states from the pseudocubic (or rhombohedral) phase;[1–4] hence a much larger change is observed. On the other hand, the dielectric constant of 0.6PMN-0.4PT is rather stable under the applied stress when compared to the near MPB 0.7PMN-0.3PT composition. This suggests the influence of different crystal structures and domain states. As stated above, the 0.7PMN-0.3PT composition contains mixed tetragonal-rhombohedral phases with more possible domain states (14), while the 0.6PMN-0.4PT contains mainly tetragonal phases with only 6 domain states, hence a much smaller change in the dielectric constant. In addition, since the measurements were carried out at room temperature, which is far below the transition temperature of 210 °C for the 0.6PMN-0.4PT composition, the domain is much less mobile and the change in the dielectric constant is also much less. Most of the more recent studies agree that the phase composition near the MPB is likely some form of monoclinic or possibly several phases together.[40–42] It is probably not rhombohedral and tetragonal phases. However, the hypothesis given above is still reasonable; i.e., the 0.6PMN-0.4PT composition is tetragonal, a phase very resistant to stress induced change, and the 0.7PMN-0.3PT composition certainly has a much more complicated phase composition that is highly vulnerable to stress induced domain switching (regardless of what the phase composition actually is). Moreover, the deaging mechanism is also expected to play a role in the increase in the dielectric loss tangent at a higher stress. During the aging process, some of the domain walls become pinned by impurities and structural imperfections. When a large enough stress is applied to the aged samples, it causes structural changes and redistribution of impurities. As a result, the domain walls that were pinned during aging can become active again. This deaging can increase the dielectric loss tangent, as observed in the 0.6PMN-0.4PT composition.

### B. Ferroelectric properties under perpendicular stress

The polarization versus electric field (*P-E*) hysteresis loops of 0.9PMN-0.1PT, 0.8PMN-0.2PT, 0.7PMN-0.3PT, and 0.6PMN-0.4PT ceramics under different compressive stresses applied perpendicular to the electric field are shown in Figs. 3(a)–3(d), respectively. It should first be noticed that generally the area of the *P-E* loops increases with increasing perpendicular compressive stress. The changes follow a similar trend for all the ceramic compositions. However, the observations are in contrast to the case when the stress was applied in parallel to the electric field reported in our previous investigations.[24,26,28,33,43] The *P-E* loop area indicates the polarization dissipation energy of a ferroelectric material under one full cycle of electric field application.[18,44] This amount of energy loss is directly related to the amount of domains participating in the switching process during the application of the electric field.[18,19] For a given composition, the increase in the loop area with increasing compressive stress indicates enhanced dissipation energy under the applied stress in the perpendicular direction, in contrast to the parallel case.[28] A possible explanation for such observation will be discussed later.

The changes in the hysteresis parameters, i.e., the dissipation energy, the saturation polarization ($P_{sat}$), the remanent polarization ($P_r$), and the coercive field ($E_c$), with the compressive stresses are plotted in Figs. 4(a)–4(d), respectively. At a given stress, the composition-dependent hysteresis parameters follow the trend observed in previous investigations.[7,15,23,27,30,36] Here, electrostrictive 0.9PMN-0.1PT and 0.8PMN-0.2PT compositions with slim *P-E* loops show lower dissipation energy as compared to piezoelectric compositions with a square-type loop. Similarly, the remanent polarization is smallest in the electrostrictive 0.9PMN-0.1PT composition, while the highest polarization is obtained in the near MPB 0.7PMN-0.3PT composition. The highest coercive field is observed in the tetragonal 0.6PMN-0.4PT composition, as expected. Considering the stress dependence, it can generally be seen that in every composition, the dissipation energy, the polarizations, and the coercive field increase almost linearly as the perpendicular compressive stress increases. It should, however, be noticed that the saturation polarization of the 0.7PMN-0.3PT composition actually decreases with increasing stress. This is in contrast to every other compositions and properties. An obvious explanation for this unusual behavior is currently not available and work is ongoing to understand the behavior. Nonetheless, the increase in all the parameters is generally less than 20% when the compressive is increased from 0 to 140–170 MPa, with the coercive field being changed less dramatically than the other parameters. The results of the changes in the hysteresis parameters of the PMN-PT ceramics with increasing perpendicular compressive stress are in agreement with the previous investigations on many ferroelectric ceramics.[20,22,27,30,31]

To understand, at least qualitatively, these experimental results on the ferroelectric properties of the PMN-PT ceramics, one can interpret the changes in terms of domain-

Downloaded 14 Apr 2009 to 202.28.246.2. Redistribution subject to AIP license or copyright; see http://jap.aip.org/jap/copyright.jsp

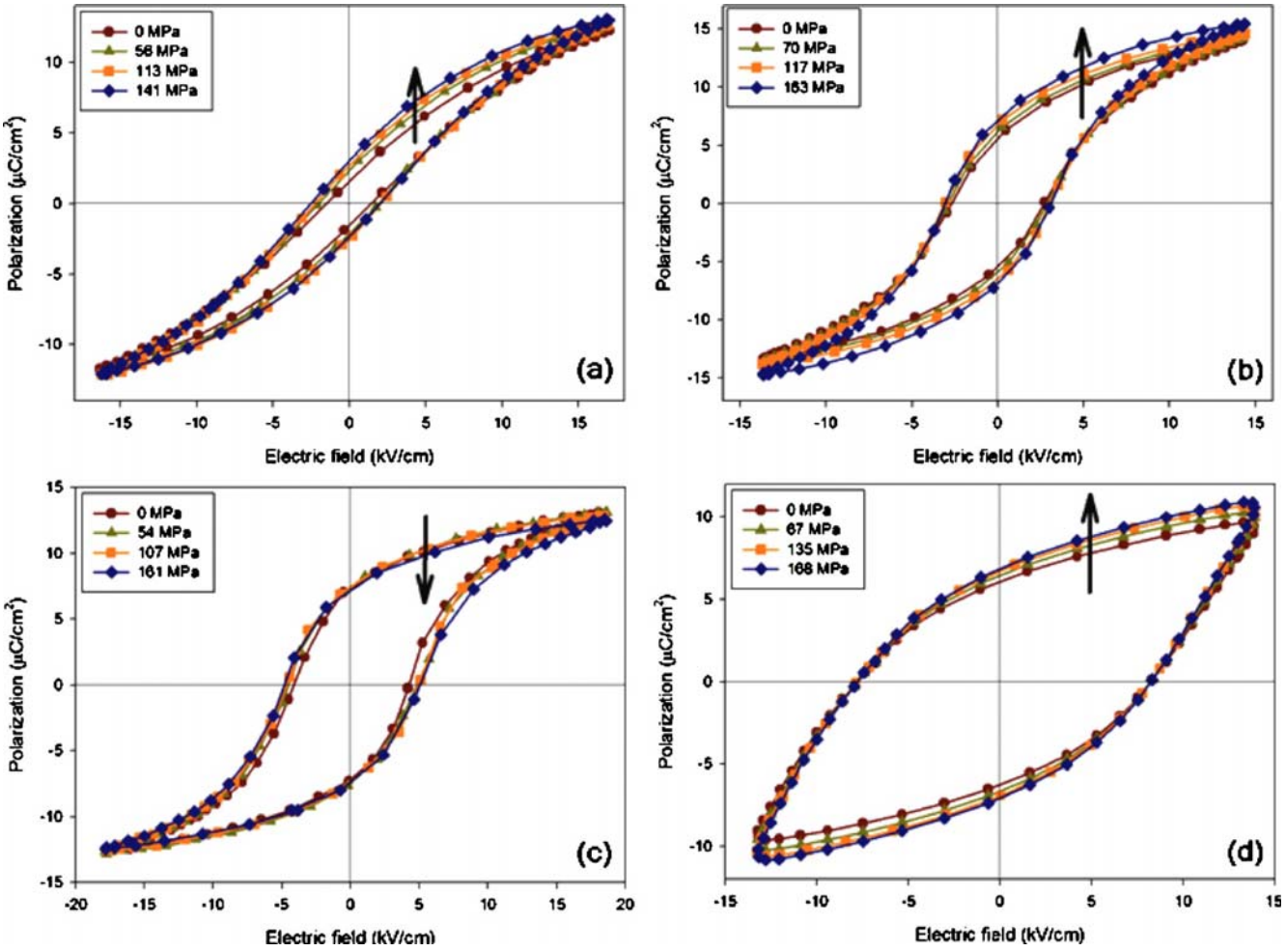



FIG. 3. (Color online) Polarization–electric field (*P-E*) hysteresis loops as a function of compressive stress applied perpendicular to the electric field for (a) 0.9PMN-0.1PT, (b) 0.8PMN-0.2PT, (c) 0.7PMN-0.3PT, and (d) 0.6PMN-0.4PT ceramics (measured at 25 °C and 50 Hz) (arrow indicates changes in polarization with increasing stress).

reorientation processes. When the compressive stress is applied perpendicular to the electric field direction, the applied stress tends to force the polarization of the individual domains to lie in a plane normal to the stress direction through the non-180° (i.e., 90° domain switching in tetragonal composition and 71° (or 109°) domain switching in rhombohedral composition) ferroelastic domain switching processes.[18–21,31] Since the applied electric field direction also lies in this plane, it takes a lower than usual applied electric field to reorient the domains perpendicular to the stress direction (or along the electric field direction), resulting in a higher value of the saturation polarization ($P_{sat}$), as shown in Fig. 4(b). When the electric field is reduced to zero, some of the domains cannot rotate back to the applied compressive stress direction, resulting in a higher than usual remanent polarization ($P_r$), as depicted in Fig. 4(c). Similarly, it takes a larger than usual electric field to force the polarizations to become zero; hence a larger coercive field is observed, as shown in Fig. 4(d). Furthermore, considering the increase in the hysteresis loss with increasing the compressive stress, as shown in Fig. 4(a), it indicates that since the perpendicular stress favors domains parallel or antiparallel to the applied electric field, more and more ferroelectric domains participate in the polarization reversal. Consequently, both the saturation and remanent polarizations become higher with increasing the perpendicular compressive stress. However, for the 0.7PMN-0.3PT composition it is noticed that the saturation polarization decreases slightly at high stresses, as depicted in Fig. 4(b). The exact explanation is not clearly known, but it could be attributed to the competing influences of the above mentioned mechanism and the stress induced decrease in the switchable part of spontaneous polarization,[21,23,39] with the latter being stronger; hence the decrease in the saturation polarization is observed at higher stresses.

More interestingly, one would be able to estimate from the *P-E* loops obtained in this study the large-signal dielectric permittivity by using Eq. (1), which gives

$$\varepsilon = \frac{\Delta P}{\Delta E}, \tag{1}$$

where $\Delta P$ is the polarization difference between +1.0 and −1.0 kV/cm. The calculated dielectric permittivity can be called *differential permittivity*, which includes the reversible (intrinsic dielectric property) and irreversible (extrinsic do-

Downloaded 14 Apr 2009 to 202.28.246.2. Redistribution subject to AIP license or copyright; see http://jap.aip.org/jap/copyright.jsp

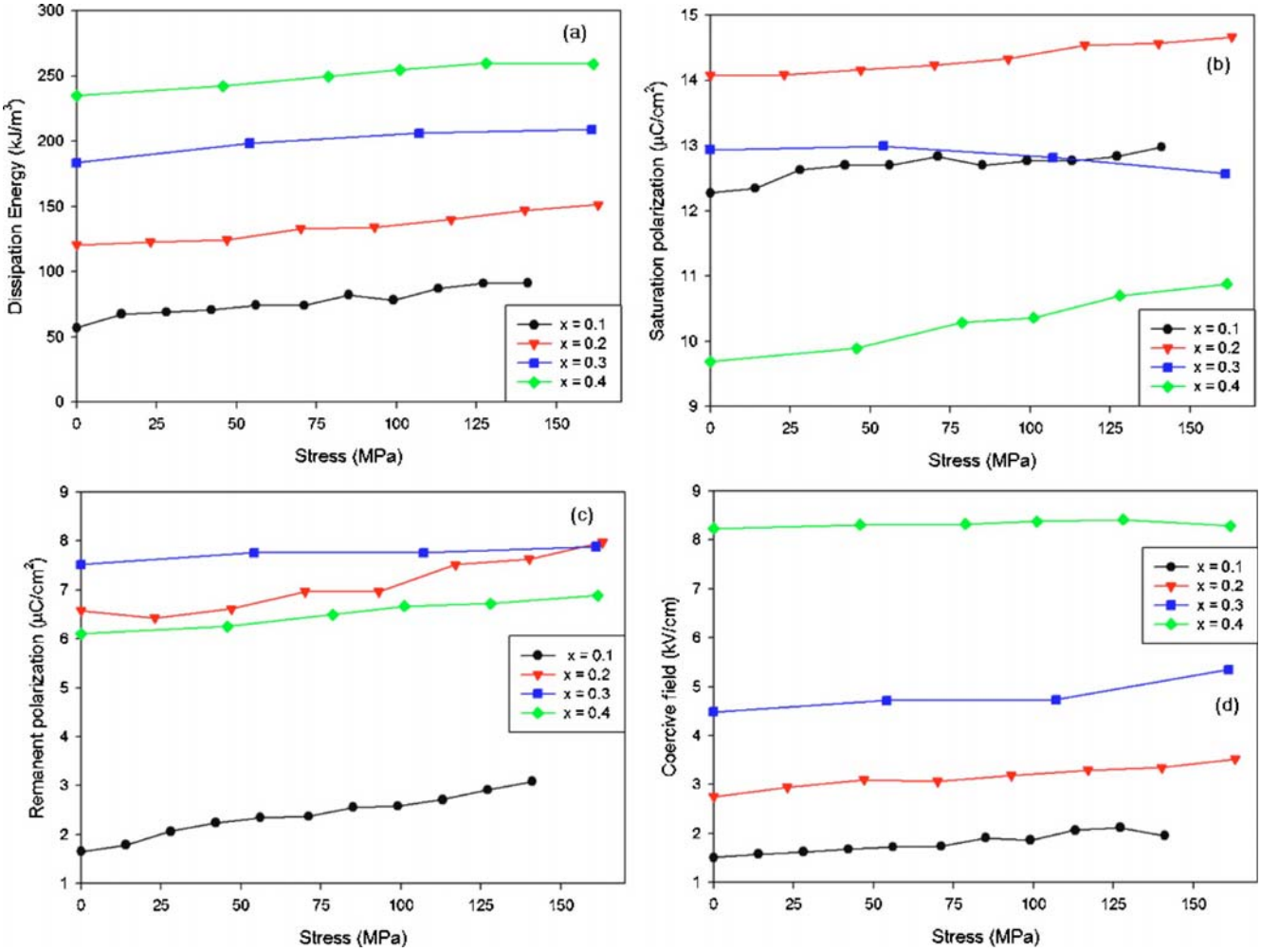



FIG. 4. (Color online) Changes in polarization–electric field ($P$-$E$) hysteresis parameters of $(1-x)$PMN-$(x)$PT ceramics with compressive stress applied perpendicular to the electric field: (a) dissipation energy $\langle A \rangle$, (b) saturation polarization ($P_{sat}$), (c) remanent polarization ($P_r$), and (d) coercive field ($E_c$) (measured at 25 °C and 50 Hz).

main switching related property) contributions of the materials.[18,33] As shown in Fig. 5 and listed in Table I, the differential permittivity is three to five times larger than the low-field relative permittivity. This clearly indicates a significant contribution from the domain switching to the dielectric properties. Though some variations in the data are present in the differential relative permittivity as shown in Fig. 5, it is even more interesting to observe that the differential relative permittivity of all the compositions tends to increase with the applied stress, which is opposite to the decreasing trend for the low-field dielectric constant shown in Fig. 2(a). This is attributed to the enhanced polarizations in the electric field direction as a result of the perpendicular stress, as stated above. The direct comparison between the high-field and low-field dielectric constants clearly signifies the importance of the experimental conditions used to determine the dielectric properties, as well as the stress-dependent dielectric properties.

This study has served as an extension of our previous work on the parallel stress-dependent dielectric and ferroelectric properties,[24,28] as well as other earlier reports, which mainly focused on only 0.9PMN-0.1PT compositions.[7,15,23,27,30] The results presented in this study have shown that the dielectric and ferroelectric properties in PMN-PT ceramics under perpendicular stress differ significantly from those under the parallel stress case reported in previous investigations.[24,28] Finally, the information obtained here is practically very useful for the design and calculation consideration of devices employing the PMN-PT ceramics.

## IV. CONCLUSIONS

The dielectric and ferroelectric properties of $(1-x)$PMN-$(x)$PT $(x=0.1-0.4)$ ceramics are investigated under compressive stress applied perpendicular to the electric field. The experimental results reveal that the superimposed perpendicular compression stress reduces the dielectric constant but increases the dielectric loss tangent of all the compositions. On the other hand, for the ferroelectric properties the applied stress noticeably enhances the dissipation energy, the polarizations, and the coercive field of all the compositions. In addition, the differential dielectric permittivity is found to increase with increasing compressive stress. These results can be interpreted through the non-180° ferroelastic domain

Downloaded 14 Apr 2009 to 202.28.246.2. Redistribution subject to AIP license or copyright; see http://jap.aip.org/jap/copyright.jsp

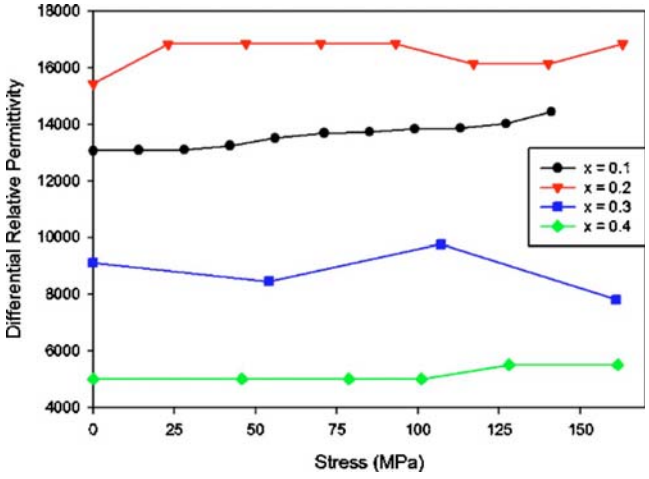



FIG. 5. (Color online) Changes in differential relative permittivity of $(1-x)$PMN-$(x)$PT ceramics with compressive stress applied perpendicular to the electric field (determined from $\pm 1$ kV/cm of the *P-E* loops measured at 25 °C and 50 Hz).

switching processes, the stress clamping of domain walls, the deaging mechanism, and the stress induced enhancement in the switchable part of spontaneous polarization. Finally, the influences of the stress applied in the perpendicular direction to the electric field are generally opposite to those of the parallel stress.

## ACKNOWLEDGMENTS

Supports from the Thailand Research Fund (TRF), Commission on Higher Education (CHE), Royal Golden Jubilee PhD Program, Faculty of Science, and Graduate School of Chiang Mai University are gratefully acknowledged.

[1]Y. H. Xu, *Ferroelectric Materials and Their Applications* (North-Holland, Los Angeles, 1991).
[2]A. J. Moulson and J. M. Herbert, *Electroceramics: Materials, Properties, Applications* (Wiley, Chichester, 2003).
[3]G. H. Haertling, J. Am. Ceram. Soc. **82**, 797 (1999).
[4]L. E. Cross, Mater. Chem. Phys. **43**, 108 (1996).
[5]S.-J. Jang, Ph.D. thesis, The Pennsylvania State University, 1979.
[6]K. Uchino, *Piezoelectric Actuators and Ultrasonic Motors* (Kluwer, Boston, 1997).
[7]D. Viehland, J. Li, E. McLaughlin, J. Powers, R. Janus, and H. Robinson, J. Appl. Phys. **95**, 1969 (2004).
[8]T. R. Shrout, Z. Chang, N. Kim, and S. Markgraf, Ferroelectr., Lett. Sect. **12**, 63 (1990).
[9]D. Viehland, M. Kim, Z. Xu, and J. Li, Appl. Phys. Lett. **67**, 2471 (1995).
[10]G. Smolenskii and A. Agranovskaya, Sov. Phys. Solid State **1**, 1429 (1960).
[11]C. Randall, D. Barber, and R. Whatmore, J. Microsc. **45**, 275 (1987).
[12]X. Dai, Z. Xu, and D. Viehland, Philos. Mag. B **70**, 33 (1994).
[13]J. Kuwata, K. Uchino, and S. Nomura, Jpn. J. Appl. Phys., Part 1 **21**, 1298 (1982).
[14]S. E. Park and T. R. Shrout, J. Appl. Phys. **82**, 1804 (1997).
[15]D. Viehland and J. Powers, Appl. Phys. Lett. **78**, 3112 (2001).
[16]D. Stansfield, *Underwater Electroacoustic Transducers* (Bath University Press, Bath, 1991).
[17]M. Mitrovic, G. P. Carmen, and F. K. Straub, Int. J. Solids Struct. **38**, 4357 (2001).
[18]D. Zhou, M. Kamlah, and D. Munz, J. Eur. Ceram. Soc. **25**, 425 (2005).
[19]R. Yimnirun, S. Wongsaenmai, S. Ananta, and E. Meechoowas, J. Phys. D **36**, 1615 (2003).
[20]Q. M. Zhang, J. Zhao, K. Uchino, and J. Zheng, J. Mater. Res. **12**, 226 (1997).
[21]G. Yang, S. F. Liu, W. Ren, and B. K. Mukherjee, Proc. SPIE **3992**, 103(2000).
[22]O. Steiner, A. K. Tagantsev, E. L. Colla, and N. Setter, J. Eur. Ceram. Soc. **19**, 1243 (1999).
[23]J. Zhao and Q. M. Zhang, Proceedings of the IEEE International Symposium on Applications of Ferroelectrics, 1996 (unpublished), p. 971.
[24]R. Yimnirun, M. Unruan, Y. Laosiritaworn, and S. Ananta, J. Phys. D **39**, 3097 (2006).
[25]R. Yimnirun, S. Ananta, and S. Chamunglap, Mater. Chem. Phys. **102**, 165 (2007).
[26]R. Yimnirun, S. Wongsaenmai, R. Wongmaneerung, N. Wongdamnern, A. Ngamjarurojana, S. Ananta, and Y. Laosiritaworn, Phys. Scr., T **T129**, 184 (2007).
[27]J. Zhao, A. E. Glazounov, and Q. M. Zhang, Appl. Phys. Lett. **74**, 436 (1999).
[28]M. Unruan, R. Wongmaneerung, A. Ngamjarurojana, S. Ananta, Y. Laosiritaworn, and R. Yimnirun, J. Appl. Phys. (unpublished).
[29]M. Unruan, S. Wongsaenmai, Y. Laosiritaworn, S. Ananta, and R. Yimnirun, J. Phys. D **41**, 085406 (2008).
[30]J. Zhao, Q. M. Zhang, and V. Mueller, Proceedings of the IEEE International Symposium on Applications of Ferroelectrics, 1998 (unpublished), p. 361.
[31]F. X. Li, S. Li, and D. N. Fang, Mater. Sci. Eng., B **120**, 119 (2005).
[32]A. Udomporn, Ph.D. thesis, Chiang Mai University, 2004.
[33]R. Yimnirun, S. Ananta, A. Ngamjarurojana, and S. Wongsaenmai, Appl. Phys. A: Mater. Sci. Process. **81**, 1227 (2005).
[34]R. Yimnirun, Y. Laosiritaworn, S. Wongsaenmai, and S. Ananta, Appl. Phys. Lett. **89**, 162901 (2006).
[35]R. Yimnirun, P. J. Moses, R. J. Meyer, and R. E. Newnham, Rev. Sci. Instrum. **74**, 3429 (2003).
[36]D. Viehland and J. Powers, J. Appl. Phys. **89**, 1820 (2001).
[37]G. Yang, S. F. Liu, W. Ren, and B. K. Mukherjee, Ferroelectrics **262**, 207 (2001).
[38]H. Krueger, J. Acoust. Soc. Am. **43**, 583 (1968).
[39]R. Yimnirun, Y. Loasiritaworn, and S. Wongsaenmai, J. Phys. D **39**, 759 (2006).
[40]A. K. Singh and D. Pandey, Phys. Rev. B **67**, 064102 (2003).
[41]C.-S. Tu, V. H. Schmidt, I.-C. Shih, and R. Chien, Phys. Rev. B **67**, 020102 (2003).
[42]V. Topolov and Z.-G. Ye, Phys. Rev. B **70**, 094113 (2004).
[43]R. Yimnirun, S. Wongsaenmai, S. Ananta, and Y. Laosiritaworn, Appl. Phys. Lett. **89**, 242901 (2006).
[44]M. E. Lines and A. M. Glass, *Principles and Applications of Ferroelectrics and Related Materials* (Oxford University Press, Oxford, 1977).

Downloaded 14 Apr 2009 to 202.28.246.2. Redistribution subject to AIP license or copyright; see http://jap.aip.org/jap/copyright.jsp

ELSEVIER

Journal of Alloys and Compounds 465 (2008) 522–526

Journal of ALLOYS AND COMPOUNDS

www.elsevier.com/locate/jallcom

# Effect of niobate B-site precursors on phase formation and particle size of lead nickel niobate powders

O. Khamman, R. Yimnirun, S. Ananta *

*Department of Physics, Faculty of Science, Chiang Mai University, Chiang Mai 50200, Thailand*

Received 26 May 2007; accepted 1 November 2007
Available online 19 December 2007

**Abstract**

A perovskite phase of $Pb(Ni_{1/3}Nb_{2/3})O_3$ or PNN powders has been synthesized by a rapid vibro-milling technique. Both $NiNb_2O_6$ and $Ni_4Nb_2O_9$ have been employed as nickel niobate precursors, with the formation of the PNN phase investigated as a function of calcination conditions by DTA and XRD techniques. Morphology and phase composition have been determined via a combination of SEM and EDX techniques. The nickel niobate precursor and calcination condition have been found to have a pronounced effect on the phase and morphology evolution of the calcined PNN powders. It is seen that optimization of calcination conditions can lead to a single-phase PNN in both methods. However, the formation temperature for single-phase PNN powders was lower for the synthetic method employing a $NiNb_2O_6$ precursor.
© 2007 Elsevier B.V. All rights reserved.

*Keywords:* Lead nickel niobate; Nickel niobate; Perovskite; Relaxor ferroelectrics

## 1. Introduction

The excellent dielectric broadening and electrostrictive properties make lead nickel niobate, $Pb(Ni_{1/3}Nb_{2/3})O_3$ or PNN, a promising material for capacitor, electrostrictive actuator, and electromechanical transducer devices [1–3]. Because of these important technological applications, there has been a great deal of interest in preparation of single-phase PNN powders as well as in the sintering and dielectric properties of PNN-based ceramics [3–7].

However, it is well-documented that the formation of PNN perovskite via the solid-state reaction is often accompanied by the occurrence of unwanted pyrochlore-type phases because of the volatilization of PbO and the low dispersion of NiO [4–6]. Hence, several material processing techniques, for example, combustion [7], co-precipitation [8] and hydrothermal [9], have been introduced as alternative to the solid-state reaction of mixed oxides to minimize the amount of pyrochlore phase formed. All of these techniques are aimed at reducing the temperature of preparation of the compound even though they are more involved and complicated than the mixed oxide route.

The columbite-precursor method which was first developed by Swart and Shrout [10] is probably one of the most fundamental, practical routine method which has been used, and it has been modified intensively for the preparation of PNN powder in the last decade [4–6]. In this method, an intermediate step to give columbite-type $NiNb_2O_6$ precursor is used to bypass the formation of the pyrochlore phases. Alternatively, the use of $Ni_4Nb_2O_9$ precursor in place of $NiNb_2O_6$ has been proposed for the fabrication of pyrochlore-free PNN [11]. However, the preparation of PNN using $Ni_4Nb_2O_9$ precursor, to date, has not been extensive as that of PNN using $NiNb_2O_6$ precursor. The potential of this alternative route was evaluated in comparison with conventional columbite route to produce PNN materials.

The purpose of this work was to compare the two B-site precursor synthetic routes of PNN formation and the characteristics of the resulting powders. The phase formation and morphology of the powders calcined at various conditions will be studied and discussed.

## 2. Experimental

$Pb(Ni_{1/3}Nb_{2/3})O_3$ was synthesized by a similar methodology of B-site precursor mixed oxide synthetic route (Fig. 1), as reported earlier [6,7,12]. Starting precursors were as follows: PbO (JCPDS file number 77-1971), NiO (JCPDS file number 73-1519) and $Nb_2O_5$ (JCPDS file number 30-0873) (Aldrich, 99% purity). These three oxide powders exhibited an average particle size in the range

* Corresponding author.
*E-mail address:* suponananta@yahoo.com (S. Ananta).

0925-8388/$ – see front matter © 2007 Elsevier B.V. All rights reserved.
doi:10.1016/j.jallcom.2007.11.002

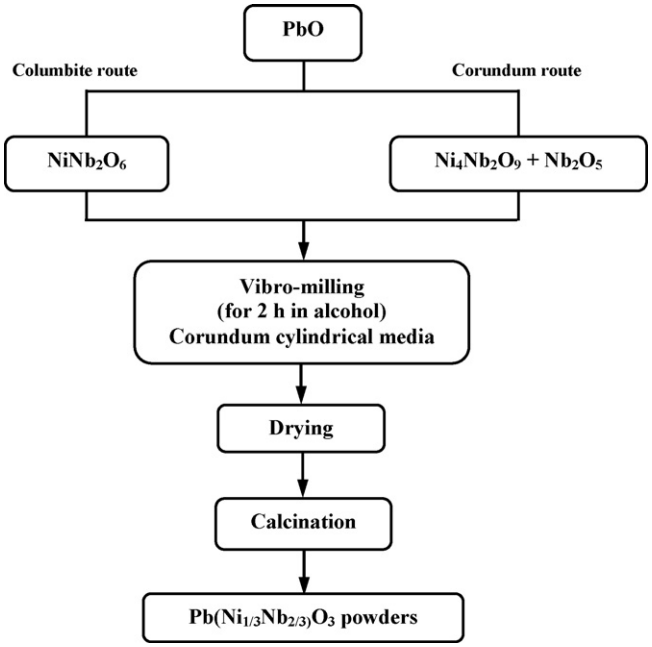



Fig. 1. A two-stage solid-state reaction routes for PNN powders.

of 3.0–5.0 μm. First, two intermediate phases of nickel niobate: $NiNb_2O_6$ and $Ni_4Nb_2O_9$ were separately prepared by the solid-state reaction method previously reported [13,14], employing an optimized calcination conditions of 900 °C for 4 h with heating/cooling rates of 30 °C/min and 1050 °C for 2 h, with heating/cooling rates of 30 °C/min, respectively. The following reaction sequences were then proposed for the formation of PNN:

1. The columbite route:

$$3PbO(s) + NiNb_2O_6(s) \rightarrow 3Pb(Ni_{1/3}Nb_{2/3})O_3(s) \quad (1)$$

2. The corundum route:

$$12PbO(s) + Ni_4Nb_2O_9(s) + 3Nb_2O_5(s) \rightarrow 12Pb(Ni_{1/3}Nb_{2/3})O_3(s) \quad (2)$$

Instead of employing a ball-milling procedure ($ZrO_2$ media under acetone for 48 h [6]), a McCrone vibro-milling was used. In order to reduce the processing time, the milling process was carried for only 2 h (instead of 12 h [12]) with corundum media in isopropanol. After drying at 120 °C for 2 h, various calcination conditions were applied in order to investigate the formation of PNN phase in each calcined powders.

The reactions of the uncalcined powders taking place during heat treatment were investigated by differential thermal analysis (DTA, Shimadzu) using a heating rate of 10 °C/min in air from room temperature up to 1200 °C. Calcined powders were subsequently examined by room temperature X-ray diffraction (XRD; Philips PW 1729 diffractometer) using Ni-filtered CuKα radiation, to identify the phases formed and optimum calcination conditions for the manufacture of PNN powders. The mean crystallite size was determined using the diffraction peak (1 1 0) of the perovskite pattern by using Scherrer equation [15]. The grain size and morphologies of calcined PNN powders were observed by scanning electron microscopy (SEM; JEOL JSM-840A). The chemical composition of the phases formed was also elucidated by an energy-dispersive X-ray (EDX) analyser with an ultra-thin window. EDX spectra were quantified with the virtual standard peaks supplied with the Oxford Instruments eXL software.

## 3. Results and discussion

DTA result for the mixtures synthesized by both B-site precursor methods is shown in Fig. 2. In general, similar trend of

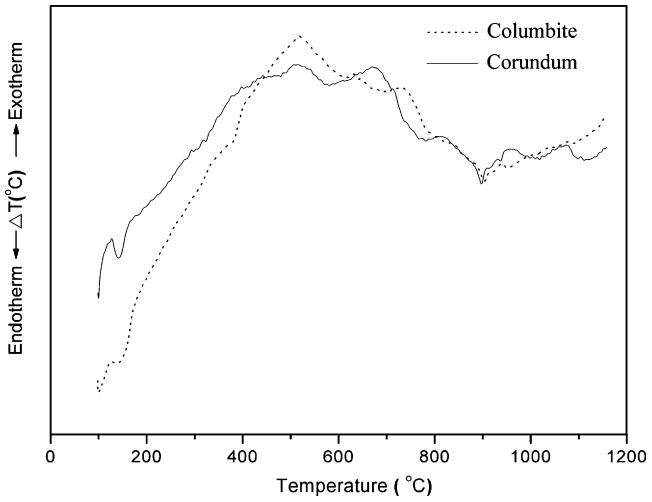



Fig. 2. DTA curves of the mixtures derived from columbite- and corundum-routes.

thermal characteristics is observed in both precursors. In the temperature range from room temperature to ~150 °C, both samples show small thermal peaks in the DTA curves, which are related to the first weight loss. These DTA peaks can be attributed to the decomposition of the organic species such as rubber lining from the milling process similar to our earlier reports [11–14]. By increasing the temperature up to ~700 °C, the solid-state reaction occurs between oxide precursors. The broad exothermic characteristic in both DTA curves represents that reaction, which has a maximum at ~450 and 600 °C for columbite- and corundum-routes, respectively. However, it is to be noted that there is no obvious interpretation of these peaks, although it is likely to correspond to a phase transition reported by a number of workers [4,6,12]. The different temperature, intensities and shapes of the thermal peaks for the two precursors here probably are related to the different starting materials especially nickel niobate and consequently, caused by the removal of species differently bonded in the network, reactivity of different species (difference in type and dispersion of NiO) in the powders. These data were used to define the range of temperatures for XRD investigation between 500 and 1150 °C. It is to be noted that a significant thermal change in DTA curves observed at temperatures above 800 °C may be attributed to the PbO volatilization typically found in lead-based ferroelectrics, consistent with other investigators [8,16,17].

To study the phase development with increasing calcination temperature in each synthetic route, they were calcined at various temperatures for 2 h in air with constant heating/cooling rates of 10 °C/min, followed by phase analysis using XRD technique. As shown in Fig. 3 (columbite route), for the uncalcined powder and the powder calcined at 500 °C, only X-ray peaks of PbO and $NiNb_2O_6$ precursors are present. Similarly, it is seen that unreacted precursors of PbO, $Nb_2O_5$ and $NiNb_2O_6$ are detected from the original mixture up to 550 °C for the corundum route (Fig. 4). These observations indicate that no reaction was yet triggered during the vibro-milling or low firing processes, in agreement with literature [11,18,19]. It is seen that PNN crystallites were developed in the powders at a calcination temperature

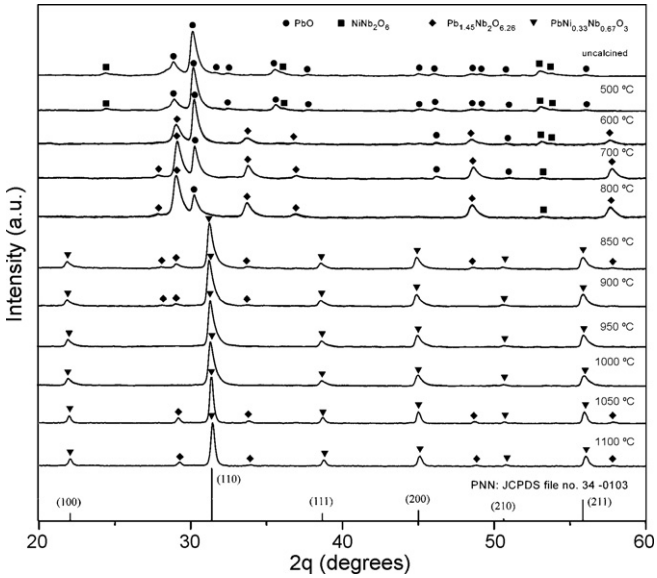



Fig. 3. XRD patterns of the columbite-route powders calcined at various conditions for 2 h with heating/cooling rates of 10 °C/min.

of 850 °C for columbite route and as low as 600 °C for corundum route.

In general, the strongest reflections apparent in the majority of these XRD patterns indicate the formation of the lead nickel niobate, PNN (▼). These can be matched with JCPDS file number 34-0103 for the cubic phase, in space group *Pm3m* (no. 221) with cell parameters $a = 403$ pm [20], consistent with other workers [6,21]. According to Fig. 3, the formation of $Pb_{1.45}Nb_2O_{6.26}$ (♦) phase has been found at ~600 °C, which is associated to the second DTA response in Fig. 2. This pyrochlore phase has a cubic structure with cell parameter $a = 1056$ pm in space group *F3dm* (no. 227) (JCPDS file number 84-1731) [22].

Upon calcination at 850 °C, the peak corresponding to PbO disappeared (not detectable by XRD method). By increasing the calcination temperature from 850 to 1000 °C, the yield of the PNN phase increases significantly until at 950 and 1000 °C, a single-phase of perovskite PNN is formed. However, for the present study, it can be seen that at the temperature range of 1050–1100 °C, some peaks of the pyrochlore $Pb_{1.45}Nb_2O_{6.26}$ phase reappear, mixing with the major phase of PNN. This could be attributed mainly to the PbO volatilization, leading to the decomposition of the perovskite phase to the pyrochlore phase, in agreement with the DTA observations at the same temperature range and also the literature [16,17].

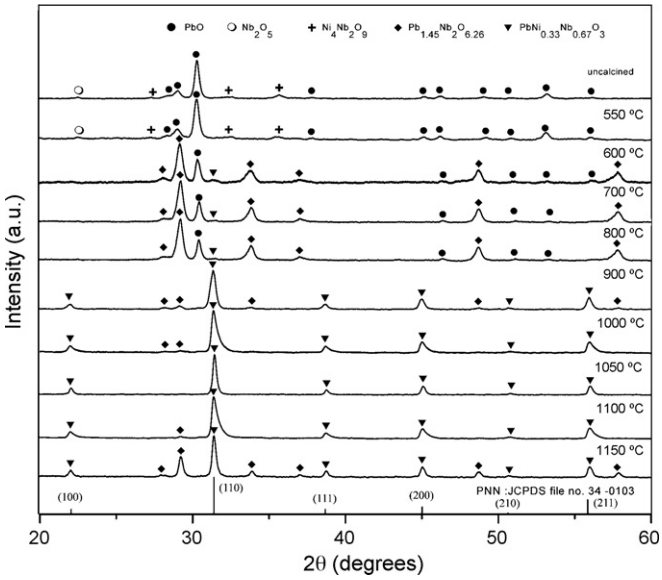



Fig. 4. XRD patterns of the corundum-route powders calcined at various conditions for 2 h with heating/cooling rates of 10 °C/min.

From Fig. 4, it is seen that calcination at 600 °C resulted in some new peaks of the perovskite PNN (▼) and pyrochlore $Pb_{1.45}Nb_2O_{6.26}$ (♦) phases [22], mixing with the unreacted PbO phase. As the firing temperature increased to 900 °C, the intensity of the PNN peaks was further enhanced and PNN becomes the predominant phase, in good agreement with the earlier DTA result. This study also shows that PNN is the only detectable phase in the corundum-route powders after calcination only at 1050 °C, whilst above 1050 °C, the pyrochore $Pb_{1.45}Nb_2O_{6.26}$ phase is formed again (probably due to the PbO partially evaporization [8,17]).

It is well-established that the perovskite-type PNN tend to form together with the pyrochlore-type $PbO–Nb_2O_5$ compounds, depending on calcination conditions [4,8,11]. In the work reported here, evidence for the formation of PNN phase, which coexists with the cubic pyrochlore phase, is found after calcination at temperature ~600–1150 °C, in agreement with literature [4,6,23]. It should be noted that no evidence of the pyrochlore $Pb_2Nb_2O_7$ [19], $Pb_3Nb_2O_8$ [8] and $Pb_3Nb_4O_{13}$ [23,24] was found in this study, nor was there any indication of the $Pb_{15}NiNb_{10}O_{41}$ reported by Balzer and Langbein [24] being present. In general, the formation temperature for high purity PNN observed in the powders derived from a combination of a B-site mixed oxide synthetic route and a carefully determined calcination condition (especially with a rapid vibromilling technique) in this work are also close to those reported for the powders prepared via many other conventional mixed oxide methods [5,6,12].

Based on the DTA and XRD data, it may be concluded that, over a wide range of calcination conditions, single-phase perovskite PNN cannot be straightforwardly formed via a two-step B-site precursor method, as verified by a number of researchers [4–7]. The experimental work carried out here suggests that the optimal calcination conditions for single-phase PNN are 950 °C (columbite route) and 1050 °C (corundum route), for 2 h with heating/cooling rates of 10 °C/min. The optimized formation temperature of single-phase PNN was lower for the columbite route probably due to the higher degree of reactivity with less reacting species involved [4]. As suggested by several workers [4,6], the degree of cation mixing in precursors significantly affects the phase formation behavior in the B-site synthesis of PNN. This observation may be accounted by the fact that the columbite route possibly provides faster chemical reaction rate (only the reaction between PbO and $NiNb_2O_6$) and is able to enhance the formation of perovskite PNN phase by increasing the reactivity of NiO [6]. Moreover, the minimum firing temperature required for the manufacturing of single-

phase columbite $NiNb_2O_6$ (~950 °C [13]) is lower than that of corundum $Ni_4Nb_2O_9$ (~1250 °C [14]).

Therefore, in general, the methodology presented in this work provides a simple method for preparing perovskite PNN powders via a solid-state mixed oxide synthetic route. It is interesting to note that, by using either columbite- or corundum-routes, with an optimal calcination condition, the reproducible, low cost and flexible process involving simple solid-state reaction synthetic route can produce high purity perovskite PNN (with impurities undetected by XRD technique) from relatively impure and inexpensive commercially available raw materials.

To further study the influence of precursor on the morphological characteristics of the resulting PNN powders, a combination of SEM and EDX is used to examine the powders obtained, as shown in Figs. 5 and 6 and Table 1. In general, it is seen that the calculated crystallite size of columbite-route PNN powders is slightly lower than the corundum-route PNN powders, in good agreement with SEM results SEM micrographs of the calcined PNN powders derived from columbite- and corundum-precursor methods are shown in Fig. 5(a) and (b), respectively. In general, the particles are agglomerated and basically irregular in shape, with a substantial variation in particle size. Observed

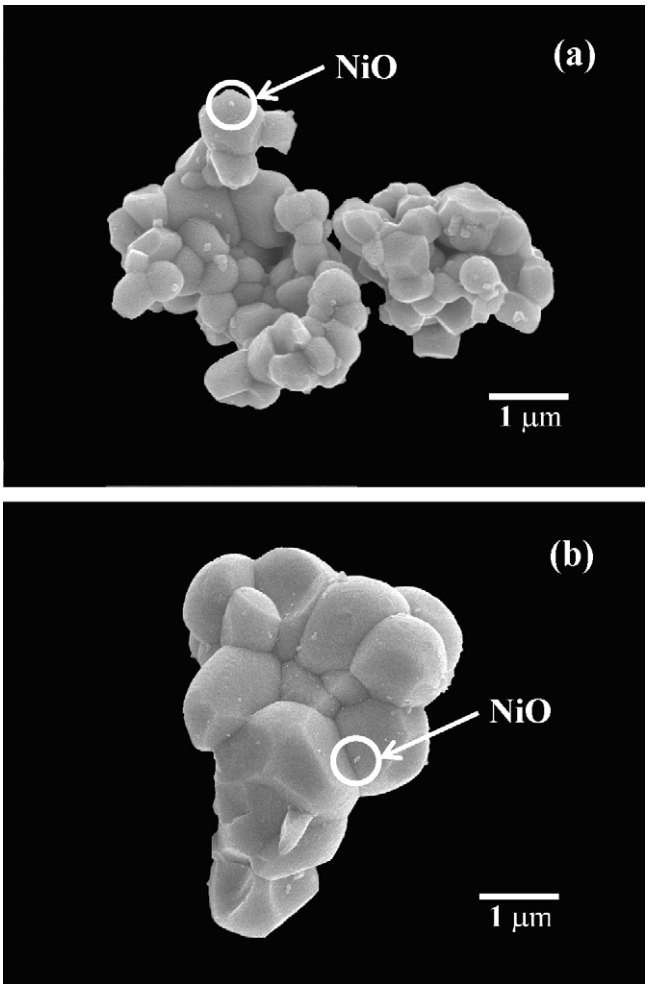



Fig. 5. SEM micrographs of the (a) columbite- and (b) corundum-route PNN powders.

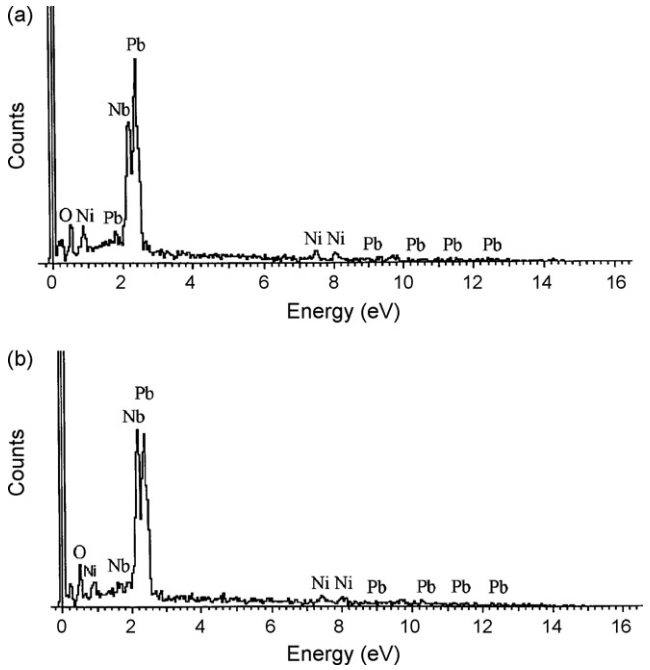



Fig. 6. EDX analysis of the (a) columbite- and (b) corundum-route PNN powders after calcined at their optimized conditions.

diameters range from 0.2 to 1.0 and 0.4 to 2.0 μm for columbite- and corundum-routes, respectively. These particle size data were directly estimated from SEM micrographs. Even though these data are not precisely determined, they were shown to provide estimated comparison between different nickel niobate precursors.

The primary particles in the agglomerates are, however, submicron in size. Additionally, the observed morphology reveals considerable difference in homogeneity, uniformity, size and shape between the two PNN powders. It is obviously evident that the columbite-route powders exhibit more heterogeneous morphology than the corundum-route powders. The columbite-route powders consist mainly of irregular round shape primary particles with a diameter of ~1 μm or less (Fig. 5(a)). In general, it is seen that primary particle in columbite-route powders is clearly smaller in size than the corundum-route powders. The averaged particle size of columbite-precursor PNN powders with finer particle size is regarded as advantage for better reactivity. However, it is seen that higher degree of agglomeration with more angular particle morphology is observed in the powders produced by the corundum route (Fig. 5(b)). The strong inter-particle bond within each aggregate is evident by the formation of a well-established necking between neighboring particles. This observation could be attributed to the mechanism of sur-

Table 1
Particle size data of both PNN powders measured by XRD and SEM techniques

| Measurement techniques | Particle size range (average) | |
|---|---|---|
| | Columbite route | Corundum route |
| XRD[a] (nm, ±2.00) | 22.31 | 23.40 |
| SEM (μm, ±0.20) | 0.22–1.00 (0.50) | 0.40–2.40 (1.11) |

[a] Crystallite size.

face energy reduction of the ultra-fine powders, i.e., the smaller the powder the higher the specific surface area [25]. This finding is also similar to that observed in PMN powders synthesized by Wongmaneerung et al. [26].

In addition, EDX analysis using a 20 nm probe from a large number of particles of the two calcined PNN powders (Fig. 6) confirmed that the parent composition is $Pb(Ni_{1/3}Nb_{2/3})O_3$, in good agreement with XRD results. A combination of SEM and EDX techniques has demonstrated that a NiO-rich phase (spherical particles with diameter ~50–100 nm) exists near the PNN parent phase, as small circles in Fig. 5. Moreover, a variation of the Pb/Ni/Nb ratio was also found, similar to that of PMN powders [26]. The existence of discrete nano-sized NiO phase points to poor reactivity of NiO, although the concentration is too low for detection by XRD [15], similar with other lead-based perovskite compounds [18,19,26].

## 4. Conclusions

This work demonstrated that single-phase perovskite $Pb(Ni_{1/3}Nb_{2/3})O_3$ powders can be successfully formed by employing either columbite or corundum B-site precursor method via a rapid vibro-milling. Evidence for the formation of a cubic pyrochlore phase, which coexists with the perovskite PNN parent phase, is found at calcination temperature ranging from 800 to 1050 °C. Amongst the two B-site precursor methods, it is seen that lower optimized calcination temperature for the production of pure lead nickel niobate powders with smaller particle size can be obtained by using $NiNb_2O_6$ precursor (the columbite route).

## Acknowledgements

We thank the Thailand Research Fund (TRF), the Commission on Higher Education (CHE), the Royal Golden Jubilee Ph.D. Program, the Faculty of Science, Chiang Mai University for all supports.

## References

[1] A.J. Moulson, J.M. Herbert, Electroceramics, second ed., Wiley, 2003.
[2] G. Haertling, J. Am. Ceram. Soc. 82 (1999) 797–818.
[3] F. Levassort, P. Tran-Huu-Hue, E. Ringaard, M. Lethiecq, J. Eur. Ceram. Soc. 21 (2001) 1361–1365.
[4] T.R. Shrout, A. Halliyal, Am. Ceram. Soc. Bull. 66 (1987) 704–711.
[5] E.F. Alberta, A.S. Bhalla, J. Phys. Chem. Solids 63 (2002) 1759–1769.
[6] C.H. Lu, W.J. Hwang, Ceram. Int. 22 (1996) 373–379.
[7] M.M.A. Sekar, A. Halliyal, J. Am. Ceram. Soc. 81 (1998) 380–388.
[8] Y. Yoshikawa, Key Eng. Mater. 206–213 (2002) 87–90.
[9] C.H. Lu, W.J. Hwang, J. Appl. Phys. 38 (1999) 5478–5482.
[10] S.L. Swartz, T.R. Shrout, Mater. Res. Bull. 17 (1982) 1245–1256.
[11] O. Khamman, R. Yimnirun, S. Ananta, Mater. Lett. 61 (2007) 4466–4470.
[12] E.F. Alberta, A.S. Bhalla, Mater. Lett. 54 (2002) 47–54.
[13] O. Khamman, R. Yimnirun, S. Ananta, Mater. Lett. 61 (2007) 639–643.
[14] O. Khamman, R. Yimnirun, S. Ananta, Mater. Lett. 61 (2007) 2565–2570.
[15] H.P. Klug, L.E. Alexander, X-ray Diffraction Procedures, second ed., Wiley, 1974.
[16] T. Zhong, Y.D. Hou, M.K. Zhu, B.C. Xu, J.L. Tang, J.B. Liu, H. Wang, H. Yan, Mater. Lett. 59 (2005) 1169–1172.
[17] K.P. Chen, C. Li, C. Lei, X. Zhang, Y. Huang, J. Mater. Sci. Lett. 21 (2002) 1785–1787.
[18] S. Ananta, Mater. Lett. 58 (2004) 2781–2786.
[19] R. Wongmaneerung, R. Yimnirun, S. Ananta, Mater. Lett. 60 (2006) 1447–1452.
[20] Powder Diffraction File No. 34-0103, International Centre for Diffraction Data, Newton Square, PA, 2000.
[21] C.H. Lu, W.J. Hwang, Jpn. J. Appl. Phys. 38 (1999) 5478–5482.
[22] Powder Diffraction File No. 84-1731, International Centre for Diffraction Data, Newton Square, PA, 2000.
[23] A.I. Agranovskaya, Bull. Acad. Sci. USSR Phys. Ser. 1 (1960) 1271–1277.
[24] B. Balzer, H. Langbein, Cryst. Res. Technol. 32 (1997) 955–962.
[25] J.S. Reeds, Principles of Ceramic Processing, second ed., Wiley, 1995.
[26] R. Wongmaneerung, T. Sarakonsri, R. Yimnirun, S. Ananta, Mater. Sci. Eng. B 132 (2006) 292–299.

ELSEVIER

Journal of Alloys and Compounds 466 (2008) 264–267

Journal of ALLOYS AND COMPOUNDS

www.elsevier.com/locate/jallcom

# Synthesis and properties of $Pb(Co_{1/3}Nb_{2/3})O_3$ ceramics

Muangjai Unruan [a], Naratip Vittayakorn [b], Rewadee Wongmaneeruang [a], Anurak Prasatkhetragarn [a], Supon Ananta [a], Rattikorn Yimnirun [a,*]

[a] *Department of Physics, Faculty of Science, Chiang Mai University, Chiang Mai 50200, Thailand*
[b] *Department of Chemistry, Faculty of Science, King Mongkut's Institute of Technology Ladkrabang, Bangkok 10520, Thailand*

Received 7 June 2007; received in revised form 3 November 2007; accepted 11 November 2007
Available online 22 November 2007

**Abstract**

In this study, $Pb(Co_{1/3}Nb_{2/3})O_3$ or PCN ceramics have been produced by sintering PCN powders synthesized from lead oxide (PbO) and cobalt niobate ($CoNb_2O_6$) with an effective method developed for minimizing the level of PbO loss during sintering. Attention has been focused on relationships between sintering conditions, phase formation, density, microstructural development, dielectric and ferroelectric properties of the sintered ceramics. The densities of sintered PCN ceramics increased with increasing sintering temperature. However, it was observed that at too high temperature the density began to decrease. Change of dielectric properties with sintering temperature also followed the same trend as the density. Based on X-ray diffraction analysis, density data, SEM micrograph, and dielectric properties, the optimum sintering temperature for a high purity PCN ceramic was found to be about 1100 and 1150 °C. A strongly diffused dielectric peak also showed a typical characteristic of ferroelectric relaxors. The P–E hysteresis loops observed at −70 °C were of slim-loop type with small remnant polarization values, which confirmed relaxor ferroelectric behavior of PCN ceramics.
© 2007 Elsevier B.V. All rights reserved.

*Keywords:* Dielectric properties; Sintering; PCN

## 1. Introduction

Lead-base relaxor ferroelectrics, particularly lead magnesium niobate, $Pb(Mg_{1/3}Nb_{2/3})O_3$ (PMN) belong to a technologically important class of complex $Pb(B'B'')O_3$ perovskite materials [1]. PMN has advantages of having broader operating temperature rang, especially over the room temperature rang. This is a direct result of a diffuse paraelectric–ferroelectric phase transition in the vicinity of room temperature. In addition, as a result of their unique microstructure features PMN ceramics exhibit low loss and non-hysteretic characteristics [2]. However, little attention has been devoted to the other lead-base relaxor ferroelectrics, $Pb(A_{1/3}B_{2/3})O_3$ (A is $Mg^{2+}$, $Co^{2+}$, $Ni^{2+}$ or $Zn^{2+}$ and B is $Nb^{5+}$ or $Ta^{5+}$), discovered by Bokov and Mylnikova [3], with the perovskite structure and the dielectric maxima temperature ($T_m$) lower than room temperature except for that of $Pb(Zn_{1/3}Nb_{2/3})O_3$. Although $Mg^{2+}$, $Co^{2+}$, $Ni^{2+}$ and $Zn^{2+}$ have similar radii, the temperatures at which spontaneous polarization occurs in $Pb(A_{1/3}B_{2/3})O_3$ differ [4].

Therefore, in this study one of lesser studied ceramics in the $Pb(A_{1/3}B_{2/3})O_3$ system, i.e. $Pb(Co_{1/3}Nb_{2/3})O_3$ (PCN) is investigated. Synthesis method, physical properties, microstructure, dielectric and ferroelectric properties of the ceramic are discussed.

## 2. Experimental method

PCN ceramics were prepared from starting PbO and $CoNb_2O_6$ (or CN) powders by a conventional mixed oxide method. CN powders were obtained from the columbite method [5], while PCN powders were prepared by a simple mixed oxide method. To obtain the perovskite-phase PCN, the cobalt niobate ($CoNb_2O_6$) powders were first prepared by mixing CoO (99.9%) and $Nb_2O_5$ (99.9%) powders in the proper proportion and vibro-milling for 1 h. After drying, the mixtures were calcined at 1100 °C for 4 h to yield so-called columbite powders ($CoNb_2O_6$). Subsequently, the columbite powders were mixed with PbO (99.9%) by the vibro-milling method and calcined at 950 °C for 4 h to form the perovskite-phase PCN powders. Then PCN powders were pressed hydraulically to form disc-shaped pellets 8 mm in diameter and 2 mm thick, with 3 wt% polyvinyl alcohol as a binder. The pellets were placed in the alumina crucible. Finally, for optimization purposes the pellets were sintered at 1050, 1100, 1150 and 1200 °C for 2 h. The phase formation of the sintered ceramics was studied by the X-ray diffraction (XRD) technique. The densities of sintered spec-

* Corresponding author. Tel.: +66 53 943 367; fax: +66 53 943 445.
*E-mail address:* rattikornyimnirun@yahoo.com (R. Yimnirun).

0925-8388/$ – see front matter © 2007 Elsevier B.V. All rights reserved.
doi:10.1016/j.jallcom.2007.11.071

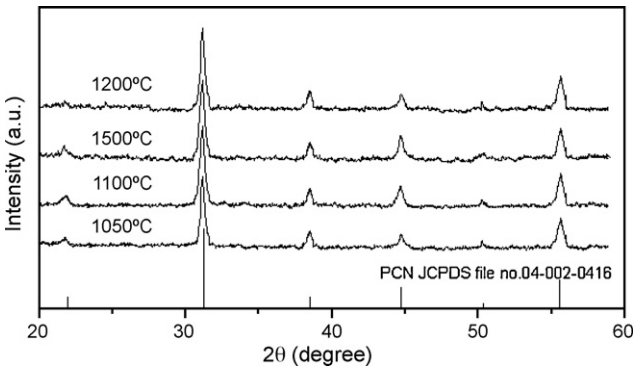



Fig. 1. XRD diffraction patterns of the sintered PCN ceramics.

imens were measured by Archimedes method. The microstructure analyses were undertaken by scanning electron microscopy (SEM: JEOL Model JSM 840A). The grain size was determined from SEM micrographs by a linear intercept method.

Before studying the dielectric properties, the specimens were lapped to obtain parallel faces. After coating with silver paint as electrode on the faces, the specimens were heated at 750 °C for 12 min to ensure contact between the electrode and the surface of the ceramic. The dielectric properties (dielectric constant ($\varepsilon_r$) and dielectric loss (tan $\delta$)) were measured at temperatures between −120 and 50 °C. The capacitance was measured with a HP4284A LCR meter in connection with a Delta Design 9023 temperature chamber and a sample holder (Norwegian Electroceramics). The dielectric constant ($\varepsilon_r$) was then calculated from a parallel-plate capacitor equation, e.g. $\varepsilon_r = Cd/\varepsilon_o A$, where $C$ is the capacitance of the specimens, $d$ and $A$ are, respectively, the thickness and the area of the electrode and $\varepsilon_o$ is the dielectric permittivity of vacuum ($8.854 \times 10^{-12}$ Fm$^{-1}$). Finally, the polarization–electric field (P–E) hysteresis loops at −70 °C were obtained using a standardized ferroelectric tester system (RT66A) with driving frequency of 4 Hz.

## 3. Results and discussion

The phase formation behavior of the sintered ceramics is revealed by an XRD method. The XRD patterns are presented in Fig. 1, with the corresponding JCPDS pattern also shown. In general, the strongest reflections apparent in the majority of the XRD patterns indicate the formation of perovskite lead cobalt niobate phase. These can be matched with JCPDS file number 04-002-0416 for the $Pb(Co_{0.33}Nb_{0.67})O_3$. Based on the XRD analysis, the optimum sintering temperature for the formation of a high purity PCN phase was found at 1100 °C.

The densities of PCN ceramics sintered at different temperatures are listed in Table 1. It is clear that the density usually increases with increasing sintering temperature. This is believed to be a result of more completed solid-state reactions at higher sintering temperatures. However, it is also observed that at too high temperature the density begins to decrease. Lead-loss is generally accepted to be the reason for the decreasing density [6].

The SEM micrographs of fractured surfaces of all PCN ceramics are shown in Fig. 2. PCN ceramic sintered at 1050 °C has small grain size with variation in grain shape. However, the other ceramics exhibit different morphology showing a possible pyrochlore formation (with pyramidal-shaped grains) and also over-sintered specimens. Table 1 also shows that the average grain size of PCN ceramics sintered at 1050 °C is relatively small, as compared to those sintered at higher temperatures. The average grain size increases with increasing sintering temperatures. However, it is also observed that at very high temperature the grain size begins to decrease, which is similar to the trend observed for the density. Change of dielectric properties with sintering temperature also followed the same trend as the density. The dielectric constant reaches maximum values at sintering temperature of 1150 °C.

Temperature and frequency dependencies of $\varepsilon_r$, as calculated from the capacitance of the sample and its geometry, and tan $\delta$ were measured continuously by increasing temperature from −120 to 50 °C and frequency rang from 100 Hz to 100 kHz. The temperature dependence of $\varepsilon_r$ and tan $\delta$ for the PCN ceramics are plotted in Fig. 3. As the measuring temperature increases the maximum dielectric constant ($\varepsilon_{max}$) appears at −30 °C, this temperature is called dielectric maxima temperature ($T_m$). It should be noticed that $T_m$ obtained in this study is different from previous studies [3,7–9], which reported $T_m$ of −70 °C for single crystal PCN and stress-dependent $T_m$ for PCN ceramics ranging from −20 to −50 °C. It could be said that the $T_m$ values obtained in this study fall within the previously reported values. This is because in this current study the dielectric properties, which are used to determine $T_m$, of the PCN ceramic were measured under compressive stress from a rather heavy sample holder used in the measurement system. In addition, the ceramics may also contain internal residual stress. Therefore, the $T_m$ values obtained in this study are slightly lower than the previously reported value under stress-free condition. There is also insignificant change of $T_m$ with different sintering temperatures. The tan $\delta$ shows only very small decrease with decreasing temperature below the $T_m$ and tan $\delta$ becomes very high above the temperature of maximum dielectric constant. Based on X-ray diffraction analysis, density data, SEM micrograph, and dielectric properties, the optimum sintering

Table 1
Characteristics of PCN ceramics

| Sintering temperature (°C) | Density (g/cm$^3$) | Average grain size (μm) | Dielectric properties | |
|---|---|---|---|---|
| | | | $\varepsilon_{max}$ | tan $\delta$ |
| 1050 | 7.58 | 1.83 | 2178 | 0.0594 |
| 1100 | 8.06 | 4.11 | 2657 | 0.0592 |
| 1150 | 8.07 | 6.35 | 2673 | 0.0578 |
| 1200 | 7.98 | 4.58 | 2248 | 0.0507 |

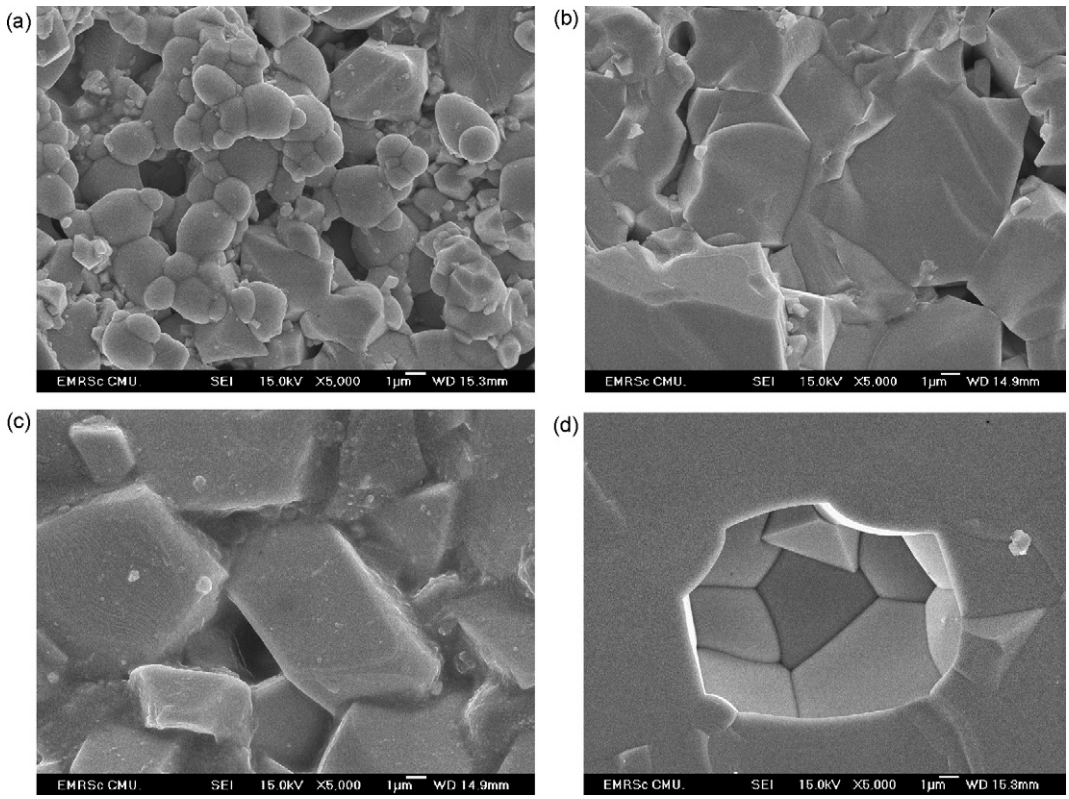



Fig. 2. SEM micrographs of PCN ceramics at different sintering temperature: (a) 1050 °C; (b) 1100 °C; (c) 1150 °C; and (d) 1200 °C.

temperature for a high purity PCN ceramic is found to be about 1100 and 1150 °C.

A strongly diffused dielectric peak is characteristic of ferroelectric relaxors. Frequency-dependent dielectric properties below $T_m$ are also observed (Fig. 4.), further indicating relaxor behavior of PCN ceramics. However, one would expect to see a strong shift in $T_m$ with frequency, as expected for typical relaxors, such behavior is not clearly visible because very high tan $\delta$ above $T_m$ causes $\varepsilon_r$ to increase rapidly.

The hysteresis loops at −70 °C of PCN ceramics sintered at different temperatures are shown in Fig. 5. It can be seen that slim P–E loops with small remnant polarization values are generally obtained for all ceramics. The slim-loop nature of the P–E curves suggests that most of the aligned dipole moments switch back to a randomly oriented state upon removal of the field. This behavior has previously been observed in ferroelectric relaxors [10]. In relaxor ferroelectric materials, micro- to macro-domain transition occurs. In the absence of any external field, the domain structure of relaxor ferroelectrics contains randomly oriented micropolar regions. However, when an electric field is applied, the micro-domains orient along the field direction and the macro-domains occur [10]. The P–E loops observed here also support that the PCN ceramics exhibit relaxor ferroelectric behavior.

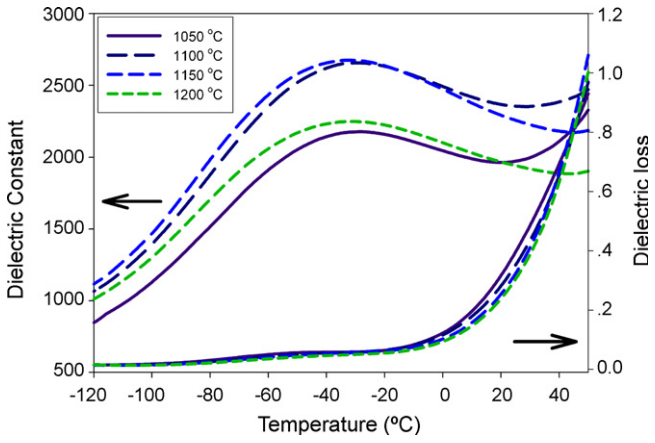



Fig. 3. Temperature dependence of dielectric properties of PCN ceramics at 1 kHz.

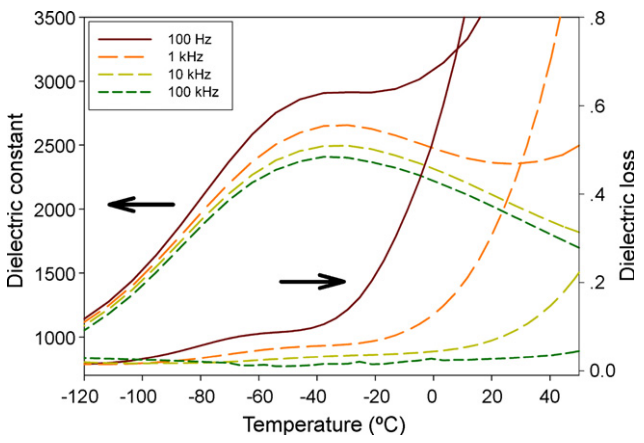



Fig. 4. Temperature and frequency dependence of dielectric properties of PCN ceramic sintered at 1100 °C.

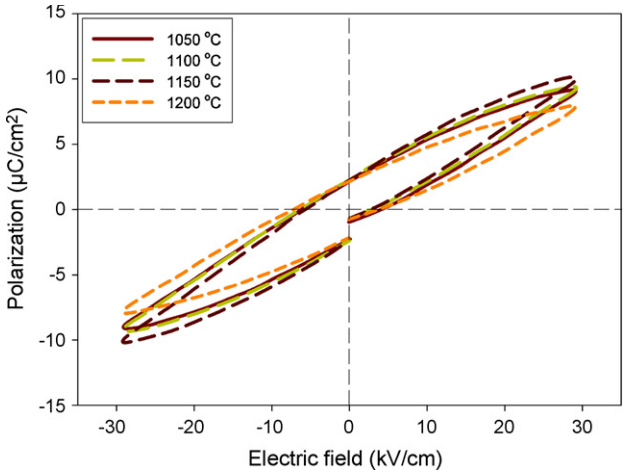



Fig. 5. P–E hysteresis loops of PCN ceramics measured at −70 °C (4 Hz).

## 4. Conclusions

In this study, PCN ceramics were prepared by the columbite precursor method. The PCN ceramics with perovskite structure and a high purity single phase are obtained. Density of these ceramics increases with increasing sintering temperature. However, at too high temperature the density begins to decrease. Change of dielectric properties with sintering temperature also follows the same trend as the density. Based on X-ray diffraction analysis, density data, SEM micrograph, and dielectric properties, the optimum sintering temperature for a high purity PCN ceramic is found to be about 1100 and 1150 °C. The samples exhibit a relaxor behavior around the maximum dielectric constant, characterized by a strongly diffused dielectric peak at −30 °C. The hysteresis loops measured at −70 °C show slim P–E loops with small remnant polarization values. This behavior has been observed in ferroelectric relaxors.

## Acknowledgments

This work is supported by the Thailand Research Fund (TRF) and Commission on Higher Education (CHE). Additional supports from the Faculty of Science and Graduate School of Chiang Mai University are gratefully acknowledged.

## References

[1] K. Vladimir, B. Jaroslav, Ceramics-Silikaty 47 (2003) 8.
[2] L.E. Cross, Ferroelectrics 76 (1987) 241.
[3] V.A. Bokov, I.E. Mylnikova, Sov. Phys. Solid State (Eng. Transl.) 2 (1961) 2428.
[4] T. Kudo, T. Yazaki, F. Naito, S. Sugaya, J. Am. Ceram. Soc. 53 (1969) 326.
[5] S.L. Swartz, T.R. Shrout, Mater. Res. Bull. 17 (1982) 1245.
[6] R. Yimnirun, S. Ananta, P. Laoratanakul, J. Eur. Ceram. Soc. 25 (2005) 3225.
[7] Landolt-Bornstein, in: T. Mitsui, S. Nomura (Eds.), Ferroelectrics and Related Substances, vol. 16, Springer-Verlag, Berlin, 1981.
[8] Y. Yamashita, Jpn. J. Appl. Phys. 33 (1994) 5328.
[9] T. Huchiga, S. Fujimoto, N. Yasuda, J. Phys. D: Appl. Phys. 20 (1987) 1291.
[10] A. Peláiz-Barranco, I. González-Carmenate, F. Calderón-Piñar, Solid State Commun. 134 (2005) 519–522.

# Changes in ferroelectric properties of ceramics in lead magnesium niobate–lead titanate system with compressive stress

Muangjai Unruan,[1] Rewadee Wongmaneerung,[2] Athipong Ngamjarurojana,[1] Yongyut Laosiritaworn,[1] Supon Ananta,[1] and Rattikorn Yimnirun[1,a)]
[1]*Department of Physics, Faculty of Science, Chiang Mai University, Chiang Mai 50200, Thailand*
[2]*Department of Physics, Faculty of Science, Maejo University, Chiang Mai 50290, Thailand*

(Received 1 May 2008; accepted 10 July 2008; published online 22 September 2008)

Effects of compressive stress on the ferroelectric properties of $Pb(Mg_{1/3}Nb_{2/3})O_3-PbTiO_3$ (PMN-PT) ceramics were investigated. The ceramics with the formula $(1-x)Pb(Mg_{1/3}Nb_{2/3})O_3-(x)PbTiO_3$ or $(1-x)PMN-(x)PT$ $(x=0.1-0.5)$ were prepared by a conventional mixed-oxide method. Dense perovskite-phase PMN-PT ceramics with a uniform microstructure were obtained. The ferroelectric properties were measured under compressive stress (0–75 MPa) using a homebuilt compressometer in conjunction with a modified Sawyer–Tower circuit. The experimental results revealed that the superimposed compression stress significantly reduced both the dissipation energy and the polarizations of the near morphotropic phase boundary compositions, i.e., 0.8PMN-0.2PT, 0.7PMN-0.3PT, and 0.6PMN-0.4PT, while the stress influence was much less in other compositions. On the contrary, the applied compressive stress showed little or no influence on the coercive field. These results were interpreted through the non-180° ferroelastic domain switching processes and the stress induced decrease in the switchable part of domains. © *2008 American Institute of Physics*. [DOI: 10.1063/1.2977684]

## I. INTRODUCTION

Lead magnesium niobate, $Pb(Mg_{1/3}Nb_{2/3})O_3$ (PMN), and its solid solution with lead titanate, $PbTiO_3$ (PT), so-called PMN-PT, are of great interest due to their high polarizabilities and excellent electrical properties suitable for various applications. These compounds have dielectric constants in excess of 20 000, making them potential candidates for capacitive applications. In addition, they also exhibit a large electrostriction at temperatures above their phase transition temperatures. This behavior extends their use to transducer and actuator applications.[1–5] The $(1-x)Pb(Mg_{1/3}Nb_{2/3})O_3-(x)PbTiO_3$ or $(1-x)PMN-(x)PT$ ceramic compositions with $x<0.2$ have been studied for electrostrictive applications,[4–7] while those with $x>0.2$ can be utilized as piezoelectric materials.[4,6,8,9] The differences between the electrostrictive and piezoelectric compositions of PMN-PT are due to differences in the degree of long-range polar order.[4,7,10] In the compositions with lower PT content, relaxor ferroelectric characteristics with polar clusters or nanodomains are observed.[4,11,12] On the other hand, long-range polar order with normal micron-sized ferroelectric domains exists in the compositions with higher PT content.[4,9,10]

Practically, when used in specific applications PMN-PT ceramics are often subjected to mechanical loading either deliberately in the design of the device itself or because the device is used to change shapes such as in many smart structure applications or the device is used under environmental stresses.[8,13–17] A prior knowledge of how the material properties change under different load conditions is crucial for the proper design of a device and for suitable selection of materials for a specific application. Despite this fact, material constants used in any design calculations are often obtained from a stress-free measuring condition, which in turn may lead to incorrect or inappropriate actuator and transducer designs. It is therefore important to determine the properties of these materials as a function of applied stress. Previous investigations on the stress-dependent electrical properties of many ceramic systems have clearly emphasized the importance of the matter.[7,15,18–29] Recently, the stress dependence of dielectric and ferroelectric properties has been investigated in materials such as PZT, PMN, BT, PZT-BT, PMN-PZT, and PZN-PZT.[19–22,30–32] In addition, our previous investigation on the influence of the applied stress on the dielectric properties of PMN-PT ceramic systems also revealed that the superimposed compression stress significantly reduced both the dielectric constant and the dielectric loss tangent of 0.9PMN-0.1PT ceramic, while the changes were not as significant in the other PMN-PT ceramic compositions.[24] The results clearly showed that the effects of stress on the dielectric properties depended significantly on ceramic compositions and stress levels. Since PMN-PT ceramics are practically employed in many electromechanical devices, there have been previous reports on the electromechanical properties of electrostrictive 0.9PMN-0.1PT and piezoelectric 0.7PMN-0.3PT ceramics under various mechanical and electrical loading conditions.[7,15,23,33] However, there has been no systematic study on the influence of an applied compressive stress on the ferroelectric properties of ceramics in the PMN-PT system. Therefore, it is the aim of this study to determine the ferroelectric properties of the $(1-x)PMN-(x)PT$, with $0.1\leq x\leq 0.5$, ceramics as a function of compressive stress.

a)Author to whom correspondence should be addressed. Electronic mail: rattikornyimnirun@yahoo.com.

 © 2008 American Institute of Physics

Author complimentary copy. Redistribution subject to AIP license or copyright, see http://jap.aip.org/jap/copyright.jsp

## II. EXPERIMENTAL METHOD

Perovskite-phase PMN powders were obtained from the columbite method, while PT powders were prepared by a simple mixed-oxide method.[34] The $(1-x)Pb(Mg_{1/3}Nb_{2/3})O_3-(x)PbTiO_3$ ceramics were then prepared from starting PMN and PT powders by the mixed-oxide method. Finally, for optimization purpose the pellets were sintered at a temperature between 1220 and 1240 °C for 2 h. Optimum sintering conditions for all ceramics were established by identifying the conditions for maximizing both the bulk density and the yield of perovskite. However, since the PMN-PT compositions having high PT content in the range $0.6 \leq x \leq 0.9$ could not be fabricated in a bulk form with high density, these compositions could not be characterized any further for the rest of the study. Their comparatively large $c/a$ values, which give rise to serious internal stress, are responsible for the frequent crack developments around the phase transition temperature during cooling of these sintered samples. In the present study, only compositions in the pseudobinary system $(1-x)$PMN$-x$PT $(0.1 \leq x \leq 0.5)$ have been fabricated from the calcined $(1-x)$PMN$-x$PT powders, employing a normal sintering method, i.e., pressureless sintering technique. Details of the processing and characterizations were provided elsewhere.[34]

Before studying the dielectric properties, the specimens were lapped to obtain parallel faces. After coating with silver paint as electrode at the faces, the specimens were heated at 750 °C for 12 min to ensure the contact between the electrode and surface of the ceramic. The ferroelectric hysteresis polarization-field ($P$-$E$) loops were characterized by using a computer controlled modified Sawyer–Tower circuit. The electric field of 15 kV/cm was applied to a sample by a high voltage ac amplifier (Trek, model 610D) with the input sinusoidal signal with a frequency of 60 Hz from a signal generator (Goodwill, model GAG-809). The detailed descriptions of this system were explained elsewhere.[35,36] To study the effects of the compressive stress on the ferroelectric properties, the uniaxial compressometer was constructed for simultaneous and parallel applications of the mechanical stress and the electric field.[37] Measurements were performed as a function of mechanical stress applied discretely between 0 and 75 MPa. During the measurements, a desired stress was first applied to the sample and then the electric field was applied. The ferroelectric hysteresis ($P$-$E$) loop was recorded at room temperature (25 °C) for both loading and unloading conditions. The parameters obtained from the loops were the maximum polarization ($P_{max}$), the remnant polarization ($P_r$), and the coercive field ($E_c$), which were defined as the points where the loops reach the maximum polarization, cross the zero field, and cross the zero polarization, respectively. The measurements reported were for the samples during their first mechanical stress cycle. It should also be noted that the reported ferroelectric parameters were obtained after a total of 10 cycles of the electric field was applied to the sample at each constant stress level.

## III. RESULTS AND DISCUSSION

It should be mentioned here that the results from x-ray diffraction studies,[30,34] not shown here, indicated that complete crystalline solutions of perovskite structure were formed throughout the composition range between $x=0.1$ and 0.5. In general, only a (pseudo)cubic symmetry is observed at low values of PT concentration, in good agreement with other workers.[38,39] By the influence of PT, however, several peaks split for $x \geq 0.4$, indicating the development of tetragonal symmetry, consistent with earlier work on PMN-PT ceramics.[9,40] Similar microstructure characteristics were observed in these samples, i.e., uniformly sized grains with a high degree of grain close packing, and almost no abnormal grain growth. In each ceramic composition grain size ranges between 0.4 and 3.7 $\mu$m, with similar averaged grain size for all compositions. By applying the linear intercept method to scanning electron microscopy micrographs of polished and thermally etched specimens, mean grain sizes of about 1.72–2.11 $\mu$m are estimated for these samples. Bulk density values are found to decrease slightly with $x$ (in the units of g/cm$^3$; the value decreases gradually from 7.98 in 0.9PMN-0.1PT to 7.78 in 0.5PMN-0.5PT). These characteristics indicate that dense perovskite-phase PMN-PT ceramics with a uniform microstructure have been obtained. Since the physical and microstructure features of all ceramic compositions are not significantly different, these parameters should not play an important role in the composition-dependent ferroelectric properties under compressive stress.

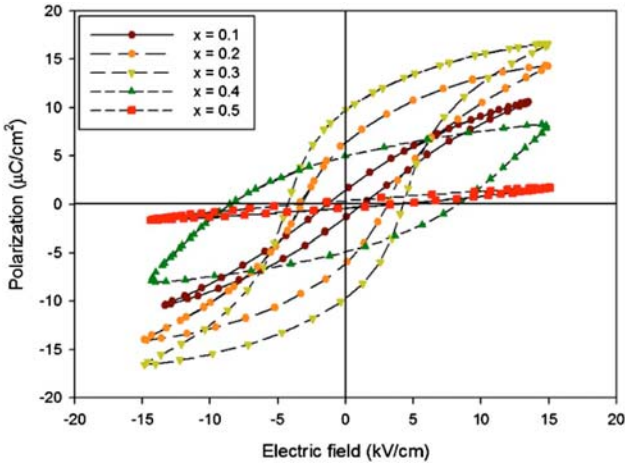



FIG. 1. (Color online) Polarization–electric field ($P$-$E$) hysteresis loops for the $(1-x)$PMN$-(x)$PT ceramics under stress-free condition (measured at 25 °C and 60 Hz).

Figure 1 illustrates a series of polarization-field ($P$-$E$) hysteresis loops for the PMN-PT ceramics under stress-free condition. It is clearly evident that the shape of $P$-$E$ loops varies greatly with the ceramic compositions. With a large amount of normal ferroelectric PT contents, the polarization loop of 0.6PMN-0.4PT is well developed, showing a large remnant polarization ($P_r$: remaining polarization when electric field is decreased to zero) and coercive field ($E_C$). The hysteresis loop is of a typical "square" form as a result of domain switching in an applied field. This is a typical characteristic of a phase that contains long-range interaction between dipoles in the ferroelectric microdomain state.[1,4,5] This confirms that the composition is of a normal ferroelectric phase with tetragonal symmetry. It should be noted that a

Author complimentary copy. Redistribution subject to AIP license or copyright, see http://jap.aip.org/jap/copyright.jsp

similar observation is expected in the 0.5PMN-0.5PT composition. However, with a even larger amount of PT content, one would expect a much higher applied field to fully reveal the well-developed *P-E* loop. Therefore, the more open loop was not obtained at this relatively low electric field of 15 kV/cm. More importantly, the 0.7PMN-0.3PT ceramic shows the largest polarization values with small coercive fields ($E_C$), confirming that the composition is near the morphotropic phase boundary (MPB) of the PMN-PT system. The other compositions with more PMN content show more of "slim" hysteresis loops, a characteristic of the suppressed ferroelectric interaction.[1,4,5] This is typically found in the relaxor ferroelectrics with polar nanoregions. This also has resulted in a decrease in the values of both $P_r$ and $E_C$ due to an increased pseudocubic nonferroelectric phase content.[1,4,5]

The polarization versus electric field (*P-E*) hysteresis loops of the 0.9PMN-0.1PT, 0.7PMN-0.3PT, and 0.5PMN-0.5PT ceramics under different compressive stresses are shown in Figs. 2(a)–2(c), respectively. It should be noticed that generally the area of the *P-E* loops decreases with increasing compressive stress. The changes follow a similar trend for all the ceramic compositions. The *P-E* loop area indicates the polarization dissipation energy of a ferroelectric material under one full cycle of electric field application.[18,41] This amount of the energy loss is directly related to the amount of domains participating in the switching process during the application of electric field.[18,19] For a given composition, the decrease in the loop area with increasing compressive stress is a result of the stress-induced domain wall suppression.[18,35]

The changes in the hysteresis parameters, i.e., the dissipation energy, the maximum polarization ($P_{max}$), the remnant polarization ($P_r$), and the coercive field ($E_C$), with the compressive stresses are plotted in Fig. 3. Generally, it can be seen that both the dissipation energy and the polarizations decrease as the compressive stress increases. On the contrary, the applied compressive stress shows little or no influence on the coercive field. More interestingly, the decrease in the dissipation energy and the polarizations with the compressive stress for the near MPB compositions, i.e., 0.8PMN-0.2PT, 0.7PMN-0.3PT, and 0.6PMN-0.4PT, is clearly more pronounced than that of the 0.9PMN-0.1PT and 0.5PMN-0.5PT compositions. The changes are clearly more observable in 0.7PMN-0.3PT and 0.6PMN-0.4PT compositions, which are closer to the reported MPB composition.[1,4,5] The reductions in both the dissipation energy and the polarization values are generally less than 20% when the compressive is increased from 0 to 75 MPa. As also depicted in Fig. 3, it should be noticed that even though the loading and unloading experiments were performed on all compositions, the results differ insignificantly. In addition, only slight decreases in the polarization values of all the ceramics are also observed after a complete cycle of the mechanical stress. This observation suggests a stress-induced decrease in the switchable part of the polarization at high stress levels.[21,23] The results of the changes in the hysteresis parameters of the PMN-PT ceramics with increasing compressive stress are in agreement with the previous investigations on many ferroelectric ceramics.[18,20–23,35,42,43]

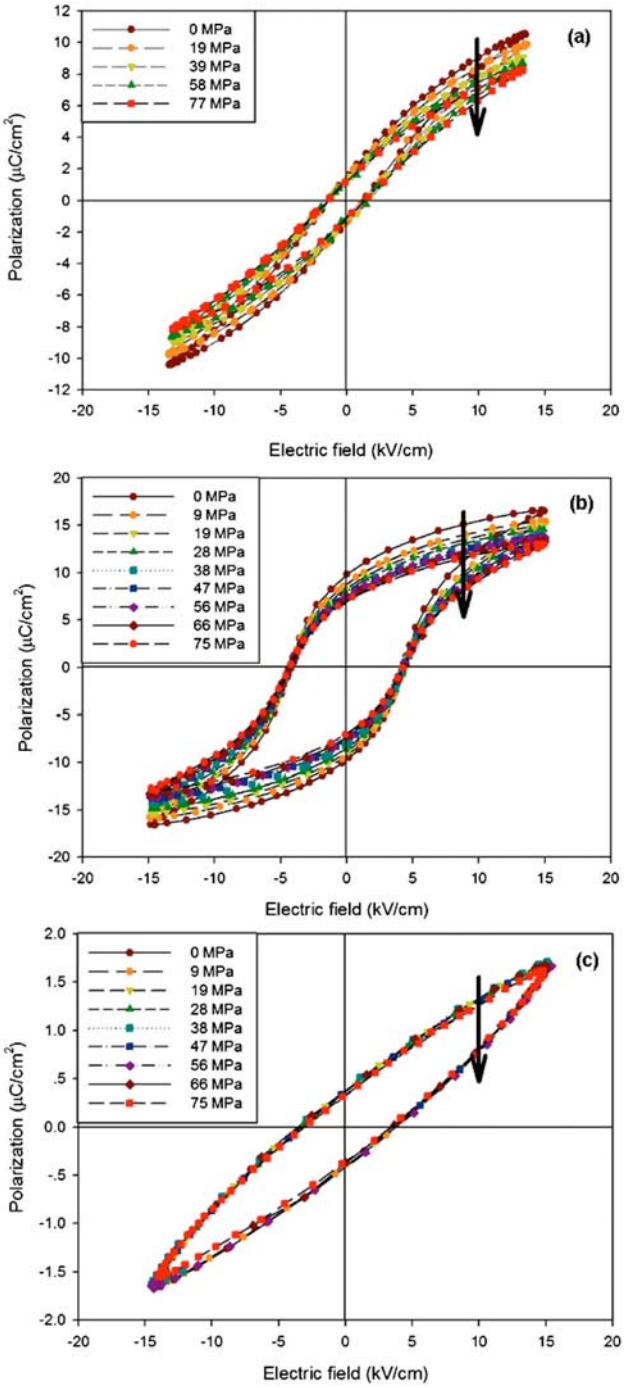



FIG. 2. (Color online) *P-E* hysteresis loops as a function of compressive stress for (a) 0.9PMN-0.1PT, (b) 0.7PMN-0.3PT, and (c) 0.5PMN-0.5PT ceramics (measured at 25 °C and 60 Hz under loading).

To understand, at least qualitatively, these experimental results on ferroelectric properties of the PMN-PT ceramics, one can interpret the changes in terms of domain-reorientation processes. When the compressive stress is applied in the direction parallel to the polar axis (poling) direction, the applied stress tends to keep the ferroelectric domains aligned with their polar axes away from the stress direction through the non-180° ferroelastic domain switching processes.[18–21] Therefore, it takes a larger than usual applied electric field to reorient the domains along the stress direc-

Author complimentary copy. Redistribution subject to AIP license or copyright, see http://jap.aip.org/jap/copyright.jsp

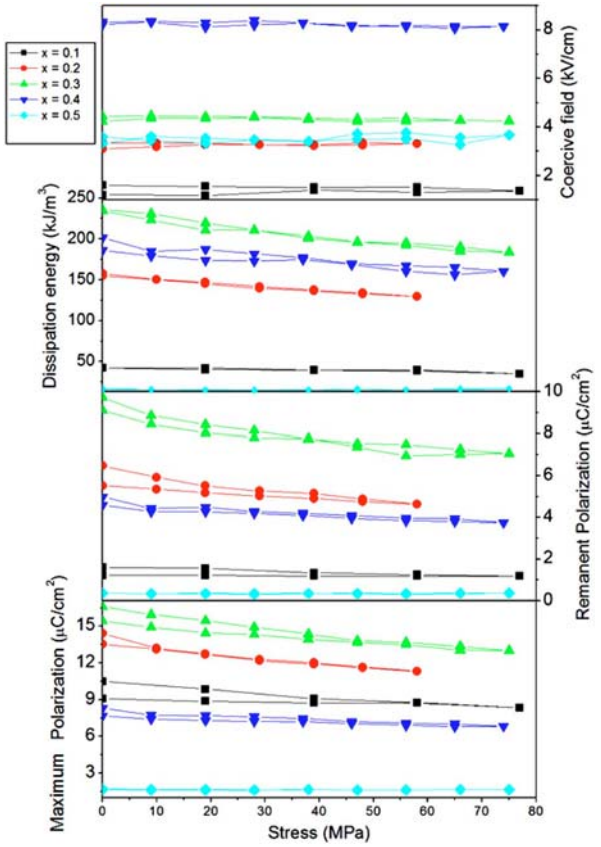



FIG. 3. (Color online) Changes in ferroelectric hysteresis parameters with compressive stress for $(1-x)$PMN$-(x)$PT ceramics (measured at 25 °C and 60 Hz) during loading and unloading.

tion, resulting in a lower value of the maximum polarization ($P_{max}$), as shown in Figs. 2 and 3. When the electric field is reduced to zero the domains tend to rotate back away from the applied compressive stress direction, resulting in a lower than usual remnant polarization ($P_r$), as depicted in Figs. 2 and 3.[21,23,33] Furthermore, considering the decrease in the hysteresis loss with increasing the compressive stress, it indicates that more and more ferroelectric domains are constrained by the applied stress and cannot be reoriented by the electric field so as to participate in the polarization reversal. Consequently, both the maximum and remnant polarizations become lower with increasing compressive stress.[20] The above mentioned arguments are particularly applicable to the closer to MPB compositions, i.e., 0.8PMN-0.2PT, 0.7PMN-0.3PT, and 0.6PMN-0.4PT, with more mobile microdomains. However, for the 0.9PMN-0.1PT composition it is observed that the changes in hysteresis parameters with the applied stress are rather small, as depicted in Figs. 2 and 3. This is due to the fact that this ceramic composition behaves more like a relaxor material.[4] Since the experiment was carried out at room temperature, the nanodomain states still predominate in this ceramic composition.[4,11] Therefore, this shows less stress-induced changes in polarizations.[7] For 0.5PMN-0.5PT composition, as described above, the rather small values in the hysteresis parameters may contribute greatly to the weak changes with stress. In addition, since the measuring temperature is far below its transition temperature of 250 °C,[34] the domains may be much less mobile in this ceramic composition; hence, much weaker changes in the hysteresis parameters with stress are observed. Most importantly, the results presented in this study have shown the different contributions to the stress-dependent ferroelectric properties in PMN-PT ceramics. This study has served as an extension to our previous work on the stress-dependent dielectric properties[30] as well as other earlier reports, which mainly focused on only 0.9PMN-0.1PT compositions.[7,15,23,33] Finally, the information obtained here is practically very useful for the design and calculation consideration of devices employing the PMN-PT ceramics.

## IV. CONCLUSIONS

In this study, the ferroelectric properties of $(1-x)Pb(Mg_{1/3}Nb_{2/3})O_3-(x)PbTiO_3$ or $(1-x)$PMN$-(x)$PT ($x=0.1-0.5$) ceramics are measured under compressive stress up to 75 MPa. It has been found that both the dissipation energy and the polarizations decrease as the compressive stress increases. On the contrary, the applied compressive stress shows little or no influence on the coercive field. The changes in the ferroelectric properties are more significant in the near MPB compositions, i.e., 0.8PMN-0.2PT, 0.7PMN-0.3PT, and 0.6PMN-0.4PT. These observations are interpreted through the non-180° ferroelastic domain switching processes and the stress-induced decrease in the switchable part of domains.

## ACKNOWLEDGMENTS

Financial supports from the Thailand Research Fund (TRF), Commission on Higher Education (CHE), Royal Golden Jubilee Ph.D. Program, and Faculty of Science and Graduate School of Chiang Mai University are gratefully acknowledged.

[1] Y. H. Xu, *Ferroelectric Materials and their Applications* (North-Holland, Los Angeles, 1991).
[2] A. J. Moulson and J. M. Herbert, *Electroceramics: Materials, Properties, Applications* (Wiley, Chichester, 2003).
[3] G. H. Haertling, J. Am. Ceram. Soc. **82**, 797 (1999).
[4] L. E. Cross, Mater. Chem. Phys. **43**, 108 (1996).
[5] S. Jang, Ph.D. thesis, The Pennsylvania State University, 1979.
[6] K. Uchino, *Piezoelectric Actuators and Ultrasonic Motors* (Kluwer, Boston, 1997).
[7] D. Viehland, J. Li, E. McLaughlin, J. Powers, R. Janus, and H. Robinson, J. Appl. Phys. **95**, 1969 (2004).
[8] T. R. Shrout, Z. Chang, N. Kim, and S. Markgraf, Ferroelectr., Lett. Sect. **12**, 63 (1990).
[9] D. Viehland, M. Kim, Z. Xu, and J. Li, Appl. Phys. Lett. **67**, 2471 (1995).
[10] G. Smolenskii and A. Agranovskaya, Sov. Phys. Solid State **1**, 1429 (1960).
[11] C. Randall, D. Barber, and R. Whatmore, J. Microsc. **45**, 275 (1987).
[12] X. Dai, Z. Xu, and D. Viehland, Philos. Mag. B **70**, 33 (1994).
[13] J. Kuwata, K. Uchino, and S. Nomura, Jpn. J. Appl. Phys., Part 1 **21**, 1298 (1982).
[14] S. E. Park and T. R. Shrout, J. Appl. Phys. **82**, 1804 (1997).
[15] D. Viehland and J. Powers, Appl. Phys. Lett. **78**, 3112 (2001).
[16] D. Stansfield, *Underwater Electroacoustic Transducers* (Bath University, Bath, 1991).
[17] M. Mitrovic, G. P. Carmen, and F. K. Straub, Int. J. Solids Struct. **38**, 4357 (2001).
[18] D. Zhou, M. Kamlah, and D. Munz, J. Eur. Ceram. Soc. **25**, 425 (2005).
[19] R. Yimnirun, S. Ananta, E. Meechoowas, and S. Wongsaenmai, J. Phys. D **36**, 1615 (2003).

Author complimentary copy. Redistribution subject to AIP license or copyright, see http://jap.aip.org/jap/copyright.jsp

[20]Q. M. Zhang, J. Zhao, K. Uchino, and J. Zheng, J. Mater. Res. **12**, 226 (1997).
[21]G. Yang, S. F. Liu, W. Ren, and B. K. Mukherjee, Proceedings of the SPIE Symposium on Smart Structures and Materials, 2000 (unpublished), Vol. 3992, p. 103.
[22]O. Steiner, A. K. Tagantsev, E. L. Colla, and N. Setter, J. Eur. Ceram. Soc. **19**, 1243 (1999).
[23]J. Zhao and Q. M. Zhang, Proceedings of the IEEE International Symposium on Applications of Ferroelectrics, 1996 (unpublished), p. 971.
[24]N. A. Pertsev, A. G. Zembilgotov, and A. K. Tagantsev, Phys. Rev. Lett. **80**, 1988 (1998).
[25]S. P. Alpay and A. L. Roytburd, J. Appl. Phys. **83**, 4714 (1998).
[26]N. A. Pertsev, V. G. Koukhar, R. Waser, and S. Hoffmann, Appl. Phys. Lett. **77**, 2596 (2000).
[27]A. Y. Emelyanov, N. A. Pertsev, and A. L. Kholkin, Phys. Rev. B **66**, 214108 (2002).
[28]Z.-G. Ban and S. P. Alpay, Appl. Phys. Lett. **82**, 3499 (2003).
[29]G. Akcay, S. P. Alpay, G. A. Rossetti, Jr., and J. F. Scott, J. Appl. Phys. **103**, 024104 (2008).
[30]R. Yimnirun, M. Unruan, Y. Laosiritaworn, and S. Ananta, J. Phys. D **39**, 3097 (2006).
[31]R. Yimnirun, S. Ananta, and S. Chamunglap, Mater. Chem. Phys. **102**, 165 (2007).
[32]R. Yimnirun, S. Wongsaenmai, R. Wongmaneerung, N. Wongdamnern, A. Ngamjarurojana, S. Ananta, and Y. Laosiritaworn, Phys. Scr., T **129**, 184 (2007).
[33]J. Zhao, A. E. Glazounov, and Q. M. Zhang, Appl. Phys. Lett. **74**, 436 (1999).
[34]A. Udomporn, Ph.D. thesis, Chiang Mai University, 2004.
[35]R. Yimnirun, S. Ananta, A. Ngamjarurojana, and S. Wongsaenmai, Appl. Phys. A: Mater. Sci. Process. **81**, 1227 (2005).
[36]R. Yimnirun, Y. Laosiritaworn, S. Wongsaenmai, and S. Ananta, Appl. Phys. Lett. **89**, 162901 (2006).
[37]R. Yimnirun, P. J. Moses, R. J. Meyer, and R. E. Newnham, Rev. Sci. Instrum. **74**, 3429 (2003).
[38]L. B. Kong, J. Ma, W. Zhu, and O. K. Tan, Mater. Res. Bull. **37**, 23 (2002).
[39]Y. C. Liou, Mater. Sci. Eng., B **103**, 281 (2003).
[40]L. F. Brown, R. L. Carlson, J. M. Sempsrott, G. T. Standford, and J. J. Fitzgerald, Proc.-IEEE Ultrason. Symp. **1**, 561 (1997).
[41]M. E. Lines and A. M. Glass, *Principles and Applications of Ferroelectrics and Related Materials* (Oxford University Press, Oxford, 1977).
[42]R. Yimnirun, Y. Loasiritaworn, and S. Wongsaenmai, J. Phys. D **39**, 759 (2006).
[43]R. Yimnirun, S. Wongsaenmai, S. Ananta, and Y. Laosiritaworn, Appl. Phys. Lett. **89**, 242901 (2006).

**Author complimentary copy. Redistribution subject to AIP license or copyright, see http://jap.aip.org/jap/copyright.jsp**

J. Phys.: Condens. Matter **20** (2008) 415202 (5pp) doi:10.1088/0953-8984/20/41/415202

# Scaling and stress dependence of sub-coercive field dynamic hysteresis in $0.6Pb(Zr_{1/2}Ti_{1/2})O_3$–$0.4Pb(Zn_{1/3}Nb_{2/3})O_3$ ceramic

**R Yimnirun**[1], **N Wongdamnern, N Triamnak, M Unruan, A Ngamjarurojana, S Ananta and Y Laosiritaworn**

Department of Physics, Faculty of Science, Chiang Mai University, Chiang Mai 50200, Thailand

E-mail: rattikornyimnirun@yahoo.com

Received 2 February 2008, in final form 23 August 2008
Published 12 September 2008
Online at stacks.iop.org/JPhysCM/20/415202

**Abstract**

The scaling behavior of sub-coercive field dynamic ferroelectric hysteresis under the influence of stress was investigated in rhombohedral $0.6Pb(Zr_{0.5}Ti_{0.5})O_3$–$0.4Pb(Zn_{1/3}Nb_{2/3})O_3$ (0.6PZT–0.4PZN) bulk ceramic. The scaling relation of hysteresis area $\langle A\rangle$ against frequency $f$, field amplitude $E_0$, and stress $\sigma$ for the minor loops takes the form of $\langle A - A_{\sigma=0}\rangle \propto f^{-0.36}E_0^{4.03}\sigma^{0.19}$, indicating the difference in the energy dissipation between the stressed and stress-free conditions. While the scaling obtained is very similar to that of soft and hard PZT ceramics, slightly faster responses to $f$ and $E_0$ indicate the ease of polarization orientation in this ceramic with a simpler domain structure compared to commercial PZT ceramics. However, the difference in mechanical properties of these materials could contribute to a variation in the response to stress. While the $E_0$ exponent obtained in this study agreed well with that derived from the Monte Carlo simulation based on the Q-state planar Potts model, the difference in the $f$ exponent obtained experimentally and theoretically was attributed to the depolarizing effects presented in the bulk ceramics.

(Some figures in this article are in colour only in the electronic version)

## 1. Introduction

Dynamic hysteresis characteristics have become an important consideration because the hysteresis area $\langle A\rangle$ as a function of the field amplitude $E_0$ and frequency $f$ presents much information that is critical for many ferroelectric applications [1, 2]. Theoretical studies have been carried out to understand the dynamic response of hysteresis curves in spin and polarization systems [3–7]. In particular, attention is focused on power-law scaling

$$\langle A\rangle \propto f^m E_0^n \tag{1}$$

(where $m$ and $n$ are exponents that depend on the dimensionality and symmetry of the system). Based on three-dimensional models, it has been suggested that $m = 1/3$ and $n = 2/3$ as $f \to 0$, whereas $m = -1$ and $n = 2$ as $f \to \infty$ [3, 5, 8]. Experimental investigations on a few thin-film systems have also been reported with variation in the scaling relations obtained [9–12]. On the contrary, there are only a few reports on the hysteresis scaling behavior of bulk ferroelectric ceramics [13–16].

Our previous investigations have already shown stress-dependent scaling behaviors in commercial soft and hard lead zirconate titanate (Pb(Zr, Ti)$O_3$; PZT) ceramics [14, 15]. The results suggested that the scaling behavior depended strongly on the dimensionality of the system, and also suggested that the different states of domains existing in the ceramics may play a key role in controlling the scaling behavior. Unfortunately, it was too difficult to retrieve such

[1] Author to whom any correspondence should be addressed.

 © 2008 IOP Publishing Ltd Printed in the UK

information for the domain structures of commercial ceramics. Therefore, this study was aimed at a ferroelectric material with a distinct domain configuration. Previous works on $0.6Pb(Zr_{0.5}Ti_{0.5})O_3$–$0.4Pb(Zn_{1/3}Nb_{2/3})O_3$ (0.6PZT–0.4PZT) ceramics with rhombohedral structure have reported excellent electrical properties suitable for various applications [17–20]. Due to its many potential applications and relatively simple domain configuration, the 0.6PZT–0.4PZN ceramic was thus chosen for this study. Practically, ferroelectric ceramics are normally used under sub-coercive field conditions in most applications; it is therefore of interest to obtain scaling relations for such conditions. Interestingly, earlier works showed that the scaling behavior of the minor and saturated loops was significantly different [11, 12].

More importantly, in many applications the ceramic specimens are often subjected to mechanical loading, either from the design of the device itself or from operating conditions which induce stresses [1, 21]. Therefore, prior knowledge of how the material properties change under different load conditions in materials is inevitably crucial for the proper design of a device and for suitable selection of materials for a specific application. In many previous investigations the electrical properties of ceramics were found to strongly depend on stresses ($\sigma$) [22–26]. Since $f$, $E_0$, and $\sigma$ have been reported to impose significant influence on the dynamic hysteresis responses of ferroelectric ceramics, it is therefore the major aim of this study to obtain the stress-dependent scaling behavior of sub-coercive field dynamic hysteresis in 0.6PZT–0.4PZN ceramic.

## 2. Experimental procedures

Disc-shaped samples of tetragonal structure 0.6PZT–0.4PZN ceramic with a diameter of 10 mm and thickness of 1 mm were used in this study. Details on the fabrication and characterization of this material can be found elsewhere [19, 20]. Its basic properties are: dielectric constant (1 kHz) $\varepsilon_r = 1616$; Curie temperature $T_C = 284\,^\circ$C; piezoelectric strain constants $d_{33} = 457$ pm V$^{-1}$; planar coupling factor $k_p = 0.59$; mechanical quality factor $Q_m = 62$; coercive field (10 Hz) $E_c = 12$ kV cm$^{-1}$. The dynamic hysteresis ($P$–$E$) loops were characterized at room temperature (25 °C) by a modified Sawyer–Tower circuit with $f$ ranging from 2 to 100 Hz and $E_0$ from 0 to 10.5 kV cm$^{-1}$. The field was applied to a sample by a high voltage AC amplifier (Trek 610D) with the input sinusoidal signal from a function generator (HP 3310A). The $P$–$E$ loops were recorded by a digital oscilloscope (HP 54645A, 100 MHz). A detailed description of this system is given elsewhere [25]. Effects of the external stress on the dynamic hysteresis were investigated with the compressometer developed for simultaneous applications of the mechanical stress and the electric field [26]. The compressive stress, applied parallel to the electric field direction, was supplied by the servohydraulic load frame and monitored with the pressure gauge. The $P$–$E$ loops were recorded as a function of mechanical stress applied discretely between 0 and 163 MPa for each applied field and frequency. At each constant stress, the loop was obtained after 20 sampling cycles to average out the noise deformation.

## 3. Results and discussion

The hysteresis loops at different $f$ but fixed $E_0$ (10.5 kV cm$^{-1}$) and $\sigma$ (27 MPa), at different $E_0$ but fixed $f$ (10 Hz) and $\sigma$ (27 MPa), and at different $\sigma$ but fixed $E_0$ (10.5 kV cm$^{-1}$) and $f$ (10 Hz) are shown in figures 1(a), (b), and (c), respectively. For a particular applied stress, as expected, the dependence of the loop pattern and area $\langle A\rangle$ on $f$ and $E$ is remarkable. At fixed $E_0$, the loop area $\langle A\rangle$ and remnant polarization ($P_r$) decrease with an increase of frequency, as shown in figure 1(a). The dependence of the hysteresis loop on $E_0$ is depicted in figure 1(b). Similar observations have also been reported in soft and hard PZT ceramics [27–29]. In addition, the $P$–$E$ loop area $\langle A\rangle$ is found to decrease steadily with increasing stress, as reported in previous investigations [24–26].

To obtain suitable scaling relations, one can first follow the suggested scaling law given in equation (1) to determine exponents $m$ and $n$ directly from the experimental data. By plotting $\langle A\rangle$ against $f$ at fixed $E_0$, one obtains the exponent $m$. On the other hand, the exponent $n$ can be obtained by plotting $\langle A\rangle$ against $E_0$ at fixed $f$. In conjunction with the least-square-fitting method, the exponents $m = -0.36 \pm 0.03$ and $n = 4.03 \pm 0.06$ were obtained. As plotted in figure 2, it is revealed that the experimental data can be fitted (with $R^2 = 0.99$), within the measured uncertainty, by

$$\langle A\rangle \propto f^{-0.36} E_0^{4.03}. \tag{2}$$

Here, the first interesting observation is that the minor-loop scaling in PZN-modified PZT bulk ceramics is generally similar to that of PZT thin film [5, 9], as well as that of the minor loop of PZT bulk ceramics [13, 15]. This is attributed to the fact that the main polarization orientation mechanism in thin-films and in sub-coercive field conditions for bulk ceramics is likely from the same reversible 180° domain rotation (which also occurs at a much faster rate than the irreversible process), as the irreversible non-180° domain switching normally accompanied by mechanical strain occurs at a higher $E$-field [13, 15, 30–34]. More importantly, the scaling relation obtained in equation (2) indicates that $\langle A\rangle$ decays slightly more quickly with $f$ and grows faster with $E_0$ than in commercial soft PZT bulk ceramic with $\langle A\rangle \propto f^{-0.33} E_0^3$ [13]. This indicates the ease of the polarization orientation process in rhombohedral 0.6PZT–0.4PZN ceramics that leads to faster polarization orientation kinetics, as compared to complex domain structures of commercial PZT bulk ceramics which require a higher energy barrier for the polarization orientation process.

Considering the $E_0$ exponent of 4.03, which is approximately of the same order as that in PZT thin film [5, 9], as well as those in minor loops of PZT bulk ceramics [13, 15], the reversible domain wall vibration is also believed to play an additional role in the dependence of hysteresis area on $E_0$ at a sub-coercive field. In the nucleation and growth concept [5, 9, 35] domain reversal can be characterized by simultaneous contributions from both the new domain nucleation rate and the domain boundary motion velocity, with the latter responding faster to the electric field [36, 37]. Since the reversible domain wall vibration makes a greater

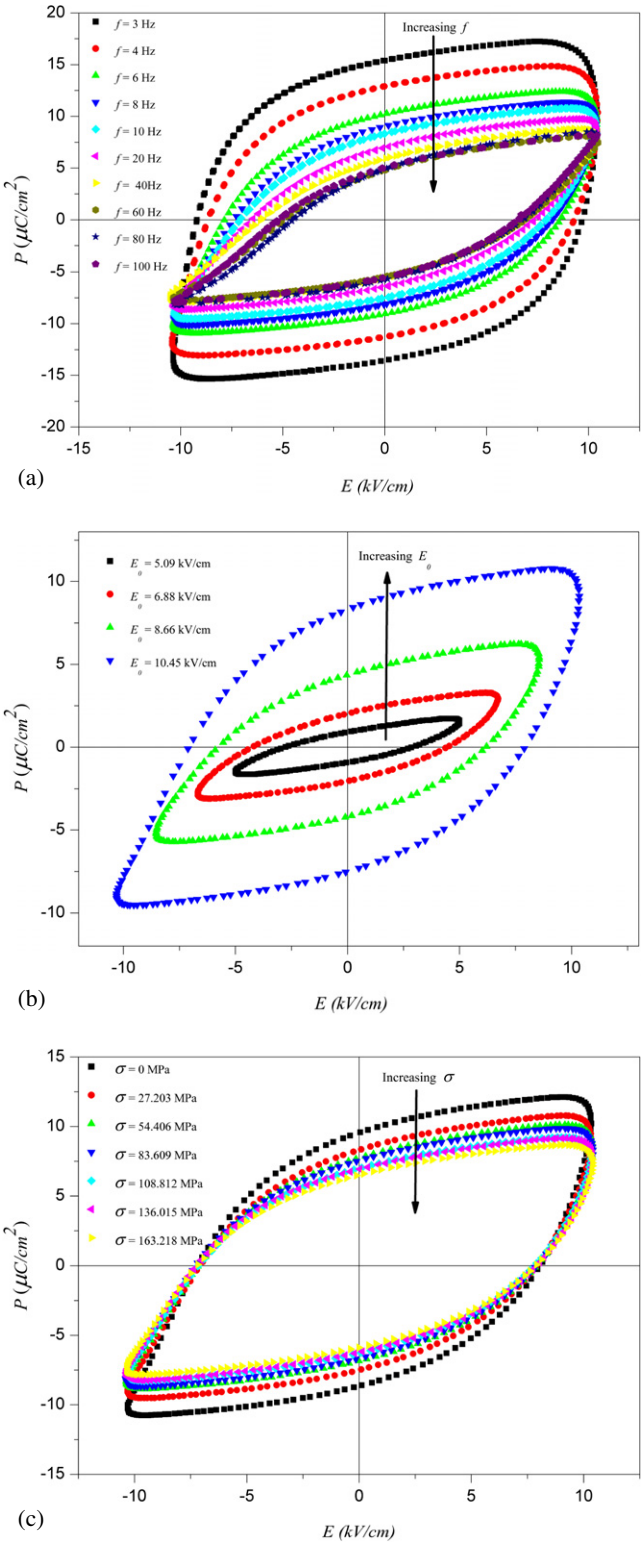



**Figure 1.** Hysteresis loops under sub-coercive field conditions for 0.6PZT–0.4PZN ceramic (a) at various $f$, $E_0 = 10.5$ kV cm$^{-1}$, and $\sigma = 27$ MPa; (b) at various $E_0$, $f = 10$ Hz, and $\sigma = 27$ MPa; and (c) at various $\sigma$, $f = 10$ Hz, and $E_0 = 10.5$ kV cm$^{-1}$.

contribution to the dependence of hysteresis area with $E_0$ in sub-coercive conditions, the response to $E_0$ occurs at much faster rate than at a higher field amplitude. It should also be

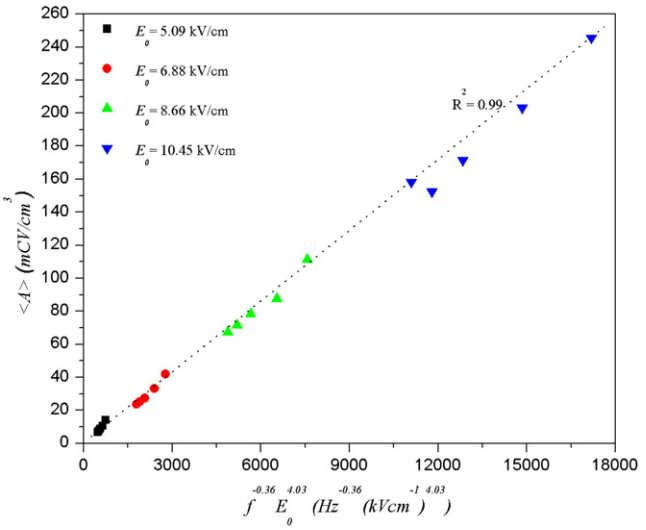



**Figure 2.** Scaling of hysteresis area $\langle A\rangle$ against $f^{-0.36}E_0^{4.03}$ for 0.6PZT–0.4PZN ceramic under sub-coercive field conditions.

noted that the $E_0$ exponent $n = 4.03$ agrees very well with the $n$ value of 4 obtained from the previous simulation study using the Monte Carlo method based on the Q-state planar Potts model [38].

In addition, the $f$ exponent of $-0.36$ is smaller in absolute value than that obtained theoretically from $(\Phi^2)^2$ and $(\Phi^2)^3$ models for non-saturated loops (exponent $-1$) [3]. The difference could be attributed to depolarizing effects from space charges on grain boundaries, induced electric field from interface layers, immobile defects etc [39], acting as a buffer to the polarization-reversal mechanism in bulk ceramics. As a result, the hysteresis area must show a relatively weaker dependence on $f$ than that of the theoretical models. Furthermore, the value of the $f$ exponent is believed to be related to available domain states in the material, previously proposed in our investigations [13, 14], or growth dimension in the growth kinetics model proposed by Ishibashi and Orihara based on the Kolmogorov–Avrami model [40, 41].

To investigate the scaling behavior under the effect of applied stresses, the stress ($\sigma$) term should be included, i.e.

$$\langle A\rangle \propto f^m E_0^n \sigma^p. \tag{3}$$

However, due to the increasing number of exponents, to simplify the problem the validity of the scaling law $\langle A\rangle(\sigma) \propto f^{-0.36}E_0^{4.03}$ is assumed for all applied stresses. Consequently, the area $\langle A\rangle$ for each stress is plotted against $f^{-0.36}E_0^{4.03}$, as shown in figure 3(a), and it can be seen from the least-square linear fits that reasonably good linear relations can be found. As a result, the condition of universality having $m = -0.36$ and $n = 4.03$ in 0.6PZT–0.4PZN bulk ceramic is confirmed. Hence, $\langle A\rangle \propto (a + b\sigma^c) f^{-0.36}E_0^{4.03}$ may be written and by substituting the fitted parameters, it is found that

$$\langle A\rangle - \langle A_{\sigma=0}\rangle = \langle A - A_{\sigma=0}\rangle \propto f^{-0.36}E_0^{4.03}\sigma^{0.19}, \tag{4}$$

where $\langle A_{\sigma=0}\rangle$ refers to the stress-free hysteresis area which will be a dominant term for zero stress. The data-collapsing

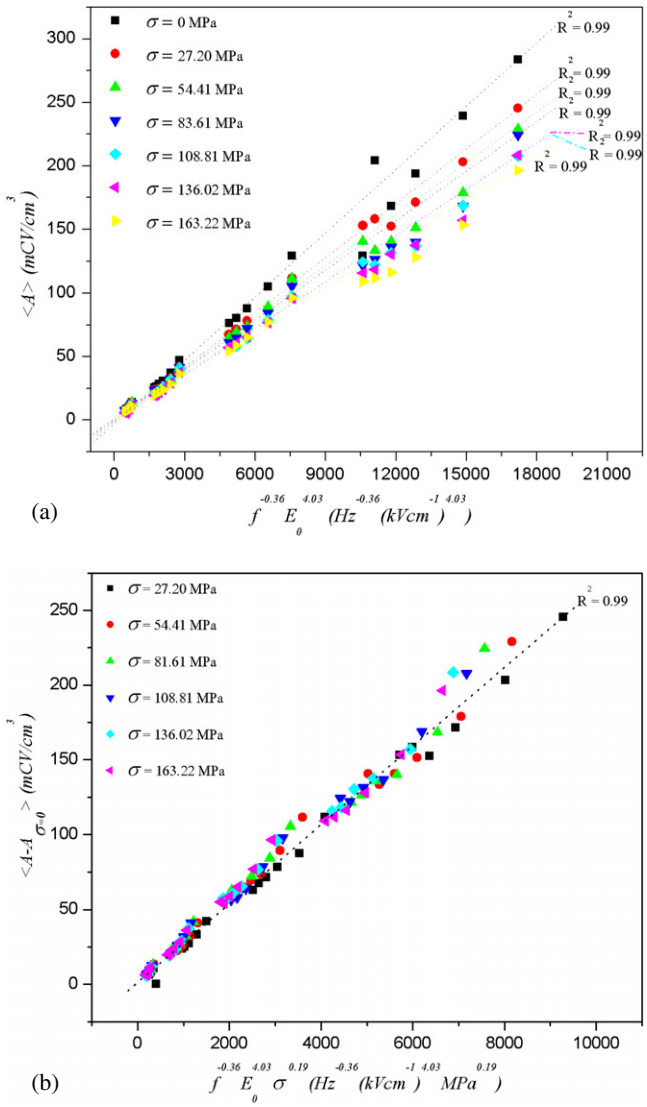



**Figure 3.** (a) Scaling of hysteresis area $\langle A \rangle$ against $f^{-0.36}E_0^{4.03}$ at various $\sigma$. (b) The collapse of the scaling area $\langle A - A_{\sigma=0} \rangle$ against $f^{-0.36}E_0^{4.03}\sigma^{0.19}$ on the same linear-line (with small fluctuation) for 0.6PZT–0.4PZN ceramic under sub-coercive field conditions.

of the scaling area from all $f$, $E_0$, and $\sigma$ was found to confirm equation (4) as evident in figure 3(b). Note that from the appearance of stress $\sigma$, $\langle A - A_{\sigma=0} \rangle$, referring to the difference in energy dissipation between under-stress and stress-free conditions, increases with increasing stress suggesting a decay of $\langle A \rangle$ with $\sigma$ at a rate of $\sigma^{0.19}$ as observed in experiments. Therefore, the difference in the hysteresis area between stressed and stress-free conditions scales with frequency, field amplitude, and stress via the exponents $m = -0.36 \pm 0.03$, $n = 4.03 \pm 0.06$, and $p = 0.19 \pm 0.03$.

To understand the scaling relation obtained in equation (4), at least qualitatively, one needs to consider the following statements. Since the $P$–$E$ loop area indicates the polarization dissipation energy subjected to one full cycle of electric field application, the loop area is therefore directly related to the volume involved in the switching process during the application of electric field [25, 26, 42]. When the compressive stress is applied in the direction parallel to the direction of the polar axis, the applied stress tends to keep the ferroelectric domains aligned with their polar axes away from the stress direction through the non-180° ferroelastic domain switching processes. Therefore, it takes a larger than usual applied electric field to reorient the domains along the stress direction, resulting in lower values of the saturation polarization. When the electric field is reduced to zero the domains tend to rotate back away from the applied compressive stress direction, resulting in a lower than usual remnant polarization ($P_r$). Therefore, both the saturation and remnant polarizations become lower with increasing compressive stress, hence the coercivity is also lower [24–26]. The polarization dissipation energy is consequently found to decrease with increasing applied stress, indicating that the sample volume contributing to polarization reversal decreases with increasing stress. Similar observations have also been reported in other investigations [22–26, 43, 44].

Furthermore, it is noted that the stress term with exponent $p = 0.19$ is noticeably different from that for soft and hard PZT bulk ceramics with $p = 0.44$ and 0.37, respectively [14, 15]. The difference could be attributed to a variation of mechanical properties of these materials. While no other stress-dependent scaling investigation is available for a direct comparison, Viehland *et al* [45] reported a power law-like relation between the hysteresis loss and the applied stress in PMN-PT crystals. In addition, many of the theoretical treatments to explain the stress effect on the hysteresis behavior have been primarily based on constitutive models, micro-mechanical and analytical approaches, thermodynamic phenomenology, and Rayleigh law and Preisach model approaches [46–56]. While these theoretical treatments are useful in understanding hysteresis behavior in ferroelectric materials under the application of stress, none of them derive a direct relation between the hysteresis loss and the applied stress in ferroelectric materials. It is also interesting to point out that recent theoretical and experimental investigations have related the stress dependence of the minor hysteresis loop parameters to the dislocation density in ferromagnetic materials [57–60]. Further investigations, both theoretical and experimental, of the stress-dependent scaling behavior are clearly needed as the stress relations are useful in predicting the practical limitations of devices when used under stress.

## 4. Conclusions

The scaling behavior of the sub-coercive field dynamic ferroelectric hysteresis of rhombohedral 0.6PZT–0.4PZN bulk ceramics under the effect of mechanical stress has been investigated. The scaling relation for the minor loops takes the form of $\langle A - A_{\sigma=0} \rangle \propto f^{-0.36}E_0^{4.03}\sigma^{0.19}$, indicating the difference in the energy dissipation between the stressed and stress-free conditions. While the scaling obtained is very similar to that of soft and hard PZT ceramics, slightly faster responses to $f$ and $E_0$ indicate the ease of polarization orientation in this ceramic with a simpler domain structure compared to commercial PZT ceramics. In addition, a difference in the response to stress could be attributed to

a variation in the mechanical properties of these materials. Finally, the $E_0$ exponent obtained in this study agrees well with that derived from the Monte Carlo simulation based on the Q-state planar Potts model. The difference in the $f$ exponent obtained experimentally and theoretically can be attributed to the depolarizing effects presented in the bulk ceramics.

## Acknowledgments

Financial support from the Thailand Research Fund (TRF), Commission on Higher Education (CHE), Royal Golden Jubilee PhD Program, Faculty of Science and Graduate School of Chiang Mai University is gratefully acknowledged.

## References

[1] Uchino K 2000 *Ferroelectric Devices* (New York: Dekker)
[2] Auciello O, Scott J F and Ramesh R 1998 *Phys. Today* **51** (7) 22
[3] Rao M, Krishnamurthy H R and Pandit R 1990 *Phys. Rev.* B **42** 856
[4] Acharyya M and Chakrabarti B K 1995 *Phys. Rev.* B **52** 6550
[5] Liu J-M, Chan H L W, Choy C L, Zhu Y Y, Zhu S N, Liu Z G and Ming N B 2001 *Appl. Phys. Lett.* **79** 236
[6] Zuo H B, Zhang M F, Han J C and Liu J M 2007 *Mater. Lett.* **61** 2697
[7] Sarjala M, Seppälä E T and Alava M J 2008 *Physica* B **403** 418
[8] Rao M and Pandit R 1991 *Phys. Rev.* B **43** 3373
[9] Liu J-M, Chan H L W, Choy C L and Ong C K 2001 *Phys. Rev.* B **65** 014416
[10] Pan B, Yu H, Wu D, Zhou X H and Liu J-M 2003 *Appl. Phys. Lett.* **83** 1406
[11] Kim Y-H and Kim J-J 1997 *Phys. Rev.* B **55** R11933
[12] Park J-H, Kim C-S, Choi B-C, Moon B K, Jeong J H and Kim I W 2003 *Appl. Phys. Lett.* **83** 536
[13] Yimnirun R, Laosiritaworn Y, Wongsaenmai S and Ananta S 2006 *Appl. Phys. Lett.* **89** 162901
[14] Yimnirun R, Wongsaenmai S, Ananta S and Laosiritaworn Y 2006 *Appl. Phys. Lett.* **89** 242901
[15] Yimnirun R, Wongmaneerung R, Wongsaenmai S, Ngamjarurojana A, Ananta S and Laosiritaworn Y 2007 *Appl. Phys. Lett.* **90** 112908
[16] Yimnirun R, Wongmaneerung R, Wongsaenmai S, Ngamjarurojana A, Ananta S and Laosiritaworn Y 2007 *Appl. Phys. Lett.* **90** 112906
[17] Jiang X P, Fang J W, Zeng H R, Chu B J, Li G R, Chen D R and Yin Q R 2000 *Mater. Lett.* **44** 219
[18] Fan H and Kim H E 2002 *J. Appl. Phys.* **91** 317
[19] Vittayakorn N, Rujijanagul G, Tunkasiri T, Tan X and Cann D P 2003 *J. Mater. Res.* **18** 2881
[20] Vittayakorn N, Rujijanagul G, Tan X and Cann D P 2006 *J. Electroceram.* **16** 141
[21] Uchino K 1997 *Piezoelectric Actuators and Ultrasonic Motors* (Boston, MA: Kluwer–Academic)
[22] Zhao J, Glazounov A E and Zhang Q M 1999 *Appl. Phys. Lett.* **74** 436
[23] Viehland D and Powers J 2001 *J. Appl. Phys.* **89** 1820
[24] Zhou D, Kamlah M and Munz D 2005 *J. Eur. Ceram. Soc.* **25** 425
[25] Yimnirun R, Laosiritaworn Y and Wongsaenmai S 2006 *J. Phys. D: Appl. Phys.* **39** 759
[26] Yimnirun R, Ananta S, Ngamjarurojana A and Wongsaenmai S 2005 *Appl. Phys.* A **81** 1227
[27] Hall D A and Stevenson P J 1999 *Ferroelectrics* **228** 139
[28] Garcia J E, Perez R and Albareda A 2001 *J. Phys. D: Appl. Phys.* **34** 3279
[29] Morozov M, Damjanovic D and Setter N 2005 *J. Eur. Ceram. Soc.* **25** 2483
[30] Trolier-McKinstry S, Gharb N B and Damjanovic D 2006 *Appl. Phys. Lett.* **88** 202901
[31] Lai B-K, Ponomareva I, Naumov I I, Kornev I, Fu H, Bellaiche L and Salamo G S 2006 *Phys. Rev. Lett.* **96** 137602
[32] Ricinschi D and Okuyama M 2007 *Ferroelectrics* **349** 111
[33] Tsurumi T, Sasaki T, Kakemoto H, Harigai T and Wada S 2004 *Japan. J. Appl. Phys.* **43** 7618
[34] Lee K and Baik S 2006 *Annu. Rev. Mater. Res.* **36** 81
[35] Gunton J D, San Miguel M and Sahmi P S 1983 *Phase Transitions and Critical Phenomena* vol 8, ed C Domb and J L Lebowitz (London: Academic) p 267
[36] Stadler H L and Zacumanids P L 1963 *J. Appl. Phys.* **34** 3255
[37] Liu J-M, Pan B, Wang K F and Yu H 2004 *Ceram. Int.* **30** 1471
[38] Liu J-M, Chan H L W and Choy C L 2002 *Mater. Lett.* **52** 213
[39] Bolten D, Böttger U and Waser R 2004 *Appl. Phys. Lett.* **84** 2379
[40] Ishibashi Y and Orihara N 1995 *Integr. Ferroelectr.* **9** 57
[41] Liu J M, Wang W M, Liu Z G, Chan H L and Choy C L 2002 *Appl. Phys.* A **75** 507
[42] Lines M E and Glass A M 1977 *Principles and Applications of Ferroelectrics and Related Materials* (Oxford: Clarendon)
[43] Kumazawa T, Kumagai Y, Miura H, Kitano M and Kushida K 1998 *Appl. Phys. Lett.* **72** 608
[44] Lu X, Zhu J, Li X, Zhang Z, Zhu X, Wu D, Yan F, Ding Y and Wang Y 2000 *Appl. Phys. Lett.* **76** 3103
[45] Veihland D, Ewart L, Powers J and Li J F 2001 *J. Appl. Phys.* **90** 2479
[46] Damjanovic D 1997 *J. Appl. Phys.* **82** 1788
[47] Landis C M 2004 *Curr. Opin. Solid State Mater. Sci.* **8** 59
[48] Achuthan A and Sun C T 2005 *J. Appl. Phys.* **97** 114103
[49] Kamlah M and Jiang Q 1999 *Smart Mater. Struct.* **8** 441
[50] Li W F and Weng G J 2002 *J. Appl. Phys.* **91** 3806
[51] Massad J E and Smith R C 2003 *J. Intell. Mater. Syst. Struct.* **14** 455
[52] Meyer V, Sallese J M, Fazan P, Bard C and Pecheux F 2003 *Solid State Electron.* **47** 1479
[53] Shieh J, Huber J E and Fleck N A 2003 *Acta Mater.* **51** 6123
[54] Guillon O, Delobelle P, Thiebaud F, Walter V and Perreux D 2004 *Ferroelectrics* **308** 95
[55] Belov A Y and Kreher W S 2005 *Mater. Sci. Eng.* B **118** 7
[56] Li L B, Lu X M, Chen Q D, Wu X M and Zhu J S 2008 *J. Appl. Phys.* **103** 034112
[57] Takahashi S, Zhang L, Kobayashi S, Kamada Y, Kikuchi H and Ara K 2005 *J. Appl. Phys.* **98** 033909
[58] Hu R, Soh A K, Zheng G P and Ni Y 2006 *J. Magn. Magn. Mater.* **301** 458
[59] Kobayashi S, Fujiwara T, Tsunoda M, Takahashi S, Kikuchi H, Kamada Y, Ara K and Shishido T 2007 *J. Magn. Magn. Mater.* **310** 2638
[60] Takahashi S, Kobayashi S, Kamada Y and Shishido T 2008 *J. Magn. Magn. Mater.* **320** 2056

J. Phys. D: Appl. Phys. **41** (2008) 205415 (5pp) doi:10.1088/0022-3727/41/20/205415

# Power-law scaling of sub-coercive field dynamic hysteresis response in $0.7Pb(Zr_{1/2}Ti_{1/2})O_3$–$0.3Pb(Zn_{1/3}Nb_{2/3})O_3$ ceramic

**R Yimnirun[1], N Wongdamnern, N Triamnak, T Sareein, M Unruan, A Ngamjarurojana, S Ananta and Y Laosiritaworn**

Department of Physics, Faculty of Science, Chiang Mai University, Chiang Mai 50200, Thailand

E-mail: rattikornyimnirun@yahoo.com

Received 2 February 2008, in final form 19 August 2008
Published 1 October 2008
Online at stacks.iop.org/JPhysD/41/205415

**Abstract**

Scaling behaviour of sub-coercive field dynamic ferroelectric hysteresis under the influence of stress was investigated in rhombohedral 0.7PZT–0.3PZN bulk ceramic. The scaling relation of hysteresis area $\langle A\rangle$ against frequency $f$, field amplitude $E_0$ and stress $\sigma$ for the minor loops takes the form of $\langle A - A_{\sigma=0}\rangle \propto f^{-0.35}E_0^{3.47}\sigma^{0.38}$, which is very similar to that of soft and hard PZT ceramics. However, slightly faster responses to $f$ and $E_0$ indicate the ease of polarization orientation in this simpler domain structure ceramic as compared with commercial PZT ceramics. This study suggests that the domain structures play a significant role in controlling dynamic hysteresis behaviour of ferroelectric materials.

(Some figures in this article are in colour only in the electronic version)

## 1. Introduction

The dynamic hysteresis characteristics have become of important consideration since hysteresis area $\langle A\rangle$ as a function of the field amplitude $E_0$ and frequency $f$ presents useful information critical for many ferroelectric applications [1, 2]. Theoretical studies have been carried out to understand the dynamic response of hysteresis curves in spin and polarization systems [3–7]. In particular, attention is focused on the power-law scaling

$$\langle A\rangle \propto f^m E_0^n \tag{1}$$

(where $m$ and $n$ are exponents that depend on the dimensionality and symmetry of the system). Based on three-dimensional models, it has been suggested that $m = 1/3$ and $n = 2/3$ as $f \to 0$, whereas $m = -1$ and $n = 2$ as $f \to \infty$ [3, 5, 8]. Experimental investigations on a few thin-film systems have also been reported with variation in the scaling relations obtained [9–12]. In contrast, there are only a few reports on the scaling behaviour studies of ferroelectric hysteresis loops of bulk ferroelectric ceramics [13–16].

Our previous investigations have already shown interesting stress-dependent scaling behaviour in commercial soft and hard lead zirconate titanate, $Pb(Zr,Ti)O_3$ or PZT, ceramics [14, 15]. The results suggested that the scaling behaviour depended strongly on the dimensionality of the system, and also led to the belief that the different states of domains existing in the ceramics may play a key role in controlling the scaling behaviour. Unfortunately, it was too difficult to retrieve such information on the domain structures of commercial ceramics. Therefore, this study was aimed at a suitable potential ferroelectric material with a distinct domain configuration. Previous works on $0.7Pb(Zr_{0.5}Ti_{0.5})O_3$–$0.3Pb(Zn_{1/3}Nb_{2/3})O_3$ (or 0.7PZT–0.3PZT) ceramics with a rhombohedral structure have reported excellent electrical properties suitable for various applications [17–20]. Therefore, due to its many potential practical applications and a relatively simpler domain structure as compared with commercial PZT ceramics [18, 20], the 0.7PZT–0.3PZN ceramic was chosen for this study. Practically, ferroelectric ceramics are used under sub-coercive field condition in most applications; it is therefore of interest to obtain scaling relations for such a condition. Interestingly, earlier works showed that the scaling

[1] Author to whom any correspondence should be addressed.

 © 2008 IOP Publishing Ltd Printed in the UK

behaviour of the minor and saturated loops was significantly different [11, 12].

More importantly, in many applications the ceramic specimens are often subjected to mechanical loading, either from the design of the device itself or from operating conditions which induce stresses [1, 21]. Therefore, prior knowledge of how the material properties change under different load conditions in materials is inevitably crucial for the proper design of a device and for suitable selection of materials for a specific application. In many previous investigations the electrical properties of ceramics were found to depend strongly on stresses ($\sigma$) [22–26]. Since $f$, $E_0$ and $\sigma$ have been reported to impose a significant influence on the dynamic hysteresis responses of ferroelectric ceramics, it is therefore the major aim of this study to obtain the stress-dependent scaling behaviour of sub-coercive field dynamic ferroelectric hysteresis in the 0.7PZT–0.3PZN ceramic.

## 2. Experimental procedures

Disc-shaped samples of tetragonal-structure 0.7PZT–0.3PZN ceramic with a diameter of 10 mm and a thickness of 1 mm were used in this study. Details on the fabrication and characterization of this material can be found elsewhere [19, 20]. Its basic properties are dielectric constant (1 kHz) $\varepsilon_r = 1625$; Curie temperature $T_C = 313\,^\circ$C; piezoelectric strain constant $d_{33} = 443\,\mathrm{pm\,V^{-1}}$; planar coupling factor $k_p = 0.57$; mechanical quality factor $Q_m = 66$; coercive field (10 Hz) $E_c = 13.1\,\mathrm{kV\,cm^{-1}}$. The dynamic hysteresis ($P$–$E$) loops were characterized at room temperature (25 °C) by using a modified Sawyer–Tower circuit with $f$ covering from 2 to 100 Hz and $E_0$ from 0 to 12 kV cm$^{-1}$. The electric field was applied to a sample by a high voltage ac amplifier (Trek 610D) with the input sinusoidal signal from a function generator (HP 3310A). The $P$–$E$ loops were recorded by a digital oscilloscope (HP 54645A, 100 MHz). The detailed descriptions of this system are explained elsewhere [25]. Effects of the external stress on the dynamic hysteresis were investigated with the compressometer, which was developed for simultaneous applications of the mechanical stress and the electric field [26]. The compressive stress, applied parallel to the electric field direction, was supplied by the servohydraulic load frame and monitored with the pressure gauge. The $P$–$E$ loops were recorded as a function of the mechanical stress applied discretely between 0 and 167 MPa for each applied field and frequency. At each constant stress, the loop was obtained after 20 sampling cycles to average out the noise deformation.

## 3. Results and discussion

The hysteresis profiles for various frequencies $f$, field amplitude $E_0$ and stress $\sigma$ are obtained. The hysteresis loops at different $f$ but fixed $E_0$ (12 kV cm$^{-1}$) and $\sigma$ (27 MPa), at different $E_0$ but fixed $f$ (10 Hz) and $\sigma$ (27 MPa) and at different $\sigma$ but fixed $E_0$ (12 kV cm$^{-1}$) and $f$ (10 Hz) are shown in figures 1(*a*), (*b*) and (*c*), respectively. For a particular applied stress, as expected, the dependence of the loop pattern and

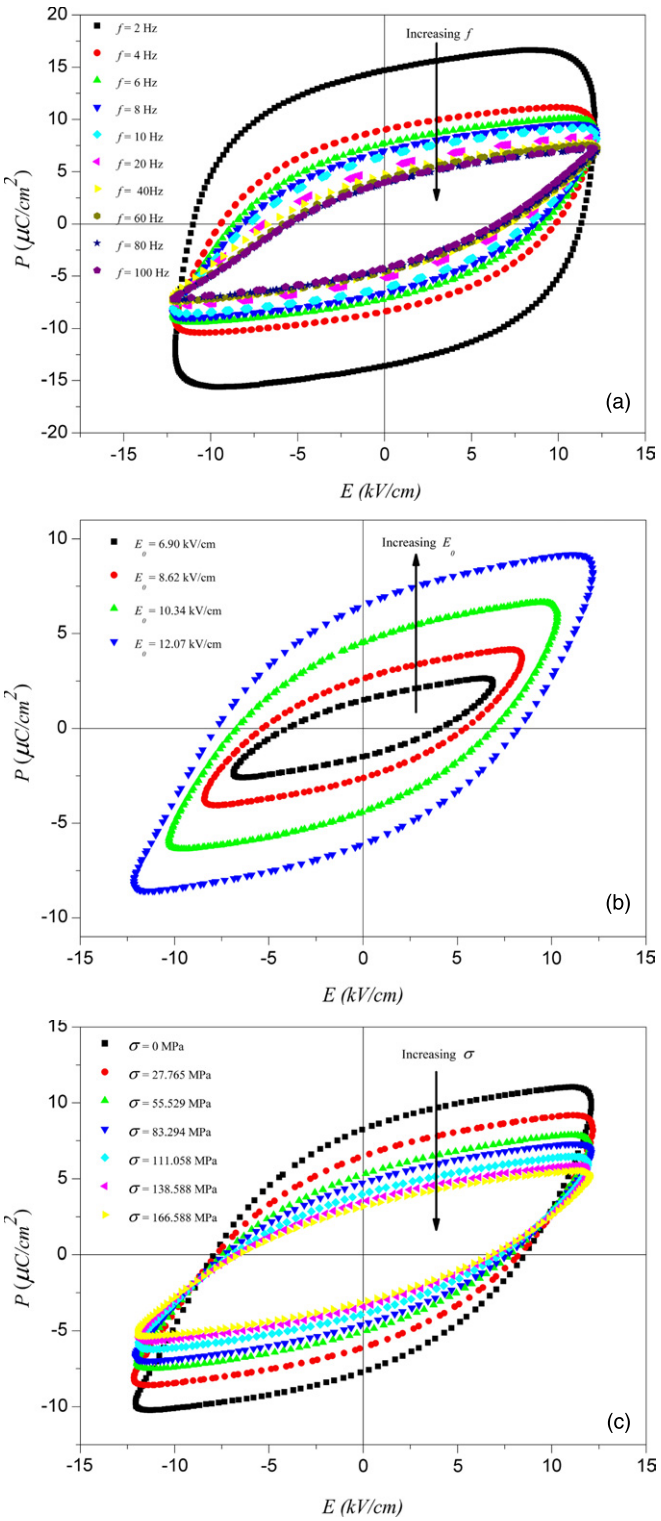



**Figure 1.** Hysteresis loops under sub-coercive field condition for the 0.7PZT–0.3PZN ceramic (*a*) at various $f$; $E_0 = 12\,\mathrm{kV\,cm^{-1}}$ and $\sigma = 27$ MPa, (*b*) at various $E_0$; $f = 10$ Hz and $\sigma = 27$ MPa and (*c*) at various $\sigma$; $f = 10$ Hz and $E_0 = 12\,\mathrm{kV\,cm^{-1}}$.

area $\langle A \rangle$ on $f$ and $E$ is remarkable. At fixed $E_0$, the loop area $\langle A \rangle$ and remanent polarization ($P_r$) decrease with an increase in frequency, as shown in figure 1(*a*). The dependence of the hysteresis loop on $E_0$ is depicted in figure 1(*b*). Similar observations have also been reported in soft and hard PZT ceramics [27–29]. In addition, the $P$–$E$ loop area $\langle A \rangle$ is

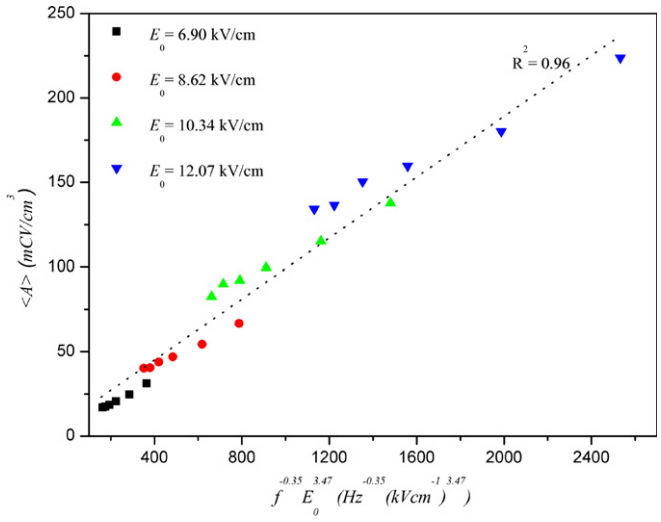



**Figure 2.** Hysteresis area $\langle A\rangle$ against $f^{-0.35}E_0^{3.47}$ for the 0.7PZT–0.3PZN ceramic under sub-coercive field condition. At each electric field, the data points are from some of the measured frequencies.

found to decrease steadily with increasing stress. Several previous investigations also reported similar stress-dependent behaviour [24–26].

To obtain a suitable scaling relation for the bulk ceramic, one can first follow the suggested scaling law given in equation (1) to determine exponent $m$ and $n$ directly from the experimental data. By plotting $\langle A\rangle$ against $f$ at fixed $E_0$, one obtains the exponent $m$. On the other hand, the exponent $n$ can be obtained from plotting $\langle A\rangle$ against $E_0$ at fixed $f$. As plotted in figure 2, it is revealed that the experimental data can be fitted (with $R^2 = 0.96$), within the measured uncertainty, by

$$\langle A\rangle \propto f^{-0.35}E_0^{3.47}. \tag{2}$$

Here, the first interesting observation is that the minor-loop scaling in PZN-modified PZT bulk ceramics is generally similar to that of the PZT thin film [5, 9], as well as that of the minor loop of PZT bulk ceramics [13, 15]. As explained in our previous investigation [13], this was attributed to the fact that the polarization orientation mechanism in thin films and in sub-coercive field condition for bulk ceramics is likely from the 180° domain reversal [30–34]. This explains why the scaling behaviour of PZT bulk ceramics at low $E$-fields is similar to that of thin films. More importantly, the scaling relation obtained in equation (2) indicates that $\langle A\rangle$ decays slightly more quickly with $f$ and grows more quickly with $E_0$ than the minor-loop scaling relations obtained earlier for commercial soft PZT bulk ceramic with $\langle A\rangle \propto f^{-0.33}E_0^3$ [13]. This clearly indicates the ease of the polarization orientation process in rhombohedral 0.7PZT–0.3PZN ceramics that leads to faster polarization orientation kinetics, as compared with complex domain structures of commercial PZT bulk ceramics which require higher energy barrier for the polarization orientation process. Furthermore, the scaling relations obtained here also support our previous proposed hypothesis that the domain structures play a major role in controlling dynamic hysteresis behaviour of ferroelectric materials [13, 15].

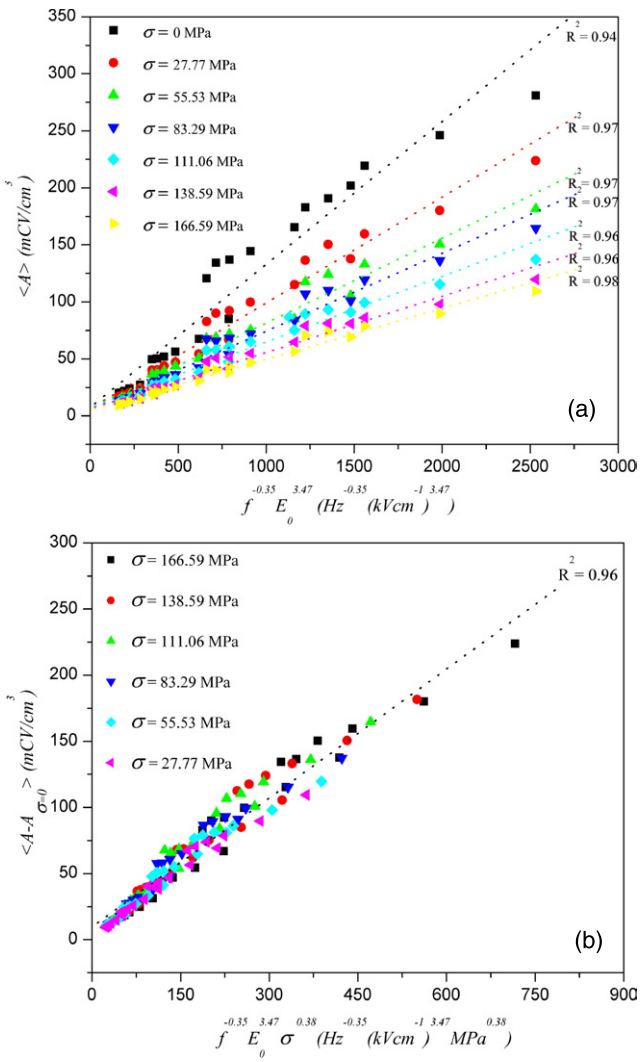



**Figure 3.** (*a*) Hysteresis area $\langle A\rangle$ against $f^{-0.35}E_0^{3.47}$ at various $\sigma$, (*b*) the collapse of the scaling area $\langle A - A_{\sigma=0}\rangle$ against $f^{-0.35}E_0^{3.47}\sigma^{0.38}$ on the same linear line (with small fluctuation) for the 0.7PZT–0.3PZN ceramic under sub-coercive field condition. At each stress, the data points are from some of the measured electric fields and frequencies.

To investigate the scaling behaviour under the effect of applied stresses, instead of including only the field amplitude $E_0$ and the frequency term $f$, the scaling relation should also include the stress ($\sigma$) term, i.e.

$$\langle A\rangle \propto f^m E_0^n \sigma^p. \tag{3}$$

However, due to increasing number of exponents, to simplify the problem, the validity of the scaling law $\langle A\rangle(\sigma) \propto f^{-0.35}E_0^{3.47}$ is assumed for all applied stresses. Consequently, the area $\langle A\rangle$ for each stress is plotted against $f^{-0.35}E_0^{3.47}$, as shown in figure 3(*a*), and it can be seen from the least-square linear fits that reasonably good linear relations can be found. As a result, the condition of universality having $m = -0.35$ and $n = 3.47$ in the 0.7PZT–0.3PZN bulk ceramic is confirmed. Consequently, $\langle A\rangle \propto (a + b\sigma^c)f^{-0.35}E_0^{3.47}$ may be written and by substituting the fitted parameters, it is found that

$$\langle A\rangle - \langle A_{\sigma=0}\rangle = \langle A - A_{\sigma=0}\rangle \propto f^{-0.35}E_0^{3.47}\sigma^{0.38}, \tag{4}$$

where $\langle A_{\sigma=0}\rangle$ refers to a stress-free hysteresis area which will be a dominant term for zero stress. The data-collapsing of the scaling area from all $f$, $E_0$ and $\sigma$ was found to confirm equation (4) as evident in figure 3(*b*). Note that from the appearance of stress $\sigma$, $\langle A - A_{\sigma=0}\rangle$, referring to the difference in energy dissipation between under-stress and stress-free conditions, increases with increasing stress suggesting a decay of $\langle A\rangle$ with $\sigma$ at a rate of $\sigma^{0.38}$ as observed in experiments. As a result, it can be concluded that the difference in the hysteresis area between under-stress and stress-free condition scales with frequency, field amplitude and stress via exponents $m = -0.35$, $n = 3.47$ and $p = 0.38$. However, at a particular fixed stress, equation (4) gives $f^{-0.35}E_0^{3.47}$ which is the original form for how the area scales with the frequency and the field amplitude.

To understand the stress-dependent scaling relation obtained in equation (4), at least qualitatively, one needs to consider the following statements. Since the $P$–$E$ loop area indicates the polarization dissipation energy subjected to one full cycle of electric field application, the loop area is therefore directly related to the volume involved in the switching process during the application of the electric field [25, 26, 35]. Hence, when mechanical stress is applied, more and more ferroelectric domains are constrained by the applied stress and cannot be re-oriented by the electric field so as to participate in the polarization reversal. Consequently, both the saturation and remanent polarizations become lower with increasing compressive stress. The polarization dissipation energy is consequently found to decrease with increasing applied stress, indicating that the sample volume contributing to polarization reversal decreases with the increasing stress. Similar observations have also been reported in other investigations [22–26, 36, 37]. Furthermore, it is noted that this stress-dependent scaling relation, in particular the stress term with exponent $p = 0.38$, is slightly different, but still in the same range, from that for soft and hard PZT bulk ceramics with $p = 0.44$ and 0.37, respectively, as obtained in our previous investigations [14, 15]. An explanation for the difference is not clearly known, but could be attributed to the difference in mechanical properties of these materials. Unfortunately, there have been no other stress-dependent scaling investigations available for an independent comparison. In addition, there has been no quantitative theoretical treatment to include the stress term in the scaling relation. Many of the theoretical treatments to explain the stress effect on the hysteresis behaviour have been primarily based on constitutive models, thermodynamic phenomenology and the Rayleigh law approach [38–40]. Further investigations, both theoretical and experimental, on the stress-dependent scaling behaviour are clearly required.

## 4. Conclusion

The scaling behaviour of the sub-coercive field dynamic ferroelectric hysteresis of rhombohedral 0.7PZT–0.3PZN bulk ceramics under the effect of mechanical stress has been investigated. The scaling relation for the minor loops takes the form of $\langle A - A_{\sigma=0}\rangle \propto f^{-0.35}E_0^{3.47}\sigma^{0.38}$, which is very similar to that of soft and hard PZT ceramics. However, slightly faster responses to $f$ and $E_0$ indicate the ease of polarization orientation in this simpler domain structure ceramic as compared with commercial PZT ceramics. As a result, this study suggests that the domain structures play a significant role in controlling dynamic hysteresis behaviour of ferroelectric materials.

## Acknowledgments

Financial support from the Thailand Research Fund (TRF), the Commission on Higher Education (CHE), the Royal Golden Jubilee PhD Program, Faculty of Science and Graduate School of Chiang Mai University is gratefully acknowledged.

## References

[1] Uchino K 2000 *Ferroelectric Devices* (New York: Dekker)
[2] Auciello O, Scott J F and Ramesh R 1998 *Phys. Today* **51**(7) 22
[3] Rao M, Krishnamurthy H R and Pandit R 1990 *Phys. Rev.* B **42** 856
[4] Acharyya M and Chakrabarti B K 1995 *Phys. Rev.* B **52** 6560
[5] Liu J-M, Chan H L W, Choy C L, Zhu Y Y, Zhu S N, Liu Z G and Ming N B 2001 *Appl. Phys. Lett.* **79** 236
[6] Zuo H B, Zhang M F, Han J C and Liu J-M 2007 *Mater. Lett.* **61** 2697
[7] Sarjala M, Seppälä E T and Alava M J 2008 *Physica* B **403** 418
[8] Rao M and Pandit R 1991 *Phys. Rev.* B **43** 3373
[9] Liu J-M, Chan H L W, Choy C L and Ong C K 2001 *Phys. Rev.* B **65** 014416
[10] Pan B, Yu H, Wu D, Zhou X H and Liu J-M 2003 *Appl. Phys. Lett.* **83** 1406
[11] Kim Y-H and Kim J-J 1997 *Phys. Rev.* B **55** R11933
[12] Park J-H, Kim C-S, Choi B-C, Moon B K, Jeong J H and Kim I W 2003 *Appl. Phys. Lett.* **83** 536
[13] Yimnirun R, Laosiritaworn Y, Wongsaenmai S and Ananta S 2006 *Appl. Phys. Lett.* **89** 162901
[14] Yimnirun R, Wongsaenmai S, Ananta S and Laosiritaworn Y 2006 *Appl. Phys. Lett.* **89** 242901
[15] Yimnirun R, Wongmaneerung R, Wongsaenmai S, Ngamjarurojana A, Ananta S and Laosiritaworn Y 2007 *Appl. Phys. Lett.* **90** 112908
[16] Yimnirun R, Wongmaneerung R, Wongsaenmai S, Ngamjarurojana A, Ananta S and Laosiritaworn Y 2007 *Appl. Phys. Lett.* **90** 112906
[17] Jiang X P, Fang J W, Zeng H R, Chu B J, Li G R, Chen D R and Yin Q R 2000 *Mater. Lett.* **44** 219
[18] Fan H and Kim H E 2002 *J. Appl. Phys.* **91** 317
[19] Vittayakorn N, Rujijanagul G, Tunkasiri T, Tan X and Cann D P 2003 *J. Mater. Res.* **18** 2881
[20] Vittayakorn N, Rujijanagul G, Tan X and Cann D P 2006 *J. Electroceram.* **16** 141
[21] Uchino K 1997 *Piezoelectric Actuators and Ultrasonic Motors* (Boston: Kluwer)
[22] Zhao J, Glazounov A E and Zhang Q M 1999 *Appl. Phys. Lett.* **74** 436
[23] Viehland D and Powers J 2001 *J. Appl. Phys.* **89** 1820
[24] Zhou D, Kamlah M and Munz D 2005 *J. Eur. Ceram. Soc.* **25** 425
[25] Yimnirun R, Laosiritaworn Y and Wongsaenmai S 2006 *J. Phys. D: Appl. Phys.* **39** 759
[26] Yimnirun R, Ananta S, Ngamjarurojana A and Wongsaenmai S 2005 *Appl. Phys. A—Mater.* **81** 1227
[27] Hall D A and Stevenson P J 1999 *Ferroelectrics* **228** 139
[28] Garcia J E, Perez R and Albareda A 2001 *J. Phys. D: Appl. Phys.* **34** 3279

[29] Morozov M, Damjanovic D and Setter N 2005 *J. Eur. Ceram. Soc.* **25** 2483
[30] Trolier-McKinstry S, Gharb N B and Damjanovic D 2006 *Appl. Phys. Lett.* **88** 202901
[31] Lai B-K, Ponomareva I, Naumov I I, Kornev I, Fu H, Bellaiche L and Salamo G S 2006 *Phys. Rev. Lett.* **96** 137602
[32] Ricinschi D and Okuyama M 2007 *Ferroelectrics* **349** 111
[33] Tsurumi T, Sasaki T, Kakemoto H, Harigai T and Wada S 2004 *Japan. J. Appl. Phys.* **43** 7618
[34] Lee K and Baik S 2006 *Ann. Rev. Mater. Res.* **36** 81
[35] Lines M E and Glass A M 1977 *Principles and Applications of Ferroelectrics and Related Materials* (Oxford: Clarendon)
[36] Kumazawa T, Kumagai Y, Miura H, Kitano M and Kushida K 1998 *Appl. Phys. Lett.* **72** 608
[37] Lu X, Zhu J, Li X, Zhang Z, Zhu X, Wu D, Yan F, Ding Y and Wang Y 2000 *Appl. Phys. Lett.* **76** 3103
[38] Damjanovic D 1997 *J. Appl. Phys.* **82** 1788
[39] Landis C M 2004 *Curr. Opin. Solid. St. Mater.* **8** 59
[40] Achuthan A and Sun C T 2005 *J. Appl. Phys.* **97** 114103

Functional Materials Letters
Vol. 1, No. 2 (2008) 133–137
© World Scientific Publishing Company

World Scientific
www.worldscientific.com

# SCALING BEHAVIOR OF DYNAMIC HYSTERESIS IN PZT-BASED FERROELECTRIC BULK CERAMICS

RATTIKORN YIMNIRUN
*Department of Physics, Faculty of Science*
*Chiang Mai University*
*Chiang Mai 50200 Thailand*
*rattikor@chiangmai.ac.th*

Received 4 February 2008
Revised 8 March 2008

The scaling relations for the hysteresis loops of soft and hard PZT bulk ceramics were obtained in the forms of $\langle A\rangle \propto f^{-0.25}E_0$ and $\langle A\rangle \propto f^{-0.28}E_0^{0.89}$, respectively, while those for the minor loops took the forms of $\langle A\rangle \propto f^{-1/3}E_0^3$ and $\langle A\rangle \propto f^{-0.43}E_0^{3.19}$. The similarity of the scaling relations suggested that the scaling behaviors of the two types of bulk ceramics were in the same universality class and that the complex defects contributed only slightly to the dynamic behaviors. Finally, this study implied that the domain structures played significant role in controlling dynamic hysteresis behavior of ferroelectric materials.

*Keywords*: Scaling; hysteresis; PZT; ceramics.

## 1. Introduction

The dynamic hysteresis, i.e., hysteresis area $\langle A\rangle$ as a function of the field amplitude $E_0$ and frequency $f$ has become an important consideration in many applications.[1,2] Hence, there have been reports on the scaling behavior of the dynamic hysteresis in ferromagnetic and ferroelectric thin films.[3–5] Many theoretical studies have been focused on scaling law

$$\langle A\rangle \propto f^{\alpha}E_0^{\beta}, \tag{1}$$

(where $\alpha$ and $\beta$ are exponents that depend on the dimensionality and symmetry of the system) of hysteresis curves in polarization systems.[3,4] Earlier investigations have reported the scaling relations for high-$f$ region with $\alpha$ and $\beta$ values, respectively, of $-1$ and 2 for $(\Phi^2)^2$ and $(\Phi^2)^3$ model, and of $-0.33$ and 3 for PZT thin films.[3–5]

Apart from its theoretical importance, since reliable measurement of the hysteresis at ultra-high frequency is still a big challenge, it is technologically helpful to understand the scaling behavior so that the ultra-high frequency of the hysteresis can be predicted. Hence, there has been a great deal of interest in the scaling behavior of the dynamic hysteresis in ferromagnetic and ferroelectric thin films.[4,5] On a contrary, bulk ferroelectric materials are useful and widely used in many applications. Furthermore, to date, there has been no report on the studies of scaling behavior of ferroelectric hysteresis loops of bulk ceramics.

Lead zirconate titanate ($Pb(Zr_{1-x}Ti_x)O_3$ or PZT) ceramics are among the lead-based complex perovskites that have been investigated extensively, both from academic and commercial viewpoints with various applications.[1,2] However, PZT ceramics are usually modified by dopants. Generally, donor (higher-valency) additives induce "soft" piezoelectric behaviors with higher dielectric and piezoelectric activities, while acceptor (lower-valency) additives result in "hard" piezoelectric

behaviors.[2] These soft and hard PZT ceramics are available commercially and employed widely in many sensor and actuator applications. In addition to the dimension and symmetry of the system, the scaling behavior depends on domain dynamics, which should be noticeably different in hard and soft PZT ceramics with distinct types of complex defects.[1,6] Therefore, it is of interest to investigate and compare the scaling behaviors of dynamic hysteresis in these important commercial soft and hard PZT bulk ceramics.

## 2. Experimental

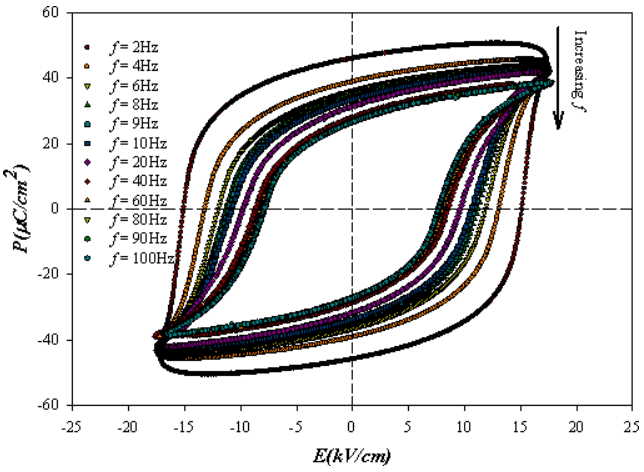
The disk-shaped samples of commercially available soft and hard PZT ceramics (APC-855 and 840, APC International, Ltd., USA) with diameter of 8 mm and thickness of 1 mm were used in this study. The dynamic hysteresis (P–E) loops were characterized at room temperature (25°C) by using a modified Sawyer–Tower circuit with $f$ covering from 1 to 100 Hz and $E_0$ from 0 to 18 and 40, in units of kV/cm, for soft and hard PZT, respectively. The electric field was applied to a sample by a high voltage AC amplifier (Trek 610D) with the input sinusoidal signal from a function generator (HP 3310A). The P–E loops were recorded by a digital oscilloscope (HP 54645A, 100 MHz). Each loop was obtained after averaging over 20 sampling cycles to average out the noise deformation. The hysteresis loop obtained was very consistent with that obtained by a standardized ferroelectric testing unit, RT66A (Radiant Technologies Inc., NM), which ensures the reliability of the measurements.

## 3. Results and Discussion

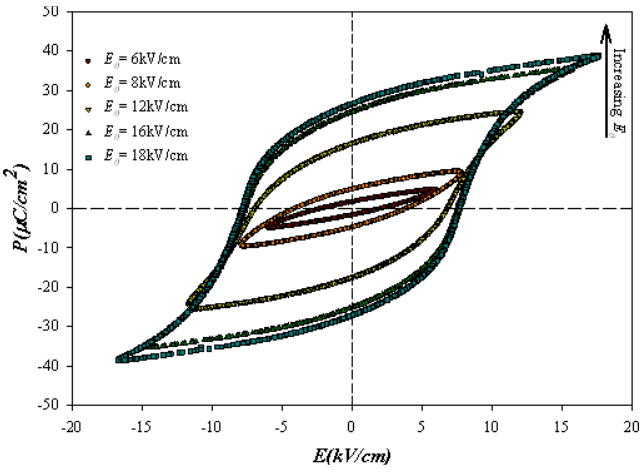
### 3.1. *Soft PZT ceramic*

The hysteresis loops at different $f$ but fixed $E_0$ (18 kV/cm), and at different $E_0$ but fixed $f$ (100 Hz) are shown in Fig. 1. The loop area $\langle A \rangle$, remanent polarization ($P_r$), and coercive field ($E_c$) decrease with an increase of frequency, as shown in Fig. 1(a). The dependence of the hysteresis loop on $E_0$ is depicted in Fig. 1(b). For small fields (6 and 8 kV/cm), the loop does not saturate. With further increase in $E_0$, $\langle A \rangle$, $P_r$ and $E_c$ increase until well saturated loop is achieved.

To obtain the suitable scaling relation for the bulk ceramic, one can fit the data with $\langle A \rangle \propto f^m E_0^n$ where $m$ and $n$ are exponents to be determined directly from the experimental data. By plotting




(a)




(b)

Fig. 1. Hysteresis loops for soft PZT ceramic (a) at various $f$ and $E_0 = 18$ kV/cm, and (b) at various $E_0$ and $f = 100$ Hz.

$\langle A \rangle$ against $f$ at fixed $E_0$, one obtains the exponent $m$. On the other hand, the exponent $n$ can be obtained from plotting $\langle A \rangle$ against $E_0$ at fixed $f$. As plotted in Fig. 2, it is revealed that the high E-field data can be much better fitted (with $R^2 = 0.97$), within the measured uncertainty, by

$$\langle A \rangle \propto f^{-0.25} E_0 \qquad (2)$$

It should also be noted that there is more deviation from the minor loops without saturation at small field amplitudes, and these data were excluded from the fitting reported in Eq. (2). The scaling relation obtained for low E-fields takes the form of $\langle A \rangle \propto f^{-0.33} E_0^3$, which is similar to that of thin films.[4,5] It is important to explain the fundamental nature of this similarity. Probable reasons would lie in the complexities of the domain structure of PZT, which also depends on the

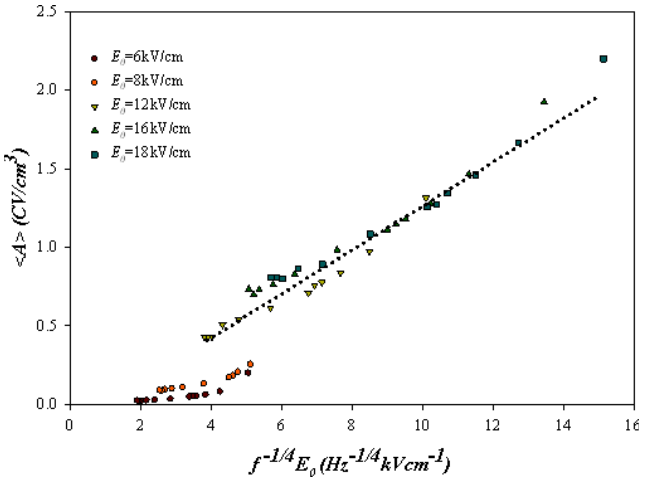


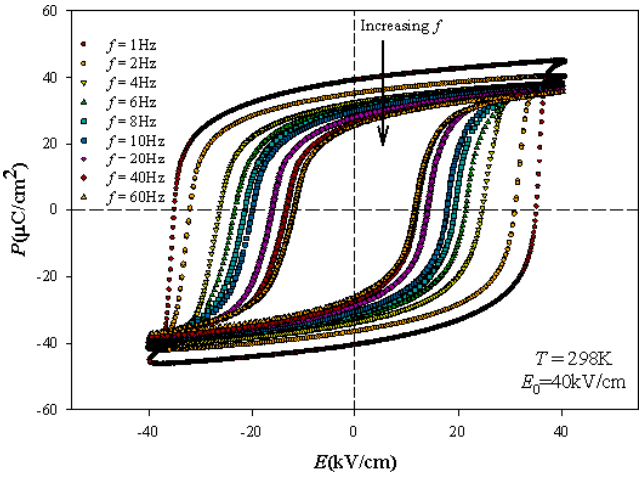

Fig. 2. Scaling of hysteresis area $\langle A\rangle$ against $f^{-0.25}E_0$ for soft PZT ceramic.

dimensionality of the material.[7] A number of recent studies have explored this behavior and reported that it is likely that different domain walls are being activated at different fields.[7,8] Generally, PZT ceramics have 180° and non-180° domain structures. As the non-180° domain switching is normally accompanied by mechanical strain, it occurs at higher E-field than 180° domain reversal does.[7–9] Therefore, under low E-fields, one would expect 180° domain reversal to occur at very fast rate (high frequencies). It is also well known that non-180° domain wall motion is typically very heavily clamped in thin films.[9] Therefore, main switching contribution in thin films would be from the 180° domain reversal. This explains why the scaling behavior of PZT bulk ceramics at low E-fields is similar to that of thin-films.

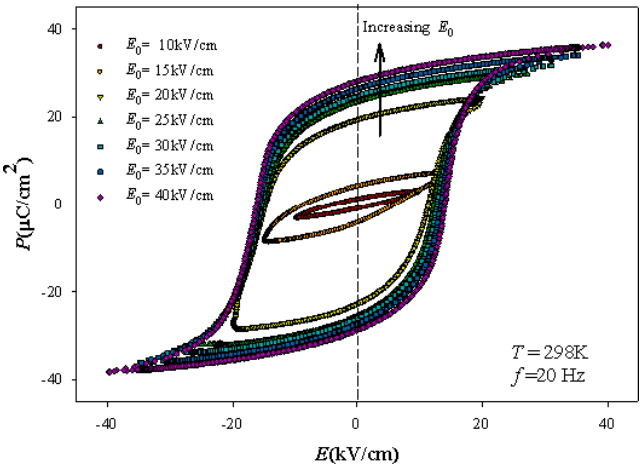
### 3.2. *Hard PZT ceramic*

The hysteresis loops at different $f$ but fixed $E_0$ (40 kV/cm), and at different $E_0$ but fixed $f$ (20 Hz) are shown in Fig. 3. The loop area $\langle A\rangle$, remanent polarization ($P_r$) and coercive field ($E_c$) decrease with an increase of frequency, as shown in Fig. 3(a). The dependence of the hysteresis loop on $E_0$ is depicted in Fig. 3(b). For small fields (10 and 15 kV/cm), the loops do not saturate. With further increase in $E_0$, $\langle A\rangle$, $P_r$ and $E_c$ increase until well saturated loop is achieved.

Attempt to obtain a scaling can be done by fitting the data with $\langle A\rangle \propto f^m E_0^n$ where $m$ and $n$ are exponents to be determined directly from the experimental data. By following the same procedure employed for soft PZT and by least-square-fitting




(a)




(b)

Fig. 3. Hysteresis loops for hard PZT bulk ceramic (a) at various $f$ and $E_0$ = 40 kV/cm and (b) at various $E_0$ and $f$ = 20 Hz.

method, for the high $E$-field data (saturated loops) the exponents $m = -0.28$ and $n = 0.89$ were obtained. As plotted in Fig. 4, it is revealed that the high $E$-field data can be fitted well ($R^2 \sim 0.98$), within the measured uncertainty, by

$$\langle A\rangle \propto f^{-0.28} E_0^{0.89} \tag{3}$$

Furthermore, the exponents $m = -0.43$ and $n = 3.19$ were obtained and fitted reasonably well ($R^2 \sim 0.92$) for the minor loop data. This form of the minor loop scaling is also similar to that of soft PZT ceramic, as well as that of thin films, as explained above.

### 3.3. *Comparison and mechanism*

The scaling relations obtained in Eqs. (2) and (3) indicate that area $\langle A\rangle$ decays more slowly with $f$

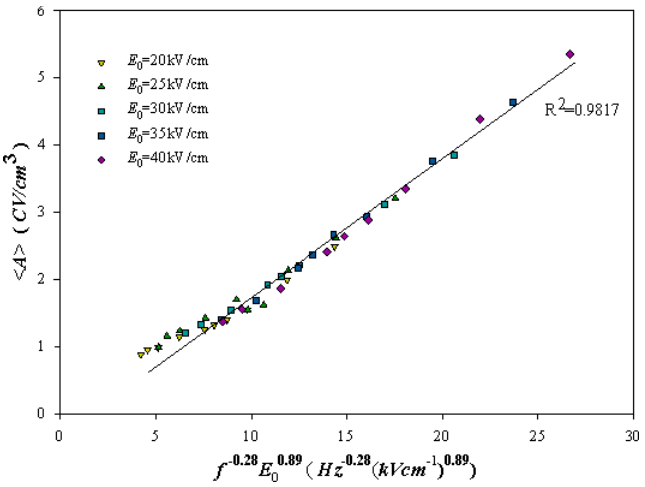



Fig. 4. Scaling of hysteresis area $\langle A\rangle$ against $f^{-0.28}E_0^{0.89}$ for hard PZT ceramic.

and grows more slowly with $E$ than the theoretical prediction, $\langle A\rangle \propto f^{-1}E_0^2$.[3,5] It is also interesting to note that the area $\langle A\rangle$ also decays slightly slower with $f$, but grows much more slowly with $E$ than the PZT thin film, $\langle A\rangle \propto f^{-0.33}E_0^{3.5}$ An explanation for the difference may come from the polarization-interaction terms as considered in the $(\Phi^2)^2$ and $(\Phi^2)^3$ models, in which the polarization-flip just has one contribution, i.e. polarization-reversal.[3,5] This requires overcoming high energy barrier. Potts model used by Liu *et al.*[10] also has the polarization orientation in various domains in directions not anti-parallel to the direction of $E$, hence requires lower energy barrier for polarization-flip to occur, which results in a higher exponent of 3 in the $E_0$ term, as compared to the exponent of 2 in the theoretical models. However, in ceramics, there are influences of many depolarizing effects, arisen from domain walls, grain boundaries, space charges, immobile defects etc., which may retard the external field. Consequently, the energy barrier is very much higher, which leads to slower polarization-flip kinetics. Therefore, a low exponent for the $E_0$ term is expected from the ceramics rather than the $(\Phi^2)^2$, $(\Phi^2)^3$ in Potts models and thin films. In addition, the $f$-term shows an exponent of $-0.25$, smaller in absolute value than that of PZT thin-film (exponent is $-0.33$). To explain the difference, not only the contribution from the domain switching and ionic-type in thin films,[10] one may need to consider the additional contributions to hysteresis properties from space charges on grain boundaries, induced electric-field from interface layers, immobile defects, etc.[1,2,6] Since our system is a bulk ceramic type; therefore, these depolarizing effects, acting as a buffer to polarization–reversal mechanism, will be stronger than those in thin film structure. As a result, the hysteresis area must show a relatively weaker dependence on $f$ than that observed in thin films.

It is even more interesting to observe that the scaling behaviors for the soft PZT bulk ceramic are to some extent similar to those of the hard counterpart. By a direct comparison, the exponents $m$ and $n$ for the two ceramics are not significantly different. The similar scaling behaviors for the two types of ceramics suggest that though the complex defects contribute greatly to the difference on the electrical properties, but they contribute only slightly to the dynamic behaviors. All these observations suggest that bulk PZT ceramics with similar domain structures should have very comparable dynamic hysteresis and scaling behavior.[11,12] Our recent studies on PZN-modified PZT ceramics also showed similar scaling behavior, which further supports the significant role of domain states in controlling scaling behavior in ferroelectric materials.

## 4. Conclusions

The scaling relations for the hysteresis loops of soft and hard PZT bulk ceramics were obtained in the forms of $\langle A\rangle \propto f^{-1/4}E_0$ and $\langle A\rangle \propto f^{-0.28}E_0^{0.89}$, respectively, while those for the minor loops take the form of $\langle A\rangle \propto f^{-1/3}E_0^3$ and $\langle A\rangle \propto f^{-0.43}E_0^{3.19}$. The similarity of the scaling relations suggests that the scaling behaviors of the two types of bulk ceramics are in the same universality class and that the complex defects contribute only slightly to the dynamic behaviors.

## Acknowledgments

This work was funded by the Thailand Research Fund (TRF), Commission on Higher Education (CHE).

## References

1. J. F. Scott, *Ferroelectr. Rev.* **1**, 1 (1998).
2. K. Uchino, *Ferroelectric Devices* (Marcel Dekker, New York, 2000).
3. M. Acharyya and B. K. Chakrabarti, *Phys. Rev. B* **52**, 6560 (1995).
4. J.-M. Liu *et al.*, *Phys. Rev. B* **65**, 014416 (2001).
5. B. Pan *et al.*, *Appl. Phys. Lett.* **83**, 1406 (2003).
6. W. Chang, A. H. King and K. J. Bowman, *Appl. Phys. Lett.* **88**, 242901 (2006).

7. K. Lee and S. Baik, *Ann. Rev. Mater. Res.* **36**, 81 (2006).
8. A. Gruverman, O. Auciello and H. Tokumoto, *Ann. Rev. Mater. Sci.* **28**, 101 (1998).
9. S. Trolier-McKinstry, N. B. Gharb and D. Damjanovic, *Appl. Phys. Lett.* **88**, 202901 (2006).
10. J.-M. Liu *et al.*, *J. Phys.: Condens. Matter* **16**, 1189 (2004).
11. R. Yimnirun *et al.*, *Appl. Phys. Lett.* **89**, 162901 (2006).
12. R. Yimnirun *et al.*, *Appl. Phys. Lett.* **90**, 112908 (2007).

Functional Materials Letters
Vol. 1, No. 3 (2008) 229–233
© World Scientific Publishing Company

World Scientific
www.worldscientific.com

# EFFECT OF NICKEL NIOBATE *B*-SITE PRECURSORS ON PHASE FORMATION, MICROSTRUCTURE AND DIELECTRIC PROPERTIES OF PEROVSKITE PNN CERAMICS

S. ANANTA*, R. YIMNIRUN and O. KHAMMAN
*Department of Physics, Faculty of Science, Chiang Mai University*
*Chiang Mai, 50200, Thailand*
**suponananta@yahoo.com*

Received 6 February 2008
Revised 25 March 2008

Relaxor perovskite lead nickel niobate (PNN) ceramics were fabricated by using *B*-site precursor method, in which both columbite-$NiNb_2O_6$ and corundum-$Ni_4Nb_2O_9$ were separately employed as nickel niobate *B*-site precursors. It has been found that optimization of sintering condition can successfully lead to highly dense and pure PNN ceramics in both routes. Between the two *B*-site precursor routes, pure perovskite PNN ceramics with slightly better densification and dielectric properties can be produced by using the columbite-route.

*Keywords*: Lead nickel niobate; perovskite; sintering; dielectric properties.

## 1. Introduction

Lead nickel niobate, $Pb(Ni_{1/3}Nb_{2/3})O_3$ or PNN, is one of the piezo-based perovskite functional materials which has been extentively studied as potential candidates for electroceramic components such as multilayer capacitor, actuator and transducer applications.[1–3] However, as is well-known, a practical limitation to the utilization of this compound in device applications has been the lack of a simple, reproducible preparation technique for a pure perovskite phase with consistent properties. The formation of perovskite PNN is often accompanied by the occurrence of one or more undesirable phases, which significantly degrade the overall electrical properties of the products.[4–7] To avoid the formation of unwanted phases, several methods have been introduced.[6–10] So far, the columbite method,[4–6] in which prefabricated $NiNb_2O_6$ is reacted with an appropriate proportion of PbO, has been widely accepted as one of the promising methods for the preparation of phase-pure PNN-based materials. There has been a great deal of interest in the preparation of single phase PNN powders as well as in the sintering and electrical properties of PNN-based ceramics.[4–9] To date, only our previous work[11,12] on the preparation of PNN powders by using a corundum $Ni_4Nb_2O_9$ precursor have been reported. Interestingly, effect of a corundum $Ni_4Nb_2O_9$ precursor on phase formation, microstructure and dielectric properties of PNN ceramics under various sintering temperatures has not been reported.

In the present study, an attempt has been made to fabricate and characterize the PNN ceramics by using two different *B*-site precursors i.e. columbite-$NiNb_2O_6$ and corundum-$Ni_4Nb_2O_9$. Their dielectric properties with respect to temperature and frequency were also examined, compared and explained on the basis of their final composition, densification and microstructural development.

## 2. Experimental

$Pb(Ni_{1/3}Nb_{2/3})O_3$ powders were synthesized by employing two different *B*-site precursors (i.e.

columbite- versus corundum-route) mixed oxide synthetic route, as reported earlier.[11,12] Starting precursors were as follows: PbO (JCPDS file no. 77-1971), NiO (JCPDS file no. 73-1519) and $Nb_2O_5$ (JCPDS file no. 30-873) (Aldrich, 99% purity). The three oxide powders have an average particle size in the range of 3.0–5.0 $\mu$m. First, two intermediate phases of nickel niobate of $NiNb_2O_6$ and $Ni_4Nb_2O_9$ were separately prepared by the solid-state reaction method previously reported.[13,14] The appropriate amount of PbO was then added to the $NiNb_2O_6$ and $Ni_4Nb_2O_9$, vibro-milled and calcined in closed alumina crucible. All batches of powder were prepared using a simple mixed oxide method via a rapid-vibro milling technique for only 2 h (instead of 12 h in Ref. 3) with corundum media in isopropyl alcohol. The detailed process can be found in our previous works.[11–14] The columbite and corundum-route mixtures were then calcined for 2 h with heating/cooling rates of 10°C/min at 950°C and 1050°C, respectively.[11,12] Ceramic fabrication was achieved by adding 3 wt.% polyvinyl alcohol (PVA) binder, prior to pressing as pellets in a pseudo-uniaxial die press. Each pellet was placed in an alumina crucible together with an atmosphere powder of identical chemical composition. After debinding at 500°C for 1 h, sintering was carried out with a constant dwell time of 2 h using heating/cooling rates of 5°C/min at various temperatures between 1100 and 1250°C.

Densities of the final sintered products were measured using the Archimedes principle. Sintered ceramics were examined by X-ray diffraction (Siemen D-500 diffractometer) using Cu$K_\alpha$ radiation at room temperature. The microstructural development was characterized using a scanning electron microscopy (JEOL JSM-840A). Mean grain size of the sintered ceramics was subsequently estimated by employing the linear intercept method.[15] In order to evaluate the dielectric properties, dense ceramics were polished to form flat, parallel faces and then coated with gold electrodes. The dielectric properties were measured at various frequency using a LCR meter (HIOKI 3532-50), on cooling through the transition range (−150 to 50°C) with a rate of 3°C/min (instead of 4°C/min in Ref. 3).

## 3. Results and Discussion

The X-ray diffraction (XRD) patterns of columbite- and corundum-route PNN ceramics sintered at various temperatures are given in Figs. 1(a)–1(c) and 1(d)–1(f), respectively. In general, all XRD patterns show 100% perovskite $Pb(Ni_{1/3}Nb_{2/3})O_3$ phase and could be matched with JCPDS file no. 34-103,[16] in agreement with other works.[7,9] To a first approximation, this phase has a pseudo-cubic perovskite-type structure with cell parameter $a = 403$ pm in space group $Pm3m$ (no. 221). It should be noted that no evidence of either unreacted precursors or pyrochlore-type phases such as $Pb_{1.45}Nb_2O_{6.26}$, $Pb_3Nb_2O_8$, $Pb_3Nb_4O_{13}$ and $Pb_{15}NiNb_{10}O_{41}$ has been found here whereas these phases were found in other works.[7,10,12,17]

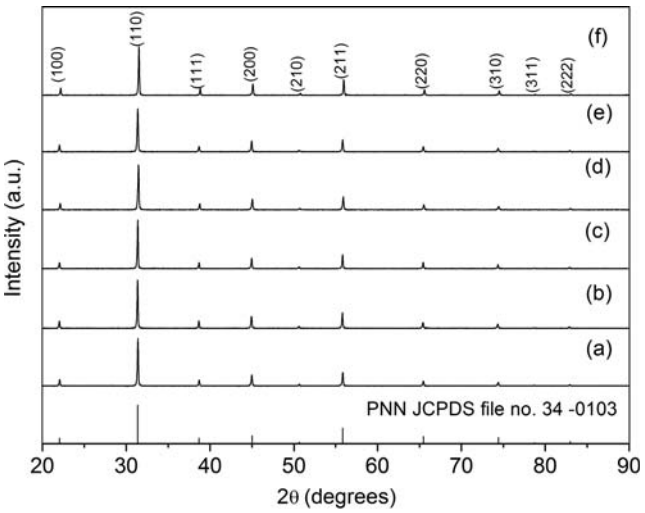



Fig. 1. XRD patterns of the columbite-route PNN ceramics sintered at (a) 1100°C, (b) 1150°C and (c) 1200°C, and the corundum-route PNN ceramics sintered at (d) 1100°C, (e) 1150°C and (f) 1200°C.

The densification data of all the samples are shown in Table 1. The density of about 92–96% and 93–95% of the theoretical value can be achieved for columbite- and corundum-route PNN ceramics, respectively. Density increases as sintering temperature increases from 1100 to 1200°C, consistent with Ref. 3. However, further increase in the sintering temperature up to 1250°C caused the critical damage of the PNN samples (with some melted areas), in contrast to earlier report.[3] This may be attributed to the loss of lead oxide at high sintering temperatures, which is similar to the results found in other Pb-based perovskite systems.[18,19]

It can be noticed that the pure PNN ceramics with higher maximum density can be produced at the optimized sintering temperature of 1200°C by using both $B$-site precursors. Based on the results obtained here, it may be concluded that the optimal sintering temperature for the production of

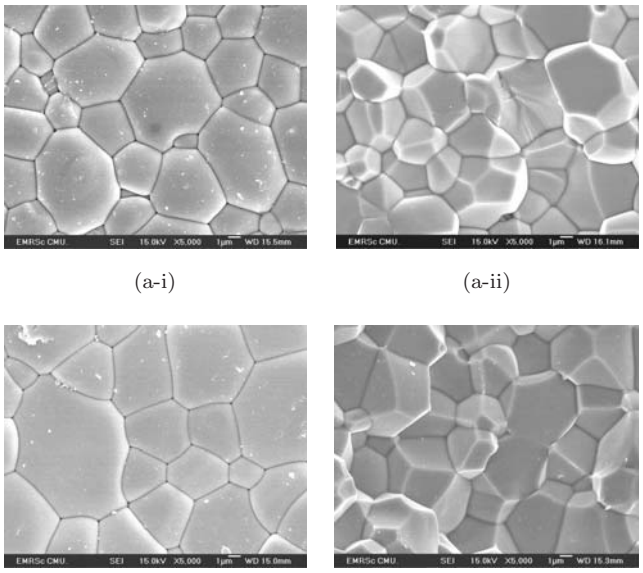
Table 1. Physical and dielectric properties of columbite- and corundum-route PNN ceramics.

| Preparation route | | Columbite route | | | Corundum route | | |
|---|---|---|---|---|---|---|---|
| Sintering condition (°C) for 2 h | 1200[3] | 1100 | 1150 | 1200 | 1100 | 1150 | 1200 |
| *Physical properties* | | | | | | | |
| Relative density (%)[a] | 94 | 92 | 95 | 96 | 93 | 94 | 95 |
| Grain size range | — | 1.2–4.2 | 1.3–5.0 | 2.0–12.3 | 0.5–3.3 | 0.8–4.4 | 1.7–8.0 |
| (mean) ($\mu$m)[b] | (3.7) | (2.2) | (3.3) | (5.4) | (1.8) | (2.2) | (4.1) |
| *Dielectric properties* | | | | | | | |
| $\varepsilon_{r,25°C}$ | 1593 | | | 1660 | | | 1543 |
| $\tan\delta_{25°C}$ | 0.0162 | | | 0.0064 | | | 0.0048 |
| $T(\varepsilon_{r,\max})$ | −110 | | | −115 | | | −117 |
| $\varepsilon_{r,\max}$ | 3403 | | | 3636 | | | 3430 |
| $\tan\delta_{\max}$ | 0.0029 | | | 0.0096 | | | 0.0121 |
| Diffusivity ($\gamma$) | 1.79 | | | 1.92 | | | 1.90 |

[a]The estimated precision of the relative density is ±0.1%.
[b]The estimated precision of the grain size is ±10%.

columbite- and corundum-route PNN ceramics with a maximum bulk density is 1200°C for 2 h (in good agreement with other researchers[3,6]), with heating/cooling rates of 5°C/min.

SEM micrographs of as-sintered (i) and fracture (ii) surfaces of columbite- and corundum-route PNN ceramics with maximum bulk density are compared in Fig. 2. In general, typical perovskite PNN microstructure consisting of highly dense grain-packing is observed in both samples and in good agreement with previous works.[3,6,7] The grain sizes are in the range of 2–12 $\mu$m and 1–8 $\mu$m for columbite- and corundum-route PNN ceramics, respectively. The results also indicate that grain size tends to increase with sintering temperature, as in the PMN and PT studies.[18,19] Micrographs of fracture surface (Figs. 2(a-ii) and 2(b-ii)) show highly dense microstructures consisting of equiaxed grains, in agreement with other researchers.[3] The PNN ceramics also have an intergranular fracture mechanism, indicating that the grain boundaries are mechanically weaker than the grains,[20] similar to the results previously observed in the relaxor perovskite systems.[4,5,18]



(a-i) (a-ii)

(b-i) (b-ii)

Fig. 2. SEM micrographs of (i) as-sintered and (ii) fracture surfaces for (a) columbite- and (b) corundum-route PNN ceramics with maximum bulk density.

In order to evaluate the dielectric properties i.e. dielectric constant ($\varepsilon_r$) and dielectric loss ($\tan\delta$), both columbite- and corundum-route PNN ceramics with the maximum bulk density were measured at frequencies between 1 and 100 kHz in the temperature range from −150 to +50°C as shown in Figs. 3(i) and 3(ii). In general, the typical relaxor behavior[2,3] with the characteristic dispersive frequency dependence of the dielectric maxima has been observed in both PNN samples. The maximum dielectric constants of 3636 and 3430 measured at 1 kHz were obtained at the temperatures about −115°C and −117°C for columbite- and corundum-route samples, respectively, which are close to previously reported values.[3,4,9]

Characteristics of PNN ceramics obtained by different *B*-site precursor methods in this work and those reported in other works are also compared in Table 1. By comparison to the corundum-route PNN ceramic, dielectric properties of columbite-route ceramic are slightly better, consistent with the density values observed. Though the difference in the dielectric properties could be caused by the

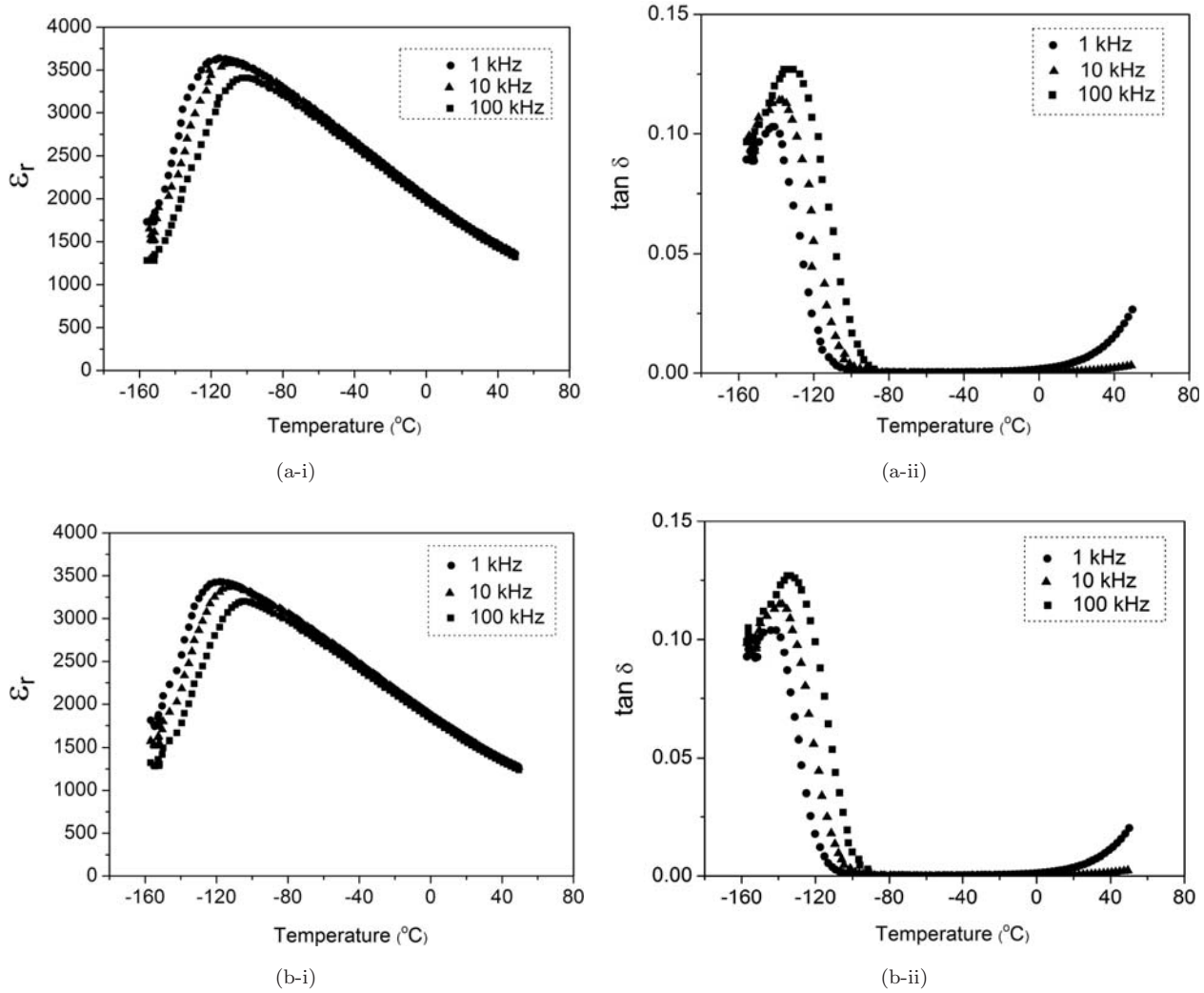



Fig. 3. Temperature dependence of (i) dielectric constant ($\varepsilon_r$) and (ii) dielectric loss ($\tan\delta$) for (a) columbite- and (b) corundum-route PNN ceramics with maximum bulk density.

grain-size effect,[2,21] this should not be the sole reason in the current study because the grain size of the ceramics obtained in both routes is very similar, as listed in Table 1. However, it is observed that the PNN ceramics with larger average grain size and wider grain size range exhibit better dielectric properties. This observation suggests that the grain size along with the microstructural heterogeneous arrangement observed play role together in controlling the dielectric properties. It should also be noted that the dielectric properties and dielectric maximum temperature ($T_{\max}$) obtained in this study are similar to previous investigation,[6] and are close to those reported for single crystal PNN.[22] On the other hand, previous reports on PNN ceramics by other groups showed noticeable deterioration in dielectric properties and shift in $T_{\max}$, which are likely caused by the inclusion of the unwanted secondary phases, which can cause the off-stoichiometry composition or chemical heterogeneity leading to more diffuse phase transition response and $T_{\max}$ shifting. The secondary phase is usually a non-ferroelectric compound so it can definitely destroy the overall dielectric properties and act like a pore in some sense for ferroelectric materials.[23,24]

Unlike the normal ferroelectrics, the dielectric behavior of PNN ceramics cannot be described by the Curie–Weiss law. Their behaviors tally well with the law $1/\varepsilon \propto (T - T_{\max})$.[2] The dielectric constant can be written in the form:

$$\frac{1}{\varepsilon} = \frac{1}{\varepsilon_{\max}} + \frac{(T - T_{\max})^{\gamma}}{2\varepsilon_{\max}\delta^2}, \qquad (1)$$

where $\gamma$ is the diffusivity which expresses the degree of dielectric relaxation in the relaxor ferroelectric

materials and $\delta$ is diffusion parameter and gives an estimation of the relaxor characteristic of the transition. The diffusion exponent for columbite- and corundum-route PNN ceramics is $\gamma = 1.92$ and 1.90, respectively (Table 1), which is higher than reported values of 1.79,[3] 1.75,[7] 1.57[9] and 1.50,[24] but is very close to 2.0,[2] indication of close to completely disordered relaxor behavior in the ceramics sintered by both routes.

By comparison, the diffusion exponent for corundum-route sintered PNN ceramic is smaller than that observed in columbite-route sample. The similar observation has been reported in the PMN ceramics.[21] It may be caused by the different densification of the samples between the two routes. It should also be noticed that the difference in the diffusion exponent $\gamma$ between the PNN ceramics obtained in this present work and those reported earlier[3,7,9,24] could be attributed to the inclusion of secondary phases, which also cause the deterioration in dielectric properties and shift in dielectric maximum temperature ($T_{max}$) in previous investigations.[23,24] Furthermore, for a perovskite ferroelectric, it can be established that the diffusion could be caused by grain-size dependence.[2,21] Therefore, this effect can partly be the cause of the increase of diffusion exponent in columbite-route PNN ceramic. Most importantly, it should be noted that the effect of corundum-$Ni_4Nb_2O_9$ *B*-site precursor on phase formation, microstructure and dielectric properties of perovskite PNN ceramics has been reported here for the first time.

## 4. Conclusions

Highly dense and pure relaxor perovskite PNN ceramics can be successfully produced by employing either columbite- or corundum-route precursor method under optimized sintering temperatures. Between the two *B*-site precursor methods, it is seen that the production of pure PNN ceramics with larger grain size, higher density and better dielectric properties can be obtained via a columbite *B*-site precursor route.

## Acknowledgments

This work was supported by the Thailand Research Fund (TRF) and the Commission on Higher Education (CHE).

## References

1. K. Niwa, M. Kondo, M. Hida and K. Kurihara, *Jpn. Ceram. Trans.* **150**, 401 (2004).
2. A. J. Moulson and J. M. Herbert, *Electroceramics*, 2nd edn. (Wiley, Chichester, 2003).
3. E. F. Alberta and A. S. Bhalla, *Mater. Lett.* **54**, 47 (2002).
4. T. R. Shrout and A. Halliyal, *Am. Ceram. Soc. Bull.* **66**, 704 (1987).
5. N. Vittayakorn, G. Rujijanagul, X. Tan, M. A. Marquardt and D. P. Cann, *J. Appl. Phys.* **96**, 5103 (2004).
6. L. Veitch, *B.S. Thesis*, Pennsylvania State University, University Park, PA, 1982.
7. C. H. Lu and H. J. Hwang, *Ceram. Int.* **22**, 373 (1996).
8. M. M. A. Sekar and A. Halliyal, *J. Am. Ceram. Soc.* **81**, 380 (1998).
9. C. H. Lu and H. J. Hwang, *Jpn. J. Appl. Phys.* **38**, 5478 (1999).
10. Y. Yoshikawa, *Key Eng. Mater.* **206–213**, 87 (2002).
11. O. Khamman, R. Yimnirun and S. Ananta, *Mater. Lett.* **61**, 4466 (2007).
12. O. Khamman, R. Yimnirun and S. Ananta, *J. Alloys. Compd.* (2007) in press, doi: 10.1016/j.jallcom.2007.11.002.
13. O. Khamman, R. Yimnirun and S. Ananta, *Mater. Lett.* **61**, 639 (2007).
14. O. Khamman, R. Yimnirun and S. Ananta, *Mater. Lett.* **61**, 2565 (2007).
15. R. L. Fullman, *Trans AIME* **197**, 447 (1953).
16. Powder Diffraction File No. 34-103. International Centre for Diffraction Data, Newton Square, PA, 2000.
17. B. Balzer and H. Langbein, *Cryst. Res. Technol.* **32**, 955 (1997).
18. S. Ananta and N. W. Thomas, *J. Eur. Ceram. Soc.* **19**, 1873 (1999).
19. A. Udomporn, K. Pengpat and S. Ananta, *J. Eur. Ceram. Soc.* **24**, 185 (2004).
20. O. Guillon, F. Thiebaud, D. Perreux, C. Courtoris, P. Champagne, A. Leriche and J. Crampon, *J. Eur. Ceram. Soc.* **25**, 2421 (2005).
21. S. Wagner, D. Kahraman, H. Kungl, M. J. Hoffmann, C. Schuh, K. Lubitz, H. Murmann-Biesenecker and J. A. Schmid, *J. Appl. Phys.* **98**, 021102 (2005).
22. V. A. Bokov and I. E. Myl'nikova, *Sov. Phys. Solid State* **3**(3), 613 (1961).
23. G. A. Smolenskii and A. I. Agranovskaya, *Sov. Phys. Solid State* **1**, 1429 (1959).
24. S. Sharma, R. Sati and R. N. P. Choudhary, *Can. J. Phys.* **71**, 322 (1993).

J. Phys. D: Appl. Phys. **41** (2008) 245405 (4pp) doi:10.1088/0022-3727/41/24/245405

# Changes in the dielectric properties of $Pb(Zr_{1/2}Ti_{1/2})O_3$–$Pb(Co_{1/3}Nb_{2/3})O_3$ ceramics under compressive stress applied perpendicularly to the electric field

**Muangjai Unruan, Anurak Prasatkhetragarn, Yongyut Laosiritaworn, Supon Ananta and Rattikorn Yimnirun**[1]

Department of Physics, Faculty of Science, Chiang Mai University, Chiang Mai, 50200, Thailand

E-mail: rattikornyimnirun@yahoo.com

Received 11 May 2008, in final form 15 September 2008
Published 27 November 2008
Online at stacks.iop.org/JPhysD/41/245405

**Abstract**

The effects of compressive stress, applied perpendicularly to the electric field, on the dielectric properties of $(1-x)Pb(Zr_{1/2}Ti_{1/2})O_3$–$(x)Pb(Co_{1/3}Nb_{2/3})O_3$ ($x = 0.1$–$0.5$) ceramics were investigated. The results showed that compressive stress had pronounced effects on the dielectric properties of PZT–PCN ceramics. With increasing compressive stress the dielectric constant decreased, while the dielectric loss tangent increased. The observations were interpreted mainly in terms of competing influences of the domain switching through non-180° domain walls, clamping of domain walls and de-ageing mechanisms. The observed changes in the dielectric properties under perpendicular compressive stress were exactly opposite to those under parallel stress.

(Some figures in this article are in colour only in the electronic version)

## 1. Introduction

Much attention regarding lead-based relaxor ferroelectrics has been focused on lead magnesium niobate ($Pb(Mg_{1/3}Nb_{2/3})O_3$, or PMN), which is widely accepted as a prototype relaxor material. However, there is a series of relaxor materials based on the $Pb(B_{1/3}Nb_{2/3})O_3$ system which also possesses interesting properties [1–3]. This study is focused on lead cobalt niobate ($Pb(Co_{1/3}Nb_{2/3})O_3$, or PCN). However, the temperature related to the maximum dielectric constant ($T_{max}$) of PCN in the relaxor phase is very low ($T_{max} = -30\,^{\circ}C$) [4]. Thus, in order to increase the $T_{max}$ of PCN, lead zirconate titanate ($PbZr_{0.5}Ti_{0.5}O_3$, or PZT) was added to PCN to form a solid solution of PZT–PCN ceramics. The solid solution of PZT and PCN is expected to synergistically combine the properties of both normal ferroelectric PZT and relaxor ferroelectric PCN, and to exhibit better piezoelectric and dielectric properties than those of the single-phase PZT and PCN [5, 6]. Our recent investigations have already revealed very interesting electrical properties of PZT–PCN ceramic systems [7, 8].

Piezoelectric and ferroelectric ceramics are widely used in devices such as actuators and transducers. However when they are used in these devices the ceramics are often subjected to self-induced or environmental stresses [9–13]. A prior knowledge of the effects of stresses on the material properties is crucial for proper design of a device and for suitable selection of materials for a specific application [12, 13]. Therefore it is very important to obtain experimental data in order to better understand how these materials behave under stress. Stress-dependent dielectric properties have been investigated in $BaTiO_3$ (BT); $Pb(Zr_{0.52}Ti_{0.48})O_3$ (PZT); $Pb(Mg_{1/3}Nb_{2/3})O_3$ (PMN); $Pb(Mg_{1/3}Nb_{2/3})O_3$–$PbTiO_3$ (PMN–PT); $Pb(Mg_{1/3}Nb_{2/3})O_3$–$Pb(Zr_{0.52}Ti_{0.48})O_3$ (PMN–PZT); and $Pb(Zr_{0.52}Ti_{0.48})O_3$–$BaTiO_3$ (PZT–BT) [14–22]. The effects of stress on the dielectric properties of these ceramics depend significantly on compositions and stress levels. However, no study has been conducted on the stress effect on dielectric properties

[1] Author to whom any correspondence should be addressed.

 © 2008 IOP Publishing Ltd Printed in the UK

**Table 1.** Characteristics of $(1-x)$PZT–$(x)$PCN ceramics with optimized processing conditions (measured at 10 kHz) [7, 8].

| Ceramic | Density ($g\,cm^{-3}$) | Grain size range ($\mu$m) | Average grain size ($\mu$m) | $T_{max}$ (°C) | Room-temperature stress-free dielectric properties | |
|---|---|---|---|---|---|---|
| | | | | | $\varepsilon_r$ | tan$\delta$ |
| 0.9PZT–0.1PCN | 7.39 | 4.54–19.56 | 7.45 | 367 | 893 | 0.206 |
| 0.8PZT–0.2PCN | 7.46 | 2.60–12.35 | 4.13 | 320 | 1106 | 0.105 |
| 0.7PZT–0.3PCN | 7.62 | 0.43–9.53 | 2.82 | 298 | 619 | 0.148 |
| 0.6PZT–0.4PCN | 7.42 | 0.6–10.75 | 2.77 | 236 | 776 | 0.239 |
| 0.5PZT–0.5PCN | 7.31 | 0.47–9.53 | 2.61 | 210 | 1061 | 0.112 |

of PZT–PCN ceramics. Our recent investigation showed that the dielectric constant of PZT–PCN ceramics increased significantly with increasing compressive stress applied parallel to the electric field direction, while the dielectric loss tangent showed an opposing trend [23]. Recently, many investigations also reported changes in the electrical properties of ferroelectric ceramics under compressive stress applied perpendicularly to the electric field [16, 18, 24–28]. Therefore, it is the aim of this study to examine the dielectric properties of PZT–PCN ceramics under such compressive stress. This study, along with our previous investigation, will provide a complete picture of how compressive stress applied in orthogonal directions affects the dielectric properties of this ceramic system.

## 2. Experimental method

Dense perovskite-phase $(1-x)Pb(Zr_{1/2}Ti_{1/2})O_3$–$(x)Pb(Co_{1/3}Nb_{2/3})O_3$ ($x = 0.1$–$0.5$) ceramics with uniform microstructure and high density values were prepared from PbO, columbite $CoNb_2O_6$, and wolframite $ZrTiO_4$ powders by the mixed-oxide method [7, 8, 23]. Details of ceramic processing and characterizations have already been provided elsewhere [7, 8]. PZT–PCN ceramics show a perovskite structure having a symmetry varying between tetragonal and pseudo-cubic types, and with a morphotropic phase boundary (MPB) composition between $x = 0.2$ and 0.3. Though the grain size of the ceramics varies considerably from <0.47 to 19.6 $\mu$m, the average grain size only varies between 3 and 7 $\mu$m [7, 8]. Table 1 summarizes the physical characteristics of the PZT–PCN ceramics used in this study. It is important to note that, since there was no significant difference in either the density or the average grain size of all the ceramic compositions (except for the 0.9PZT–0.1PCN composition, which contained larger grains), these parameters should not play an important role in the composition-dependent dielectric properties under compressive stress.

The sintered specimens were cut into rectangular bars (typical dimensions: $6 \times 2 \times 2\,mm^3$) and then lapped to obtain parallel faces. Silver paint was applied onto the two ($6 \times 2\,mm^2$) opposite faces, and the two electrodes were attached with silver wires for electrical measurement. The specimens were heated at 750 °C for 12 min to ensure contact between the electrodes and the ceramic surface. To study the effects of stress on the dielectric properties of the ceramic, a compressometer was constructed for simultaneous applications of mechanical stress perpendicular to the electric field [29–31]. The compressometer cell consisted of a cylindrical brass cell with a heavy brass base, a brass ram and a precisely guided loading platform which provided true uniaxial stress during mechanical loading. Compressive stress was supplied by a servohydraulic load frame, and the applied stress level was monitored with the load frame's pressure gauge. Measurements were performed as a function of mechanical prestress applied discretely. The dielectric properties were measured at room temperature using a LCR-meter (Instek LCR-821) with an applied voltage of 1 V at 10 kHz.

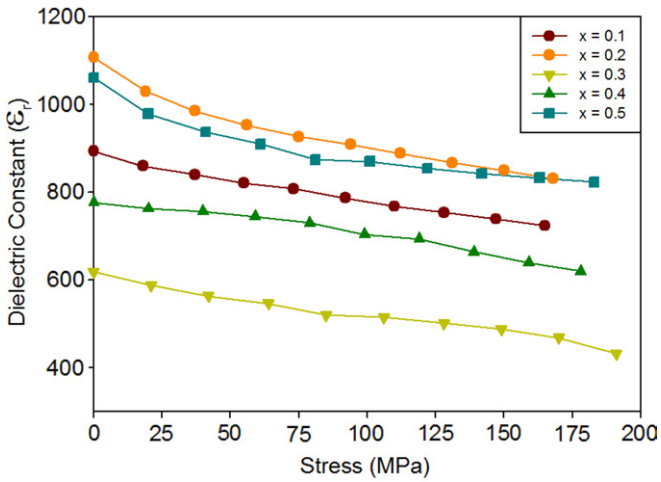



**Figure 1.** Changes in dielectric constant ($\varepsilon_r$) with compressive stress applied perpendicularly to the electric field direction for $(1-x)$PZT–$(x)$PCN ceramics (measured at 25 °C and 10 kHz).

## 3. Results and discussion

The room-temperature dielectric properties of $(1-x)$PZT–$(x)$PCN ceramic as a function of perpendicular compressive stress are depicted in figures 1 and 2. It should be noted that even though the loading and the unloading experiments were performed on all compositions, the results differed insignificantly. Hence, only the average values are plotted. Figure 1 shows that the dielectric constant decreases with increasing stress, for all compositions. At a maximum applied stress of 180 MPa, the decrease in the dielectric constant varies slightly: from approximately 25–30% for the near MPB 0.8PZT–0.2PCN and 0.7PZT–0.3PCN compositions, to 15–20% for the other compositions. On the other hand, the dielectric loss tangent (tan $\delta$) increases monotonically with the

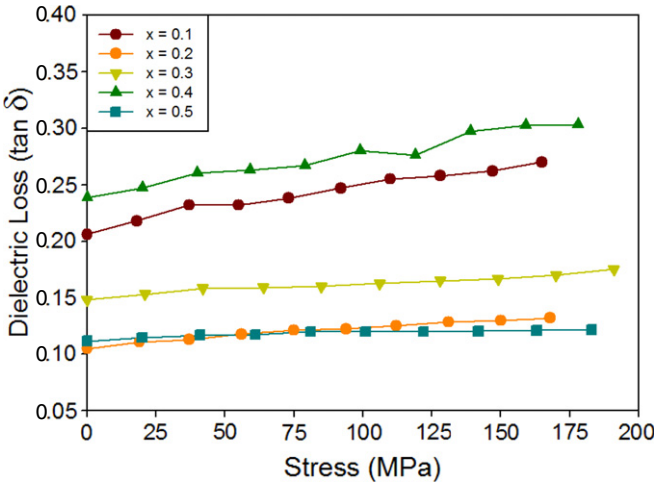



**Figure 2.** Changes in dielectric loss tangent (tan $\delta$) with compressive stress applied perpendicularly to the electric field direction for $(1-x)$PZT–$(x)$PCN ceramics (measured at 25 °C and 10 kHz).

applied stress increase, as displayed in figure 2. The dielectric loss tangent increases by 10–20% at the maximum stress value, with the higher changes observed for compositions near the MPB. In the case of compressive stress applied perpendicularly to the direction of the electric field, only limited testing has been carried out on hard and soft PZT, PIN–PT and PMN–PT ceramics [18, 20, 24, 32, 33]. The results presented here are very similar to those obtained earlier for the Pb-based perovskite ceramics mentioned above.

However, since the dielectric constant of the sample was measured using capacitance, there is a change in sample capacitance due to the geometrical deformation under stress. The variation of the sample dielectric constant ($\Delta\varepsilon_r$) can be expressed as $\varepsilon_r^* X^*((1+2\upsilon)/E)$, where $X$ is the applied stress, $\upsilon$ is Poisson's ratio and $E$ is Young's modulus [20, 29]. By applying the estimated values of $\upsilon \sim 0.3$ and $E \sim 100$ GPa for PZT–based ceramics [19, 24, 34] and $\varepsilon_r$ given in table 1, it can be estimated that at the maximum stress of 180 MPa, the variation of the sample dielectric constant due to geometrical deformation is <0.5%. Therefore, this variation should not be an important factor in the dielectric properties change under stress seen in figures 1 and 2.

To understand these experimental results, at least qualitatively, various effects must be considered. When compressive stress is applied, the domain structure of ferroelectric ceramics may undergo domain switching through non-180° domain walls, de-ageing, and clamping of domain walls [11, 14, 19, 28]. Here, the stress clamping of domain walls, which results in a decrease in domain wall mobility, and the stress-induced decrease in the switchable part of spontaneous polarization are expected to play roles in the decrease in the dielectric constant under compressive stress [10, 17, 28]. In addition, the continuous decrease in the dielectric constant can also be attributed to the switching of 90° domains. This is a particularly important contribution because when compressive stress is applied perpendicularly to the electric field direction, the applied stress tends to force the polarization of the individual domains to lie in a plane normal to the stress direction through the non-180° (i.e. 90° in tetragonal composition, and 71°/109° in rhombohedral composition) ferroelastic domain switching processes [14–17, 28]. Therefore, a greater decrease in the dielectric constant of the compositions near MPB (i.e. 0.8PZT–0.2PCN and 0.7PZT–0.3PCN) is attributed to more available domain states in the compositions [1–3]; hence a much greater change is observed.

The cause of the stress dependence of the dielectric loss tangent is more complex. As is seen in the changes in the dielectric constant, the clamping of domain walls under compressive perpendicular stress results in a decrease in domain wall mobility; hence this should reduce the dielectric loss tangent at a similar rate [17, 28]. However, a noticeable increase in the dielectric loss tangent is observed for all compositions. This can probably be explained by an additional, obviously larger, contribution from the de-ageing mechanism. During the ageing process, some of the domain walls become pinned by impurities and structural imperfections. When a large enough stress is applied to the aged samples, it causes structural changes and a redistribution of impurities. As a result, the domain walls that were pinned during ageing can become active again. This de-ageing can increase the dielectric responses. Therefore, the competing influence between the domain clamping and de-ageing mechanisms can cause a slight increase in the dielectric loss response to the applied stress.

In addition, only slight decreases in the dielectric properties of all the ceramics were observed after a complete cycle of mechanical stress. This suggests a small stress-induced decrease in the switchable part of the polarization at the maximum applied stress, which exceeds the expected coercive stress for ferroelastic switching in PZT–PCN ceramics (reported as 130–150 MPa for hard PZT ceramics) [35].

## 4. Conclusions

The dielectric properties of $(1-x)$Pb$(Zr_{1/2}Ti_{1/2})O_3$–(x)Pb$(Co_{1/3}Nb_{2/3})O_3$ ($x$ = 0.1–0.5) ceramics were determined under compressive stress applied perpendicularly to the electric field. The results clearly showed that perpendicular compressive stress had pronounced effects on the dielectric properties of PZT–PCN ceramics. With increasing compressive stress, the dielectric constant of the ceramics decreased, while the dielectric loss tangent increased. The observations were interpreted mainly in terms of competing influences of the domain switching through non-180° domain walls, clamping of domain walls, and de-ageing mechanisms. The observed changes in the dielectric properties under perpendicular compressive stress were exactly opposite to those under parallel stress.

## Acknowledgments

This work was jointly supported by the Thailand Research Fund (TRF), Commission on Higher Education (CHE), Royal Golden Jubilee PhD Program, Faculty of Science and Graduate School of Chiang Mai University.

## References


[1] Uchino K 2000 *Ferroelectric Devices* (New York: Dekker)
[2] Jaffe B, Cook W R and Jaffe H 1971 *Piezoelectric Ceramics* (New York: Academic)
[3] Xu Y 1991 *Ferroelectric Materials and Applications* (Los Angeles, CA: North-Holland)
[4] Unruan M, Vittayakorn N, Wongmaneeruang R, Prasatkhetragarn A, Ananta S and Yimnirun R 2008 *J. Alloys Compounds* **466** 264
[5] Kudo T, Yazaki T, Naito F and Sugaya S 1970 *J. Am. Ceram. Soc.* **53** 326
[6] Hachiga T, Fujimoto S and Yasuda N 1987 *J. Phys. D: Appl. Phys.* **20** 1291
[7] Vittayakorn N, Wirunchit S, Traisak S, Yimnirun R and Rujijanagul G 2008 *Curr. Appl. Phys.* **8** 128
[8] Prasartkhetragarn A, Vittayakorn N, Ananta S, Yimnirun R and Cann D P 2008 *Japan. J. Appl. Phys.* **47** 998
[9] Kuwata J, Uchino K and Nomura S 1982 *Japan. J. Appl. Phys.* **21** 1298
[10] Park S E and Shrout T R 1997 *J. Appl. Phys.* **82** 1804
[11] Viehland D and Powers J 2001 *Appl. Phys. Lett.* **78** 3112
[12] Stansfield D 1991 *Underwater Electroacoustic Transducers* (Bath: Bath University Press)
[13] Uchino K 1997 *Piezoelectric Actuators and Ultrasonic Motors* (Boston, MA: Kluwer)
[14] Zhou D, Kamlah M and Munz D 2005 *J. Eur. Ceram. Soc.* **25** 425
[15] Wongsaenmai S, Ananta S, Meechoowas E and Yimnirun R 2003 *J. Phys. D.* **36** 1615
[16] Zhang Q M, Zhao J, Uchino K and Zheng J 1997 *J. Mater. Res.* **12** 226
[17] Yang G, Liu S F, Ren W and Mukherjee B K 2000 *Proc. SPIE Symp. Smart Struct. Mater.* **3992** 103
[18] Steiner O, Tagantsev A K, Colla E L and Setter N 1999 *J. Eur. Ceram. Soc.* **19** 1243
[19] Zhao J and Zhang Q M 1996 *Proc. IEEE Int. Symp. Appl. Ferroelectr.* **1** 971
[20] Yimnirun R, Unruan M, Laosiritaworn Y and Ananta S 2006 *J. Phys. D: Appl. Phys.* **39** 3097
[21] Yimnirun R, Ananta S and Chamunglap S 2007 *Mater. Chem. Phys.* **102** 165
[22] Yimnirun R, Wongsaenmai S, Wongmaneerung R, Wongdamnern N, Ngamjarurojana A, Ananta S and Laosiritaworn Y 2007 *Phys. Scr.* **T129** 184
[23] Unruan M, Prasatkhetragarn A, Laosiritaworn Y, Ananta S and Yimnirun R 2008 *Phys. Scr.* **77** 045702
[24] Zhao J, Glazounov A E and Zhang Q M 1999 *Appl. Phys. Lett.* **74** 436
[25] Unruan M, Wongmaneerung R, Ngamjarurojana A, Ananta S, Laosiritaworn Y and Yimnirun R 2008 *J. Appl. Phys.* **104** 064107
[26] Unruan M, Wongsaenmai S, Laosiritaworn Y, Ananta S and Yimnirun R 2008 *J. Phys. D: Appl. Phys.* **41** 085406
[27] Zhao J, Zhang Q M and Mueller V 1998 *Proc. IEEE Int. Symp. Appl. Ferroelectr.* **1** 361
[28] Li F X, Li S and Fang D N 2005 *Mater. Sci. Eng.* B **120** 119
[29] Yimnirun R, Moses P J, Meyer R J and Newnham R E 2003 *Rev. Sci. Instrum.* **74** 3429
[30] Yimnirun R, Ananta S, Ngamjarurojana A and Wongsaenmai S 2005 *Appl. Phys.* A **81** 1227
[31] Yimnirun R, Loasiritaworn Y and Wongsaenmai S 2006 *J. Phys. D: Appl. Phys.* **39** 759
[32] Yang G, Liu S F, Ren W and Mukherjee B K 2001 *Ferroelectrics* **262** 207
[33] Krueger H 1967 *J. Acoust. Soc. Am.* **43** 583
[34] Viehland D and Powers J 2001 *J. Appl. Phys.* **89** 1820
[35] Calderon-Moreno J M 2001 *Mater. Sci. Eng.* A **315** 227

# Stress dependence and scaling of subcoercive field dynamic hysteresis in $0.5Pb(Zr_{1/2}Ti_{1/2})O_3-0.5Pb(Zn_{1/3}Nb_{2/3})O_3$ ceramic

R. Yimnirun,[a] N. Wongdamnern, N. Triamnak, M. Unruan, A. Ngamjarurojana, S. Ananta, and Y. Laosiritaworn
*Department of Physics, Faculty of Science, Chiang Mai University, Chiang Mai 50200, Thailand*

(Received 1 February 2008; accepted 5 October 2008; published online 17 November 2008)

Stress dependence and scaling behavior of subcoercive field dynamic ferroelectric hysteresis were investigated in rhombohedral $0.5Pb(Zr_{1/2}Ti_{1/2})O_3-0.5Pb(Zn_{1/3}Nb_{2/3})O_3$ (0.5PZT–0.5PZN) bulk ceramic with profound relaxor characteristics. The scaling relation of hysteresis area $\langle A\rangle$ against frequency $f$, field amplitude $E_0$, and stress $\sigma$ for the minor loops takes a form of $\langle A-A_{\sigma=0}\rangle \propto f^{-0.34}E_0^{3.68}\sigma^{0.35}$, which is very similar to that of soft and hard lead zirconate titanate ceramics with the same disrupted domains. This study suggests that the domain structures play a significant role in controlling the dynamic hysteresis behavior of ferroelectric materials. © *2008 American Institute of Physics*. [DOI: 10.1063/1.3021287]

## I. INTRODUCTION

The dynamic hysteresis characteristics have become important consideration since hysteresis area $\langle A\rangle$ as a function of the field amplitude $E_0$ and frequency $f$ presents lots of information critical for many ferroelectric applications.[1,2] Theoretical studies have been carried out to understand the dynamic response of hysteresis curves in spin and polarization systems.[3–7] In particular, attention is focused on scaling law,

$$\langle A\rangle \propto f^m E_0^n \tag{1}$$

(where $m$ and $n$ are exponents that depend on the dimensionality and symmetry of the system). Based on three-dimensional models, it has been suggested that $m=1/3$ and $n=2/3$ as $f\rightarrow 0$, whereas $m=-1$ and $n=2$ as $f\rightarrow\infty$.[3,5,8] Experimental investigations on a few thin-film systems have also been reported with variation in the scaling relations obtained.[9–12] On the contrary, there are only few reports on the scaling behavior studies of ferroelectric hysteresis loops of bulk ferroelectric ceramics.[13–16]

Our previous investigations have already shown interesting stress-dependent scaling behaviors in commercial soft and hard lead zirconate titanate, $Pb(Zr,Ti)O_3$ or PZT, ceramics.[14,15] The results suggested that the scaling behavior depended strongly on the dimensionality of the system, and it was also led to believe that the different states of domains existing in the ceramics may play a key role in controlling the scaling behavior. As an extension to our previous investigations,[14,15] this current study was aimed at a suitable potential ferroelectric material with similar domain configuration to commercial PZT bulk ceramics. Previous works on rhombohedral $0.5Pb(Zr_{0.5}Ti_{0.5})O_3-0.5Pb(Zn_{1/3}Nb_{2/3})O_3$ (or 0.5PZT–0.5PZT) ceramics with disrupted domains have shown excellent electrical properties with profound relaxor characteristics suitable for various applications.[17–20] Therefore, due to its many potential practical applications and relatively similar domain configuration as compared to commercial soft and hard PZT ceramics, the 0.5PZT–0.5PZN ceramic was chosen for this study. Practically, ferroelectric ceramics are used under subcoercive field condition in most applications; it is therefore of interest to obtain scaling relations for such condition. Interestingly, earlier works showed that the scaling behavior of the minor and saturated loops was significantly different.[11,12]

More importantly, in many applications the ceramic specimens are often subjected to mechanical loading, either from the design of the device itself or from operating conditions which induce stresses.[1,21] Therefore, prior knowledge of how the material properties change under different load conditions in materials is inevitably crucial for proper design of a device and for suitable selection of materials for a specific application. In many previous investigations the electrical properties of ceramics were found to depend strongly on stresses ($\sigma$).[22–26] Since $f$, $E_0$, and $\sigma$ have been reported to impose significant influence on the dynamic hysteresis responses of ferroelectric ceramics, it is therefore the major aim of this study to obtain the stress-dependent scaling behavior of subcoercive field dynamic ferroelectric hysteresis in 0.5PZT–0.5PZN ceramic.

## II. EXPERIMENT

The disk-shaped samples of tetragonal-structure 0.5PZT–0.5PZN ceramic with diameter of 10 mm and thickness of 1 mm were used in this study. Details on the fabrication and characterization of this material can be found elsewhere.[19,20] Its basic properties are dielectric constant (1 kHz) $\varepsilon_r=1566$, Curie temperature $T_C=256$ °C; piezoelectric strain constants $d_{33}=497$ pm/V, planar coupling factor $k_p=0.60$, mechanical quality factor $Q_m=54$, and coercive field (10 Hz) $E_c=10$ kV/cm. The dynamic hysteresis ($P$-$E$) loops were characterized at room temperature (25 °C) by using a modified Sawyer–Tower circuit with $f$ covering from 2 to 100 Hz and $E_0$ from 0 to 9.6 kV/cm. The electric field was applied to a sample by a high voltage ac amplifier (Trek

[a]Author to whom correspondence should be addressed, Electronic mail: rattikornyimnirun@yahoo.com.

 © 2008 American Institute of Physics

Author complimentary copy. Redistribution subject to AIP license or copyright, see http://jap.aip.org/jap/copyright.jsp

610D) with the input sinusoidal signal from a function generator (HP 3310A). The *P-E* loops were recorded by a digital oscilloscope (HP 54645A, 100 MHz). The detailed descriptions of this system were explained elsewhere.[25] Effects of the external stress on the dynamic hysteresis were investigated with the compressometer, which was developed for simultaneous applications of the mechanical stress and the electric field.[26] The compressive stress, applied parallel to the electric field direction, was supplied by the servohydraulic load frame and monitored with the pressure gauge. The *P-E* loops were recorded as a function of mechanical stress applied discretely between 0 and 168 MPa for each applied field and frequency. At each constant stress, the loop was obtained after 20 sampling cycles to average out the noise deformation.

## III. RESULTS AND DISCUSSION

The hysteresis profiles for various frequencies $f$, field amplitude $E_0$, and stress $\sigma$ are obtained. The hysteresis loops at different $f$ but fixed $E_0$ (9.6 kV/cm) and $\sigma$ (27 MPa), at different $E_0$ but fixed $f$ (10 Hz) and $\sigma$ (27 MPa), and at different $\sigma$ but fixed $E_0$ (9.6 kV/cm) and $f$ (10 Hz) are shown in Figs. 1(a)–1(c), respectively. For a particular applied stress, as expected, the dependence of the loop pattern and area $\langle A \rangle$ on $f$ and $E$ is remarkable. At fixed $E_0$, the loop area $\langle A \rangle$ and remnant polarization ($P_r$) decrease with an increase in frequency, as shown in Fig. 1(a). The dependence of the hysteresis loop on $E_0$ is depicted in Fig. 1(b). Similar observations have also been reported in soft and hard PZT ceramics.[27–29] In addition, the *P-E* loop area $\langle A \rangle$ is found to decrease steadily with increasing stress. Several previous investigations also reported similar stress-dependent behavior.[24–26]

To obtain the suitable scaling relation for the bulk ceramic, one can first follow the suggested scaling law given in Eq. (1) to determine exponents $m$ and $n$ directly from the experimental data. By plotting $\langle A \rangle$ against $f$ at fixed $E_0$, one obtains the exponent $m$. On the other hand, the exponent $n$ can be obtained from plotting $\langle A \rangle$ against $E_0$ at fixed $f$. As plotted in Fig. 2, it is revealed that the experimental data can be fitted (with $R^2=0.99$), within the measured uncertainty, by

$$\langle A \rangle \propto f^{-0.34} E_0^{3.68}. \quad (2)$$

Here, the first interesting observation is that the minor-loop scaling in 0.5PZT–0.5PZN bulk ceramics is generally similar to that of PZT thin film,[5,9] as well as that of minor loop of PZT bulk ceramics.[13,15] As explained in our previous investigation,[13] this was attributed to the fact that main polarization orientation mechanism in thin films and in subcoercive field condition for bulk ceramics is likely from the 180° domain reversal.[30–34] This explains why the scaling behavior of PZT bulk ceramics at low electric fields is similar to that of thin films. More importantly, the scaling relation obtained in Eq. (2) is generally very similar to that of the minor-loop scaling relations obtained earlier for commercial soft and hard PZT bulk ceramics with $\langle A \rangle \propto f^{-0.33} E_0^3$ and $\langle A \rangle \propto f^{-0.43} E_0^{3.19}$, respectively.[13,15] This clearly indicates that the polarization orientation process in rhombohedral

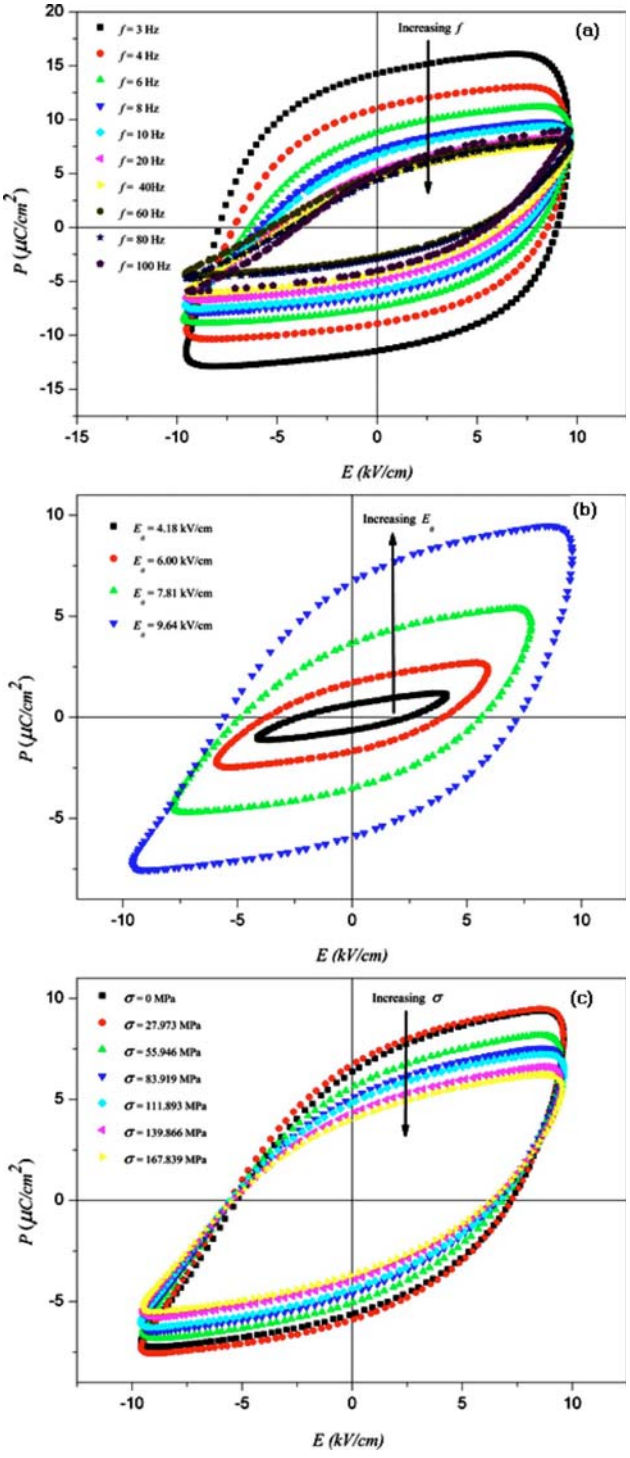



FIG. 1. (Color online) Hysteresis loops under subcoercive field condition for 0.5PZT–0.5PZN ceramic (a) at various $f$, $E_0=9.6$ kV/cm, and $\sigma=27$ MPa; (b) at various $E_0$, $f=10$ Hz and $\sigma=27$ MPa; and (c) at various $\sigma$, $f=10$ Hz, and $E_0=9.6$ kV/cm.

0.5PZT–0.5PZN ceramics with disrupted domains is similar to that in commercial PZT bulk ceramics with the same complex domain structures Therefore, the scaling relations obtained here clearly support our previous proposed hypothesis that the domain structures play major role in controlling dynamic hysteresis behavior of ferroelectric materials.[13,15]

To investigate the scaling behavior under the effect of

Author complimentary copy. Redistribution subject to AIP license or copyright, see http://jap.aip.org/jap/copyright.jsp

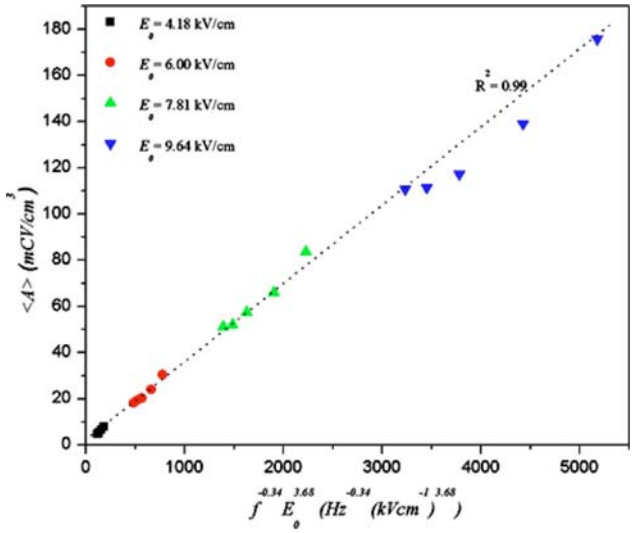



FIG. 2. (Color online) Scaling of hysteresis area $\langle A\rangle$ against $f^{-0.34}E_0^{3.68}$ for 0.5PZT–0.5PZN ceramic under subcoercive field condition.

applied stresses, instead of including only the field amplitude $E_0$ and the frequency term $f$, the scaling relation should also include the stress ($\sigma$) term, i.e.,

$$\langle A\rangle \propto f^m E_0^n \sigma^p. \tag{3}$$

However, due to increasing number of exponents, to simplify the problem, the validity of the scaling law $\langle A\rangle(\sigma) \propto f^{-0.34}E_0^{3.68}$ is assumed for all applied stresses. Consequently, the area $\langle A\rangle$ for each stress is plotted against $f^{-0.34}E_0^{3.68}$, as shown in Fig. 3(a), and it can be seen from the least–squares linear fits that reasonably good linear relations can be found. As a result, the condition of universality having $m=-0.34$ and $n=3.68$ in 0.5PZT–0.5PZN bulk ceramic is confirmed. Consequently, $\langle A\rangle \propto (a+b\sigma^c)f^{-0.34}E_0^{3.68}$ may be written and by substituting the fitted parameters, it is found that

$$\langle A\rangle - \langle A_{\sigma=0}\rangle = \langle A - A_{\sigma=0}\rangle \propto f^{-0.34}E_0^{3.68}\sigma^{0.35}, \tag{4}$$

where $\langle A_{\sigma=0}\rangle$ refers to stress–free hysteresis area which will be a dominant term for zero stress. The data collapsing of the scaling area from all $f$, $E_0$, and $\sigma$ was found to confirm Eq. (4) as evident in Fig. 3(b). Note that from the appearance of stress $\sigma$, $\langle A-A_{\sigma=0}\rangle$, referring to the difference in energy dissipation between under stress and stress–free conditions, increases with increasing stress suggesting a decay of $\langle A\rangle$ with $\sigma$ at a rate of $\sigma^{0.35}$ as observed in experiments. As a result, it can be concluded that the difference of the hysteresis area between under stress and stress-free condition scales with frequency, field amplitude and stress via exponents $m=-0.34$, $n=3.68$, and $p=0.35$. However, at a particular fixed stress, Eq. (4) gives $f^{-0.34}E_0^{3.68}$ which is the original form for how the area scales with the frequency and the field amplitude.

To understand the stress-dependent scaling relation obtained in Eq. (4), at least qualitatively, one needs to consider the following statements. Since the *P-E* loop area indicates the polarization dissipation energy subjected to one full cycle of electric field application, the loop area is therefore directly

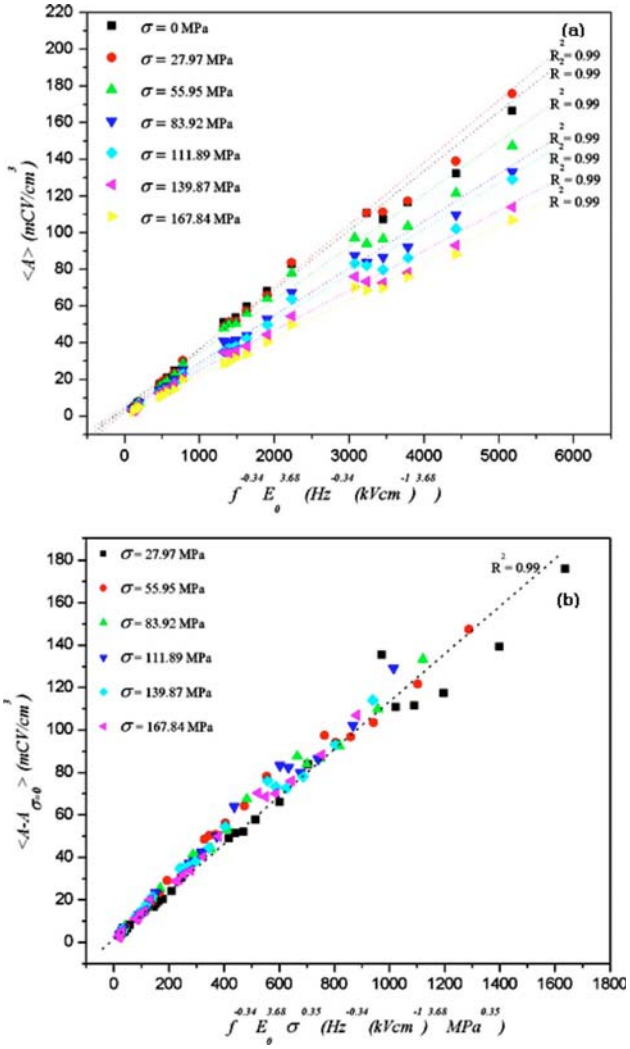



FIG. 3. (Color online) (a) Scaling of hysteresis area $\langle A\rangle$ against $f^{-0.34}E_0^{3.68}$ at various $\sigma$. (b) The collapse of the scaling area $\langle A-A_{\sigma=0}\rangle$ against $f^{-0.34}E_0^{3.68}\sigma^{0.35}$ on a same linear line (with small fluctuation) for 0.5PZT–0.5PZN ceramic under subcoercive field condition.

related to volume involved in the switching process during the application of electric field.[25,26,35] Hence, when the mechanical stress is applied, more and more ferroelectric domains are constrained by the applied stress and cannot be reoriented by the electric field so as to participate in the polarization reversal. Consequently, both the saturation and remnant polarizations become lower with increasing compressive stress. The polarization dissipation energy is consequently found to decrease with increasing applied stress, indicating that the sample volume contributing to polarization reversal decreases with increasing stress. Similar observations have also been reported in other investigations.[22–26,36,37] Furthermore, it is noted that this stress-dependent scaling relation, in particular the stress term with exponent $p=0.35$, is slightly different, but still in the same range, from that for soft and hard PZT bulk ceramics with $p=0.44$ and 0.37, respectively, as obtained in our previous investigations.[14,15] An explanation for the difference is not clearly known but could be attributed to the difference in mechanical properties of these materials. Unfortunately, there have been no other

Author complimentary copy. Redistribution subject to AIP license or copyright, see http://jap.aip.org/jap/copyright.jsp

stress-dependent scaling investigations available for independent comparison. In addition, there has been no quantitative theoretical treatment to include the stress term in the scaling relation. Many of the theoretical treatments to explain the stress effect on the hysteresis behavior have been primarily based on constitutive models, thermodynamic phenomenology, and Rayleigh law approach.[38–40] Further investigations, both theoretical and experimental, on the stress-dependent scaling behavior are clearly required.

## IV. CONCLUSION

The scaling behavior of the subcoercive field dynamic ferroelectric hysteresis of rhombohedral 0.5PZT–0.5PZN bulk ceramics under the effect of mechanical stress has been investigated. The scaling relation for the minor loops takes the form of $\langle A - A_{\sigma=0} \rangle \propto f^{-0.34} E_0^{3.68} \sigma^{0.35}$, which is very similar to that of soft and hard PZT ceramics with the same disrupted domains. As a result, this study suggests that the domain structures play a significant role in controlling the dynamic hysteresis behavior of ferroelectric materials.

## ACKNOWLEDGMENTS

Financial supports from the Thailand Research Fund (TRF), Commission on Higher Education (CHE), Royal Golden Jubilee PhD. Program, Faculty of Science and Graduate School of Chiang Mai University are gratefully acknowledged.

[1] K. Uchino, *Ferroelectric Devices* (Dekker, New York, 2000).
[2] O. Auciello, J. F. Scott, and R. Ramesh, Phys. Today **51**, 22 (1998).
[3] M. Rao, H. R. Krishnamurthy, and R. Pandit, Phys. Rev. B **42**, 856 (1990).
[4] M. Acharyya and B. K. Chakrabarti, Phys. Rev. B **52**, 6550 (1995).
[5] J.-M. Liu, H. L. W. Chan, C. L. Choy, Y. Y. Zhu, S. N. Zhu, Z. G. Liu, and N. B. Ming, Appl. Phys. Lett. **79**, 236 (2001).
[6] H. B. Zuo, M. F. Zhang, J. C. Han, and J. M. Liu, Mater. Lett. **61**, 2697 (2007).
[7] M. Sarjala, E. T. Seppälä, and M. J. Alava, Physica B **403**, 418 (2008).
[8] M. Rao and R. Pandit, Phys. Rev. B **43**, 3373 (1991).
[9] J.-M. Liu, H. L. W. Chan, C. L. Choy, and C. K. Ong, Phys. Rev. B **65**, 014416 (2001).
[10] B. Pan, H. Yu, D. Wu, X. H. Zhou, and J.-M. Liu, Appl. Phys. Lett. **83**, 1406 (2003).
[11] Y.-H. Kim and J.-J. Kim, Phys. Rev. B **55**, R11933 (1997).
[12] J.-H. Park, C.-S. Kim, B.-C. Choi, B. K. Moon, J. H. Jeong, and I. W. Kim, Appl. Phys. Lett. **83**, 536 (2003).
[13] R. Yimnirun, Y. Laosiritaworn, S. Wongsaenmai, and S. Ananta, Appl. Phys. Lett. **89**, 162901 (2006).
[14] R. Yimnirun, S. Wongsaenmai, S. Ananta, and Y. Laosiritaworn, Appl. Phys. Lett. **89**, 242901 (2006).
[15] R. Yimnirun, R. Wongmaneerung, S. Wongsaenmai, A. Ngamjarurojana, S. Ananta, and Y. Laosiritaworn, Appl. Phys. Lett. **90**, 112908 (2007).
[16] R. Yimnirun, R. Wongmaneerung, S. Wongsaenmai, A. Ngamjarurojana, S. Ananta, and Y. Laosiritaworn, Appl. Phys. Lett. **90**, 112906 (2007).
[17] K. Uchino, *Piezoelectric Actuators and Ultrasonic Motors* (Kluwer, Boston, 1997).
[18] J. Zhao, A. E. Glazounov, and Q. M. Zhang, Appl. Phys. Lett. **74**, 436 (1999).
[19] D. Viehland and J. Powers, J. Appl. Phys. **89**, 1820 (2001).
[20] D. Zhou, M. Kamlah, and D. Munz, J. Eur. Ceram. Soc. **25**, 425 (2005).
[21] R. Yimnirun, Y. Laosiritaworn, and S. Wongsaenmai, J. Phys. D **39**, 759 (2006).
[22] R. Yimnirun, S. Ananta, A. Ngamjarurojana, and S. Wongsaenmai, Appl. Phys. A: Mater. Sci. Process. **81**, 1227 (2005).
[23] X. P. Jiang, J. W. Fang, H. R. Zeng, B. J. Chu, G. R. Li, D. R. Chen, and Q. R. Yin, Mater. Lett. **44**, 219 (2000).
[24] H. Fan and H. E. Kim, J. Appl. Phys. **91**, 317 (2002).
[25] N. Vittayakorn, G. Rujijanagul, T. Tunkasiri, X. Tan, and D. P. Cann, J. Mater. Res. **18**, 2882 (2003).
[26] N. Vittayakorn, G. Rujijanagul, X. Tan, and D. P. Cann, J. Electroceram. **16**, 141 (2006).
[27] D. A. Hall and P. J. Stevenson, Ferroelectrics **228**, 139 (1999).
[28] J. E. Garcia, R. Perez, and A. Albareda, J. Phys. D **34**, 3279 (2001).
[29] M. Morozov, D. Damjanovic, and N. Setter, J. Eur. Ceram. Soc. **25**, 2483 (2005).
[30] S. Trolier-McKinstry, N. B. Gharb, and D. Damjanovic, Appl. Phys. Lett. **88**, 202901 (2006).
[31] B.-K. Lai, I. Ponomareva, I. I. Naumov, I. Kornev, H. Fu, L. Bellaiche, and G. S. Salamo, Phys. Rev. Lett. **96**, 137602 (2006).
[32] D. Ricinschi and M. Okuyama, Ferroelectrics **349**, 111 (2007).
[33] T. Tsurumi, T. Sasaki, H. Kakemoto, T. Harigai, and S. Wada, Jpn. J. Appl. Phys., Part 1 **43**, 7618 (2004).
[34] K. Lee and S. Baik, Annu. Rev. Mater. Res. **36**, 81 (2006).
[35] M. E. Lines and A. M. Glass, *Principles and Applications of Ferroelectrics and Related Materials* (Clarendon, Oxford, 1977).
[36] T. Kumazawa, Y. Kumagai, H. Miura, M. Kitano, and K. Kushida, Appl. Phys. Lett. **72**, 608 (1998).
[37] X. Lu, J. Zhu, X. Li, Z. Zhang, X. Zhu, D. Wu, F. Yan, Y. Ding, and Y. Wang, Appl. Phys. Lett. **76**, 3103 (2000).
[38] D. Damjanovic, J. Appl. Phys. **82**, 1788 (1997).
[39] C. M. Landis Curr. Opin. Solid. Solid Mater. Sci. **8**, 59 (2004).
[40] A. Achuthan and C. T. Sun, J. Appl. Phys. **97**, 114103 (2005).

Author complimentary copy. Redistribution subject to AIP license or copyright, see http://jap.aip.org/jap/copyright.jsp

# Changes in dielectric and ferroelectric properties of $Fe^{3+}/Nb^{5+}$ hybrid-doped barium titanate ceramics under compressive stress

M. Unruan, T. Sareein, J. Tangsritrakul, S. Prasertpalichatr, A. Ngamjarurojana, S. Ananta, and R. Yimnirun[a)]
*Department of Physics, Faculty of Science, Chiang Mai University, Chiang Mai, 50200, Thailand*

(Received 29 October 2008; accepted 3 November 2008; published online 16 December 2008)

The influences of compressive stress on the dielectric and ferroelectric properties of $Fe^{3+}/Nb^{5+}$ hybrid-doped barium titanate ($BaTiO_3$) ceramics were investigated. Superimposed compressive stress had a pronounced effect on the electrical properties of the ceramics. The response of low-field dielectric properties to stress changed from soft to hard piezoelectric behavior with increasing $Nb^{5+}$ content. While ferroelectric properties decreased with stress, hardening behavior was observed with increasing $Nb^{5+}$ content in hybrid-doped $BaTiO_3$ ceramics. A mechanism based on induced change in the acceptor valence by the donor dopant in hybrid-doped $BaTiO_3$ ceramics was proposed to explain the results obtained. © *2008 American Institute of Physics*. [DOI: 10.1063/1.3042228]

Barium titanate [$BaTiO_3$ (BT)] based materials are well known electroceramics that find applications as dielectric materials in capacitors.[1–4] Historically BT was the first polycrystalline piezoelectric; but it was soon replaced by $Pb(Zr,Ti)O_3$ (PZT) ceramic because the latter has much better piezoelectric properties. Since then, PZT has dominated piezoelectric applications to date. However, PZT is now facing a major challenge due to the environmental hazard from its toxic lead.[5,6] Recently BT has regained a great deal of interest due to the introduction of the large recoverable electrostrain in doped BT-based materials.[7–14] The mechanism to explain this behavior is based on the universal "symmetry-conforming principle" of point defects.[7–11] This provides a way to produce high-performance, lead-free piezoelectrics based on BT. Since then, doped BT systems, especially Mn-doped $(Ba,Sr)TiO_3$, have been investigated extensively.[10–12] Interestingly, acceptor/donor-doped BT (the so-called hybrid-doped BT) systems, such as $Mn^{3+}/La^{3+}$-doped BT and $Mn^{3+}/Nb^{5+}$-doped BT, also show the same large electrostrain behavior.[13,14] This is of particular interest, as opposite electrical properties, including ferroelectric aging effects, can be expected between acceptor-doped and donor-doped ferroelectrics. It should also be noticed that the acceptor dopant employed in the previous hybrid-doped BT investigations mentioned above was always the $Mn^{3+}$ cation, without any particular reason given. Therefore, one might wonder if the same behavior is realizable in hybrid-doped BT using other acceptor dopants. Our recent investigation showed that dielectric and ferroelectric aging behaviors in $Fe^{3+}/Nb^{5+}$ hybrid-doped BT ceramics differed noticeably from those observed in $Mn^{3+}$-based hybrid-doped BT systems. Nonetheless, the opposing roles of the acceptor and donor dopants on electrical properties were still observed. Most importantly, the potential of high-performance, lead-free piezoelectrics based on BT was confirmed in $Fe^{3+}/Nb^{5+}$-doped BT ceramics.

However, when used in piezoelectric devices, ceramics are often subjected to self-induced or environmental stresses.[15,16] A prior knowledge of the effects of stresses on the material properties is crucial for proper design of a device and for suitable selection of materials for a specific application.[17,18] Therefore, it is very important to obtain experimental data in order to understand how these materials behave under stress.[19–21] Recently, the compressive-stress dependence of electrical properties has been studied in various materials.[19–26] The results clearly showed that the effects of applied stress on electrical properties depended significantly on ceramic compositions and stress levels. Although there have been many previous reports on the electrical properties of hybrid-doped BT ceramics, the influences of applied stress on the electrical properties of hybrid-doped BT ceramics are yet to be reported. Therefore, it is the aim of this study to determine the dielectric and ferroelectric properties of the $Fe^{3+}/Nb^{5+}$ hybrid-doped BT ceramics as a function of compressive stress. This paper will reveal the opposing and competing dielectric responses to applied stress of acceptor-dominant and donor-dominant hybrid-doped BT ceramics. More interestingly, it will also be shown that while $Fe^{3+}$ and $Nb^{5+}$ normally act as acceptor and donor, respectively, when added individually in BT system, the added $Nb^{5+}$ could enhance the hardening effect in hybrid-doped BT ceramics.

In this study, a series of $Fe^{3+}$ and $Nb^{5+}$ hybrid-doped BT ceramics with $Fe^{3+}$ fixed at 1 mol %, but with $Nb^{5+}$ varying from 0.5 to 1.5 mol %, were prepared via a mixed-oxide method with a formula $Ba(Ti_{0.99-x}Fe_{0.01}Nb_x)O_3$ when $x=0.005$, 0.01, and 0.015 (abbreviated as BT−1Fe−$y$Nb with $y=100x$ hereafter). Hence, samples of acceptor-dominant $y=0.5$, equal-doping $y=1$, and donor-dominant $y=1.5$ were obtained. It should be noted that x-ray diffraction analysis showed all sintered ceramics to be single-phase perovskite materials with tetragonal symmetry. Since this paper only deals with the stress dependence study, detailed investigations of temperature- and frequency-dependent dielectric and ferroelectric properties will be presented in another publication. Room temperature (25 °C) dielectric properties and ferroelectric hysteresis loops were measured using a home-

a)Author to whom correspondence should be addressed. Electronic mail: rattikornyimnirun@yahoo.com.

 © 2008 American Institute of Physics

Downloaded 16 Dec 2008 to 202.28.27.3. Redistribution subject to AIP license or copyright; see http://jap.aip.org/jap/copyright.jsp

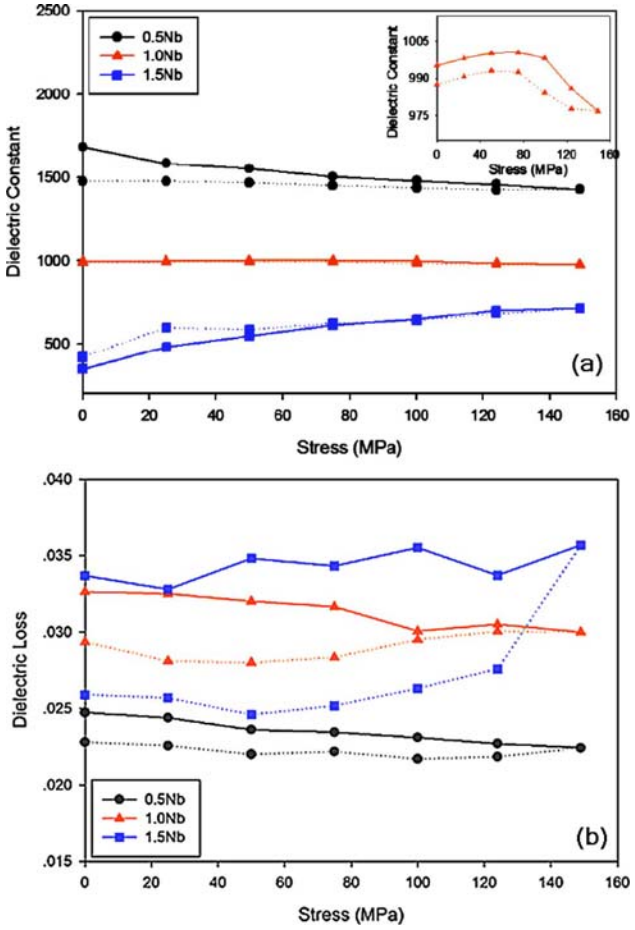



FIG. 1. (Color online) (a) Changes in dielectric constant ($\varepsilon_r$) and (b) changes in dielectric loss tangent (tan $\delta$) with compressive stress applied parallel to the electric field direction for $Ba(Ti_{0.99-x}Fe_{0.01}Nb_x)O_3$ ceramics when $x=0.005$ (0.5 Nb), 0.01 (1.0 Nb), and 0.015 (1.5 Nb) (measured at 25 °C and 10 kHz).

built compressometer developed for simultaneous applications of mechanical stress and electric field.[22,24] Low-field dielectric properties were measured by a *LCR*-meter (Instek LCR-821) with applied voltage of 1 V. The dielectric constant and loss were determined at a frequency of 10 kHz. The ferroelectric (*P-E*) hysteresis loops were characterized using a modified Sawyer–Tower circuit with a fixed 50 Hz frequency and $E_0$ of 15 kV/cm. The electric field was applied to a sample by a high-voltage ac amplifier (Trek 610D) with the input sinusoidal signal from a function generator (HP 3310A). The *P-E* loops were recorded by a digital oscilloscope (HP 54645A, 100 MHz). Prior to all measurements, the samples were "deaged" by holding at 250 °C for 30 min, followed by a quick cooling to room temperature.

The room temperature dielectric properties at 10 kHz of $Ba(Ti_{0.99-x}Fe_{0.01}Nb_x)O_3$ ceramics as a function of compressive stress are depicted in Fig. 1. The measurements were performed with mechanical stress increased to the maximum (solid lines), and then gradually removed to zero (dotted lines). Generally, the results showed only slightly different dielectric properties between loading and unloading conditions; this differs from results previously observed in other ceramic systems and is likely caused by the stress-induced depoling mechanism at high stress.[25–28] Nonetheless, there are observable changes in both the dielectric constant and the dielectric loss tangent with stress. The different dielectric responses to the applied stress are clearly evident. For the acceptor-dominant BT–1Fe–0.5Nb composition, both the dielectric constant and dielectric loss tangent decrease with increasing stress. On the other hand, the trend is reversed in the donor-dominant BT–1Fe–1.5Nb composition. Interestingly, for the equal-doping BT–1Fe–1Nb composition the dielectric properties (both dielectric constant and dielectric loss tangent) show very little change with stress. However, when taking a closer look [inset of Fig. 1(a)] one can see that the dielectric constant first increases when the stress is increased to 80 MPa, then decreases when the applied stress is increased further. Similar behavior is also noticeable in the dielectric loss tangent, as shown in Fig. 1(b). The changes in dielectric properties under compressive stress obtained in this study are in part similar to those for BT, PZT, and lead magnesium niobate-lead titanate (PMN-PT) systems, as seen in earlier investigations.[22,24,25,27,29] Under applied compressive stress, the domain structure of ceramics may undergo domain reorientation through non-180° domain walls, as well as stress-induced depinning of the domain walls. Hence, an increase in dielectric properties is observed in the BT–1Fe–1.5Nb composition (similar behavior was observed in hard Fe-doped PZT).[23,25,27,28] On the other hand, stress clamping of domain walls, which results in a decrease in domain wall mobility, is expected to play a role in the decrease in dielectric properties in the BT–1Fe–0.5Nb composition (as reported in soft La-doped PZT).[23,25] The competing influences of domain reorientation and stress clamping of domain wall mechanisms are believed to be a reason for the change in dielectric properties under stress in the BT–1Fe–1Nb composition (mixing behaviors of hard and soft materials). The possible reason for the hardening effect with increasing donor content in hybrid-doped BT ceramic will be discussed later.

The polarization versus electric field (*P-E*) hysteresis loops of $Ba(Ti_{0.99-x}Fe_{0.01}Nb_x)O_3$ ceramics under different compressive stresses are shown in Fig. 2. It should first be noticed that generally the area of the *P-E* loops decreases with increasing compressive stress. The changes follow a similar trend for all ceramic compositions. The *P-E* loop area indicates the polarization dissipation energy of a ferroelectric material under one full cycle of electric field application.[20,30] This amount of energy loss is directly related to the amount of domain participating in the switching process during the application of the electric field.[20,25] For a given composition, the decrease in the loop area with increasing compressive stress is a result of stress-induced domain wall suppression.[30] The changes in hysteresis parameters, i.e., dissipation energy, saturation polarization ($P_{sat}$), remnant polarization ($P_r$), and coercive field ($E_c$), with compressive stresses are plotted in Fig. 3. Generally, it can be seen that all hysteresis parameters decrease as compressive stress increases. As is also depicted in Fig. 3, it should be noted that even though the loading and unloading experiments were performed on all compositions, the results differ only slightly (similar to the changes in low-field dielectric properties). In addition, only slight decreases in the polariza-

Downloaded 16 Dec 2008 to 202.28.27.3. Redistribution subject to AIP license or copyright; see http://jap.aip.org/jap/copyright.jsp

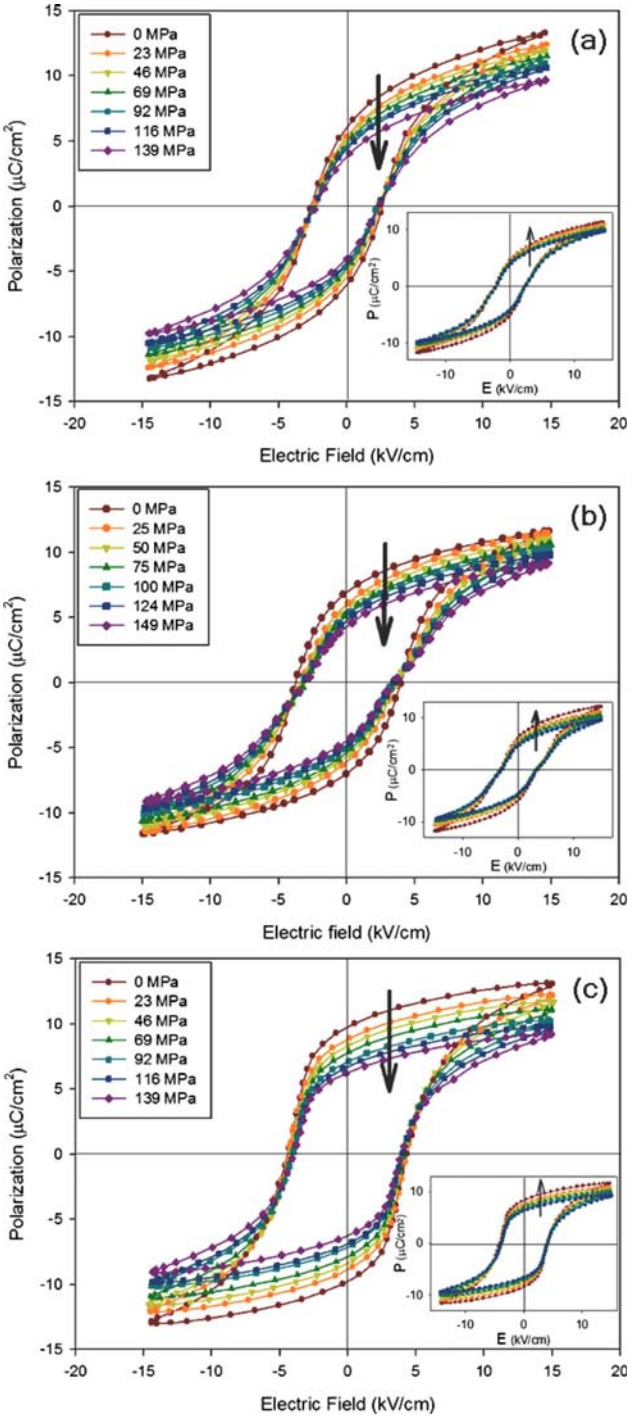



FIG. 2. (Color online) Polarization-electric field ($P$-$E$) hysteresis loops as a function of compressive stress for (a) $Ba(Ti_{0.985}Fe_{0.01}Nb_{0.005})O_3$, (b) $Ba(Ti_{0.98}Fe_{0.01}Nb_{0.01})O_3$, and (c) $Ba(Ti_{0.978}Fe_{0.01}Nb_{0.015})O_3$ ceramics (measured at 25 °C and 50 Hz under loading). The inset in each figure indicates the $P$-$E$ loops during unloading.

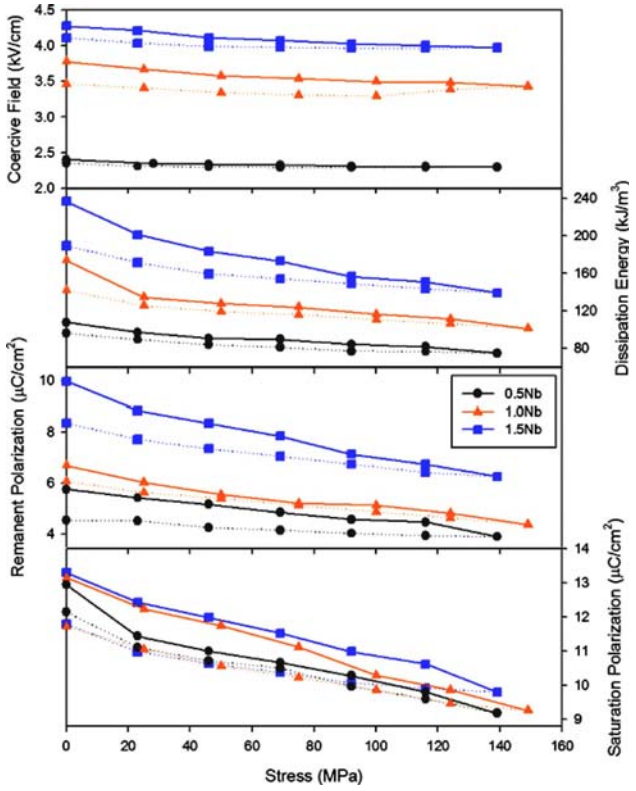



FIG. 3. (Color online) Changes in ferroelectric hysteresis parameters with compressive stress for $Ba(Ti_{0.99-x}Fe_{0.01}Nb_x)O_3$ ceramics when $x=0.005$ (0.5 Nb), 0.01 (1.0 Nb), and 0.015 (1.5 Nb) during stress loading (solid lines) and unloading (dotted lines) (measured at 25 °C and 50 Hz).

tion values of all the ceramics are also observed after a complete cycle of mechanical stress. This observation suggests a stress-induced decrease in the switchable part of the polarization at high stress levels.[23,25] The results of changes in the hysteresis parameters of $Ba(Ti_{0.99-x}Fe_{0.01}Nb_x)O_3$ ceramics with increasing compressive stress are in agreement with previous investigations of many ferroelectric ceramics.[18–20,24,26,29] To understand the experimental results of the changes in ferroelectric properties under compressive stress, as depicted in Fig. 3, one can interpret the changes in terms of domain-reorientation processes. When compressive stress is applied in a direction parallel to the electric field, the applied stress tends to keep the ferroelectric domains aligned away from the stress direction, through the non-180° ferroelastic domain switching processes.[27–29] Therefore, it takes a greater than usual applied electric field to reorient the domains along the stress direction, resulting in a lower value of the saturation polarization ($P_{sat}$). When the electric field is reduced to zero, the domains tend to rotate back away from the applied compressive-stress direction, resulting in lower than usual remnant polarization ($P_r$) and hence a lower coercive field ($E_c$) required to bring the remnant polarization to zero.[25,29] Furthermore, the decrease in hysteresis loss with increasing compressive stress indicates that more and more ferroelectric domains are constrained by the applied stress and cannot be reoriented by the electric field so as to participate in the polarization reversal.[25,29] Consequently, both the saturation and remnant polarizations become lower with increasing compressive stress.

Another important and even more interesting finding is that $Ba(Ti_{0.99-x}Fe_{0.01}Nb_x)O_3$ ceramics become ferroelectrically harder with increasing donor (Nb) concentration, as seen from the low-field dielectric behavior in Fig. 1; and there is also more dissipation loss, larger coercivity, and lower polarization, as seen in Figs. 2 and 3. This is unexpected, as Nb is well known as a softening dopant in donor-monodoped BT and $Pb(Zr,Ti)O_3$ ceramics.[1–3,26,30] One

Downloaded 16 Dec 2008 to 202.28.27.3. Redistribution subject to AIP license or copyright; see http://jap.aip.org/jap/copyright.jsp

would wonder about the probable cause of this unexpected behavior. For equal-doped BT–1Fe–1Nb compositions, there are two possible microscopic distributions of $Fe^{3+}$ and $Nb^{5+}$ dopants.[13,14] The first is that $Fe^{3+}$ and $Nb^{5+}$ form $Fe^{3+}$–$Nb^{5+}$ pairs. In this case, the average *B*-site valence at the defect pair is 4+, which is the same as the host *B*-site $Ti^{4+}$. Thus, charge neutrality is kept at the defect pairs, and therefore no vacancy is formed.[13] If this was the case, we would not observe the mixed response to applied stress of the low-field dielectric properties; while the acceptor-dominant BT–1Fe–0.5Nb composition and the donor-dominant BT–1Fe–1.5Nb composition would behave like hard and soft materials, respectively. However this is not the case at all, as shown in our experimental results in Figs. 1 and 2. To understand this peculiar behavior in a hybrid-doped BT ceramic, we need to first analyze its possible defect structure. The common point of view states that donor doping creates *A*-site vacancies ($V''_{Ba}$), while acceptor doping causes oxygen vacancies ($V_O^{\bullet\bullet}$) for charge compensation.[1–3,30–32] In contrast to the formation of $Fe^{3+}$–$Nb^{5+}$ pairs, it is possible that $Fe^{3+}$ and $Nb^{5+}$ are distributed in the *B*-site sublattices and are allowed to be apart from each other.[13,14] As their concentration is very low, the chance of forming pairs is thus very low. By assuming this random distribution, one can expect the formation of immobile defect dipoles $2Nb^{\bullet}_{Ti}$–$V''_{Ba}$ and mobile defect dipoles $2Fe'_{Ti}$–$V_O^{\bullet\bullet}$ in their respective *B*-site sublattices,[13,14] which in turn cause the separated soft and hard properties in the *B*-site sublattices. In addition to these assumptions, it is important to point out one possible mechanism which is likely responsible for the observed peculiar hardening effect with increasing donor (Nb) concentration in the hybrid-doped BT ceramics. Previous investigations by Albertsen *et al.*[33] and Kishi *et al.*[34,35] on donor-acceptor charge complex formation in BT ceramics have suggested that an acceptor with lower valence state (in this case $Fe^{2+}$, as opposed to $Fe^{3+}$) is more stable in acceptor-donor doped BT ceramics. The consequence of the (partial) change in acceptor valence from $Fe^{3+}$ to $Fe^{2+}$ is the (partial) formation of electrically stronger (based on electrostatic Coulombic interaction) $Fe''_{Ti}$–$V_O^{\bullet\bullet}$ defect dipoles. In comparison with the equal-doping BT–1Fe–1Nb composition, a higher concentration of $Fe''_{Ti}$–$V_O^{\bullet\bullet}$ defect dipoles can be expected with the addition of $Nb^{5+}$, i.e., the BT–1Fe–1.5Nb composition. Hence, hardening effects are observed with decreased low-field dielectric properties (and increased dielectric properties with applied compressive stress, as observed in hard PZT ceramics), and increased dissipation loss and coercivity. On the other hand, with the lower $Nb^{5+}$ content in the BT–1Fe–0.5Nb composition, a relatively lower concentration of $Fe''_{Ti}$–$V_O^{\bullet\bullet}$ defect dipoles is expected; hence the ceramic is, by comparison, softer, with higher low-field dielectric properties (and lowered dielectric properties with applied compressive stress, as observed in soft PZT ceramics) and lower dissipation loss and coercivity, as clearly shown in Figs. 1–3.

In summary, the influences of compressive stress on the dielectric and ferroelectric properties of $Fe^{3+}/Nb^{5+}$ hybrid-doped BT ceramics are investigated. The superimposed compressive stress shows pronounced influences on the electrical properties of the ceramics. The response of the low-field dielectric properties to stress changes from soft to hard piezoelectric behavior with increasing $Nb^{5+}$ content. While ferroelectric properties decrease with stress, hardening behavior is observed with increasing $Nb^{5+}$ content in the hybrid-doped BT ceramics. A mechanism based on the induced change in the acceptor valence by the donor dopant in hybrid-doped BT ceramics is proposed to explain the results obtained.

This work was jointly supported by the Thailand Research Fund (TRF), the Commission on Higher Education (CHE), the Royal Golden Jubilee Ph.D. Program, and the Faculty of Science and the Graduate School of Chiang Mai University.

[1] B. Jaffe, W. R. Cook, and H. Jaffe, *Piezoelectric Ceramics* (Academic, New York, 1971).
[2] Y. H. Xu, *Ferroelectric Materials and Their Applications* (North Holland, Los Angeles, 1991).
[3] A. J. Moulson and J. M. Herbert, *Electroceramics: Materials, Properties, Applications* (Wiley, Chichester, 2003).
[4] K. Uchino, *Ferroelectric Devices* (Dekker, New York, 2000).
[5] C. Ang, Z. Yu, Z. Jing, R. Y. Guo, A. S. Bhalla, and L. E. Cross, Appl. Phys. Lett. **80**, 3424 (2002).
[6] Y. M. Chiang, G. W. Farrey, and N. A. Soukhojak, Appl. Phys. Lett. **73**, 3683 (1998).
[7] X. Ren and K. Otsuka, Phys. Rev. Lett. **85**, 1016 (2000).
[8] X. Ren, Nature Mater. **3**, 91 (2004).
[9] L. X. Zhang, W. Chen, and X. Ren, Appl. Phys. Lett. **85**, 5658 (2004).
[10] L. X. Zhang and X. Ren, Phys. Rev. B **71**, 174108 (2005).
[11] L. X. Zhang and X. Ren, Mater. Sci. Eng., A **438–440**, 354 (2006).
[12] M. M. Ahmad, K. Yamada, P. Meuffels, and R. Waser, Appl. Phys. Lett. **90**, 112902 (2007).
[13] W. Liu, W. Chen, L. Yang, Y. Wang, L. X. Zhang, C. Zhou, S. Li, and X. Ren, Mater. Sci. Eng., A **438–440**, 350 (2006).
[14] W. Liu, W. Chen, L. Yang, Y. Wang, L. X. Zhang, C. Zhou, S. Li, and X. Ren, Appl. Phys. Lett. **89**, 172908 (2006).
[15] K. Uchino, *Piezoelectric Actuators and Ultrasonic Motors* (Kluwer Academic, Boston, 1997).
[16] D. Stansfield, *Underwater Electroacoustic Transducers* (Bath University Press, Bath, 1991).
[17] S. Park and T. R. Shrout, J. Appl. Phys. **82**, 1804 (1997).
[18] D. Viehland and J. Powers, Appl. Phys. Lett. **78**, 3112 (2001).
[19] C. S. Lynch, Acta Mater. **44**, 4137 (1996).
[20] D. Zhou, Z. Wang, and M. Kamlah, J. Appl. Phys. **97**, 084105 (2005).
[21] G. Yang, Z. Yue, T. Sun, H. Gou, and L. Li, J. Phys. D **41**, 045307 (2008).
[22] W. Chaisan, R. Yimnirun, and S. Ananta, Phys. Scr., T **T129**, 205 (2007).
[23] D. Damjanovic, J. Appl. Phys. **82**, 1788 (1997).
[24] R. Yimnirun, M. Unruan, Y. Laosiritaworn, and S. Ananta, J. Phys. D **39**, 3097 (2006).
[25] Q. M. Zhang, J. Zhao, K. Uchino, and J. Zheng, J. Mater. Res. **12**, 226 (1997).
[26] M. Morozov, D. Damjanovic, and N. Setter, J. Eur. Ceram. Soc. **25**, 2483 (2005).
[27] J. Y. Li, R. C. Rogan, E. Ustundag, and K. Bhattacharya, Nature Mater. **4**, 776 (2005).
[28] G. Yang, S. F. Liu, W. Ren, and B. K. Mukherjee, Ferroelectrics **262**, 207 (2001).
[29] R. Yimnirun, Y. Loasiritaworn, and S. Wongsaenmai, J. Phys. D **39**, 759 (2006).
[30] M. E. Lines and A. M. Glass, *Principles and Applications of Ferroelectrics and Related Materials* (Oxford University Press, Oxford, 1977).
[31] S. Pruvost, G. Sebald, L. Lebrun, and D. Guyomar, J. Appl. Phys. **102**, 064104 (2007).
[32] T. Granzow, E. Suvaci, H. Kungl, and M. J. Hoffmann, Appl. Phys. Lett. **89**, 262908 (2006).
[33] K. Albertsen, D. Hennings, and O. Steigelmann, J. Electroceram. **2**, 193 (1998).
[34] H. Kishi, N. Kohzu, Y. Iguchi, J. Sugino, M. Kato, H. Ohsato, and T. Okuda, Jpn. J. Appl. Phys., Part 1 **39**, 5533 (2000).
[35] H. Kishi, N. Kohzu, Y. Iguchi, J. Sugino, M. Kato, H. Ohsato, and T. Okuda, J. Eur. Ceram. Soc. **21**, 1643 (2001).

Downloaded 16 Dec 2008 to 202.28.27.3. Redistribution subject to AIP license or copyright; see http://jap.aip.org/jap/copyright.jsp

Available online at www.sciencedirect.com
ScienceDirect
Current Applied Physics 9 (2009) 249–252
Current Applied Physics
An official journal of the KPS
www.elsevier.com/locate/cap
www.kps.or.kr

# Ferroelectric properties of $Pb(Zr_{1/2}Ti_{1/2})O_3$–$Pb(Zn_{1/3}Nb_{2/3})O_3$ ceramics under compressive stress

Rattikorn Yimnirun *, Narit Triamnak, Muangjai Unruan, Athipong Ngamjarurojana, Yongyut Laosiritaworn, Supon Ananta

*Department of Physics, Faculty of Science, Chiang Mai University, Chiang Mai 50200, Thailand*

Received 25 December 2006; received in revised form 11 February 2008; accepted 12 February 2008
Available online 29 February 2008

**Abstract**

Effects of compressive stress on the ferroelectric properties of ceramics in PZT–PZN system were investigated. The ceramics with a formula $(1-x)Pb(Zr_{1/2}Ti_{1/2})O_3$–$xPb(Zn_{1/3}Nb_{2/3})O_3$ or $(1-x)$PZT–$(x)$PZN ($x = 0.1$–$0.5$) were prepared by a conventional mixed-oxide method. The ferroelectric properties under the compressive stress of the PZT–PZN ceramics were observed at the stress levels up to 170 MPa using a compressometer in conjunction with a modified Sawyer–Tower circuit. It was found that with increasing compressive stress the area of the ferroelectric hysteresis ($P$–$E$) loops, the saturation polarization ($P_{sat}$), the remnant polarization ($P_r$), and the coercive field ($E_c$) decreased. These results were interpreted through the non-180° ferroelastic domain switching processes.
© 2008 Elsevier B.V. All rights reserved.

*PACS:* 77.84.−s; 77.80.Fm; 77.84.Dy; 77.80.−e

*Keywords:* Ferroelectric properties; PZT–PZN; Stress

## 1. Introduction

In many practical sensor and actuator applications, piezoelectric and ferroelectric ceramics are often subjected to mechanical loading, either deliberately in the design of the device itself or because the device is used to change shapes as in many smart structure applications or the device is used under environmental stresses such as in underwater transducers [1–3]. A prior knowledge of how the material properties change under different load conditions is therefore very crucial for proper design of a device and for suitable selection of materials for a specific application. Despite the fact, material constants used in many design calculations are often obtained from a stress-free measuring condition, which in turn may lead to incorrect or inappropriate actuator and transducer designs [4,5]. It is therefore important to determine the properties of these materials as a function of applied stress. Previous investigations on the stress-dependent dielectric and electrical properties of many ceramic systems, such as BT, PZT, PMN, PMN–PT, PZT–BT, and PMN–PZT have clearly emphasized the importance of the subject [6–13]. In this paper, the stress dependence of the ferroelectric properties of ceramics in PZT–PZN system is presented.

Recently, there have been a great deal of interest in lead zirconate titanate-lead zinc niobate ($Pb(Zr_{1/2}Ti_{1/2})O_3$–$Pb(Zn_{1/3}Nb_{2/3})O_3$ or PZT–PZN) systems because of their high dielectric, piezoelectric, and ferroelectric properties [14–16]. PZN is a ferroelectric material with frequency dependent dielectric relaxation behavior, as well as diffuse phase transition at 140 °C [17]. A single crystal of PZN shows extremely high dielectric and piezoelectric constants [18]. PZT also has high piezoelectric properties, particularly compositions (Zr:Ti ~ 52:48) close to a morphotropic phase boundary (MPB) between the tetragonal and the rhombohedral phases [19]. Therefore, PZT is the most popular ferroelectric material used in electronic devices

* Corresponding author. Tel.: +66 53 943 367; fax: +66 53 943 445.
*E-mail address:* rattikornyimnirun@yahoo.com (R. Yimnirun).

1567-1739/$ - see front matter © 2008 Elsevier B.V. All rights reserved.
doi:10.1016/j.cap.2008.02.007

[4,19,20]. As both PZT and PZN possess excellent electrical properties, enhanced properties can thus be expected from ceramics in PZT–PZN system. There have been many previous reports on the electrical properties of PZT–PZN ceramics [14–16]. Earlier report on the stress-dependent dielectric properties of PZT–PZN also showed very interesting results [21]. However, there has been no systematic study on the influence of an applied stress on the ferroelectric properties of the PZT–PZN ceramics. Therefore, it is the aim of this study to determine the ferroelectric properties of the $(1-x)$PZT–$(x)$PZN ceramics as a function of compressive stress.

## 2. Experiments and measurements

In this study, $(1-x)Pb(Zr_{1/2}Ti_{1/2})O_3$–$(x)Pb(Zn_{1/3}Nb_{2/3})O_3$ (with $x = 0.1$–$0.5$) ceramics were prepared from starting PZT and PZN powders by a conventional mixed-oxide method via vibro-milling technique [22]. Perovskite-phase PZN powders were obtained from the columbite method with zinc niobate ($ZnNb_2O_6$) selected as the precursor, while PZT powders were prepared by a simple mixed-oxide method [23]. For optimization purpose, the sintering was carried out at temperatures between 1200 and 1250 °C for 2 h. Details of the processing and characterizations were provided elsewhere [22–24].

Before studying the dielectric properties, the specimens were lapped to obtain parallel faces. After coating with silver paint as electrode at the faces, the specimens were heated at 750 °C for 12 min to ensure the contact between the electrodes and surfaces of ceramic. The ferroelectric hysteresis ($P$–$E$) loops were characterized by using a computer controlled modified Sawyer–Tower circuit. The electric field was applied to a sample by a high voltage AC amplifier (Trek, model 610D) with the input sinusoidal signal with a frequency of 100 Hz from a signal generator (Goodwill, model GAG-809). The detailed descriptions of this system were explained elsewhere [9,10]. To study the effects of the compressive stress on the ferroelectric properties, the uniaxial compressometer was constructed for simultaneous and parallel applications of the mechanical stress and the electric field [12]. Measurements were performed as a function of mechanical stress applied discretely between 0 and 170 MPa. During the measurements, a desired stress was first applied to the sample and then the electric field was applied. The ferroelectric hysteresis ($P$–$E$) loop was recorded at room temperature (25 °C) for both loading and unloading conditions. The parameters obtained from the loops were the saturation polarization ($P_{sat}$), the remnant polarization ($P_r$), and the coercive field ($E_c$), which were defined as the points where the loops reach the maximum polarization, cross the zero field, and cross the zero polarization, respectively. The measurements reported were for the samples during their first mechanical stress cycle. It should also be noted that the reported ferroelectric parameters were obtained after a total of 10 cycles of the electric field was applied to the sample at each constant stress level.

## 3. Results and discussion

The polarization vs. electric field ($P$–$E$) hysteresis loops of the 0.9PZT–0.1PZN, 0.7PZT–0.3PZN, and 0.5PZT–0.5PZN ceramics under different compressive stresses are shown in Figs. 1–3, respectively. It should first be noticed that the area of the $P$–$E$ loops decreases with increasing compressive stress. The changes follow a similar trend for all the ceramics. The $P$–$E$ loop area indicates the polarization dissipation energy of a ferroelectric material under one full cycle of electric field application [23]. This amount of the energy loss is directly related to the amount of domain participating in the switching process during the application of electric field [10]. Unlike in the PMN–PZT system, in which the stress-free loop area decreases with increasing PMN content, as the ceramics gradually change from ferroelectric PZT with macro-domain states to electrostrictive PMN with nano-domain states [13,17], the stress-free loop areas of all the ceramics are generally very similar. For a given composition, the decrease in the loop area with increasing the compressive stress is a result of the stress-induced domain wall suppression [10].

The changes in the saturation polarization ($P_{sat}$), the remnant polarization ($P_r$), and the coercive field ($E_c$) with the compressive stresses are plotted in Figs. 4–6, respectively. It should first be noticed that, thought the values are not significantly different, the stress-free values of the $P_{sat}$ and $P_r$ are generally largest (with $E_c$ nearly minimal) for the near MPB compositions ($x = 0.3$–$0.4$). In addition, the $P_r$ values for the tetragonal compositions, i.e., 0.9PZT–0.1PZN and 0.8PZT–0.2PZN, are lower than those of the rhombohedral compositions (0.6PZT–0.4PZN and 0.5PZT–0.5PZN). However, the trend for $E_c$ is reversed. These observations are anticipated because the ceramic systems gradually change from the compositions with tetragonal structure

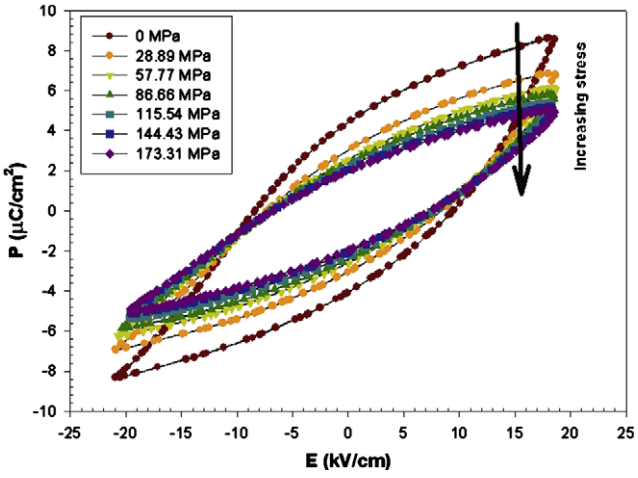



Fig. 1. Polarization vs. electric field ($P$–$E$) hysteresis loops as a function of compressive stress for 0.9PZT–0.1PZN ceramic (loading cycle).

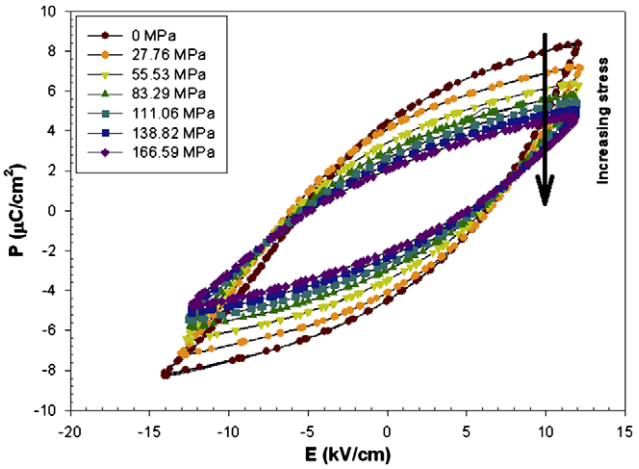



Fig. 2. Polarization vs. electric field ($P$–$E$) hysteresis loops as a function of compressive stress for 0.7PZT–0.3PZN ceramic (loading cycle).

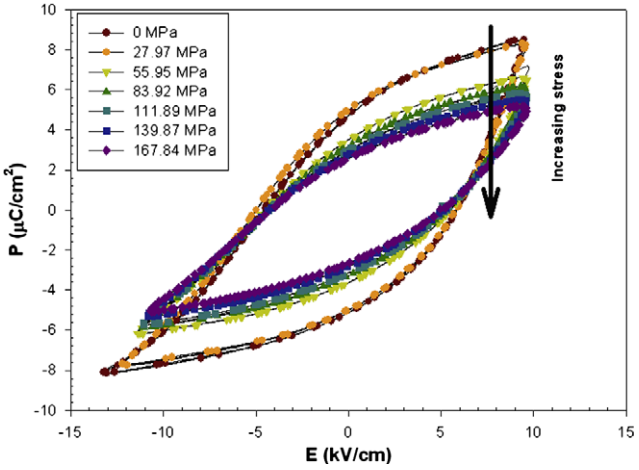



Fig. 3. Polarization vs. electric field ($P$–$E$) hysteresis loops as a function of compressive stress for 0.5PZT–0.5PZN ceramic (loading cycle).

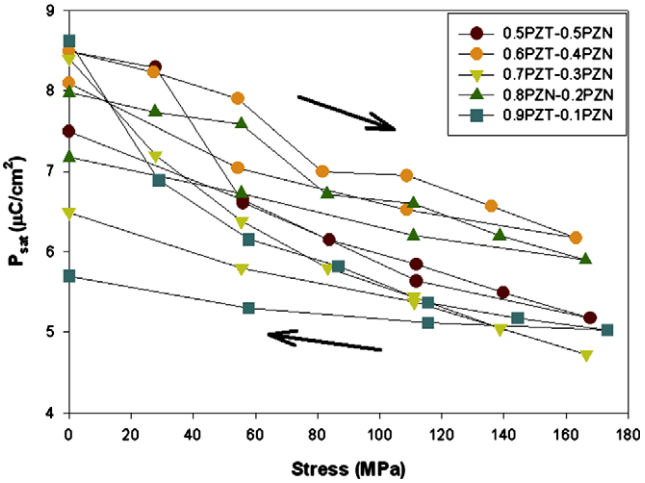



Fig. 4. Changes in saturation polarization ($P_{sat}$) with compressive stress for $(1-x)$PZT–$x$PZN ceramics (loading and unloading).

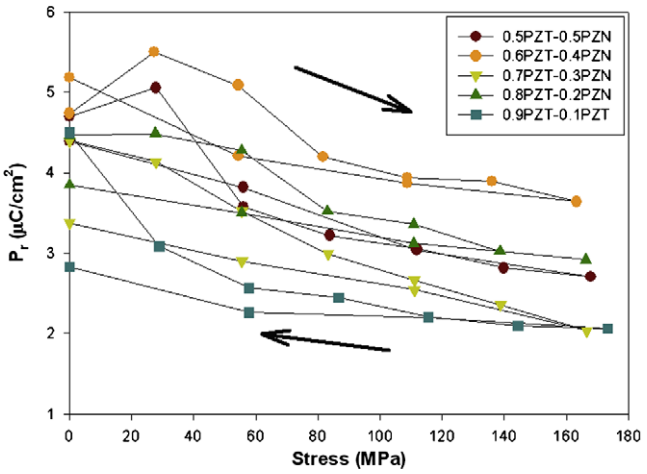



Fig. 5. Changes in remnant polarization ($P_r$) with compressive stress for $(1-x)$PZT–$x$PZN ceramics (loading and unloading).

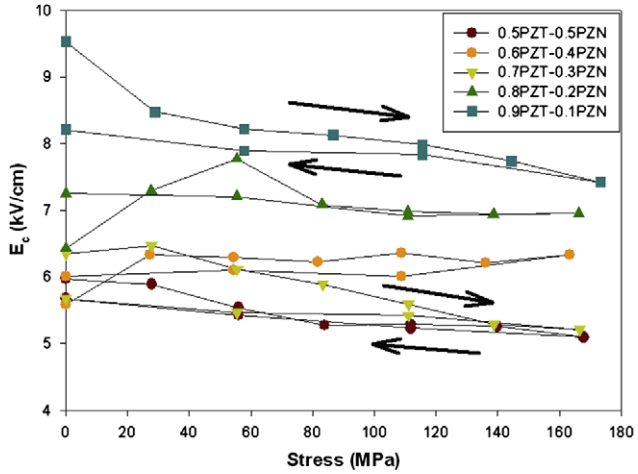



Fig. 6. Changes in coercive field ($E_c$) with compressive stress for $(1-x)$PZT–$x$PZN ceramics (loading and unloading).

($x = 0.1$ and 0.2) with high $E_c$ and low $P_r$ to the near MPB compositions with the highest polarization values, and finally to the compositions with rhombohedral structure ($x = 0.4$ and 0.5) with low $E_c$ and high $P_r$, as mentioned in previous investigation [14–17]. This clearly clarifies the existence of the MPB near $x = 0.3$ and 0.4, as reported earlier [21]. Figs. 4 and 5 clearly show that both the saturation and remnant polarizations decrease as the compressive stress increases. In both cases, the decrease is generally very similar with the polarization values at 170 MPa are approximately 50–75% of the stress-free values. In addition, noticeable decreases in the polarization values of all the ceramics are also observed after a complete cycle of the mechanical stress. This observation suggests a significant stress-induced depoling in PZT–PZN ceramics, resulting in the observed decrease of the polarization values under high stress levels [11,25]. Interestingly, as opposed to the polarizations, the applied compressive stress shows little or no influence on the coercive field, as demonstrated in Fig. 6.

To understand, at least qualitatively, these experimental results on ferroelectric PZT–PZN ceramics, one can interpret the changes in terms of domain-reorientation processes. When the compressive stress is applied in the direction parallel to the polar axis (poling) direction, the applied stress tends to keep the ferroelectric domains aligned with their polar axes away from the stress direction through the non-180° ferroelastic domain switching processes [6,7,11,25]. Therefore, it takes larger than usual applied electric field to reorient the domains along the stress direction, resulting in lower value of the saturation polarization ($P_{sat}$), as shown in Figs. 1–4. When the electric field is reduced to zero the domains tend to rotate back away from the applied compressive stress direction, resulting in lower than usual remnant polarization ($P_r$), as depicted in Figs. 1–3 and 5 [7,25]. Furthermore, considering the decrease of the hysteresis loss with increasing the compressive stress, it indicates that more and more ferroelectric domains are constrained by the applied stress and cannot be re-oriented by the electric field so as to participate in the polarization reversal. Consequently, both the saturation and remnant polarizations become lower with increasing the compressive stress. [12]. The results of the changes of the hysteresis parameters of the ferroelectric PZT–PZN ceramics with increasing compressive stress are in agreement with the previous investigations on many ferroelectric ceramics [5,7,12,26,27].

## 4. Conclusions

In this study, effects of compressive stress on the ferroelectric properties of ceramics in the PZT–PZN system are investigated. The ferroelectric properties under the compressive stress are observed at stress levels up to 170 MPa using a compressometer in conjunction with a modified Sawyer–Tower circuit. The results show that the area of the ferroelectric hysteresis ($P$–$E$) loops, the saturation polarization ($P_{sat}$), the remnant polarization ($P_r$), and the coercive field ($E_c$) decrease with increasing compressive stresses. The non-180° ferroelastic domain switching processes are responsible for the changes observed. Furthermore, noticeable decreases in the polarization values of all the ceramic are also observed after a complete cycle of the mechanical stress, indication of a significant stress-induced de-poling in PZT–PZN ceramics. Finally, this study undoubtedly shows that the applied compressive stress has significant influences on the hysteresis properties of the PZT–PZN ceramics.

## Acknowledgment

Financial support from the Thailand Research Fund (TRF) and Commission on Higher Education (CHE) is gratefully acknowledged.

## References

[1] L.E. Cross, Ferroelectrics 76 (1987) 241.
[2] Y.H. Xu, Ferroelectric Materials and Their Applications, North Holland, Los Angeles, 1991.
[3] D. Viehland, J. Powers, J. Appl. Phys. 89 (2001) 1820.
[4] K. Uchino, Piezoelectric Actuators and Ultrasonic Motors, Kluwer Academic, Boston, 1997.
[5] D. Viehland, J.F. Li, E. McLaughlin, J. Powers, R. Janus, H. Robinson, J. Appl. Phys. 95 (2004) 1969.
[6] Q.M. Zhang, J. Zhao, K. Uchino, J. Zheng, J. Mater. Res. 12 (1997) 226.
[7] D. Zhou, M. Kamlah, D. Munz, J. Eur. Ceram. Soc. 25 (2005) 425.
[8] R. Yimnirun, Ferroelectrics 331 (2006) 9.
[9] R. Yimnirun, S. Ananta, S. Chamunglap, Mater. Chem. Phys. 102 (2007) 165.
[10] R. Yimnirun, S. Ananta, A. Ngamjarurojana, S. Wongsaenmai, Curr. Appl. Phys. 6 (3) (2006) 520.
[11] G. Yang, S.F. Liu, W. Ren, B.K. Mukherjee, Proc. SPIE Symp. Smart Struct. Mater. 3992 (2000) 103.
[12] R. Yimnirun, M. Unruan, Y. Laosiritaworn, S. Ananta, J. Phys. D 39 (2006) 3097.
[13] R. Yimnirun, Int. J. Mod. Phys. B 20 (23) (2006) 3409.
[14] N. Vittayakorn, G. Rujijanagul, T. Tunkasiri, X. Tan, D.P. Cann, J. Mater. Res. 18 (2003) 2882.
[15] H. Fan, H.-E. Kim, J. Appl. Phys. 91 (2002) 317.
[16] N. Vittayakorn, G. Rujijanagul, X. Tan, H. He, M.A. Marquardt, D.P. Cann, J. Electroceram. 16 (2006) 141.
[17] A.A. Bokov, I.P. Rayevskii, V.G. Smotrakov, O.I. Prokopalo, Phys. Status Solidi A 93 (1986) 411.
[18] K. Uchino, Solid State Ionics 108 (1998) 43.
[19] M.E. Lines, A.M. Glass, Principles and Applications of Ferroelectrics and Related Materials, Oxford, 1977.
[20] A.J. Moulson, J.M. Herbert, Electroceramics: Materials, Properties, Applications, Wiley, Chichester, 2003.
[21] R. Yimnirun, A. Ngamjarurojana, Y. Laosiritaworn, Supon Ananta, Narit Triamnak, Ferroelectrics 355 (2007) 257.
[22] R. Yimnirun, R. Tipakontitikul, S. Ananta, Int. J. Mod. Phys. B 20 (16) (2006) 2415.
[23] A. Ngamjarurojana, O. Khamman, R. Yimnirun, S. Ananta, Mater. Lett. 60 (2006) 2867.
[24] A. Ngamjarurojana, O. Khamman, S. Ananta, R. Yimnirun, J. Electroceram. (2008), doi: 10.1007/s10832-007-9290-4.
[25] G. Yang, W. Ren, S.F. Liu, A.J. Masys, B.K. Mukherjee, Proc. IEEE Ultrason. Symp. 2 (2000) 1005.
[26] I.J. Fritz, J. Appl. Phys. 49 (1978) 788.
[27] C.S. Lynch, Acta Mater. 44 (1996) 4137.

Available online at www.sciencedirect.com
ScienceDirect
Current Applied Physics 9 (2009) 268–273
Current Applied Physics
An official journal of the KPS
www.elsevier.com/locate/cap
www.kps.or.kr

# Synthesis and electrical properties of $Pb(Mg_{1/3}Nb_{2/3})O_3$–$PbTiO_3$ ceramics

R. Wongmaneerung, R. Yimnirun, S. Ananta *

*Department of Physics, Faculty of Science, Chiang Mai University, Chiang Mai 50200, Thailand*

Received 24 December 2006; received in revised form 15 February 2008; accepted 20 February 2008
Available online 29 February 2008

**Abstract**

Ceramic compositions of a combination between lead magnesium niobate, $Pb(Mg_{1/3}Nb_{2/3})O_3$, and lead titanate, $PbTiO_3$, were fabricated by using $Mg_4Nb_2O_9$ precursor technique. Their electrical properties with respect to temperature and frequency were examined and the effect of sintering conditions on phase formation, densification, microstructure and electrical properties of the ceramics were examined. It has been found that optimisation of sintering condition can lead to a highly dense and pyrochlore-free PMN–PT ceramics. The gradual decreasing of the physical properties of the sintered ceramics was related to the gradual decrease of density and inhomogeneous microstructure. The results also revealed that for the lower concentration of lead titanate a relaxor behavior is noticed with a high electrostrictive effect, which was almost hysteretic free. However, higher amount of lead titanate led to a normal ferroelectric behavior.
© 2008 Elsevier B.V. All rights reserved.

*PACS:* 77.22.Ch; 77.84.Dy; 77.80.–e; 77.80.Fm

*Keywords:* Dielectric properties; Ferroelectric properties; Lead magnesium niobate titanate

## 1. Introduction

The complex perovskite lead magnesium niobate–lead titanate, $(1-x)Pb(Mg_{1/3}Nb_{2/3})O_3$–$xPbTiO_3$ (PMN–PT), are extensively used as multilayer capacitors, electrostrictive actuators, sensors and many other electronic and microelectromechanical devices [1,2]. This is due to their excellent electrical and electromechanical properties including high relative permittivity, a broad maximum in the dielectric constant, large electrostrictivity, associated with a low thermal expansion and excellent voltage stability [1–3]. However, these importance properties are depend strongly on the purity of the raw materials and method of preparation, since they can be limited by the formation of the unwanted pyrochlore phases with poor electrical properties upon processing [4–6]. Throughout the years, considerable efforts with various preparation techniques have been proposed and used to fabricate pyrochlore-free PMN–PT ceramics [7–9]. Among these, the columbite method [6], in which prefabricated $MgNb_2O_6$ is reacted with an appropriate proportion of PbO, has been widely used in the synthesized of phase-pure perovskite PMN-based ceramics. Numerous studies [10–13] have been reported in the literature in which the columbite method was modified by using different set of reactants as precursor materials. To our knowledge there are no reports so far on the preparation of PMN–PT ceramics by using a corundum $Mg_4Nb_2O_9$ precursor. In our previous work, pure-perovskite PMN could be prepared by using $Mg_4Nb_2O_9$ precursor. This suggested that the same process would be adaptable for the formation of PMN–PT solid solutions and also would be easier than conventional methods, because the PMN structure can be stabilized by the presence of PT.

In the present study, ceramics in the $(1-x)$PMN–$x$PT system were fabricated by using the solid-state reaction technique with $Mg_4Nb_2O_9$ as a key B-site precursor. Their

* Corresponding author. Tel.: +66 53 943367; fax: +66 53 943445.
*E-mail address:* suponananta@yahoo.com (S. Ananta).

1567-1739/$ - see front matter © 2008 Elsevier B.V. All rights reserved.
doi:10.1016/j.cap.2008.02.009

electrical properties with respect to temperature and frequency were examined, compared and explained on the basis of their final composition, densification, and structural development.

## 2. Experimental

The system under investigation was $(1-x)Pb(Mg_{1/3}Nb_{2/3})O_3$–$xPbTiO_3$ or $(1-x)$PMN–$x$PT, where $x$ changed from 0.1 to 0.5 at regular interval of 0.1. The starting materials were commercially available oxide powders of PbO, MgO, $Nb_2O_5$ and $TiO_2$ (Aldrich, 99.9% purity) with an average particle size of 3–5 μm. PMN powders were first synthesised from these oxides using a modified mixed oxide synthetic route described in our earlier work [14]. In this method, MgO and $Nb_2O_5$ are reacted at 950 °C for 2 h to form the corundum precursor $Mg_4Nb_2O_9$ [15]. The following reaction was employed for the formation of PMN [14]:

$$12PbO(s) + 3Nb_2O_5(s) + Mg_4Nb_2O_9(s) \rightarrow 12Pb(Mg_{1/3}Nb_{2/3})O_3(s) \quad (1)$$

The resulting PMN was then reacted with PbO and $TiO_2$ at 800 °C for 2 h with heating/cooling rates of 30 °C/min to obtain PMN–PT. The mixing process was carried out by vibro-milling the mixture of raw materials for 2 h with corundum media in isopropyl alcohol (IPA). After wet-milling, the slurry was dried, sieved and calcined in closed alumina crucibles.

Green pellets were pressed into disks and sintered at various temperatures between 900 and 1250 °C (no organic binders or any other additives were used). Each pellet to be sintered was supported by $PbZrO_3$ setters and enclosed in double alumina crucibles together with the atmosphere powder of identical composition (to minimize the possibility of PbO volatilization). Densities of the sintered pellets were determined by using the Archimedes principles. Room temperature X-ray diffraction (XRD; Philips PW 1729 diffractometer) using Ni filtered Cu $K_\alpha$ radiation, was used to identified the phases formed and optimum sintering condition for the manufacture of each PMN–PT composition, with the microstructural development examined by scanning electron microscopy (SEM; JEOL JSM-840A), operating at 20 kV and equipped with an energy-dispersive X-ray (EDX) analyser. For the electrical measurements the ceramics were polished using 1 μm alumina, cleaned with ultrasonic, dried and sputtered with gold. The dielectric measurement were made using an automated measurement system i.e. an LCR meter (HP-4174A), a nitrogen-fed furnace (9023 Delta design) and a desktop computer (HP-200 series). Hysteresis measurements were made using a modified Sawyer–Tower circuit controlled by a PC. This system is also capable of simultaneous measurement of strain using an LVDT and lock-in amplifier (SR830 DSP, Stanford Research).

## 3. Results and discussion

The X-ray diffraction patterns from sintered PMN–PT ceramics with maximum perovskite and bulk density are given in Fig. 1, where complete crystalline solutions of perovskite structure were formed throughout the whole composition ranges. Optimum sintering conditions for all ceramics were established by identifying the conditions for maximizing both the bulk density and the yield of perovskite. In general, only a pseudo-cubic symmetry was observed at low values of PT concentration, in good agreement with other workers [12,13,16]. By the influence of PT, however, several peaks split for $x \geqslant 0.4$, indicating the development of tetragonal symmetry, which continued with a further increase in PT concentration. For example, (002)/(200) peaks splitting the diffraction line around $2\theta$ of 44–46° confirming their tetragonal symmetry, consistent with literature [12,17].

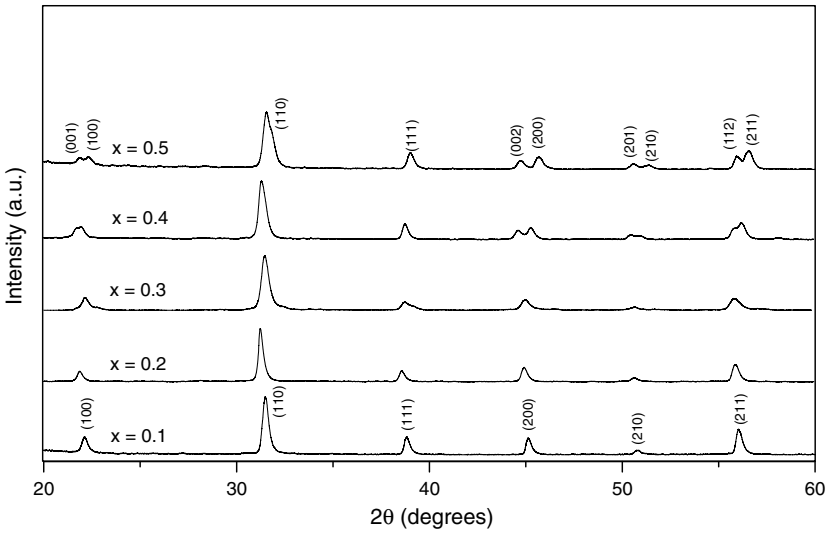



Fig. 1. XRD patterns of the $(1-x)$PMN–$x$PT ceramics sintered at their optimum conditions.

Table 1
Phase and densification characteristics of $(1-x)$PMN–$x$PT ceramics from various sintering conditions

| Composition $x$ | Optimum sintering condition (°C for 2 h) | Concentration of perovskite phase (%) | Density[a] (g/cm$^3$) | Grain-size[b] (μm) |
|---|---|---|---|---|
| 0.1 | 1240 | 100 | 7.98 | 0.42–3.66 |
| 0.2 | 1240 | 100 | 7.94 | 0.44–3.02 |
| 0.3 | 1240 | 100 | 7.86 | 0.41–2.80 |
| 0.4 | 1220 | 100 | 7.83 | 0.41–3.45 |
| 0.5 | 1220 | 100 | 7.78 | 0.48–3.72 |

[a] The estimated precision of the density is ±0.05 g/cm$^3$.
[b] The estimated precision of the grain size is ±0.05 μm.

The densification data of all compositions are given in Table 1. In general, the bulk density was found to decrease slightly with $x$, which could be due to the lower melting point of PT compared to PMN. Thus, the admixture of PMN could be considered as a useful technique for promoting the densification of PT, along with its other significant advantage of bringing the Curie range down to lower temperatures as demonstrated by a number of workers [4,18,19]. It can be seen that the ceramic sintered at 1220–1240 °C having the highest relative density with grain size range of about 0.4–3.7 μm, was of the best interest for further investigation.

SEM micrographs of both as fired and fracture surfaces of all compositions are shown in Fig. 2, indicating representative microstructures. In general, similar microstructural characteristics were observed in these samples, i.e. uniformly sized grains with a high degree of grain close-packing. Almost no abnormal grain growth was observed, although some small particles of MgO and PbO (identified by EDX) with diameter about 0.28–0.55 μm were found at the grain boundaries and triple junctions of some samples (e.g. $x = 0.2$). By applying the linear intercept method to these micrographs, mean grain sizes of about 0.3–3.35 μm were estimated as given in Table 1. It should be seen as a rough approximation since the micrographs exhibit only two dimensional images of the unpolished samples. Apart from the grain size, the effect of chemical composition on the grain shape was also noticed. It is likely that the degree of angularity tend to increase with $x$. The fraction of the larger size was increased with the increase of PT content. This may be attributed to the perovskite increases stability, which facilitates the formation with the increase of PT content.

The experimental work carried out here suggests that complex perovskite $(1-x)$PMN–$x$PT ceramics with a high degree of grain packing microstructures can be achieved by sintering powders derived from the B-site ($Mg_4Nb_2O_9$) precursor method. However, small amounts of MgO and PbO phases can still be detected in some compositions, indicating their poor homogeneity due to the limitation of a mixed oxide processing. According to TEM observation by Goo et al. [20], MgO tends to be segregated in the PMN grains as submicrometer inclusions and this segregation leads to a shortage of MgO on the whole, a situation liable to affect the formation of pyrochlore phase.

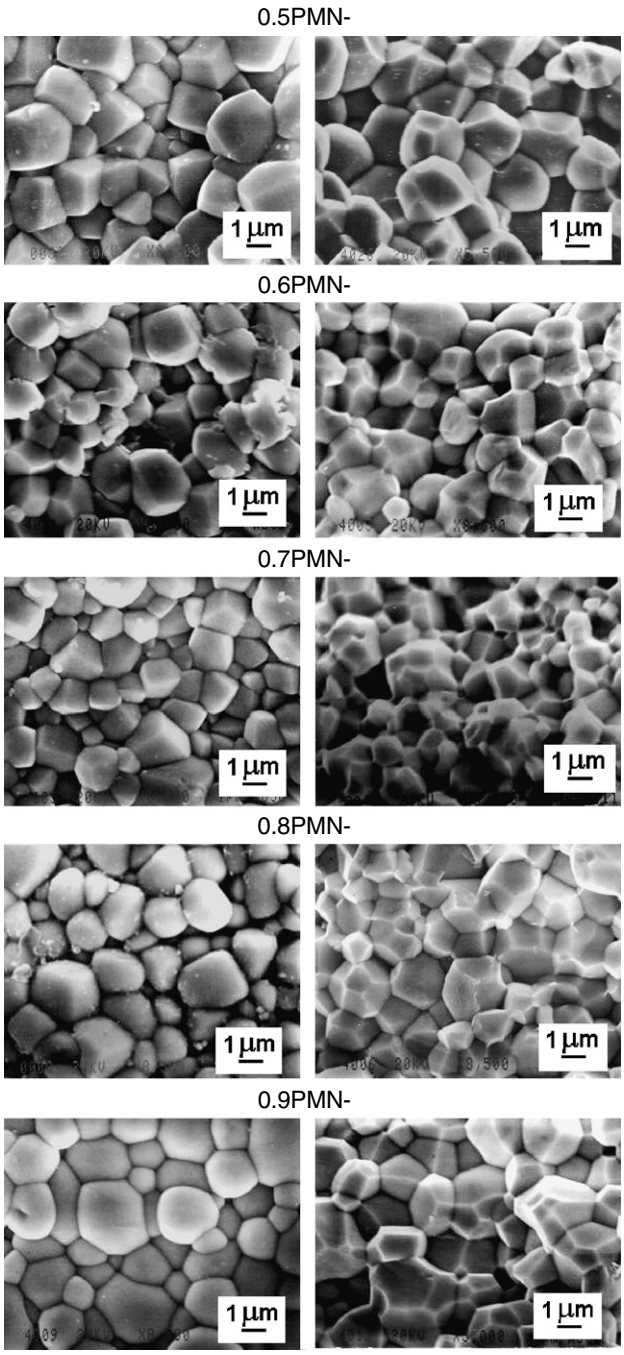



Fig. 2. SEM micrographs of the $(1-x)$PMN–$x$PT ceramics sintered at their optimum conditions.

The dielectric properties, e.g. dielectric constant ($\varepsilon_r$) and dielectric loss tangent ($\tan\delta$), are measured as functions of both temperature and frequency, as shown in Fig. 3a–b. As listed in Table 2, the Curie temperature ($T_C$) (determined at measuring frequency of 1 kHz) increases from 38 °C in 0.9PMN–0.1PT to 250 °C in 0.5PMN–0.5PT. This is a direct result of PT addition to PMN ($T_C \sim -8$ °C) since

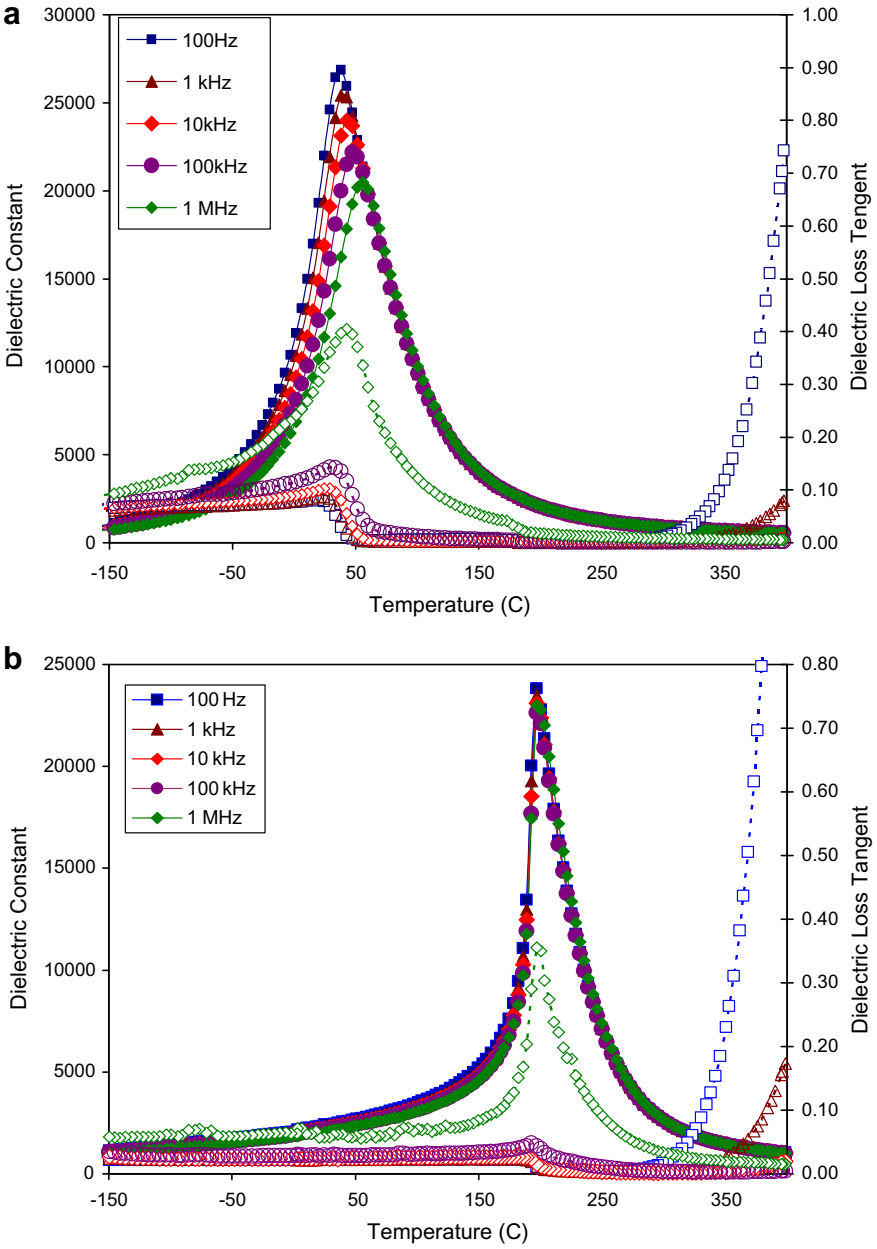



Fig. 3. Temperature and frequency dependences of dielectric properties of (a) 0.9PMN–0.1PT and (b) 0.7PMN–0.3PT ceramics (open markers with dotted lines indicate data for the dielectric loss tangent ($\tan\delta$) at the same frequency).

Table 2
Dielectric and ferroelectric properties of $(1-x)$PMN–$x$PT ceramics

| Composition $x$ | $T_C$ (°C) | Dielectric properties[a] | | Ferroelectric properties[b] | | |
|---|---|---|---|---|---|---|
| | | $\varepsilon_r$ | $\tan\delta$ | $P_{sat}$ (mC/m$^2$) | $P_r$ (mC/m$^2$) | $E_c$ (MV/m) |
| 0.1 | 38 | 19400 | 0.087 | 100 | 13 | 0.196 |
| 0.2 | 140 | 3520 | 0.043 | 160 | 55 | 0.236 |
| 0.3 | 197 | 2320 | 0.022 | 179 | 100 | 0.391 |
| 0.4 | 220 | 2134 | 0.021 | 127.5 | 84 | 0.891 |
| 0.5 | 250 | 1010 | 0.025 | 75 | 53 | 1.279 |

[a] Measured at 25 °C and 1 kHz.
[b] Measured at 25 °C and 0.1 Hz.

PT itself has a Curie temperature of 490 °C [21]. As shown in Fig. 3a, for 0.9PMN–0.1PT ceramic both $\varepsilon_r$ and $\tan\delta$ exhibit strong temperature-frequency dependence below the transition temperature. This is a typical behavior of relaxor ferroelectrics [22], in which a strong temperature-frequency dependence is observed and the temperatures of maximum dielectric constant and dielectric loss tangent are shifted to higher temperature with increasing frequency. The maximum value of the dielectric constant decreases with increasing frequency, while that of the dielectric loss tangent increases. The dielectric properties then become frequency independence above the transition temperature [23]. PMN is a well-known relaxor ferroelec-

tric material as a result of a short-range ordered structure with a nanometer scale heterogeneity in composition [23]. Small addition of PT–PMN causes an increase in $T_C$, but the strong relaxor behavior still exists. In addition, since 0.9PMN–0.1PT ceramic has a pseudo-cubic symmetry it is therefore intrinsically electrostrictive (i.e. its electrically-induced strain is quadratically proportional to the applied electric field and is non-hysteretic, as shown later in Fig. 4b) [24]. With its enhanced dielectric properties at room temperature, as listed in Table 2, it is widely employed in transducers and actuators [25].

Further increase in PT contents leads to more observable normal ferroelectric behavior because PT is intrinsically a normal ferroelectric [24]. For instance, the dielectric properties of 0.7PMN–0.3PT ceramic, as plotted in Fig. 3b, exhibit a mixture of both normal and relaxor characteristics, in which the transition temperature is not shifted as much as for relaxor 0.9PMN–0.1PT ceramic. Similar tendency has also been observed in several prior investigations [23,26,27]. It should be noted that 0.7PMN–0.3PT ceramic composition is close to MPB of the PMN–PT system. Therefore, its structural symmetry is a mixture of pseudo-cubic and tetragonal, as shown in Fig. 1, which in turn causes a mixture of normal and relaxor characteristics observed for dielectric properties. With a tetragonal symmetry, the 0.5PMN–0.5PT ceramic, on the other hand, exhibits a normal ferroelectric behavior (not shown), in which the dielectric properties change significantly with temperature, but are nearly independent of frequency, except in the vicinity of the phase transformation temperature. This is a typical characteristic of normal ferroelectric ceramics with a long-range ordered structure [23]. It should also be noted here that the dielectric properties in all ceramics increase significantly at high

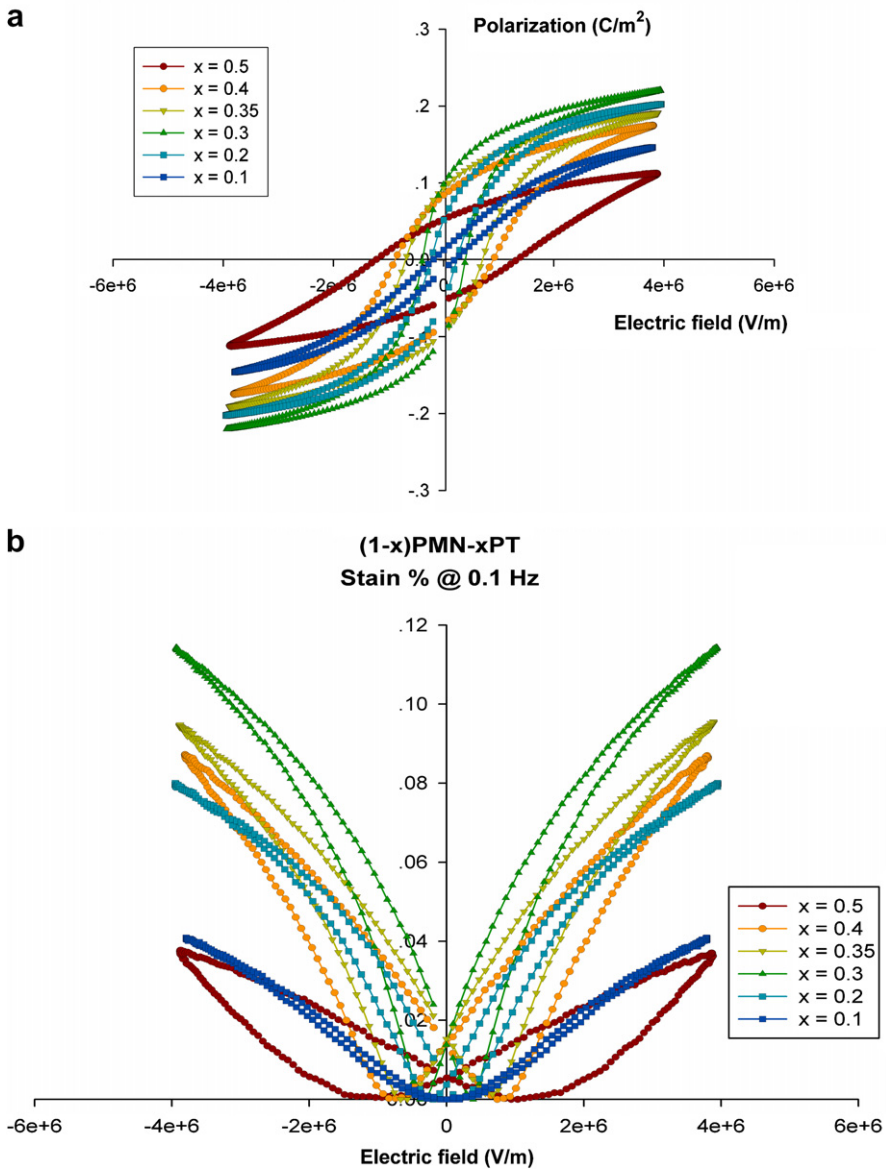



Fig. 4. (a) $P$–$E$ and (b) s-E hysteresis loops of $(1-x)$PMN–$x$PT ceramics.

temperature as a result of thermally activated space charge conduction [26]. It can be concluded that when PT is added to form the binary system with PMN, the $T_C$ increases monotonically, as shown in Table 2 and Fig. 3, and the dielectric behavior is shifted from relaxor ferroelectric towards normal ferroelectric.

Fig. 4a illustrates a series of polarization-field ($P$–$E$) hysteresis loops for the PMN–PT ceramics. It is clearly evident that the shape of $P$–$E$ loops varies greatly with the ceramic compositions. With large amount of normal ferroelectric PT contents, the polarization loops of 0.5PMN–0.5PT and 0.6PMN–0.4PT are well developed showing large remnant polarization ($P_r$: remaining polarization when electric field is decreased to zero). The hysteresis loops are of a typical "square" form as a result of domain switching in an applied field. This is a typical characteristic of a phase that contains long-range interaction between dipoles in the ferroelectric micro-domain state [22,25]. This confirms that these compositions are of a normal ferroelectric phase with tetragonal symmetry, as indicated by the dielectric measurements and XRD analysis. The 0.7PMN–0.3PT ceramic shows largest polarization values with small coercive field ($E_c$), confirming that the composition is near the MPB of PMN–PT system. The other compositions with more PMN content show more of "slim" hysteresis loops, a characteristic of the suppressed ferroelectric interaction [22,25]. This is typically found in the relaxor ferroelectrics with polar nano-regions. This also has resulted in decreasing of the values of both $P_r$ and $E_C$, as seen in Table 2, due to an increased pseudo-cubic non-ferroelectric phase content [25–27]. A similar behavior is also observed from the strain-electric field (s-E) relation, as plotted in Fig. 4b. As can be seen, the near hysteresis-free electrostrictive behavior normally observed in relaxor ferroelectric is obtained in 0.9PMN–0.1PT ceramic. With increasing amount of PT, the s-E loops become more of "butterfly" type typically obtained in normal ferroelectric state. The field-induced strain increases with increasing amount of PT to 30 mol% (near MPB composition), reaching the maximum value of ~0.12%. Further increase in the PT content results in the decrease of the induced strain. Therefore, it can be concluded that the ferroelectric properties of the ceramics in PMN–PT system move gradually from the relaxor ferroelectric state in PMN to the normal ferroelectric state in 0.5PMN–0.5PT, crossing the MPB near 0.7PMN–0.3PT [22,25].

## 4. Conclusions

Dense and pure-perovskite PMN–PT relaxor ceramics could be produced by using corundum $Mg_4Nb_2O_9$ as a B-site precursor. They possess very high dielectric constants and fundamental dielectric and electromechanical properties which can be greatly varied by composition and sintering condition. Dielectric relaxor behavior for the rhombohedral sample was found to lower concentration of PT, where high electrostrictive effect was observed. A higher amount of lead titanate induced a normal ferroelectric behavior with high polarization value and high electric field induced-strain.

## Acknowledgements

This work was supported by the Thailand Research Fund (TRF), the Commission on Higher Education (CHE), the Faculty of Science, Chiang Mai University.

## References

[1] A.J. Moulson, J.M. Herbert, Electroceramics, second ed., Wiley, Chichester, 2003.
[2] K. Uchino, Ferroelectric Devices, Marcel Dekker, New York, 2000.
[3] G.H. Haertling, J. Am. Ceram. Soc. 82 (1999) 797.
[4] S.L. Swartz, T.R. Shrout, W.A. Schulze, L.E. Cross, J. Am. Ceram. Soc. 67 (1984) 311.
[5] J.P. Guha, J. Eur. Ceram. Soc. 23 (2003) 133.
[6] S.L. Swartz, T.R. Shrout, Mater. Res. Bull. 17 (1982) 1245.
[7] A. Watanabe, H. Haneda, Y. Moriyoshi, S. Shirasaki, S. Kuramoto, H. Yamamura, J. Mater. Sci. 27 (1992) 1245.
[8] K.R. Han, S. Kim, H.J. Koo, J. Am. Ceram. Soc. 81 (1998) 2998.
[9] J. Wang, D.M. Wan, J.M. Xue, W.B. Ng, Adv. Mater. 11 (1999) 210.
[10] X. Zhang, C. Lei, K. Chen, J. Am. Ceram. Soc. 88 (2005) 335.
[11] A. Ianculescu, A. Braileanu, I. Pasuk, C. Popescu, J. Therm. Anal. Calorim. 80 (2005) 663.
[12] S. Fengbing, L. Qiang, Z. Haisheng, L. Chunhong, Z. Shixi, S. Dezhong, Mater. Chem. Phys. 83 (2004) 135.
[13] D.H. Suh, D.H. Lee, N.K. Kim, J. Eur. Ceram. Soc. 22 (2002) 219.
[14] R. Wongmaneerung, T. Sarakonsri, R. Yimnirun, S. Ananta, Mater. Sci. Eng. B 132 (2006) 292.
[15] S. Ananta, Mater. Lett. 58 (2004) 2530.
[16] Y.C. Liou, Mater. Sci. Eng. B 103 (2003) 281.
[17] D. Viehland, M.C. Kim, J.F. Li, Z. Xu, Appl. Phys. Lett. 67 (1995) 2471.
[18] S.W. Choi, J.M. Jang, A.S. Bhalla, Ferroelectrics 189 (1996) 27.
[19] J. Kelly, M. Leonard, C. Tantigate, A. Safari, J. Am. Ceram. Soc. 80 (1997) 957.
[20] E. Goo, T. Yamamoto, K. Okazaki, J. Am. Ceram. Soc. 69 (1996) C188.
[21] B. Jaffe, W.R. Cook, H. Jaffe, Piezoelectric Ceramics, Academic Press, New York, 1977.
[22] L.E. Cross, Mater. Chem. Phys. 43 (1996) 108.
[23] V. Koval, C. Alemany, J. Briancin, H. Brunckova, K. Saksl, J. Eur. Ceram. Soc. 23 (2003) 1157.
[24] S.E. Park, T.R. Shrout, Mater. Res. Innovations 1 (1997) 20.
[25] L.E. Cross, Ferroelectrics 76 (1987) 241.
[26] R. Yimnirun, S. Ananta, P. Laoratanakul, J. Eur. Ceram. Soc. 25 (2005) 3225.
[27] R. Yimnirun, S. Ananta, P. Laoratanakul, Mater. Sci. Eng. B 112 (2004) 79.

Available online at www.sciencedirect.com
ScienceDirect
Current Applied Physics 9 (2009) 422–425
Current Applied Physics
An official journal of the KPS
www.elsevier.com/locate/cap
www.kps.or.kr

# Dielectric properties of PIN–PT ceramics under compressive stress

R. Yimnirun *, S. Wongsaenmai, S. Ananta, N. Triamnak

*Department of Physics, Faculty of Science, Chiang Mai University, Chiang Mai 50200, Thailand*

Received 25 December 2006; received in revised form 30 September 2007; accepted 26 March 2008
Available online 4 April 2008

**Abstract**

Lead indium niobate, $Pb(In_{1/2}Nb_{1/2})O_3$ or (PIN), is an interesting ferroelectric material, because it can be changed from a disordered state to ordered state by long-time thermal annealing. However, the temperature related to the maximum dielectric constant ($T_{max}$) of PIN in relaxor phase is low (at 1 kHz, $T_{max} = 66$ °C). In this study, to increasing $T_{max}$ of PIN, lead titanate, $PbTiO_3$(PT) was thus added to PIN with compositions $(1 - x)$PIN–$x$PT (for $x = 0.1$–$0.5$). The influence of stress on the dielectric properties of $(1 - x)$PIN–$x$PT ceramics was then investigated. The dielectric properties were measured under various uniaxial compressive stress up to 400 MPa. The results showed that the superimposed compression load reduced the dielectric constant in 0.9PIN–0.1PT. For the other compositions, the dielectric constants first increased with the compressive stress, and then decreased when the stress was further increased up to 400 MPa. The dielectric loss tangent of all composition was found to decrease with increasing compressive stress.
© 2008 Elsevier B.V. All rights reserved.

*PACS:* 77.84.Dy; 77.80.−e; 77.80.Fm

*Keywords:* Dielectric properties; PIN–PT; Stress

## 1. Introduction

Piezoelectric and ferroelectric ceramics are widely used in devices such as actuators and transducers. However, when they are used in devices specified above, these ceramics are often subjected to self-induced or under environmental stresses [1–3]. A prior knowledge of the effects of stresses on the material properties is crucial for proper design of a device and for suitable selection of materials for a specific application [4–6]. Therefore, it is very important to obtain experimental data, as well as to better understand how these materials behave under stress. Recently, the compressive stress dependence of dielectric properties has been studied in materials such as $BaTiO_3$ (BT), $Pb(Zr_{0.52}Ti_{0.48})O_3$ (PZT), $Pb(Mg_{1/3}Nb_{2/3})O_3$ (PMN), $Pb(Mg_{1/3}Nb_{2/3})O_3$–$PbTiO_3$ (PMN–PT), $Pb(Mg_{1/3}Nb_{2/3})O_3$–$Pb(Zr_{0.52}Ti_{0.48})O_3$ (PMN–PZT), and $Pb(Zr_{0.52}Ti_{0.48})O_3$–$BaTiO_3$ (PZT–BT) [7–13]. The results clearly showed that the effects of stress on the dielectric properties depended significantly on ceramic compositions and stress levels.

Recently, there have been a great deal of interest in lead indium niobate, $Pb(In_{1/2}Nb_{1/2})O_3$ or PIN, because it can be obtained in a disordered state and can be made to exhibit a transition from disordered state to ordered state by long-time thermal annealing. In the disordered state, PIN is a relaxor ferroelectric (RFE) with rhombohedral symmetry. On the other hand, the ordered PIN structure is antiferroelectric (AFE) with orthorhombic symmetry [14]. However, the temperature related to the maximum dielectric constant ($T_{max}$) of PIN in RFE phase is low (at 1 kHz, $T_{max} = 66$ °C) [15,16]. Thus, to enhance the dielectric properties of PIN (as well as increasing $T_{max}$), lead titanate, $PbTiO_3$ (PT) is added to PIN with compositions $(1 - x)$PIN–$x$PT (for $x = 0.1$–$0.5$). Practically, there have been many previous reports on the electrical properties of PIN and PT ceramics, but there has been no systematic study on the influence of an applied stress on the dielectric properties of the PIN–PT ceramics. Therefore, it is the aim of this study to

* Corresponding author. Tel.: +66 53 943 367; fax: +66 53 943 445.
*E-mail address:* rattikornyimnirun@yahoo.com (R. Yimnirun).

1567-1739/$ - see front matter © 2008 Elsevier B.V. All rights reserved.
doi:10.1016/j.cap.2008.03.013

determine the dielectric properties of the $(1-x)$PIN–$(x)$PT ceramics as a function of compressive stress.

## 2. Experimental method

$(1-x)Pb(In_{1/2}Nb_{1/2})O_3$–$(x)PbTiO_3$ (for $x = 0.1$–$0.5$) ceramics were prepared from two stage mixed-oxide method. First, $InNbO_4$ was prepared from oxide powders of $Nb_2O_5$ and $In_2O_3$. The powders were mixed by via a rapid vibratory mill for 30 min in alcohol. After drying, the mixture was calcined at 1100 °C for 2 h to obtain the intermediate precursor $InNbO_4$ [17]. Next, the precursor was mixed with appropriate amount of PbO and $TiO_2$ by via a rapid vibratory mill for 30 min. For optimization purpose, the mixtures were calcined at temperatures between 800 and 900 °C for 2 h. After calcination, the powders were pressed hydraulically to form disc-shaped pellets 10 mm in diameter and 1 mm thick, with 3 wt% polyvinyl alcohol as a binder. Finally, the disc-shaped pellets were sintered at temperatures between 1100 and 1125 °C for 2 h. Detailed preparation process is given elsewhere [18].

Before studying the dielectric properties under the compressive stress, the specimens were lapped to obtain parallel faces. After coating with silver paint as electrode at the faces, the specimens were heated at 750 °C for 12 min to ensure the contact between the electrode and surface of ceramic. The ceramics were poled at 150 °C under a field of 25 kV/cm and field-cooled to room temperature. To study effects of the stress on the dielectric properties of the ceramic, the compressometer was constructed for simultaneous applications of the mechanical stress and the electric field [19]. The compressometer cell consisting of a cylindrical brass cell with a heavy brass base, a brass ram and a precisely guided loading platform provides true uniaxial stress during mechanical loading. The prepared specimen is carefully placed between the two alumina blocks and the electric field is applied to the specimen via the copper shims attached to the alumina blocks. With this setting, the uniaxial compressive stress is applied parallel to the electric field direction. The uniaxial compressive stress is supplied by the servohydraulic load frame and the applied stress level is monitored with the pressure gage of the load frame. Measurements are performed as a function of mechanical pre-stress applied discretely [20]. The dielectric properties were measured by LCR-meter (Instrek LCR-821). The room temperature (25 °C) capacitance and the dielectric loss tangent are determined at frequency range 1–200 kHz under compressive pre-stress levels of 0–400 MPa. The dielectric constant was then calculated from a parallel-plate capacitor equation, e.g., $\varepsilon_r = Cd/\varepsilon_0 A$, where $C$ is the capacitance of the specimens, $d$ and $A$ are, respectively, the thickness and the area of the electrode, and $\varepsilon_0$ is the dielectric permittivity of vacuum ($8.854 \times 10^{-12}$ F/m).

## 3. Results and discussion

Since this work reports the dielectric properties of PIN–PT ceramics under the application of compressive pre-stress, the following paragraph is only served as preliminary information on structural and dielectric characteristics under stress-free condition, which are of important in the discussion of the influence of stress on the dielectric properties of the ceramics. More information on the above mentioned characteristics can be found in previous publications [21,22]. By X-ray diffraction method, the phase and structural information of the PIN–PT ceramics was established [22]. In general, pseudo-cubic symmetry was observed at low PT contents ($x = 0.1$, 0.2 and 0.3), in agreement with other workers [23,24]. However, by the influence of PT, the tetragonal symmetry had developed in compositions with $x = 0.4$ and 0.5. The dielectric constant ($\varepsilon_r$) was also measured as functions of both temperature and frequency, as previously described in details in previous publications [21,22]. In compositions $x = 0.4$ and 0.5, the dielectric properties were nearly independent of frequency, except in the vicinity of the phase transformation temperature; a typical characteristic of normal ferroelectrics [23,24]. At low PT contents, the dielectric behavior was shifted towards that of relaxor materials. The dielectric properties of the compositions with $x \leqslant 0.3$ exhibited a diffuse phase transition with dielectric peak broadening [24]. As listed in Table 1, the high value of dielectric constant under stress-free condition at room temperature is obtained in ceramic composition with $x = 0.4$, because of its vicinity to the morphotropic phase boundary (MPB) of PIN–PT system, as reported earlier [14,21,22].

The dielectric properties at 100 kHz of $(1-x)$PIN–$(x)$PT ceramics as a function of compressive stress are depicted in Figs. 1 and 2. For better comparison, the dielectric properties of each composition under stress are normalized to the stress-free values. Clearly, there is a significant change of both the dielectric constant and the dielectric loss tangent with stress from 0 to 400 MPa and returning to stress-free condition. As depicted in Fig. 1, the changes of the dielectric constant with the stress can be divided into two groups. For pseudo-cubic compositions ($x = 0.1$–$0.3$), the dielectric constant changes drastically with the applied stress. The dielectric constant changes more than 5–35%, when the stress reaches 400 MPa. The change of the dielectric constant during loading and unloading does not follow the same path. The dielectric constant of these compositions either initially increases then decreases until maximum stress, or only

Table 1
Characteristics of PIN–PT ceramics with optimized processing conditions Refs. [21,22]

| Ceramic | Sintering temperature (°C) | Density (g/cm$^3$) | $T_{max}$ (°C) | Stress-free dielectric properties | |
|---|---|---|---|---|---|
| | | | | $\varepsilon_{r,\ room}$ | $\varepsilon_{r,\ max}$ |
| 0.9PIN–0.1PT | 1100 | 7.78 | 134 | 2275 | 5756 |
| 0.8PIN–0.2PT | 1125 | 7.85 | 213 | 863 | 6863 |
| 0.7PIN–0.3PT | 1125 | 7.81 | 292 | 689 | 6154 |
| 0.6PIN–0.4PT | 1125 | 7.85 | 355 | 1132 | 6674 |
| 0.5PIN–0.5PT | 1125 | 7.80 | 398 | 483 | 13422 |

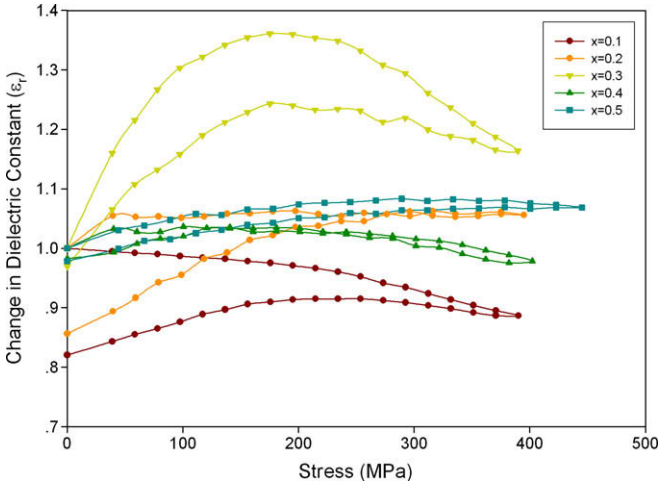



Fig. 1. Relative changes of dielectric constant ($\varepsilon_r$) with compressive stress for $(1-x)$PIN–$(x)$PT ceramics (measured at 25 °C and 100 kHz).

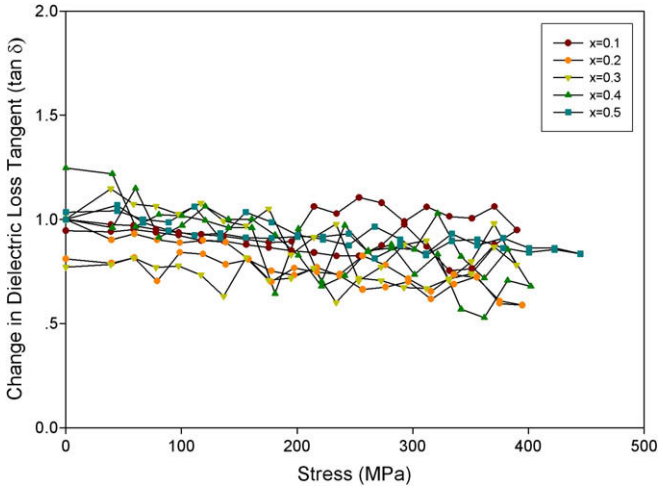



Fig. 2. Relative changes of dielectric loss tangent ($\tan\delta$) with compressive stress for $(1-x)$PIN–$(x)$PT ceramics (measured at 25 °C and 100 kHz).

decreases with increasing stress. On the other hand, for the tetragonal compositions, with $x$ values of 0.4 and 0.5, the dielectric constant shows very little change with stress. In addition, the compressive stress dependence of the dielectric loss tangent ($\tan\delta$) is observed, as shown in Fig. 2. It can be seen that the dielectric loss tangents during loading and unloading are not significantly different. It is also noticed that the changes in the dielectric properties with the compressive stress obtained in this study are in parts similar to those for PMN–PZT and PMN–PT systems in earlier investigations [10,11].

To understand these experimental results, at least qualitatively, various effects have to be considered. When a compressive stress is applied to the ferroelectric materials in the direction parallel to the poling direction, the domain structure in the material will change to maintain the domain energy at a minimum, because the stress will move some of the polarization away from the poling direction; during this process some of the domains engulf other domains or change shape irreversibly. Under a stress, the domain structure of ferroelectric ceramics may undergo domain switching through non-180° domain walls, de-aging, de poling and clamping of domain walls [10].

The experimental observations, both the drastic change case and the very little change case, can be attributed to competing influences, in an opposite way, of the intrinsic contribution of domains and the extrinsic contribution of re-polarization and growth of micro-polar regions. Under the applied compressive stress, the non-180° domain wall density increases. Hence, the increase of the dielectric constant is observed. The de-aging mechanism, which also increases the dielectric constant [9–11], is also expected to play a role here. Therefore, a combination of the domain switching and the de-aging mechanisms is believed to be a reason for the increase of the dielectric constant during low-stress application, i.e., PIN–PT with $x = 0.2$, 0.3, 0.4 and 0.5. With further increase in the stress, the stress clamping of domain walls, which results in a decrease of domain wall mobility, and the stress induced decrease in switchable part of spontaneous polarization are expected to play a role in the decrease of the dielectric constant [9,10]. In addition, in case of 0.9PIN–0.1PT the continuous decrease in the dielectric constant can be attributed to the switching of 90° domains, which causes the significant decrease in the dielectric constant, as seen in Fig. 1. The cause of the stress dependence of the dielectric loss tangent is a little more straightforward. As depicted in Fig. 2, the clamping of the domain walls under the compressive stress results in a decrease of domain wall mobility and reduces the dielectric loss tangent [25]. This is a reversible effect with the domain wall mobility returning to near the original values, when the applied stress is removed, as seen in Fig. 2 that the dielectric loss tangents return to near their original values after a stress cycle. In addition, a significant decrease in the dielectric constant after a full cycle of stress application has been observed and attributed to the stress induced decrease in switchable part of spontaneous polarization at high stress and the irreversible 90° domain switching [10,25].

## 4. Conclusions

In this study, the dielectric properties of PIN–PT ceramics with a formula $(1-x)Pb(In_{1/2}Nb_{1/2})O_3$–$(x)PbTiO_3$ (for $x = 0.1$–0.5) prepared by a two stage mixed-oxide method are measured under the compressive stress from 0 to 400 MPa. The results clearly show that the superimposed compression stress has pronounced effects on both the dielectric constant and the dielectric loss tangent of PIN–PT ceramics. The observations are mainly interpreted in terms of competing influences of the intrinsic contribution, and the extrinsic contribution from domain switching through non-180° domain walls, clamping of domain walls, de-aging, and the stress induced decrease in switchable part of spontaneous polarization.

## Acknowledgements

This work was supported by the Thailand Research Fund (TRF), Commission on Higher Education (CHE), Development and Promotion of Science and Technology Talents Project (DPST), Faculty of Science and Graduate School of Chiang Mai University.

## References

[1] J. Kuwata, K. Uchino, S. Nomura, Jpn. J. Appl. Phys. 21 (1982) 1298.
[2] S. Park, T.R. Shrout, J. Appl. Phys. 82 (4) (1997) 1804.
[3] D. Viehland, J. Powers, Appl. Phys. Lett. 78 (20) (2001) 3112.
[4] L.E. Cross, Ferroelectric 76 (1987) 241.
[5] K. Uchino, Piezoelectric Actuators and Ultrasonic Motors, Kluwer Academic, Boston, 1997.
[6] D. Stansfield, Underwater Electroacoustic Transducers, Bath University Press, Bath, 1991.
[7] R. Yimnirun, S. Ananta, S. Chamunglap, Mater. Chem. Phys. 102 (2007) 165.
[8] R. Yimnirun, S. Ananta, A. Ngamjarurojana, S. Wongsaenmai, Curr. Appl. Phys. 6 (3) (2006) 520.
[9] G. Yang, S.F. Liu, W. Ren, B.K. Mukherjee, Proc. SPIE Sym. Smart Struct. Mater. 3992 (2000) 103.
[10] R. Yimnirun, M. Unruan, Y. Laosiritaworn, S. Ananta, J. Phys. D 39 (2006) 3097.
[11] R. Yimnirun, Int. J. Mod. Phys. B 20 (23) (2006) 3409.
[12] D. Zhou, M. Kamlah, D. Munz, J. Eur. Ceram. Soc. 25 (2005) 425.
[13] S. Wongsaenmai, S. Ananta, E. Meechoowas, R. Yimnirun, J. Phys. D 36 (2003) 1615.
[14] E.F. Alberta, A.S. Bhalla, J. Kor. Phys. Soc. 32 (1998) 1265.
[15] A. Halliyal, U. Kumar, U. Kumar, R.E. Newnham, L.E. Cross, Am. Ceram. Soc. Bull. 66 (4) (1987) 671.
[16] J.R. Belsick, A. Halliyal, U. Kumar, R.E. Newnham, Am. Ceram. Soc. Bull. 66 (4) (1987) 664.
[17] N. Yasuda, M. Fujie, Jpn. J. Appl. Phys. 31 (1992) 3128.
[18] S. Wongsaenmai, O. Khamman, S. Ananta, R. Yimnirun, J. Electroceram., in press. doi: 10.1007/s10832-007-9311-3.
[19] R. Yimnirun, S. Ananta, A. Ngamjarurojana, S. Wongsaenmai, Appl. Phys. A: Mater. Sci. Proc. 81 (2005) 1227.
[20] R. Yimnirun, Y. Laosiritaworn, S. Wongsaenmai, J. Phys. D: Appl. Phys. 39 (2006) 759.
[21] S. Wongsaenmai, A. Bhalla, X. Tan, S. Ananta, R. Yimnirun, Ferroelectr. Lett. 34 (2007) 36.
[22] Wongsaenmai, X. Tan, S. Ananta, R. Yimnirun, J. Alloys Comps. 454 (2008) 331.
[23] N. Vittayakorn, G. Rujijanagul, T. Tunkasiri, X. Tan, D.P. Cann, J. Mater. Res. 18 (2003) 2882.
[24] N. Vittayakorn, G. Rujijanagul, X. Tan, H. He, M.A. Marquardt, D.P. Cann, J. Electroceram. 16 (2006) 141.
[25] Q.M. Zhang, J. Zhao, K. Uchino, J. Zheng, J. Mater. Res. 12 (1997) 226.

International Journal of Modern Physics B
Vol. 23, No. 1 (2009) 105–111
© World Scientific Publishing Company

World Scientific
www.worldscientific.com

# ELECTRICAL PROPERTIES OF Nb-DOPED $Pb(Zr_{0.52}Ti_{0.48})O_3$ CERAMICS

PIYACHON KETSUWAN, YONGYUT LAOSIRITAWORN,
SUPON ANANTA and RATTIKORN YIMNIRUN*

*Department of Physics, Faculty of Science,*
*Chiang Mai University, Chiang Mai 50200, Thailand*
**rattikornyimnirun@yahoo.com*

Received 30 July 2008

The $Pb(Zr_{0.52}Ti_{0.48})O_3$ ceramics with 0.75, 1.0, 1.25 and 1.50%wt of $Nb_2O_5$ addition were prepared by a conventional mixed oxide technique. It was found that the average grain size of the ceramics decreased from 6 to 1 $\mu$m with increasing doping concentration to 1.5%wt. The room temperature dielectric constant and $d_{33}$ reached maximum values of 1050 and 285 pC/N, respectively, at 1%wt Nb-doping. The electrical coercivity ($E_c$) of Nb-doped PZT decreased, while the polarization values increased, with increasing doping concentration. Most importantly, this study shows that $Nb_2O_5$-doped PZT ceramics exhibits soft piezoelectric and enhanced ferroelectric behaviors, and the optimum properties can be obtained using suitable doping concentration.

*Keywords*: Ferroelectric properties; dielectric properties; Nb-doped PZT.

## 1. Introduction

$Pb(Zr_{0.52}Ti_{0.48})O_3$ is a composition near the morphotropic phase boundary (MPB) of $Pb(Zr,Ti)O_3$ that separates rhombohedral and tetragonal ferroelectric forms with the coexistence of the 14 orientation states: 6-tetragonal and 8-rhombohedral. That is essential to allow the strong polarization for piezoelectricity. As the MPB is nearly vertical on the phase diagram, intrinsic property persists over a wide temperature range.[1] Almost all useful PZT ceramics are doped or modified to improve properties for specific applications.[2] Lead zirconate titanate solid solution modifications are controlled by aliovalent cation additions. The excess charge cation addition is called donor doped or soft PZTs, and the charge deficient cation is acceptor doped or hard PZTs. One approach of modification is off-valent donor doping, such as $Nb^{5+}$ replacing $Zr^{4+}$. This makes the domain wall move more easily and results in enhanced dielectric constant and coupling factor but reduced electric coercivity.[3]

*Corresponding author.

However, there have only been a few reports on the effect of doping concentration of electrical properties of Nb-doped PZT ceramics prepared with conventional mixed-oxide method.[4–7] This study is therefore aimed at detailed and comprehensive investigation on the effect of doping $Pb(Zr_{0.52}Ti_{0.48})O_3$ with 0.75, 1.0, 1.25 and 1.50%wt of $Nb_2O_5$ addition on dielectric, piezoelectric and ferroelectric properties.

## 2. Experimental Method

The $Pb(Zr_{0.52}Ti_{0.48})O_3$ ceramics with addition of 0.75, 1.0, 1.25 and 1.50%wt $Nb_2O_5$ were prepared by conventional mixed oxide technique from PbO (Fluka 99.0%), $ZrO_2$ (Fluka 99.0%), $TiO_2$ (Fluka 99.9%) and $Nb_2O_5$ (Aldrich 99.9%) powders. After ball milling in ethanol for 24 h, the slurry was dried and calcined at 975°C for 2 h.[8] Then, the calcined powder was pressed into discs ($d$ = 10 mm). The pellets were placed inside a closed alumina crucible covered with lead zirconate ($PbZrO_3$) powder to compensate the PbO volatilization and sintered at 1250°C for 2 h.

The X-ray diffraction (XRD) was used for structure and phase formation analysis. The microstructure was observed by scanning electron microscope (SEM). The bulk densities of sintered discs were measured by the Archimedes method. The dielectric, piezoelectric and ferroelectric properties were determined by automated LCR-meter, $d_{33}$-meter and a Sawyer-Tower circuit, respectively. The specimens were poled under 20 kV/cm at 120°C for 30 min in silicone oil.[9,10]

## 3. Results and Discussion

The X-ray diffraction pattern of $Nb_2O_5$ doped $Pb(Zr_{0.52}Ti_{0.48})O_3$ ceramics with varying concentration is shown in Fig. 1. The peak intensity indicates the formation of perovskite phases, which could be matched with JCPDS file 73-2022 for rhombohedral phase of PZT and JCPDS file 33-0784 for tetragonal phase of PZT. It should be noticed that the coexistence of tetragonal and rhombohedral phase for the undoped and doped PZT at 0.75 and 1.0%wt, which was characterized by (020) and (200) peaks. Finally, the rhombohedral phase became dominant at 1.25 and 1.5%wt.

The densification behavior of the specimens is shown in Fig. 2. The density increases at first with increasing doping concentration from 0.75 to 1.0%wt. Then a drop of the densification is observed when the concentration is further increased. However, the density of doped specimens is smaller than the undoped condition. The surface morphology of sintered ceramics was observed by using scanning electron microscope (SEM), as shown in Fig. 3. The mean grain size of the ceramics was determined by using the line intercept method. The mean grain size tends to decrease with increasing doping concentration. Similar observations have been reported in other systems.[4,6,7] This observation indicates that $Nb_2O_5$ addition had inhibited grain growth during the solid-solution process, as also reported earlier.[11,12]

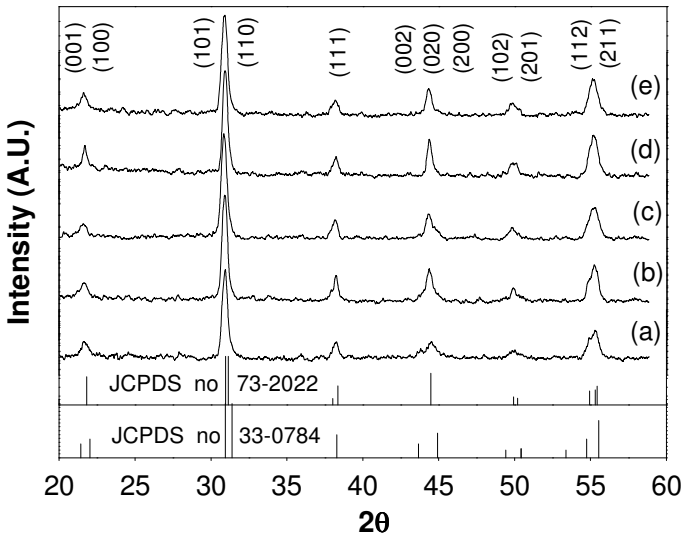



Fig. 1. XRD pattern of $Nb_2O_5$-doped $Pb(Zr_{0.52}Ti_{0.48})O_3$ ceramics sintered at 1250°C for 2 h with varying concentration (a) 0%wt, (b) 0.75%wt, (c) 1.0%wt, (d) 1.25%wt and (e) 1.5%wt.

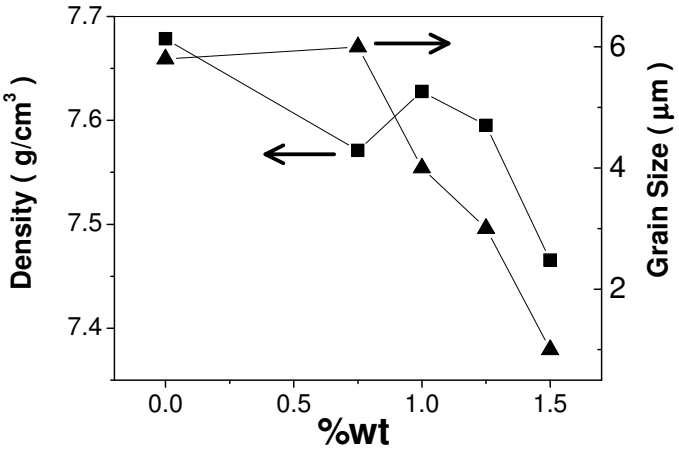



Fig. 2. Dependence of density and grain size of $Nb_2O_5$-doped $Pb(Zr_{0.52}Ti_{0.48})O_3$ ceramics on the doping concentration.

The room temperature dielectric constant and piezoelectric $d_{33}$-constant show a similar trend that is observed on densification behavior. The $\varepsilon_r$ and $d_{33}$-constants increase with increasing doping from 0.75 to 1.0%wt. Then a drop of the $\varepsilon_r$ and $d_{33}$ is observed when the concentration is further increased, as shown in Fig. 4. In addition, both values of $Nb_2O_5$ doped samples are better than those of the undoped sample. This trend is also observed in $Pb(Zr_{0.51}Ti_{0.49})O_3$ ceramics doped with 5.5 mol% $Nb_2O_5$ as reported by Chu *et al.*[7]

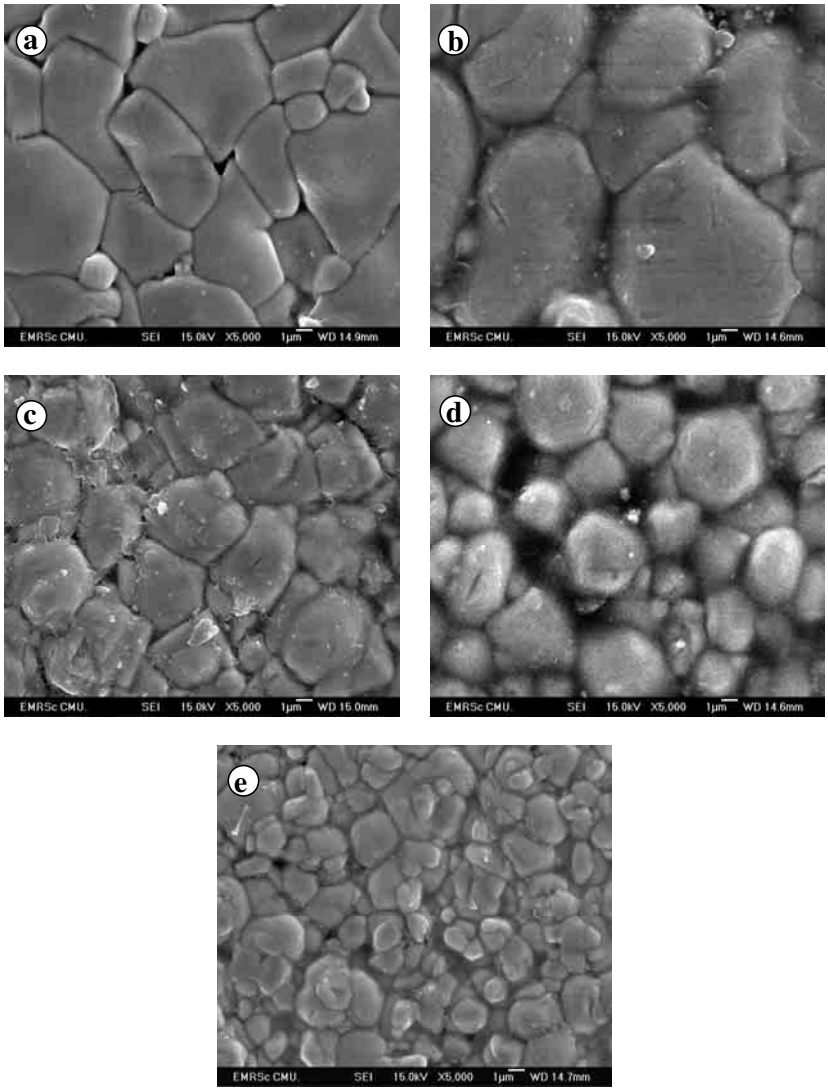



Fig. 3. SEM micrographs of $Nb_2O_5$-doped $Pb(Zr_{0.52}Ti_{0.48})O_3$ ceramics with doping concentration (a) 0%wt, (b) 0.75%wt, (c) 1.0%wt, (d) 1.25%wt and (e) 1.5%wt.

The ferroelectric hysteresis behavior of $Pb(Zr_{0.52}Ti_{0.48})O_3$ with addition of 0.75, 1.0, 1.25 and 1.50%wt $Nb_2O_5$ is shown in Fig. 5. The electrical coercivity ($E_c$) is seen to decrease, while the polarization values increase with increasing doping concentration. These observations clearly indicate the soft piezoelectric behavior of Nb-doped PZT, as expected.

It should also be noted that earlier investigations[11,13,14] observed enhanced electrical properties, particularly dielectric properties, with decreasing grain size in

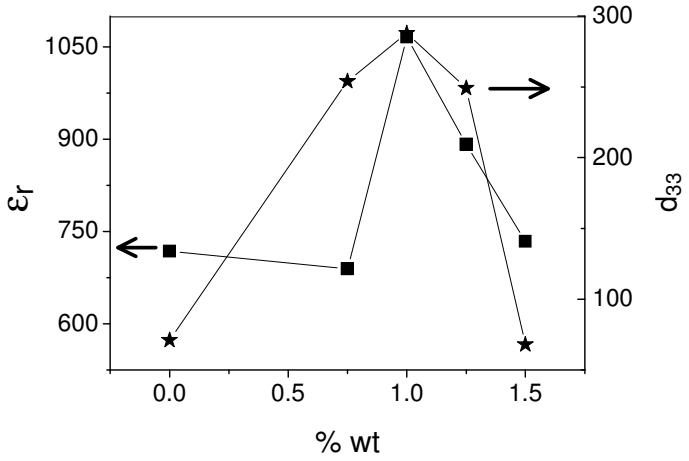



Fig. 4. The room temperature dielectric constant measured at 1 kHz and piezoelectric $d_{33}$-constant as a function of doping concentration of $Nb_2O_5$-doped $Pb(Zr_{0.52}Ti_{0.48})O_3$ ceramics.

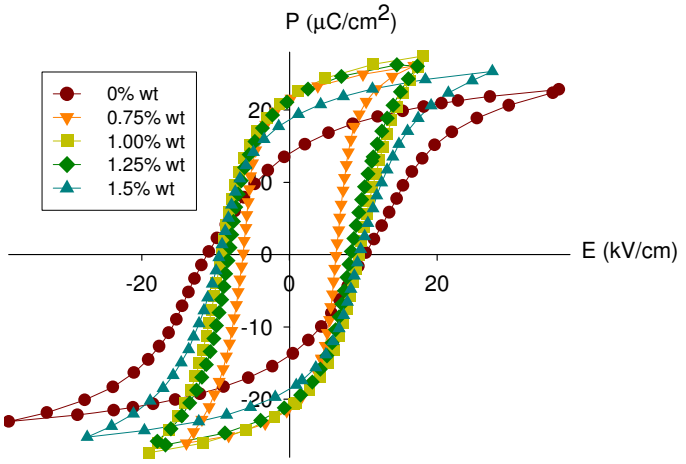



Fig. 5. P-E hysteresis loops of $Nb_2O_5$-doped $Pb(Zr_{0.52}Ti_{0.48})O_3$ ceramics.

perovskite ferroelectrics, such as PZT-based and BT-based ceramics. Therefore, one could state that the enhanced electrical properties observed in this study are partly due to decreasing grain size, as observed in Fig. 3. However, it should also be pointed out that there is a competing influence of the decreased density, which generally deteriorates electrical properties. These two competing microstructural features result in nearly constant dielectric constant ($\varepsilon_r$) in undoped and 0.75%wt $Nb_2O_5$ doped PZT ceramics, as shown in Fig. 4. However, with further increase in $Nb_2O_5$ concentration to 1.0%wt, the significant increase of $\varepsilon_r$ is observed, possibly due to increased density and decreased grain size simultaneously. Although the grain

size continues to decrease with higher $Nb_2O_5$ concentration, the dielectric constant decreases significantly, likely due to a strong decrease in the density. Another possible reason for the decrease in the dielectric constant, as well as the $d_{33}$ constant, beyond 1.0%wt $Nb_2O_5$ addition is a phase transition from mixed tetragonal and rhombohedral to mainly rhombohedral, as described earlier and shown in Fig. 1.

In addition to the relationship between the phase and microstructural features, and the electrical properties as described above, enhanced electrical properties can also be attributed to the softening effect with addition of $Nb_2O_5$ into PZT ceramics. As is well-known, a soft doping ion may soften the properties of piezoelectric ceramics, i.e., dielectric constant ($\varepsilon_r$) and piezoelectric $d_{33}$ constant are enhanced, while the coercivity is reduced, as observed in Figs. 4 and 5. When ions with small ionic radius like $Nb^{5+}$ enter into the perovskite lattice of PZT, they occupy the B-sites to replace $Zr^{4+}/Ti^{4+}$ ions. Since the doping ions have higher valence than +4, extra positive charges entering the lattice and Pb vacancies have to be created to ensure electroneutrality. In a lattice having Pb vacancies, transfer of atoms is easier than in a perfect lattice; thus domain motions can be caused by a smaller electric field.[13,15] Therefore, the coercivity of $Nb_2O_5$ doped PZT ceramics is reduced, as compared to undoped PZT, as seen in Fig. 5. In addition, Pb-vacancies are negatively charged, and these can be paired with $Nb^{5+}$ ions to form defect dipoles, which can be aligned when there is a spontaneous polarization or when there is an applied electric field. This will create a larger polarization, and hence explain why the doped PZT has larger polarization values than the undoped PZT, as seen in Fig. 5. The decrease in the $d_{33}$ constant and the polarization values for PZT ceramics containing more than 1.0%wt $Nb_2O_5$ is likely due to the significant decrease in the density and the phase transition from mixed tetragonal and rhombohedral to mainly rhombohedral, as described earlier.

## 4. Conclusion

The effects of doping on the electrical properties of $Pb(Zr_{0.52}Ti_{0.48})O_3$ ceramics with addition of 0.75, 1.0, 1.25 and 1.50%wt $Nb_2O_5$ were investigated. The density increases at first with increasing doping concentration from 0.75 to 1.0%wt. Then a drop of the densification is observed when the concentration is further increased. It was found that the average grain size of the ceramics decreased from 6 to 1 $\mu$m with increasing $Nb_2O_5$ doping concentration to 1.5%wt. The room temperature dielectric constant and $d_{33}$ reached maximum values of 1050 and 285 pC/N, respectively, at 1%wt Nb-doping. The electrical coercivity decreases, while the polarization values increase, with increasing doping concentration.

## Acknowledgments

This work was supported by the Thailand Research Fund (TRF), Commission on Higher Education (CHE), Graduate School and Faculty of Science, Chiang Mai University.

## References


1. L. E. Cross, *Mater. Chem. Phys.* **43**, 108 (1996).
2. G. H. Haertling, *J. Amer. Ceram. Soc.* **82**(4), 797 (1999).
3. K. Okazaki and K. Nagata, *J. Amer. Ceram. Soc.* **56**, 82 (1973).
4. M. Takahashi and S. Takahashi, *Jpn. J. Appl. Phys.* **9**, 1009 (1970).
5. M. D. Durruthy, *J. Mater. Sci.* **34**, 2311 (1999).
6. C. L. Huang, B. H. Chen and L. Wu, *Solid State Commun.* **130**, 19 (2004).
7. S. Y. Chu, T. Y. Chen, I. T. Tsai and W. Water, *Sensor and Actuators A* **113**, 198 (2004).
8. W. Chaisan, R. Yimnirun, S. Ananta and D. P. Cann, *Mater. Lett.* **59**(28), 3732 (2005).
9. R. Yimnirun, S. Ananta and P. Laoratanakul, *J. Eur. Ceram. Soc.* **25**(13), 3225 (2005).
10. R. Yimnirun, *Ferroelectrics* **331**, 9 (2006).
11. V. Singh, H. H. Kumar, D. K. Kharat, S. Hait and M. P. Kulkarni, *Mater. Lett.* **60**, 2964 (2006).
12. D. M. Hammer and M. J. Hoffmann, *J. Am. Ceram. Soc.* **81**, 3277 (1998).
13. R. F. Zhang, H. P. Zhang, J. Ma, Y. Z. Chen and T. S. Zhang, *Solid State Ionics* **166**, 219 (2004).
14. R. Yimnirun, R. Tipakorntitikul and S. Ananta, *Int. J. Mod. Phys. B* **20**(17), 2415 (2006).
15. W. Qiu and H. H. Hng, *Mater. Chem. Phys.* **75**, 151 (2002).

International Journal of Modern Physics B
Vol. 23, No. 3 (2009) 403–410
© World Scientific Publishing Company

World Scientific
www.worldscientific.com

# DIELECTRIC PROPERTIES OF LEAD MAGNESIUM NIOBATE-LEAD TITANATE CERAMICS PREPARED BY MIXED-OXIDE METHOD

RATTIKORN YIMNIRUN

*Department of Physics, Faculty of Science, Chiang Mai University, Chiang Mai 50200 Thailand*
*rattikornyimnirun@yahoo.com*

Received 9 September 2006

In this study, the $(1-x)\mathrm{Pb}(\mathrm{Mg}_{1/3}\mathrm{Nb}_{2/3})\mathrm{O}_{3-x}\mathrm{PbTiO}_3$ (when $x = 0.1$, 0.3 and 0.5) ceramics were prepared from PMN and PT powders by a mixed-oxide method. The dielectric properties of the ceramics were measured as functions of both temperature ($-150$–$400^\circ$C) and frequency (100 Hz–1 MHz). The results indicated that the dielectric properties of pseudo-cubic phase 0.9PMN-0.1PT and tetragonal phase 0.5PMN-0.5PT ceramics followed that of relaxor and normal ferroelectric behaviors, respectively, while the dielectric behaviors of a near MPB phase 0.7PMN-0.3PT ceramic showed a mixture of normal and relaxor ferroelectric behaviors. In addition, the Curie temperature ($T_C$) increased with increasing PT contents, while the diffusivity decreased. This confirmed a gradual transition from a relaxor ferroelectric behavior in 0.9PMN-0.1PT to a normal ferroelectric behavior in 0.5PMN-0.5PT. The difference in dielectric behaviors was attributed to the structural symmetry of the ceramics.

*Keywords*: PMN-PT; dielectric properties.

## 1. Introduction

Ceramics are one of the many classes of electronic materials. The electronic industries are demanding smaller, higher packing density and higher frequency electronic devices.[1] Among those features, volume efficiency can be easily improved by reduction of the dimensions of devices and by increasing the dielectric constant of the materials used. This is particular in the case for capacitor industry, in which uses of high dielectric constant ceramics are of great success. A family of materials which dominates the industry is lead-based ferroelectrics, especially lead magnesium niobate, $\mathrm{Pb}(\mathrm{Mg}_{1/3}\mathrm{Nb}_{2/3})\mathrm{O}_3$ or PMN, and its solid solution with lead titanate, $\mathrm{PbTiO}_3$ or PT, the so-called PMN-PT compounds, which show dielectric constant in excess of 20,000, making them candidate materials for capacitors.[2] In addition, they exhibit electrostrictive behavior at temperatures above their transition temperatures. This particular feature leads to their uses in transducers and actuators.[3,4]

Lead magnesium niobate (PMN) is generally established as a representative of relaxor ferroelectrics. Although the Curie temperature of PMN is well below room temperature,[5] it can be easily shifted upward with PT addition, a normal ferroelectric compound which has a transition at 490°C. A spontaneous phase transition is indicated in the solid solution PMN-PT as a result of a change in the degree of ordering induced by substitution of cationic sites. An addition of ∼28% PT causes the material to revert to a normal ferroelectric tetragonal phase with $T_C \sim 130$°C. The $(1-x)$PMN-$(x)$PT system also shows a morphotropic phase boundary (MPB) near $x \sim 0.4$, separating pseudo-cubic phase and tetragonal phases. As observed in other systems such as PZN-PT and PZT, anomalously large dielectric and piezoelectric properties are observed for compositions lying near the MPB.[6] This study is aimed at investigating the dielectric properties, as functions of both temperature and frequency, of ceramics in PMN-PT system. In particular, three compositions, 0.9PMN-0.1PT, 0.7PMN-0.3PT and 0.5PMN-0.5PT representing pseudo-cubic, near MPB and tetragonal phases, respectively, are chosen for the study to examine the roles of MPB, as well as to establish the structure-property relations for the PMN-PT system.

## 2. Materials and Methods

The $Pb(Mg_{1/3}Nb_{2/3})O_3$–$PbTiO_3$ ceramics were prepared from PMN and PT powders by a mixed-oxide method. Perovskite-phase PMN powders were obtained via a well-known columbite method,[7] while PT powders were prepared by a more conventional mixed-oxide method. For PMN powders, the magnesium niobate ($MgNb_2O_6$) powders were first prepared by mixing starting MgO (>98%) (Fluka, Switzerland) and $Nb_2O_5$ (99.9%) (Aldrich, Germany) powders and then calcining the mixed powders at 1100°C for 3 hours with the heating/cooling rates of 20°C/min. This yielded a so-called columbite powder ($MgNb_2O_6$). The columbite powders were subsequently ball-milled with PbO (99%) for 24 hours. The mixed powders were calcined at 800°C for 1 hour with the heating/cooling rates of 20°C/min. X-ray diffraction analysis was employed to confirm the formation of perovskite-phase PMN. PT powders were prepared from reagent-grade PbO (99%) and $TiO_2$ (98.5%) starting powders (Fluka, Switzerland). These powders were ball-milled for 24 hours and then calcined at 600°C for 1 hour with the heating/cooling rates of 20°C/min. The $(1-x)Pb(Mg_{1/3}Nb_{2/3})O_{3-x}PbTiO_3$ powders (when $x = 0.1$, 0.3 and 0.5) were subsequently prepared from the precursor PMN and PT powders by a mixed-oxide technique. Initially, PMN and PT powders for a given composition were weighed and then ball-milled in ethanol for 24 hours. The mixed powders were calcined for 2 hours at 900, 800 and 750°C for compositions with $x = 0.1$, 0.3 and 0.5, respectively, with the heating/cooling rates of 20°C/min. To fabricate PMN-PT ceramics, the calcined powders were pressed hydraulically to form disc-shaped pellets 15 mm in diameter and 2 mm thick, with 5 wt.% polyvinyl alcohol (PVA) as a binder. The pellets were stacked in a covered alumina crucible. Finally, the sintering was

carried out at a sintering temperature for 2 hours with 15 min/°C heating and cooling rates. The sintering temperature was optimized at 1240°C for compositions with $x = 0.1$ and 0.3, and at 1220°C for composition with $x = 0.5$. More details of the powder and ceramic preparation studies were described thoroughly in previous publication[8] and will not be included in this present context, which is focused on the dielectric properties of the successfully prepared ceramics.

The dielectric properties of the sintered ceramics were studied as functions of both temperature and frequency with an automated dielectric measurement system. The computer-controlled dielectric measurement system consisted of an LCR-meter (Hewlett–Packard Precision LCR-Meter HP 4284A), a temperature chamber (Delta Design 9023) and a computer system. The detailed description of this system was explained elsewhere.[9] For dielectric property characterizations, the sintered samples were lapped to obtain parallel faces, and the faces were then coated with silver paint as electrodes. The samples were heat-treated at 750°C for 12 min to ensure the contact between the electrodes and the ceramic surfaces. The capacitance and the dielectric loss tangent were determined over the temperature of −150 and 400°C with the frequency ranging from 100 Hz to 1 MHz. The measurements were carried out on cooling continuously. Before each cooling run, the samples were first heated up to 400°C and then cooling run was performed at the rate of 4°C/min. The dielectric constant was then calculated from $\varepsilon_r = Cd/\varepsilon_0 A$, where $C$ is the capacitance of the sample, $d$ and $A$ are the thickness and the area of the electrode, respectively and $\varepsilon_0$ is the dielectric permittivity of vacuum ($8.854 \times 10^{-12} F/m$).

## 3. Results and Discussion

The experimental results on physical properties, the phase formation behavior and microstructure features of all the sintered ceramics are presented and discussed thoroughly elsewhere.[10] Hence, these results will not be shown here. However, it should be stated here that the sintered ceramics are in perovskite phase with a pseudo-cubic crystal structure for 0.9PMN-0.1PT, and with a tetragonal crystal structure for 0.5PMN-0.5PT. It is of interest to see that 0.7PMN-0.3PT composition shows a mixed pseudo-cubic and tetragonal symmetry, which confirms that the MPB of the PMN-PT system lies between $x = 0.3$ and 0.4.[6] Table 1 includes the density and grain-size range for all ceramic compositions. It should be noted that

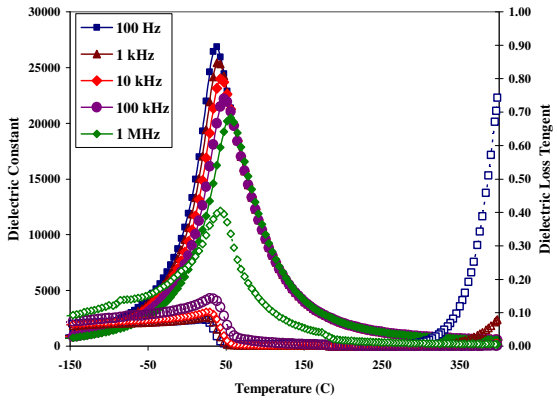
Table 1. Physical and dielectric properties of PMN-PT ceramics (at 1 kHz).

| Ceramic | Density ($g/cm^3$) | Grain size ($\mu m$) | $T_C$ (°C) | Maximum properties | | Room temp. properties | | Diffusivity ($\gamma$) |
|---|---|---|---|---|---|---|---|---|
| | | | | $\varepsilon_r$ | $\tan\delta$ | $\varepsilon_r$ | $\tan\delta$ | |
| 0.9PMN-0.1PT | 7.98 | 0.42 – 3.66 | 38 | 25400 | 0.049 | 19400 | 0.087 | 1.96 |
| 0.7PMN-0.3PT | 7.86 | 0.41 – 2.80 | 197 | 23500 | 0.011 | 2320 | 0.022 | 1.63 |
| 0.5PMN-0.5PT | 7.78 | 0.48 – 3.76 | 250 | 23200 | 0.085 | 1010 | 0.025 | 1.14 |

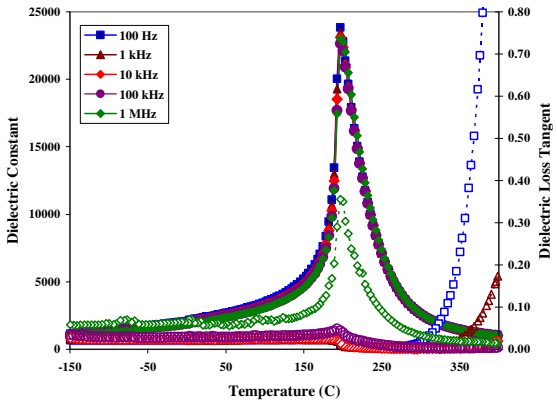
a variation in these physical features could impose significant effects on dielectric properties. However, as seen in Table 1, the density and the grain size range are not significantly different, and are not expected to show marked effects on the dielectric properties of the ceramics. Therefore, in this case, it is reasonable to assume that the dielectric properties of the ceramics are mainly influenced by their structural symmetry, as will be discussed in the following context.

The dielectric properties, e.g., dielectric constant ($\varepsilon_r$) and $\tan\delta$, are measured as functions of both temperature and frequency, as shown in Figs. 1(a)–1(c). As listed in Table 1, the Curie temperature ($T_C$) (determined at measuring frequency of 1 kHz) increases from 38°C in 0.9PMN-0.1PT to 250°C in 0.5PMN-0.5PT. This is a direct result of PT addition to PMN ($T_C \sim -8$°C) since PT itself has a Curie temperature of 490°C.[11] The maximum dielectric constant for all the ceramics studied is in excess of 20,000. This is clearly a reason for their potential applications in capacitors.[1–4] As shown in Fig. 1(a), for 0.9PMN-0.1PT ceramic, both dielectric constant ($\varepsilon_r$) and dielectric loss tangent ($\tan\delta$) exhibit strong temperature-frequency dependence below the transition temperature. This is a typical dielectric behavior of relaxor ferroelectrics,[3] in which a strong temperature-frequency dependence is observed and the temperatures of maximum dielectric constant and dielectric loss tangent are shifted to higher temperature with increasing frequency. The maximum value of the dielectric constant decreases with increasing frequency, while that of the dielectric loss tangent increases. The dielectric properties then become frequency independent above the transition temperature.[12–14] PMN is a well-known relaxor ferroelectric material with diffused phase transition (DPT) as a result of a short-range ordered structure with a nanometer scale heterogeneity in composition.[12] Small addition of PT to PMN causes an increase in $T_C$, but the strong relaxor behavior still exists. In addition, since 0.9PMN-0.1PT ceramic has a pseudo-cubic symmetry, it is therefore intrinsically electrostrictive (i.e., its electrically-induced strain is quadratically proportional to the applied electric field and is nonhysteretic).[4] With its enhanced dielectric properties at room temperature, as listed in Table 1, it is widely employed in transducers and actuators.[2–4]

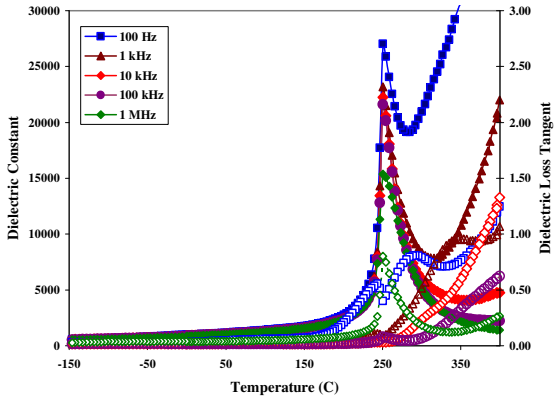
Further increase in PT contents leads to more observable normal ferroelectric behavior because PT is intrinsically a normal ferroelectric.[3,4] The dielectric properties of 0.7PMN-0.3PT ceramic, as plotted in Fig. 1(b), exhibit a mixture of both normal and relaxor characteristics, in which the transition temperature is not shifted as much as for relaxor 0.9PMN-0.1PT ceramic. Similar tendency has also been observed in several prior investigations.[12–14] It should be noted that 0.7PMN-0.3PT ceramic composition is close to MPB of the PMN-PT system. Therefore, its structural symmetry is a mixture of pseudo-cubic and tetragonal, which in turn causes a mixture of normal and relaxor characteristics observed for dielectric properties. With a tetragonal symmetry, the 0.5PMN-0.5PT ceramic, on the other hand, exhibits a normal ferroelectric behavior with a very sharp phase transition. As plotted in Fig. 1(c), the dielectric properties of 0.5PMN-0.5PT ceramic change significantly with temperature, but are nearly independent of frequency, except in the vicinity




(a)




(b)




(c)

Fig. 1. (Color on line) Temperature and frequency dependences of dielectric properties of (a) 0.9PMN-0.1PT ceramic, (b) 0.7PMN-0.3PT ceramic and (c) 0.5PMN-0.5PT ceramic (open markers with dotted lines indicate data for the dielectric loss tangent ($\tan\delta$) at the same frequency).

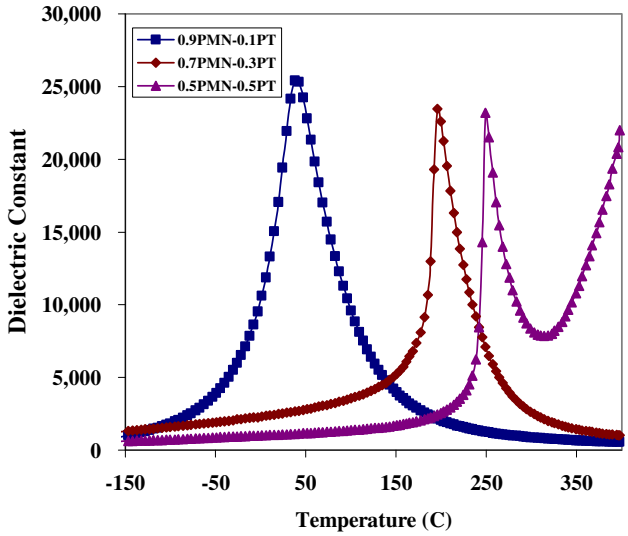



Fig. 2. (Color on line) Temperature dependence of dielectric constant of PMN-PT ceramics (measured at 1 kHz).

of the phase transformation temperature. This is a typical characteristic of normal ferroelectric ceramics with a long-range ordered structure.[3,12] It should also be noted here that the dielectric properties in all ceramics increase significantly at high temperature as a result of thermally activated space charge conduction.[13,14]

When PT is added to form the binary system with PMN, the $T_C$ increases monotonically, as shown in Table 1 and Fig. 2, and the dielectric behavior is shifted from relaxor ferroelectric towards normal ferroelectric. The degree of broadening or diffuseness is used to assess such behavior in the observed dielectric variation. This could be estimated with the diffusivity ($\gamma$) using the expression $\ln(1/\varepsilon_r - 1/\varepsilon_{\max})$ versus $(T - T_{\max})^{\gamma}$. The value of $\gamma$ can vary from 1, for normal ferroelectrics with a normal Curie–Weiss behavior, to 2, for completely disordered relaxor ferroelectrics.[13–16] The plots in Fig. 3 show that the variation is very linear. The mean value of the diffusivity ($\gamma$) is extracted from these plots by fitting a linear equation. The values of $\gamma$ listed in Table 1 vary between 1.14 for 0.5PMN-0.5PT and 1.96 for 0.9PMN-0.1PT. These results confirm that diffuse phase transition occur in 0.9PMN-0.1PT ceramic ($\gamma = 1.96$) with a nearly complete disorder characteristic, while a strong normal ferroelectric behavior is observed for 0.5PMN-0.5PT ceramic with $\gamma = 1.14$. With the $\gamma$ value of 1.63, 0.7PMN-0.3PT ceramic is expected to possess a mixed behavior, as is confirmed by the dielectric data plotted in Fig. 1(b). In addition, it should also be noted that even if it is established that the diffuseness could be caused by the decrease of grain size in a perovskite ferroelectric material,[12] the observed difference of the degree of the diffuseness in this study is not a result of the grain size variation because of the uniformity of the grain size range of the ceramics studied.

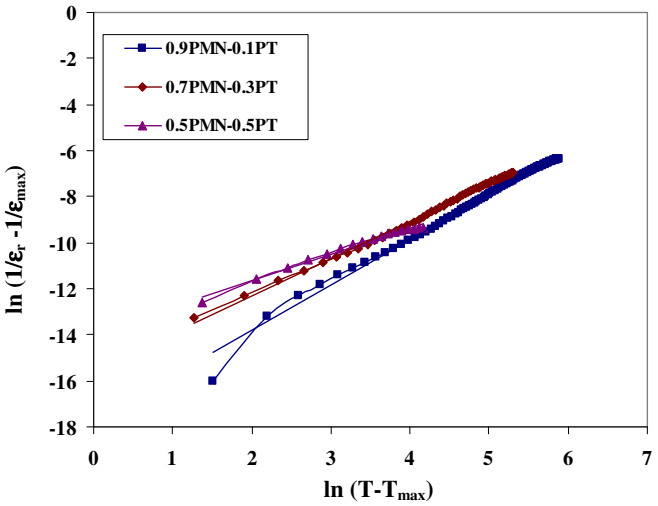



Fig. 3. (Color on line) Variation of $\ln(1/\varepsilon_r - 1/\varepsilon_{\max})$ versus $\ln(T - T_{\max})$ of PMN-PT ceramics in the paraelectric region at 1 kHz.

## 4. Conclusion

The $(1-x)\mathrm{Pb}(\mathrm{Mg}_{1/3}\mathrm{Nb}_{2/3})\mathrm{O}_{3-x}\mathrm{PbTiO}_3$ (when $x = 0.1$, 0.3 and 0.5) ceramics are prepared from PMN and PT powders by a mixed-oxide method. The dielectric properties of the ceramics are determined as functions of both temperature and frequency with an automated dielectric measurement system. The measurement takes place over the temperature range of $-150$°C and 400°C with measuring frequency between 100 Hz and 1 MHz. The results indicate that the dielectric properties of pseudo-cubic phase 0.9PMN-0.1PT and tetragonal phase 0.5PMN-0.5PT ceramics follow that of relaxor and normal ferroelectric behaviors, respectively, while the dielectric behaviors of a near MPB phase 0.7PMN-0.3PT ceramic show a mixture of normal and relaxor ferroelectric behavior. In contrast to an increase in $T_C$ with increasing PT contents, the degree of broadening or diffuseness shows a decrease, which confirms a transition from a relaxor ferroelectric behavior in 0.9PMN-0.1PT to a normal ferroelectric behavior in 0.5PMN-0.5PT. The difference in dielectric behaviors is attributed to the structural symmetry of the ceramics.

## Acknowledgments

The author expresses his gratitude for financial support from the Thailand Research Fund (TRF). Help with the sample preparation by Dr. A. Udomporn and with the dielectric measurements by Dr. Y. Somiya are gratefully acknowledged.

## References

1. A. J. Moulson and J. M. Herbert, *Electroceramics: Materials, Properties, Applications*, 2nd edn. (John Wiley & Sons Ltd, New York, 2003).

2. G. H. Haertling, *J. Am. Ceram. Soc.* **82**(4), 797 (1999).
3. L. E. Cross, *Mater. Chem. Phys.* **43**, 108 (1996).
4. S. E. Park and T. R. Shrout, *Mater. Res. Innov.* **1**, 20 (1997).
5. G. A. Smolenskii and A. I. Agranovskaya, *Sov. Phys.-Solid State* **1**, 1429 (1960).
6. S. W. Choi, J. M. Tang and A. S. Bhalla, *Ferroelectrics* **189**, 27 (1996).
7. S. L. Swartz and T. R. Shrout, *Mater. Res. Bull.* **17**, 1245 (1982).
8. A. Udomporn and S. Ananta, *Mater. Lett.* **58**, 1154 (2004).
9. Q. Jiang, Electrically induced fatigue effects and reliability in piezoelectric and electrostrictive ceramics, Ph.D. thesis, The Pennsylvania State University, University Park (1992).
10. A. Udomporn, Preparation and structural characterization of lead magnesium niobate-lead titanate ceramics, Ph.D. thesis, Chiang Mai University, Chiang Mai (2004).
11. B. Jaffe, W. R. Cook and H. Jeffe, *Piezoelectric Ceramics* (Academic Press, New York, 1997).
12. V. Koval, C. Alemany, J. Briancin, H. Brunckova and K. Saksl, *J. Eur. Ceram. Soc.* **23**, 1157 (2003).
13. R. Yimnirun, S. Ananta and P. Laoratanakul, *Mater. Sci. Eng. B* **112**, 79 (2004).
14. R. Yimnirun, S. Ananta and P. Laoratanakul, *J. Eur. Ceram. Soc.* **25**, 3225 (2005).
15. E. F. Alberta and A. S. Bhalla, *J. Phys. Chem. Solids* **63**, 1759 (2002).
16. W. Chaisan, R. Yimnirun, S. Ananta and D. P. Cann, *Mater. Lett.* **59**, 3732 (2005).

Materials Chemistry and Physics 114 (2009) 569–575

Contents lists available at ScienceDirect

Materials Chemistry and Physics

journal homepage: www.elsevier.com/locate/matchemphys

# Effect of two-stage sintering on phase formation, microstructure and dielectric properties of perovskite PMN ceramics derived from a corundum $Mg_4Nb_2O_9$ precursor

R. Wongmaneerung[a], R. Yimnirun[b], S. Ananta[b,*]

[a] Department of Physics, Faculty of Science, Maejo University, Chiang Mai 50290, Thailand
[b] Department of Physics, Faculty of Science, Chiang Mai University, Chiang Mai 50200, Thailand

ARTICLE INFO

*Article history:*
Received 31 January 2008
Received in revised form
16 September 2008
Accepted 2 October 2008

*Keywords:*
Lead magnesium niobate
Perovskite
Sintering
Dielectric properties

ABSTRACT

Pure and dense relaxor perovskite ceramics of lead magnesium niobate (PMN) have been successfully fabricated by using a combination between a corundum $Mg_4Nb_2O_9$ *B*-site precursor and a two-stage sintering techniques. Effect of doubly sintering on phase formation, microstructure and dielectric properties of the PMN ceramics was determined via XRD, SEM and dielectric measurement. It has been found that under suitable two-stage sintering schemes, dense and pure perovskite PMN ceramics derived from a corundum *B*-site precursor route can be successfully achieved with better dielectric properties than those of ceramics from either a conventional or a two-stage sintered columbite *B*-site precursor methods.
© 2008 Elsevier B.V. All rights reserved.

## 1. Introduction

Relaxor perovskite ferroelectric lead magnesium niobate, $Pb(Mg_{1/3}Nb_{2/3})O_3$ (PMN), -based-ceramics are widely employed for electronic applications such as multilayer capacitors, electrostrictive actuators and components working by induced piezoelectric effect [1,2]. Principal role in the properties of the niobates plays intrinsic cationic substitution which form additional anharmonic electron–phonon interaction [3] determining the principal electronic and optical properties. However, the main hindrance to the utilization of these PMN-based materials in electronic device applications has been the lack of simple, reproducible fabrication technique for dense and pure perovskite phase [4–6]. Moreover, it would also be highly desirable for these materials to be fired at relatively low temperatures, permitting the use of low-cost electrode materials, e.g. copper or nickel [1,2]. It is well-known that the fabrication of PMN via a solid-state reaction method is complicated by the formation of an undesired lead-niobate-based pyrochlore phases during the final stage of reaction between mixed oxides and the high volatility of lead oxide [5–8]. Several approaches have been introduced to minimize the pyrochlore phases and improve the reproducibility of their dielectric properties [9–12]. These involve modification of solid-state or wet chemical methods, but most of them leave 3–5 wt% pyrochlore phase in the sintered products [7,8]. In connection with this, a "columbite" method [8] where $MgNb_2O_6$ is formed first, followed by its reaction with PbO to form the perovskite PMN, has become one of the most effective solid-state reaction method which has been widely employed to produce PMN since 1982 [8]. Alternatively, different kinds of precursor such as $Pb_3Nb_2O_8$ [13] or "corundum" $Mg_4Nb_2O_9$ [14] have been introduced instead of $MgNb_2O_6$. Amongst all the approaches reported so far, most attention has been concentrated on the powder processing, whereas investigation of modified sintering techniques for the production of PMN ceramics has not been widely carried out [15]. In practice, sintering is a crucial stage which can significantly affect the densification and the dielectric properties of the PMN ceramics more strongly than the choice of reaction precursors.

In our previous work [15], a combination between the columbite *B*-site precursor and the two-stage sintering techniques has been proposed to achieve the densification of PMN ceramic bodies without significant grain growth. However, so far, no work has been done on the investigation of the two-stage sintering PMN ceramics derived from a corundum *B*-site precursor route. Therefore, in this work, an attempt has been made to fabricate and characterize the relaxor perovskite PMN ceramics by employing a combination of the corundum precursor and the two-stage sintering methods. The influence of doubly sintering condition on phase formation,

* Corresponding author. Tel.: +66 53 943376; fax: +66 53 943445.
*E-mail address:* suponananta@yahoo.com (S. Ananta).

0254-0584/$ – see front matter © 2008 Elsevier B.V. All rights reserved.
doi:10.1016/j.matchemphys.2008.10.003

microstructure and dielectric properties of the PMN ceramics is investigated.

## 2. Materials and methods

The starting materials were commercially available oxide powders of PbO, MgO and $Nb_2O_5$ (Aldrich, 99% purity) with an average particle size of 3–5 μm. A corundum *B*-site precursor route [16] employing intermediate phase of $Mg_4Nb_2O_9$ was adopted for the preparation of PMN powders. In this method, MgO and $Nb_2O_5$ were reacted at 1050 °C for 4 h with heating/cooling rates of 10 °C $min^{-1}$ to form $Mg_4Nb_2O_9$ [17,18], prior to reaction with PbO at 950 °C for 1 h with heating/cooling rates of 30 °C $min^{-1}$ [16]. All powders were prepared by using a simple mixed oxide method via a rapid-vibro milling technique for 30 min with corundum media in isopropyl alcohol, as detail described in our previous works [17–19]. Ceramic fabrication was achieved by adding 3 wt% polyvinyl alcohol (PVA) binder, prior to pressing as pellets in a pseudo-uniaxial die press. Each pellet was placed in an alumina crucible together with an atmosphere powder of identical chemical composition. After the binder burn out at 500 °C for 1 h, sintering was carried out with a dwell time of 1 h at each step, with constant heating/cooling rates of 20 °C $min^{-1}$ applied. Three sets of the first sintering temperature ($T_1$) were designed for the two-stage sintering case: 1025, 1050 and 1075 °C. Variation of the second sintering temperature ($T_2$) between 950 and 1025 °C was carried out for each case.

Densities of the final sintered products were measured by using the Archimedes principle. Sintered ceramics were examined by room-temperature X-ray diffraction (Siemen D-500 diffractometer) using Cu Kα radiation to identify the phase formed. The microstructural development was characterized using a scanning electron microscopy (JEOL JSM-840A). Mean grain size of the sintered ceramics was subsequently estimated by employing the linear intercept method [20]. In order to evaluate the dielectric properties, dense ceramics were polished to form flat, parallel faces and then coated with gold electrodes. The dielectric properties were measured at various frequencies using a LCR meter (HIOKI 3532-50), on cooling through the transition range (−50 to 100 °C) with a rate of 3 °C $min^{-1}$.

## 3. Results and discussion

X-ray diffraction patterns of the PMN ceramics doubly sintered at various conditions are displayed in Fig. 1, indicating the formation of both perovskite and impurity phases in each case. The results indicated that a single phase of perovskite PMN (yield of 100% within the limitations of the XRD technique) is found at only three sets of sintering conditions: i.e. at 1025/1000 °C, 1050/1025 °C and 1075/1025 °C. The strongest reflections in the majority of all XRD traces indicate the formation of the $Pb(Mg_{1/3}Nb_{2/3})O_3$ perovskite phase, which could be matched with JCPDS file no. 81-861, in agreement with other works [21,22]. To a first approximation, this major phase has a cubic phase in space group *Pm*3*m* (no. 221) with cell parameter *a* = 404.41 pm [23]. For other doubly sintering conditions, additional weak reflections of the pyrochlore-type phase previously observed in normal sintered PMN case [20] are found to co-exist along with the perovskite PMN. It should be attributed to many factors, including the poor mixing of the employed powders derived from the mechanical milling technique and the PbO evaporation [21,22]. Whilst it is possible to obtain better mixing through planetary- or jet-milling method [1], these mechanical millings can lead to seriously higher contaminations (which in turn lead to another problem of getting rid of all of them). Hence, one has to balance between these two factors in each case. In addition, as suggested in the literature [24], the PbO evaporation could also be determined by measuring weigh loss by assuming that the PbO is the only evaporating component in the system, which in most case is still incorrect.

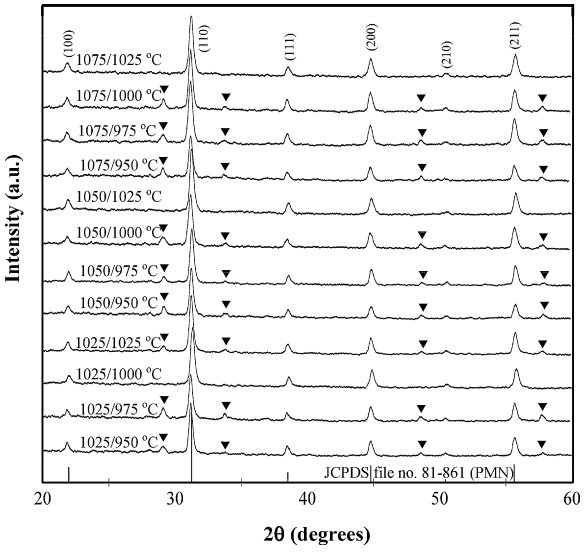



**Fig. 1.** XRD patterns of PMN ceramics doubly sintered at various conditions.

Nonetheless, this minor phase could be correlated with pyrochlore phase of composition $Pb_{1.86}(Mg_{0.24}Nb_{1.76})O_{6.5}$ (marked by ▼), and could be matched with JCPDS file no. 82-388 [25]. This phase has a pyrochlore-type structure with a cubic unit cell *a* = 10.60 Å, space group *Fd*3*m* (no. 227). Moreover, no evidence of other pyrochlore phases such as $Pb_2Nb_2O_7$, $Pb_3Nb_4O_{13}$, and $Pb_{1.83}Nb_{1.71}Mg_{0.29}O_{6.39}$ has been observed here whereas these phases were found in other works [5,8,15]. By comparison with other processing routes, it is found that only one set of double-sintering condition was found to produce a single phase perovskite PMN (at 1025/1100 °C) in the two-stage sintered columbite-route PMN [15] whilst a minimum temperature of up to 1225 °C is required for the normal sintered columbite-route PMN ceramics [21]. This observation indicates that the $Mg_4Nb_2O_9$ precursor is a better precursor to get rid of the unwanted pyrochlore phase, probably due to the better chemical reactivity between PbO and $Mg_4Nb_2O_9$.

In order to evaluate the relative amounts of perovskite and pyrochlore phases in each doubly sintering condition, the following approximation was employed, as in the earlier PMN and PFN studies [15]:

$$\text{perovskite phase(wt\%)} = \frac{I_p}{I_p + I_m} \times 100$$

Here $I_p$ and $I_m$ refer to the intensities of the (1 1 0) perovskite and (2 2 2) minor phase peaks, respectively, these being the most intense reflections in the XRD patterns of both phases. For the purposes of estimating the concentration of minor phase present, Eq. (1) has been applied to the diffraction patterns obtained (Table 1). Table 1 also presents the relative density and grain size data of the two-stage sintered PMN samples compared with conventional case [21]. Generally, it is evident that as the sintering temperature increases, the density of almost all the samples increases. The two-stage sintered corundum-route PMN ceramics reaches a maximum density of ~97% at 1075/1025 °C, each for 1 h (normal sintered columbite-route PMN samples exhibit equivalent densification after sintered at 1275 °C for 2 h [21]). On the other hand, two-stage sintered columbite-route PMN ceramics exhibit less densification and a sintering scheme of 1125/1100 °C, each for 2 h, is required to reach a densification level of ~91% [15]. Moreover, it can be seen that the relative density of the two-stage sintered corundum-route PMN ceramics increases from 85 to 97% with increasing sintering temperature, whilst grain size changes only slightly (about 2.1–2.9 μm). This is probably because the two stage sintering proceeds in a "frozen" microstructure and has the effect on grain growth. Hence, the kinetics are sufficient for reaching fairly high density, whilst providing the benefit of suppression grain growth [26,27]. The physical characteristics of various two-stage sintered PMN samples obtained by different *B*-site precursors are also compared in Table 1. Apart from employing shorter dwell time and faster heating/cooling rates, it can be noticed that

**Table 1**
Physical properties of PMN ceramics doubly sintered at various conditions.

| $T_1$ (°C) | $T_2$ (°C) | Perovskite phase[a] (wt%) | Relative density[b] (%) | Grain size range (mean)[c] (μm) |
|---|---|---|---|---|
| 1025 | 950 | 83.5 | 90 | 1.1–2.9 (2.0) |
| 1025 | 975 | 92.0 | 91 | 1.1–3.0 (2.0) |
| 1025 | 1000 | 100 | 94 | 1.2–3.0 (2.1) |
| 1025 | 1025 | 96.4 | 96 | 1.0–2.9 (1.9) |
| 1050 | 950 | 87.1 | 85 | 1.2–2.8 (2.0) |
| 1050 | 975 | 89.1 | 93 | 1.3–3.0 (2.2) |
| 1050 | 1000 | 92.4 | 94 | 1.3–3.0 (2.2) |
| 1050 | 1025 | 100 | 96 | 1.4–3.2 (2.3) |
| 1075 | 950 | 84.3 | 93 | 1.5–3.4 (2.5) |
| 1075 | 975 | 88.6 | 94 | 1.5–3.8 (2.7) |
| 1075 | 1000 | 92.0 | 95 | 1.6–4.0 (2.8) |
| 1075 | 1025 | 100 | 97 | 1.6–4.2 (2.9) |
| 1025 | 1100 | 100 | 91 | 2.0–7.0 (4.5) (Ref. [14]) |
| 1275 | – | 100 | 96 | 3.2–15.6 (9.4) (Ref. [20]) |

[a] The estimated precision of the perovskite phases is ±1%.
[b] The estimated precision of the density is ±1%.
[c] The estimated precision of the grain size is ±10%.

optimized sintering temperature and/or dwell time of the two-stage sintered corundum-route PMN ceramics in this work is lower than the normal sintering [21] and equivalent to the two-stage sintered columbite-route PMN ceramics [15]. This observation could be attributed mainly to the effectiveness of a combination between the two-stage sintering and the corundum *B*-site precursor methods.

As-fired and fracture surface SEM micrographs of corundum-route PMN samples doubly sintered with different schemes are shown in Fig. 2(i) and (ii), respectively. Clearly, the free surface microstructure of the two-stage sintered corundum-route PMN ceramics is significantly different from those of the normal and the two-stage sintered columbite-route PMN sample [15,21] which exhibits highly dense microstructure with abnormal grains of size around ~3–4 μm due to the recrystallization during firing and variation of stoichiometric compositions [28]. Their grain sizes are in the range of 1–4 μm which is significantly lower than those observed in the normal and the two-stage sintered columbite-route PMN ceramics (Table 1) [15,21]. Moreover, with careful observation (Fig. 2(i)), it can be found that PMN grains in two-stage sintered sample also exhibit whisker-like shape, similar to the results observed by Chaisan et al. [29]. With sizes of ~300–500 nm in length and ~60–100 nm in width, these whiskers are seen to distribute and coat on the grains (only at the surfaces). By using an energy dispersive X-ray (EDX) analysis, the chemical composition of these whiskers is identified as $Pb(Mg_{0.33}Nb_{0.67})O_3$. Even though exact mechanism of the microstructure observed here is not well established, but it should be noted that the various features of microstructure in PMN ceramics depend on the grain growth rate in the different planes [30]. However, the sintered process and growth environment also play an important role in the formation of microstructures [31]. In this work, the occurrence of a typical abnormal grain growth commonly found in the PMN-based systems [32–35] is observed and is likely to be caused by atom attachment to surface or boundary steps either produced by two-dimensional nucleation and lateral growth mechanism or existing at screw dislocations or the coalescence of grains and the consequent formation of grain boundaries with re-entrant edges [34,35]. MgO inclusion may act as a sintering inhibitor because of grain size. Therefore, grain growth is suppressed during the sintering process. It is possible that small amount of MgO are dissolved in the PbO-rich liquid or PMN at high firing temperatures, and its segregation at the grain–liquid interface and grain boundary may have made their step energies finite and hence made them sufficiently singular to cause these abnormal grain growth, as found in the PMN-PT system [32,33]. However, in this work grain boundaries inside these abnormal grains were not clearly observed by SEM. To answer this question, the crystallographic orientation of the grains should be examined further by using other techniques such as TEM or electron backscattered diffraction.

In general, SEM micrographs of fracture surfaces (Fig. 2(ii)) shows highly dense microstructures consisting of equiaxed grains, in agreement with other workers [6,15,21]. The grains are similar in shape, with significant variation in size (0.2–3.5 μm). Moreover, micrograph shows a few pores at triple points. Minor phases can be found in these micrographs, in particular at the grain boundaries and at the triple point junctions. These phases could be clearly distinguished from the microstructure features of the perovskite parent phase, in term of brightness (too bright and too dark). EDX analysis (Table 2) shows the chemical composition of the minor phases, neighbouring the parent PMN phase (marked as "1"), to be $Pb(Mg_{0.6}Nb_{1.9})O_{6.35}$ (bright area; marked as "2") in contrast to the XRD result (Fig. 1), and MgO (dark area; marked as "3"), although the concentration is too low for detection by X-ray, in consistent with earlier work [16]. In addition, it is seen that the PMN samples also have an intergranular fracture mechanism, indicating that the grain boundaries are mechanically weaker than the grains [31], similar to the results previously observed in the two-stage sintered columbite-route PMN ceramics [15].

The dielectric properties of PMN ceramics doubly sintered at various conditions were measured at frequencies between 100 Hz and 100 kHz in the temperature range from −120 to +100 °C as shown in Fig. 3. In general, the typical relaxor behavior [1,2] with the characteristic dispersive frequency dependence of the dielectric maxima has been observed in all samples. Fig. 4(a) and (b) shows a comparison of the dielectric properties at 1 kHz of PMN ceramics doubly sintered at various conditions. It is clear that the maxima in the dielectric constant versus temperature plots increase noticeably with increase in the sintering temperature. Similar trend is also observed for $T(\varepsilon_{r,max})$ and $\tan\delta_{max}$. The dielectric properties

**Table 2**
Dielectric properties (at 1 kHz) of PMN ceramics doubly sintered at various conditions.

| EDX positions | Composition (at%) | | | Possible phase |
|---|---|---|---|---|
| | Pb (M) | Mg (K) | Nb (L) | |
| 1 | 50.83 | 17.05 | 32.12 | $Pb(Mg_{0.33}Nb_{0.67})O_3$ |
| 2 | 28.21 | 16.97 | 54.82 | $Pb(Mg_{0.6}Nb_{1.9})O_{6.35}$ |
| 3 | – | 100 | – | MgO |

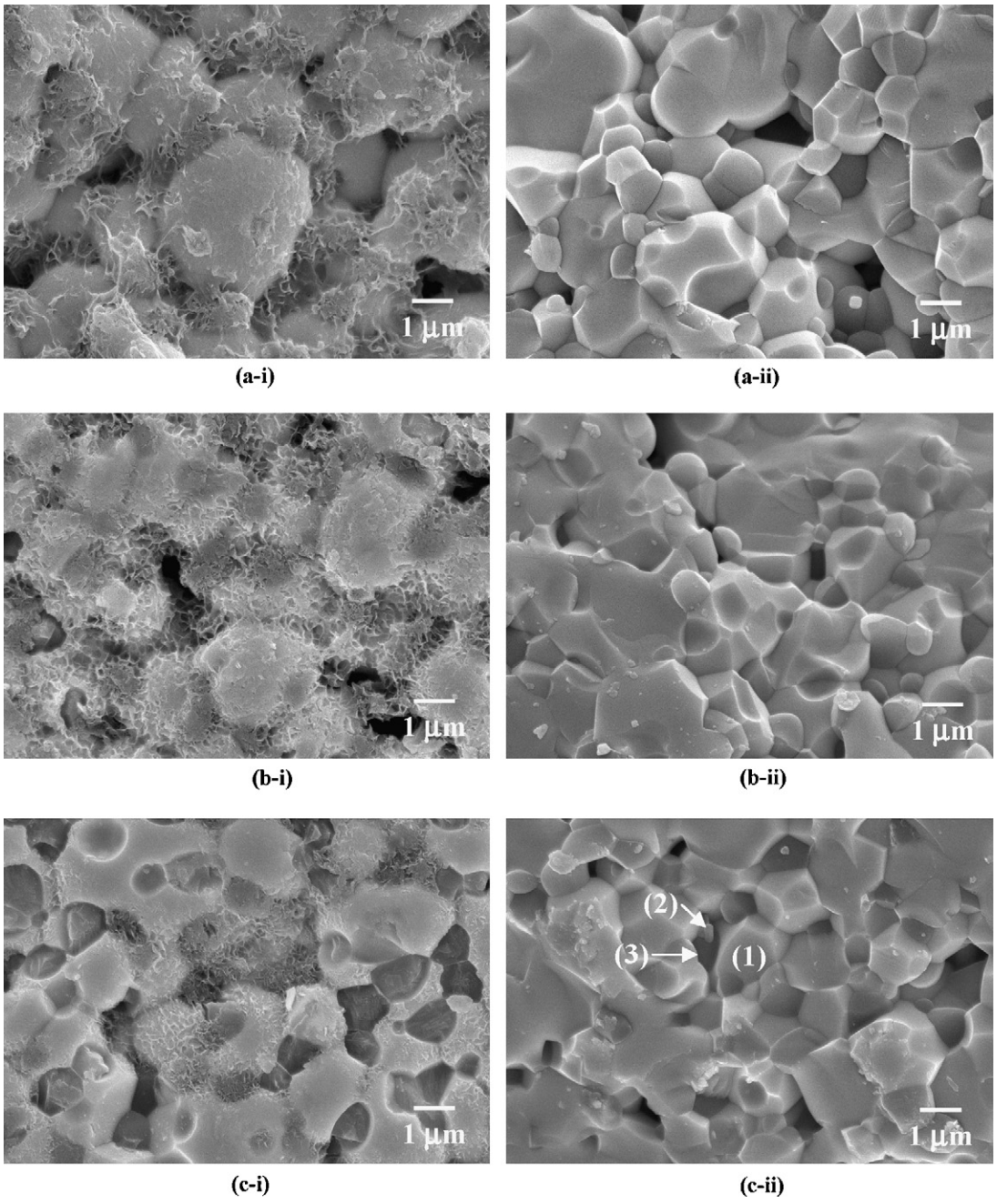



**Fig. 2.** SEM micrographs of as-fired (i) and fracture surfaces (ii) of PMN ceramics doubly sintered at (a) 1025/1000 °C, (b) 1050/1025 °C and (c) 1075/1025 °C, for constant dwell time of 1 h at each stage.

at room temperature also show the same dependency on sintering temperature, i.e. both $\varepsilon_{r,25\,^\circ C}$ and $\tan\delta_{25\,^\circ C}$ increase. Hence, it can be stated that the magnitude of both dielectric constant and dielectric loss in PMN ceramics depend considerably upon the heat treatment conditions. As also listed in Table 3, all doubly sintered PMN samples exhibit the maximum dielectric constant of about 20,708–24,291 at 1 kHz with temperature of maximum dielectric constant, $T(\varepsilon_{r,max})$, of about −15 to −18 °C, in good agreement with other researchers [5–10]. As listed in Table 2, it can be noticed that the presence of MgO phase may slightly shift the temperature of $\varepsilon_{r,max}$. In addition, since the grain size of all the doubly sintered corundum-route PMN ceramics are not significantly different (ranging from 2.1 to 2.9 μm, as listed in Table 1), the difference in dielectric properties should be attributed to the difference in density, which increases from 94 to 97% with increasing sintering temperature (as listed in Table 1). The statement that the density plays a crucial role in controlling the dielectric properties is further supported when comparing the dielectric properties of the doubly sintered corundum-route PMN ceramics with those of the normal sintered and doubly sintered columbite-route PMN ceramics, as listed in Table 3. Here, one can clearly see that the dielectric constant values (both $\varepsilon_{r,25\,^\circ C}$ and $\varepsilon_{r,max}$) in doubly sintered corundum-route PMN ceramics are very close to those observed in the normal sintered PMN [36]. It should be noted that these ceramics have very different grain size (2.9 and 9.4 μm, respectively, as listed in Table 1), but similar density values, i.e. 96–97%. On the other hand, as listed in Tables 1 and 3, the dielectric constants of the doubly sintered columbite-route and corundum-route PMN

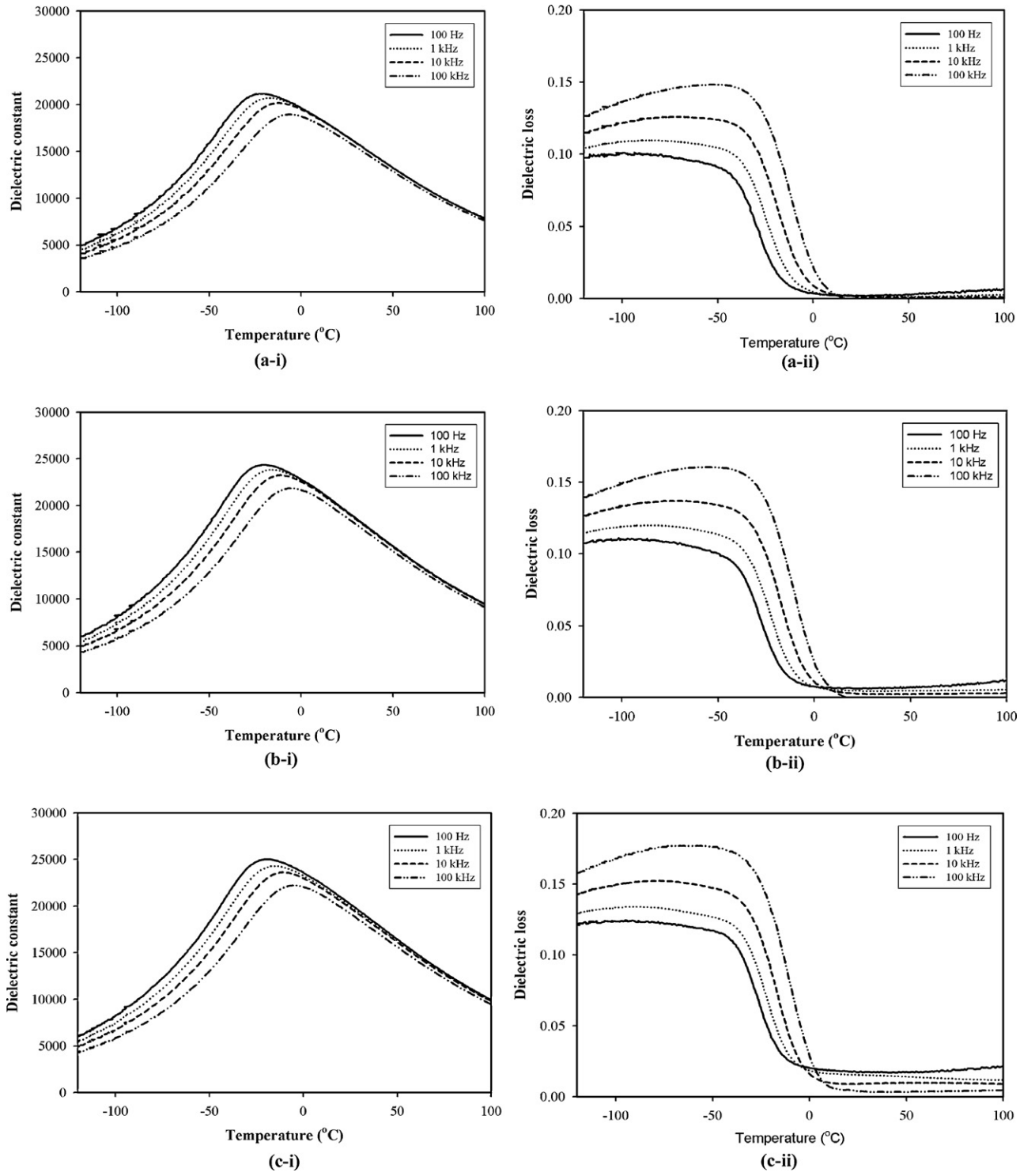



**Fig. 3.** Variation with temperature of: (i) dielectric constant ($\varepsilon_r$) and (ii) dielectric loss ($\tan\delta$) for PMN ceramics doubly sintered at: (a) 1025/1000 °C, (b) 1050/1025 °C and (c) 1075/1025 °C, for constant dwell time of 1 h at each stage.

ceramics with very different density (91 and 97%, respectively) are significantly different, even though they have similar average grain size. This clearly indicates that density, not the average grain size, could be the controlling factor for such observation [37]. It should be noted that the presence of MgO results in an enhancement of the dielectric constant of PMN ceramics, as also observed by Lu and Lee [38]. This was originally attributed to the elimination of the pyrochlore phase, consistent with the XRD results.

The degree of broadening or diffuseness in the observed dielectric variation could be estimated with the diffusivity ($\gamma$) using the expression $(\varepsilon_{r,max}/\varepsilon_r) - 1$ versus $(T - T_{max})^2$. The value of $\gamma$ can vary from 1 to 2, for completely disordered relaxor ferroelectrics [39,40]. The plots in Fig. 5 show that the variation is very linear. The mean value of $\gamma$ is extracted from those plots by fitting a linear equation. The values of $\gamma$ for all doubly sintered corundum-route PMN samples are generally very similar (varying between 1.66 and 1.79),

**Table 3**
EDX analysis on doubly sintered PMN ceramics derived from a corundum *B*-site precursor route.

| Dielectric properties (1 kHz) | Sintering temperatures ($T_1/T_2$) (°C) and dwell time of each step (h) | | | | |
|---|---|---|---|---|---|
| | Columbite-route | | Corundum-route | | |
| | 1275, 2 (Ref. [20]) | 1025/1100, 2 (Ref. [14]) | 1025/1000, 1 | 1050/1025, 1 (this work) | 1075/1025, 1 |
| $\varepsilon_{r,25\,°C}$ | 18,268 | 9,500 | 15,372 | 18,313 | 19,023 |
| Tan $\delta_{25\,°C}$ | 0.01 | 0.001 | 0.001 | 0.004 | 0.009 |
| $T_{\varepsilon r,max}$ | −9 | −10 | −17.5 | −16.3 | −15 |
| $\varepsilon_{r,max}$ | 24,003 | 13,910 | 20,708 | 23,823 | 24,291 |
| tan $\delta_{max}$ | 0.20 | 0.12 | 0.11 | 0.12 | 0.14 |
| Diffusivity ($\gamma$) | – | – | 1.79 | 1.66 | 1.67 |

indication of close to completely disordered relaxor behavior in the ceramics sintered by this route.

Here, the effect of two-stage sintering on phase formation, microstructure and dielectric properties of the PMN ceramics derived from a corundum *B*-site precursor route was investigated and compared with both the normal and the two-stage sintered columbite-routes. The different microstructural characteristics, density and amount of secondary phase present in sintered PMN ceramics strongly influence the dielectric properties of these materials, leading to superior electrical behavior in two-stage sintered corundum-route PMN sample. In comparison to the normal sintering method, although a disadvantage of the proposed two-stage sintering method is a greater time requirement, the significant reduction in firing temperature is a possible development, particularly with regard to the drive towards electrodes of lower cost for electronic products [1,2,26]. In general, these PMN ceramics exhibit complex microstructures which are a result of variation

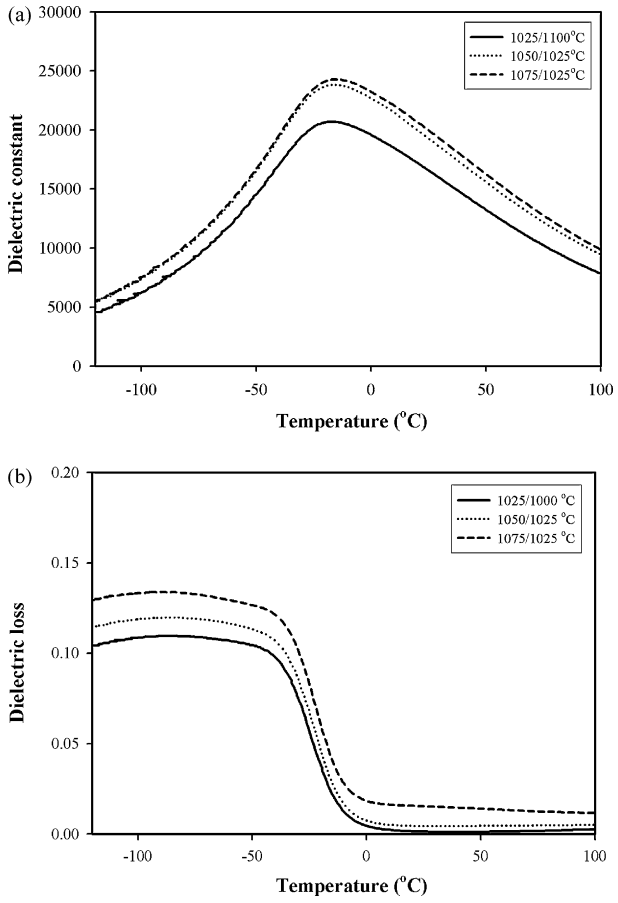



**Fig. 4.** Variation with temperature of: (a) dielectric constant and (b) dielectric loss at 1 kHz for PMN ceramics doubly sintered at various conditions.

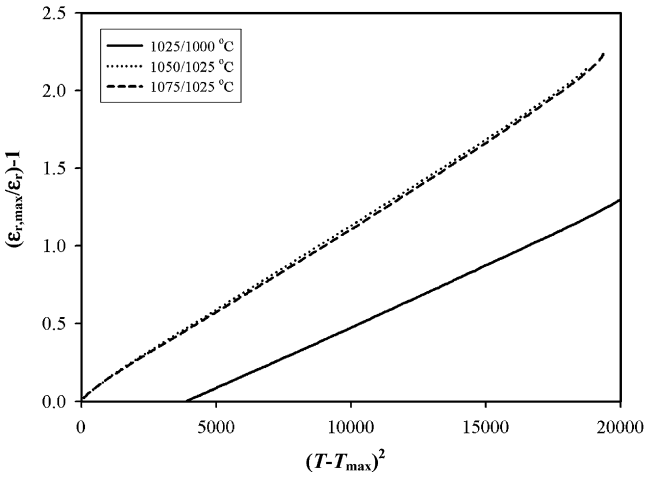



**Fig. 5.** Dependence of $(\varepsilon_{r,max}/\varepsilon_r) - 1$ with $(T - T_{max})^2$ for PMN ceramics doubly sintered at various conditions.

in grain size, shape and orientation, variation in chemical homogeneity and densification, and the presence of additional minor phase, pores and (micro) cracks. These factors, which are strongly influence by the sintering conditions, have an important effect on the dielectric properties. Furthermore, the PMN ceramics showed a comparable perovskite yield, maximum density, and dielectric properties to those obtained by the partial oxalate [36], or even better than those fabricated by the sol–gel [11], the freeze-drying [41], and the citrate-gel [42] methods.

## 4. Conclusion

This work demonstrated that, under suitable processing conditions, the properties of the PMN ceramics derived from a combination between the corundum *B*-site precursor and the two-stage sintering methods are equivalent to (or even better than) those obtained from a well-known columbite route (either a normal or a two-stage sinterings). It has been found that the two-stage sintering can effectively suppress the grain growth in perovskite PMN.

## Acknowledgements

This work was supported by the Thailand Research Fund (TRF) and the Commission on Higher Education (CHE).

## References

[1] A.J. Moulson, J.M. Herbert, Electroceramics, 2nd ed., Wiley, Chichester, 2003.
[2] G.H. Haertling, J. Am. Ceram. Soc. 82 (1999) 797.
[3] I.V. Kityk, M. Makowska-Janusik, M.D. Fontana, M. Aillerie, A. Fahmi, Cryst. Res. Technol. 36 (2001) 577.
[4] S.J. Jang, L.E. Cross, K. Uchino, J. Am. Ceram. Soc. 64 (1981) 209.

[5] M. Lejeune, J.P. Boilot, Ceram. Int. 8 (1982) 99.
[6] S.L. Swartz, T.R. Shrout, W.A. Schulze, L.E. Cross, J. Am. Ceram. Soc. 67 (1984) 311.
[7] J. Chen, A. Gorton, H.M. Chen, M. Harmer, J. Am. Ceram. Soc. 69 (1986) C303.
[8] S.L. Swartz, T.R. Shrout, Mater. Res. Bull. 17 (1982) 1245.
[9] M. Lejeune, J.P. Boilot, Am. Ceram. Soc. Bull. 64 (1984) 679.
[10] J.P. Guha, H.U. Anderson, J. Am. Ceram. Soc. 69 (1986) C287.
[11] F. Chaput, J.P. Boilot, M. Lejeune, R. Papiernik, L.G. Pfaizgrag, J. Am. Ceram. Soc. 72 (1989) 1355.
[12] Y.C. Liou, J.H. Chen, Ceram. Int. 30 (2004) 17.
[13] K. Sreedhar, A. Mitra, Mater. Res. Bull. 32 (1997) 1643.
[14] P.A. Joy, K. Sreedhar, J. Am. Ceram. Soc. 80 (1997) 770.
[15] S. Ananta, N.W. Thomas, J. Eur. Ceram. Soc. 19 (1999 2917).
[16] R. Wongmaneerung, T. Sarakonsri, R. Yimnirun, S. Ananta, Mater. Sci. Eng. B 132 (2006) 292.
[17] R. Wongmaneerung, T. Sarakonsri, R. Yimnirun, S. Ananta, Mater. Sci. Eng. B 130 (2006) 246.
[18] S. Ananta, Mater. Lett. 58 (2004) 2530.
[19] S. Ananta, Mater. Lett. 58 (2004) 2834.
[20] R.L. Fullman, Trans. AIME 197 (1953) 447.
[21] S. Ananta, N.W. Thomas, J. Eur. Ceram. Soc. 19 (1999) 629.
[22] S. Ananta, N.W. Thomas, J. Eur. Ceram. Soc. 19 (1999) 155.
[23] Powder Diffraction File No. 81-861, International Centre for Diffraction Data, Newton Square, PA, 2000.
[24] H.C. Ling, A.M. Jackson, M.F. Yan, W.W. Rhodes, J. Mater. Res. 5 (1990) 629.
[25] Powder Diffraction File No. 82-338, International Centre for Diffraction Data, Newton Square, PA, 2000.
[26] P. Lucas, W.T. Petuskey, J. Am. Ceram. Soc. 84 (2001) 2150.
[27] H.T. Kim, Y.H. Han, Ceram. Int. 30 (2004) 1719.
[28] S.H. Hur, J.K. Lee, K.W. Park, H.S. Hong, S.J. Park, Mater. Lett. 35 (1998) 78.
[29] W. Chaisan, R. Yimnirun, S. Ananta, Ferroelectrics 346 (2007) 84.
[30] M.H. Lin, J.F. Chou, H.Y. Lu, J. Eur. Ceram. Soc. 20 (2000) 517.
[31] O. Guillon, F. Thiebaud, D. Perreux, C. Courtoris, P. Champagne, A. Leriche, J. Crampon, J. Eur. Ceram. Soc. 25 (2005) 2421.
[32] C.E. Seo, D.Y. Yoon, J. Am. Ceram. Soc. 88 (2005) 963.
[33] U.J. Chung, J.k. Park, N.M. Hwang, H.Y. Lee, D.Y. Kim, J. Am. Ceram. Soc. 85 (2002) 965.
[34] S.B. Lee, N.M. Hwang, D.Y. Yoon, M.F. Henry, Metal. Mater. Trans. A 31 (2000) 985.
[35] H.K. Lee, J.S. Kim, N.M. Hwang, D.Y. Kim, J. Eur. Ceram. Soc. 20 (2000) 731.
[36] S.M. Gupta, C.S. Harendranath, A.R. Kulkarni, Ceram. Int. 23 (1997) 191.
[37] R. Wongmaneerung, R. Yimnirun, S. Ananta, Appl. Phys. A 86 (2007) 249.
[38] C.H. Lu, J.T. Lee, J. Ceram. Soc. Jpn. 103 (1995) 1122.
[39] R. Rai, S. Sharma, Solid State Commun. 129 (2004) 305.
[40] E.F. Alberta, A.S. Bhalla, J. Phys. Chem. Sol. 63 (2002) 1759.
[41] W.B. Ng, J. Wang, S.C. Ng, L.M. Gan, J. Mater. Chem. 8 (1998) 2239.
[42] Y.S. Hang, H.B. Park, S.J. Kim, J. Eur. Ceram. Soc. 18 (1998) 613.

# Dynamic ferroelectric hysteresis scaling of $BaTiO_3$ single crystals

N. Wongdamnern,[1] A. Ngamjarurojana,[1] Y. Laosiritaworn,[1,2] S. Ananta,[1] and R. Yimnirun[1,2,a)]
[1]*Department of Physics, Faculty of Science, Chiang Mai University, Chiang Mai 50200, Thailand*
[2]*Research Center in Theoretical and Computational Physics, Thailand Center of Excellence in Physics, Chiang Mai 50200, Thailand*

(Received 27 September 2008; accepted 17 January 2009; published online 25 February 2009)

The scaling behavior of the dynamic hysteresis of ferroelectric $BaTiO_3$ single crystals was investigated. Two sets of the scaling relation of hysteresis area $\langle A \rangle$ against frequency $f$ and field amplitude $E_0$ were clearly established. Above the coercive field, the scaling took a form of $\langle A \rangle \propto f^{-0.195} E_0^{0.950}$. On the other hand, the scaling in the form of $\langle A \rangle \propto f^{1.667E_0-2.804} E_0^{4.157}$ was obtained under subcoercive field condition. While these scaling relations were generally comparable to previously reported ones, it was found that the $f$ and $E_0$ exponents depended on $E_0$ and $f$, respectively, which was in contrast to the prior theoretical prediction and experimental investigations. © *2009 American Institute of Physics*. [DOI: 10.1063/1.3086317]

## I. INTRODUCTION

The dynamic hysteresis, i.e., hysteresis area $\langle A \rangle$ as a function of the field amplitude $E_0$ and frequency $f$ has become important consideration in many applications, whose performance is related to the signal amplitude and frequency, as well as in more recently developed ferroelectric random access memories (Fe-RAMs).[1–4] Therefore, it is technologically helpful to understand the scaling behavior so that the ultrahigh frequency hysteresis can be predicted in devices. Hence, there have been reports on the scaling behavior of the dynamic hysteresis in ferromagnetic and ferroelectric thin films, with some discrepancies between theoretical and experimental results.[5–14] Many theoretical studies have been focused on the power-law scaling,

$$\langle A \rangle \propto f^{\alpha} E_0^{\beta}, \tag{1}$$

(where $\alpha$ and $\beta$ are exponents that depend on the dimensionality and symmetry of the system) of hysteresis curves in polarization systems.[5–9]

Earlier investigations[5,6,8,14–16] have reported the scaling relations in thin films of some ferroelectric materials, such as $Pb(Zr,Ti)O_3$ (or PZT), $Bi_4Ti_3O_{12}$, and $SrBi_2Ta_9O_4$, as summarized in Table I. We also reported the scaling relations for soft and hard PZT bulk ceramics.[17–20] Most recently the scaling behavior of a ferroelectric liquid crystal was also reported.[21] As listed in Table I, it is interesting to observe that scaling behaviors of different materials derived from theoretical models, thin-film, and bulk ceramics are generally comparable (only slight difference in exponents $m$ and $n$), suggesting that materials with similar domain structures should have very comparable dynamic hysteresis and scaling behavior, as previously proposed in our recent investigations.[17,19,22] It could be stated that the dynamic hysteresis (hence the scaling behavior) is mainly controlled by available domain states and polarization switching mechanism. Our previous investigations in soft and hard PZT bulk ceramics have shown indirect evidence of the influence of the different domain states on the dynamic hysteresis behavior.

However, giving the complexity of the dopant types and concentrations in the commercial ceramics investigated, it was too complicated to directly evaluate the domain state contribution to dynamic behavior in the ceramics. It is thus

TABLE I. Dynamic scaling exponents for different systems [refer to Eq. (1)].

| System | $\alpha$ | $\beta$ | Refs. |
|---|---|---|---|
| $(\Phi^2)^2$ and $(\Phi^2)^3$ models | −1 | 2 | 5 and 6 |
| $Q$-state Potts model | | | |
| Saturated Loops | | 1 | 14 |
| Minor Loops | | 4 | 14 |
| | −0.66 | 2 | 15 |
| Nd-doped $Bi_4Ti_3O_{12}$ thin-Film | −0.33 | 2 | 16 |
| $SrBi_2Ta_9O_4$ thin-film | −0.33 | 3 | 14 |
| $Pb(Zr,Ti)O_3$ thin-films | −0.33 | 1 | 41 |
| $PbTiO_3$/polymer Composite | −1 | 2 | 42 |
| Soft PZT bulk ceramic | | | |
| Saturated Loops | −0.25 | 1 | 17 |
| Minor Loops | −0.33 | 3 | 17 |
| Hard PZT bulk ceramic | | | |
| Saturated Loops | −0.28 | 0.89 | 19 |
| Minor Loops | −0.43 | 3.19 | 19 |
| PZT-PZN bulk ceramic | | | |
| Minor Loops | −0.42 | 3.65 | 22 |
| $Na_{0.5}Bi_{0.5}TiO_3$ ceramic | | | |
| Minor Loops | −0.39 | 2.63 | 43 |
| {001}-$BaTiO_3$ single crystals | | | |
| Saturated Loops | $-0.195 \pm 0.016$ | $0.950 \pm 0.056$ | This work |
| Minor Loops | $(1.667)E_0 - 2.804$ | $4.157 \pm 0.092$ | This work |

a)Author to whom correspondence should be addressed. E-mail: rattikornyimnirun@yahoo.com.

 © 2009 American Institute of Physics

Author complimentary copy. Redistribution subject to AIP license or copyright, see http://jap.aip.org/jap/copyright.jsp

more suitable to study such influence in material with more distinct domain structures, particularly single crystals of simple ferroelectric materials, of which the scaling behavior has surprisingly yet to be reported. Thus, we present the results on the scaling behaviors of the dynamic hysteresis of tetragonal $BaTiO_3$ single crystals. As will be seen, the dynamic hysteresis and scaling behaviors of the $BaTiO_3$ single crystal are comparatively very similar to those of the other more complex materials previously reported. More interestingly, it is found that an intercorrelation of $f$ and $E_0$ exponents is obtained, which is in contrast to the prior theoretical prediction and experimental investigations.

## II. EXPERIMENTAL

The dynamic hysteresis ($P$-$E$) loops of tetragonal {001}-$BaTiO_3$ single crystals grown by the Remeika process[23,24] containing $a$-$c$ domains[25,26](triangular-shaped plates with 5 mm edge length and thickness of 0.5 mm) were characterized at room temperature (25 °C) by using a modified Sawyer-Tower circuit with $f$ covering from 1 to 300 Hz and $E_0$ from 0 to 6.6 kV/cm. Measurements were parallel to the tetragonal (001) direction. The electric field was applied to a sample by a high voltage ac amplifier (Trek 610D) with the input sinusoidal signal from a function generator (HP 3310A). The $P$-$E$ loops were recorded by a digital oscilloscope (HP 54645A, 100 MHz). Each loop was obtained after 20 sampling cycle to average out the noise deformation.

## III. RESULTS AND DISCUSSION

The hysteresis loops at different $E_0$ but fixed $f$ (100 Hz), and at different $f$ but fixed $E_0$ (6.0 kV/cm) are shown in Fig. 1. As shown in Fig. 1(a), for applied fields lower than the coercive field, the loop does not saturate. With further increase in $E_0$ beyond $E_c$, the loop area $\langle A\rangle$, remanent polarization ($P_r$), and coercive field ($E_c$) increase until well saturated loop is achieved. Similar observations have been reported in ferroelectric thin films and bulk ceramics.[8,10,14,17,19,22] The $\langle A\rangle$, $P_r$, and $E_c$ decrease with an increase in frequency, as shown in Fig. 1(b). As already established in our previous investigations,[17,19,22] the scaling behavior can be divided into two distinct regimes; that for the saturated loops ($E_0 > E_c$) and the other for the minor loops ($E_0 < E_c$). The same can be applied for the case of the $BaTiO_3$ single crystals, as seen in an inset of Fig. 1(a) that the change in $\langle A\rangle$ with $E_0$ follows two distinctly different trends with the applied field amplitude $E_0 = E_c$ (1.7 kV/cm)[25,27] being a critical turning point. It should be noted that the $E_c$ is generally frequency dependent [$E_c(f)$], but in this case the measuring frequency range is not too extensive to cause large variation in $E_c$, as seen in an inset of Fig. 1(a). Thus, the fixed $E_c$ of 1.7 kV/cm can be used effectively.

Thus, to obtain the scaling relations for the $BaTiO_3$ single crystals, one can fit the data with Eq. (1) where exponents $\alpha$ and $\beta$ are determined directly from the experimental data. By plotting $\langle A\rangle$ against $f$ at fixed $E_0$, one obtains the exponent $\alpha$. On the other hand, the exponent $\beta$ can be obtained from plotting $\langle A\rangle$ against $E_0$ at fixed $f$. In conjunction with the least square-fitting method, the methodology outlined above is applied to obtain the exponents $\alpha$ and $\beta$ from the saturated loop ($E_0 > E_c$) and the minor loop data ($E_0 < E_c$). Figures 2(a) and 2(b) show a variation in exponent $\alpha$ with $E_0$ and a variation in exponent $\beta$ with $f$, respectively. Evidently, the two exponents depend slightly on the frequency $f$ and significantly on the field amplitude $E_0$, with $E_0 = E_c$ being the critical turning point. The variations in both exponents obtained here are in strong contrast to most of the previous investigations,[5–9,11,14–22] in which the scaling exponents are normally treated as constant and depend only on the dimensionality and symmetry of the system, not the frequency $f$ and field amplitude $E_0$, as stated previously in Eq. (1).

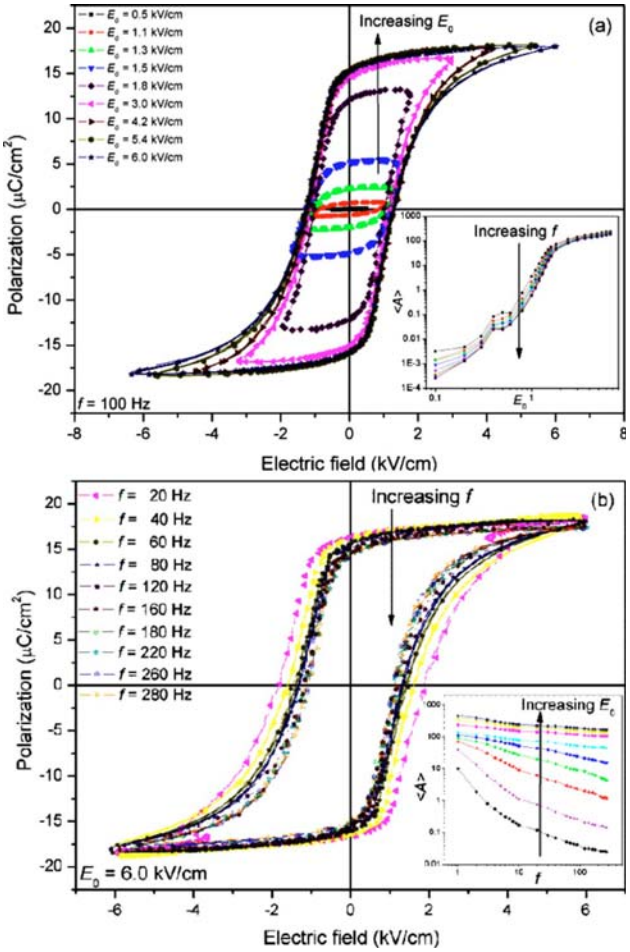



FIG. 1. (Color online) Hysteresis loops for {001}-$BaTiO_3$ single crystals (a) at various $E_0$ and $f$=100 Hz and (b) at various $f$ and $E_0$=6.0 kV/cm. Shown in insets are changes in $\langle A\rangle$ with $f$ and $E_0$ at some measuring conditions.

From Fig. 2(a), two linear relations can be obtained for the variation in $f$-exponent $\alpha$ with $E_0$. With $E_0 < E_c$, a strong field-dependent relation $\alpha = (1.667)E_0 - 2.804$ (with $R^2 \sim 0.97$) is obtained, while a much weaker field-dependent relation $\alpha = -(8.07 \times 10^{-3})E_0 - 0.163$ (with $R^2 \sim 0.93$) is attained at $E_0 > E_c$. Furthermore, as displayed in Fig. 2(b), two very weak frequency-dependent relations are obtained for the variation in $E_0$-exponent $\beta$ with $f$, e.g., $\beta = (6.105 \times 10^{-4})f + 4.065$ (with $R^2 \sim 0.94$) and $\beta = (3.730 \times 10^{-4})f + 0.894$ (with $R^2 \sim 0.95$) for $E_0 < E_c$ and $E_0 > E_c$, respectively. It is impor-

Author complimentary copy. Redistribution subject to AIP license or copyright, see http://jap.aip.org/jap/copyright.jsp

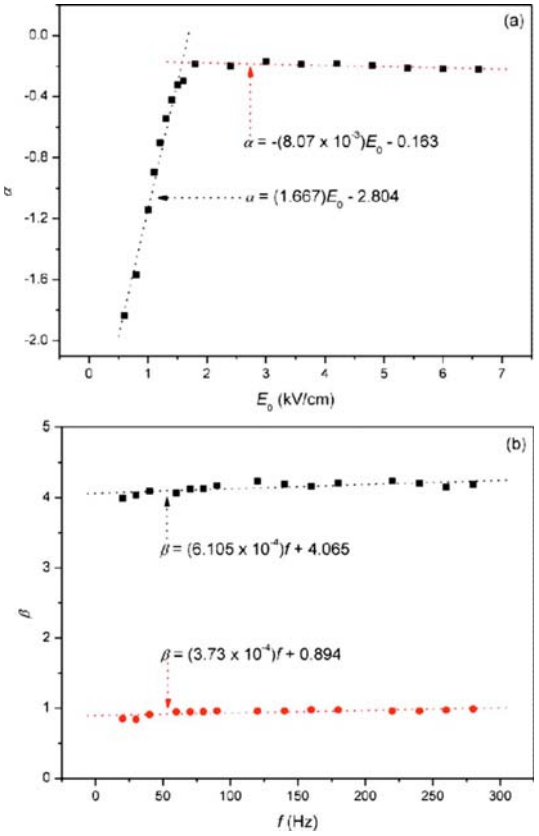



FIG. 2. (Color online) (a) Variation in exponent $\alpha$ with $E_0$ and (b) variation in exponent $\beta$ with $f$ in subcoercive field ($0.1 \leq E_0 \leq 1.6$ kV/cm) (black square markers) and beyond coercive field ($1.8 \leq E_0 \leq 6.6$ kV/cm) (red circle markers) conditions. Dotted lines indicate linear relations fitted to data in each regime.

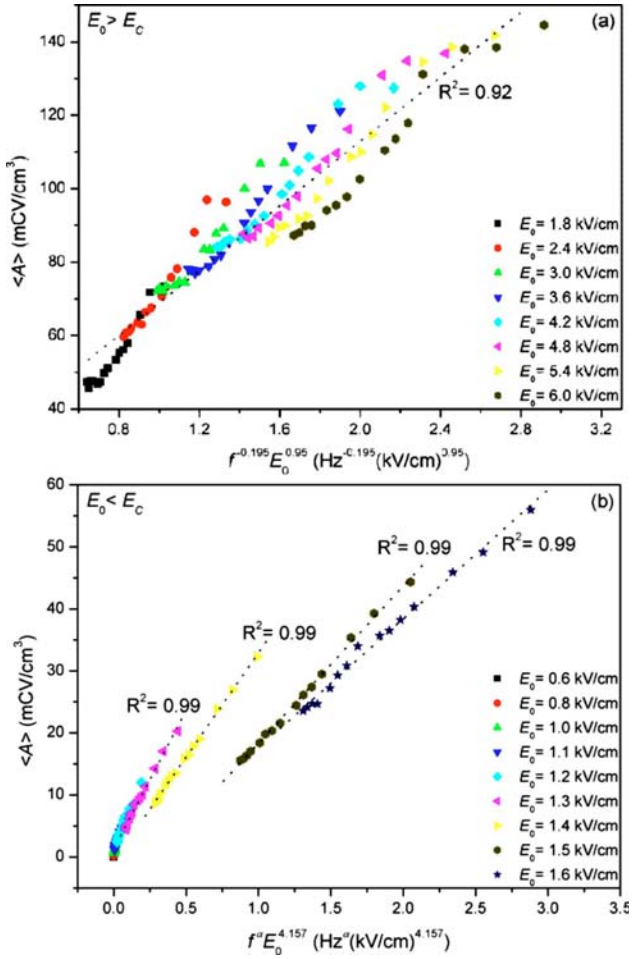



FIG. 3. (Color online) Scaling of hysteresis for {001}-$BaTiO_3$ single crystals (a) area $\langle A \rangle$ against $f^{-0.195}E_0^{0.95}$ and for the saturated loops ($E_0 > E_c$) (b) area $\langle A \rangle$ against $f^{\alpha}E_0^{4.157}$ for the minor loops ($E_0 < E_c$). The dotted lines represent the fitting.

tant to point out that not only the complex scaling behaviors of a ferroelectric prototype $BaTiO_3$ single crystal are revealed but the relations expressed above also provide useful and critical information in understanding the scaling behaviors in other ferroelectric materials previously reported, as listed in Table I, and will be discussed later.

Obviously, with very small coefficients to $E_0$ and $f$ terms (for the whole range of $E_0$ and $f$ used in this study), one can estimate the exponents $\alpha = -0.195 \pm 0.016$ and $\beta = 0.950 \pm 0.056$ when $E_0 > E_c$. As plotted in Fig. 3(a), it is revealed that the saturated loop data can be fitted reasonably well ($R^2 \sim 0.92$), within the measured uncertainty, by

$$\langle A \rangle \propto f^{-0.195} E_0^{0.950}. \tag{2}$$

On the other hand, for the case of $E_0 < E_c$ only the exponent $\beta = 4.157 \pm 0.092$ can be estimated, while the relation $\alpha = (1.667)E_0 - 2.804$ has to be used due to its strong field-dependent nature. Therefore, the scaling relation for the minor loops of the $BaTiO_3$ single crystals takes the form of

$$\langle A \rangle \propto f^{1.667E_0 - 2.804} E_0^{4.157}, \tag{3}$$

which fitted very well ($R^2 \sim 0.99$) with the minor loop data at each $E_0$, as plotted in Fig. 3(b).

The scaling relation obtained in Eq. (2) for the saturated loops of $BaTiO_3$ single crystals indicates that $\langle A \rangle$ decays more slowly with $f$ and grows more slowly with $E_0$ than the theoretical prediction from $(\Phi^2)^2$ and $(\Phi^2)^3$ models, as well as most of the other ferroelectric materials in both thin-film and bulk forms, as compared in Table I. In the saturated loop case, when comparing the $E_0$-exponent $\beta$ listed in Table I, it is very interesting to observe that the $\beta$ value (approximately 1) in our present study on $BaTiO_3$ single crystal is similar to those obtained earlier for the bulk ceramics and that directly estimated from Monte Carlo method based on $Q$-state planar Potts model,[14] while it is much lower than those derived from $(\Phi^2)^2$ and $(\Phi^2)^3$ models and ferroelectric thin films ($\beta \sim 2-3$). A qualitative explanation for the difference may come from the polarization-interaction terms as considered in the $(\Phi^2)^2$ and $(\Phi^2)^3$ models, in which the polarization flip just has one contribution, i.e., polarization reversal.[5,6] Similarly, as explained thoroughly in our previous reports,[17,20] main polarization switching contribution in thin films would also be from the 180° domain reversal. Hence, a similar polarization switching kinetics is expected in the two cases. On the other hand, in the single crystals and bulk ceramics, there are influences of many depolarizing effects[17] arisen from domain walls, boundaries, space charges, immobile defects, etc., which may retard the external field. Consequently, the energy barrier is very much higher, which leads to slower

Author complimentary copy. Redistribution subject to AIP license or copyright, see http://jap.aip.org/jap/copyright.jsp

polarization-flip kinetics. Therefore, a lower exponent for the $E_0$ term is expected in these types of materials.

A more quantitative approach to explain a near linear dependence of hysteresis area with electric field amplitude $E_0$ can be drawn upon the domain reversal nature through the nucleation and growth concept,[28] which was theoretically established very nicely for $BaTiO_3$ materials.[7,8] Here the domain reversal can be characterized by an effective characteristic time [combining simultaneous contributions from both the new domain nucleation rate ($\tau_n \propto E_0^{-2/3}$) and the domain boundary motion velocity ($\tau_v \propto E_0^{-4/3}$)] $\tau' = \sqrt{\tau_n \tau_v} \propto E_0^{-1}$.[16,29] If this effective characteristic time represents the response of the domain reversal to the varying external field at a given frequency, it should be inversely proportional to the hysteresis area $\langle A \rangle$. Therefore, it can be assumed that $\langle A \rangle \propto E_0$, which is in very good agreement with the present study.

Furthermore, in the case of saturated loops, the $f$-exponent $\alpha$ of $BaTiO_3$ single crystal is smallest in absolute value among those listed in Table I. In our previous reports, the depolarizing effects, acting as a buffer to polarization-reversal mechanism, were already discussed as the reason of a relatively weaker dependence on $f$ in bulk ceramics than that observed in thin films and predicted from theoretical models.[17,19] As for the smallest response to $f$ in the single crystals, an explanation may simply be a result of a near saturation of polarization in the single crystals under the applied field beyond its coercive field, as shown in Fig. 1(a), under which the crystal is nearly in a single-domain-like state, unlike in thin films and bulk ceramics with multidomain states.[1,30,31] This has resulted in a relatively weaker dependence on $f$ than those observed in most of the other ferroelectric thin films and bulk ceramics. It should also be noted here that a deviation of the experimentally obtained scaling relations from the theoretical prediction may be due to the fact that the models[5,6] is relevant to the insulating defect-free single domain samples with very low dielectric anisotropy and low electroelastic coupling, which clearly is not the case for the $BaTiO_3$ single crystals with a well-known large dielectric anisotropy.[1,25,30,31]

For the minor loop scaling relation in Eq. (3) and as listed in Table I, the $E_0$-exponent $\beta$ ($\sim$4.157) in the $BaTiO_3$ single crystals is approximately in the same order (3–4) as to that in PZT thin film,[8,14] as well as those in minor loops of PZT and PZN-modified PZT bulk ceramics.[17,19,22] As explained in our previous investigations,[17,19] this is attributed to the fact that the main polarization orientation mechanism in thin films and in subcoercive field condition for single crystals and bulk ceramics is likely from the reversible 180° domain rotation (which also occurs at much faster rate than the irreversible process), as the irreversible non-180° domain switching is normally accompanied with mechanical strain, it occurs at higher $E$-field than 180° domain rotation does. Therefore, under low $E$-fields, one would expect the 180° domain rotation to occur first.[32–37] This explains why the scaling behavior of the single crystals and bulk ceramics at low $E$ fields is similar to that of thin films and why the response to $E_0$ at subcoercive field occurs at much faster response ($\beta \sim 2-4$) than that at higher field amplitude ($\beta \sim 1$). It should also be noticed that the $\beta$=4.157 obtained experimentally in this study agrees very well with the $\beta$ value of 4 obtained from the previous simulation study using Monte Carlo method based on $Q$-state planar Potts model.[14]

Another important implication of this study is the fact that the $f$-exponent $\alpha$ is strongly field dependent in subcoercive field condition, as seen in Fig. 2(a). This may provide a hint to explain such variation in the $\alpha$ value, as listed in Table I, which may be caused from an experimental limitation to fully achieve the saturation state in most of the previous high-field dynamic hysteresis studies available in literature. In fact, the $\alpha$ value for all previous investigations falls between $-0.195$ (that of saturated loop of $BaTiO_3$ obtained here, believed to be the upper limit of the $f$ exponent) and $-1$ [theoretically obtained from $(\Phi^2)^2$ and $(\Phi^2)^3$ models for non-saturated loops]. The upper limit of the $\alpha$ value is believed to be related to available domain states in the material, previously proposed in our investigations,[19,22] or growth dimension in growth kinetics model proposed by Ishibashi and Orihara[38,39] based on Kolmogorov-Avrami model. Nonetheless, more investigations are clearly required to support this hypothesis.

It should also be noticed that the scaling relations obtained in this current study is only applicable to high frequency limit. This is because at lower frequency range ($<1$ Hz) another set of scaling relations must be formulated, as seen in both previous theoretical and experimental works that $\langle A \rangle$ is rapidly increasing, then turning to zero at much lower frequency. In addition, the high frequency limit in prior investigations in thin films is usually in the range of 1–100 kHz, the maximum frequency of 300 Hz used in this study may not be viewed as a high frequency limit as compared to those cases. The range of excitation parameters in this study is limited by equipments used. The field amplitude used here is reasonable as saturated $P$-$E$ loops are already obtained. Therefore, while the higher field amplitude could be obtained, no new information is revealed. The major limitation in this current study is probably the frequency range of 1–300 Hz, which seems rather narrow, as compared to previous investigations in thin films. However, this can be explained very easily. All of the previous investigations on scaling behavior of ferroelectric materials are on thin films. Therefore, it is much easier to apply only 1–10 V to obtain saturated $P$-$E$ loops and most of the function generators can provide this voltage in very wide frequency range (0.0001 Hz to $>1$ MHz). As a result, most of the previous investigations were carried out in boarder range, as compared to current study in much thicker samples. Since this work was carried out on single crystal plates with nearly 1 mm thick, the amplifier can only provide high electric field (6 kV/cm) up to 300 Hz.

Based on the arguments mentioned, the scaling relations are considered applicable within the range of the experimental conditions. Nevertheless, it is interesting to point out that, through extrapolation of the scaling relations presented in Fig. 2 for exponents $\alpha$ and $\beta$ to the range of field amplitude of 10–50 kV/cm and frequency of 1–10 kHz used in the case of many previous thin-film studies, one could easily obtain the exponents $\alpha$ and $\beta$ close to those previously reported as listed in Table I. For instance, with $E_0$ of 25 kV/cm and $f$ of

Author complimentary copy. Redistribution subject to AIP license or copyright, see http://jap.aip.org/jap/copyright.jsp

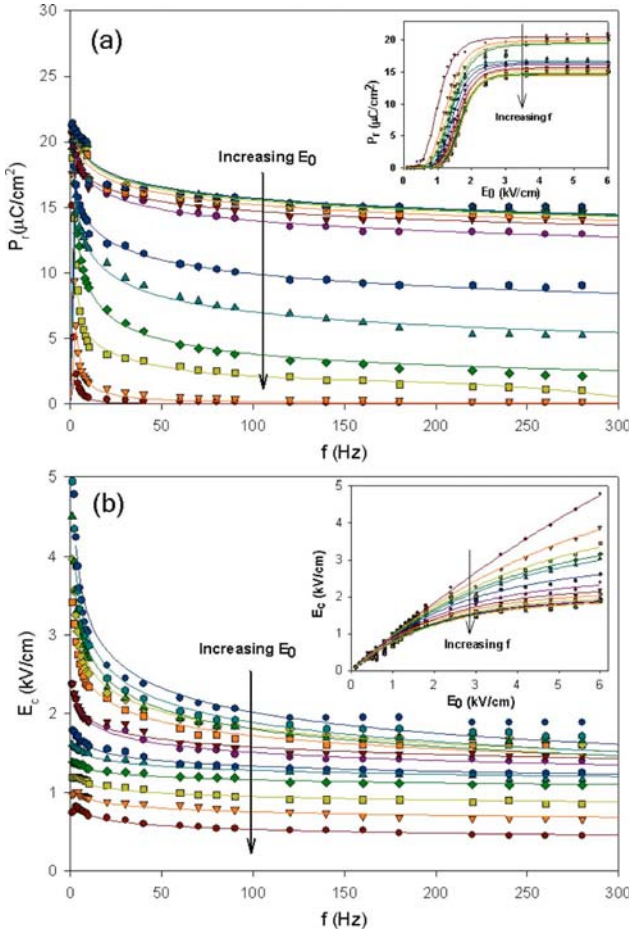



FIG. 4. (Color online) Linear plots between (a) $P_r$ and $f$ for various $E_0$ and (b) $E_c$ and $f$ for various $E_0$. Solid lines indicate power-law fitting to the data. Also shown in insets of respective figure are linear plots of $P_r$ and $E_c$ with $E_0$ for various $f$.

5 kHz, the exponents $\alpha$ and $\beta$ of $-0.365$ and 2.759 (as compared to $-0.33$ and 2–3 for thin films) can be obtained. More importantly, it should still be emphasized that the scaling relations obtained in this study is mostly applicable within the range of excitation parameters mentioned above.

Finally, we look at the measured $P_r$ and $E_c$ as functions of $f$ and $E_0$, as plotted in Fig. 4. One can observe decaying of both $P_r$ and $E_c$ with $f$, while both parameters increase to saturation with $E_0$, as seen in insets of Fig. 4. As the frequency of the applied field increases, it is expected for $P_r$ to decrease because some of the domains cannot follow the applied field. Hence, it takes lower electric field to force the polarizations to become zero, hence lower coercive field is observed. It is important to note that both $P_r$ and $E_c$ will not increase indefinitely as $f \rightarrow 0$. As reported in many previous investigations,[7,8,11,14–16,39] the two parameters reach maxima at certain $f$, then begin to decrease to finite values (usually called static $P_r$ and $E_c$) as $f \rightarrow 0$. However, due to an equipment limitation such very low $f$ range could not be performed in this study. Nonetheless, the measured $P_r$ and $E_c$ as functions of $f$ seen in Fig. 4 imply power-law relations between the two parameters and $f$, as also widely reported in literature.[2,4,38,39] On the other hand, as seen from insets of Fig. 4 rather complex relations with $E_0$ are obtained, hence will not be discussed here. Therefore, with least-square fitting method with $R^2 > 0.95$ (with some variation), the power-law scaling of $P_r(f)$ and $E_c(f)$ for saturated loop data ($E_0 > 1.7$ kV/cm) takes the forms of

$$P_r \propto f^{-0.079}, \tag{4}$$

$$E_c \propto f^{-0.164}. \tag{5}$$

Since approaching saturation the hysteresis area can be roughly estimated with $(2P_r)(2E_c)$,[20,40] so an empirical relation $\langle A \rangle \propto f^{-0.243}$ is available from Eqs. (4) and (5). Although at fixed $E_0$ this relation is not too far from Eq. (2) with $\langle A \rangle \propto f^{-0.195}$, the difference in the $f$-exponent could arrive from the complex relations between $P_r$, $E_c$, and $E_0$, as displayed in insets of Fig. 4 and discussed above. Nonetheless, these two scaling methods seem to agree reasonably well.[41–43] So once the scaling of area to the frequency is found, it is possible to guess how the $E_c$ would scale with $f$ if the scaling relation between $P_r$ and $f$ is known or vice versa. Similarly, scaling of area to frequency and to temperature has also been reported in previous investigations.[20,39]

## IV. CONCLUSIONS

Two sets of the scaling relation for $BaTiO_3$ single crystals are established based upon the coercive field. The scaling in the form of $\langle A \rangle \propto f^{-0.195} E_0^{0.950}$ is obtained when $E_0 > E_C$, while the scaling takes the form of $\langle A \rangle \propto f^{1.667E_0 - 2.804} E_0^{4.157}$ when $E_0 < E_C$. Although, these scaling relations that are comparable to those of the other more complex materials, the intercorrelation between the $f$ and $E_0$ exponents is obtained, which is in contrast to the prior theoretical prediction and experimental investigations.

## ACKNOWLEDGMENTS

This work was financially supported by the Thailand Center of Excellence in Physics (through the Research Center in Theoretical and Computational Physics). Partial supports for N.W., A.N., and S.A. from the Thailand Research Fund (TRF), Commission on Higher Education (CHE), Graduate School and Faculty of Science, Chiang Mai University are also acknowledged. Thanks are also due to Edward M. Sabolsky of Penn State University for providing the single crystals.

[1] B. Jaffe, W. R. Cook, and H. Jaffe, *Piezoelectric Ceramics* (Academic, New York, 1971).
[2] J. F. Scott, Ferroelectr. Rev. **21**, 1 (1998).
[3] K. Uchino, *Ferroelectric Devices* (Marcel Dekker, New York, 2000).
[4] R. Waser, U. Böttger, and M. Grossmann, in *Ferroelectric Random Access Memories*, edited by H. Ishiwara, M. Okuyama, and Y. Arimoto (Springer-Verlag, Berlin, Heidelberg, 2004).
[5] M. Rao, H. R. Krishnamurthy, and R. Pandit, Phys. Rev. B **42**, 856 (1990).
[6] M. Acharyya and B. K. Chakrabarti, Phys. Rev. B **52**, 6550 (1995).
[7] J.-M. Liu, H. L. W. Chan, C. L. Choy, and C. K. Ong, Phys. Rev. B **65**, 014416 (2001).
[8] J.-M. Liu, H. L. W. Chan, C. L. Choy, Y. Y. Zhu, S. N. Zhu, Z. G. Liu, and N. B. Ming, Appl. Phys. Lett. **79**, 236 (2001).
[9] M. Rao and R. Pandit, Phys. Rev. B **43**, 3373 (1991).
[10] Q. Jiang, H. N. Yang, and G. C. Wang, Phys. Rev. B **52**, 14911 (1995).
[11] B. Pan, H. Yu, D. Wu, X. H. Zhou, and J.-M. Liu, Appl. Phys. Lett. **83**, 1406 (2003).
[12] Y.-H. Kim and J.-J. Kim, Phys. Rev. B **55**, R11933 (1997).

Author complimentary copy. Redistribution subject to AIP license or copyright, see http://jap.aip.org/jap/copyright.jsp

[13]J.-H. Park, C.-S. Kim, B.-C. Choi, B. K. Moon, J. H. Jeong, and I. W. Kim, Appl. Phys. Lett. **83**, 536 (2003).
[14]J.-M. Liu, H. L. W. Chan, and C. L. Choy, Mater. Lett. **52**, 213 (2002).
[15]J.-M. Liu, B. Pan, H. Yu, and S. T. Zhang, J. Phys.: Condens. Matter **16**, 1189 (2004).
[16]J.-M. Liu, B. Pan, K. F. Wang, and H. Yu, Ceram. Int. **30**, 1471 (2004).
[17]R. Yimnirun, Y. Laosiritaworn, S. Wongsaenmai, and S. Ananta, Appl. Phys. Lett. **89**, 162901 (2006).
[18]R. Yimnirun, S. Wongsaenmai, S. Ananta, and Y. Laosiritaworn, Appl. Phys. Lett. **89**, 242901 (2006).
[19]R. Yimnirun, R. Wongmaneerung, S. Wongsaenmai, A. Ngamjarurojana, S. Ananta, and Y. Laosiritaworn, Appl. Phys. Lett. **90**, 112908 (2007).
[20]R. Yimnirun, R. Wongmaneerung, S. Wongsaenmai, A. Ngamjarurojana, S. Ananta, and Y. Laosiritaworn, Appl. Phys. Lett. **90**, 112906 (2007).
[21]S. S. Bhattacharyya, M. Rahman, A. Mukherjee, B. K. Chaudhuri, and A. Yoshizawa, Appl. Phys. Lett. **92**, 122909 (2008).
[22]R. Yimnirun, N. Wongdamnern, N. Triamnak, M. Unruan, A. Ngamjarurojana, S. Ananta, and Y. Laosiritaworn, J. Appl. Phys. **103**, 086105 (2008).
[23]E. M. Sabolsky, A. R. James, S. Kwon, S. Trolier-Mckinstry, and G. L. Messing, Appl. Phys. Lett. **78**, 2551 (2001).
[24]E. M. Sabolsky, S. Trolier-Mckinstry, and G. L. Messing, J. Appl. Phys. **93**, 4072 (2003).
[25]F. Jona and G. Shirane, *Ferroelectric Crystals* (Dover, New York, 1993).
[26]B. Jiang, Y. Bai, J. L. Cao, Y. Su, S. Q. Shi, W. Chu, and L. Qiao, J. Appl. Phys. **103**, 116102 (2008).
[27]W. J. Merz, Phys. Rev. **91**, 513 (1953).
[28]J. D. Gunton, M. San Miguel, and P. S. Sahmi, in *Phase Transitions and Critical Phenomena*, edited by C. Domb and J. L. Lebowitz (Academic, London, 1983), Vol. 8, p. 267.
[29]H. L. Stadler and P. L. Zacumanids, J. Appl. Phys. **34**, 3255 (1963).
[30]M. E. Caspari and W. J. Merz, Phys. Rev. **80**, 1082 (1950).
[31]M. E. Lines and A. M. Glass, *Principles and Applications of Ferroelectrics and Related Materials* (Oxford University Press, Oxford, 1977).
[32]N. Uchida and T. Ikeda, Jpn. J. Appl. Phys. **4**, 867 (1965).
[33]A. Gruverman, O. Auciello, and H. Tokumoto, Annu. Rev. Mater. Sci. **28**, 101 (1998).
[34]D. Bolten, U. Böttger, and R. Waser, Appl. Phys. Lett. **84**, 2379 (2004).
[35]T. Tsurumi, T. Sasaki, H. Kakemoto, T. Harigai, and S. Wada, Jpn. J. Appl. Phys. **43**, 7618 (2004).
[36]S. Trolier-McKinstry, N. B. Gharb, and D. Damjanovic, Appl. Phys. Lett. **88**, 202901 (2006).
[37]K. Lee and S. Baik, Annu. Rev. Mater. Res. **36**, 81 (2006).
[38]Y. Ishibashi and N. Orihara, Integr. Ferroelectr. **9**, 57 (1995).
[39]J. M. Liu, W. M. Wang, Z. G. Liu, H. L. Chan, and C. L. Choy, Appl. Phys. (Berlin) **A75**, 507 (2002).
[40]G. L. Yuan, J.-M. Liu, S. T. Zhang, D. Wu, Y. P. Wang, Z. G. Liu, H. L. W. Chan, and C. L. Choy, Appl. Phys. Lett. **84**, 954 (2004).
[41]J.-M. Liu, H. P. Li, C. K. Ong, and L. C. Lim, J. Appl. Phys. **86**, 5198 (1999).
[42]B. Pan, Y. Yang, L. C. Yu, J. M. Liu, K. Li, Z. G. Liu, and H. L. W. Chan, Mater. Sci. Eng., B **99**, 179 (2003).
[43]N. Wongdamnern, T. Sareein, and R. Yimnirun (to be published).

**Author complimentary copy. Redistribution subject to AIP license or copyright, see http://jap.aip.org/jap/copyright.jsp**

Journal of Alloys and Compounds 475 (2009) 473–478

Contents lists available at ScienceDirect

Journal of Alloys and Compounds

journal homepage: www.elsevier.com/locate/jallcom

# Fabrication and dielectric properties of lead titanate nanocomposites

R. Wongmaneerung[a], A. Rujiwatra[b], R. Yimnirun[c], S. Ananta[c,*]

[a] Department of Physics, Faculty of Science, Maejo University, Chiang Mai 50290, Thailand
[b] Department of Chemistry, Faculty of Science, Chiang Mai University, Chiang Mai 50200, Thailand
[c] Department of Physics, Faculty of Science, Chiang Mai University, Chiang Mai 50200, Thailand

ARTICLE INFO

*Article history:*
Received 14 January 2008
Received in revised form 8 July 2008
Accepted 13 July 2008
Available online 6 September 2008

*Keywords:*
Lead titanate
Perovskite
Composites
Microstructure
Dielectric properties

ABSTRACT

A simple powder mixing and pressure-less sintering process for fabrication of $PbTiO_3$ (PT) nanocomposites (micron-sized PT matrix reinforced with either PT nanoparticles or nanofibers) has been developed to enhance both densification and dielectric properties. The potentiality of a ceramic-nanocomposite technique as a low-cost and simple ceramic fabrication to obtain highly dense and pure PT/PT composites was demonstrated. It has been found that both densification and dielectric properties of the composites fabricated in this work were significantly enhanced, as compared to the two-stage sintering and the conventional PT ceramics.

© 2008 Elsevier B.V. All rights reserved.

## 1. Introduction

Pure and dense lead titanate ($PbTiO_3$ or PT) ceramic, which is of interest as a component in commercial electroceramic materials, is regarded to be one of the most difficult lead-based perovskite ferroelectric ceramics to produce [1–3]. The most important properties of PT ceramics are high Curie temperature (~490 °C), large mechanical-quality factor and pyroelectric coefficient [4,5]. Moreover, PT when combined with other oxides can form a series of ferroelectric materials that exhibit many of the most desirable dielectric, piezoelectric and pyroelectric properties for use in electronic and electro-optic devices at high frequency and high temperature, such as infrared sensors, actuators and hydrophones [1–3]. However, PT ceramic is mechanically weak due to large distortion of the tetragonal phase at room temperature which is characterized by the ratio between the lattice parameters ($c/a$, hereafter called tetragonality, ~1.06 [6,7]). Apart from general problems of PbO volatilization and associated high porosity, the stress induced by cooling through the phase transition can create cracking in bulk ceramics.

To overcome these problems, several techniques have been introduced, such as utilizing nanopowders, using additives, employing spark-plasma sintering and carrying out appropriated milling and sintering conditions [8–13]. All these techniques are aimed at reducing the lattice tetragonality of bulk ceramics, even though they inevitably affect the phase formation, structure and electrical properties of materials in different ways. Amongst all the issues reported so far, most attention has been concentrated on the use of additives and chemically derived powder processing, whereas investigations on modified particle packing or composite techniques have not been widely carried out [14,15].

Recently, ceramic-nanocomposites in which nanosized phases were dispersed within the matrix grains and/or at the grain boundaries have emerged as a novel approach of improving materials properties [16]. The mechanical properties of ceramics are known to be improved significantly by dispersing ceramic-nanoparticles into the ceramic-matrix grains or grain boundaries. However, the degree of improvement in their properties is dependent on the type of composite system involved [16]. Few studies have reported on ferroelectric matrix/metal nanodispersoid [17] and ferroelectric matrix/non-ferroelectric nanodispersoid [18] composite systems, and it is not yet clear how these dispersoids affect the properties of nanocomposites. Moreover, the problem of property trade-off, i.e., a deterioration of electrical properties still remains unsolved. In other words, the improvement of mechanical property can only be realized only by sacrificing electrical properties. So far, a little has been reported on the fabrication of ferroelectric matrix/ferroelectric nanodispersoid composite systems [19]. However, no work on the perovskite PT ceramic-nanocomposites has been reported yet.

Therefore, in this work, ferroelectric matrix/ferroelectric nanodispersoid PT composite has been developed to resolve these problems. With this new scheme, instead of using only micron-

* Corresponding author. Tel.: +66 53 943367; fax: +66 53 943445.
*E-mail address:* suponananta@yahoo.com (S. Ananta).

0925-8388/$ – see front matter © 2008 Elsevier B.V. All rights reserved.
doi:10.1016/j.jallcom.2008.07.074

sized PT powders as reported in our previous works [13,20], two different types of PT nanodispersoid (nanoparticles and nanofibers) were adopted as starting materials. The influence of both PT nanodispersoids on densification, microstructure and dielectric properties of the composites will be discussed and compared with the conventional method.

## 2. Experimental procedure

The starting PT materials for the fabrication of self-reinforced PT matrix/PT nanodispersoid composites were micron-sized PT powders, nanopowders, and nanofibers (Fig. 1), which were synthesized via ball-milling, vibro-milling, and hydrothermal techniques, respectively. The characteristics of each starting PT materials and their processing details are described in our previous works [21–23]. The powder mixtures (matrix:dispersoid ratio of 1:1) were formed into pellets by adding 3 wt.% polyvinyl alcohol (PVA) binder, prior to pressing in a pseudo-uniaxial die press at 100 MPa. It should be noted here that preliminary study of other matrix:dispersoid ratios, e.g. 0.7:0.3 and 0.6:0.4 was carried out and the complete solid-solution microstructure type commonly observed in the conventional PT processing was observed in all cases, indicating the solubility effect of the perovskite PT/PT (although their morphologies are different) limiting the possibility of composite formation. Each pellet was placed in an alumina crucible together with an atmosphere powder of identical chemical composition [20]. Such a composite cannot be fabricated by hot-pressing in the reduced atmosphere because the Pb-based perovskite is easily decomposed in the atmosphere. In this work, the composites were prepared by using simple pressure-less sintering method. Sintering was carried out at various temperatures (1000–1225 °C), for 1 h with heating/cooling rates of 1 °C/min [13,20] applied. These firing conditions were advocated from our previous work on PT ceramics with experimental details presented in Refs. [13,20].

Densities of the sintered products were determined by using the Archimedes principle. X-ray diffraction (XRD; Siemens-D500 diffractometer) was carried out at room temperature using Cu Kα radiation to identify the phase formed. The lattice parameters and tetragonality factor ($c/a$) of the sintered ceramics were calculated from the XRD patterns [24]. The microstructural development was characterized using a scanning electron microscopy (SEM; JEOL JSM-840A), equipped with an energy dispersive X-ray (EDX) analyzer. Mean grain sizes of the sintered ceramics were subsequently estimated by employing the linear intercept method [25]. In order to evaluate the dielectric properties, densified ceramics were polished to form flat and parallel faces. The samples were coated with silver-paste electrodes which were fired on both sides of the samples at 700 °C for 1 h. The dielectric properties were measured using a HIOKI 3532-50 LCR meter, on cooling through the transition range (550–25 °C) with a rate of 5 °C/min at high frequencies ranging from 1 to 5 MHz. Values of the dielectric constant were corrected for porosity by using the relationship $\varepsilon_r = \varepsilon_{r(measured)} \times$ theoretical density/sintered density [26].

## 3. Results and discussion

X-ray diffraction patterns of the PT composites reinforced with various PT dispersoids and sintered at various temperatures are displayed in Fig. 2, indicating the formation of single phase perovskite in all cases. The strongest reflections in the majority of all XRD traces indicate the formation of the PT perovskite phase of lead titanate which could be matched with JCPDS file no. 6-452, in agreement with other works [10–13]. To a first approximation, this phase has a tetragonal perovskite-type structure in space group $P4/mmm$ with cell parameters $a = 389.93$ pm and $c = 415.32$ pm [27]. All the peaks were assigned to PT, and no reaction phase between different PT starting materials was detected. Moreover, there is no significant difference between the PT nanocomposites reinforced with either PT nanopowders or nanofibers, after sintered at temperatures ranging from 1150 to 1200 °C. This observation could be attributed mainly to the high purity of the employed starting materials together with the optimized firing conditions. The samples sintered with temperature below 1150 °C were broken into pieces after sintering process, whilst the samples sintered at 1225 °C exhibited severe melted areas. Thus, no further characterization can be performed on these samples.

It should be noted that a single phase of perovskite is found in all PT composites similar with the two-stage sintering samples [20], in contrast to the observations for the conventional case [13] (Table 1). No evidence of pyrochlore phase of $PbTi_3O_7$ composition

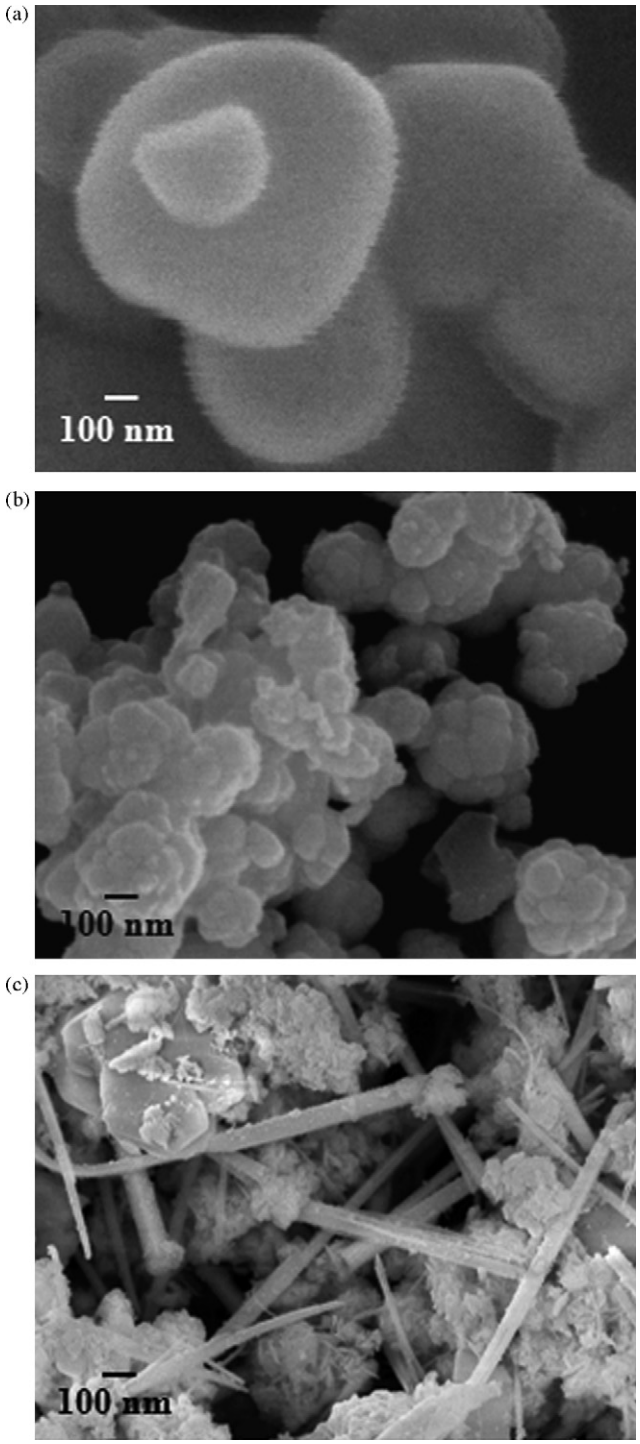



**Fig. 1.** SEM micrographs of the starting PT dispersoids: (a) micron-sized powders, (b) nanopowders, and (c) nanofibers.

reported earlier by other workers [21,28] was found, nor was any evidence of other second phases [29] being present. This could be due to the lower firing temperature of the nanocomposite samples as compared to the conventional PT ceramics, leading to a smaller degree of lead losses and consequently avoiding the pyrochlore formation, in consistent with other works [30,31], whilst a sufficient arrangement of grain-packing required for ceramic densification still be reached. However, many other factors come into play, e.g. homogeneity of materials, reactivity of starting powders, and pro-

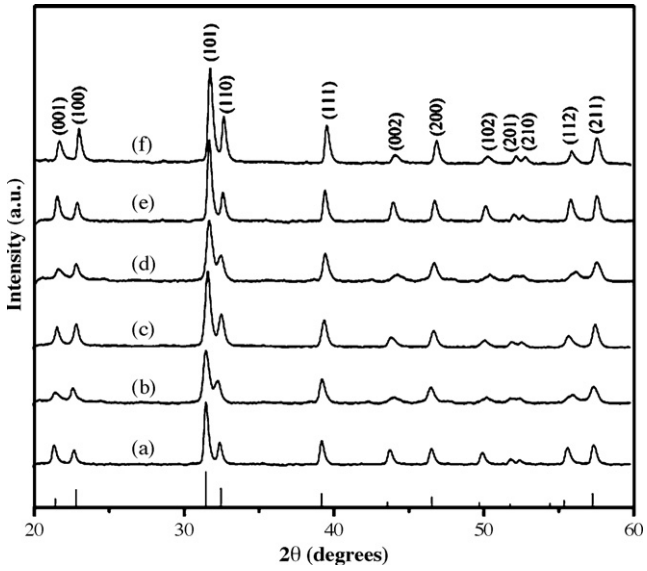



**Fig. 2.** XRD patterns of PT composites reinforced with PT nanopowders after sintered at (a) 1150 °C, (b) 1175 °C and (c) 1200 °C, and reinforced with PT nanofibers after sintered at (d) 1150 °C, (e) 1175 °C and (f) 1200 °C, for 2 h.

cessing variables. These XRD results clearly show that, in general, the different processing methods used for preparing PT ceramics gave rise to a different phase formation in the sintered materials. The absence of minor phase in composite samples was related to the more reactive process used.

Table 1 also shows tetragonality factor ($c/a$), relative density and average grain size of each nanocomposite sample, comparing with the conventional and the two-stage sintered samples, respectively. Generally, it is evident that as the sintering temperature increases, the density of almost all the samples increases. However, it can be seen that the sintering behavior of PT ceramics derived from different processing techniques were dissimilar. Two-stage sintering PT ceramics reached a maximum density of ~97% at 900/1200 °C [20]. Whilst conventional PT samples exhibit reduced densification, and a temperature of 1225 °C was required to reach a densification level of ~94% [13]. On the other hand, both types of PT nanocomposites sintered at 1200 °C exhibit the highest relative density of about 98% with a smallest average grain size of less than 1.0 μm. By comparison with conventional PT ceramics, lower values of tetragonality ($c/a$) are found in all nanocomposite cases, equivalent to those observed in the two-stage sintering case, indicating lower internal stress in these nanocomposites. More interestingly, all nanocomposite samples do not suffer from severe stresses as a result of the high $c/a$ ratio so they have not broken into pieces after experienced the sintering process or once subjected to a cycle of high temperature measurement of dielectric properties, as reported previously for the conventional and two-stage sintering PT cases [13,20].

Microstructural features (free and fracture surfaces) of both PT nanocomposites sintered at different temperatures for 2 h are shown in Figs. 3 and 4. It was found that average grain sizes increase with the sintering temperature (Fig. 3). The PT nanodispersoids were found to locate both within the matrix and at the grain boundaries (see enlarged insertion in Fig. 3(d)). The microstructure of the composites is that of the nanocomposites classified as "nanomicro" and "nanofiber" types [16].

Representative fracture surfaces for both types of PT nanocomposites are given in Fig. 4. It is seen that a uniform grain shape of typical perovskite ceramics [9,30,31] is observed, with sizes in the range of 0.2–2.8 μm. It should be noted that the average grain size of both PT nanocomposites is <1.7 μm, which is less than the critical value of 3 μm [11,32,33] and gives rise to a volumetric percentage enough to buffer the anisotropic stress caused by the phase transition [32]. Here, it is believed that PT nanodispersoids with random orientations result in lower internal stress in composite samples because they compensate the anisotropy of thermal expansion coefficients.

By comparison with conventional PT ceramics [13], almost clean microstructures with highly uniform, denser angular grain-packing and more homogeneous are generally observed in both types of self-reinforced PT nanocomposites. These microstructures are typical of a solid-state sintering mechanism. In the present study (Figs. 3 and 4), the microstructural features of both types of PT nanocomposites with various sintering temperatures ranging from 1150 to 1200 °C are not significantly different. However, it should be noted that higher angularly grains were evidenced for higher sintering temperature. The observation that the sintering temperature effect may also play an important role in obtaining a high angularity grains of perovskite ceramics is also consistent with other similar systems [30,31]. Moreover, abnormal grain growth probably due to the inhibition of grain growth mechanism during doubly sintering process [20,34] was also found in some samples, as shown in Figs. 3(c and d) and 4(f). It is also of interest to point out that evidence of intergranular fracture has been found for the existence of microcracks (arrowed) along the grain boundaries of the composite samples self-reinforced with PT nanoparticles (Fig. 4(a–c)). The different microstructure evolution of PT nanocomposites confirms the importance of the processing method including the morphological characteristics of the dispersed phase, consistent with other works [32,35]. Whilst the grain size of both nanocomposites is approximately the same, the density and microstructure of PT samples sintered at higher temperatures indicated that the composite

**Table 1**
Sintering behavior of PT ceramics derived from different fabrication techniques

| Processing [Ref.] | Sintering temperature (°C) | Perovskite phase[a] (%) | Relative density[b] (%) | Tetragonality factor ($c/a$) | Grain size[c] (μm) | Average grain size (μm) |
|---|---|---|---|---|---|---|
| Normal sintering [13] | 1225 | 89.20 | 93.00 | 1.063 | 41.0–83.0 | 62.0 |
| Two-stage sintering [20] | 900/1200 | 100.00 | 97.02 | 1.061 | 1.0–2.2 | 1.6 |
| Composite reinforced with nanopowders | 1150 | 100.00 | 96.33 | 1.059 | 0.2–0.6 | 0.40 |
| | 1175 | 100.00 | 97.02 | 1.053 | 0.3–1.0 | 0.65 |
| | 1200 | 100.00 | 97.85 | 1.061 | 0.6–2.0 | 1.30 |
| Composite reinforced with nanofibers | 1150 | 100.00 | 95.68 | 1.053 | 0.3–1.3 | 0.80 |
| | 1175 | 100.00 | 96.76 | 1.058 | 0.4–1.3 | 0.85 |
| | 1200 | 100.00 | 97.45 | 1.061 | 0.5–2.8 | 1.65 |

[a] The estimated precision of the perovskite phase is ±0.1%.
[b] The estimated precision of the density is ±0.1%.
[c] The estimated precision of the grain size is ±10%.

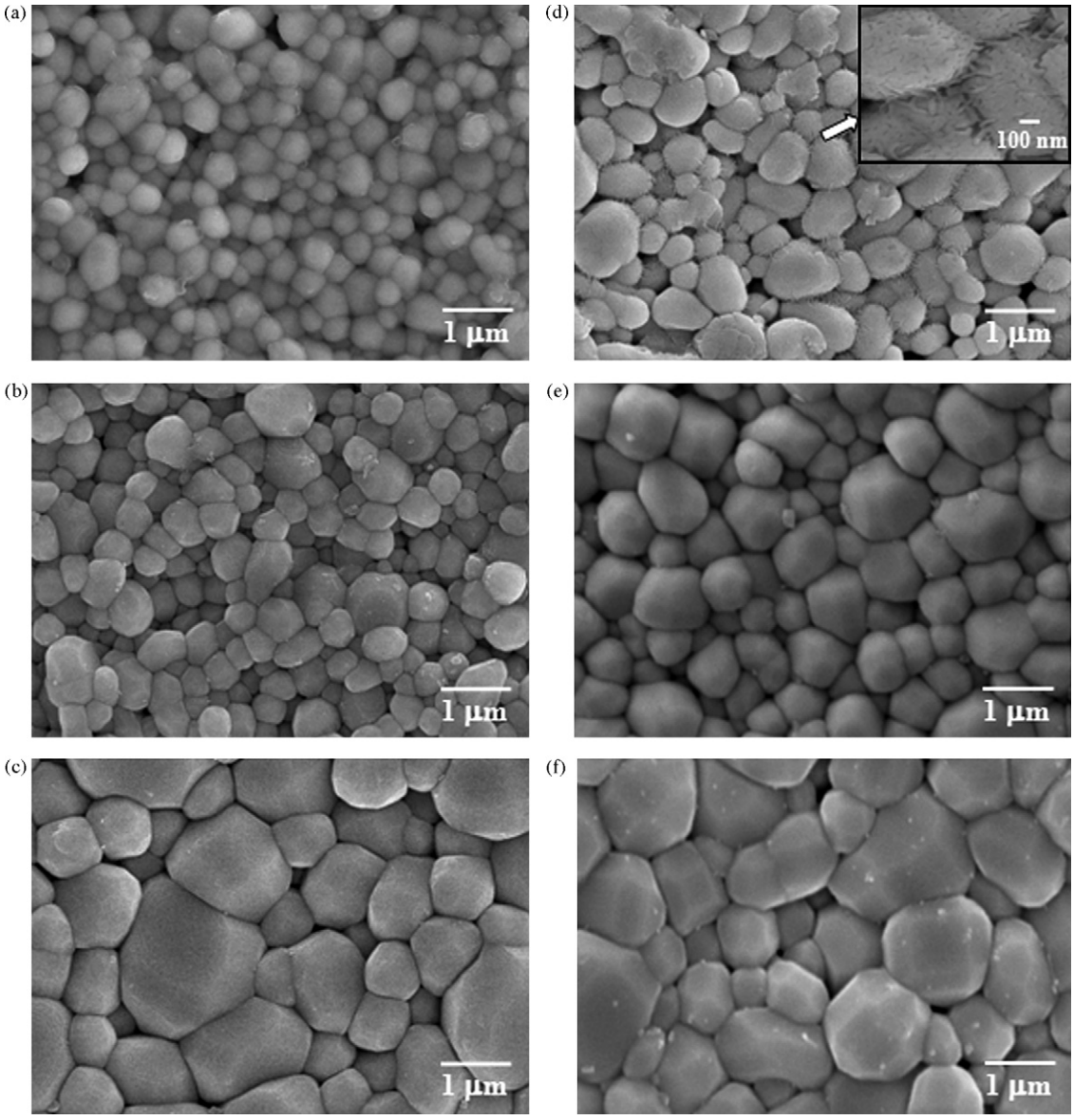



**Fig. 3.** Free surface of PT composites reinforced with PT nanopowders after sintered at (a) 1150 °C, (b) 1175 °C and (c) 1200 °C, and reinforced with PT nanofibers after sintered at (d) 1150 °C, (e) 1175 °C and (f) 1200 °C, for 2 h.

method of PT matrix reinforced with PT nanofibers was preferable for obtaining dense PT ceramics.

Interestingly, all the nanocomposite samples sintered at 1150–1200 °C remained unbroken. It may be assumed that the nanocomposites consisting of very fine dispersoids suffer less deformation, caused by the high value of $c/a$ ratio, than the ceramics with significantly large grains (Table 1). Consequently, the experimental work carried out here suggests that the optimum conditions for forming the highly dense PT samples in this work are both types of PT/PT nanocomposites sintered at 1200 °C, 2 h dwell time, and 1 °C/min heating/cooling rates.

The dielectric properties of PT samples fabricated with different techniques are also compared in Table 2. In general, they all behave as typical normal ferroelectric materials [3]. The Curie temperatures are about the same for all samples measured whilst the variation of dielectric constant and dielectric loss of both types of PT nanocomposites seems to be somewhat related to the sintering temperatures. This observation indicates that densification and the presence of the second phases accompanied with porosities are the key factors responsible for the dielectric response of the products. Moreover, this study demonstrated that the dielectric properties of PT ceramics are also influenced by microstructural features and arrangement especially the microcracks and final density rather than by only grain size itself.

**Table 2**
Dielectric properties of PT ceramics derived from different fabrication techniques

| Processing [Ref.] | Frequency (MHz) | $T_C$ (°C) | $\varepsilon_{25°}$ | $\varepsilon_{r,max}$ | $\tan\delta_{max}$ |
|---|---|---|---|---|---|
| Normal sintering [13] | 1 | 482 | 243 | 7680 | 1.07 |
| Two-stage sintering [20] | 1 | 484 | 209 | 8198 | 0.95 |
| Composite reinforced with nanopowders | 1 | 486 | 244 | 8523 | 1.09 |
| | 3 | 486 | 245 | 7517 | 0.91 |
| | 5 | 487 | 247 | 7144 | 0.76 |
| Composite reinforced with nanofibers | 1 | 488 | 248 | 9104 | 0.81 |
| | 3 | 489 | 246 | 7110 | 0.57 |
| | 5 | 489 | 242 | 6801 | 0.45 |

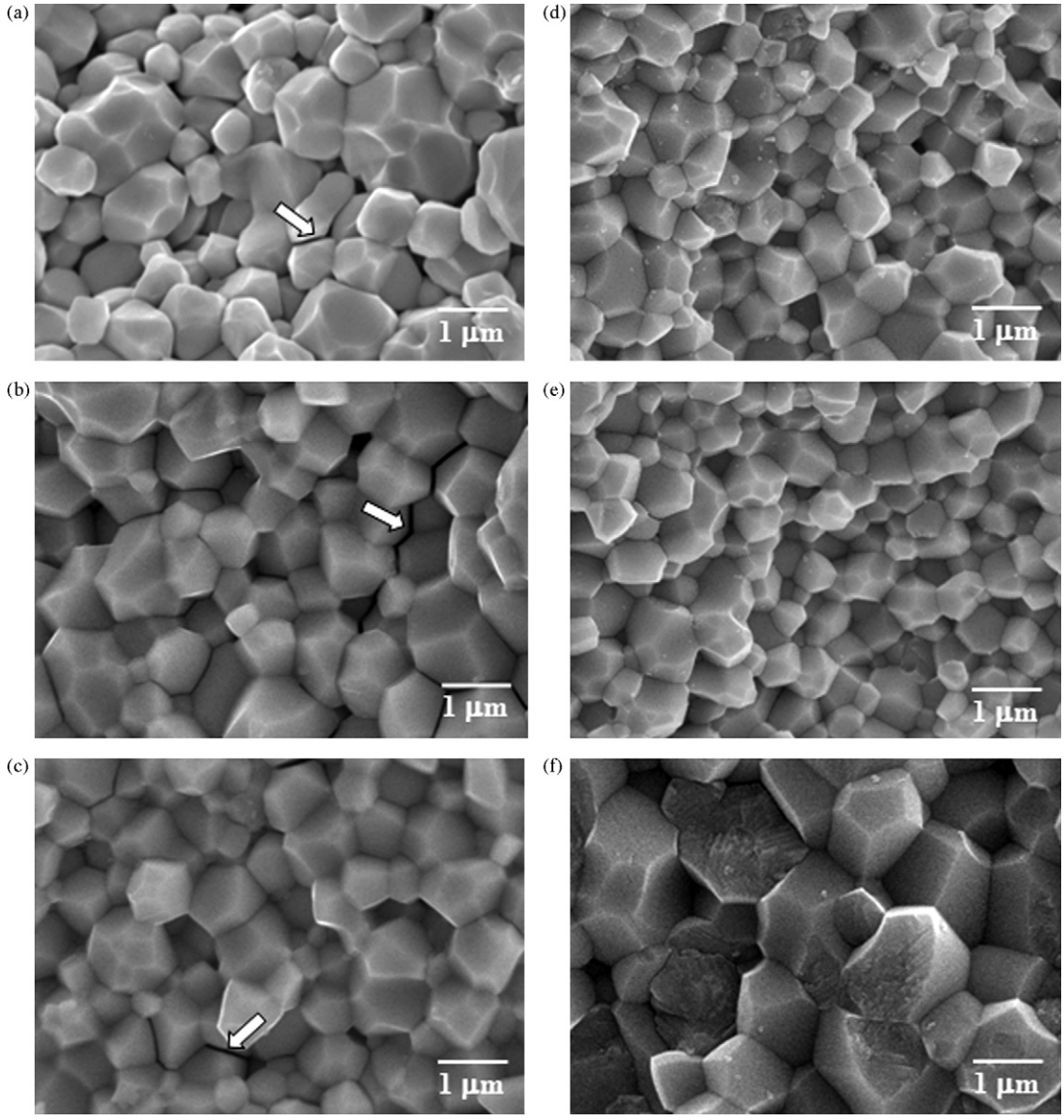



**Fig. 4.** Fracture surface of PT composites reinforced with PT nanopowders after sintered at (a) 1150 °C, (b) 1175 °C and (c) 1200 °C, and reinforced with PT nanofibers after sintered at (d) 1150 °C, (e) 1175 °C and (f) 1200 °C, for 2 h.

The different microstructure and the different amount of secondary phases present in the sintered PT ceramics strongly influence the dielectric properties of these materials, leading to relatively superior dielectric behavior in PT/PT nanocomposites. The secondary phases in conventional PT sample are interconnected at grain boundaries and, as suggested by Wang and Schulze [31], exert more influence on the dielectric properties than when they are isolated. The influence of densification and microcracks on dielectric properties of these PT composites can be clearly observed in Fig. 5, where the dielectric constant and dissipation factor as a function of temperature are shown, respectively.

The maximum dielectric constant values at 1 MHz in both PT nanocomposites were 2–5% higher than in two-stage sintering and conventional PT samples (Table 2). As mentioned earlier, the reason for this is the high amount of secondary phase present in conventional PT ceramics and the presence of a PbO-rich secondary phase, with low dielectric constant, which could form a continuous layer between grains, decreasing the dielectric constant of the two-stage sintering samples [13,36].

The results obtained in this work suggest that, in general, these PT/PT nanocomposites exhibit complex microstructures which are inherently heterogeneous. The heterogeneity is a result of variation in grain size and orientation; variation in chemical homogeneity; and the presence and distribution of additional minor phase, pores and (micro) cracks. These factors, which are strongly influenced by the sintering conditions, have an important effect on the dielectric properties of the materials and their reproducibility. However, these results suggest that better densification can be introduced into piezoceramics by fabricating ceramic-nanocomposites reinforced with piezoelectric nanodispersoids. Two aspects of this study are significant: (i) reductions in the maximum required sintering temperature (or the required prolong firing time) are possible as compared to the conventional (or the two-stage sintering) method and (ii) a framework has been established for developing self-reinforced piezoceramic-nanocomposite technique for better

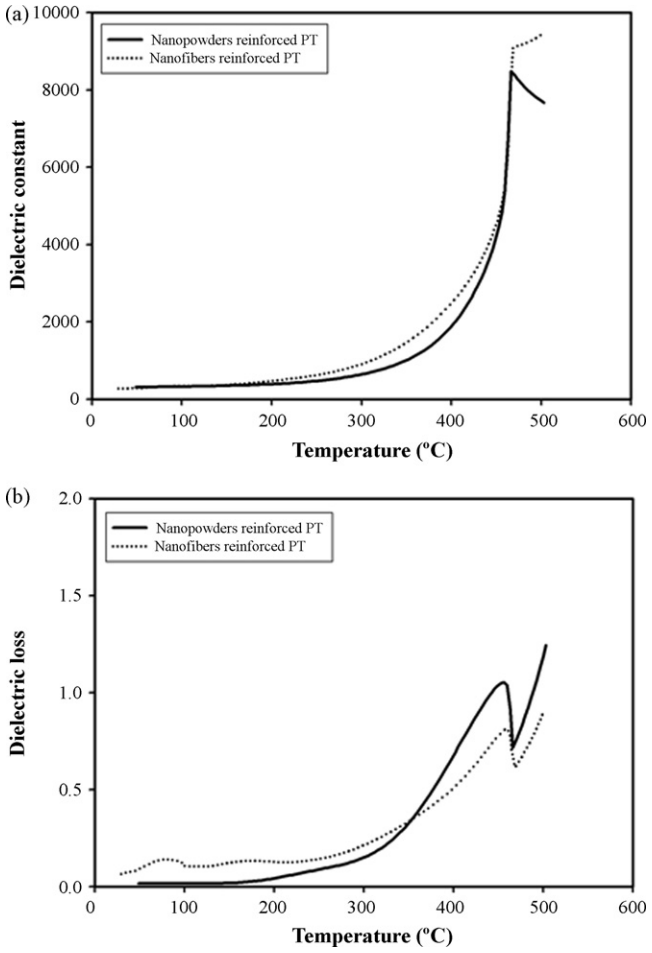



**Fig. 5.** Variation with temperature of (a) dielectric constant ($\varepsilon_r$) and (b) dielectric loss ($\tan\delta$) at 1 MHz for PT composites reinforced with PT nanopowders compared with those reinforced with PT nanofibers.

densification with retainable electrical properties of other piezoelectric materials, particularly those containing low melting point constituents.

For better understanding and verifying the attractiveness of the nanocomposite technique further, a systematic study on the effect of another piezoelectric nanodispersoids such as $BaTiO_3$ or PZT on the phase formation, densification, microstructure and electrical properties of the piezoelectric-based ceramic-nanocomposites is required.

## 4. Conclusions

The potentiality of a ceramic-nanocomposite technique as a low-cost and simple ceramic fabrication to obtain highly dense and pure PT/PT composites was demonstrated. It has been found that both densification and dielectric properties of the composites fabricated in this work were significantly enhanced, as compared to the two-stage sintering and the conventional PT ceramics, which is likely due to the fine-grain and reduced tetragonality as well as anisotropies of stress and domain motion in the composites.

## Acknowledgements

We thank the Thailand Research Fund (TRF), the Commission on Higher Education (CHE) and the National Nanotechnology Center (NANOTEC), NSTDA, for all support.

## References

[1] B. Jaffe, W.R. Cook, H. Jaffe, Piezoelectric Ceramics, Academic Press, New York, 1971.
[2] G.H. Haertling, J. Am. Ceram. Soc. 82 (1999) 797–818.
[3] A.J. Moulson, J.M. Herbert, Electroceramics, 2nd ed., Wiley, Chichester, 2003.
[4] T. Takahashi, Am. Ceram. Soc. Bull. 69 (1990) 691–695.
[5] L.E. Cross, Mater. Chem. Phys. 43 (1996) 108–115.
[6] G. Shirane, S. Hoshino, J. Phys. Soc. Jpn. 6 (1951) 265–270.
[7] G. Shirane, R. Pepinsky, B.C. Frazer, Acta Crystallogr. 9 (1956) 131–140.
[8] H. Takeuchi, S. Jyomura, E. Yamamoto, Y. Ito, J. Acoust. Soc. Am. 72 (1982) 1114–1120.
[9] L.B. Kong, W. Zhu, O.K. Tan, J. Mater. Sci. Lett. 19 (2000) 1963–1966.
[10] T. Suwannasiri, A. Safari, J. Am. Ceram. Soc. 76 (1993) 3155–3158.
[11] T. Takeuchi, M. Tabuchi, I. Kondoh, N. Tamari, H. Kageyama, J. Am. Ceram. Soc. 83 (2000) 541–544.
[12] J.S. Forrester, J.S. Zobec, D. Phelan, E.H. Kisi, J. Solid State Chem. 177 (2004) 3553–3559.
[13] A. Udomporn, K. Pengpat, S. Ananta, J. Eur. Ceram. Soc. 24 (2004) 185–188.
[14] F. Ye, L. Liu, J. Zhang, M. Iwasa, C.L. Su, Compos. Sci. Technol. 65 (2005) 2233–2239.
[15] R. Gadow, F. Kern, A. Killinger, Mater. Sci. Eng. B 148 (2008) 58–64.
[16] T. Ohji, Y.K. Jeong, Y.H. Choa, K. Niihara, J. Am. Ceram. Soc. 81 (1998) 1453–1460.
[17] H.T. Chung, D.S. Cheong, C.S. Kim, Mater. Lett. 59 (2005) 920–924.
[18] S. Jiansirisomboon, A. Watcharapasorn, Curr. Appl. Phys. 8 (2008) 48–52.
[19] H. Beltran, N. Maso, E. Cordoncillo, A.R. West, J. Electroceram. 18 (2007) 277–282.
[20] R. Wongmaneerung, R. Yimnirun, S. Ananta, Appl. Phys. A 86 (2007) 249–255.
[21] A. Udomporn, S. Ananta, Mater. Lett. 58 (2004) 1154–1159.
[22] R. Wongmaneerung, R. Yimnirun, S. Ananta, Mater. Lett. 60 (2006) 2666–2671.
[23] A. Rujiwatra, N. Thammajak, T. Sarakonsri, R. Wongmaneerung, S. Ananta, J. Crystal Growth 289 (2006) 224–230.
[24] H. Klug, L. Alexander, X-ray Diffraction Procedures for Polycrystalline and Amorphous Materials, 2nd ed., Wiley, New York, 1974.
[25] R.L. Fullman, Trans. AIME 197 (1953) 447–452.
[26] S.L. Swartz, T.R. Shrout, W.A. Schulze, L.E. Cross, J. Am. Ceram. Soc. 67 (1984) 311–315.
[27] JCPDS-ICDD Card no. 6-452, International Centre for Diffraction Data, Newtown Square, PA, 2000.
[28] J. Tartaj, C. Moure, L. Lascano, P. Durán, Mater. Res. Bull. 36 (2001) 2301–2310.
[29] M.L. Calzada, M. Alguero, L. Pardo, J. Sol–Gel Sci. Technol. 13 (1998) 837.
[30] S. Ananta, N.W. Thomas, J. Eur. Ceram. Soc. 19 (1999) 1873–1881.
[31] H.C. Wang, W.A. Schulze, J. Am. Ceram. Soc. 73 (1990) 825–832.
[32] Y. Matsuo, H. Sasaki, J. Am. Ceram. Soc. 49 (1966) 229–230.
[33] S.R. Dhage, Y.B. Khollam, H.S. Potdar, S.B. Deshpande, B.D. Sarwade, D.K. Date, Mater. Lett. 56 (2002) 564–570.
[34] S. Ananta, N.W. Thomas, J. Eur. Ceram. Soc. 19 (1999) 2917–2930.
[35] S. Chattopadhyay, P. Ayyub, V.R. Palkar, M. Multani, Phys. Rev. B 52 (1995) 13177–13179.
[36] M. Villegas, A.C. Caballero, M. Kosec, C. Moure, P. Duran, J.F. Fernandez, J. Mater. Res. 14 (1999) 891–897.

Journal of Alloys and Compounds 474 (2009) 241–245

Contents lists available at ScienceDirect

Journal of Alloys and Compounds

journal homepage: www.elsevier.com/locate/jallcom

# Effects of addition of BT on structural phase formation and electrical properties of relaxor ferroelectric $Pb(In_{0.5}Nb_{0.5})_{(1-x)}Ti_{(x)}O_3$ ceramics

S. Wongsaenmai [a,*], S. Ananta [b], R. Yimnirun [b]

[a] Department of Physics, Faculty of Science, Maejo University, Chiang Mai 50290, Thailand
[b] Department of Physics, Faculty of Science, Chiang Mai University, Chiang Mai 50200, Thailand

ARTICLE INFO

*Article history:*
Received 18 January 2008
Received in revised form 11 June 2008
Accepted 15 June 2008
Available online 13 August 2008

*Keywords:*
Relaxor ferroelectric
Wolframite precursor method
Vibro-milling technique
PBINT

ABSTRACT

In this study, the solid solution of $Pb(In_{0.5}Nb_{0.5})_{(1-x)}Ti_{(x)}O_3$ with 20 mol% of BT (where $x = 0.0$, 0.1, 0.2 and 0.3) ceramics was prepared by the wolframite precursor method via a vibro-milling technique. The concentration of 20 mol% of BT was the lowest amount of BT to help stabilize the perovskite phase formation of PIN ceramics in this study. The variation of $x$ between 0.0 and 0.3 ($0.0 \leq x \leq 0.3$; $\Delta x = 0.1$) was chosen based on the non-MPB composition of this PINT system to focus on the compositions with relaxor behavior. The phase formation of the ceramics was investigated as a function of compositions. The XRD patterns investigation showed that the ceramics gradually changed from the pseudo-cubic to tetragonal phase between the compositions $x = 0.2$ and 0.3, indicating a shift in the MPB of the PINT system with BT addition. Correspondingly, large dielectric constant maximum ($\varepsilon_m$) was observed over the same compositions. The remanent polarization ($P_r$) was also maximized at this composition, which indicated enhanced electrical properties near the MPB of this PBINT system. These results clearly indicated that the addition of BT had strong influence on phase formation and the electrical properties of the PINT system.
© 2008 Elsevier B.V. All rights reserved.

## 1. Introduction

The relaxor ferroelectric ceramics, which have the $Pb(B'B'')O_3$ complex perovskite structure, show broad dielectric transition maxima, high dielectric constant over a wide temperature range and frequency dispersion of dielectric properties and high electrostrictive strains [1,2]. These owning excellent properties attract for application as multilayer capacitor, piezoelectric transducer and electrostrictive actuator [2,3]. It is known that the main problem of these materials is the difficult to obtain the single-phase perovskite because of its inherently small electronegativity difference and low tolerance factor [4]. It has reported that the addition of the largest electronegativity difference and tolerance factor such as BT to PZN- and PMN-based system helps to stabilize the perovskite phase formation [5,6]. Lead indium niobate (PIN) is of interest for its chemical ordering study. It is a member of relaxor family with a 1:1 stoichiometric of B-site ordering which can be brought from disordered state into ordered state by thermal treatment [7]. The disordered state of PIN exhibits relaxor behavior which shows broad dielectric maximum near 66 °C [8,9]. In contrast, the ordered state shows antiferroelectric behavior with a sharp peak in dielectric constant vs. temperature curve observed at 168 °C [8,10]. However, the most interesting in this material is the solid solution with PT normal ferroelectric, because of their $T_c$ higher than 250 °C near the MPB for the single crystal [11]. It is difficult to eliminate the pyrochlore phase in preparation, even though the wolframite precursor method was used. Interestingly, the addition of BT to help elimination the pyrochlore phase was reported in other systems of PZN-PT–BT and PMN-PT–BT [12,13]. In this present work, the addition of BT to PINT system was obtained by the wolframite precursor method to obtain the pure phase perovskite via vibro-milling technique. The phase formation and transition were investigated from the XRD patterns and the lattice parameters. The possible MPB of this PBINT system was examined with XRD patterns and electrical properties.

## 2. Experimental

The powders of $Pb(In_{0.5}Nb_{0.5})_{(1-x)}Ti_{(x)}O_3$ with 20 mol% of BT (where $x = 0.0$, 0.1, 0.2, and 0.3, abbreviated as PBINT) were synthesized by the wolframite precursor method via a vibro-milling technique. The concentration of 20 mol% of BT was lowest amount of BT to help stabilize the perovskite phase formation of PIN ceramics in this study. The secondary phase was found in the compositions lower than that of 20 mol% of BT (results are not shown). The wolframite ($InNbO_4$) was first prepared by mixing starting indium oxide ($In_2O_3$) and niobium oxide ($Nb_2O_5$) (Aldrich, 99.9% purity). Mixed powders were milled by a vibratory laboratory mill (McCrone micronizing mill) for 0.5 h and calcined at optimized calcination temperature of 900 °C for 4 h to obtain the intermediate precursor $InNbO_4$ [14,15]. The wolframite precursor powders were subsequently mixed with lead oxide (PbO) (Fluka, 99%

* Corresponding author. Tel.: +66 53 873525; fax: +66 53 872206.
*E-mail address:* wongsaenmai@yahoo.com (S. Wongsaenmai).

0925-8388/$ – see front matter © 2008 Elsevier B.V. All rights reserved.
doi:10.1016/j.jallcom.2008.06.112

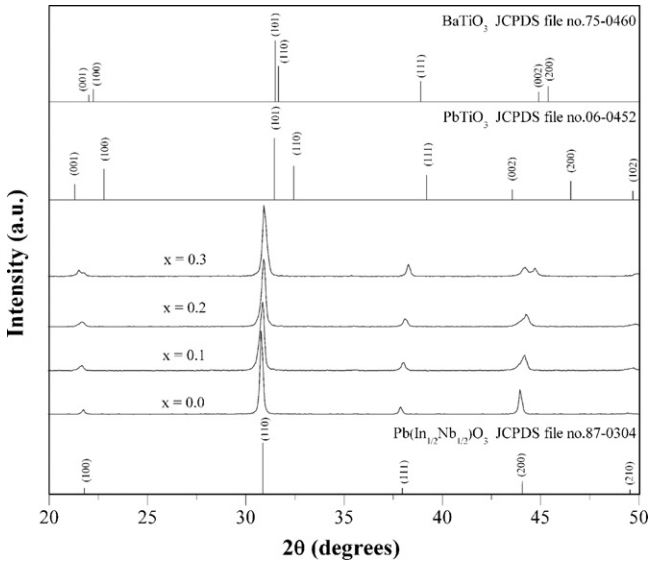



**Fig. 1.** XRD patterns of PBINT ceramics obtained at optimum sintering temperature.

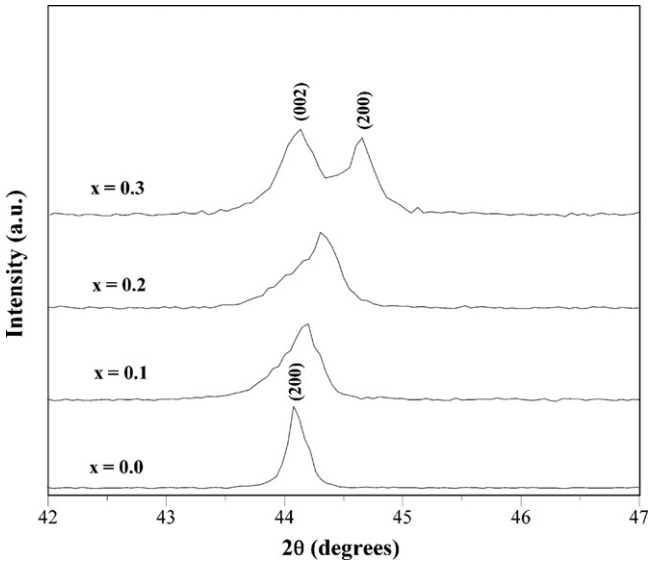



**Fig. 2.** Selected region XRD patterns of PBINT ceramics.

purity), $BaCO_3$ (Fluka, 99% purity) and titanium oxide ($TiO_2$) (Riedel-de Haën, 99% purity) according to the compositions of $Pb(In_{0.5}Nb_{0.5})_{(1-x)}Ti_{(x)}O_3$ with 20 mol% of BT where $x = 0.0$, 0.1, 0.2, and 0.3 and re-milled for 0.5 h. Excess amount of PbO (2 mol%) and $In_2O_3$ (2 mol%) were added in this stage. After drying at 120 °C for 2 h, the mixtures were calcined at temperature between 1050 and 1150 °C for 2 h with heating/cooling rate of 5 °C/min to determine optimum firing condition for every composition, in closed alumina crucible. After that, the calcined powders were pressed hydraulically to form disc-shaped pellets 10 mm in diameter and 2 mm thick, using 3 wt.% polyvinyl alcohol as binder. The pellets with composition between $x = 0.0$ and 0.3 were sintered in a closed alumina crucible at temperature between 1250 and 1300 °C for 2 h with heating/cooling rate of 10 °C/min. To prevent PbO evaporation, the pellets were placed on the same powder.

The phase formation of the sintered ceramics was analyzed by X-ray diffraction (XRD), using Cu Kα radiation to determine the phases formed and optimum firing temperatures for the formation of desired phase. The relative amount of the perovskite phase was determined from the relative intensities of the major XRD peaks of perovskite (1 1 0) and pyrochlore (2 2 2) ($I_{perov(1\,1\,0)}/I_{perov(1\,1\,0)} + I_{pyro(2\,2\,2)}$) [16]. Lattice parameters of the perovskite phases were determined by Cohen's method in conjunction with the least squares method [17]. The microstructure was investigated by scanning electron microscopy (SEM, JEOL Model JSM 840A). For the evaluation of electrical properties, gold electrodes were sputtered on both sides of the samples. The dielectric properties were measured with an LCR meter (HP-4284A, Hewlett-Packard, Santa Clara, CA) in conjunction with an environmental chamber (9023, Delta Design, Poway, CA). A heating rate of 2 °C/min and frequency of 1 kHz were used during measurement. Ferroelectric hysteresis loops were evaluated at various temperatures (25, −20, −50 and −80 °C) with a standardized ferroelectric test system (RT-66A, Radiant Technologies, Albuquerque, NM). A peak electric field of 30 kV/cm was applied.

## 3. Results and discussion

The XRD patterns of the dense PBINT ceramics as function of PT concentration at room temperature are shown in Fig. 1. It is evident that a complete crystalline solid solution of pure perovskite phase occurs throughout the studied compositional range of the PBINT system. The main difference of these XRD patterns can be observed on the peak of (2 0 0) reflection near $2\theta \sim 44–45°$, because the single (2 0 0) reflection peak indicates the pseudo-cubic phase, whereas the splitting in two peaks of (2 0 0)/(2 0 0) shows the tetragonal phase. For better viewing, the selected region of the (2 0 0) reflections near $2\theta \sim 44–45°$ are shown in Fig. 2, which exhibits the phase transformation from the pseudo-cubic to the tetragonal phase near the compositions of $x = 0.2$ and 0.3. Therefore, it can be expected that the MPB of this system lies between the compositions $x = 0.2$ and 0.3.

It is also supported by the lattice parameters, as listed in Table 1, that the region near same the compositions between $x = 0.2$ and 0.3 shows rapid increase in the tetragonality factor of $c/a$ to 1.01. It is also seen that the addition of PT leads to shrinking of the $a$-axis while the $c$-axis expands, resulting in the average lattice parameter decrease. In comparison to the PINT system, the average lattice parameter of composition $x = 0.0$ (as $a = 0.4127$ nm) is larger than that of the PIN ceramics (as $a = 0.4117$ nm) [18]. However, the average lattice parameter decreases with increasing PT concentration for both of PINT and PBINT ceramic systems. It is expected that diffusion of the smaller Ti cation into B-site results in a decrease in lattice constant and the partial substitution of the larger Ba cation into A-site causes an increase in the average lattice parameters [19–21]. From the results of the XRD patterns and the lattice parameters, it is believed that the MPB of the PBINT system lies between the compositions $x = 0.2$ and 0.3. Additionally, it is also indicated that the addition of BT induces a shift of the MPB in the PINT system. Similar shift of the MPB has been reported in other systems such as PMN-PT and PZN-PT [13,22,23].

Fig. 3 shows the SEM micrographs of the PBINT ceramics. The grain size was estimated from the SEM observation, as listed in Table 1, together with the density. In general, the irregular grains

**Table 1**
Physical properties and the lattice parameters of PBINT ceramics

| Composition ($x$) | Calcination temperature (°C) | Sintering temperature (°C) | Lattice constant (nm) | | | | Bulk density (g/cm$^3$) | Percentage of theoretical density (%) | Grain size (μm) |
|---|---|---|---|---|---|---|---|---|---|
| | | | $a$ | $c$ | $c/a$ | $(a^2c)^{1/3}$ | | | |
| 0.0 | 1150 | 1300 | 0.4126 | – | 1 | 0.4127 | 7.89 | 93.2 | 1.90 |
| 0.1 | 1000 | 1250 | 0.4100 | – | 1 | 0.4100 | 7.78 | 90.1 | 2.13 |
| 0.2 | 1050 | 1250 | 0.4096 | – | 1 | 0.4096 | 7.84 | 92.6 | 2.26 |
| 0.3 | 1050 | 1250 | 0.4052 | 0.4109 | 1.01 | 0.4067 | 7.86 | 97.1 | 2.58 |

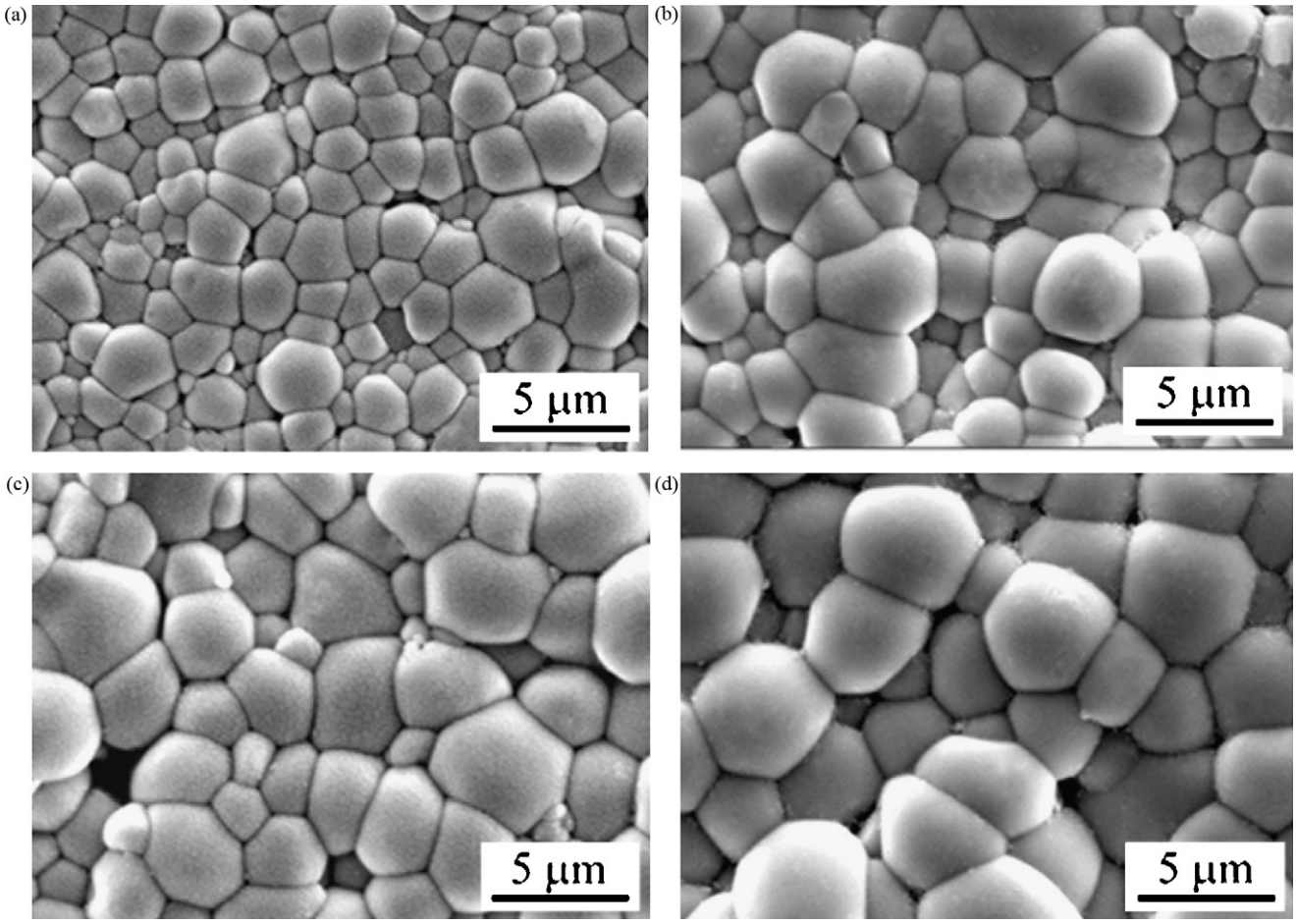



**Fig. 3.** SEM micrographs of PBINT with various compositions: (a) $x = 0.0$, (b) $x = 0.1$, (c) $x = 0.2$ and (d) $x = 0.3$.

and porosities can be observed, while the pyrochlore phase could not be found in the microstructure, good agreement with the XRD investigation. Clearly, the addition of PT and BT helps to stabilize the perovskite phase, a result of their difference in electronegativity and tolerance factor [5]. Additionally, the relative densities in the range of 90–97% theoretical density are obtained. These densities strongly influence the electrical properties, which will be presented in the following part. Moreover, the average grain size is in the range of 1–3 μm, indicating the fine grain size for this system [24]. The average grain size increased from 1.90 μm for the composition of $x = 0.0$–approximately 2.58 μm for the composition of $x = 0.3$. However, it should be noticed that the microstructure of all the compositions also represents two distinct grain sizes, i.e. large grains (~5 μm) and submicron grains. It is clearly evident that the addition of PT noticeably enhances grain growth.

The temperature dependence of the dielectric constant (at 1 kHz) as a function of composition is displayed in Fig. 4. All compositions show broad maximum of the dielectric constant. More details of the dielectric properties underlying frequency and their relaxor behavior have been reported in our previous work [25]. The dielectric constant maxima ($\varepsilon_m$) slightly increase with the composition of $x = 0.1$ and then drastically increase with more PT concentrations.

As listed in Table 2, large dielectric constant maxima are obtained at the composition of $x = 0.2$ ($\varepsilon_m = 17{,}366$ at 1 kHz) and $x = 0.3$ ($\varepsilon_m = 18{,}541$ at 1 kHz). It is known that the solid solution of lead-based relaxor and normal ferroelectric (PT) shows extra high dielectric constant maximum near the MPB [26]. Based on the XRD patterns and the lattice parameters, the maximization of the dielectric properties near the MPB has also been correlated with the reduction of the lattice distortion, as previously reported in the PZT system [27]. The temperatures of dielectric constant maximum ($T_m$) are also summarized in Table 2. It can be seen that increasing PT concentration leads to a shift of $T_m$ to a higher temperature,

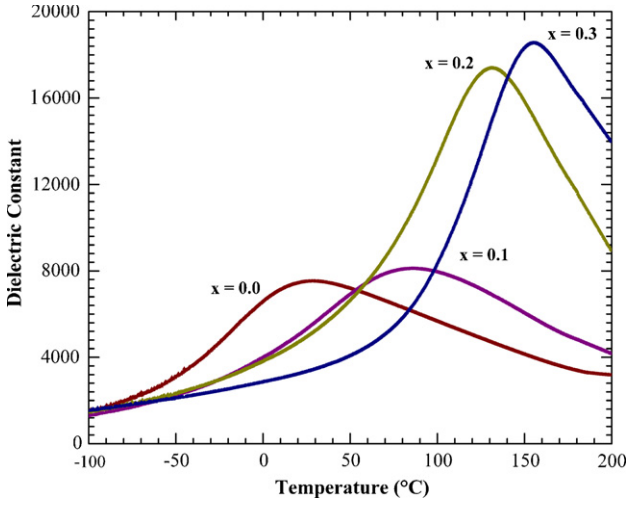



**Fig. 4.** Temperature dependence of the dielectric constant at 1 kHz for PBINT ceramics.

**Table 2**
Dielectric properties of PBINT ceramics at 1 kHz

| Composition ($x$) | $T_m$ (°C) | Dielectric properties | | | |
|---|---|---|---|---|---|
| | | 25 °C | | At $T_m$ | |
| | | $\varepsilon_r$ | tan $\delta$ | $\varepsilon_m$ | tan $\delta$ |
| 0.0 | 26 | 7500 | 0.030 | 7591 | 0.029 |
| 0.1 | 85 | 5326 | 0.076 | 8093 | 0.027 |
| 0.2 | 130 | 4953 | 0.068 | 17,366 | 0.038 |
| 0.3 | 155 | 3339 | 0.039 | 18,541 | 0.047 |

as expected since the transition temperature of PT is very high (~490 °C) [28]. However, it should be noticed that the $T_m$ in PBINT is lower than that in the PINT system even at the same composition, as reported in our previous work [29]. The $T_m$ is shifted to lower temperature by the addition of BT, with similar results observed in PMN-PT–BT and PZN-PT–BT systems [12,13]. This is probably related to BT-based solid solutions tend to posses pinched-type phase transition due to the lack of lone-pair electron associated with lead ions [26,30].

Fig. 5 illustrates a series of the polarization ($P$–$E$) hysteresis loops at various temperatures (25, −20, −50 and −80 °C) with a driving electric field of 30 kV/cm for PBINT ceramics. All ceramics show well-developed hysteresis loops with decreasing temperature. The composition $x$ = 0.0 shows the slim-type hysteresis loop at room temperature, and the loop opens up with decreasing temperatures, indicating the development in the volume fraction of local polar regions with decreasing temperature [31]. It is also observed that the hysteresis loops differ in shapes depending on the composition. The typical "slim" hysteresis loops is found at the composition $x$ = 0.0, then the loop shape gradually changes to the typical "square" hysteresis loops with increasing PT concentration. The square type loops are due to abruptly switching of a domain structure with an electric field, which is typical for a phase of strong normal ferroelectric PT that contains long-range corporations between dipoles in the ferroelectric micro-domain [27]. On the other hand, the slim-type loop is owing to more sluggish reversal, typical of a phase with a suppressed long-range of interaction micro-domain. The value of the polarization parameters such as the remanent polarization ($P_r$), the saturated polarization ($P_s$) and the coercive fields ($E_c$) evaluated from the hysteresis loop are also listed in Table 3. The $E_c$ is seen to be strongly depending on temperature for all compositions, while the $P_r$ changes only slightly.

The variations of the values of hysteresis loops parameters; i.e. the remanent polarization ($P_r$) and the coercive fields ($E_c$), evaluated from the hysteresis loops are shown in Fig. 6. The maximum of the $P_r$ is observed near the compositions $x$ = 0.2 and 0.3, indication of the MPB region of this PBINT system. It is generally accepted that the domain wall can easily move around the MPB because of the coexistence of the pseudo-cubic and tetragonal phases in ferro-

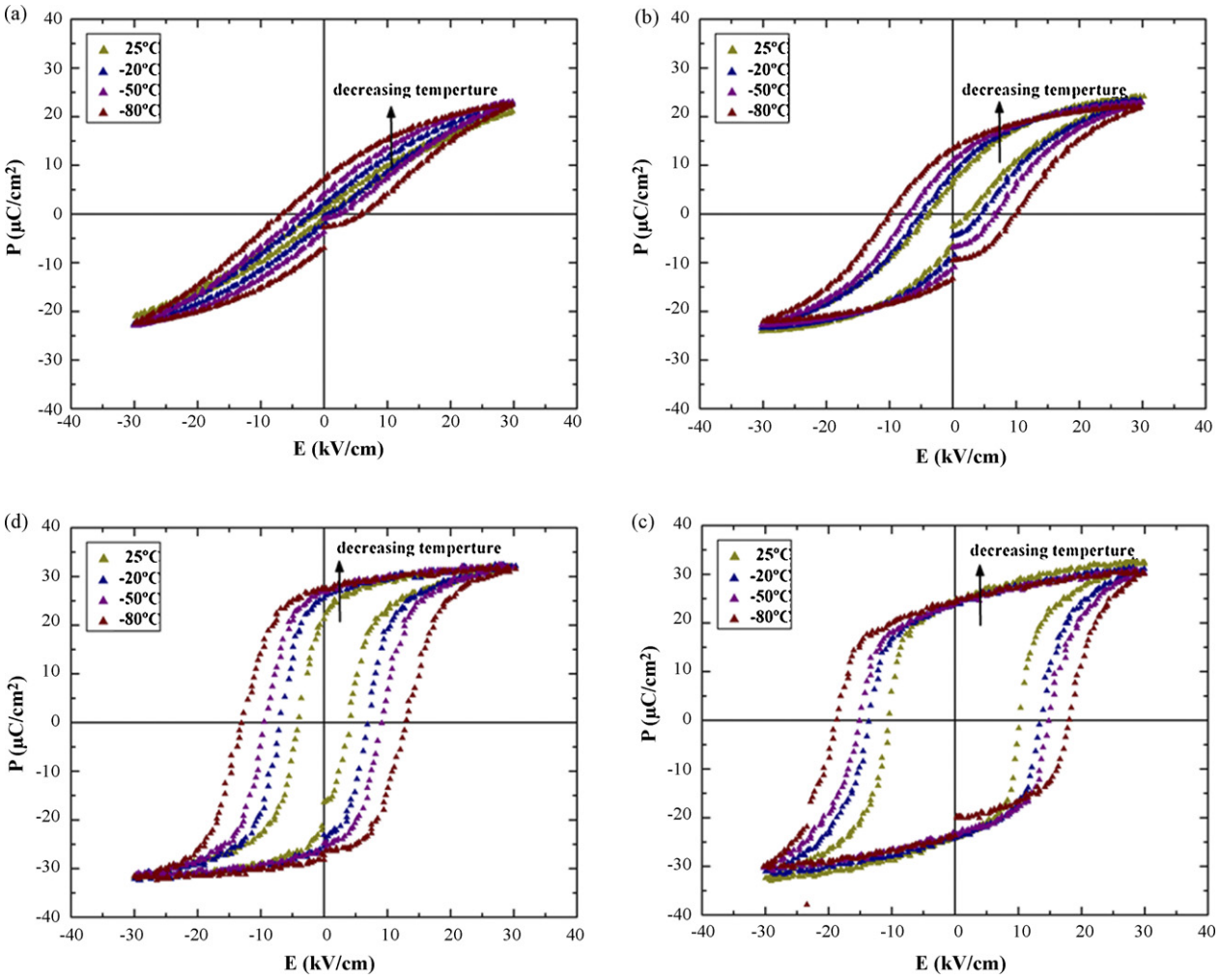



**Fig. 5.** Hysteresis loops of PBINT as a function of temperature 25, −20, −50 and −80 °C for various compositions (a) $x$ = 0.1, (b) $x$ = 0.2 (c) $x$ = 0.3 and (d) $x$ = 0.4.

**Table 3**
Ferroelectric properties of PBINT ceramics

| Composition ($x$) | Ferroelectric properties | | | | | | | |
|---|---|---|---|---|---|---|---|---|
| | At 25 °C | | | | At −80 °C | | | |
| | $P_r$ (μm/cm$^2$) | $P_s$ (μm/cm$^2$) | $E_c$ (kV/cm) | $R_{sq}$[a] | $P_r$ (μm/cm$^2$) | $P_s$ (μm/cm$^2$) | $E_c$ (kV/cm) | $R_{sq}$[a] |
| 0.0 | 1.09 | 20.22 | 0.29 | 0.84 | 7.08 | 22.43 | 6.02 | 0.41 |
| 0.1 | 6.67 | 24.12 | 2.67 | 0.42 | 14.70 | 24.24 | 9.78 | 0.74 |
| 0.2 | 22.48 | 31.84 | 4.24 | 0.94 | 28.40 | 32.79 | 13.04 | 1.12 |
| 0.3 | 24.60 | 31.44 | 10.08 | 1.11 | 25.75 | 32.47 | 18.08 | 1.25 |

[a] Hysteresis loop squareness.

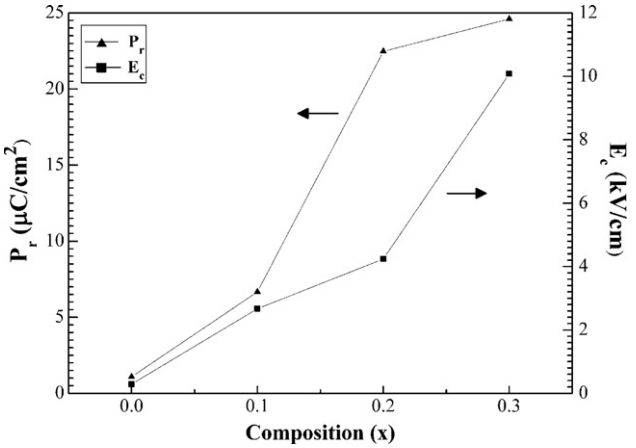



**Fig. 6.** Composition dependence of the $P_r$ and $E_c$ of PBINT ceramics at room temperature.

electric materials, which induces the high $P_r$ [32]. In addition, the linear increase of the $E_c$ indicates the increasing in the extent of the tetragonal phase with increasing PT concentration, which makes domain switching more difficult [33].

Finally, the ferroelectric characteristic of the ceramics can also be assessed with the hystersis loop squareness ($R_{sq}$), which is typically understood to be ratio of $P_r/P_s$, where $P_r$ is the remanent polarization at zero electric field and $P_s$ is the saturated polarization obtained at some finite field strength below the dielectric breakdown. One can also use the loop squareness to measure not only the deviation in the polarization axis but also that in the electric field axis with the empirical expression, $R_{sq} = (P_r/P_s) + (P_{1.1E_c}/P_r)$ where $P_{1.1E_c}$ is the polarization at the field equal to $1.1E_c$. For the ideal square loop, $R_{sq}$ is equal to 2.00. The $R_{sq}$ parameter, listed in Table 3 for all compositions at 25 and −80 °C, clearly shows more loop squareness with increasing PT concentration.

From the results of this study, it believed that the MPB of the PBINT system lies between the compositions $x = 0.2$ and 0.3. This is confirmed by the phase transformation observed in the XRD patterns, and the examined lattice parameters. The electrical properties; i.e. dielectric constant and the $P$–$E$ hysteresis loops also exhibit excellent values near these compositions. These results clearly indicate that the addition of BT has strong effect on phase formation, microstructure and the electrical properties of the PINT system. In comparison with the PINT system, the addition of BT leads to a shift of the MPB region, increases the grain size, and enhances the electrical properties.

## 4. Conclusion

The pure phase of solid solution of $Pb(In_{0.5}Nb_{0.5})_{(1-x)}Ti_{(x)}O_3$ with 20 mol% of BT (where $x = 0.0$, 0.1, 0.2 and 0.3) ceramics was obtained by the wolframite precursor method via a vibro-milling technique. The XRD investigation showed that the ceramics gradually changed from the pseudo-cubic to tetragonal phase between the compositions $x = 0.2$ and 0.3. Correspondingly, large dielectric constant maximum ($\varepsilon_m$) were also obtained at the same compositions. The remanent polarization ($P_r$) also maximized near these compositions, which indicated enhanced electrical properties near the MPB composition. These results clearly indicated that the addition of BT had strong effect on phase formation, microstructure and the electrical properties of the PINT system.

## Acknowledgements

This work was supported by the Thailand Research Fund (TRF), Commission on Higher Education (CHE), and Ministry of University Affairs in Thailand.

## References

[1] R.E. Newnham, S. Trolier-Mckinstry, Ceram. Trans. 32 (1993) 1–18.
[2] T.R. Shrout, A. Halliyal, Am. Ceram. Soc. Bull. 66 (1987) 704–711.
[3] L.E. Cross, Mater. Chem. Phys. 43 (1996) 108–115.
[4] C.A. Randall, A.S. Bhalla, T.R. Shrout, L.E. Cross, J. Mater. Res. 5 (1990) 829–834.
[5] A. Halliyal, U. Kumar, R.E. Newnham, L.E. Cross, Am. Ceram. Soc. Bull. 66 (1987) 671–676.
[6] D.H. Kang, K.H. Yoon, J. Mater. Sci. 26 (1991) 56–60.
[7] C.A. Randall, A.S. Bhalla, Jpn. J. Appl. Phys. 29 (1990) 327–333.
[8] E.F. Alberta, A.S. Bhalla, J. Phys. Chem. Solids 63 (2002) 1759–1769.
[9] J. Wang, K.Z. Baba-Kishi, H.L.W. Chan, C.L. Choy, C.W. Tai, A.S. Bhalla, Ferroelectrics 272 (2002) 267–272.
[10] M. Iwata, S. Katagiri, H. Orihara, M. Maeda, I. Suzuki, H. Ohwa, N. Yasuda, Y. Ishibashi, Ferroelectrics 301 (2004) 179–183.
[11] N. Yasuda, H. Ohwa, M. Kume, K. Hayashi, Y. Hosono, Y. Yamashita, J. Cryst. Growth 229 (2001) 299–304.
[12] U. Kumar, L.E. Cross, A. Halliyal, J. Am. Ceram. Soc. 75 (1992) 2155–2164.
[13] L. Ruan, L. Li, Z. Gui, J. Mater. Sci. Lett. 16 (1997) 1020–1022.
[14] S. Wongsaenmai, S. Ananta, R. Yimnirun, Mater. Lett. 61 (2007) 2426–2429.
[15] S. Wongsaenmai, S. Ananta, R. Yimnirun, J. Mater. Sci. 42 (2007) 3754–3760.
[16] S.L. Swartz, T.R. Shrout, Mater. Res. Bull. 17 (1982) 1245–1250.
[17] B.D. Cullity, Elements of X-ray Diffraction, Addison–Wesley, New York, 1978.
[18] S. Wongsaenmai, X. Tan, S. Ananta, R. Yimnirun, Appl. Phys. A 88 (2007) 323–328.
[19] R.D. Shannon, Acta Crystallogr. A 32 (1976) 751–767.
[20] B.A. Malkov, Yu.N. Venevtsev, Inorg. Mater. (Transl. of Neorg. Mater.) 13 (1977) 1182–1192.
[21] S. Nomura, H. Arima, Jpn. J. Appl. Phys. 11 (1972) 358–364.
[22] W. Zhu, A.L. Andrei, P.Q. Mantas, J.L. Baptista, J. Am. Ceram. Soc. 84 (2001) 1740–1744.
[23] J.C. Bruno, T.C. Boni, C. Cavalheiro, M.A. Zaghete, Mater. Res. Bull. 43 (2008) 297–304.
[24] M. Pham-Thi, C. Augier, H. Dammak, P. Gaucher, Ultrasonics 44 (2006) e627–e631.
[25] S. Wongsaenmai, S. Ananta, R. Yimnirun, R. Guo, A.S. Bhalla, Ferroelectr. Lett. Sect. 34 (2007) 36–45.
[26] B. Jaffe, W.R. Cook, H. Haffe, Piezoelectric Ceramics, Academi Press, New York, 1971.
[27] M.R. Soares, A.M.R. Senos, P.Q. Mantes, J. Eur. Ceram. Soc. 19 (1999) 1865–1871.
[28] R. Wongmaneerung, R. Yimnirun, S. Ananta, Appl. Phys. A 86 (2007) 249–255.
[29] S. Wongsaenmai, S. Ananta, R. Yimnirun, Mater. Sci. Eng., submitted for publication.
[30] R.E. Newham, J. Mater. Educ. 5 (1983) 947–982.
[31] C.H. Wang, J. Eur. Ceram. Soc. 22 (2002) 2033–2038.
[32] V. Sundar, R.E. Newnham, Ferroelectrics 135 (1992) 431–446.
[33] J.T. Zeng, K.W. Kwok, H.L.W. Chan, J. Am. Ceram. Soc. 89 (2006) 2828–2832.

Journal of Alloys and Compounds 475 (2009) 456–462

Contents lists available at ScienceDirect

Journal of Alloys and Compounds

journal homepage: www.elsevier.com/locate/jallcom

# Effects of SiC nanofibers addition on microstructure and dielectric properties of lead titanate ceramics

R. Wongmaneerung[a,*], P. Singjai[b], R. Yimnirun[b], S. Ananta[b]

[a] Department of Physics, Faculty of Science, Maejo University, Chiang Mai 50290, Thailand
[b] Department of Physics, Faculty of Science, Chiang Mai University, Chiang Mai 50200, Thailand

ARTICLE INFO

*Article history:*
Received 31 May 2008
Received in revised form 8 July 2008
Accepted 10 July 2008
Available online 23 August 2008

*Keywords:*
Lead titanate
Perovskite
Composite
Dielectric properties

ABSTRACT

Dense perovskite ferroelectric $PbTiO_3$ (or PT) ceramics reinforced with SiC nanofibers have been successfully fabricated by a simple solid-state mixed oxide and conventional sintering method. Phase formation, densification, microstructure and dielectric properties of the composites were investigated as a function of SiC content. Addition of SiC nanofibers to a PT matrix did not result in unexpected reaction phase. Microstructural observations revealed that some SiC nanofibers were heterogeneously dispersed in PT matrix and at the matrix boundaries. The grain size was decreased significantly with addition of SiC nanofiber. Though the densification and mechanical strength were improved, the dielectric properties of PT/SiC composites were degraded dramatically.

© 2008 Elsevier B.V. All rights reserved.

## 1. Introduction

Perovskite ferroelectric lead titanate ($PbTiO_3$ or PT) based ceramics which exhibit excellent dielectric, piezoelectric and pyroelectric properties have been widely employed in sensor, transducer and actuator applications, especially for devices working at high-temperature and high-frequency conditions [1–3]. However, pure and dense PT ceramic is regarded to be one of the most difficult lead-based perovskite ferroelectrics to produce especially via a simple solid-state reaction method [2,3]. It suffers from low mechanical properties and the resulting poor electrical reliability mainly due to large distortion of the tetragonal phase at room temperature [3]. This phase transformation causes a complicated stress system in the ferroelectric material, and then results in the generation of internal stress and mechanically twined microstructure at room temperature. For further high-power applications used under severe circumstances, its poor mechanical and electrical reliability become a critical limitation on the application of this material. Especially in multilayer piezoelectric actuators, the high electric driving field needed to produce a large displacement may cause mechanical and electrical degradation [2,3]. Therefore, improving mechanical properties of PT-based materials is worthwhile.

To overcome such problems, several techniques have been introduced [4–9]. Amongst all the issues reported so far, most attention has been concentrated on the use of additives and chemically derived powder processing, whereas investigations on modified particle packing or composite techniques have not been widely carried out [10,11]. Recently, Niihara [12] had reported that small amount of submicro- or nano-scale second phase could largely improve the mechanical properties of ceramic matrix. In the past few years, this composite idea has been applied to some perovskite ferroelectric ceramics such as $BaTiO_3$/SiC [13], PZT/SiC [14] and PZT/Ag [15] systems. However, to our knowledge, the fabrication of PT composites reinforced with SiC nanofibers has not been reported so far.

Therefore, in this work, small amount SiC nanofibers (0.1–5.0 wt%) reinforced PT ceramics are fabricated by conventional sintering method. The effect of SiC additions on densification, microstructure and dielectric properties of the composites have been discussed and compared with the monolithic PT ceramics.

## 2. Experimental procedure

Monolithic $PbTiO_3$ (PT) ceramics and PT/SiC composites were prepared using a conventional ceramic fabrication method. The starting materials were $PbTiO_3$ powders (average particle size ~1–5 μm) and β-SiC nanofibers (average diameter ~80–100 and ~15–100 μm in length), as shown in Fig. 1. Characteristic properties of starting materials and detail of their fabrication procedures were already described elsewhere [16,17]. Briefly, different amounts (0.1–5.0 wt% or 0.03–1.55 vol%) of SiC nanofibers were ultrasonically dispersed in ethanol for 10 min before mechanically vibro-mixing [16] with the PT powders and 1 wt% of PVA binder for 30 min. The slurry was dried at 120 °C and sieved into a fine powder. The mixed powders of each composition were pressed into green pellet under a uniaxial press at 100 MPa, placed on high purity alumina spacer inside a closed alumina crucible. The PVA binder was

* Corresponding author.
*E-mail address:* re_nok@yahoo.com (R. Wongmaneerung).

0925-8388/$ – see front matter © 2008 Elsevier B.V. All rights reserved.
doi:10.1016/j.jallcom.2008.07.051

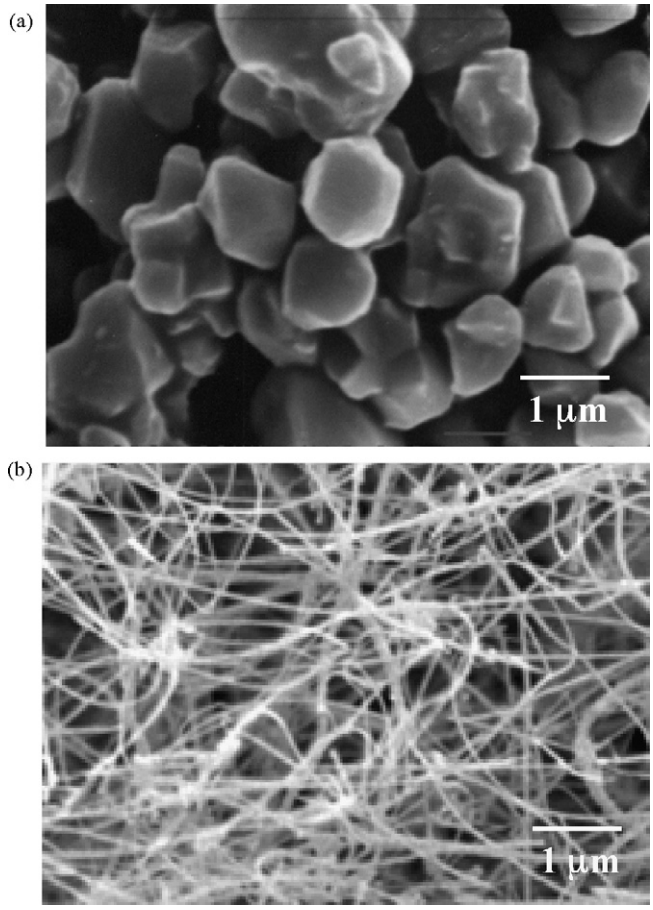



**Fig. 1.** SEM micrographs of the fabricated (a) PT powders and (b) SiC nanofibers.

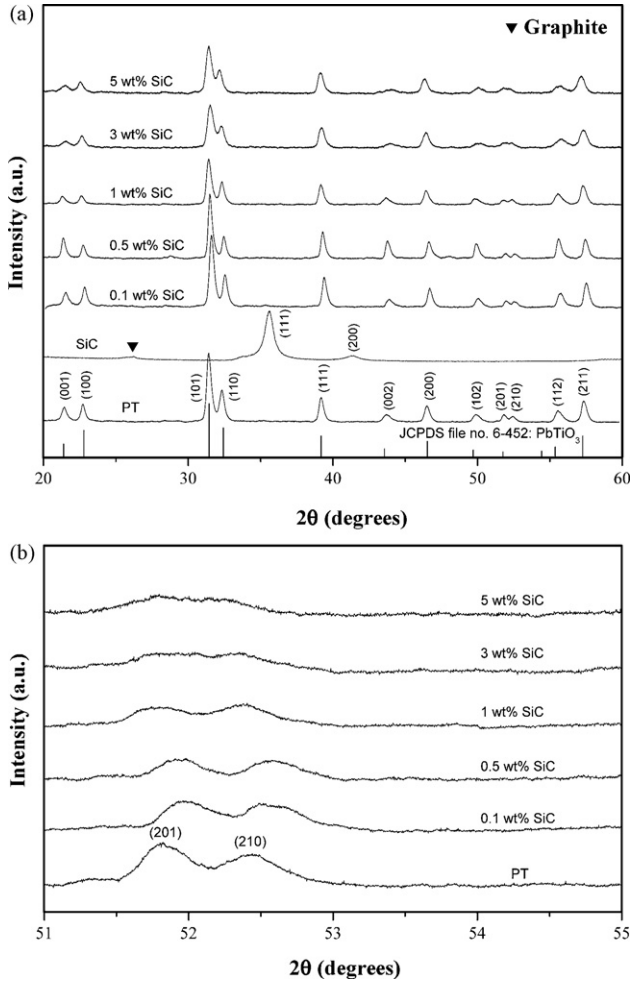



**Fig. 2.** XRD patterns of monolithic PT ceramics and PT/SiC composites after sintered at 1200 °C for 1 h with heating/cooling rates of 1 °C/min.

burnt out at 550 °C with heating/cooling rates of 10 °C/min and sintered at 1200 °C for 1 h with slow heating/cooling rates of 1 °C/min (in order to avoid the sample damage after sintering [9,18]). A PbO atmosphere was also maintained during sintering using PT powders with identical chemical composition in order to minimize the lead loss due to evaporation [9,18].

Phase identification of the sintered samples was characterized by using room temperature X-ray diffraction technique (XRD; Siemens-D500 diffractometer) with Cu $K_{\alpha 1}$ radiation. The lattice parameters and tetragonality factor ($c/a$) of the sintered samples were calculated from the XRD patterns [18,19]. The bulk density was determined by using the Archimedes principle in distilled water, and the relative density calculated using the theoretical density of PT [1]. Microstructure and fracture surface of the samples were examined with a scanning electron microscopy (SEM; JEOL JSM-840A). The average grain size of each composition was determined by linear intercept method using SEM photograph [9]. For electrical measurement, silver paste was fired on both sides of the polished samples at 600 °C as electrode. The dielectric properties were studied as a function of temperature. The capacitance was measured with a HP4284A LCR meter in connection with a Delta Design 9023 temperature chamber and a chamber holder capable of high temperature measurement, on cooling through the transition range (550–25 °C) with a rate of 5 °C/min at high frequencies range from 1 to 5 MHz.

## 3. Results and discussion

X-ray diffraction patterns of the monolithic PT and PT/SiC composites sintered at 1200 °C for 1 h are shown in Fig. 2(a), indicating the formation of only single phase perovskite in all cases. All the peaks were identified as tetragonal $PbTiO_3$, which could be matched with JCPDS file no. 6-452 [20], in agreement with other works [4–9]. No reaction phases between the PT matrix and SiC addition were observed in these XRD patterns. Moreover, there is no trace of the SiC phase was detected in all composites. The amount of SiC remaining in the composite may have been too small to be detected by XRD, and peak broadening due to particle size effects may have also been a factor [19]. It should be noted that the XRD patterns show some sign of peak splitting, e.g. (2 0 1)/(2 1 0) peaks which is an indication of tetragonal PT phase [16,20] however, the splitting was less well defined in the higher amount of SiC-containing samples, as shown in Fig. 2(b).

Table 1 also shows tetragonality factor ($c/a$), relative density and grain sizes of all compositions. The values of $c/a$ for all PT/SiC composites are significantly lower than that of monolithic PT ceramics, indicating lower internal stress in these PT/SiC composites. With increasing SiC content, the $c/a$ value, the density and the average grain size was decreased, in consistent with other similar perovskite-based systems [13,14]. More interestingly, all composite

**Table 1**
Physical properties of PT/SiC composites after sintered at 1200 °C for 1 h with heating/cooling rates of 1 °C/min

| SiC nanofiber (wt%) | Tetragonality ($c/a$) | Relative density (%) | Grain size[a] (mean) (μm) |
|---|---|---|---|
| 0.0 | 1.063 | 94 | 20.0–65.0 (36) |
| 0.1 | 1.061 | 95 | 0.5–2.2 (0.8) |
| 0.5 | 1.061 | 91 | 0.5–2.6 (0.7) |
| 1.0 | 1.060 | 90 | 0.2–1.6 (0.6) |
| 3.0 | 1.057 | 84 | 0.1–0.9 (0.4) |
| 5.0 | 1.057 | 72 | 0.1–0.7 (0.3) |

[a] The estimated precision of the grain size is ±10%.

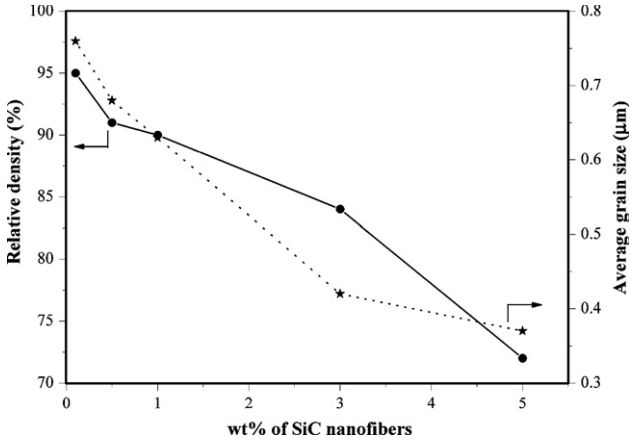



**Fig. 3.** Variation of relative density and average grain size of PT/SiC composites with SiC content.

samples do not suffer from severe stresses as a result of the high $c/a$ ratio so they have not broken into pieces after experienced the sintering process or once subjected to a cycle of high temperature measurement of dielectric properties, as reported previously for the conventional and two-stage sintering PT cases [9,18]. Arlt et al. [21] have shown that for the grain size of less than 1 μm, the lower value of $c/a$ ratio was found with the reduction of grain size. In the present study, the average grain size of all PT/SiC composites is obviously smaller than 1 μm (Table 1 and Fig. 3). Thus, it is believed that the major factor to reduce the tetragonality factor is mainly attributed to the grain growth suppression effect of SiC addition [13,14].

However, there is little change in the tetragonality factor of PT composites when the content of SiC is higher than 3.0 wt%. Furthermore, there is no SiC phase appearing in any PT/SiC composites. Thus, it can be estimated that the solubility of SiC in PT matrix is higher than 5 wt% (or 1.55 vol%) [22]. It is well known that PT system has an $ABO_3$-type perovskite structure. The A-sites are occupied by $Pb^{2+}$ ions and the B-sites by $Ti^{4+}$ ions. Although a dopant can go either to the A- or B-site, its distribution on the two sites being a function of the valence and ionic radius of the dopants [1,3]. However, in this study, the possibility of a $Si^{4+}$ ion substitution which will create an oxygen vacancy to compensate charge neutrality and the distortion of oxygen octahedron structure [3] resulting in the variation of tetragonality ($c/a$) should not be the case since no sufficient ionization or diffusion can be expected for SiC at 1200 °C.

The influence of SiC additions on the relative density of PT composites sintered at 1200 °C for 1 h in air is also shown in Table 1 and Fig. 3. Generally, it is evident that the monolithic PT ceramics and PT/SiC composites (with less than 1 wt% SiC) could be sintered to above 90% of the theoretical density even at a temperature as low as 1200 °C. As the SiC content increases (especially at 0.5 wt% SiC), the relative density of the samples decrease in good agreement with those found for the PZT/SiC [20], PZT/$Al_2O_3$ [23], $BaTiO_3$/$Al_2O_3$ [24] and $BaTiO_3$/NiO [25] composites. In the case of $BaTiO_3$/$Al_2O_3$ and $BaTiO_3$/NiO systems [24,25], it was also shown that addition of secondary phase caused enlargement of particle size in green body, resulting in low density observed in sintered samples. In this work, the addition of SiC nanofibers into PT matrix had the same effect as those of $Al_2O_3$ and NiO. The inhibition of densification was evidenced from the large fraction of opened pores in 1.0 and 5.0 wt% SiC/PT samples (Figs. 4c(ii) and d(ii)) compared to the monolithic PT (Fig. 4a(i)). It should be noted that remarkable change of average grain size was observed on addition of a non-perovskite SiC phase, and the small quantity added had quite significant effect on the sinterability of PT ceramics by suppressing the liquid-phase (PbO-rich phases) sintering mechanism commonly found for typical monolithic PT [9,18]. This sintering behavior can be associated with the grain growth suppression of SiC nanofibers inside the PT matrix. In this system, the formation of oxygen vacancies due to $Si^{4+}$ ion substitution in the perovskite structure is not considered to be another reason responsible for the sintering behaviour of PZT/SiC composites. Thus, the assumption of oxygen vacancies accelerate mass transfer and densification, which result in high relative density observed in other system [15,26] is not valid in this study.

A distribution of SiC fibers in a matrix may decrease the sintering rate by inducing tensile mean stress in the matrix [27,28]. The effects are less pronounced for a PT matrix, wherein the tensile mean stress approaches the sintering potential, resulting in substantial retardation of sintering, as observed experimentally. However, the SiC nanofiber has a diminished retardation effect in a lower strength ferroelectric typed of PT matrix, because the stresses are more readily relaxed. The specific source of this difference is not yet understood. Several researchers [27–29] have found that application of an initial gap between the fiber and matrix to delay stress development, are shown to be crucial requirements for densification of ceramic matrix materials.

Microstructural features, free (i) and fracture (ii) surfaces, of the monolithic PT ceramics and PT/SiC composites sintered at 1200 °C for 1 h are displayed in Fig. 4. The grain structure of both monolithic PT ceramics and PT/SiC composites were more or less equiaxed. Growth of the matrix grains in the PT/SiC composites is thought to be inhibited by reaction between the matrix and SiC phases [28,30]. In general, the small grain size results in high mechanical properties. Because of the relatively low reactivity between PT and SiC [28], SiC has significant effect on overall microstructural arrangement and therefore also the mechanical properties [3,12]. Observation of the microstructure by SEM showed that the SiC phase was randomly dispersed in the PT matrix. The average grain size of PT matrix (determined by a linear intercept as shown in Table 1) is also given as a function of SiC content in Fig. 3. The average grain sizes were found to decrease with the addition of SiC, indicating that SiC inhibited grain growth as earlier proposed by other workers [13,14]. The SiC nanofibers were found to locate both within the matrix and at the grain boundaries (see enlarged insertion in Fig. 4e(i)). The overall microstructural arrangement of the PT/SiC composites found in this study can be roughly classified as “nanofiber” types according to the model advocated by Kuntz et al. [30].

As mentioned previously, a small quantity of dispersed fiber is enough to control the grain growth mechanism and as a consequence to effectively reinforce the PT matrix. It seems that the grain boundary movement is depressed by the SiC fibers, as can be seen in Fig. 4(c). This may be caused by the grain boundary pinning force of SiC, which depressed the migration of PT grain boundaries during the sintering process [31], pointed out by other researchers [23,24]. In general, spontaneous cracking of polycrystalline ceramics results from the internal stresses between grains, owing to incompatible strains from either thermal expansion anisotropy or phase transformation [2,3,32]. The spontaneous cracking observed in the present study must be caused by the paraelectric to ferroelectric phase transformation.

Generally, the fracture mode of pure perovskite PT ceramics is known to be an intergranular [9,18]. In the present study, the fracture mode of 0.1 wt% SiC composite (Fig. 4b(ii)) is predominantly intergranular-type as well as that of monolithic PT ceramic (Fig. 4a(ii)), because the clear grain boundary can be observed. In general, the samples with intergranular fracture include the pores and impurities in the grain boundaries are weaker compared to those of the other part. In comparison with the typical monolithic PT ceramics [5,9], almost clean microstructures with highly uniform, denser angular grain-packing and more homogeneous are

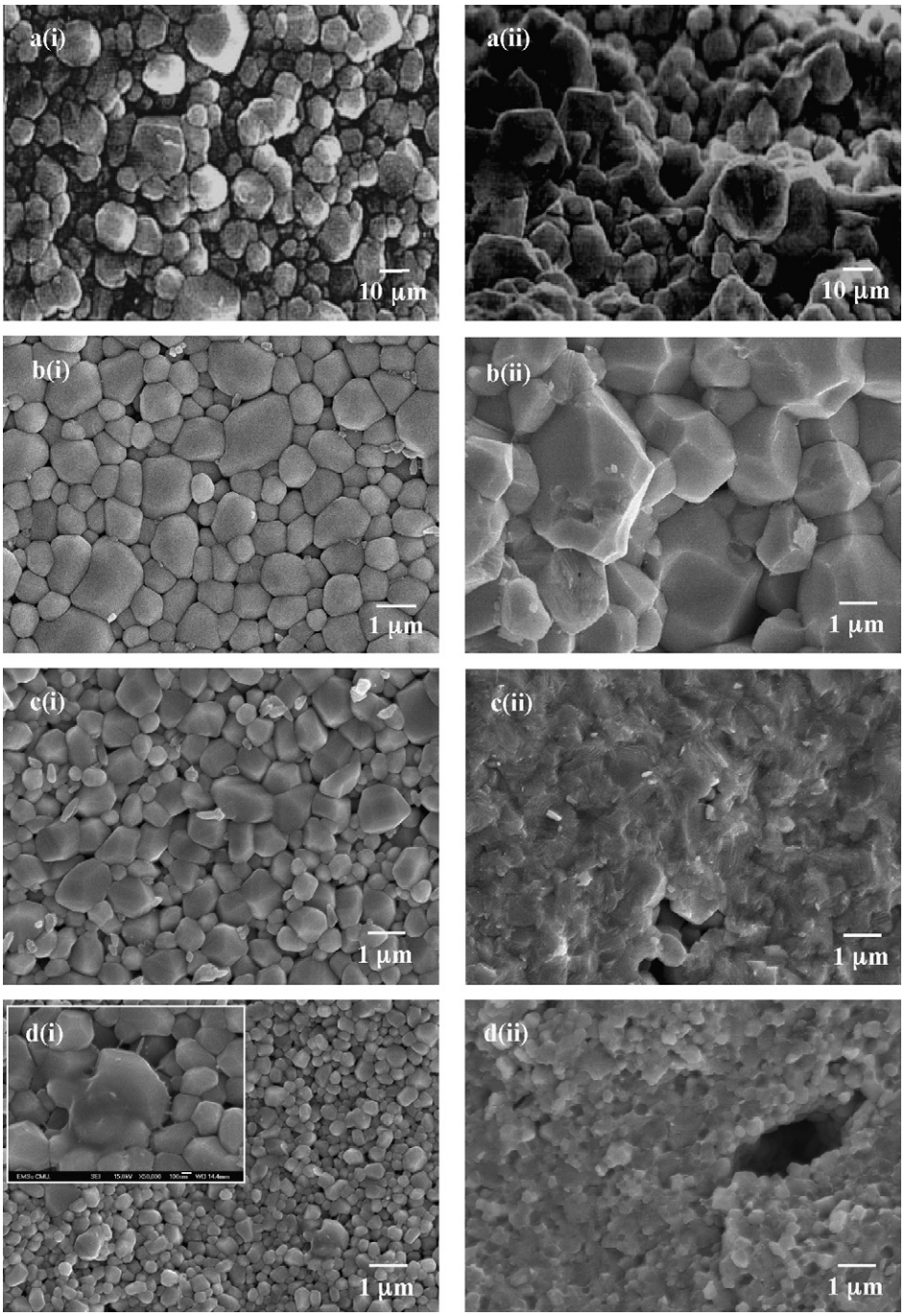



**Fig. 4.** Free (i) and fracture (ii) surfaces of (a) monolithic PT ceramics and PT/SiC composites with (b) 0.1 wt%, (c) 1 wt% and (d) 5 wt% of SiC content.

generally observed in PT/SiC composites. Interestingly, all samples remained unbroken. On the other hand, with increasing SiC content, the grain boundary in the fracture surface became obscure as shown in Fig. 4c(ii) and d(ii), and the fracture changed from intergranular to transgranular surface. This kind of characteristic was also found for the PZT/SiC composites earlier reported by Chen et al. [33]. Furthermore, it should be noted that the average grain size of both PT nanocomposites is <1.5 μm, which is less than the critical value of 3 μm [9,28] and gives rise to a volumetric percentage enough to buffer the anisotropic stress caused by the phase transition [3,28]. The reduced grain size of the composites is considered to be responsible for the improvement of their mechanical properties [5,6,18].

The influence of SiC content upon the dielectric-temperature characteristics of PT/SiC nanocomposite ceramics at various high frequencies over the temperature range of 25–550 °C is illustrated in Fig. 5, owing to the fact that the most desirable dielectric properties of PT ceramics for use in electronic devices are at high frequency range (MHz–GHz) and not much work has been reported on the electrical properties at frequency higher than 100 kHz. Thus, the high frequency range available from the dielectric equipment testing of 1–5 MHz has been performed in this study. The dielectric constant ($\varepsilon_r$) and dielectric loss ($\tan\delta$) values at room temperature and a ferroelectric–paraelectric phase transition temperature ($T_C$) are also listed in Table 2. Generally, they all behave as typical normal ferroelectric materials [1–3]. Moreover, it can be seen that except

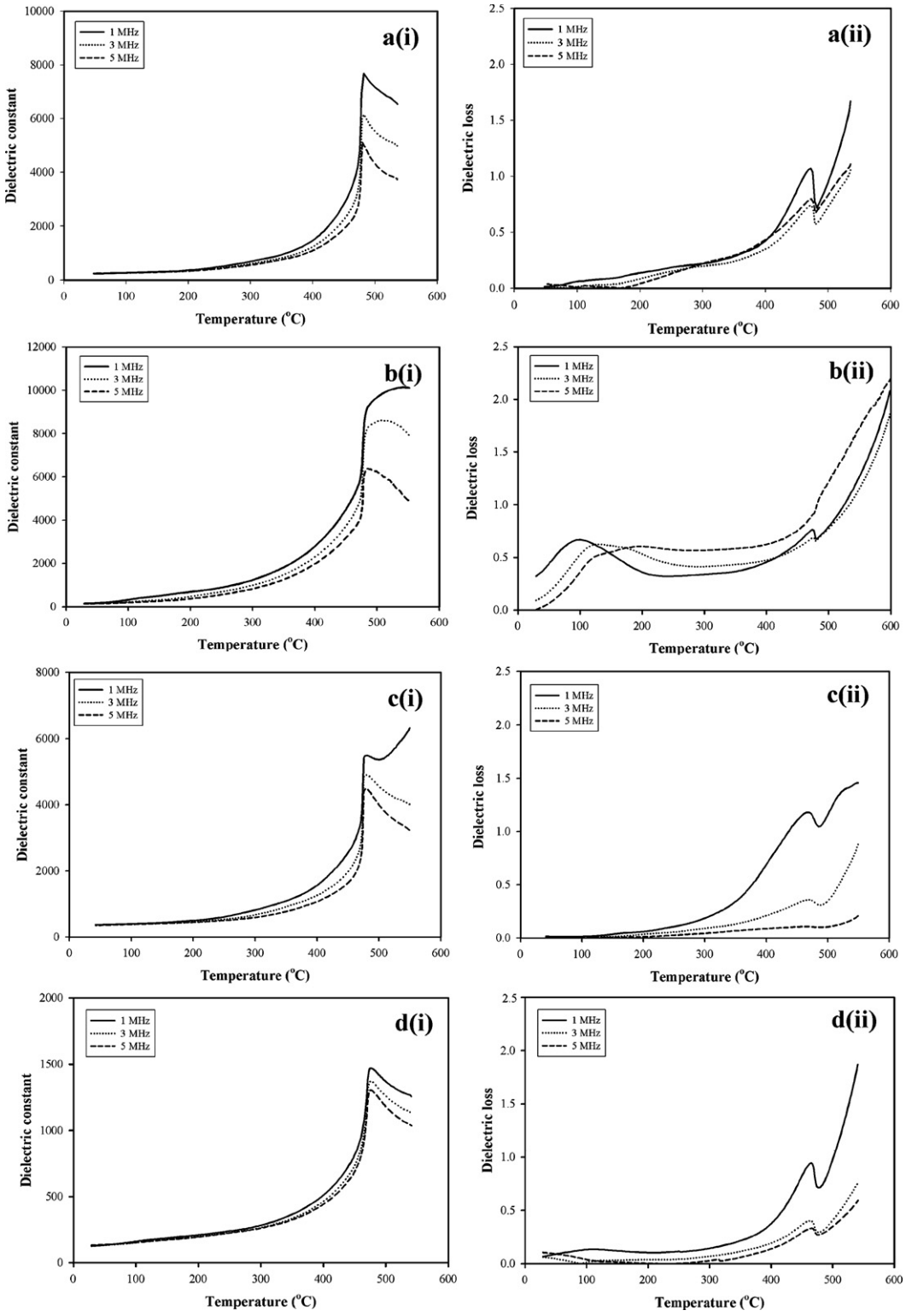



**Fig. 5.** Variation with temperature of dielectric constant ($\varepsilon_r$) and dielectric loss ($\tan\delta$) at 1 MHZ for (a) monolithic PT ceramics and PT/SiC composites with (b) 0.1 wt%, (c) 1 wt% and (d) 5 wt% of SiC content.

at 0.1 wt% SiC, increasing the SiC content caused a reduction in the dielectric constant (and increase in dielectric loss for PT/SiC composites with SiC > 0.1 wt%). Similar trend in dielectric values at $T_C$ was also observed. The reduction in $\varepsilon_r$ and also the increase in $\tan\delta$ with the content of SiC additive could be attributed mainly to an increase in porosity, as can be seen in Fig. 4. It can be said that the SiC nanofibers did not so much react with PT matrix. Other reason which is possible is that the presence of more non-ferroelectric SiC phase. The SiC fiber seems to be acting in the same way as porosity because the SiC is nonpiezoelectric material. Domain wall motion clamping due to the reduced grain size [34] is also considered to be another possible reason responsible for the low dielectric con-

**Table 2**
Dielectric properties of PT/SiC composites measured at 1 MHz

| SiC nanofiber (wt%) | $T_C$ (°C) | $\varepsilon_{25°C}$ | $\tan\delta_{25°C}$ | $\varepsilon_{r,max}$ | $\tan\delta_{max}$ |
|---|---|---|---|---|---|
| 0.0 | 482 | 243 | 0.02 | 7680 | 1.07 |
| 0.1 | 485 | 149 | 0.32 | 9337 | 0.76 |
| 1.0 | 482 | 268 | 0.08 | 5493 | 1.18 |
| 5.0 | 475 | 128 | 0.02 | 1470 | 0.95 |

stant of SiC/PT composites. The results on dielectric measurement were also in agreement with a previous report in the perovskite-based PZT/SiC and $BaTiO_3$/SiC systems [13,14,33]. In those cases, the domain clamping due to oxygen vacancies and reduction in grain size was thought to cause the decrease in dielectric constant. In this work, the grain size of these composites was rather small therefore domain clamping due to grain size was probably one of the main factors. Furthermore, this work demonstrated that the dielectric properties of PT/SiC nanocomposite ceramics are also influenced by microstructural features and arrangement especially the microcracks and final density. It is seen that with the increase of SiC content, the peak of $T_C$ kept a clear shape and shifted towards lower temperatures (Table 2 and Fig. 6). The shift of the phase transformation temperature in these PT/SiC composites might be due to a relaxation of transformation-induced internal stress by the SiC fiber dispersed in the PT matrix. Similar effect was also found in the MgO/$BaTiO_3$ nanocomposites where $T_C$ of the $BaTiO_3$ dispersoids shifted to lower temperatures upon the incorporation of Mg ion [35].

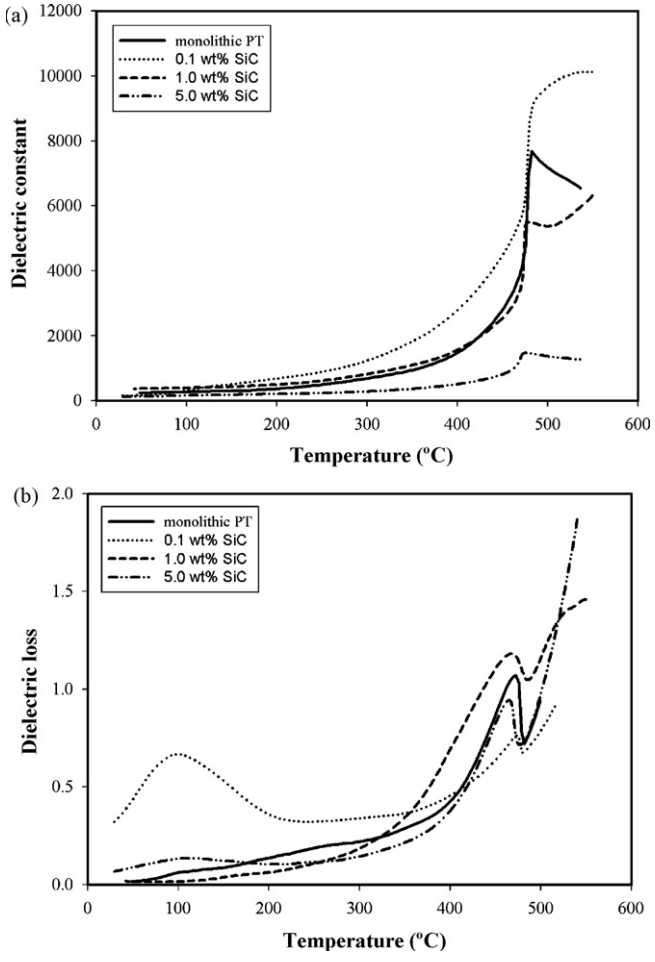



**Fig. 6.** Variation with temperature of (a) dielectric constant and (b) dielectric loss at 1 MHz of PT/SiC composites as a function of SiC content.

The results obtained in this work suggest that these composites exhibit complex microstructures which are inherently heterogeneous. The heterogeneity is a result of variation in grain size, fiber length and orientation, variation in chemical homogeneity; and the presence and distribution of additional phases and pores. These factors have an important effect on the dielectric properties of the materials. Although improving mechanical properties of PT-based ceramics is worthwhile, the problem of dielectric properties trade-off especially a deterioration of dielectric constant still remains unsolved. Further work on the PT ceramics reinforced with the piezoelectric nanomaterials, e.g. PZT, $BaTiO_3$ or ZnO nanofibers should be very helpful for gaining better understanding of these piezoceramic nanocomposite systems.

## 4. Conclusions

The influence of SiC nanofiber addition on phase formation, microstructure and dielectric properties of perovskite PT ceramics fabricated by a simple, inexpensive solid-state reaction method has been examined and reported for the first time. If small amount of 0.1 wt% SiC nanofibers was added into perovskite PT matrix, dense PT/SiC composites with good mechanical and dielectric properties could be successfully produced by a simple mixed oxide and conventional sintering method. Addition of SiC nanofibers was found to inhibit densification and suppress grain growth, in agreement with results from other ferroelectric nanocomposite systems. The dielectric properties were also influenced by SiC addition in analogous with the porosity.

## Acknowledgements

This work was supported by the Thailand Research Fund (TRF), the Commission on Higher Education (CHE), the National Nanotechnology Center (NANOTEC) and the Faculty of Science, Chiang Mai University and Maejo University.

## References

[1] B. Jaffe, W.R. Cook, H. Jaffe, Piezoelectric Ceramics, Academic Press, New York, 1971.
[2] G.H. Haertling, J. Am. Ceram. Soc. 82 (1999) 797–818.
[3] A.J. Moulson, J.M. Herbert, Electroceramics, 2nd ed., Wiley, Chichester, 2003.
[4] H. Takeuchi, S. Jyomura, E. Yamamoto, Y. Ito, J. Acoust. Soc. Am. 72 (1982) 1114–1120.
[5] L.B. Kong, W. Zhu, O.K. Tan, J. Mater. Sci. Lett. 19 (2000) 1963–1966.
[6] T. Suwannasiri, A. Safari, J. Am. Ceram. Soc. 76 (1993) 3155–3158.
[7] T. Takeuchi, M. Tabuchi, I. Kondoh, N. Tamari, H. Kageyama, J. Am. Ceram. Soc. 83 (2000) 541–544.
[8] J.S. Forrester, J.S. Zobec, D. Phelan, E.H. Kisi, J. Solid State Chem. 177 (2004) 3553–3559.
[9] A. Udomporn, K. Pengpat, S. Ananta, J. Eur. Ceram. Soc. 24 (2004) 185–188.
[10] J.S. Reed, Principles of Ceramic Processing, 2nd ed., Wiley, New York, 1995.
[11] T. Nagai, H.J. Hwang, M. Yasuoka, M. Sando, K. Niihara, J. Am. Ceram. Soc. 81 (1998) 425–453.
[12] K. Niihara, J. Ceram. Soc. Jpn. 99 (1991) 974–982.
[13] H.J. Hwang, K. Niihara, J. Mater. Sci. 33 (1998) 549–558.
[14] T. Yamamoto, H. Igarashi, K. Okazaki, Ferroelectrics 63 (1985) 281–288.
[15] H.J. Hwang, M. Yasuoka, M. Sando, M. Toriyama, J. Am. Ceram. Soc. 82 (1999) 2417–2422.
[16] R. Wongmaneerung, R. Yimnirun, S. Ananta, Mater. Lett. 60 (2006) 1447–1452.
[17] T. Jintakosol, P. Singjai, Key Eng. Mater. 353–358 (2007) 2171–2174.
[18] R. Wongmaneerung, R. Yimnirun, S. Ananta, Appl. Phys. A 86 (2007) 249–255.
[19] H. Klug, L. Alexander, X-ray Diffraction Procedures for Polycrystalline and Amorphous Materials, 2nd ed., Wiley, New York, 1974.
[20] JCPDS-ICDD Card no. 6-452. International Centre for Diffraction Data. Newtown Square, PA, 2000.
[21] G. Arlt, D. Hennings, G. de With, J. Appl. Phys. 58 (1985) 1619–1625.
[22] R.B. Atkin, R.M. Fulrath, J. Am. Ceram. Soc. 53 (1970) 51–52.
[23] K. Tajima, H.J. Hwang, M. Sando, K. Niihara, Key Eng. Mater. 161–163 (1999) 505.
[24] S. Jiansirisomboon, A. Watcharapasorn, Cur. Appl. Phys. 8 (2008) 48–52.
[25] W.H. Tzing, W.H. Tuan, Ceram. Int. 25 (1999) 69–75.
[26] P.H. Xiang, X.L. Dong, C.D. Feng, N. Zhong, J.K. Guo, Ceram. Int. 30 (2004) 765–772.

[27] Y. Matsuo, H. Sasaki, J. Am. Ceram. Soc. 49 (1966) 229–230.
[28] Y. Xu, A. Zangvil, A. Kerber, J. Eur. Ceram. Soc. 17 (1997) 921–928.
[29] C.H. Hsueh, J. Am. Ceram. Soc. 71 (1988) C442–C444.
[30] J.D. Kuntz, G.D. Zhan, A.K. Mukherjee, MRS Bull. 1 (2004) 22–27.
[31] M. Hillert, Acta Metall. 36 (1988) 3177–3181.
[32] R.C. Pohanka, S.W. Freiman, B.A. Bender, J. Am. Ceram. Soc. 61 (1978) 72–75.
[33] H. Chen, H. Yang, X. Dong, Y. Wang, Phys. Stat. Sol. (a) 203 (2006) R61–R63.
[34] T. Yamamoto, K. Yamamoto, R. Tanaka, K. Okazaki, T. Ueyama, Jpn. J. Appl. Phys. 28 (1989) 63–66.
[35] T. Nagai, H.J. Hwang, M. Yasuoka, M. Sando, K. Niihara, Ceram. Trans. 85 (1997) 369–378.

Current Applied Physics 9 (2009) 802–806

Contents lists available at ScienceDirect

Current Applied Physics

journal homepage: www.elsevier.com/locate/cap

# Effects of Zr/Ti ratio on dielectric and ferroelectric properties of $0.8Pb(Zr_xTi_{1-x})O_3$–$0.2Pb(Co_{1/3}Nb_{2/3})O_3$ ceramics

Anurak Prasatkhetragarn [a,*], Muangjai Unruan [a], Athipong Ngamjarurojana [a], Yongyut Laosiritaworn [a], Supon Ananta [a], Rattikorn Yimnirun [a], David P. Cann [b]

[a] Department of Physics, Faculty of Science, Chiang Mai University, 239 Huay Kaew Road, Chiang Mai 50200, Thailand
[b] Materials Science, School of Mechanical, Industrial and Manufacturing Engineering, Oregon State University, Corvallis, OR 97331, United States

ARTICLE INFO

*Article history:*
Received 9 July 2008
Accepted 23 July 2008
Available online 14 August 2008

*PACS:*
85.50.–n
77.22.–d
77.22.Ch
77.80.Bh

*Keywords:*
PZT–PCN
MPB
Zr/Ti ratio
Dielectric properties
Ferroelectric properties

ABSTRACT

The influences of Zr/Ti ratio on electrical properties of the $0.8Pb(Zr_xTi_{1-x})O_3$–$0.2Pb(Co_{1/3}Nb_{2/3})O_3$ ceramics prepared by a mixed-oxide method (with $x = 0.46$, 0.48, 0.50, 0.52, and 0.54) have been investigated in order to identify the morphotropic phase boundary composition in this system. With XRD analysis, the crystal structure of dense specimens appeared to change gradually from tetragonal to rhombohedral with increasing Zr content. The dielectric properties measurements showed a maximum dielectric constant at $x = 0.50$, while the transition temperature decreased with increasing Zr content in the system. Moreover, all ceramics showed diffused phase transition behaviors with a minimum diffusivity at $x = 0.50$. In addition, the Polarization–Electric field ($P$–$E$) hysteresis loops of the ceramic systems also changed significantly with the Zr content. Interestingly, the loop squareness parameter reached maximum around $x = 0.50$. Other ferroelectric hysteresis parameters showed noticeable change at $x = 0.50$. These results clearly showed the significance of Zr/Ti ratio in controlling the electrical properties of the PZT–PCN ceramic systems.

© 2008 Elsevier B.V. All rights reserved.

## 1. Introduction

Lead-based perovskite-type solid solutions consisting of relaxor and normal ferroelectrics have attracted great interest at the compositions close to the morphotropic phase boundary (MPB) because of their excellent dielectric, piezoelectric, and electrostrictive properties, which are useful in actuating and sensing applications [1]. Lead zirconate titanate, $Pb(Zr_xTi_{1-x})O_3$ or PZT ceramics have been investigated from both fundamental and applied viewpoints [1,2]. The MPB of PZT is located at a $PbTiO_3$:$PbZrO_3$ of 0.52:0.48 and separates the Ti-rich tetragonal phase from the Zr-rich rhombohedral phase [3]. Furthermore, the MPB composition has a high $T_c$ of 390 °C, which allows piezoelectric devices to be operated at relatively high temperatures. Most commercial PZT ceramics are designed in the vicinity of the MPB with various doping methods in order to achieve high properties [2,4–7]. Recently, many piezoelectric ceramic materials have been developed from binary systems containing a combination of relaxor and normal ferroelectric materials [2] that yield high dielectric permittivities (e.g., $Pb(Zr_{1/2}Ti_{1/2})O_3$–$Pb(Ni_{1/3}Nb_{2/3})O_3$ (PZT–PNN) [4], and $Pb(Zr_{1/2}Ti_{1/2})O_3$–$Pb(Mg_{1/3}Nb_{2/3})O_3$ (PZT–PMN) [5]), excellent piezoelectric coefficients (e.g., $Pb(Zr_{1/2}Ti_{1/2})O_3$–$Pb(Zn_{1/3}Nb_{2/3})O_3$ (PZT–PZN) [6]), and high pyroelectric coefficients (e.g., $Pb(Ni_{1/3}Nb_{2/3})O_3$–$PbTiO_3$–$PbZrO_3$ (PNN–PT–PZ) [7]).

Lead cobalt niobate, $Pb(Co_{1/3}Nb_{2/3})O_3$ or PCN, which exhibits a perovskite structure and a Curie temperature of ≈−30 °C, is a relaxor ferroelectric material with a high dielectric constant [8,9]. On the basis of the above mentioned approach, solid solutions of PZT and PCN are expected to synergistically combine the properties of both the normal ferroelectric PZT and relaxor ferroelectric PCN, which could exhibit electrical properties that are better than those of the single-phase PZT and PCN [8–11]. Our previous investigation on $(1-x)$PZT–$(x)$PCN ceramic systems has already shown excellent electrical properties with the MPB at $x = 0.2$. Previously, the influences of Zr/Ti ratio on electrical properties have been extensively investigated in PZT [12–15], PZT–PZN [16], PZT–PMMN [17], and PZT–$SiO_2$ [18]. However, there have been no systematic studies on the relationship between Zr/Ti ratio, physical and electrical properties of ceramics within specific morphotropic phase boundary compositions of PZT and PCN.

* Corresponding author. Tel.: +66 53 941921x443; fax: +66 53 943445.
*E-mail address:* Prasatkhetragarn@yahoo.com (A. Prasatkhetragarn).

1567-1739/$ - see front matter © 2008 Elsevier B.V. All rights reserved.
doi:10.1016/j.cap.2008.07.019

Therefore, the overall purpose of this study is to determine the influence of Zr/Ti ratio on phase formation, microstructure, dielectric and ferroelectric properties of $0.8Pb(Zr_xTi_{1-x})O_3$–$0.2Pb(Co_{1/3}Nb_{2/3})O_3$ where $x = 0.46$, 0.48, 0.50, 0.52, and 0.54) ceramic systems.

## 2. Experimental procedure

The specimens studied were fabricated according to the formula: $0.8Pb(Zr_xTi_{1-x})O_3$–$0.2Pb(Co_{1/3}Nb_{2/3})O_3$, where $x = 0.46$, 0.48, 0.50, 0.52, and 0.54. Raw materials of PbO, $ZrO_2$, $TiO_2$, CoO, and $Nb_2O_5$ with >99% purity were used to prepare samples. The columbite $CoNb_2O_6$ precursor was weighed and introduced into the batch calculations. The $CoNb_2O_6$ powder was prepared at calcination temperature of 1100 °C for 2 h [8]. In the present work, the $0.8Pb(Zr_xTi_{1-x})O_3$–$0.2Pb(Co_{1/3}Nb_{2/3})O_3$ samples were prepared from PbO, $ZrO_2$, $TiO_2$, and $CoNb_2O_6$ powders using the solid-state reaction of these raw materials. The powders were mixed by a vibratory-milling technique in ethanol for 6 h. After drying, the product was calcined in an alumina crucible at a temperature of 950 °C [19]. The calcined powders were uniaxially cold-pressed at 5000 psi into disc-shaped pellets with a diameter of 12.7 mm and a thickness of 1 mm, with 3 wt% poly vinyl alcohol (PVA) added as a binder. Following binder burnout at 500 °C, the pellets were sintered at 1200 °C for 2 h at a heating/cooling rate of 5 °C/min [19].

The phase structure of the powders was analyzed via X-ray diffraction (XRD; Bruker-AXS D8). The microstructures of the sintered samples were examined using scanning electron microscopy (SEM; JEOL JSM-840A). The dielectric properties of the samples were measured using an automated measurement system. An Agilent 4284A LCR meter was used to measure the dielectric properties over a wide temperature range using a NorECS ProboStat high temperature measurement cell. The room temperature ferroelectric properties were examined using a simple Sawyer–Tower circuit at fixed measuring frequency of 50 Hz.

## 3. Results and discussion

Perovskite phase formation and crystal structure were determined by XRD at room temperature. The XRD patterns of $0.8Pb(Zr_xTi_{1-x})O_3$–$0.2Pb(Co_{1/3}Nb_{2/3})O_3$, where $x = 0.46$, 0.48, 0.50, 0.52 and 0.54 are correlated with JCPDS file number 70-4057, as shown in Fig. 1, showing a perovskite structure for all compositions. The pyrochlore phase is not observed in this system. In the XRD patterns, the crystal structure of the specimens appears to change gradually from tetragonal to rhombohedral with increasing Zr content, as presented in Fig. 1(a). There also appears an MPB between tetragonal and rhombohedral phases around Zr/Ti = 50/50. As shown in Fig. 1(b), XRD peak profiles of the (200) and (002) peaks at $x = 0.46$ and 0.48 indicate the tetragonal phase. At the $x = 0.50$ composition, (020) peak is observed, indicating the coexistence of the tetragonal and rhombohedral phases, as shown in Fig. 1(c). The (020) peak in compositions $x = 0.52$ and 0.54 has indicated that the crystal has transformed into rhombohedral phase. Previously, a similar behavior was also observed with increasing Zr content in PZT, PZT–PZN, PZT–PMMN, and PZT–$SiO_2$ based ceramics [13–18].

Effects of Zr/Ti ratio on the microstructure of the $0.8Pb(Zr_xTi_{1-x})O_3$–$0.2Pb(Co_{1/3}Nb_{2/3})O_3$ ceramics are displayed in Fig. 2. The grain size of the ceramics varies considerably from 1.00 to 11.31 μm, as listed in Table 1. However, the average grain size only slightly increases with increasing Zr content. Since the grain size of PZT-based materials strongly depends on the composition ratio, nucleation energy, and growth energy, the compositions with lower Zr content need higher growth energy. This trend is similar to those reported in the literature [14,20]. Since the microstructure of all compositions does not differ significantly, it should not play an important role in controlling electrical properties of this ceramic system.

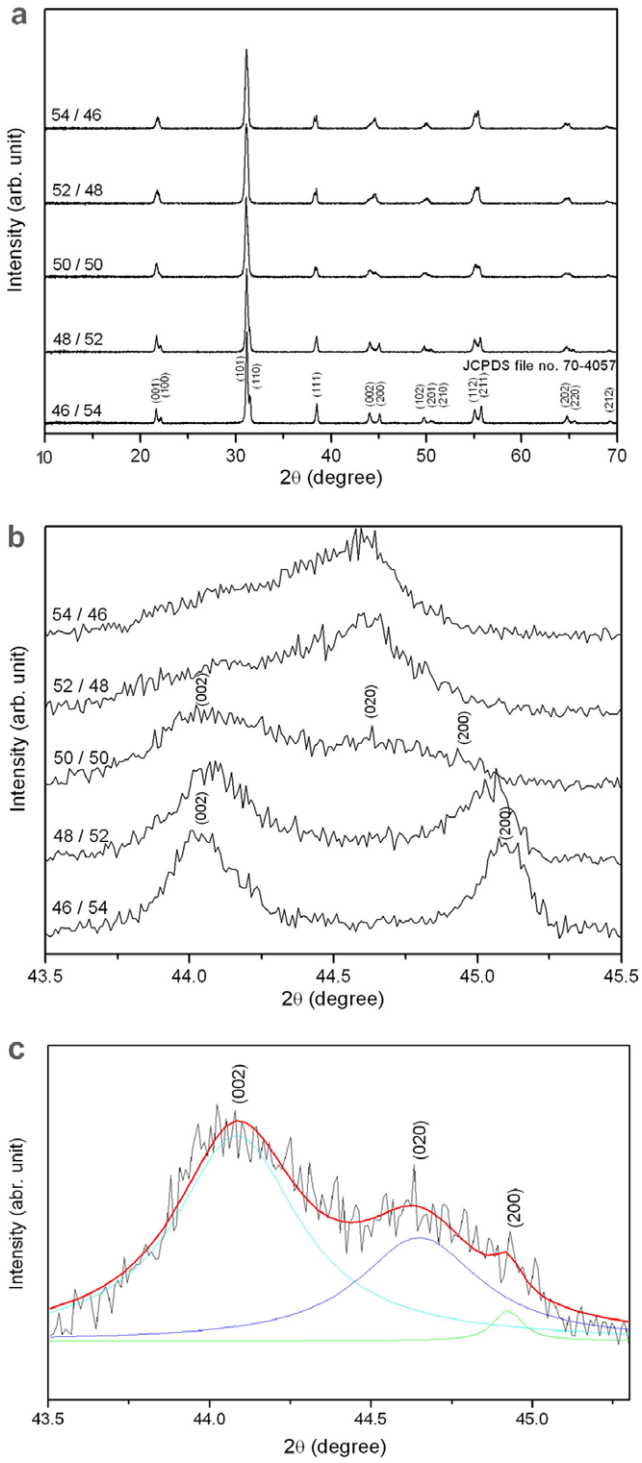



**Fig. 1.** XRD patterns of $0.8Pb(Zr_xTi_{1-x})O_3$–$0.2Pb(Co_{1/3}Nb_{2/3})O_3$ ceramics; (a) with $x = 0.46$, 0.48, 0.50, 0.52 and 0.54, (b) the (200) and (002) peaks profile at various Zr/Ti ratios and (c) coexistence of tetragonal/rhombohedral phases at $x = 0.50$ composition.

Temperature dependences of the dielectric constant ($\varepsilon_r$) and dielectric loss tangent ($\tan\delta$) of the $0.8Pb(Zr_xTi_{1-x})O_3$–$0.2Pb(Co_{1/3}Nb_{2/3})O_3$ ceramics are displayed in Fig. 3. At room temperature

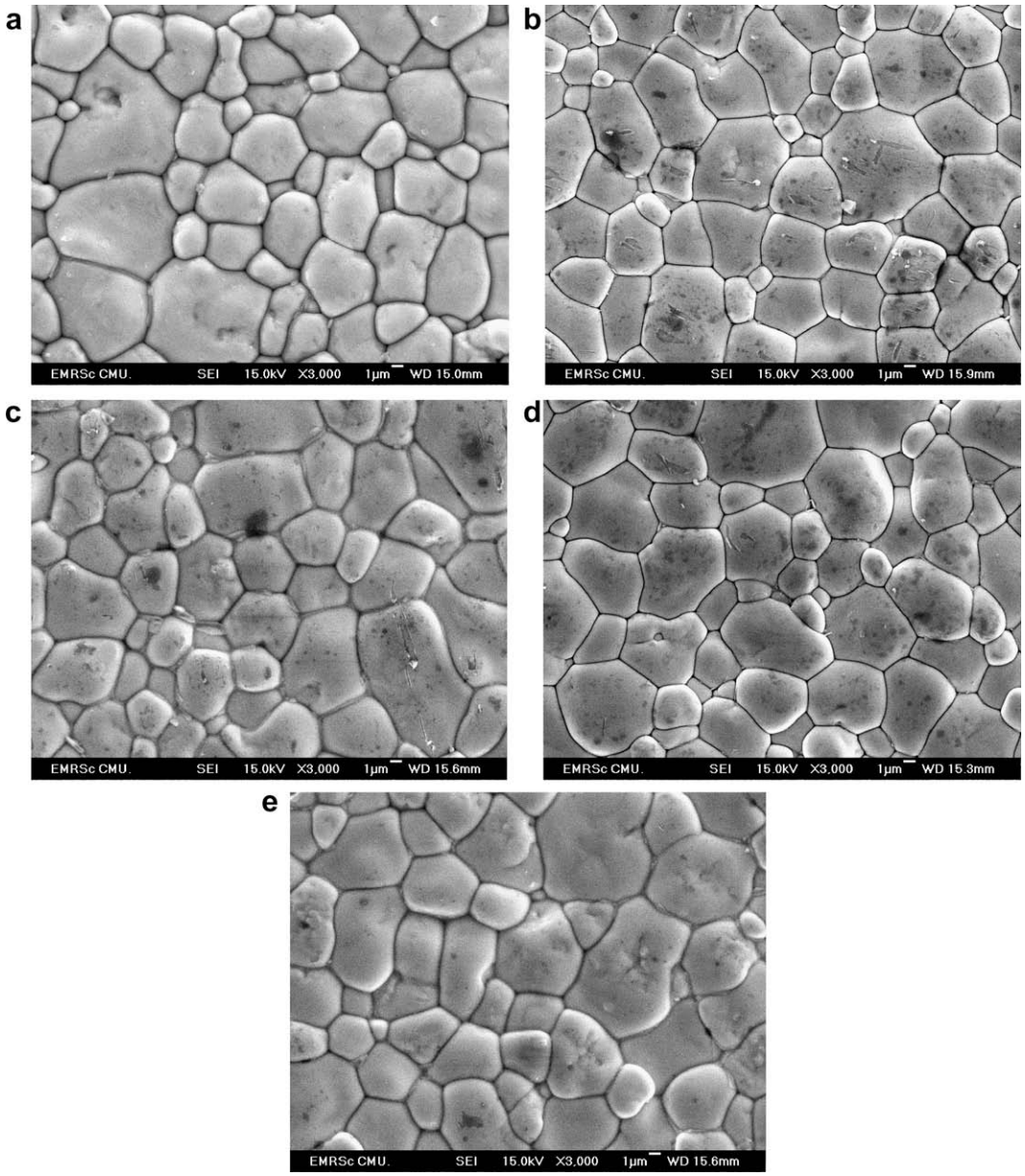



**Fig. 2.** SEM micrographs of $0.8Pb(Zr_xTi_{1-x})O_3$–$0.2Pb(Co_{1/3}Nb_{2/3})O_3$ with increasing Zr content: (a) $x = 0.46$, (b) $x = 0.48$, (c) $x = 0.50$, (d) $x = 0.52$, and (e) $x = 0.54$.

**Table 1**
Physical properties of $0.8Pb(Zr_xTi_{1-x})O_3$–$0.2Pb(Co_{1/3}Nb_{2/3})O_3$ ceramics

| Zr/Ti ratio | Density ($g/cm^3$) | Grain size range (μm) | Average grain size (μm) |
|---|---|---|---|
| 46/54 | 7.93 ± 0.05 | 1.21–10.99 | 4.34 |
| 48/52 | 7.94 ± 0.05 | 1.19–10.21 | 4.36 |
| 50/50 | 7.95 ± 0.05 | 1.41–11.12 | 4.54 |
| 52/48 | 7.91 ± 0.05 | 1.38–11.31 | 4.66 |
| 54/46 | 7.93 ± 0.05 | 1.00–9.20 | 4.72 |

(RT), with increasing Zr content, the dielectric constant and tan $\delta$ tend to increase because the transition temperature of the ceramics shifts towards RT; hence, the value of the dielectric properties measured at RT increases, as listed in Table 2. Many previous works on PZT–PZN, PZT–PNN, and PZT–PMN have reported a similar behavior [4–6]. The maximum dielectric constant ($\varepsilon_{max}$) at 1 kHz is also listed in Table 2. The $\varepsilon_{max}$ increases at Zr = 0.46,

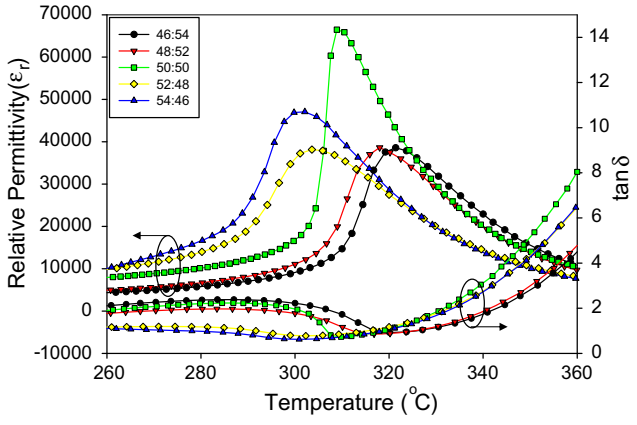



**Fig. 3.** Temperature dependences of dielectric properties of $0.8Pb(Zr_xTi_{1-x})O_3$–$0.2Pb(Co_{1/3}Nb_{2/3})O_3$ ceramics, where $x = 0.46$, 0.48, 0.50, 0.52, and 0.54.

**Table 2**
Dielectric properties of $0.8Pb(Zr_xTi_{1-x})O_3$–$0.2Pb(Co_{1/3}Nb_{2/3})O_3$ ceramics

| Zr/Ti ratio | Dielectric properties (at 1 kHz) | | | | | | |
|---|---|---|---|---|---|---|---|
| | $T_{max}$ | $\varepsilon_{RT}$ | $\tan\delta$ | $\varepsilon_{max}$ | $\tan\delta$ | $\gamma$ | $\delta$ |
| 46/54 | 321 | 835 | 0.0437 | 38,580 | 0.9232 | 1.71 | 15.98 |
| 48/52 | 318 | 875 | 0.0467 | 38,630 | 0.8548 | 1.65 | 15.64 |
| 50/50 | 310 | 929 | 0.0484 | 66,590 | 0.7797 | 1.52 | 15.41 |
| 52/48 | 304 | 951 | 0.0547 | 38,150 | 0.7302 | 1.86 | 16.75 |
| 54/46 | 301 | 979 | 0.0657 | 47,200 | 0.6215 | 1.89 | 16.82 |

0.48 and 0.50 and then decreases at Zr = 0.52 and 0.54, whereas $\tan\delta$ tends to decrease with increasing Zr content, clearly indicating the maximum dielectric constant at MPB composition of Zr/Ti = 50/50. In addition, a clear transition in $T_{max}$ (defined as the temperature at which $\varepsilon_r$ is maximum at 1 kHz) is observed. It is noticed that an increase in Zr mole fraction leads to a decrease in $T_{max}$, most likely due to crystal structure of the materials was changed from tetragonal to rhombohedral, as shown in XRD patterns in Fig. 1. This result suggests that the transition temperature of 0.8PZT–0.2PCN system can be varied over a range from 301 to 321 °C by controlling the Zr/Ti ratio in the system. Similar behavior is also reported in previous works [13–18].

To further understand the dielectric behavior of the PZT–PCN system, the permittivity of a first-order normal ferroelectric can be described by the Curie–Weiss law and a second-order relaxor ferroelectric can be described by a simple quadratic law [21]. This arises from the fact that the total number of relaxor contributing to the permittivity response in the vicinity of the permittivity peak is temperature dependent, and the temperature distribution of this number is given by a Gaussian function about a mean value $T_0$ with a standard deviation $\delta$. The relative permittivity can be derived via using the following equation:

$$\frac{\varepsilon_m}{\varepsilon(f,T)} = 1 + \frac{(T - T_m(f))^\gamma}{2\delta^2} \quad (1)$$

where $\varepsilon_m$ is the maximum value of the permittivity at $T = T_m(f)$. The value of $\gamma$ is the expression of the degree of dielectric relaxation, while $\delta$ is used to measure the degree of diffuseness of the phase transition. In a material with a "pure" diffuse phase transition, $\gamma$ is expected to be 2 [10]. As listed in Table 2, the values of $\gamma$ vary with Zr/Ti ratio between 1.52 and 1.89, which confirms that diffuse phase transition occurs in the PZT–PCN system. It is important to note that in perovskite ferroelectrics it has been established that $\gamma$ and $\delta$ can be affected by Zr/Ti ratio and structure of the materials. The values of $\gamma$ and $\delta$ decrease with increasing Zr from 0.46 to 0.50 mol%, and then increase when Zr content increases further, as tabulated in Table 2. It is interesting to observe that the phase transition is least diffused at MPB, possibly due to a sharp increase of dielectric permittivity at MPB. A similar behavior has also been observed in PZT–PZN systems [16].

The Polarization–Electric field ($P$–$E$) hysteresis loops of $0.8Pb(Zr_xTi_{1-x})O_3$–$0.2Pb(Co_{1/3}Nb_{2/3})O_3$ ceramics measured at 15 kV/cm are presented in Fig. 4. To assess effect of Zr/Ti ratio on

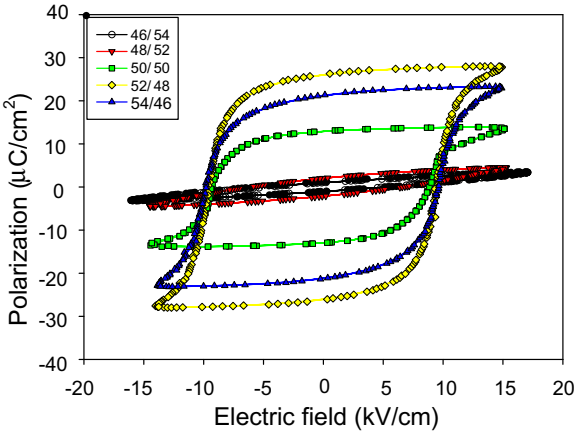



**Fig. 4.** $P$–$E$ loops of $0.8Pb(Zr_xTi_{1-x})O_3$–$0.2Pb(Co_{1/3}Nb_{2/3})O_3$ ceramics, where $x = 0.46$, 0.48, 0.50, 0.52, and 0.54.

ferroelectric characteristics of 0.8PZT–0.2PCN ceramics, the ferroelectric parameters have been extracted from the experimental data, as summarized in Table 3. The remnant polarization ($P_r$) and coercive field ($E_c$) increase with increasing Zr content. However, the decrease in the remnant polarization at $x = 0.54$ could be caused by Zr-rich rhombohedral phase in this composition [22]. The ferroelectric parameters have been normalized in forms of $P_r/P_{max}$ and $E_c/E_{max}$ values, where $P_{max}$ is the polarization value at the maximum applied field ($E_{max}$). These normalized values are also listed in Table 3. It can be seen that $P_r/P_{max}$ increases with increasing Zr content and reaches the maximum values at Zr/Ti = 50/50 composition and then decreases, while $E_c/E_{max}$ increases with increasing Zr content. Furthermore, the ferroelectric characteristics can be assessed with the hysteresis loop squareness ($R_{sq}$) [19], which can be calculated from the empirical expression $R_{sq} = (P_r/P_s) + (P_{1.1E_c}/P_s)$, where $P_s$ is the saturated polarization obtained at some finite field strength below the dielectric breakdown and $P_{1.1E_c}$ is the polarization at the field equal to $1.1E_c$. For the ideal square loop, $R_{sq}$ is equal to 2.00 [23]. As listed in Table 3, the loop squareness parameter $R_{sq}$ increases from 0.90 in Zr/Ti = 54/46 to reach the maximum value of 1.49 in Zr/Ti = 50/50 and then decrease to 1.45 in Zr/Ti = 46/54. As is well known, the values of the dielectric and ferroelectric properties of a solid solution with MPB usually maximize approximately at the MPB composition. It is seen that the highest $R_{sq}$ at Zr/Ti of 50/50 indicates the MPB of this system. This behavior has also been found in previous investigation [14]. This observation could be due to easy polarization rotation in the MPB region with coexistence of the tetragonal and rhombohedral phase [14]. Fig. 5 summarizes the dielectric and ferroelectric properties of $0.8Pb(Zr_xTi_{1-x})O_3$–$0.2Pb(Co_{1/3}Nb_{2/3})O_3$ with various Zr/Ti ratios. Clearly, substantial changes of the electrical properties are observed at Zr/Ti ratio of 50/50, which confirm the MPB of this ceramic system at Zr/Ti = 50/50. An anomaly of electrical properties at the MPB has also been observed in solid solutions of PZT–PNN, PZT–PZN, and PZT–PMN [4–7,24].

**Table 3**
Ferroelectric properties of $0.8Pb(Zr_xTi_{1-x})O_3$–$0.2Pb(Co_{1/3}Nb_{2/3})O_3$ ceramics

| Zr/Ti ratio | Ferroelectric properties | | | | | |
|---|---|---|---|---|---|---|
| | $P_r$ (μC/cm²) | $P_s$ (μC/cm²) | $E_c$ (kV/cm) | $P_r/P_{max}$ | $E_c/E_{max}$ | Loop squareness ($R_{sq}$) |
| 46/54 | 1.00 | 1.25 | 5.23 | 0.33 | 0.35 | 0.90 |
| 48/52 | 2.09 | 2.48 | 6.78 | 0.46 | 0.45 | 1.00 |
| 50/50 | 12.91 | 13.71 | 8.89 | 0.93 | 0.60 | 1.49 |
| 52/48 | 26.16 | 27.75 | 9.50 | 0.93 | 0.65 | 1.47 |
| 54/46 | 21.34 | 22.91 | 9.65 | 0.92 | 0.66 | 1.45 |

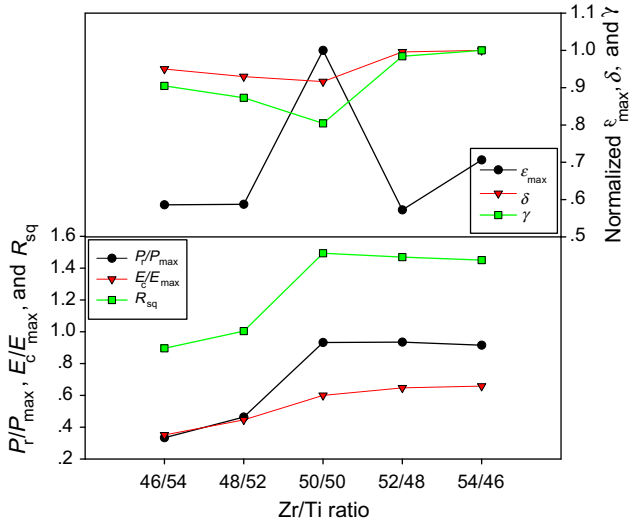



**Fig. 5.** Relationship of dielectric and ferroelectric parameter $P_r/P_{max}$, $E_c/E_{max}$, $R_{sq}$, and normalized $\varepsilon_{max}$, $\delta$, and $\gamma$ with various Zr/Ti ratio.

## 4. Conclusions

In this study, ceramics in the $0.8Pb(Zr_xTi_{1-x})O_3$–$0.2Pb(Co_{1/3}Nb_{2/3})O_3$ system, $x = 0.46$, 0.48, 0.50, 0.52, and 0.54, are successfully prepared by a solid-state mixed-oxide technique. The XRD analysis indicates that the tetragonal and rhombohedral phases coexist around Zr/Ti = 50/50. The surface micrographs show that average grain size slightly increases with increasing Zr content. At 1 kHz, the maximum dielectric constant ($\varepsilon_{max}$) of 65,600 is observed at Zr/Ti = 50/50. However, the diffusivity ($\gamma$) and diffuseness parameter ($\delta$) reach minimum at Zr/Ti = 50/50. Moreover, the ferroelectric parameters; remnant polarization ($P_r$) and coercive field ($E_c$), increase with increasing Zr content, while the highest loop squareness ($R_{sq}$) of 1.49 is observed at the MPB composition. Most importantly, a combination of XRD analysis, dielectric and ferroelectric measurements shows that the MPB between the tetragonal and rhombohedral phases exists around Zr/Ti ratio of 50/50. Finally, this study shows that the Zr/Ti ratio could be used to tailor electrical properties in PZT–PCN ceramics.

## Acknowledgments

The authors wish to express profound gratitude to Materials Science Groups, Oregon State University for ceramics preparation and measurement. This work was supported by the Commission on Higher Education (CHE), the Thailand Research Fund (TRF), the Faculty of Science, the Graduate School of Chiang Mai University, and Naresuan University Phayao.

## References

[1] A.J. Moulson, J.M. Herbert, Electroceramics: Materials, Properties, Applications, Wiley, Chichester, UK, 2003.
[2] L.E. Cross, Mater. Chem. Phys. 43 (1996) 108.
[3] S.-E. Park, T.R. Shrout, IEEE Trans. Ultrason. Ferroelectron. Freq. Control 44 (1997) 1140.
[4] N. Vittayakorn, G. Rujijanagul, X. Tan, M.A. Marquardt, D.P. Cann, J. Appl. Phys. 96 (2004) 5103.
[5] R. Yimnirun, S. Ananta, P. Laoratanakul, J. Eur. Ceram. Soc. 25 (2005) 3235.
[6] H. Fan, G.T. Park, J.J. Choi, J. Ryu, H.E. Kim, J. Mater. Res. 17 (2002) 180.
[7] D. Luff, R. Lane, K.R. Brown, H.J. Marshallsay, Trans. J. Br. Ceram. Soc. 73 (1974) 251.
[8] M. Unruan, N. Vittayakorn, R. Wongmaneeruang, A. Prasatkhetragarn, S. Ananta, R. Yimnirun, J. Alloy Compd. (in press).
[9] T. Hachiga, S. Fujimoto, N. Yasuda, J. Phys. D 20 (1987) 1291.
[10] T. Kudo, T. Yazaki, F. Naito, S. Sugaya, J. Am. Ceram. Soc. 53 (1970) 326.
[11] Z. Brankovic, G. Brankovic, J.A. Varela, J. Mater. Sci. 14 (2003) 37.
[12] R. Guo, L.E. Cross, S.-E. Park, B. Noheda, D.E. Cox, G. Shirane, Phys. Rev. Lett. 84 (2000) 5423.
[13] Y.H. Lee, J.K. Lee, K.S. Hong, J. Korean Phys. Soc. 42 (2003) 1395.
[14] P. Khaenamkaew, S. Muensit, I.K. Bdikin, A.L. Kholkin, Mater. Chem. Phys. 102 (2007) 159.
[15] Z.J. Wang, Y. Aoki, L.J. Yan, H. Kokawa, R. Maeda, J. Crystal Growth 267 (2004) 92.
[16] S.H. Lee, C.B. Yoon, S.M. Lee, H.E. Kim, J. Eur. Ceram. Soc. 26 (2006) 111.
[17] H. Chen, J. Long, Z. Meng, Mater. Sci. Eng. B 99 (2003) 433.
[18] X. Wang, X. Yao, H. Ishiwara, Mater. Sci. Eng. B 137 (2007) 278.
[19] A. Prasatkhetragarn, N. Vittayakorn, S. Ananta, R. Yimnirun, D.P. Cann, Jpn. J. Appl. Phys. 47 (2008) 998.
[20] Q. Zhang, R.W. Whatmore, J. Phys. D: Appl. Phys. 34 (2001) 2296.
[21] A.A. Bokov, Z.G. Ye, Solid State Commun. 116 (2000) 105.
[22] B. Jaffe, W.R. Cook Jr., H. Jaffe, Piezoelectric Ceramics, Academic Press, London, UK, 1971.
[23] G.H. Haertling, W.J. Zimmer, Am. Ceram. Soc. Bull. 45 (1966) 1084.
[24] N. Vittayakorn, G. Rujijanagul, T. Tankasiri, X. Tan, D.P. Cann, Mater. Sci. Eng. B 108 (2004) 258.

J Mater Sci (2009) 44:1868–1872
DOI 10.1007/s10853-008-3235-4

# The morphotropic phase boundary and electrical properties of $(1 - x)Pb(Zn_{1/2}W_{1/2})O_3$–$xPb(Zr_{0.5}Ti_{0.5})O_3$ ceramics

**O. Khamman · X. Tan · S. Ananta · R. Yimnirun**

Received: 20 November 2008 / Accepted: 29 December 2008 / Published online: 3 February 2009
© Springer Science+Business Media, LLC 2009

**Abstract** Ceramics in the solid solution of $(1 - x)Pb(Zn_{1/2}W_{1/2})O_3$–$xPb(Zr_{0.5}Ti_{0.5})O_3$ system, with $x = 0.80$, 0.85, 0.90, and 0.95, were synthesized with the solid-state reaction technique. The perovskite phase formation in the sintered ceramics was analyzed with X-ray diffraction. It shows that the rhombohedral and the tetragonal phases coexist in the ceramic with $x = 0.90$, indicating the morphotropic phase boundary (MPB) within this pseudo-binary system. Dielectric and ferroelectric properties measurements indicate that the transition temperature decreases while the remanent polarization increases with the addition of $Pb(Zn_{1/2}W_{1/2})O_3$. In the composition of $x = 0.85$ which is close to the MPB in the rhombohedral side, a high piezoelectric property with $d_{33} = 222$ pC/N was observed.

## Introduction

Lead-containing perovskite ferroelectrics are of great importance to engineering technologies due to their unique dielectric and piezoelectric properties [1]. Lead zirconate titanate, $Pb(Zr_{1-y}Ti_y)O_3$, is the most studied system for piezoelectric applications in transducers and actuators [1–4]. The best piezoelectric properties are found in compositions close to the morphotropic phase boundary (MPB), roughly $Pb(Zr_{0.5}Ti_{0.5})O_3$ [1]. To further enhance their piezoelectric properties, other complex compounds have been incorporated into the $Pb(Zr_{0.5}Ti_{0.5})O_3$, such as $Pb(Ni_{1/3}Nb_{2/3})_3$ [5], $Pb(Zn_{1/3}Nb_{2/3})O_3$ [6], $Pb(Mg_{1/3}Nb_{2/3})O_3$ [7], and $Pb(Mg_{1/2}W_{1/2})O_3$ [8].

Lead zinc tungstate, $Pb(Zn_{1/2}W_{1/2})O_3$, is a complex perovskite compound with $Zn^{2+}$ and $W^{6+}$ ordered on the B-site of the $ABO_3$ perovskite lattice [9]. When cooling through the Curie temperature of 130 °C, it transforms from the cubic to a tetragonal structure. However, whether the tetragonal phase is ferroelectric or antiferroelectric is still unknown [9]. It should be noted that perovskite $Pb(Zn_{1/2}W_{1/2})O_3$ can only be synthesized under high pressure [10]. The conventional solid-state reaction method invariably leads to the mixture of $Pb_2WO_5$ and ZnO [11]. To the authors' knowledge, the complex perovskite $Pb(Zn_{1/2}W_{1/2})O_3$ has not been reported in literature to be incorporated into $Pb(Zr_{1-y}Ti_y)O_3$ for solid solutions. In addition to identifying the MPB and investigating the dielectric, piezoelectric, and ferroelectric properties in the $(1 - x)Pb(Zn_{1/2}W_{1/2})O_3$–$xPb(Zr_{0.5}Ti_{0.5})O_3$ solid solution system, the present study aims to determine the solubility limit of $Pb(Zn_{1/2}W_{1/2})O_3$ in $Pb(Zr_{0.5}Ti_{0.5})O_3$ and to explore if long range cation order can be developed in $Pb(Zr_{0.5}Ti_{0.5})O_3$-based solid solutions [8].

## Experimental

Ceramics in the $(1 - x)Pb(Zn_{1/2}W_{1/2})O_3$–$xPb(Zr_{0.5}Ti_{0.5})O_3$ pseudo-binary system with $x = 0.80$, 0.85, 0.90, and 0.95 were prepared with a two-step reaction method. First, powders of $ZnWO_4$ and $ZrTiO_4$ were synthesized. The $ZnWO_4$ precursor was formed by reacting ZnO (99.9%) with $WO_3$ (99.9%) at 1000 °C for 4 h while the $ZrTiO_4$ precursor was formed by reacting $ZrO_2$ (99%) with $TiO_2$

O. Khamman · S. Ananta · R. Yimnirun
Department of Physics, Faculty of Science, Chiang Mai University, Chiang Mai 50200, Thailand

X. Tan (✉)
Department of Materials Science and Engineering, Iowa State University, Ames, IA 50011, USA
e-mail: xtan@iastate.edu

(99.9%) at 1400 °C for 4 h. Appropriate amount of $ZnWO_4$ and $ZrTiO_4$ were then mixed with PbO (99.9%, with 2 mol% excess) and milled, dried, and calcined at 900 °C for 4 h. The green compact of ceramics was formed by uniaxially pressing powders containing 2 wt% polyvinyl alcohol binder. Sintering was carried out at temperatures between 1100 and 1175 °C. To prevent PbO loss from the pellets, a PbO atmosphere was provided with a bed of $PbZrO_3$ powder placed in the vicinity of the pellets.

The density of the ceramics was measured by the Archimedes method, and the grain size was examined by scanning electron microscopy (SEM). The X-ray diffraction was used to verify the phase purity and determine the crystal structure. The ceramic pellets were polished and then electroded with gold for dielectric measurements. The samples were heated from room temperature at 2 °C/min for the measurement. For the piezoelectric measurement, samples were poled under 30 kV/cm for 10 min at 120 °C. The piezoelectric coefficient $d_{33}$ was measured using a $d_{33}$ meter 24 h after poling. The polarization hysteresis measurement was carried out with a standardized ferroelectric test system at room temperature with a frequency of about 4 Hz.

## Results and discussion

The measured density of the sintered ceramic pellets in the pseudo-binary system $(1-x)Pb(Zn_{1/2}W_{1/2})O_3$–$xPb(Zr_{0.5}Ti_{0.5})O_3$ is listed in Table 1. The relative density for all the pellets was found to be above 90%. The addition of $Pb(Zn_{1/2}W_{1/2})O_3$ seems to enhance the sinterability of the solid solution ceramics. SEM micrographs of the fracture surfaces of the ceramic pellets are shown in Fig. 1. It can be seen that grains are uniform with clear grain boundaries. The average grain size determined from these micrographs is also listed in Table 1. Obviously, incorporating up to 10 mol% of $Pb(Zn_{1/2}W_{1/2})O_3$ into $Pb(Zr_{0.5}Ti_{0.5})O_3$ significantly increases the grain size. However, beyond 10 mol%, it appears to show the opposite effect.

X-ray diffraction patterns of the $(1-x)Pb(Zn_{1/2}W_{1/2})O_3$–$xPb(Zr_{0.5}Ti_{0.5})O_3$ solid solution ceramics are presented in Fig. 2. Within the detection limit of the diffractometer, sintered ceramics are phase pure with the perovskite structure with $x$ down to 0.80. Further increase in $Pb(Zn_{1/2}W_{1/2})O_3$ content invariably leads to the formation of second phases. Therefore, the solubility limit of $Pb(Zn_{1/2}W_{1/2})O_3$ in $Pb(Zr_{0.5}Ti_{0.5})O_3$ is 20 mol%. Furthermore, the X-ray diffraction data in the range of 15–20° for $2\theta$ (not shown in Fig. 2) did not display any diffraction intensity peak, suggesting the absence of long range cation order in these sintered ceramics [8].

**Table 1** Characteristics of the sintered $(1-x)Pb(Zn_{1/2}W_{1/2})O_3$–$xPb(Zr_{0.5}Ti_{0.5})O_3$ ceramics

| $x$ | Relative density (%) | Grain size (μm) |
|---|---|---|
| 0.80 | 95 | 11.5 |
| 0.85 | 92 | 28.5 |
| 0.90 | 91 | 41.8 |
| 0.95 | 90 | 20.8 |

Close examination indicates significant changes in the pseudo-cubic $(200)_c$ peak when composition varies, as marked with the dashed box in Fig. 2. For the composition of $x = 0.95$, the X-ray diffraction pattern shows an obvious $(200)_c$ peak splitting which is indicative of the tetragonal symmetry of the perovskite structure. As the $Pb(Zn_{1/2}W_{1/2})O_3$ content increases in the solid solution, the $(200)_c$ peak transforms to a single peak which suggests a rhombohedral distortion of the perovskite structure. The results show that a morphotropic phase boundary (MPB), separating the rhombohedral from the tetragonal phase, exists at $x = 0.90$ in the pseudo-binary $(1-x)Pb(Zn_{1/2}W_{1/2})O_3$–$xPb(Zr_{0.5}Ti_{0.5})O_3$ solid solution system. It is interesting to notice that the phase evolution sequence in the present $Pb(Zn_{1/2}W_{1/2})O_3$–$Pb(Zr_{0.5}Ti_{0.5})O_3$ system is very similar to that in the $Pb(Ni_{1/3}Nb_{2/3})O_3$–$Pb(Zr_{0.5}Ti_{0.5})O_3$ [5] and the $Pb(Zn_{1/3}Nb_{2/3})O_3$–$Pb(Zr_{0.5}Ti_{0.5})O_3$ systems [6].

The temperature dependence of dielectric constant $\varepsilon_r$ and loss tangent tan $\delta$ measured at 1 kHz for the ceramics are plotted in Fig. 3. It is shown that with increasing $Pb(Zn_{1/2}W_{1/2})O_3$ content in the $(1-x)Pb(Zn_{1/2}W_{1/2})O_3$–$xPb(Zr_{0.5}Ti_{0.5})O_3$ solid solution, the paraelectric–ferroelectric transition temperature $T_m$ decreases continuously. Overall, all the ceramics show very high dielectric permittivity. The dielectric constant at $T_m$, denoted as $\varepsilon_m$ hereafter, shows the highest value of 38410 in the composition of $x = 0.90$. This composition, as revealed by the X-ray diffraction patterns shown in Fig. 2, is the MPB composition. Therefore, the results from the dielectric measurement are in support of the x-ray diffraction data. The values of $T_m$ and $\varepsilon_m$ for the ceramic series are listed in Table 2 for clarity.

It is also noticed from Fig. 3 that the paraelectric–ferroelectric transition peak becomes broadened slightly with increasing $Pb(Zn_{1/2}W_{1/2})O_3$ content. In addition, a new dielectric anomaly emerges around 260 °C in the composition of $x = 0.80$. Detailed comparison of the dielectric constant under different measuring frequencies between compositions of $x = 0.80$ and 0.95 is shown in Fig. 4. A weak frequency dependence is seen in the dielectric constant.

The broadened dielectric peak suggests that the dielectric constant $\varepsilon_r$ at temperatures above $T_m$ should follow a general expression [5, 12]:

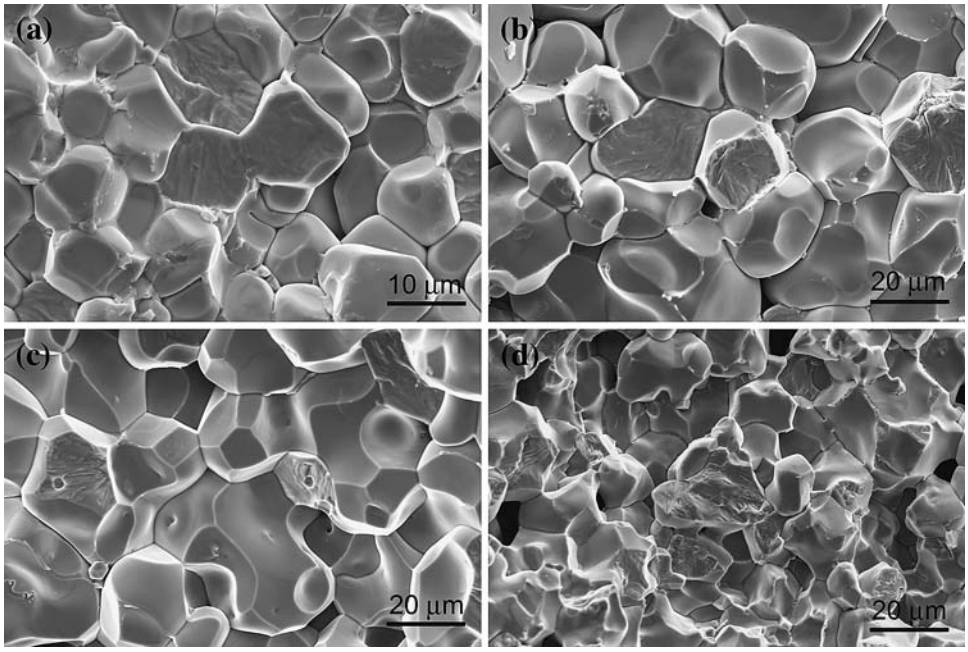



**Fig. 1** SEM micrographs revealing the fracture surfaces of $(1 - x)Pb(Zn_{1/2}W_{1/2})O_3$–$xPb(Zr_{0.5}Ti_{0.5})O_3$ ceramics. **a** $x = 0.80$, **b** $x = 0.85$, **c** $x = 0.90$, **d** $x = 0.95$

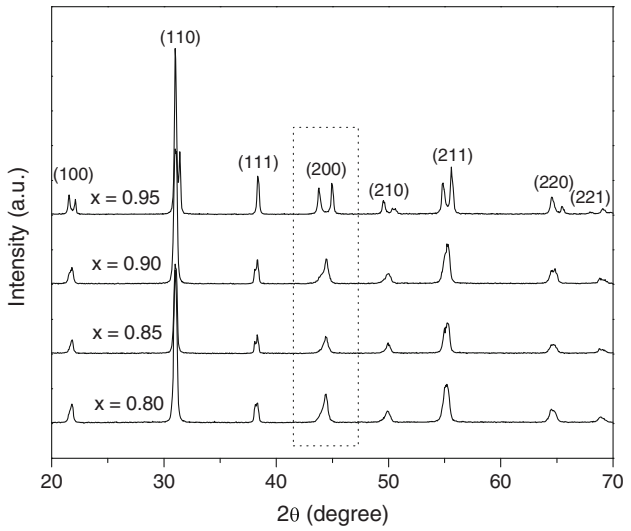



**Fig. 2** X-ray diffraction spectra for the sintered $(1 - x)Pb(Zn_{1/2}W_{1/2})O_3$–$xPb(Zr_{0.5}Ti_{0.5})O_3$ ceramics. The intensity peaks are index with the pseudo-cubic perovskite structure. The $(200)_c$ peak in the dashed box reveals the change of distortion

$$\frac{\varepsilon_m}{\varepsilon_r} = 1 + \frac{[T - T_m]^\gamma}{2\delta^2} \quad (1)$$

where $\gamma$ is a parameter indicating the degree of dielectric relaxation while the parameter $\delta$ can be used to evaluate the degree of the diffuseness of the phase transition. When $\gamma = 1$, Eq. 1 becomes the Curie–Weiss law, while for $\gamma = 2$ this equation becomes the quadratic relationship describing the classic relaxor ferroelectric $Pb(Mg_{1/3}Nb_{2/3})O_3$ [13]. According to Eq. 1, the values of ln $[(\varepsilon_m/\varepsilon_r) - 1]$ are plotted against ln $(T - T_m)$ in Fig. 5 for all the sintered

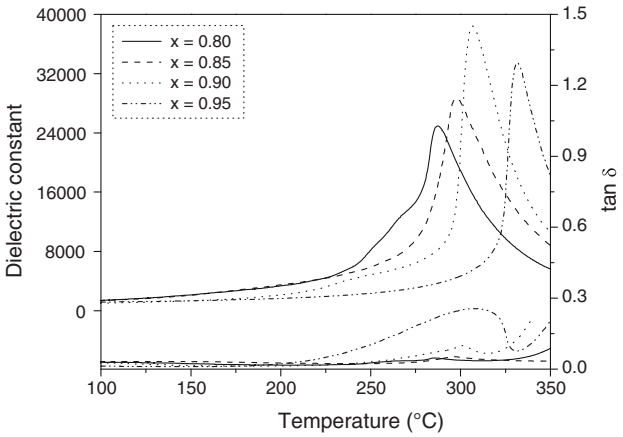



**Fig. 3** Dielectric constant $\varepsilon_r$ and loss tangent tan $\delta$ as a function of temperature measured at 1 kHz during heating in the $(1 - x)Pb(Zn_{1/2}W_{1/2})O_3$–$xPb(Zr_{0.5}Ti_{0.5})O_3$ ceramics

**Table 2** Dielectric and piezoelectric properties of the $(1 - x)Pb(Zn_{1/2}W_{1/2})O_3$–$xPb(Zr_{0.5}Ti_{0.5})O_3$ ceramics

| $x$ | $\varepsilon_m$ | $T_m$ (°C) | $\gamma$ | $\delta$ | $d_{33}$ (pC/N) |
|---|---|---|---|---|---|
| 0.80 | 24930 | 287 | 1.55 | 8.07 | 142 |
| 0.85 | 28730 | 297 | 1.55 | 7.50 | 222 |
| 0.90 | 38410 | 306 | 1.53 | 7.39 | 188 |
| 0.95 | 33480 | 331 | 1.43 | 6.13 | 136 |

ceramics, using the data obtained at 1 kHz. Remarkably good linearity within the measurement temperature range above $T_m$ is evident. Using the intercept and the slope of the fitted lines in Fig. 5, $\gamma$ and $\delta$ for each composition are determined and listed in Table 2. It is found that with

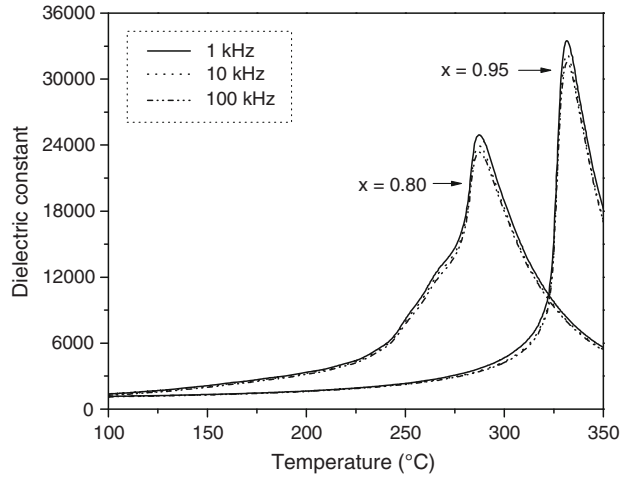



**Fig. 4** Dielectric constant $\varepsilon_r$ as a function of temperature measured at 1, 10, and 100 kHz during heating in the $0.20Pb(Zn_{1/2}W_{1/2})O_3{-}0.80Pb(Zr_{0.5}Ti_{0.5})O_3$ and the $0.05Pb(Zn_{1/2}W_{1/2})O_3{-}0.95Pb(Zr_{0.5}Ti_{0.5})O_3$ ceramics

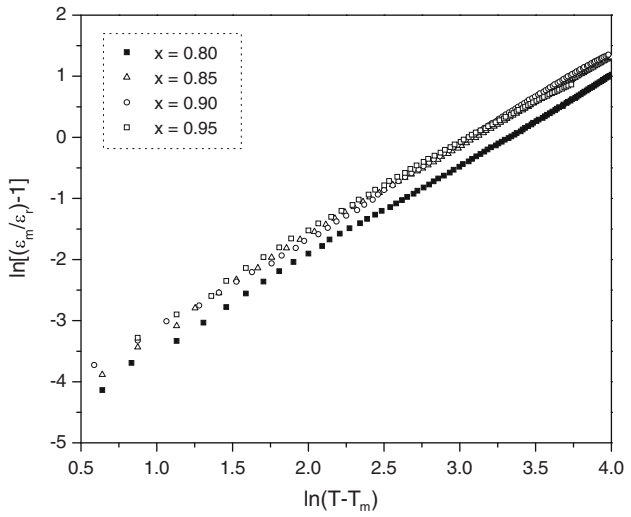



**Fig. 5** The ln $[(\varepsilon_m/\varepsilon_r) - 1]$ vs. ln $(T - T_m)$ plot for the $(1 - x)Pb(Zn_{1/2}W_{1/2})O_3$–$xPb(Zr_{0.5}Ti_{0.5})O_3$ ceramics

increasing amount of $Pb(Zn_{1/2}W_{1/2})O_3$ in the $(1 - x)Pb(Zn_{1/2}W_{1/2})O_3$–$xPb(Zr_{0.5}Ti_{0.5})O_3$ solid solution, both the relaxation parameter $\gamma$ and the diffuseness parameter $\delta$ increases. This is indicative of an increasing degree of disorder of the electrical dipole moments in the solid solution ceramics.

The piezoelectric property of the poled ceramics was measured at room temperature with a quasi-static $d_{33}$ meter and is also listed in Table 2. The highest $d_{33}$ value (222 pC/N) is found in the ceramic of $0.15Pb(Zn_{1/2}W_{1/2})O_3$–$0.85Pb(Zr_{0.5}Ti_{0.5})O_3$, a composition close to the MPB in the rhombohedral side. Optimizing processing conditions is expected to further increase the piezoelectric property.

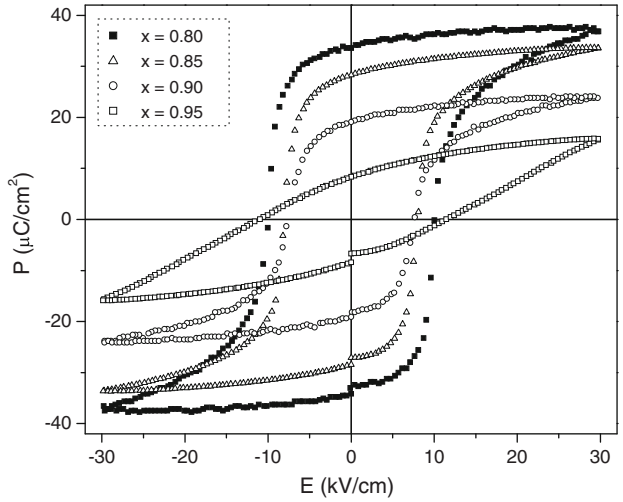



**Fig. 6** Polarization versus electric field hysteresis loops measured at room temperature at 4 Hz in the $(1 - x)Pb(Zn_{1/2}W_{1/2})O_3$–$xPb(Zr_{0.5}Ti_{0.5})O_3$ ceramics

Finally, the ferroelectric properties of the sintered ceramics were evaluated with the electrical polarization versus field hysteresis loop measurements. As shown in Fig. 6, all samples exhibit a profound hysteretic behavior. In the ceramic of $0.05Pb(Zn_{1/2}W_{1/2})O_3$–$0.95Pb(Zr_{0.5}Ti_{0.5})O_3$, a non-saturated hysteresis loop is observed at a peak electric field of 30 kV/cm. However, saturated loops are seen in ceramics with a higher content of $Pb(Zn_{1/2}W_{1/2})O_3$. In addition, the remanent polarization $P_r$ is observed to increase dramatically with increasing $Pb(Zn_{1/2}W_{1/2})O_3$ content. In the ceramic with composition of $x = 0.80$, $P_r$ reached 33.6 μC/cm$^2$. The shape of the ferroelectric hysteresis loop can be quantitatively assessed with the so-called squareness parameter $R_{sq}$, defined previously in literature [14]:

$$R_{sq} = \left(\frac{P_r}{P_s}\right) + \left(\frac{P_{1.1E_c}}{P_r}\right) \quad (2)$$

where $P_s$ is the saturation polarization, $E_c$ is the coercive field, $P_{1.1E_c}$ is the polarization at the field of $1.1E_c$. For a perfect square loop, $R_{sq}$ is equal to 2.00. With the data presented in Fig. 6, the loop squareness parameter $R_{sq}$ is calculated. The result is listed in Table 3, together with the remanent polarization $P_r$ and the coercive field $E_c$. Incorporating $Pb(Zn_{1/2}W_{1/2})O_3$ obviously enhances the ferroelectric properties significantly.

## Conclusions

Phase pure perovskite ceramics in the $(1 - x)Pb(Zn_{1/2}W_{1/2})O_3$–$xPb(Zr_{0.5}Ti_{0.5})O_3$ system can be prepared with the solid-state reaction method with up to 20 mol% of

**Table 3** Ferroelectric properties of the $(1 - x)Pb(Zn_{1/2}W_{1/2})O_3$–$xPb(Zr_{0.5}Ti_{0.5})O_3$ ceramics

| $x$ | $P_r$ (μC/cm$^2$) | $E_c$ (kV/cm) | $R_{sq}$ |
|---|---|---|---|
| 0.80 | 33.6 | 10.1 | 1.24 |
| 0.85 | 28.4 | 8.2 | 1.36 |
| 0.90 | 19.2 | 7.8 | 1.20 |
| 0.95 | 8.4 | 11.4 | 0.66 |

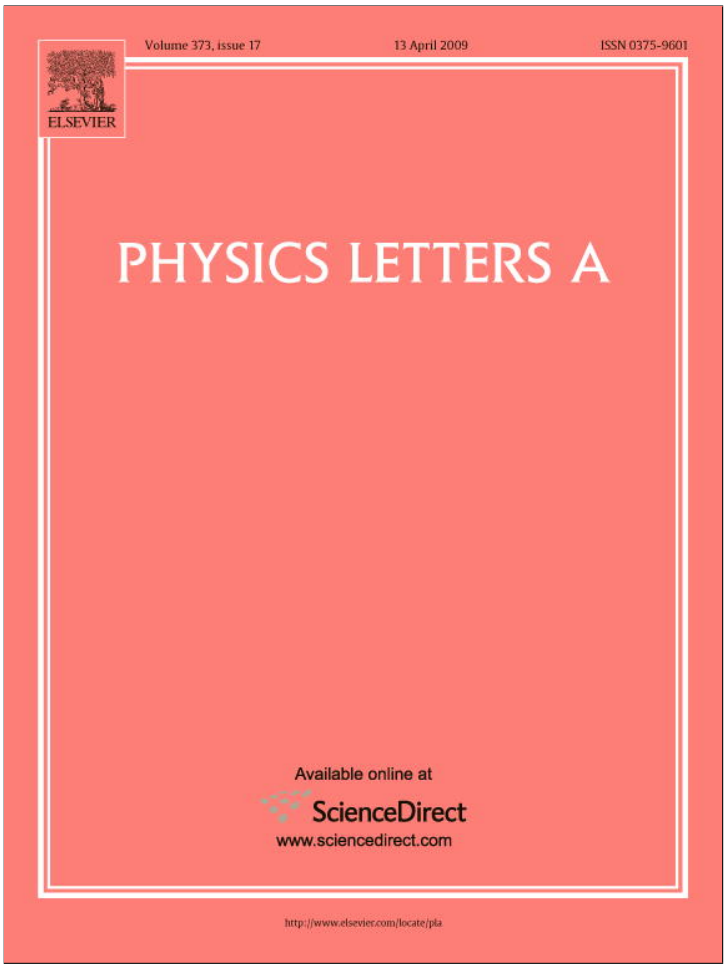
$Pb(Zn_{1/2}W_{1/2})O_3$. In the composition range for a stable perovskite structure, the MPB composition is identified at $x = 0.90$. This MPB separates the tetragonal phase from the rhombohedral phase. At the MPB composition, a remarkably high dielectric constant $\varepsilon_m$ of 38410 is observed at the ferroelectric transition temperature $T_m$. In the ceramic of $0.15Pb(Zn_{1/2}W_{1/2})O_3$–$0.85Pb(Zr_{0.5}Ti_{0.5})O_3$, a composition in the rhombohedral side of MPB, the best piezoelectric property ($d_{33} = 222$ pC/N) is detected. Furthermore, the addition of $Pb(Zn_{1/2}W_{1/2})O_3$ in $Pb(Zr_{0.5}Ti_{0.5})O_3$ dramatically enhances the ferroelectric properties, manifested by the large increase in the remanent polarization and the hysteresis loop squareness parameter. Therefore, the $(1 - x)Pb(Zn_{1/2}W_{1/2})O_3$–$xPb(Zr_{0.5}Ti_{0.5})O_3$ solid solution offers a new material system for various device applications.

**Acknowledgements** This work was supported by the National Science Foundation through the CAREER grant DMR-0346819 and the Thailand Research Fund (TRF), the Commission on Higher Education (CHE), and the Faculty of Science, Chiang Mai University, Thailand.

## References

1. Jaffe B, Cook WR, Jaffe H (1971) Piezoelectric ceramics. Academic Press, London
2. Haertling GH (1999) J Am Ceram Soc 82:797
3. Cross LE (1996) Mater Chem Phys 43:108
4. Uchino K (2000) Ferroelectric devices. Marcel Dekker, Inc, New York
5. Vittayakorn N, Rujijanagul G, Tan X, Marquardt MA, Cann DP (2004) J Appl Phys 96:5103
6. Vittayakorn N, Rujijanagul G, Tan X, He H, Marquardt MA, Cann DP (2006) J Electroceram 16:141
7. Yimnirun R, Ananta S, Laoratanakul P (2005) J Eur Ceram Soc 25:3235
8. White D, Zhao X, Besser MF, Tan X (2008) J Mater Sci 43:5258. doi:10.1007/s10853-008-2772-1
9. Okai B, Yoshimoto J, Fujita T (1974) J Phys Soc Jpn 37:281
10. Fujita T, Fukunaga O, Nakagawa T, Nomura S (1970) Mater Res Bull 5:759
11. Lee WJ, Kim NK (2008) J Mater Sci 43:3608. doi:10.1007/s10853-008-2574-5
12. Uchino K, Nomura S (1982) Ferroelectr Lett 44:55
13. Smolenskii GA (1970) J Phys Soc Jpn 28(Suppl):26
14. Jin B, Kim J, Kim SC (1997) Appl Phys A 65:53

Provided for non-commercial research and education use.
Not for reproduction, distribution or commercial use.




This article appeared in a journal published by Elsevier. The attached copy is furnished to the author for internal non-commercial research and education use, including for instruction at the authors institution and sharing with colleagues.

Other uses, including reproduction and distribution, or selling or licensing copies, or posting to personal, institutional or third party websites are prohibited.

In most cases authors are permitted to post their version of the article (e.g. in Word or Tex form) to their personal website or institutional repository. Authors requiring further information regarding Elsevier's archiving and manuscript policies are encouraged to visit:

http://www.elsevier.com/copyright

Author's personal copy

Physics Letters A 373 (2009) 1583–1587

Contents lists available at ScienceDirect

Physics Letters A

www.elsevier.com/locate/pla

# Influences of compressive stress and aging on dielectric properties of sodium bismuth titanate ceramics

T. Sareein, M. Unruan, A. Ngamjarurojana, S. Jiansirisomboon, A. Watcharapasorn, R. Yimnirun *

*Department of Physics, Faculty of Science, Chiang Mai University, Chiang Mai, 50200, Thailand*

ARTICLE INFO

*Article history:*
Received 15 December 2008
Received in revised form 17 February 2009
Accepted 23 February 2009
Available online 5 March 2009
Communicated by A.R. Bishop

*PACS:*
77.80.-e
77.80.Fm
77. 84.-s

*Keywords:*
Dielectric properties
NBT
Compressive stress
Aging

ABSTRACT

The influences of compressive stress and aging on dielectric properties of undoped and Fe-doped sodium bismuth titanate (NBT) ceramics were investigated. The dielectric properties were decreased significantly with the compressive stress applied parallel to the electric field direction, while the changes were reversed with the stress applied perpendicularly. In addition, lower changes of the dielectric properties with stress were observed in Fe-NBT ceramics, likely caused by an enhanced relaxor characteristic with the acceptor doping, which also reduced the aging rate in the ceramics. Finally, the aging behavior of the NBT and Fe-NBT ceramics followed the slightly stretched exponential law, and the aging rate in both ceramics was found to decrease with frequency, a result of the pinning of the polarization components. These observations clearly confirmed the role of the acceptor dopant in enhancing the relaxor ferroelectric characteristics in the NBT-based ceramics.

© 2009 Elsevier B.V. All rights reserved.

## 1. Introduction

Sodium bismuth titanate, $Na_{0.5}Bi_{0.5}TiO_3$ (NBT), and NBT-based ceramics are currently considered as a potential lead-free ferroelectric material to replace the widely used lead-based perovskite materials because of lead-free control atmosphere and lack of lead pollution [1–10]. While several previous investigations have suggested that the NBT exhibits strong ferroelectric properties with a large remnant polarization, $P_r = 38\ \mu C/cm^2$, and a phase transition point from ferroelectric to antiferroelectric should occur above 200 °C, many experiments do not confirm this hypothesis [1,2,4,10]. At present researchers accept that rather coexistence of rhombohedral and tetragonal phases takes place above 200 °C, not antiferroelectric [11]. In addition, this material system has been investigated in terms of variation in their dielectric and piezoelectric properties due to processing conditions, various dopants, and the formation of solid solution with other compounds [2,4–7,9,10].

Piezoelectric and ferroelectric ceramics are widely used in devices such as actuators and transducers. However, when they are used in devices, these ceramics are often subjected to self-induced or under environmental stresses. A prior knowledge of the effects of stresses on the material properties is crucial for proper design of a device and for suitable selection of materials for a specific application. Therefore, it is very important to obtain experimental data, as well as to better understand how these materials behave under stress [12–15]. Recently, the compressive stress dependence of dielectric properties has been studied in lead-based ferroelectric materials [16–23]. Interestingly, there have been many previous reports on the electrical properties of NBT-based ceramics [4–9], but there has been no systematic study on the influence of an applied stress on the dielectric properties of the NBT ceramics. Earlier investigations have already revealed significance of stress-induced ferroelectric phase transition, and domain structure and birefringence in NBT single crystals and NBT-based ceramics [24–31]. In addition to practical implication of stress influence, aging, usually regarded as an unwanted effect [32–35], has also been a subject of interest in lead-free materials, as it has been reported that aging of piezoelectric properties of lead-free materials is dramatic, hence limiting their potential uses in many applications [36–42]. Though aging behavior has been investigated extensively in lead-based materials [33,43–47], the aging behavior of the dielectric properties of NBT-based ceramics has yet to be reported.

Therefore, this study is aimed to examine the dielectric properties of the $Na_{0.5}Bi_{0.5}TiO_3$ ceramics as a function of compressive stress applied parallel and perpendicular to an electric field direction. Aging behavior of the dielectric properties of the ceramics is also investigated. This study is also extended to Fe-doped NBT

* Corresponding author at: School of Physics, Institute of Science, Suranaree University of Technology, Nakhon Ratchasima 30000, Thailand.
*E-mail address:* rattikornyimnirun@yahoo.com (R. Yimnirun).

0375-9601/$ – see front matter © 2009 Elsevier B.V. All rights reserved.
doi:10.1016/j.physleta.2009.02.065

Author's personal copy



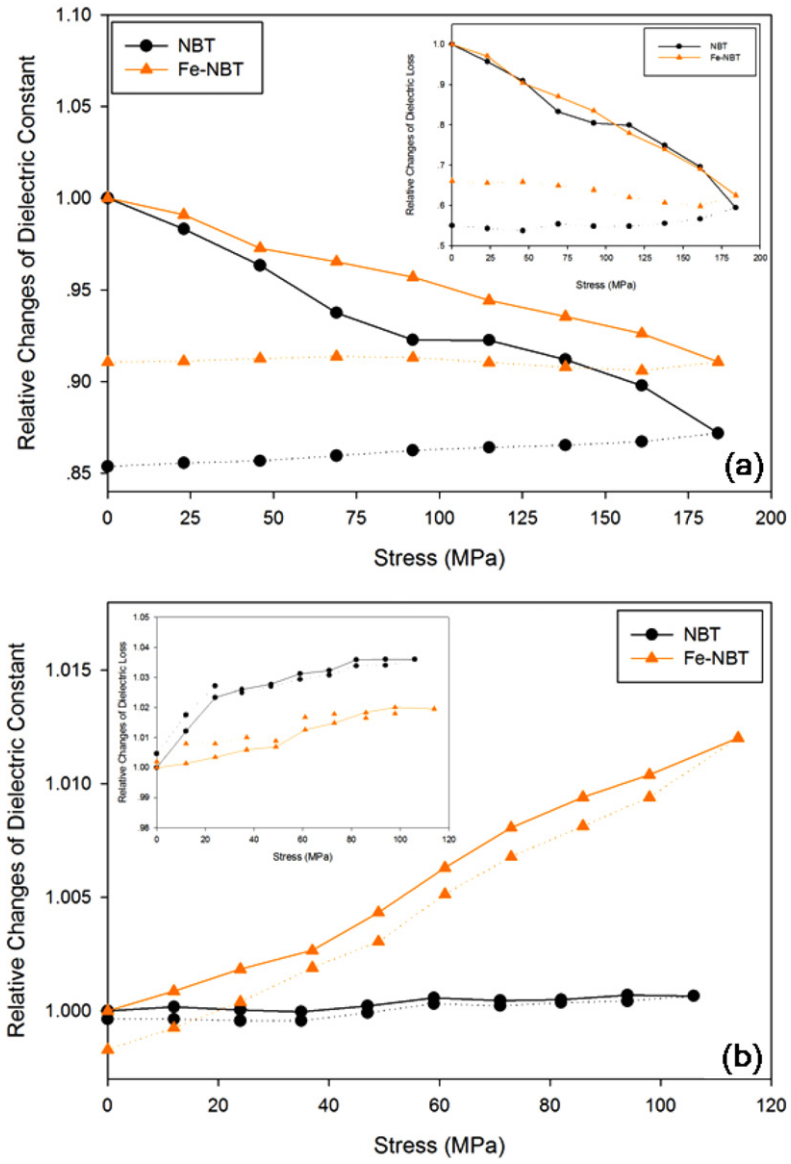



**Fig. 1.** Relative changes of dielectric constant ($\varepsilon_r$) and relative changes of dielectric loss tangent (tan $\delta$) (inset) for NBT and Fe-NBT ceramics with compressive stress applied parallel (a) and perpendicular (b) to an electric field direction (measured at 25 °C and 10 kHz). Solid lines indicate changes during loading, and dotted lines indicate changes during unloading. Opposite trends are observed in the two stress directions.

ceramics since it is well established that lower-valence doping entails aging and previous investigations already showed significantly different responses to stress in undoped and doped (both lower-valence and higher-valence) lead-based materials [18,19,22,23]. Therefore, it is of very interest to also conduct the same experiments in the Fe-doped NBT ceramics.

## 2. Experimental

In this study, $Na_{0.5}Bi_{0.5}TiO_3$ (NBT hereafter) and Fe-doped $Na_{0.5}Bi_{0.5}TiO_3$ (Fe-NBT hereafter) powders were prepared from binary oxides and carbonate, i.e. $Bi_2O_3$ (>98%, Fluka), $Na_2CO_3$ (99.5%, Carlo Erba), $TiO_2$ (>99%, Riedel-de Haën) and $Fe_2O_3$ (99.9%, Fluka) with the nominal composition $Na_{0.5}Bi_{0.5}Ti_{1-x}Fe_xO_{3-0.5x}$, where $x = 0.0$ and 0.015. The powder mixtures were ball milled in ethanol using zirconia milling media for 24 h, calcined at 800 °C for 2 h. The calcined powders were re-ground using agate mortar and pestle, sieved, pressed into pellets and sintered at temperature of 1050 °C for 2 h. Detailed preparation process is given elsewhere [48]. The sintered specimens were then cut as rectangular bars (typical dimensions $6 \times 2 \times 2$ mm$^3$) and lapped to obtain parallel faces. After coating with silver paint as electrode, the effects of the compressive stress on the dielectric properties of the aged ceramics (the specimens were left at 25 °C for 4 weeks to achieve a fully aged state) were investigated with the compressometer. The compressive stress was applied both parallel and perpendicular to an electric field direction [49,50]. The low-field dielectric properties were measured by LCR-meter (Instrek LCR-821) with applied voltage of 1 V. The room temperature (25 °C) dielectric constant and dielectric loss tangent were determined at frequency 10 kHz. For aging study, the samples were heated to 550 °C and kept for 30 min to remove the aging effect and ensure them to start from unaged states. Then, they were immediately cooled to room temperature. The aging effect was characterized by measuring the changes in the dielectric properties with aging time.

## 3. Results and discussion

By X-ray diffraction method, both NBT and Fe-NBT ceramics were single phase with a rhombohedral structure. SEM micro-

Author's personal copy



**Table 1**
Room temperature stress-free dielectric properties and fitting parameters of Eq. (1) to the data in Fig. 3.

| Ceramic | Stress-free (10 kHz) | | $K_\infty$ | | | $K_1$ | | | $\tau$ (second) | | |
|---|---|---|---|---|---|---|---|---|---|---|---|
| | $\varepsilon_r$ | $\tan\delta$ | 1 kHz | 10 kHz | 100 kHz | 1 kHz | 10 kHz | 100 kHz | 1 kHz | 10 kHz | 100 kHz |
| NBT | 595 | 0.0269 | 616.4 | 576.4 | 533.5 | 37.4 | 29.4 | 20.2 | 8530 | 19062 | 20762 |
| Fe-NBT | 640 | 0.0224 | 679.2 | 635.5 | 588.9 | 28.5 | 26.4 | 19.6 | 8817 | 22890 | 29469 |

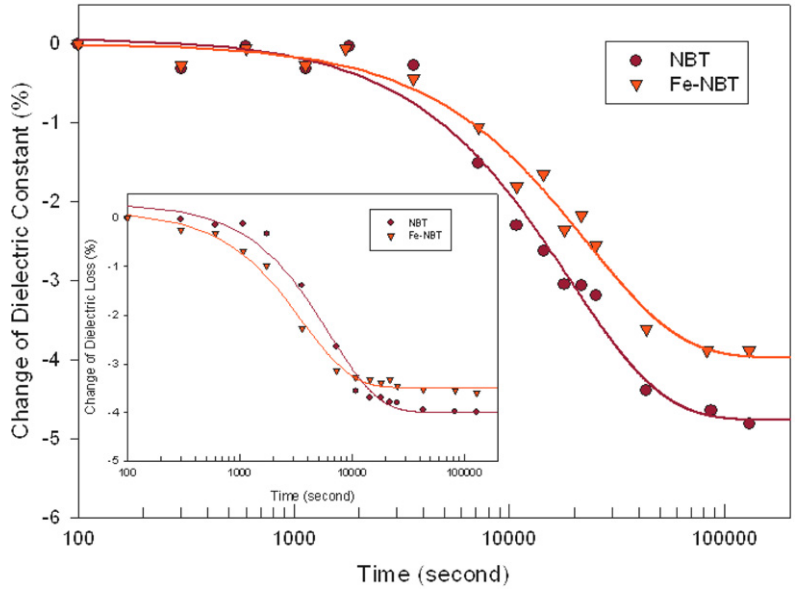



**Fig. 2.** Dielectric constant and dielectric loss tangent (inset) aging at 25 °C and 10 kHz for NBT and Fe-NBT ceramics. The solid lines are the fitting of the data with Eq. (1). Apparently, dielectric constant of NBT ages more quickly than that of Fe-NBT.

graphs revealed dense and well developed grain morphology with almost no porosity and the measured density of about 92–95% of the theoretical value [48]. For the Fe-doped NBT, the defect equation could be written as the following: $Fe_2O_3 = 2Fe'_{Ti} + 3O_O^x + V_O^{\bullet\bullet}$. It has to be noted that the defect reaction only assumed ionic defect compensation. In addition, it was assumed that Fe ions preferentially substituted Ti sites. The latter assumption was based on the fact that the ionic radius of Fe ion ($r_{Fe}^{3+} = 0.69$ Å) was much closer to the ionic radius of Ti ion ($r_{Ti}^{4+} = 0.61$ Å) than those of Bi ion ($r_{Bi}^{3+} \sim 1.38$ Å) and Na ion ($r_{Na}^{+} = 1.39$ Å). Therefore, one could expect defect complexes $2Fe'_{Ti} - V_O^{\bullet\bullet}$, which should facilitate the aging effect associated with acceptor doping on B site based on the symmetry-conforming principle of point defects, as reported in previous investigations [40,41,51].

The room temperature dielectric properties at 10 kHz of NBT and Fe-NBT ceramics as a function of compressive stress applied parallel and perpendicular to the electric field direction are depicted in Fig. 1(a) and (b), respectively. For better comparison, the dielectric properties of each ceramic under stress are normalized to the stress-free values, which are listed in Table 1. Clearly, there are observable changes of both the dielectric constant and the dielectric loss tangent with stress, in both cases of the compressive stress being applied either parallel or perpendicular to the electric field direction. For the case of stress parallel to the electric field direction, the dielectric constant and dielectric loss of both NBT and Fe-NBT ceramics are seen to significantly decrease with stress (10–15% for dielectric constant and 35-45% for dielectric loss at maximum stress), as displayed in Fig. 1(a). The cause of the decrease in the dielectric properties is likely from the clamping of the domain walls under the compressive stress, which results in a decrease of domain wall mobility and significantly reduced dielectric constant and dielectric loss [16–20]. In addition, a significant decrease in the dielectric properties after a full cycle of stress application is attributed to the stress induced decrease in switchable parts of domains at high stress [18–23]. The results obtained in this study are in parts similar to those for BT, PZT, PMN-PZT, PIN-PT, and PMN-PT systems in earlier investigations [16,17,19,23,49,50]. More interestingly, slightly lower changes of the dielectric properties with stress are observed in Fe-NBT ceramics. The cause for this observation is possibly due to an enhanced relaxor characteristic in Fe-doped NBT ceramics, as previously reported in La-doped and Mn-doped PMN-PT ceramics [44,45], implying that the doping Fe ions (and their associated defect complexes) break the polar regions to smaller size and reduce the crystal anisotropy in these regions, hence lesser contribution from the domains and domain walls [44,45]. This is consistent with other experimental results, i.e. the aging rate is also reduced in Fe-NBT ceramics, which will be discussed later.

For the case of stress applied perpendicular to the electric field direction, as depicted in Fig. 1(b), the changes of the dielectric properties with the stress are significantly different from the parallel stress case. Both the dielectric constant and dielectric loss increase (however, only 0–3%) with the applied stress. Interestingly, the results observed in this current study are in parts similar to earlier studies on commercial PZT ceramics, PIN-PT, and PMN-PT ceramics [19,22,23,49,50]. In this case, a combination of the de-aging and the polarization re-orientation mechanisms is believed to be a reason for the increase of the dielectric properties with stress. During aging process, some of the domain walls become pinned by impurities and structural imperfections. When a large enough stress is applied to the aged samples, it causes structural changes and redistribution of impurities. As a result, the domain walls that were pinned during aging can become active again [19,22,23]. This de-aging can increase the dielectric responses, as seen in Fig. 1(b). The perpendicular stress can also move some of the polarizations towards the electric field direc-

Author's personal copy



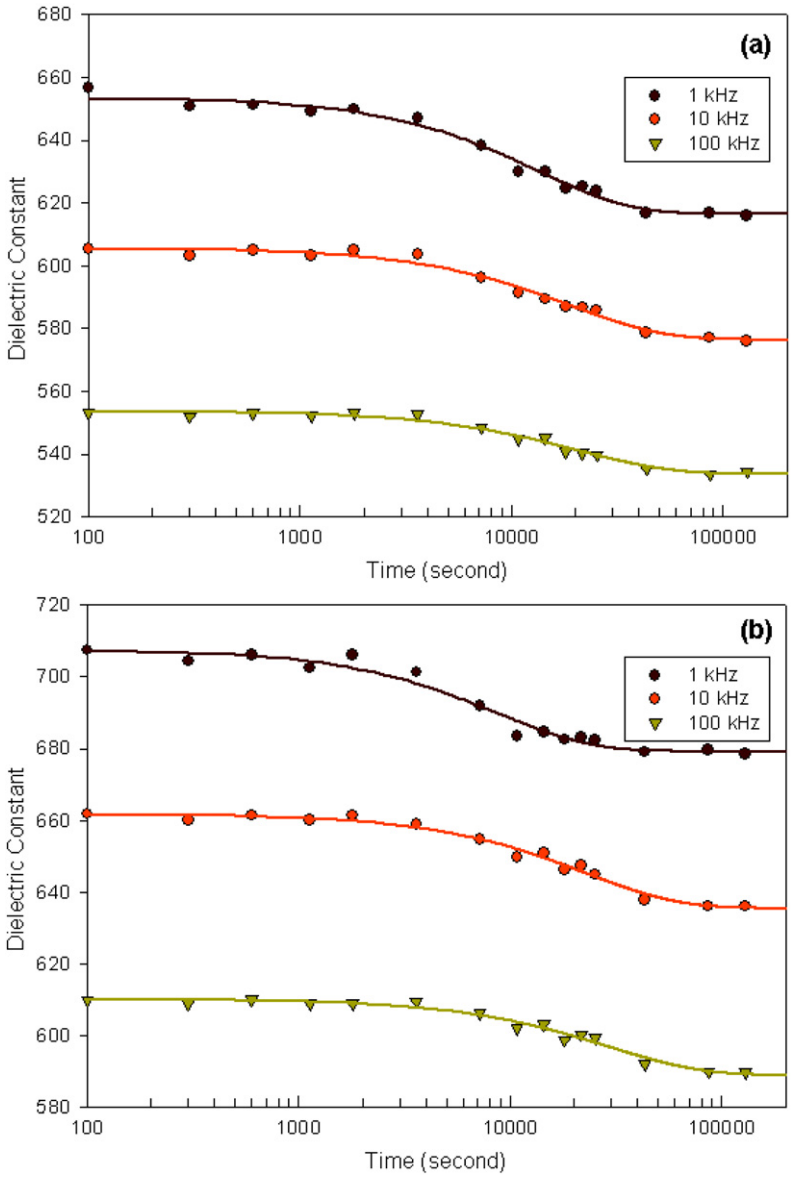



**Fig. 3.** Frequency dependent dielectric constant aging at 25 °C for (a) NBT and (b) Fe-NBT ceramics. The solid lines are the fitting of the data with Eq. (1). The data show that the relaxation time $\tau$ increases with frequency in both ceramics.

tion, hence an increase in the dielectric constant with the applied stress is observed [49,50]. An unexpected larger change of the dielectric constant obtained for Fe-NBT ceramics is believed to be a result of more easily polarization re-orientation process in the ceramics with mobile oxygen vacancies ($V_O^{\bullet\bullet}$) [19,23].

The room temperature aging of the low-field dielectric constant and dielectric loss of NBT and Fe-NBT ceramics is shown in Fig. 2. It is obvious that the aging observed in these ceramics is not linear with logarithmic time. The linear logarithmic time law of the aging successfully applied in normal ferroelectrics is related to the relaxation of the domain structure in the material towards an equilibrium configuration [43–45]. In a relaxor ferroelectric, deviation of the aging behavior from the linear logarithmic time behavior is a result of the lack of the macrodomain structure [44,45]. In this case, the time dependence may follow the stretched exponential law [36,38,39,44,45], which can be expressed, for small signal parameters, as

$$K = K_\infty + K_1 \exp\left[-(t/\tau)^\upsilon\right] \tag{1}$$

where $K_\infty$ represents the part which is not time dependent and the second term on the right-hand side of the equation represent the time dependent part, which becomes zero as $t \to \infty$. The time constant (relaxation time) $\tau$ reflects the aging rate. As is evident from the solid curves in Fig. 2, which are fitting to Eq. (1), the stretched exponential function (*however only slightly, as to say not purely exponential*) can describe the experimental data quite well for NBT and FE-NBT ceramics, clearly confirming their relaxor ferroelectric behavior [1,2,4]. It should also be noted that the value of $\upsilon$ fitted from in Eq. (1) varies between 0.97–1.00 in all cases. Previous investigations on PMN-PT ceramics [44,45] also reported a similar value when the aging was determined away from their transition temperatures, which is also the case for this present study. Therefore, for better comparison, the value of $\upsilon$ was fixed at 1.00 to obtain the fitting parameters for the data in Figs. 2 and 3, as listed in Table 1. As shown in Fig. 2, it is noticed that the Fe-NBT ceramics show slightly weaker dielectric properties aging (larger relaxation time $\tau$) than the NBT ceramics. The increased relaxation time $\tau$ in Fe-doped NBT ceramics reflects an increase in the activation energy for the motion of the micropolar domains [44,45], which is consistent with the results on the stress-dependent dielectric properties discussed above. This clearly suggests that, as opposed to the aging behavior in normal fer-

Author's personal copy



roelectrics, acceptor doping does not promote aging in lead-free relaxor ferroelectrics.

Fig. 3 shows the frequency-dependent aging behavior of the NBT and Fe-NBT ceramics. It is observed that in both ceramics the aging rate decreases (relaxation time $\tau$ increases) with measuring frequency, as also listed in Table 1. While $K_\infty$ and $K_1$ decrease with the measuring frequency, $K_1/K_\infty$ does not change very much in the experimental frequency range. To explain the frequency-dependent aging behavior in NBT and Fe-NBT ceramics, it has been previously proposed that the frequency dependent aging could be a result of the pinning of the polarization components which have low relaxation time or high activation energy by the defect field [45,52,53]. In a relaxor ferroelectric, local micropolar domains exist with the size of the domains distributing statistically over a broad range. The energy involved in reorienting a polar microdomain under an internal defect electric bias field $E_{\text{def}}$ is proportional to $\nu P E_{\text{def}}$ where $P$ is the polarization and $\nu$ is the volume of the micropolar domain. Therefore, the micropolar regions with large $\nu$ which have longer relaxation times will be pinned more effectively by $E_{\text{def}}$ than the micropolar domains of smaller size, which have shorter relaxation time. Similar observations have been reported in acceptor-doped PMN ceramics, PMN-PT ceramics and BT-based ceramics [36–39, 43–45].

## 4. Conclusions

The dielectric properties of the NBT and Fe-NBT ceramics responded to the compressive stress applied parallel and perpendicular to the electric field direction in opposite manner. A combination of the clamping of the domain walls, the de-aging, and the polarization re-orientation mechanisms seemed to be the major factors causing the changes observed. In addition, enhanced relaxor behavior as well as reduced aging rate in Fe-NBT samples was likely the main cause of the less dependence on stress of the dielectric properties. Finally, the aging rate in both undoped and acceptor-doped NBT ceramics in this study was found to decrease with frequency, indicating the pinning effect on polarization components. The applied slightly stretched exponential law was also found to explain well this aging behavior. The results of this study suggested that the relaxor ferroelectric characteristics in the NBT-based ceramics could be enhanced by acceptor doping.

## Acknowledgements

This work was jointly supported by the Thailand Research Fund (TRF), Commission on Higher Education (CHE), the Thailand Center of Excellence in Physics (through the Research Center in Theoretical and Computational Physics), Royal Golden Jubilee Ph.D. Program, Faculty of Science and Graduate School of Chiang Mai University.

## References

[1] G.A. Smolensky, V.A. Isupov, A.I. Agranovskaya, N.N. Ktainik, Sov. Phys. Solid State 2 (1961) 2651.
[2] H. Nagata, T. Takenaka, J. Eur. Ceram. Soc. 21 (2001) 1299.
[3] Y. Saito, H. Takao, T. Tani, T. Nonoyama, K. Takatori, T. Homma, T. Nagaya, M. Nakamura, Nature 432 (2004) 7013.
[4] S.E. Park, K.S. Hong, J. Mater. Res. 12 (1997) 2152.
[5] K. Roleder, I. Franke, A.M. Glazer, P.A. Thomas, S. Miga, J. Suchanicz, J. Phys.: Condens. Matter 14 (2002) 5399.
[6] Y. Lin, S. Zhao, N. Cai, J. Wu, X. Zhou, C.W. Nan, Mater. Sci. Eng. B 99 (2003) 449.
[7] L. Liu, M. Zhu, Y. Hou, H. Yan, R. Liu, J. Mater. Res. 22 (2007) 1188.
[8] T.R. Shrout, S.J. Zhang, J. Electroceram. 19 (2007) 111.
[9] S.H. Lee, C.B. Yoon, S.M. Lee, H.E. Kim, K.W. Lee, J. Mater. Res. 23 (2008) 115.
[10] S.T. Lau, C.H. Cheng, S.H. Choy, D.M. Lin, K.W. Kwok, H.L.W. Chan, J. Appl. Phys. 103 (2008) 104105.
[11] G.O. Jones, P.A. Thomas, Acta Crystallogr. B 58 (2002) 168.
[12] S. Park, T.R. Shrout, J. Appl. Phys. 82 (1997) 1804.
[13] D. Viehland, J. Powers, Appl. Phys. Lett. 78 (2001) 3112.
[14] K. Uchino, Piezoelectric Actuators and Ultrasonic Motors, Kluwer Academic, Boston, 1997.
[15] D. Stansfield, Underwater Electroacoustic Transducers, Bath Univ. Press, Bath, 1991.
[16] G. Yang, S.F. Liu, W. Ren, B.K. Mukherjee, Proc. SPIE Sym. Smart Struct. Mater. 3992 (2000) 103.
[17] R. Yimnirun, S. Ananta, S. Chamunglap, Mater. Chem. Phys. 102 (2007) 165.
[18] D. Zhou, M. Kamlah, D. Munz, J. Eur. Ceram. Soc. 25 (2005) 425.
[19] Q.M. Zhang, J. Zhao, K. Uchino, J. Zheng, J. Mater. Res. 12 (1997) 226.
[20] O. Steiner, A.K. Tagantsev, E.L. Colla, N. Setter, J. Eur. Ceram. Soc. 19 (1999) 1243.
[21] R. Yimnirun, Y. Laosiritaworn, S. Wongsaenmai, J. Phys. D: Appl. Phys. 39 (2006) 759.
[22] J. Zhao, A.E. Glazounov, Q.M. Zhang, Appl. Phys. Lett. 74 (1999) 436.
[23] G. Yang, S.F. Liu, W. Ren, B.K. Mukherjee, Ferroelectrics 262 (2001) 207.
[24] J. Suchanicz, J. Phys. Chem. Solids 62 (2001) 1271.
[25] J. Suchanicz, R. Rosiek, J.P. Mercurio, S. Said, Ferroelectrics 300 (2004) 107.
[26] J. Suchanicz, J.P. Mercurio, S. Said, B. Garbarz-Glos, Phys. Status Solidi A 193 (2002) 179.
[27] V.A. Isupov, T.V. Kruzina, Izv. Akad. Nauk SSSR Ser. Fiz. 47 (1983) 616.
[28] V.A. Isupov, T.V. Kruzina, Izv. Akad. Nauk SSSR Ser. Fiz. 48 (1984) 1178.
[29] T.V. Kruzina, V.M. Duda, J. Suchanicz, Mater. Sci. Eng. B 87 (2001) 48.
[30] J. Suchanicz, T.V. Kruzina, Ferroelectrics 317 (2005) 109.
[31] J. Suchanicz, J.P. Mecurio, P. Marchet, T.V. Kruzina, Phys. Status Solidi B 225 (2001) 459.
[32] K. Carl, K.H. Haerdtl, Ferroelectrics 17 (1978) 473.
[33] W.A. Schulze, K. Ogino, Ferroelectrics 87 (1988) 361.
[34] U. Robels, G. Arlt, J. Appl. Phys. 73 (1993) 3454.
[35] D.C. Lupascu, Y.A. Genenko, N. Balke, J. Am. Ceram. Soc. 89 (2006) 224.
[36] T. Nomura, N. Kawano, J. Yamamatsu, T. Arashi, Y. Nakano, A. Sato, Jpn. J. Appl. Phys. 34 (1995) 5398.
[37] D.A. Hall, M.M. Ben-Omran, J. Phys.: Condens. Matter 10 (1998) 9129.
[38] T. Tsurumi, M. Shono, H. Kakemoto, S. Wada, K. Saito, H. Chazono, Jpn. J. Appl. Phys. Part B 44 (2005) 6989.
[39] J. Portelles, S. Garcia, E. Martinez, O. Raymond, N.S. Almodovar, J.L. Heiras, J.M. Siqueiros, J. Appl. Phys. 97 (2005) 054105.
[40] Z. Feng, X. Ren, Appl. Phys. Lett. 91 (2007) 032904.
[41] H. Bao, L. Zhang, Y. Wang, W.F. Liu, C. Zhou, X. Ren, Appl. Phys. Lett. 91 (2007) 142903.
[42] G.L. Yuan, Y. Yang, S.W. Or, Appl. Phys. Lett. 91 (2007) 122907.
[43] H. Dederichs, G. Arlt, Ferroelectrics 68 (1986) 281.
[44] W.Y. Pan, Q.Y. Jiang, L.E. Cross, Ferroelectrics 82 (1988) 111.
[45] Q.M. Zhang, J. Zhao, L.E. Cross, J. Appl. Phys. 79 (1996) 3181.
[46] D.A. Hall, P.J. Stevenson, Ferroelectrics 187 (1996) 23.
[47] M.I. Toacsan, A. Ioachim, L. Nedelcu, H.V. Alexandru, Prog. Solid State Chem. 35 (2007) 531.
[48] A. Watcharapasorn, S. Jiansirisomboon, T. Tunkasiri, Mater. Lett. 61 (2007) 2986.
[49] M. Unruan, S. Wongsaenmai, Y. Laosiritaworn, S. Ananta, R. Yimnirun, J. Phys. D: Appl. Phys. 41 (2008) 541.
[50] M. Unruan, A. Ngamjarurojana, Y. Laosiritaworn, S. Ananta, R. Yimnirun, J. Appl. Phys. 104 (2008) 034101.
[51] X. Ren, Nature Mater. 3 (2004) 91.
[52] W. Pan, E. Furman, G.O. Dayton, L.E. Cross, J. Mater. Sci. Lett. 5 (1986) 647.
[53] T.B. Wu, M. Shyu, C. Chung, H. Lee, J. Am. Ceram. Soc. 78 (1995) 2168.

Provided for non-commercial research and education use.
Not for reproduction, distribution or commercial use.




This article appeared in a journal published by Elsevier. The attached copy is furnished to the author for internal non-commercial research and education use, including for instruction at the authors institution and sharing with colleagues.

Other uses, including reproduction and distribution, or selling or licensing copies, or posting to personal, institutional or third party websites are prohibited.

In most cases authors are permitted to post their version of the article (e.g. in Word or Tex form) to their personal website or institutional repository. Authors requiring further information regarding Elsevier's archiving and manuscript policies are encouraged to visit:

http://www.elsevier.com/copyright

Author's personal copy

Materials Letters 63 (2009) 1281–1284

Contents lists available at ScienceDirect

Materials Letters

journal homepage: www.elsevier.com/locate/matlet

# Phase formation, microstructure, and dielectric properties of $(1-x)$PZT–$(x)$PCN ceramics

A. Prasatkhetragarn [a,*], P. Ketsuwan [b], S. Ananta [c], R. Yimnirun [d], D.P. Cann [e]

[a] Department of Materials Science, School of Science and Technology, Naresuan University at Phayao, Phayao 56000, Thailand
[b] Department of Physics, School of Science and Technology, Naresuan University at Phayao, Phayao 56000, Thailand
[c] Department of Physics, Faculty of Science, Chiang Mai University, Chiang Mai 50200, Thailand
[d] School of Physics, Institute of Science, Suranaree University of Technology, Nakorn Ratchasima 30000, Thailand
[e] Materials Science, School of Mechanical, Industrial and Manufacturing Engineering, Oregon State University, Corvallis, OR 97331, USA

ARTICLE INFO

*Article history:*
Received 16 October 2008
Accepted 26 February 2009
Available online 11 March 2009

*Keywords:*
PZT–PCN
MPB
Phase formation
Microstructure
Dielectric properties

ABSTRACT

Ceramics in a PZT–PCN system with the formula $(1-x)Pb(Zr_{1/2}Ti_{1/2})O_3$–$(x)Pb(Co_{1/3}Nb_{2/3})O_3$, where $x=0.0$, 0.1, 0.2, 0.3, 0.4, 0.5, and 1.0, were prepared using a solid-state mixed-oxide technique with columbite—$CoNb_2O_6$ and wolframite—$ZrTiO_4$ precursors. The crystal structure of the specimens studied with X-ray diffraction (XRD) analysis showed a coexistence between tetragonal and pseudo cubic phases at composition $x=0.2$. The SEM micrograph showed that the average grain size significantly decreased with increasing PCN content. A maximum dielectric constant was observed at composition $x=0.2$, while the transition temperature strongly decreased with increasing PCN content. All ceramics also showed diffused phase transition behaviors with a minimum diffusivity at $x=0.2$. The morphotropic phase boundary (MPB) lay at the 0.8PZT–0.2PCN composition.

© 2009 Elsevier B.V. All rights reserved.

## 1. Introduction

Lead zirconate titanate, $PbZr_{1-x}Ti_xO_3$ or PZT ceramics have been investigated from both fundamental and applied viewpoints [1,2]. Most commercial PZT ceramics are designed in the vicinity of the MPB with various doping methods in order to achieve high properties [2–7]. Recently, many piezoelectric ceramic materials have been developed from binary systems containing a combination of relaxor and normal ferroelectric materials [4] that yield high dielectric permittivities (e.g., PZT–PNN [5], and PZT–PMN [6]), excellent piezoelectric coefficients (e.g., PZT–PZN [7]), and high pyroelectric coefficients (e.g., PNN–PT–PZ [8]).

Lead cobalt niobate, $Pb(Co_{1/3}Nb_{2/3})O_3$ or PCN, which exhibits a perovskite structure and a Curie temperature of $\approx -30$ °C, is a relaxor ferroelectric material with a high dielectric constant [9,10]. On the basis of the above mentioned approach, solid solutions of PZT and PCN are expected to synergistically combine the properties of both the normal ferroelectric PZT and relaxor ferroelectric PCN, which could exhibit electrical properties that are better than those of the single-phase PZT and PCN [9–12]. Therefore, the overall purpose of this study is to determine the phase formation, microstructure, and dielectric properties of ceramics in a $(1-x)Pb(Zr_{1/2}Ti_{1/2})O_3$–$(x)Pb(Co_{1/3}Nb_{2/3})O_3$ (where $x=0.0$, 0.1, 0.2, 0.3, 0.4, 0.5, and 1.0) system prepared with the columbite–wolframite precursors method via a vibratory-milling technique.

## 2. Experimental procedure

In the present work, $(1-x)Pb(Zr_{1/2}Ti_{1/2})O_3$–$(x)Pb(Co_{1/3}Nb_{2/3})O_3$ samples with compositions of $x=0.0$, 0.1, 0.2, 0.3, 0.4, 0.5, and 1.0 were prepared from $ZrTiO_4$ [13], $CoNb_2O_6$, and PbO powders. PZT–PCN powders were synthesized using the solid-state reaction of these raw materials and mixed by a vibratory-milling technique in ethanol for 6 h. After drying, the product was calcined in an alumina crucible at a temperature of 900 °C [14]. The calcined powders were uniaxially cold-pressed at 2.5 t into disc-shaped pellets with a diameter of 12.7 mm and a thickness of 1 mm, with 3 wt.% poly (vinyl alcohol) (PVA) added as a binder. Following binder burnout at 500 °C, the pellets were sintered at 1200 °C for 2 h at a heating/cooling rate of 5 °C/min [14].

The phase structure of the powders and ceramics were analyzed via X-ray diffraction (XRD; Bruker-AXS D8). The microstructures of the sintered samples were examined using scanning electron microscopy (SEM; JEOL JSM-840A). The dielectric properties of the samples were measured using an automated measurement system. An Agilent 4284A LCR meter was used to measure the dielectric properties over a wide temperature range using a NorECS ProboStat high temperature measurement cell.

## 3. Results and discussion

The XRD patterns of $(1-x)$PZT–$(x)$PCN ceramics with various $x$ values are shown in Fig. 1. The XRD data show a range in symmetry between the tetragonal (JCPDS file no. 70-4057) and pseudo cubic

* Corresponding author. Tel.: +66 54 466666x1716; fax: +66 54 466664.
*E-mail address:* Prasatkhetragarn@yahoo.com (A. Prasatkhetragarn).

0167-577X/$ – see front matter © 2009 Elsevier B.V. All rights reserved.
doi:10.1016/j.matlet.2009.02.063

Author's personal copy



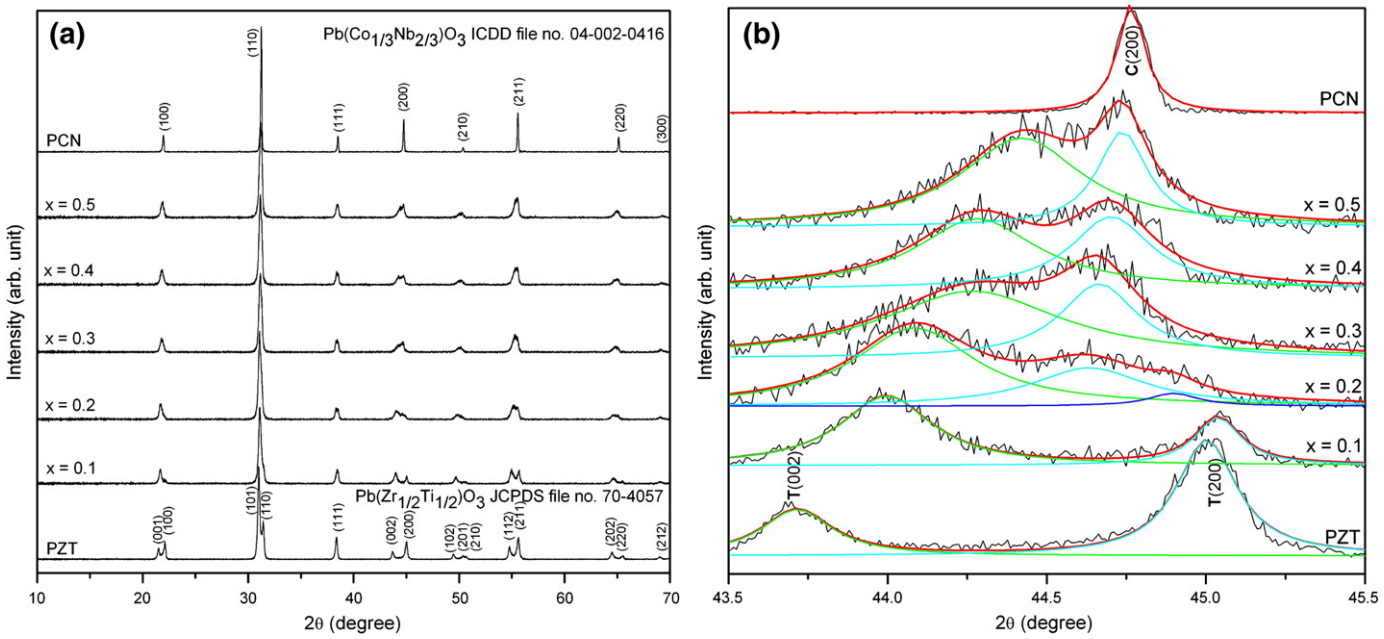



**Fig. 1.** XRD patterns of (a) $(1-x)$PZT–$(x)$PCN ceramics (where $x=0$, 0.1, 0.2, 0.3, 0.4, 0.5, and 1) and (b) (002)/(200) peak profile.

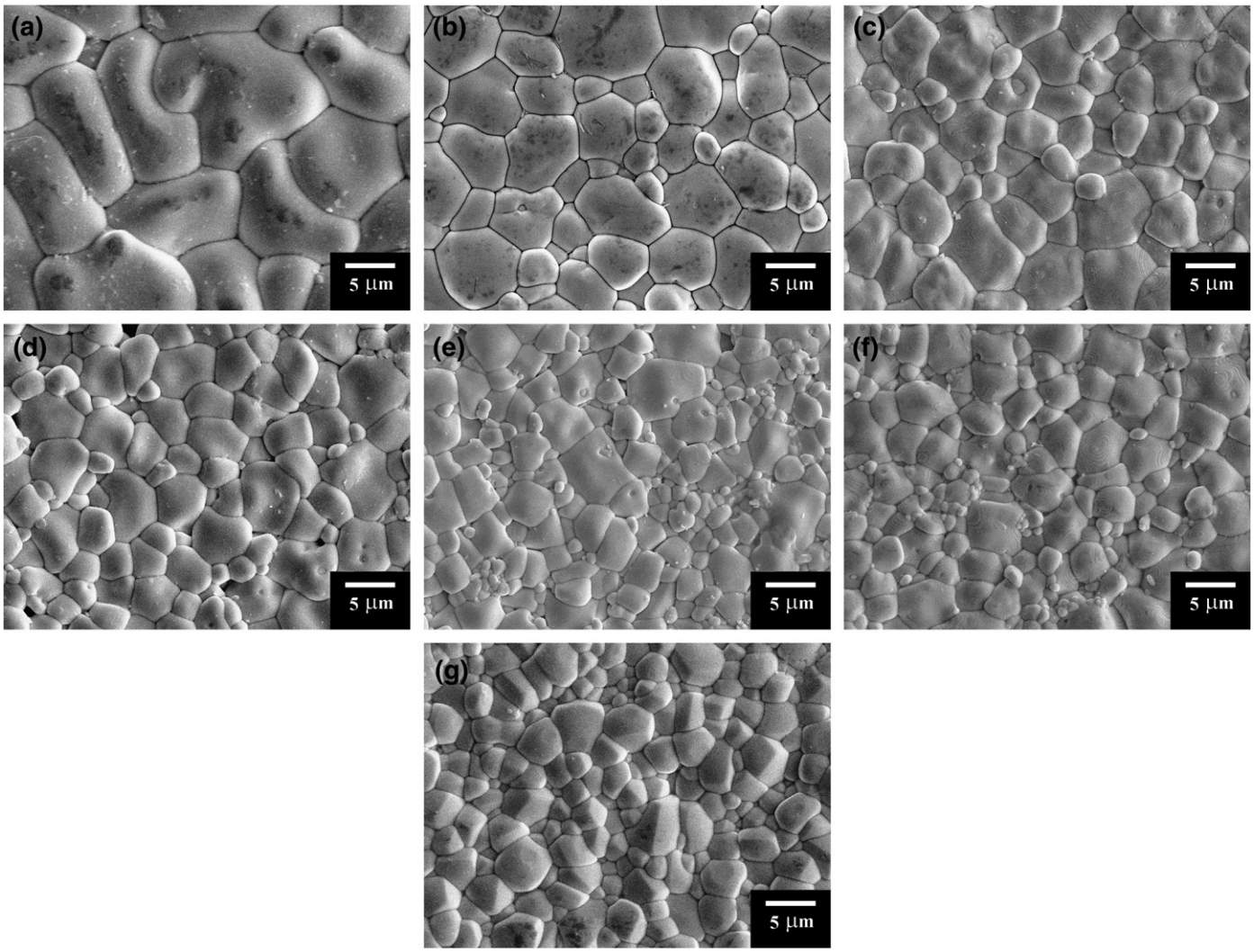



**Fig. 2.** SEM images of $(1-x)$PZT–$(x)$PCN ceramics with various compositions: (a) $x=0$, (b) $x=0.1$, (c) $x=0.2$, (d) $x=0.3$, (e) $x=0.4$, (f) $x=0.5$, and (g) $x=1$.

Author's personal copy



**Table 1**
Physical properties and dielectric properties of $(1-x)$PZT–$(x)$PCN ceramics.

| $x$ value | Physical properties | | | Dielectric properties (at 1 kHz) | | | | | | |
|---|---|---|---|---|---|---|---|---|---|---|
| | Density (g/cm$^3$) | Grain size range (μm) | Average grain size (μm) | $T_m$ (°C) | $\varepsilon_{RT}$ | tan $\delta_{RT}$ | $\varepsilon_m$ | tan $\delta_m$ | $\gamma$ | $\delta$ |
| 0.0 | 7.93 | 3.68–18.55 | 10.93 | 392 | 685 | 0 | 26670 | 1.111 | 1.57 | 15.97 |
| 0.1 | 7.93 | 1.84–14.54 | 4.14 | 358 | 703 | 0.02 | 51700 | 0.864 | 1.53 | 15.55 |
| 0.2 | 7.95 | 1.25–10.94 | 3.79 | 310 | 758 | 0.05 | 65700 | 2.188 | 1.49 | 15.28 |
| 0.3 | 7.94 | 0.75–9.94 | 3.16 | 270 | 785 | 0.07 | 47100 | 1.716 | 1.65 | 16.13 |
| 0.4 | 7.92 | 0.44–9.94 | 2.48 | 229 | 945 | 0.11 | 37900 | 1.653 | 1.72 | 16.66 |
| 0.5 | 7.91 | 0.43–8.77 | 2.12 | 175 | 1508 | 0.12 | 27000 | 0.613 | 1.79 | 16.81 |
| 1.0 | 7.94 | 0.54–6.85 | 3.08 | −25 | 3905 | 1.44 | 3800 | 0.081 | 1.95 | 17.54 |

(ICDD file no. 04-002-0416) perovskite types [13,15]. It is clear that the structure of the PZT–PCN compositions gradually changes from tetragonal to pseudo cubic with increasing PCN content. However, the 200 peak of pseudo cubic phase is first observed at composition $x=0.2$, while 200 peak of tetragonal phase is also present in this composition, as shown in Fig. 1(b). This observation is obviously associated with the composition showing the coexistence of two symmetries, which in this case are the tetragonal and pseudo cubic phases. To a first approximation, it could be said that the composition with $x=0.2$ is close to the MPB of the $(1-x)$PZT–$(x)$PCN system.

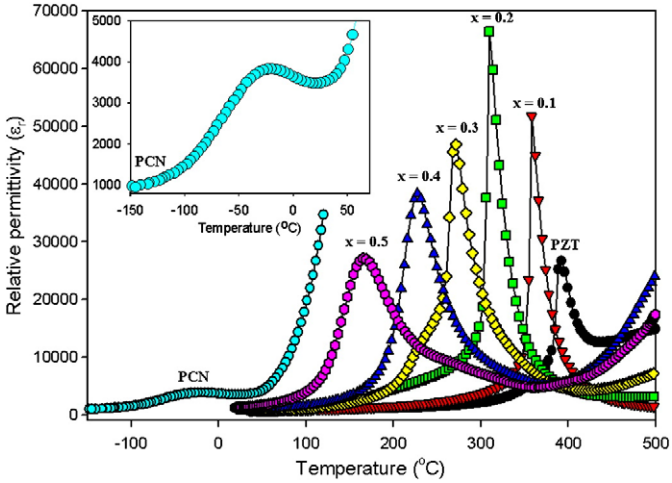



**Fig. 3.** Relative permittivity ($\varepsilon_r$) of $(1-x)$PZT–$(x)$PCN ceramics at 1 kHz.

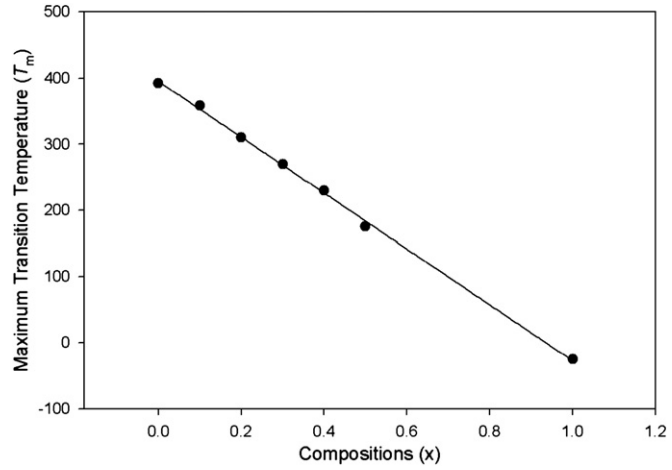



**Fig. 4.** Relationship of maximum transition temperature ($T_m$) and composition variation ($x$).

The SEM images in Fig. 2 reveal that the addition of PCN resulted in significant changes in the microstructure of the ceramics. The images also show that the grain size of the ceramics varied considerably from 0.43 to 18.55 μm (Table 1). However, the average grain size significantly decreased with an increase in the content of PCN. Interestingly, the density results can be correlated to the microstructure because high-density 0.8PZT–0.2PCN ceramics show high degrees of grain close packing, whereas low−density 0.5PZT–0.5PCN ceramics contain many closed pores.

Temperature dependences of the dielectric constant ($\varepsilon_r$) of the $(1-x)$PZT–$(x)$PCN ceramics with various $x$ values ($x=0$, 0.1, 0.2, 0.3, 0.4, 0.5, and 1) are shown in Fig. 3. The $\varepsilon_{max}$ increases from $x=0$ (pure PZT) and shows maximum value at $x=0.2$ and then decreases from $x=0.3$ to 1.0, clearly indicating the maximum dielectric constant at MPB composition of $x=0.2$. In addition, a clear transition in $T_m$ decrease with increasing PCN mole fraction, most likely because the crystal structure of the materials was changed from tetragonal to pseudo cubic, as confirmed with XRD patterns in Fig. 1. This result suggests that the transition temperature of $(1-x)$PZT–$(x)$PCN system can be varied over a range from −25 to 392 °C by controlling the PCN content in the system, as shown in Fig. 4.

As listed in Table 1, all ceramics also showed diffused phase transition behaviors with a minimum diffusivity ($\gamma$) and diffuseness parameter ($\delta$) at $x=0.2$. It is clear that the addition of PCN increases the degree of disorder in $(1-x)$PZT–$(x)$PCN over the compositional range ($x=0$, 0.1, 0.2, 0.3, 0.4, 0.5, and 1), with the highest degree of diffuseness exhibited in the pure PCN composition. Different dielectric behaviors could also be caused by grain size variation [6,13], as noted in Table 1. A similar behavior has also been observed in PZT–PNN [5], PZT–PMN [6] systems.

## 4. Conclusions

In this study, ceramics within the $(1-x)Pb(Zr_{1/2}Ti_{1/2})O_3$–$(x)Pb(Co_{1/3}Nb_{2/3})O_3$ solid solution system (where $x=0.0$, 0.1, 0.2, 0.3, 0.4, 0.5, and 1.0) were successfully prepared using a solid-state mixed-oxide technique. The PZT ceramic was identified by XRD analysis as a single-phase tetragonal perovskite, while the addition of PCN resulted in a gradual shift from tetragonal symmetry to pseudo cubic symmetry, with a possible MPB between the two phases located near the 0.8PZT–0.2PCN composition. The SEM micrograph showed that the average grain size significantly decreases with increasing PCN content. At 1 kHz, a maximum dielectric constant was observed at composition of $x=0.2$, while the transition temperature strongly decreased with increasing PCN content. All ceramics also showed diffused phase transition behaviors with a minimum diffusivity at $x=0.2$.

## Acknowledgements

The authors wish to express profound gratitude to the Materials Science Groups, Oregon State University for ceramics preparation and measurement. This work was supported by the Commission on Higher

Author's personal copy



Education (CHE), the Thailand Research Fund (TRF), and Naresuan University at Phayao.

## References

[1] Moulson AJ, Herbert JM. Electroceramics: materials, properties, applications. Chichester, U.K.: Wiley; 2003.
[2] Roleder K. Key Eng Mater 1998;155–156:123.
[3] Kuwata J, Uchino K, Nomura S. Ferroelectrics 1981;37:579.
[4] Park S-E, Shrout TR. IEEE Trans Ultrason Ferroelectr Freq Control 1997;44:1140.
[5] Vittayakorn N, Rujijanagul G, Tan X, Marquardt MA, Cann DP. J Appl Phys 2004;96:5103.
[6] Yimnirun R, Ananta S, Laoratanakul P. J Eur Ceram Soc 2005;25:3235.
[7] Fan H, Park GT, Choi JJ, Ryu J, Kim HE. J Mater Res 2002;17:180.
[8] Luff D, Lane R, Brown KR, Marshallsay HJ. Trans J Br Ceram Soc 1974;73:251.
[9] Unruan M, Vittayakorn N, Wongmaneeruang R, Prasatkhetragarn A, Ananta S, Yimnirun R. J Alloy Compd 2008;466:264.
[10] Hachiga T, Fujimoto S, Yasuda N. J Phys D 1987;20:1291.
[11] Kudo T, Yazaki T, Naito F, Sugaya S. J Am Ceram Soc 1970;53:326.
[12] Brankovic Z, Brankovic G, Varela JA. Ferroelectrics 2007;365:203.
[13] Prasatkhetragarn A, Yimnirun R, Ananta S. Ferroelectrics 2007;356:203.
[14] Prasatkhetragarn A, Vittayakorn N, Ananta S, Yimnirun R, Cann DP. Jpn J Appl Phys 2008;47:998.
[15] Vittayakorn N, Wirunchit S, Traisak S, Yimnirun R, Rujijanagul G. Curr Appl Phys 2008;8:128.

# Dielectric and ferroelectric properties of lead zirconate titanate-lead nickel niobate ceramics under compressive stress

M. Unruan,[1,a)] A. Prasartketrakarn,[1] A. Ngamjarurojana,[1] Y. Laosiritaworn,[1] S. Ananta,[1] and R. Yimnirun[2]
[1]*Department of Physics and Materials Science, Faculty of Science, Chiang Mai University, Chiang Mai 50200, Thailand*
[2]*School of Physics, Institute of Science, Suranaree University of Technology, Nakhon Ratchasima 30000, Thailand*

(Received 23 December 2008; accepted 21 February 2009; published online 23 April 2009)

Dielectric and ferroelectric properties of complex perovskite lead zirconate titanate-lead nickel niobate ceramic system were investigated under the influence of the compressive stress. The results showed that the dielectric properties, i.e., dielectric constant ($\varepsilon_r$) and dielectric loss (tan $\delta$), and the ferroelectric characteristics, i.e., the area of the ferroelectric hysteresis ($P$-$E$) loops, the maximum polarization ($P_{max}$), and the remanent polarization ($P_r$) changed significantly with increasing compressive stress. These changes depended greatly on the ceramic compositions. The experimental results on the dielectric properties could be explained by the deaging phenomenon. The stress-induced domain wall motion suppression and non-180° ferroelectric domain switching processes were responsible for the changes observed for the ferroelectric parameters. In addition, a significant decrease in those parameters after a cycle of stress was observed and attributed to the stress-induced decrease in switchable part of spontaneous polarization. This study clearly showed that the applied stress has significant influence on the electrical properties of complex perovskite ceramics. © *2009 American Institute of Physics*. [DOI: 10.1063/1.3106659]

## I. INTRODUCTION

There has recently been a great deal of interest in lead zirconate titanate-lead nickel niobate [$Pb(Zr_{1-x}Ti_x)O_3$-$Pb(Ni_{1/3}Nb_{2/3})O_3$ or (PZT-PNN)] ceramics because of their high longitudinal coupling coefficients, as well as good dielectric and excellent piezoelectric properties.[1–3] PZT is a normal ferroelectric material, which has been extensively investigated in the literatures because of its high dielectric properties and high piezoelectric coefficient. The high piezoelectric properties of PZT have been observed for compositions near the morphotropic phase boundary (MPB), i.e., at lead zirconate ($PbZrO_3$ or PZ):lead titanate($PbTiO_3$ or PT)=0.52:0.48.[4–6] PNN is a relaxor ferroelectric material originally reported by Smolenskii and Agranovskaya.[7] It exhibits the excellent dielectric broadening and electrostrictive properties and shows a diffuse phase transition around −120 °C with a peak permittivity of about 4000 at 1 kHz.[8]

Practically, piezoelectric and ferroelectric ceramics are often subjected to mechanical loading either deliberately in the design of the device itself or because the device is used to change shapes as in many smart structure applications or the device is used under environmental stresses.[9–13] A prior knowledge of how the material properties change under different load conditions is crucial for proper design of a device and for suitable selection of materials for a specific application.[12,13] It is therefore important to determine the properties of these materials as a function of applied stress. Previous investigations on the stress-dependence electrical properties of many ceramic systems emphasized the importance of the matter.[11,14–18] Recently, the uniaxial stress dependence of dielectric and ferroelectric properties has been investigated in materials such as barium titanate (BT), lead magnesium niobate (PMN), PMN-PT, PZT-BT, and PMN-PZT.[16–21] The results clearly showed that the effects of stress on the dielectric and ferroelectric properties depended significantly on ceramic compositions and stress levels. Interestingly, there has been no systematic study on the influence of an applied stress on the dielectric and ferroelectric properties of the PZT-PNN ceramics. Therefore, it is the aim of this study to determine the dielectric and ferroelectric properties of the $(1-x)$PZT-$(x)$PNN ceramics as a function of compressive stress.

## II. EXPERIMENTAL

In this study, $(1-x)$PZT-$(x)$PNN (with $x=0.1-0.5$) ceramics were prepared using the columbite precursor method. The columbite structure ($NiNb_2O_6$) and wolframite structure ($ZrTiO_4$) were synthesized first. The calcined $NiNb_2O_6$ and $ZrTiO_4$ powders were mixed with PbO in a stoichiometric ratio to form the composition $(1-x)$PZT-$(x)$PNN, with $x=0.1-0.5$. For optimization purpose, the sintering was carried out at temperatures between 1100 and 1250 °C for 4 h. Details of the processing and characterizations were provided elsewhere.[2]

Before studying the electrical properties, the specimens were lapped to obtain parallel faces. After coating with silver paint as electrode at the faces, the specimens were heated at 750 °C for 12 min to ensure the contact between the electrode and surface of ceramic. To study effects of the com-

a)Author to whom correspondence should be addressed. Electronic mail: muangjaiunruan@yahoo.com.

 © 2009 American Institute of Physics

Author complimentary copy. Redistribution subject to AIP license or copyright, see http://jap.aip.org/jap/copyright.jsp

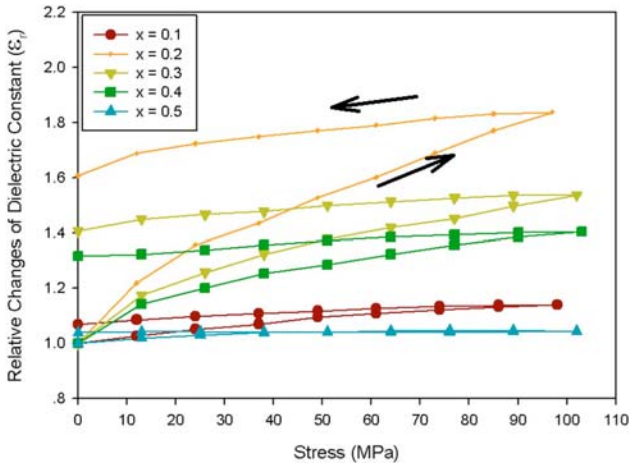



FIG. 1. (Color online) Relative changes in dielectric constant ($\varepsilon_r$) with compressive stress for $(1-x)$PZT-$(x)$PNN ceramics (measured at 25 °C and 10 kHz; solid arrows indicate loading direction).

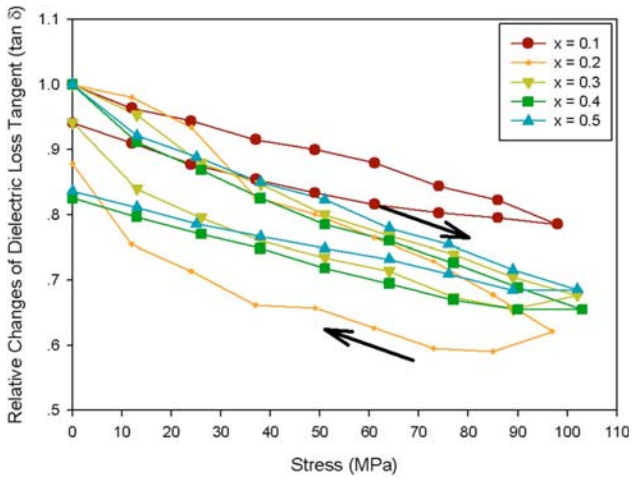



FIG. 2. (Color online) Relative changes in dielectric loss tangent (tan $\delta$) with compressive stress for $(1-x)$PZT-$(x)$PNN ceramics (measured at 25 °C and 10 kHz; solid arrows indicate loading direction).

pressive stress on the dielectric and ferroelectric properties of the ceramics, the compressometer was constructed.[16–18] The dielectric properties were measured by LCR meter (Instrek LCR-821). The room temperature (25 °C) capacitance and the dielectric loss tangent were obtained at frequency of 10 kHz under compressive stress. The dielectric constant was then calculated from a parallel-plate capacitor equation, e.g., $\varepsilon_r = Cd/\varepsilon_0 A$, where $C$ is the capacitance of the specimens, $d$ and $A$ are respectively the thickness and the area of the electrode, and $\varepsilon_0$ is the dielectric permittivity of vacuum $(8.854 \times 10^{-12}$ F/m).

The ferroelectric hysteresis ($P$-$E$) loops were characterized by using a computer controlled modified Sawyer–Tower circuit. The electric field was applied to a sample by a high voltage ac amplifier (Trek, model 610D) with the input sinusoidal signal with a frequency of 50 Hz from a signal generator (Goodwill, model GAG-809). The ferroelectric hysteresis ($P$-$E$) loop was recorded at room temperature (25 °C) for both loading and unloading conditions. The parameters obtained from the loops were the maximum polarization ($P_{max}$), the remanent polarization ($P_r$), and the coercive field ($E_c$), which were defined as the points where the loops reach the maximum polarization, cross the zero field, and cross the zero polarization, respectively.

## III. RESULTS AND DISCUSSION

### A. Dielectric properties under stress

The experimental results of the compressive stress dependence of the dielectric properties during loading and unloading for the ceramics in PZT-PNN system are displayed in Figs. 1 and 2. For better comparison, the dielectric properties of each composition under stress are normalized to the stress-free values. Clearly, there is a considerable change in both the dielectric constant and the dielectric loss tangent with the compressive stress. As depicted in Fig. 1, the dielectric constant is seen to increase with increasing stress in all compositions. The increase in the dielectric constant varies from approximately 4%–14% in the near pseudocubic relaxor ferroelectric 0.5PZT-0.5PNN and tetragonal ferroelectric 0.9PZT-0.1PNN compositions to 40%–54% in the rhombohedral relaxor ferroelectric 0.6PMN-0.4PNN and 0.7PZT-0.3PNN compositions. For the MPB 0.8PZT-0.2PNN composition, the dielectric constant increases drastically with the stress. The dielectric constant increases more than 80% when the stress reaches 100 MPa and returns to 160% of its original value when the stress is removed. On the other hand, the dielectric loss tangent (tan $\delta$) is seen to decrease significantly (20%–40%) with increasing stress, as displayed in Fig. 2. The changing of the dielectric properties with increasing and decreasing stress does not follow the same path. It is also noticed that the changes in the dielectric properties with the compressive stress obtained in this study are in parts similar to those for systems in earlier investigations.[17,19,22]

To understand these experimental results, various effects have to be considered. When a mechanical stress is applied to a ferroelectric material, the domain structure in the material will change to maintain the domain energy at a minimum; during this process some of the domains engulf other domains or change shape irreversibly. Under a compressive stress, the domain structure of ferroelectric ceramics may undergo domain switching, clamping of domain walls, and deaging mechanisms.[14,15,19,23] In this study, the results on the compressive stress dependence of the dielectric properties can easily be explained with the above statements. When the compressive stress is applied in the direction parallel to the polar axis (poling) direction, the stress will move some of the polarization away from the poling direction, resulting in a change in domain structures.[15,19,24,25] This change increases the non-180° domain wall density. Hence the increase in the dielectric constant with the applied stress is observed. The deaging mechanism, which also increases the dielectric constant,[15,18–20] is also expected to play a role here. Therefore, a combination of the domain switching and the deaging mechanisms is believed to be a reason for the increase in the dielectric constant with increasing applied stress in the PZT-PNN system, as shown in Fig. 1. The cause of the stress dependence of the dielectric loss tangent is mainly due to the clamping of the domain walls under compressive stress,

Author complimentary copy. Redistribution subject to AIP license or copyright, see http://jap.aip.org/jap/copyright.jsp

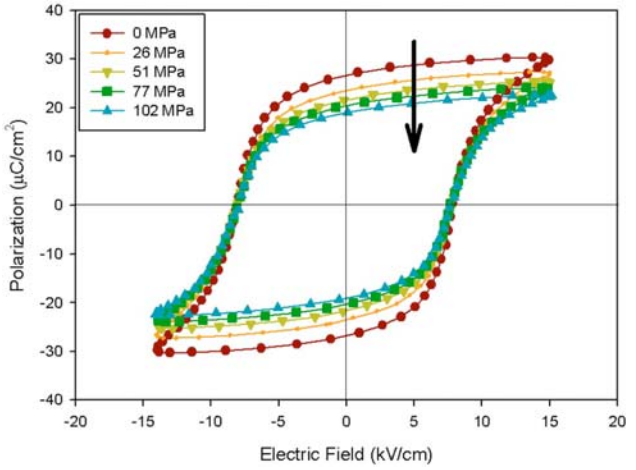



FIG. 3. (Color online) Polarization vs electric field ($P$-$E$) hysteresis loops as a function of compressive stress for 0.7PZT-0.3PNN ceramic (loading cycle).

which results in a decrease in domain wall mobility. The deaging mechanism, which also decreases the dielectric loss tangent,[15,22] is also expected to play a role in controlling the change in the dielectric loss tangent with the stress, as observed in Fig. 2.

It should also be noted here that the applied stress could also affect the ferroelectric phase transitions of the ceramics, which consequently change the observed dielectric properties significantly.[15,25] The applied compressive stress has been found to move the Curie temperature ($T_C$) up to the order of approximately 0.1 °C/MPa in 0.9PMN-0.1PT.[15] In addition, the influence of stress on the properties of ferroelectric materials is strongly dependent on the temperature, especially when the temperature is higher or lower than $T_C$. In this study, since $(1-x)$PZT-$(x)$PNN (with $x=0.1-0.5$) ceramics exhibit $T_C$ ranging from 130 °C ($x=0.5$) to 330 °C ($x=0.1$),[2] the change in the dielectric properties with stress in the vicinity of $T_C$ and the stress-induced shift in $T_C$ is rather insignificant because of their high $T_C$, as compared to the measurement temperature of 25 °C. Therefore, the stress-related ferroelectric phase transition is not expected to have significant effects on the changes in dielectric properties of PZT-PNN ceramics under the applied stress observed in this study.

### B. Ferroelectric properties under stress

The polarization versus electric field ($P$-$E$) hysteresis loops of the 0.7PZT-0.3PNN ceramic under different compressive stresses are shown in Fig. 3 as a simple representative for the other compositions with similar behavior. It should first be noticed that the area of the $P$-$E$ loops decreases with increasing compressive stress. The changes follow similar trend for all the ceramics. The $P$-$E$ loop area indicates the polarization dissipation energy of a ferroelectric material under one full cycle of electric field application. This amount of the energy loss is directly related to the amount of domain participating in the switching process during the application of electric field.[14,17] For a given composition, the decrease in the loop area with increasing the compressive stress is a result of the stress-induced domain wall suppression.[14,26]

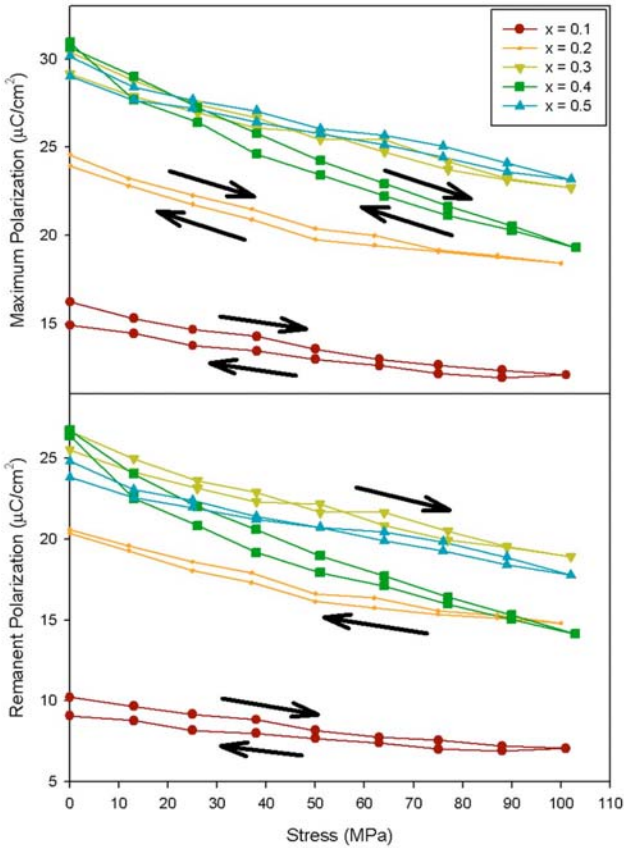



FIG. 4. (Color online) Changes in remanent polarization ($P_r$) and maximum polarization ($P_{max}$) with compressive stress for $(1-x)$PZT-$x$PNN ceramics (loading and unloading).

The changes in the remanent polarization ($P_r$), maximum polarization ($P_{max}$), and the coercive field ($E_c$) with the compressive stresses are plotted in Figs. 4 and 5, respectively. The changes in the maximum polarization ($P_{max}$) with stress are similar to the $P_r$. Figure 4 clearly shows that the

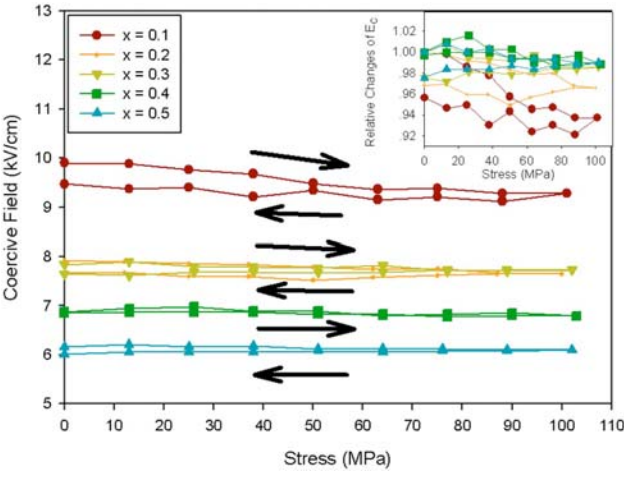



FIG. 5. (Color online) Changes in coercive field ($E_c$) with compressive stress for $(1-x)$PZT-$x$PNN ceramics (loading and unloading).

Author complimentary copy. Redistribution subject to AIP license or copyright, see http://jap.aip.org/jap/copyright.jsp

maximum and remanent polarizations decrease as the compressive stress increases. The decrease is generally very similar to the polarization values at 100 MPa, which are approximately 30%–45% of the stress-free values. In addition, noticeable decreases in the polarization values of all the ceramic are also observed after a complete cycle of the mechanical stress. This observation suggests a significant stress-induced depoling in PZT-PNN ceramics, resulting in the observed decrease in the polarization values under high stress levels.[19,27] Since the remanent polarization decreases as the compressive stress increases, it takes lower than usual electric field to force the polarizations to become zero; hence lower coercive field is observed, as demonstrated in Fig. 5.

To understand, at least qualitatively, these experimental results on ferroelectric properties of the PZT-PNN ceramics, one can interpret the changes in terms of domain-reorientation processes. When the compressive stress is applied in the direction parallel to the polar axis (poling) direction, the applied stress tends to keep the ferroelectric domains aligned with their polar axes away from the stress direction through the non-180° ferroelastic domain switching processes.[14,15] Therefore, it takes larger than usual for the applied electric field to reorient the domains along the stress direction, resulting in lower value of the maximum polarization ($P_{max}$), as shown in Figs. 3 and 4. When the electric field is reduced to zero the domains tend to rotate back away from the applied compressive stress direction, resulting in lower than usual remanent polarization ($P_r$),[19,28,29] as depicted in Figs. 3 and 4. Furthermore, considering the decrease in the hysteresis loss with increasing compressive stress, it indicates that more and more ferroelectric domains are constrained by the applied stress and cannot be reoriented by the electric field so as to participate in the polarization reversal. Consequently, both the maximum and remanent polarizations become lower with increasing compressive stress.[15] The results of the changes in the hysteresis parameters of the ferroelectric ceramics with increasing compressive stress are in agreement with the previous investigations on many ferroelectric ceramics.[11,14,18,30]

## IV. CONCLUSIONS

In this study, effects of compressive stress on the dielectric properties of PZT-PNN ceramics with a formula of $(1-x)$PZT-$(x)$PNN ($x=0.1-0.5$) have been investigated under compressive stress using a compressometer in conjunction with an automatic LCR meter and a modified Sawyer–Tower circuit. The superimposed compression stress had pronounced effects on both the dielectric constant and the dielectric loss tangent of PZT-PNN ceramics, especially in MPB 0.8PZT-0.2PNN composition. The area of the ferroelectric hysteresis ($P$-$E$) loops, the maximum polarization ($P_{max}$), the remanent polarization ($P_r$), and the coercive field ($E_c$) decrease with increasing compressive stresses. The observations were mainly interpreted in terms of domain switching through non-180° domain walls, deaging, and the stress-induced domain wall suppression mechanisms. Furthermore, noticeable decreases in the polarization values of all the ceramic are also observed after a complete cycle of the mechanical stress, indication of a significant stress-induced depoling in PZT-PNN ceramics. Finally, this study undoubtedly shows that the applied compressive stress has significant influences on the dielectric and ferroelectric properties of the PZT-PNN ceramics.

## ACKNOWLEDGMENTS

Financial supports from the Thailand Research Fund (TRF), Commission on Higher Education (CHE), Royal Golden Jubilee (RGJ) Ph.D. Program, Thailand Excellent Center in Physics, and Faculty of Science and Graduate School of Chiang Mai University are gratefully acknowledged.

[1] M. Kondo, M. Hida, M. Tsukuda, K. Kurihara, and N. Kamehara, Jpn. J. Appl. Phys., Part 1 **36**, 6043 (1997).
[2] N. Vittayakorn, G. Rujijanagul, X. Tan, M. A. Marquardt, and D. P. Cann, J. Appl. Phys. **96**, 5103 (2004).
[3] D. Luff, R. Lane, K. R. Brown, and H. J. Marshallsay, Trans. J. Br. Ceram. Soc. **73**, 251 (1974).
[4] J. Moulson and J. M. Herbert, *Electroceramics: Materials, Properties, Applications* (Chapman and Hall, New York, 1990).
[5] B. Jaffe, W. R. Cook, and H. Jaffe, *Piezoelectric Ceramic* (RAN, New York, 1971).
[6] Y. H. Xu, *Ferroelectric Materials and Their Applications* (North-Holland, Los Angeles, 1991).
[7] G. A. Smolenskii and A. L. Agranovskaya, Sov. Phys. Tech. Phys. **13**, 80 (1958).
[8] V. A. Bokov and I. E. Mylnikova, Sov. Phys. Solid State **2**, 2428 (1960).
[9] J. Kuwata, K. Uchino, and S. Nomura, Jpn. J. Appl. Phys., Part 1 **21**, 1298 (1982).
[10] S. E. Park and T. R. Shrout, J. Appl. Phys. **82**, 1804 (1997).
[11] D. Viehland and J. Powers, Appl. Phys. Lett. **78**, 3112 (2001).
[12] D. Stansfield, *Underwater Electroacoustic Transducers* (Bath University Press, Bath, UK, 1991).
[13] K. Uchino, *Piezoelectric Actuators and Ultrasonic Motors* (Kluwer, Boston, 1997).
[14] D. Zhou, M. Kamlah, and D. Munz, J. Eur. Ceram. Soc. **25**, 425 (2005).
[15] Q. M. Zhang, J. Zhao, K. Uchino, and J. Zheng, J. Mater. Res. **12**, 226 (1997).
[16] R. Yimnirun, Ferroelectrics **331**, 9 (2006).
[17] R. Yimnirun, S. Ananta, and S. Chamunglap, Mater. Chem. Phys. **102**, 165 (2007).
[18] R. Yimnirun, S. Ananta, A. Ngamjarurojana, and S. Wongsaenmai, Curr. Appl. Phys. **6**, 520 (2006).
[19] G. Yang, S. F. Liu, W. Ren, and B. K. Mukherjee, Proc. SPIE Symposium on Smart Structures and Materials **3992**, 103 (2000).
[20] R. Yimnirun, M. Unruan, Y. Laosiritaworn, and S. Ananta, J. Phys. D **39**, 3097 (2006).
[21] R. Yimnirun, S. Ananta, E. Meechoowas, and S. Wongsaenmai, J. Phys. D **36**, 1615 (2003).
[22] M. Unruan, S. Wongsaenmai, Y. Laosiritaworn, S. Ananta, and R. Yimnirun, J. Phys. D **41**, 541 (2008).
[23] G. Yang, S. F. Liu, W. Ren, and B. K. Mukherjee, Ferroelectrics **262**, 207 (2001).
[24] D. Audigier, Cl. Richard, Cl. Descamps, M. Troccaz, and L. Eyraud, Ferroelectrics **154**, 219 (1994).
[25] I. J. Fritz, J. Appl. Phys. **49**, 4922 (1978).
[26] R. Yimnirun, S. Ananta, A. Ngamjarurojana, and S. Wongsaenmai, Appl. Phys. A: Mater. Sci. Process. **81**, 1227 (2005).
[27] G. Yang, W. Ren, S. F. Liu, A. J. Masys, and B. K. Mukherjee, Proc.-IEEE Ultrason. Symp. **2**, 1005 (2000).
[28] J. Zhao and Q. M. Zhang, Proceedings of the 10th IEEE International Symposium on Applications of Ferroelectrics, Vol. 2, pp. 971–974 (1996).
[29] J. Zhao, A. E. Glazounov, and Q. M. Zhang, Appl. Phys. Lett. **74**, 436 (1999).
[30] C. S. Lynch, Acta Mater. **44**, 4137 (1996).

Author complimentary copy. Redistribution subject to AIP license or copyright, see http://jap.aip.org/jap/copyright.jsp

# Dielectric and Ferroelectric Properties of PZT-PNN Ceramics Under Compressive Stress

M. Unruan*, A. Prasartketrakarn, A. Ngamjarurojana, Y. Laosiritaworn, S. Ananta and R. Yimnirun,

Department of Physics, Faculty of Science, Chiang Mai University,

Chiang Mai 50200, Thailand

## Abstract

Dielectric and ferroelectric properties of complex perovskite PZT-PNN ceramic system were investigated under the influence of the compressive stress. The results showed that the dielectric properties, i.e. dielectric constant ($\varepsilon_r$) and dielectric loss (tan $\delta$), and the ferroelectric characteristics, i.e. the area of the ferroelectric hysteresis (P-E) loops, the maximum polarization ($P_{max}$), and the remanent polarization ($P_r$) changed significantly with increasing compressive stress. These changes depended greatly on the ceramic compositions. The experimental results on the dielectric properties could be explained by the de-aging phenomenon. The stress-induced domain wall motion suppression and non-180º ferroelectric domain switching processes were responsible for the changes observed for the ferroelectric parameters. In addition, a significant decrease in those parameters after a cycle of stress was observed and attributed to the stress induced decrease in switchable part of spontaneous polarization. This study clearly showed that the applied stress has significant influence on the electrical properties of complex perovskite ceramics.

**Keywords:** Dielectric Properties; Ferroelectric Properties; Stress; Perovskite Ceramics

* Corresponding author: Department of Physics, Faculty of Science, Chiang Mai University, Chiang Mai 50200, Thailand; Fax No. 6653-943-445; E-mail: muangjaiunruan@yahoo.com

# 1 Introduction

There have recently been a great deal of interest in lead zirconate titanate-lead nickel niobate ($Pb(Zr_{1-x}Ti_x)O_3$-$Pb(Ni_{1/3}Nb_{2/3})O_3$ or (PZT-PNN)) ceramics because of their high longitudinal coupling coefficients, as well as good dielectric and excellent piezoelectric properties [1-3]. Lead zirconate titanate ($Pb(Zr_{1-x}Ti_x)O_3$ or PZT) is a normal ferroelectric material which has been extensively investigated in the literatures because of their high dielectric properties and high piezoelectric coefficient. The high piezoelectric properties of PZT have been observed for compositions near the morphotropic phase boundary (MPB), i.e. at $PbZrO_3$:$PbTiO_3$ = 0.52:0.48 [4-6]. Lead nickel niobate ($Pb(Ni_{1/3}Nb_{2/3})O_3$ or PNN) is a relaxor ferroelectric material originally reported by Smolenskii and Agranovskaya [7]. It exhibits the excellent dielectric broadening and electrostrictive properties and shows a diffuse phase transition around -120 $^{o}$C with a peak permittivity of about 4000 at 1 kHz [8].

Practically, piezoelectric and ferroelectric ceramics are often subjected to mechanical loading, either deliberately in the design of the device itself or because the device is used to change shapes as in many smart structure applications or the device is used under environmental stresses [9-13]. A prior knowledge of how the material properties change under different load conditions is crucial for proper design of a device and for suitable selection of materials for a specific application [12,13]. It is therefore important to determine the properties of these materials as a function of applied stress.

Previous investigations on the stress-dependence electrical properties of many ceramic systems have emphasized the importance of the matter [11,14-18]. Recently, the uniaxial stress dependence of dielectric and ferroelectric properties has been investigated in materials such as BT, PZT, PMN, PMN-PT, PZT-BT, and PMN-PZT [16-21]. The results clearly showed that the effects of stress on the dielectric and ferroelectric properties depended significantly on ceramic compositions and stress levels. Interestingly, there has been no systematic study on the influence of an applied stress on the dielectric and ferroelectric properties of the PZT-PNN ceramics. Therefore, it is the aim of this study to determine the dielectric and ferroelectric properties of the (*1-x*)PZT-(*x*)PNN ceramics as a function of compressive stress.

## 2 Experimental

In this study, (*1-x*)$Pb(Zr_{1/2}Ti_{1/2})O_3$–(*x*)$Pb(Ni_{1/3}Nb_{2/3})O_3$ (with x = 0.1-0.5) ceramics were prepared using the columbite precursor method. The columbite structure ($NiNb_2O_6$) and wolframite structure ($ZrTiO_4$) were synthesized first. The calcined $NiNb_2O_6$ and $ZrTiO_4$ powders were mixed with PbO in a stoichiometric ratio to form the composition (*1-x*)$Pb(Zr_{1/2}Ti_{1/2})O_3$–(*x*)$Pb(Ni_{1/3}Nb_{2/3})O_3$, with x = 0.1-0.5. For optimization purpose, the sintering was carried out at temperatures between 1100 and 1250 °C for 4 h. Details of the processing and characterizations were provided elsewhere [2].

Before studying the electrical properties, the specimens were lapped to obtain parallel faces. After coating with silver paint as electrode at the faces, the specimens were heated at 750°C for 12 min to ensure the contact between the electrode and surface of ceramic. To study effects of the compressive stress on the dielectric and

ferroelectric properties of the ceramics, the compressometer was constructed [16-18]. The dielectric properties were measured by LCR-meter (Instrek LCR-821). The room temperature (25 °C) capacitance and the dielectric loss tangent were obtained at frequency of 10 kHz under compressive stress. The dielectric constant was then calculated from a parallel-plate capacitor equation, e.g. $\varepsilon_r = Cd / \varepsilon_0 A$, where C is the capacitance of the specimens, d and A are, respectively, the thickness and the area of the electrode, and $\varepsilon_0$ is the dielectric permittivity of vacuum ($8.854 \times 10^{-12}$ F/m).

The ferroelectric hysteresis (P-E) loops were characterized by using a computer controlled modified Sawyer-Tower circuit. The electric field was applied to a sample by a high voltage AC amplifier (Trek, model 610D) with the input sinusoidal signal with a frequency of 50 Hz from a signal generator (Goodwill, model GAG-809). The ferroelectric hysteresis (P-E) loop was recorded at room temperature (25 °C) for both loading and unloading conditions. The parameters obtained from the loops were the maximum polarization ($P_{max}$), the remanent polarization ($P_r$), and the coercive field ($E_c$), which were defined as the points where the loops reach the maximum polarization, cross the zero field, and cross the zero polarization, respectively.

# 3 Results and Discussion

## 3.1 Dielectric Properties Under Stress

The experimental results of the compressive stress dependence of the dielectric properties during loading and unloading for the ceramics in PZT-PNN system are displayed in Figs. 1 and 2. For better comparison, the dielectric properties of each composition under stress are normalized to the stress-free values. Clearly, there is a

considerable change of both the dielectric constant and the dielectric loss tangent with the compressive stress. As depicted in Fig. 1, the dielectric constant is seen to increase with increasing stress in all compositions. The increase of the dielectric constant varies from approximately 4-14 % in the near pseudo-cubic relaxor ferroelectric 0.5PZT-0.5PNN and tetragonal ferroelectric 0.9PZT-0.1PNN compositions to 40-54% in the rhombohedral relaxor ferroelectric 0.6PMN-0.4PNN and 0.7PZT-0.3PNN compositions. For the morphotropic phase boundary (MPB) 0.8PZT-0.2PNN composition, the dielectric constant increases drastically with the stress. The dielectric constant increases more than 80% when the stress reaches 100 MPa and returns to 160% of its original value when the stress is removed. On the other hand, the dielectric loss tangent (tan $\delta$) is seen to decrease significantly (20-40%) with increasing stress, as displayed in Fig. 2. The changing of the dielectric properties with increasing and decreasing the stress do not follow the same path. It is also noticed that the changes in the dielectric properties with the compressive stress obtained in this study are in parts similar to those for BT, PZT, PMN-PZT, PMN-PT and PIN-PT systems in earlier investigations [17,19,22].

To understand these experimental results, various effects have to be considered. When a mechanical stress is applied to a ferroelectric material, the domain structure in the material will change to maintain the domain energy at a minimum; during this process some of the domains engulf other domains or change shape irreversibly. Under a compressive stress, the domain structure of ferroelectric ceramics may undergo domain switching, clamping of domain walls and de-aging mechanisms [14,15,19,23]. In this study, the results on the compressive stress dependence of the dielectric properties can easily be explained with the above statements. When the compressive stress is applied in the direction parallel to the polar axis (poling) direction, the stress

will move some of the polarization away from the poling direction resulting in a change in domain structures [15,19,24,25]. This change increases the non-180º domain wall density. Hence the increase of the dielectric constant with the applied stress is observed. The de-aging mechanism, which also increases the dielectric constant [15,19,20,26], is also expected to play a role here. Therefore, a combination of the domain switching and the de-aging mechanisms is believed to be a reason for the increase of the dielectric constant with increasing applied stress in the PZT-PNN system, as shown in Fig. 1. The cause of the stress dependence of the dielectric loss tangent, as mainly due to the clamping of the domain walls under compressive stress, which results in a decrease in domain wall mobility. The de-aging mechanism, which also decrease the dielectric loss tangent [15, 22] is also expected to play a role in controlling the change of the dielectric loss tangent with the stress, as observed in Fig. 2.

### 3.2 Ferroelectric Properties Under Stress

The polarization versus electric field (P-E) hysteresis loops of the 0.7PZT-0.3PNN ceramic under different compressive stresses are shown in Fig. 3 as a simple representative for the other compositions with similar behavior. It should first be noticed that the area of the P-E loops decreases with increasing compressive stress. The changes follow similar trend for all the ceramics. The P-E loop area indicates the polarization dissipation energy of a ferroelectric material under one full cycle of electric field application. This amount of the energy loss is directly related to the amount of domain participating in the switching process during the application of electric field [14,17]. For a given composition, the decrease in the loop area with increasing the

compressive stress is a result of the stress-induced domain wall suppression [14,27].

The changes in the remanent polarization ($P_r$), maximum polarization ($P_{max}$) and the coercive field ($E_c$) with the compressive stresses are plotted in Figs. 4 and 5, respectively. The changes in the maximum polarization ($P_{max}$) with stress are similar to the $P_r$. Figure 4 clearly shows that the maximum and remanent polarizations decrease as the compressive stress increases. The decrease is generally very similar with the polarization values at 100 MPa are approximately 30-45% of the stress-free values. In addition, noticeable decreases in the polarization values of all the ceramic are also observed after a complete cycle of the mechanical stress. This observation suggests a significant stress-induced de-poling in PZT-PNN ceramics resulting in the observed decrease of the polarization values under high stress levels [19,28]. Since the remanent polarization decreases as the compressive stress increases, it takes lower than usual electric field to force the polarizations to become zero, hence lower coercive field is observed, as demonstrated in Fig. 5.

To understand, at least qualitatively, these experimental results on ferroelectric properties of the PZT-PNN ceramics, one can interpret the changes in terms of domain-reorientation processes. When the compressive stress is applied in the direction parallel to the polar axis (poling) direction, the applied stress tends to keep the ferroelectric domains aligned with their polar axes away from the stress direction through the non-180º ferroelastic domain switching processes [14,15]. Therefore, it takes larger than usual applied electric field to reorient the domains along the stress direction, resulting in lower value of the maximum polarization ($P_{max}$), as shown in Fig. 3 and 4. When the electric field is reduced to zero the domains tend to rotate back away from the applied compressive stress direction, resulting in lower than usual remanent polarization ($P_r$), as

depicted in Figs. 3 and 4 [19,29,30]. Furthermore, considering the decrease of the hysteresis loss with increasing the compressive stress, it indicates that more and more ferroelectric domains are constrained by the applied stress and cannot be re-oriented by the electric field so as to participate in the polarization reversal. Consequently, both the maximum and remanent polarizations become lower with increasing the compressive stress [15]. The results of the changes of the hysteresis parameters of the ferroelectric ceramics with increasing compressive stress are in agreement with the previous investigations on many ferroelectric ceramics [11,14,26,31].

## 4 Conclusions

In this study, effects of compressive stress on the dielectric properties of PZT-PNN ceramics with a formula $(1\text{-}x)Pb(Zr_{1/2}Ti_{1/2})O_3–(x)Pb(Ni_{1/3}Nb_{2/3})O_3$ or *(1-x)*PZT-*(x)*PNN ($x$ = 0.1-0.5) have been investigated under compressive stress using a compressometer in conjunction with an automatic LCR meter and a modified Sawyer-Tower circuit. The superimposed compression stress had pronounced effects on both the dielectric constant and the dielectric loss tangent of PZT-PNN ceramics, especially in morphotropic phase boundary (MPB) 0.8PZT-0.2PNN composition. The area of the ferroelectric hysteresis (P-E) loops, the maximum polarization ($P_{max}$) the remanent polarization ($P_r$) and the coercive field ($E_c$) decrease with increasing compressive stresses. The observations were mainly interpreted in terms of domain switching through non-180° domain walls, de-aging, and the stress-induced domain wall suppression mechanisms. Furthermore, noticeable decreases in the polarization values of all the ceramic are also observed after a complete cycle of the mechanical stress, indication of a significant stress-induced de-

poling in PZT-PNN ceramics. Finally, this study undoubtedly shows that the applied compressive stress has significant influences on the dielectric and ferroelectric properties of the PZT-PNN ceramics.

## 5 Acknowledgments

Financial supports from the Thailand Research Fund (TRF), Commission on Higher Education (CHE), Faculty of Science and Graduate School of Chiang Mai University are gratefully acknowledged.

## 6 References

[1] M. Kondo, M. Hida, M. Tsukuda, K. Kurihara and N. Kamehara, *Jpn. J. Appl. Phys.*, **36** (1997) 6043.

[2] N. Vittayakorn, G. Rujijanagul, X. Tan, M. A. Marquardt and D. P. Cann, *J. Appl. Phys.*, **96 (9)** (2004) 5103.

[3] D. Luff, R. Lane, K. R. Brown and H. J. Marshallsay, *Trans. J. Br. Ceram. Soc.,* **73** (1974) 251.

[4] J. Moulson and J.M. Herbert, *Electroceramics: Materials, Properties, Applications*, Chapman and Hall, New York, 1990.

[5] B. Jaffe, W.R. Cook and H. Jaffe, *Piezoelectric Ceramic*, R.A.N. Publishers, 1971.

[6] Y.H. Xu, *Ferroelectric Materials and Their Applications*, North Holland, Los

Angeles, 1991.

[7] G.A. Smolenskii and A.L. Agranovskaya, *Sov. Phys. Tech. Phys*., **13** (1958) 80.

[8] V. A. Bokov and I. E. Mylnikova, *Sov. Phys. Solid State*, **2**, (1960) 2428.

[9] J. Kuwata, K. Uchino and S. Nomura, *Jpn. J. Appl. Phys*., **21** (1982) 1298.

[10] S.E. Park and T.R. Shrout, *J. Appl. Phys*., **82** (1997) 1804.

[11] D. Viehland and J. Powers, *Appl. Phys. Lett*., **78** (20) (2001) 3112.

[12] D. Stansfield, *Underwater Electroacoustic Transducers*, Bath University Press, Bath, 1991.

[13] K. Uchino, *Piezoelectric Actuators and Ultrasonic Motors*, Kluwer, Boston, 1997.

[14] D. Zhou, M. Kamlah and D. Munz, *J. Euro. Ceram. Soc*., **25** (2005) 425.

[15] Q.M. Zhang, J. Zhao, K. Uchino and J. Zheng, *J. Mater. Res*., **12** (1997) 226.

[16] R. Yimnirun, *Ferroelectrics*, **331** (2006) 9.

[17] R. Yimnirun, S. Ananta and S. Chamunglap, *Mater. Chem. Phys*., **102** (2007) 165.

[18] R. Yimnirun, S. Ananta, A. Ngamjarurojana and S. Wongsaenmai*, Curr. Appl. Phys*., **6** (2006) 520.

[19] G. Yang, S.F. Liu, W. Ren and B.K. Mukherjee, *Proc. SPIE Sym. Smart Struct. Mater*., **3992** (2000) 103.

[20] R. Yimnirun, M. Unruan, Y. Laosiritaworn and S. Ananta, *J. Phys. D: Appl. Phys*.,

**39** (2006) 3097.

[21] R. Yimnirun, *Inter. J. Mod. Phys. B* (2007) *in press*.

[22] M. Unruan, S. Wongsaenmai, Y. Laosiritaworn, S. Ananta and R. Yimnirun, *J. Phys. D: Appl. Phys*., **41** (2008) in press.

[23] G. Yang, S.F. Liu, W. Ren and B.K. Mukherjee, *Ferroelectrics*, **262** (2001) 207.

[24] D. Audigier, Cl. Richard, Cl. Descamps, M. Troccaz and L. Eyraud, *Ferroelectrics*, **154** (1994) 219.

[25] I.J. Fritz, *J. Appl. Phys*., **49** (1978) 4922.

[26] R. Yimnirun, S. Ananta, A. Ngamjarurojana and S. Wongsaenmai, 2006 *Curr. Appl. Phys*, **6** (2006) 52.

[27] R. Yimnirun, S. Ananta, A. Ngamjarurojana and S. Wongsaenmai, *Appl. Phys. A*, **81(6)** (2005) 1227.

[28] G. Yang, W. Ren, S.F. Liu, A.J. Masys and B.K. Mukherjee, *Proc. of the IEEE Ultrasonic Symposium*, (2000) 1005.

[29] J. Zhao and Q.M. Zhang, *Proc. of the IEEE International Symposium on Applications of Ferroelectrics*, (1996) 971.

[30] J. Zhao, A.E. Glazounov and Q.M. Zhang, *Appl. Phys. Lett*., **74**, (1999) 436.

[32] C.S. Lynch, *Acta Mater*., **44**, (1996) 4137.

## Caption of Figures

**Figure 1.** Relative changes of dielectric constant ($\varepsilon_r$) with compressive stress for (1-*x*)PZT-(*x*)PNN ceramics (measured at 25 ºC and 10 kHz; solid arrows indicate loading direction).

**Figure 2.** Relative changes of dielectric loss tangent (tan $\delta$) with compressive stress for (1-*x*)PZT-(*x*)PNN ceramics (measured at 25 ºC and 10 kHz; solid arrows indicate loading direction).

**Figure 3.** Polarization vs. electric field (P-E) hysteresis loops as a function of compressive stress for 0.7PZT-0.3PNN ceramic (loading cycle).

**Figure 4.** Changes in remanent polarization ($P_r$) and maximum polarization ($P_{max}$) with compressive stress for (*1-x*)PZT-*x*PNN ceramics (loading and unloading).

**Figure 5.** Changes in coercive field ($E_c$) with compressive stress for (*1-x*)PZT-*x*PNN ceramics (loading and unloading).

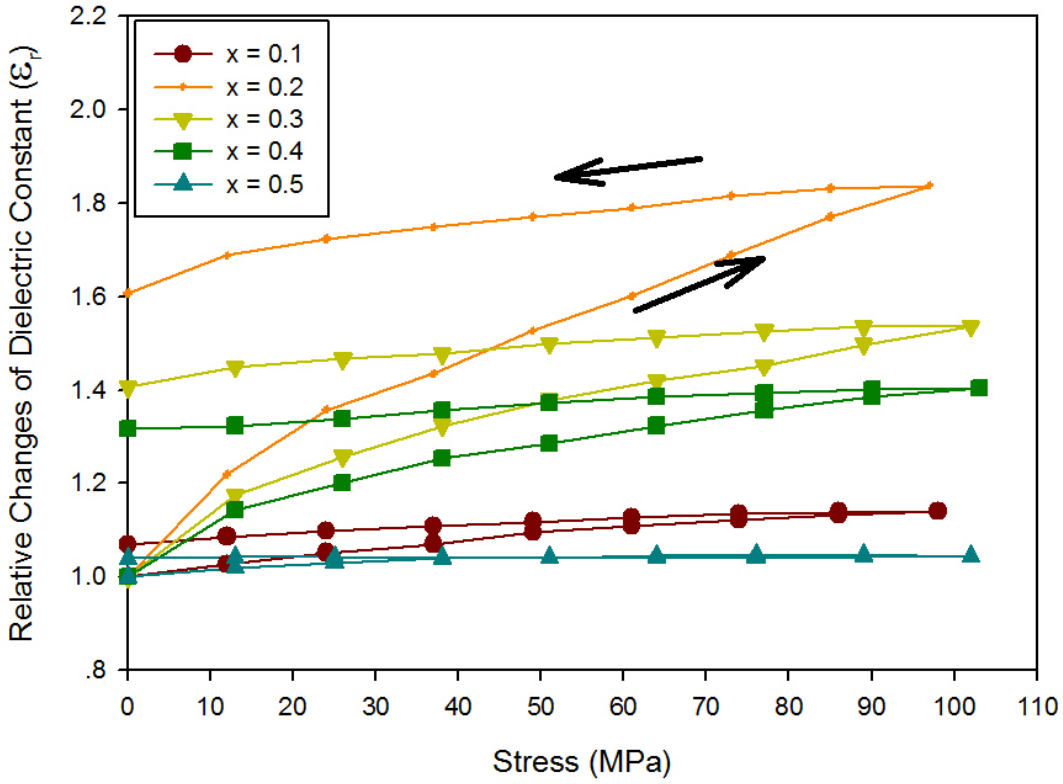

x = 0.1
x = 0.2
x = 0.3
x = 0.4
x = 0.5
Relative Changes of Dielectric Constant (ε_r)
Stress (MPa)
2.2
2.0
1.8
1.6
1.4
1.2
1.0
.8
0
10
20
30
40
50
60
70
80
90
100
110

**Fig. 1**

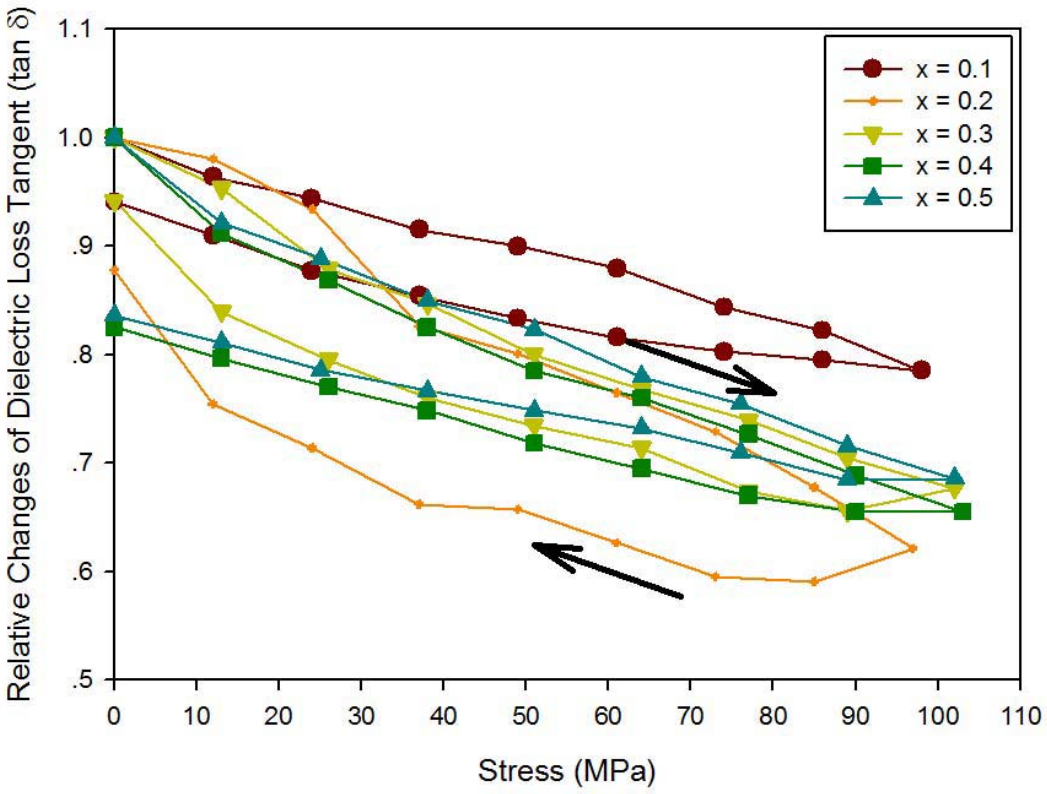

Relative Changes of Dielectric Loss Tangent (tan δ)
1.1
1.0
.9
.8
.7
.6
.5
0
10
20
30
40
50
60
70
80
90
100
110
Stress (MPa)
x = 0.1
x = 0.2
x = 0.3
x = 0.4
x = 0.5

**Fig. 2**

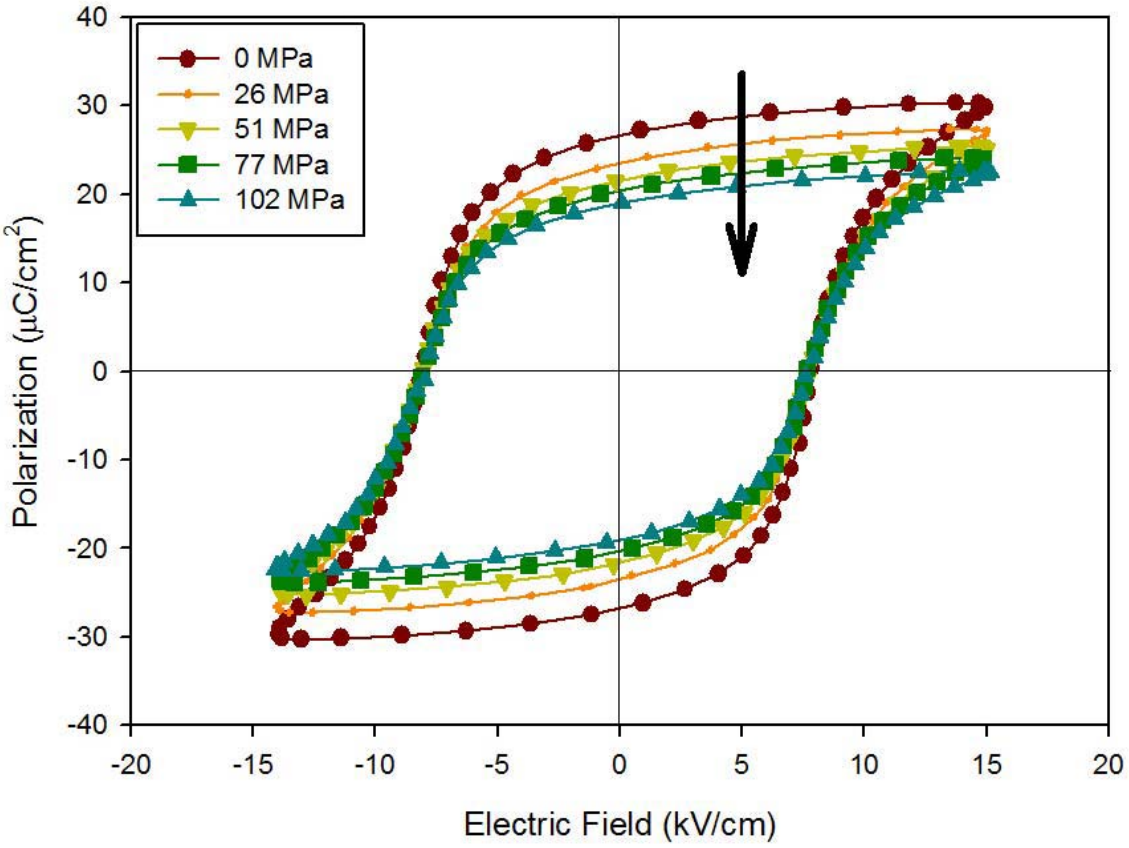

0 MPa
26 MPa
51 MPa
77 MPa
102 MPa
Polarization (μC/cm²)
Electric Field (kV/cm)
40
30
20
10
0
-10
-20
-30
-40
-20
-15
-10
-5
0
5
10
15
20

**Fig. 3**

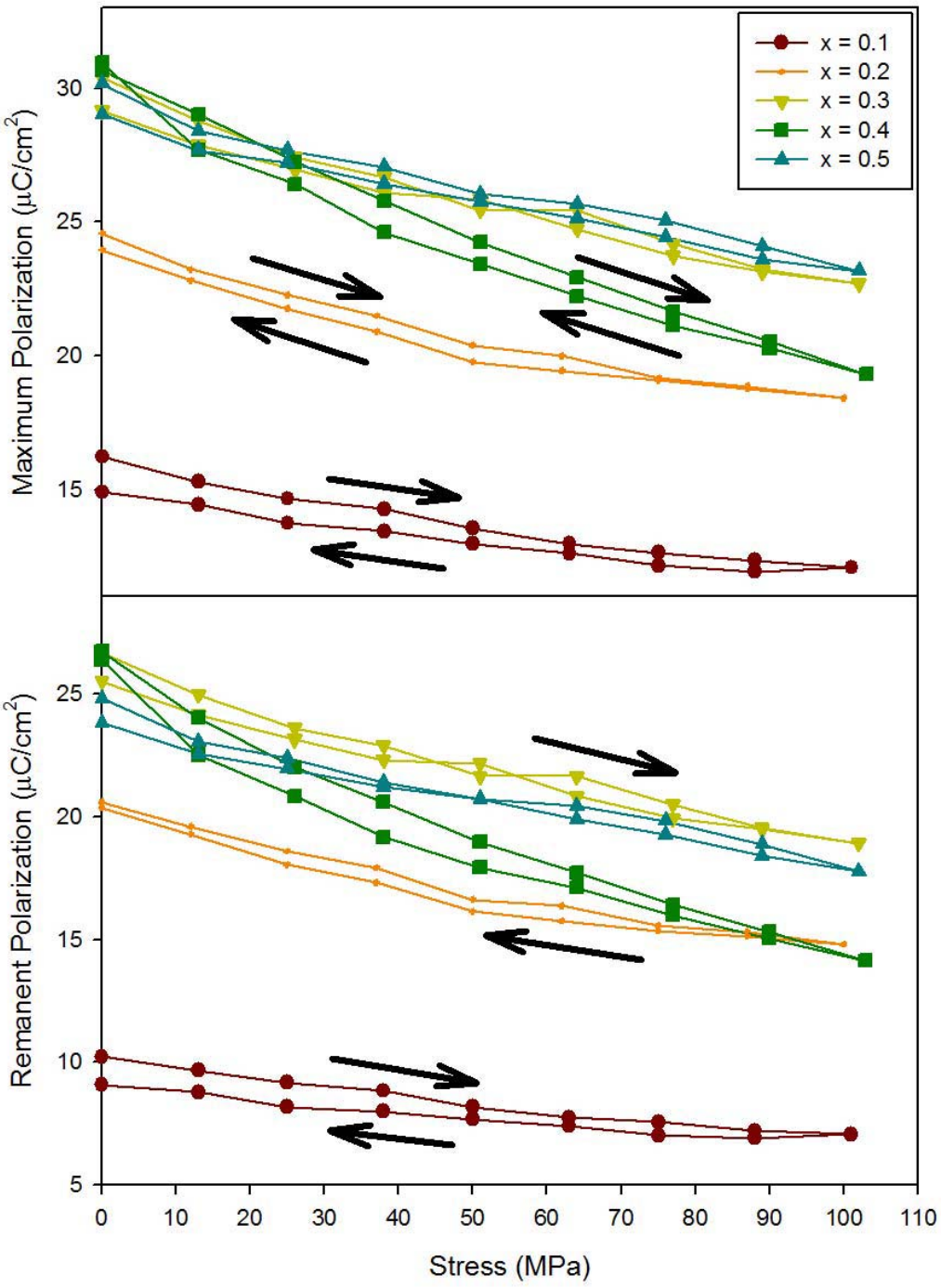

x = 0.1
x = 0.2
x = 0.3
x = 0.4
x = 0.5
Maximum Polarization (μC/cm²)
Remanent Polarization (μC/cm²)
Stress (MPa)
30
25
20
15
10
5
0
10
20
30
40
50
60
70
80
90
100
110

**Fig. 4**

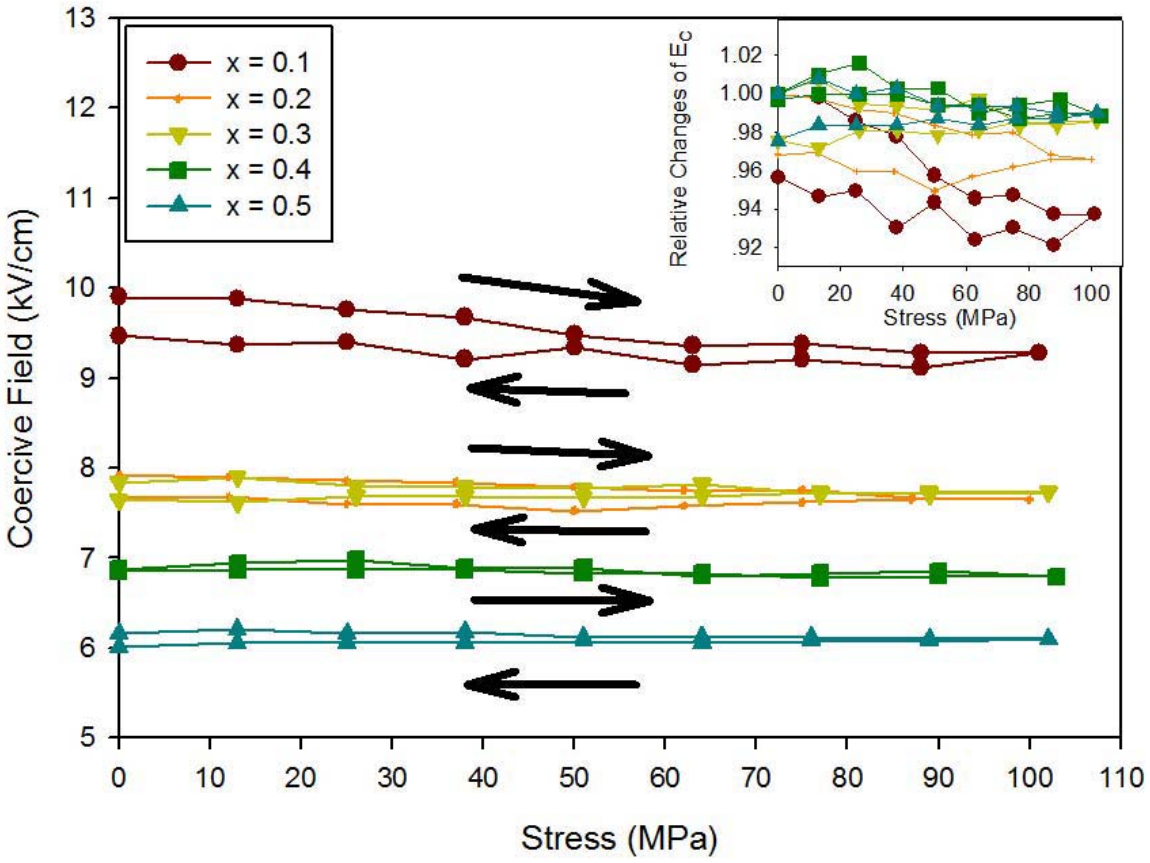

x = 0.1
x = 0.2
x = 0.3
x = 0.4
x = 0.5
Coercive Field (kV/cm)
Stress (MPa)
Relative Changes of Ec
Stress (MPa)

**Fig. 5**

# Dielectric and ferroelectric properties of lead zirconate titanate-lead nickel niobate ceramics under compressive stress

M. Unruan,[1,a)] A. Prasartketrakarn,[1] A. Ngamjarurojana,[1] Y. Laosiritaworn,[1] S. Ananta,[1] and R. Yimnirun[2]
[1]*Department of Physics and Materials Science, Faculty of Science, Chiang Mai University, Chiang Mai 50200, Thailand*
[2]*School of Physics, Institute of Science, Suranaree University of Technology, Nakhon Ratchasima 30000, Thailand*

(Received 23 December 2008; accepted 21 February 2009; published online 23 April 2009)

Dielectric and ferroelectric properties of complex perovskite lead zirconate titanate-lead nickel niobate ceramic system were investigated under the influence of the compressive stress. The results showed that the dielectric properties, i.e., dielectric constant ($\varepsilon_r$) and dielectric loss (tan $\delta$), and the ferroelectric characteristics, i.e., the area of the ferroelectric hysteresis ($P$-$E$) loops, the maximum polarization ($P_{max}$), and the remanent polarization ($P_r$) changed significantly with increasing compressive stress. These changes depended greatly on the ceramic compositions. The experimental results on the dielectric properties could be explained by the deaging phenomenon. The stress-induced domain wall motion suppression and non-180° ferroelectric domain switching processes were responsible for the changes observed for the ferroelectric parameters. In addition, a significant decrease in those parameters after a cycle of stress was observed and attributed to the stress-induced decrease in switchable part of spontaneous polarization. This study clearly showed that the applied stress has significant influence on the electrical properties of complex perovskite ceramics. © *2009 American Institute of Physics*. [DOI: 10.1063/1.3106659]

## I. INTRODUCTION

There has recently been a great deal of interest in lead zirconate titanate-lead nickel niobate [$Pb(Zr_{1-x}Ti_x)O_3$-$Pb(Ni_{1/3}Nb_{2/3})O_3$ or (PZT-PNN)] ceramics because of their high longitudinal coupling coefficients, as well as good dielectric and excellent piezoelectric properties.[1–3] PZT is a normal ferroelectric material, which has been extensively investigated in the literatures because of its high dielectric properties and high piezoelectric coefficient. The high piezoelectric properties of PZT have been observed for compositions near the morphotropic phase boundary (MPB), i.e., at lead zirconate ($PbZrO_3$ or PZ):lead titanate($PbTiO_3$ or PT)=0.52:0.48.[4–6] PNN is a relaxor ferroelectric material originally reported by Smolenskii and Agranovskaya.[7] It exhibits the excellent dielectric broadening and electrostrictive properties and shows a diffuse phase transition around −120 °C with a peak permittivity of about 4000 at 1 kHz.[8]

Practically, piezoelectric and ferroelectric ceramics are often subjected to mechanical loading either deliberately in the design of the device itself or because the device is used to change shapes as in many smart structure applications or the device is used under environmental stresses.[9–13] A prior knowledge of how the material properties change under different load conditions is crucial for proper design of a device and for suitable selection of materials for a specific application.[12,13] It is therefore important to determine the properties of these materials as a function of applied stress. Previous investigations on the stress-dependence electrical properties of many ceramic systems emphasized the importance of the matter.[11,14–18] Recently, the uniaxial stress dependence of dielectric and ferroelectric properties has been investigated in materials such as barium titanate (BT), lead magnesium niobate (PMN), PMN-PT, PZT-BT, and PMN-PZT.[16–21] The results clearly showed that the effects of stress on the dielectric and ferroelectric properties depended significantly on ceramic compositions and stress levels. Interestingly, there has been no systematic study on the influence of an applied stress on the dielectric and ferroelectric properties of the PZT-PNN ceramics. Therefore, it is the aim of this study to determine the dielectric and ferroelectric properties of the $(1-x)$PZT-$(x)$PNN ceramics as a function of compressive stress.

## II. EXPERIMENTAL

In this study, $(1-x)$PZT-$(x)$PNN (with $x=0.1-0.5$) ceramics were prepared using the columbite precursor method. The columbite structure ($NiNb_2O_6$) and wolframite structure ($ZrTiO_4$) were synthesized first. The calcined $NiNb_2O_6$ and $ZrTiO_4$ powders were mixed with PbO in a stoichiometric ratio to form the composition $(1-x)$PZT-$(x)$PNN, with $x=0.1-0.5$. For optimization purpose, the sintering was carried out at temperatures between 1100 and 1250 °C for 4 h. Details of the processing and characterizations were provided elsewhere.[2]

Before studying the electrical properties, the specimens were lapped to obtain parallel faces. After coating with silver paint as electrode at the faces, the specimens were heated at 750 °C for 12 min to ensure the contact between the electrode and surface of ceramic. To study effects of the com-

a)Author to whom correspondence should be addressed. Electronic mail: muangjaiunruan@yahoo.com.

 © 2009 American Institute of Physics

Downloaded 23 Apr 2009 to 202.28.246.2. Redistribution subject to AIP license or copyright; see http://jap.aip.org/jap/copyright.jsp

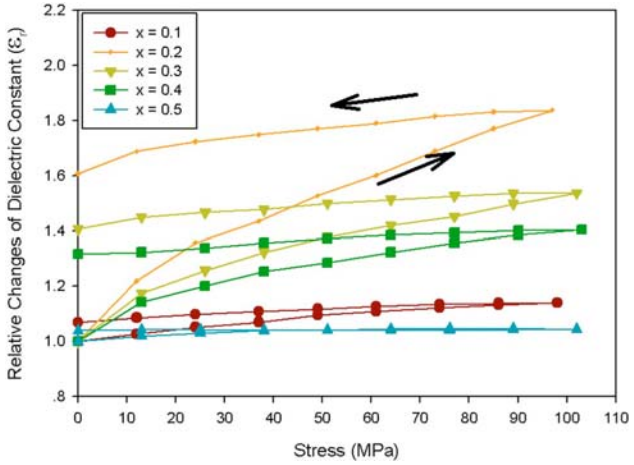



FIG. 1. (Color online) Relative changes in dielectric constant ($\varepsilon_r$) with compressive stress for $(1-x)$PZT-$(x)$PNN ceramics (measured at 25 °C and 10 kHz; solid arrows indicate loading direction).

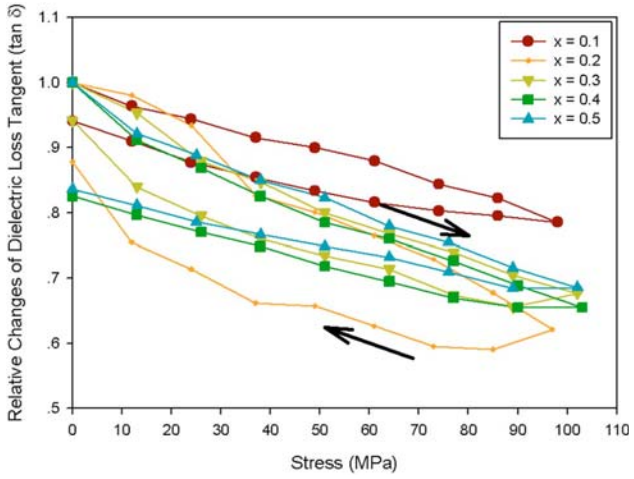



FIG. 2. (Color online) Relative changes in dielectric loss tangent (tan $\delta$) with compressive stress for $(1-x)$PZT-$(x)$PNN ceramics (measured at 25 °C and 10 kHz; solid arrows indicate loading direction).

pressive stress on the dielectric and ferroelectric properties of the ceramics, the compressometer was constructed.[16–18] The dielectric properties were measured by LCR meter (Instrek LCR-821). The room temperature (25 °C) capacitance and the dielectric loss tangent were obtained at frequency of 10 kHz under compressive stress. The dielectric constant was then calculated from a parallel-plate capacitor equation, e.g., $\varepsilon_r = Cd/\varepsilon_0 A$, where $C$ is the capacitance of the specimens, $d$ and $A$ are respectively the thickness and the area of the electrode, and $\varepsilon_0$ is the dielectric permittivity of vacuum $(8.854 \times 10^{-12}$ F/m).

The ferroelectric hysteresis ($P$-$E$) loops were characterized by using a computer controlled modified Sawyer–Tower circuit. The electric field was applied to a sample by a high voltage ac amplifier (Trek, model 610D) with the input sinusoidal signal with a frequency of 50 Hz from a signal generator (Goodwill, model GAG-809). The ferroelectric hysteresis ($P$-$E$) loop was recorded at room temperature (25 °C) for both loading and unloading conditions. The parameters obtained from the loops were the maximum polarization ($P_{max}$), the remanent polarization ($P_r$), and the coercive field ($E_c$), which were defined as the points where the loops reach the maximum polarization, cross the zero field, and cross the zero polarization, respectively.

## III. RESULTS AND DISCUSSION

### A. Dielectric properties under stress

The experimental results of the compressive stress dependence of the dielectric properties during loading and unloading for the ceramics in PZT-PNN system are displayed in Figs. 1 and 2. For better comparison, the dielectric properties of each composition under stress are normalized to the stress-free values. Clearly, there is a considerable change in both the dielectric constant and the dielectric loss tangent with the compressive stress. As depicted in Fig. 1, the dielectric constant is seen to increase with increasing stress in all compositions. The increase in the dielectric constant varies from approximately 4%–14% in the near pseudocubic relaxor ferroelectric 0.5PZT-0.5PNN and tetragonal ferroelectric 0.9PZT-0.1PNN compositions to 40%–54% in the rhombohedral relaxor ferroelectric 0.6PMN-0.4PNN and 0.7PZT-0.3PNN compositions. For the MPB 0.8PZT-0.2PNN composition, the dielectric constant increases drastically with the stress. The dielectric constant increases more than 80% when the stress reaches 100 MPa and returns to 160% of its original value when the stress is removed. On the other hand, the dielectric loss tangent (tan $\delta$) is seen to decrease significantly (20%–40%) with increasing stress, as displayed in Fig. 2. The changing of the dielectric properties with increasing and decreasing stress does not follow the same path. It is also noticed that the changes in the dielectric properties with the compressive stress obtained in this study are in parts similar to those for systems in earlier investigations.[17,19,22]

To understand these experimental results, various effects have to be considered. When a mechanical stress is applied to a ferroelectric material, the domain structure in the material will change to maintain the domain energy at a minimum; during this process some of the domains engulf other domains or change shape irreversibly. Under a compressive stress, the domain structure of ferroelectric ceramics may undergo domain switching, clamping of domain walls, and deaging mechanisms.[14,15,19,23] In this study, the results on the compressive stress dependence of the dielectric properties can easily be explained with the above statements. When the compressive stress is applied in the direction parallel to the polar axis (poling) direction, the stress will move some of the polarization away from the poling direction, resulting in a change in domain structures.[15,19,24,25] This change increases the non-180° domain wall density. Hence the increase in the dielectric constant with the applied stress is observed. The deaging mechanism, which also increases the dielectric constant,[15,18–20] is also expected to play a role here. Therefore, a combination of the domain switching and the deaging mechanisms is believed to be a reason for the increase in the dielectric constant with increasing applied stress in the PZT-PNN system, as shown in Fig. 1. The cause of the stress dependence of the dielectric loss tangent is mainly due to the clamping of the domain walls under compressive stress,

Downloaded 23 Apr 2009 to 202.28.246.2. Redistribution subject to AIP license or copyright; see http://jap.aip.org/jap/copyright.jsp

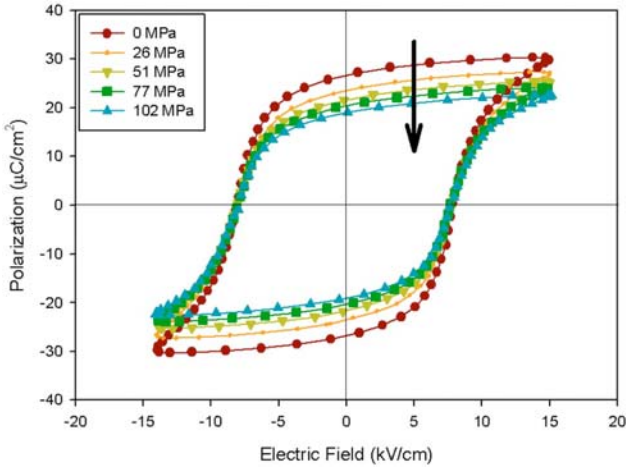



FIG. 3. (Color online) Polarization vs electric field ($P$-$E$) hysteresis loops as a function of compressive stress for 0.7PZT-0.3PNN ceramic (loading cycle).

which results in a decrease in domain wall mobility. The deaging mechanism, which also decreases the dielectric loss tangent,[15,22] is also expected to play a role in controlling the change in the dielectric loss tangent with the stress, as observed in Fig. 2.

It should also be noted here that the applied stress could also affect the ferroelectric phase transitions of the ceramics, which consequently change the observed dielectric properties significantly.[15,25] The applied compressive stress has been found to move the Curie temperature ($T_C$) up to the order of approximately 0.1 °C/MPa in 0.9PMN-0.1PT.[15] In addition, the influence of stress on the properties of ferroelectric materials is strongly dependent on the temperature, especially when the temperature is higher or lower than $T_C$. In this study, since $(1-x)$PZT-$(x)$PNN (with $x=0.1-0.5$) ceramics exhibit $T_C$ ranging from 130 °C ($x=0.5$) to 330 °C ($x=0.1$),[2] the change in the dielectric properties with stress in the vicinity of $T_C$ and the stress-induced shift in $T_C$ is rather insignificant because of their high $T_C$, as compared to the measurement temperature of 25 °C. Therefore, the stress-related ferroelectric phase transition is not expected to have significant effects on the changes in dielectric properties of PZT-PNN ceramics under the applied stress observed in this study.

### B. Ferroelectric properties under stress

The polarization versus electric field ($P$-$E$) hysteresis loops of the 0.7PZT-0.3PNN ceramic under different compressive stresses are shown in Fig. 3 as a simple representative for the other compositions with similar behavior. It should first be noticed that the area of the $P$-$E$ loops decreases with increasing compressive stress. The changes follow similar trend for all the ceramics. The $P$-$E$ loop area indicates the polarization dissipation energy of a ferroelectric material under one full cycle of electric field application. This amount of the energy loss is directly related to the amount of domain participating in the switching process during the application of electric field.[14,17] For a given composition, the decrease in the loop area with increasing the compressive stress is a result of the stress-induced domain wall suppression.[14,26]

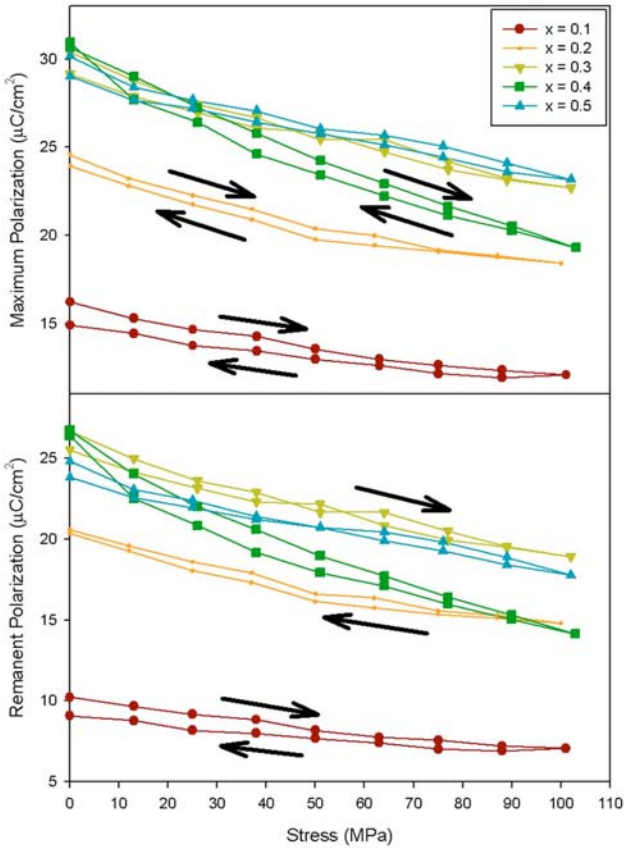



FIG. 4. (Color online) Changes in remanent polarization ($P_r$) and maximum polarization ($P_{max}$) with compressive stress for $(1-x)$PZT-$x$PNN ceramics (loading and unloading).

The changes in the remanent polarization ($P_r$), maximum polarization ($P_{max}$), and the coercive field ($E_c$) with the compressive stresses are plotted in Figs. 4 and 5, respectively. The changes in the maximum polarization ($P_{max}$) with stress are similar to the $P_r$. Figure 4 clearly shows that the

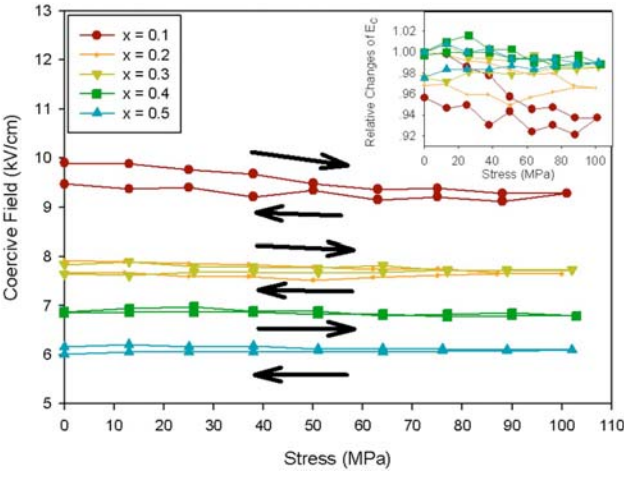



FIG. 5. (Color online) Changes in coercive field ($E_c$) with compressive stress for $(1-x)$PZT-$x$PNN ceramics (loading and unloading).

Downloaded 23 Apr 2009 to 202.28.246.2. Redistribution subject to AIP license or copyright; see http://jap.aip.org/jap/copyright.jsp

maximum and remanent polarizations decrease as the compressive stress increases. The decrease is generally very similar to the polarization values at 100 MPa, which are approximately 30%–45% of the stress-free values. In addition, noticeable decreases in the polarization values of all the ceramic are also observed after a complete cycle of the mechanical stress. This observation suggests a significant stress-induced depoling in PZT-PNN ceramics, resulting in the observed decrease in the polarization values under high stress levels.[19,27] Since the remanent polarization decreases as the compressive stress increases, it takes lower than usual electric field to force the polarizations to become zero; hence lower coercive field is observed, as demonstrated in Fig. 5.

To understand, at least qualitatively, these experimental results on ferroelectric properties of the PZT-PNN ceramics, one can interpret the changes in terms of domain-reorientation processes. When the compressive stress is applied in the direction parallel to the polar axis (poling) direction, the applied stress tends to keep the ferroelectric domains aligned with their polar axes away from the stress direction through the non-180° ferroelastic domain switching processes.[14,15] Therefore, it takes larger than usual for the applied electric field to reorient the domains along the stress direction, resulting in lower value of the maximum polarization ($P_{max}$), as shown in Figs. 3 and 4. When the electric field is reduced to zero the domains tend to rotate back away from the applied compressive stress direction, resulting in lower than usual remanent polarization ($P_r$),[19,28,29] as depicted in Figs. 3 and 4. Furthermore, considering the decrease in the hysteresis loss with increasing compressive stress, it indicates that more and more ferroelectric domains are constrained by the applied stress and cannot be reoriented by the electric field so as to participate in the polarization reversal. Consequently, both the maximum and remanent polarizations become lower with increasing compressive stress.[15] The results of the changes in the hysteresis parameters of the ferroelectric ceramics with increasing compressive stress are in agreement with the previous investigations on many ferroelectric ceramics.[11,14,18,30]

## IV. CONCLUSIONS

In this study, effects of compressive stress on the dielectric properties of PZT-PNN ceramics with a formula of $(1-x)$PZT-$(x)$PNN ($x=0.1-0.5$) have been investigated under compressive stress using a compressometer in conjunction with an automatic LCR meter and a modified Sawyer–Tower circuit. The superimposed compression stress had pronounced effects on both the dielectric constant and the dielectric loss tangent of PZT-PNN ceramics, especially in MPB 0.8PZT-0.2PNN composition. The area of the ferroelectric hysteresis ($P$-$E$) loops, the maximum polarization ($P_{max}$), the remanent polarization ($P_r$), and the coercive field ($E_c$) decrease with increasing compressive stresses. The observations were mainly interpreted in terms of domain switching through non-180° domain walls, deaging, and the stress-induced domain wall suppression mechanisms. Furthermore, noticeable decreases in the polarization values of all the ceramic are also observed after a complete cycle of the mechanical stress, indication of a significant stress-induced depoling in PZT-PNN ceramics. Finally, this study undoubtedly shows that the applied compressive stress has significant influences on the dielectric and ferroelectric properties of the PZT-PNN ceramics.

## ACKNOWLEDGMENTS

Financial supports from the Thailand Research Fund (TRF), Commission on Higher Education (CHE), Royal Golden Jubilee (RGJ) Ph.D. Program, Thailand Excellent Center in Physics, and Faculty of Science and Graduate School of Chiang Mai University are gratefully acknowledged.

[1] M. Kondo, M. Hida, M. Tsukuda, K. Kurihara, and N. Kamehara, Jpn. J. Appl. Phys., Part 1 **36**, 6043 (1997).
[2] N. Vittayakorn, G. Rujijanagul, X. Tan, M. A. Marquardt, and D. P. Cann, J. Appl. Phys. **96**, 5103 (2004).
[3] D. Luff, R. Lane, K. R. Brown, and H. J. Marshallsay, Trans. J. Br. Ceram. Soc. **73**, 251 (1974).
[4] J. Moulson and J. M. Herbert, *Electroceramics: Materials, Properties, Applications* (Chapman and Hall, New York, 1990).
[5] B. Jaffe, W. R. Cook, and H. Jaffe, *Piezoelectric Ceramic* (RAN, New York, 1971).
[6] Y. H. Xu, *Ferroelectric Materials and Their Applications* (North-Holland, Los Angeles, 1991).
[7] G. A. Smolenskii and A. L. Agranovskaya, Sov. Phys. Tech. Phys. **13**, 80 (1958).
[8] V. A. Bokov and I. E. Mylnikova, Sov. Phys. Solid State **2**, 2428 (1960).
[9] J. Kuwata, K. Uchino, and S. Nomura, Jpn. J. Appl. Phys., Part 1 **21**, 1298 (1982).
[10] S. E. Park and T. R. Shrout, J. Appl. Phys. **82**, 1804 (1997).
[11] D. Viehland and J. Powers, Appl. Phys. Lett. **78**, 3112 (2001).
[12] D. Stansfield, *Underwater Electroacoustic Transducers* (Bath University Press, Bath, UK, 1991).
[13] K. Uchino, *Piezoelectric Actuators and Ultrasonic Motors* (Kluwer, Boston, 1997).
[14] D. Zhou, M. Kamlah, and D. Munz, J. Eur. Ceram. Soc. **25**, 425 (2005).
[15] Q. M. Zhang, J. Zhao, K. Uchino, and J. Zheng, J. Mater. Res. **12**, 226 (1997).
[16] R. Yimnirun, Ferroelectrics **331**, 9 (2006).
[17] R. Yimnirun, S. Ananta, and S. Chamunglap, Mater. Chem. Phys. **102**, 165 (2007).
[18] R. Yimnirun, S. Ananta, A. Ngamjarurojana, and S. Wongsaenmai, Curr. Appl. Phys. **6**, 520 (2006).
[19] G. Yang, S. F. Liu, W. Ren, and B. K. Mukherjee, Proc. SPIE Symposium on Smart Structures and Materials **3992**, 103 (2000).
[20] R. Yimnirun, M. Unruan, Y. Laosiritaworn, and S. Ananta, J. Phys. D **39**, 3097 (2006).
[21] R. Yimnirun, S. Ananta, E. Meechoowas, and S. Wongsaenmai, J. Phys. D **36**, 1615 (2003).
[22] M. Unruan, S. Wongsaenmai, Y. Laosiritaworn, S. Ananta, and R. Yimnirun, J. Phys. D **41**, 541 (2008).
[23] G. Yang, S. F. Liu, W. Ren, and B. K. Mukherjee, Ferroelectrics **262**, 207 (2001).
[24] D. Audigier, Cl. Richard, Cl. Descamps, M. Troccaz, and L. Eyraud, Ferroelectrics **154**, 219 (1994).
[25] I. J. Fritz, J. Appl. Phys. **49**, 4922 (1978).
[26] R. Yimnirun, S. Ananta, A. Ngamjarurojana, and S. Wongsaenmai, Appl. Phys. A: Mater. Sci. Process. **81**, 1227 (2005).
[27] G. Yang, W. Ren, S. F. Liu, A. J. Masys, and B. K. Mukherjee, Proc.-IEEE Ultrason. Symp. **2**, 1005 (2000).
[28] J. Zhao and Q. M. Zhang, Proceedings of the 10th IEEE International Symposium on Applications of Ferroelectrics, Vol. 2, pp. 971–974 (1996).
[29] J. Zhao, A. E. Glazounov, and Q. M. Zhang, Appl. Phys. Lett. **74**, 436 (1999).
[30] C. S. Lynch, Acta Mater. **44**, 4137 (1996).

Downloaded 23 Apr 2009 to 202.28.246.2. Redistribution subject to AIP license or copyright; see http://jap.aip.org/jap/copyright.jsp

Journal of Alloys and Compounds xxx (2008) xxx–xxx

Contents lists available at ScienceDirect

Journal of Alloys and Compounds

journal homepage: www.elsevier.com/locate/jallcom

# Effect of magnesium niobate precursors on phase formation, microstructure and dielectric properties of perovskite lead magnesium niobate ceramics

R. Wongmaneerung[a,*], R. Yimnirun[b], S. Ananta[b]

[a] Department of Physics, Faculty of Science, Maejo University, Chiang Mai 50290, Thailand
[b] Department of Physics, Faculty of Science, Chiang Mai University, Chiang Mai 50200, Thailand

ARTICLE INFO

*Article history:*
Received 2 January 2008
Received in revised form 28 October 2008
Accepted 30 October 2008
Available online xxx

*Keywords:*
Lead magnesium niobate
Perovskite
Relaxor
*B*-site precursor

ABSTRACT

Lead magnesium niobate, $Pb(Mg_{1/3}Nb_{2/3})O_3$ or PMN, ceramics were fabricated by using *B*-site precursor method where both $MgNb_2O_6$ and $Mg_4Nb_2O_9$ were employed as magnesium niobate precursors. It has been found that under suitable sintering condition highly dense and pure $Pb(Mg_{1/3}Nb_{2/3})O_3$ ceramics can be successfully achieved in both processing routes. In addition, pure perovskite $Pb(Mg_{1/3}Nb_{2/3})O_3$ ceramic with slightly higher dielectric constant can be produced at lower sintering temperature by using a corundum-route.

© 2008 Elsevier B.V. All rights reserved.

## 1. Introduction

Lead magnesium niobate, $Pb(Mg_{1/3}Nb_{2/3})O_3$ or PMN, is one of the most widely investigated perovskite relaxor ferroelectric materials, which has been extensively studied because of its high dielectric constant and electrostrictive coefficient [1–4]. The excellent properties make it a promising material for capacitor, actuator and transducer applications [5–7]. As is well-known, in the preparation of PMN via the conventional solid-state reaction using PbO, MgO and $Nb_2O_5$ [8,9], significant amount of the pyrochlore-type phases with relatively low dielectric constant are inevitably formed with PMN and these phases significantly degrade the overall electrical properties of the products. In order to avoid the formation of pyrochlores, several methods have been introduced [10–13]. So far, the columbite method [12,13], in which prefabricated $MgNb_2O_6$ is reacted with an appropriate proportion of PbO, has been widely accepted as one of the promising methods for the preparation of phase-pure PMN-based materials. To date, only a few work [10,11] on the preparation of PMN powders by using a corundum $Mg_4Nb_2O_9$ precursor have been reported. Moreover, effects of $Mg_4Nb_2O_9$ precursor on phase formation, microstructure and dielectric properties of PMN ceramics has not been adequately characterized. Thus, in the present study, the PMN ceramics were fabricated by using both $MgNb_2O_6$ and $Mg_4Nb_2O_9$ as precursor. Their dielectric properties with respect to temperature and frequency were examined, compared and explained on the basis of their final composition, densification, and microstructural development.

## 2. Experimental

PMN powders were synthesized by employing two different *B*-site precursors (i.e. columbite-route versus corundum-route) mixed oxide synthetic route, as reported earlier [12,13]. Starting precursors were as follows: PbO (JCPDS file no. 77-1971), MgO (periclase: JCPDS file no. 71-1176) and $Nb_2O_5$ (JCPDS file no. 80-2493) (Aldrich, 99% purity). These three oxide powders exhibited an average particle size in the range of 3.0–5.0 μm. First, two intermediate phases of magnesium niobate: $MgNb_2O_6$ and $Mg_4Nb_2O_9$ were separately prepared by the solid-state reaction method previously reported [14–16]. The appropriate amount of PbO was then added to the $MgNb_2O_6$ and $Mg_4Nb_2O_9$, and vibro-milled in isopropanol alcohol for 1 h. Columbite- and corundum-route mixtures were then calcined at 900 and 950 °C, respectively, for 1 h with heating/cooling rates of 30 °C/min [15].

Green pellets were pressed into disks and sintered at various temperatures between 1100 and 1290 °C. Densities of the sintered pellets were determined by using the Archimedes principles. Room temperature X-ray diffraction (XRD; Philips PW 1729 diffractometer) was used to identify the phases formed and optimum sintering condition. The relative amounts of perovskite and pyrochlore phases were determined from XRD patterns of the samples by measuring the major peak intensities for the perovskite and pyrochlore phases. The following qualitative equation [12] was used.

$$\%\text{Perovskite} = 100 \times \frac{I_{per}}{I_{per} + I_{pyr}} \quad (1)$$

Here, $I_{per}$ refers to the intensity of the perovskite (1 1 0) peak and $I_{pyr}$ refers to the intensity of the pyrochlore (2 2 2) peak.

The microstructural development was examined by scanning electron microscopy (SEM; JEOL JSM-840A). Average grain size of the sintered ceramics was

* Corresponding author. Tel.: +66 81 8554973.
*E-mail address:* re_nok@yahoo.com (R. Wongmaneerung).

0925-8388/$ – see front matter © 2008 Elsevier B.V. All rights reserved.
doi:10.1016/j.jallcom.2008.10.152

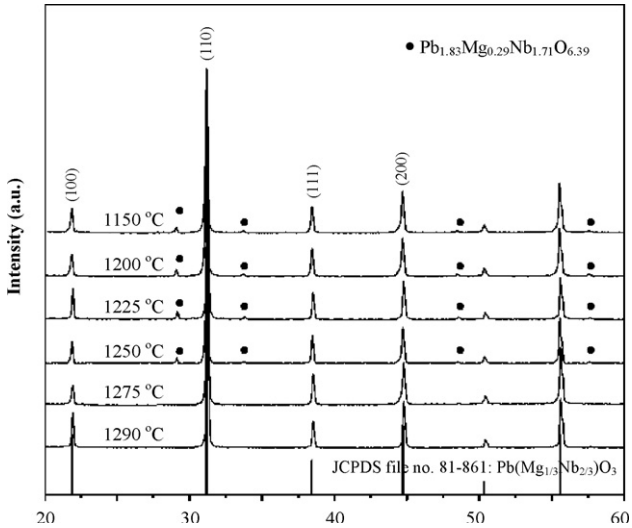



**Fig. 1.** XRD patterns of the columbite-route PMN ceramics sintered at various temperatures.

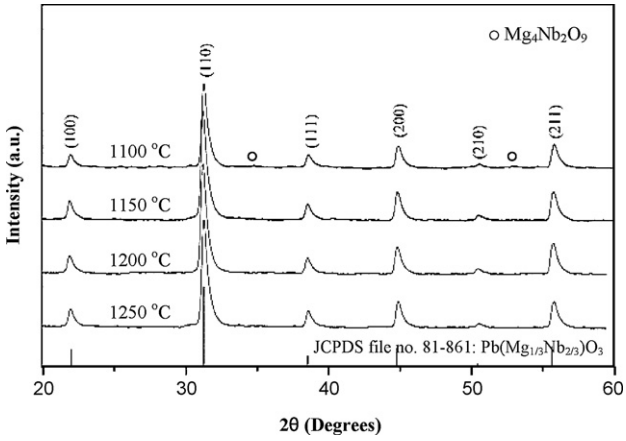



**Fig. 2.** XRD patterns of the corundum-route PMN ceramics sintered at various temperatures.

estimated by using a linear intercept method [17], in which the linear intercept length is determined by laying a series of uniformly distributed test lines on the planar section and counting the number of times the grain boundaries are intercepted. In this work, five samples from each processing condition were used in determining the average grain size and the standard deviation of the grain size was estimated as ±0.05 μm. For the dielectric measurement, ceramic surfaces were parallel polished and sputtered with gold. Dielectric characterization was performed with a LCR meter (HP-4284A, Hewlett-Packard) in conjunction with an environmental chamber (9023, Delta Design). A heating rate of 3 °C/min was used during the measurement.

## 3. Results and discussion

The X-ray diffraction patterns of columbite- and corundum-route PMN ceramics sintered at various temperatures are given in Figs. 1 and 2, respectively. As shown in Fig. 1, the strongest reflections in the majority of the XRD patterns indicate the formation of PMN phase, which could be matched with JCPDS file no. 81-861 [18], in agreement with other works [16,19]. To a first approximation, this phase has a pseudo-cubic perovskite-type structure with cell parameter $a = 404.41$ pm in space group *Pm3m* (no. 221). However, some additional reflections (marked by ●), which correlate with a pyrochlore phase of composition $Pb_{1.83}Mg_{0.29}Nb_{1.71}O_{6.39}$ (JCPDS file no. 33-769 [20]) are found in XRD patterns of columbite-route PMN samples sintered at low sintering temperatures (1150–1250 °C). This phase has orthorhombic structure with cell parameter $a = 105.9$ pm in space group *Fd3m* (no. 227) [21]. As shown in Fig. 2, XRD patterns of corundum-route PMN ceramics which sintered above 1100 °C show 100% perovskite phase and could be matched with JCPDS file no. 81-861 [18], similar to PMN phase occurs in columbite-route. It should be noted that no evidence of pyrochlore phases such as $Pb_2Nb_2O_7$, $Pb_3Nb_2O_8$ and $Pb_5Nb_4O_{15}$ has been found here whereas these phases were found in other works [22,23]. However, some additional reflections (marked by ○), which correlate with $Mg_4Nb_2O_9$ phase are found in XRD patterns of PMN sample sintered at 1100 °C. This observation indicates that $Mg_4Nb_2O_9$ was formed at this low temperature at which the complete reaction between PbO and $Mg_4Nb_2O_9$ could not occur. This is likely due to the poor reactivity of the solid-state reaction method commonly found in the mixed oxide perovskite compounds.

For the purpose of estimating the concentration of pyrochlore phase present, Eq. (1) has been applied to the obtained diffraction patterns, as given in Table 1. It can be noticed that pure PMN ceramics can be produced at the lower optimized sintering temperature by using corundum precursor. Moreover, the dense PMN ceramics can be formed by using both *B*-site precursors. Based on the XRD data obtained here, it may be concluded that the optimal sintering temperature for the production of columbite- and corundum-route PMN ceramic is 1275 °C for 4 h with heating/cooling rates of 10 °C/min, and 1250 °C for 2 h with heating/cooling rates of 10 °C/min, respectively.

The densification data of all samples are shown in Table 1. It is observed that the density of about 93–95% and 89–92% of the theoretical value can be achieved for columbite- and corundum-route PMN ceramics, respectively. Density increases as sintering temperature increases. Further, increase in the sintering temperature up to 1300 °C caused to the decrease in density values. This may be attributed to the loss of lead oxide at high sintering temperatures,

**Table 1**
Phase and densification characteristics of columbite- and corundum-route PMN ceramics from various sintering conditions.

| Preparation route | Sintering temperature (°C) | Perovskite phase[a] (%) | Pyrochlore phase[a] (%) | Relative density[b] (%) |
|---|---|---|---|---|
| Columbite | 1150 | 96.76 | 3.24 | 96.48 |
| | 1200 | 96.72 | 3.28 | 96.85 |
| | 1225 | 96.10 | 3.90 | 96.11 |
| | 1250 | 97.37 | 2.63 | 95.24 |
| | 1275 | 100.00 | 0.00 | 95.37 |
| | 1290 | 100.00 | 0.00 | 93.64 |
| Corundum | 1100 | 100.00 | 0.00 | 89.32 |
| | 1150 | 100.00 | 0.00 | 90.83 |
| | 1200 | 100.00 | 0.00 | 91.76 |
| | 1250 | 100.00 | 0.00 | 92.14 |

[a] The estimated precision of the perovskite and pyrichlorephase is ±0.1%.
[b] The estimated precision of the density is ±0.1%.

Please cite this article in press as: R. Wongmaneerung, et al., J. Alloys Compd. (2008), doi:10.1016/j.jallcom.2008.10.152

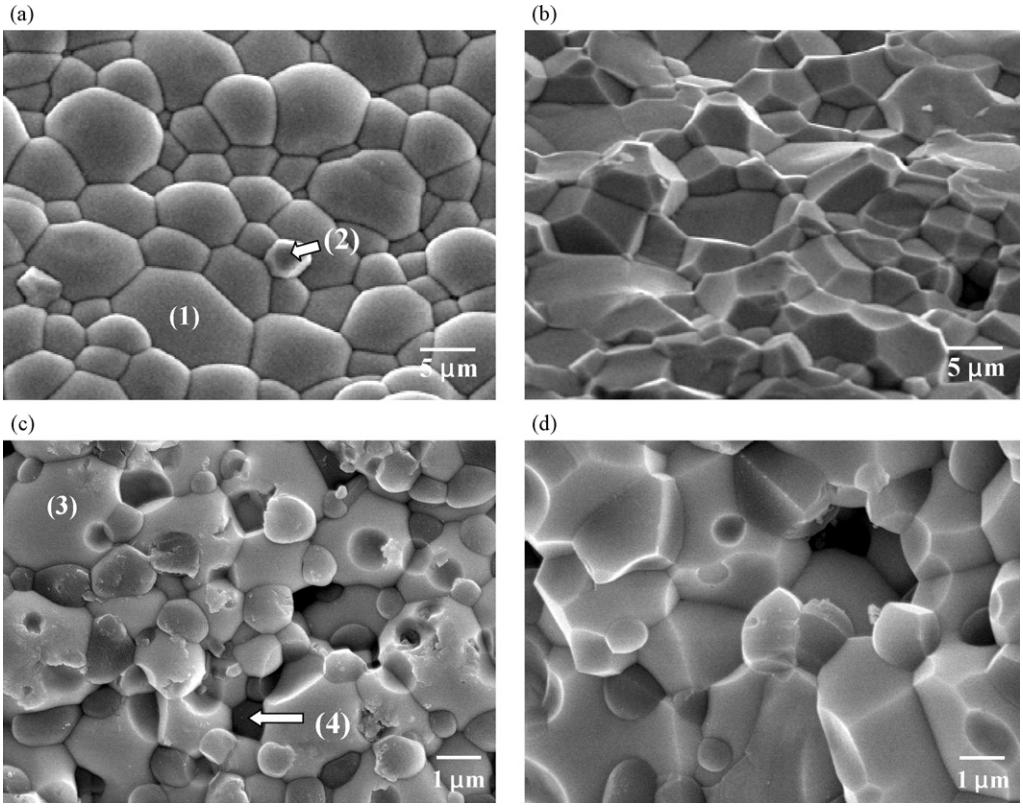



**Fig. 3.** SEM micrographs of (a) as-sintered and (b) fracture surfaces for columbite-route PMN ceramics, (c) as-sintered and (d) fracture surfaces for corundum-route PMN ceramics with maximum bulk density.

which is similar to the results found in other Pb-based perovskite systems [24,25].

Microstructural development was investigated by scanning electron microscopy. Free and fracture surface micrographs of columbite- and corundum-route PMN ceramics with maximum bulk density are compared in Fig. 3. In general, typical PMN microstructure consisting of highly dense grain-packing and round microstructural is observed in both samples and in good agreement with previous works [26,27]. Moreover, the grain sizes are in the range of 2–12 μm and 0.8–2.3 μm for columbite- and corundum-route PMN ceramics, respectively. In columbite-route sample, it is seen that a few facet grain is observed on the surface. By employing the combination of SEM/EDX techniques, more information is obtained as shown in Table 2 and Fig. 4 (a). EDX analysis of the facet grains (marked as "(2)") indicated the chemical composition of $Pb_6(MgNb_{10})O_{32}$ or $Pb_{1.83}(Mg_{0.37}Nb_{3.06})O_{10}$, although the concentration is too low for XRD detection, consistent with earlier work [28]. It is, therefore, intriguing to note the advantage of a combination between SEM and EDX techniques, which lies in its ability to reveal microstructural features often missed by the XRD diffraction method which requires at least 5 wt% of the component [29]. It should be noted that in this sample, no unreacted MgO and PbO liquid phase has been found on the grain boundary [22,26,30]. This phase is mainly observed between perovskite grains (marked as "(1)"). It should be noted here that EDX is now the most commonly used elemental analysis available within the SEM technique. This

**Table 2**
Chemical compositions of both PMN ceramics from EDX analyzer.

| EDX positions | Composition (at%) | | | Possible phase |
|---|---|---|---|---|
| | Mg (K) | Nb (L) | Pb (M) | |
| (1) | 16.13 | 33.34 | 50.52 | Pb3(MgNb2)O9 |
| (2) | 7.17 | 58.41 | 34.76 | $Pb_6(MgNb_{10})O_{32}$ |
| (3) | 17.06 | 28.33 | 54.62 | Pb3(MgNb2)O9 |
| (4) | 100.00 | – | – | MgO |

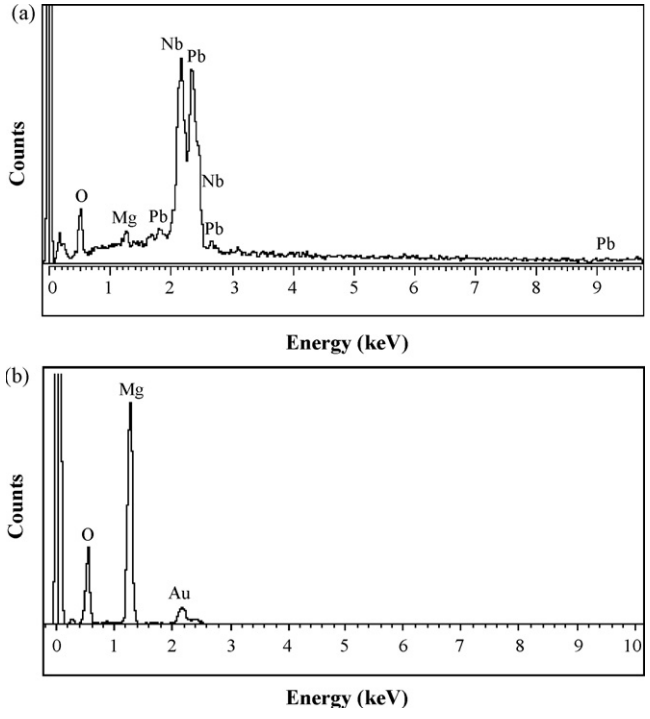



**Fig. 4.** EDX analysis of (a) the pyrochlore phase and (b) the MgO phase from both PMN ceramics (some spectra indexed as Au come from coated electrode).

Please cite this article in press as: R. Wongmaneerung, et al., J. Alloys Compd. (2008), doi:10.1016/j.jallcom.2008.10.152

**Table 3**
Comparison of $\varepsilon_{r,max}$ and grain size of PMN ceramics obtained by various methods.

| Sample from | Lejeune and Boilot [8] | Liou et al. [45] | Han and Kim [46] | This work | This work |
|---|---|---|---|---|---|
| Processing | Mixed oxide with $MgCO_3$ | Simplified columbite | Mixed oxide with $Mg(NO_3)_2$ | Columbite | Corundum |
| Calcination temperature/time | 800/2 h | 1100/3 h | 950/2 h | 900/1 h | 950/1 h |
| Sintering temperature/time | 900/2 h | 1250/2 h | 900/2 h | 1275/4 h | 1250/2 h |
| Relative density | 96.0% | 93.6% | 95.6% | 95.4% | 92.1% |
| $\varepsilon_{r,max}$ | 15400 | 17060 | n.a. | 12984 | 16566 |
| Grain size (μm) | n.a. | 7.1 | 2–4 | 2–12 | 0.8–2.3 |

technique offers a means of rapidly evaluating the elemental constituents of a sample; major constituents (10 wt% or more) can be indicated in 10 s and a 100-s accumulation is often sufficient for identification of minor elements (on the order of 1 wt%). In addition to rapid qualitative analysis, accurate quantitative analysis can also be achieved with EDX technique. However, there are techniques for microanalysis of inorganic materials. One of these techniques is electron probe microanalyzer (EPMA). The EPMA's usefulness is compositional information, using characteristic X-ray lines, with a spatial resolution on the order of 1 μm can be obtained from a sample. The EPMA technique will be used for analysis of the PMN samples and the results will be presented in the future. Nonetheless, for the purpose of comparison, the EDX results obtained in this study are used for preliminary analysis.

For corundum-route PMN sample, the as-sintered ceramic (Fig. 3 (c)) shows few apparent open pores at grain boundaries and triple points; but cracks and microcracks are not observed. These could be caused by MgO inclusions (the dark area) present at triple points. It seems that the grain boundary movement is depressed by the MgO phase; hence the open pores were formed. Furthermore, the dark areas are determined by SEM/EDX to be MgO inclusions (marked as "(4)" in the microstructure in Fig. 4 (b)) neighbouring the parent PMN phase (marked as "(3)") as shown in Table 2, similar to the inclusions observed in a series of non-stoichiometric PMN compositions as reported earlier [31]. Furthermore, there were the MgO inclusions previously observed by Goo et al. [32] in a stoichiometric PMN doped with excess MgO. It is believed to be another cause for the lower density values in corundum-route PMN ceramic compared to columbite-route. Similar finding was also reported in SiC reinforced PZT ceramics [33]. Moreover, the microstructure in Fig. 3 (c) displays few small grains. EDX analysis indicated the chemical composition of $Pb(Mg_{1/3}Nb_{2/3})O_3$. It is evident that the coarsening of big grains over small grains is through a process coherent with a solid-state sintering mechanism. Micrographs of fracture surface (Fig. 3 (b) and (d)) show highly dense microstructures consisting of equiaxed grains in agreement with other researchers [26,27,34]. The PMN ceramics also have an intergranular fracture mechanism, indicating that the grain boundaries are mechanically weaker than the grains [35].

In order to evaluate the dielectric properties, both columbite- and corundum-route PMN ceramics with the maximum bulk density were measured at frequencies between 1 and 100 kHz in the

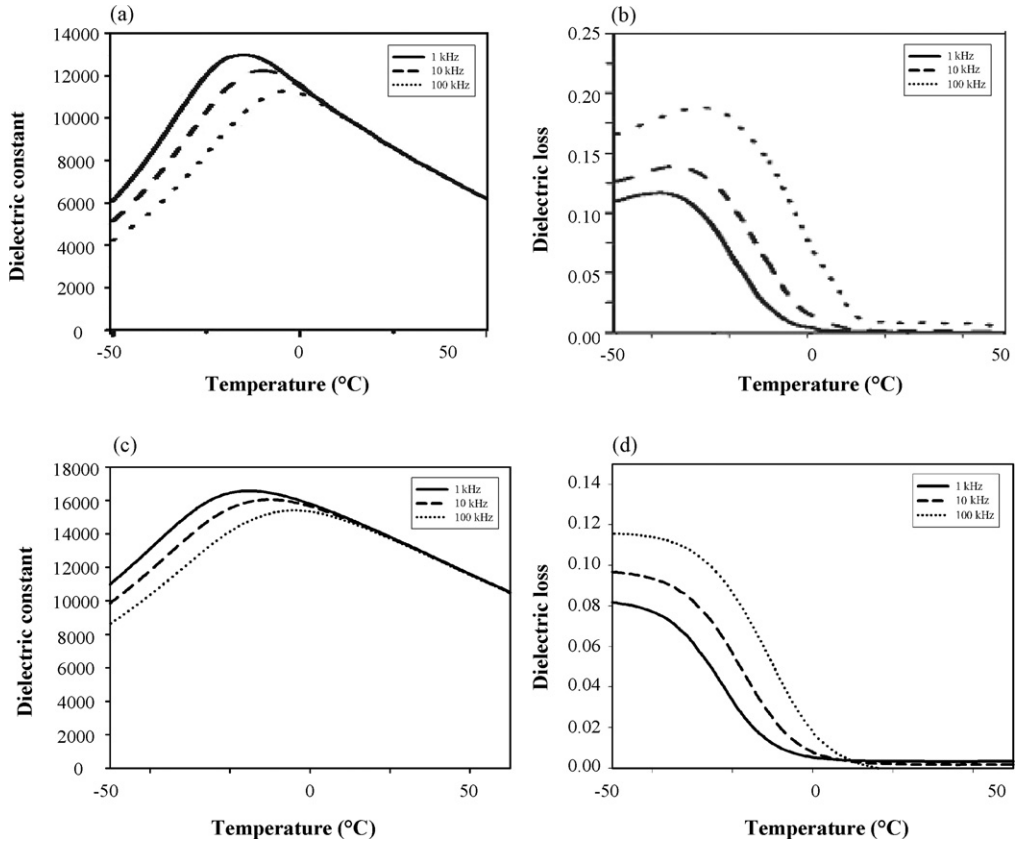



**Fig. 5.** Temperature dependence of (a) dielectric constant ($\varepsilon_r$) and (b) dielectric loss ($\tan\delta$) for the columbite-route PMN ceramic, (c) dielectric constant ($\varepsilon_r$) and (d) dielectric loss ($\tan\delta$) for the corundum-route PMN ceramic.

Please cite this article in press as: R. Wongmaneerung, et al., J. Alloys Compd. (2008), doi:10.1016/j.jallcom.2008.10.152

**Table 4**
Dielectric properties of PMN ceramics.

| Preparation route | Frequency (kHz) | $T_{max}$ (°C) | $\Delta T_{max}$ (°C) (1–100 kHz) | $\varepsilon_{r,max}$ | $\tan\delta_{max}$ | Diffusivity ($\gamma$) | Diffuseness parameter ($\delta$) |
|---|---|---|---|---|---|---|---|
| Columbite | 1 | −10.6 | 13.05 | 12960.7 | 0.12 | 1.98 | 42.03 |
| | 10 | −5.2 | | 12458.9 | 0.14 | 1.97 | 39.58 |
| | 100 | 2.5 | | 11855.7 | 0.19 | 1.92 | 37.28 |
| Corundum | 1 | −15.6 | 11.45 | 16566.5 | 0.07 | 1.79 | 35.64 |
| | 10 | −10.0 | | 16042.0 | 0.08 | 1.76 | 35.28 |
| | 100 | −4.1 | | 15406.5 | 0.11 | 1.73 | 32.73 |

temperature range from −50 to +50 °C as shown in Fig. 5. In general, the typical relaxor behavior [36,37] with the characteristic dispersive frequency dependence of the dielectric maxima has been observed in both PMN samples. The dielectric constant ($\varepsilon_r$) and dielectric loss ($\tan\delta$) are compared in Fig. 5. The maximum dielectric constant reached 12984 and 16566 at 1 kHz, the temperatures for $\varepsilon_{r,max}$ are −10 °C and −15 °C for columbite- and corundum-route samples, respectively, which are close to previously published values [26,38,39]. It can be noticed that the presence of MgO phase may slightly shift the temperature of $\varepsilon_{r,max}$. Characteristics of various PMN obtained by different methods in this work and those reported in other works are compared in Table 3. By comparison to columbite-route PMN ceramic, $\varepsilon_{r,max}$ of corundum-route ceramic is slightly higher. It should be noted that the presence of MgO resulted in an enhancement of the dielectric constant of PMN ceramics. This was originally attributed to the elimination of the pyrochlore phase [39], in agreement with the XRD results. Moreover, it should be noted that an increase of dielectric constant could be a combination of various effects; i.e. (i) phase present, (ii) density/porosity of the sample and (iii) grain size. Here it is observed that smaller grain size leads to an enhanced the dielectric constant. There are two other interesting features in this study. Firstly, the sample containing a small amount of MgO phase shows a high dielectric constant with similar results reported by Wang and Schulze [38]. The second feature is seen in Table 1, e.g. while the density of corundum-route PMN sample is low compared to columbite-route sample, the sample still exhibits all the characteristics of a relaxor materials.

Unlike the normal ferroelectrics, the dielectric behavior of PMN ceramics cannot be described by the Curie-Weiss law equation. Their behaviors tally well with the law $1/\varepsilon \propto (T - T_m)^2$. The dielectric constant can be written in the form [40]:

$$\frac{1}{\varepsilon} = \frac{1}{\varepsilon_m} + \frac{(T - T_m)^2}{2\varepsilon_m \delta^2} \quad (2)$$

Here $\gamma$ is the expression of the degree of dielectric relaxation in the relaxor ferroelectric materials and $\delta$ is diffuseness parameter and gives an estimation of the relaxor characteristic of the transition.

Fig. 6 shows dependencies of the $(\varepsilon_m/\varepsilon) - 1$ versus $(T - T_m)^2$, with determined values of the two diffuseness parameters ($\gamma$ and $\delta$). The diffuseness exponent for columbite-route sintered PMN ceramic is $\gamma = 1.98$ (Table 4), which is higher than reported value of 1.64 [41] but is very close to 2.0 [42]. Moreover, the diffuseness exponent tends to decrease while the frequency increases. By comparison, the diffuseness exponent for corundum-route sintered PMN ceramic is much smaller than those observed in columbite-route sample. It may be caused by the presence of MgO. The MgO inclusions might affect the low-frequency contributions to the dielectric constant. This interaction would be modeled by $\delta$ in Eq. (2) as shown in Table 4 and would suggest that the MgO phase could slightly decrease the diffuseness of the phase transition, in agreement with previous report [38]. Furthermore, for a perovskite ferroelectric, it can be established that the diffuseness could be caused by grain size dependence [43,44]. Therefore, this effect can partly be the cause of the increase of diffuseness exponent

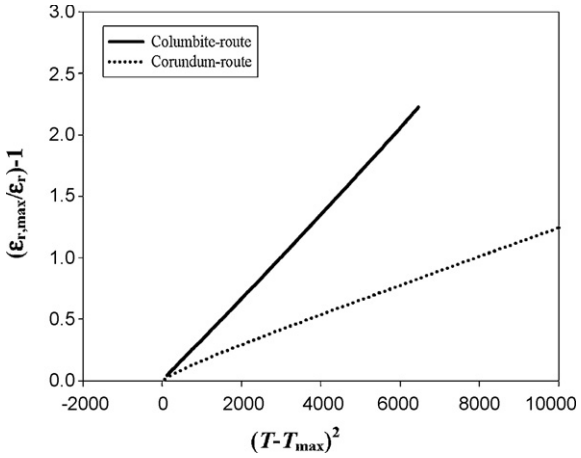



**Fig. 6.** Dependence of $(\varepsilon_{r,max}/\varepsilon_r) - 1$ with $(T - T_{max})^2$ for (a) columbite- and (b) corundum-route PMN ceramics.

in columbite-route PMN ceramic. Finally, it should be noted that the dielectric constant is increased with decreasing grain size. The factor leading to this result is probably the variation in the stress to which the grains are subjected as they cool through the Curie point. Moreover, the columbite-route PMN ceramic containing a small amount of pyrochlore phase ($Pb_{1.83}Mg_{0.29}Nb_{1.71}O_{6.39}$) shows a low dielectric constant. This observation is clearly a result of the paraelectric pyrochlore phase with a low dielectric constant at room temperature of 130; hence reducing the dielectric properties of the columbite-route PMN ceramic sample.

## 4. Conclusion

Results indicate that using different magnesium niobate precursors to produce PMN ceramics greatly influences phase formation, microstructure and dielectric properties of the resulting products. It has been concluded that the single-phase perovskite PMN ceramics can be successfully formed by employing either columbite- or corundum-route precursor method under optimized sintering temperatures. Between the two *B*-site precursor methods, it is seen that lower optimized sintering temperature for the production of pure PMN ceramics can be obtained by using corundum-route, whereas the large obtainable grain size was found in the columbite-route PMN ceramics. Moreover, the presence of MgO phase in the microstructures of corundum-route PMN ceramics may lead to the pyrochlore elimination and results in enhancement of the dielectric properties.

## Acknowledgements

This work was supported by the Thailand Research Fund (TRF) and the Commission on Higher Education (CHE).

Please cite this article in press as: R. Wongmaneerung, et al., J. Alloys Compd. (2008), doi:10.1016/j.jallcom.2008.10.152

## References

[1] G.A. Smolenskii, A.I. Agranovskaya, Sov. Phys. Tech. Phys. (Engl. Transl.) 3 (7) (1958) 1380.
[2] V.V. Kirillov, V.A. Isupov, Ferroelectrics 5 (1973) 3.
[3] E.P. Smirnova, O.V. Rubinshtein, B.A. Isupov, Ferroelectrics 143 (1993) 263.
[4] L.E. Cross, S.J. Jang, R.E. Newnham, K. Uchino, Ferroelectrics 23 (1980) 187.
[5] A.J. Moulson, J.M. Herbert, Electroceramics, 2nd ed., John Wiley & Sons, Chichester, 2003.
[6] G.H. Haertling, J. Am. Ceram. Soc. 82 (1999) 797.
[7] S.J. Jang, K. Uchino, S. Nomura, L.E. Cross, Ferroelectrics 27 (1980) 31.
[8] M. Lejeune, J.P. Boilot, Mater. Res. Bull. 20 (1985) 493.
[9] J.P. Guha, J. Mater. Sci. 36 (2001) 5219.
[10] P.A. Joy, K. Sreedhar, J. Am. Ceram. Soc. 80 (1997) 770.
[11] C.H. Lu, H.S. Yang, Mater. Sci. Eng. B 84 (2001) 159.
[12] S.L. Swartz, T.R. Shrout, Mater. Res. Bull. 17 (1982) 1245.
[13] Y.-C. Liou, J.-H. Chen, Ceram. Int. 30 (2004) 17.
[14] S. Ananta, Mater. Lett. 58 (2004) 2781.
[15] R. Wongmaneerung, T. Sarakonsri, R. Yimnirun, S. Ananta, Mater. Sci. Eng. B 132 (2006) 292.
[16] S. Ananta, N.W. Thomas, J. Eur. Ceram. Soc. 19 (1999) 155.
[17] W.E. Lee, W.M. Rainforth, Ceramic Microstructures Property Control by Processing, Chapman & Hall, London, 1994.
[18] Powder Diffraction File No. 81-861, International Centre for Diffraction Data, Newton Square, PA, 2000.
[19] S. Ananta, N.W. Thomas, J. Eur. Ceram. Soc. 19 (1999) 629.
[20] Powder Diffraction File No. 33-769, International Centre for Diffraction Data, Newton Square, PA, 2000.
[21] A. Mergen, W.E. Lee, J. Eur. Ceram. Soc. 17 (1997) 1033.
[22] J. Wang, X. Junmin, W. Dongmei, N. Weibeng, Solid State Ionics 124 (1999) 271.
[23] P. Lucas, W.T. Petuskey, J. Am. Ceram. Soc. 84 (9) (2001) 2150.
[24] E.R. Nielsen, E. Ringgaard, M. Kosec, J. Eur. Ceram. Soc. 22 (2002) 1847.
[25] A. Boutarfaia, Ceram. Int. 26 (2000) 583.
[26] A.L. Costa, C. Galassi, G. Fabbri, E. Roncari, C. Capiani, J. Eur. Ceram. Soc. 21 (2001) 1165.
[27] J.P. Guha, H.U. Anderson, J. Am. Ceram. Soc. 69 (1986) C-287.
[28] S. Ananta, Mater. Lett. 58 (2004) 2530.
[29] H. Klug, L. Alexander, X-Ray Diffraction Procedures for Polycrystalline and Amorphous Materials, 2nd ed., John Wiley & Sons Ltd., New York, 1974.
[30] L.B. Kong, J. Ma, W. Zhu, O.K. Tan, J. Mater. Sci. Lett. 20 (2001) 1241.
[31] M.F. Yan, H.C. Ling, W.W. Rhodes, J. Mater. Res. 4 (4) (1989) 930.
[32] E. Goo, T. Yamamoto, K. Okazaki, J. Am. Ceram. Soc. 68 (8) (1986) C-188.
[33] T. Yamamoto, H. Igarashi, K. Okazaki, Ferroelectrics 63 (1985) 281.
[34] S. Ananta, N.W. Thomas, J. Eur. Ceram. Soc. 19 (1999) 2917.
[35] O. Guillon, F. Thiebaud, D. Perreux, C. Courtoris, P. Champagne, A. Leriche, J. Crampon, J. Eur. Ceram. Soc. 25 (2005) 2421.
[36] L.E. Cross, Ferroelectrics 76 (1987) 241.
[37] L.E. Cross, Ferroelectrics 151 (1994) 305.
[38] H.-C. Wang, W.A. Schulze, J. Am. Ceram. Soc. 73 (4) (1990) 825.
[39] S.L. Swartz, T.R. Shrout, W.A. Schulze, L.E. Cross, J. Am. Ceram. Soc. 67 (5) (1984) 311.
[40] Z. Li, L. Zhang, X. Yao, J. Mater. Res. 16 (2001) 834.
[41] K. Uchino, S. Nomura, Ferroelectr. Lett. 44 (3) (1982) 55.
[42] M. Kuwabara, S. Takahashi, K. Goda, K. Oshima, K. Watanabe, Jpn. J. Appl. Phys. 31 (9B) (1992) 3241.
[43] V. Koval, C. Alemany, J. Briančin, H. Bruncková, J. Electroceram. 10 (2003) 19.
[44] R. Yimnirun, S. Ananta, P. Laoratanakul, J. Eur. Ceram. Soc. 25 (2005) 3235.
[45] Y.-C. Liou, L. Wu, S.S. Liou, Jpn. J. Appl. Phys. 33 (9B) (1994) L1320.
[46] K.R. Han, S. Kim, J. Mater. Sci. 35 (2000) 2055.

Please cite this article in press as: R. Wongmaneerung, et al., J. Alloys Compd. (2008), doi:10.1016/j.jallcom.2008.10.152

Current Applied Physics xxx (2009) xxx–xxx

Contents lists available at ScienceDirect

Current Applied Physics

journal homepage: www.elsevier.com/locate/cap

# Dielectric and ferroelectric properties of 0.8PZT–0.2PCN ceramics under sintering conditions variation

Anurak Prasatkhetragarn [a,*], Muangjai Unruan [b], Athipong Ngamjarurojana [b], Yongyut Laosiritaworn [b], Supon Ananta [b], Rattikorn Yimnirun [b], David P. Cann [c]

[a] Department of Materials Science, School of Science and Technology, Naresuan University at Phayao, Phayao 56000, Thailand
[b] Department of Physics, Faculty of Science, Chiang Mai University, Chiang Mai 50200, Thailand
[c] Materials Science, School of Mechanical, Industrial and Manufacturing Engineering, Oregon State University, Corvallis, OR 97331, USA

ARTICLE INFO

*Article history:*
Received 10 August 2008
Accepted 12 January 2009
Available online xxxx

*PACS:*
77.84.-s
77.84.Dy

*Keywords:*
PZT–PCN
Sintering conditions
Dielectric properties
Ferroelectric properties

ABSTRACT

The influences of sintering conditions on electrical properties of the $0.8Pb(Zr_{1/2}Ti_{1/2})O_3$–$0.2Pb(Co_{1/3}Nb_{2/3})O_3$ ceramics have been investigated with sintering temperatures of 1175, 1200, 1225, and 1250 °C and dwell times for 2, 6, and 10 h. The crystal structure of dense specimens showed coexistence between tetragonal, rhombohedral and pseudo cubic phases in all sintering temperatures, while tetragonal-rich phase appeared with increasing dwell times. A maximum dielectric constant was observed at sintering condition of 1200 °C for 2 h, while the transition temperature slightly increased with increasing dwell time. All ceramics also showed diffused phase transition behaviors with a minimum diffusivity at sintering condition of 1200 °C for 2 h. In addition, the polarization–electric field ($P$–$E$) hysteresis loops of the ceramic systems also changed significantly with sintering conditions. Interestingly, the ferroelectric parameters; remnant polarization ($P_r$) and loop squareness ($R_{sq}$) tended to increase with increasing sintering temperatures and dwell times.

© 2009 Elsevier B.V. All rights reserved.

## 1. Introduction

Ferroelectric and related materials continue to be exploited for numerous applications, including recent concepts of "smart" or "intelligent" systems, whereby multifunctional components are required [1]. Nowadays, substantial research and development has been devoted to ferroelectric materials consisting of relaxor and normal ferroelectrics have attracted great interest at the compositions close to the morphotropic phase boundary (MPB) because of their excellent dielectric, piezoelectric, and electrostrictive properties, which are useful in actuating and sensing applications [1,2]. Lead zirconate titanate, $Pb(Zr_xTi_{1-x})O_3$ or PZT ceramics have been investigated from both fundamental and applied viewpoints [2,3]. The MPB of PZT is located at a $PbTiO_3$:$PbZrO_3$ of 0.52:0.48 and separates the Ti-rich tetragonal phase from the Zr-rich rhombohedral phase [4]. Furthermore, the MPB composition has a high $T_c$ of 390 °C, which allows piezoelectric devices to be operated at relatively high temperatures. Most commercial PZT ceramics are designed in the vicinity of the MPB with various doping methods in order to achieve high properties [3,5–8]. Recently, many piezoelectric ceramic materials have been developed from binary systems containing a combination of relaxor and normal ferroelectric materials [3] that yield high dielectric permittivities {e.g., $Pb(Zr_{1/2}Ti_{1/2})O_3$–$Pb(Ni_{1/3}Nb_{2/3})O_3$ (PZT–PNN), and $Pb(Zr_{1/2}Ti_{1/2})O_3$–$Pb(Mg_{1/3}Nb_{2/3})O_3$ (PZT–PMN)} [5,6], excellent piezoelectric coefficients {e.g., $Pb(Zr_{1/2}Ti_{1/2})O_3$–$Pb(Zn_{1/3}Nb_{2/3})O_3$ (PZT–PZN)} [7], and high pyroelectric coefficients {e.g., $Pb(Ni_{1/3}Nb_{2/3})O_3$–$PbTiO_3$–$PbZrO_3$ (PNN–PT–PZ)} [8].

Lead cobalt niobate, $Pb(Co_{1/3}Nb_{2/3})O_3$ or PCN, which exhibits a perovskite structure and a Curie temperature of ≈−30 °C, is a relaxor ferroelectric material with a high dielectric constant [9,10]. On the basis of the above mentioned approach, solid solutions of PZT and PCN are expected to synergistically combine the properties of both the normal ferroelectric PZT and relaxor ferroelectric PCN, which could exhibit electrical properties that are better than those of the single-phase PZT and PCN [9–12]. Our previous investigation on $(1-x)$PZT–$(x)$PCN ceramic systems has already shown excellent electrical properties with the MPB at $x = 0.2$ [13]. Previously, the influences of sintering conditions on electrical properties have been extensively investigated in PZT [14], PZT–PMN [15,16], PZT–PZN [17], PMS–PZT [18], PMN–PNN–PZT [19], PCW–PMN–PZT [20], PZT–PMN–PZN [21], PFW–PT [22], KNN–ST [23], and BNT–BT [24]. However, there have been no systematic studies on the relationship between sintering temperature and dwell time variation on physical and electrical properties of ceramics within specific morphotropic phase boundary compositions of PZT and PCN. Therefore, the overall purpose of this

* Corresponding author. Tel.: +66 53 943367; fax: +66 53 943445.
*E-mail address:* Prasatkhetragarn@yahoo.com (A. Prasatkhetragarn).

1567-1739/$ - see front matter © 2009 Elsevier B.V. All rights reserved.
doi:10.1016/j.cap.2009.01.005

study is to examine the influence of sintering conditions on phase formation, microstructure, dielectric and ferroelectric properties of $0.8Pb(Zr_{1/2}Ti_{1/2})O_3$–$0.2Pb(Co_{1/3}Nb_{2/3})O_3$ ceramic systems.

## 2. Experimental procedure

The specimens studied were fabricated according to the formula: $0.8Pb(Zr_{1/2}Ti_{1/2})O_3$–$0.2Pb(Co_{1/3}Nb_{2/3})O_3$. Raw materials of PbO, $ZrO_2$, $TiO_2$, CoO, and $Nb_2O_5$ with >99% purity were used to prepare samples. The columbite $CoNb_2O_6$ and wolframite $ZrTiO_4$ precursors were weighed and introduced into the batch calculations. $CoNb_2O_6$ and $ZrTiO_4$ powders were prepared at calcination temperatures of 1100 and 1450 °C for 2 h, respectively [25,26]. In this work, the $0.8Pb(Zr_{1/2}Ti_{1/2})O_3$–$0.2Pb(Co_{1/3}Nb_{2/3})O_3$ samples were prepared from PbO, $ZrTiO_4$, and $CoNb_2O_6$ powders using the solid-state reaction of these raw materials. The powders were mixed by a vibratory–milling technique in ethanol for 6 h. After drying, the product was calcined in an alumina crucible at a temperature of 950 °C [25]. The calcined powders were uniaxially cold-pressed at 5000 psi into disc-shaped pellets with a diameter of 12.7 mm and a thickness of 1 mm, with 3 wt% poly (vinyl alcohol) (PVA) added as a binder. Following binder burnout at 500 °C, the pellets were sintered at various sintering temperatures of 1175, 1200, 1225, and 1250 °C for 2, 6, and 10 h with fixed heating/cooling rate of 5 °C/min.

The phase structure of the powders was analyzed via X-ray diffraction (XRD; Bruker-AXS D8). The microstructures of the sintered samples were examined using scanning electron microscopy (SEM; JEOL JSM-840A). The dielectric properties of the samples were measured using Agilent 4284A LCR meter over a wide temperature range using a NorECS ProboStat high temperature measurement cell. The room temperature ferroelectric properties were examined using a simple Sawyer–Tower circuit at fixed measuring frequency of 50 Hz.

## 3. Results and discussions

Perovskite phase formation and crystal structure were determined by XRD at room temperature. The XRD patterns of $0.8Pb(Zr_{1/2}Ti_{1/2})O_3$–$0.2Pb(Co_{1/3}Nb_{2/3})O_3$ ceramics with various sintering temperatures and dwell times are shown in Figs. 1 and 2, respectively, showing perovskite structure for all compositions. The pyrochlore phase is not observed in this system. For sintering temperature variation, sintered ceramics with various sintering temperature of 1175, 1200, 1225 and 1250 °C are correlated with JCPDS file number 70-4057, as displayed in Fig. 1a. In the XRD patterns, the crystal structure of all specimens appears coexistence between tetragonal and pseudo cubic phases in 0.8PZT–0.2PCN system. As shown in Fig. 1b, XRD peak profiles of the (002)/(200) peaks of tetragonal phase and (200) peak of pseudo cubic phase appeared around $2\theta$ of ≈44°–45°. However, a separate peak at (111) peak, as shown in Fig. 1a, confirmed that the rhombohe-

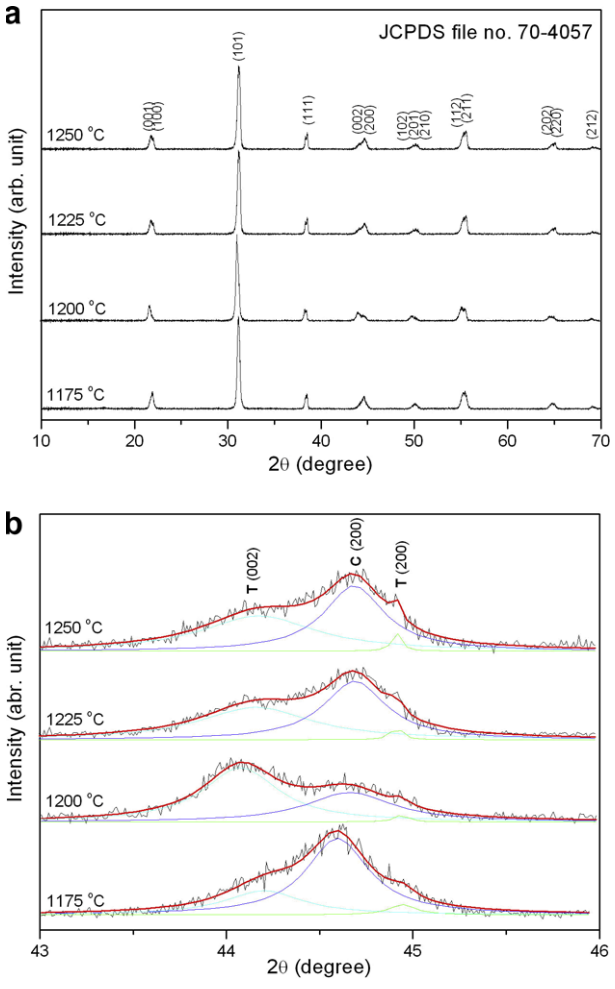



**Fig. 1.** XRD patterns of $0.8Pb(Zr_{1/2}Ti_{1/2})O_3$–$0.2Pb(Co_1/3Nb_{2/3})O_3$ ceramics with; (a) sintering temperature of 1175, 1200, 1225 and 1250 °C and (b) coexistence of T(002), T(200) and C(200) peaks profile.

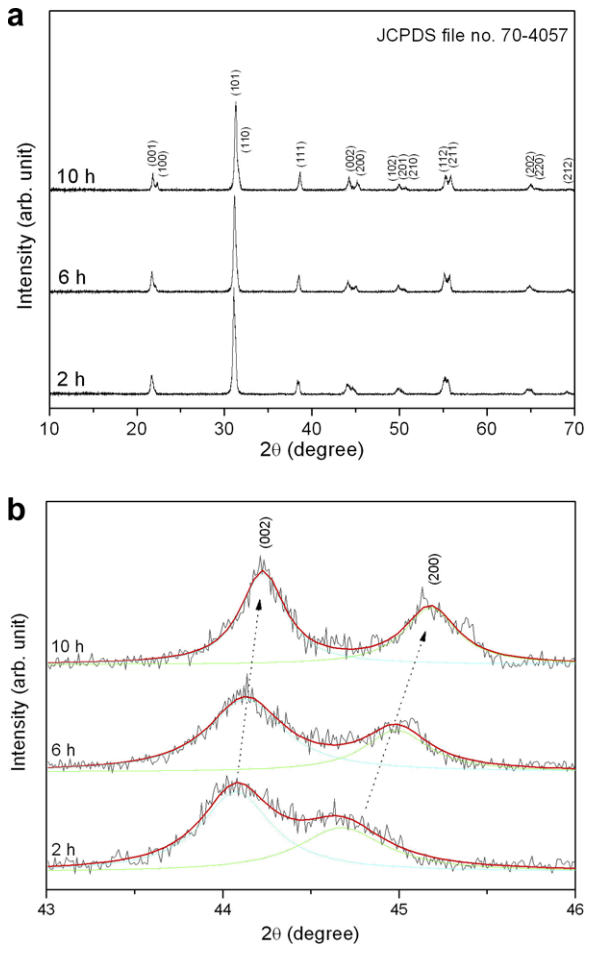



**Fig. 2.** XRD patterns of $0.8Pb(Zr_{1/2}Ti_{1/2})O_3$–$0.2Pb(Co_{1/3}Nb_{2/3})O_3$ ceramics with; (a) dwell times for 2, 6, and 10 h and (b) the (002)/(200) peaks profile with various dwell times.

Please cite this article in press as: A. Prasatkhetragarn et al., Dielectric and ferroelectric properties of 0.8PZT–0.2PCN ceramics under ..., Curr. Appl. Phys. (2009), doi:10.1016/j.cap.2009.01.005

dral phase is also observed in this system with increasing sintering temperature. It should be noticed that this ceramic system shows coexistence of tetragonal, rhombohedral, and pseudo cubic phases. For samples with fixed sintering temperature of 1200 °C and dwell times variations for 2, 6 and 10 h, the XRD patterns also show single-phase without pyrochlore phase, as shown in Fig. 2a. The tetragonal-rich phase is observed with increasing dwell time for 6 and 10 h, indicating the structural change in 0.8PZT–0.2PCN system, as shown in Fig. 2b. Clearly, these observations show that the sintering conditions have affected the crystal structure of 0.8PZT–0.2PCN ceramics. Previously, a similar behavior was also observed with increasing sintering temperatures in PZT, PZT–PMN, PZT–PZN, PZT–PNN, PMS–PZT, PMN–PNN–PZT, PZT–PMN–PZN, PCW–PMN–PZT, PZT–PMWSN, and PFW–PT [14–22,27].

Effects of sintering conditions on the microstructure of the $0.8Pb(Zr_{1/2}Ti_{1/2})O_3$–$0.2Pb(Co_{1/3}Nb_{2/3})O_3$ ceramics are displayed in Fig. 3. The grain size of the ceramics varies considerably from 0.57 to 13.76 μm, as listed in Table 1. The average grain size and density of this ceramics tend to increases with increasing sintering temperatures and dwell times probably due to the grain growth is

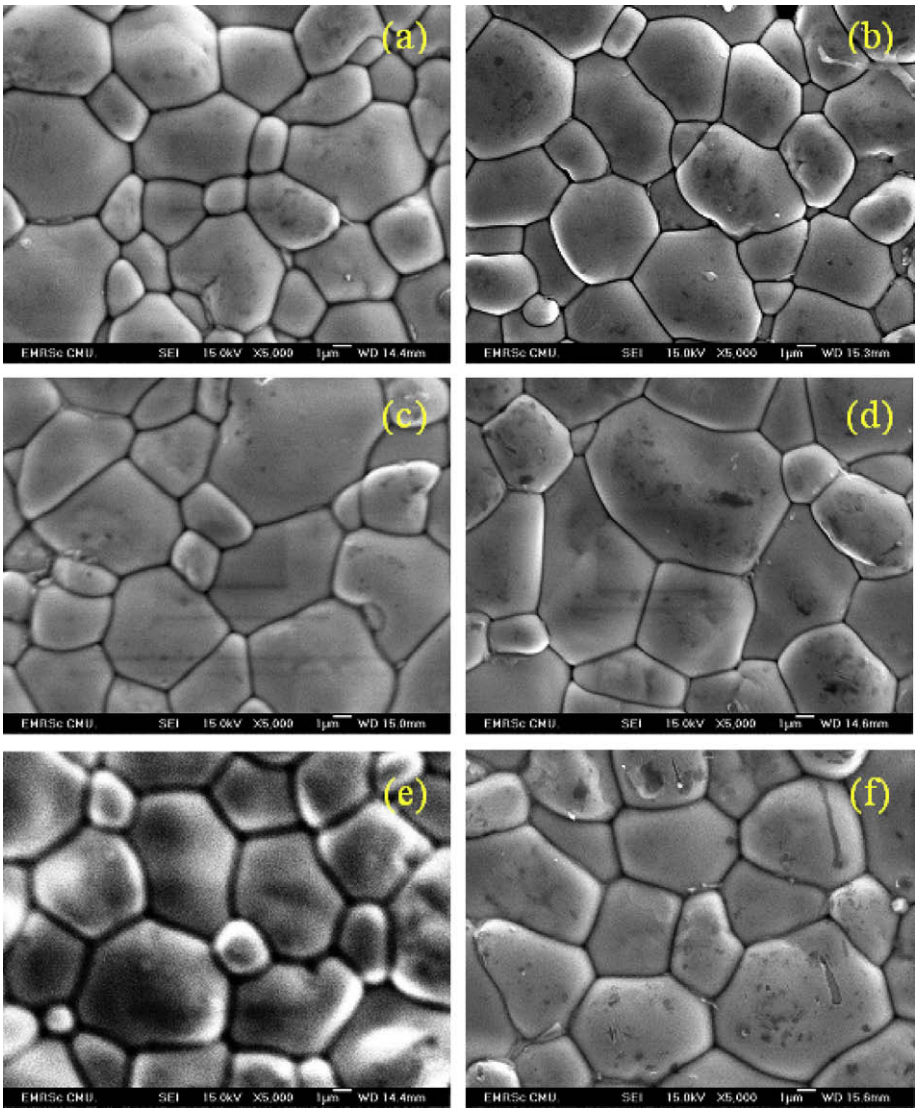



**Fig. 3.** SEM micrographs of $0.8Pb(Zr_{1/2}Ti_{1/2})O_3$–$0.2Pb(Co_{1/3}Nb_{2/3})O_3$ with various sintering temperatures of (a) 1175, (b) 1200, (c) 1225, (d) 1250, and various dwell times for (e) 6 h and (f) 10 h.

**Table 1**
Physical properties of 0.8PZT–0.2PCN ceramics at various sintering condition.

| Sintering conditions | | Density ($g/cm^3$) | Grain size range (μm) | Average grain size (μm) |
|---|---|---|---|---|
| Temperature (°C) | Dwell time (h) | | | |
| 1175 | 2 | 7.89 ± 0.05 | 0.57–10.31 | 4.19 |
| 1200 | 2 | 7.91 ± 0.05 | 0.81–9.67 | 4.55 |
| 1225 | 2 | 7.93 ± 0.05 | 1.29–12.24 | 5.95 |
| 1250 | 2 | 7.94 ± 0.05 | 1.71–13.76 | 7.94 |
| 1200 | 6 | 7.92 ± 0.05 | 1.95–10.43 | 5.05 |
| 1200 | 10 | 7.94 ± 0.05 | 0.81–12.00 | 5.97 |

Please cite this article in press as: A. Prasatkhetragarn et al., Dielectric and ferroelectric properties of 0.8PZT–0.2PCN ceramics under ..., Curr. Appl. Phys. (2009), doi:10.1016/j.cap.2009.01.005

controlled by boundary diffusion [28]. This indicates that the sintering process can enhance the diffusion mechanism and promote the densification of the sample with higher relative density [28]. Therefore, the grain size and density of PZT–PCN ceramics strongly depend on the sintering conditions. This trend is similar to those reported in the literature [14–24,27].

Temperature dependences of the dielectric constant ($\varepsilon_r$) and dielectric loss tangent (tan $\delta$) of the $0.8Pb(Zr_{1/2}Ti_{1/2})O_3$–$0.2Pb(Co_{1/3}Nb_{2/3})O_3$ ceramics at various sintering temperatures of 1175, 1200, 1225, and 1250 °C and dwell times for 2, 6,and 10 h are displayed in Figs. 4 and 5, respectively. The maximum dielectric constant ($\square_{max}$) at 1 kHz is also listed in Table 2. For sintering temperature variation, the $\square_{max}$ tends to increase from 28300 at 1175 °C up to 64500 at 1200 °C and then decrease to 39200 at 1250 °C, while tan $\delta$ tends to increase with increasing sintering temperature, clearly indicating that the sintering temperature has strong influence on the optimum dielectric properties of 0.8PZT–0.2PCN system. In addition, a clear transition in $T_{max}$ (defined as the temperature at which $\square_r$ is maximum at 1 kHz) is observed. It is noticed that an increased sintering temperature does not significantly change $T_{max}$ of the ceramics, as shown in Table 2. At fixed sintering temperature of 1200 °C, and various dwell times for 2, 6, and 10 h, the dielectric constant shows maxima at 2 h dwell time, and then decreases with increasing dwell times. While board peaks at $\square_{max}$ have been observed, $T_{max}$ shows slightly

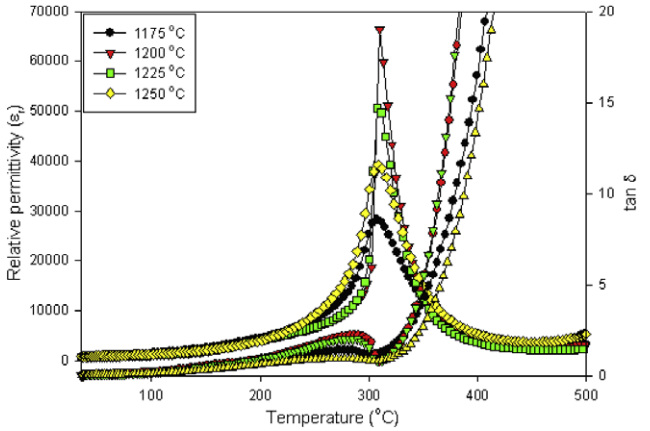



**Fig. 4.** Temperature dependences of dielectric properties of $0.8Pb(Zr_{1/2}Ti_{1/2})O_3$–$0.2Pb(Co_{1/3}Nb_{2/3})O_3$ at various sintering temperature with fixed dwell time for 2 h and heating/cooling rates of 5 °C/min.

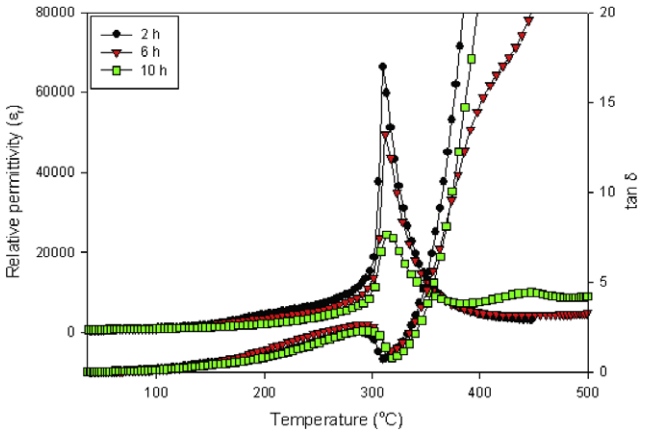



**Fig. 5.** Temperature dependences of dielectric properties of $0.8Pb(Zr_{1/2}Ti_{1/2})O_3$–$0.2Pb(Co_{1/3}Nb_{2/3})O_3$ with various dwell times (sintered at 1200 °C and heating/cooling rates of 5 °C/min).

**Table 2**
Dielectric properties of 0.8PZT–0.2PCN ceramics at various sintering conditions.

| Sintering conditions | | Dielectric properties (at 1 kHz) | | | | | | |
|---|---|---|---|---|---|---|---|---|
| Temperature (°C) | Dwell time (h) | $T_{max}$ (°C) | $\varepsilon_{RT}$ | tan $\delta$ | $\varepsilon_{max}$ | tan $\delta$ | $\gamma$ | $\delta$ |
| 1175 | 2 | 308 | 983 | 0.0552 | 28300 | 0.419 | 1.73 | 16.52 |
| 1200 | 2 | 309 | 929 | 0.0467 | 64500 | 0.73 | 1.49 | 15.28 |
| 1225 | 2 | 309 | 880 | 0.042 | 51000 | 1.11 | 1.73 | 16.08 |
| 1250 | 2 | 309 | 716 | 0.0418 | 39200 | 1.089 | 1.81 | 16.81 |
| 1200 | 6 | 312 | 778 | 0.0382 | 49500 | 1.26 | 1.55 | 15.4 |
| 1200 | 10 | 315 | 736 | 0.0432 | 24600 | 0.808 | 1.62 | 15.71 |

increase with increasing dwell time, probably caused by a shift to a tetragonal-rich phase composition as shown in Fig. 2. Similar behavior is also reported in previous works [15,17,21,22,24,28].

To further understand the dielectric behavior of the 0.8PZT–0.2PCN ceramic with various sintering conditions, the permittivity of a first-order normal ferroelectric can be described by the Curie–Weiss law and a second-order relaxor ferroelectric can be described by a simple quadratic law [29]. The relative permittivity can then be derived via using

$$\frac{\varepsilon_m}{\varepsilon(f,T)} = 1 + \frac{(T - T_m(f))^{\gamma}}{2\delta^2} \quad (1)$$

where $\varepsilon_m$ is the maximum value of the permittivity at $T = T_m(f)$. The value of $\gamma$ is the expression of the degree of dielectric relaxation, while $\delta$ is used to measure the degree of diffuseness of the phase transition. In a material with a "pure" diffuse phase transition, $\gamma$ is expected to be 2 [30]. As listed in Table 2, the values of $\gamma$ vary with sintering conditions between 1.49 and 1.81, which confirms that diffuse phase transition occurs in the 0.8PZT–0.2PCN ceramics. It is important to note that in perovskite ferroelectrics it has been established that $\gamma$ and $\delta$ can be affected by sintering conditions and structure of the materials. The values of $\gamma$ and $\delta$ decrease with increasing sintering temperature from 1175 to 1200 °C, and then increase when sintering temperature increases further, as shown in Table 2. For dwell time variation, the values of $\gamma$ and $\delta$ tend to increase with increasing dwell time as also shown in Table 2. However, the results show minimum $\gamma$ and $\delta$ values at sintering temperature of 1200 °C and dwell times for 2 h. It is interesting to observe that the phase transition is least diffused at this optimized sintering condition, possibly due to a sharp increase of dielectric permittivity at MPB. A similar behavior has also been observed in PZT–PNN and PZT–PMN systems [5,6].

The polarization–electric field ($P$–$E$) hysteresis loops of $0.8Pb(Zr_{1/2}Ti_{1/2})O_3$–$0.2Pb(Co_{1/3}Nb_{2/3})O_3$ ceramics measured at 15 kV/cm are presented in Figs. 6 and 7. To assess effect of sintering conditions on ferroelectric characteristics of 0.8PZT–0.2PCN ceramics, the ferroelectric parameters have been extracted from the experimental data, as summarized in Table 3. For sintering temperature variation, the remnant polarization ($P_r$) increases with increasing sintering temperature. However, the largest remnant polarization at sintering temperature of 1250 °C could be caused by effects of grain size, which reaches maximum in this condition [23], as listed in Table 1. However, with fixed sintering temperature at 1200 °C and various dwell times, the $P_r$ also increases with increasing dwell times, while $E_c$ shows the same behavior as in sintering temperature variation case. Furthermore, the ferroelectric characteristics can be assessed with the hysteresis loop squareness ($R_{sq}$) [25], which can be calculated from the empirical expression $R_{sq} = (P_r/P_s) + (P_{1.1Ec}/P_s)$, where $P_s$ is the saturated polarization obtained at some finite field strength below the dielectric breakdown and $P_{1.1Ec}$ is the polarization at the field equal to $1.1E_c$. For the ideal square loop, $R_{sq}$ is equal to 2.00 [31]. As listed in Table 3, the loop squareness parameter $R_{sq}$ increases to 1.47 at sintering tempera-

Please cite this article in press as: A. Prasatkhetragarn et al., Dielectric and ferroelectric properties of 0.8PZT–0.2PCN ceramics under ..., Curr. Appl. Phys. (2009), doi:10.1016/j.cap.2009.01.005

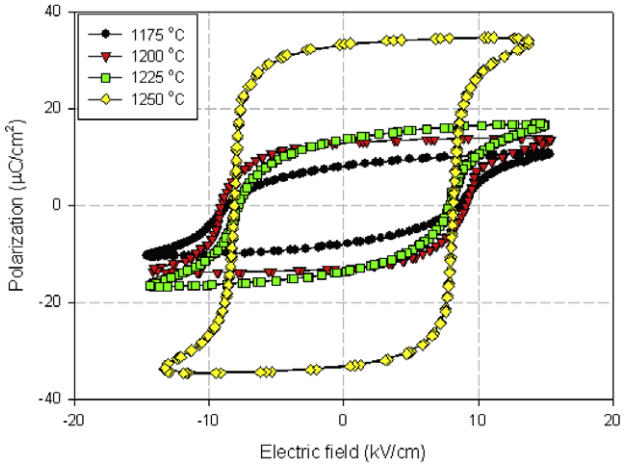



**Fig. 6.** *P–E* loops of $0.8Pb(Zr_{1/2}Ti_{1/2})O_3$–$0.2Pb(Co_{1/3}Nb_{2/3})O_3$ at various sintering temperatures with fixed dwell time for 2 h and heating/cooling rates of 5 °C/min.

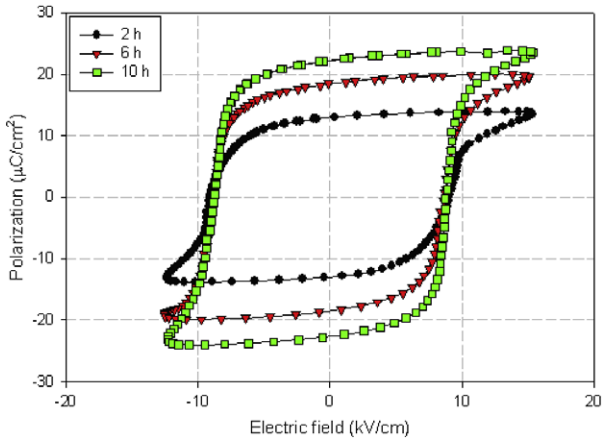



**Fig. 7.** *P–E* loops of $0.8Pb(Zr_{1/2}Ti_{1/2})O_3$–$0.2Pb(Co_{1/3}Nb_{2/3})O_3$ with various dwell times (sintered at 1200 °C and heating/cooling rates of 5 °C/min).

**Table 3**
Ferroelectric properties of 0.8PZT–0.2PCN ceramics at various sintering conditions.

| Sintering conditions | | Ferroelectric Properties | | | | | |
|---|---|---|---|---|---|---|---|
| Temperature (°C) | Dwell time (h) | $P_r$ (μC/cm²) | $P_s$ (μC/cm) | $E_c$ (kV/cm) | $P_r/P_{max}$ | $E_c/E_{max}$ | Loop squareness ($R_{sq}$) |
| 1175 | 2 | 8.06 | 10.73 | 8.7 | 0.75 | 0.58 | 1.06 |
| 1200 | 2 | 12.91 | 13.88 | 9.13 | 0.93 | 0.61 | 1.47 |
| 1225 | 2 | 13.61 | 16.79 | 7.84 | 0.81 | 0.53 | 1.16 |
| 1250 | 2 | 33.29 | 34.43 | 8.14 | 0.97 | 0.59 | 1.58 |
| 1200 | 6 | 18.46 | 19.99 | 8.76 | 0.92 | 0.58 | 1.48 |
| 1200 | 10 | 22.33 | 23.91 | 8.85 | 0.93 | 0.58 | 1.53 |

ture of 1200 °C and dwell time for 2 h. However, larger $R_{sq}$ value at 1250 °C could be due to easy polarization rotation in the MPB region with coexistence of the tetragonal and pseudo cubic phase and/or effects of maximum grain size in this sintering condition. Similar behavior is also reported in PZT–PMN and PZT–PZN [32,33].

## 4. Conclusions

In this study, the influence of sintering conditions on phase formation and electrical properties of the $0.8Pb(Zr_{1/2}Ti_{1/2})O_3$–$0.2Pb(Co_{1/3}Nb_{2/3})O_3$ ceramics with various sintering temperature of 1175, 1200, 1225, and 1250 °C and dwell times for 2, 6, and 10 h have been investigated. The XRD analysis indicates that the tetragonal, pseudo cubic and rhombohedral phases coexist for all compositions sintered at various temperatures, while the tetragonal-rich phase appears with increasing dwell time. The surface micrographs show that average grain size increases with increasing sintering temperature and dwell time. At 1 kHz, the maximum dielectric constant ($\varepsilon_{max}$) of 64500 is observed in ceramics sintered at 1200 °C for 2 h, while the diffusivity ($\gamma$) and diffuseness parameter ($\delta$) reach minima. Moreover, the ferroelectric parameters; remnant polarization ($P_r$) and loop squareness ($R_{sq}$) increase with increasing sintering temperatures and dwell times, while coercive field ($E_c$) does not show specific trend. Finally, this study shows that the sintering conditions play critical role on physical and electrical properties of the PZT–PCN ceramics.

## Acknowledgements

The authors wish to express profound gratitude to Materials Science Groups, Oregon State University for ceramics preparation and measurement. This work was supported by the Commission on Higher Education (CHE), the Thailand Research Fund (TRF), the Faculty of Science, the Graduate School of Chiang Mai University, and Naresuan University Phayao.

## References

[1] G.H. Haertling, J. Am. Ceram. Soc. 82 (1999) 797.
[2] A.J. Moulson, J.M. Herbert, Electroceramics: Materials Properties Applications, Wiley, Chichester, UK, 2003.
[3] L.E. Cross, Mater. Chem. Phys. 43 (1996) 108.
[4] S.-E. Park, T.R. Shrout, IEEE Trans. Ultrason. Ferroelectr. Freq. Control. 44 (1997) 1140.
[5] N. Vittayakorn, G. Rujijanagul, X. Tan, M.A. Marquardt, D.P. Cann, J. Appl. Phys. 96 (2004) 5103.
[6] R. Yimnirun, S. Ananta, P. Laoratanakul, J. Eur. Ceram. Soc. 25 (2005) 3235.
[7] H. Fan, G.T. Park, J.J. Choi, J. Ryu, H.E. Kim, J. Mater. Res. 17 (2002) 180.
[8] D. Luff, R. Lane, K.R. Brown, H.J. Marshallsay, Trans. J. Br. Ceram. Soc. 73 (1974) 251.
[9] M. Unruan, N. Vittayakorn, R. Wongmaneeruang, A. Prasatkhetragarn, S. Ananta, R. Yimnirun, J. Alloy Compd., in press.
[10] T. Hachiga, S. Fujimoto, N. Yasuda, J. Phys. D 20 (1987) 1291.
[11] T. Kudo, T. Yazaki, F. Naito, S. Sugaya, J. Am. Ceram. Soc. 53 (1970) 326.
[12] Z. Brankovic, G. Brankovic, J.A. Varela, J. Mater. Sci. 14 (2003) 37.
[13] A. Prasatkhetragarn, P. Ketsuwan, M. Unruan, A. Ngamjarurojana, S. Ananta, R. Yimnirun, D.P. Cann, Mater. Lett., submitted for publication.
[14] H. Maiwa, O. Kimura, K. Shoji, H. Ochiai, J. Eur. Ceram. Soc. 25 (2005) 2383.
[15] J. Yue, M. Leung, E. Haemmerle, M. Hodgson, G. Li, W. Gao, J. Alloy Compd., in press.
[16] J. Yoo, C. Lee, Y. Jeong, K. Chung, D. Lee, D. Paik, Mater. Chem. Phys. 90 (2005) 386.
[17] Y.D. Hou, M.K. Zhu, H. Wang, B. Wang, H. Yan, C.S. Tian, Mater. Lett. 58 (2004) 1508.
[18] Z.G. Zhu, B.S. Li, G.R. Li, W.Z. Zhang, Q.R. Yin, Mater. Sci. Eng. B 117 (2005) 216.
[19] Y. Jeong, J. Yoo, S. Lee, J. Hong, Sensor Actuator A 135 (2007) 215.
[20] K. Chung, J. Yoo, C. Lee, D. Lee, Y. Jeong, H. Lee, Sensor Actuator A 125 (2006) 340.
[21] C.H. Wang, S.J. Chang, P.C. Chang, Mater. Sci. Eng. B 111 (2004) 124.
[22] C.S. Hong, S.Y. Chu, W.C. Su, R.C. Chang, H.H. Nien, Y.D. Juang, J. Alloy Compd. 459 (2008) 1.
[23] R.C. Chang, S.Y. Chu, Y.P. Wong, C.S. Hong, H.H. Huang, J. Alloy Compd. 456 (2008) 308.
[24] L. Liu, H. Fan, S. Ke, X. Chen, J. Alloy Compd. 458 (2008) 504.
[25] A. Prasatkhetragarn, N. Vittayakorn, S. Ananta, R. Yimnirun, D.P. Cann, Jpn. J. Appl. Phys. 47 (2008) 998.
[26] A. Prasatkhetragarn, R. Yimnirun, S. Ananta, Ferroelectrics 356 (2007) 203.
[27] J.H. Cho, I.K. Park, H.G. Kim, H.T. Chung, J. Am. Ceram. Soc. 80 (1997) 1523.
[28] C.Y. Chen, Y. Hu, H.L. Lin, Mater. Chem. Phys. 99 (2006) 26.
[29] A.A. Bokov, Z.G. Ye, Solid State Commun. 116 (2000) 105.
[30] Y.-M. Chiang, D.P. Birnie, W.D. Kingery, Physical Ceramics, Wiley, Chichester, UK, 1997. p. 522.
[31] G.H. Haertling, W.J. Zimmer, Am. Ceram. Soc. Bull. 45 (1966) 1084.
[32] S. Wongsaenmai, Y. Laosiritaworn, S. Ananta, R. Yimnirun, Mater. Sci. Eng. B (2005).
[33] N. Vittayakorn, G. Rujijanagul, D.P. Cann, J. Alloy. Compd. 440 (2007) 259.

# Dielectric Properties of Complex Perovskite PZBT-PMNT Ceramic Under Compressive Stress

**Rattikorn Yimnirun*, Muangjai Unruan, Rewadee Wongmaneerung, Orawan Khamman, Wanwilai Chaisan, and Supon Ananta**

Department of Physics, Faculty of Science, Chiang Mai University,

Chiang Mai 50200, Thailand

*Author for Correspondence, E-mail: rattikornyimnirun@yahoo.com

## ABSTRACT

Effects of compressive stress on the dielectric properties of complex perovskite PZBT-PMNT ceramic were investigated. The dielectric properties measured under stress-free condition showed a composite nature with two distinct temperatures of dielectric maximum associated with PZBT and PMNT. The dielectric properties under the compressive stress were observed at stress levels up to 230 MPa using a homebuilt compressometer. The results clearly showed that the superimposed compression load significantly reduced both the dielectric constant and the dielectric loss tangent in every measuring frequency. The change of the dielectric constant with stress was attributed to competing influences of the intrinsic contribution of non-polar matrix and the extrinsic contribution of re-polarization and growth of micro-polar regions, while the clamping of the domain walls contributed to the change in dielectric loss tangent with stress. Finally, the stress induced decrease in switchable part of spontaneous polarization was seen as a cause for a large drop of the dielectric constant after a stress cycle.

**Keywords:** Dielectric Properties, PZBT-PMNT, Stress

## 1. INTRODUCTION

Complex perovskite ferroelectric ceramics have been studied extensively because they can be applied in several micro- and nano-electronic devices such as multilayer capacitors, microactuators and miniaturized transducers [1-5]. Among them, barium titanate ($BaTiO_3$ or BT), lead titanate ($PbTiO_3$ or PT), lead zirconate titanate ($Pb(Zr_{1-x}Ti_x)O_3$ or PZT), lead magnesium niobate ($Pb(Mg_{1/3}Nb_{2/3})O_3$ or PMN) ceramics and a variety of their solid solutions have been investigated extensively and continuously since the late 1940s [1,3,4]. Two of the most studied ferroelectric compounds, PZT and BT ceramics are representative perovskite piezoelectric and ferroelectric prototypes, respectively, because of their excellent electrical properties. While BT has a high dielectric constant with a relatively low Curie temperature ($T_C$) (~120 ºC), PZT has a higher $T_C$ of 390 ºC which allows PZT-based piezoelectric devices to be operated at relatively higher temperatures [2,4]. Although BT ceramic has better mechanical properties than PZT, the sintering temperature is also higher [1,3,6]. Thus, mixing PZT with BT is expected to decrease the sintering temperature of BT-based ceramics while maintaining excellent dielectric properties. Our earlier studies have already revealed the optimized electrical properties in 0.5PZT-0.5BT ceramic with $\varepsilon_r \sim 4000$ at $T_C$ of 160 ºC [7,8].

Another family of ferroelectric materials which are of great interest due to their high polarizabilities is lead-based relaxor ferroelectrics. PMN has very good dielectric properties [2,3,5]. However, the temperature related to the maximum dielectric constant ($T_{max}$) of PMN is very low (~ -10°C) [5]. Therefore, PT is systematically added to PMN to enhance the dielectric properties of PMN (as well as increasing $T_{max}$). In particular, 0.9PMN-0.1PT ceramics, which have $T_{max} \sim 40$ °C and $\varepsilon_{r,max} > 20000$, have been a subject of many investigations and, more importantly, have been widely

applied for capacitor, actuator and transducer applications [9-12]. However, since there have always been a need to obtain ceramic with board dielectric peak and maximum dielectric constant for various applications, especially in capacitive components [2-5], and with the complimentary characteristics between 0.5PZT-0.5BT and 0.9PMN-0.1PT ceramics, it is expected that excellent dielectric properties can be obtained from a mixture composition of the two ceramics. It is, therefore, one of the aims of this study to explore the dielectric properties of the mixture composition of 0.5PZT-0.5BT and 0.9PMN-0.1PT.

In most applications, however, ceramics are often subjected to mechanical loading, either deliberately in the design of the device itself or because the device is used to change shapes as in many smart structure applications or the device is used under environmental stresses [13-15]. A prior knowledge of how the materials behave under different load conditions is therefore very crucial for proper design of a device and for suitable selection of materials for a specific application. Therefore, it is very important to determine the properties of the materials as a function of applied stress. Previous investigations on the stress-dependence dielectric and electrical properties of many ceramic systems, such as PZT, PMN-PZT, and PMN-PT have clearly emphasized the importance of the subject [15-22]. Therefore, the major aim of this study is to investigate the influences of the compressive stress on the dielectric properties of complex perovskite PZBT-PMNT ceramic.

## 2. EXPERIMENTAL DETAILS

The ceramic composition with a formula $[0.5Pb(Zr_{0.52}Ti_{0.48})O_3–0.5BaTiO_3]$-$[0.9Pb(Mg_{1/3}Nb_{2/3})O_3\text{-}0.1PbTiO_3]$ (abbreviated as PZBT-PMNT hereafter) was selected for this study as outlined above. The PZBT-PMNT powders were prepared

from $0.5Pb(Zr_{0.52}Ti_{0.48})O_3–0.5BaTiO_3$ (abbreviated as PZBT hereafter) and $0.9Pb(Mg_{1/3}Nb_{2/3})O_3$-$0.1PbTiO_3$ (abbreviated as PMNT hereafter) starting powders via a simple mixed-oxide method [7,23]. The detailed descriptions of the PZBT and PMNT powders processing and characterization were presented elsewhere and will not be discussed here [7,8,23]. The PZBT-PMNT ceramics were then fabricated via the same mixed-oxide method. After mixing the powders by ball-milling method and drying process, the mixed powders were pressed hydraulically to form disc-shaped pellets 10 mm in diameter and 2 mm thick, with 3 wt.% polyvinyl alcohol as a binder. The pellets were placed on the alumina powder-bed inside alumina crucible and surrounded with atmosphere powders of the same composition. Finally, the pellets were sintered at 1250 °C for 2 h.

For dielectric property characterizations, the sintered samples were lapped to obtain parallel faces disc-shaped specimens with diameter of 8 mm and thickness of 1 mm, and the faces were then coated with silver paint as electrodes. The samples were then heat-treated at 750 °C for 12 min to ensure the contact between the electrodes and the ceramic surfaces. The samples were subsequently poled in a silicone oil bath at a temperature of 120 °C by applying a dc field of 20 kV/cm for 30 min and then field-cooled to room temperature. The dielectric properties of the sintered ceramics were studied under stress-free condition as functions of both temperature and frequency with an automated dielectric measurement system. The capacitance and the dielectric loss tangent were determined over the temperature range of 25 and 400 °C with the frequency ranging from 1 kHz to 5 MHz. The measurements were carried out on cooling continuously at the rate of 3 °C/min. To study the effects of the compressive stress on the dielectric properties, the compressometer was constructed [20,24]. The dielectric properties were measured by LCR-meter (Instrek LCR-821). The room

temperature (25 °C) capacitance and the dielectric loss tangent were obtained at frequency range 10 to 200 kHz under the compressive stress levels up to 230 MPa. The dielectric constant was then calculated from a parallel-plate capacitor equation, e.g. $\varepsilon_r = Cd/\varepsilon_0 A$, where C is the capacitance of the specimens, d and A are, respectively, the thickness and the area of the electrode, and $\varepsilon_0$ is the dielectric permittivity of vacuum ($8.854 \times 10^{-12}$ F/m).

## 3. RESULTS AND DISCUSSION

The stress-free dielectric properties, e.g. dielectric constant ($\varepsilon_r$) and tan $\delta$, as functions of both temperature and frequency are plotted in Fig. 1. It is clearly seen that there are two distinct dielectric anomalies. The first dielectric peak at lower temperature region with higher dielectric constant is associated with the PMNT component, which has $T_{max}$ near 40 ºC [12]. A strong dielectric dispersion below $T_{max}$ also indicates a relaxor ferroelectric behavior. In this case, the temperatures of maximum dielectric constant and dielectric loss tangent are shifted to higher temperature with increasing frequency. The maximum value of the dielectric constant decreases with increasing frequency, while that of the dielectric loss tangent increases. The dielectric properties then become frequency independence above the transition temperature [25,26]. Even though these descriptions are not clearly seen on the first dielectric peak because of the appearance of the second dielectric peak, it could still be said that the relaxor behavior exists. The second dielectric peak occurs over temperature range 150-200 ºC, which should be associated with the PZBT component with $T_C$ near 162 ºC [7,8]. A diffuse phase transition with small frequency dispersion of the dielectric maxima is also observed within this second dielectric peak, similar to earlier reported observation for the PZBT component [8]. These observations of the two distinct dielectric peaks

should indicate the composite nature of the PZBT-PMNT ceramic. Moreover, it should also be noted that significant increase in the dielectric constant dielectric loss at high temperatures is a result of thermally activated space charge conduction [25,26].

The fractional changes of the dielectric properties of the PZBT-PMNT ceramic under the compressive stress during loading and unloading are shown in Figs. 2 and 3. There is a significant change of the dielectric properties of the ceramic with increasing stress from 0 to 230 MPa and returning to stress-free condition. As seen in Fig. 2, the dielectric constant decreases monotonically with increasing the compressive stress, then increases only slightly when the compressive stress is gradually removed. The changing of the dielectric constant with increasing and decreasing the applied stress does not follow the same path. In every frequency, the dielectric constant with increasing the compressive stress is larger in value than that with decreasing stress. It is also of interest to see that the stress-free dielectric constant value decreases significantly after a stress cycle. It can be seen very clearly that the dielectric constant decreases as much as 25% at the maximum applied stress and only returns to slightly less than 85% of its original value when the stress is removed. As displayed in Fig. 3, though following a similar trend, the change in the dielectric loss tangent value is less significant, as it only decreases about 10-20% at the maximum stress and almost returns to its original value after a stress cycle. Similar observations have been reported for other ceramic systems, such as BT, PZT, PMN, PMN-PT and PMN-PZT [17,20,22,27-28]. It should also be noted that since the dielectric constant of the sample was measured through the capacitance, there is a change of sample capacitance due to the geometrical deformation under stress. The variation of the sample dielectric constant ($\Delta\varepsilon_r$) can be expressed as $\varepsilon_r * X * ((1+2\upsilon)/E)$, where X is the applied stress, $\upsilon$ is the Poisson's ratio, and E is the Young's modulus [29,30]. By applying the estimated

values of $\upsilon \sim 0.3$ and $E \sim 100$ GPa for the ceramic [15,16,18,22,31] and $\varepsilon_r \sim 4000$, it can be estimated that at the maximum stress of 230 MPa, the variation of the sample dielectric constant due to the geometrical deformation is < 0.5%. Therefore, this variation should not be an important factor in the variation of the dielectric constant under stress observed in Fig. 2.

To understand these experimental results, at least qualitatively, various effects have to be considered. Normally, the properties of ferroelectric materials are derived from both the intrinsic contribution of domains and extrinsic contributions of re-polarization and growth of micro-polar regions [16,17,20,22,27,28]. When a compressive stress is applied to the ferroelectric materials, the domain structure in the materials will change to maintain the domain energy at a minimum; during this process some of the domains engulf other domains or change shape irreversibly. Under the applied stress, the domain structure of ferroelectric ceramics may undergo domain switching through non-180° domain walls, de-aging, clamping of domain walls, and stress induced decrease in switchable part of spontaneous polarization [21,27,31,32,33].

The situation for the PZBT-PMNT system is quite complex because this system is a mixing between the relaxor ferroelectric PMNT and the normal ferroelectric PZBT. Therefore, there is a competing mechanism between the two types of materials, depending upon temperature. Since the stress experiment was carried out at room temperature (~25 °C) which is just below the $T_{max}$ of PMNT (~40 °C) [12], the dielectric properties of the PZBT-PMNT ceramic undet stress should be dominated by the PMNT contribution. Therefore, the experimental observations, which show decreases in both dielectric constant and dielectric loss tangent with increasing stress, can be attributed to competing influences of the intrinsic contribution of non-polar

matrix and the extrinsic contribution of re-polarization and growth of micro-polar regions. Since the dielectric response of both contributions is affected by the applied stress in an opposite way, the behavior of the PZBT-PMNT ceramic depends on the ratio between the micro-polar region and the non-polar matrix, in this case the non-polar matrix still dominates [27,28]. Hence, the dielectric responses of the PZBT-PMNT ceramic are observed to decrease significantly with increasing the compressive stress, as seen in Figs. 2 and 3. More interestingly, it is worth noting that our earlier investigations on the stress-dependent dielectric properties of the two members, i.e. PZBT [32] and PMNT [22], revealed that under a similar loading condition the dielectric constant of the PMNT ceramic decreased nearly 70%, whereas the PZBT ceramic showed approximately 5-10% increase in the dielectric constant. Clearly, the apparent suppression of the dielectric constant change with stress observed in this current study supports the composite nature of the PZBT-PMNT ceramic, as also revealed by the free-stress dielectric properties measurements shown in Fig. 1.

The cause of the stress dependence of the dielectric loss tangent is a little more straightforward than that of the dielectric constant. As depicted in Fig. 3, the clamping of the domain walls under the compressive stress results in a decrease of domain wall mobility and reduces the dielectric loss tangent [22,27]. This is a reversible effect with the domain wall mobility returning to near the original values when the applied stress is removed, as seen in Fig. 3 that the dielectric loss tangents return to near their original values after a stress cycle. In addition, a significant decrease in the dielectric constant after a full cycle of stress application has been observed, and attributed to the stress induced decrease in switchable part of spontaneous polarization at high stress [21,31].

## 4. CONCLUSIONS

The dielectric properties of complex perovskite PZBT-PMNT ceramic were investigated in this study. The dielectric properties measured under stress-free condition showed two distinct dielectric peaks associated with PZBT and PMNT. The dielectric properties under the compressive stress were observed using a homebuilt compressometer. The results clearly showed that the superimposed compression load significantly reduced both the dielectric constant and the dielectric loss tangent in every measuring frequency. The change of the dielectric properties with stress was attributed to competing influences of the intrinsic contribution of non-polar matrix and the extrinsic contribution of re-polarization and growth of micro-polar regions. Other contributions include the clamping of the domain walls and the stress induced decrease in switchable part of spontaneous polarization. This study clearly indicated that the complex perovskite PZBT-PMNT ceramic possessed a composite nature, as confirmed by the dielectric measurements.

## ACKNOWLEDGMENTS

Financial supports from the Thailand Research Fund (TRF), Faculty of Science and Graduate School of Chiang Mai University are gratefully acknowledged.

## REFERENCES


[1] B. Jaffe, W.R. Cook. Piezoelectric Ceramics, R.A.N. Inc., New York, 1971.

[2] L.E. Cross, Mater. Chem. Phys. 43 (1996) 108.

[3] G.H. Haertling, J. Am. Ceram. Soc. 82(4) (1999) 797.

[4] N. Setter, J. Euro. Ceram. Soc. 21 (2001) 1279.

[5] A.J. Moulson, J.M. Herbert. Electroceramics: Materials, Properties, Applications, 2nd Ed., John Wiley & Sons Ltd, New York, 2003.

[6] W. Chaisan, S. Ananta, T. Tunkasiri, Cur. Appl. Phys. 4 (2004) 182.

[7] W. Chaisan, R. Yimnirun, S. Ananta, D.P. Cann, Mater. Lett. 59 (2005) 3737.

[8] W. Chaisan, R. Yimnirun, S. Ananta, D.P. Cann, Mater. Sci. Eng. B. (2006) *in press*

[9] S. Jiang, D. Zhou, S. Gong, W. Lu, Sensors Actuat. A69 (1998) 1.

[10] Y.C. Liou, J. Mater. Sci. 103 (2003) 281.

[11] A. Safari, R.K. Panda, V.F. Janas, Appl. Ferro. Ceram. Mater. 1 (2000) 1.

[12] S. Huang, C. Feng, L. Chen, X. Wen, Integrated Ferroelectrics 74 (2005) 45.

[13] L.E. Cross, Ferroelectrics. 76 (1987) 241.

[14] Y.H. Xu, Ferroelectric Materials and Their Applications, North Holland, Los Angeles, 1991.

[15] D. Viehland, J. Powers, J. Appl. Phys. 89(3) (2001) 1820.

[16] J. Zhao, A.E. Glazounov, Q.M. Zhang, Appl. Phys. Lett. 74 (1999) 436.

[17] Q.M. Zhang, J. Zhao, K. Uchino, J. Zheng, J. Mater. Res. 12 (1997) 226.

[18] D. Viehland, J.F. Li, E. McLaughlin, J. Powers, R. Janus, H. Robinson, J. Appl. Phys. 95 (2004) 1969.

[19] D.Zhou, M. Kamlah, D. Munz, J. Euro. Ceram. Soc. 25 (2005) 425.

[20] R. Yimnirun, S. Ananta, E. Meechoowas, S. Wongsaenmai, J. Phys. D: Appl. Phys. 36 (2003) 1615.

[21] R. Yimnirun, Y. Loasiritaworn, S. Wongsaenmai, J. Phys. D: Appl. Phys. 39 (2006) 759.

[22] R. Yimnirun, M. Unruan, Y. Loasiritaworn, S. Ananta, J. Phys. D: Appl. Phys. 39 (2006) 3097.

[23] A. Udomporn, PhD Thesis, Chiang Mai University, 2004.

[24] R. Yimnirun, S. Ananta, A. Ngnamjarurojana, S. Wongsaenmai, Appl. Phys. A: Mater. 81(6) (2005) 1227.

[25] R. Yimnirun, S. Ananta, P. Laoratanakul, Mater. Sci. Eng. B. 112 (2004) 79.

[26] R. Yimnirun, S. Ananta, P. Laoratanakul, J. Euro. Ceram. Soc. 25(13) (2005) 3225

[27] G. Yang, W. Ren, S.F. Liu, A.J. Masys, B.K. Mukherjee, Proc. IEEE Ultra. Symp. 1 (2000) 1005.

[28] O. Steiner, A.K. Tagantsev, E.L. Colla, N. Setter, J. Euro. Ceram. Soc. 19 (1999) 1243.

[29] P. Preu, S. Haussuhl, Solid State Commun., 45(7) (1983) 619.

[30] R. Yimnirun, P.J. Moses, R.J. Meyer, R.E. Newnham, Rev. Sci. Instrum. 74 (2003) 3429

[31] J. Zhao, Q.M. Zhang, Proc. IEEE ISAF. 2 (1996) 971.

[32] R. Yimnirun, Ferroelectrics 331 (2006) 9.

[33] R. Yimnirun, S. Ananta, A. Ngnamjarurojana, S. Wongsaenmai, Curr. Appl. Phys. 6(3) (2006) 520.

## List of Figure Captions

**Fig. 1.** Temperature and frequency dependences of dielectric properties of PZBT-PMNT ceramic under stress-free condition (solid circle indicates dielectric peak associated with PMNT, and dotted circle indicates dielectric peak associated with PZBT).

**Fig. 2.** Relative changes of dielectric constant ($\varepsilon_r$) as a function of compressive stress for PZBT-PMNT ceramic.

**Fig. 3.** Relative changes of dielectric loss tangent (tan $\delta$) as a function of compressive stress for PZBT-PMNT ceramic.

.

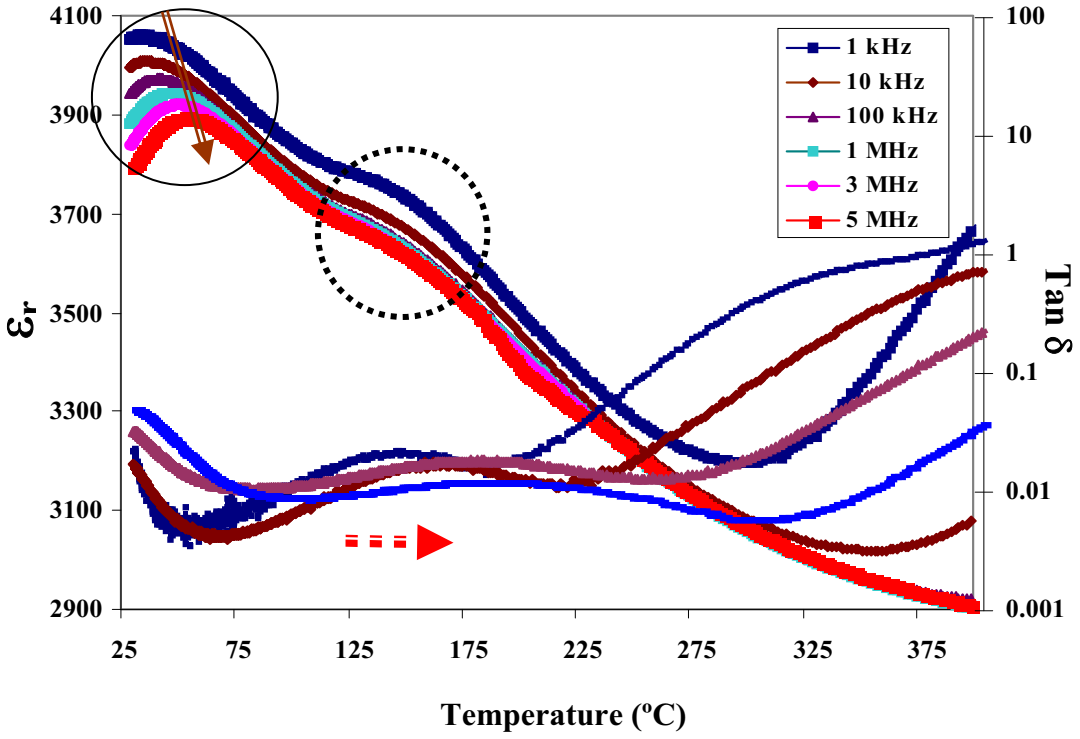



**Fig. 1.** Temperature and frequency dependences of dielectric properties of PZBT-PMNT ceramic under stress-free condition (solid circle indicates dielectric peak associated with PMNT, and dotted circle indicates dielectric peak associated with PZBT).

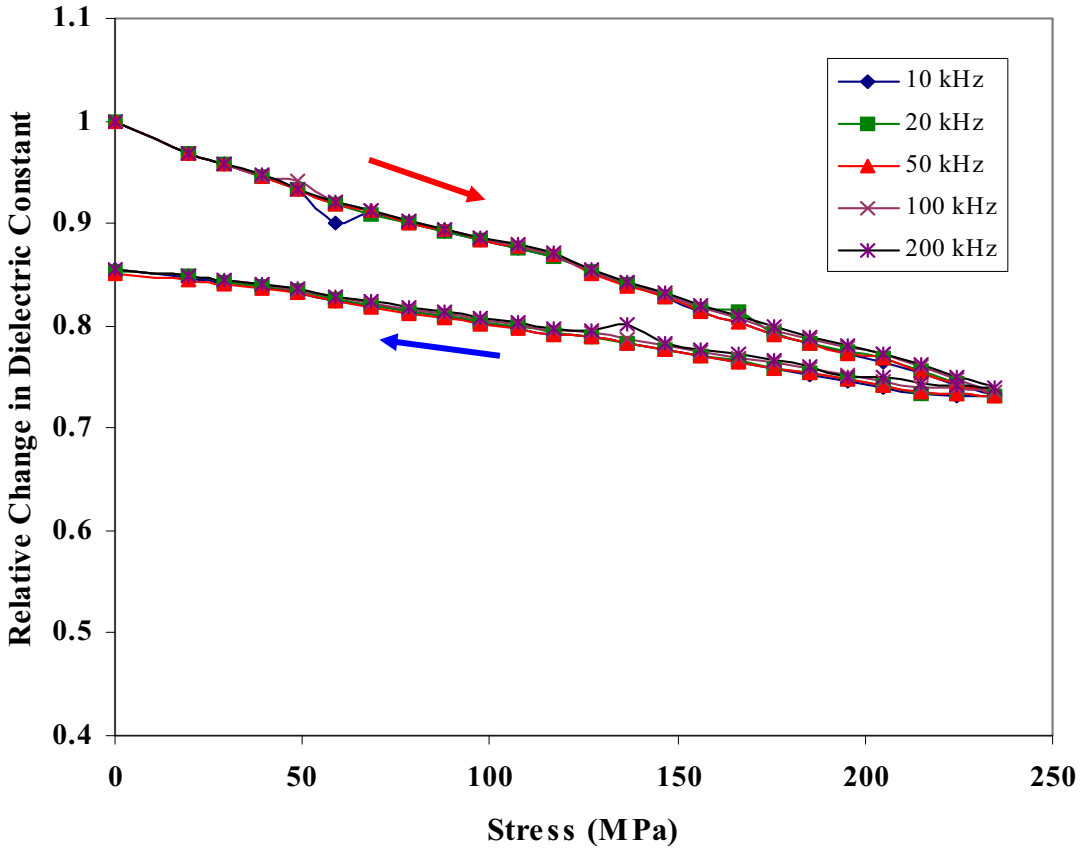



**Fig. 2.** Relative changes of dielectric constant ($\varepsilon_r$) as a function of compressive stress for PZBT-PMNT ceramic.

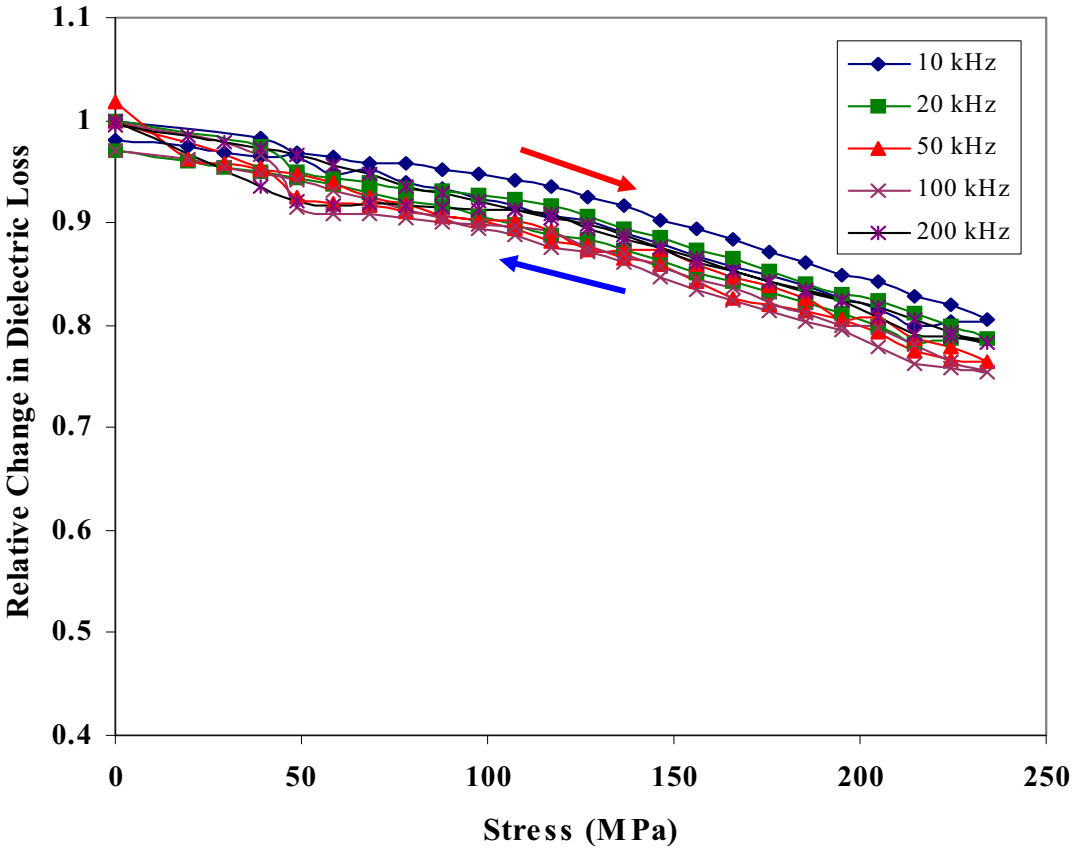



**Fig. 3.** Relative changes of dielectric loss tangent (tan δ) as a function of compressive stress for PZBT-PMNT ceramic.

# Ferroelectric Hysteresis Behavior in 0-3 PZT-Cement Composites: Effects of Frequency and Electric Field

**A. Chaipanich*, N. Jaitanong and R. Yimnirun**

*Department of Physics, Faculty of Science, Chiang Mai University,*

*Chiang Mai 50200, Thailand*

Lead zirconate titanate (PZT) -cement composites of 0-3 connectivity were produced and the effects of the frequency and electric field on the ferroelectric polarization-electric field (*P-E*) hysteresis of the composites were investigated. It was found that there was an increase in both the *instantaneous* remnant polarization ($P_{ir}$) and coercive field ($E_{ic}$) when the applied field increased. The *instantaneous* remnant polarization ($P_{ir}$) was found to reduce when the frequency was increased. The ferroelectric hysteresis loops only existed when the composites were subjected to lower frequency; i.e. at 20 and 40 Hz. At higher frequency, the loops tended to stretch out, showing more of a lossy characteristic.

Keywords: PZT, cement, composite, polarization, ferroelectric hysteresis

* Corresponding author

E-mail address: arnon@chiangmai.ac.th Fax: 66 53 357512

Piezoelectric-cement based composites have recently been developed for civil engineering applications [1-12]. The benefit from the use of such piezoelectric-cement based composite is that these composites possess better matching to the host structure, concrete than normal piezoelectric ceramic or other type of piezoelectric composites. Li *et al.* [1] showed that cement-based piezoelectric composites of 0-3 white Portland cement-lead zirconate titanate (PZT) composite can overcome the matching problem and that ≈40%-50% PZT by volume, the acoustic impedance is close to that of concrete (8.95 $x10^6$ $kg{\cdot}m^{-2}{\cdot}s^{-1}$) as compared to that of PZT at 21.2 $x10^6$ $kg{\cdot}m^{-2}{\cdot}s^{-1}$. However, the study on the ferroelectric hysteresis, which is an important behavior for materials with ferroelectric properties [13] that can be used to give indication of the difficulty of the poling process involved, of piezoleclectric-cement composites is limited. It is thus the aim of this current work to investigate the ferroelectric hysteresis behavior of the piezoleclectric-cement composites. Effects of the frequency and the amplitude of the applied electric field on the hysteresis behavior will be examined to provide the basis for the poling process of the piezoleclectric-cement composites.

In this work a 0-3 of PZT ceramic particles were mixed with normal Portland cement (PC) to form PZT-PC composites [7]. Lead zirconate titanate (PZT) ceramic particles having median size 450μm of composition $Pb(Zr_{0.52}Ti_{0.48})O_3$ were produced from PZT pellet sintered at 1250ºC for 3 h. PZT ceramic particles were then mixed with Portland cement (PC) to produce 0-3 connectivity PZT-PC composites of 50:50 by volume. Thereafter, the composites were placed for curing at 60ºC and 98% relative humidity for 3 days before measurements [7]. Phase characterizations of the composites were carried out by room temperature X-ray diffraction (XRD; Philips PW 1729 diffractometer) using Ni-filtered CuK radiation. The room temperature ferroelectric

hysteresis (*P–E*) loops were characterized using a computer controlled modified Sawyer-Tower circuit [14]. The electric field was applied to a sample by a high-voltage ac amplifier with the input sinusoidal signal with a frequency of 20-100 Hz from a signal generator.

X-ray diffraction pattern of 0-3 PZT–PC composite, as shown in Fig. 1, was found to show diffraction pattern mostly as attributed to that of PZT showing the perovskite phase at 2θ of 22.023, 30.942, 31.387, 38.283, 44.917, 50.417 and 55.524 degree, where the matching XRD peaks can be seen when compared to the PZT ceramic. In addition, rhombohedral calcium carbonate ($CaCO_3$) (2θ= 29.072), dicalcium silicate (2θ= 32.013, 32.117 and 32.939) and hydrated peak of hexagonal calcium hydroxide (2θ= 34.111) can also be noticed and these peaks can be clearly seen in the pure Portland cement XRD pattern. Nonetheless, these detectable phases do not account for all the phases present in the cement matrix. For example, calcium silicate hydrate which is the primary cement hydration product is generally known to be amorphous with poor crystalline form and thus amorphous characteristic can also be noticed from the XRD pattern. The overall detectable crystallized products when compared to the total phases of Portland cement are therefore relatively small; although the presence can still be seen. It thus further explains as to why these peaks of hydrated cement phases are even lesser in intensity in the XRD pattern of PZT-cement composite at 50% PZT by vol. since the crystallized perovskite structure of PZT would dominantly give a stronger diffraction resulting in high intensity peaks as seen in the XRD pattern.

It can be seen from Fig. 2 that when the composite was subjected to different electric field, the *P-E* hysteresis loops can be seen at all different electric field. It must first be noted that all ferroelectric hysteresis loops (*P-E* loops) of the PZT-cement

composites show a "lossy" feature with round tips as a result of cement matrix in the composites. It is believed that when an external electrical field acts on the cement matrix many weak conducting ions such as $Ca^{2+}$, $OH^-$, $Si^{4+}$, $Al^{3+}$ begin to migrate besides the polarization of electron. These ions cause higher conducting loss in the composites, hence a lossy feature is then observed in all the P-E loops obtained [19]. However, this study primarily aims at comparing the effects of the frequency and amplitude of the applied electric field on the hysteresis behavior, as reported in PZT ceramics and other monolithic materials [15-18]. Therefore, the ferroelectric parameters obtained here are used exclusively for comparison purpose among themselves. From the *P*-*E* loops seen in Fig. 2 (a), one can define two parameters based on the x- and y-axes intercepts. With a lossy behavior, it is impossible to achieve the fully saturated loops, hence the typical hyteresis parameters; i.e. the remnant polarization ($P_r$) and the coercive field ($E_c$) cannot be extracted. For comparison, we define the y-axis intercept at a given applied field as the "*instantaneous*" remnant polarization ($P_{ir}$), while the x-axis intercept is called the "*instantaneous*" coercive field ($E_{ic}$).

From Fig. 2(a), an increase in the amplitude of the field $E_0$ makes the loop larger and increases its angle to the *E* axis of inclination. Furthermore, it can be seen that there is an increase in the so called "*instantaneous*" remnant polarization ($P_{ir}$) and the "*instantaneous*" coercive field ($E_{ic}$) which represents the polarization at zero field and electric field at zero polarization at each measured frequency and $E_0$ when the electric field ($E_0$) increases from 10 kV/cm to 25 kV/cm. At frequency of 60 Hz, $P_{ir}$ can be seen to increase from 1.25 to 4.65 μC/cm$^2$ and $E_{ic}$ increases from 6.05 to 14.27 kV/cm for the hysteresis loops with the electric field of 10 kV/cm and 25 kV/cm, respectively. The increase in both the "*instantaneous*" parameters is due to the electric charge in a polar

material when induced with increasing an external electric field. The plots of the "*instantaneous*" polarization and coercive field against different $E_0$ at fixed $f$ (60 Hz) can be seen in Fig. 2 (b). It can be observed that when the electric field increases there is an increase in the "*instantaneous*" remnant polarization and that this increase appear to be almost linear. The "*instantaneous*" coercive field was found to increase in a similar manner. Previous investigations on the ferroelectric hysteresis behavior of the ferroelectric materials under sub-coercive field condition also showed similar changes of the hysteresis parameters with the applied field [16,18].

When the hysteresis loops were plotted at 25 kV/cm and with varying frequency from 20 to 100 Hz (Fig. 3 (a)), a typical hysteresis loops can still be seen at lower frequency (20 and 40 Hz). However at higher frequency i.e. 100 Hz, the loop tends to stretched out more and the loop no longer resemble a typical hysteresis. The "*instantaneous*" remnant polarization ($P_{ir}$) and "*instantaneous*" coercive field ($E_{ic}$) can be seen to decrease with an increase in frequency. The observation that the $P_{ir}$ and $E_{ic}$ decreases with increasing frequency is ascribed to the delayed response of the polarization reversal to the varying external field. Similar behavior was observed in previous study on ferroelectric ceramics [13-15].

It should be noted here that a loss from the cement can be seen to be more sensitive at higher frequency especially at 100 Hz where an oval shaped typical of a resistance is seen. It is understood that at the high frequency the interfacial polarizations cannot follow the change of the electric field due to the longer time taken for the space charge polarization to occur [16]. It is believed that when an external electrical field acts on the cement matrix many weak conducting ions such as $Ca^{2+}$, $OH^{-}$, $Si^{4+}$, $Al^{3+}$ begin to

migrate besides the polarization of electron. These ions move slowly when it reaches the interface of PZT and cement or in the defect areas and there is an accumulation effect which in turn results in the polarization of a space charge, and at lower frequency all the polarization can follow these changes of electrical field [19].

**I think we need to compare our results with previous P-E studies on PZT-PC composites here. Could you please provide some comparison of our results with those from the published paper by Chinese group [refs 20, 21]?**

Fig. 3 (b) shows the "*instantaneous*" remnant polarization $P_{ir}$ and the "*instantaneous*" coercive field $E_{ic}$ measured at different frequencies at fixed $E_0$=25 kV/cm. It can be seen that $P_{ir}$ can be seen to decrease increases from 6.10 to 4.24 to μC/cm$^2$ when increasing $f$ from 20 to 100 Hz. The $E_{ic}$ on the other hand can be seen to increase from 12.25 to 16.86 kV/cm with increasing frequency and the saturation seems to occur when the frequency reaches 80 Hz, where there is little difference in the coercive field between the results at 80 and 100 Hz.

From the above results, it was found that both the "*instantaneous*" remnant polarization ($P_{ir}$) and the "*instantaneous*" coercive field ($E_{ic}$) increase when the electric field ($E_0$) increases from 10 kV/cm to 25kV/cm. When the hysteresis loops were plotted at 25 kV/cm and with varying frequency from 20 to 100 Hz, $P_{ir}$ was found to decrease with an increase in frequency while $E_{ic}$ still increases. At higher frequency (≥80 Hz), the loop tends to stretch out more and no longer exhibit ferroelectric *P-E* hysteresis loop. It is understood that at the higher frequency a space charge polarization from conducting ions at the interface cannot follow the change of the electric field, thereby leading to a non-ferroelectric appearance. It should also be noted here that fully saturated P-E loops

cannot be achieved for the 0-3 PZT–PC composite studied here as a result of its highly lossy characteristics due to the presence of the weak conducting ions in the cement matrix, which in turns leads to poling difficulties in this type of the composites.

The authors gratefully acknowledge the Thailand Research Fund (TRF) and the Commission on Higher Education (CHE) for financial support.

## References

[1] Z. Li, D. Zhang, K. Wu, J. Am. Ceram. Soc., **85** (2002), p.305.

[2] C. Xin, S. Huang, C. Jun, X. Ronghua, L. Futian, L. Lingchao, J. Eur. Ceram. Soc., **25** (2005), p. 3223.

[3] A.Chaipanich, T. Tunkasiri, Curr App Phys., **7** (2007), p285.

[4] B. Dong, Z. Li, Compos. Sci. Technol.**65** (2005), p.1363.

[5] S. Huang, J. Chang, R. Xu, F. Liu, L. Lu, Z. Ye, X. Cheng, Smart Mater. Struct.,**13** (2004) 270

[6] Z. Li, B. Dong, D. Zhang, Cem. Concr. Compos., **27** (2005), p. 27.

[7] A. Chaipanich , N. Jaitanong, T. Tunkasiri, Matls. Letts., **61** (2007), p.5206.

[8] A. Chaipanich and N. Jaitanong, Adv. Mats. Res., **55-57**(2008), p.381.

[9] N. Jaitanong, K. Wongjinda, P. Tammakun, G. Rujijanagul and A. Chaipanich, Adv. Mats.Res., **55-57** (2008), p.377.

[10] N. Jaitanong, A. Chaipanich , T. Tunkasiri, Ceram Inter., **34** (2008), p.793.

[11] A. Chaipanich, Curr App Phys., **7** (2007), p. 574.

[12] A. Chaipanich Curr App Phys., **7** (2007), p. 537.

[13] J.-M. Liu, H. L. W. Chan, C. L. Choy, Y. Y. Zhu, S. N. Zhu, Z. G. Liu, N. B. Ming, Appl. Phys. Lett., **79** (2001), p.236.

[14] R.Yimnirun, S. Ananta, Y. Laosiritaworn, A.Ngamjarurojana, and S.Wongsaenmai, Ferroelectrics, **358** (2007), p.3.

[15] R.Yimnirun, Y. Laosiritaworn, S. Ananta, and S.Wongsaenmai, Appl. Phys. Lett., **89** (2006), p 162901-1

[16] R. Yimnirun, N. Wongdamnern, N. Triamnak, M. Unruan, A. Ngamjarurojana, S. Ananta, and Y. Laosiritaworn, J. Appl. Phys. **103** (2008), p 086105-1

[17] N. Wongdamnern, A. Ngamjarurojana, Y. Laosiritaworn, S. Ananta, and R. Yimnirun, J. Appl. Phys. *Submitted*

[18] R. Yimnirun, N. Wongdamnern, N. Triamnak, M. Unruan, A. Ngamjarurojana, S. Ananta, and Y. Laosiritaworn, J. Phys. D: Appl. Phys. **41** (2008), p 205415-1

[19] X. Cheng, S.Huang, J. Chang, and Z. Li, J. Appl. Phys., **101**(2007)

[20] ? P-E loop of PC-PZT composites

[21] ? P-E loop of PC-PZT composites

## Figure Captions

**Figure 1** XRD Diffraction pattern of 0-3 PZT-PC composites with comparison to PZT and PC patterns

**Figure 2** Effects of electric field amplitude on (a) the ferroelectric (*P*-*E*) hysteresis loops and (b) on *instantaneous* remnant polarization ($P_{ir}$) and *instantaneous* coercive field ($E_{ic}$) of PZT-PC composites (with fixed *f* of 60 Hz)

**Figure 3** Effects of electric field frequency on (a) the ferroelectric (*P*-*E*) hysteresis loops and (b) on *instantaneous* remnant polarization ($P_{ir}$) and *instantaneous* coercive field ($E_{ic}$) of PZT-PC composites (with $E_0$ fixed at 25 KV/cm)

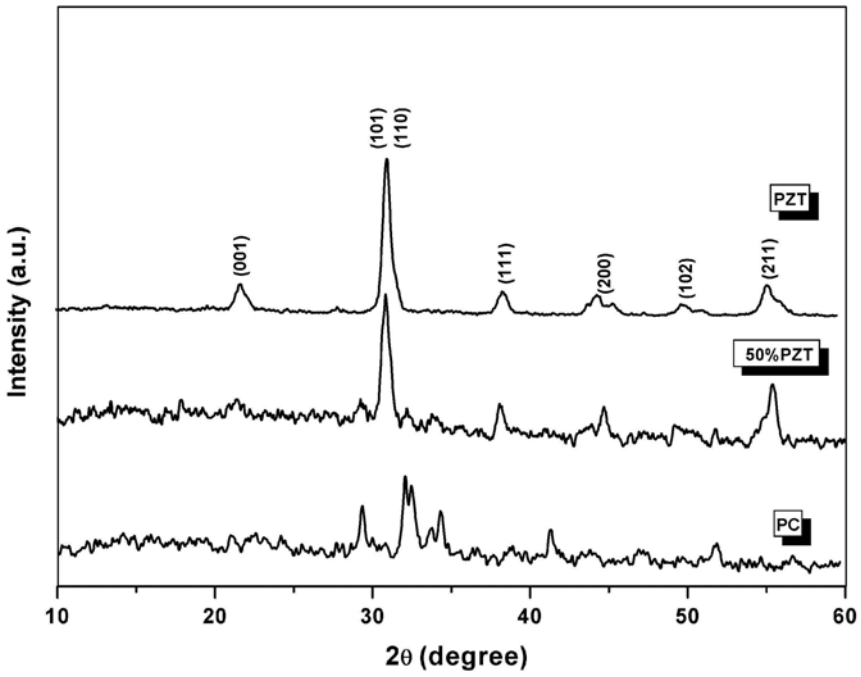
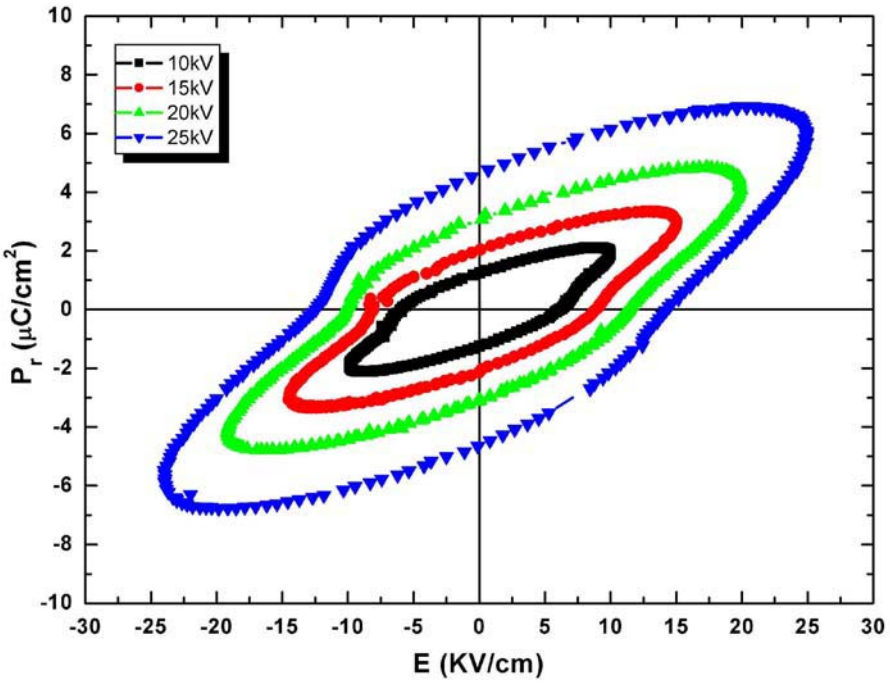
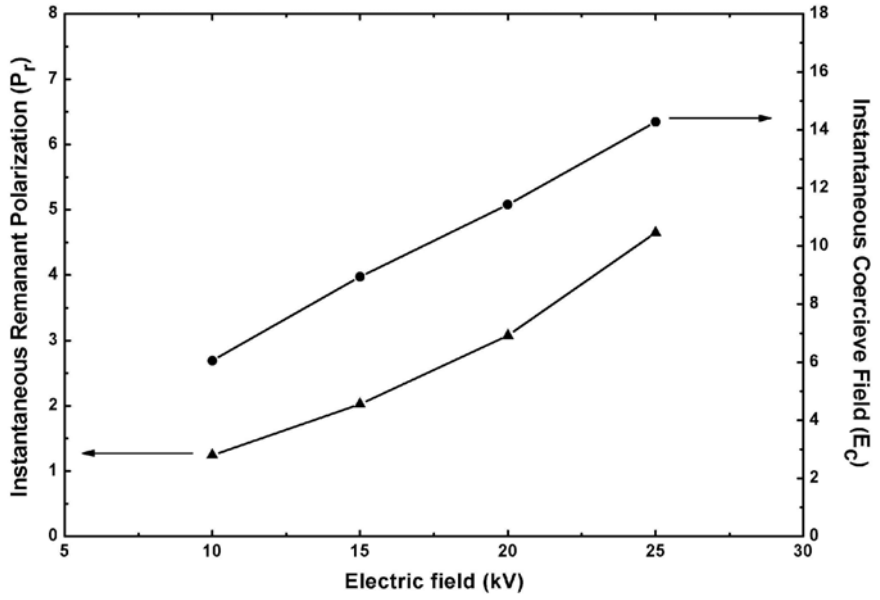

Intensity (a.u.)
(001)
(101)
(110)
(111)
(200)
(102)
(211)
PZT
50%PZT
PC
10
20
30
40
50
60
2θ (degree)

**Figure 1**

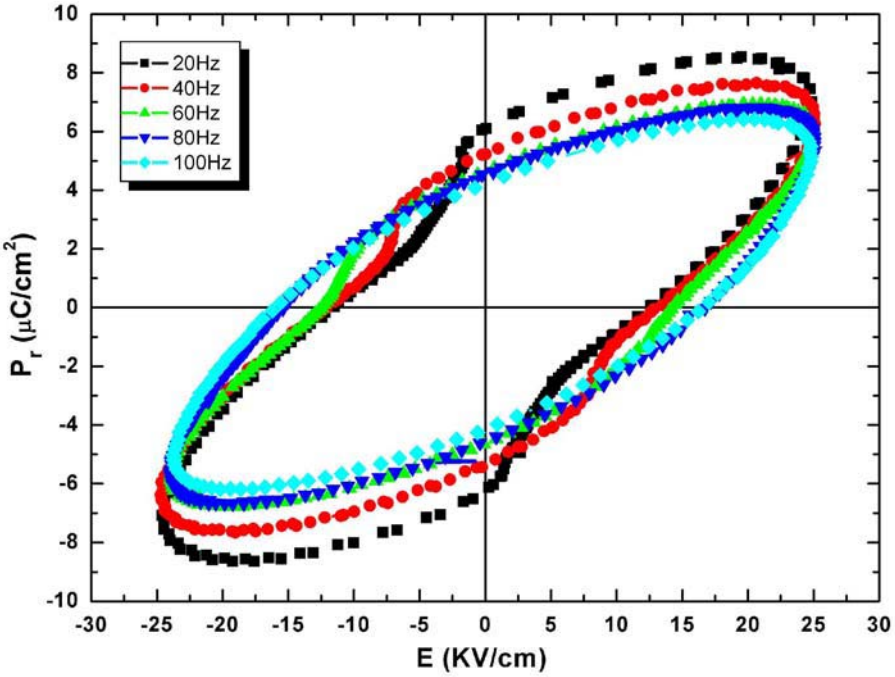

10kV
15kV
20kV
25kV
P_r (μC/cm^2)
E (KV/cm)

(a)

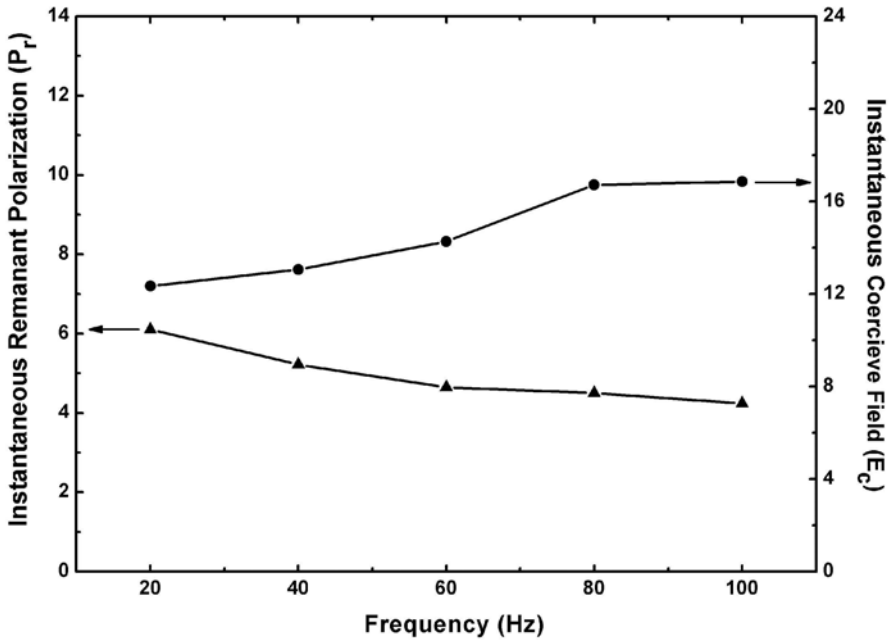

Instantaneous Remanant Polarization (P_r)
Instantaneous Coercieve Field (E_C)
Electric field (kV)

(b)

**Figure 2**


20Hz
40Hz
60Hz
80Hz
100Hz
P_r (μC/cm^2)
E (KV/cm)

(a)


Instantaneous Remanant Polarization (P_r)
Instantaneous Coercieve Field (E_c)
Frequency (Hz)

(b)

**Figure 3**

Phys. Scr. **T129** (2007) 184–189 doi:10.1088/0031-8949/2007/T129/042

# Stress- and temperature-dependent scaling behavior of dynamic hysteresis in soft PZT bulk ceramics

**R Yimnirun, S Wongsaenmai, R Wongmaneerung, N Wongdamnern, A Ngamjarurojana, S Ananta and Y Laosiritaworn**

Department of Physics, Faculty of Science, Chiang Mai University, Chiang Mai 50200, Thailand

E-mail: rattikornyimnirun@yahoo.com

Received 1 March 2007
Accepted for publication 13 July 2007
Published 27 November 2007
Online at stacks.iop.org/PhysScr/T129/184

**Abstract**

Effects of electric field-frequency, electric field-amplitude, mechanical stress, and temperature on the hysteresis area, especially the scaling form, were investigated in soft lead zirconate titanate (PZT) bulk ceramics. The hysteresis area was found to depend on the frequency and field-amplitude with the same set of exponents as the power-law scaling for both with and without stresses. The inclusion of stresses into the power-law was obtained in the form of $\langle A - A_{\sigma=0}\rangle \propto f^{-0.25} E_0 \sigma^{0.44}$ which indicates the difference in energy dissipation between the under-stress and stress-free conditions. The power-law temperature scaling relations were obtained for hysteresis area $\langle A\rangle$ and remanent polarization $P_r$, while the coercivity $E_C$ was found to scale linearly with temperature $T$. The three temperature scaling relations were also field-dependent. At fixed field amplitude $E_0$, the scaling relations take the forms of $\langle A\rangle \propto T^{-1.1024}$, $P_r \propto T^{-1.2322}$ and $(E_{C0} - E_C) \propto T$.

PACS numbers: 77.22.Ch, 77.84.Dy, 77.84.−s

(Some figures in this article are in colour only in the electronic version.)

## 1. Introduction

Lead zirconate titanate ($Pb(Zr_{1-x}Ti_x)O_3$ or PZT) ceramics are among the lead-based complex perovskites that have been investigated extensively, both from academic and commercial viewpoints with various applications [1–3]. However, PZT ceramics are usually modified with dopants. Generally, donor (higher-valency) additives induce 'soft' piezoelectric behavior with higher dielectric and piezoelectric activities, while acceptor (lower-valency) additives result in 'hard' piezoelectric behavior [1–3]. Most of the previous investigations have been focused on soft PZT ceramics because of their extensive uses in sensors and actuators [1–3]. In many of these applications, the dynamic hysteresis, i.e. hysteresis area $\langle A\rangle$ as a function of the field amplitude $E_0$ and frequency $f$ has become an important consideration [1–4]. Hence, there have been reports on the scaling behavior, which indicates the dependence of the hysteresis area $\langle A\rangle$ on relevant parameters, of the dynamic hysteresis in ferromagnetic and ferroelectric thin films [5–13]. Many theoretical studies have been focused on the scaling law.

$$\langle A\rangle \propto f^{\alpha} E_0^{\beta}, \tag{1}$$

where $\alpha$ and $\beta$ are exponents that depend on the dimensionality and symmetry of the system of hysteresis curves in polarization systems [5–8]. Earlier investigations have reported the scaling relations for high-$f$ region with $\alpha$ and $\beta$ values, respectively, of $-1$ and 2 for $(\Phi^2)^2$ and $(\Phi^2)^3$ models, and of $-0.33$ and 3 for PZT thin-film [6, 8, 9]. In contrast, there are only very few reports on the scaling behavior studies of ferroelectric hysteresis loops of bulk ferroelectric ceramics [14–17].

More importantly, in many applications the ceramic specimens are often subjected to mechanical loading, either from the design of the device itself or from operating conditions which induce stresses [1–3, 18]. Therefore, a prior knowledge of how the material properties change under different load conditions in materials is inevitably crucial for proper design of a device and for suitable

 © 2007 The Royal Swedish Academy of Sciences Printed in the UK 

selection of materials for a specific application. In many previous investigations the electrical properties of ceramics were found to depend strongly on stresses ($\sigma$) [19–23]. Additionally, it is well known that the size and shape of the hysteresis loop in the ferroelectric state depend strongly on temperature $T$ [1–3, 24]. The temperature dependence of ferroelectric properties is of interest in view of not only technological applications, but also in fundamental senses. The theoretical investigation by Rao *et al* has already proposed a temperature scaling for ferromagnetic materials, which indicates that the hysteresis area decreases with increasing temperature [5, 8]. Experimental results on ferromagnetic thin-films have revealed various temperature scaling relations [5, 6, 8, 10]. Interestingly, there has been no report on the temperature scaling of dynamic hysteresis in ferroelectrics, both theoretical and experimental. Since $f$, $E_0$, $\sigma$ and $T$ have been reported to impose significant influence on the dynamic hysteresis responses of ferroelectric ceramics, it is therefore the aim of this study to establish the scaling behavior of the dynamic hysteresis responses of soft PZT bulk ceramics under the influence of external stress and temperature. In this present study, the scaling behavior indicates the dependence of the hysteresis area $\langle A \rangle$ on frequency $f$, field amplitude $E_0$, stress $\sigma$ and temperature $T$.

## 2. Experimental

Disk-shaped samples of a commercially available soft PZT ceramic (PKI-552, Piezo Kinetics Inc., USA) with diameter of 10 mm and thickness of 1 mm were used in this study. For the stress-dependent studies, the dynamic hysteresis ($P$–$E$) loops were characterized at room temperature (25 °C) by using a modified Sawyer–Tower circuit with $f$ covering from 2 to 100 Hz and $E_0$ from 0 to 18 kV cm$^{-1}$. The electric field was applied to a sample by a high voltage AC amplifier (Trek 610D) with the input sinusoidal signal from a function generator (HP 3310A). The $P$–$E$ loops were recorded by a digital oscilloscope (HP 54645A, 100 MHz). Effects of the external stress on the dynamic hysteresis were investigated with the compressometer, which was developed for simultaneous applications of the mechanical stress and the electric field [22, 23]. The compressive stress, applying parallel to the electric field direction, was supplied by the servohydraulic load frame and monitored with the pressure gauge. The $P$–$E$ loops were recorded as a function of mechanical stress applied discretely between 0 and 24 MPa for each applied field and frequency. At each constant stress, the loop was obtained after 20 sampling cycles to average out the noise deformation. For the temperature-dependent studies, the stress-free $P$–$E$ hysteresis loops were obtained over a temperature range of 298–453 K with $E_0$ up to 40 kV cm$^{-1}$ ($f$ was fixed at 4 Hz).

## 3. Results and discussion

### 3.1. Stress-dependent case

The hysteresis profiles for various frequencies $f$, field-amplitude $E_0$, and stress $\sigma$ are obtained. For a particular applied stress, as expected, the dependence of the loop pattern

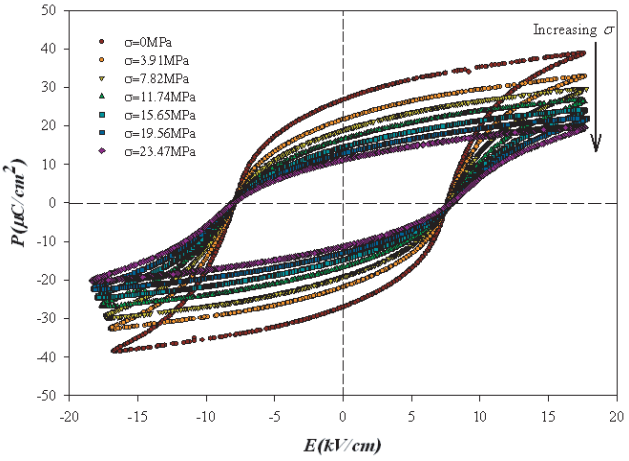



**Figure 1.** Hysteresis loops for soft PZT ceramic at various $\sigma$ ($f = 100$ Hz and $E_0 = 18$ kV cm$^{-1}$).

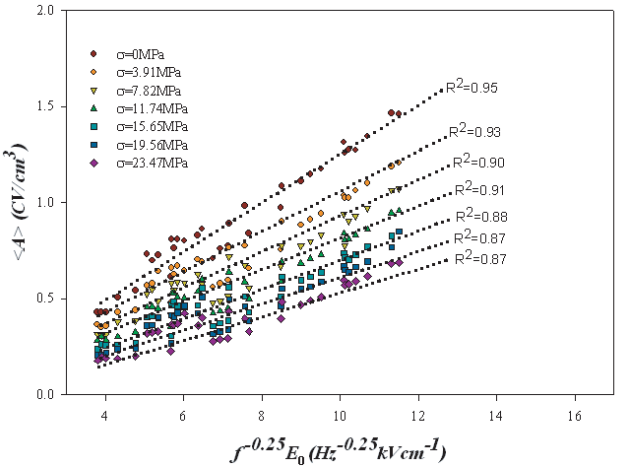



**Figure 2.** Scaling of hysteresis area $\langle A \rangle$ against $f^{-0.25}E_0$ for soft PZT ceramic at various $\sigma$.

and area $\langle A \rangle$ on $f$ and $E$ is remarkable. At fixed $E_0$, the loop area $\langle A \rangle$, remanent polarization ($P_r$), and coercive field ($E_C$) decrease with increasing frequency. For the dependence of the hysteresis loop on $E_0$, the loop does not saturate at small fields (6 and 8 kV cm$^{-1}$). With further increase in $E_0$, $\langle A \rangle$, $P_r$ and $E_C$ increase until well saturated loop is achieved. Similar stress-free observations have been reported in thin-films and bulk ceramics [7, 11, 14–17].

Figure 1 displays the hysteresis loops under different compressive stress during loading at fixed $f$ of 100 Hz and fixed $E_0$ of 18 kV cm$^{-1}$. The $P$–$E$ loop area $\langle A \rangle$ is found to decrease steadily with increasing stress. To investigate the scaling behavior under the effect of applied stresses, instead of including only the field amplitude $E_0$ and the frequency term $f$, the scaling relation should also include the stress ($\sigma$) term, i.e.

$$\langle A \rangle \propto f^m E_0^n \sigma^p. \tag{2}$$

However, due to increasing number of exponents, to simplify the problem, the validity of the scaling law $\langle A \rangle(\sigma) \propto f^{-0.25}E_0$ is assumed, inspired by a stress-free investigation on bulk PZT [14], for all applied stresses. Consequently, the area $\langle A \rangle$ for each stress is plotted against $f^{-0.25}E_0$, as shown in figure 2, and it can be seen from the least-square linear fits

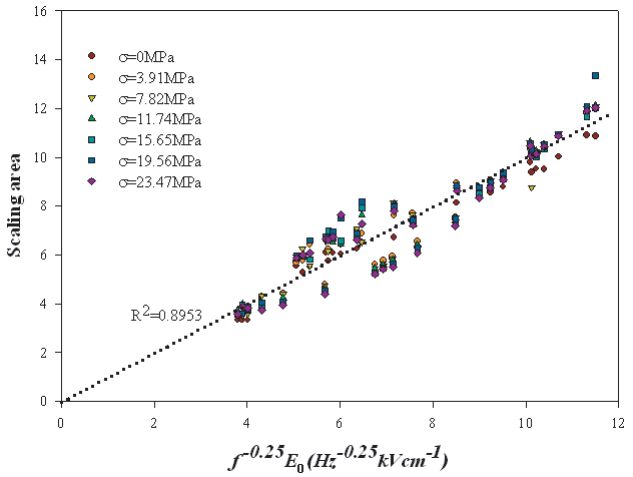



**Figure 3.** The collapse of the scaling area $(\langle A\rangle - F(\sigma))/(\sigma)$ against $f^{-0.25}E_0$ on the same linear-line (with small fluctuation) for soft PZT ceramic.

that reasonably good linear relations can be found. As a result, the condition of universality having $m = -0.25$ and $n = 1$ in soft PZT bulk ceramic systems is confirmed whereas the proportional constant in equation (2) may still be a function of $\sigma$. Therefore, equation (2) is generalized by writing,

$$\langle A\rangle = G(\sigma)\, f^{-0.25}E_0 + F(\sigma), \tag{3}$$

where both $G(\sigma)$ and $F(\sigma)$ are assumed to be a function of $\sigma$ representing slope-function and $y$-intercept-function for a 'linear-relation' in equation (3), and their values are presented via linear-fit functions in figure 2. Next, to obtain the scaling form as indicating in equation (2), the slope-function $G(\sigma)$ is assumed to take a form of power-law function, i.e. $G(\sigma) = a + b\sigma^c$, and a nonlinear fit for $G(\sigma)$ gives $a = 0.136 \pm 0.021$, $b = -0.019 \pm 0.015$ and $c = 0.439 \pm 0.173$ with $R^2 \approx 0.994$. However, for the $y$-intercept-function $F(\sigma)$, the scattering data in $F(\sigma)$ do not follow a trivial power-law scaling form. Instead, the reasonably well-fitted function that suits $F(\sigma)$ in the current study is found to take a quadratic function. So $F(\sigma) = a_0 + a_1\sigma + a_2\sigma^2$ is written and a least square fit is performed to give $a_0 = -0.019 \pm 0.006$, $a_1 = 0.002 \pm 0.001$ and $a_2 = -1.149 \times 10^{-4} \pm 4.850 \times 10^{-4}$ with $R^2 \approx 0.878$. As a result, from equation (3), it is therefore possible to write the scaling area

$$\frac{\langle A\rangle - F(\sigma)}{G(\sigma)} = f^{-0.25}E_0 \tag{4}$$

and by plotting this scaling area $(\langle A\rangle - F(\sigma))/G(\sigma)$ against $f^{-0.25}E_0$ all the data should collapse on to a single linear line having a $y$-intercept at zero. The data-collapsing of the scaling area from all $f$, $E_0$ and $\sigma$ was found to confirm equation (4) as evident in figure 3. On the other hand, it is of interest if the scaling of $\langle A\rangle$ in a form given by equation (2) is allowed. Therefore, by discarding minor loops which usually occur at very low $E_0$, $F(\sigma) \equiv \langle A\rangle\ (E_0 \to 0)$ will be small in comparison to $\langle A\rangle$ and can be discarded in equation (4) at some intermediately high fields. Consequently, $\langle A\rangle \propto (a + b\sigma^c)\, f^{-0.25}E_0$ may be written and by substituting the fitted parameters, it is found that

$$\langle A\rangle - \langle A_{\sigma=0}\rangle = \langle A - A_{\sigma=0}\rangle \propto f^{-0.25}E_0\sigma^{0.44}, \tag{5}$$

where $\langle A_{\sigma=0}\rangle$ refers to stress-free hysteresis area which will be a dominant term for zero stress. Note that from the appearance of stress $\sigma$, $\langle A - A_{\sigma=0}\rangle$, referring to the difference in energy dissipation between under-stress and stress-free conditions, increases with increasing stress suggesting a decay of $\langle A\rangle$ with $\sigma$ at a rate of $\sigma^{0.44}$ as observed in experiments. As a result, it can be concluded that the difference in the hysteresis area between under-stress and stress-free conditions scales with frequency, field-amplitude and stress via exponents $m = -0.25$, $n = 1$ and $p = 0.44$. However, at a particular fixed stress, equation (5) gives $f^{-0.25}E_0$ which is the original form for how the area scales with the frequency and the field-amplitude [14].

To understand the scaling relation obtained, at least qualitatively, one needs to consider the following statements. Since the $P$–$E$ loop area indicates the polarization dissipation energy subjected to one full cycle of electric field application, the loop area is therefore directly related to volume involved in the switching process during the application of electric field [22–24]. Hence, when the mechanical stress is applied, more and more ferroelectric domains are constrained by the applied stress and cannot be re-oriented by the electric field so as to participate in the polarization reversal. Consequently, both the saturation and remanent polarizations become lower with increasing compressive stress. The polarization dissipation energy is consequently found to decrease with increasing applied stress, indicating that the sample volume contributing to polarization reversal decreases with the increasing stress. Similar observations have also been reported in other investigations [19–23]. Though this study has revealed a significant influence of the external stress on the scaling behavior in bulk ceramics, there has been no quantitative theoretical treatment to include the stress-term in the scaling relation. An earlier theoretical investigation by Rao and Pandit [8] has already proposed the inclusion of temperature term in the scaling relation, in addition to $f$ and $E_0$ terms. Many of the theoretical treatments to explain the stress effect on the hysteresis behavior have been primarily based on constitutive models, thermodynamic phenomenology and Rayleigh law approach [25–27]. This clearly has triggered a need to include a stress-term in the previous theoretical models [5–7].

### *3.2. Temperature-dependent case*

The hysteresis loops for various electric field amplitudes $E_0$ and temperatures $T$ were obtained and it was found that both $E_0$ and $T$ played a crucial role on the hysteresis area $\langle A\rangle$. For example, with increasing $E_0$, a transition from a minor loop at low field to a saturated s-shape loop at high field occurs. This is expected because with higher field there is more electrical energy supplied into the system resulting in more 'electrical driving force' acting on electric dipole moments [24]. Consequently, the polarization has more tendency to follow the external electric field which in turn reduces the phase lag between the polarization and the field signals. As a result, the saturated loops are obtained at high fields instead of the minor loops at low fields. On the other hand, with increasing temperature, the loop area is notably reduced in size. This is caused by the fact that higher temperature

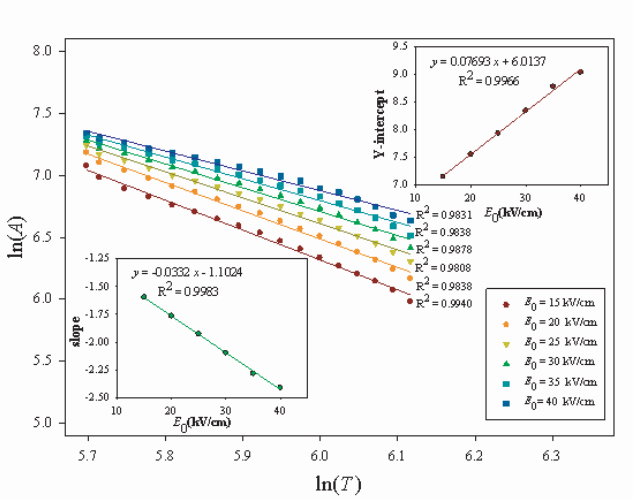



**Figure 4.** Double logarithmic plot between ln $(A)$ and ln $(T)$ for various $E_0$ where the linear relations are found but the $y$-intercepts and slopes seem to be $E_0$-dependent. The insets show those linear relations with $E_0$.

provides higher thermal fluctuation to the polarization which reduces the ferroelectric interaction among the dipoles [24]. Therefore, even $E_0$ is fixed, the polarization direction is easily tuned with the electric field at higher temperatures due to the smaller ferroelectric interaction providing a reduction in both remanent polarization ($P_r$) and coercivity ($E_C$). For this reason, the hysteresis loop area is reduced with increasing temperature. Similar observations have been reported in many other ferroelectric systems [28–31]. More interestingly, the observed temperature dependence of these hysteresis parameters prompts a question whether there exist temperature scaling relations for these parameters.

Figure 4 shows the relation between $\langle A \rangle$ and $T$ in a double logarithmic form where good linear fits are apparent ($R^2$ close to 1). This implies a power-law relation between the hysteresis area and temperature, i.e. $\langle A \rangle \propto T^{\gamma}$, and for each $E_0$ the exponent $\gamma$ can be extracted from the slope, i.e. $\gamma = \mathrm{d}\ln\langle A \rangle / \mathrm{d}\ln T$. However, both the slope $\gamma$ and the $y$-intercept seem to vary with $E_0$. Thus, to prove this $E_0$ dependence, both the slope $\gamma$ and the $y$-intercept are plotted as a function of $E_0$ (insets in figure 4), and the linear dependences on $E_0$ are noticeable. The linear least square fits of both slopes and $y$-intercepts with $E_0$ give $y = -0.0332x - 1.1024$ with $R^2 = 0.9983$ for the slope (lower inset), and $y = 0.0769x + 6.0137$ with $R^2 = 0.9966$ for the $y$-intercept (upper inset). However, the $y$-intercept refers to the value of $\ln\langle A \rangle$ at the limit $\ln T$ approaching zero and from the fitting $\ln\langle A \rangle$ is not ceased at this limit which is not really sound because at low temperatures dynamic of the dipoles or domain walls freeze. This could be caused by the fact that domain wall motion at high temperature is very different from that at very low temperature [32, 33]. Consequently, this study does not imply there is a finite hysteresis area at $T$ approaching zero (i.e. in this case $\ln T = 0$ or $T = 1$) but the quantity $\ln\langle A \rangle$ at $\ln T = 0$ here comes from an empirical fit to fulfill the validity of the linear fit. Therefore, upon the proposed assumptions and fitting techniques, by integrating all the relevant fits, it is

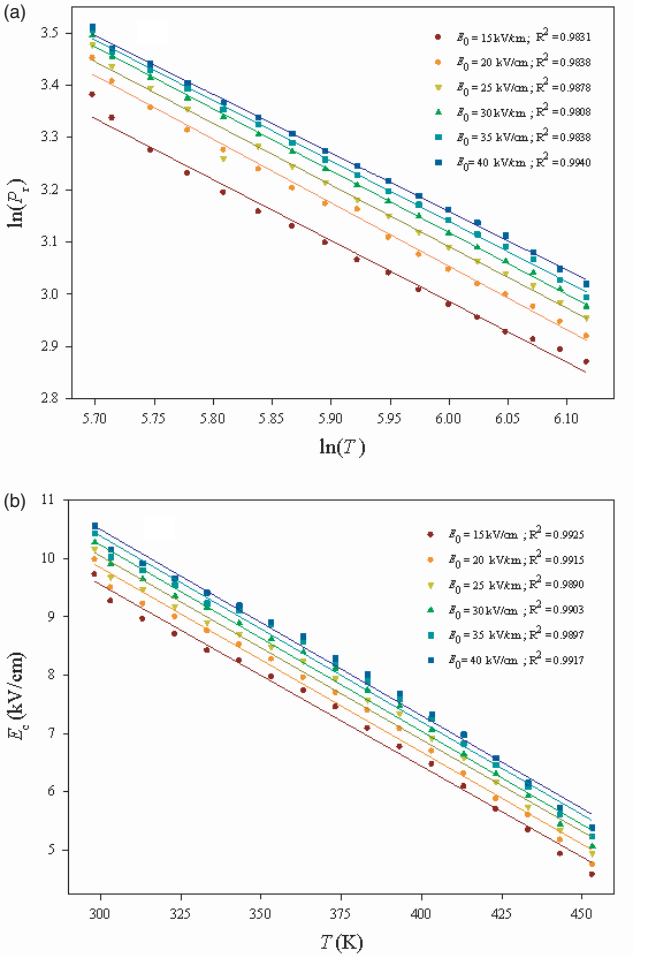



**Figure 5.** (a) Double logarithmic plot between ln $(P_r)$ and ln $(T)$, and (b) linear plot between $E_C$ and $T$.

found that

$$\langle A \rangle = \exp\left(0.0769E_0 + 6.0137\right) T^{-(0.0332E_0 + 1.1024)}. \quad (6)$$

Through similar mathematical treatment performed on $\langle A \rangle$, temperature dependent relations for $P_r$ and $E_C$ are also obtained. Figure 5(a) shows the relation between $P_r$ and $T$ in a double logarithmic plot. As is evident, the power-law relation seems suitable for the fit since good $R^2$ are attained. It is found that

$$P_r = \exp(-0.0068E_0 + 10.305) T^{(0.0022E_0 - 1.2322)}. \quad (7)$$

The relation between $E_C$ and $T$ is shown in figure 5(b). Surprisingly, linear relations are apparent so an approximation on $y = ax + b$ could be used to fit the data. Nonlinear fits between $E_C$ and $T$ are also performed (not shown) and the linear dependence of $E_C$ and $T$ is confirmed. Therefore, it could be estimated that

$$E_C = (-0.00003E_0 - 0.03085)\, T + (0.0459E_0 + 18.319)\,. \quad (8)$$

The temperature dependences of $\langle A \rangle$, $P_r$ and $E_C$ shown in equations (6)–(8) are also slightly $E_0$-dependent. Obviously, small coefficients to $E_0$ (for the whole range of $E_0$ used in this study) suggest that at fixed $E_0$

$$\langle A \rangle \propto T^{-1.1024}, \quad (9)$$

$$P_{\mathrm{r}} \propto T^{-1.2322}, \tag{10}$$

$$(E_{\mathrm{C0}} - E_{\mathrm{C}}) \propto T. \tag{11}$$

$E_{\mathrm{C0}}$ in equation (11) can be viewed as the coercivity at $T \sim 0$ K. However, as $T \to 0$, thermal energy is low causing a non-symmetric hysteresis loop, hence $E_{\mathrm{C0}}$ cannot be meaningfully defined. Here, $E_{\mathrm{C0}}$ is used for proposing the fit, which is valid for the experimental range in this study.

The quantitative results obtained in equations (9)–(11) could also be explained in terms of domain switching as a function of temperature and field. Generally, the domain switching is caused by the domain wall movement leading to either extension or contraction of the ferroelectric domains, and determines the average polarization value. In soft PZT ceramics, the oxygen vacancy is a key factor which controls how the ferroelectric domain grows and shrinks. In particular, oxygen vacancy is mobile and usually gets stuck at the ferroelectric domain [34–36]. This causes domain wall clamping and decelerates the domain switching. Therefore, if the trapped oxygen vacancies are high in number, the polarization switching is rarely allowed and the polarization will be suppressed due to the pinned domain wall [37]. Nevertheless, the oxygen vacancy can become less trapped if an external electric field is applied [38]. This is since there is more electric driving energy on the ferroelectric dipoles and, starting from boundaries with low oxygen vacancy density, the domain walls move across the boundaries allowing bigger domain switching whereas the oxygen vacancies move aside and get accumulated at other boundaries. This is why higher $P_{\mathrm{r}}$ and $E_{\mathrm{C}}$ are found with increasing applied field. On the other hand, temperature also has some prominent effect on the domain wall movement. With increasing temperature, there is higher level of thermal fluctuation in the system, that causes the oxygen vacancy to become less entrapped [39]. Therefore, the external field need not be as high as those at low temperatures to unlock the domain switching. This leads to the reduction in $E_{\mathrm{C}}$ with increasing temperature. In the case of $P_{\mathrm{r}}$, the higher temperature induces higher level of thermal fluctuation on the domain wall motion and reduces the stability of the polarization in each domain. Thus the average $P_{\mathrm{r}}$ tends to decrease with increasing temperature. As a result, the hysteresis area $\langle A \rangle$ is also reduced with increasing temperature. In general, this temperature- and field-dependent domain switching phenomenon is universal to all ferroelectric systems. However, the behavior may be different in detail due to different levels of complex defect, types and percentages of doping, crystal structures and domain states [31, 34, 36–39].

More importantly, equations (9)–(11) present simple relations for the temperature scaling of ferroelectric hysteresis parameters. It should be noted that there have only been few theoretical treatments to include temperature term in dynamic hysteresis scaling of ferromagnetics [5, 6, 8]. Considering relatively successful applications of the treatments to $E$- and $f$-dependent ferroelectric hysteresis [5–9], it would be worthwhile to compare our experimental results with the theoretically derived scaling. Theoretical scaling relations have been proposed as $\langle A \rangle \propto T^{-\gamma}$ with $\gamma$ being 0.7, 1.18 and 1.98 for continuum 3D $(\Phi^2)^2$, 2D and 3D Ising models, respectively [5, 6, 8]. An explanation for the variation may come from the different polarization-interaction terms as considered in these models. It could be seen that our experimentally obtained temperature scaling of $\langle A \rangle$ (with $\gamma \sim 1.1$) falls between the values obtained from the models. The difference could be attributed to additional contributions from depolarizing effects within the ceramics (arisen from domain walls, grain boundaries, space charges, immobile defects etc) [14–17], as compared to physically over-simplified polarization-interaction proposed in the theoretical models [5, 6, 8].

Furthermore, the relation $E_{\mathrm{c}} \propto (T - \mathrm{T_c})^{-0.35}$ drawn from the 3D $(\Phi^2)^2$ model is significantly different from the linear relation obtained from our study, which further clarifies that the theoretical models cannot be applied to ferroelectric bulk ceramics. This study clearly serves as a survey to show that more improvement of the theoretical approach is needed to predict the scaling behavior in bulk ferroelectric ceramics. Interestingly, different forms of temperature scaling of $E_{\mathrm{C}}$ extracted from the previous experimental data on PZT thin films also indicate dimensional dependence of the coercivity, as reported in previous investigations [26, 35].

## 4. Conclusions

The scaling behavior of the dynamic hysteresis of soft PZT bulk ceramics under the effects of mechanical stress and temperature has been investigated. With the presence of external stress, the scaling law for the loop-area yields the same set of exponents as frequency and field-amplitude in stress-free condition which confirms the condition of universality in the bulk system. The difference in energy dissipation between the under-stress and stress-free conditions is found to scale with $f^{-0.25} E_0 \sigma^{0.44}$. Additionally, power-law temperature scaling relations have been found for hystersis area $\langle A \rangle$ and remanent polarization $P_{\mathrm{r}}$, while the coercivity $E_{\mathrm{C}}$ scales linearly with temperature. The three temperature scaling relations are field-dependent. At fixed $E_0$, the scaling relations take the forms of $\langle A \rangle \propto T^{-1.1024}$, $P_r \propto T^{-1.2322}$ and $(E_{\mathrm{C0}} - E_{\mathrm{C}}) \propto T$.

## Acknowledgments

Financial support from the Thailand Research Fund (TRF), Commission on Higher Education (CHE), Faculty of Science and Graduate School of Chiang Mai University is gratefully acknowledged.

## References

[1] Jaffe B, Cook W R and Jaffe H 1971 *Piezoelectric Ceramics* (New York: Academic)
[2] Xu Y H 1991 *Ferroelectric Materials and Their Applications* (Los Angeles: North-Holland)
[3] Uchino K 2000 *Ferroelectric Devices* (New York: Dekker)
[4] Auciello O, Scott J F and Ramesh R 1998 *Phys. Today* **22** 1
[5] Rao M, Krishnamurthy H R and Pandit R 1990 *Phys. Rev.* B **42** 856
[6] Acharyya M and Chakrabarti B K 1995 *Phys. Rev.* B **52** 6560
[7] Liu J-M, Chan H L W, Choy C L, Zhu Y Y, Zhu S N, Liu Z G and Ming N B 2001 *Appl. Phys. Lett.* **79** 236

[8] Rao M and Pandit R 1991 *Phys. Rev.* B **43** 3373
[9] Liu J-M, Chan H L W, Choy C L and Ong C K 2001 *Phys. Rev.* B **65** 014416
[10] Jiang Q, Yang H N and Wang G C 1995 *Phys. Rev.* B **52** 14911
[11] Pan B, Yu H, Wu D, Zhou X H and Liu J-M 2003 *Appl. Phys. Lett.* **83** 1406
[12] Kim Y-H and Kim J-J 1997 *Phys. Rev.* B **55** R11933
[13] Park J-H, Kim C-S, Choi B-C, Moon B K, Jeong J H and Kim I W 2003 *Appl. Phys. Lett.* **83** 536
[14] Yimnirun R, Laosiritaworn Y, Wongsaenmai S and Ananta S 2006 *Appl. Phys. Lett.* **89** 162901
[15] Yimnirun R, Wongsaenmai S, Ananta S and Laosiritaworn Y 2006 *Appl. Phys. Lett.* **89** 242901
[16] Yimnirun R, Wongmaneerung R, Wongsaenmai S, Ngamjarurojana A, Ananta S and Laosiritaworn Y 2007 *Appl. Phys. Lett.* **90** 112906
[17] Yimnirun R, Wongmaneerung R, Wongsaenmai S, Ngamjarurojana A, Ananta S and Laosiritaworn Y 2007 *Appl. Phys. Lett.* **90** 112908
[18] Uchino K 1997 *Piezoelectric Actuators and Ultrasonic Motors* (Boston, MA: Kluwer Academic)
[19] Zhao J, Glazounov A E and Zhang Q M 1999 *Appl. Phys. Lett.* **74** 436
[20] Viehland D and Powers J 2001 *J. Appl. Phys.* **89** 1820
[21] Zhou D, Kamlah M and Munz D 2005 *J. Eur. Ceram. Soc.* **25** 425
[22] Yimnirun R, Laosiritaworn Y and Wongsaenmai S 2006 *J. Phys. D: Appl. Phys.* **39** 759
[23] Yimnirun R, Ananta S, Ngamjarurojana A and Wongsaenmai S 2005 *Appl. Phys.* A **81** 1227
[24] Lines M E and Glass A M 1977 *Principles and Applications of Ferroelectrics and Related Materials* (Oxford: Clarendon)
[25] Damjanovic D 1997 *J. Appl. Phys.* **82** 1788
[26] Tsurumi T, Sasaki T, Kakemoto H, Harigai T and Wada S 2004 *Japan. J. Appl. Phys.* **43** 7618
[27] Achuthan A and Sun C T 2005 *J. Appl. Phys.* **97** 114103
[28] Liu J-M, Pan B, Yu H and Zhang S T 2004 *J. Phys.: Condens. Matter* **16** 1189
[29] Yuan G L, Liu J-M, Zhang S T, Wu D, Wang Y P, Liu Z G, Chan H L W and Choy C L 2004 *Appl. Phys. Lett.* **84** 954
[30] Lin D, Xiao D, Zhu J and Yu P 2006 *Appl. Phys. Lett.* **88** 062901
[31] Pandey S K, Thakur O P, Kumar A, Prakash C, Chatterjee R and Goel T C 2006 *J. Appl. Phys.* **100** 014104
[32] Gruverman A, Auciello O and Tokumoto H 1998 *Ann. Rev. Mater. Sci.* **28** 101
[33] Lee K and Baik S 2006 *Ann. Rev. Mater. Res.* **36** 81
[34] Chang W, King A H and Bowman K 2006 *Appl. Phys. Lett.* **88** 242901
[35] Tsurumi T, Nam S-M, Kil Y-B and Wada S 2002 *Key Eng. Mater.* **214–215** 123
[36] Jullian C, Li J F and Viehland D 2004 *J. Appl. Phys.* **95** 4316
[37] He L X and Vanderbilt D 2003 *Phys. Rev.* B **68** 134103
[38] Dimos D, Al-Shareef H N, Warren W L and Tuttle B A 1996 *J. Appl. Phys.* **80** 1682
[39] Hauke T, Mueller V, Beige H and Fousek J 1998 *Phys. Rev.* B **57** 10424

IOP Publishing Physica Scripta
Phys. Scr. **T129** (2007) 205–208 doi:10.1088/0031-8949/2007/T129/046

# Changes in ferroelectric properties of barium titanate ceramic with compressive stress

**Wanwilai Chaisan, Rattikorn Yimnirun and Supon Ananta**

Department of Physics, Faculty of Science, Chiang Mai University, Chiang Mai 50200, Thailand

E-mail: wanwilai_chaisan@yahoo.com

Received 26 February 2007
Accepted for publication 17 August 2007
Published 28 November 2007
Online at stacks.iop.org/PhysScr/T129/205

**Abstract**
In this work, barium titanate (BT) ceramic was prepared using a conventional mixed oxide method. The effect of uniaxial compressive stress on the ferroelectric properties of BT ceramics were investigated. The changes in ferroelectric properties were observed at stress up to 60 MPa using a compressometer in conjunction with a modified Sawyer–Tower circuit. The results showed that applied stress had a significant influence on the ferroelectric properties of BT ceramics. Ferroelectric characteristics, i.e. the area of the ferroelectric hysteresis ($P$–$E$) loop, the saturation polarization ($P_{sat}$), the remanent polarization ($P_r$) and the loop squareness ($R_{sq}$), decreased with increasing compressive stress, while the coercive field ($E_c$) remained constant. Stress-induced domain wall motion suppression and non-180° ferroelectric domain switching processes are responsible for the changes observed.

PACS numbers: 77.80.−e, 77.84.−s, 77.84.Dy

## 1. Introduction

Barium titanate ($BaTiO_3$; BT), which exhibits a perovskite structure and a Curie temperature ∼120 °C, is a classical ferroelectric material which has been extensively exploited both for fundamental research and for technological utilization over the past decades [1, 2]. Owing to its high dielectric constant, large mechanical-quality factor, large pyroelectric coefficient, non-toxic handling, low cost of manufacturing and being a lead-free ferroelectric ceramic, BT is an environmentally friendly material, thus making it a strong candidate for various electronic applications in this global climatic situation. These include commercial capacitors, positive temperature coefficient resistors, high-density optical data storage, ultrasonic transducers, piezoelectric devices and semiconductors [3–6]. In many of these applications, BT ceramics are often subjected to mechanical loading, either deliberately in the design of the device itself or the device is used under environmental stresses. Despite this fact, material constants used in any design calculations are often obtained from a stress-free measuring condition, which in turn may lead to incorrect or inappropriate actuator and transducer designs [7]. It is therefore important to determine the electrical properties of BT ceramics as a function of applied stress. Previous investigations on stress-dependence of electrical properties of many ferroelectric ceramics, such as lead zirconate titanate (PZT), lead magnesium niobate (PMN) and PMN–lead titanate (PT) [7, 8], have clearly emphasized the importance of this subject. These works reported that the electrical properties of these ceramics changed significantly on the application of stress. Yimnirun *et al* [7] and Zhou *et al* [9] investigated the effect of external stress on the ferroelectric properties of soft PZT ceramics. Their results showed that the ferroelectric characteristics, i.e. the area of the ferroelectric hysteresis ($P$–$E$) loops, the saturation polarization ($P_{sat}$), the remanent polarization ($P_r$) and the loop squareness ($R_{sq}$), decrease with increasing compressive stress. For BT, the stress dependence on its electrical properties has been widely studied for many decades. Konkol and Piotrowska [10] have studied the effect of one-dimensional stress on the permittivity ($\varepsilon$) of BT ceramics. Their work showed that the $\varepsilon$ value increased with pressure below 100 kg cm$^{-2}$ and increased more slowly after pressure above 100 kg cm$^{-2}$ as domain movement is restricted. After removal of stress, the $\varepsilon$ slowly decreased to the original value. Moreover, Kim *et al* [11] observed the change in domain configuration under external stress and explained it in terms of elastic strain energy minimization. However, there are few works studying the ferroelectric

 © 2007 The Royal Swedish Academy of Sciences Printed in the UK 

properties of BT under stress. Desu [12] studied the influence of stress on the ferroelectric properties of BT thin film and reported that the coercive fields of BT thin film increased while remanent polarization decreased with increasing compressive stress. Sinyakov and Flerova [13] studied the hysteresis loop behavior of BT single crystal with tensile stress. Nevertheless, as well known, the experimental results of thin films and single crystals are always totally different from bulk ceramics because of their different microstructures [14].

Thus far, there have been no systematic studies on the ferroelectric properties of BT bulk ceramics and even though, as mentioned above, there have been many works on electrical properties of BT ceramics since 1940s [1, 2], there are no previous reports on the P–E hysteresis loop results under various environmental stresses of BT bulk ceramics. Therefore, this work will be the first to investigate the dependence of hysteresis loop with stress for BT ceramic. The major purpose of this work is to report the results of P–E hysteresis loops of BT ceramic under various compressive stresses and to discuss these new experimental results. Moreover, the ferroelectric data, i.e. the saturation polarization ($P_s$), the remanent polarization ($P_r$), the coercive field ($E_c$) and the loop squareness ($R_{sq}$), of BT ceramic under compressive stress will also be reported.

## 2. Experimental procedure

Investigations were performed on BT ceramics produced by the conventional mixed oxide method. The x-ray diffraction test at room temperature showed that BT ceramics have a pure perovskite phase with tetragonal symmetry, matched with JCPDS file no 5-0626 with unit cell parameters $a = 3.994$ Å and $c = 4.038$ Å, space group *P4 mm* (no 99) [15]. Disk samples with a diameter of 12.5 mm and a thickness of 0.8 mm were chosen for the electrical measurements and the samples were electroded by silver painting.

The ferroelectric hysteresis (*P–E*) loops were characterized by using a computer controlled modified Sawyer–Tower circuit. The electric field was applied to a sample by a high voltage ac amplifier (Trek, model 610D) with the input sinusoidal signal with a frequency of 100 Hz from a signal generator (Goodwill, model GAG-809). To study the effect of the compressive stress on the ferroelectric properties, the uniaxial compressometer was constructed. The detailed descriptions of this system are explained elsewhere [7, 16]. During the measurements, the specimen was immersed in silicone oil to prevent high-voltage arcing during electric loading. Measurements were performed as a function of mechanical stress applied discretely between 0 and 60 MPa. During the measurements, a desired stress was first applied to the sample and then the electric field was applied. The ferroelectric hysteresis (*P–E*) loop was recorded at room temperature (25 °C). The parameters obtained from the loops were the saturation polarization ($P_s$), the remanent polarization ($P_r$) and the coercive field ($E_c$), which are defined as the points where the loops reach the maximum polarization, cross the zero field and the zero polarization, respectively.

## 3. Results and discussion

The polarization versus electric field (*P–E*) hysteresis loops of the BT ceramics under different compressive stress are shown in figure 1. It should first be noted that the area of these *P–E* hysteresis loops slightly decreases with increasing stress. The *P–E* loop area represents the unit-volume polarization dissipation energy of a ferroelectric material subject to one full cycle of electric field loading [17]. The change in polarization dissipation energy is plotted in figure 2 as a function of compressive stress, in which the dissipation energy is found to decrease linearly with the stress increment. The polarization dissipation energy is also termed energy loss consumed for self-heating of the specimen and related directly to the number of domains participating in the switching process during an electric loading cycle [9]. From figure 2, it is clear that the number of domains contributing to polarization reversal gradually decreases with increasing compressive stress. In the stress-free state (0 MPa), the dissipation energy is $1.10 \times 10^5$ J m$^{-3}$, whereas at maximum stress (60 MPa), the dissipation energy decreases to $0.9 \times 10^5$ J m$^{-3}$ (~20% of the stress-free state), which implies that a lower number of domains participate in polarization reversal under high compressive stress.

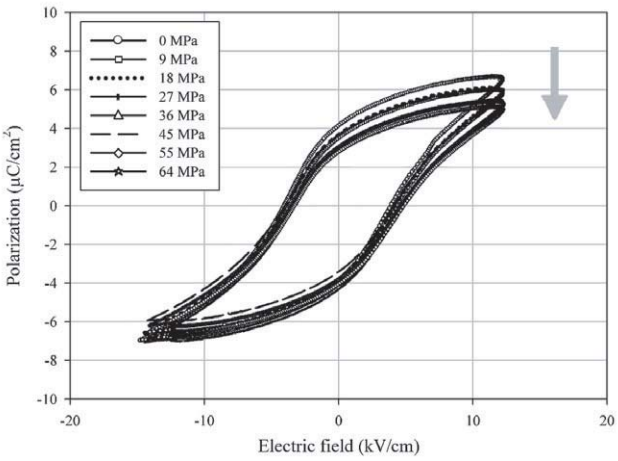



**Figure 1.** Polarization versus electric field (*P–E*) hysteresis loops as a function of compressive stress for BT ceramic.

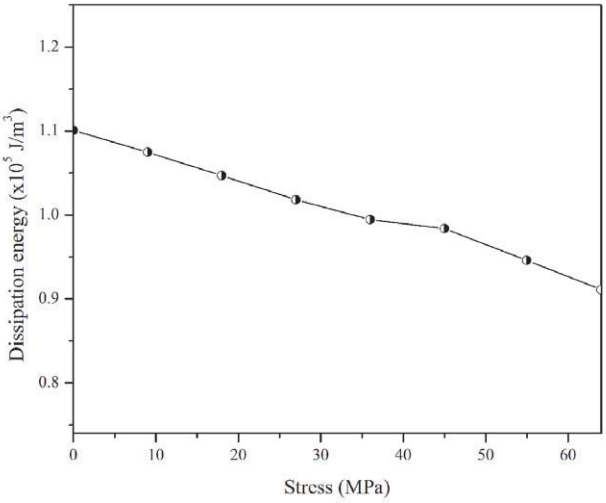



**Figure 2.** Changes in dissipation energy (hysteresis loop area) with compressive stress for BT ceramic.

The changes in the saturation polarization ($P_s$), remanent polarization ($P_r$) and coercive field ($E_c$) with the compressive

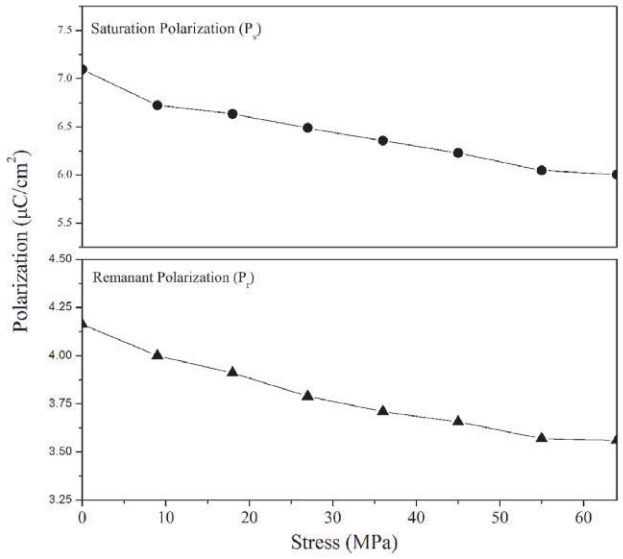



**Figure 3.** Changes in saturated polarization ($P_s$) and remanent polarization ($P_r$) with compressive stress for BT ceramic.

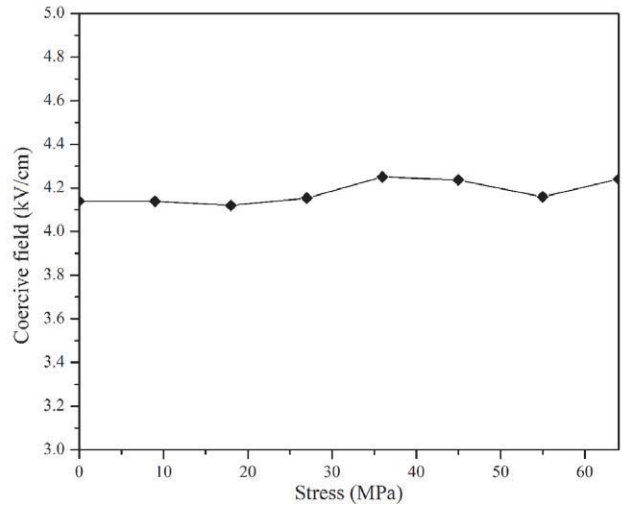



**Figure 4.** Changes in coercive field ($E_c$) with compressive stress for BT ceramic.

stress are plotted in figures 3 and 4, respectively. Similarly to the trend observed in the dissipation energy, figure 3 clearly shows that both the $P_s$ and $P_r$ decrease as the compressive stress increases. This suggests a significant stress induced decrease in the switchable part of the spontaneous polarization of the BT ceramic resulting in the observed decrease in the polarization value under high stress [18]. In contrast, the applied stress shows little or no influence on the coercive field ($E_c$), as plotted in figure 4. These results clearly indicate that BT ceramics are not suitable for high compressive stress applications. It should be noted here that previous works on other ceramics systems, such as PZT, PLZT and PMN–PT, showed a similar tendency [9, 19, 20].

The ferroelectric characteristics of the BT ceramic can also be assessed with the hysteresis loop squareness ($R_{sq}$), which can be calculated from the empirical expression [21, 22]:

$$R_{sq} = \frac{P_r}{P_s} + \frac{P_{1.1E_c}}{P_r}, \quad (1)$$

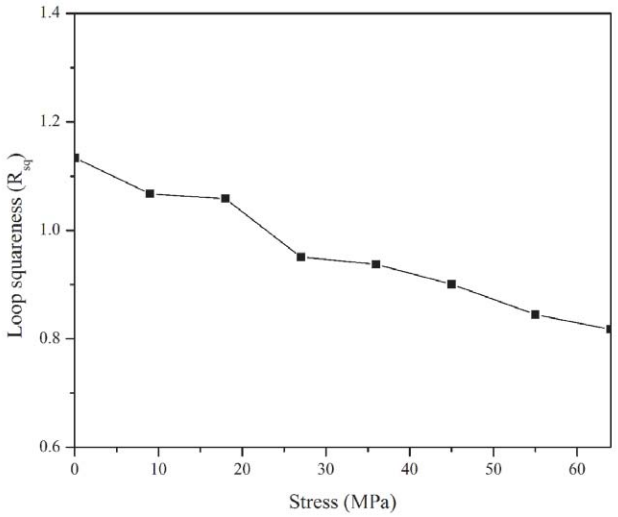



**Figure 5.** Changes in loop squareness ($R_{sq}$) with compressive stress for BT ceramic.

where $P_r$ is the remanent polarization, $P_s$ is the saturated polarization obtained at some finite field strength below the dielectric breakdown and $P_{1.1E_c}$ is the absolute value of the polarization at the field equal to $1.1E_c$. For the ideal square loop, $R_{sq}$ is equal to 2. As shown in figure 5, the $R_{sq}$ values gradually decrease with increasing compressive stress. This observation is clearly a result of the decrease in polarization under the compressive stress. From these results, it can be said that the ferroelectric characteristics of BT ceramic decrease considerably under application of compressive stress.

To understand these experimental results on the BT ceramic, one can interpret the changes in terms of domain-reorientation processes. When the compressive stress is applied in the direction parallel to the poling direction, the applied stress tends to keep the ferroelectric domains aligned with their polar axes away from the stress direction through the non-180° domain switching processes. Therefore, it takes a larger than usual applied electric field to reorient the domain along the stress direction, resulting in a lower value of the saturated polarization (figure 3). When the electric field is reduced to zero the domain tends to rotate back away from the stress direction, resulting in a lower than usual remanent polarization (figure 3). Moreover, the decrease in the dissipation energy with increasing compressive stress indicates that more and more ferroelectric domains are constrained by the stress and cannot be reoriented by the electric field so as to participate in the polarization reversal. Consequently, both the saturated and remanent polarizations become lower with increasing compressive stress. The results of the changes in the ferroelectric characteristics of the BT ceramic with increasing compressive stress are in agreement with previous investigations of many ferroelectric ceramics [7, 9, 23].

## 4. Conclusions

In this study, the effects of compressive stress on the ferroelectric properties of BT ceramic are investigated. Ferroelectric properties under compressive stress are observed up to 60 MPa using a compressometer in conjunction with

a modified Saywer–Tower circuit. The results show that the area of the hysteresis loops, which corresponds to the dissipation energy, the saturation polarization ($P_s$), the remanent polarization ($P_r$) and the loop squareness ($R_{sq}$) decrease with increasing compressive stress, whereas the coercive field ($E_c$) appears unaffected by stress. The non-180° ferroelectric domain switching and stress-induced domain wall suppression processes are responsible for the changes observed. These values ($P_s$, $P_r$, $R_{sq}$ and $E_c$) confirmed that the ferroelectric characteristics of BT ceramic decrease considerably under the application of compressive stress.

## Acknowledgments

This work is supported by the Thailand Research Fund (TRF), the Commission on Higher Education (CHE) and the Faculty of Science, Chiang Mai University.

## References

[1] Moulson A J and Herbert J M 2003 *Electroceramics: Materials, Properties, Applications* (Chichester, UK: Wiley)
[2] Haertling G H 1999 *J. Am. Ceram. Soc.* **82** 797–818
[3] Uchino K 1998 *Piezoelectrics and Ultrasonic Applications* (Dordrecht: Kluwer)
[4] Uchino K 2000 *Ferroelectric Devices* (New York: Dekker)
[5] Hennings D 1987 *J. High Technol. Ceram.* **3** 91–111
[6] Sreekantan S, Noora A, Ahmad Z, Othman R and West A 2007 *J. Mater. Process. Technol.* at press
[7] Yimnirun R, Laosiritaworn Y and Wongsaenmai S 2006 *J. Phys. D: Appl. Phys.* **39** 759–64
[8] Steiner O, Tagantsev A K, Colla E L and Setter N 1999 *J. Eur. Ceram. Soc.* **19** 1243–6
[9] Zhou D, Kamlah M and Munz D 2005 *J. Eur. Ceram. Soc.* **25** 425–32
[10] Konkol R and Piotrowska A 1976 *Mater. Sci.* **2** 127–8
[11] Kim S B, Chung T J and Kim D Y 1993 *J. Eur. Ceram. Soc.* **12** 147–51
[12] Desu S B 1993 *J. Electrochem. Soc.* **140** 2981–7
[13] Sinyakov E V and Flerova S A 1970 *Phys. Solid State* **12** 2728–30
[14] Chiang Y-M, Birnie D P and Kingery W D 1997 *Physical Ceramics* (New York: Wisley)
[15] JCPDS-ICDD card no. 5-0626. International Centre for Diffraction Data, Newtown, PA, 2002
[16] Park S E and Shrout T R 1997 *J. Appl. Phys.* **82** 1804–11
[17] Lines M E and Glass A M 1997 *Principles and Applications of Ferroelectrics and Related Materials* (Oxford: Clarendon)
[18] Yang G, Ren W, Liu S F, Masys A J and Mukherjee B K 2000 *Proc. 2000 IEEE Ultrason. Symp. (San Juan, Puerto Rico)* p 1005–8
[19] Lynch C S 1996 *Acta Mater.* **44** 4137–48
[20] Zhao J and Zhang Q M 1996 *Ferroelectrics* **2** 971–4
[21] Chaisan W, Yimnirun R, Ananta S and Cann D P 2007 *Mat. Chem. Phys.* **104** 103–8
[22] Haertling G H and Zimmer W J 1966 *Am. Ceram. Soc. Bull.* **45** 1084–9
[23] Yimnirun R, Ananta S, Ngamjarurojana A and Wongsaenmai S 2005 *Appl. Phys. A: Mat. Sci. Proc.* **81** 1227–31

Available online at www.sciencedirect.com
ScienceDirect
Ceramics International 34 (2008) 731–734
CERAMICS INTERNATIONAL
www.elsevier.com/locate/ceramint

# Comparative studies of dynamic hysteresis responses in hard and soft PZT ceramics

N. Wongdamnern *, N. Triamnak, A. Ngamjarurojana, Y. Laosiritaworn, S. Ananta, R. Yimnirun

*Department of Physics, Faculty of Science, Chiang Mai University, Chiang Mai 50200, Thailand*

Available online 29 September 2007

**Abstract**

Lead zirconate titanate (PZT) is a ferroelectric material with very interesting and useful dynamic hysteresis properties. Normally, PZT is doped with donors or acceptors to yield better electrical properties. Soft and hard PZT ceramics are respectively donor- and acceptor-doped PZT, which are commercially available and widely employed in various applications. Previous investigations have mainly been focused on the dynamic hysteresis at room temperature and under stress-free condition. However, when used, these ceramics are normally subjected to stress. More importantly, the ambient temperature is usually not at room temperature. Therefore, this study was to investigate dynamic hysteresis behavior of both hard and soft PZT ceramics with varying compressive stress and temperature. The results clearly revealed the influence of external stress and temperature on the dynamic hysteresis of both types of PZT ceramics. Increasing stress and temperature resulted in a decrease of the hysteresis area of the two types of PZT ceramics.
© 2007 Elsevier Ltd and Techna Group S.r.l. All rights reserved.

*Keywords:* A. Dynamic hysteresis; B. Hard PZT; C. Soft PZT

## 1. Introduction

Lead zirconate titanate ($Pb(Zr_{1-x}Ti_x)O_3$ or PZT) ceramics are among the lead-based complex perovskites that have been investigated extensively, from both academic and commercial viewpoints. They are employed extensively in sensor and actuators applications, as well as smart systems [1–6]. The most widely studied and used PZT compositions are in the vicinity of the morphotropic phase boundary (MPB) between the tetragonal and rhombohedral ferroelectric phases [1,4,6–8]. However, to meet the requirements for specific applications, PZT ceramics are usually modified with dopants [1,4,9,10]. Generally, donor (higher valency) additives induce 'soft' piezoelectric behaviors with higher dielectric and piezoelectric activities suitable for sensor and actuator applications. On the other hand, acceptor (lower valency) additives result in 'hard' piezoelectric behaviors particularly suitable for ultrasonic motor applications [1,2,4–6].

However, in these applications, PZT ceramics are often subjected to mechanical loading under different temperatures, either deliberately in the design of the device itself or the use in changing shapes for many smart structure applications or the uses under environmental stresses or environmental heats [1–7]. A prior knowledge of how the material properties change under different conditions is therefore crucial for proper design of a device and for suitable selection of materials for a specific application. Despite that fact, material constants used in many design calculations are often obtained from a stress-free measuring condition or room temperature condition, which in turn may lead to incorrect or inappropriate designs of actuator and transducer. It is therefore important to determine the properties of these materials as functions of applied stress and temperature. Previous investigations on the stress dependence of dielectric and electrical properties of many ceramic systems, i.e. undoped-PZT, PLZT, BT, PMN–PT, PZT–BT and PMN–PZT, have clearly emphasized the importance of the subject [11–19]. The present study aims at studying technically important and commercially available soft and hard PZT ceramics. Many investigations have already revealed interesting results on the dielectric and piezoelectric properties of the

* Corresponding author. Tel.: +66 53 943367; fax: +66 53 943445.
*E-mail address:* nat_4169@hotmail.com (N. Wongdamnern).

0272-8842/$34.00 © 2007 Elsevier Ltd and Techna Group S.r.l. All rights reserved.
doi:10.1016/j.ceramint.2007.09.048

soft and hard PZT ceramics under stress [13–15,19]. However, there has been no work on the stress and temperature dependence of the ferroelectric properties of the ceramics. Therefore, this study is undertaken to investigate the influences of the uniaxial compressive stress and temperature on the ferroelectric properties of the soft and hard PZT ceramics.

## 2. Experimental procedure

A commercially available soft PZT (PKI-552, Piezo Kinetics Inc., USA) and hard PZT ceramics (APCI-840, USA) were used in this study. Soft PZT properties presented (measured by the supplier) a longitudinal charge coefficient $d_{33}$ = 550 pm/V; a planer coupling factor $k_p$ = 0.63, a dielectric constant (1 kHz) $\varepsilon_r$ = 3400, a Curie temperature $T_c$ = 200 °C and a bulk density = 7.6 g/cm$^3$. Hard PZT properties presented $d_{33}$ = 290 pm/V, $k_p$ = 0.59, $\varepsilon_r$ = 1250, $T_c$ = 325 °C and a bulk density = 7.6 g/cm$^3$. The disc-shaped samples with a diameter of 6.27 mm and a thickness of 1 mm were pre-poled by the supplier.

The ferroelectric hysteresis (*P–E*) loops were characterized using a computer controlled modified Sawyer-Tower circuit. The electric field was applied to a sample by a high-voltage ac amplifier (Trek, model 610D) with the input sinusoidal signal with a frequency of 50 Hz from a signal generator (Goodwill, model GAG-809). To study the effects of the uniaxial stress and temperature on the ferroelectric properties, the uniaxial compressometer was constructed with heating system. The compressometer with heater were developed for simultaneous applications of the mechanical stress, the temperature and the electric field. The compressometer cell with heating system consisting of a cylindrical brass cell with a heavy brass base, a brass ram, precisely guided loading platform provides true uniaxial stress during mechanical loading, while the heater provides desired heat to increase the temperature up to 200 °C. The prepared specimen was carefully placed between the two alumina blocks and the electric field was applied to the specimen via the copper shims attached to the alumina blocks. With this setting, the uniaxial compressive stress was applied parallel to the electric field direction and heat was applied to the brass and passed to sample through silicone oil. During the measurements, the specimen was immersed in silicone oil to prevent high-voltage arcing during electric loading. The uniaxial compressive stress was supplied by the servohydraulic load frame and the applied stress was monitored with the pressure guage of the load frame. Heating of the sample was applied by 300 W heater, which was tightened to brass and the applied heat was monitored and controlled by multimeter and computer interface. Measurements were performed as functions of mechanical compressive stress and temperature. Mechanical stress was applied discretely between 0 and 324 MPa and temperature was applied discretely between 25 and 160 °C. The ferroelectric hysteresis (*P–E*) loop was recorded at discrete temperature for each mechanical loading condition. The measurements reported were for the samples during mechanical loading. It should also be noted that the reported ferroelectric parameters were obtained after a total of 10 cycles of the electric field were applied to the sample at constant stress and temperature.

## 3. Results and discussion

The polarization versus electric field (*P–E*) hysteresis loops of the soft and hard PZT ceramics under different compressive stress during loading are shown in Figs. 1 and 2, respectively. It should first be noticed that the area of the *P–E* loops decreases steadily with increasing the compressive stress in both soft and hard PZT ceramics. The *P–E* loop area indicates the polarization dissipation energy of a ferroelectric material subjected to one full cycle of electric field application. This amount of energy loss is directly related to volume involved in the switching process during the application of electric field [2]. Therefore, the decrease in the loop area with increasing stress is a result of the stress-induced domain wall motion suppression [19]. The polarization dissipation energy is consequently found to decrease with increasing the applied stress, indicating that the sample volume contributing to polarization reversal decreases with the increasing compressive stress.

The change in the saturated polarization ($P_{sat}$), the remanent polarization ($P_r$), and the coercive field ($E_c$) with the uniaxial

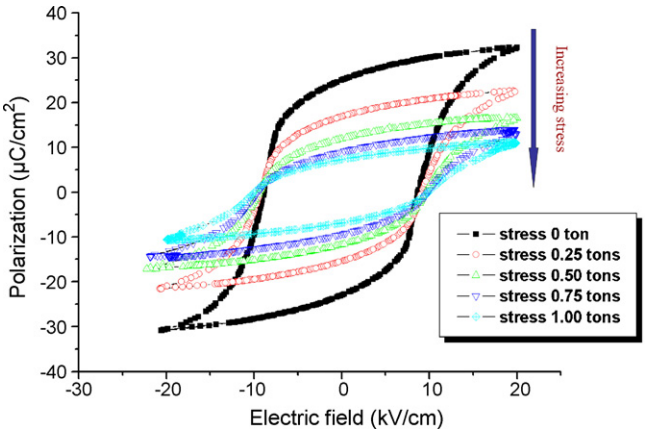



Fig. 1. Polarization vs. electric field (*P–E*) hysteresis loops as a function of compressive stress for soft PZT ceramic during loading.

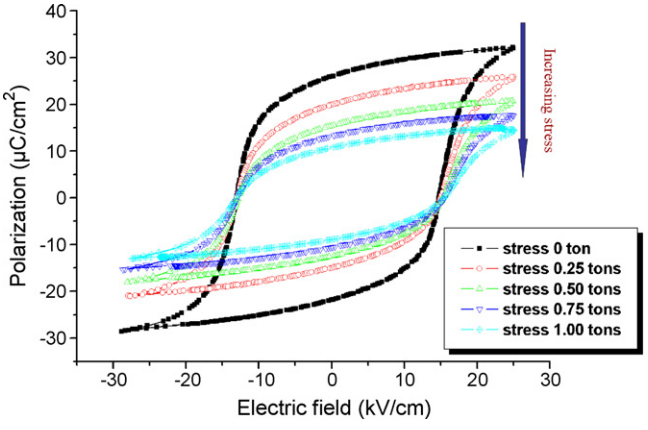



Fig. 2. Polarization vs. electric field (*P–E*) hysteresis loops as a function of compressive stress for hard PZT ceramic during loading.

compressive stress is similar to the trend observed in the dissipation energy (loop area). Both the saturated and remanent polarization decrease as the compressive stress increases. This suggests a significant stress-induced decrease in the switchable part of the spontaneous polarization of the soft and hard PZT ceramics resulting in the observed decrease in the polarization values, as well as the dissipation energy, under high stress [15,23]. In contrast, the applied stress shows little or no influence on the coercive field ($E_c$). It should also be noted that previous investigations on other ceramic systems, such as BT, PLZT, PMN–PT and PMN–PZT, showed a similar tendency [11,12,19–22,24].

To understand, these experimental results on the soft and hard PZT ceramics, one can interpret the changes in term of domain-reorientation processes [13–19]. When uniaxial compressive stress is applied in the direction parallel to the poling direction, the applied stress tends to keep the ferroelectric domain aligned with their polar axes away from the stress direction through the non-180° ferroelectric domain switching processes. Therefore, it takes a larger than usual applied electric field to reorient the domains along the stress direction, resulting in a lower value of the saturated polarization ($P_s$). When the electric field is reduced to zero the domain tend to rotate back away from the applied stress direction, resulting in a lower than usual remanent polarization ($P_r$). Furthermore, the decrease in the dissipation energy with increasing compressive stress indicates that more and more ferroelectric domains are constrain by the stress and cannot be reoriented by the electric field so as to participate in the polarization reversal. Consequently, both the saturated and remanent polarizations become lower with increasing compressive stress [19]. The results of changes in the ferroelectric characteristics of the soft and hard PZT ceramics with increasing compressive stress are in agreement with the previous investigations of many ferroelectric ceramics [11,12,18–25].

The ($P$–$E$) hysteresis loops of the soft and hard PZT ceramics under different temperatures are shown in Figs. 3 and 4, respectively. In both cases, area of the $P$–$E$ loops decreases steadily with increasing the temperature, indicating that polarization dissipation energy decreases when the temperature increases. This is caused by that higher temperature provides

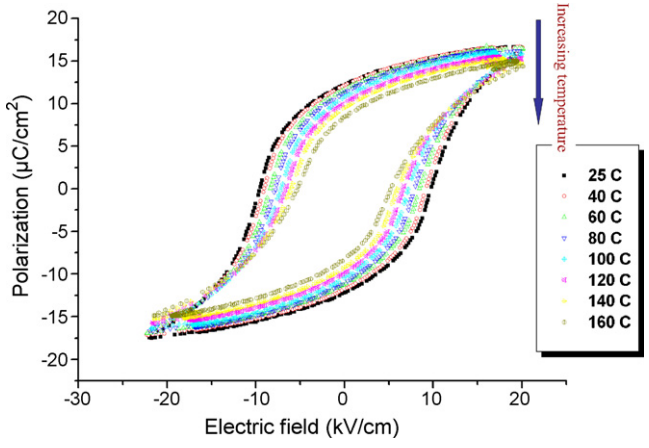



Fig. 3. Polarization vs. electric field ($P$–$E$) hysteresis loops as a function of temperature for soft PZT ceramic.

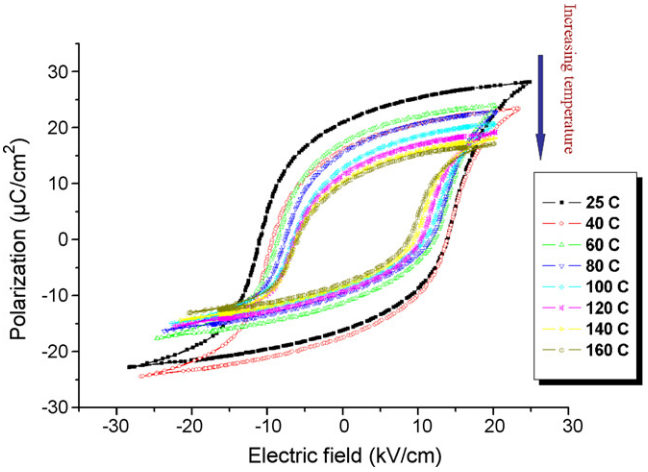



Fig. 4. Polarization vs. electric field ($P$–$E$) hysteresis loops as a function of temperature for hard PZT ceramic.

higher thermal fluctuation to the polarization order parameter, which reduces the ferroelectric interaction among the dipoles. Therefore, even $E_0$ is fixed, the polarization direction is easily turned with the electric field at higher temperatures due to the smaller ferroelectric interaction providing a reduction in both remanent polarization ($P_r$) and coercivity ($E_c$). For this reason, the hysteresis loop area is reduced with increasing the temperature. Additionally, slightly asymmetric $P$–$E$ loops are also observed in the hard PZT, as displayed in Figs. 2 and 4. The observation could be attributed to the presence of the complex defects, which provide the internal field-bias. Therefore, the ferroelectric interaction between these defect dipoles which are trapped near domain walls, and the other dipoles in the domain makes the polarization switching and domain reorientation processes, as well as the domain wall motions, more difficult in one field direction than the other direction. This results in asymmetric loops, and the differences between $E_c^+$ and $E_c^-$, and $P_r^+$ and $P_r^-$, as observed in Figs. 2 and 4.

## 4. Conclusions

In this study, the effects of stress and temperature on the ferroelectric properties of soft and hard PZT ceramics are investigated. The results show that in both types of PZT ceramics the ferroelectric characteristics, i.e. the area of the ferroelectric hysteresis ($P$–$E$) loops, which corresponds to the energy dissipation, the saturated polarization ($P_{sat}$) and the remanent polarization ($P_r$), decrease with increasing compressive stress, while the coercive field ($E_c$) is virtually unaffected by the applied stress. The non-180° ferroelectric domain switching and stress-induced domain wall suppression processes are responsible for the changes observed. Similar decrease of the ferroelectric parameters is also observed with increasing temperature. The cause for the thermal effect is believed to reduce ferroelectric interaction due to higher thermal fluctuation. More importantly, this study undoubtedly shows that the applied stress and the temperature have significant influences on the ferroelectric properties of the soft and hard PZT ceramics.

## Acknowledgments

The Thailand Research Fund (TRF), Commission on Higher Education (CHE), The Development and Promotion of Science and Technology Talents Project (DPST), Faculty of Science and Graduate School of Chiang Mai University are gratefully acknowledged for financial supports.

## References

[1] B. Jaffe, W.R. Cook, H. Jaffe, Piezoelectric ceramics, J. Sound Vib. 20 (4) (1971) 562–563.
[2] G.H. Heartling, Ferroelectric ceramics: history and technology, J. Am. Ceram. Soc. 82 (1999) 797–818.
[3] L.E. Cross, Ferroelectric materials for electromechanical transducer applications, Mater. Chem. Phys. 43 (1996) 108–115.
[4] A.J. Moulson, J.M. Herbert, Electroceramics, Properties, Applications, 2nd ed., Wiley–Interscience, New York, 2003.
[5] K. Uchino, Ferroelectric Devices, vol. 16, Marcel Dekker, Inc., New York, 2000.
[6] Y.H. Xu, Ferroelectric Materials and Their Applications, JAJR Trading, Inc., USA, 1991.
[7] L.E. Cross, Relaxor ferroelectrics, Ferroelectrics 76 (1987) 241–267.
[8] W. Cao, L.E. Cross, Theoretical model for the morphotropic phase boundary in lead zirconate–lead titanate solid solution, Phys. Rev. B 47 (1993), 4825–4830.
[9] S. Takahashi, Effect of impurity doping in lead zirconate titanate ceramics, Ferroelectrics 41 (1982) 143–156.
[10] F. Kulcsar, Electromechanical properties of lead titanate zirconate ceramics modified with certain three or five-valent additives, J. Am. Ceram. Soc. 42 (7) (1959) 343–349.
[11] I.J. Fritz, Uniaxial stress effects in a 95/5 lead zirconate titanate ceramic, J. Appl. Phys. 49 (9) (1978) 4922–4928.
[12] C.S. Lynch, The effect of uniaxial stress on the electro-mechanical response of 8/65/35 PLZT, Acta Mater. 44 (10) (1996) 4137–4148.
[13] Q.M. Zhang, J. Zhao, K. Uchino, J. Zheng, Change of the weak field properties of $Pb(ZrTi)O_3$ piezoceramics with compressive uniaxial stresses and its links to the effect of dopants on the stability of the polarizations in the materials, J. Mater. Res. 12 (1997) 226–234.
[14] J. Zhao, A.E. Glazounov, Q.M. Zhang, Change in electromechanical properties of 0.9PMN–0.1PT relaxor ferroelectric induced by uniaxial compressive stress directed perpendicular to the electric field, Appl. Phys. Lett. 74 (1999) 436–438.
[15] G. Yang, S.F. Lui, W. Ren, B.K. MukHerjee, Effect of uniaxial stress and DC bias field on the piezoelectric, dielectric, and elastic properties of piezoelectric ceramics, in: Proceedings of the IEEE Ultrasonic Symposium 1005 on Smart Structures and Materials, SPIE 3992, 2000, pp. 103–113.
[16] D. Viehland, J. Powers, Effect of uniaxial stress upon the electromechanical properties of various piezoelectric ceramics and single crystals, J. Appl. Phys. 89 (2001) 1820–1825.
[17] R. Yimnirun, S. Ananta, E. Meechoowas, S. Wongsaenmai, Effect of uniaxial stress on dielectric properties of lead magnesium niobate–lead zirconate titanate ceramics, J. Phys. D: Appl. Phys. 36 (2003) 1615–1619.
[18] D. Viehland, J.F. Li, E. McLaugHlin, J. Powers, R. Janus, H. Robinson, Effect of uniaxial stress on the large-signal electromechanical properties of electrostrictive and piezoelectric lead magnesium niobate lead titanate ceramics, J. Appl. Phys. 95 (2004) 1969–1972.
[19] D. Zhou, M. Kamlah, D. Munz, Effects of bias electric fields on the nonlinear ferroelastic behavior of soft lead zirconate titanate piezoceramics, J. Eur. Ceram. Soc. 25 (2005) 425–432.
[20] D. Fang, C. Li, Nonlinear electric-mechanical behavior of a soft. PZT-51 ferroelectric ceramic, J. Mater. Sci. 34 (1999) 4001–4010.
[21] O. Guillon, P. Delobelle, F. Thiebaud, V. Walter, D. Perreux, Uniaxial electromechanical behavior of a soft PZT: experiments and modeling, Ferroelectrics 308 (2004) 95–111.
[22] J. Zhao, Q.M. Zhang, Effect of mechanical stress on the electromechanical performance of PZT and PMN–PT ceramics, in: Proceedings of IEEE 10th International Symposium on Applications of Ferroelectrics (ISAF), vol. 2, 1996, pp. 971–974.
[23] G. Yang, W. Ren, S.F. Liu, A.J. Masys, B.K. Mukherjee, Effect of uniaxial stress and dc bias field on the piezoelectric, dielectric, and elastic properties of piezoelectric ceramics, in: Proceedings of the IEEE Ultrasonic Symposium 1005 on Ultrasonics Symposium, vol. 2, 2000, pp. 1005–1008.
[24] R. Yimnirun, S. Ananta, A. Ngamjarurojana, S. Wongsaenmai, Uniaxial stress dependence of ferroelectric properties of $X$PMN–$(1-X)$PZT ceramic systems, Appl. Phys. A: Mater. Sci. Process. 81 (6) (2005) 1227–1231.
[25] R. Yimnirun, Y. Laosiritaworn, S. Wongsaenmai, Effect of uniaxial compressive pre-stress on ferroelectric properties of soft PZT ceramics, J. Phys. D: Appl. Phys. 39 (2006) 759–764.

Available online at www.sciencedirect.com
ScienceDirect
Ceramics International 34 (2008) 809–812
CERAMICS INTERNATIONAL
www.elsevier.com/locate/ceramint

# Artificial neural network modeling of ceramics powder preparation: Application to $NiNb_2O_6$

W. Laosiritaworn [a,*], O. Khamman [b], S. Ananta [b], R. Yimnirun [b], Y. Laosiritaworn [b]

[a] *Department of Industrial Engineering, Faculty of Engineering, Chiang Mai University, Chiang Mai 50200, Thailand*
[b] *Department of Physics, Faculty of Science, Chiang Mai University, Chiang Mai 50200, Thailand*

Available online 7 October 2007

**Abstract**

This paper studied the modeling of the synthesis process of $NiNb_2O_6$ (NN) powder using an artificial neural network (ANN). The characteristic of interest was the amount of NN phase percentage produced from the synthesis process. Three controlling factors affecting the mentioned characteristic were dwell time, calcined temperature and heating/cooling rate. Design of experiments (DoE) technique was used to analyze the relationship of controlling factors to the amount of NN phase. The results show that calcined temperature is the most important factor affecting the amount of NN phase. The dwell time and heating/cooling rate are less significant on the phase but longer dwell time and higher heating/cooling rate are appreciable for the slightly higher purity. Multiple regression was also used to compare the results and the ANN was found to significantly outperform the regression analysis.
© 2008 Elsevier Ltd and Techna Group S.r.l. All rights reserved.

*Keywords:* Powders preparation; Artificial neural network

## 1. Introduction

Typically, in preparing ceramic powder, several techniques ranging from mechanical milling to chemical method can be used [1]. However, due to many factors involved such as milling time, dwell time, calcined temperature, heating/cooling rate, etc., lots of experimental combinations are possible. Therefore, to search for the optimal condition in obtaining the powder with a pure preferred phase at low cost could be difficult. This method of trial-and-error experiment is not economical and the optimal experimental setting cannot be guaranteed. Consequently, there is a need for a technique which can be used to find the relation between the relevant parameters to obtain the powder with a high purity phase in a cost efficient way. Thus, there comes the objective of this study to suit such a situation using an artificial neural network.

Artificial neural network (ANN) is one of several artificial intelligence tools which has been widely used in various applications due to its ability to learn from samples, and fault tolerance. In this study, it is used to predict the percentage of the desired material in ceramic powder preparation. The $NiNb_2O_6$ (NN) powder was chosen as a case study due to its interesting in being used as a precursor to prepare $Pb(Ni_{1/3}Nb_{2/3})O_3$ [9] which is a potential candidate for electroceramics applications [1–3].

In this study, by following the NN powder preparation technique suggested in Ref. [9], the percentage of the obtained NN phase relevant to the condition of preparation including dwell time, calcined temperature and heating/cooling rate was investigated. Fifty-one experimental samples have been used to construct the ANN model. Once the ANN has been assembled, it was used to predict the percentage of NN phase of the unseen input conditions. Therefore, this minimizes the need to conduct an actual experimentation. Design of experiments (DoE) was then used to analyze the effect of controlling factors to the percentage of NN phase. Multiple regression model was also used for a comparison purpose.

### 1.1. Background theories

#### 1.1.1. Artificial neural network

Artificial neural network (ANN) is 'an interconnected assembly of simple processing elements, *units* or *nodes*, whose

* Corresponding author.
*E-mail address:* wimalin@eng.cmu.ac.th (W. Laosiritaworn).

0272-8842/$34.00 © 2008 Elsevier Ltd and Techna Group S.r.l. All rights reserved.
doi:10.1016/j.ceramint.2007.09.102

functionality is loosely based on the animal neuron. The processing ability of the network is stored in the inter-unit connection strengths, or *weights*, obtained by a process of adaptation to, or *learning* from, a set of training patterns' [4].

Inspired by how the brain and nerve cells work, ANN is constructed by connecting simple processing elements or neurons together. Neurons can be located in the input layer, the output layer or the hidden layers. The input layer takes data from the outside of a neural network and sends it to hidden layer neurons. The output layer sends the information back outside the network.

ANN training can be supervised or unsupervised (self-organising). This paper is focused on supervised training. The back-propagation algorithm is the most extensively adopted algorithm for network training [5] and is the type of network used in this research.

#### 1.1.2. Statistical design of experiments

Statistical DoE was first developed in the early 1920s by Sir Ronald Fisher to determine the effect of multiple factors on the outcome of agricultural trials. The work of statisticians [6,7] with an interest in this area has provided a firm foundation for practitioners. DoE is a statistical and structural method used to analyze relationships between factors affecting processes (independent variables) and the output of those processes (dependent variables). DoE techniques are widely used, both by researchers, for characterisation, optimisation, and modelling [8].

## 2. Experimental procedures

### 2.1. NN powder preparation

The NN powder was synthesized by the solid-state reaction of thoroughly ground mixtures of NiO and $Nb_2O_5$ powders milling in the required stoichiometric ratio. The detailed description of the NN powder preparation is given elsewhere [9]. In this study, the NN powder was synthesized by varying dwell time from 1 to 48 h, calcined temperature from 500 to 1200 °C, and heating/cooling rate from 3 to 30 °C/min. Then the obtained powder is investigated by X-ray diffraction (XRD) technique to calculate the percentage of NN phase. However, if there exist more than two phases in the XRD pattern, the NN percentage is set as unclassified. Controlling factors in the experiments were set by trial-and-error and percentage of NN phase were recorded. Fifty-one records of experimental data were available.

### 2.2. Multiple regression analysis

A multiple regression model has the following form:

$$y = \beta_0 + \beta_1 x_1 + \beta_2 x_2 + \cdots + \beta_k x_k,$$

where $\beta_0$ is the intercept, $\beta_1, \ldots, \beta_k$ refer to parameters representing the contribution of the independent variables, and $x_1, \ldots, x_k$ are independent variables.

Of the 51 records available, 41 records were randomly selected and used to fit regression equation while the remaining 10 records was used as independent test set. The regression equation is as follows:

$$y = -103.905 + 0.189x_1 + 0.810x_2 + 0.616x_3,$$

where $y$ is the percentage of NN phase obtained, while $x_1$, $x_2$ and $x_3$ refer to calcined temperature, dwell time and heating/cooling rate, respectively. The results from regression analysis are compared with the result from ANN in the next section.

### 2.3. Artificial neural network training and testing

The same data set used to fit regression equation was used to train ANN. The training was carried out with 41 records and the remaining 10 records for testing ANN performance. Qnet v2000 software was used to develop an ANN model. The network developed consisted of three layers. Input layer has three neurons representing calcined temperature, dwell time and heating/cooling rate while the output layer has one neuron which represents the prediction of percentage of NN phase obtained. Hidden layer neurons were selected by trial-and-error and the appropriate number of hidden neurons were 17. Root mean square error of the training and testing data were 0.039701 and 0.049907, respectively, and the correlation coefficient of training and testing data were 0.977587 and

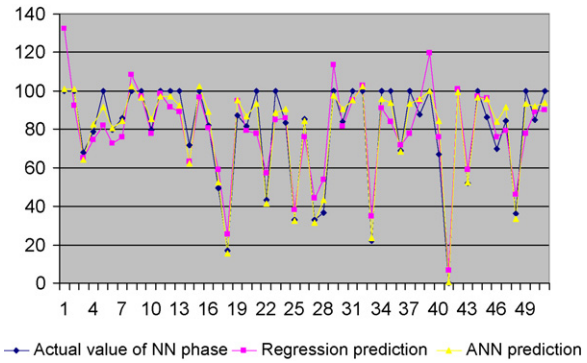



Fig. 1. The comparison of actual value with regression prediction and ANN prediction.

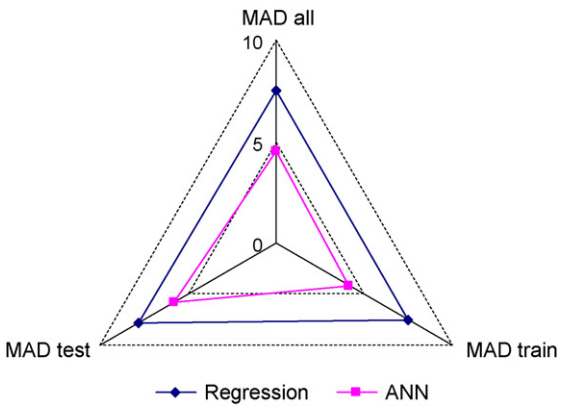



Fig. 2. MAD of results from regression model and ANN model.

Table 1
ANOVA analysis

| Source | d.f. | Seq SS | Adj SS | Adj MS | *F* | *P* |
|---|---|---|---|---|---|---|
| Calcined temperature | 4 | 148162.3 | 148162.3 | 37040.6 | 3532.83 | 0 |
| Dwell time | 6 | 2207 | 2207 | 367.8 | 35.08 | 0 |
| Heating/cooling rate | 2 | 525.1 | 525.1 | 262.6 | 25.04 | 0 |
| Calcined temperature × dwell time | 24 | 280.9 | 280.9 | 11.7 | 1.12 | 0.363 |
| Calcined temperature × heating/cooling rate | 8 | 2907.1 | 2907.1 | 363.4 | 34.66 | 0 |
| Dwell time × heating/cooling rate | 12 | 1317.7 | 1317.7 | 109.8 | 10.47 | 0 |
| Error | 48 | 503.3 | 503.3 | 10.5 | | |
| Total | 104 | 155903.4 | | | | |

d.f.: degree of freedom; Seq SS: sequencial sum of squares; Adj SS: adjusted sum of squares; Adj MS: adjusted mean square; *F*: *F*-statistic; *P*: *p*-value.

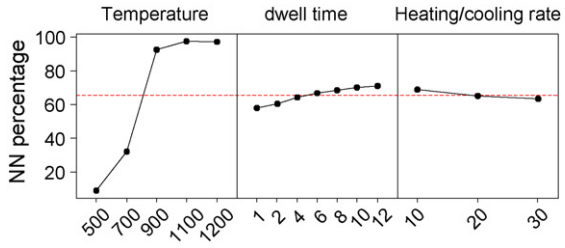



Fig. 3. Main effect plot (data means) of NN percentage.

0.947345, respectively. As the correlation coefficient of both training and testing data were very close to 1, the model is a good approximation of real experimentations.

Fig. 1 shows the actual data of percentage of NN phase compared with the prediction from regression and ANN. Fig. 2 is the radar chart that illustrates mean absolute deviation (MAD) of the overall, training and testing data of the results from both regression and ANN. It can be concluded from both figures that ANN significantly outperform multiple regression, as a result ANN model was used for further analysis.

### 2.4. Design of experimental analysis

After the ANN had been properly trained, it was used to predict experimental results. Experiments were set at five levels for the calcined temperature ranging from 500 to 1200 °C, seven levels for the dwell time ranging from 1 to 12 h and three levels for the heating/cooling rate ranging from 10 to 30 °C/min, with all possible combinations of experimental setting of 105. These experimental settings were fed to the trained ANN to obtain the prediction of the NN phase.

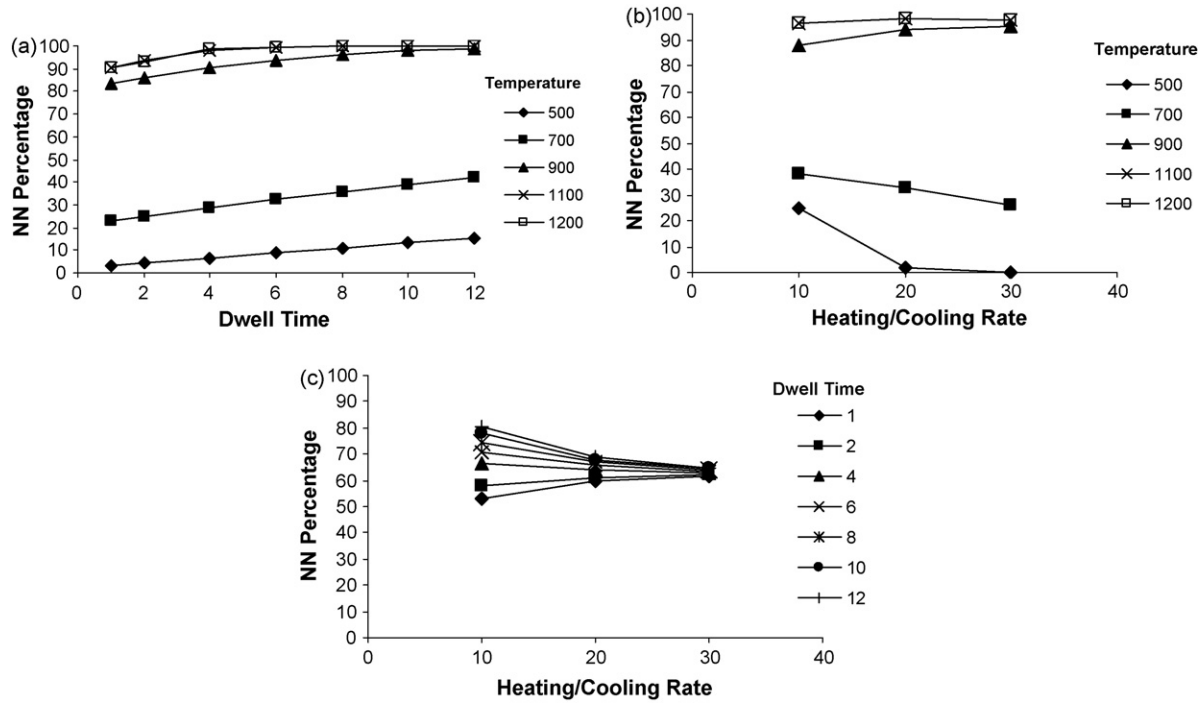



Fig. 4. Interaction plot (data means) of NN percentage: (a) between temperature and dwell time; (b) between temperature and heating/cooling rate; (c) between heating/cooling rate and dwell time.

## 3. Results and discussion

Analysis of variance (ANOVA) was carried out to identify significant factors and factor interactions to the percentage of NN. The ANOVA analysis was prepared by using MINITAB release 14. Table 1 summarises the significant factors of each response at the 95% confidence level. Significant factors at the 95% confidence level were the factor that has $P$ value lower than 0.05. As a result, calcined temperature, dwell time, heating/cooling rate, interaction of calcined temperature and heating/cooling rate and interaction of dwell time and heating/cooling rate are found to be significant with different levels.

The relation among the experimental parameters in obtaining the high purity NN phase can be analysed by the main effect plot (Fig. 3), which shows the effect of each controlling factors on the NN percentage. The graph indicated that calcined temperatures has the highest effect on NN percentage and there is a steep decrease in NN percentage at temperature below 900 °C. Dwell time and heating/cooling rate have less effect than calcined temperature but their effects are still significant according to the ANOVA analysis.

The interaction plot (data mean) of NN percentage is shown in Fig. 4. Each sub-figure represents the interaction between a pair of preparation conditions in obtaining the NN phase. Since there are three relevant parameters considered in this study, when a pair is chosen, each data point in the considered sub-figure is calculated from the average over the remaining parameter. For instance, Fig. 4(a) shows the interaction of temperature and time of the obtained NN phase in which each data point is calculated from the average over all considered heating/cooling rate.

It can be summarised from Fig. 4(a) that the calcined temperature has prominent effect on the percentage of NN phase, where a very high percentage is obtained only for the temperature above (or equal to) 900 °C. A huge leap in the percentage is found in calcined temperature between 700 and 900 °C, but the longer dwell time only slightly enhances the percentage. Slight dependence on heating/cooling rate of the NN phase is also found (Fig. 4(b)). The strong reliance on the temperature is again apparent. On the other hand, Fig. 4(c) shows the relation of heating/cooling rate of the NN phase with varying dwell time. As can be seen, the high percentage is found for low heating/cooling rate but high dwell time. The description underlying all these phenomena can be given via thermodynamics of phase transformation. Presumably, to grow the NN phase, the thermal energy must be at the right condition corresponding to the energy barrier. If the calcined temperature is too low, the thermal energy might not be enough to trick out the NN phase. However, even the heating/cooling rate does not have a significant effect on the percentage of NN phase, but when the rate is too high, there might not be enough time for the NN phase to get growing so a longer dwell time is needed.

## 4. Conclusions

The ANN technique was used to study the relation among calcined temperature, dwell time and heating/cooling rate in obtaining the high percentage of NN phase. In this study, the high accuracy ANN model of NN synthesis process, was constructed from a minority of training examples, in predicting the results from an untrained experiment. Also from the prediction, a significant effect from the relevant parameters to the percentage of NN phase is apparent. The most important factor to obtain the high percentage is the calcined temperature while the dwell time has a moderate effect on the phase, and the heating/cooling rate has the least significant. The major advantage of ANN is that it allows the through analysis of the relationship of controlling factors to the amount of NN phase without conducting experiments randomly. The traditional trial-and-error experiment might results in conducting many experiments, yet the optimal solution might never be found. The techniques adopted in this article could also be applied to other process which will results in a more economical and structure way for data analysis.

## Acknowledgements

The authors would like to acknowledge Thailand Research Fund (TRF) and the Commission on Higher Education (CHE) for financial support.

## References

[1] J.S. Reed, Principles of Ceramic Processing, 2nd ed., Wiley, New York, 1995.
[2] G.H. Haertling, Ferroelectric ceramics: history and technology, J. Am. Ceram. Soc. 82 (1999) 797–818.
[3] A.J. Moulson, J.M. Herbert, Electroceramics, 2nd ed., Wiley, Chichester, 2003.
[4] K. Gurney, An Introduction to Neural Networks, UCL Press Limited, London, 1997.
[5] C.A.O. Nascimento, R. Giudici, R. Guardani, Neural network based approach for optimization of industrial chemical processes, Comput. Chem. Eng. 24 (2000) 2303–2314.
[6] G.E.P. Box, W.G.J. Hunter, S. Hunter, Statistics for Experimenters: An Introduction to Design, Data Analysis, and Model Building, Wiley, New York, 1987.
[7] D.C. Montgomery, Design and Analysis of Experiments, 5th ed., John Wiley & Sons Inc., New York, 2001.
[8] J. Antony, R.K. Roy, Improving the process quality using statistical design of experiments: a case study, Qual. Assur. 6 (1999) 87–95.
[9] O. Khamman, R. Yimnirun, S. Ananta, Phase and morphology evolution of corundum-type $Ni_4Nb_2O_9$ powders synthesized by solid-state reaction, Mater. Lett. 61 (2006) 2565–2570.

Available online at www.sciencedirect.com
ScienceDirect
Ceramics International 34 (2008) 705–708
CERAMICS INTERNATIONAL
www.elsevier.com/locate/ceramint

# Piezoelectric properties of low temperature sintering in $Pb(Zr,Ti)O_3$–$Pb(Zn,Ni)_{1/3}Nb_{2/3}O_3$ ceramics for piezoelectric transformer applications

A. Ngamjarurojana [a,*], S. Ural [b], S.H. Park [b], S. Ananta [a], R. Yimnirun [a], K. Uchino [b]

[a] *Department of Physics, Faculty of Science, Chiang Mai University, Chiang Mai 50200, Thailand*
[b] *International Center for Actuators and Transducers, Materials Research Institute, Pennsylvania State University, University Park, PA 16802, USA*

Available online 25 September 2007

**Abstract**

In this study, in order to develop low-temperature sintering ceramics for a multilayer piezoelectric transformer application, we explored CuO and $Bi_2O_3$ as sintering aids at low temperature (900 °C) sintering condition for Sb, Li and Mn-substituted $0.8Pb(Zr_{0.48}Ti_{0.52})O_3$–$0.16Pb(Zn_{1/3}Nb_{2/3})O_3$–$0.04Pb(Ni_{1/3}Nb_{2/3})O_3$ ceramics. These substituted ceramics have excellent piezoelectric and dielectric properties such as $d_{33} \sim 347$ pC/N, $k_p \sim 0.57$ and $Q_m \sim 1469$ when sintered at 1200 °C. The addition of CuO decreased the sintering temperature through the formation of a liquid phase. However, the piezoelectric properties of the CuO-added ceramics sintered below 900 °C were lower than the desired values. The additional $Bi_2O_3$ resulted in a significant improvement in the piezoelectric properties. The composition Sb, Li and Mn-substituted $0.8Pb(Zr_{0.48}Ti_{0.52})O_3$–$0.16Pb(Zn_{1/3}Nb_{2/3})O_3$–$0.04Pb(Ni_{1/3}Nb_{2/3})O_3$ + 0.5 wt% CuO + 0.5 wt% $Bi_2O_3$ showed the value of $k_p = 0.56$, $Q_m = 1042$ (planar mode), $d_{33} = 350$ pC/N, when it was sintered at 900 °C for 2 h. These values indicated that the newly developed composition might be suitable for multilayer piezoelectric transformer application.
© 2007 Elsevier Ltd and Techna Group S.r.l. All rights reserved.

*Keywords:* Low temperature sintering; Piezoelectric transformer and vibration velocity

## 1. Introduction

The materials for piezoelectric actuators, ultrasonic motors and piezoelectric transformers applications should have compromised characteristics between hard and soft piezoelectrics, implying high electromechanical coupling factor ($k$) and piezoelectric constant ($d$) with high mechanical quality factor ($Q_m$) [1].

However, the sintering temperature of lead zirconate titanate (PZT)-based high-power compositions is usually too high, approximately 1200 °C, to use base metal electrodes such as Ag and Cu. Therefore, Ag/Pd alloy is generally used as the electrode to suppress the migration of Ag into the ceramics at high temperature. Consequently, lowering of the sintering temperature of piezoelectric ceramics is essential for the fabrication of cost-effective multilayer piezoelectric devices. Furthermore, low temperature sintering can provide advantages such as compatibility with low temperature cofired ceramics (LTCC), the reduction of energy consumption, and the reduced PbO volatilization.

Previously, various techniques were employed to obtain the low temperature sinterable PZT composition. The addition of dopants, which improves solid-state sintering, and the addition of oxides and compounds, which have low melting points for liquid-phase sintering are the most popular methods [2–4]. Some of the oxides and compounds that have been used for assisting liquid-phase sintering [5–9]. Even though these techniques were able to obtain dense ceramics at low sintering temperature, piezoelectric properties were not satisfactory enough to be used in industry.

Previously, we developed the Sb, Li and Mn-substituted $Pb(Zr_{0.48}Ti_{0.52})O_3$–$Pb(Zn_{1/3}Nb_{2/3})O_3$–$Pb(Ni_{1/3}Nb_{2/3})O_3$ ceramics with excellent dielectric and piezoelectric properties when sintered at 1200 °C [10]. The aim of this study was to

* Corresponding author. Tel.: +66 53 941921x445; fax: +66 53 943445.
*E-mail address:* Ngamjarurojana@yahoo.com (A. Ngamjarurojana).

0272-8842/$34.00 © 2007 Elsevier Ltd and Techna Group S.r.l. All rights reserved.
doi:10.1016/j.ceramint.2007.09.012

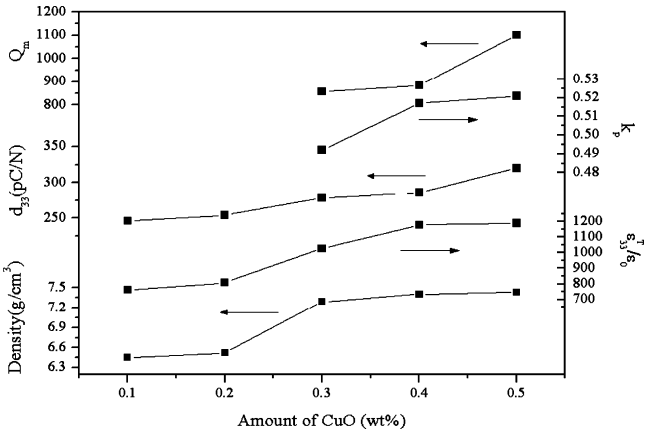



Fig. 1. Density, dielectric permittivity ($\varepsilon_{33}^{T}/\varepsilon_0$), piezoelectric constant ($d_{33}$), electromechanical coupling factor ($k_p$) and mechanical quality factor ($Q_m$) and of the specimens sintered at 900 °C for 2 h in $Pb(Zr,Ti)O_3$–$Pb(Zn,Ni)_{1/3}Nb_{2/3}O_3$ + $x$ wt% CuO ceramics.

lower the sintering temperature of this composition for providing Ag or Cu cofiring compatible high-power piezoelectric ceramics, aiming at layered structure piezoelectric actuators and transformer applications. We therefore investigated the effect of CuO and $Bi_2O_3$ addition in the Sb, Li and Mn-substituted $Pb(Zr_{0.48}Ti_{0.52})O_3$–$Pb(Zn_{1/3}Nb_{2/3})O_3$–$Pb(Ni_{1/3}Nb_{2/3})O_3$ ceramics as a solution for low temperature sinterable high power ceramics.

## 2. Experimental procedure

The specimens studied in this research were fabricated according to the formula: $0.8Pb(Zr_{0.48}Ti_{0.52})O_3$–$0.16Pb(Zn_{1/3}Nb_{2/3})O_3$–$0.04Pb(Ni_{1/3}Nb_{2/3})O_3$ with Sb, Li and Mn substitution $(Pb(Zr,Ti)O_3$–$Pb(Zn,Ni)_{1/3}Nb_{2/3}O_3)$ + $x$ wt% CuO + $y$ wt% $Bi_2O_3$, where $x = 0.1$–$0.5$; $y = 0$–$0.5$, respectively. Raw materials of PbO, $ZrO_2$, $TiO_2$, ZnO, NiO, $Nb_2O_5$, $Sb_2O_5$, $Li_2CO_3$, $MnO_2$, CuO and $Bi_2O_3$ with >99% purity were used to prepare samples by a conventional ceramic sintering process. The obtained mixture was ball-milled using zirconia ball media with isopropanal as a medium in a polyethylene jar for 24 h. The mixed slurry was dried and calcined at 750 °C for 2 h. The calcined powders were ball-milled again with additives and consolidated into disks of 12.5 mm diameter and rectangular plates using isostatic pressing about 150 MPa. PbO-rich atmosphere sintering of the ceramics was performed in a high-purity alumina crucible at the temperature of 850–900 °C for 2 h. The crystal structure and symmetry of the sintered bodies were examined by X-ray diffraction (XRD) and sintered densities were measured by the Archimedes method. Silver electrode (Dupont, QS 171) was printed on the lapped surfaces for electrode. The electrode specimens were poled in silicone oil at 150 °C by applying a dc field of 3 kV/mm for 30 min. The piezoelectric constant ($d_{33}$) was measured using a quasi-static piezoelectric $d_{33}$ meter (Model ZJ-3d, Institute of Acoustics Academic Sinica, China). The planar coupling coefficient ($k_p$)

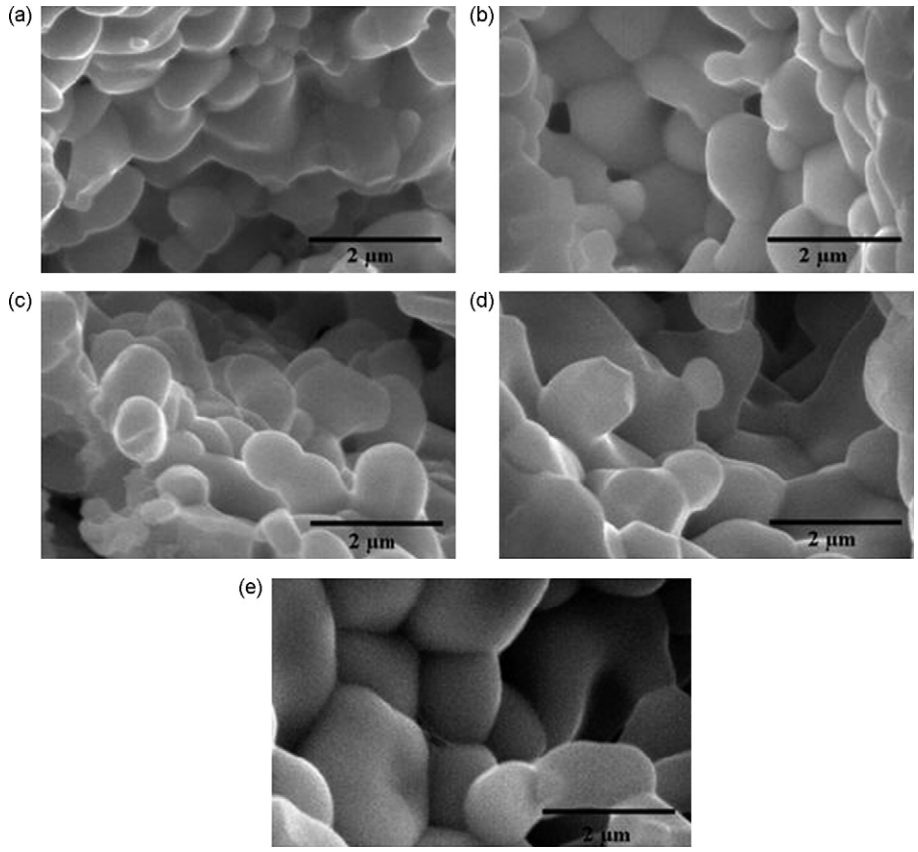



Fig. 2. SEM images of the samples sintered at 900 °C for 2 h in $Pb(Zr,Ti)O_3$–$Pb(Zn,Ni)_{1/3}Nb_{2/3}O_3$ + $x$ wt% CuO ceramics.: (a) $x = 0.1$, (b) $x = 0.2$, (c) $x = 0.3$, (d) $x = 0.4$ and (e) $x = 0.5$.

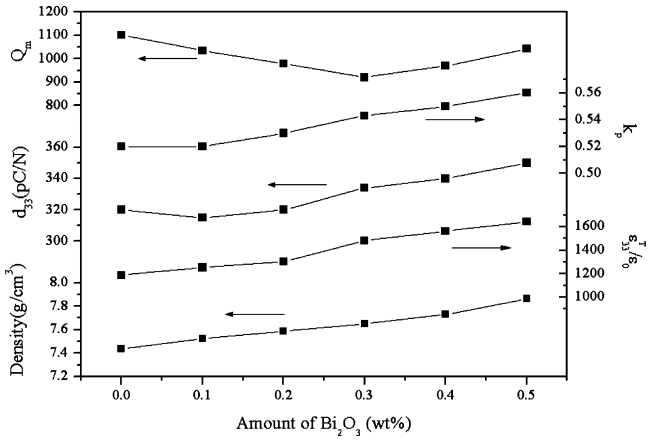



Fig. 3. Density, dielectric permittivity $(\varepsilon_{33}^{T}/\varepsilon_0)$, piezoelectric constant ($d_{33}$), electromechanical coupling factor ($k_p$) and mechanical quality factor ($Q_m$) and of the specimens sintered at 900 °C for 2 h in $Pb(Zr,Ti)O_3$–$Pb(Zn,Ni)_{1/3}Nb_{2/3}O_3$ + 0.5 wt% CuO + $y$ wt% $Bi_2O_3$ ceramics.

and the mechanical quality factor ($Q_m$) were determined by the resonance and anti-resonance technique using an impedance analyzer (Model HP4294A, Hewlett-Packard, CA).

## 3. Results and discussion

### 3.1. Effect of CuO addition

Initially, the effect of the addition of CuO on the sinterability, crystal structure, piezoelectric and dielectric properties was investigated in $Pb(Zr,Ti)O_3$–$Pb(Zn,Ni)_{1/3}Nb_{2/3}O_3$-based ceramics. The sintering temperature of all the specimens was fixed at 900 °C, which is cofiring compatible temperature for Ag and low temperature cofired ceramics (LTCC) substrate. Density, dielectric permittivity $(\varepsilon_{33}^{T}/\varepsilon_0)$, electromechanical coupling factor ($k_p$), mechanical quality factor and piezoelectric constant ($d_{33}$) were plotted as a function of the amount of CuO addition in Fig. 1. The density was increased with the increase of CuO contents approximately from 6.4 to 7.8 g/cm$^3$. This improvement of the density might be related to the formation of the liquid phase. Moreover, the variation of piezoelectric and dielectric properties showed similar trend to that of density. Therefore, the improved piezoelectric and dielectric properties, which were observed in the range of $x \geq 0.3$, might be due to the increased density as well as increased grain size shown in Fig. 2. This hardening effect that could be confirmed by the enhancement of $Q_m$ value approximately from 600 to 1200 as shown in Fig. 1. Therefore, Cu ions could be expected to enter B site and act as a hardener. Fig. 2 shows the SEM images of the $Pb(Zr,Ti)O_3$–$Pb(Zn,Ni)_{1/3}Nb_{2/3}O_3$ + $x$ wt% CuO ceramics sintered at 900 °C for 2 h. As the CuO addition amount increased, grain growth happened whereas small grains disappeared. This grain growth with CuO addition can be explained with liquid phase sintering. Previously, we showed that the addition of CuO can reduce the sintering temperature of the $Pb(Zr,Ti)O_3$–$Pb(Ni,Nb)O_3$ system by the formation of a liquid phase [11]. Thus, this liquid phase formation can also be an explanation for the $Pb(Zr,Ti)O_3$–$Pb(Zn,Ni)_{1/3}Nb_{2/3}O_3$ + $x$ wt% CuO ceramics.

### 3.2. Effect of $Bi_2O_3$ addition

$Bi_2O_3$ has low melting temperature (817 °C) and it was reported $Bi_2O_3$ can form liquid phase with ZnO at approximately 750 °C. Therefore, $Bi_2O_3$ was added to $Pb(Zr,Ti)O_3$–$Pb(Zn,Ni)_{1/3}Nb_{2/3}O_3$ + 0.5 wt% CuO in order to further improve the piezoelectric properties of the specimens sintered at low temperature. Density, dielectric permittivity $(\varepsilon_{33}^{T}/\varepsilon_0)$, electromechanical coupling factor ($k_p$), mechanical quality

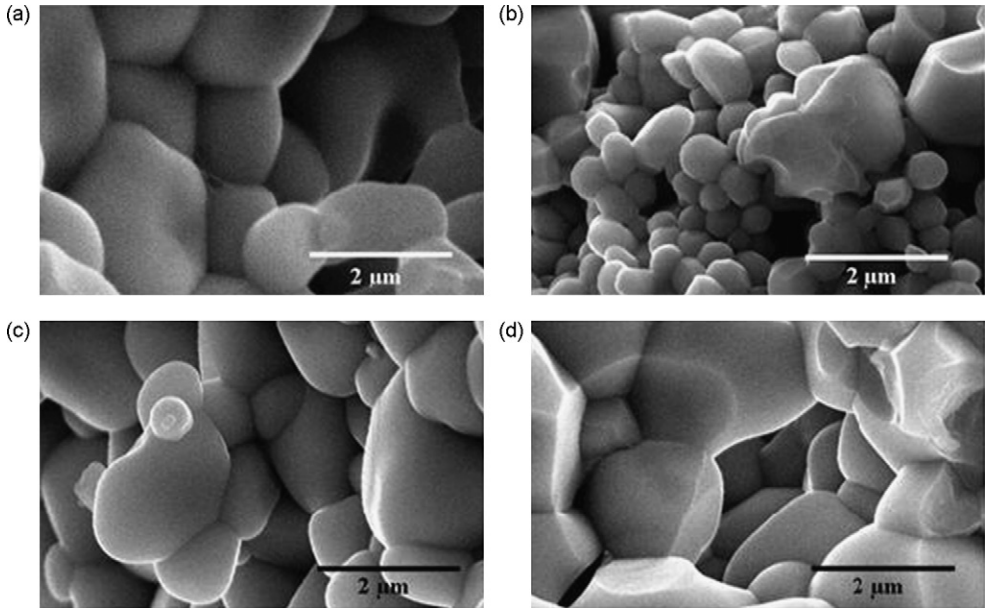



Fig. 4. SEM images of the samples sintered at 900 °C for 2 h in $Pb(Zr,Ti)O_3$–$Pb(Zn,Ni)_{1/3}Nb_{2/3}O_3$ + 0.5 wt% CuO + $y$ wt% $Bi_2O_3$ ceramics.: (a) $y = 0$, (b) $y = 0.1$, (c) $y = 0.3$ and (d) $y = 0.5$.

factor and piezoelectric constant ($d_{33}$) of $Pb(Zr,Ti)O_3$–$Pb(Zn,Ni)_{1/3}Nb_{2/3}O_3$ + 0.5 wt% CuO + $y$ wt% $Bi_2O_3$ ceramics sintered at 900 °C for 2 h are plotted as a function of the amount of $Bi_2O_3$ addition in Fig. 3. When $Bi_2O_3$ was added, density was increased and this increased density improved the dielectric and piezoelectric properties as seen in Fig. 3. The density of the specimens was improved when the amount of $Bi_2O_3$ was added and this increase might be due to the formation of liquid phase. In addition, $Q_m$ was decreased and $\varepsilon_{33}^T/\varepsilon_0$ and $d_{33}$ were increased with the amount of $Bi_2O_3$ addition in the range of $0.0 \leq y \leq 0.3$. Therefore, their variations could happen because Bi ions entered A site, since they acted as softener in this range. On the contrary, $Q_m$ exhibits a minimum profile at 0.3 wt% of $Bi_2O_3$ addition. In addition, $\varepsilon_{33}^T/\varepsilon_0$, $d_{33}$ and $Q_m$ were increased with the amount of $Bi_2O_3$ addition above 0.3 wt%. Thus, Bi ions might act as both hardener and softener in this range and their variations might be able to occur because Bi ions entered B site and A site, respectively. Fig. 4 shows the SEM images of the $Pb(Zr,Ti)O_3$–$Pb(Zn,Ni)_{1/3}Nb_{2/3}O_3$ + 0.5 wt% CuO + $y$ wt% $Bi_2O_3$ ceramics sintered at 900 °C for 2 h. When the amount of $Bi_2O_3$ was more than 0.3 wt%, the small grains almost disappeared and average grain size increased. Even though apparent liquid phase formation was not observed in the SEM images, $Bi_2O_3$ addition might induce small amount of liquid phase and it could be expected to help grain growth due to its low melting point.

## 4. Conclusions

In this study, we developed CuO and $Bi_2O_3$ as sintering aids at low temperature sintering condition (900 °C) for Sb, Li and Mn-substituted $Pb(Zr,Ti)O_3$–$Pb(Zn,Ni)_{1/3}Nb_{2/3}O_3$ ceramics. The addition of CuO decreased the sintering temperature through the formation of a liquid phase. However, the piezoelectric properties of the CuO-added ceramics sintered below 900 °C were lower than the desired values. The additional $Bi_2O_3$ resulted in a significant improvement in the piezoelectric properties.

At the sintering temperature of 900 °C, the electromechanical coupling factor ($k_p$), piezoelectric constant ($d_{33}$), mechanical quality factor ($Q_m$) of Sb, Li and Mn-substituted $0.8Pb(Zr_{0.48}Ti_{0.52})O_3$–$0.16Pb(Zn_{1/3}Nb_{2/3})O_3$–$0.04Pb(Ni_{1/3}Nb_{2/3})O_3$-based ceramics with 0.5 wt% CuO and 0.5 wt% $Bi_2O_3$ show the optimal value of 0.56, 350 pC/N and 1042, respectively. These values indicated that the newly developed composition might be suitable for multilayer piezoelectric transformer application.

## Acknowledgements

This work was supported by the Thailand Research Fund (TRF) and Commission on Higher Education (CHE). The authors are thankful to the Graduate School and Faculty of Science, Chiang Mai University and the Ministry of Education for financial support.

## References

[1] K. Uchino, J.R. Giniewicz, Micromechatronics, Marcel Dekker, New York, 2003.
[2] S. Takahashi, Sintering $Pb(Zr,Ti)O_3$ ceramics at low temperature, Jpn. J. Appl. Phys. 19 (4) (1980) 771–1771.
[3] P.G. Lucuta, F. Constantinescu, D. Barb, Structural dependence on sintering temperature of lead zirconate–titanate solid solutions, J. Am. Ceram. Soc. 68 (10) (1985) 533–537.
[4] G. Zhilun, L. Longtu, G. Suhua, Z. Xiaowen, Low-temperature sintering of lead-based piezoelectric ceramics, J. Am. Ceram. Soc. 72 (3) (1989) 486–491.
[5] S. Kaneko, D. Dong, K. Murakami, Effect of simultaneous addition of $BiFeO_3$ and $Ba(Cu_{0.5}W_{0.5})O_3$ on lowering of sintering temperature of $Pb(Zr,Ti)O_3$ ceramics, J. Am. Ceram. Soc. 68 (4) (1998) 1013–1018.
[6] X. Wang, K. Murakami, S. kaneko, High-performance $PbZn_{1/3}Sb_{2/3}O_3$–$PbNi_{1/2}Te_{1/2}O_3$–$PbZrO_3$–$PbTiO_3$ ceramics sintered at a low temperature with the aid of complex additives $Li_2CO_3$–$Bi_2O_3$–$CdCO_3$, Jpn. J. Appl. Phys. 39 (9) (2000) 5556–5559.
[7] T. Hayashi, T. Inoue, Y. Akiyama, Low-temperature sintering and properties of (Pb, Ba, Sr)(Zr, Ti, Sb)$O_3$ piezoelectric ceramics using sintering aids, Jpn. J. Appl. Phys. 38 (9) (1999) 5547–5552.
[8] L. Wu, C.H. Wang, The dielectric and piezoelectric properties of 0.125PMN–0.875PZT ceramics-doped with $4PbO{\cdot}B_2O_3$, Jpn. J. Appl. Phys. 32 (6) (1993) 2757–2761.
[9] D.E. Wittmer, R.C. Buchanan, Low temperature densification of lead zirconate titanate with vanadium pentoxide additive, J. Am. Ceram. Soc. 64 (3) (1981) 485–490.
[10] S.-H. Park, S. Ural, C.-W. Ahn, S. Nahm, K. Uchino, Piezoelectric properties of Sb-, Li-, and Mn-substituted $Pb(Zr_xTi_{1-x})O_3$–$Pb(Zn_{1/3}Nb_{2/3})O_3$–$Pb(Ni_{1/3}Nb_{2/3})O_3$ ceramics for high-power applications, Jpn. J. Appl. Phys. 45 (9) (2006) 2667–2673.
[11] C.-W. Ahn, H.-C. Song, S. Nahm, S. Priya, S.-H. Park, K. Uchino, H.-G. Lee, H.-J. Lee, Effect of ZnO and CuO on the sintering temperature and piezoelectric properties of a hard piezoelectric ceramic, J. Am. Ceram. Soc. 89 (3) (2006) 921–925.

Available online at www.sciencedirect.com
ScienceDirect
Ceramics International 35 (2009) 181–184
CERAMICS INTERNATIONAL
www.elsevier.com/locate/ceramint

# Monte Carlo investigation of hysteresis properties in ferroelectric thin-films under the effect of uniaxial stresses

Y. Laosiritaworn [a,*], S. Ananta [a], J. Poulter [b], R. Yimnirun [a]

[a] Department of Physics, Faculty of Science, Chiang Mai University, Chiang Mai 50200, Thailand
[b] Department of Mathematics, Faculty of Science, Mahidol University, Bangkok 10400, Thailand

Accepted 1 October 2007
Available online 23 February 2008

**Abstract**

The uniaxial stress dependence of the hysteresis behavior of ferroelectric films was studied. The DIFFOUR model was modified to include the uniaxial stress effect. Both the uniaxial stress and the external electric field were applied on the out-of-plane direction of the films. The polarization was measured with varying the magnitude of the applied stress and the electric field frequency via the dynamics of the polarization reversal in terms of hysteresis. The study was taken by means of Monte Carlo simulations using the spin-flip Metropolis algorithm. From the results, the district dependence of hysteresis behavior on frequency between low frequency and high frequency was prominent. On the other hand, the remanent and the coercivity significantly decreased with increasing applied stresses. Moreover, the areas under the hysteresis loops also decreased indicating smaller magnitude of energy dissipation. The results agree well with related experiments where applicable.
© 2008 Elsevier Ltd and Techna Group S.r.l. All rights reserved.

*Keywords:* Ferroelectric thin-films; Monte Carlo; Uniaxial stress; Hysteresis

## 1. Introduction

Ferroelectric thin-films have recently been of wide interest in view of both technological and fundamental importance [1,2]. Of a particular interest is the technological applicability such as high-speed ferroelectric recording media in which high areal densities and high reliability are in demand [1]. Therefore, it is necessary to understand the response of ferroelectric domain switching to electric field corresponding to specific material structures in detail. Nevertheless, for the sake of simplicity, theoretical studies on ferroelectric multi-layers are usually performed on an ideal stress-free system. However, real materials used in many applications are often affected by crystalline anisotropy caused by external mechanical stress, or internal strain induced by misfit in lattice spacing at the interfaces between ferroelectric layers and the substrate. Furthermore, ferroelectric thin-films under stresses were found to have their polarization behavior altered leading to substantial changes in phase transition between ferroelectric and paraelectric phases [3,4]. Consequently, it is very important to include the applied stress to model real materials.

In this work, the uniaxial stress dependence of the ferroelectric dynamic properties in thin-films was studied. To outline, the study was firstly done by proposing the DIFFOUR Hamiltonian that includes the uniaxial stress effect. Then, by means of Monte Carlo simulations, the polarization along the out-of-plane direction is investigated with varying the field frequency and uniaxial stress via the dynamics of the hysteresis. Finally, all the descriptions to these results are given in detail.

## 2. Methodologies

### 2.1. Spin Hamiltonian

In this study, the DIFFOUR Hamiltonian [5–7]

$$H = \sum_i \left( \frac{P_0^2}{2m} - \frac{a}{2}u_i^2 + \frac{b}{2}u_i^4 \right) - \sum_{<ij>} U_{ij}\vec{u}_i \cdot \vec{u}_j - E(t)\sum_i u_{iz} \quad (1)$$

was considered where $\vec{u}_i$ is the ferroelectric dipole spin at site $i$, $P_0^2/2m$ is the kinetic energy, $a$ and $b$ are the double-well

* Corresponding author. Fax: +66 53943445.
*E-mail address:* yongyut_laosiritaworn@yahoo.com (Y. Laosiritaworn).

0272-8842/$34.00 © 2008 Elsevier Ltd and Techna Group S.r.l. All rights reserved.
doi:10.1016/j.ceramint.2007.10.034

potential parameters for the ferroelectric spins, and $U_{ij}$ is the ferroelectric interaction. However, in this study, only the case that $\vec{u}_i$ is constant in magnitude was considered to underline the dynamics of the spin orientation in response to the field. Therefore, by proposing appropriate reference energy and introducing the stress effect, the Hamiltonian can be rewritten as

$$H = \sum_{<ij>} U_{ij}(\Delta l)\hat{u}_i \cdot \hat{u}_j - E(t)\sum_i u_{iz}, \tag{2}$$

where $\hat{u}_i$ is a unit vector referring to one of the possible 14 ferroelectric spin directions (6 from tetragonal and 8 from rhombohedral structures), $<ij>$ represents summation over the nearest pairs, and $u_{iz}$ is the spin's $z$ component. $E(t) = E_0 \sin(2\pi ft)$ is the electric field acting only on the out-of-plane direction of the films, where $f$ and $E_0$ refer to frequency and amplitude respectively. Helical and free-boundary conditions were used for the in-plane ($xy$) and the out-of-plane ($z$) directions. In this picture, the magnitude of $\hat{u}_i$ is dimensionless, so both $U_{ij}$ and $E$ have a unit of energy. $U_{ij}(\Delta l)$ is a function of lattice distortion $\Delta l$, arising from the applied stress, and assumed to take a Lennard–Jones potential-like [8], i.e.

$$U_{ij}(r_{ij}) = U_0\left[\left(\frac{r_0}{r_{ij}}\right)^{12} - 2\left(\frac{r_0}{r_{ij}}\right)^{6}\right]. \tag{3}$$

Here, $r_0$ is the lattice spacing at a specific thermal equilibrium, $U_0$ is the ferroelectric interaction associated to $r_0$ ($\Delta l = 0$), and $r_{ij}$ is the distance between site $i$ and $j$. For zero stress (strain), $r_{ij} = r_0$ and $U_{ij} = -U_0$ so the system prefers ferroelectric phase. Since the Young's modulus is defined as $Y \equiv P/((r_{ij} - r_0)/r_0)$ where $P$ is the stress (pressure), it is possible to write $r_{ij}/r_0 = 1 - (P/Y)$ and Eq. (3) as $U^z_{ij} = U_0[(1-(P/Y))^{-12} - 2(1-(P/Y))^{-6}]$. However, along the $xy$ direction, there also exists the lattice distortion caused by the stress along the $z$ direction. The ratio of the distortions between these two directions is defined as the Poisson ratio $\varepsilon \equiv -\Delta r^{xy}/\Delta r^z$ (where for many systems ranging from metal to ceramics, $\varepsilon \approx 0.3$ [9]). As a result, it is possible to write $\varepsilon = -\Delta r^{xy}/\Delta r^z = -(r^{xy}_{ij} - r_0)/(r^z_{ij} - r_0) = ((1 - r^{xy}_{ij})/r_0)/(r^z_{ij}/(r_0 - 1))$ which gives $r^{xy}_{ij}/r_0 = 1 - \varepsilon((r^z_{ij}/r_0) - 1) = 1 + \varepsilon(P/Y)$. Consequently, the ferroelectric interaction along the $xy$ direction is $U^{xy}_{ij} = U_0[(1+(\varepsilon P/Y))^{-12} - 2(1+(\varepsilon P/Y))^{-6}]$. As a result, the Hamiltonian can be written as

$$H = \sum_{<ij> \in \text{in-plane}} U^{xy}_{ij}\hat{u}_i\hat{u}_j + \sum_{<ij> \in \text{out-of-plane}} U^z_{ij}\hat{u}_i\hat{u}_j - E(t)\sum_i u_{iz}. \tag{4}$$

### 2.2. Monte Carlo simulation

Throughout this study, $U_0$ was set as 1, so this re-defines the unit of temperature $T$ as $J/k_B$ (where $k_B$ is the Boltzmann's constant), and electric field amplitude $E_0$ as a unit of $U_0$. The simulations were done at a temperature in the ferroelectric phase (where there exists hysteresis loops), i.e. $T = 1.0\ J/k_B$. The ratio $P/Y$ was varied from 0.00 to 0.16. The simulation was done on bi-layer ferroelectric films where each single layer consists of ferroelectric unit cells connecting along the in-plane direction. The ferroelectric spins are assumed to reside in the unit cells and the system consists of $N = L \times L \times 2$ spins where $L \times L$ refers to number of spins in one monolayer. To minimize finite size effect, large $L$ is required so in this study $L = 40$ was chosen. Trial simulations for larger sizes were also performed and it is found that for the range of parameters used in this study, the difference in hysteresis behavior is not significant. The unit time step was defined from one full simulation update of all sites of the lattice, i.e. 1 Monte Carlo step per site (mcs). The field frequency was varied from 0.001 to 4 $\text{mcs}^{-1}$ and the field amplitude is fixed at $E_0/U_0 = 4$.

With the Hamiltonian proposed in Eq. (3), each system was assigned an initial random configuration and later on was passed to the thermal Monte Carlo updates, using the Metropolis algorithm [10]. In updating the system, each spin is assigned a new random direction, and the probability of accepting that new direction is proportional to

$$\text{probability} = \exp\left(-\frac{\Delta H}{k_B T}\right) \tag{5}$$

where $\Delta H$ is the energy differences between of the original and the new updating state. If the energy difference is less than zero, or a uniform random number in the range [0,1) is less than the probability given in Eq. (5), the new direction is accepted and the system is successfully updated, or else the considered spin is left untouched. The whole procedure is repeated until the simulation ends.

In measuring, with varying the uniaxial stress and the applied field frequency, each simulation waited for a few cycles to obtain steady hysteresis loops, and then the polarization per spin along the $z$ direction was calculated, i.e.

$$p_r = \frac{1}{N}\left[\sum_i u_{iz}\right]. \tag{6}$$

Then, 1000 steady hysteresis loops were used to calculate average hysteresis loop for each condition.

## 3. Results and discussion

From the simulation results, with varying field frequency and stress, significant changes to the hysteresis loop were found. Fig. 1a shows the patterns for hysteresis loops for frequencies ranging from 0.001 to 0.320 $\text{mcs}^{-1}$. As can be seen, 2 distinct behaviors can be found for low frequency region, e.g. $f \leq 0.125\ \text{mcs}^{-1}$ and for high frequency region, e.g. $f > 0.125\ \text{mcs}^{-1}$. At low frequencies, the loops get bigger with increasing frequency. This is because, at low frequency, the field period is high and hence the sweeping time of the field per one hysteresis cycle is large. Ferroelectric spins then have time to follow the field leading to low phase-lag between the polarization and field and hence to a small hysteresis loop.

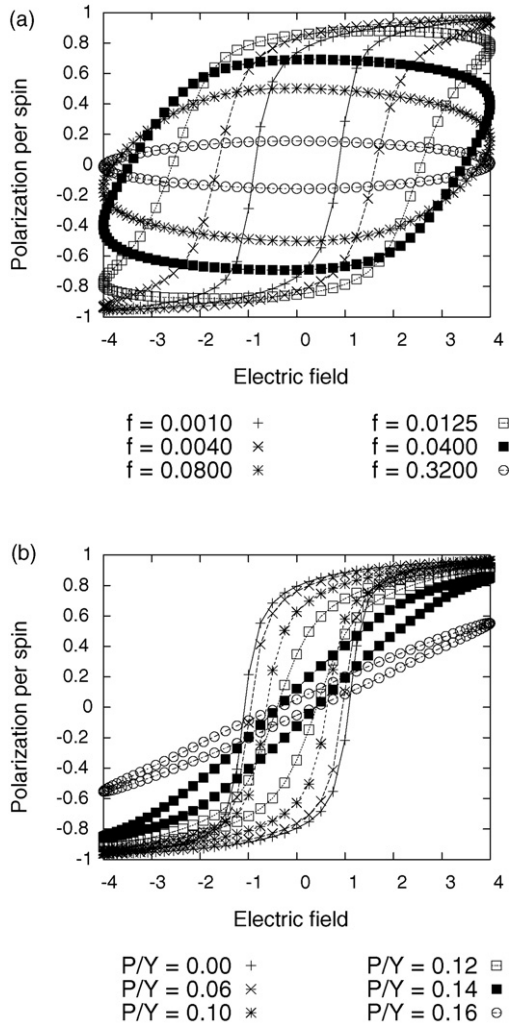



Fig. 1. Hysteresis loops of the bi-layered films (a) at zero-stress but varying frequency from $f = 0.0010$ to $f = 0.3200$ mcs$^{-1}$, and (b) at $f = 0.0010$ mcs$^{-1}$ but varying stress from $P/Y = 0.00$ to $P/Y = 0.16$.

However, with increasing the frequency in the low frequency region, the phase lag gets bigger and hence the hysteresis loop becomes larger. However, if the frequency is still increased, the loop reaches a maximum size at a certain frequency. Beyond this point, the frequency is very high which limits the dynamics of the spins and results in a smaller loop with an oval shape-like.

However, with a non-zero stress, e.g. in Fig. 1b, the decrease of the remanent $p_r$, the coercivity $E_C$, and the hysteresis loop-area were found. The reason is that the stress causes the $z$ direction to become a 'hard axis'. As a result, the spins prefer to align in the $xy$ direction or have their $z$-components align in an anti-parallel pattern to lower the energy. Consequently, both $p_r$ and $E_C$ reduce. In comparison with experiments, qualitatively, the decrease of the coercivity and the loop-area with increasing stress has trends that agree reasonably well with an experiment on ferroelectric material [11].

On the other hand, Fig. 2 shows the hysteresis loop area as a function of frequency for various stresses. The loop area increases for low frequency region and decreases for high

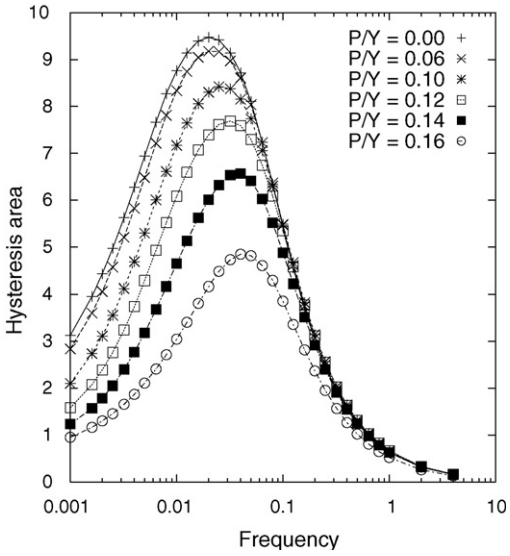



Fig. 2. Stress dependent of the hysteresis areas (arbitrary unit) of the bi-layered films as a function of the electric field frequency (mcs$^{-1}$ unit) with varying stresses from $P/Y = 0.00$ to $P/Y = 0.16$.

frequency region with increasing frequency. At a particular frequency, the loop area is smaller for larger stresses. This is because the $z$ direction is the stress induced 'hard axis'. In this way, the spins are loosely coupled along the $z$ direction and hence it will be easier for the spins to catch up with the field so the inclined oval loop occurs with small loop area. However, with increasing the frequency at low frequencies, the phase lag gets larger but with higher stresses it will require higher frequency to reach the loop-area maximum point. This is why the frequency at the maximum area shifts to higher frequency for larger stress. Notice that the maximum area is smaller for larger stress because of smaller $p_r$ and $E_C$.

## 4. Conclusions

In this study, Monte Carlo simulations were performed to study ferroelectric thin-films under the influence of uniaxial stress on ferroelectric hysteresis properties. The objective is to investigate the behavior of the spin-reversal along the out-of-plane direction with changes in the magnitude of the stress and the electric field frequency. With increasing frequency, it is found that the hysteresis area increases for low frequency and decreases for high frequency. On the other hand, the applied stress reduces $p_r$, $E_C$ and the hysteresis area. This is due the stress causing the out-of-plane direction to be a 'hard axis' and the hysteresis results in smaller loop-area. The results qualitatively agree well with experiments where applicable.

## Acknowledgement

The authors would like to acknowledge financial supports from the Commission on Higher Education and the Thailand Research Fund (TRF).

## References

[1] J.F. Scott, Ferroelectric Memories, Springer-Verlag, Berlin, 2002.
[2] G.H. Haertling, Ferroelectric Ceramics: History and Technology, Journal of American Ceramic Society 82 (1999) 797–818.
[3] X. Lu, J. Zhu, Z. Liu, X. Xu, Y. Wang, Phase transition related stress in ferroelectric thin films, Thin Solid Films 375 (2000) 15–18.
[4] J. Mendiola, M.L. Calzada, P. Ramos, M.J. Martin, F. Agulló-Rueda, On the effects of stresses in ferroelectric (Pb,Ca)$TiO_3$ thin films, Thin Solid Films 315 (1998) 195–201.
[5] T. Janssen, J.A. Tjon, One-dimensional model for a crystal with displacive modulation, Physical Review B 24 (1981) 2245–2248.
[6] J.-M. Liu, Q.C. Li, W.M. Wang, X.Y. Chen, G.H. Cao, X.H. Liu, Z.G. Liu, Scaling of dynamic hysteresis in ferroelectric spin systems, Journal of Physics: Condensed Matter 13 (2001) L153–L161.
[7] J.-M. Liu, W.M. Wang, Z.G. Liu, H.L. Chan, C.L. Choy, Dynamic hysteresis in ferroelectric systems: experiment and Monte Carlo simulation, Applied Physics A 75 (2002) 507–514.
[8] S.J. Mitchell, D.P. Landau, Phase separation in a compressible 2D Ising model, Physical Review Letter 97 (2006) 025701.
[9] W.D. Callister, Materials Science and Energineering: An Introduction, John Wiley & Sons, New York, 2003.
[10] N. Metropolis, A.W. Rosenbluth, M.N. Rosenbluth, A.H. Teller, E. Teller, Equation of state calculations by fast computing machines, Journal of Chemical Physics 21 (1953) 1087–1092.
[11] R. Yimnirun, Y. Laosiritaworn, S. Wongsaenmai, Effect of uniaxial compressive pre-stress on ferroelectric properties of soft PZT ceramics, Journal Physics D 39 (2006) 759–764.

Available online at www.sciencedirect.com
ScienceDirect
Ceramics International 35 (2009) 121–124
CERAMICS INTERNATIONAL
www.elsevier.com/locate/ceramint

# Preparation and characterization of ceramic nanocomposites in the PZT–BT system

Wanwilai Chaisan *, Rattikorn Yimnirun, Supon Ananta

*Department of Physics, Faculty of Science, Chiang Mai University, Chiang Mai 50200, Thailand*

Accepted 1 October 2007
Available online 23 February 2008

**Abstract**

Nanocomposites of the $(1-x)$PZT-$x$BT system were fabricated by the bimodal particle concept. The effect of fabricating conditions on structural characteristics and dielectric properties of the ceramics was investigated using XRD, SEM, and a standard dielectric measurement. The ceramic–solid solutions and -nanocomposites in the PZT–BT system were comparatively explored. It was clearly seen that the microstructures and the dielectric properties of PZT–BT ceramic-nanocomposites are totally different from those of ceramic–solid solutions. The dielectric behavior of ceramic-nanocomposites displayed superimposition of two phase transitions with a lower maximum value of the dielectric constant than that of the solid solutions.
© 2008 Elsevier Ltd and Techna Group S.r.l. All rights reserved.

*Keywords:* B. Nanocomposites; C. Dielectric properties; D. PZT; BT

## 1. Introduction

Piezoelectric ceramics (e.g. $Pb(Zr_x,Ti_{(1-x)})O_3$, $BaTiO_3$ and its related compounds), which are widely used as transducers, pressure sensors and actuators, suffer from mechanical and electrical deterioration in service because of fatigue damage. When piezoelectric devices are used in severe circumstances, such as high stress or high power applications, problems that are related to reliability (i.e. degradation of electrical properties and fatigue fracture) become more critical and important. Therefore, it is necessary to investigate the electrical behavior of piezoelectric ceramics and to design microstructure that possesses excellent electrical properties. Both $BaTiO_3$ (BT) and $Pb(Zr,Ti)O_3$ (PZT) are among the most common ferroelectric materials and have been studied extensively since the late 1940s [1,2]. These two ceramics have distinct characteristics that make each individual ceramic suitable for different applications. The compound PZT has highly desirable piezoelectric properties which can be applied in transducer applications. Furthermore, it has a high $T_C$ of 390 °C which allows piezoelectric devices to be operated at relatively high temperatures. BT is a normal ferroelectric material which exhibits a high dielectric constant, a lower $T_C$ (∼120 °C) and better mechanical properties [1–3]. Thus, mixing PZT with BT is expected to decrease the sintering temperature of BT-based ceramics, allowing a desirable move towards electrodes of lower cost [4]. Moreover, the nano-reinforced structure is believed to improve densification and mechanical properties of the ceramic composite. Therefore, ceramic-nanocomposites of the lead zirconate titanate–barium titanate ($(1-x)$PZT-$x$BT) system with various compositions, were fabricated using a modified mixed-oxide synthetic route and a bimodal particle concept. The effect of processing parameters on the arrangement of phases, microstructural evolution and electrical properties of the ceramics was carefully investigated using XRD, SEM and dielectric measurements.

## 2. Experimental procedure

Ceramic-nanocomposites in the system $(1-x)$PZT-$x$BT ($0.1 \leq x \leq 0.5$; $\Delta x = 0.1$) have been fabricated from PZT powder and BT nanopowder, employing a normal sintering method. Reagent grade PbO, $ZrO_2$, $TiO_2$ and $BaCO_3$ powders (Fluka, >99% purity) were used as starting materials. Powder of each end member (PZT and BT) was first formed in order to avoid unwanted pyrochlore phases. For the preparation of BT

* Corresponding author. Tel.: +66 53 943367; fax: +66 53 943445.
*E-mail address:* wanwilai_chaisan@yahoo.com (W. Chaisan).

0272-8842/$34.00 © 2008 Elsevier Ltd and Techna Group S.r.l. All rights reserved.
doi:10.1016/j.ceramint.2007.10.032

nanopowder, a vibratory laboratory mill (McCrone Micronizing Mill) powered by a 1/30 HP motor was employed for 30 h with zirconia media in ethanol. The well-mixed powder was calcined at 1300 °C for 2 h in an alumina crucible. With a modified mixed-oxide method [5], the PZT powders were prepared using a lead zirconate ($PbZrO_3$) as precursor in order to reduce the occurrence of undesirable phase. Pure $PbZrO_3$ phase was first formed by reacting PbO with $ZrO_2$ at 800 °C for 2 h. $PbZrO_3$ powder was then mixed with PbO and $TiO_2$ and milled, dried and calcined at 900 °C for 2 h to form single phase PZT.

The $(1 - x)$PZT–$x$BT mixed powders were then formulated from the BT and PZT components by employing the similar mixed-oxide procedure. In the mixing process, the calculated relevant proportions of constituents were weighed, suspended in ethanol and intimately mixed in a ball-mill with zirconia media. Drying was carried out for 2 h and the dried powder was then ground into the fine powders. The powders were then isostatically cold-pressed into pellets with a diameter of 15 mm and a thickness of 2 mm at a pressure of 4 MPa and sintered at 1200 °C for 2 h.

Densities of sintered ceramics were measured by Archimedes method and X-ray diffraction (XRD using $CuK_\alpha$ radiation) was employed to identify the phases formed. The grain morphology and size were directly imaged using scanning electron microscopy (SEM). For electrical measurements, silver paste was fired on both sides of the polished samples at 750 °C for 12 min as the electrodes. Dielectric properties of the sintered ceramics were studied as a function of both temperature and frequency. The capacitance was measured with a HP4284A LCR meter in connection with a Delta Design 9023 temperature chamber and a sample holder capable of high temperature measurement. Dielectric constant ($\varepsilon_r$) was calculated using the geometric area and thickness of the discs.

## 3. Results and discussion

XRD patterns of all sintered ceramic-nanocomposites are shown in Fig. 1. Here the peak positions and intensities of the XRD patterns vary according to the amount and chemical composition of the phases present. It is seen that the diffraction peaks shifted towards a higher angle with increasing $x$ and the XRD peaks of all ceramic-nanocomposites are broader than those of solid-solution case in our earlier work [6]. These can be interpreted in terms of co-existing perovskite phases, i.e. PZT, BT and their reacted intermediate phases. Moreover, with careful observation, it is found that the sintered samples of $0.3 \leq x \leq 0.5$ nanocomposites exhibit the perovskite structure with traces of unwanted phase ($\bigtriangledown$) occurring at $2\theta \sim 28°$. It is believed that this unwanted phase is $ZrO_2$ matched with JCPDS file no. 37-1484 [7]. Compositional fluctuations due to the evaporation of lead oxide within surface regions are believed to be responsible for the occurrence of free $ZrO_2$ phase in the sintered $(1 - x)$PZT-$x$BT ceramics of $0.3 \leq x \leq 0.5$ nanocomposites. Another possibility was put forward by Fushimi and Ikeda [8], who suggested that melting of PT-PZ solid solution can change from congruent to incongruent and induce $ZrO_2$ to form at ~1340 °C. On the other hand, Brankovic et al. [9] suggested that incomplete reaction of the starting precursors can also result in the persistence of free $ZrO_2$ phase. Since no trace of $ZrO_2$ has been observed for sintered samples of $x = 0.1$ and 0.2, it is believed that the segregation of $ZrO_2$ may be associated with loss of Pb content and also depend on the level of BT content, similar with observations made in other perovskite systems [10,11].

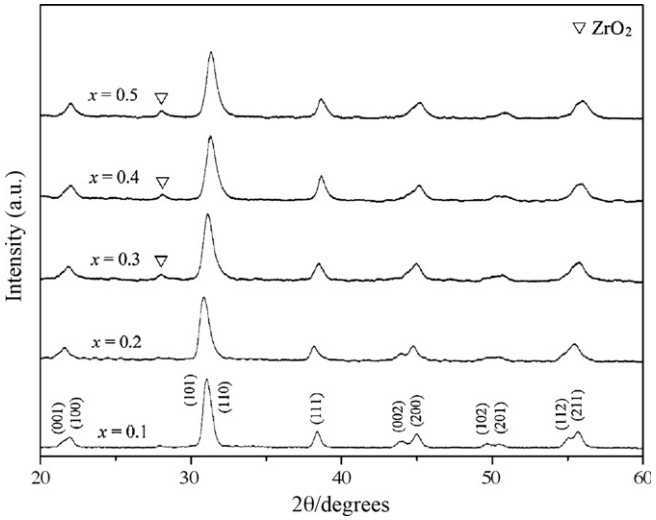



Fig. 1. XRD patterns of the $(1 - x)$PZT-$x$BT ceramic-nanocomposites sintered at 1200 °C for 2 h.

The microstructural morphology of $(1 - x)$PZT-$x$BT ceramic-nanocomposites was initially examined by SEM. Micrographs of as-fired surface of all ceramic-nanocomposites are shown in Fig. 2(a–e). In general, high porosity, heterogeneous microstructures consisting mainly of two ranges of particles (in respect of size and shape) were found in all samples. A distribution of very small spherical BT particles (brighter phase with diameter ~200–500 nm) is found over the PZT grains, especially for rich-BT samples. Large pore-sizes of the order of 2 μm were also observed. These poorly sintered samples could be attributed to several factors, including the effect of different particle size fractions between the two end components, ineffective mixing and the use of low density green bodies produced by conventional uniaxial die-pressing.

Densities in the range 4.80–6.21 g/cm$^3$ were obtained, which are considerably lower than the values obtained for sintered PZT–BT solid solution ceramics in our earlier work [6]. In order to preserve the ceramics with a nanostructural arrangement, it is possible that the sintering temperature employed in this work is not enough for driving the densification mechanism to achieve dense PZT/BT ceramic-nanocomposites. However, so far, there are no reports on the production of highly dense PZT/BT ceramic-nanocomposites by a pressureless sintering method. Moreover, the scope for improving pressureless sintering by raising the temperature is limited by the melting point of PZT (~1400 °C) whilst the hot-pressing technique can cause severe PbO-volatilization problems [12].

The temperature dependence of the dielectric constant ($\varepsilon_r$) measured at 1 MHz for $(1 - x)$PZT–$x$BT nanocomposites with

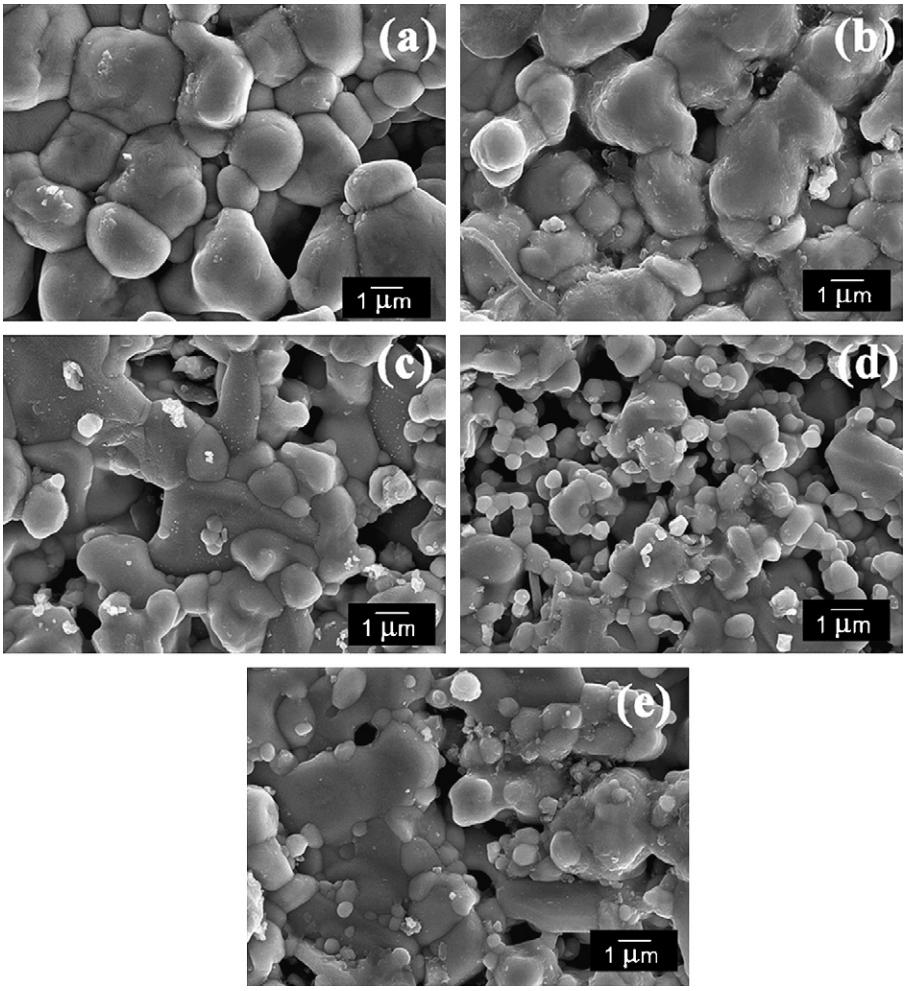



Fig. 2. SEM micrographs of as-fired surfaces of the sintered $(1-x)$PZT-$x$BT ceramic-nanocomposites with $x$ = (a) 0.1, (b) 0.2, (c) 0.3, (d) 0.4 and (e) 0.5.

$0.1 \leq x \leq 0.5$ is shown in Fig. 3. All ceramic-nanocomposites display dielectric peak superimposition of the two phase transitions ($T_1$ and $T_2$) with no frequency dependence. The shape of dielectric peak for each composition seems to be the two peaks merged into a mound. The height of the mound was lower than those of solid solutions [6]. The phase transition temperatures, $T_1$ and $T_2$, and dielectric data are illustrated in Fig. 3 and list in Table 1. As is well known, the dielectric constant of pure PZT and pure BT showed anomalies at 390 and 130 °C, respectively. Therefore, ceramic-nanocomposites between PZT and BT are expected to show a transition temperature between 390 and 130 °C. An attempt was made to characterize the dielectric temperature of PZT–BT as a function of $x$. However, difficulties were encountered in indexing the measured dielectric peak broadening obtained. As seen in Fig. 3, with increasing of $x$, $T_1$ and $T_2$ decrease moving toward

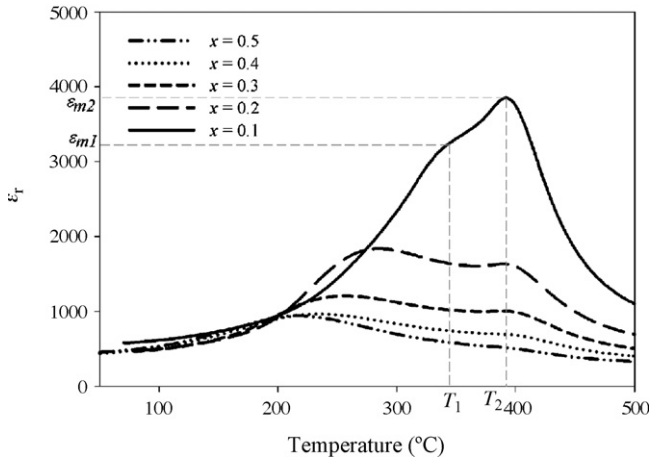



Fig. 3. Comparison of dielectric constant ($\varepsilon_r$) at 1 MHz for $(1-x)$PZT-$x$BT ceramic-nanocomposites.

Table 1
Dielectric properties of ceramic-nanocomposites in the $(1-x)$PZT–$x$BT system

| Compositions ($x$) | $T_1$ (°C) | $\varepsilon_{m1}$ | $T_2$ (°C) | $\varepsilon_{m2}$ |
|---|---|---|---|---|
| 0.1 | 340 | 3200 | 392 | 3800 |
| 0.2 | 285 | 1800 | 390 | 1600 |
| 0.3 | 257 | 1200 | 388 | 1000 |
| 0.4 | 234 | 960 | 385 | 700 |
| 0.5 | 216 | 940 | 380 | 530 |

$\varepsilon_{m1}$ and $\varepsilon_{m2}$ are the maximum dielectric constant at $T_1$ and $T_2$, respectively (see also Fig. 3).

the Curie temperature of BT. $T_1$ refers to transition temperature of BT and $T_2$ refers to transition temperature of PZT. There are various proposals for explaining the dielectric response of composite materials. Ausloos [13] studied effective dielectric constant theories of composite solids. Their work reported that the broad spectrum of dielectric constant is the results of clustering effects, the shape of particle (or cluster) effect and particle heterogeneity effect. In this work, it is possible that the incorporation of BT nanoparticles into a PZT matrix may hinder domain wall motion sufficiently to reduce the dielectric constant [14]. Moreover, the presence of unwanted $ZrO_2$ phase (confirmed by XRD) and high porosity (confirmed by SEM) are other reasons for the low dielectric constants in ceramic-nanocomposites with composition of $x > 0.2$. However, by neglect accounting for the porosity, the maximum dielectric constant ($\varepsilon_{max}$) of all ceramic-nanocomposites was back-calculated to 100% density for a better comparison with the solid solutions. Although the dielectric values of ceramic-nanocomposites are still lower than those of the solid solutions, the broadening is greater which infers the operating temperature with the moderate dielectric constant (∼1000–4000) of these ceramics is much wider in range, suitable for certain electronic devices.

## 4. Conclusions

Ceramics-nanocomposites in the system $(1 - x)$PZT-$x$BT were successfully processes by employing the bimodal particle concept. All PZT–BT compositions in this study were of the perovskite structure with tetragonal symmetry. The dielectric properties of all the ceramic-nanocomposites are strongly influenced by the presence of secondary phases and densification mechanism. The dielectric peak shows superimposition of the two phase transitions with no frequency dependence and the dielectric value is lower than that of solid solutions for all compositions, explained by theory of the dielectric response for composite materials. With increasing of $x$, the phase transition temperatures of all ceramics decrease moving toward to Curie temperature of BT.

## Acknowledgement

I would like to thank the Thailand Research Fund (TRF), Commission on Higher Education (CHE) and the Faculty of Science, Chiang Mai University for all financial support.

## References

[1] G.H. Haertling, Ferroelectric ceramics: history and technology, J. Am. Ceram. Soc. 82 (4) (1999) 797–818.
[2] B. Jaffe, W.R. Cook, H. Jaffe, Piezoelectric Ceramics, Academic Press, London, 1971.
[3] A.J. Moulson, J.M. Herbert, Electroceramics: Materials, Properties, Applications, John Wiley & Sons Ltd., Chichester, 2003.
[4] J. Chen, Z. Shen, F. Liu, X. Liu, J. Yun, Preparation and properties of barium titanate nanopowder by conventional and high-gravity reactive precipitation methods, Scripta Mater. 49 (2003) 509–514.
[5] W. Chaisan, S. Ananta, T. Tunkasiri, Synthesis of barium titanate-lead zirconate titanate solid solutions by a modified mixed-oxide synthetic route, Curr. Appl. Phys. 4 (2–4) (2004) 182–185.
[6] W. Chaisan, R. Yimnirun, S. Ananta, D.P. Cann, Dielectric properties of solid solutions in the lead zirconate titanate-barium titanate system prepared by a modified mixed-oxide method, Mater. Lett. 59 (2005) 3732–3737.
[7] JCPDS-ICDD card no. 37-1484, International Centre for Diffraction Data, Newtown Square, PA, 2002.
[8] S. Fushimi, T. Ikeda, Phase equilibrium in the system PbO-$TiO_2$-$ZrO_2$, J. Am. Ceram. Soc. 50 (1967) 129–132.
[9] Z. Brankovic, G. Brankovic, J.A. Varela, PZT ceramics obtained from mechanochemically synthesized powders, J. Mater. Sci. 14 (2003) 37–41.
[10] F. Xia, X. Yao, Piezoelectric and dielectric properties of PZN-BT-PZT solid solutions, J. Mater. Sci. 34 (1999) 3341–3343.
[11] N. Vittayakorn, G. Rujijanagul, T. Tunkasiri, X. Tan, D.P. Cann, Influence of processing conditions on the phase transition and ferroelectric properties of $Pb(Zn_{1/3}Nb_{2/3})O_3$-$Pb(Zr_{1/2}Ti_{1/2})O_3$ ceramics, Mater. Sci. Eng. B 108 (2004) 258–265.
[12] V.L. Balkevich, C.M. Flidlider, Hot-pressing of some piezoelectric ceramics in the PZT system, Ceramurgia Inter. 2 (1976) 81–87.
[13] M. Ausloos, Dielectric response of composite materials, J. Phys. C: Solid State Phys. 18 (1985) L1163–L1167.
[14] S.R. Panteny, C.R. Bowen, R. Stevens, Piezoelectric Particulate Reinforced Nanocomposites, The Alden Group, Oxford, 2000.

Available online at www.sciencedirect.com
ScienceDirect
Ceramics International 35 (2009) 173–176
CERAMICS INTERNATIONAL
www.elsevier.com/locate/ceramint

# Effect of vibro-milling time on phase formation and particle size of barium titanate nanopowders

W. Chaisan *, R. Yimnirun, S. Ananta

*Department of Physics, Faculty of Science, Chiang Mai University, Chiang Mai 50200, Thailand*

Accepted 1 October 2007
Available online 26 February 2008

**Abstract**

Barium titanate (BT) nanopowder was synthesized by a solid state reaction via a rapid vibro-milling technique. The effect of milling time on phase formation and particle size of BT powder was investigated. Powder samples were characterized using XRD (X-ray diffraction) and SEM techniques. It was found that the resulting BT powders have a range of particle size depending on milling times. Production of a single-phase BT nanopowder can be successfully achieved by employing a combination of 30 h milling time and calcination conditions of 1200 °C for 2 h.
© 2008 Elsevier Ltd and Techna Group S.r.l. All rights reserved.

*Keywords:* A. Milling; Powders: solid state reaction; D. $BaTiO_3$

## 1. Introduction

Barium titanate ($BaTiO_3$ or BT), which exhibits a perovskite structure and a Curie temperature ~120 °C, is a classical ferroelectric material that has been extensively exploited both for academic and technological utilizations over the past decades [1,2]. Owing to its high dielectric constant, large mechanical-quality factor, large pyroelectric coefficient, non-toxic handling and low cost of manufacturing, compared to several lead-based perovskite ferroelectrics, BT-based ceramics have been a strong candidates for several electronic applications, including ultrasonic transducers, multilayer capacitors, pyroelectric detectors, semiconductors with positive temperature coefficient of resistance (PTCR) and electro-optic devices [3,4]. To fabricate them, a fine powder of perovskite phase with a minimal degree of particle agglomeration is needed as the starting material to achieve a dense and uniform microstructure at a given sintering temperature. In order to improve the sintering behavior of ceramics, a crucial focus of powder synthesis in recent years has been the formation of uniform-sized, single morphology particulates ranging in size from nanometer to micrometers.

The development of a method to produce nanopowders of precise stoichiometry and desired properties is complex, depending on a number of variables such as nature and purity of starting materials, processing history, temperature, etc. To obtain nanosized BT powders, many investigations have focused on several chemistry-based preparation routes, such as sol–gel [5], sol-precipitation [6], hydrothermal reaction [7], besides the more conventional solid state reaction of mixed oxides [8]. All these techniques are aimed at reducing the particle size and temperature of preparation of the compound even though they are more involved and complicated in approach than the solid state reaction. The advantage of using mechanical milling for preparation of nanosized powders lies in its ability to produce mass quantities of powders in the solid state using simple equipment and low cost starting precursors [9,10]. The ball-milling technique is a very popular solid state reaction because of easy and low cost technique, however the size of particle from this technique is still large (micrometer). Thus, the potentiality of vibro-milling technique will be then focused in order to achieve the nanosized powder. Although some research has been done in the preparation of BT nanopowders via a vibro-milling technique [11], to our knowledge a systematic study regarding the influence of milling time on the preparation of BT nanopowders has not yet been reported. Therefore, in this work, the effect of milling time on phase formation, and particle size of BT nanopowders was investigated in this connection. The potential of the vibro-

* Corresponding author. Tel.: +66 53 943376; fax: +66 53 943445.
*E-mail address:* wanwilai_chaisan@yahoo.com (W. Chaisan).

0272-8842/$34.00 © 2008 Elsevier Ltd and Techna Group S.r.l. All rights reserved.
doi:10.1016/j.ceramint.2007.10.035

milling technique as a simple and low-cost method to obtain usable quantities of single-phase BT powders at low temperature and with nanosized particles was also examined.

## 2. Experimental procedure

Commercially available powders of $BaCO_3$ and $TiO_2$ (anatase form), (Fluka, >99% purity) were used as starting materials. $BaTiO_3$ powder was synthesized by the solid state reaction of these raw materials. A vibratory laboratory mill (McCrone Micronizing Mill) powered by a 1/30 HP motor was employed for preparing the stoichiometric $BaTiO_3$ powder [9]. The mixed powder was vibro-milled for 0.5 h with corundum media in isopropyl alcohol (IPA). Drying was carried out for 2 h at 120 °C. Various calcination temperatures ranging from 700 to 1400 °C were selected to investigate the phase development of BT. Moreover, in order to investigate the effect of milling time on phase formation and particle size, the milling times were then ranged from 0.5 to 30 h. All powders were examined by room temperature X-ray diffraction (XRD; Siemens-D500 diffractometer) using Ni-filtered Cu Kα radiation, to identified the phase formed and the optimum firing temperature for the production of single-phase BT powders under various milling conditions. The crystallite size and tetragonality factor (*c*/*a*) were also estimated from these XRD patterns [12]. The morphologies of the powders observed by scanning electron microscopy (JEOL JSM-840 A SEM).

## 3. Results and discussion

From the TG-DTA data in previous work [13], the range of calcination temperatures between 700 and 1400 °C were designed for BT powder to investigate the phase formation. To study the phase development with increasing calcination temperature in BT powder prepared from vibro-milling technique for 0.5 h, it was calcined for 2 h in air at various temperatures, up to 1400 °C, followed by phase analysis using XRD. As shown in Fig. 1, for the uncalcined powder, only X-ray peaks of precursors, $BaCO_3$ (●) and $TiO_2$ (◆), which could be matched with JCPDS file numbers 5-0378 [14] and 21-1272 [15], respectively, are presented, indicating that no reaction had yet been triggered during the milling process. In this work, it is seen that the desired perovskite $BaTiO_3$ (▽) was already observed in the powder calcined at 700 °C, accompanying with unreacted $BaCO_3$ and $TiO_2$ precursors as

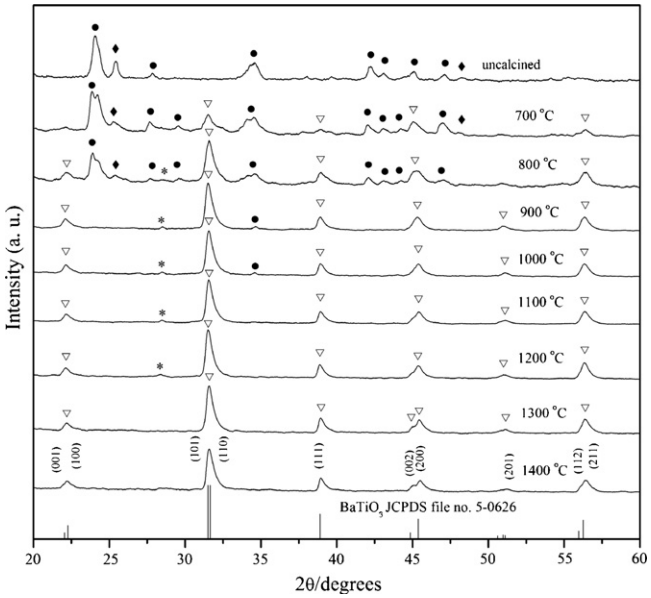



Fig. 1. XRD patterns of BT powders calcined at various temperatures for 2 h with heating/cooling rates of 10 °C/min (● = $BaCO_3$, ◆ = $TiO_2$, ▽ = $BaTiO_3$ and * = $Ba_2TiO_4$).

separated phases, in good agreement with literature [16,17]. Moreover, the unknown phase (★) started to occur at $2\theta \sim 28.5^\circ$, consistent with earlier work of Simon-Seveyrat et al. [18]. According to the literature [19,20], the reaction sequence of the phase formation in the BT mixture can be described as follow.

$$2BaCO_3 + TiO_2 \rightarrow Ba_2TiO_4 + 2CO_2 \quad (1)$$

$$Ba_2TiO_4 + TiO_2 \rightarrow 2BaTiO_3 \quad (2)$$

It was believed that this unknown phase corresponds to $Ba_2TiO_4$, which could be matched with JCPDS file numbers 72-0135 [21], always found in conventional mixed oxide processing [16,22]. As the temperature increased to 1000 °C, the intensity of the $BaTiO_3$ peaks was further enhanced. The starting materials completely disappeared after calcination at 1100 °C, however, the unwanted $Ba_2TiO_4$ phase still be detected. Upon calcination at 1300 °C, an essentially mono-phasic of $BaTiO_3$ phase was obtained. This observation agrees well with other workers [23,24]. This BT phase was indexable according to a tetragonal perovskite-type structure with lattice parameters $a = 3.994$ Å and $c = 4.038$ Å, space group *P*4*mm* (no. 99), consistent with JCPDS file number 5-0626 [25].

Table 1
Effect of milling time on the optimum calcination temperature and the variation of particle size of BT powders measured by different techniques

| Milling time (h) | Perovskite phase (%) | Calcination temperature (°C) | XRD | | SEM | |
|---|---|---|---|---|---|---|
| | | | *A* (nm) | *c*/*a* | *D* (nm) | *P* (nm) |
| 0.5 | 100 | 1300 | 38.32 | 1.0090 | 610 | 250–1400 |
| 10 | 100 | 1250 | 32.09 | 1.0059 | 260 | 100–500 |
| 15 | 100 | 1250 | 32.38 | 1.0036 | 490 | 100–1000 |
| 20 | 100 | 1250 | 31.95 | 1.0058 | 590 | 250–700 |
| 25 | 100 | 1200 | 31.60 | 1.0065 | 390 | 250–700 |
| 30 | 100 | 1200 | 31.56 | 1.0056 | 250 | 100–400 |

*A* = crystallite size, *c*/*a* = tetragonality factor, *D* = average particle size, *P* = particle size range.

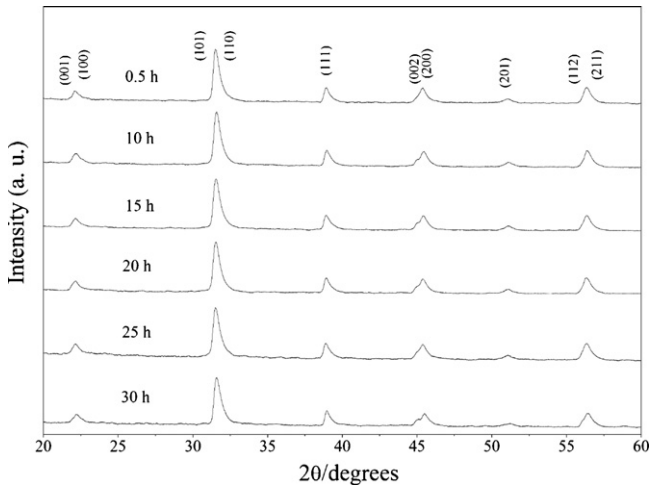



Fig. 2. XRD patterns of BT powders milled at different times.

Having established the optimum calcination temperature of BT powder vibro-milled for 0.5 h, an attempt was also made to calcine the BT powder under various milling times. The optimum calcination temperature of each powder was reported in Table 1 and the XRD patterns of all BT powders are shown in Fig. 2. It has been observed that with increasing milling time, all diffraction lines broaden, e.g., (0 0 2) and (2 0 0) peaks, an indication of a continuous decrease in particle size and of the introduction of lattice strain. These values indicate that the prolonged milling treatment affects the particle size and evolution of crystallinity of the phase formed. For BT powders, the longer the milling time, the lower the required (optimum) firing temperature. Additionally, the crystallite size and tetragonality factor ($c/a$) were estimated from these XRD patterns as also given in Table 1. The calculated crystalline size value was also found to decrease with increasing milling time. Though, the relative intensities of the Bragg peaks and the calculated tetragonality factor ($c/a$) for the powders exhibit independent of milling time, it is well documented that, as Scherer's analysis provides only a measurement of the extension of the coherently diffracting domains, the crystallite sizes determined by this method can be significantly under estimation [26]. In addition to strain, factors such as dislocations, stacking faults, heterogeneities in composition and instrumental broadening can attribute to peak broadening, making it almost impossible to extract a reliable particle size solely from XRD [27].

In this connection, SEM was also employed for particle size measurement (Table 1). The morphological evolution of the powders as a function of milling time was also revealed, as illustrated in the SEM micrographs (Fig. 3). At first sight, the morphological characteristic of BT powders with various milling times is similar for all cases. In general, the particles are agglomerated and basically irregular shape, with a substantial variation in particle sizes. The powders consist of primary particles with nanometers in size. Increasing milling time over the range 0.5–30 h, the powders exhibit spatial fluctuation in their particle sizes. The extent of the fluctuation depends on the milling time as well as on the calcination temperature applied. In this study, it is seen that the optimum milling time for the production of the smallest nanosized BT powder with low firing temperature was found to be at 30 h. The finding of this

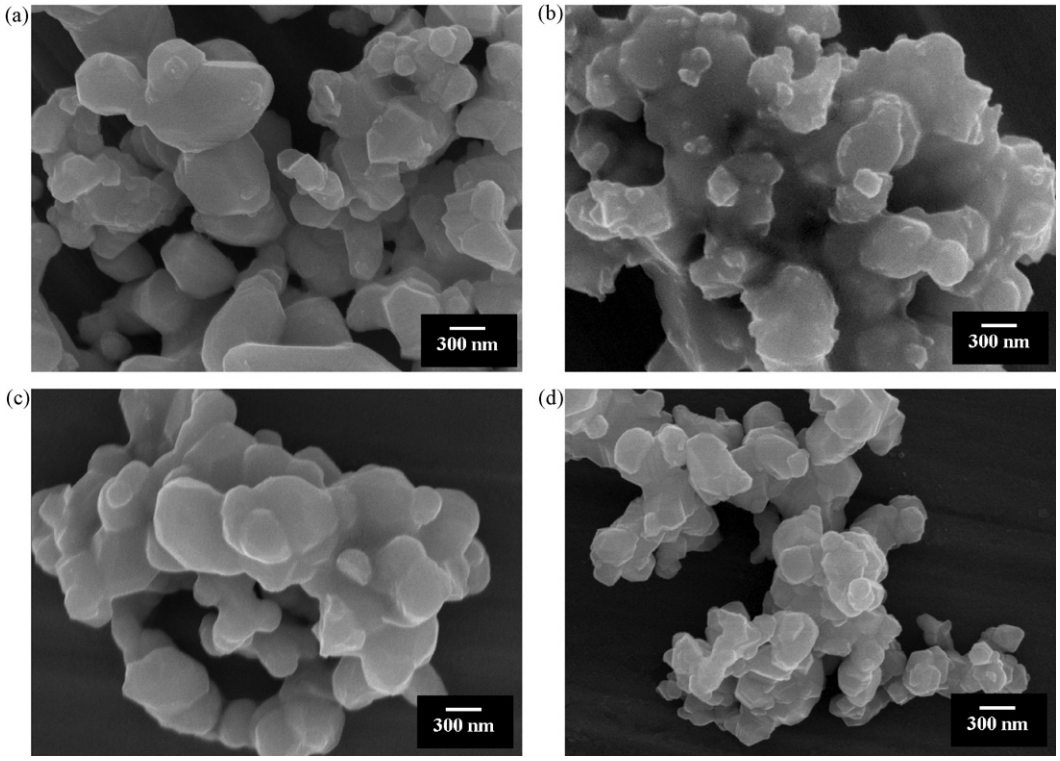



Fig. 3. SEM micrographs of BT powders after milling times of (a) 0.5, (b) 15, (c) 25 and (d) 30 h (calcined at their optimized conditions).

investigation indicates a strong relationship between the vibro-milling process and the yield of BT nanopowders.

## 4. Conclusions

The synthesis of perovskite BT nanopowder by a solid state reaction and the influence of milling time on its formation were studied. It was established that the milling time influences not only the development of the solid state reaction of BT phase but also particle size and morphology. It was shown that the increase of vibro-milling time significantly decreases the calcination temperature and particle size. A single phase of BT nanopowder can be successfully produced by employing a combination of 30 h milling time and calcination condition of 1200 °C for 2 h.

## Acknowledgements

I would like to thank the Thailand Research Fund (TRF), Commission on Higher Education (CHE) and the Faculty of Science, Chiang Mai University for all financial support.

## References

[1] A.J. Moulson, J.M. Herbert, Electroceramics: Materials, Properties, Applications, John Wiley & Sons Ltd., Chichester, 2003.
[2] G.H. Haertling, Ferroelectric ceramics: history and technology, J. Am. Ceram. Soc. 82 (4) (1999) 797–818.
[3] K. Uchino, Piezoelectrics and Ultrasonic Applications, Kluwer, Deventer, 1998.
[4] Y. Xu, Ferroelectric Materials and their Applications, Elsevier Science Publishers B.V., 1991.
[5] S. Tangwiwat, S. Milne, Barium titanate sols prepared by a diol-based sol–gel route, J. Non-Cryst. Solids 351 (12/13) (2005) 976–980.
[6] W. Luan, L. Gao, J. Guo, Study on drying stage of nanoscale powder preparation, NanoStruct. Mater. 10 (7) (1998) 1119–1125.
[7] S. Kwon, D. Yoon, Effects of heat treatment and particle size on the tetragonality of nano-sized barium titanate powder, Ceram. Int. 33 (7) (2007) 1357–1362.
[8] J. Chen, Z. Shen, F. Liu, X. Liu, J. Yun, Preparation and properties of barium titanate nanopowder by conventional and high-gravity reactive precipitation methods, Scripta Mater. 49 (2003) 509–514.
[9] R. Wongmaneerung, R. Yimnirun, S. Ananta, Effect of vibro-milling time on phase formation and particle size of lead titanate nanopowders, Mater. Lett. 60 (12) (2006) 1447–1452.
[10] R. Wongmaneerung, T. Sarakonsri, R. Yimnirun, S. Ananta, Effects of milling method and calcination condition on phase and morphology characteristics of $Mg_4Nb_2O_9$ powders, Mat. Sci. Eng. B 130 (2006) 246–253.
[11] B.D. Stojanovic, C. Jovalekic, V. Vukotic, A.Z. Simoes, J.A. Varela, Ferroelectric properties of mechanically synthesized nanosized barium titanate, Ferroelectrics 319 (2005) 65–73.
[12] C. Suryanarayana, M.G. Norton, X-Ray Diffraction: A Practical Approach, Plenum Press, New York, 1998.
[13] W. Chaisan, Preparation and Characterization of Ceramic Nanocomposite in the PZT-BT and $TiO_2$-$SnO_2$ Systems, Ph.D. Thesis, Chiang Mai University, Chiang Mai, Thailand, 2006.
[14] JCPDS-ICDD card no. 5-0378, International Centre for Diffraction Data, Newtown Square, PA, 2002.
[15] JCPDS-ICDD card no. 21-1272, International Centre for Diffraction Data, Newtown Square, PA, 2002.
[16] V. Berbenni, A. Marini, G. Bruni, Effect of mechanical milling on solid state formation of $BaTiO_3$ from $BaCO_3$–$TiO_2$ (rutile) mixtures, Thermochim. acta 374 (2) (2001) 151–158.
[17] E. Brzozowski, M.S. Castro, Synthesis of barium titanate improved by modifications in the kinetics of the solid state reaction, J. Eur. Ceram. Soc. 20 (2000) 2347–2351.
[18] L. Simon-Seveyrat, A. Hajjaji, Y. Emziane, B. Guiffard, D. Guyomar, Re-investigation of Synthesis of $BaTiO_3$ by conventional solid-state reaction and oxalate coprecipitation route for piezoelectric applications, Ceram. Int. 33 (1) (2007) 35–40.
[19] A. Beauger, J.C. Mutin, J.C. Niepce, Synthesis reaction of metatitanate $BaTiO_3$. Part 2: study of solid-solid reaction interfaces, J. Mat. Sci. 18 (1983) 3543–3550.
[20] L.B. Kong, J. Ma, H. Huang, R.F. Zhang, W.X. Que, Barium titanate derived from mechanochemically activated powders, J. Alloys Compd. 337 (2002) 226–230.
[21] JCPDS-ICDD card no. 72-0135, International Centre for Diffraction Data, Newtown Square, PA, 2002.
[22] J.K. Lee, K.S. Hong, J.W. Jang, Roles of Ba/Ti ratios in the dielectric properties of $BaTiO_3$ ceramics, J. Am. Ceram. Soc. 84 (9) (2001) 2001–2006.
[23] W. Chaisan, S. Ananta, T. Tunkasiri, Synthesis of barium titanate-lead zirconate titanate solid solutions by a modified mixed-oxide synthetic route, Cur. Appl. Phys. 4 (2–4) (2004) 182–185.
[24] W. Chaisan, R. Yimnirun, S. Ananta, D.P. Cann, Dielectric properties of solid solutions in the lead zirconate titanate-barium titanate system prepared by a modified mixed-oxide method, Mater. Lett. 59 (2005) 3732–3737.
[25] JCPDS-ICDD card no. 5-0626, International Centre for Diffraction Data, Newtown, PA, 2002.
[26] C. Suryanarayana, Mechanical alloying and milling, Prog. Mater. Sci. 46 (2001) 1–184.
[27] H. Klug, L.E. Alexander, X-ray Diffraction Procedures for Polycrystalline and Amorphous Materials, Wiley, New York, 1974.